

NASA SP-412

# Apollo-Soyuz Test Project

## Summary Science Report



Volume I

National Aeronautics and Space Administration

# Apollo-Soyuz Test Project Summary Science Report

## Volume I

Astronomy, Earth Atmosphere and Gravity Field,  
Life Sciences, and Materials Processing

Prepared by  
NASA Lyndon B. Johnson Space Center



*Scientific and Technical Information Office* 1977  
NATIONAL AERONAUTICS AND SPACE ADMINISTRATION  
Washington, D.C.



## EDITORIAL BOARD

The material submitted for the "Apollo-Soyuz Test Project Summary Science Report" was reviewed by a NASA Editorial Review Board consisting of the following members: R. Thomas Giuli (Chairman), J. Vernon Bailey, Richard R. Baldwin, Leland J. Casey, P. Donald Gerke, John K. Holcomb, David N. Holman, W. Wilson Lauderdale, Harold Kernaghan, James M. Sanders, Robert S. Snyder, Orion E. Tollefsbol, Lyle Vande Zande, and William L. Young.

In two volumes:

Volume I: Astronomy, Earth Atmosphere and  
Gravity Field, Life Sciences,  
and Materials Processing

Volume II: Earth Observations and  
Photography

### Library of Congress Cataloging in Publication Data

Lyndon B. Johnson Space Center.

Apollo-Soyuz Test Project : summary science report.

(NASA SP ; 412)

1. Apollo-Soyuz Test Project. I. Title. II. Series:

United States. National Aeronautics and Space Administration.

NASA SP ; 412.

TL788.4.L9 1977 500.5 77-11892

---

For sale by the National Technical Information Service  
Springfield, Virginia 22151 Price — \$13.75

## Foreword

International cooperation was the keynote of the Apollo-Soyuz Test Project. During the 3 years after the project was officially initiated by a U.S.-U.S.S.R. agreement on May 24, 1972, the great effort in coordination, communication, and integration culminated in the highly successful flight from July 15 to 24, 1975. The 9-day flight marked the first time that manned spacecraft of two nations have met in space for joint engineering and scientific investigations.

The principal objective of the project was to develop a compatible docking system and rendezvous and crew transfer procedures that might be appropriate for future international manned space missions. This objective was successfully accomplished.

An additional objective of major importance was the program of scientific investigations conducted during the mission. A science program was planned by NASA that made abundant use of the experimental opportunities afforded by the mission parameters and spacecraft capabilities. The 2-day docked phase of the flight was used to conduct three experiments that required joint scientific activities within the two spacecraft. Subsequent to the docked phase, two additional joint scientific experiments were conducted that required complicated, precise maneuvering of the Apollo spacecraft relative to, and in the proximity of, the Soyuz spacecraft. The remaining unilateral phases of the mission were likewise used effectively by each country to perform scientific experiments on a unilateral basis. In addition to the five joint U.S.-U.S.S.R. experiments, the Apollo crewmen conducted 23 unilateral experiments. Two of these were provided by the Federal Republic of Germany—a further illustration of the international scope of the mission. Not only was scientific research served by this mission, but worldwide space-science awareness was promoted through extensive home television broadcasting and filming of flight experimentation and in-flight science demonstrations.

This report discusses the joint experiments and the U.S.-conducted unilateral experiments. It provides detailed descriptions of the scientific concepts and experiment design and operation, and it presents the scientific results that have accrued from approximately 1 year of postflight analysis. The scientific value of this international venture will contribute significantly to the development of future international science collaboration on the Space Shuttle flights and other projects.

CHESTER M. LEE  
*ASTP Program Director*  
GLYNN S. LUNNEY  
*ASTP Technical Director*





# Contents

	Page
1. SUMMARY OF SCIENTIFIC RESULTS <i>R. T. Giuli</i>	1
2. MISSION DESCRIPTION <i>S. N. Hardee</i>	23
3. SOFT X-RAY OBSERVATIONS (MA-048) <i>S. Shulman, S. Naranan, W. Snyder, D. Yentis, R. Cruddace, H. Friedman, G. Fritz, and R. Henry</i>	39
4. EXTREME ULTRAVIOLET SURVEY (MA-083) <i>S. Bowyer, B. Margon, M. Lampton, F. Paresce, and R. Stern</i>	49
5. INTERSTELLAR HELIUM GLOW (MA-088) <i>S. Bowyer, J. Freeman, M. Lampton, and F. Paresce</i>	71
6. ARTIFICIAL SOLAR ECLIPSE (MA-148) <i>G. M. Nikolskiy, A. I. Simonov, I. S. Kim, R. T. Giuli, M. D. Jenness, and A. N. Lunde</i>	85
7. CRYSTAL ACTIVATION (MA-151) <i>J. I. Trombka, E. L. Eller, R. L. Schmadebeck, C. S. Dyer, R. C. Reedy, D. W. Barr, J. S. Gilmore, R. J. Prestwood, B. P. Bayhurst, D. G. Perry, A. R. Smith, R. C. Cordi, R. H. Pehl, J. S. Eldridge, E. Schonfeld, and A. E. Metzger</i>	101
8. ULTRAVIOLET ABSORPTION (MA-059) <i>T. M. Donahue, R. D. Hudson, W. T. Rawlins, J. Anderson, F. Kaufman, and M. B. McElroy</i>	109
9. STRATOSPHERIC AEROSOL MEASUREMENTS (MA-007) <i>T. J. Pepin, M. P. McCormick, W. P. Chu, F. Simon, T. J. Swissler, R. R. Adams, K. H. Crumbly, and W. H. Fuller, Jr.</i>	127
10. DOPPLER TRACKING (MA-089) <i>G. C. Weiffenbach, M. D. Grossi, and P. W. Shores</i>	137
11. GEODYNAMICS (MA-128) <i>F. O. Vonbun, W. D. Kahn, W. T. Wells, and T. D. Conrad</i>	177



# ASTP SUMMARY SCIENCE REPORT

12.	LIGHT FLASH OBSERVATIONS (MA-106)	193
	<i>T. F. Budinger, C. A. Tobias, R. H. Huesman, F. T. Upham, T. F. Wieskamp, J.-U. Schott, and E. Schopper</i>	
13.	BIOSTACK III (MA-107)	211
	<i>Horst Bücker, M. Delpoux, S. Fogel, M. Freeling, E. H. Graul, G. Horneck, A. R. Kranz, H. Planel, W. Rüther, U. Scheidemann, C. Thomas, C. A. Tobias, B. Toth, T. Yang, O. C. Allkofer, R. Beaujean, E. V. Benton, W. Enge, R. Facius, H. Francois, W. Heinrich, D. Hildebrand, C. Jacquot, R. Kaiser, J. P. Massué, E. Obst, D. D. Peterson, R. Pfohl, G. Portal, G. Reitz, M. Schäfer, E. Schopper, J.-U. Schott, and G. Siegmon</i>	
14.	ZONE-FORMING FUNGI (MA-147)	227
	<i>T. D. Rogers, M. E. Brower, and G. R. Taylor</i>	
15.	MICROBIAL EXCHANGE (AR-002)	237
	<i>G. R. Taylor, K. D. Kropp, M. R. Henney, S. S. Ekblad, A. A. Baky, T. O. Groves, T. C. Molina, J. G. Decelle, C. F. Carmichael, N. J. Gehring, E. L. Young, I. L. Shannon, W. J. Frome, and N. R. Funderburk</i>	
16.	CELLULAR IMMUNE RESPONSE (MA-031)	257
	<i>B. Sue Criswell and Kathy Cobb</i>	
17.	POLYMORPHONUCLEAR LEUKOCYTE RESPONSE (MA-032)	263
	<i>R. Russell Martin, Glenn A. Warr, Margaret J. Putman, Diane H. Kentor, and Carolinda L. Holleman</i>	
18.	KILLIFISH HATCHING AND ORIENTATION (MA-161)	281
	<i>H. W. Scheld, A. Baky, J. F. Boyd, V. B. Eichler, P. M. Fuller, R. B. Hoffman, J. R. Keefe, K. P. Kuchnow, J. M. Oppenheimer, G. A. Salinas, and R. J. von Baumgarten</i>	
19.	ELECTROPHORESIS TECHNOLOGY (MA-011)	307
	<i>R. E. Allen, G. H. Barlow, M. Bier, P. E. Bigazzi, R. J. Knox, F. J. Micale, G. V. F. Seaman, J. W. Vanderhoff, C. J. Van Oss, W. J. Patterson, F. E. Scott, P. H. Rhodes, B. H. Nerren, and R. J. Harwell</i>	
20.	ELECTROPHORESIS (MA-014)	335
	<i>K. Hannig, H. Wirth, and E. Schoen</i>	
21.	MULTIPURPOSE ELECTRIC FURNACE (MA-010)	353
	<i>A. Boese, J. McHugh, and R. Seidensticker</i>	
22.	SURFACE-TENSION-INDUCED CONVECTION (MA-041)	367
	<i>R. E. Reed, W. Uelhoff, and H. L. Adair</i>	
23.	MONOTECTIC AND SYNTECTIC ALLOYS (MA-044)	403
	<i>L. L. Lacy and C. Y. Ang</i>	

## CONTENTS

24.	INTERFACE MARKING IN CRYSTALS (MA-060) <i>H. C. Gatos, A. F. Witt, M. Lichtensteiger, and C. J. Herman</i>	429
25.	ZERO-G PROCESSING OF MAGNETS (MA-070) <i>D. J. Larson, Jr.</i>	449
26.	CRYSTAL GROWTH FROM THE VAPOR PHASE (MA-085) <i>H. Wiedemeier, H. Sadeek, F. C. Klaessig, M. Norek, and R. Santandrea</i>	471
27.	HALIDE EUTECTIC GROWTH (MA-131) <i>A. S. Yue, C. W. Yeh, and B. K. Yue</i>	491
28.	MULTIPLE MATERIALS MELTING (METALS), PART OF EXPERIMENT MA-150 <i>L. I. Ivanov, V. N. Kubasov, V. N. Pimenov, K. P. Gurov, E. V. Demina, Yu. S. Malkov, and V. M. Lazarenko</i>	501
29.	MULTIPLE MATERIALS MELTING (GERMANIUM-SILICON SOLID SOLUTIONS), PART OF EXPERIMENT MA-150 <i>V. S. Zemskov, V. N. Kubasov, I. N. Belokurova, A. N. Titkov, I. L. Shulpina, V. I. Safarov, and N. B. Guseva</i>	539
30.	CRYSTAL GROWTH (MA-028) <i>M. D. Lind</i>	555
	APPENDIX A — Recovery of Atmospheric Parameters From Radio Tracking Data of the Geodynamics Experiment <i>P. E. Schmid and S. Rangaswamy</i>	563
	APPENDIX B — Abbreviations and Acronyms	571
	APPENDIX C — Units and Unit-Conversion Factors	575
	APPENDIX D — Hardware Vendors	579



# 1. Summary of Scientific Results

*R. T. Giuli<sup>a</sup>*

## ABSTRACT

The Apollo-Soyuz Test Project science and technology program conducted by the Apollo crew consisted of 28 separate experiments, including 5 conducted jointly with the Soyuz crew. Cosmic sources of extreme-ultraviolet and X-ray radiation were discovered. The interstellar medium in the vicinity of the solar system was investigated. The solar corona was photographed using spacecraft occultation of the solar disk. The radioactivation of potentially useful gamma-ray detectors by cosmic particle bombardment was measured, and the effects of cosmic particle impact upon living cells were investigated using three different techniques in three separate experiments. The concentrations of two atomic species and the aerosol component of the upper atmosphere were measured by resonance absorption spectroscopy and solar extinction photometry, respectively. The Earth surface structure was investigated using photographic and visual observations, and the subsurface structure was investigated by gravity-field measurements employing highly precise spacecraft-to-spacecraft tracking techniques. Zero-g effects on the embryogenesis of fish vestibular systems and on the rhythmicity of fungal growth patterns were investigated. Microbial growth and microbial transfer among crewmembers were measured. Mixtures of biological cells were separated into pure samples by use of two different electrophoresis techniques. Seven sets of solid materials were processed by high-temperature melting, and one set was processed by ambient-temperature diffusion.

## INTRODUCTION

The Apollo crew participated in 28 scientific and technological experiments during the joint Apollo-Soyuz Test Project (ASTP) mission of July 1975. These experiments included five conducted jointly with the Soyuz crew and two provided by the Federal Republic of Germany. In addition to these unilateral Apollo and joint Apollo-Soyuz experiments, a number of unilateral Soyuz experiments were performed. This report summarizes only the 28 experiments falling into the first two categories. Together, the selected experiments formed a well-integrated program of complementary scientific objectives. In several cases, related experiments used different experimental techniques in pursuit of similar scientific objectives. The scientific results and operational experiences from these experiments are being used to determine the best techniques to pursue in future space missions. The experiments are listed by discipline and topic in table 1-I. The designations in parentheses denote the notation used for the jointly conducted experiments. The 28 experiments were selected from 161 proposals submitted from 9 countries (table 1-II).

The purpose of the ASTP Summary Science Report is to provide, in one document, a complete description of the experiment concepts, instrumentation, and operations; and to describe their results as provided by approximately 1 year of postmission analysis. The document is in two volumes; the second volume will pertain to the Earth Observations and Photography Experiment. This first volume pertains to all the other ASTP experiments.

---

<sup>a</sup>NASA Lyndon B. Johnson Space Center.

## ASTP SUMMARY SCIENCE REPORT

TABLE 1-I.—ASTP Experiments

<i>Topic</i>	<i>Experiment no.</i>	<i>Experiment name</i>
<i>Space sciences</i>		
Astronomy	MA-048	Soft X-Ray Observations
	MA-083	Extreme Ultraviolet Survey
	MA-088	Interstellar Helium Glow
	MA-148	Artificial Solar Eclipse <sup>a</sup> (AS-4)
	MA-151	Crystal Activation
Earth studies	MA-059	Ultraviolet Absorption <sup>a</sup> (AS-5)
	MA-007	Stratospheric Aerosol Measurements
	MA-136	Earth Observations and Photography
	MA-089	Doppler Tracking
	MA-128	Geodynamics
<i>Life sciences</i>		
Particle radiation effects on living cells	MA-106	Light Flash Observations
	MA-107	Biostack III <sup>b</sup>
	MA-147	Zone-Forming Fungi <sup>a</sup> (AS-1)
Human immune system	AR-002	Microbial Exchange <sup>a</sup> (AS-2)
	MA-031	Cellular Immune Response
	MA-032	Polymorphonuclear Leukocyte Response
Vestibular system	MA-161	Killifish Hatching and Orientation
<i>Materials processing</i>		
Biological materials	MA-011	Electrophoresis Technology
	MA-014	Electrophoresis <sup>b</sup>
Solid materials	MA-010	Multipurpose Furnace
	MA-041	Surface-Tension-Induced Convection
	MA-044	Monotectic and Syntectic Alloys
	MA-060	Interface Marking in Crystals
	MA-070	Zero-g Processing of Magnets
	MA-085	Crystal Growth From the Vapor Phase
	MA-131	Halide Eutectic Growth
	MA-150	Multiple Materials Melting <sup>a</sup> (AS-3)
	MA-028	Crystal Growth

<sup>a</sup>Joint U.S.-U.S.S.R. experiment.<sup>b</sup>Federal Republic of Germany experiment.**ASTRONOMY**

The astronomy experiments are listed in table 1-I in order of the distance away from the Earth that the objects of study lie. The soft X-ray objects lie deep in our galaxy and even beyond our galaxy. The extreme-ultraviolet (EUV) objects lie within a few hundred light-years from the solar system, and the portion of the interstellar medium (ISM)

investigated in the Interstellar Helium Glow Experiment lies within a few astronomical units from the solar system. The corona photographed during the Artificial Solar Eclipse Experiment is within approximately 50 solar radii from the Sun. Finally, two crystal detectors that have potential application for future gamma-ray astronomy payloads were carried onboard the Apollo spacecraft to measure their susceptibility to



TABLE 1-II.—*Experiment Proposals Submitted to NASA*

<i>Origin</i>	<i>Number</i>
United States	135
Federal Republic of Germany	8
France	7
India	4
U.S.S.R.	3
Ireland	1
Scotland	1
Sweden	1
Switzerland	1
TOTAL	161

radioactivation by local cosmic particle bombardment.

### Concepts and Operations

The Soft X-Ray Observations Experiment was an attempt to obtain higher performance (viz, higher angular resolution) from a rocket-class instrument by taking advantage of the longer observing time available with an Earth-orbiting stabilized platform. The instrument (fig. 1-1), which was bolted into the scientific instrument bay of the Apollo service module, consisted of a gas proportional counter with an aluminum honeycomb collimator that provided a  $4^\circ$  circular field of view. Pointing of the instrument was accomplished by pointing of the spacecraft; there was no separate instrument pointing system. The three main objectives of the experiment were as follows.

1. To scan the celestial sphere to determine the structure of the known, soft X-ray background and hence possibly the source or sources of this background
2. To obtain the low-energy spectra of known X-ray sources for which higher energy spectra have previously been obtained so that distance estimates for these sources can be derived
3. To obtain high-time-resolution observations of discrete sources to discover X-ray pulsars

Soon after initiating operation, the instrument developed a high-voltage-breakdown characteristic that permitted operation only for periods of 2 minutes at a time. However, during those 2-minute periods, the instrument performed well, and new procedures were developed during the mission in near real time, which utilized the entire Apollo crew to properly phase spacecraft pointing and instrument switching. The result was a cumulation of approximately 1 hour of high-quality data that yielded successful achievements in all three objectives, especially the first and third.

The Extreme Ultraviolet Survey Experiment was an attempt to pioneer a new field of astronomy. Discrete sources of EUV radiation outside the solar system had never before been observed because EUV radiation (defined here as radiation with wavelengths between 10 and 100 nm) is highly susceptible to absorption by the ISM, which is mostly diffuse hydrogen gas. The previously supposed ISM density would not allow detectable amounts of EUV radiation to travel

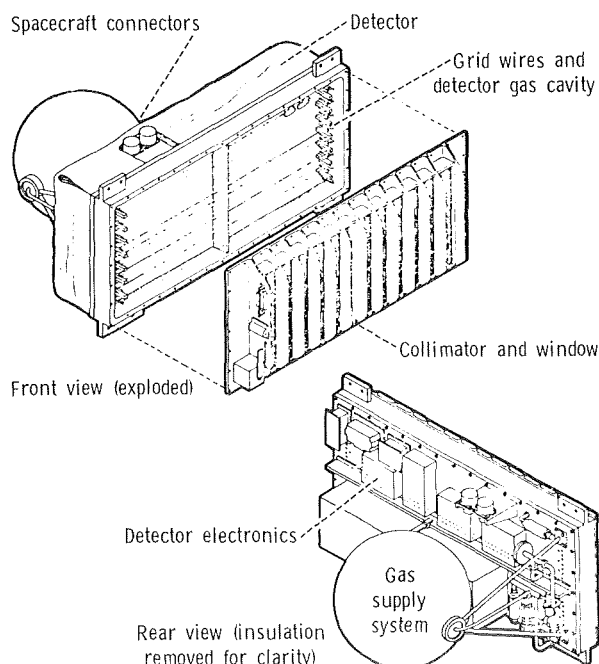


FIGURE 1-1.—Soft X-ray instrument.

more than a few tens of light-years, and few potential EUV sources exist within that distance of the solar system. Furthermore, the technology required for detecting faint EUV radiation was, to a large extent, undeveloped. In recent years, however, four favorable events occurred: The estimate of the ISM density decreased, observations in other wavelengths suggested that many strong EUV sources may exist within a few hundred light-years of the solar system, the requisite technology improved, and a suitable flight opportunity arrived. The instrument (fig. 1-2) consisted of grazing-incidence focusing optics, EUV-transmitting filters, and channel electron multiplier detectors. The EUV instrument was bolted into the service module instrument bay together with the soft X-ray instrument, and instrument pointing was achieved by spacecraft pointing. An in-flight pointing "raster scan" was performed to obtain precise definition of the instrument line-of-sight direction relative to the spacecraft axis. This exercise allowed the higher-resolution ( $2.5^\circ$  field of view) detector to be used exclusively during the flight, which maximized the instrument sensitivity and contributed in a major way to the outstanding achievements of this experiment.

The Interstellar Helium Glow Experiment was an attempt to determine unambiguously the temperature and density of the ISM in the vicinity of the solar system. A by-product of the investiga-

tion was to be the determination of the velocity of the local ISM relative to the Sun. The technique was to detect EUV radiation originating from the Sun that is resonantly backscattered by the helium component of the ISM, specifically neutral helium (He I, 58.4 nm) and once-ionized helium (He II, 30.4 nm). Previous observations of the ultraviolet resonance line (Lyman  $\alpha$ , 121.6 nm) of the ISM hydrogen component have not yielded definitive results because it is not possible to separate the solar-scattered contribution of that radiation from the unknown contribution transmitted through the ISM from galactic sources. However, as has been discussed, there should be little EUV radiation transmitted from great distances; therefore, the ambiguity is removed for the helium resonance radiation. Thus, the property of EUV radiation that poses problems for EUV stellar astronomy (high susceptibility to absorption by the ISM) is the very property that makes the Interstellar Helium Glow Experiment feasible. The instrument (fig. 1-3) utilized essentially the same technology as the EUV survey instrument, except that the grazing-incidence optics were nonfocusing, wide field-of-view collectors. The instrument was bolted into the service module instrument bay

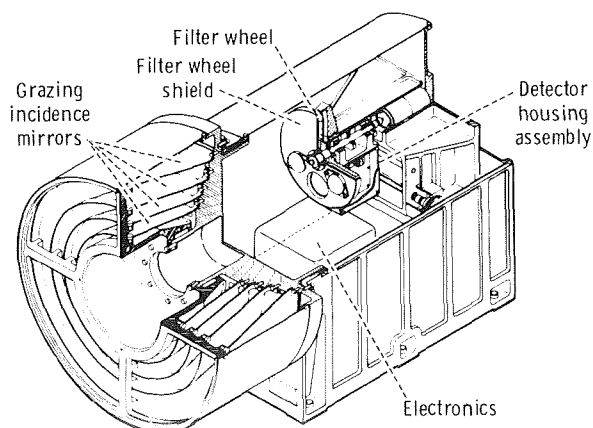


FIGURE 1-2.—Extreme-ultraviolet survey instrument.

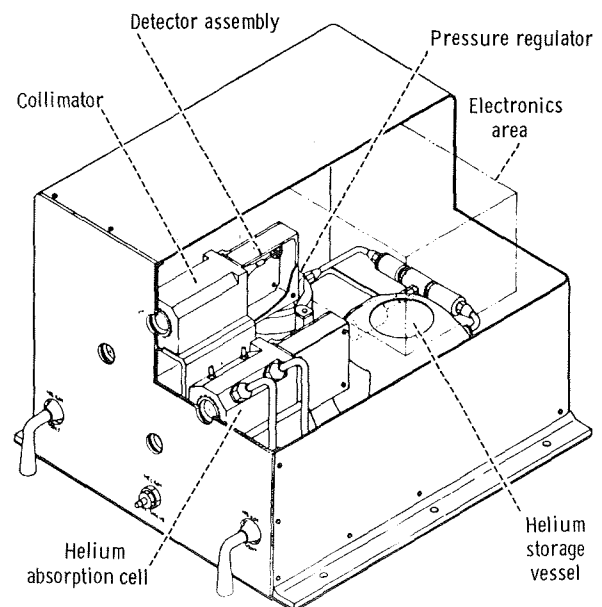


FIGURE 1-3.—Helium glow instrument.

with the soft X-ray and EUV instruments, and the entire sky was scanned by a series of spacecraft roll maneuvers. Although one of the detectors failed during the flight, the instrument functioned well, and 10 hours of data were obtained.

The Artificial Solar Eclipse Experiment was an attempt to demonstrate the feasibility of photographing the solar corona from one spacecraft by occulting the solar disk radiation with another spacecraft. The Apollo spacecraft backed away from the Soyuz spacecraft in the solar direction (fig. 1-4) until, at a separation of approximately 200 m, the Apollo subtended an angle of approximately 2 solar diameters, as seen from Soyuz. Soyuz photography was performed in the solar direction through a vignetting light baffle designed to block the bright sunlight reflected from the Earth beyond the terminator. All operations were performed successfully.

The Crystal Activation Experiment was an attempt to learn more about the propensity of certain types of crystals to be radioactivated by particle bombardment in the Earth-orbital environment. The crystals (germanium and thallium-

activated sodium iodide) are potentially important for use as detectors in future gamma-ray astronomy payloads. The problem is that cosmic-ray particles such as high-energy protons (and secondary neutrons produced in the spacecraft structure by these protons) can induce X-ray and gamma-ray activity by way of spallation interactions with the detector material. This detector background cannot be distinguished from the signal produced by incident gamma rays; hence, it is difficult to account for the background contribution to the total signal when attempting to measure the intensity of gamma rays coming from astronomical sources. Consequently, the background properties of the detectors must be investigated separately, as in this experiment. The experiment consisted of carrying a sample of each of the crystals into orbit and then measuring the induced radioactivity after the mission. To detect the short-half-life species, the measurements began on the recovery ship approximately 1.5 hours after atmospheric reentry of the command module. Those and subsequent laboratory measurements were successful.

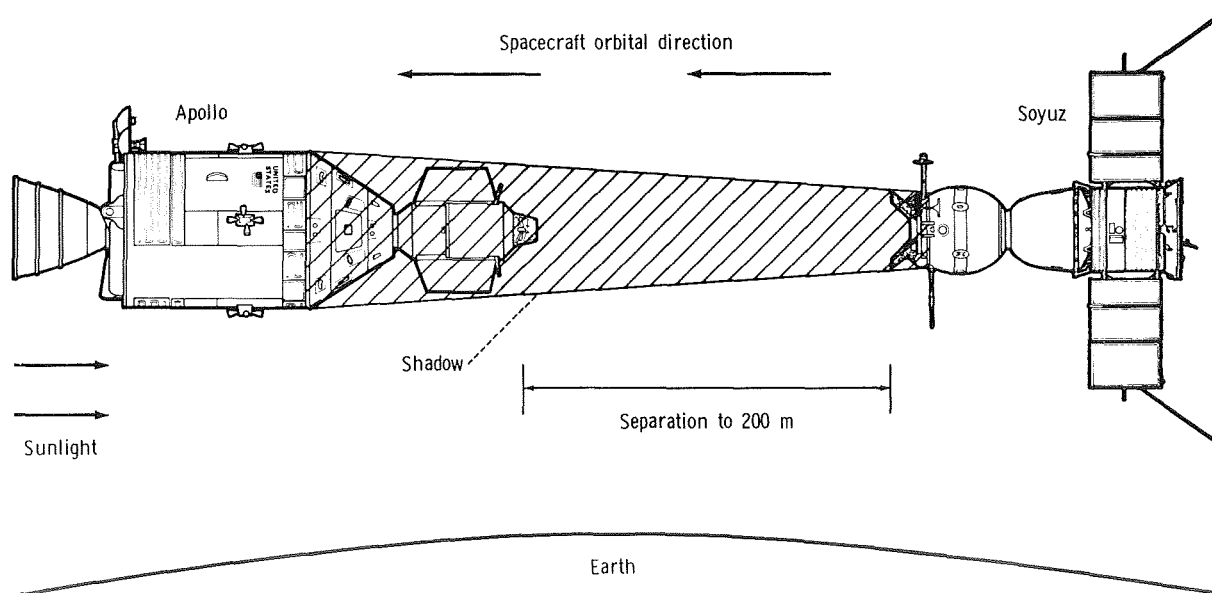


FIGURE 1-4.—Spacecraft orientation for artificial solar eclipse.

## Results

The Soft X-ray Observations Experiment resulted in several important discoveries. For example, the previously known binary X-ray source in the Small Magellanic Cloud (a companion galaxy of our galaxy), SMC X-1, was discovered to be an X-ray pulsar as well, thus identifying the compact component of the binary to be a rotating neutron star. This is the first pulsar discovered outside our galaxy, and it has the shortest pulse period (0.7157 second) of any known X-ray binary pulsar. Two important observations of extended structure in the soft X-ray background were obtained. The first is associated with a known (optically) supernova remnant in the constellation Centaurus. The second is a previously known X-ray source in the constellation Cygnus, designated Cyg X-6. However, the ASTP observations in conjunction with a rocket experiment by the same investigators, have shown for the first time that Cyg X-6 is an extended X-ray source and is not associated with any optical or radio object.

The Extreme Ultraviolet Survey Experiment achieved the first detection of discrete sources of EUV radiation outside the solar system. To date, four such sources have been positively identified in the data. They are stars that were previously known optically to be the white dwarfs HZ 43 and Feige 24, the dwarf nova SS Cygni, and the M-dwarf flare star Proxima Centauri. The two most intense sources are the white dwarfs, and this experiment determined that they are much hotter than was previously believed. In fact, they are now the hottest, most luminous white dwarfs known; preliminary analysis indicates the effective temperature of HZ 43 may be 110 000 K, at which temperature it would be the first known white dwarf whose total luminosity exceeds that of the Sun. The EUV data were also useful in providing more reliable estimates of the ISM mean densities in the directions of the white dwarfs: 0.01 to 0.02 hydrogen atoms  $\text{cm}^{-3}$ . The dramatic new physical interpretation for the EUV objects establishes the importance of observing such objects at EUV wavelengths when their peak energy emission occurs at those wavelengths. Thus, this

experiment has provided strong indication that the new field of EUV stellar astronomy may become important.

The Interstellar Helium Glow Experiment analysis is still underway. No definite conclusions have been obtained at this writing; no current theoretical models fit the data in their present state of analysis.

Data from the Artificial Solar Eclipse Experiment were analyzed exclusively by the U.S.S.R. investigators, and their results are published in this document. They report that the corona is detectable on 19 of the 55 exposures suitable for analysis, and they have obtained a coronal intensity distribution along the ecliptic westward from the Sun which extends to nearly 50 solar radii.

Results of the Crystal Activation Experiment indicated that, because of the geomagnetic shielding of the low ASTP orbit, the induced activation was a factor of 3 less than that incurred on a similar experiment flown on the Apollo 17 lunar mission. The contribution to the activation by secondary neutrons demonstrates that such detectors used in gamma-ray astronomy experiments should be placed far from heavy material.

## EARTH STUDIES

The Earth studies experiments are listed in table 1-I in order of the distance above the Earth's surface that the subjects of study are located. The Ultraviolet Absorption Experiment was an investigation of the atomic composition of the tenuous upper atmosphere at the spacecraft altitude, and the Stratospheric Aerosol Measurements Experiment measured the aerosols in the tropopause at an altitude of approximately 20 km. The Earth Observations and Photography Experiment studied a multitude of Earth surface features on land and in the oceans, and the Earth subsurface structure was investigated by means of two variations of gravity-field measurements with two spacecraft-to-spacecraft tracking experiments, the Doppler Tracking Experiment and the Geodynamics Experiment.

### Concepts and Operations

The Ultraviolet Absorption Experiment was an attempt to apply a new technique, resonance absorption spectroscopy, to the investigation of the upper atmosphere. This technique had never before been employed in a space mission experiment, and it appeared feasible to measure the concentrations of neutral atomic oxygen (O) and neutral atomic nitrogen (N) at the relatively low ASTP orbital altitude of 220 km. The former measurement would serve as a comparison with previous results from mass spectrometry experiments, and the latter measurement would constitute the first reliable measurement of N at such altitudes. Thus, this experiment could provide a first assessment of a technique that might be developed as a powerful method for measuring and monitoring the constituents of the upper atmosphere. The concept of the experiment was to produce collimated beams of resonance radiation for O and N on the Apollo spacecraft and illuminate an array of corner reflectors mounted on the Soyuz spacecraft at a known distance from Apollo. The portion of the beam striking the retroreflectors was returned to a collecting mirror on the docking module and was focused on the entrance slit of a spectrophotometer. To prevent Doppler effects (due to spacecraft orbital velocity) from shifting the lamp frequency away from the atmospheric absorption frequency, it was necessary to maneuver the Apollo spacecraft such that the light beams traveled between the two spacecraft perpendicularly to their orbital velocity vectors. Primarily because of this constraint, the spacecraft maneuvers required for the three data takes (at approximate spacecraft separations of 150, 500, and 1000 m) became the most intricately planned maneuvers ever performed by an Apollo spacecraft during a scientific experiment. Figure 1-5 shows the planned maneuver schematic for the 500-m data take. A reflected signal (resonance absorption data) was obtained for this run but not for the 150-m data take and only sporadically for the 1000-m data take. An anomaly occurred during the 500-m data take that has been interpreted as a degradation of the corner reflectors. Reso-

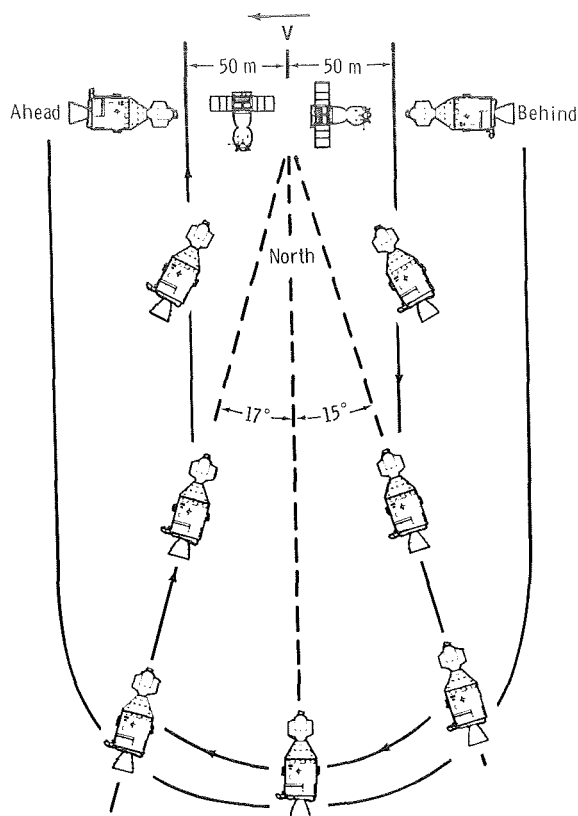


FIGURE 1-5.—Spacecraft maneuver for Ultraviolet Absorption Experiment.

nance fluorescence (resonance scattering) data were obtained during the 150-m data take.

The Stratospheric Aerosol Measurements Experiment was an attempt to perform the first remote sensing of the atmospheric aerosol layers from an orbiting spacecraft, using solar extinction photometry. The concept was to monitor the extinction of direct sunlight at orbital sunrise and sunset, as the Sun-spacecraft line of sight traversed upward and downward through the lower 150 km of atmosphere (fig. 1-6). For this purpose, a photometer sensitive to  $1\text{-}\mu\text{m}$  radiation (the wavelength range most sensitive to aerosol extinction) was mounted in a command module window and data were collected during two sunsets (Northern Hemisphere) and two sunrises (Southern Hemisphere). High-quality data were obtained.

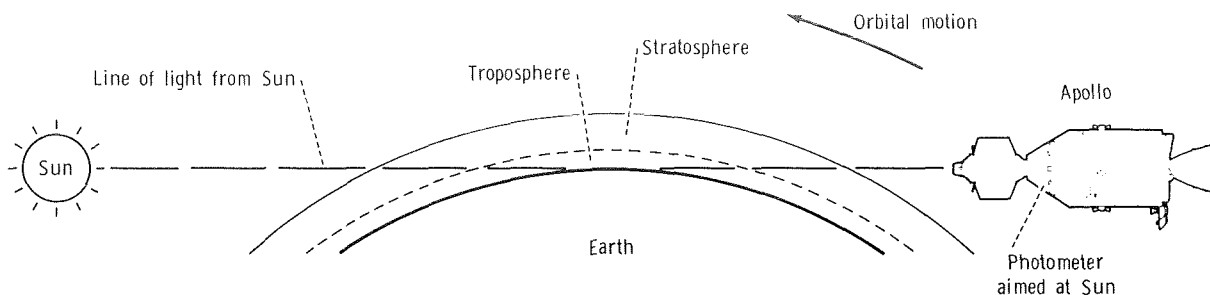


FIGURE 1-6.—Sunrise orientation for stratospheric aerosol measurements.

The Earth Observations and Photography Experiment was an attempt to use the recognition and interpretive capabilities of human observers to refine the selection of Earth surface features for photography and to provide *in situ* contributions to analysis of these features. The phenomena to be observed were selected from the categories of geology, deserts, oceanography, hydrology, and meteorology. For the ASTP experiment, a Principal Investigator assembled a team of scientific investigators representing topics of special interest in the previously mentioned fields. A comprehensive crew training program involving classroom studies and aircraft flyover exercises was conducted, and an extensive flight-planning effort was made to ensure the acquisitions of as much data as real-time cloud cover would allow. Many useful observations and photographs were obtained. Postmission data assessment was used to define a scientific analysis program that is underway at the time of this writing.

The Doppler Tracking Experiment was one of two ASTP experiments that represented attempts to test the feasibility of performing refined measurements of the Earth's gravity-field structure with horizontal scale sizes of approximately 250 to 1000 km. Such measurements would be useful in describing the subsurface structure of the Earth to depths of several hundred kilometers, and it is anticipated that such information would have great importance for understanding tectonic plate processes. Surface gravimetry is useful only for gravity structure determinations on a scale of less than approximately 100 km, and single-satellite orbit perturbation measurements are useful only for scale sizes greater than 2000 km. In principle, however, two spacecraft in orbit can

recover the gravity-field structure of the desired scale size by performing very high accuracy Doppler measurements between the vehicles while one of them is being accelerated by the gravity-field anomaly. Roughly, the smallest anomaly scale size recoverable is about equal to the altitude of the lower spacecraft, and the largest scale size is comparable to the separation of the spacecraft. The spacecraft-to-spacecraft tracking technique used in the Doppler Tracking Experiment was the low-low technique, in which the two spacecraft traveled in the same orbit at some suitable separation (fig. 1-7). The two spacecraft were the Apollo command and service module (CSM) and the docking module, which was jettisoned from the CSM in a spin-stabilized mode (end over end) for the purpose of this experiment. A transmitter in the docking module provided phase-coherent

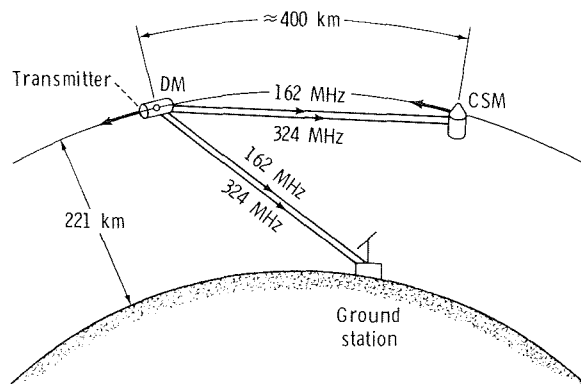


FIGURE 1-7.—Doppler tracking low-low spacecraft orientation.

dual-frequency transmission to the CSM to account for ionospheric effects in the Doppler measurement. This feature introduced the possibility of studying the horizontal scale of electron concentrations in the ionosphere and of detecting traveling ionospheric disturbances and boundaries of ionospheric turbulence. Consequently, ionospheric studies became a secondary objective of the experiment. After the docking module was jettisoned, the CSM moved to an initial separation distance of 310 km and drifted to a separation distance of 430 km by the end of the data take (nine revolutions later, approximately 14 hours).

The Geodynamics Experiment was the other ASTP experiment designed to detect and recover gravity-field fine structure, and it used the high-low spacecraft-to-spacecraft tracking technique. The low spacecraft was the Apollo vehicle, and the high spacecraft was the geosynchronous Applications Technology Satellite (ATS) 6, which was located over the east coast of Africa during the experiment (fig. 1-8). The Geodynamics Experiment data link in figure 1-8 was from the ATS ranging station in Madrid to ATS-6, to Apollo,

back to ATS-6, and to Madrid. The Apollo Spaceflight Tracking and Data Network (STDN) link was used for spacecraft orbit determination. The experiment involved no dedicated spacecraft hardware; the Apollo/ATS-6 communications link was developed for other reasons. Data were acquired on 108 passes under the ATS-6 spacecraft.

## Results

The Ultraviolet Absorption Experiment successfully measured the concentrations of O and N at the ASTP altitude. The values were obtained by combining the resonance fluorescence data of the 150-m data take with combined fluorescence and absorption data of the 500-m data take. Preliminary values are  $[O] = 1.15 \times 10^9 \text{ cm}^{-3}$  and  $[N] = 8.6 \times 10^6 \text{ cm}^{-3}$ . Continuing analysis is expected to refine these values, but they are already in good agreement with the oxygen measurements of the Atmospheric Explorer Satellite extrapolated to the time and location of the ASTP measurements.

The Stratospheric Aerosol Measurements Experiment yielded high-quality photometry and photography results. The aerosol layer peaked at an altitude of approximately 20 km in the Northern Hemisphere and somewhat lower in the Southern Hemisphere; the peak concentration was approximately 50 percent higher in the Northern Hemisphere. These results, combined with balloon-sampling measurements made in Australia before and after the ASTP mission, are consistent with seasonal, meridional transport of aerosols after the eruption of Volcan de Fuego in Guatemala in October 1974. The results are very encouraging for developing the solar extinction technique for long-term spaceborne monitoring of the Earth's atmosphere.

The Earth Observations and Photography Experiment data have been assessed, and an analysis program has been defined and is underway. Because the analysis program was delayed until postmission data assessment was completed, the scientific results will be reported in volume II of the ASTP Summary Science Report.

The Doppler Tracking Experiment was not

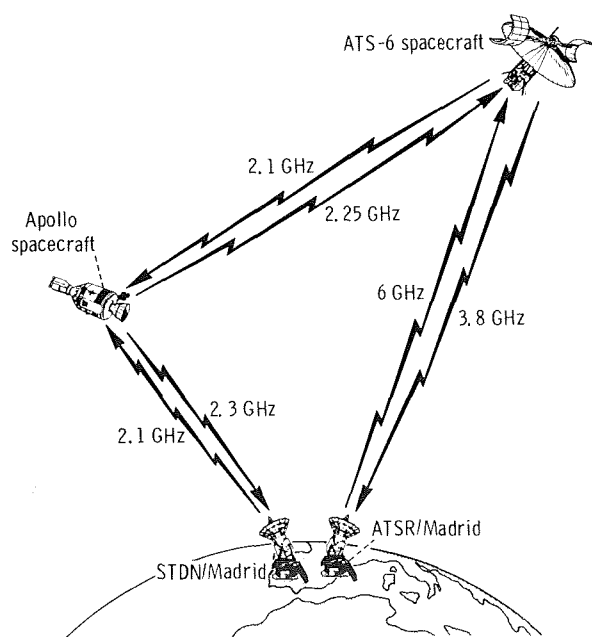


FIGURE 1-8.—Geodynamics high-low spacecraft orientation.

able to achieve its prime objective of measuring gravity-field anomalies. The data were degraded by a single-frequency noise level much higher than anticipated and too high to allow extraction of gravity-field signatures. The source of the noise is not known. The ionospheric investigation was highly successful. Analysis is continuing, but preliminary results are as follows.

1. Changes in the columnar electron content between the two spacecraft were accurately measured and yielded gradients as high as  $10^6$  electrons  $\text{m}^{-3} \text{m}^{-1}$  on both the dayside (typical density,  $5 \times 10^{11}$  electrons/ $\text{m}^3$ ) and nightside (typical density,  $3 \times 10^9$  electrons/ $\text{m}^3$ ) ionosphere.

2. Traveling ionospheric disturbances were detected; the most noticeable one occurred off the coast of California. This disturbance was a nine-cycle wave with peak-to-peak electron density perturbation of 35 percent, with wavelength of 690 km (as would be seen from the ground), and with spatial extent of 7200 km along the Apollo orbital track. The ionospheric results from the Doppler Tracking Experiment are particularly noteworthy because they are the first such measurements of the ionosphere in the region of 200 km altitude.

The Geodynamics Experiment resulted in successful detection and recovery of gravity-field signatures with resolution within  $0.010 \text{ cm/sec}^2$  (10 mgal). Areas in which such anomalies were recovered are the Indian Ocean Depression, the Himalayan Anomalous Region, an area in west central Africa near the Banqui magnetic anomaly, and the Zagros thrust zone, which is at the juncture of the African and Eurasian tectonic plates. The high-quality gravity measurements of the Geodynamics Experiment were an extremely encouraging demonstration of the validity of the high-low spacecraft-to-spacecraft tracking technique. This technique may be developed to provide global coverage for gravity-field measurements with future space projects. An additional benefit from the Geodynamics Experiment was the use of the data for tropospheric studies. Analysis of the atmospheric refraction of the Apollo/ATS link near the horizon yielded refractivity, pressure, and temperature profiles that closely matched radiosonde determinations. This result has potential application for space monitor-

ing of meteorological properties of the troposphere.

## **PARTICLE RADIATION EFFECTS ON LIVING CELLS**

With the advent of space flight, interest arose as to the effects upon humans and other living organisms of exposure to cosmic particle radiation. While the effects of protons are now fairly well understood, recent interest has developed in understanding the implications of the highly charged and energetic (HZE) component of cosmic rays for long-duration space travel. Such particles can deposit energy in tissue at a linear rate exceeding  $1 \text{ GeV cm}^2 \text{ g}^{-1}$ , and such energy deposition is capable of killing a cell if the particle passes sufficiently near the cell nucleus. The implications are particularly important for nonregenerative cells such as those in the central nervous system. Three ASTP experiments were designed to investigate the effects of HZE impact on living cells. The Light Flash Observations Experiment yielded measurements of visual effects produced by impact with the astronauts' eyes, the Biostack III Experiment yielded measurements of mutations eventually produced in animals and plants that were flown in the dormant stage (egg, seed), and the Zone-Forming Fungi Experiment was an attempt to observe the real-time mutations that might occur in a ring of fungal cells as they grew during the flight.

### **Concepts and Operations**

The light flash experiment was an attempt to record the visual sensations caused by impact of HZE particles on the dark-adapted retinæ of two astronauts, and to correlate their observations of the intensities and shapes of the resulting flashes with measurements by particle detectors placed close to the astronauts' eyes. The objective was to determine quantitatively the frequency, character, latitudinal dependence, and identity of cosmic particles that cause the flash phenomena. The ultimate objective is to assess the radiation hazards



for long-duration, Earth-orbiting and interplanetary missions. The two detectors used were a silver chloride crystal device that measured particle identity and energy transfer, and a silicon solid-state device that measured particle spectra (energies) and directions and also provided better time resolution than the silver chloride crystals. The orientation of the retinæ with respect to the Earth's magnetic field (fig. 1-9) was important for interpreting the flashes. Data were obtained on two orbits, one of them using only the solid-state detector.

The Biostack III Experiment was an attempt to confirm and extend the studies of HZE particle impact on biological systems begun with the Biostack I and II Experiments during the Apollo 16 and 17 missions. A feature of the ASTP mission was that the geomagnetic shielding yielded a radiation dose an order of magnitude lower than on the lunar missions. The experiment consisted of two cylindrical containers with layers of dormant biological objects interleaved with sheets of particle detectors. The interleaving enabled accurate determination of the location of the hits on the biological objects, which consisted of plant seeds and eggs of lower animals such as brine shrimp.

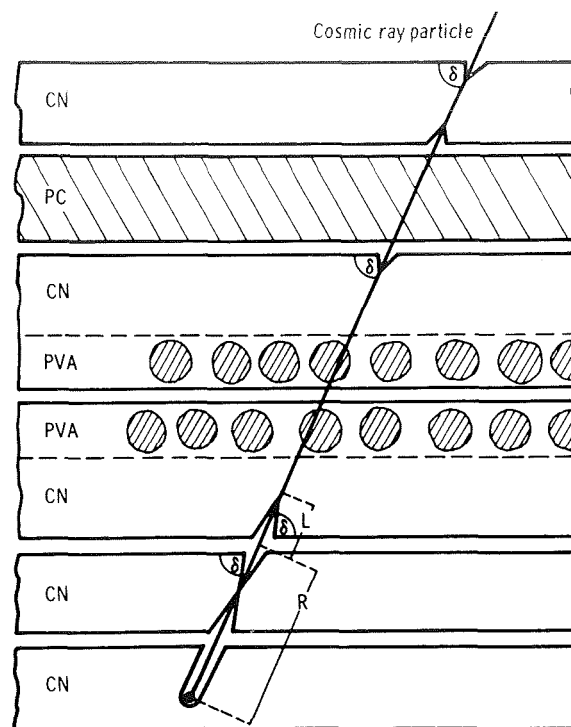


FIGURE 1-10.—Biostack III typical sample/detector layers.

Figure 1-10 shows a representative section of one of the cylinders. The dip angle  $\delta$  helps locate the impacted biological object, the cone length  $L$  determines energy loss, and the residual range  $R$  determines particle charge. The cylinders were stored in the command module in a location of minimum shielding to ambient cosmic radiation.

The Zone-Forming Fungi Experiment had two objectives. One objective was to study radiation effects, especially HZE-impact effects, upon the growth rates and development of growing cultures of *Streptomyces* (*Actinomyces* in the U.S.S.R.) *levoris* Kras carried onboard the two spacecraft. The other objective was to ascertain the possible effect of space-flight factors on the rhythmicity of the growth patterns exhibited in the cultures. The cultures were grown in Petri dishes with particle detectors placed above and below the dishes for determination of particle impact characteristics. Two such assemblies were packaged together in a device (fig. 1-11), and two such devices were

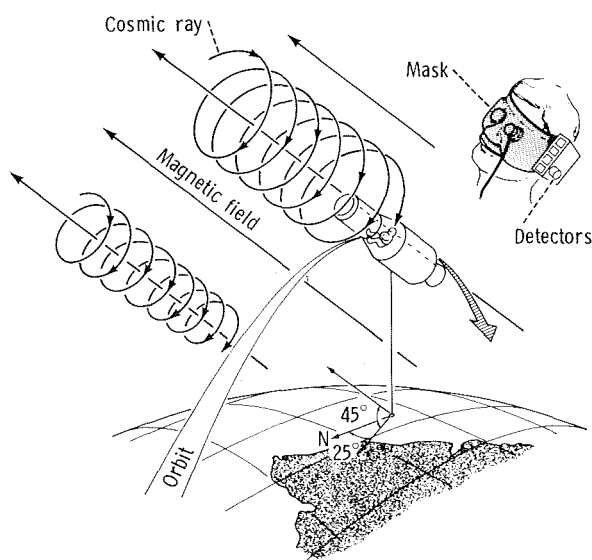


FIGURE 1-9.—Orientation for light flash experiment.

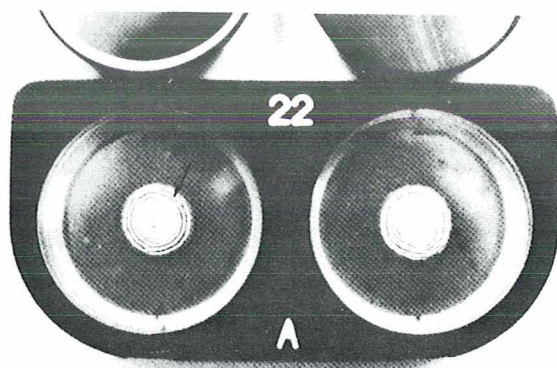


FIGURE 1-11.—Zone-forming fungi culture device.

launched in each spacecraft. During the docked portion of the flight, one device from each spacecraft was exchanged.

### Results

The light flash experiment data for the silver chloride crystals did not correlate well with either the astronaut event-rate observations or the abundances calculated for the ASTP altitude. This discrepancy was probably due to inadequate time resolution for the crystals (viz, the decay time of unfixed heavy-ion tracks was too long). The events observed in the region of the South Atlantic Anomaly, when compared to similar observations performed during the Skylab 4 mission (at an altitude of 440 km), suggest a physical interpretation for the mechanism of light flash production. This mechanism is inelastic collisions of protons with nuclei of carbon, nitrogen, or oxygen in the retina. The arguments leading to this interpretation include the relative abundances of protons with energy loss  $\geq 15 \text{ keV } \mu\text{m}^{-1}$  at the two altitudes, the relative shielding of the spacecraft (Skylab shielding was much less than that of the command module), and the orientation of the retina with respect to the magnetic field in the South Atlantic Anomaly.

The Biostack III Experiment analysis is partially completed. The biological objects that underwent impact have been identified. Objects adjacent to them are being used as controls. Growth and development studies and genetic studies are

still in progress. Preliminary results are as follows.

1. Growth of *Bacillus subtilis* spores was significantly reduced for impacts of particles that passed within  $4 \mu\text{m}$  of the spore centers.

2. Seeds of *Zea mays* showed significant retardation in growth and development, and two impacted seeds failed to germinate.

3. No effects have yet been detected on the germination, growth, and development of the impacted seeds of *Arabidopsis thaliana*.

4. Most of the impacted animal eggs showed serious damage during development. For example, the *Artemia salina* eggs displayed a significantly reduced hatching rate, and developmental anomalies at the extremities and at the abdomen were evident.

In comparison of the dosimetry results of Biostack III with those of Biostack I and II, it was noted that, despite the much lower radiation dose for the ASTP mission, the Biostack III frequency of nuclear disintegration stars was nearly twice that of Biostack II. Little is known about their potential biological effects, but increased attention is being given to nuclear stars in the Biostack III analysis, especially since this radiation component reaches maximum intensity at altitudes of approximately 20 km, which is the region of the atmosphere where supersonic transports fly.

The Zone-Forming Fungi Experiment results showed that definite differences occurred among the various cultures in their zone growth rates and morphologies, but the differences occurred non-uniformly. No specific property of space flight (for example, HZE radiation or weightlessness) can be correlated with any of the observed differences. Investigations are continuing to determine whether the resulting abnormal spore morphology will appear in subculture.

### HUMAN IMMUNE SYSTEM

The investigation of the effect of space-flight factors on the infectious disease process has been a continuing one in both the United States and the U.S.S.R. since the advent of the space program. The ASTP mission provided a unique opportunity to study the process because of the relatively large number of subjects (five crewmen and two

spacecraft) that originated from widely separated environments and that were suddenly brought together under space-flight conditions. The Apollo-Soyuz investigation of the immune system comprised three experiments. The Microbial Exchange Experiment emphasized measurements of several microbial species but also included measurements of species-specific antibodies. The Cellular Immune Response Experiment and Polymorphonuclear Leukocyte Response Experiment investigated cell function.

### Concepts and Operations

The Microbial Exchange Experiment was an attempt to monitor alterations in three factors: the composition of microbial populations inhabiting the Apollo and Soyuz crewmembers and spacecraft, the ability of each crewmember to resist infection, and the ability of certain microorganisms to cause infection. The purpose was to address the overall problem of space-flight effects on the balance between the immune system and infectious microorganisms. Because the two crews came from widely separated geographical and ecological areas, it was possible to identify specific marker microbes for study of cross-contamination patterns. The autoflora and immunocompetence levels of each crewmember were established through repeated sampling and analyses before flight so that flight changes could be measured and intercrew transfer of marker organisms could be identified. Likewise, certain immunological parameters of the blood and saliva of each crewmember were studied to detect changes in the ability of the person to resist infection. This was the first space experiment to monitor species-specific antibodies. During flight, microbial samples were obtained by specially designed swabs (fig. 1-12) from 15 areas in each spacecraft and from 6 locations on each crewmember. The devices were launched and recovered in the Soyuz spacecraft, and initial laboratory studies were performed in Moscow by U.S. and U.S.S.R. investigators.

The Cellular Immune Response Experiment and Polymorphonuclear Leukocyte Response Experiment were laboratory investigations of im-

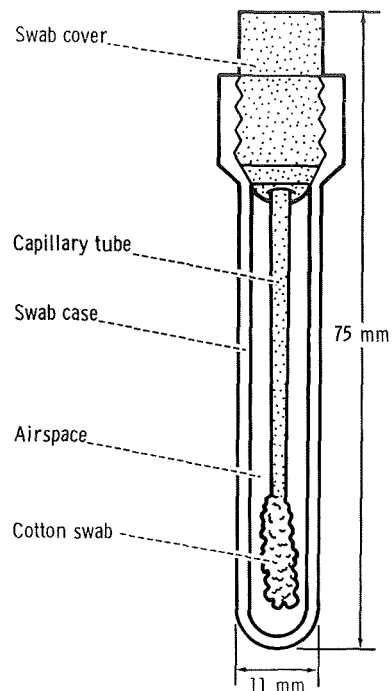


FIGURE 1-12.—Microbial exchange collection device.

une system cell function as affected by space-flight factors. These studies involved blood sample analysis before and after the mission; no in-flight data were acquired. The investigations pertained only to the Apollo crewmembers. In the former experiment, the parameters studied were white blood cell concentrations, lymphocyte numbers, B- and T-lymphocyte distributions in peripheral blood, and lymphocyte responsiveness. In the latter experiment, the studies included total leukocyte count, differential count, measurement of leukocyte adhesion, evaluation of leukocyte migration and chemotaxis, and assessment of phagocytic ability.

### Results

The Microbial Exchange Experiment results were consistent with those of studies on previous missions and added results unique to ASTP. A variety of potential pathogens were recovered from each of the prime and backup crewmembers before and after the flight, but no disease events

occurred. The yeast *Candida albicans* and the bacteria *Staphylococcus aureus* were transferred from one Apollo crewmember to another, but no microbial transfer occurred between crews. No other medically significant changes in the microbial population occurred. The total load of aerobic bacteria inhabiting the skin and upper respiratory tract was essentially the same for all 10 crewmembers and was not significantly changed during flight. Likewise, no significant change in the presence of species-specific antibodies could be attributed to the mission.

The Cellular Immune Response Experiment analysis showed significant depression of the lymphocyte responsiveness from premission levels, but the lymphocyte population remained essentially unchanged. The possibility that the immunosuppression was caused by inhalation of toxic gases rather than usual space-flight factors cannot be assessed; no data are available on the effects of toxic gases on lymphocytic responses. Similar response depression was not observed on the various Apollo lunar missions, but it was observed on the much longer Skylab 3 and 4 missions.

The Polymorphonuclear Leukocyte Response Experiment analysis detected no substantial change in the leukocyte functions from premission tests. It is noted, however, that the time scale for turnover of the leukocytes, from insertion into the bloodstream by the bone marrow to deposit in the tissues, is only a few hours. Thus, the postmission leukocytes tested were not the ones present during weightlessness, so it is not possible to describe the changes in leukocyte function as a function of time of exposure to space-flight conditions. Thus, this study cannot draw conclusions on the possible effects of extended missions on leukocyte function.

## VESTIBULAR SYSTEM

### Concepts and Operations

The Killifish Hatching and Orientation Experiment was the second in a series to determine the effects of space flight on certain portions of the life cycle of certain organisms. The emphasis was on the function and development of the vestibular

system and on calcium metabolism as it related to otolith development. A similar experiment in demonstration form was conducted during the Skylab 3 mission. The Skylab experiment consisted of a plastic bag of synthetic seawater containing 2 juvenile killifish (*Fundulus heteroclitus*) and another bag containing 50 fertilized eggs. The juveniles exhibited looping swimming motion for several days, until they gradually adapted to visual cues for orientation. The orbit-hatched fry, however, exhibited no initial disorientation. They appeared to depend on visual cues for orientation in orbit, and those alive after recovery appeared to depend only on visual cues for orientation on the recovery ship, with no vestibular input. The animals died soon after recovery and were not preserved sufficiently to prevent deterioration. Typical otoliths were not visible in microscopic sections of these fish. The Apollo-Soyuz experiment was designed to extend the Skylab experiment, with emphasis on vestibular disturbance and embryonic development. Since otolith development is largely a matter of calcium metabolism, study of the otolith development was important not only for understanding the effects of space flight on the vestibular system, but possibly for using the otolith as a model for space research on calcium metabolism in general. The experiment consisted of two sets of five seawater-filled plastic bags. One set contained immature fry (21 days old at launch) that had been reared from hatching in tanks presenting various visual environments. The other set contained numbers of fertilized eggs of different ages since fertilization. Figure 1-13 is a photograph of the two sets of bags. The data consisted of filming the swimming behavior of the juveniles and the orbit-hatchlings at various stages of the mission. Postflight analysis included swimming-behavior testing, light and electron microscopy of the vestibular system, and continued zero-g aircraft testing.

### Results

The Killifish Hatching and Orientation Experiment analysis revealed that both the juveniles and the hatchlings exhibited normal vestibular function after flight. The juveniles' postflight swimming patterns suggested abnormal swim bladders.



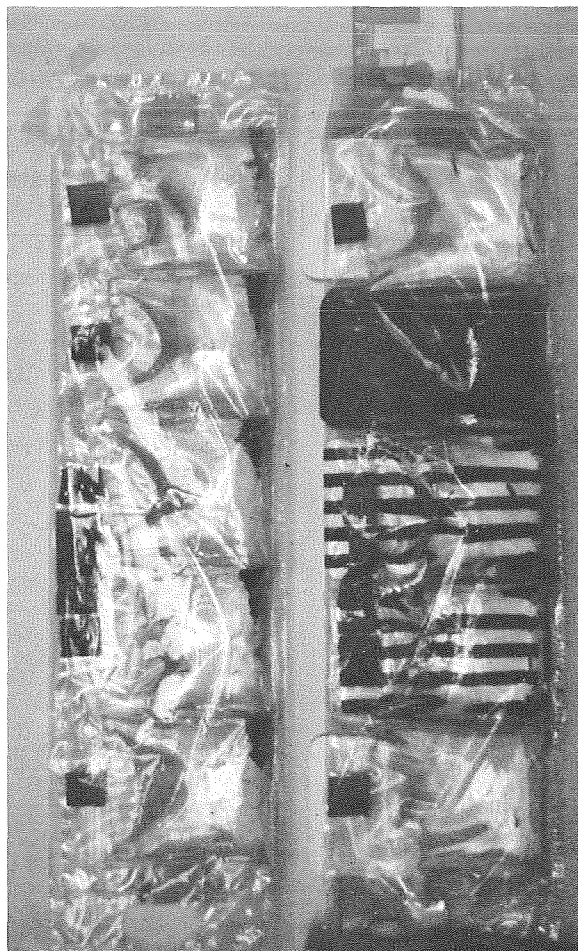


FIGURE 1-13.—Killifish egg and fish containers.

Subsequent testing of maturing fish implied subtle changes in geotactic response and enhanced sensitization to environmental influences as compared with controls. Microscopy has revealed no significant effects on the development of the central nervous system, the peripheral vestibular apparatus, the eye, or the cardiovascular system.

### BIOLOGICAL MATERIALS PROCESSING

For various types of biological research, it is necessary to acquire pure samples of single-type live cells from a mixture of different types of live cells. The separation process is often not amenable to centrifuge or filter techniques because the

different types of cells are not sufficiently dissimilar in size, shape, or mass, and the cells may be too fragile to survive in a viable form.

Electrophoresis is a separation method based on the fact that live cells have a surface charge, the quantity of which is related to the cells' biological function. Thus, if a mixture of different types of cells is placed in an electrolytic buffer solution (the composition of which is compatible with the biological vitality of the cells), and if an electric field is applied, the different types of cells should separate into individual zones according to their individual electrophoretic mobilities. However, in ground-based laboratories, the performance of the electrophoresis process is limited by effects that are mostly associated with a one-g environment. For example, the density difference between cell zones and the buffer solution often causes sedimentation, and Joule heating of the electrophoretic column by the electric field often causes destabilizing convection currents. In principle, these performance limitations may be eliminated in a zero-g or micro-g environment. On the Apollo-Soyuz mission, two experiments successfully demonstrated, for the first time in a space environment, two types of electrophoresis. They were the Electrophoresis Technology Experiment and the Electrophoresis Experiment.

### Concepts and Operations

The Electrophoresis Technology Experiment was an attempt to demonstrate the static column, or zonal, method by electrophoresing several sets of mixtures of cells. The method uses a static column of buffer solution (fig. 1-14) with the electric field aligned along the column. A sample of cell mixture is introduced at one end, and the individual cell zones travel down the column at different speeds. Five different mixtures of cells were to be processed: a mixture of rabbit, human, and horse fixed red blood cells; human peripheral blood lymphocytes; human fetal kidney cells; fixed rabbit and human red blood cells; and fresh rabbit and human red blood cells. The last two mixtures were processed by means of

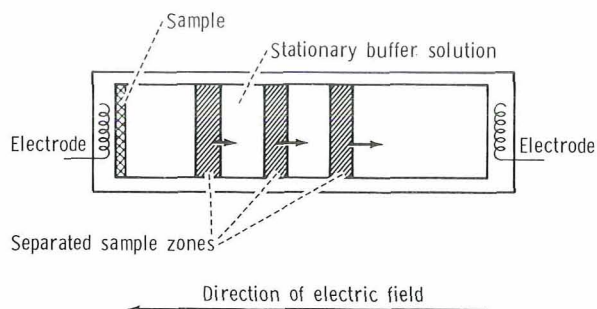


FIGURE 1-14.—Electrophoresis technology static column concept.

isotachopheresis, which is a zone-boundary-sharpening type of zonal electrophoresis. The interest in processing kidney cells was to assess the feasibility of isolating urokinase-producing cells. Urokinase is an enzyme that has the ability to dissolve blood clots, and there is much interest in this enzyme for eventual medical application. The supply of urokinase is far too low to meet the demands, and although it is obtainable from cultures of kidney cells, only 5 percent of the cells in the kidney cortex produce it. If urokinase-producing cells can be isolated from the rest, for example by space processing, the potential exists for increased rates of production. To assess this possibility, a pharmaceutical company participated in the kidney cell processing portion of this experiment. The various mixtures (eight in all, because the first three were duplicated) were launched in a cryogenic freezer to maintain cell viability. After the mixtures were processed, the columns were frozen with the cell zones in place, and they were stored and returned in the freezer for laboratory analysis. Thus, this experiment addressed the three technological requirements for eventual application of electrophoresis on space missions: (1) preservation of cell viability before processing, (2) processing, and (3) preservation of viability after processing.

The Electrophoresis Experiment was an attempt to demonstrate improved performance of the free-flow method in a micro-g environment over that attainable on the ground. In this method, the buffer solution flows continuously (fig. 1-15), and the cell mixture is continuously inserted into

the flow. The electric field is aligned perpendicularly to the flow so that the cells separate from each other laterally into streams. Four mixtures were processed in this experiment: rat bone marrow cells, fixed rabbit and human red blood cells, rat spleen cells, and rat lymph node cells with human red blood cells as markers. Except for the mixture of fixed cells, the mixtures were freshly prepared before they were launched in the Apollo command module. The rat lymph cells were frozen (stored in the cryogenic freezer of the Electrophoresis Technology Experiment) and the others were cooled until processing began approximately 1 day after launch. The separated streams were detected photo-optically and the data were stored on magnetic tape; no attempt was made to preserve the cells after processing.

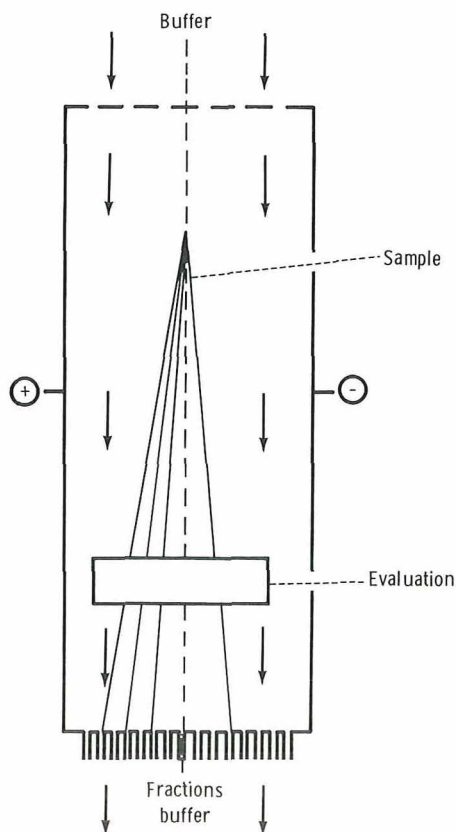


FIGURE 1-15.—Electrophoresis continuous flow concept.

## Results

The Electrophoresis Technology Experiment, by separating the fixed red blood cell species from their mixture, provided the first successful demonstration of zonal electrophoresis in a space environment. The lymphocytes did not electrophorese successfully. A probable reason is that the cells lost viability due to pH fluctuations; postmission assessment revealed only 6 percent viability. The isotachopheresis was partly successful; only front boundaries developed. No zone separation or rear boundaries were evident because the processing time was too short. From a research application viewpoint, the most significant result was the kidney cell separation. Zones were formed and yielded concentrations of urokinase-producing cells, as demonstrated by subsequent laboratory culturing. Although the lymphocyte processing was not successful, preservation techniques were developed in preparation for the experiment that may eventually allow blood donors to donate blood years in advance of intended use, as opposed to some present requirements of donating within 2 days of intended use.

The Electrophoresis Experiment developed an anomaly in its photo-optical detection system. During flight, the lamps were 42 percent brighter than their nominal values, which resulted in saturation of the photodiode detector array. Consequently only optical absorptions greater than 30 percent were detectable, and 30 percent was the upper limit expected for light absorption by the separated streams. However, absorption pulses did appear on the data tape with a distribution similar to that expected for the separated streams. Subsequent ground tests revealed that the cells subjected to electrophoresis tend to aggregate irregularly in the regions of the electrophoretically separated streams such that the pulse distributions do provide good representations of the separated cell-stream distributions. On the basis of this indirect evidence for successful electrophoresis, the result was that electrophoresis was accomplished with a tenfold increase in the throughput rate and with at least as sharp cell separation as is achievable in a one-g environment. The rat spleen cells achieved the sharpest separation. The rat lymph node cells achieved excellent

separation and apparently exhibited the greatest tendency to form aggregations (viz, provided the greatest number of pulse data). The rat bone marrow cells indicated good separation in spite of few data (viz, they tended not to aggregate), and insufficient data were available for conclusions concerning the separation of human and rabbit red blood cells.

## SOLID MATERIALS PROCESSING

Two types of solid materials processing were conducted on the ASTP mission: high-temperature and low-temperature. The high-temperature processing consisted of melting and solidifying seven sets of materials samples in an electric furnace. They constituted seven separate experiments to investigate mechanical, optical, electrical, and/or magnetic properties of pure and mixed substances that were processed in the absence of sedimentation and thermal convection effects during their liquid phases. Three of the experiments were extensions of furnace investigations begun during Skylab missions, three were entirely new investigations, and one was a jointly conducted experiment. The low-temperature processing was a single experiment that attempted to grow commercially important crystals in water at ambient Apollo cabin temperature. This was the first such experiment performed in a space environment. The development and implementation of this experiment also incorporated cost sharing between NASA and a commercial firm.

The Multipurpose Furnace Experiment was actually a development effort to provide a facility for processing the seven high-temperature experiments during the mission. The ASTP furnace was developed from the Skylab furnace and provided higher processing temperatures (nominally 1423 K) with no increase in power requirement. Also, circuitry was added to allow controlled, variable-rate cooldown; and a helium-injection rapid-cooldown system was developed to reduce the cool-to-touch time from 20 hours to as few as 3 hours. Thus, more experiments could be processed during the mission. Each experiment provided a set of three stainless steel cartridges (fig. 1-16), and each cartridge contained between one

and three ampoules of material to be processed. All three cartridges were processed simultaneously. The furnace system operated extremely well throughout the mission, except during the first use of the helium cooldown system. This anomaly resulted in a longer soak time for the first experiment, but no notable degradation was observed in the scientific results and no further system anomalies occurred during the mission.

The Surface-Tension-Induced Convection Experiment was an attempt to detect the convective mixing in melted material in micro-g that might be due to surface-tension gradients arising from compositional gradients. The material selected was pure lead interfaced to an alloy of lead and 0.05 atomic percent gold, and samples were processed in both wetting and nonwetting ampoules. The processed samples revealed that incomplete mixing occurred in a pattern not explainable by diffusion. The flow pattern occurred where the material contacted the nonwetting ampoule surface, and the best explanation appears to be that the flow was induced by interfacial tension gradients arising most likely from the compositional gradient, a demonstration of the Marangoni

effect. These results are surprising because they suggest that the well-known hydrodynamic no-slip condition may not be valid in micro-g conditions. (However, see discussion of Interface Marking in Crystals Experiment.)

The Monotectic and Syntectic Alloys Experiment was an investigation of the effects of micro-g melting and solidification of two materials, aluminum antimonide (AlSb) and lead-zinc (Pb-Zn). Aluminum antimonide is potentially an efficient solar-cell material, perhaps 30 to 50 percent more efficient than silicon. The problems with this material have been difficulty in obtaining stoichiometric homogeneity in the compound and the fact that this material is highly reactive with moisture. This latter problem may be caused by electromotive force effects due to the presence of Al-rich and Sb-rich secondary phases that occur within the compound in one-g processing. The samples processed during ASTP reveal major improvements in macroscopic and microscopic homogeneity. They contain an average of 4 times, and a maximum of 20 times, less of the undesirable secondary phase. Small amounts of the Al-rich phase are found only along parts of the grain boundaries, whereas samples

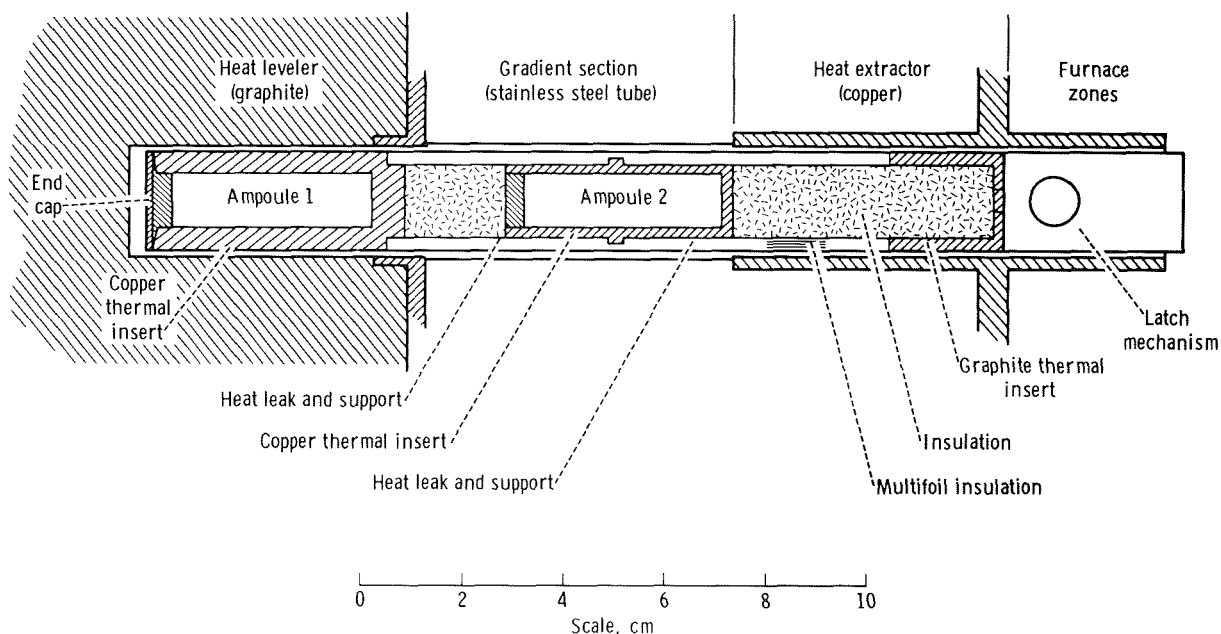


FIGURE 1-16.—Multipurpose furnace typical cartridge assembly.



processed in one-g conditions contain major grains of both the Al-rich and Sb-rich phases. The Pb-Zn system was studied to investigate the phase-segregation effects in micro-g conditions for this immiscible system. Because of the large density differences between lead and zinc, it is difficult in one-g conditions to prevent gravity separation during resolidification. It was hoped that the space-processed samples would result in a dispersion of fine particles of superconducting lead in a zinc-rich composition. However, the space-processed samples failed to mix, even though the soak temperature was 40 K above the published miscibility gap. Although some Pb particles were dispersed in the Zn matrix, the bulk of the lead remained in the same position as before melting.

The Interface Marking in Crystals Experiment was designed to investigate the crystal growth and segregation characteristics in a directionally solidifying material. For this purpose, gallium-doped germanium crystals grown on Earth were partly melted and resolidified as 55-millisecond current pulses ( $19.1 \text{ A cm}^{-2}$ ) were transmitted across the traveling solid/melt interface at intervals of 4 seconds. The Peltier cooling by the current pulses at the interface caused time-identifiable demarcations that enabled determination of growth rates. Many new results were revealed. No wetting of the ampoule by the material occurred, as opposed to ground-based processing. The possibility that wetting inversion in space is a phenomenon occurring for many systems has significant implications for materials-processing technology in space applications. The measured growth rate increased rapidly from 0 to  $7 \mu\text{m sec}^{-1}$  at the onset of cooling, continued to increase over a distance of 2.5 cm, and then reached a constant value of  $10.5 \mu\text{m sec}^{-1}$ . The growth-rate behavior was the same for the ground-processed samples, an indication that the heat transfer was dominated by conduction (since laminar convection was present in the ground-based tests). All segregation theories assume a step-function jump from zero to constant-growth rate; therefore, these results require the development of a modified segregation theory. The segregation results show that, as expected, the dopant concentration increased in the bands as the interface

traveled over approximately 1.5 cm. However, with continuing growth (at a rate that was still increasing), the dopant concentration decreased rather than reaching an expected steady-state value. It is most likely that this unexpected behavior is a feature of the geometry of the growth system rather than a characteristic of growth in micro-g conditions.

The Zero-g Processing of Magnets Experiment was designed to investigate the possibility of enhancing the magnetic coercive strength of materials, which may have important technological application in the future. The two magnetic materials tested were alloys of manganese-bismuth (Mn-Bi) and copper-cobalt-cerium (Cu-Co-Ce). The results were significant. Chemical homogeneity was substantially enhanced macroscopically and microscopically. Primary single crystals were grown that exceeded the sizes of Earth-grown crystals by a factor of 10. (Crystal size was limited by the ampoule dimension.) The Mn-Bi samples yielded significantly improved coercive strength, exceeding previously reported values by 20 to 100 percent. In the unannealed state, values exceeding  $15 \text{ MA m}^{-1}$  were achieved; at this writing, measurements are underway for the annealed state. The Cu-Co-Ce samples did not show enhanced magnetic properties. The problem with the flight samples was similar to problems encountered with Earth-based processing of rare earth materials. The material reacted with the crucible material of the ampoule to form an intermetallic reaction layer, which resulted in spurious nucleation of the magnetic phase ahead of the regrowth interface.

The Crystal Growth From the Vapor Phase Experiment was an extension of a Skylab experiment to generalize and characterize the micro-g crystal growth of a class of compounds from the vapor phase. The Skylab experiment revealed that improved crystalline perfection and much greater than expected mass transport rates occurred for germanium selenide (GeSe) and germanium telluride (GeTe) using germanium tetraiodide as a transport agent. Crystal growth from the vapor phase for such compounds in the IV to VI class of materials is of major interest because the electronic properties are critically dependent on the degree of chemical homogeneity and

crystalline perfection. The ASTP experiment included new compounds and solid solutions transported with different transport agents in higher temperature gradients. The results confirm the Skylab results and extend the conclusions to more complex systems. They also provide experimental evidence for the cause of the enhanced transport rates over the theoretically predicted values. The homogeneity improvement in distribution of tellurium in the germanium-selenium-tellurium starting sample is approximately a factor of 10. The corresponding improvement in distribution of selenium in the germanium-sulfur-selenium starting sample is less pronounced. In micro-g conditions, the transport rates were equal to or lower than rates on the ground, but they were three to five times greater than any diffusion theory would predict for micro-g conditions. Furthermore, the enhanced rates cannot be explained solely on the basis of a diffusion process. The enhanced rates are most probably related to thermochemical effects of gas-phase reactions that have not been included in current vapor transport models.

The Halide Eutectic Growth Experiment was an attempt to grow continuous fibers of lithium fluoride (LiF) in a matrix of sodium chloride (NaCl). The objective was to demonstrate the advantages of micro-g processing for obtaining infrared-transmitting fiber optics. This experiment was an extension of a similar Skylab experiment in which long fibers of sodium fluoride were grown in a matrix of sodium chloride. For the Apollo-Soyuz experiment, ingots of the LiF-NaCl eutectic were partly melted and directionally resolidified in micro-g conditions. Continuous LiF fibers were obtained, which yielded improved transmittance over a wider wavelength range with better image quality compared to ground-processed samples.

The Multiple Materials Melting Experiment had several objectives. This jointly conducted experiment was analyzed exclusively by the U.S.S.R. investigators, and their results are published in this document. Three ampoules containing different materials were placed in each cartridge. One sample consisted of an aluminum rod with seven tungsten balls fused to one end and a rod of tungsten-rhenium alloy fused to the other. The

objectives were to investigate formulation of compounds with components of highly different specific weights and to investigate diffusion and formation of intermetallic phases as a result of interaction of refractory inclusions in a meltable matrix. The inclusions were shifted during space processing, perhaps due to in-flight spacecraft accelerations. The second ampoule contained an antimony-doped germanium-silicon solid solution. The purpose was to obtain monocrystals of homogeneous distribution of this semiconductor material. Monocrystals were obtained with and without seeding by means of directional solidification, but with heterogeneous distribution of components possibly due to radial temperature gradients in the furnace. The third ampoule contained aluminum powder and small pieces of copper-aluminum eutectic to investigate, for example, sphere formation. The space-processed samples showed no significant differences from the ground-processed samples.

The Crystal Growth Experiment was the first attempt in space to demonstrate the possibility of growing commercially important crystals by diffusion of appropriate reactants toward each other through pure water at low temperature (viz, ambient spacecraft cabin temperature). Low-temperature methods avoid some of the complications associated with high-temperature processing, such as phase transitions, component volatility, thermally induced strain, and contamination from the container. The most successful ground-based, low-temperature crystal growth process has been the gel method, in which reactants diffuse toward each other through a gel. The function of the gel is to support the growing crystals and suppress convection. The main problems are reduced diffusion rates through the gel and multiple nucleation of crystals in the gel, which combine to prevent the growth of large single crystals, and possible contamination of the crystals by the gel material. Because the crystals presumably do not need convection suppression or crystal support in micro-g conditions, the gel can be replaced by pure water. The crystals were grown in reactors (fig. 1-17); compartment A contained the water, and the reactants were stored in compartments B and C. After the joint phase of the mission was completed and the Apollo and

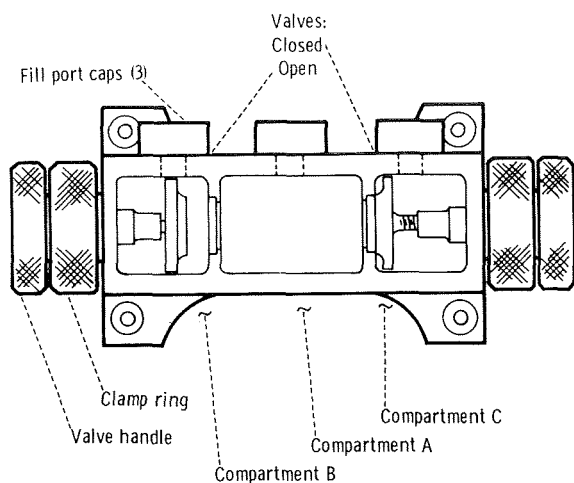


FIGURE 1-17.—Crystal growth reactor.

Soyuz spacecraft had separated, compartments B and C were opened and the reactants diffused toward each other. The crystals grown were calcium tartrate, calcium carbonate, and lead sulfide. The best crystals obtained were the calcium tartrate, with prismatic shapes as long as 2 mm and plate shapes as long as 5 mm. Many rhombohedral calcium carbonate crystals as large as 0.5 mm on a side were formed. The lead sulfide reaction was less successful, but it produced small crystals as large as 0.1 mm. However, the lead sulfide reaction was not complete at time of reentry. The need for temperature control was evident for all the reactions; the temperature in the command module ranged from 289 to 297 K during the flight. The crystals obtained were of a size and quality comparable to the best obtainable in one-g conditions in the same length of time.



## 2. Mission Description

*S. N. Hardee<sup>a</sup>*

### ABSTRACT

The Apollo-Soyuz mission was the first manned space flight conducted jointly by two nations. The United States and the U.S.S.R. achieved a substantial degree of success in (1) obtaining flight experience for rendezvous and docking of manned spacecraft and developing a docking system that would be suitable for use as a standard international system, (2) demonstrating in-flight intervehicular crew transfer, and (3) conducting a series of science and applications experiments. The Apollo and Soyuz spacecraft, with minor exceptions, were similar to those flown on previous missions, but a new Apollo module, the docking module, was built specifically for this mission. The mission started with the Soyuz launch on July 15, 1975, followed by the Apollo launch on the same day. Docking of the two spacecraft occurred on July 17, and joint operations were conducted for 2 days. Both spacecraft landed safely and on schedule; the Soyuz landing in the U.S.S.R. occurred on July 21, and the Apollo landing near Hawaii occurred on July 24. Twenty-eight science experiments were performed during the mission.

### INTRODUCTION

The first international manned space flight, the Apollo-Soyuz Test Project (ASTP) (fig. 2-1), was highly successful. The primary objectives of the joint U.S.-U.S.S.R. project were to test systems for manned spacecraft rendezvous and docking that would be suitable for use as a standard international system and to demonstrate crew transfer

between spacecraft. An additional objective was to conduct a program of science and applications experimentation. Joint and unilateral experiments that provided data and experience in the fields of Earth resources, Earth gravity, Earth atmosphere, astronomy, solar science, life sciences, and space processing were conducted. (The arrangement of these experiments within this report is given in the Table of Contents.) Some of these experiments were conducted in pioneering fields. For example, the first measurements of atomic nitrogen in the Earth's atmosphere at orbit altitudes were made, and a search for discrete sources of 5- to 100-nm (50 to 1000 Å) extreme ultraviolet (EUV) radiation outside the solar system was made for the first time. In addition, space science awareness was promoted through extensive commercial television (TV) broadcasting and filming of flight experimentation and through in-flight science demonstrations.

### SPACECRAFT DESCRIPTION

An overview of the two spacecraft and the docking module (DM) is shown in figure 2-2, and the ASTP experiment locations are shown in figure 2-3.

#### Apollo Spacecraft Description

The Apollo spacecraft used for this mission was similar in most respects to those employed to ferry crews to and from the Skylab space station, but it differed in some significant aspects that will be pointed out in this discussion. The significant differences among four generations of Apollo spacecraft are summarized in table 2-I.

---

<sup>a</sup>NASA Lyndon B. Johnson Space Center.

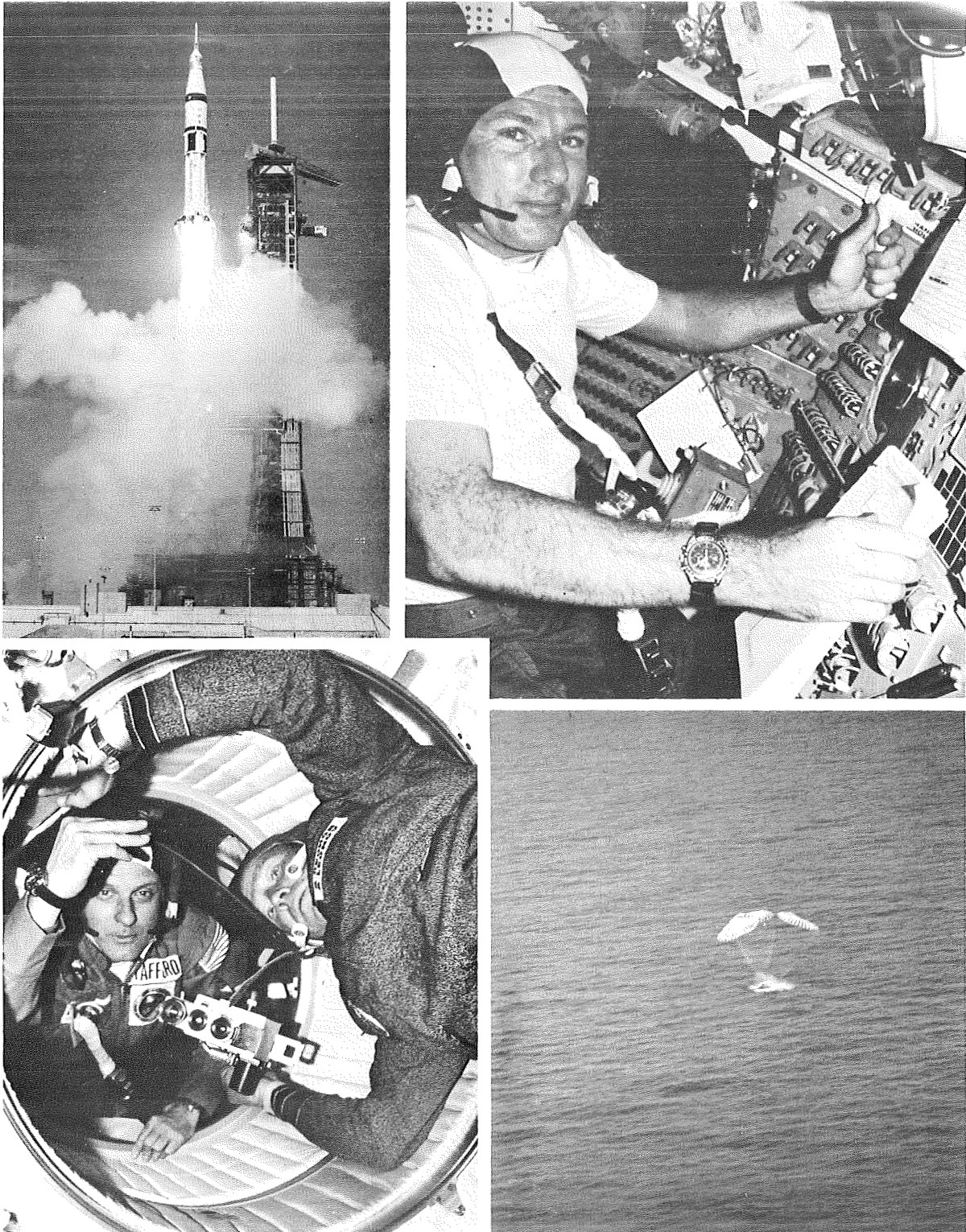


FIGURE 2-1.—Pictorial summary of Apollo-Soyuz mission.

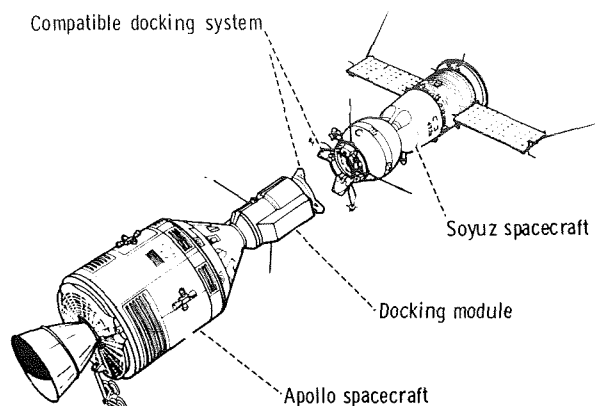


FIGURE 2-2.—Apollo-Soyuz rendezvous and docking configuration.

*Command and service module.*—The Apollo command and service module (CSM) flown on the Apollo-Soyuz mission was closely similar to the command and service modules used for the Skylab flights, but some modifications were made to fit mission needs. Additional controls for the docking system and special CSM-to-DM umbilicals were added together with experiment packages and their controls. Also, the steerable high-gain antenna used for deep-space communications during the Apollo lunar missions but not needed for the Skylab missions was reinstalled on the Apollo-Soyuz command and service module. The antenna was used to establish a relay link with Applications Technology Satellite 6

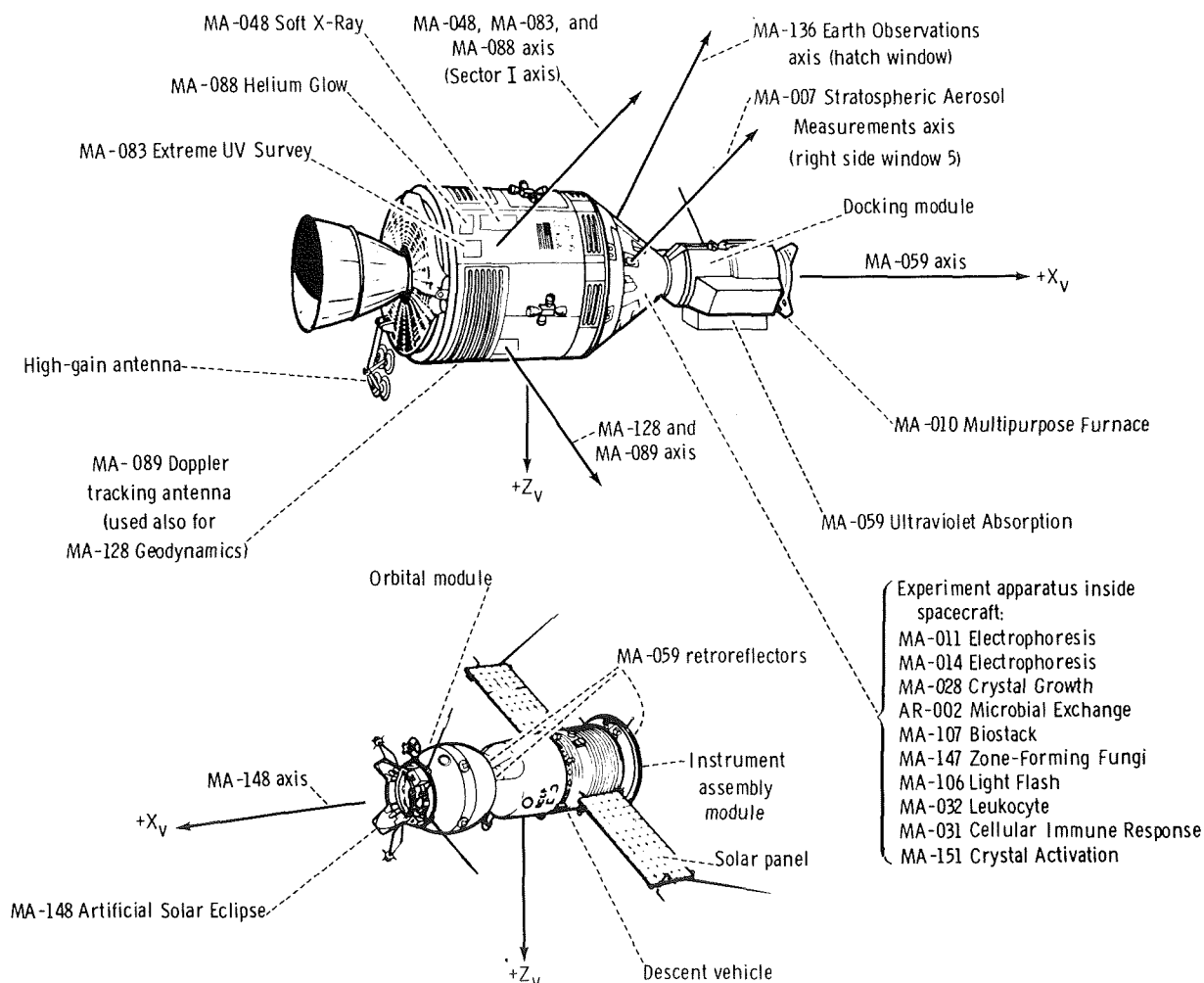


FIGURE 2-3.—ASTP experiment mounting locations.

TABLE 2-I.—Significant Apollo Spacecraft Configuration Differences

System	Area of difference	Mission			
		ASTP	Skylab	<sup>a</sup> Apollo 11 to 14	<sup>b</sup> Apollo 15 to 17
Command module					
Electrical power system	Lunar module umbilicals			X	X
	Skylab tunnel umbilical		X		
	Docking module umbilicals	X			
	Drag-through umbilical	X	X		
Experiments	Stowable	X	X	X	X
	Coldplate mounted	X			
Television	Cameras and monitors	X	X	X	X
	Video tape recorder	X			
Communications	Speaker box	X	X		
	ATS-6 equipment	X			
Environmental control system (ECS)	Extravehicular activity capability		X		X
Displays and controls	Experiments	X	X		X
	Docking module	X			
	Compatible docking system	X			
	ATS-6 communications	X			
Stowage	Apollo Block II			X	X
	Skylab		X		
	Modified Skylab	X			
Service module					
Experiments	Scientific instrument bay	X			X
	Lunar sounder				X
	Doppler tracking receiver	X			
	Remotely controlled doors	X			X
	Extravehicular retrieval capability				X
Service propulsion system	Propellant utilization gaging system (flight)			X	X
	Propellant utilization gaging system (ground)	X	X		
	Four propellant, two pressurant tanks			X	X
	Two propellant, one pressurant tank	X	X		
Environmental control system	Heaters deactivated	(c)	X		
	Coldplates for experiment cooling and ATS-6 equipment	X			

<sup>a</sup> Lunar-landing missions.<sup>b</sup> Lunar-landing missions with expanded scientific data return capability.<sup>c</sup> ESC radiator heater motor switches placed in open position before launch.



TABLE 2-I.—Concluded

System	Area of difference	Mission			
		ASTP	Skylab	<sup>a</sup> Apollo 11 to 14	<sup>b</sup> Apollo 15 to 17
Service module - concluded					
Reaction control system (RCS)	Propellant storage module	X	X		
	RCS quad heaters	X	X		
Thermal protection	Increased cork insulation	X	X		
	<sup>d</sup> Additional cork insulation	X			
Communications	Rendezvous radar transponder			X	X
	ATS-6 power amplifier system	X			
	High-gain antenna	X		X	X
Electrical power system	Two fuel cells		X		
	Three fuel cells	X		X	X
	Descent batteries		X		
	Extra water tank		X		
	Increased cryogenic storage capacity			X	X
	Return enhancement battery			X	X
Spacecraft adapter					
Panels	Jettisonable	X		X	X
	Deployable		X		
Structural support	Lunar module			X	X
	Docking module	X			

<sup>a</sup> Lunar-landing missions.<sup>b</sup> Lunar-landing missions with expanded scientific data return capability.<sup>d</sup> For long-duration RCS firings.

(ATS-6) in synchronous orbit to provide communications with the Mission Control Center for 55 percent of each orbit.

*Docking module.*—The docking module was basically an airlock that permitted the crewmen to transfer between the two spacecraft, which had different internal pressures and atmosphere constituents. The docking module had docking facilities on each end that enabled rigid coupling of the Apollo and Soyuz spacecraft and was a cylindrical pressure vessel with an internal diameter of 1.42 m and an overall length of 3.15 m between the docking interfaces.

The principal external attachments to the docking module were a Doppler transmitter antenna for the Doppler Tracking Experiment, an ultraviolet spectrometer for the Ultraviolet Absorption Experiment, a docking target that enabled the Soyuz crew to observe the Apollo docking approach through the Soyuz periscope, three very high frequency (VHF) antennas, three adapter mountings, a vent housing, and four gas storage tanks. The external and internal arrangements of the docking module are shown in figure 2-4.

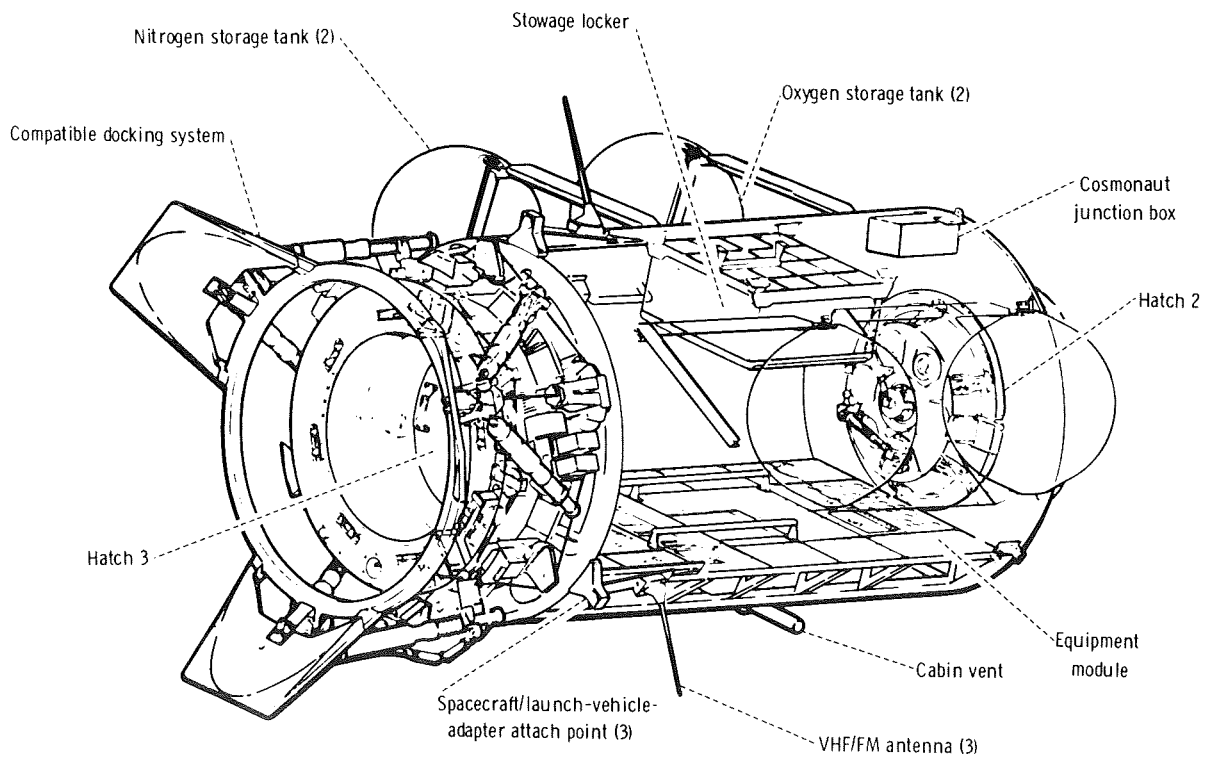
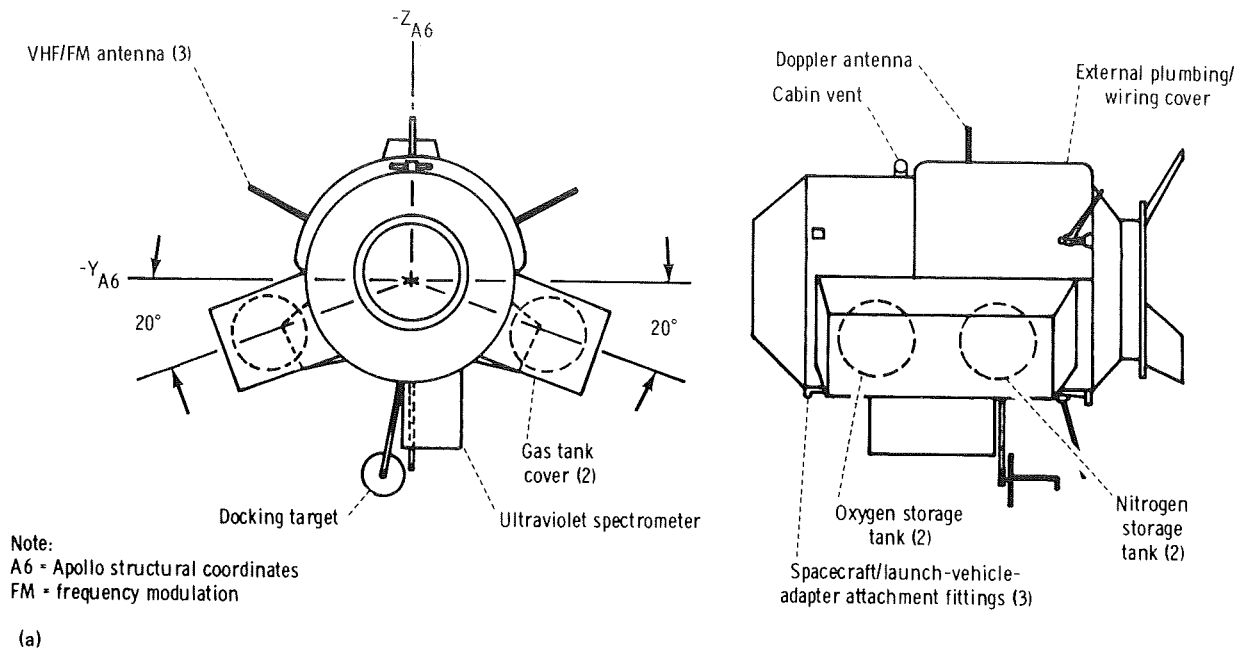


FIGURE 2-4.—Docking module. (a) Exterior. (b) Interior.

### Soyuz Spacecraft Description

The Soyuz spacecraft consisted of three modules, which are discussed in the order of their proximity to the Apollo spacecraft when docked.

The orbital module, which provided the Soyuz portion of the compatible docking system, was used for work and rest by the crew during orbit. The module contained a side hatch for crew entry before launch, a forward hatch for crew transfer to and from the docking module, and an aft tunnel for crew transfer to the descent vehicle. Two windows were provided: one forward of the side hatch for earthward viewing, and the other on the opposite side of the module for outward viewing.

The descent vehicle, with the main controls and crew couches, was occupied by the cosmonauts during launch, dynamic orbital operations, descent, and landing.

The instrument assembly module, which contained subsystems required for power, communications, propulsion, and other functions, was located at the aft end of the Soyuz spacecraft. Two sets of winglike solar battery panels were mounted 180° apart on the exterior of the module.

### TRACKING AND COMMUNICATIONS

Flight control personnel maintained contact with the Apollo and Soyuz spacecraft through the Spaceflight Tracking and Data Network (STDN). This network consisted of a complex of fixed ground stations, portable ground stations, specially equipped aircraft, and an instrumented ship. The mission was supported by 14 Spaceflight Tracking and Data Network stations, as well as by a U.S.S.R. network consisting of 7 ground stations and 2 ships. Communications opportunities with the use of the Spaceflight Tracking and Data Network alone encompassed 17 percent of the mission time; but, for the first time, an Applications Technology Satellite that increased the total communications coverage to 63 percent was employed (fig. 2-5). The increased coverage with the ATS-6 was of significant importance to several science experiments. The Apollo-Soyuz Test Project communications are shown schematically in figure 2-6.

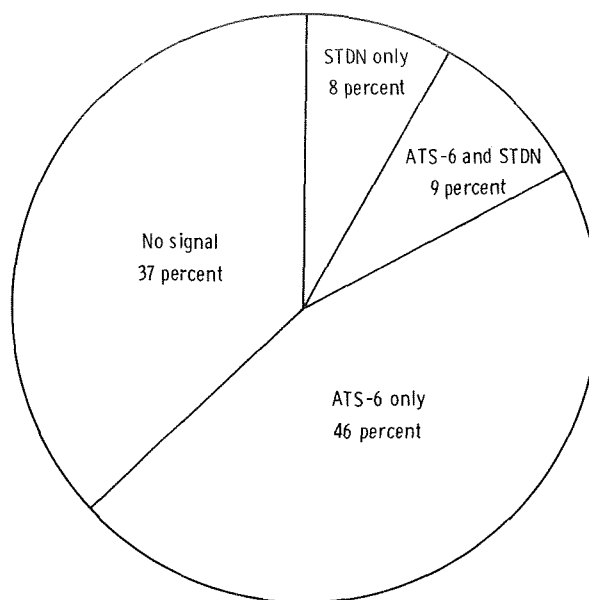


FIGURE 2-5.—Communications with command and service module for 24-hour period.

### NARRATIVE FLIGHT SUMMARY

#### Launch and Rendezvous Maneuvers Phase

The Soyuz spacecraft, manned by Alexei A. Leonov, commander, and Valeri N. Kubasov, flight engineer, was launched from the Baykonur, Kazakhstan, launch complex at 12:20 UT on July 15, 1975. It was launched in a northeasterly direction and was inserted into a 186- by 222-km orbit at an inclination of 51.8°. On the fourth orbit after lift-off, the first of two maneuvers to circularize the Soyuz orbit at 223 km was initiated. The second circularization maneuver occurred on the 17th Soyuz orbit.

Seven and one-half hours after the Soyuz launch, the Apollo spacecraft, manned by Thomas P. Stafford, commander, Vance D. Brand, command module pilot, and Donald K. Slayton, docking module pilot, was launched from the NASA John F. Kennedy Space Center in a northeasterly direction and was inserted into a 149- by 168-km orbit, also with an inclination of 51.8°. One hour fourteen minutes after lift-off, the Apollo command and service module was separated from the Saturn-IVB stage, and the crew began the

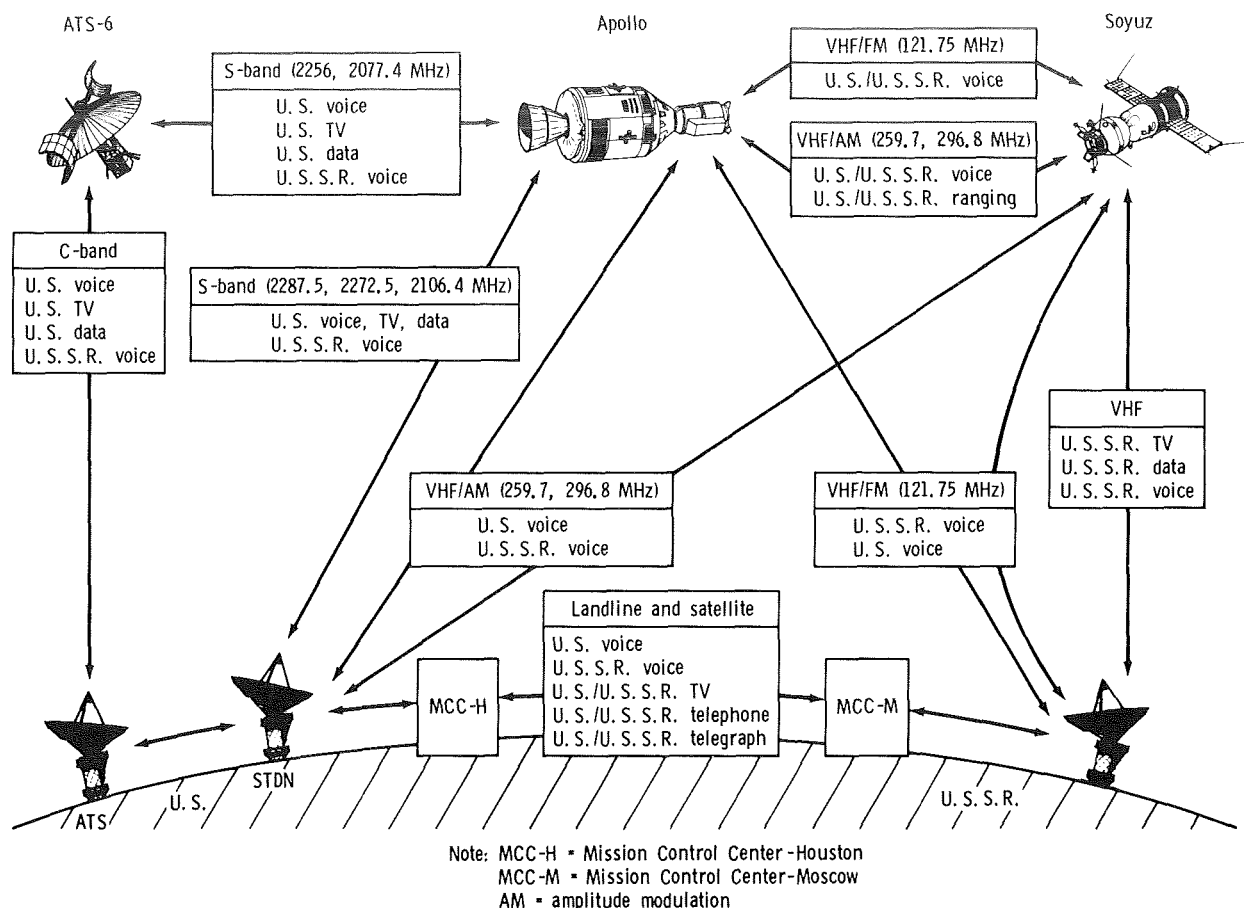


FIGURE 2-6.—Apollo-Soyuz communication overview.

transposition and docking procedure to extract the docking module from the launch vehicle. Although these operations were generally normal, the removal of the docking probe was hindered by a misrouted pyrotechnic connector cable. A corrective procedure given to the crew was used successfully to remove the probe, and extraction was completed at 22:24 UT. After performance of an evasive maneuver to avoid recontact with the launch vehicle, a circularization maneuver at the third apogee, and additional phasing and plane correction maneuvers, the first day of maneuver activities was concluded for both crews.

Before the end of the day, several science experiment operations were performed. The Zone-Forming Fungi (ZFF) Experiment, which had been photographed at 12-hour intervals beginning July 13, 1975, was again photographed at 12:30

Soyuz ground elapsed time (GET). Simultaneously, the Biostack Experiment was activated for approximately 12 hours of operation. The first Geodynamics Experiment data take was initiated at 15:12 GET and continued through the next three ATS-6 passes by the Apollo spacecraft. Major mission events and data collection periods are shown in figure 2-7.

The second day was devoted primarily to pre-docking checkout activities, rendezvous maneuvers, and science experiments. The first biostack data take was concluded at 25:38 GET, and the killifish experiment was initiated at 27:18 GET. Earth observations activities were initiated after starting the killifish experiment and extended into the period of Ultraviolet Absorption (UVA) Experiment lamp burn-in, which started at 27:40 GET. Multipurpose furnace experiment

preparations were also made during the lamp burn-in period, and the ultraviolet absorption crew optical alignment sight calibrations were made. After another Geodynamics Experiment data take, multipurpose furnace operations were started with the Surface-Tension-Induced Convection Experiment cartridges. Simultaneously, the Electrophoresis Experiment (EPE) was prepared and operated; the Extreme Ultraviolet Survey, Helium Glow (HeG), and Soft X-Ray Experiments were checked out; several geodynamics data takes were made; and zone-forming fungi photographs were taken. Unfortunately, a malfunction developed in the Soft X-Ray Experiment after only 10 minutes of normalcy during the initial operation of the experiment on the second day of flight. However, good data were obtained again, intermittently, during the sixth through eighth days of flight.

### **Joint Phase**

Docking occurred on the 36th Soyuz orbit and the 29th Apollo revolution. The time of docking was 51 hours 49 minutes Soyuz GET on July 17, 1975; and the orbit of the docked spacecraft was nearly circular at 223 km with an eccentricity of less than 1 km. The Apollo and Soyuz spacecraft remained docked for approximately 2 days.

After docking, hatch 1 was opened, and several transfers of both crews, television tours of both spacecraft and of the United States and the U.S.S.R., a news conference, and official ceremonies were conducted. The Surface-Tension-Induced Convection Experiment in the multipurpose furnace was continued during this period, and the collection of microbial samples for the Microbial Exchange Experiment was accomplished by the two crews. The multipurpose furnace was shut down at 58:05 GET and was reinitiated for the U.S.S.R. Multiple-Materials Melting Experiment at 58:45 GET.

Several other science experiments were conducted during this first docked phase. The Zone-Forming Fungi Experiment was photographed again; several Earth observations and geodynamics data takes were made; the Microbial Exchange Experiment was conducted; the

U.S.S.R. multiple-materials melting was concluded; and the zero-g processing of magnets in the multipurpose furnace was conducted.

After the two spacecraft had been docked for nearly 44 hours, the first undocking was performed normally, and the joint Artificial Solar Eclipse Experiment was performed. A second docking was then performed at 96:14 GET to test the docking system with the Soyuz docking system active.

Final undocking was 99:06 GET, after which the Ultraviolet Absorption Experiment was conducted to conclude the joint phase of the flight. The Apollo spacecraft began stationkeeping 18 m ahead of the Soyuz spacecraft. The Apollo spacecraft then was maneuvered to a 150-m displacement out of the Soyuz orbital plane. At 99:40 GET, a 10-minute data take was performed as the command and service module swept through a 30° arc at the 150-m radius from the Soyuz spacecraft. Similarly, a 500-m out-of-plane data take was made starting at 101:18 GET. After the 500-m data take, the command and service module was positioned back into the Soyuz orbital plane, and an in-plane final evasive maneuver was begun at 102:22 GET.

During the 150-m data take, no reflected signal was detected by the spectrometer. Assessment of the problem by ground personnel indicated a contaminated Soyuz side reflector or possible locking of the star tracker onto a different light source. Therefore, the Soyuz aft reflector was used for the 500-m data take.

### **Soyuz Deorbit and Landing**

The Soyuz deorbit maneuver was performed at 141:50 GET. The reentry vehicle was brought to a safe landing in Kazakhstan at 10:51 UT on July 21, 1975, after a flight of 142 hours 31 minutes.

### **Apollo Orbit Continuation Phase**

The Apollo spacecraft continued in orbit for approximately 5 days after separation from the Soyuz spacecraft. Following the ultraviolet absorption joint phase data takes, one revolution of

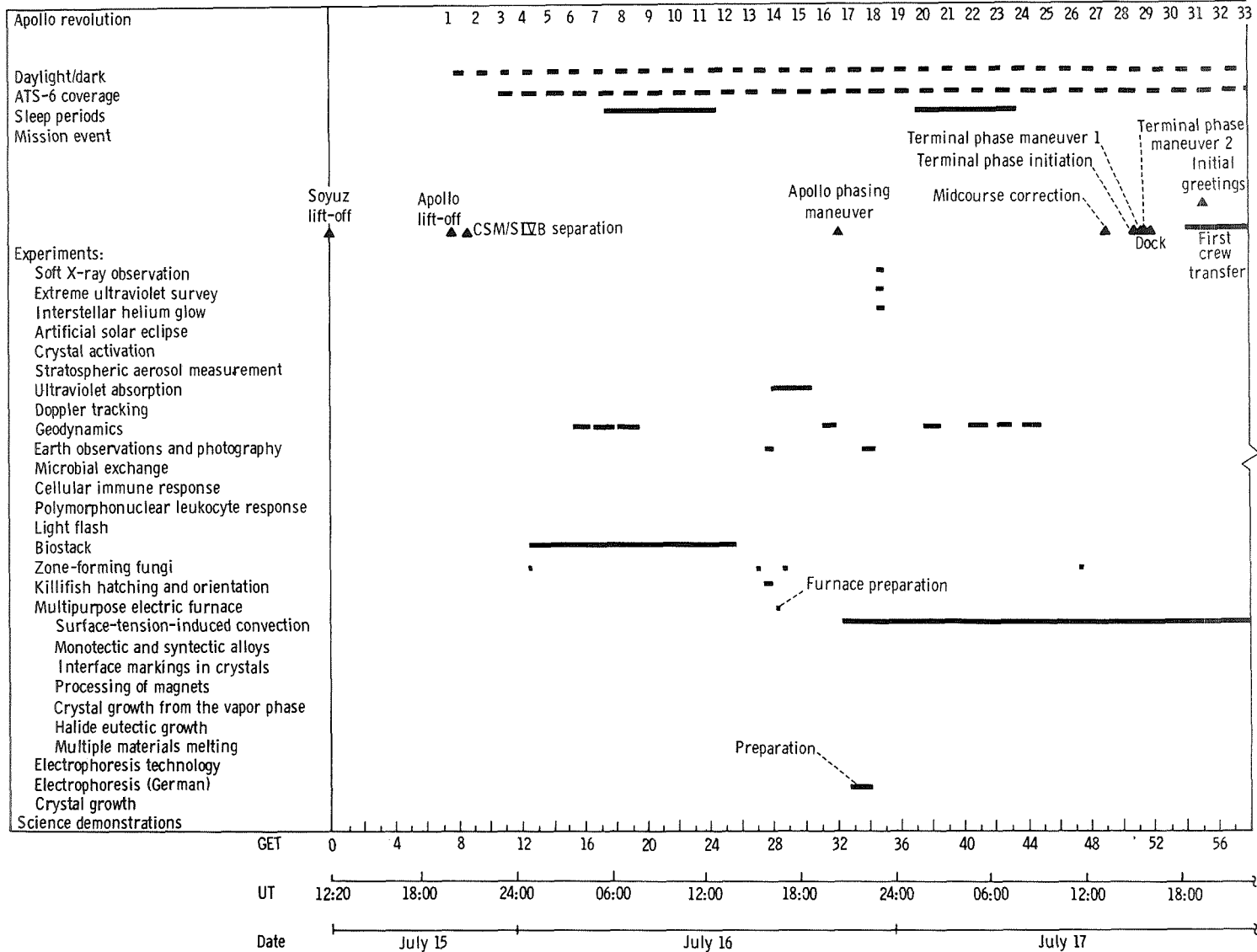


FIGURE 2-7.—Major mission events and data collection periods correlated to UT and GET.



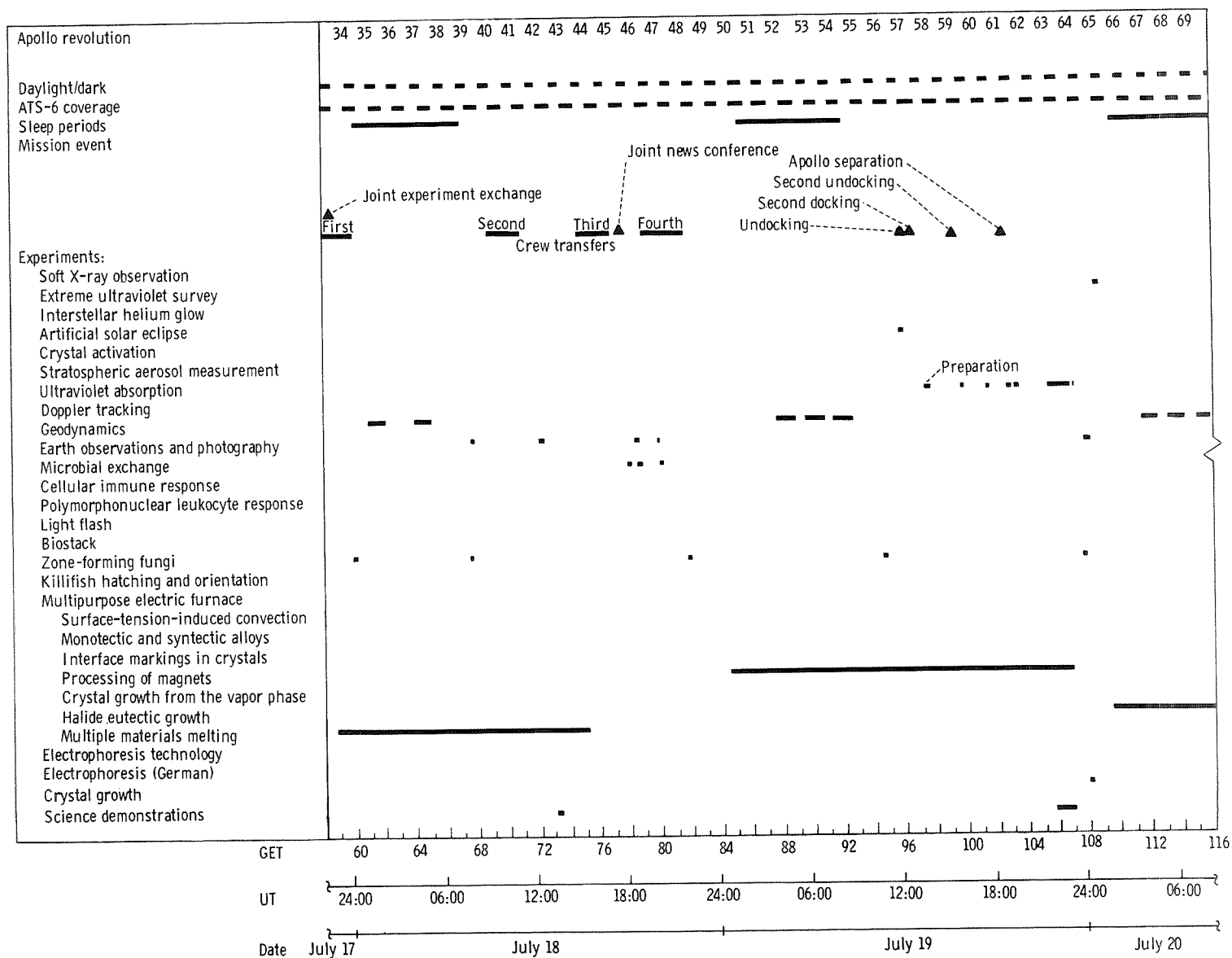


FIGURE 2-7.—Continued.

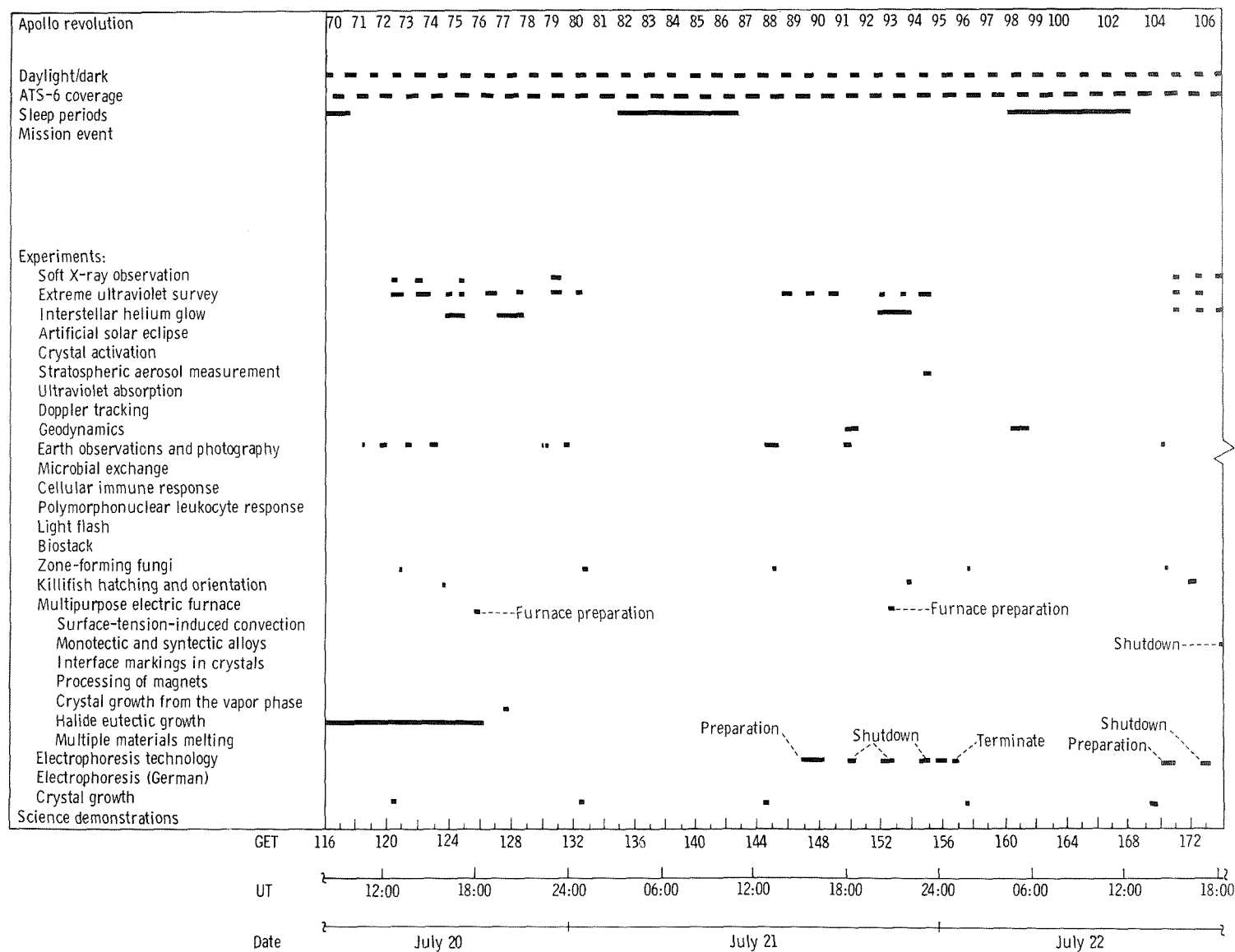


FIGURE 2-7.—Continued.

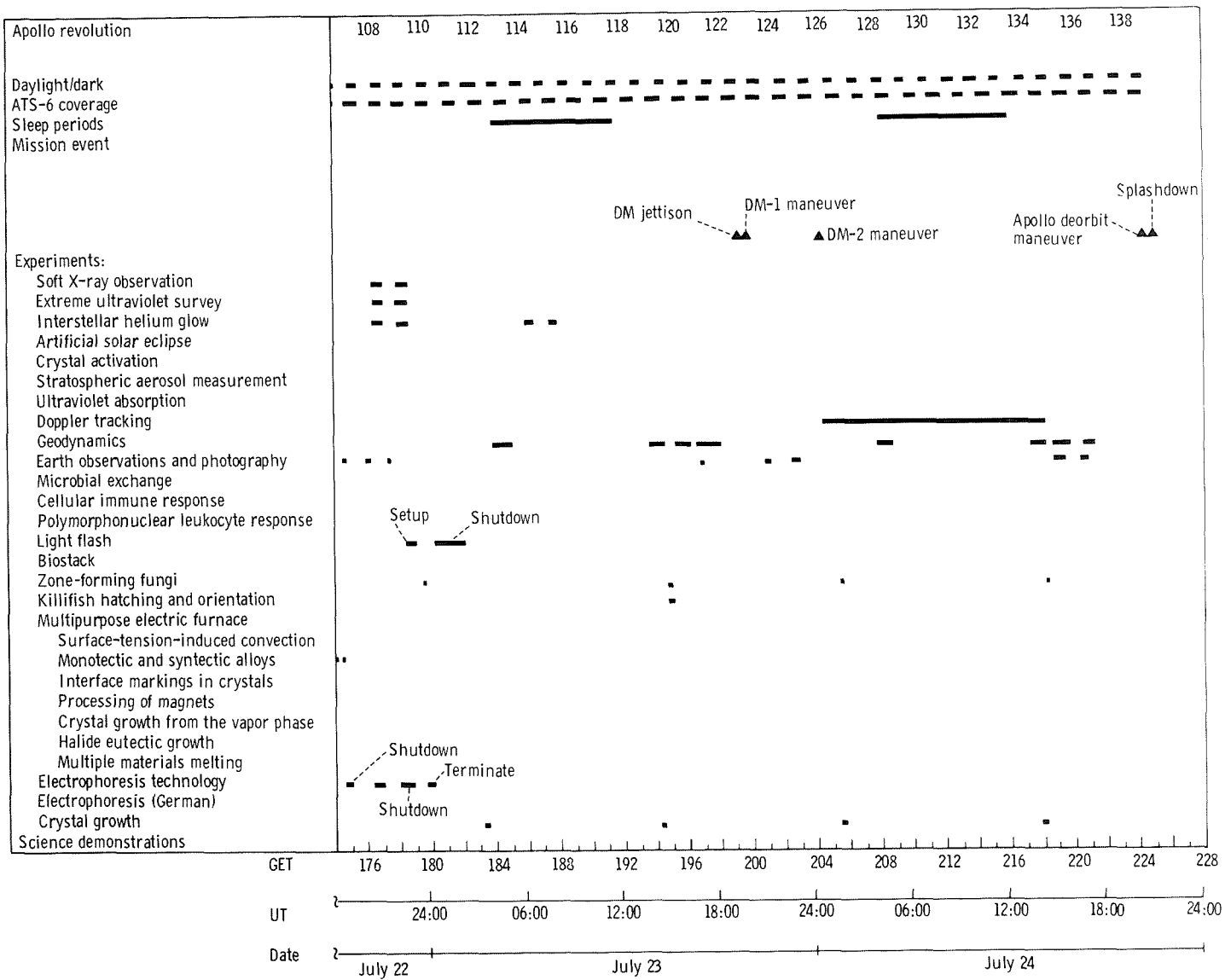


FIGURE 2-7.—Concluded.

Apollo out-of-plane data was obtained and a spacecraft test roll maneuver of  $360^\circ$  was performed to measure resonant fluorescence background and ambient atmosphere gas pileup. The experiment was shut down at 107:07 GET.

The multipurpose furnace zero-g processing of magnets was concluded at 106:50 GET, and the Halide Eutectic Experiment was initiated in the furnace at 109:20 GET. In the interim, zone-forming fungi photographs and Earth observations were made; the Crystal Growth Experiment (CGE) was initiated; and a raster scan for the extreme ultraviolet survey was made. After several Geodynamics Experiment data takes and several Earth observations, the extreme ultraviolet experiment was started. The Crystal Growth and Zone-Forming Fungi Experiments were then examined and photographed before the Helium Glow Experiment scans were made. Helium glow data-take periods consisted of sweeping the  $15^\circ$  field of view across regions of the celestial sphere by rolling the Apollo spacecraft about the longitudinal axis. Several excellent roll scan data takes were made. The killifish observations were again made during this period.

Extreme ultraviolet and helium glow scans, Earth observations, geodynamics data takes, and crystal growth and zone-forming fungi observations were continued at intervals; the multipurpose furnace Crystal Growth From the Vapor Phase Experiment was conducted; and the Biostack III Experiment was turned on at 132:00 GET. The Electrophoresis Technology Experiment was initiated at 147:30 GET and was shut down at 152:10; it was started again 18 hours later. The Stratospheric Aerosol Measurements (SAM) Experiment operations were initiated at 154:30 GET, and shutdown occurred at 158:00 GET. The multipurpose furnace Interface Marking in Crystals Experiment was also conducted during this period, as was the Monotectic and Syntectic Alloys Experiment.

During revolution 109, an extreme ultraviolet finding of special significance was made when an intense EUV source was discovered. This discovery was the first known detection of a cosmic source of extreme ultraviolet radiation. The Light Flash Observations Experiment was also initiated during revolution 109. The unmanned portion of

this experiment started at 179:13 GET, and the manned portion was initiated during the following revolution. These times were selected so that the two data-take periods would include passage through the South Atlantic Anomaly and would be descending passes (i.e., from northwest to southeast) to provide data at the maximum available geomagnetic latitude and to provide South Atlantic Anomaly data. Periodic zone-forming fungi, geodynamics, crystal growth, Earth observations, helium glow, killifish experiment, soft X-ray, and electrophoresis technology operations were also conducted during this period.

The docking module was jettisoned at 199:27 GET to prepare for the Doppler Tracking Experiment, which required a 300-km separation of the command and service module from the docking module. After jettison, the Apollo crew photographed the docking module and then maneuvered the command and service module to the same orbit as the docking module at a range of 300 km. The data-take period began at 204:20 GET and continued for approximately 14 hours with intentional command and service module attitude changes during the interim. During these 14 hours, periodic crystal growth, zone-forming fungi, geodynamics, and Earth observations operations were continued.

### **Apollo Deorbit and Landing**

After several minor changes in orbit (during the joint phase and the orbit continuation phase) due to decay and maneuvers, the final Apollo orbit was a nominal 213 km with a 13-km difference between apogee and perigee. The Apollo deorbit maneuver was performed at 224:17 GET; and, after a flight of 217 hours 28 minutes, the command module landed approximately 1.3 km from the target point. The time of splashdown was 21:18 UT on July 24, 1975. The command module assumed the stable II attitude for approximately 4.5 minutes after splashdown. The crew remained in the command module during recovery operations and were onboard the U.S.S. *New Orleans* approximately 41 minutes after splashdown.

After shipboard ceremonies, during which the crewmen appeared to be in good condition, it was

learned that they had been exposed to oxidizer vapors for several minutes when an arming function and a manual backup function were overlooked during the entry phase of the mission. The crewmen were immediately given intensive medical care. The necessary changes in medical examination schedules and the therapy given the crew potentially affected the Cellular Immune

Response Experiment and the Polymorphonuclear Leukocyte Response Experiment. These experiments were complementary experiments that were conducted by preflight and postflight blood sampling and analysis. Despite this impact, scientifically useful results were obtained in these experiments.



### 3. Soft X-Ray Observations

#### Experiment MA-048

*S. Shulman,<sup>a</sup> S. Naranan,<sup>ab</sup> W. Snyder,<sup>c</sup> D. Yentis,<sup>a</sup> R. Cruddace,<sup>a</sup> H. Friedman,<sup>a†</sup> G. Fritz,<sup>a</sup> and R. Henry<sup>c</sup>*

#### ABSTRACT

The Soft X-Ray Experiment was designed to observe celestial X-ray sources in the energy range from 0.1 to 10 keV. The X-ray spectra and fast-time variability were measured to characterize the emission from a number of such sources. A new X-ray pulsar was discovered, and a new X-ray-emitting supernova remnant was detected.

#### OBJECTIVES

The objectives of the Apollo-Soyuz Test Project (ASTP) Soft X-Ray Experiment were to study the spectra of a large number of known celestial X-ray sources in the range from 0.1 to 10 keV, to search for periodicities and other variability in these sources, and to more precisely map the soft X-ray diffuse background. Celestial X-ray sources have been observed from rockets and satellites for approximately a decade, and more than 200 sources have been located. Figure 3-1 is a map of the sky in galactic coordinates showing the sources located by the *Uhuru* small astronomy satellite (SAS-1). The concentration in the galactic plane indicates a class of sources within the galaxy, and the uniform distribution at high latitudes indicates a class of extragalactic objects.

The objective of spectral measurements in the range from 0.1 to 10 keV is twofold. First, detailed comparison of the spectra of many sources would provide the capability to classify X-ray sources more precisely in terms of the X-ray emission mechanism and the relevant physical parameters such as size, density, temperature, magnetic field strength, and relativistic particle content. Second, the low-energy parts of the spectra (less than 2 keV) are affected by absorption in the intervening interstellar material. A measure of the absorption can be used to establish a fairly precise distance scale for the X-ray sources. The distances in turn yield the absolute luminosities and the relationship to other features of galactic structure such as the spiral arms.

The search for periodicities and fast-time variability was conducted by recording the counts in 3-millisecond intervals for three broad energy bands. The objective was to search for new pulsars (presumably rotating neutron stars) and for other types of sources where intensity variations on a fast-time scale might provide information on the source structure, size, and emission mechanisms.

The third objective of the experiment was to map the soft X-ray background. At energies of approximately 0.25 keV, there is an observable diffuse emission from all directions in the sky. Figure 3-2 is a map obtained from data taken during an Aerobee rocket flight. To map a significant portion of the sky during the 5-minute flight, a wide field of view (10° by 10°) and a rapid scan rate were used. As a result, the statistical precision of the map is poor, and the minimum contrast features that can be detected are quite bright. The increased observing time available with the ASTP instrument provided the opportunity to use a 4°

---

<sup>a</sup>Naval Research Laboratory.

<sup>b</sup>On leave from Tata Institute of Fundamental Research, Bombay, India.

<sup>c</sup>Johns Hopkins University.

<sup>†</sup>Principal Investigator.



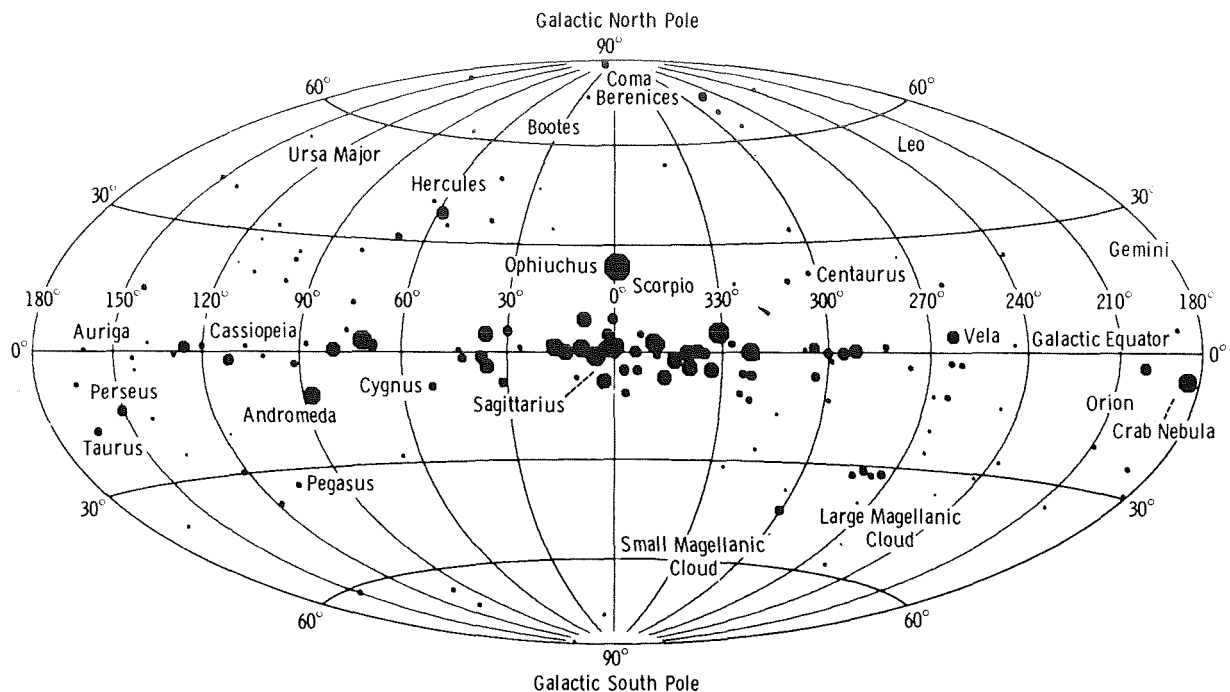


FIGURE 3-1.—Map of 2- to 10-keV X-ray sources as determined by the *Uhuru* satellite.

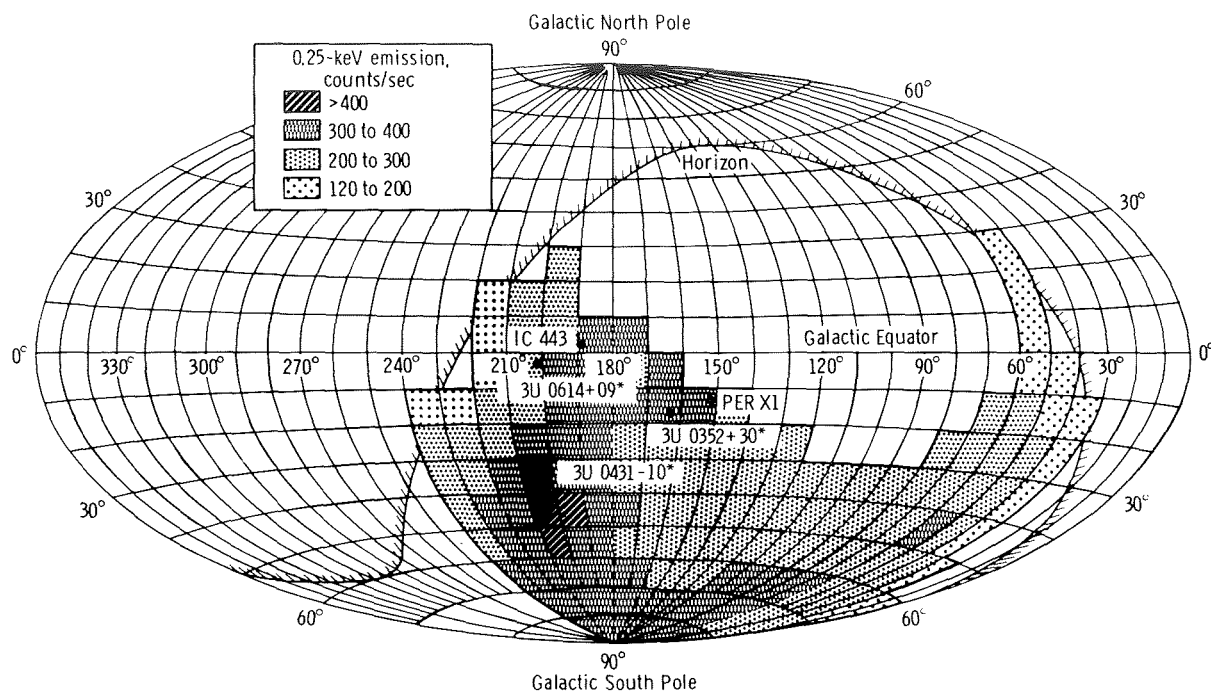
by 4° field of view and to obtain approximately 10 times as much data in each resolution element. With increased resolution, an attempt is being made to determine the origins of the soft X-ray diffuse background.

### INSTRUMENT DESCRIPTION

The X-ray instrument is a large-area proportional counter very similar to those that have been flown on sounding rockets by several groups. The proportional counter detects individual X-ray photons when they interact in the detector gas. This interaction produces photoelectrons that drift toward a high-voltage anode and produce secondary electrons. In the high electric field region near the anode, the secondary electrons initiate an electron avalanche, which produces an electronic pulse that can easily be amplified and detected. In the proportional counter (as opposed to the Geiger counter), the total charge in the avalanche pulse is proportional to the original number of sec-

ondary electrons; thus, information about the energy of the detected X-ray is preserved.

The detector gas is a standard mixture of 90 percent argon and 10 percent methane (P10 gas) at  $110 \text{ kN/m}^2$  (1.1 atm). The detector anodes are nominally operated at 2700 V, and the instrument contains a feedback system to adjust this voltage to keep the gain constant during variations in detector temperature. The gas is contained by a  $2\text{-}\mu\text{m}$  polycarbonate window that requires an elaborate support structure to withstand the  $110\text{-kN/m}^2$  (1.1 atm) pressure. This thin window is necessary to permit the detection of X-rays in the 0.1- to 2-keV energy range: these X-rays would be absorbed by more conventional window materials such as  $50\text{-}\mu\text{m}$  beryllium. Aluminum honeycomb is part of the window support structure and also provides the instrument collimation that gives a circular field of view with a full-width half-maximum (FWHM) response of 4°. The effective area for X-ray detection is  $1200 \text{ cm}^2$ . The front face of the detector, including the honeycomb and support ribs, is shown in figure 3-3.



\* Source designations from the Uhuru catalog.

FIGURE 3-2.—Map of diffuse 0.25-keV X-ray emission from a Naval Research Laboratory (NRL) rocket observation.

Because a thin window is required for the low-energy X-ray observations, a gas supply is required to replenish gas that escapes through small pinholes in the window. Typical leak rates into vacuum range from 10 to 100 cm<sup>3</sup> Pa/min (10 to 100 cm<sup>3</sup> atm/min). A 30.5-cm (12 in.) diameter reservoir tank was incorporated into the experiment and was pressurized to 17 000 kN/m<sup>2</sup> (170 atm) approximately 35 days before launch. With this gas supply system, the detector could also be completely emptied and refilled by astronaut command to remove atmospheric contaminants that diffused into the detector before launch. The gas tank is a prominent feature in the rear view of the instrument shown in figure 3-4.

The electronic design of the instrument is shown in figure 3-5. There are two sets of anodes in the detector, one for X-ray data and one for the veto of charged particles. Each set has a separate preamplifier and discriminator. A data pulse is accepted and analyzed only if no pulse is detected within a few microseconds in the veto section. Data pulses that are accepted are then pulse height

analyzed, and the pulse height is stored for telemetry readout. The analysis is accomplished by a 9-bit analog-to-digital (A-D) converter that uses a successive approximation scheme. Each pulse height is also sorted into one of three energy bins for accumulation in the 3-microsecond fast-timing bins. The electronics are mounted on the rear of the detector as shown in figure 3-4.

The crucial parameters of gain and resolution were measured during laboratory calibrations. These parameters are required to determine the spectrum of X-rays incident on the detector. The detector response is convolved with the incident photon spectrum to give the counts observed in each pulse-height bin of the spectral data. Mathematically, this is described as follows:

$$N(V_1, V_2) = \int_{E_1=G(V_1)}^{E_2=G(V_2)} dE \int_0^\infty T(E') A(E') R(E', E) N(E') dE' \quad (3-1)$$

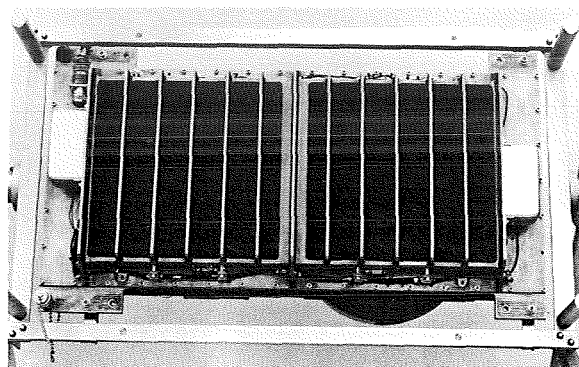


FIGURE 3-3.—Front view of the ASTP X-ray detector.

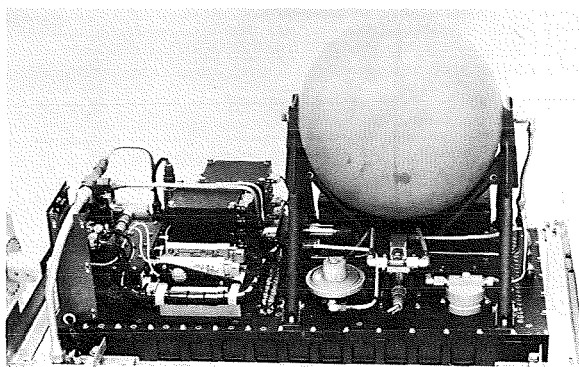


FIGURE 3-4.—Rear view of the ASTP X-ray detector with the electromagnetic interference shield removed.

where  $N$  is the counting rate,  $V_1$  and  $V_2$  are the boundaries of the pulse-height channel,  $T(E')$  is the window transmission as a function of energy,  $A(E')$  is the gas absorption as a function of energy,  $R(E', E)$  is the resolution function,  $N(E')$  is the incident photon spectrum, and  $G(V)$  is the pulse-height gain function. The functions  $T$  and  $A$  can be calculated from measurements made at a number of different laboratories. The gain  $G(V)$  and the resolution function  $R(E', E)$  are determined by laboratory calibrations with monochromatic X-rays incident on the detector. The peak in the spectral data yields the gain, and

the shape of the spectral data yields the resolution function. At most energies, the resolution function is Gaussian; however, at low energies, a Poisson function gives a better fit because the parameters must all be greater than zero.

The gain calibration is given in figure 3-6. Energy is plotted as a function of channel number rather than channel voltage. The instrument gain is linear to within 10 percent over the entire range from 0.1 to 8 keV. A significant nonlinearity of approximately 10 percent is noticeable at the higher energies. The resolution function averaged over the entire sensitive area of the detector at an

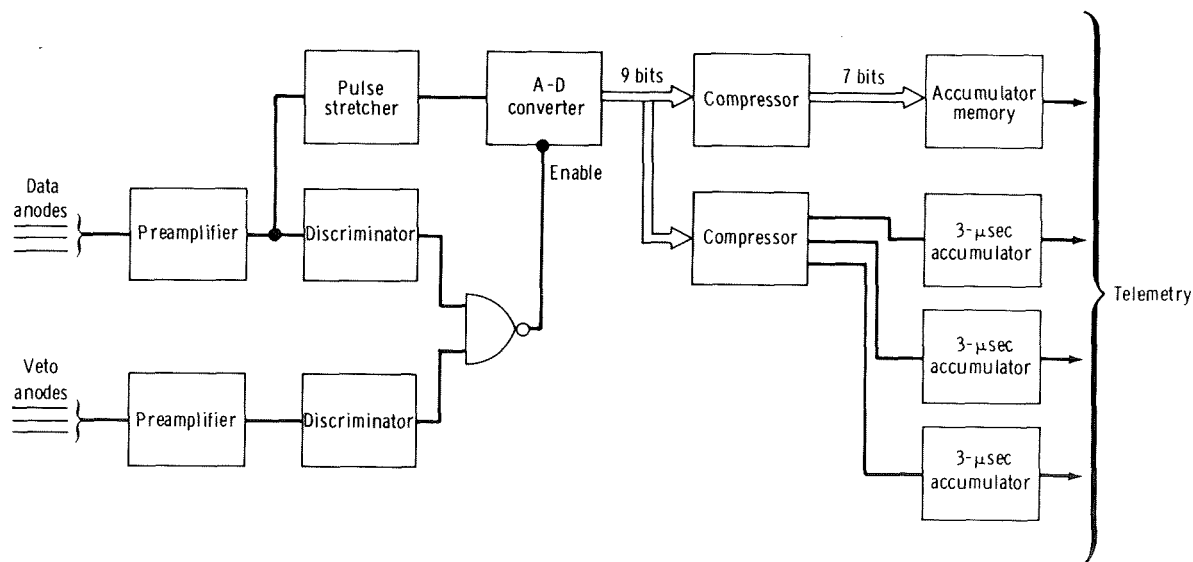


FIGURE 3-5.—Simplified block diagram of the detector electronics.

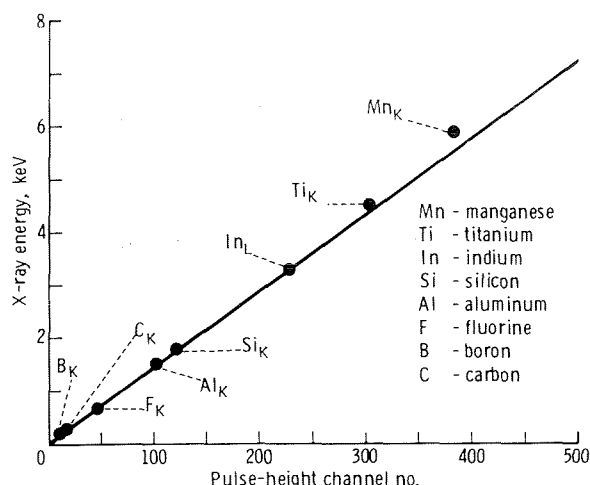


FIGURE 3-6.—Laboratory gain calibration of the ASTP detector.

energy of 5.98 keV ( $Mn_K$ ) is shown in figure 3-7. The FWHM of the function is approximately 27 percent. The FWHM at any single point in the detector is considerably better (approximately 20 percent), but slight gain variations from point to point broaden the average resolution. The FWHM resolution is plotted as a function of energy in figure 3-8.

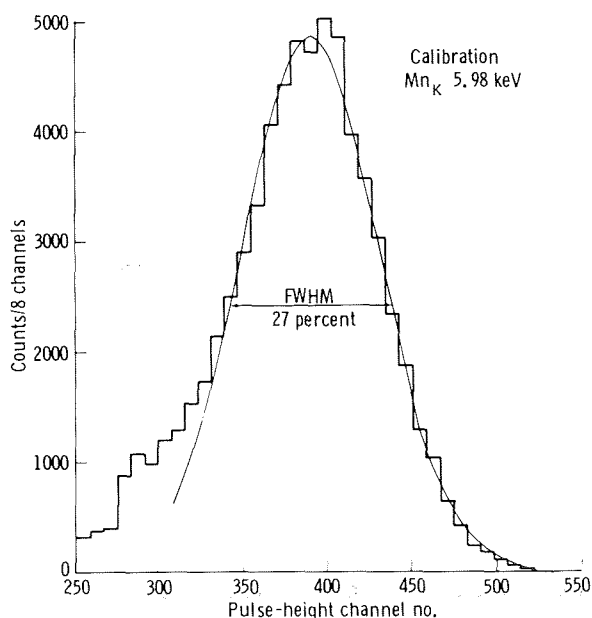


FIGURE 3-7.—Laboratory calibration spectrum of the  $Mn_K$  X-ray line at 5.98 keV.

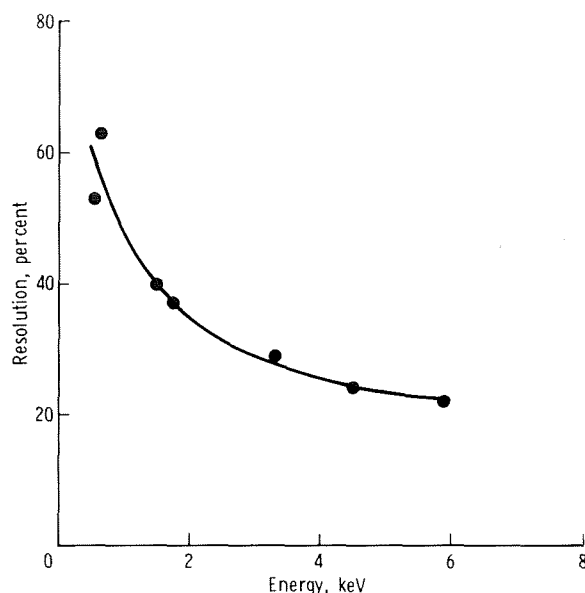


FIGURE 3-8.—Detector resolution as a function of energy calibration.

A quick in-flight calibration was provided by two radioactive sources mounted on rotary solenoids, which could be switched into the detector field of view by astronaut command. The housings for these assemblies are shown mounted to the end ribs in figure 3-3.

The flight window was installed on the detector in April 1975. The leak rate measured in vacuum was approximately  $3 \text{ cm}^3 \text{ Pa/min}$  ( $3 \text{ cm}^3 \text{ atm/min}$ ). This rate remained stable through testing, installation, and launch. No degradation was observed during the flight.

### IN-FLIGHT ANOMALIES

The X-ray experiment was activated together with the other scientific instrument bay experiments approximately 35 hours after launch. Several minutes after the initial activation and calibration, an excessively high count rate was noted in the lowest spectral channels. This pattern of several minutes of normal operation followed by a period of high count rates was observed several times during the mission. The problem apparently was caused by a high-voltage breakdown.

Problems with high-voltage breakdown in proportional counters have been evident in all programs using these detectors. In addition to the usual problems of component failures and potting breakdowns, the gas gain region of the detector amplifies any discharge or breakdown caused by sharp points, metal chips, or inadequate spacing of elements. The following paragraphs give a brief operating history for the flight.

The X-ray experiment was operated on day 5 during the raster scan for the Extreme Ultraviolet Survey (EUV) Experiment. The count rates went full scale, and a gas purge was scheduled in anticipation of a possible instrument problem. After purging, the instrument was operated on the sixth day of flight, and 25 minutes of satisfactory data were obtained before the problem reappeared. On day 7, a test was performed in which the instrument was operated with the high voltage on for 2 minutes and then off for 2 minutes. The instrument operated properly for approximately 3 of the 5 minutes during which the high voltage was on. The experiment operation procedure for day 8 was revised to incorporate the 2-minute-on mode of operation, and at least 30 more minutes of satisfactory data were obtained.

On days 8 and 9, an engineering test was performed in an attempt to determine the cause of the instrument malfunction. At the end of the data take on day 8, the instrument was left in a "contingency powerdown" mode, which evacuated the gas volume of the detector. The detector was allowed to pump down to a hard vacuum overnight, and, on day 9, the high voltage was turned on with no gas in the detector. No counts at all were observed for 30 minutes or longer. This result indicated that the malfunction occurred in the gas gain volume of the detector. High-voltage potting, power supplies, and the other high-voltage components external to the gas volume of the detector were thus eliminated as possible causes of the malfunction.

The high voltage was turned off, the detector gas volume was refilled to a nominal pressure of  $110 \text{ kN/m}^2$  (1.1 atm), and the high voltage was activated again. The detector malfunction reappeared in approximately 2 minutes, thus reaffirming the conclusion that the malfunction occurred in the gas volume of the detector.

The available data are currently being interpreted to hopefully obtain a better understanding of this malfunction. Several hypotheses have been suggested, and some laboratory tests may be needed to determine whether the characteristics of the problem can be reproduced. At present, however, no simple hypothesis convincingly explains both the intermittent nature and the preponderance of low-energy spectral counts.

Another instrumental anomaly occurred during the flight when a calibration source stuck in the field of view of the detector. The problem first occurred during the initial activation on July 21. The calibration source retracted after several momentary applications of power by the astronauts; however, the source was observed in the field of view again several orbits later, apparently because of inadvertent crew operations. No further efforts were made to dislodge the source because of the astronaut workload and the number of changes that would have been required in the Flight Plan.

In contrast to the high-voltage breakdown, the calibration source was viewed as a relatively minor problem. In analyzing the data, most of the X-ray counts caused by the calibration source can be subtracted because they occur in a narrow spectral range. (The source was iron-55 ( $^{55}\text{Fe}$ ), which emits  $\text{Mn}_K$  X-rays at an energy of 5.9 keV.) The subtraction, however, does introduce some additional statistical uncertainties into the results.

## OBSERVATIONS AND RESULTS

In spite of the instrumental problems encountered, several important observations were made with the Apollo-Soyuz X-ray instrument. Spectra of sources were obtained, regions of enhanced emission in the X-ray background were detected, and a new X-ray pulsar was detected. Thus, all the original objectives were met, although in a limited way, and the capabilities of a large-area X-ray detector with wide spectral and timing capabilities combined with a very flexible spacecraft system were effectively demonstrated. In the following subsections, the results of the most important observations are discussed in detail for each of the sources.

### SMC X-1

The source SMC X-1 was first discovered in a rocket flight (ref. 3-1) and then found to be a binary system in *Uhuru* satellite data (ref. 3-2). The binary period is 3.9 days. An optical identification has been made with a BO supergiant in the Small Magellanic Cloud (SMC). It is believed that X-rays are produced in such binary systems when matter flows from a star (such as a supergiant) onto an unseen, compact companion (i.e., a white dwarf, a neutron star, or a black hole). In several instances, a neutron star is present and its rotation produces a pulsed modulation of the X-ray emission. One of the principal reasons for the Apollo-Soyuz observation was to search for such pulsed emission.

The Apollo observation was made at 18:50 UT on July 20, 1975. The detector was scanned toward the source by a spacecraft maneuver at a rate of  $0.5^\circ \text{ sec}^{-1}$  yielding 30 seconds of off-source background data. The detector was pointed to within  $1^\circ$  of SMC X-1 for approximately 300 seconds. However, only the first 190 seconds of data are useful because the high-voltage breakdown problem occurred during the latter part of this period. The data were searched for periodicities both by Fourier analysis techniques and by folding the data modulo the suspected periods. A 0.7157-second period was detected. The pulse profiles ob-

tained by folding the data modulo this period are shown in figure 3-9. Each bin represents the superposition of 265 36-millisecond data accumulations, and the data are displayed twice to show two full periods. The 1.6- to 7-keV data show a clear double-pulse structure with both peaks nearly equal in intensity. The off-source background is 393 counts/sec, so there is a substantial rate (400 counts/sec) from the source that is not pulsed. The pulsed fraction, or ratio of pulsed to unpulsed intensity, is 25 to 30 percent at 1.6 to 7 keV. At the lower energies (0.6 to 1.6 keV), the characteristics change dramatically. No pulsations were detected with an upper limit on the pulsed fraction of 10 percent.

A detailed spectrum of SMC X-1 was obtained and is shown in figure 3-10. The data are "best fit" by the following power law incorporating absorption by interstellar material.

$$\frac{dN}{dE} = 0.04E^{-0.8 \pm 0.1} \left[ \exp -\sigma(E) N_H \right] \quad (3-2)$$

where the interstellar hydrogen column density  $N_H$  is in the range of 0 to  $2 \times 10^{21}$  atoms/cm<sup>2</sup> and  $\sigma$  is the energy-dependent attenuation cross section per hydrogen atom. This spectrum is consistent with that found by the Orbiting Solar Observatory 7 (OSO-7) hard X-ray experiment (ref. 3-3) in the energy range 7 to 35 keV.

The Small Magellanic Cloud is a small galaxy 63 kpc (1 pc = 3 light-years) away from the Milky Way. At this distance, the observed X-ray luminosity of SMC X-1 is approximately  $3 \times 10^{31}$  J/sec ( $3 \times 10^{38}$  ergs/sec), making it the most luminous binary X-ray source. The pulsations detected by the Apollo experiment have a period of 0.7157 second, making the SMC X-1 the binary source with the shortest pulsing period. The regular pulsations also indicate that the compact member is a rotating neutron star. Further observations of the pulsations will enable an orbital Doppler shift to be measured, which in turn will yield an accurate mass for the neutron star. Observations of long-term pulse period decreases will yield information on the transfer of angular momentum in the accretion process.

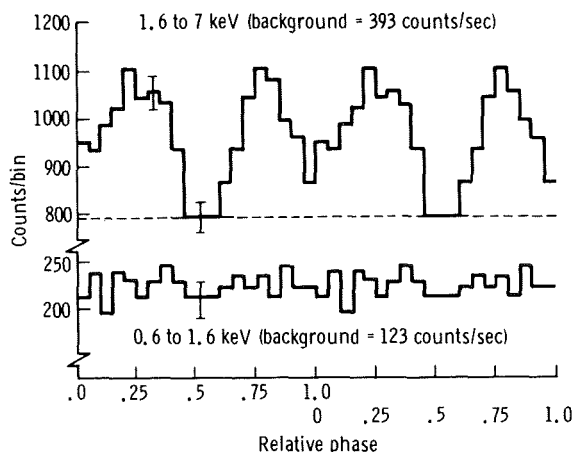


FIGURE 3-9.—Pulse profiles obtained by folding the data modulo the 0.7157-second period. The data are plotted twice to show the full profile. The dashed line indicates the estimated level of continuous emission.

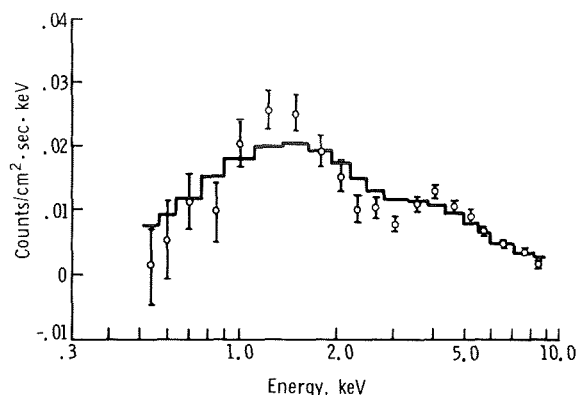


FIGURE 3-10.—The X-ray spectrum of SMC X-1. The solid line is the “best fit” power law model described in equation (3-2).

### Extended Low-Energy Sources

In spite of the limited coverage obtained, at least two important observations of extended structure in the soft X-ray background were obtained. Both regions were observed to be brighter than their surroundings in the 0.6- to 2-keV band. No such enhancement was seen in the 0.18- to 0.28-keV band, probably because the regions lie close to the galactic plane where the interstellar medium absorbs the lower energy X-rays.

The first such region observed was in the constellation Centaurus. A comparison of the 0.6- to 2-keV count rate with that in adjacent regions indicates an excess of  $0.084 \text{ count/cm}^2 \cdot \text{sec}$ . The position of maximum intensity is within  $1^\circ$  of a known radio supernova remnant ( $\alpha = 14^{\text{h}}39^{\text{m}}$ ,  $\delta = -62^\circ15'$ ; ref. 3-4), and it is suggested that this same object is also the source of the X-ray emission. The regions scanned and the location of the supernova remnant are shown in figure 3-11. The distance to the supernova remnant is estimated to be 2.5 kpc, implying an X-ray luminosity of  $2 \times 10^{28} \text{ J/sec}$  ( $2 \times 10^{35} \text{ ergs/sec}$ ). The distance is consistent with the lack of observed 0.18- to 0.28-keV X-rays, and the luminosity and diameter are consistent with a remnant similar in age ( $10^4$  years) and total energy to the Cygnus Loop.

The X-ray spectrum of this source is shown in figure 3-12. The spectrum is best accounted for by

bremsstrahlung from a hot plasma at a temperature of  $3 \times 10^6 \text{ K}$  with an interstellar hydrogen column density of  $5 \times 10^{21} \text{ atoms/cm}^2$ .

A second extended source was observed in the constellation Cygnus. It was observed previously on a rocket flight (ref. 3-5) and was designated Cyg X-6. However, because of the Apollo-Soyuz observation and another NRL rocket observation, the source was recently shown to be extended. It does not coincide with any known radio or optical supernova remnant and, in fact, is not circular in shape but rather an elongated  $1^\circ$  by  $8^\circ$  filament. The spectrum, shown in figure 3-13, is remarkably similar to that found for the Centaurus supernova remnant. The best fit is for a hot plasma at  $3 \times 10^6 \text{ K}$  with an intervening hydrogen column density of  $8.5 \times 10^{21} \text{ atoms/cm}^2$ , suggesting again that the source is at least 2 kpc away.

The nature of Cyg X-6 is of considerable interest. The elongated shape suggests that it is not a single supernova remnant. It is possible that Cyg

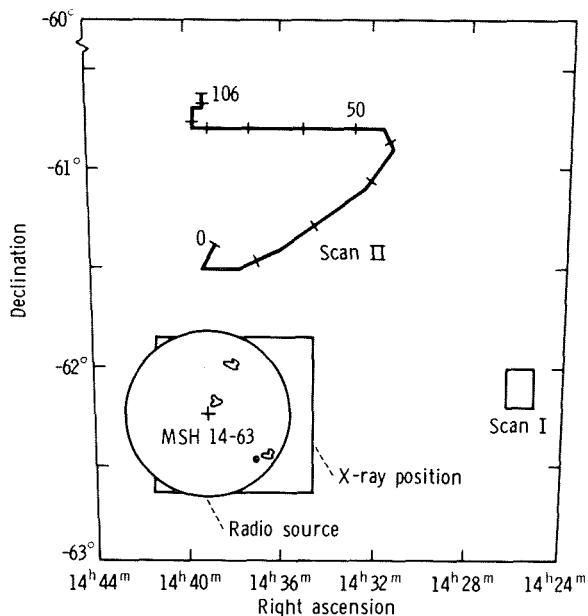


FIGURE 3-11.—Map of the region MSH 14-63 showing the Apollo scans. The best estimate of the X-ray source position is indicated. The small patches inside the remnant represent the locations of optical filaments, and the dot near the southwest rim indicates the location of the strongest continuum radio emission. Scan II is divided into time periods from 0 to 106 seconds.



X-6 is an example of an intersecting chain of remnants of the type predicted theoretically by Cox and Smith (ref. 3-6). They show that such chains are likely to occur, given the known frequency of supernova explosions and a plausible model for their evolution. When remnants do intersect, the newer one will reheat the older remnant, thus extending its X-ray-emitting lifetime.

If the minimum distance to the source suggested by the spectrum is correct, then the  $1^\circ$  by  $8^\circ$  structure is enormous, covering projected distances of 35 by 300 pc. Because the  $8^\circ$  (300 pc) extension is almost perpendicular to the galactic plane, it extends far above the 75- to 100-pc scale height of the neutral hydrogen disk. Such large hot plasma structures may be quite important both as a source of plasma that produces the soft X-ray background and as a means of redistributing that plasma into the galactic halo from its principal source in supernova events which occur primarily inside the neutral hydrogen disk.

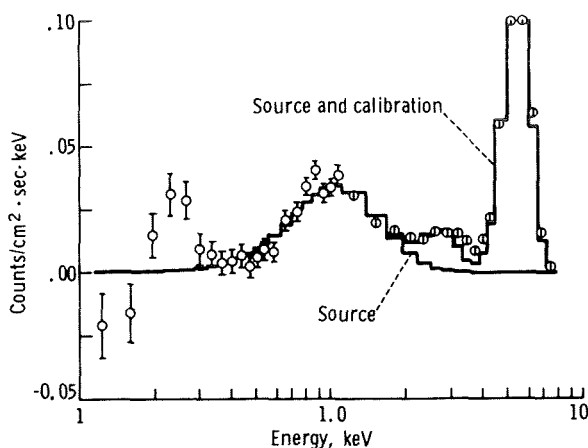


FIGURE 3-13.—The X-ray spectrum of Cyg X-6. The solid lines are the “best fit” thermal bremsstrahlung model described in the text. Top line shows the theoretical spectrum with the addition of the 5.89-keV line due to the  $^{55}\text{Fe}$  calibration source that failed to retract properly.

### HZ 43

The white dwarf HZ 43 was observed by both the University of California EUV telescope and the NRL X-ray instrument. The EUV measurements indicate that the star has a black-body spectrum at a temperature of approximately 110 000 K. The X-ray observation detected the source at wavelengths less than 10 nm (100 Å) (energies above 0.1 keV), which is far from the emission peak at 30 nm (300 Å). Figure 3-14 shows the X-ray count rates in three energy bands and shows the variations in the position of the source in the field of view. A significant signal was detected in both the 0.18- to 0.28-keV and 0.6- to 2-keV bands. The 0.18- to 0.28-keV count rate of  $(16.2 \pm 1.8) \times 10^{-3}$  count/cm<sup>2</sup> · sec is consistent with the black-body spectrum observed by the EUV telescope. However, the 0.6- to 2-keV count rate of  $(6.3 \pm 1.0) \times 10^{-3}$  count/cm<sup>2</sup> · sec is more than 100 times larger than predicted for a 110 000-K black body. The investigators searched for other sources that might have been in the field of view simultaneously and found that the coma cluster of galaxies, a known X-ray source (ref. 3-7), was seen at about 10 percent of peak response and can account for the observed 0.6- to 2-keV signal.

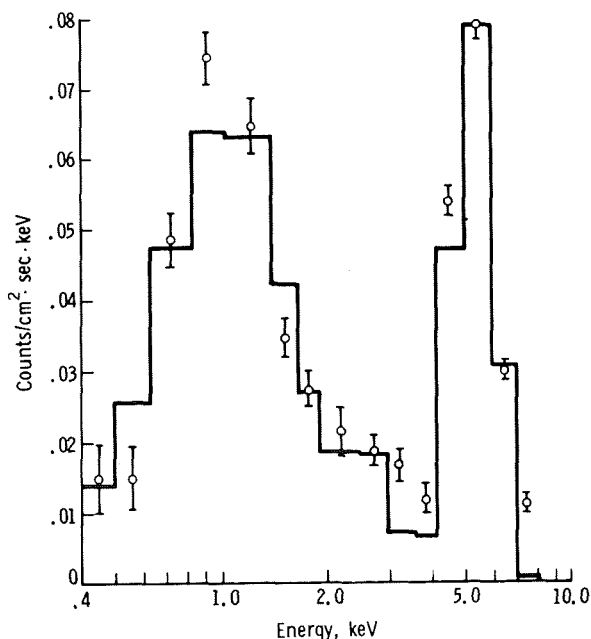


FIGURE 3-12.—The X-ray spectrum of the supernova remnant MSH 14-63. The solid line is the “best fit” thermal bremsstrahlung model (described in the text) with the addition of a 5.89-keV line due to the  $^{55}\text{Fe}$  calibration source that failed to retract properly. (See subsection entitled “In-Flight Anomalies.”)

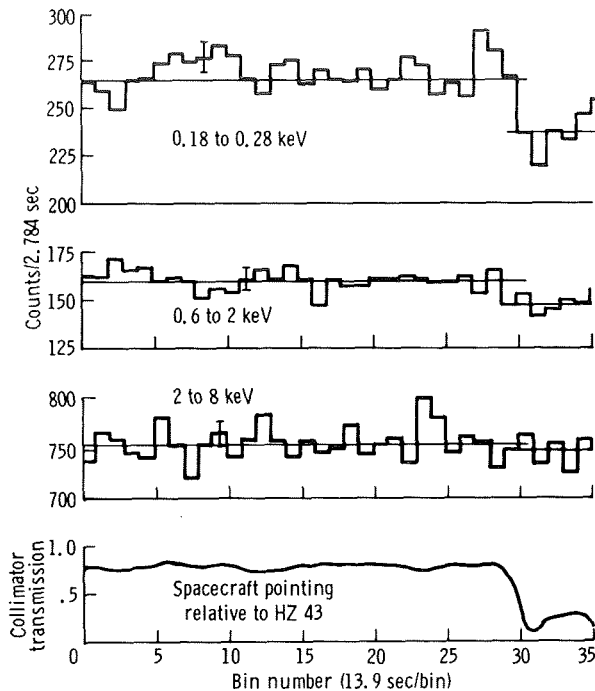


FIGURE 3-14.—Counting rates in three energy bands during the observation of HZ 43. The variation in the collimator response to the source as the spacecraft maneuvered is also shown. The horizontal lines indicate the average “on-source” rates in each energy band.

It appears, therefore, that HZ 43 has a spectrum that can be entirely accounted for by a black-body emission at 110 000 K. No evidence has been found for X-ray emission from a hot corona or for accretion at temperatures on the order of  $10^6$  to  $10^7$  K. Any such emission must be less than  $5 \times 10^{-18} \text{ J/cm}^2 \cdot \text{sec}$  ( $5 \times 10^{-11} \text{ erg/cm}^2 \cdot \text{sec}$ ) in the energy range 0.6 to 8 keV.

## REFERENCES

- 3-1. Price, R. E.; Groves, D. J.; et al.: X-Rays From the Magellanic Clouds. *Astrophys. J. (Letters)*, vol. 168, 1971, pp. L7-L9.
- 3-2. Schreier, E.; Giacconi, R.; et al.: Discovery of the Binary Nature of SMC-1 From *Uhuru*. *Astrophys. J. (Letters)*, vol. 178, 1972, pp. L71-L75.
- 3-3. Ulmer, M. P.; Baity, W. A.; Wheaton, W. A.; and Peterson, L. E.: Observations of the Binary X-Ray Source SMC X-1 From OSO-7. *Nature Phys. Sci.*, vol. 242, no. 121, 1973, pp. 121-123.
- 3-4. Downes, D.: New Radio Results on Supernova Remnants. *Astronom. J.*, vol. 76, May 1971, pp. 305-316.
- 3-5. Coleman, P. L.; Bunner, A. N.; Kraushaar, W. L.; and McCammon, D.: X-Ray Observation of a New Soft Source in Cygnus. *Astrophys. J. (Letters)*, vol. 170, 1971, pp. L47-L49.
- 3-6. Cox, Donald P.; and Smith, Barham W.: Large-Scale Effects of Supernova Remnants on the Galaxy: Generation and Maintenance of a Hot Network of Tunnels. *Astrophys. J. (Letters)*, vol. 189, 1974, pp. L105-L108.
- 3-7. Meekins, John F.; Fritz, Gilbert; Chubb, Talbot A.; and Friedman, H.: X-Rays From the Coma Cluster of Galaxies. *Nature*, vol. 231, 1971, pp. 107-108.

## 4. Extreme Ultraviolet Survey

### Experiment MA-083

*S. Bowyer,<sup>a†</sup> B. Margon,<sup>a</sup> M. Lampton,<sup>a</sup> F. Paresce,<sup>a</sup> and R. Stern<sup>a</sup>*

#### ABSTRACT

A grazing incidence telescope sensitive to radiation in the 5- to 100-nm band was flown in the Apollo service module. On 10 nighttime revolutions, the command and service module was maneuvered to point the instrument at 30 different stellar targets for periods of 1 to 20 minutes, thus constituting the first sensitive search for extreme ultraviolet radiation from non-solar sources. Several hours of supplementary data were also obtained during nighttime orbits when other experiments in the scientific instrument bay were operating.

Analysis of the data completed thus far indicates the definite detection of at least four extrasolar extreme ultraviolet sources. The probable identifications of these sources are the hot white dwarfs HZ 43 and Feige 24, the dwarf nova SS Cygni, and the M-dwarf flare star Proxima Centauri. The two white dwarfs are the most intense sources, with fluxes incident at Earth of 3 to 4 pW/m<sup>2</sup> in the 17- to 62-nm band. Optical spectrophotometric measurements of these two objects made with the 3-m telescope at the Lick Observatory have been combined with the extreme ultraviolet data to derive several physical parameters of the stars; the investigators found these two objects to be the hottest and the most luminous known white dwarfs. The shapes of their extreme ultraviolet spectra may be used to

infer that the density of the local neutral component of interstellar hydrogen is  $\leq 0.02$  atom/cm<sup>3</sup>, which is promising for future astronomical observations in this wavelength band.

The four objects thus far identified are the first extrasolar sources to be detected in the extreme ultraviolet band. Computer analysis of both the prime and supplementary data will eventually yield near-photon-limited sensitivity levels for coverage over a considerable fraction of the July night sky and may reveal additional point sources. These observations also provide the largest volume of data ever obtained on the ultrasoft component of the diffuse cosmic X-ray background. Preliminary analysis of these data indicates that spatial isotropy is restored in the 6- to 15-nm band, contrary to the well-known anisotropy of the 4.4- to 6-nm radiation.

#### INTRODUCTION

Astronomical observations of nonsolar sources in the extreme ultraviolet (EUV) region of the electromagnetic spectrum (10 to 100 nm) are of profound significance for studies of stellar evolution, stellar atmospheres, and the interstellar medium. The existence of stars producing predominantly ionizing radiation (wavelengths less than 91.2 nm) has been postulated to explain the ionization state of the interstellar medium. Such stars might represent a very hot phase of stellar evolution (refs. 4-1 and 4-2). Effective surface temperatures greater than 20 000 K have been observed, for example, among O stars, among white dwarfs of classes DAn and DAwk, among the

<sup>a</sup>University of California at Berkeley.

<sup>†</sup>Principal Investigator.

subdwarf OB stars (ref. 4-3), and among the ultraviolet (UV) excess objects observed from the European TD-1A satellite (ref. 4-4). A major deterrent to previous attempts at celestial EUV observations has been the opacity of the interstellar gas resulting from photoelectric absorption by neutral hydrogen and neutral and singly ionized helium. However, recent spectroscopic studies of interstellar matter toward nearby stars (refs. 4-5 to 4-7) indicate that, in many directions, neutral hydrogen concentrations are as low as 0.01 to 0.1 atom/cm<sup>3</sup>. Then, the absorption cross sections given in reference 4-8 indicate that direct EUV observations of sufficiently hot stars should be possible to distances of 20 to 100 pc.

Preliminary surveys at EUV wavelengths have been made from sounding rockets and have set upper limits of approximately 0.1 nW/m<sup>2</sup> for sources in limited regions of the sky (refs. 4-9 to 4-13). However, significant constraints on stellar emission models would require improvements in sensitivity of perhaps two orders of magnitude. The Apollo-Soyuz mission offered the opportunity to make extended observations of numerous candidate stars with an EUV telescope that had the requisite sensitivity. Ten nighttime orbits were used to obtain data on 30 preselected stars, 1 planet, and the EUV background radiation.

## EQUIPMENT

The EUV telescope (ref. 4-14) consisted of a 37-cm-diameter grazing incidence mirror assembly, a continually rotating (10 rpm) six-position filter wheel, and a pair of channel electron multiplier detectors. A schematic view of the instrument is shown in figure 4-1.

The parabolic optics were fabricated from aluminum coated with a nickel alloy and then overcoated with a fine layer of gold. The filter wheel included an opaque filter that permitted nearly continuous monitoring of the detector background during the mission. The field of view (FOV) of the instrument was circular with selectable diameters of 2.5° or 4.3° full width at half maximum obtained by commanding either detector into the focal position. The detailed construction

of the detector modules is described in reference 4-15. The detector not at the focal position was also monitored to further establish the stability of the background count rates. Count rates from both detectors were telemetered each 0.1 second together with the filter wheel position and other auxiliary information.

The entire system was calibrated in the laboratory with collimated radiation at numerous wavelengths between 4.4 and 265 nm. Absolute intensities were established by using National Bureau of Standards-calibrated vacuum-photodiode secondary standards above 20 nm and propane proportional counters below 20 nm. The various filters, in combination with the efficiency characteristics of the mirror assembly and detector, defined the wavelength bands illustrated in figure 4-2. The detailed response of the system is summarized in table 4-I. The filters and their band passes at 10 percent of peak transmission, the energy-integrated effective area, or grasp  $G = \int A(E) dE$  (where  $E$  is energy and  $A$  is area), and the effective energy  $E_e = \int EA(E) dE / G$  are given in table 4-I.

The experiment was mounted to a shelf in bay 1 of the service module (SM). A protective cover enclosed the instrument assembly at all times when the experiment was not in operation. At appropriate times in the Flight Plan, the crew activated a switch in the command module (CM) to open the cover. The remaining experiment controls consisted of a POWER ON/OFF switch and a two-position detector-selection switch. Both switches were located in the CM and operated by the crew.

The observing procedure consisted of opening the experiment cover, waiting 10 seconds to permit the ambient pressure in the SM bay to vent to vacuum, and then turning the instrument power on. The crewmember then selected the appropriate detector to ensure that the proper channel multiplier was always in the focal plane. The filter wheel operated automatically and continuously whenever the instrument power was on.

The telescope was oriented at preselected targets by using the spacecraft command module computer (CMC) for guidance and orientation and by using the normal Apollo reaction control system thrusters for maneuverability to point the

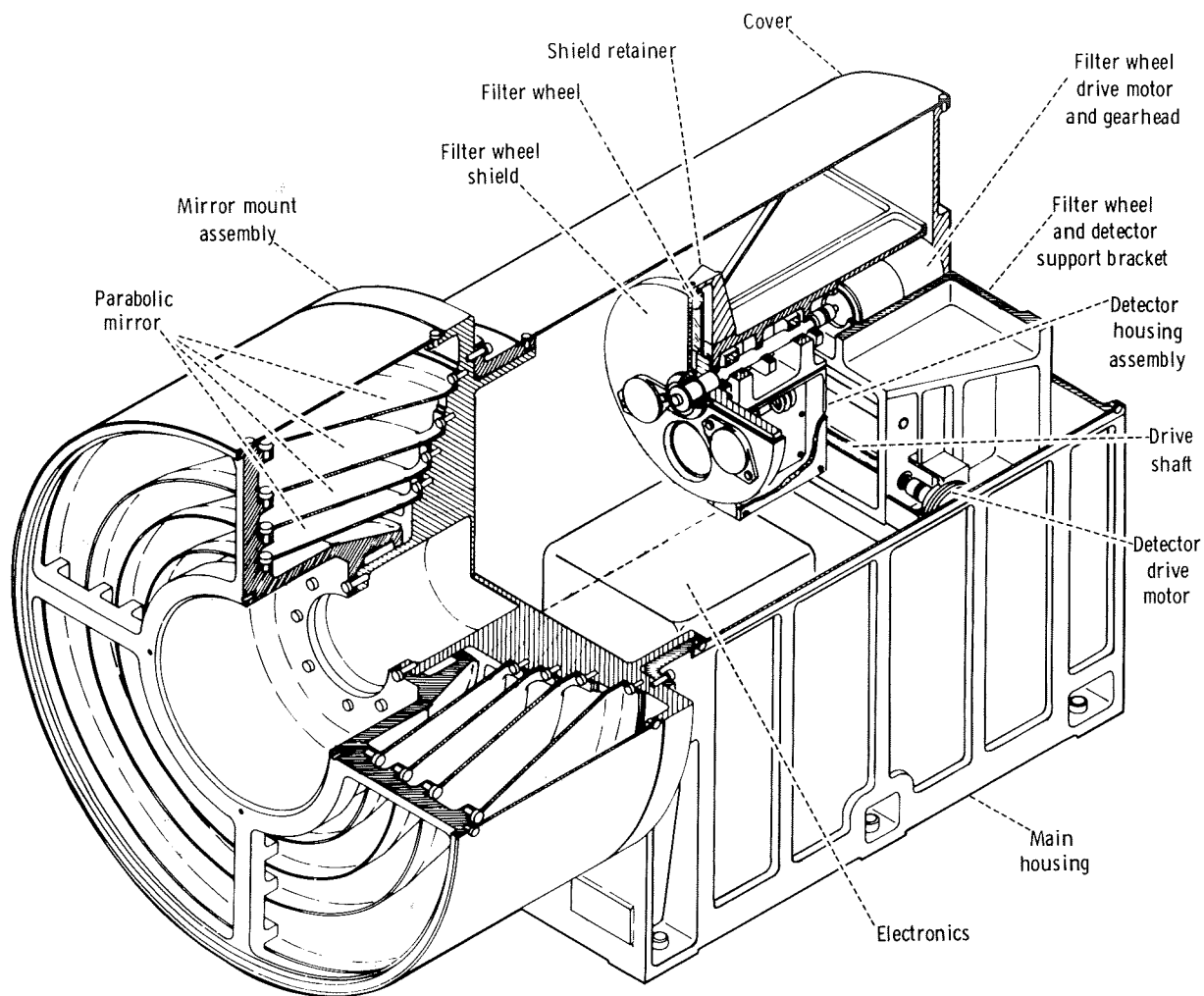


FIGURE 4-1.—A schematic diagram of the EUV telescope.

instrument line of sight at the desired position on the celestial sphere for predetermined lengths of time. The typical target observation sequence consisted of spending equal amounts of time pointing at a target and at two background points located  $3^\circ$  on each side of the target. Any statistically significant differences between the average count rates when observing target and background are then attributable to EUV emission from the object under study. Target observations lasting from 1 to 20 minutes were executed.

## RESULTS

The EUV telescope functioned perfectly during the entire mission. The background count rates remained low and reproducible, and the data show no evidence of degradation in instrument sensitivity from the laboratory-measured values.

On revolution 65 at 108 hours 26 minutes ground elapsed time, a preplanned raster scan maneuver was executed using a special erasable memory program in the CMC. This maneuver

consisted of slewing the telescope in a zigzag pattern back and forth across a star of known brightness in the far UV ( $\approx 130$  nm) where the barium fluoride filter has maximum sensitivity. Because the target position is known in celestial coordinates, a comparison of the time history of the barium fluoride count rates during this maneuver with the known command and service module (CSM) attitude enables the calculation of the actual (in-flight) alinement of the experiment with respect to the CM inertial measuring unit. This information could then be used to recompute CSM pointing data for mission targets to compensate for any changes in alinement from the nominal values caused by vibration or thermal stresses. However, analysis of the revolution 65 raster scan data, obtained on the stars  $\iota$  Aql and  $\kappa$  Aql, indicated, to an accuracy of  $0.3^\circ$ , that no change from the nominal alinement occurred.

Observation of the targets proceeded normally with occasional small deviations from the observing list caused by time-line anomalies. The rationale for target selection is discussed in reference 4-14. A list of the targets actually observed appears in table 4-II. This list is composed of 30 distinct targets. Seven targets were observed twice during the mission, one target was observed three times, and one target was observed during an extended crew sleep period while the spacecraft was in a fixed inertial attitude.

During the mission, considerable real-time planning enabled additional high-quality science data to be obtained. For example, on day 4 of the mission, the American Association of Variable Star Observers advised that the dwarf nova SS

Cygni had undergone an optical outburst. As a result, additional observations of this target were obtained on revolutions 80 and 105. Similarly, several nighttime revolutions originally intended for observing soft X-ray targets became available for the EUV survey because of difficulties with the soft X-ray experiment.

The results of the observations on targets of particular interest are given in the following discussion.

### HZ 43

As part of the preplanned observing schedule, on revolution 109 the ultrasoft X-ray source in Coma Berenices (refs. 4-16 to 4-18) was observed for 7 minutes starting at 22:26 UT on July 22, 1975. After taking background data for 1 minute, a  $3^\circ$  spacecraft roll maneuver brought the center of the instrument line of sight to a point  $1^\circ$  north of the intended target. Thus, the target was just at the edge of the  $2^\circ$  FOV of the instrument. Several roll and pitch motions of approximately  $0.5^\circ$  resulted from spacecraft motion within the attitude dead-band box and moved the FOV off and on the source. Finally, additional sky background data were obtained  $3^\circ$  off the target.

During these maneuvers, obvious increases and decreases in the detector count rates were immediately recognized. A plot of the count rate as opposed to time is shown in figure 4-3 for the 5.5 to 15, 11.4 to 15, 17 to 62, 50 to 78, and 135 to 154 nm bands with each point representing the

TABLE 4-I.—EUV Instrument Characteristics

Filter material	Band pass		Grasp, $\text{cm}^2 \text{ eV}$	Effective energy, $\text{eV}$
	eV	nm		
Parylene N	83 to 225	5.5 to 15.0	590	142
Beryllium/ parylene N	83 to 109	11.4 to 15.0	60	100
Aluminum plus carbon	20 to 73	17 to 62	270	46
Tin	16 to 25	50 to 78	108	21
Barium fluoride	8.0 to 9.2	135 to 154	.47	9

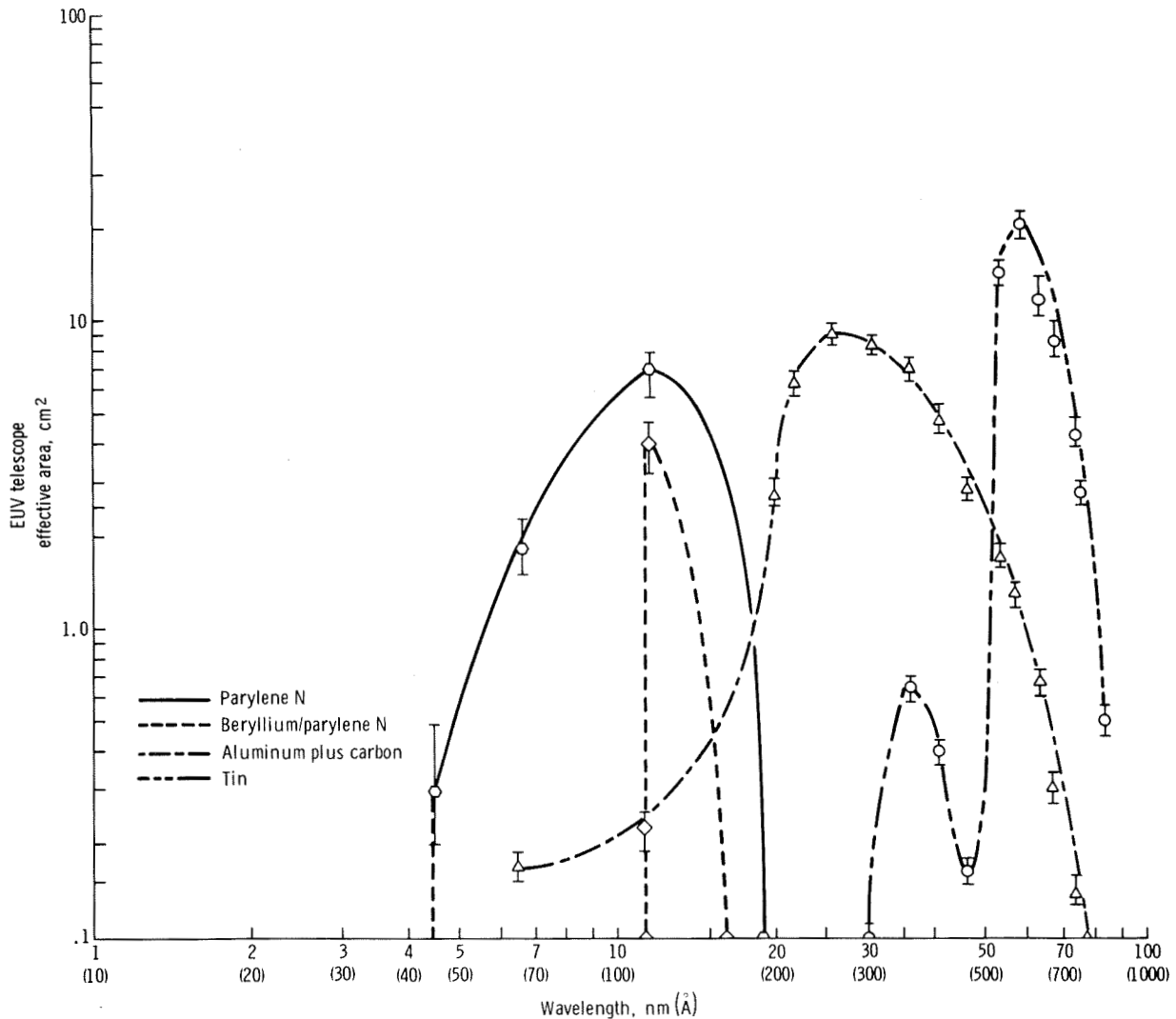


FIGURE 4-2.—Effective area of the EUV telescope as determined by the laboratory calibration data. (The response of the barium fluoride band pass, which was used primarily for instrument alignment determination, is given in table 4-I.)

average count rate during an 0.8-second time interval. Also shown is the count rate in the opaque filter position, which indicates that the observed instrumental background remained steady at 0.6 count/sec.

A crude estimate of the spectral energy distribution of an object can be made by dividing the observed count rate in each band by the appropriate energy-integrated effective area. Such an estimate is exact for continua having constant photon

fluxes per unit frequency. Listed in table 4-III are the observed background-subtracted count rates for the Coma source, corrected for atmospheric attenuation at  $E_e$  based on the Committee on Space Research International Reference Atmosphere 1965 model 2 reference atmosphere, appropriate for the observing conditions. The total energy flux in the 17- to 62-nm band is approximately 4  $\mu\text{W}/\text{m}^2$ .



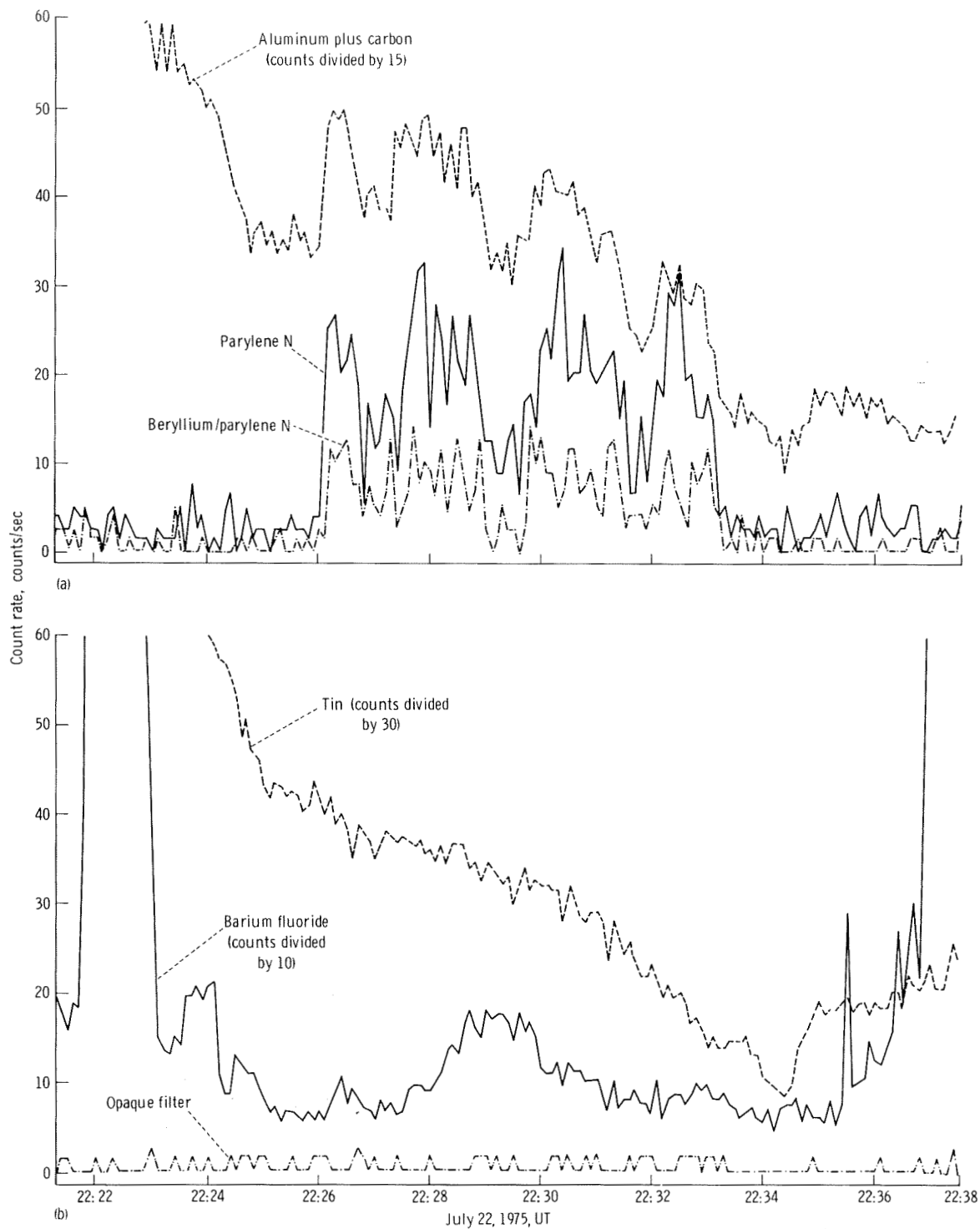


FIGURE 4-3.—The EUV data obtained during a portion of revolution 109. The trends in the aluminum and tin band passes are due to the spatial variations in the geocoronal foreground radiation. This behavior was repeated on numerous orbits. The barium fluoride count rates are dominated by the occasional observations of known blue stars. (a) Aluminum plus carbon, parylene N, and beryllium/parylene N. (b) Tin, barium fluoride, and the opaque filter.

TABLE 4-II.—Targets Observed by the EUV Telescope

Revolution	Target
72	EV Lac, AE Aqr, NGC 7293, $\epsilon$ Eri
73	VW Cep, DQ Her, 70 Oph, $\alpha$ PsA
80	EV Lac, SS Cyg, DQ Her, $\theta$ Oph, $\alpha$ Cen
88	$\alpha$ CMa B
89	NGC 6853, PSR 1929+10, $\alpha$ Aql, UV Cet, Feige 24
90	SS Cyg, 61 Cyg, BD +28°4211, Jupiter
94	HZ 29, i Boo, Prox Cen
105	SS Cyg, BD +28°4211
108	Wolf 424, $\alpha$ Cen, Z Cha, VW Hyi, UV Cet
109	PSR 1133+16, HZ 43, Prox Cen, PSR 1451-68, $\beta$ Hyi
113 to 117	Wolf 424

TABLE 4-III.—EUV Photometry of Selected Targets

Object	Revolution	Length of exposure, sec	Count rate, <sup>a</sup> counts/sec				
			Parylene N	Beryllium/ parylene N	Aluminum plus carbon	Tin	Barium fluoride
Positive detections							
HZ 43	109	427	23 ± 1	9 ± 0.6	270 ± 5	<130	<25
	104	9	25 ± 5	7 ± 3	240 ± 25	--	<80
Feige 24	89	125	2 ± 1	<1	232 ± 5	<65	<150
Proxima Centauri	109	78	4 ± 1	<1.5	<45	<120	--
	94	1100	1 ± 1	<1	<50	--	--
SS Cygni	80	135	2 ± 0.5	<1	<45	<125	<150
	90	103	1 ± 0.5	<1	<52	<120	<180
	105	372	<1	<1	<45	<80	<150
Upper limits							
Sirius B	88	74	<2.5	<2.0	<350	<625	<54 400
Jupiter	90	322	<2	<1	<70	<160	<90
PSR 1133+16	109	75	<4	<2.5	<160	<150	<960
PSR 1451-68	109	329	<5	<4	<60	<120	<240
PSR 1929+10	89	252	<2	<2	<40	<90	<120
Hercules X-1	104	582	<1	<1	<45	<180	<60

<sup>a</sup>All count rates are corrected for background and atmospheric absorption. No entry indicates rapidly changing background, short exposure, or South Atlantic Anomaly precluded useful upper limit. Rates may be converted to photon fluxes by using data in table 4-1.

The intensities of this source have been plotted as a function of wavelength in figure 4-4. Also shown is the 4.4- to 16.5-nm detection and 1-keV upper limit in reference 4-17. The data appear compatible and support the identification of the EUV object with the Coma soft X-ray source. Figure 4-4 clearly indicates that the spectrum peaks in the EUV band at approximately 30 nm.

Positional information on this source can be derived from the fact that, as the spacecraft pointing varies, the count rates are occasionally interrupted. Telemetered data on the CSM aspect have been combined with in-flight data on the experiment alignment to obtain four independent position zones for the source. These zones define a

common region that is shown in figure 4-5 superposed on the relevant star field.

The Small Astronomy Satellite-3 observations reported in reference 4-18 have given a positional error box for the soft X-ray source that is compatible with the EUV position and is also shown in figure 4-5. It is highly probable that one object is responsible for the soft X-ray and EUV emissions. It has been suggested (ref. 4-18) that the soft X-ray object is the hot white dwarf HZ 43 at  $\alpha$  (1950) =  $13^h14.0^m$ ,  $\delta$  (1950) =  $+29^\circ22'$ . This object is also marked on figure 4-5, and the EUV position is compatible with this suggestion.

Without assumption as to the optical identification of the source, a description of the spectrum may be provided by using the observed count rates to constrain parameters of emission models. The simple continuum models chosen for these calculations had photon number per unit energy functions of the following forms: power law,  $N(E) = cE^n \exp(-N_H \sigma)$ ; exponential,  $N(E) = cE^{-1} \exp(-E/kT) \exp(-N_H \sigma)$ ; and black body,  $N(E) = cE^2 [\exp(E/kT) - 1]^{-1} \exp(-N_H \sigma)$ ; where  $N$  is photon number,  $c$  is intensity coefficient,  $T$  is temperature,  $k$  is the Boltzmann constant,  $n$  is the photon power-law index, and  $N_H$  is the column density of neutral interstellar hydrogen. In each case, the energy-dependent absorption cross section per hydrogen atom  $\sigma$  has been taken from reference 4-8 with normal abundances, no ionization, and no molecular hydrogen.

The collected data can be satisfactorily fit by any of these trial spectra provided that the free parameters are appropriately chosen. Figure 4-6 shows the derived parameter constraints for these models. In each case, contours are drawn at the  $\chi^2_{min} + 6.25$  level appropriate for 90 percent statistical confidence with three free parameters (ref. 4-19). These constraints are compatible with, but much stricter than, the parameter regions derived from the soft X-ray rocket data given in reference 4-17.

Because of the strong likelihood of the association of this EUV source with the stellar system HZ 43, the investigators have obtained correlative ground-based data on the optical object using the facilities of the Lick and Allegheny Observatories. The HZ 43 system is known to consist of a very

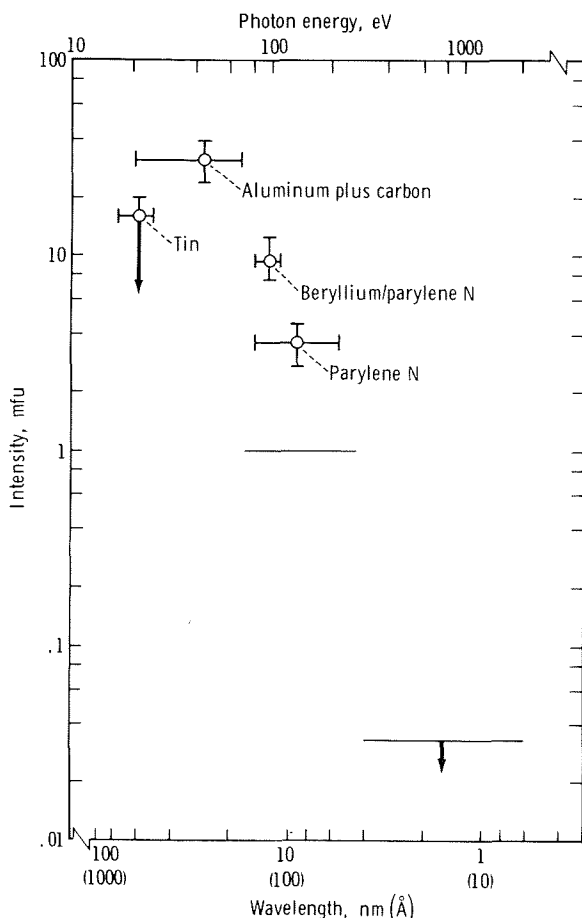


FIGURE 4-4.—Spectral intensities derived from the EUV data on the source in Coma Berenices. Soft X-ray data (ref. 4-17) are also shown.

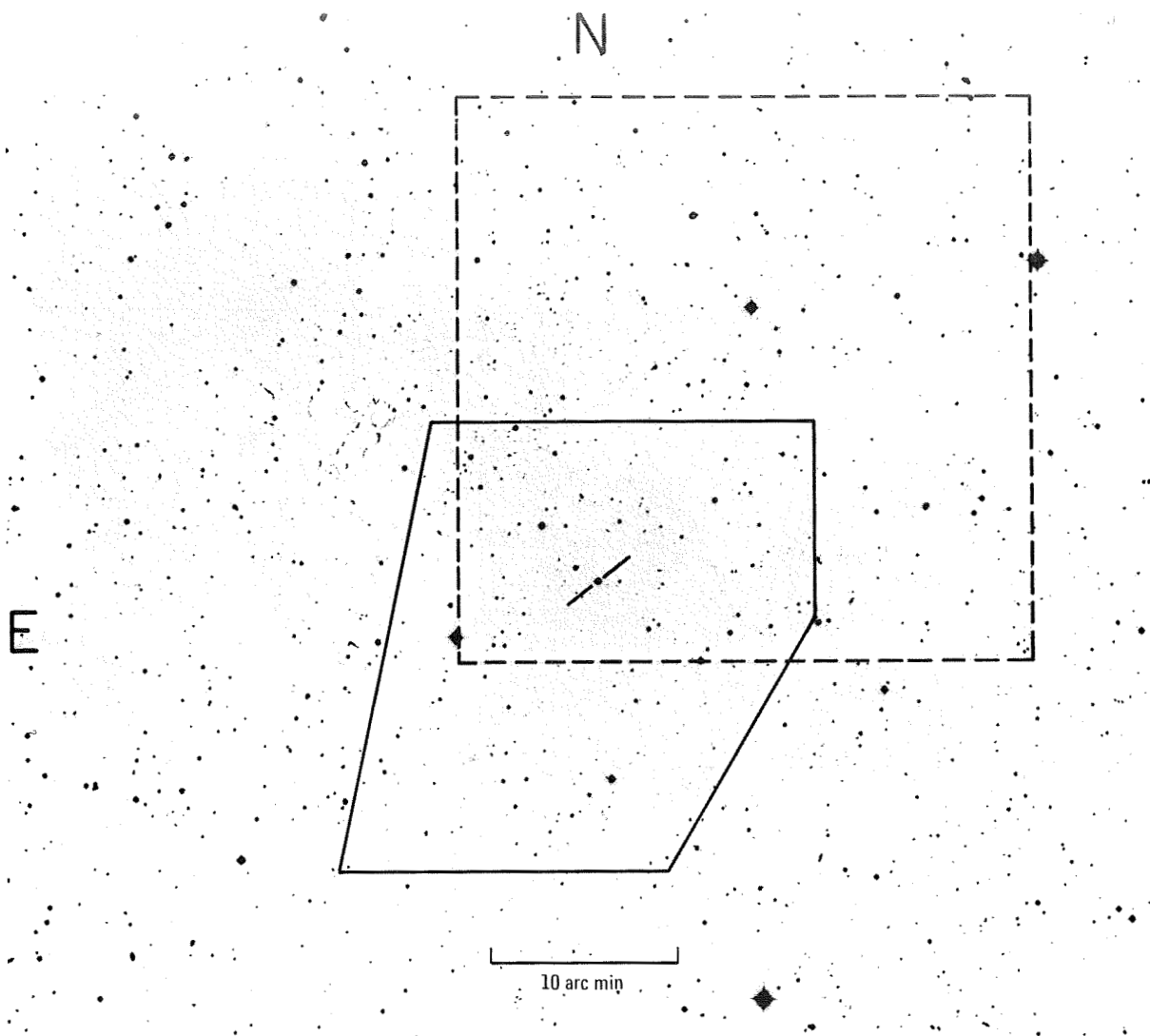


FIGURE 4-5.—Positional error box for the EUV source in Coma Berenices derived from the revolution 109 data (solid line). The broken line is the error box for the soft X-ray source observed from Small Astronomy Satellite-3 (ref. 4-18). The white dwarf HZ 43 is also marked in the center of the photograph. Enlargement is from the blue Sky Survey plate (copyright by the National Geographic Society - Palomar Observatory Sky Survey; reproduced by permission of the Hale Observatories).

blue white dwarf and a faint red comoving companion located 3 arcsecs distant from the white dwarf (see, e.g., ref. 4-20); the two objects are hereafter referred to as HZ 43A, B.

Image tube spectrophotometric measurements at a resolution of approximately 0.8 nm were obtained of HZ 43A, B (composite) and HZ 43A (blue component only), using the Robinson-Wampler image tube scanner (at the Cassegrain

focus) of the Lick Observatory 3-m reflector. The resulting spectra of the composite system and HZ 43A are shown in figure 4-7. The difference between these spectra, also shown in the figure, was used to derive the spectrum of the red star HZ 43B. The HZ 43A spectrum was found to be that of a very hot white dwarf of class DA<sub>W</sub>K; it lacks the strong spectral lines of singly ionized helium at 541.1 and 468.6 nm evident in the spectrum of

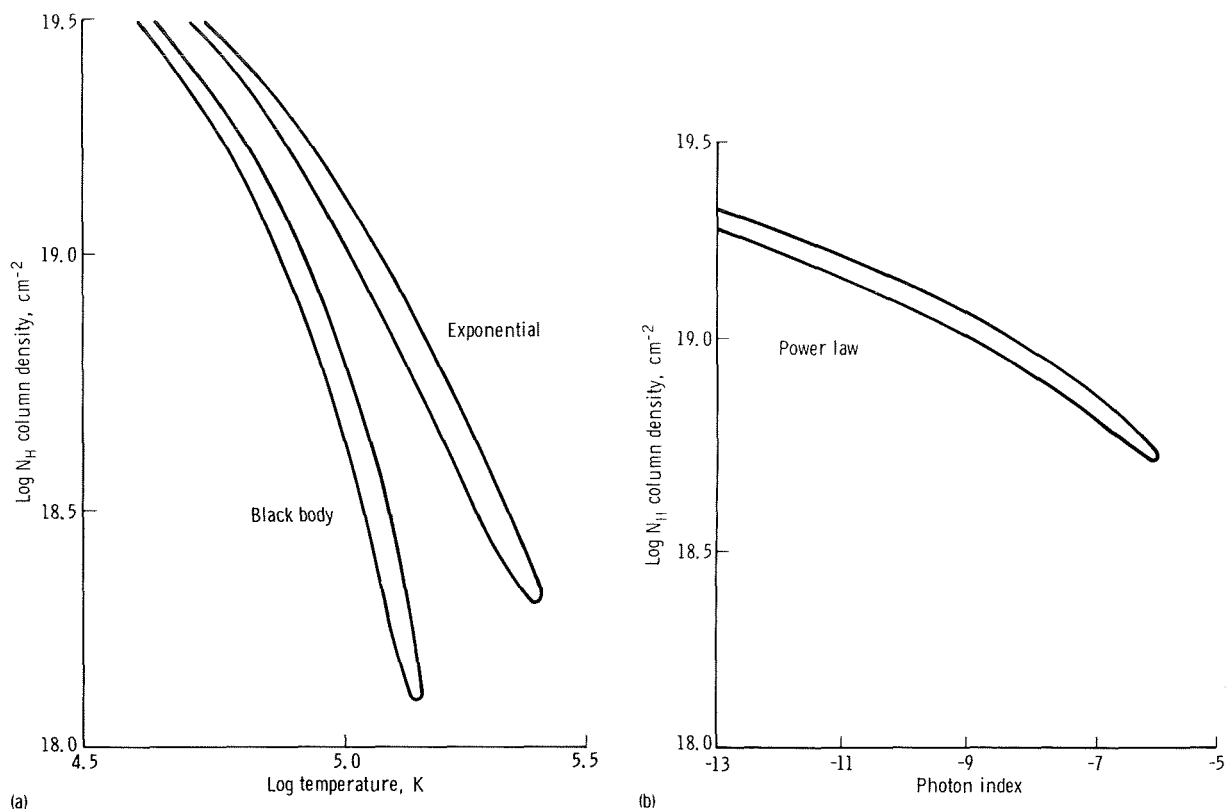


FIGURE 4-6.—Contours of constant  $\chi^2$  for the fits of black-body, exponential, and power-law spectra to the HZ 43 EUV data. Each contour has been drawn at the  $\chi^2_{\min} + 6.25$  level appropriate for 90 percent statistical confidence with three adjustable parameters (ref. 4-19). (a) Black-body and exponential contours. (b) Power-law spectra contour.

DO white dwarfs. No other features other than weak, broad Balmer absorption lines due to neutral hydrogen are evident in the scans of HZ 43A to 680 nm. In particular, none of the spectra show any trace of emission lines, nor has emission ever been reported in the literature for this star, contrary to the assertion of reference 4-18.

The derived HZ 43B spectrum is that of an M-dwarf star with weak Balmer emission lines. The explicit spectral subtype of the star has been estimated in the manner used in reference 4-21, by measuring the strengths of the titanium oxide (TiO) bands and the colors and by visually comparing the overall spectrum with spectroscopic standards. Based on these criteria, HZ 43B is classified as dM3.5. This classification, together with the known absolute brightness of stars of this type and the observed apparent brightness of HZ

43B (fig. 4-7), may be used to derive the distance of the system. The result of this procedure is a distance of 66 (+25, -18) pc.

A new trigonometric parallax has also been derived for HZ 43 using 22 plates obtained at the Allegheny Observatory between 1951 and 1967. The Allegheny material has a poor seasonal distribution, with only five plates obtained at high positive parallax factors; nevertheless, when remeasured and reduced with the latest techniques, the available material is sufficient to yield results of substantially greater accuracy than those in reference 4-22. The new parallax derived is  $\pi = 0.015 \pm 0.006$  arcsec. Recently, the U.S. Naval Observatory measured and reduced 21 plates obtained on HZ 43 with their 1.55-m reflector and found a preliminary parallax of  $\pi = 0.017 \pm 0.005$  arcsec. The agreement with the

Allegheny value is good, so the results may be combined to derive a weighted mean result of  $\pi = 0.016 \pm 0.004$  arcsec, indicating a distance of 62 (+21, -12) pc, which is in excellent agreement with the independently derived distance for HZ 43B previously described.

If the identification of the EUV object with HZ 43A is accepted, the optical and EUV data cited earlier may be combined to derive many interesting parameters of the system (see, e.g., ref. 4-23). A measurement of the monochromatic intensity of a black body at any wavelength yields a locus in a plane (solid angle, effective temperature). In figure 4-8, the EUV and optical data are combined in such a plane. Using the spectrophotometry of HZ 43A shown in figure 4-7, absolute fluxes at the top of the Earth's atmosphere have been derived

at five wavelengths in the 400- to 650-nm range. Care was taken to extract each measurement at a wavelength that was free of absorption features and thus truly applicable to the stellar continuum. The loci resulting from these intensity measurements appear in figure 4-8 as the approximately horizontal lines. The ordinate of the graph is the dimensionless ratio, stellar radius to stellar distance; an additional ordinate scale of stellar radius in kilometers is provided, assuming the parallax  $\pi = 0.016$  arcsec.

Several interesting features are immediately apparent from the optical data. The loci computed from the different optical wavelengths are not precisely coincident or congruent, undoubtedly reflecting scatter in the observational material. However, they do define a reasonably narrow

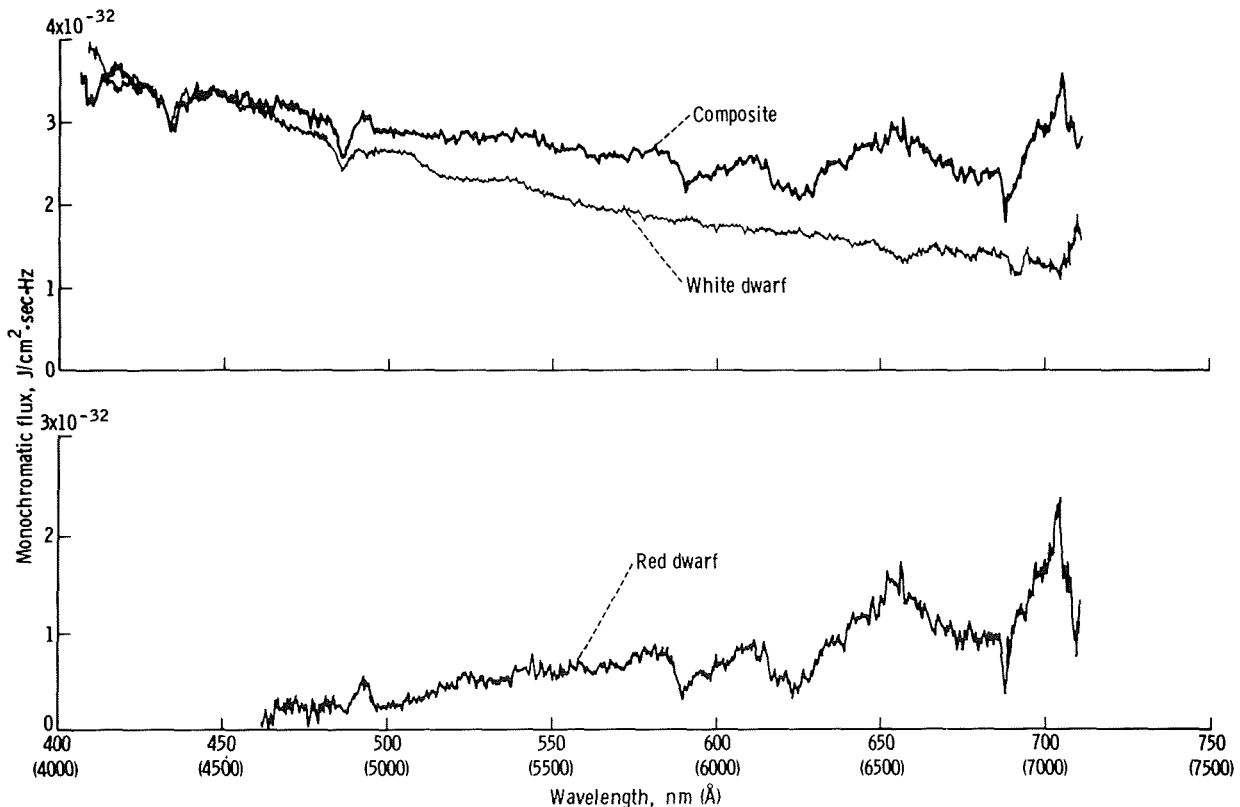


FIGURE 4-7.—Spectrophotometry of HZ 43 obtained with the image tube scanner of the Lick Observatory 3-m telescope, with 0.8-nm resolution. In the upper spectrum, the slit included both red and blue components of the system; the middle spectrum is that of the blue star only. The spectrum of the red component (lower spectrum) was derived by differencing the upper two spectra.

band that is nearly parallel to the temperature axis. This figure thus quantitatively verifies the qualitative knowledge that optical spectrophotometry is very insensitive to the precise temperature of such a hot object. Specifically, the difference in the slopes of black-body spectra at temperatures of 50 000 and 100 000 K is only  $\approx 0.1$  magnitude across the visible band, which explains the difficulty of determining such a temperature in the optical band.

Ideally, one would want to have monochromatic EUV magnitudes to compare with these optical data. At the moment, however, the only EUV data available are the broadband photometric measurements made during the Apollo-Soyuz mission. Therefore, the data shown in figure 4-6 were used to determine the parameters of five different black-body models that represent the extremes of the allowable values of the adjustable parameters. The resulting intensities were then used to define the EUV locus shown in figure 4-8. The EUV and optical data intersect and provide a common region in the plane (radius, temperature). Further, the EUV data are obviously very sensitive to temperature. The combination of the EUV and optical data accurately defines a small region of allowable effective temperature at  $110\,000 \pm 10\,000$  K and radius of  $5000 \pm 1000$  km, under the assumption of this simple black-body emission model. For such an object, the luminosity is  $6.8 L_{\odot}$ , where  $L_{\odot}$  is the solar luminosity,  $3.83 \times 10^{26}$  J/sec. These parameters are in reasonable agreement with white dwarf models; they would give to HZ 43 the highest temperature of any known white dwarf.

Using these stellar parameters, the EUV spectrum may be used to derive the equivalent column density of neutral interstellar hydrogen  $N_H$  in the line of sight to HZ 43. This value is  $N_H = 4 \times 10^{18}$  atoms/cm<sup>2</sup> or, using the parallax  $\pi = 0.016$  arcsec, a volume density of 0.02 atom/cm<sup>3</sup> is derived. This value for the volume density, although lower than many previous suggestions, is consistent with observations of stellar Lyman-alpha 121.6-nm absorption in nearby stars.

A summary spectrum of HZ 43A at all wavelengths thus far measured appears in figure

4-9. The EUV data from the Apollo-Soyuz mission are plotted as the heavy points, and the optical spectrophotometric data shown in figure 4-7 are plotted as the broken line. The radio data from reference 4-24, the UV data from reference 4-25, and the soft X-ray data from reference 4-17 are also included.

It is quite possible that the emergent spectrum of HZ 43A is considerably more complex than the simple black-body spectrum used for these calculations. However, no calculations of high temperature, high surface gravity, and pure hydrogen model atmospheres have been published. Such models are particularly important to assess the effect of wavelength-dependent opacity mechanisms, the Lyman discontinuity, and the presence of trace amounts of atmospheric helium and heavy elements. Preliminary calculations by the authors suggest that these effects may combine to lower the effective temperature from that derived in a black-body approximation.

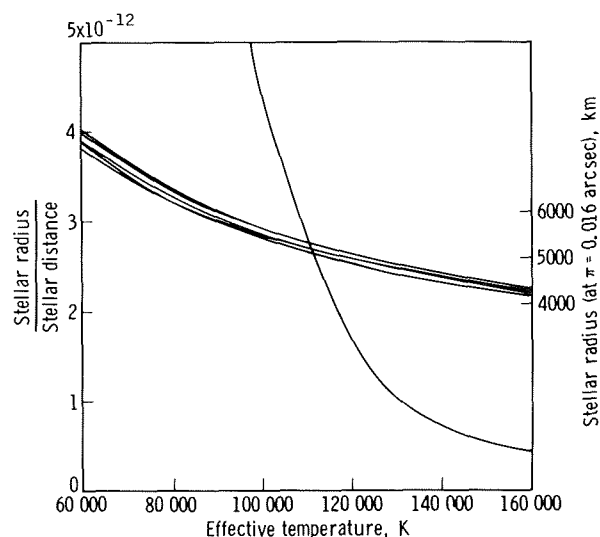


FIGURE 4-8.—Constraints on solid angle as a function of temperature for HZ 43A using the spectra shown in figure 4-7 and the EUV data in figure 4-6, under the assumption of a black-body emission model. The inferred stellar radius at the optimum parallax is also indicated.



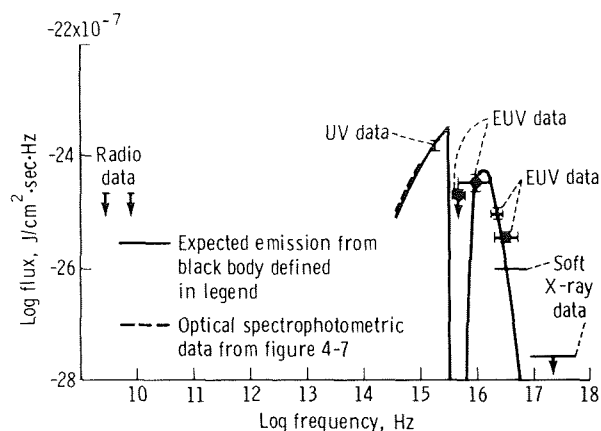


FIGURE 4-9.—The intensity of HZ 43 as observed from Earth. The solid line is the expected emission from a black body of 110 000 K effective temperature attenuated below the Lyman limit by interstellar photoelectric absorption equivalent to  $N_H = 4 \times 10^{18}$  atoms/cm<sup>2</sup>, using the EUV photoelectric cross sections in reference 4-8.

### Feige 24

On revolution 89, a preplanned observation of the hot white dwarf Feige 24 was conducted. Data telemetered during this maneuver are displayed in figure 4-10. The lowest portion of the figure displays the angular offset of the center of the FOV of the EUV telescope from Feige 24 as a function of time. These data are determined by the CMC independently of the EUV experiment. The horizontal broken line denotes the 1.2° radius of the telescope field; thus, all times located between the intersection of this line with the offset graph are times when Feige 24 was within the FOV. This interval is projected onto the time axis of the figure with the vertical broken lines.

Count rate data from the EUV telescope are displayed in the upper portion of figure 4-10. The opaque shutter data show that the detector internal background remained steady at 0.4 count/sec during the entire observation. Data from the 5.5 to 15, 11.4 to 15, and 135 to 154 nm bands have been omitted for clarity; however, they were also constant during the entire maneuver sequence, with mean rates of 3.4, 1.5, and 600 counts/sec, respectively. The strong increases in the 17- to 62- and

50- to 78-nm count rates (cf. fig. 4-10) were due to spatial variations in the geocoronal foreground radiation. This smooth variation as the CSM moves from orbital midnight to sunrise was repeatedly observed on numerous revolutions. (See figure 4-3 for an additional example.)

Figure 4-10 indicates that Feige 24 was within the telescope FOV for 2 minutes commencing at 15:50 UT. Simultaneous with the entrance of the star into the field, a sudden and large increase (200 counts/sec) was observed in the 17- to 62-nm counting rate above the geocoronal background. This new rate persisted for 122 seconds and then fell quickly (within two data samples) to a smooth extrapolation of the geocoronal count rate, exactly simultaneous with the motion of the CSM away from Feige 24. The excess number of counts

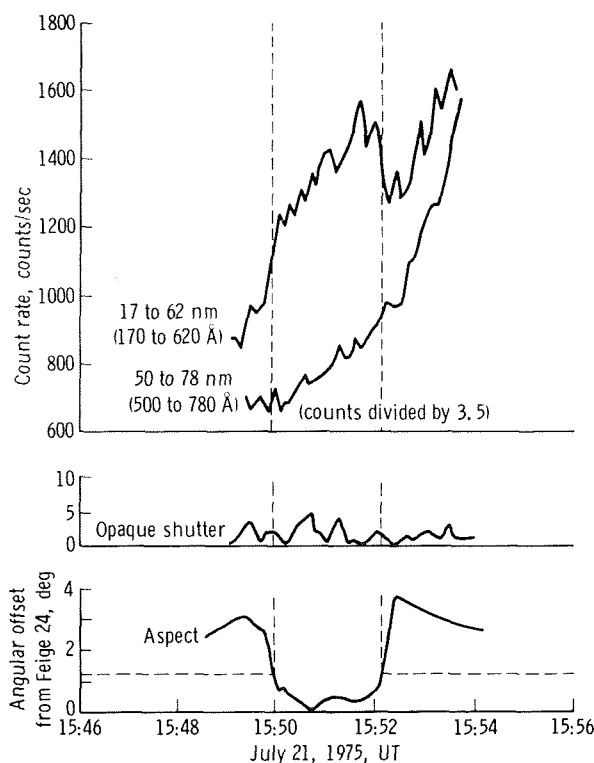


FIGURE 4-10.—Observations of the hot white dwarf Feige 24 made during the Apollo-Soyuz mission. The horizontal broken line indicates the threshold of the telescope 1.2° radius FOV; the projected vertical lines therefore encompass times when Feige 24 was within the FOV.

above the smooth background curve during this 2-minute period was  $25\,000 \pm 550$ , which is statistically significant at the 45 standard-deviation level. It is concluded with high confidence that an intense celestial source of EUV radiation has been detected at or very near Feige 24. The observed excess flux, when corrected (a 14-percent correction) for residual atmospheric absorption, corresponds to  $3\text{ pW/m}^2$  in the 17- to 62-nm band incident above the Earth's atmosphere. This is comparable to the observed intensity of HZ 43 on revolution 109. There is no evidence for nonstatistical intensity variations during the observation.

In the four other wavelength bands, upper limits to the source intensity may be obtained. In the 5.5- to 15- and 11.4- to 15-nm bands, these limits are  $0.10$  and  $0.17\text{ pW/m}^2$ , respectively, or approximately 10 percent of the observed intensity of HZ 43. It is thus clear that this source has a spectrum substantially steeper than that of HZ 43. The derived upper limit in the 50- to 78-nm band is  $0.41\text{ pW/m}^2$ , and the upper limit in the 135- to 154-nm band is  $44\text{ pW/m}^2$ , equivalent to the monochromatic magnitude of  $m_v > 8.1$  at 137 nm.

The investigators used the detailed laboratory calibration of the FOV dimensions, together with the telemetered count rate and aspect histories and the observation of several known early-type stars in the 135- to 154-nm band, to derive quantitative limits on the position of the EUV source. This position is restricted to a quadrilateral whose corners have epoch 1950 ( $\alpha, \delta$ ): ( $2^{\text{h}}30^{\text{m}}, 3^{\circ}15'$ ), ( $2^{\text{h}}37^{\text{m}}, 5^{\circ}00'$ ), ( $2^{\text{h}}42^{\text{m}}, 3^{\circ}55'$ ), and ( $2^{\text{h}}35^{\text{m}}, 2^{\circ}10'$ ). This area ( $3.8\text{ deg}^2$ ) contains Feige 24 at  $2^{\text{h}}32.5^{\text{m}}, 3^{\circ}31'$  and also the hot subdwarf O star Feige 26. The detailed maneuver history of the spacecraft makes Feige 26 an unfavorable candidate, although it cannot be completely excluded on positional grounds alone. However, if the subdwarf classification is correct, Feige 26 is almost certainly too distant to be the source observed, based on interstellar photoelectric opacity; e.g., a distance of 250 pc is suggested in reference 4-3. The observations of BD +28°4211 made during the EUV experiment on revolutions 90 and 105 also suggest that Feige 26 was not the observed source. The star BD +28°4211 is a subdwarf O of a

similar optical spectrum but 2 magnitudes brighter than and thus almost certainly closer than Feige 26. The star BD +28°4211 was not detected during the EUV experiment with an upper limit in the 17- to 62-nm band of  $0.6\text{ pW/m}^2$ , i.e., 20 percent of the flux from the source discussed here.

Without assuming the optical identification of this source, one may fit simple continuous emission models to the EUV data and constrain parameters of these models to avoid violating the observed fluxes and upper limits. This fitting procedure has been performed in a manner similar to that described earlier for HZ 43. The intensity, temperature or slope, and intervening column density of neutral hydrogen are left as free parameters in the analysis. The results are given in figure 4-11, where contours of constant  $\chi^2$  for power-law, exponential, and black-body models are given, analogous to figure 4-6 for HZ 43. This figure provides quantitative confirmation of the qualitative impression yielded by the count-rate ratio of Feige 24 to HZ 43. Feige 24 is a significantly cooler source in thermal models or has a steeper spectrum in power-law models.

The Feige 24 system is known spectroscopically to consist of a very blue DA white dwarf and an unresolved red dwarf M companion. The similarity of this system to HZ 43 immediately suggests that similar mechanisms may produce the observed EUV flux: thermal emission from the degenerate component of the system. Again, the same problem arises as for the analysis of HZ 43 — there are no published relevant model atmospheres for this combination of temperature, gravity, and composition.

In an initial attempt to understand the origin of the EUV emission from Feige 24, spectrophotometric measurements at a resolution of 0.8 nm were obtained of the star using the Cassegrain scanner of the Lick Observatory 3-m reflector. Nine observations were obtained between August 1975 and January 1976. A good signal-to-noise ratio was achieved in all cases, but wavelength coverage was dependent on other observing programs. Blue spectra (380 to 600 nm) data were obtained on August 11 and 12, 1975, and January 8 and 9, 1976. Yellow scans (480 to 720 nm) were acquired on August 11 and 12, 1975, September 2, 1975, and January 7 and 9, 1976. Finally, red and

infrared observations were made on August 12, 1975, and January 7, 1976, to extend wavelength coverage to 820 nm.

The spectrophotometry of Feige 24 is displayed in figure 4-12. Balmer emission lines due to neutral hydrogen appear in most of the scans but are highly variable in strength. When the hydrogen-alpha 685.3-nm line is strongest in emission, the neutral helium lines at 587.6, 447.1, and 667.8 nm also appear in emission. There is no trace of the ionized helium 468.6-nm line reported on one plate of Feige 24 in reference 4-20.

It is obvious from figure 4-12 that Feige 24 has an unusually variable spectrum on the time scale of days. Particularly noteworthy is the apparent anticorrelation of the M-star absorption features with the Balmer emission lines. The spectrum with strongest emission (January 9, 1976) also has

the weakest TiO and sodium features, and these latter features are strongest on nights of weakest emission (e.g., August 12, 1975). Whether this activity is due to flare star activity of the dwarf M component or to a heating (possibly periodic) of the M star by the hot white dwarf is as yet uncertain.

In a manner similar to that used in making calculations for HZ 43, the spectrophotometric data of figure 4-12 may be used to classify the M component of the Feige 24 system and to obtain a distance estimate. Based on the equivalent widths of the TiO bands in these data, the red star is of type dM1.5, yielding a distance estimate of 90 (+53, -33) pc. When combined with the EUV data of figure 4-11, this distance implies a volume density of neutral interstellar hydrogen  $n_H$  in this direction of  $0.01 \leq n_H \leq 0.1 \text{ atom/cm}^3$ .

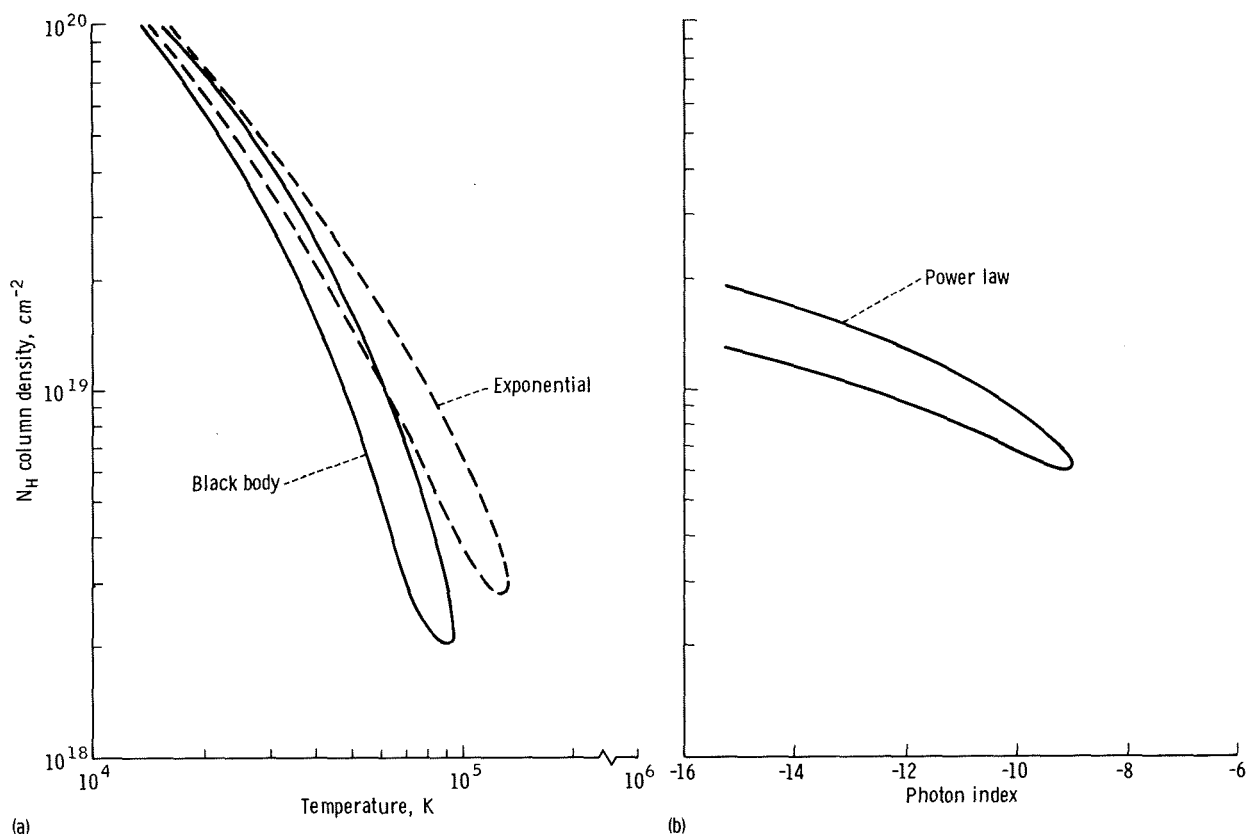


FIGURE 4-11.—Contours of constant  $\chi^2$  for fits of black-body, exponential, and power-law spectra to the Feige 24 EUV data. Each contour is drawn at the 90-percent statistical confidence level, analogous to figure 4-6. (a) Black-body and exponential contours. (b) Power-law spectra contour.

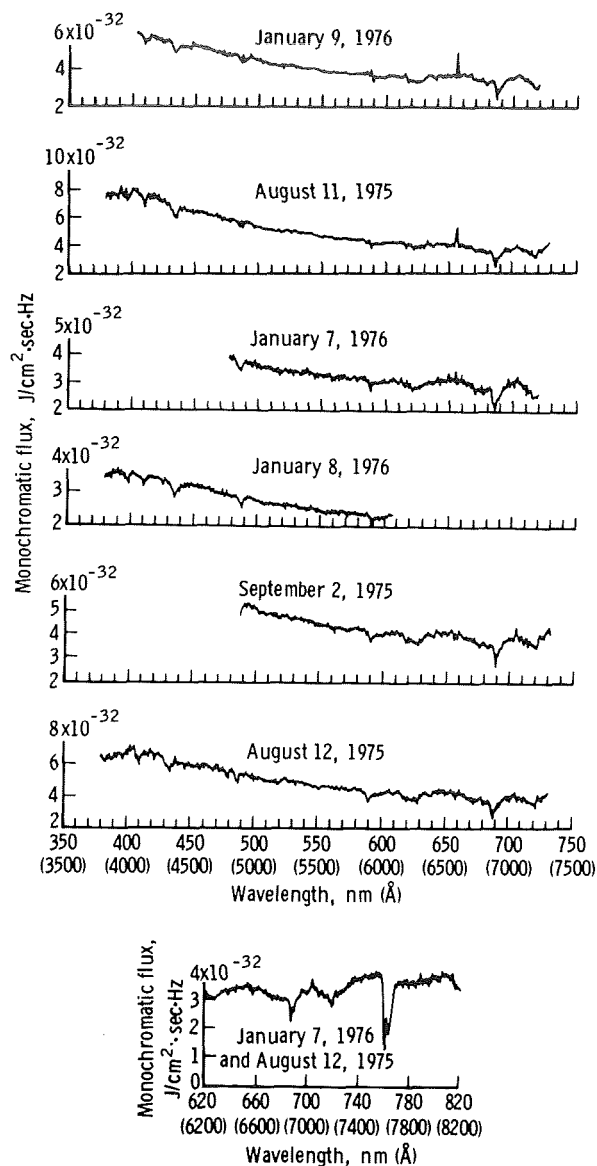


FIGURE 4-12.—Spectrophotometry of Feige 24 obtained with the image tube scanner of the 3-m telescope at the Lick Observatory. Note the prominent and variable emission feature due to neutral hydrogen at 656.3 nm. The deep absorption features at 690 and 760 nm are due to the Earth's atmosphere. (Insert at bottom shows curve of infrared data for two separate nights that have been summed for greater precision.)

### Proxima Centauri

On revolutions 94 and 109, the EUV observing program included the target Proxima Centauri, an

11th magnitude M5 dwarf star. At a distance of 1.3 pc, this object has the distinction of being the closest star to Earth other than the Sun. Table 4-III indicates that on revolution 94 there was no positive detection of flux from Proxima Centauri in any of the filters, although sensitivity was somewhat degraded by an intense South Atlantic Anomaly passage on this revolution. However, on revolution 109 there was a very strong positive detection of the target in the 5.5- to 15-nm (Parylene N) band. The data from this observation are given in figure 4-13. The rise and fall of the 5.5- to 15-nm count rates are seen to be precisely coincident with the entrance and exit of Proxima Centauri into and out of the EUV FOV; there can therefore be little doubt of the celestial nature of the detected radiation, or its identification with a source at or very near Proxima Centauri. The nearby companion  $\alpha$  Centauri can definitely be eliminated as the identification of the observed source. The spacing between the two stars is  $2.2^\circ$ , and the CSM ephemeris supplied by the NASA Lyndon B. Johnson Space Center indicates that, on this revolution, the EUV experiment received only a 5-second exposure to  $\alpha$  Centauri, which occurred just before the observed

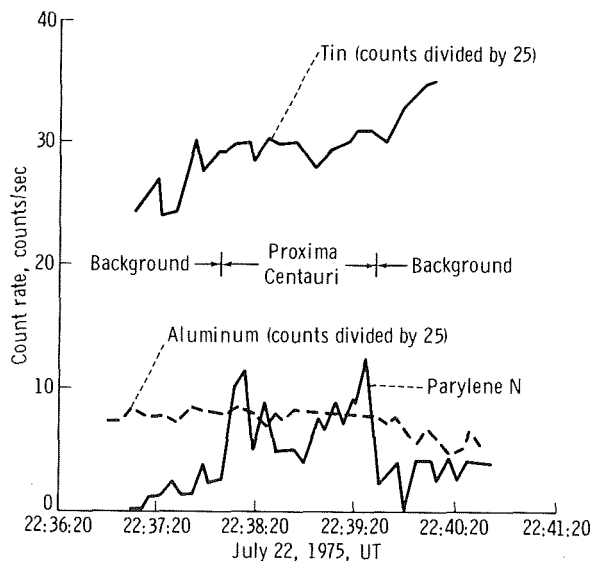


FIGURE 4-13.—Count rates from the EUV telescope during the observation of Proxima Centauri on revolution 109. The times when the star was within the telescope FOV, as computed from the CSM ephemeris, are also indicated.

increase in the 5.5- to 15-nm count rate that persisted for 80 seconds.

Data in figure 4-13 indicate that the source is not detected in the 17- to 62- or 50- to 78-nm bands. The 11.4- to 15-nm data have been omitted for clarity, but they give no statistically significant evidence for a detection. The upper limit in the 11.4- to 15-nm band is consistent with the positive flux detection in the 5.5- to 15-nm region, given the large difference in sensitivity of the parylene filter and the beryllium filter (a factor of 10 assuming a flat incident spectrum).

The revolution 109 data may be used to derive a crude spectrum for the observed source, using the technique previously described for HZ 43 and Feige 24. The results of the spectral fitting procedure are given in figure 4-14. The derivable constraints are all lower limits on the source temperature or spectral hardness, due to the weak nature of the detection. Nevertheless, it is clear from figure 4-14 that this source is quite different from those associated with HZ 43 and Feige 24, in that the spectrum is considerably harder. The flux observed at Earth in the 5.5- to 15-nm band is  $0.2 \text{ pW/m}^2$ , corresponding to an absolute luminosity of  $4.2 \times 10^{21} \text{ J/sec}$  or  $10^{-5} L_{\odot}$  at the 1.3-pc distance of Proxima Centauri.

There is little doubt that a source of this intensity in the 5.5- to 15-nm band would have been detected during the EUV observations on revolution 94. Table 4-III indicates that the upper limit on that occasion was 25 percent of the flux later observed on revolution 109. It is thus concluded with high probability that this source is variable in intensity on at least a time scale of 1 day. This variability and the nature of Proxima Centauri immediately suggest the occurrence of a stellar flare as an explanation for the observed flux. Proxima Centauri is a known optical flare star, and the luminosity of the visible flare events (300 to 700 nm) is similar to the EUV luminosity of the event observed during the Apollo-Soyuz mission.

Conclusive evidence for this hypothesis would, of course, be the simultaneous observation of an optical/EUV flare event. The time of the revolution 109 observation was such that ground-based observations of Proxima Centauri were possible only from the Eastern Hemisphere, south of the Equator. Prior arrangements were in fact made for

simultaneous optical photometry to be conducted from the Lake Tekapo, New Zealand, Mount John Observatory of the University of Canterbury; unfortunately, a major snowstorm at this time precluded any observations.

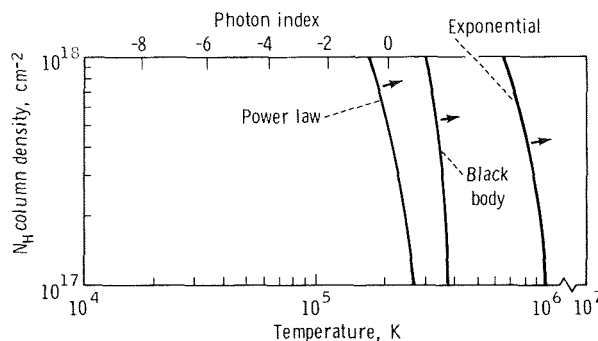


FIGURE 4-14.—Constraints on the EUV spectra of Proxima Centauri derived from the revolution 109 data. The arrows indicate that the spectral parameters must be to the right of the solid lines.

## SS Cygni

The bright dwarf nova SS Cygni was observed three times (revolutions 80, 90, and 105) during the mission. Fortunately, the object was undergoing an optical outburst at the time and was therefore 4 magnitudes (a factor of 40) brighter than normal in the visible band. Table 4-III indicates that there is a positive detection of SS Cygni in the 5.5- to 15-nm band on revolution 80, a marginal detection in this band on revolution 90, and no observable flux on revolution 105. There is no evidence for positive fluxes in any of the other band passes on any of the three observations. As is the case with Proxima Centauri, the lack of flux in the 11.5- to 15-nm band is consistent with the detection in the 5.5- to 15-nm channel because of the sensitivity ratios of the two filters.

The revolution 80 data have been used to derive constraints in the incident spectrum, and these results appear in figure 4-15. Note that the spectrum resembles that of Proxima Centauri more than HZ 43 or Feige 24; the source has a flat,

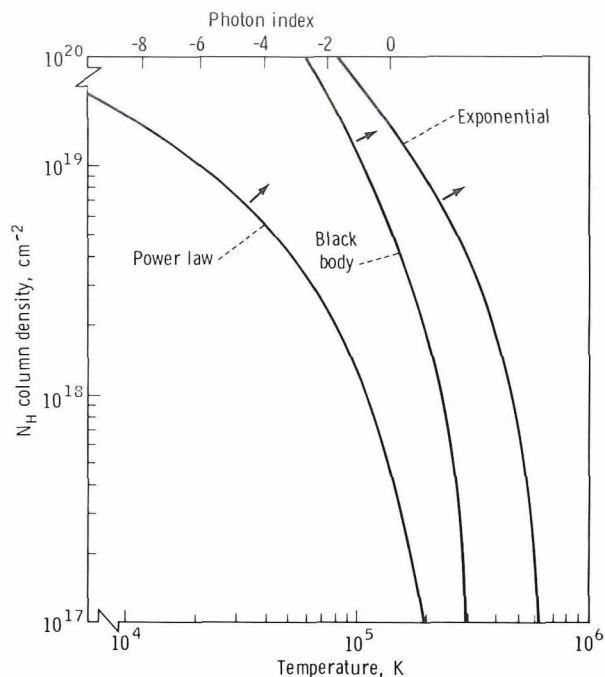


FIGURE 4-15.—Constraints on the EUV spectra of SS Cygni derived from the revolution 80 data. The arrows indicate that the spectral parameters must be to the right of the solid lines.

hard spectrum. The observed flux in the 5.5- to 15-nm range is  $0.1 \text{ pW/m}^2$ . Because the distance to SS Cygni can only be poorly estimated, it is difficult to accurately compute the interstellar absorption correction and intrinsic luminosity. If the distance to the star is assumed to be 100 pc and the volume density of neutral hydrogen is as low as  $0.1 \text{ atom/cm}^3$ , an absorption correction within the 5.5- to 15-nm range and an intrinsic luminosity of  $0.3 L_{\odot}$  or  $1 \times 10^{25} \text{ J/sec}$  can be inferred. This is considerably less than the intensity reported in the 4.4- to 8.3-nm band in reference 4-26 but not incompatible with more recent unpublished observations by the Small Astronomy Satellite-3 and Astronomical Netherlands Satellite (ANS) experiments. It seems likely that there may be a range of possible EUV/soft X-ray luminosities for this system, both in active and quiescent states.

The fact that the Apollo-Soyuz observations spanned almost 2 days presented the opportunity to search for correlations between the EUV and the variable optical intensity. A large volume of

optical photometry was successfully acquired for SS Cygni, simultaneous with the Apollo-Soyuz observations. These data include photoelectric photometry with the 0.6-m reflector at the Lick Observatory, photographic photometry with the 0.8-m reflector at the Leuschner Observatory, photoelectric photometry with the 0.8-m reflector at the Manastash Ridge Observatory, and several hundred visual magnitudes supplied by the American Association of Variable Star Observers and numerous independent professional and amateur observers. Interpretation of this large amount of heterogeneous data is not yet complete; however, preliminary results indicate that the optical outburst began on July 17, 1975, and that the system remained at or near maximum light throughout the EUV observations. It is hoped that the joint analysis of the EUV and visible data will ultimately contribute to an understanding of the cause of the outbursts.

### Selected Upper Limits

The upper limits on EUV and ultrasoft X-ray emission obtained on many of the sources in table 4-II, which were observed but not detected, provide useful new constraints on models of these objects. Detailed analysis is still underway for most of these objects, but some of the more potentially interesting results will be noted here as examples of the usefulness of the data.

Extreme ultraviolet observations of Sirius B were obtained on revolution 88. This object is important because it is the closest known white dwarf, one of the hottest, and one of only three white dwarfs with dynamically determined masses. This is one of the few objects observed during the Apollo-Soyuz mission that is so close to Earth that interstellar photoelectric opacity is negligible, even at wavelengths as long as the Lyman limit (91.2 nm). The derived upper limit in the 50- to 78-nm band is  $1.7 \text{ pW/m}^2$ , corresponding to an intrinsic luminosity of  $1.4 \times 10^{23} \text{ J/sec}$  at a distance of 2.7 pc to Sirius B. This limit is a full factor of 10 more stringent than that derived by the California Institute of Technology investigators in a sounding rocket experiment (ref. 4-27). Preliminary calculations indicate the



Apollo-Soyuz upper limit violates the predicted EUV flux for the currently accepted Sirius B model atmosphere, indicating that these theoretical models may need to be reexamined.

On revolutions 89 and 109, three radio pulsars were observed: PSR 1133+16, 1451-68, and 1929+10. There were no positive detections, with upper limits of approximately  $0.2 \text{ pW/m}^2$  obtained in the 5.5- to 15-nm band. These results are interesting because there has never been a detection of thermal radiation from a neutron star. The fact that such objects are not strong thermal X-ray sources in the 0.1- to 1-nm band constrains their surface temperatures to be less than  $5 \times 10^6 \text{ K}$  (e.g., ref. 4-28); however, until the current experiment, it has been impossible to push this limit to cooler temperatures, and thus more restrictive inferences on the equation of state, because the bulk of thermal radiation for  $5 \times 10^4 < T < 5 \times 10^6 \text{ K}$  emerges in the EUV. The Apollo-Soyuz limits may be interpreted to provide these new constraints.

On revolution 104, the binary X-ray pulsar Hercules X-1 was observed in conjunction with a soft X-ray observation. The binary phase of the pulsar during the observation was 0.72, which means that the X-ray source was uneclipsed as viewed from Earth. The source was not detected by either experiment, with the EUV experiment providing an upper limit of  $50 \text{ fW/m}^2$  in the 5.5- to 15-nm range. This limit is highly significant because it is substantially less than the positively detected intensity in this band obtained by two sounding rocket experiments (refs. 4-29 and 4-30). As reported in reference 4-29, for example, an intensity of  $2 \text{ pW/m}^2$  was observed in the 4.4- to 6.9-nm band, or a factor of 40 above the upper limit. This proves that the ultrasoft X-ray component of Hercules X-1 is time variable, perhaps as a function of the 35-day period of the system.

### Observations of the Diffuse Background Radiation

Although the 4.4- to 6-nm component of the cosmic diffuse background radiation was discovered almost a decade ago (ref. 4-31), its origin

is still not understood. This radiation is spatially anisotropic, in contrast to the diffuse X-ray background at shorter wavelengths. Also, the flux is detected in directions where the mean free path due to interstellar photoelectric opacity is known to be small. These facts indicate that this radiation is distinct from the hard X-ray background and has a relatively local galactic origin. Various investigators have searched for correlations of the intensity of this radiation with numerous other phenomena (e.g., neutral interstellar hydrogen column density, far-UV absorption lines of hot interstellar gas, low-frequency radio features, etc.) with ambiguous results. Part of the difficulty is the lack of a high-resolution all-sky survey at those wavelengths made with one instrument over a relatively short period of time.

The Apollo-Soyuz EUV observations in the 5.5- to 15-nm band represent a tremendous increase in the data available to examine this problem. A combination of data acquired during operations at or near the preselected EUV targets, during the Helium Glow Experiment great circle scans, and during the soft X-ray maneuvers encompasses a remarkably representative sample of all galactic longitudes and latitudes. The observations were made primarily with the  $2.4^\circ$ -diameter FOV, which was the best spatial resolution ever used for such a survey, and were all acquired by the same instrument over a period of time that was short compared to many solar and terrestrial phenomena. The data also extend to longer wavelengths than previously used for this work to take advantage of the sharply increasing fluxes due to the steep spectrum. Finally, data were acquired at a wide variety of different geocentric, geomagnetic, and solar coordinates, enabling a careful search to be made for noncelestial flux contributions that have been a problem in many previous brief experiments.

The reduction of this large amount of data is still underway; however, preliminary results appear in figure 4-16, where the 5.5- to 15-nm count rate (with opaque shutter background subtracted) is plotted as a function of galactic latitude for a variety of longitudes. Several interesting features are apparent in figure 4-16. Even using data strictly from EUV targeted observations, a remarkably wide spatial coverage was achieved in



galactic coordinates. To within the counting statistics of the observations, the intensity seems reasonably uniform as a function of longitude and latitude. This is in sharp contrast to 4.4- to 6-nm surveys (e.g., ref. 4-32) in which high-to-low latitude intensity contrasts of a factor of 5 are not uncommon. Thus, these data are interpreted as evidence that spatial isotropy may be gradually restored as observations are shifted to longer and longer wavelengths.

A natural (although tentative) interpretation of this phenomenon is as follows. As the wavelength of observation increases, the mean free path due

to interstellar photoelectric absorption decreases. If the radiation is in fact due to large-scale galactic features such as thermal emission from hot gas clouds or radio loops, the line of sight at these longer wavelengths will reach only the very nearest such features, which will in turn have the largest solid angles as viewed from Earth. As fewer emitting features are superposed, a large-scale intensity isotropy would be expected to emerge. Further analysis of the EUV background observations will be needed to verify the plausibility of this concept.

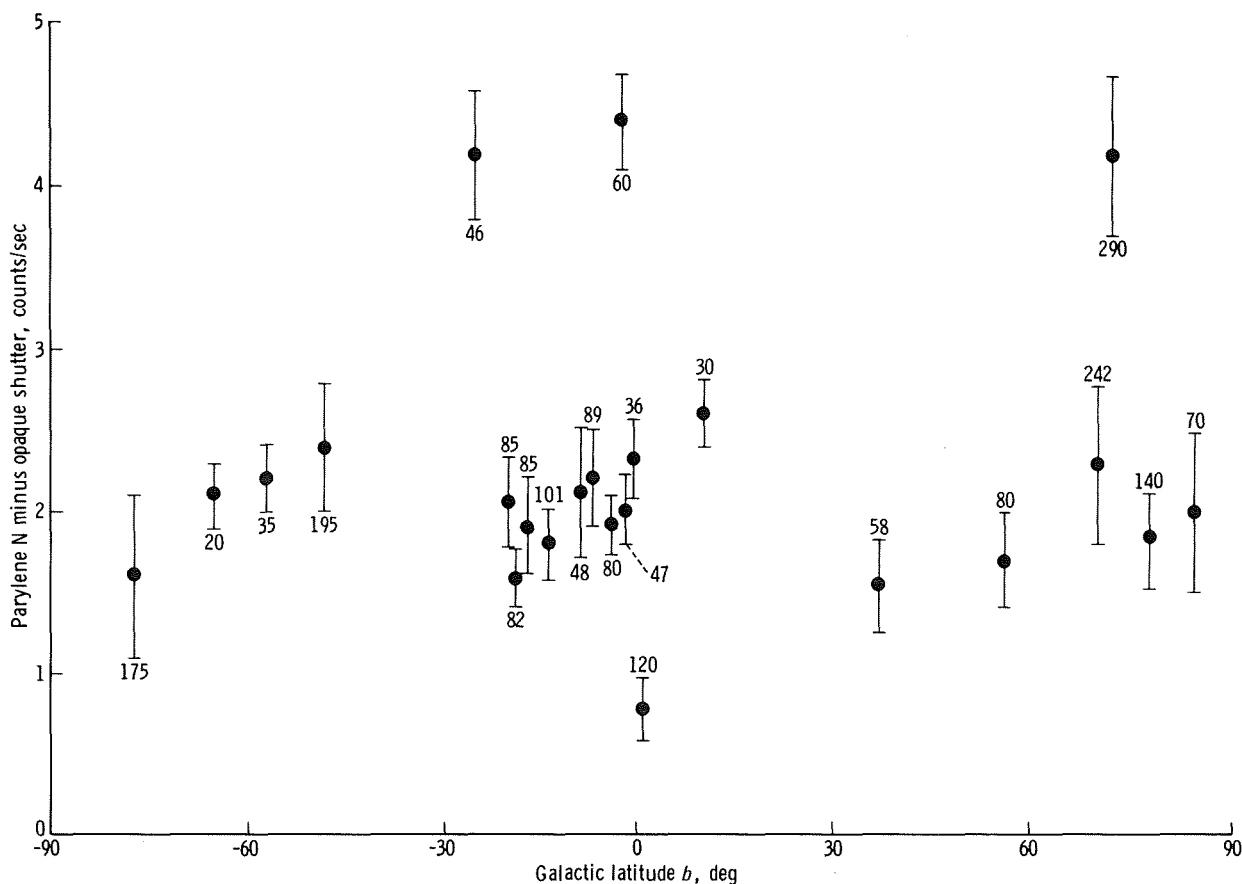


FIGURE 4-16.—The intensity of the diffuse cosmic background radiation in the 5.5- to 15-nm band as a function of galactic latitude, as observed by the EUV telescope. The galactic longitude where each data point was acquired is also indicated.

## SUMMARY

All the primary goals of the EUV Survey Experiment were achieved. Data were acquired on 30 different targets belonging to a variety of different classes of stars. Extensive and sensitive data on the EUV background radiation were also obtained. The targeted observations have resulted in the detection of at least four celestial sources of EUV radiation, the first such objects ever to be detected. The observed objects belong to three different classes of stars — hot white dwarfs, flare stars, and dwarf novae — and have different spectra and intrinsic luminosities. The investigators conclude that extrasolar EUV astronomy is not only feasible but that the varied nature of the detectable sources indicates that this field will have an impact on astronomy as a whole comparable to that obtained when previously unexplored windows in the electromagnetic spectrum have been opened.

## ACKNOWLEDGMENTS

The Lick Observatory 3-m spectrophotometry discussed here was obtained in collaboration with Dr. J. Liebert (Steward Observatory, University of Arizona) and Dr. H. Spinrad (Astronomy Department, University of California at Berkeley). The parallax for HZ 43 was obtained in collaboration with Dr. G. Gatewood (Allegheny Observatory, University of Pittsburgh).

## REFERENCES

- 4-1. Hills, J. G.: An Explanation of the Cloudy Structure of the Interstellar Medium. *Astron. & Astrophys.*, vol. 17, 1972, pp. 155-160.
- 4-2. Rose, W. K.; and Wentzel, D. G.: Ultraviolet Stars and the Interstellar Gas. *Astrophys. J.*, vol. 181, 1973, pp. 115-123.
- 4-3. Greenstein, J. L.; and Sargent, A. I.: The Nature of Faint Blue Stars in the Halo. II. *Astrophys. J. Supp. Series*, vol. 28, no. 259, 1974, pp. 157-210.
- 4-4. Carnochan, D. J.; Dworetzky, M. M.; et al.: A Search for Ultraviolet Objects. *Phil. Trans. Roy. Soc. London, A*, vol. 279, 1975, pp. 479-485.
- 4-5. Rogerson, J. B.; York, D. G.; et al.: Spectrophotometric Results From the *Copernicus* Satellite. III. Ionization and Composition of the Intercloud Medium. *Astrophys. J. (Letters)*, vol. 181, 1973, pp. L110-L115.
- 4-6. Bohlin, R. C.: *Copernicus* Observations of Interstellar Absorption at Lyman Alpha. *Astrophys. J.*, vol. 200, 1975, pp. 402-414.
- 4-7. Dupree, A. K.: Ultraviolet Observations of Alpha Aurigae From *Copernicus*. *Astrophys. J. (Letters)*, vol. 200, 1975, pp. L27-L31.
- 4-8. Cruddace, R.; Paresce, F.; Bowyer, S.; and Lampton, M.: On the Opacity of the Interstellar Medium to Ultrasoft X-rays and Extreme Ultraviolet Radiation. *Astrophys. J.*, vol. 187, 1974, pp. 497-504.
- 4-9. Riegler, G. R.; and Garmire, G. P.: Observations of the Extreme Ultraviolet Nightglow. *J. Geophys. Res.*, vol. 79, 1974, pp. 226-232.
- 4-10. Henry, P.; Bowyer, S.; et al.: An Extreme Ultraviolet Search of the Galactic Anticenter Region. *Bull. American Astron. Soc.*, vol. 6, no. 4, part I, 1974, p. 446.
- 4-11. Henry, Patrick; Bowyer, Stuart; et al.: Limits on the Space Density of 0 Subdwarfs and Hot White Dwarfs From a Search for Extreme Ultraviolet Sources. *Astrophys. J.*, vol. 205, 1976, pp. 426-429.
- 4-12. Henry, Patrick; Cruddace, Raymond; et al.: Limits on the Soft X-ray and Extreme Ultraviolet Flux From RX Andromedae and U Geminorum. *Astrophys. J. (Letters)*, vol. 197, 1975, pp. L117-L121.
- 4-13. Henry, P.; Cruddace, R.; et al.: An Extreme Ultraviolet Search of the North Galactic Polar Region. *Astrophys. J.*, vol. 195, 1975, pp. 107-110.
- 4-14. Margon, B.; and Bowyer, S.: Extreme Ultraviolet Astronomy From Apollo-Soyuz. *Sky and Telescope*, vol. 50, no. 1, 1975, pp. 4-9.
- 4-15. Hoshiko, H. H.: Helical Channel Multiplier Package Design for Space Instrumentation. *Rev. Sci. Instr.*, vol. 46, no. 3, 1975, pp. 331-332.

- 4-16. Hayakawa, Satio; Tanaka, Yasuo; et al.: Soft X-ray Emission From the Direction of the Coma Cluster. *Publ. Astron. Soc. Japan*, vol. 27, 1975, pp. 615-617.
- 4-17. Margon, B.; Malina, R.; et al.: An Ultrasoft X-ray Source in Coma Berenices. *Astrophys. J. (Letters)*, vol. 203, 1976, pp. L25-L28.
- 4-18. Hearn, D. R.; Richardson, J. A.; et al.: MX 1313+29: A Compact Source of Very Low Energy X-rays in Coma Berenices. *Astrophys. J. (Letters)*, vol. 203, 1976, pp. L21-L24.
- 4-19. Margon, B.; Lampton, M.; Bowyer, S.; and Cruddace, R.: Soft X-ray Spectroscopy of Three Extragalactic Sources. *Astrophys. J.*, vol. 197, 1975, pp. 25-29.
- 4-20. Eggen, O. J.; and Greenstein, J. L.: Spectra, Colors, Luminosities, and Motions of the White Dwarfs. *Astrophys. J.*, vol. 141, 1965, pp. 83-108.
- 4-21. Liebert, James: The Demise of the Degenerate M Stars. *Astrophys. J. (Letters)*, vol. 200, 1975, pp. L95-L98.
- 4-22. Wagman, N. E.: Photographic Determinations of the Parallaxes of 67 Stars With the Thaw Refractor, *Astronom. J.*, vol. 72, 1967, pp. 957-958.
- 4-23. Lampton, M.; Margon, B.; et al.: Discovery of a Non-solar Extreme Ultraviolet Source. *Astrophys. J. (Letters)*, vol. 203, 1976, pp. L71-L74.
- 4-24. Condon, J.: New Soft X-ray Source. *International Astronomical Union Circular No. 2790*, June 17, 1975.
- 4-25. Wu, C. C.; Wesselius, P. R.; et al.: HZ 43. *International Astronomical Union Circular No. 2805*, July 22, 1975.
- 4-26. Rappaport, S.; Cash, W.; et al.: Possible Detection of Very Soft X-rays from SS Cygni. *Astrophys. J. (Letters)*, vol. 187, 1974, pp. L5-L7.
- 4-27. Riegler, G. R.; and Garmire, G. P.: Search for Extreme Ultraviolet Radiation From Selected Stars. *Astron. & Astrophys.*, vol. 45, no. 1, 1975, pp. 213-216.
- 4-28. Greenstein, George; and McClintock, Jeffrey E.: Prospects for Detecting Blackbody X-rays From Neutron Stars. *Science*, vol. 185, Aug. 9, 1974, pp. 487-490.
- 4-29. Shulman, S.; Friedman, H.; et al.: Soft X-ray Emission From Hercules X-1. *Astrophys. J. (Letters)*, vol. 199, 1975, pp. L101-L104.
- 4-30. Catura, R. C.; and Acton, L. W.: Intense Soft X-ray Flux From Hercules X-1. *Astrophys. J. (Letters)*, vol. 202, 1975, pp. L5-L7.
- 4-31. Bowyer, C. S.; Field, G. B.; and Mack, J. E.: Detection of an Anisotropic Soft X-ray Background Flux. *Nature*, vol. 217, 1968, pp. 32-34.
- 4-32. Davidsen, A.; Shulman, S.; et al.: Observations of the Soft X-ray Background. *Astrophys. J.*, vol. 177, 1972, pp. 629-642.

## 5. Interstellar Helium Glow

### Experiment MA-088

*S. Bowyer,<sup>a†</sup> J. Freeman,<sup>a</sup> M. Lampton,<sup>a</sup> and F. Paresce<sup>a</sup>*

#### ABSTRACT

A four-channel photometer sensitive to two solar extreme-ultraviolet lines that are resonantly scattered by helium gas was developed for the Apollo-Soyuz Test Project. Two channels were used to observe the 58.4-nm line of He I (neutral), and helium gas resonant absorption cells were used to determine the intensities of the center and wings of that line. The other two channels were used to observe the 30.4-nm line of the He II (singly ionized).

The instrument surveyed much of the celestial sphere during a series of slow rolling maneuvers by the Apollo spacecraft. The experiment operated properly and usable data were obtained. Study of the distributions of observed flux and study of the ratio of 58.4-nm fluxes observed with gas cells full and empty will refine current understanding of several poorly known properties of the local interstellar medium. Study of the 30.4-nm flux distribution will refine present knowledge of the structure of the Earth's plasmasphere.

#### INTRODUCTION

Observation of interstellar gas passing through the solar system provides information about the temperature, number density, and bulk velocity of the local interstellar medium (ISM). As discussed by Danby and Camm (ref. 5-1), Blum and Fahr

(ref. 5-2), Holzer and Axford (ref. 5-3), Axford (ref. 5-4), Johnson (ref. 5-5), and Wallis (ref. 5-6), neutral atoms passing near the Sun are gravitationally focused into a density distribution for which the shape depends, in a complicated manner, both on ISM parameters and on the local effects of photoionization by the Sun, collisional ionization by the solar wind, collisions with other atoms, and the pressure of sunlight. Detailed study of this density distribution permits untangling of the various parameters, some of which are uncertain by an order of magnitude or more. In pursuit of these ends, observations have been made of ISM hydrogen (Thomas and Krassa, ref. 5-7; Bertaux and Blamont, ref. 5-8; and Thomas, ref. 5-9) and helium (Paresce et al., refs. 5-10 and 5-11; Weller and Meier, ref. 5-12; and Freeman et al., ref. 5-13) using photometers sensitive to solar radiation resonantly scattered by the species in question.

Neutral helium is perhaps the component of the ISM most suitable for such observations, for several reasons. It is second only to neutral hydrogen in abundance, and it resonantly scatters the intense solar 58.4-nm radiation ( $1s^2-1s2p$  transition). This wavelength does not readily penetrate the ISM; thus, observations of local interstellar helium do not suffer, as do Lyman- $\alpha$  observations, from confusion from a possible galactic background flux. Finally, the Sun's gravity clearly dominates the solar radiation pressure on helium, unlike hydrogen (Fahr, ref. 5-14), resulting in sharp gravitational focusing and pronounced local helium density variations.

Any such observation made from the immediate vicinity of Earth must contend with a potentially serious background problem due to resonant

---

<sup>a</sup>University of California at Berkeley.

<sup>†</sup>Principal Investigator.

scattering from helium atoms in the Earth's upper atmosphere. The temperature of the helium geocorona is approximately 1000 K, (Jacchia, ref. 5-15), corresponding to helium thermal speeds of approximately 2 km/sec and to thermal-Doppler broadening of the scattered 58.4-nm line of approximately 0.6 pm full width half maximum. On the other hand, the bulk speed of the local ISM with respect to the Sun is generally believed to be 5 to 20 km/sec (Fahr, ref. 5-14; and Thomas, ref. 5-16), and the orbital speed of the Earth is 30 km/sec; hence, there are large solid angles, the configuration of which varies throughout the year, within which the radial velocities of local interstellar helium with respect to Earth are several tens of kilometers per second. This radiation will reach Earth Doppler-shifted away from the geocoronal 58.4-nm line by several times the width of that line. Hence, a narrow-band gas absorption cell having an absorption feature sufficiently wide to contain the geocoronal line will absorb the geocoronal 58.4-nm flux while transmitting most of that scattered from the local ISM. Such a cell can be made by confining helium in the optical path leading to the detector.

The intensity observed with the gas cell filled provides an additional datum that enables more detailed fitting of ISM models to observations. For the cell used in the present instrument, this signal is produced only by helium atoms moving at a radial speed of at least 9 km/sec with respect to the photometer, and is consequently a sensitive indicator of the dynamical state of the gas. The ratio  $\epsilon_0$  of 58.4-nm fluxes seen with the gas cell full and empty is a particularly valuable datum because it does not depend on the integrated solar flux  $F$  at 58.4 nm, the density of helium  $n_{He}$  in the local ISM, the transmission of the broadband filters used in the photometer, or the quantum efficiency of the instrument's photon detector. Any model fitting that results from measurements of  $\epsilon_0$  will therefore depend only on model parameters other than  $F$  and  $n_{He}$ , and will be independent of any changes in instrument sensitivity that may have occurred between calibration and flight. The parameter  $\epsilon_0$  is clearly most useful when it can be shown that the contribution of the geocoronal 58.4-nm flux to the cell-empty count rate is small.

Observations of 30.4-nm flux have been made by Paresce et al. (refs. 5-17 and 5-18), Ogawa and Tohmatsu (ref. 5-19), and Young et al. (ref. 5-20). Although the distribution of the observed flux agrees broadly with the distribution that would be observed if the flux were due to scattering of solar 30.4-nm radiation off He II (singly ionized) trapped in the Earth's magnetosphere (Paresce et al., ref. 5-18), additional observations will refine knowledge of magnetospheric structure. Furthermore, a component of this flux scattered from the local ISM might exist. An observer within the Earth's lower magnetosphere could best detect such a component by observing from within the Earth's shadow, looking up the axis of the shadow. Positive identification of a local ISM component of 30.4-nm flux by this means would depend on detailed comparison of observations with models of the He II in the magnetosphere. Information about such a component would further clarify the interaction of the local ISM with the Sun's gravity and radiation and would facilitate correct inferences about distant ISM properties from local ISM observations. For this reason, the photometer was designed to observe local helium at both 58.4- and 30.4-nm wavelengths.

## MISSION ENVIRONMENT

The Apollo-Soyuz Test Project (ASTP) helium glow detector (HGD) was mounted to a shelf inside one bay of the Apollo service module, approximately 1 m from the spacecraft main engine. The HGD observed through a remotely operated door that was closed for launch and opened in orbit during data takes. Previous Apollo flights and engineering studies had defined the environmental stresses to which the HGD would be subjected.

Although orbital flight imposed no mechanical loads on the HGD, it did contribute to several other environmental problems. Temperatures at the instrument attachment point were predicted to vary between 273 and 328 K (0° and 55° C). The HGD was required to operate successfully at temperatures set by these limits and by the varying radiant flux reaching the instrument through its

door. There was a possibility that gas leaks from another scientific instrument in the same bay might cause the local ambient pressure to rise from 0.1 to 1.0 N/m<sup>2</sup>, which might have induced corona discharge from high-voltage elements of the HGD, resulting in possible damage to the instrument.

Degradation of the HGD optics would have occurred if they had become coated with contaminants that were purged or outgassed from Apollo systems. Transmission of extreme-ultraviolet (EUV) light at the wavelengths studied by the HGD is blocked almost completely by only 10 to 100 nm of most materials; and, in normal operation, the Apollo spacecraft exudes a diverse variety of contaminants.

The nominal 250-km altitude of the mission orbit placed the spacecraft well within the ionosphere and subjected the HGD to large fluxes of ions and electrons. The photon detectors used by the instrument respond to ions and electrons; therefore, the ionosphere fluxes posed a potential problem of severe data degradation.

## DESIGN OF INSTRUMENT

The major systems of the HGD were photon detectors, broadband spectral filters, helium gas absorption cells and associated gas supply system, and electronic components.

### Photon Detectors

The HGD included four photometers, each using a channel electron multiplier (CEM) as a photon detector. The photometers were generally similar in construction, operation, and performance to those discussed by Bowyer et al. (ref. 5-21). They featured a conical photocathode with an active diameter of 15 mm and an included angle of 22°, and a helical electron multiplier formed from capillary tubing. The fragile nature of these devices necessitated the development of a special mounting (Hoshiko, ref. 5-22).

Two identical channels were used to observe 58.4-nm radiation, and two more were primarily sensitive to 30.4-nm radiation. The band passes

within which the photometers observed were defined by the EUV transmission of 80- to 160-nm-thick metal filters (Bowyer et al., ref. 5-21; and Steele, ref. 5-23). The 58.4-nm channels were used to view the sky through gas absorption cells, each of which was capped with one tin and one aluminum filter. Together, these filters provided a band pass approximately 10 nm wide, containing the 58.4-nm line. Each collimator for the 30.4-nm channels contained a single filter, composed of a layer of aluminum and a layer of carbon, which defined a similar band pass for this wavelength.

To prevent the CEM's from detecting charged ionospheric particles, the HGD used magnetic brooms to prevent ionospheric ions and electrons from entering photometer viewports and instrument-housing vents. Each broom was an annular array of magnets that produced a transverse magnetic field of approximately 15 mT (150 G), several centimeters in depth. Other possible locations for charged-particle leaks, such as joints and clearances around screws, were carefully sealed. A positive potential of 35 V was applied to the outer extremity of each CEM in normal operation, providing additional shielding against stray thermal positive ions.

### Gas Absorption Cells

The dimensions of the helium gas absorption cells were selected so that each cell would contain an appropriate amount of gas; the thermal-Doppler-broadened helium scattering cross section near 58.4 nm was evaluated using an oscillator strength (Allen, ref. 5-24) of 0.276. Collisional broadening was not significant in the range of helium pressures and temperatures considered. Calculations indicated that a 0.1-m-long column of helium at a temperature of 300 K and a pressure of 130 N/m<sup>2</sup> absorbs more than 99 percent over a band approximately 3.5 pm full width, as shown in figure 5-1. Such a width is sufficient to absorb the geocoronal 58.4-nm line even when it is Doppler shifted by the 8-km/sec speed of an orbiting spacecraft.

Various mechanisms were considered that could reliably and repeatedly establish the design

pressure in the gas absorption cell in a flight instrument. Commercial regulators capable of delivering pressures of 100 to 200 N/m<sup>2</sup> reliably during a spacecraft mission were not available, nor were sensors for such pressures with sufficiently fast response to control a gas system by feedback.

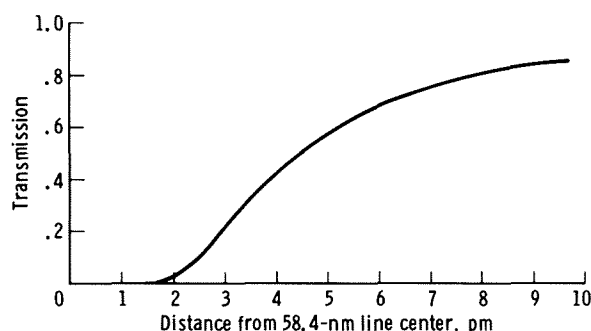


FIGURE 5-1.—Theoretical transmission of the filled gas absorption cell as a function of wavelength.

The system finally chosen for ASTP is shown in figure 5-2. Helium was supplied to the gas cells from a tank at a pressure of approximately 6 MN/m<sup>2</sup>. The gas flowed through a master solenoid valve to a regulator, where its pressure was reduced to approximately 100 kN/m<sup>2</sup>. The gas then flowed through adjustable needle valves into small transfer manifolds. To pressurize a gas cell, the fill valve was opened for a "preset" short interval, releasing into the cell the gas in the transfer manifold plus a small additional amount that leaked through the needle valve. The transfer manifold volume was selected so that it alone contained not quite enough helium to fill a cell to design pressure; and, during testing, the needle valve was adjusted until the total amount of gas released produced the desired pressure of 130 N/m<sup>2</sup>.

A thermocouple gage tube was connected to each cell for continuous in-flight monitoring of cell pressure. A thermistor was bonded to each cell to measure cell temperature. The cells also served as collimators restricting the field of view of the 58.4-nm photometer channels to 14° full width half maximum. The collimators for the

30.4-nm channels were similar in mechanical design to the gas absorption cells and provided the same field of view.

Absorption cells for the Lyman- $\alpha$  line of atomic hydrogen, which are conceptually similar to the one described here but technically quite different, have been successfully used by Morton and Purcell (ref. 5-25), Winter and Chubb (ref. 5-26), and Blamont and Madjar (ref. 5-27). Helium absorption cells have been successfully flown by Delaboudiniere and Carabetain (ref. 5-28) in observations of the Sun, and by Freeman et al. (ref. 5-13) in studies of the local ISM.

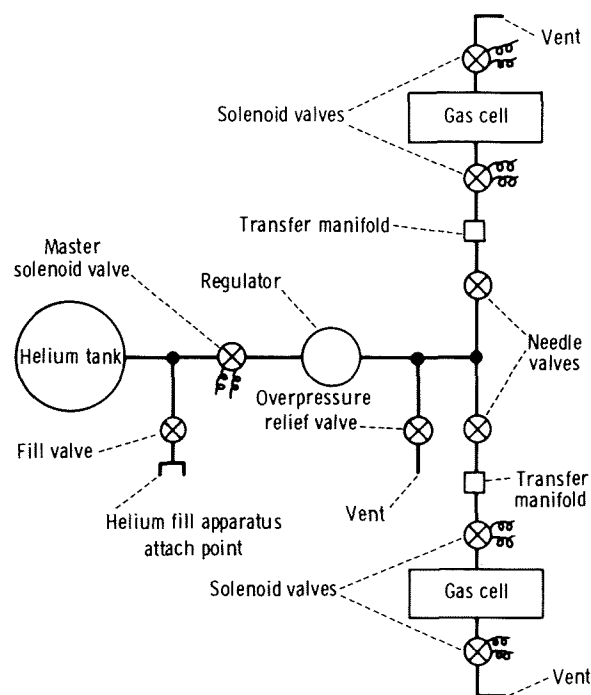


FIGURE 5-2.—Mechanical block diagram of HGD gas plumbing subsystem.

### Thin Metal Filters

The mesh-supported thin metal filters used to restrict the photometer's broadband spectral response posed special design and development problems. Several filters were torn during initial vibration tests. The filter mounts were then



modified by providing an epoxy fillet between the filter surface and the interior of the mounting ring; the problem did not recur.

Thin metal filters mounted in flight configuration were tested to determine whether they could survive repeated application and removal of the  $130\text{-N/m}^2$  cell pressure. The test fixture used automatically controlled solenoid valves to apply and remove a preset, regulated differential pressure to a filter at a rate of approximately one complete cycle every 5 seconds. High-purity dry nitrogen gas was used to establish the pressure differential, and the tests were run at atmospheric pressure in a closed chamber that was continuously purged with high-purity dry nitrogen. The filters were visually inspected for pinholes before and after

the test using backlighting under  $10\times$  magnification. Filter leak rates were measured with the test fixture before, during, and after the pressure cycling.

The number of gas absorption cell pressure cycles that each filter would undergo during calibration and flight was expected to be approximately  $2.5 \times 10^4$ . An aluminum-silicon filter was cycled  $6.9 \times 10^4$  times. It showed no pinholes before or after testing. An upper bound for its leak rate at the conclusion of the test was  $2 \times 10^{-8} \text{ m}^3/\text{sec}$ . If this leak rate were caused by a single round hole having a diameter greater than its length, the hole diameter would have been  $2 \mu\text{m}$ . The leak rate corresponds to a pressure decay time constant ( $10^5$  seconds) for helium leaking into a vacuum.

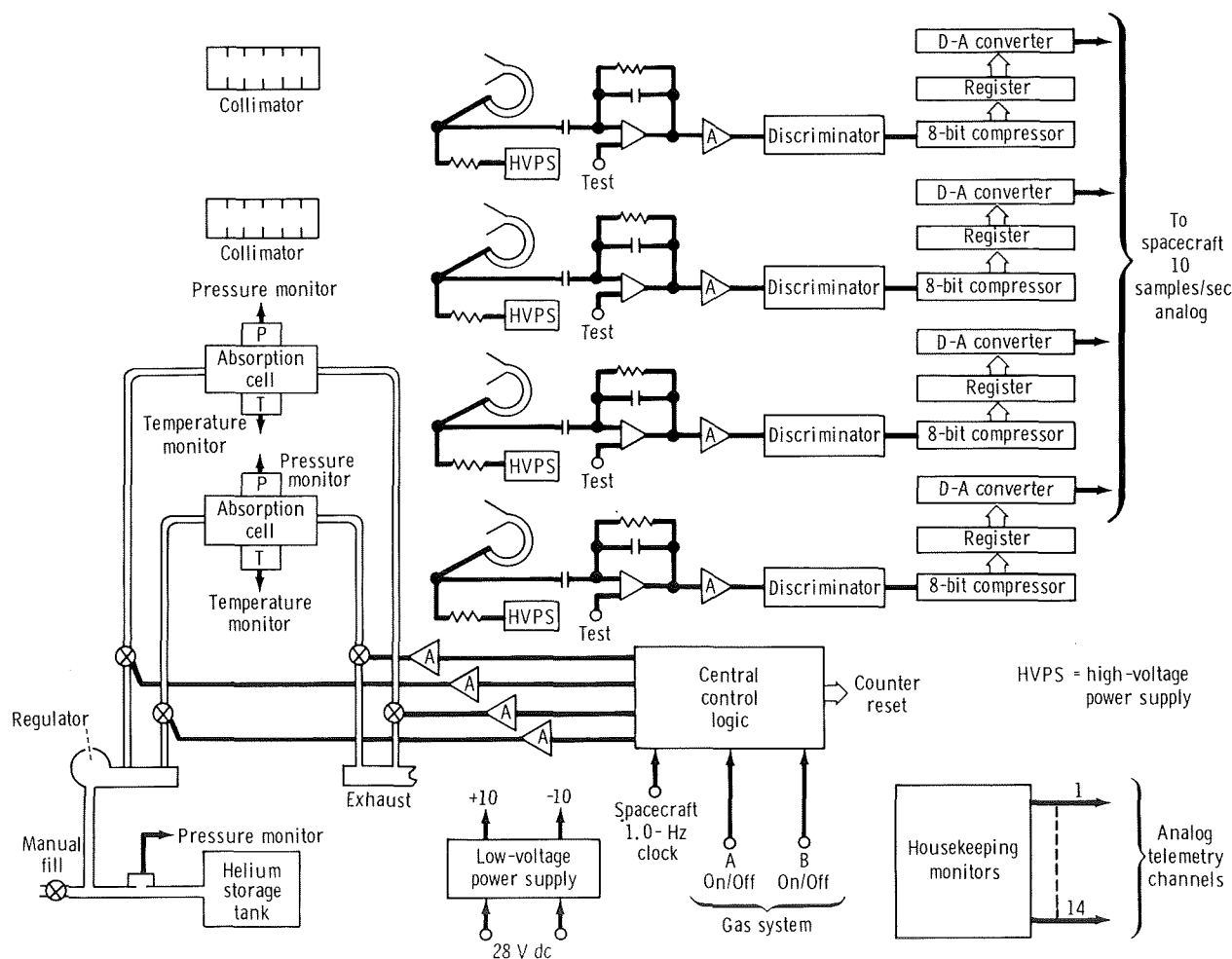


FIGURE 5-3.—Helium glow detector electronics subsystem block diagram.

A tin-germanium filter was cycled  $9.0 \times 10^4$  times. It showed no pinholes before the test and five pinholes after test. The leak rate after testing was  $2 \times 10^{-7}$  m<sup>3</sup>/sec, which corresponds to a single 6- $\mu$ m-diameter hole and to a pressure decay time constant for helium leaking into vacuum of  $10^4$  seconds, which is still far longer than the 2.5-second interval during which the absorption cell was intended to hold pressure. Pinholes of these sizes could have caused only a negligible increase in background count rate, even when the instrument viewed the  $2 \times 10^{14}$  sec<sup>-1</sup> m<sup>-2</sup> ( $2 \times 10^4$  rayleighs) of Lyman- $\alpha$  flux from the daytime sky.

### Electronics Subsystem

The HGD electronics subsystem is shown in block diagram form in figure 5-3. The amplifier system for each detector channel accepted signals as small as  $10^{-14}$  C at a maximum random rate of  $10^5$ /sec. A pulse-pair resolution of 1.0 microsecond ensured that statistical counting losses remained below 10 percent, even at maximum count rate.

The compressor and register for each channel accepted serial event pulses from the discriminator and produced an 8-bit output word representative of the number of events detected in each 0.1-second accumulation interval. The binary word was then converted by the digital-to-analog converter to an analog voltage compatible with the Apollo telemetry system. The output voltage was updated every 0.1 second in synchronization with the sampling of that voltage by the telemetry system.

Data compression was necessary because the 8-bit word used by the telemetry system allowed only 256 distinct output signals, whereas the event rates from the detector ranged up to  $10^4$  per sampling interval. An adaptive prescaler compression algorithm was selected that produced an output word the numerical value of which varied in a manner similar to the logarithm of the number of counts detected in the sampling interval.

The housekeeping parameters (gas absorption cell pressures, average absorption cell temperature, storage-tank gas pressure, and a current

monitor for the high-voltage power supplies) were sampled and telemetered for real-time monitoring at Mission Control Center.

Timing and synchronization were controlled by the central control logic subsystem, which was synchronized to the spacecraft 1.0-Hz clock. The power system converted spacecraft 28 V dc power into various regulated low voltages for electronics subsystems and into regulated high voltages for the channel electron multipliers. To minimize single-point failures, each detector had an independent high-voltage supply.

### Mechanical Features

The HGD was approximately a cube 0.35 m on each side with a mass of 21 kg. A general view of the instrument with the cover removed is shown in figure 5-4. The HGD was bolted into the Apollo spacecraft with thermally insulating mounts. The front face was coated with highly reflecting metallic tape to restrict radiative heating and cooling of the instrument. A black-coated shroud sealed the HGD to the inside of the spacecraft skin. The shroud restricted the flow of gases from the interior of the spacecraft service module into the HGD so that, when the instrument door was

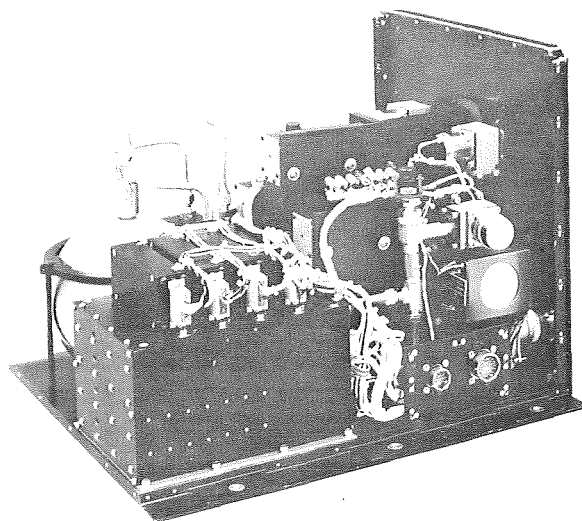


FIGURE 5-4.—Oblique view of HGD with cover removed. The optical axis points to the right.

opened, the instrument internal pressure fell to a value sufficiently low to prevent high-voltage corona discharge. The major characteristics of the HGD are summarized in tables 5-I and 5-II.

*TABLE 5-I.—Helium Glow Detector Characteristics*

Dimensions, m .....	0.33 by 0.33 by 0.43
Mass, kg .....	21
Average power, W .....	20
Gas cell pressure, N/m <sup>2</sup> .....	130

*TABLE 5-II.—Helium Glow Detector Channel Characteristics*

Channel	Design wavelength, nm	Nominal band pass, nm	Sensitivity at design wavelength, counts m <sup>2</sup> /photon
1	58.4	50 to 70	15
2	30.4	20 to 50	140
3	58.4	50 to 70	18
4	30.4	20 to 50	140

## INSTRUMENT CALIBRATION

The HGD was calibrated in the EUV calibration facility at the Space Sciences Laboratory of the University of California at Berkeley. This facility included a vacuum chamber, a grazing-incidence monochromator, several sources of EUV radiation, reference diodes for measuring ultraviolet and EUV fluxes, ion and electron guns, and such supporting equipment as pumps, manipulators, collimators, laminar-flow benches, and dehumidifiers.

The vacuum chamber had an inner diameter of 1.2 m and was 1.5 m long. An oil-diffusion pump with a liquid nitrogen cold trap provided sufficient pumping capacity to obtain a pressure of 1 to 0.1 mN/m<sup>2</sup>, even when the HGD gas absorption cells were cycling. The chamber contained a remotely controlled manipulator that could translate the HGD in any direction perpendicular to its optical axis and simultaneously pitch and yaw it. The

manipulator position was displayed on calibrated remote readouts.

A gas discharge lamp (Paresce et al., ref. 5-11), operated with various gases, provided a source of EUV light. The radiation passed through a 2.2-m McPherson grazing-incidence monochromator, a grazing-incidence paraboloidal collimator, and an adjustable stop, and then into the calibration tank. The monochromator was provided with its own diffusion pump and cold trap.

End-to-end photometric calibration of each detector channel was performed with emission lines of hydrogen, helium, neon, and argon (using a narrow, collimated monochromator output beam and a National Bureau of Standards calibrated vacuum photodiode as a reference standard). The beam intensities were adjusted to a sufficiently low level that statistical counting losses due to the 1-microsecond dead time of the CEM and electronics were insignificant. The resulting calibration curves are shown in figure 5-5.

The spatial shape of the photosensitive area of each channel was mapped at several wavelengths using a 1-mm-diameter collimated monochromator beam. The shape of each sensitive area agreed within the measurement error with the 13-mm-diameter clear aperture of each CEM. The response was constant across the region except for a small insensitive patch at the center of the CEM, where the electron-multiplier section of the device joins the photoemissive surface. This insensitive patch accounted for only a few percent of the total CEM area.

The shape of the solid angle viewed by each channel was studied by varying both the angle that the incident photon beam made with the detector optical axis and the position of the beam in the channel entrance pupil. The response remained constant as long as the beam directly illuminated the CEM. When the beam did not directly illuminate the CEM but instead reached it after one or more reflections off the interior of the gas absorption cell or collimator, the response never exceeded  $5 \times 10^{-3}$  of the direct response. Calculations indicated that, if each channel viewed an isotropic source of radiation to which it was sensitive, no more than 3 percent of the photons detected would have reached the detector by such reflections.

The photometric linearity of each channel was examined and was found to be consistent with that calculated from the Poisson statistics of photon arrival together with the known 1-microsecond dead time of the detector electronics following each event. In the laboratory, the dark rate of each channel was found to be less than 0.1 count/sec. This rate is consistent with that expected from false counting due to cosmic radiation.

The gas absorption cells were operated to verify that their pressure cycling had the correct amplitude, frequency, and phase. The pressure sensors for these measurements were those contained in the HGD, which had been separately calibrated in helium before assembly.

A source of ions and electrons could be mounted in the calibration tank to determine whether the HGD would respond when exposed

to ionospheric charged particle fluxes. The source was a high-perveance vacuum diode composed of a resistance-heated nichrome/barium oxide filament, a cylindrical mesh anode, and a surrounding electrostatic focus cup at anode potential. The diode was capable of producing up to  $2 \times 10^{10}$  positive ions/sr · sec, or up to  $2 \times 10^{14}$  electrons/sr · sec at energies up to approximately 400 eV. The source geometry was approximately that of a point source radiating into 1 sr of solid angle. The source was mounted approximately 0.1 m from the instrument and the HGD was then translated vertically and laterally to present its entire front face to the flux of particles.

The maximum flux of positive ions produced by the source ( $2 \times 10^{10}$  ions/sr · sec) did not raise any HGD count rate above background. On this basis, an upper limit to the integral of effective area over solid angle for 200-eV ion sen-

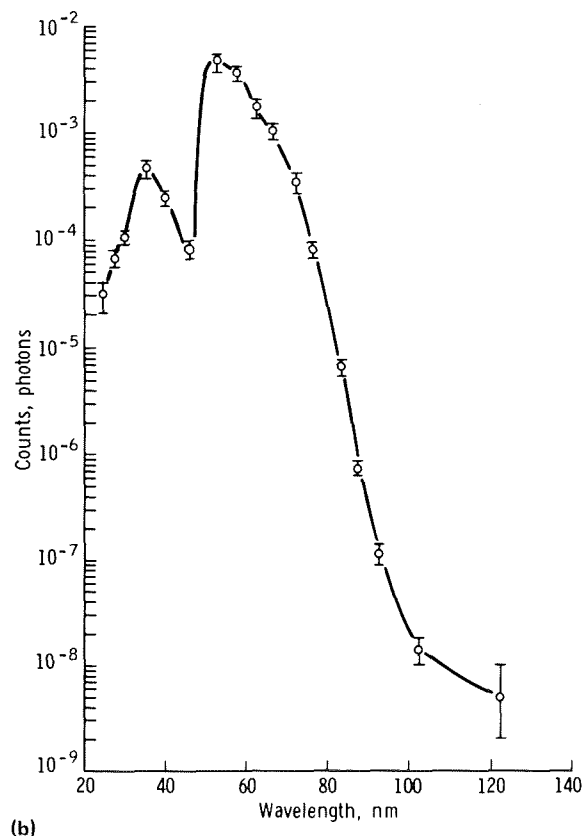
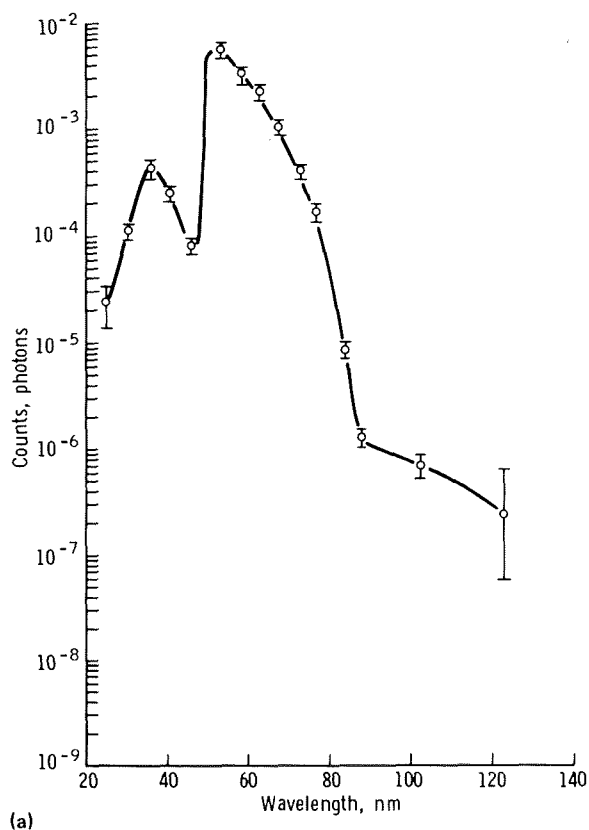


FIGURE 5-5.—Absolute end-to-end sensitivity of HGD channels as a function of wavelength. (a) 58.4-nm channel no. 1. (b) 58.4-nm channel no. 3. (c) 30.4-nm channel no. 2. (d) 30.4-nm channel no. 4.

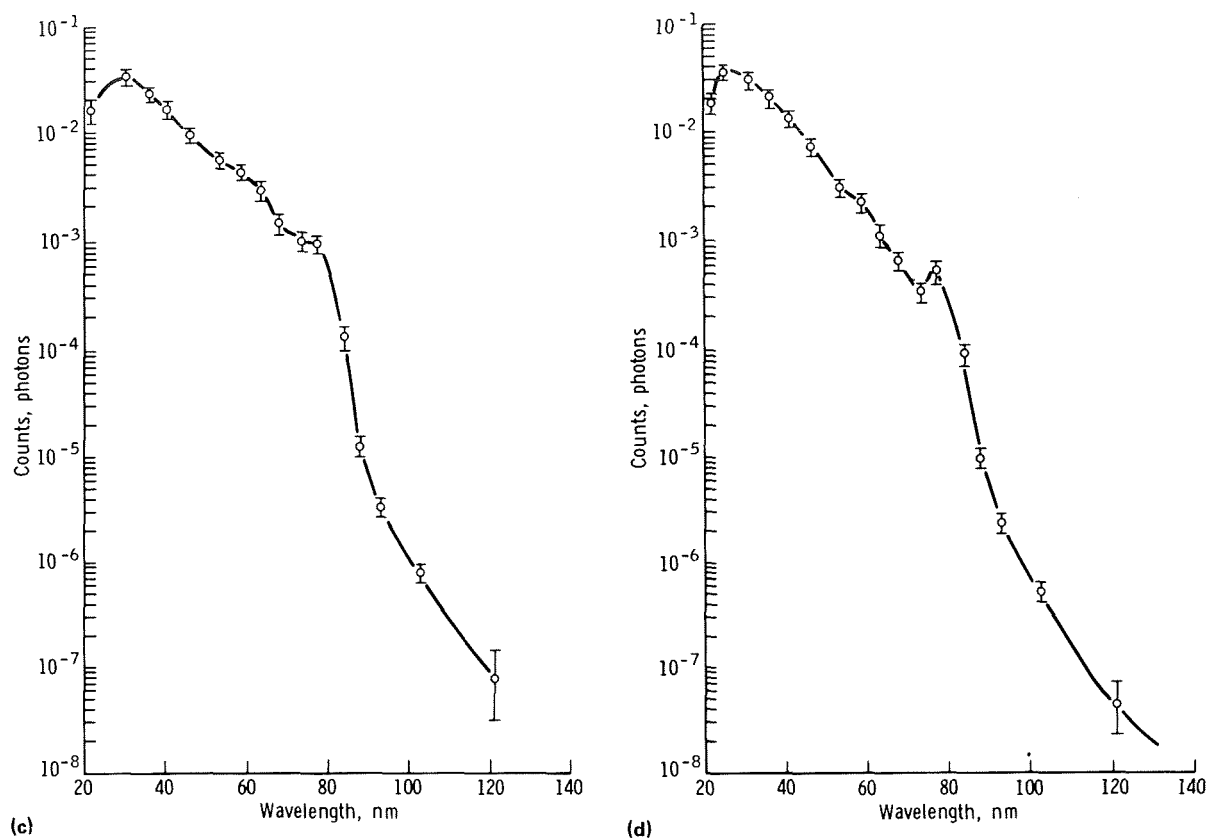


FIGURE 5-5.—Concluded.

sitivity of each HGD channel was calculated to be  $10^{-12} \text{ m}^2 \cdot \text{sr}$ . A much larger electron flux of  $2 \times 10^{14} \text{ sr}^{-1} \text{ sec}^{-1}$  was generated by the source. This flux was detectable and gave integrals of effective area over solid angle for 10-eV electrons for the various channels of  $10^{-17}$  to  $10^{-16} \text{ m}^2 \cdot \text{sr}$ .

One vent port in the front face of the HGD allowed the internal volume of the instrument to outgas to space. This port was baffled internally. An intense beam of 58.4-nm photons was directed into the port and all count rates were monitored to investigate the possibility that a combination of internal reflections and photoemission inside the instrument might cause false counts. The sensitivities detected by this method ranged from  $2.7 \times 10^{-9}$  to  $1.6 \times 10^{-8}$  counts detected per photon passing into the vent port. A similar test using a source that approximated the luminous flux of the Sun, but at a lower black-body tem-

perature of approximately 3000 K, yielded no count rate significantly above background.

An intense 58.4-nm beam was used to illuminate each of the four detectors serially, and the count rates of all four channels were simultaneously monitored. The amounts of crosstalk observed ranged from  $1.1 \times 10^{-9}$  to  $6.0 \times 10^{-9}$  counts in an unilluminated channel (per photon entering the entrance pupil of a different channel).

## FLIGHT OPERATIONS

The HGD and its protective door were controlled by switches and circuit breakers in the Apollo command module. The crewmembers also controlled a switch that could interrupt the flow of

helium to either gas absorption cell. This switch could have been used if declining tank pressure or corona discharge had indicated a leak in either gas cell. When observations were to be made, the crewmembers opened the door, waited a few moments to allow the pressure in the instrument area to drop from 0.1 to 1.0 N/m<sup>2</sup> (door closed) to 1 mN/m<sup>2</sup> or less (door open), and turned on the power. The short wait before turn-on was necessary to avoid possible corona discharge from the high-voltage electronics at pressure above 0.1 N/m<sup>2</sup>.

The door was never opened within 15 minutes after the completion of any discrete purge or vent of contaminants from the spacecraft. Dynamical calculations based on residual atmospheric drag at an altitude of 250 km indicated that a 15-minute delay was adequate to allow even contaminant particles as large as 0.01 m in diameter to drift clear of the spacecraft. Furthermore, crewmembers engaged in extravehicular activity on previous Apollo missions have not observed ice crystals or other contaminants clinging to the spacecraft near the location of the HGD.<sup>1</sup>

Four Apollo reaction-control thrusters located close to the HGD were inhibited from firing during HGD observations. The high level or redundancy of the Apollo attitude control system allowed the spacecraft to maneuver properly with the 12 remaining thrusters.

The HGD was pointed at various areas of the sky by maneuvering the spacecraft. These maneuvers were carefully planned before the flight and consisted, for the most part, of slow rolls about the spacecraft long axis, with that axis pointing in a specified fixed direction. For each axis orientation chosen, the spacecraft was rolled through several short arcs that together spanned the complete great circle normal to the axis. The times at which the various rolls were made were selected so as to minimize the zenith angles of the observations and to maximize the portion of the data taken with the spacecraft in darkness.

The observations maneuvers selected allowed the instrument to survey over three-quarters of the celestial sphere. Furthermore, the maneuvers

were chosen to permit especially detailed and repeated study of the region where the pronounced helium-density variations mentioned previously occur, and of the portion of sky that can be viewed while looking down the shadow cast by the Earth in the geocorona.

Data useful for in-flight checks of instrument calibration and sensitivity to unwanted wavelengths of light were taken while the instrument viewed the Earth and the horizon. At the last turn-off of the HGD, the instrument was intentionally operated with the door closed to check the background count rate with no light reaching the detectors.

## RESULTS

The HGD returned approximately 10 hours of data, including approximately 2 hours devoted to a systematic survey of half the celestial sphere. Previously developed software was used for reduction and rough analysis of the data. The immediate conclusions were as follows.

1. One 30.4-nm detector failed part way into the mission.
2. All functioning detectors exhibited unexpectedly high count rates when the Sun was above the horizon.
3. All functioning detectors yielded nighttime count rates that were generally comparable to previous measurements of 58.4- and 30.4-nm nighttime flux.
4. One 58.4-nm detector occasionally gave a count rate substantially higher than the other 58.4-nm detector. The variation of this count rate with spacecraft position and line-of-sight orientation suggested that detector number 1 had acquired an unwanted sensitivity to Lyman- $\alpha$  radiation at 121.6 nm.
5. Door-closed dark counting rates did not exceed 0.1 count/sec.

The objective of further reduction of 58.4-nm data has been to determine parameters of the local ISM by evaluating the chi-squared polynomial, comparing the observations with predictions made using present ISM models. The subset of cell-empty data (taken when the Sun was more than 30° below the horizon, when the line-of-sight

---

<sup>1</sup>Personal communications, R. Evans, 1974.

was within  $60^\circ$  of the zenith, and when the spacecraft was well clear of the highly charged particle fluxes in the South Atlantic Anomaly) was selected for more complete analysis.

The 53 minutes of these data were binned in 30-second intervals, using a filtering process that rejected individual data samples that were more than 3 standard deviations above or below the average sample size for the bin. The purpose of this filtering process was to ensure that the reduced data were free of spurious signals, such as might be caused by electronic noise in the telemetry system. The preliminary reduction was performed without taking into account any corrections due to absorption of 58.4-nm flux by the Earth's atmosphere above the spacecraft.

Existing ISM models were then used to calculate predicted flux levels for these observations, as a function of ISM model parameters. The chi-squared polynomial comparing prediction to observation was evaluated for each set of parameters considered. No satisfactory fit was obtained, indicating that the existing models, without correction for atmospheric absorption, did not adequately explain the observations.

The chi-squared polynomial was then reevaluated for the 17.5-minute subset of the previous data set for which the line-of-sight lay within  $30^\circ$  of the zenith. The best fit obtained was much better, though still not adequate to explain the observations. The chi-square fits obtained are summarized in table 5-III. The observed isophotes for the 17.5-minute data set together with the corre-

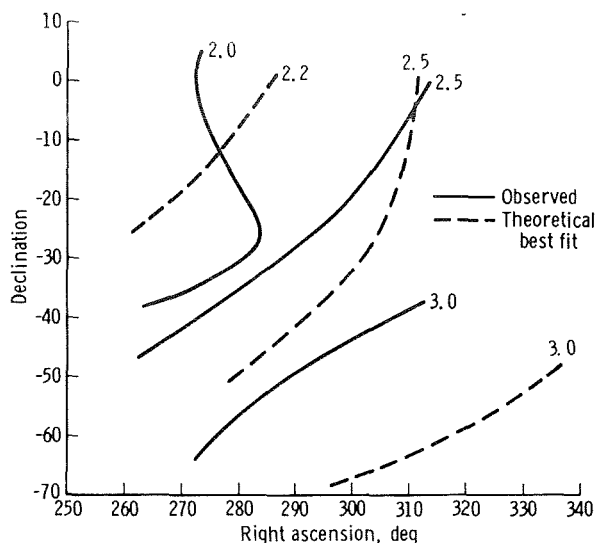


FIGURE 5-6.—Preliminary observed isophotes and best-fit theoretical isophotes for the 17.5-minute data set. (Isophotes parameterized by rayleighs.)

sponding predicted isophotes for the best fit to these data are displayed in figure 5-6.

## ACKNOWLEDGMENTS

Robert Stern, Stanford University, assisted with calibration and integration. The instrument and its ground support equipment were fabricated by Ball Brothers Research Corporation.

TABLE 5-III.—*Preliminary Fits of Cold ISM Models to Subsets of Experiment Data*

<i>Zenith angles at which data were taken, deg</i>	<i>Data points, no.</i>	<i>Degrees of freedom, no.</i>	<i>Chi square per degree of freedom</i>
0 to 60	106	102	28.8
0 to 30	35	31	11.5

## REFERENCES

- 5-1. Danby, J. M. A.; and Camm, G. L.: Statistical Dynamics and Accretion. *Monthly Notices Roy. Astron. Soc.*, vol. 117, 1957, pp. 50-71.
- 5-2. Blum, P. W.; and Fahr, H. J.: Interaction Between Interstellar Hydrogen and the Solar Wind. *Astron. & Astrophys.*, vol. 4, 1970, pp. 280-290.
- 5-3. Holzer, T. E.; and Axford, W. I.: Interaction Between Interstellar Helium and the Solar Wind. *J. Geophys. Res.*, vol. 76, Oct. 1971, pp. 6965-6970.
- 5-4. Axford, W. I.: The Interaction of the Solar Wind With the Interstellar Medium. *Solar Wind. NASA SP-308*, 1972, pp. 609-660.
- 5-5. Johnson, H. E.: Backscatter of Solar Resonance Radiation - I. *Planet. & Space Sci.*, vol. 20, June 1972, pp. 829-840.
- 5-6. Wallis, Max K.: Local Hydrogen Gas and the Background Lyman-Alpha Pattern. *Monthly Notices Roy. Astron. Soc.*, vol. 167, 1974, pp. 103-119.
- 5-7. Thomas, G. E.; and Krassa, R. F.: OGO 5 Measurements of the Lyman Alpha Sky Background. *Astron. & Astrophys.*, vol. 11, 1971, pp. 218-233.
- 5-8. Bertaux, J. L.; and Blamont, J. E.: Evidence for a Source of Extraterrestrial Hydrogen Lyman-Alpha Emission: The Interstellar Wind. *Astron. & Astrophys.*, vol. 11, 1971, pp. 200-217.
- 5-9. Thomas G. E.: Properties of Nearby Interstellar Hydrogen Deduced From Lyman- $\alpha$  Sky Background Measurements. *Solar Wind. NASA SP-308*, 1972, pp. 668-683.
- 5-10. Paresce, Francesco; Bowyer, Stuart; and Kumar, Shailendra: Evidence for an Interstellar or Interplanetary Source of Diffuse He I 584 Å Radiation. *Astrophys. J.*, vol. 183, July 1973, pp. L87-L90.
- 5-11. Paresce, F.; Kumar, S.; and Bowyer, C. S.: Continuous Discharge Line Source for the Extreme Ultraviolet. *Appl. Opt.*, vol. 10, no. 8, 1971, pp. 1904-1908.
- 5-12. Weller, C. S.; and Meier, R. R.: Observations of Helium in the Interplanetary/Interstellar Wind: The Solar-Wake Effect. *Astrophys. J.*, vol. 193, Oct. 1974, pp. 471-476.
- 5-13. Freeman, J.; Bowyer, S.; Paresce, F.; and Lampton, M.: Gas Absorption Cell Photometer for Rocket Observations of Local Interstellar Helium. *Rev. Sci. Instrumen.*, vol. 47, Mar. 1976, pp. 227-281.
- 5-14. Fahr, H. J.: The Extraterrestrial UV-Background and the Nearby Interstellar Medium. *Space Sci. Rev.*, vol. 15, Feb. 1974, pp. 483-540.
- 5-15. Jacchia, L. G.: Revised Static Models of the Thermosphere and Exosphere With Empirical Temperature Profiles. *SAO-SR-332*, Smithsonian Institution Astrophysical Observatory, Cambridge, Mass., 1971.
- 5-16. Thomas, G. E.: Interplanetary Gas of Nonsolar Origin. *Rev. Geophys. Space Phys.*, vol. 13, July 1975, pp. 1063-1065.
- 5-17. Paresce, Francesco; Bowyer, C. Stuart; Kumar, Shailendra; and Lampton, Michael: Rocket Observations of Extreme Ultraviolet Radiation in the Night Airglow. *EOS, Trans. A.G.U.*, vol. 51, 1970, p. 795.
- 5-18. Paresce, F.; Bowyer, S.; and Kumar, S.: Observations of the He II 304-Å Radiation in the Night Air. *J. Geophys. Res.*, vol. 78, Jan. 1973, pp. 71-79.
- 5-19. Ogawa, Toshihiro; and Tohmatsu, Takao: Sounding Rocket Observation of Helium 304- and 584-Å Glow. *J. Geophys. Res.*, vol. 76, Sept. 1971, pp. 6136-6145.
- 5-20. Young, James M; Weller, Charles S.; Johnson, Charles Y.; and Holmes, Julian C.: Rocket Observations of the Far UV Nightglow at Lyman  $\alpha$  and Shorter Wavelengths. *J. Geophys. Res.*, vol. 76, June 1971, pp. 3710-3722.
- 5-21. Bowyer, C. S.; Lampton, M.; Mack, J.; and Paresce, F.: A Far Ultraviolet Photometer for Space Research. *Planet. & Space Sci.*, vol. 18, June 1970, pp. 835-845.
- 5-22. Hoshiko, H. H.: Helical Channel Multiplier Package Design for Space Instrumentation. *Rev. Sci. Instrumen.*, vol. 46, Mar. 1975, pp. 331-332.
- 5-23. Steele, Gordon N.: Development and Fabrication of Large-Area Extreme-Ultraviolet Filters for the Apollo Telescope Mount. *Space Optics*. B. J. Thompson and R. R. Shannon, eds., National Academy of Sciences (Washington, D.C.), 1974, pp. 367-389.
- 5-24. Allen, C. W.: *Astrophysical Quantities*. Third ed. University of London, 1973, p. 72.



- 5-25. Morton, Donald C.; and Purcell, J. Dewitt: Observations of the Extreme Ultraviolet Radiation in the Night Sky Using an Atomic Hydrogen Filter. *Planet. & Space Sci.*, vol. 9, Aug. 1962, pp. 455-458.
- 5-26. Winter, Thomas C. Jr.; and Chubb, Talbot A.: The Determination of the Profile of the Night Sky Hydrogen Lyman Alpha Emission Line. *J. Geophys. Res.*, vol. 72, Sept., 1967, pp. 4405-4414.
- 5-27. Blamont, J. E.; and Madjar, A. Vidal: Monitoring of the Lyman Alpha Emission Line of the Sun During the Year 1969. *J. Geophys. Res.*, vol. 76, July 1971, pp. 4311-4324.
- 5-28. Delaboudiniere, J. P.; and Carabetian, C.: A Rocket Borne Absorption Cell for High Resolution Spectroscopy of the He I Line at 584 Å for Solar Observations. *Space Sci. Instrumen.*, vol. 1, Feb. 1975, pp. 91-110.

## BIBLIOGRAPHY

- Canfield, L. R.; Johnston, R. G.; and Madden, R. P.: NBS Detector Standards for the Far Ultraviolet. *Appl. Opt.*, vol. 12, no. 7, 1973, pp. 1611-1617.
- Wallis, M. K.: *Interaction Between the Interstellar Medium and Solar Wind Plasma*. *Astrophys. and Space Sci.*, vol. 20, Jan. 1973, pp. 3-18.
- Wallis, Max K.: Collisional Heating of Interplanetary Gas: Fokker-Planck Treatment. *Planet. & Space Sci.*, vol. 23, Mar. 1975, pp. 419-430.



## 6. Artificial Solar Eclipse

### Experiment MA-148\*

*G. M. Nikolskiy,<sup>a†</sup> A. I. Simonov,<sup>b</sup> I. S. Kim,<sup>a</sup> R. T. Giuli,<sup>c</sup>  
M. D. Jenness,<sup>c</sup> and A. N. Lunde<sup>c</sup>*

#### ABSTRACT

On July 19, 1975, the Apollo spacecraft successfully occulted the solar disk from the field of view of a camera mounted in the Soyuz spacecraft while performing a spacecraft separation maneuver to permit the outer solar corona to be viewable by the Soyuz camera. The camera operated automatically, and 55 frames were developed for scientific analysis.

gaseous and particle atmosphere around the Apollo spacecraft. The Apollo crew performed the required spacecraft maneuvers and photographed the eclipse shadow on the Soyuz vehicle, and the Soyuz crew photographed the corona. The ASE experiment and the method for conducting it were proposed by A. I. Simonov and G. M. Nikolskiy. The detailed trajectory computation was a joint effort of NASA and the U.S.S.R. Academy of Sciences.

#### INTRODUCTION

The Artificial Solar Eclipse (ASE) Experiment is one of the five experiments that incorporated joint activities between the U.S. and U.S.S.R. crews during the Apollo-Soyuz Test Project (ASTP) mission. The objective of this experiment was to detect the extended region of the solar corona by photographing it from the Soyuz spacecraft against the black space background, while the disk of the Sun was occulted by the Apollo spacecraft. A secondary objective was to determine the distribution of contaminant

#### OPERATIONS AND EQUIPMENT

The ASE was performed by separating the Apollo from the Soyuz shortly after orbital sunrise in such a way that Apollo occulted the Sun from view of the Soyuz orbital module (OM) hatch window. Apollo backed away from Soyuz toward the Sun to a separation distance (225 m) at which the apparent diameter of the Apollo command module (CM), as seen from Soyuz, was approximately 2 solar diameters. Apollo then reversed direction and performed an approach and docking maneuver with Soyuz. Apollo totally occulted the Sun during the separation maneuver, and Soyuz performed automatic sequence photography in the solar direction during the spacecraft separation and approach maneuvers. The orbital events are described in figure 6-1 and table 6-I. Before orbital sunrise, the Soyuz crew installed the corona-photography camera near the interior surface of the OM hatch window, looking out along the plus-X axis of the Soyuz vehicle. The frame

---

\*The joint U.S.-U.S.S.R. designation was "Experiment AS-4."

<sup>a</sup>Institute of Terrestrial Magnetism, Ionosphere, and Radiowave Propagation, U.S.S.R. Academy of Sciences.

<sup>b</sup>Space Research Institute, U.S.S.R. Academy of Sciences.

<sup>c</sup>NASA Lyndon B. Johnson Space Center.

<sup>†</sup>Principal Investigator.

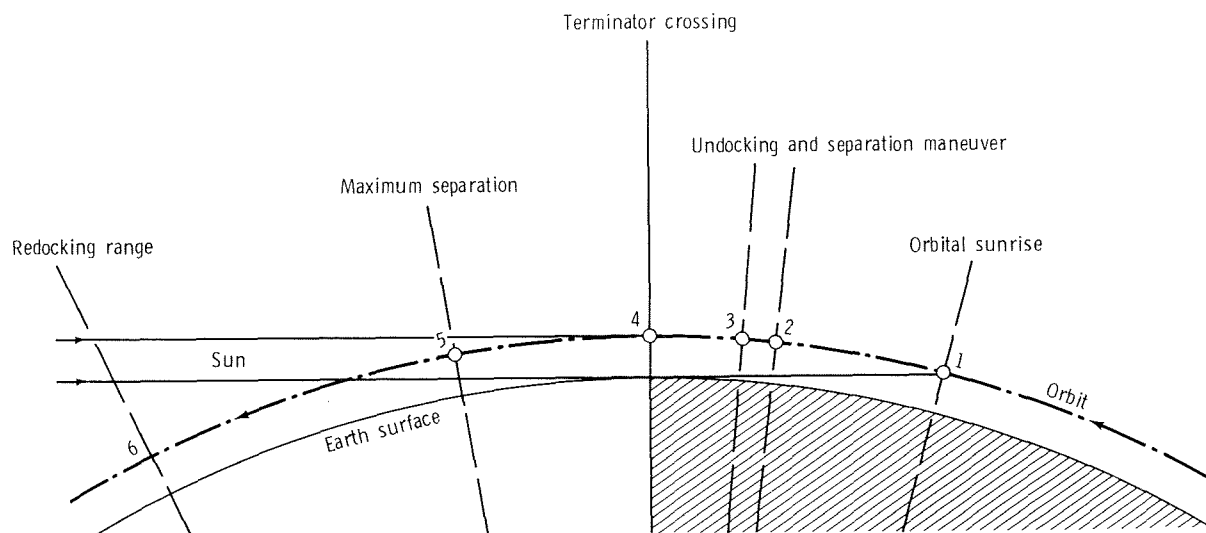


FIGURE 6-1.—Orbital schematic of artificial solar eclipse during the 57th orbit of the Apollo spacecraft and the 65th orbit of the Soyuz spacecraft. Numbers refer to events described in table 6-I.

TABLE 6-I.—Sequence of Events From First Undocking to Second Docking, July 19, 1975

Event	UT, hr:min:sec	Spacecraft separation, m	Event description
1	12:02:05	0	Orbit sunrise.
2	12:03:20	0	At undocking, spring release mechanism gives Soyuz a velocity of 0.10 m/sec along the Soyuz minus-X axis and gives Apollo a velocity of 0.05 m/sec along the Apollo minus-X axis.
	12:03:35	2.3	Apollo begins first 4-jet, minus-X, 0.38-m/sec separation maneuver (initiated after a 15-second coast period) along line of sight to Sun direction and maintains inertial attitude hold.
	12:03:38	3.3	Reaction control system (RCS) engines cut off.
	12:03:50	9.6	Apollo begins second 4-jet, minus-X, 0.50-m/sec separation maneuver after a 12-second coast period.
3	12:03:54	12.8	RCS engines cut off; separation rate, 1.03 m/sec.
4	12:05:55	137	The two spacecraft cross the Earth terminator.
5	12:07:20	225	Apollo begins a 2-m/sec, 4-jet, plus-X RCS maneuver to null the separation rate and return the Apollo vehicle to the redocking position.
	12:07:36	225	RCS engines cut off.
6	12:10:58	<17	Apollo achieves docking range and begins a 1-m/sec, 4-jet, minus-X RCS maneuver to null the closing velocity component.

size was 50 by 50 mm, the lens focal length was 90 mm, and the aperture ratio was 1:2.8. The photographs were taken in "white" light over the wavelength range of approximately 400 to 750 nm; the lens used no filter. The Kodak HS-2485 (70 mm) film was mounted in a mechanized-drive magazine on the back of the camera. A timer controlled the automated camera operation in continuously repeated cycles, with six exposures per cycle. Tables 6-II and 6-III give the timing data for the camera operation.

Before the spacecraft undocking, the Apollo crew installed a U.S.S.R. light baffle on the outside of the Soyuz OM hatch window. The baffle (fig. 6-2) shielded the hatch window from light reflected from the Soyuz docking mechanism and from the Earth. To block the intense sunlight reflected from the Earth beyond the terminator, the baffle design incorporated vignetting of the frame so that approximately one-half the frame toward the Earth was totally obscured (figs. 6-2 and 6-3).

Also during separation, the 16-mm Apollo data acquisition camera (DAC) was mounted in a CM window to view along the Apollo plus-X axis. The 75-mm focal length lens of the DAC automatically operated at 12 frames/sec, exposing SO-242 color film at 1/125 second. The purpose of the DAC photography was to monitor the motion of the umbra on the Soyuz spacecraft.

TABLE 6-II.—Interval Between Start of a Series and the Beginning of an Exposure Within the Series

Exposure no.	Exposure time, sec	Interval, sec
1	11	0
2	3.3	13.75
3	1.1	19.80
4	.33	23.65
5	.165	26.73
6	3.3	29.65

TABLE 6-III.—Interval Between the End of Undocking and the Start of a Series

Series	Interval, sec
I	20.7
II	56.4
III	92.1
IV	127.8
IX	306.3
X	342.0
XI	377.7
XII	413.4
XXI	734.7

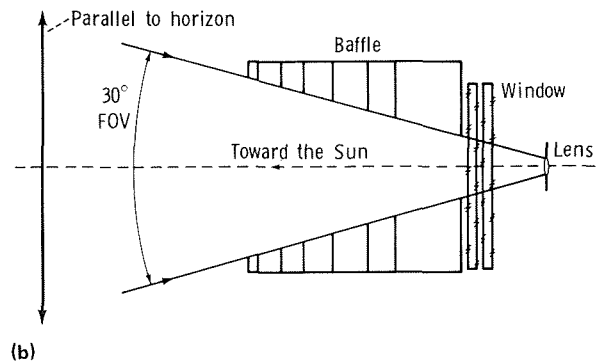
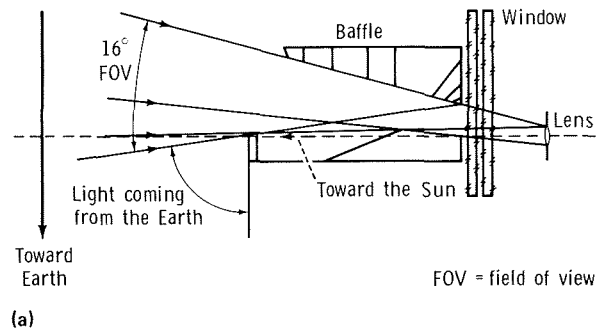


FIGURE 6-2.—Optical schematic of the baffle. (a) Side view. (b) Top view.

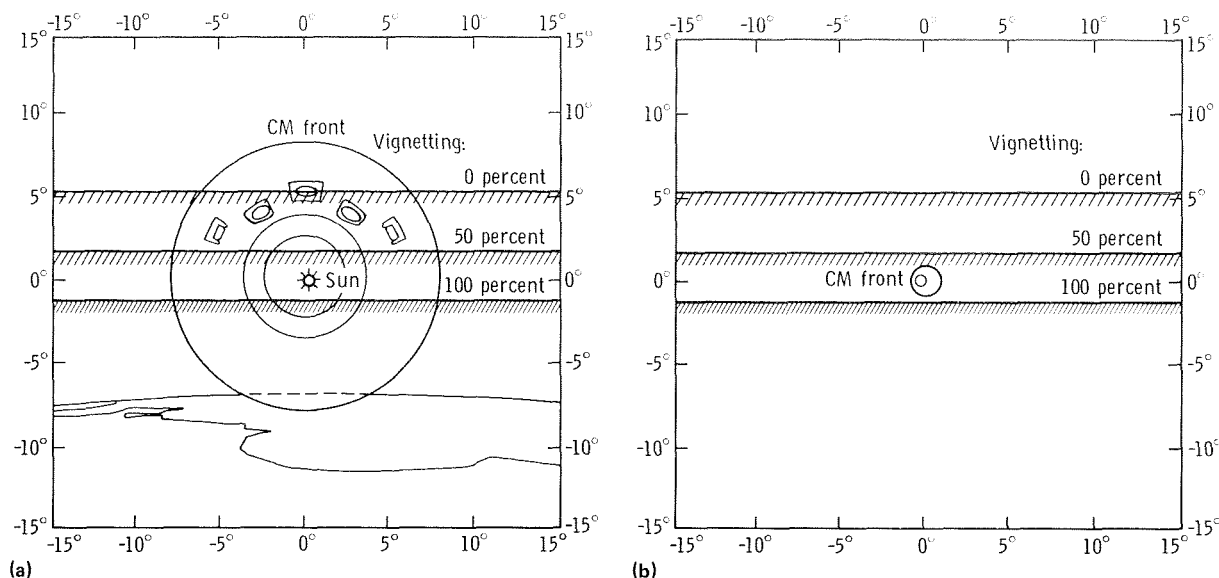


FIGURE 6-3.—View of the Apollo spacecraft as seen from the Soyuz spacecraft. The field of view is 30° with the Sun in the center of the view. The indicated vignetting is from the design of the light baffle on the Soyuz hatch window. (a) 12.8 m from Soyuz (after the second reaction control system (RCS) separation burn). (b) 225 m from Soyuz (just before the RCS approach burn).

## DESCRIPTION OF PHOTOGRAPHS

Photographs taken during the ASE experiment were processed at the Solar Activity Laboratory in Moscow. The film processing used D-19 developer and a developing time of 12 minutes at a temperature of 298 K (25° C). Relative calibration was performed by means of a tube photometer, which produced 12 marks with relative intensities within 2.4 orders of magnitude. The calibration used an unexposed emulsion that had been flown onboard the Soyuz 19 spacecraft under conditions identical to those of the ASTP mission; calibration was performed with exposures of 10, 3, 1, and 0.3 seconds.

Fifty-three frames (series I to IV, IX to XII, and XXI) contain information on the illumination around the Apollo spacecraft. The outer corona (i.e., diffuse illumination) is more concentrated toward the ecliptic and is visible on 19 frames that were the least exposed to the reaction control system (RCS) exhaust illumination. Unfortunately, the glass of the Soyuz OM hatch window was also illuminated, apparently by light coming through the OM side window and by light from

the instrument panel. The fact that frames were exposed in those portions that were fully shielded by the baffle indicates that the illumination came from the cabin. Optimum results were obtained with 0.16- and 0.33-second exposures; frames with longer exposures have high photographic density.

Three celestial objects (two stars,  $\gamma$  Geminorum and  $\alpha$  Canis Minoris, and the planet Mercury) are visible on nearly all negatives; the frames view the portion of the sky that is southwest of the Sun. The photographic resolution is 2' to 4' (0.05 to 0.1 mm), depending on the location on the frame and exposure time. The resolution is determined by a combination of several factors such as the lens quality, the emulsion grain size, and the camera vibrations. Fully visible is a narrow ring around the Apollo spacecraft. The ring results from the diffraction of solar light and creates no background at distances of more than 0.5 m from the Apollo spacecraft periphery. The interference is fully accounted for by the illumination from the RCS exhaust and by the previously mentioned cabin illumination. Visible on many frames are not only the Apollo RCS engine plumes, which can reach as far as the

frame boundaries (at a spacecraft separation of 50 m), but also the particles escaping from the jet engines with a velocity of several meters per second.

### SCALE AND SHADING DETERMINATION

For scale and shading determination, distances between stars were measured, and rectangular coordinates of the stars were calculated from the photographs. If  $x$  and  $y$  are the coordinates of the stars measured on the negatives from the solar disk center, perpendicular to and along the declination circle, respectively, then

$$\left. \begin{aligned} x &= \frac{\tan(\alpha - \alpha_{\odot}) \cos A}{\cos(A - \delta_{\odot})} \\ y &= \tan(A - \delta_{\odot}) \end{aligned} \right\} \quad (6-1)$$

where  $\alpha$  and  $\delta$  are the right ascension and declination, respectively, and the auxiliary angle  $A$  is

$$\tan A \equiv \frac{\tan \delta}{\cos(\alpha - \alpha_{\odot})} \quad (6-2)$$

A comparison of measurements with calculations indicated that the solar position on the negatives can be determined with 0.1 percent relative accuracy and that a more accurate value for the camera focal length is 90.4 mm.

Figure 6-4 shows the Apollo silhouette with respect to the Sun as seen from Soyuz at different times corresponding to different values of spacecraft separation  $d$ . The value of  $d$  is related to the apparent outer diameter  $d_A$  of Apollo as follows.

$$d = \frac{353.4}{d_A} \sim 5.8 \quad (6-3)$$

where  $d$  is the distance in meters between the Soyuz camera lens and the front end of the docking module attached to Apollo and where  $d_A$  is measured on the negatives in millimeters. Measurements of  $d_A$  were made on 24 photographs, yielding  $d$  as a function of time for both

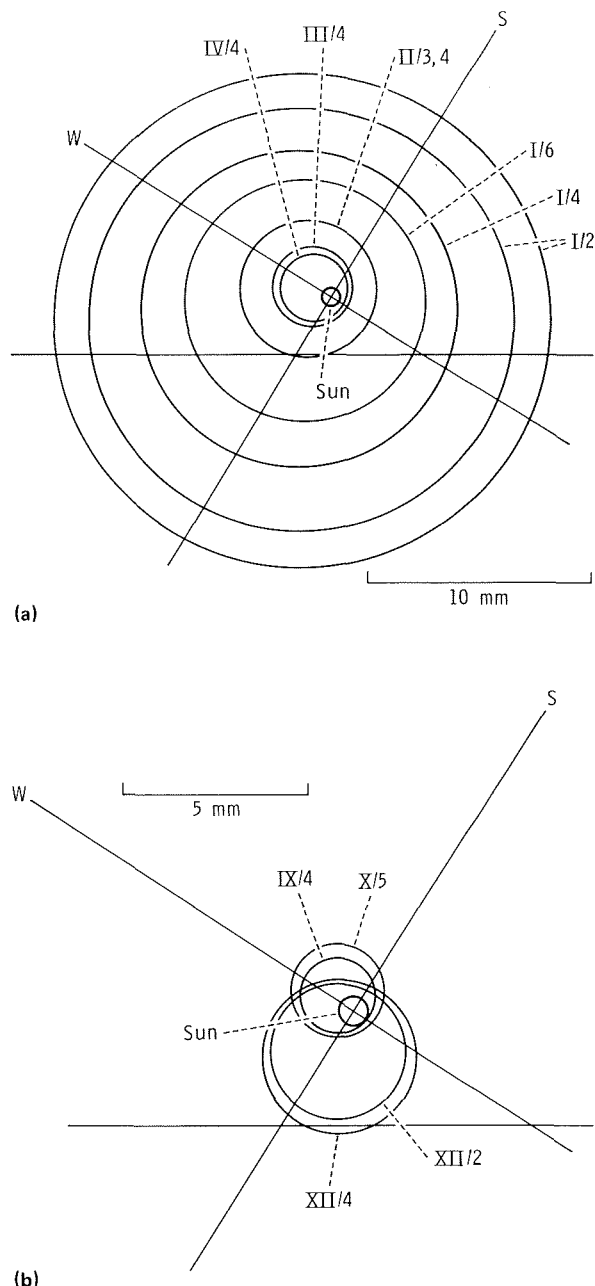


FIGURE 6-4.—Silhouette of the Apollo spacecraft with respect to the Sun (as seen on the frames indicated), corresponding to different values of  $d$  during the separation maneuver and during the approach maneuver. Shown are directions of the declination circle (S indicates south) and the orthogonal coordinate (W indicates west). Series numbers are given in Roman numerals and exposure numbers in Arabic numerals (e.g., IV/4). (a) Separation maneuver. (b) Approach maneuver.

the separation and approach phases of the maneuver (fig. 6-5). Diffraction effects contribute to uncertainty in the  $d_A$  measurements. The slopes of the lines in figure 6-5 indicate that the spacecraft separation velocity was 1.0 m/sec and that the approach velocity was 0.8 m/sec.

From 164 to 306 seconds after undocking (140 m during the separation maneuver to 185 m

during the approach maneuver), all frames were "washed out" by strong reflection of earthlight from the cone of the Apollo command module. The eclipse was again observed from 306 seconds after undocking to its end at 450 seconds (70-m spacecraft separation).

TABLE 6-IV.—Photometrically Processed Frames

Series/ exposure no.	Exposure, sec	Time after undocking, sec	Separation between spacecraft, m	Object
II/4	0.33	80.0	55	Corona
II/5	.16	83.6	58	Corona
III/4	.33	115.8	90	Corona
X/3	1.1	361.8	142	RCS plume
X/4	.33	365.7	138	RCS plume
XI/4	.33	401.4	109	Corona
XII/3	1.1	433.2	83	Corona
XII/5	.16	440.1	77	Corona

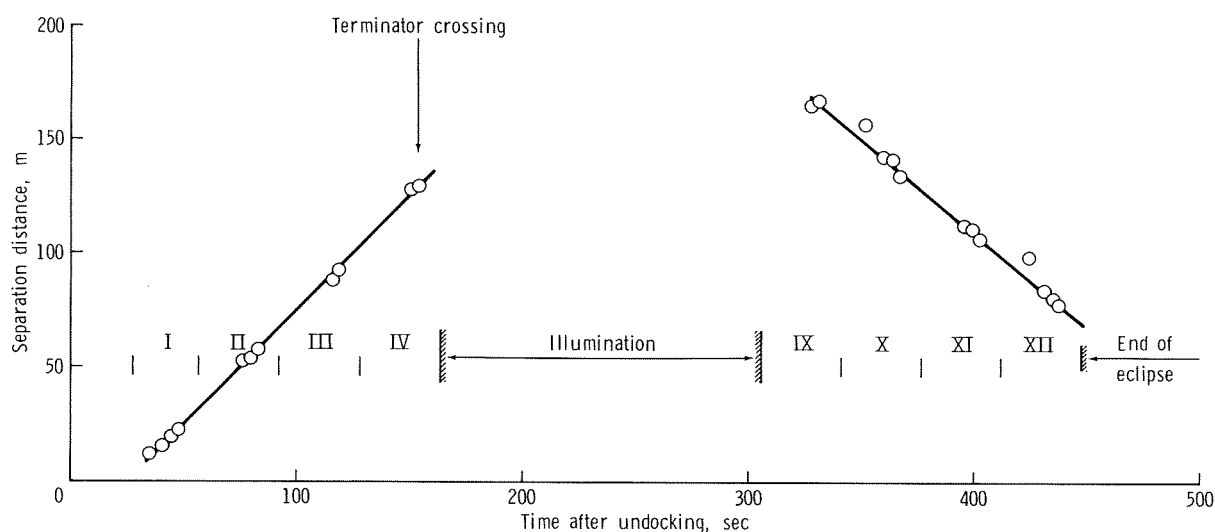


FIGURE 6-5.—The Apollo and Soyuz separation distance  $d$  as a function of time after undocking, based on measurements of the Apollo angular diameter on 24 frames. Roman numerals denote the corresponding photographic series.



### PHOTOGRAPH CALIBRATION AND PRODUCTION OF ISOPHOTES

The photographs listed in table 6-IV were selected for processing. A second-order equal-density locus was constructed for seven photographs, using a photographic method with the Sabatier effect. Individual equal-density loci were combined for each photograph. Convergence was done in reference to the stars and frame boundaries. To convert these loci into isophotes, a photometric trace with a microphotometer was performed on the negatives along the Sun-Mercury line (viz., approximately along the ecliptic) to obtain the relative intensities between the equal-density loci. The absolute photometric correlation was performed on three negatives, using the star  $\gamma$  Geminorum as a standard (+1.8 photovisual magnitude). Since the star image was entirely contained within the aperture of the microphotometer, creating an area on the negative of  $S_o = 0.1 \times 0.1 \text{ mm}^2$ , the density of the star image  $D^*$  was determined from the following equation.

$$D = D^* \frac{S_\gamma}{S_o} + D_\phi \left( 1 - \frac{S_\gamma}{S_o} \right) \quad (6-4)$$

where  $D_\phi$  is the background density near the star,  $D$  is the star density within the aperture, including the background, and  $S_\gamma = 0.005 \text{ mm}^2$  is the area of the star image. The corresponding intensity of the star was then determined from the performance curve, which was plotted from the tube photometric data. The vignetting of the lens field of view (0.5 in the  $\gamma$  Geminorum region of the frame) was taken into account. The absolute intensity is expressed in fractions of solar disk intensity by the ratio

$$\begin{aligned} \log \frac{i_\gamma}{i_\odot} &= \log \frac{S_\odot}{S_\gamma} - 0.4(m_\gamma - m_\odot) \\ &= -9.7 \end{aligned} \quad (6-5)$$

where the apparent photovisual magnitude of the Sun  $m_\odot$  is  $-26.7$  and the area of the Sun image  $S_\odot$  is  $0.5 \text{ mm}^2$ . All the intensity determinations of the  $\gamma$  Geminorum image on three different

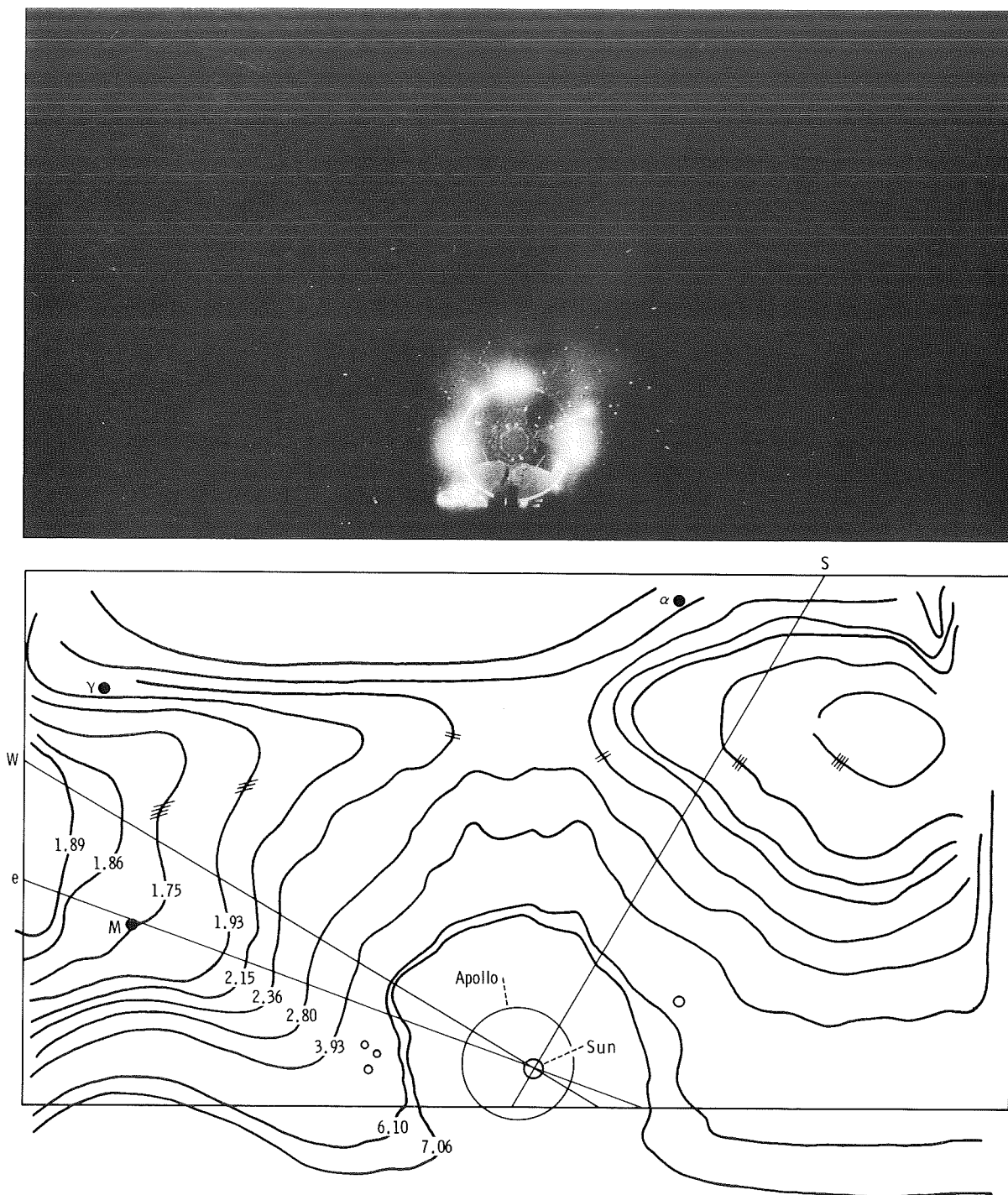
negatives, each with a 0.33-second exposure, coincide to within 10 percent. The  $\alpha$  Canis Minoris ( $-0.4$  photovisual magnitude) star measurements were performed as controls; the results coincide to within 15 percent. Figure 6-6 shows various frame positives and associated isophotes, the originals of which were originally made on a 10:1 scale of the negatives.

### PATTERN OF CORONA INTENSITY ALONG THE ECLIPTIC

As mentioned earlier, considerable illumination was coming from the OM cabin. To take this light into consideration, a frame with a 0.33-second exposure was used. This photograph was taken before undocking (series 0, frame 4) when the Soyuz hatch window was completely shaded by the Apollo spacecraft. A photometric trace was done on this frame along the ecliptic direction, and the contribution of cabin illumination to the other frames was thus determined. At an angular distance  $R$  greater than  $14^\circ$  from the Sun, the cabin light constitutes the entire illumination. At  $R = 10^\circ$ , the cabin illumination exceeds the brightness of the corona by a factor of 3, whereas at  $R < 5^\circ$ , the cabin illumination is less than one-half the total brightness. Figure 6-7 shows the corrected data on corona light intensity along the ecliptic, including corrections for the vignetting of the baffle and lens (fig. 6-8). For distances of less than  $3^\circ$  from the Sun, use of the frame XII/5 enabled the investigators to obtain measurements in the vicinity of  $R = 1.5^\circ$ . The best fit to the corrected corona data is given by the equation

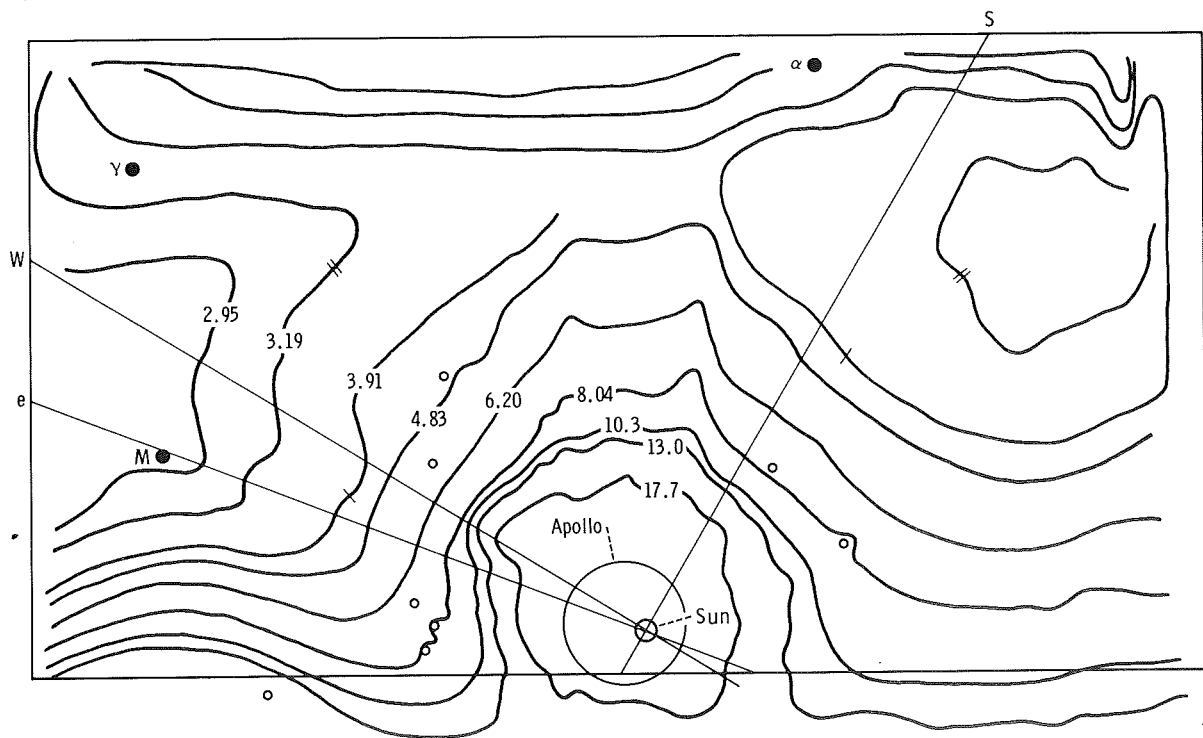
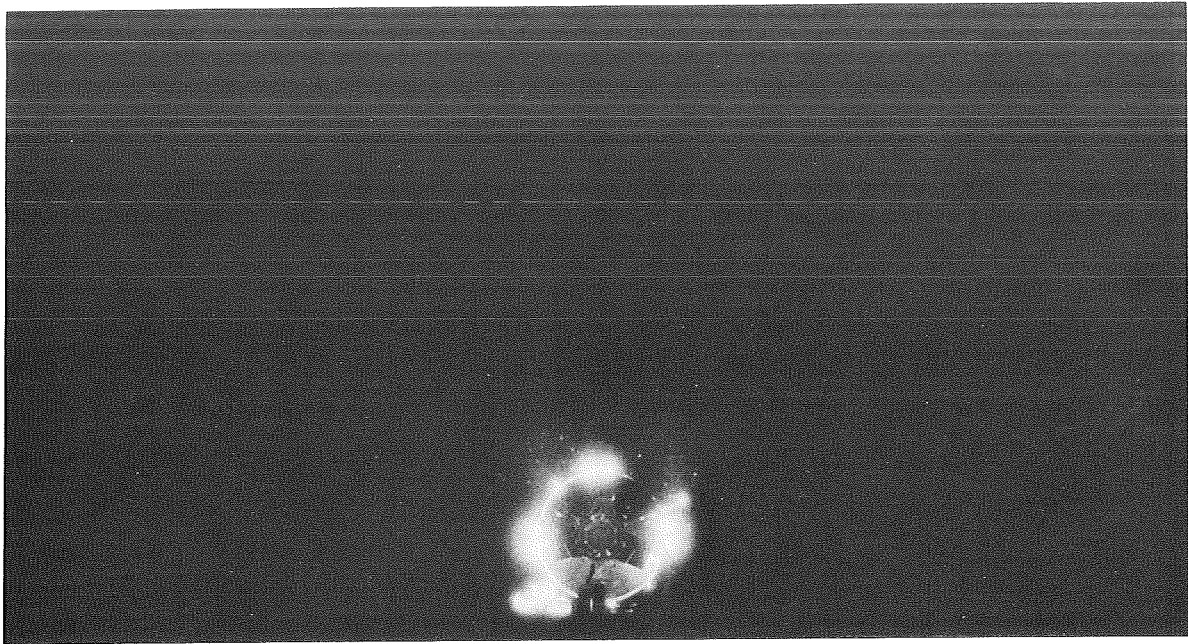
$$\frac{i}{i_\odot} = \frac{4 \times 10^{-7}}{\left( \frac{R}{R_\odot} \right)^{2.5}} \quad (6-6)$$

where  $R_\odot$  is the solar radius. All the light intensities are three times higher than the known 1954 data that were obtained by Blackwell from aircraft observations (refs. 6-1 and 6-2), and it is difficult to attribute this discrepancy to errors in absolute time tagging.



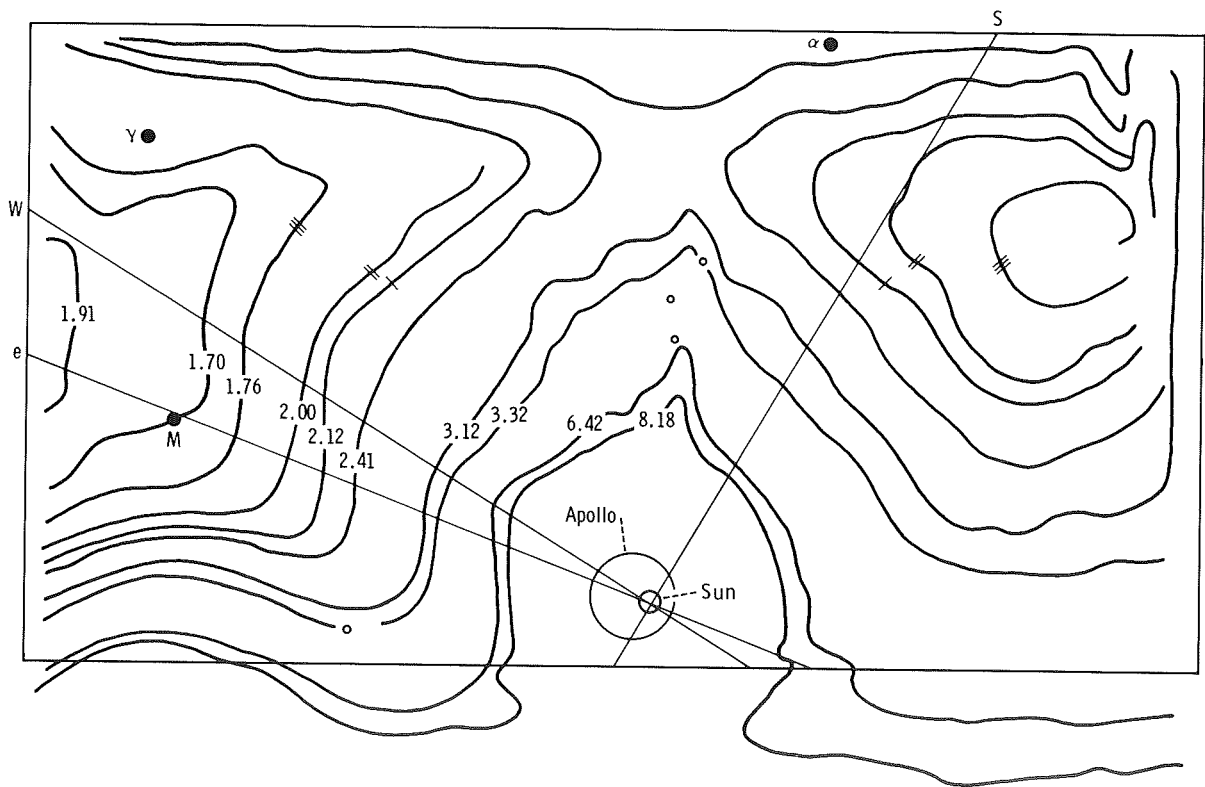
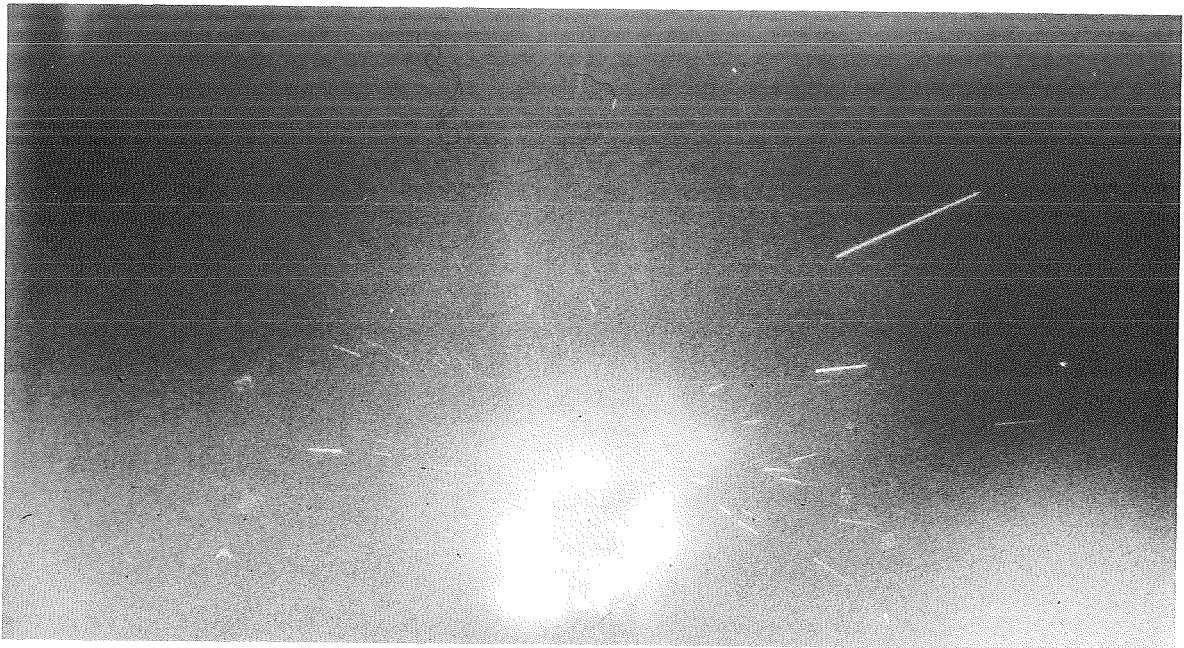
(a) Frame II/4 and isophotes.

FIGURE 6-6.—Photographic positives for designated ASE frames together with related isophote maps. Isophotes are given in  $10^{-10}$  units of solar disk center intensity. Positions of the Sun, stars  $\gamma$  Geminorum ( $\gamma$ ) and  $\alpha$  Canis Minoris ( $\alpha$ ), planet Mercury (M), and Apollo are indicated. Directions are given for the ecliptic (e), the declination circle (S), and the orthogonal coordinate (W). The lower line indicates the hypothetical 100-percent-vignetting line of the baffle.



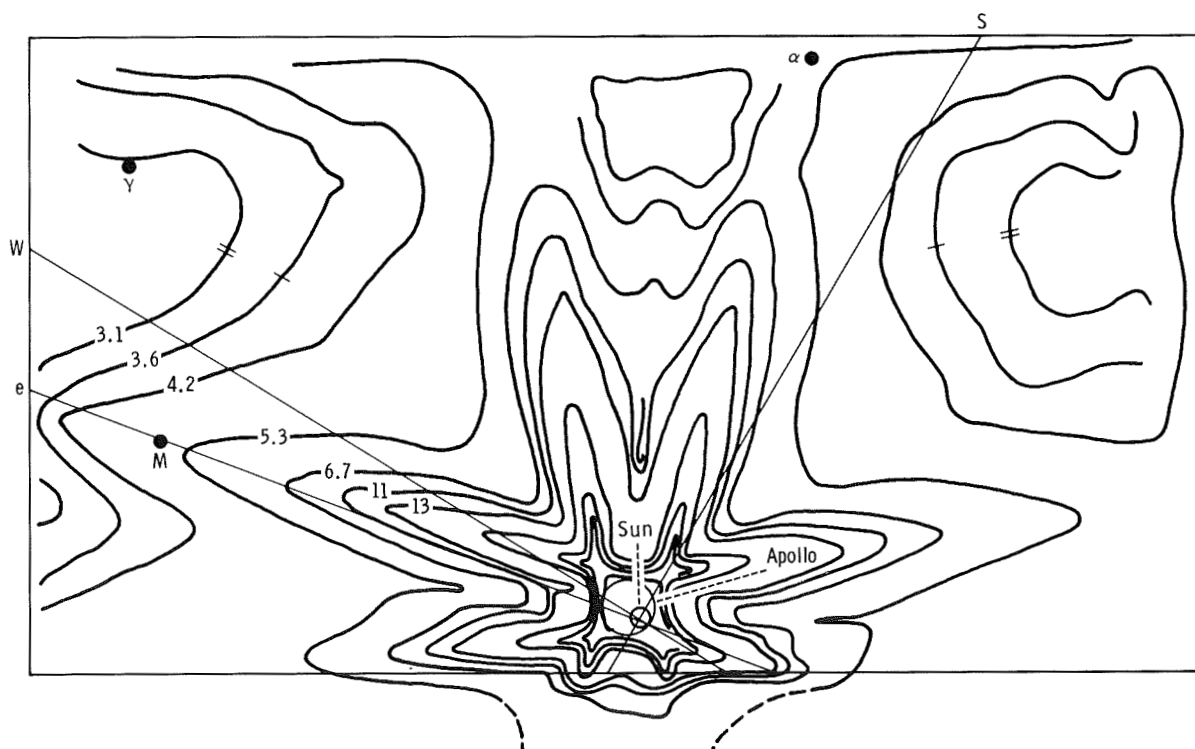
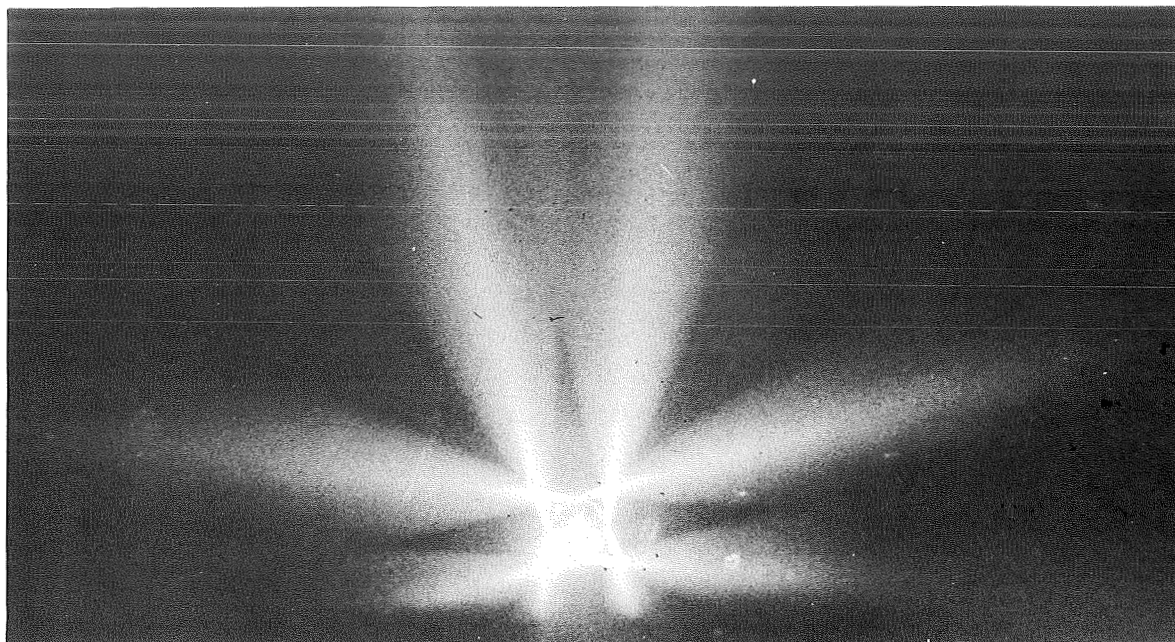
(b) Frame II/5 and isophotes.

FIGURE 6-6.—Continued.



(c) Frame III/4 and isophotes.

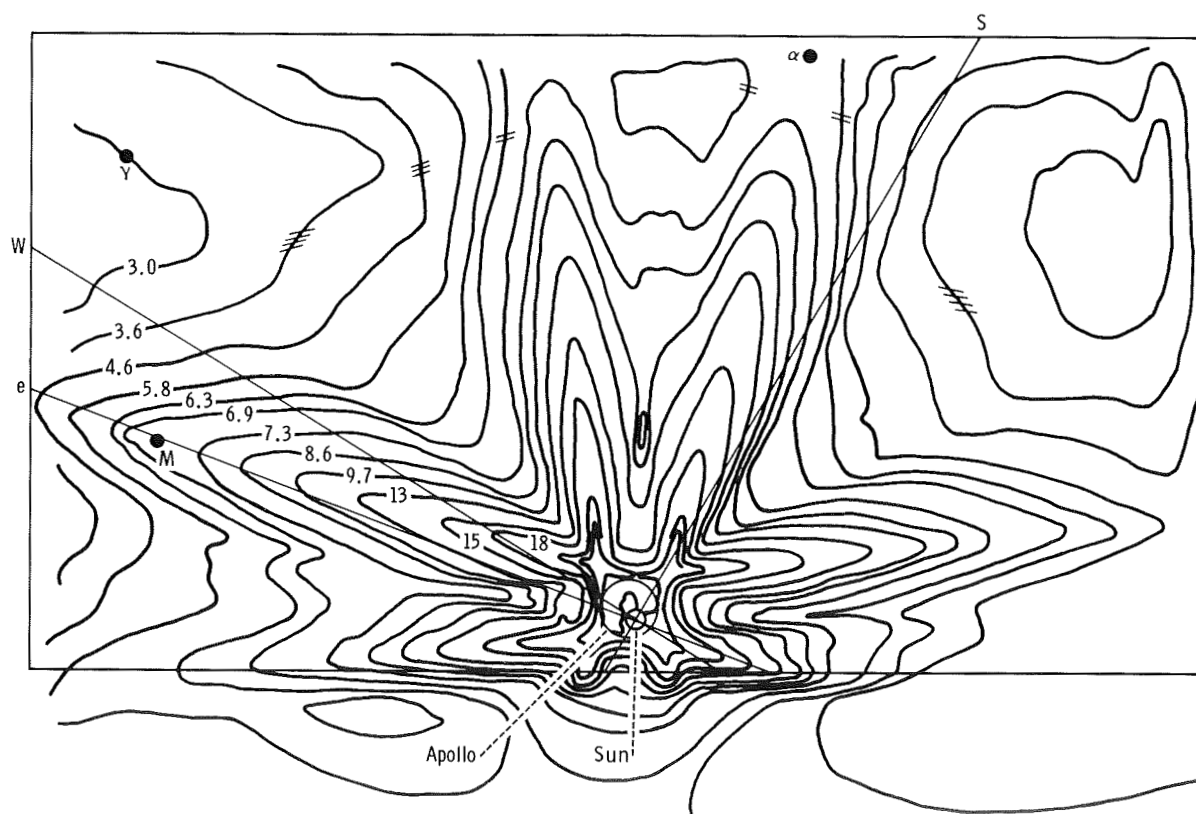
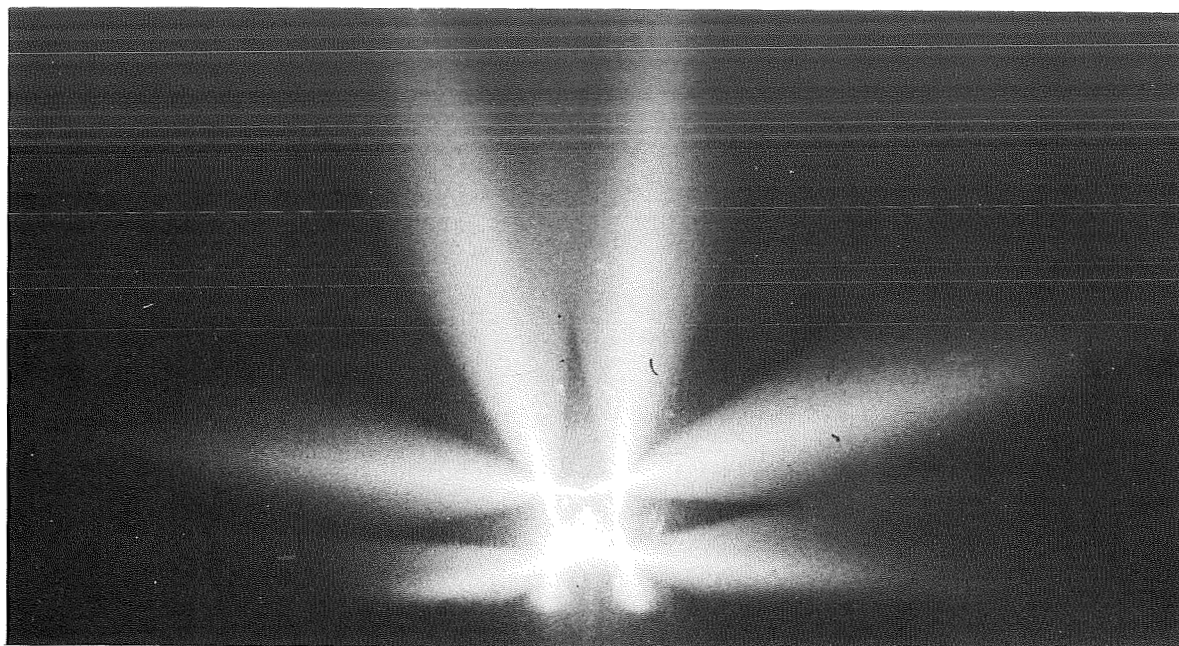
FIGURE 6-6.—Continued.



(d) Frame X/3 and isophotes.

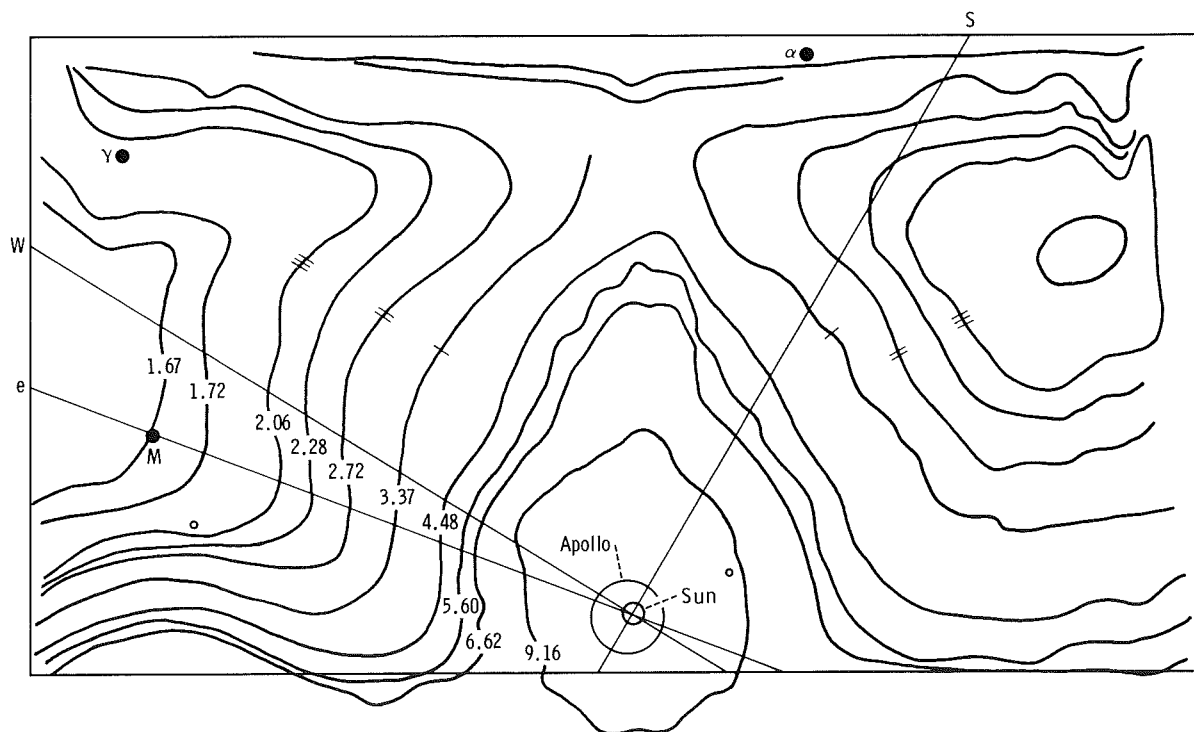
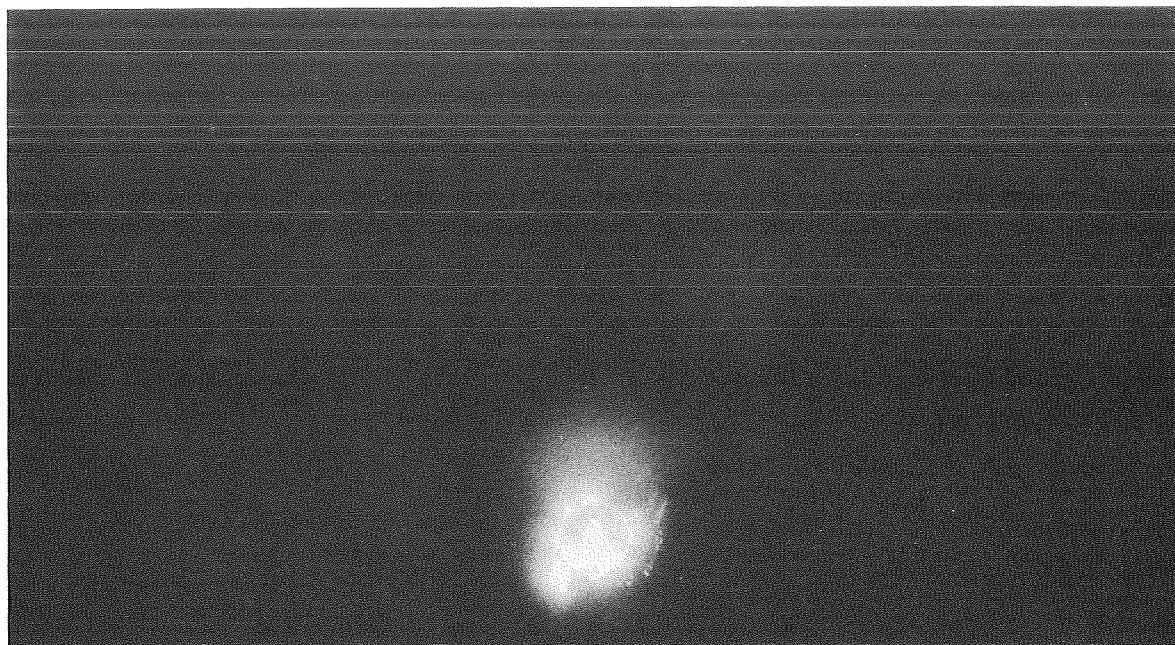
FIGURE 6-6.—Continued.





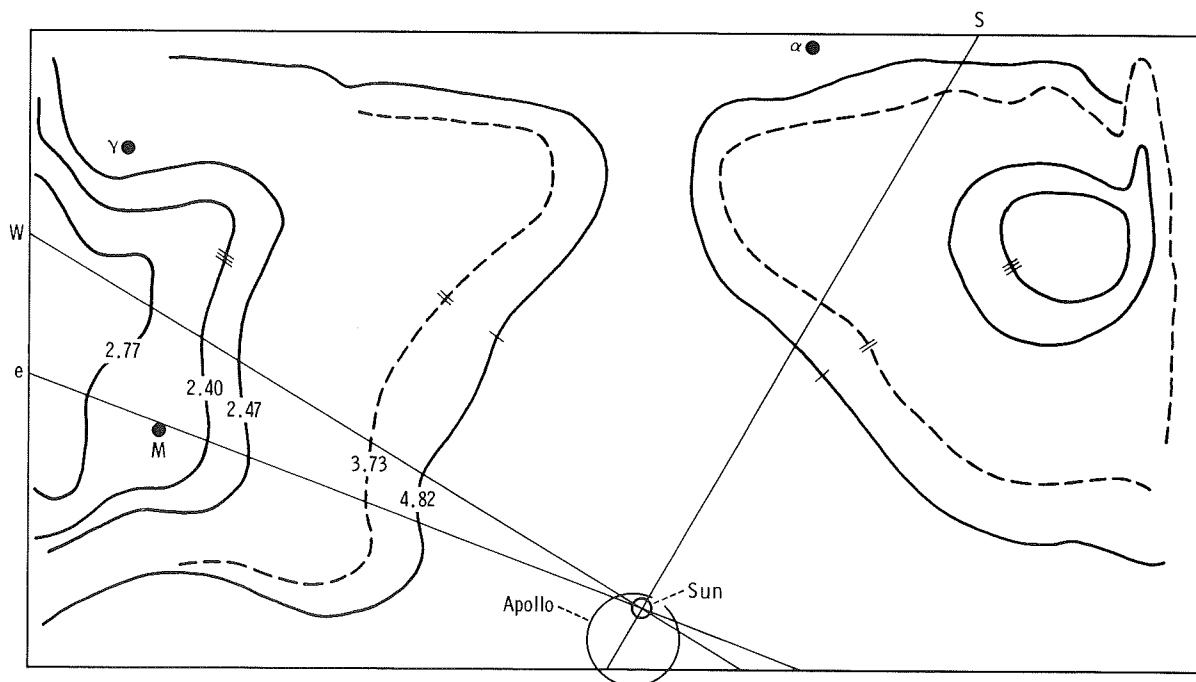
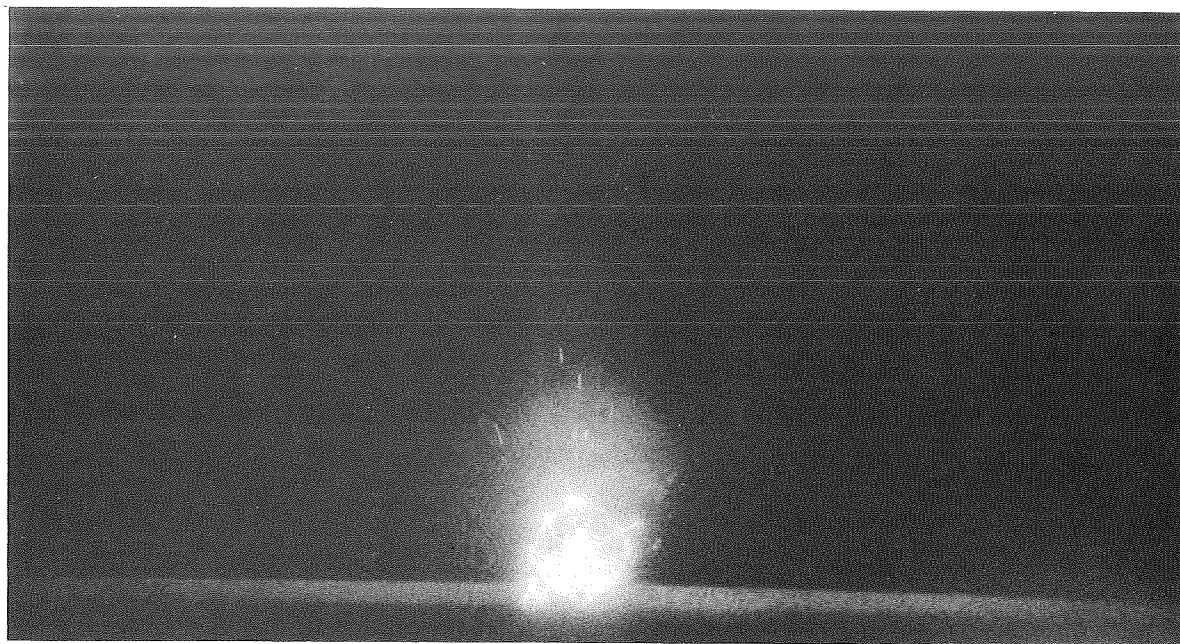
(e) Frame X/4 and isophotes.

FIGURE 6-6.—Continued.



(f) Frame XI/4 and isophotes.

FIGURE 6-6.—Continued.



(g) Frame XII/3 and isophotes.

FIGURE 6-6.—Concluded.



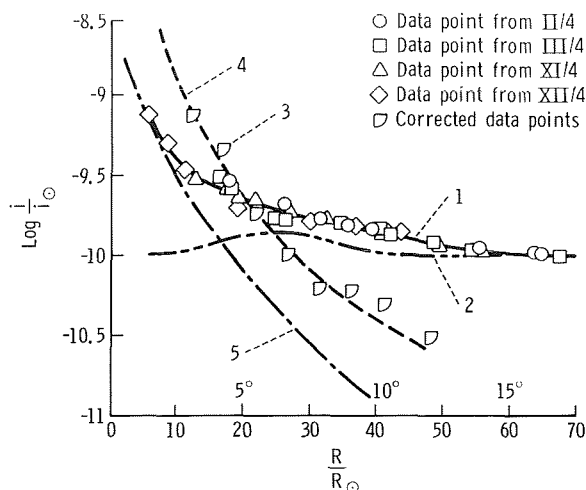


FIGURE 6-7.—Light distribution of the outer corona along the ecliptic. Number designations are as follows: 1. Light intensity distribution along the ecliptic as measured on the four indicated frames. 2. Distribution of cabin-light illumination along the ecliptic. 3. Data corrected for the cabin illumination and for lens and baffle vignetting. 4. Best fit to the corrected data (using eq. (6-6)). 5. Data obtained by Blackwell in 1954 (refs. 6-1 and 6-2).

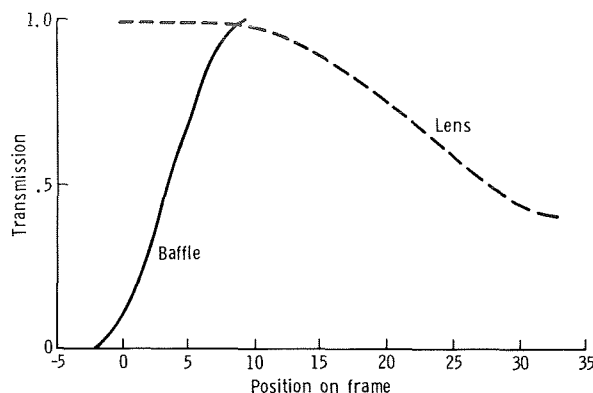


FIGURE 6-8.—Baffle and lens transmission as a function of position on the frame. The zero point is the center of a frame (optical axis of the camera). The lens vignetting curve is radially symmetric about the zero point. The baffle vignetting curve pertains only to the vertical direction; distance on the abscissa increases upward (away from the Earth). Baffle transmission is constant along any horizontal line on the frame.

## CONCLUSIONS

This preliminary analysis of the ASE experiment leads to the following conclusions.

1. The ASE experiment demonstrated that it was an effective method for studying the spatial distribution of contaminants produced by RCS engines as they function in a vacuum and in the gas-dust "atmosphere" that surrounds the space vehicles.

2. The atmosphere surrounding the space vehicle is a serious obstacle in performing observations of the dimly lit astronomical objects. This atmosphere is created, primarily, by the gas evaporation and particle condensation originating from the RCS engines.

3. Perhaps the major result of the ASE experiment is its demonstration that the simulation of solar eclipse is possible by providing an "artificial Moon" at a distance of approximately 100 m. Although diffraction phenomena on the artificial Moon did occur, they did not interfere with the observation of the outer corona. However, to obtain reliable quantitative data, it is essential to use

a "clean" artificial Moon that does not discharge gas or particles.

## REFERENCES

- 6-1. Blackwell, D. E.: A Study of the Outer Corona From a High Altitude Aircraft at the Eclipse of 1954 June 30. *Monthly Notices Roy. Astron. Soc.*, vol. 115, no. 6, 1955, pp. 629-649.
- 6-2. Blackwell, D. E.; Ingham, M. F.; and Dewhirst, D. W.: *The Zodiacal Light. Advances in Astronomy and Astrophysics*, Zdeněk Kopal, ed., vol. 5, Academic Press, Inc. (New York), 1967, pp. 1-69.



## 7. Crystal Activation

### Experiment MA-151

*J. I. Trombka,<sup>a†</sup> E. L. Eller,<sup>a</sup> R. L. Schmadebeck,<sup>a</sup> C. S. Dyer,<sup>b</sup> R. C. Reedy,<sup>c</sup> D. W. Barr,<sup>c</sup> J. S. Gilmore,<sup>c</sup> R. J. Prestwood,<sup>c</sup> B. P. Bayhurst,<sup>c</sup> D. G. Perry,<sup>c</sup> A. R. Smith,<sup>d</sup> R. C. Cordi,<sup>d</sup> R. H. Pehl,<sup>d</sup> J. S. Eldridge,<sup>e</sup> E. Schonfeld,<sup>f</sup> and A. E. Metzger<sup>g</sup>*

#### ABSTRACT

The Crystal Activation Experiment consisted of two sample packages that were flown in the command module and returned to Earth for analysis of the radioactivity induced in them during the flight. The objective of the experiment was to define the background caused by detector activation that interferes when gamma radiation is measured in the 0.02- to 10-MeV range from Earth orbit. These measurements, together with accelerator beam activation measurements and theoretical calculations, will be used to estimate this background for future or planned experiments. To aid the calculations, metals selected for their cross sections for specific neutron and proton energies were included in the samples in addition to the germanium and thallium-activated sodium iodide (NaI(Tl)), which are the usual detectors for low-energy gamma-ray measurements.

Preliminary results show that the activation of the NaI(Tl) crystal was a factor of 3 below that

from a similar measurement on Apollo 17. The identification of certain species and the level of activation observed show an important contribution from the interactions of thermal and energetic neutrons produced as secondaries in the spacecraft. The reduction of the activation by a factor of 3, compared with the Apollo 17 experiment, is consistent with the reduction in the primary cosmic ray intensity due to the geomagnetically shielded orbit.

#### INTRODUCTION

Significant background components to X-ray and gamma-ray measurements performed in space can be attributed to X-ray and gamma-ray emission induced in the spacecraft surrounding the detector and within the detector itself. Varying detector-spacecraft geometries (such as those obtainable with an extendable boom) can provide an indication of the spacecraft contribution, but in-flight measurements cannot separate the cosmic-ray-induced detector background from counts caused by the external photon flux.

Previous measurements were made on an NaI(Tl) crystal flown on Apollo 17. For that flight, the activation was mainly induced by cosmic-ray protons and by secondary neutrons produced in the spacecraft material. Because of the low-altitude Earth orbit on the Apollo-Soyuz Test Project (ASTP) mission, the Apollo-Soyuz spacecraft was exposed to a proton flux that was less intense. However, the protons had a higher

---

<sup>a</sup>NASA Robert H. Goddard Space Flight Center.

<sup>b</sup>University of Maryland.

<sup>c</sup>Los Alamos Scientific Laboratory.

<sup>d</sup>Lawrence Berkeley Laboratory.

<sup>e</sup>Oak Ridge National Laboratory.

<sup>f</sup>NASA Lyndon B. Johnson Space Center.

<sup>g</sup>NASA Jet Propulsion Laboratory.

<sup>†</sup>Principal Investigator.

average energy and therefore could have been more efficient in producing secondary neutrons. Neither the particle flux inside the spacecraft nor the cross sections for production of radioactive isotopes in the detector materials are well known. Therefore, in addition to NaI(Tl) and germanium detector crystals, the sample package included a number of metals that have good cross sections for specific energy ranges of neutrons and protons.

### SCIENTIFIC BACKGROUND

One of the major difficulties in measuring 0.02- to 10-MeV gamma radiation from space lies in distinguishing the radiation emitted by cosmic and planetary sources from the high rate of background gamma radiation produced by cosmic-ray and trapped-proton interaction with the spacecraft and the detector materials. Of these effects, the most difficult to isolate is the delayed decay of a radioactive nucleus produced by a spallation interaction within the detector material. These effects particularly complicate measurements of the diffuse sky-background gamma radiation in a spectral band that could contain important information on cosmology and the role of antimatter in the universe. The experimental confusion and theoretical possibilities have been recently reviewed by Horstman, Cavallo, and Moretti-Horstman (ref. 7-1). It is evident that advances in the field require improved knowledge of local activation effects and optimization of detector design and location against such a background.

Radioactive background has been observed in all cosmic gamma-ray experiments that have been carried into regions of trapped radiation such as in the Orbiting Solar Observatory (OSO) series of spacecraft. Such effects have been successfully explained (ref. 7-2) by a model proposed by Dyer and Morfill (ref. 7-3) in which the direct proton interactions in scintillators lead to radioactive spalled nuclei, the decay products of which are indistinguishable from an external gamma ray. The work by Dyer and Morfill and that by Fishman (ref. 7-4) demonstrated that similar interactions due to cosmic rays could also cause contamination, and this has been verified by the gamma-ray

NaI(Tl) spectrometers carried onboard Apollo 15 and Apollo 16 (ref. 7-5). As a result, an identical crystal was flown and returned on Apollo 17. Application of the spallation-activation calculation to those results showed that the level of activation was considerably enhanced by significant fluxes of secondary neutrons produced in the heavy spacecraft by cosmic-ray proton interactions (ref. 7-6). Results from activation packages flown on Skylab (ref. 7-7) also showed the presence of secondary neutrons but indicated less thermalization of this flux than that indicated by the Apollo 17 data.

For these reasons, it was considered important to include an activation package onboard the Apollo-Soyuz spacecraft to obtain further data from near-Earth orbit. For the Apollo-Soyuz orbit (222 km altitude, 51.8° inclination), part of the primary cosmic ray flux is shielded by the Earth's magnetic field, and trapped proton effects are minimized by the low orbit.

### EQUIPMENT AND EXPERIMENTAL PROCEDURE

The two assemblies shown in figures 7-1 and 7-2 were flown in the command module of the Apollo spacecraft during the Apollo-Soyuz mission. An NaI(Tl) crystal (fig. 7-1) physically identical to those flown on the Apollo 15 and 16 missions was used in this experiment. This assembly did not include the photomultiplier, the proton anticoincidence mantle, and the thermal shield that were used during the Apollo 15 and 16 missions, but it was identical to the assembly used on the Apollo 17 mission. Thus, direct comparison of the results from the two missions can be made. The detector was a 7- by 7-cm right-cylindrical crystal, hermetically sealed in a steel cylinder with a glass plate at one end. Magnesium oxide was used as an optical reflector inside the crystal assembly except at the glass window. This assembly made possible the simple procedure for optically coupling the crystal to a photomultiplier tube after flight. The second assembly (fig. 7-2) consisted of a 724-g sample of high-purity germanium; a small intrinsic germanium detector 32 mm in diameter by 8.75 mm thick, with a 0.12-mm layer of indium

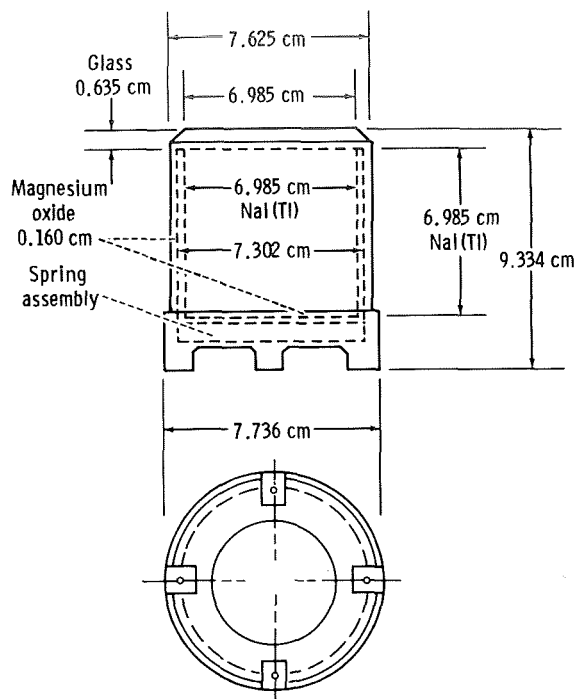


FIGURE 7-1.—The Apollo NaI(Tl) crystal assembly.

on one face; and 100-g foil disks of yttrium (Y), scandium (Sc), and depleted uranium (U) sealed in a cylinder identical with that used for containing the NaI(Tl) crystal. The lid of the container in this second assembly was made of 55 g of titanium (Ti) rather than steel.

Before the mission, background counts were taken on all materials in the laboratories where postflight low-level counting was anticipated. After splashdown, the flight (i.e., activated) NaI(Tl) was returned to the recovery ship and optically mounted on a photomultiplier tube, and pulse height spectra were obtained. The crystal counting was started approximately 1.5 hours after atmospheric entry of the command module. Before splashdown, a control (unactivated) crystal was optically sealed to the same photomultiplier tube, and the background was determined in the steel shield.

A 10.2- by 10.2-cm NaI(Tl) detector was used to measure the gamma-ray emission flux from the NaI(Tl) crystal and from the germanium after

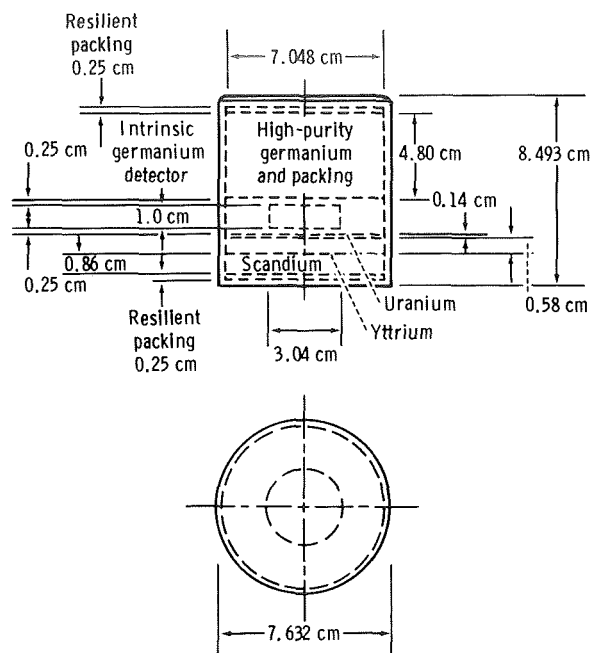


FIGURE 7-2.—Sample package showing location of metals and intrinsic germanium detector.

removal from its container. These measurements were also performed inside the steel shield, starting approximately 1.5 hours after atmospheric entry of the command module. Counting continued for 4 hours onboard the recovery carrier.

The detectors, bulk germanium, and foil disks were then returned to laboratories in the United States for further counting. The intrinsic germanium detector was returned to the Lawrence Berkeley Laboratory where the detector material was mounted on a cryostat, cooled, and low-level-counted. The foil disks and the steel container were delivered to the Los Alamos Scientific Laboratory for analysis. The NaI(Tl) crystals and the bulk germanium material were taken to the Oak Ridge National Laboratory, where the internal NaI(Tl) measurements were continued, and lithium-activated germanium (Ge(Li)) and low-level coincidence spectra were accumulated on both materials. High-resolution Ge(Li) spectra were also taken of the bulk germanium at the NASA Lyndon B. Johnson Space Center (JSC).

## RESULTS

## Lawrence Berkeley Laboratory

### Recovery Ship Measurements

The internal NaI(Tl) spectrum taken onboard the recovery ship approximately 4 hours after reentry is compared with the equivalent data from the Apollo 17 experiment in figure 7-3. The radionuclides identified from the Apollo 17 data are shown. Although the statistics are poorer, the Apollo-Soyuz data have the same general shape and are lower in intensity by a factor of approximately 3. The bulk germanium data did not show any identifiable lines but indicated a low-energy excess consistent with the presence of gallium-67 ( $^{67}\text{Ga}$ ) identified in the data taken at the Lawrence Berkeley Laboratory.

The detector was successfully brought into operation on the first attempt and showed the same noise and resolution characteristics that had been observed during preflight tests. Counting commenced at the Lawrence Berkeley Laboratory approximately 24 hours after splashdown.

The earliest spectra showed some excess count rates in continuum regions up to at least 1000 keV, and perhaps as high as 2000 keV; however, counting statistics will severely limit the quantitative results that can be obtained from these spectral distributions. Simple hand analysis indicated decay with (probably) more than one half-life, in the few-tens-of-hours range, but definitely shorter than the 78-hour half-life of  $^{67}\text{Ga}$ .

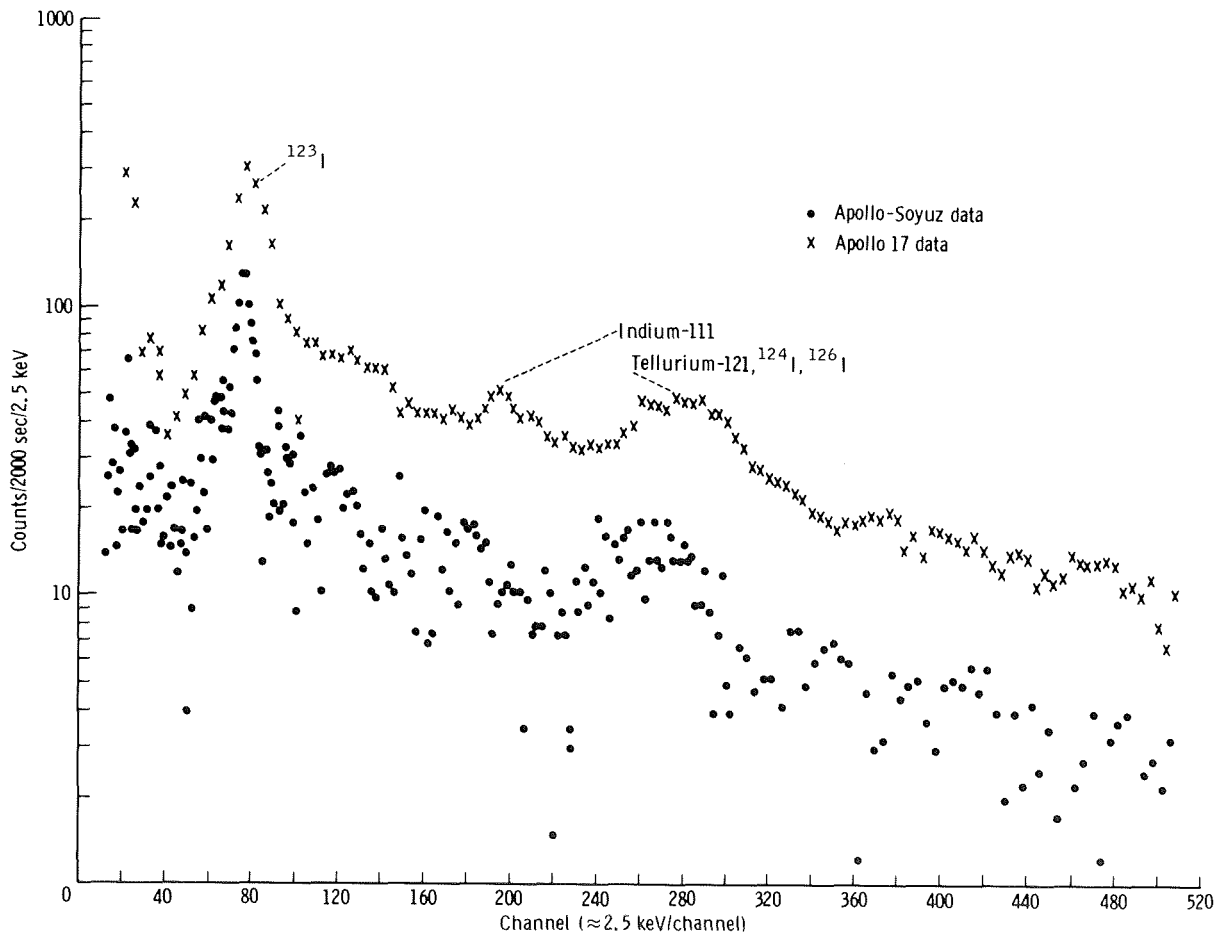


FIGURE 7-3.—Comparison of Apollo 17 and Apollo-Soyuz NaI(Tl) spectra taken 4 hours after reentry.

The prominent X-ray peak at approximately 10 keV (fig. 7-4) shows a composite decay curve that has been graphically resolved into two components, appropriate to 78-hour  $^{67}\text{Ga}$  and 12-day germanium-71 ( $^{71}\text{Ge}$ ). Identification of  $^{67}\text{Ga}$  is conclusive, based on the aforementioned evidence, the decay of a 93-keV gamma ray with a single half-life of about 80 hours, the decay of a gamma ray with apparent energy of about 195 keV (the sum of the 185 keV gamma ray and the X-ray) having approximately the same half-life, and the delayed-coincidence results described in a later paragraph. Identification of  $^{71}\text{Ge}$  is also considered conclusive, although it is based on less evidence, namely observation of the appropriate energy X-ray peak, which decays with (nearly) the  $^{71}\text{Ge}$  half-life.

Identification of the 78-hour half-life radionuclide  $^{67}\text{Ga}$  was confirmed from early spectra using delayed-coincidence measurements. In  $^{67}\text{Ga}$  decay, the lowest level (93 keV) in the stable daughter zinc-67 ( $^{67}\text{Zn}$ ) has a half-life of 9.3 microseconds; thus, the gamma ray that de-excites this level is almost always delayed in time with respect to emission of zinc fluorescent X-rays. Delayed-coincidence analysis was performed, using the X-ray events to generate a gate delayed 9 microseconds and of 27-microsecond width. A delayed-coincidence spectrum acquired during 2175 minutes of data accumulation that started 4 days after splashdown shows only the 93-keV peak and a scattering of lower energy partial absorption events. No events were stored in any of the 1420 channels above the peak region. This spectrum cannot be reconciled with any decay scheme other than that of  $^{67}\text{Ga}$ .

The most recent data indicate the appearance of at least two X-rays at energies below 10 keV, which may indicate the presence of  $^{65}\text{Zn}$  and one (or more) of the long-lived cobalt isotopes  $^{56}\text{Co}$ ,  $^{57}\text{Co}$ , and  $^{58}\text{Co}$ .

### Los Alamos Scientific Laboratory

The metal foil disks arrived at Los Alamos Scientific Laboratory 23 hours after splashdown. Analysis of the exposed foils was conducted as follows.

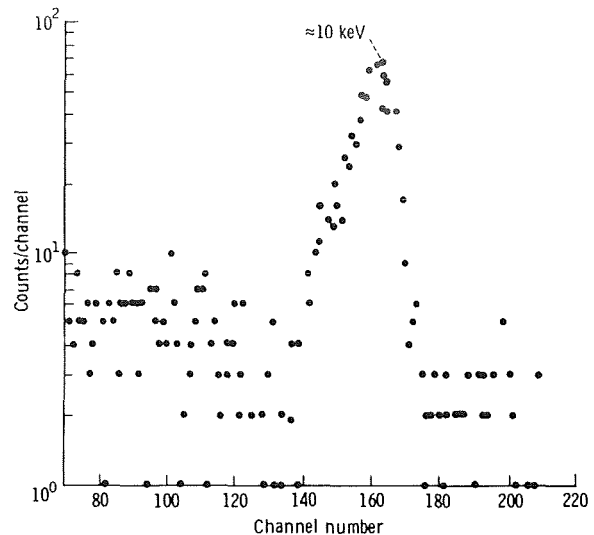


FIGURE 7-4.—Internal germanium spectrum showing doublet structure of 10-keV peak contributed by  $^{67}\text{Ga}$  and  $^{71}\text{Ge}$  (440-minute count time at 0.066 keV/channel).

1. The scandium disk was nondestructively counted for  $^{46}\text{Sc}$  to determine the thermal neutron-capture product.
2. Neptunium-239 ( $^{239}\text{Np}$ ) was chemically separated from uranium and counted to determine the epithermal neutron-capture product.
3. Molybdenum-99 ( $^{99}\text{Mo}$ ) was also chemically separated to measure the fission component.
4. The yttrium disk was dissolved and analyzed for  $^{87}\text{Y}$ , an energetic neutron- and proton-induced reaction product, and for zirconium-89 ( $^{89}\text{Zr}$ ), a low-energy-proton reaction product.
5. The titanium lid was chemically processed for scandium radionuclides produced by 1- to 20-MeV neutrons.
6. The stainless steel can was nondestructively analyzed for activities produced from iron.

The thermal neutron flux was 0.71 neutron/cm<sup>2</sup>·sec and the upper limit to the epithermal neutron flux was 0.003 neutron/cm<sup>2</sup>·sec. Table 7-1 shows the average cross sections for reactions measured in the ASTP foils as well as the flux of particles above 1 MeV and above the approximate threshold energy for each reaction determined from the ASTP foil measurements.

### Oak Ridge National Laboratory and JSC

Direct measurements of induced radionuclides were made by optically sealing a photomultiplier tube to the activated NaI(Tl) crystal. Pulse height spectra of the internal response were obtained beginning approximately 26 hours after splashdown. Such measurements are continuing to characterize the long-lived components. Indirect measurements of the induced radionuclides were made by using Ge(Li) detectors and a large anticoincidence-shielded NaI(Tl) spectrometer in the low-level facility at Oak Ridge National Laboratory (ref. 7-8).

Preliminary results from the low-level spectrometer system ( $4\pi$  system) yielded positive identification of iodine-124 ( $^{124}\text{I}$ ),  $^{126}\text{I}$ , and  $^{24}\text{Na}$  in the NaI flight detector. Tentative identification of  $^{22}\text{Na}$  was also made, but verification must await refinement of the spectral analysis. Semiquantitative disintegration-rate values are approximately one-third to one-half those found in the Apollo 17 experiment (ref. 7-6) for  $^{124}\text{I}$ ,  $^{126}\text{I}$ , and  $^{24}\text{Na}$ .

Gamma-gamma coincidence data on the germanium experiment from the  $4\pi$  system indicated the presence of at least one short-lived positron-emitting radionuclide. Decay-curve analysis of the positron-positron coincidences yielded a half-life value of 29 hours. The early measurements also show apparent gamma-gamma coincidences of 0.5 with 0.8-MeV photon and of 0.8 with 1.4-MeV photon. The radionuclide most closely fitting these characteristics is arsenic-72 ( $^{72}\text{As}$ ), a 26.0-hour positron emitter with a 0.834-MeV gamma ray in coincidence with its major positron branch. The positron-positron counting rate corrected to splashdown is approximately 2.7 counts/min with a corresponding system background of 0.1 count/min. At 41 days after splashdown, the positron-positron counting rate was only 50 percent above background. Detailed analysis of Ge(Li) spectra shows a tentative identification of  $^{67}\text{Ga}$ , a 78-hour radionuclide that decays by electron capture.

TABLE 7-1.—Summary of Threshold Reactions<sup>a</sup>

Reaction	$\phi\sigma$ , $\frac{\text{m}^2}{\text{cm}^2\text{-sec}}$ ( $\text{b}/\text{cm}^2\text{-sec}$ )	$E > 1 \text{ MeV}$			$E > \text{threshold}$	
		$<\sigma>$ , $\text{m}^2 (\text{b})$	$\phi$ , $\text{cm}^{-2} \text{sec}^{-1}$	Threshold, MeV	$<\sigma>$ , $\text{m}^2 (\text{b})$	$\phi$ , $\text{cm}^{-2} \text{sec}^{-1}$
$^{238}\text{U}(\text{n},\text{f})$	$4.30 \times 10^{-28}$ (4.30)	$1.48 \times 10^{-28}$ (1.48)	2.9	1	$1.48 \times 10^{-28}$ (1.48)	2.9
$\text{Ti}(\text{n},\text{x})^{47}\text{Sc}$	.087 (.087)	.030 (.030)	2.9	2	.035 (.035)	2.5
$\text{Ti}(\text{n},\text{x})^{46}\text{Sc}$	$\leq .32$ ( $\leq .32$ )	.023 (.023)	$\leq 36$	5	.035 (.035)	$\leq 24$
$^{27}\text{Al}(\text{n},\alpha)^{24}\text{Na}$	$\leq 15.5$ ( $\leq 15.5$ )	.014 (.014)	$\leq 1100$	5	.023 (.023)	$\leq 670$
$\text{Ti}(\text{n},\text{x})^{48}\text{Sc}$	$\leq .23$ ( $\leq .23$ )	.0073 (.0073)	$\leq 31$	5	.0115 (.0115)	$\leq 20$
$^{45}\text{Sc}(\text{n},2\text{n})^{44\text{m}}\text{Sc}$	$\leq .22$ ( $\leq .22$ )	.018 (.018)	$\leq 12$	10	.035 (.035)	$\leq 6$
$^{89}\text{Y}(\text{n},2\text{n})^{88}\text{Y}$	$\leq 1.65$ ( $\leq 1.65$ )	.110 (.110)	$\leq 15$	10	.215 (.215)	$\leq 8$
$^{89}\text{Y}(\text{n},3\text{n})^{87}\text{Y}$	$\leq .41$ ( $\leq .41$ )	.058 (.058)	$\leq 7.1$	20	.133 (.133)	$\leq 3.2$

<sup>a</sup>Uncertainty in the fluxes is estimated to be approximately  $\pm 50$  percent. Symbols are defined as follows: E is energy;  $\sigma$ , cross section;  $\phi$ , flux; n, neutron; f, fission;  $\alpha$ , alpha particle; and x, X-ray.



## DISCUSSION

The results of both internal and external monitoring of the NaI crystal showed an activation spectrum similar to that of the Apollo 17 crystal but at approximately one-third the intensity. Gallium-67 has been positively identified in the intrinsic germanium as well as in the external counting of the bulk germanium. Germanium-71 has been tentatively identified internally and  $^{72}\text{As}$ , externally.

Orbital integrations of trapped proton fluxes give a mission-averaged contribution of  $0.6 \text{ proton/cm}^2 \cdot \text{sec}$  for protons with energy greater than 100 MeV. This analysis also enables the mission-averaged cosmic ray flux to be estimated at  $0.8 \text{ particle/cm}^2 \cdot \text{sec}$ . The quantities of all positively identified radionuclides are considerably in excess of predictions based on these fluxes.

These results clearly confirm that considerable fluxes of secondary neutrons are produced by the interaction of cosmic rays with heavy spacecraft, as was the case in Apollo 17 (ref. 7-6). A considerable flux of thermal neutrons was again shown by the  $^{24}\text{Na}$  result and confirmed by the scandium activation. The very low epithermal neutron flux determined from the uranium foil disk is consistent with the low  $^{128}\text{I}$ : $^{24}\text{Na}$  ratio found in the Apollo 17 crystal. The other species observed in the NaI crystal require an energetic neutron flux (10 to 100 MeV) of  $2 \text{ neutrons/cm}^2 \cdot \text{sec}$ , consistent with the threshold detectors.

The reduction of activation between Apollo 17 and Apollo-Soyuz is approximately the same as the reduction in primary cosmic ray intensity due to geomagnetic shielding, showing that for this range the secondary neutron production is directly proportional to the primary cosmic ray intensity.

The production of secondary neutrons in heavy spacecraft and their efficient thermalization in Apollo modules again emphasize the necessity for developing codes to assess neutron production and transport, and demonstrate that gamma-ray

spectrometers are best used far removed from heavy material.

The calculations used here are being improved by comparison with controlled monoenergetic irradiation experiments, which will also yield important information on the short half-life radionuclides missed by such return procedures.

## REFERENCES

- 7-1. Horstman, H. M.; Cavallo, G.; and Moretti-Horstman, E.: *La Rivista del Nuovo Cimento*, vol. 5, 1975, p. 255.
- 7-2. Dyer, C. S.; Dunphy, P. P.; Forrest, D. J.; and Chupp, E. L.: *Proceedings of the 14th International Cosmic Ray Conference*, 1975, p. 3122.
- 7-3. Dyer, C. S.; and Morfill, G. E.: *Contribution to the Background Rate of a Satellite X-Ray Detector by Spallation Products in a Cesium Iodide Crystal. Astrophys. & Space Sci.*, vol. 14, no. 1, 1971, pp. 243-258.
- 7-4. Fishman, G. J.: *Cosmic-Ray Effects on Diffuse Gamma-Ray Measurements. Astrophys. J.*, vol. 171, 1972, pp. 163-167.
- 7-5. Trombka, J. I.; Metzger, A. E.; et al.: *The Cosmic Gamma-Ray Spectrum Between 0.3 and 27 MeV Measured on Apollo 15. Astrophys. J.*, vol. 181, 1973, pp. 737-746.
- 7-6. Dyer, C.; Trombka, J. I.; et al.: *Radioactivity Observed in the Sodium Iodide Gamma-Ray Spectrometer Returned on the Apollo 17 Mission. Space Sci. Instrum. 1*, vol. 3, 1975.
- 7-7. Fishman, G. J.: *Neutron and Proton Activation Measurements From Skylab. AIAA/AGU Paper 74-1227*, Nov. 1974.
- 7-8. Eldridge, J. S.; O'Kelley, G. D.; Northcutt, K. J.; and Schonfeld, E.: *Nondestructive Determination of Radionuclides in Lunar Samples Using a Large Low-Background Gamma-Ray Spectrometer and a Novel Application of Least-Squares Fitting. Nucl. Instr. & Meth.*, vol. 112, 1973, pp. 319-322.



## 8. Ultraviolet Absorption

### Experiment MA-059\*

*T. M. Donahue,<sup>a†</sup> R. D. Hudson,<sup>b†</sup> W. T. Rawlins,<sup>c</sup> J. Anderson,<sup>a</sup> F. Kaufman,<sup>c</sup> and M. B. McElroy<sup>d</sup>*

#### ABSTRACT

The Ultraviolet Absorption Experiment performed during the Apollo-Soyuz mission involved sending a beam of atomic oxygen and atomic nitrogen resonance radiation (130.4 and 120.0 nm), strong unabsorbable oxygen and nitrogen radiation (130.6 and 149.3 nm), and visual radiation, all filling the same 3°-wide field of view from the Apollo to the Soyuz. The radiation struck a retroreflector array on the Soyuz and was returned to a spectrometer onboard the Apollo. Lock on the retroreflector was maintained by the visual light and a star tracker. The density of atomic oxygen and atomic nitrogen between the two spacecraft was measured by observing the amount of resonance radiation absorbed when the line joining Apollo and Soyuz was perpendicular to their velocity with respect to the ambient atmosphere. By allowing the Apollo spacecraft to drift at fixed ranges of 150, 500, and 1000 m through an arc of  $\pm 15^\circ$  with respect to the perpendicular to the velocity vector, the temperature of the gas was obtained; i.e., the Doppler line profile was scanned. Information concerning oxygen

densities was also obtained by observation of resonantly fluorescent light. The absorption experiments for atomic oxygen and atomic nitrogen were successfully performed at a range of 500 m, and abundant resonance fluorescence data were obtained.

#### INTRODUCTION

The Ultraviolet Absorption (UVA) Experiment is one of the five experiments that incorporated joint activities between the U.S. and U.S.S.R. crews during the Apollo-Soyuz Test Project (ASTP) mission. The experiment provided an opportunity for the realization of a technique devised to permit the measurement of atmospheric species concentrations. This experiment involved the application of the most reliable and specific laboratory technique available for measuring the concentration of a given gaseous species—atomic absorption spectroscopy. This method is probably the most reliable available tool for quantitative analysis if the cross sections or oscillator strengths for absorption are known, if proper precautions are taken to ascertain the frequency dependence (or line shapes) of light sources and absorbers, if optical properties of the measuring devices are measured, and if corrections are made for absorption by other species (or impurities). A complementary technique, the quantitative observation of resonance fluorescence in which atomic or molecular species scatter resonance radiation from a light source into a detector, is a powerful one and was used in the ASTP UVA experiment. The species chosen for detection and measurement were neutral atomic

---

\*The joint U.S.-U.S.S.R. designation was "Experiment AS-5."

<sup>a</sup>University of Michigan.

<sup>b</sup>NASA Goddard Space Flight Center.

<sup>c</sup>University of Pittsburgh.

<sup>d</sup>Harvard University.

<sup>†</sup>Co-Principal Investigator.

oxygen (O) and neutral atomic nitrogen (N). The first was selected for several reasons.

1. Strong resonance light sources are available that produce radiation in the resonance triplet at 130.2, 130.5, and 130.6 nm, hereafter referred to as 130.4-nm radiation.

2. The absorption cross section or oscillator strength of O for the energy-state transition producing or absorbing this radiation ( $^3P_{2,1,0}$   $^3S_1$ ) is accurately known.

3. Although O is the most abundant atmospheric species at the experiment altitude (225 km), to detect the species cleanly in a mass spectrometer is difficult because of its propensity to recombine into molecular oxygen ( $O_2$ ) upon colliding with the walls of a spectrometer ion source. At lower altitudes, this recombination has caused difficulties that leave the actual density of O near 120 km uncertain by a factor of 5 or more. At an altitude of 225 km, the uncertainty is probably not very great, but it is interesting to attempt to verify other measurement methods by a new one or to prove the new method by comparison with ground truth.

Atomic nitrogen was interesting because, as of a year or so ago, the direct measurement of this species in the thermosphere had probably not yet been performed successfully. A satellite mass spectrometer result (ref. 8-1) obtained at an altitude of 400 km suggested that the partial pressure of N exceeded that of molecular nitrogen ( $N_2$ ), but the result was flawed by low mass resolution. A rocketborne mass spectrometer result by Ghosh and others (ref. 8-2) suggested that, at an altitude of 185 km, the density of N was 6 percent that of  $N_2$ , although Hickman and Nier (ref. 8-3) showed that this is an upper limit.

The problems in measuring N mass spectrometrically are similar to those of obtaining O measurements but are more serious because the density ratio of N to  $N_2$  in the thermosphere is small. The  $N_2$  can be dissociatively ionized in the spectrometer ion source; like O, N is highly reactive and can recombine not only to form  $N_2$  on instrument chamber walls but can form other compounds such as NO.

## PRINCIPLE OF THE UVA EXPERIMENT

The principle of the UVA measurement was to produce fairly well collimated beams of 130.4- and 120.0-nm radiation (resonance for O and N), and 135.6- and 149.3-nm radiation (forbidden lines of O and N that are very weakly absorbed by these species). The forbidden line radiation originated in the same sources as the resonant line radiation and hence defined the beam geometry, the reflectivity, and the transmission of the optical instrument for the resonance radiation independently of resonance absorption. The light was produced by radiofrequency-driven lamp sources and collimated by mirrors on the Apollo spacecraft. The light beams illuminated an array of corner reflectors mounted on the Soyuz spacecraft at a known distance  $x$  from the Apollo UVA light source. Thus, the portion of the beam striking the retroreflectors returned to a collecting mirror near the Apollo collimating mirror. From this mirror array, the radiation was focused on the entrance slit of a 0.75-m Ebert-Fastie scanning spectrophotometer by an auxiliary mirror. The spectral range from 120.0 to 149.3 nm was scanned every 12 seconds through 1.5-nm ranges centered on 120.0, 130.4, 135.6, and 149.3 nm. The bandwidth of the spectrometer was approximately 1.15 nm. The spectrometer was a modified backup unit for the one used on the Apollo 17 experiment (ref. 8-4).

In its simplest terms, the principle of the UVA experiment is illustrated in figure 8-1. A known flux of resonance radiation  $F$  is radiated into a solid angle  $\Omega$ . At a distance  $x$  from the source, the

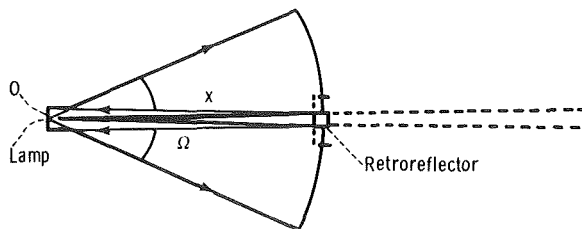


FIGURE 8-1.—Basic geometry of the UVA experiment.

irradiance is  $F/\Omega x^2$ . If the reflectivity of each surface of the retroarray is  $r$  and the retroarray surface area is  $A$ , an amount of radiation  $r^3 FA/\Omega x^2$  is returned to point O and passes through a well-defined and limited region determined by the shape of the collimating mirror, the shape of the corner reflectors, and the geometry of the retroreflector array. Essentially, light from each point on the collimating mirror that strikes a given retroreflector returns through a region of the same shape but twice the linear dimensions of the corner reflector. The pattern of light sent from a point source to a corner reflector that is a distance  $x$  from the source and back to the source is analogous to the pattern of light sent from the point source to a hole in an opaque screen at a distance  $x$  of the same shape as the reflector and then on through the aperture to a screen that is a distance  $2x$  from the source. If a fraction of this returned light  $f$  is sent to a spectrometer having a throughput  $QT$ , where  $Q$  is the quantum efficiency and  $T$  is the transmission, the counting rate  $R$  of a detector in the spectrometer will be

$$R = r^m \frac{FA}{\Omega x^2} \exp(-2\bar{\sigma}xn) fQT \quad (8-1)$$

where  $m$  is the number of reflections, six in the present case;  $\bar{\sigma}$  is the mean absorption cross section; and  $n$  is the attenuation coefficient. Obviously,  $r$  is assumed to be the same at each surface for a given wavelength.

The flux  $F$  of 130.4-nm radiation was  $5 \times 10^{13}$  photons/sec into a solid angle  $\Omega$  of 0.75 sr. Typical values for the other terms in the equation are as follows.

$$\begin{aligned} r &= 0.75 \\ m &= 6 \\ A &= 55 \text{ cm}^2 \\ f &= 0.2 \\ T &= 0.2 \\ Q &= 0.12 \text{ electron/photon} \\ \bar{\sigma} &= 10^{-13} \text{ cm}^2 \end{aligned}$$

Thus

$$R \approx 3 \times 10^{12} x^{-2} \exp(-2\bar{\sigma}xn) \quad (8-2)$$

The unattenuated counting rate  $R_0$  is  $3 \times 10^{12} x^{-2}$ , or  $3 \times 10^2$  counts/sec even at a range of 1 km. It was assumed that the minimum absorption that could be detected was 10 percent; i.e.,  $\exp(-2\bar{\sigma}xn) = 0.9$ , or  $xn = 2 \times 10^{12} \text{ cm}^{-2}$ . Thus, at 100 m, an absorber density of  $2 \times 10^9 \text{ cm}^{-3}$  should be detectable and, at 1 km, a density of  $2 \times 10^7 \text{ cm}^{-3}$  should be detectable. In this case, the counting rate will be 270 counts/sec, compared with the unabsorbed rate of 300 counts/sec.

In an experiment such as this, the spacecraft velocities are greater than the average thermal velocities of the gas particles at 1000 K (by a factor of 8 for oxygen). Hence, the frequency of the lamp signal will be shifted far away from the absorption frequency of the atoms by the Doppler effect if the light is radiated in the approximate direction of the Apollo velocity vector. It is therefore necessary to conduct the experiment with the vector between the spacecraft nearly perpendicular to the spacecraft velocity vectors. A simple calculation shows that, if the angle between the direction of emission of the light signal and the Apollo velocity vector were  $78^\circ$  with the two spacecraft 100 m apart, the absorption by  $4 \times 10^9 \text{ atoms/cm}^3$  of oxygen would be only 30 percent compared to 82 percent if the angle were  $90^\circ$ . This effect could, however, readily be turned into an advantage if the experiment were performed in such a way that one spacecraft (for example, Apollo) slowly drifted past the other at a fixed range and the angle between them varied through approximately  $30^\circ$  centered on the normal to the orbital velocity vector. The reasons are twofold. First, it would not be necessary to determine by some independent measurement when the angle of observation was  $90^\circ$  to the direction of the relative wind. This information would automatically be determined as the point at which the counting rate became minimum. Second, the change in counting rate with angle would define the Doppler line shape of the absorbing atom. Hence, the functional form of this variation would enable measuring the temperature of the absorbing atoms.

In practice, it is necessary to consider the fact that the light flux  $F$  varies with wavelength  $\lambda$  for each fine structure component of the resonance lines, and that the absorption cross section  $\sigma$  is

also a function of wavelength. Thus, the term  $F \exp(-2\bar{\sigma} nx)$  in equation (8-1) must be replaced for each fine structure component by

$$\int_i F_i(\lambda) \exp[-2nx\sigma(\lambda)] d\lambda \quad (8-3)$$

where  $F_i(\lambda)$  depends on the effective lamp temperature  $T_L$  and  $\sigma(\lambda)$  values depend on the gas temperature  $T_G$ . When there is no relative motion between source and absorber, the functional form of  $F(\lambda)$  may be written

$$\left( \frac{mc^2}{2\pi k T_L \lambda_{0i}^2} \right)^{1/2} \exp \left[ \frac{-mc^2 (\lambda - \lambda_{0i})^2}{2k T_L \lambda_{0i}^2} \right] \quad (8-4)$$

where  $\lambda_{0i}$  is the line center wavelength of the  $i$ -th fine structure component,  $m$  is the atomic mass of the gas species,  $c$  is the speed of light, and  $k$  is the Boltzmann constant. When  $u$  is the component of the atmospheric velocity along the light beam in the coordinate system in which the Apollo vehicle is at rest,  $\sigma(\lambda)$  becomes

$$\sigma_0 \exp \left\{ \frac{-mc^2 \left[ (\lambda - \lambda_0) c - u \lambda_0 \right]^2}{2k T_G \lambda_0^2 c^2} \right\} \quad (8-5)$$

Finally, because the spectrometer does not resolve the fine structure components in the spectrum, it is necessary to sum over fine structure components to obtain the predicted counting rate.

$$R = \sum R_i \quad (8-6)$$

The spectral parameters for the gases involved in this experiment are shown in table 8-I.

Figures 8-2(a) and 8-2(b) show the counting rates as a function of spacecraft separation when  $u = 0$  for O and N, respectively, at typical gas concentrations. Figures 8-3(a) and 8-3(b) show, for various values of  $T_G$ , the variation in atmospheric transmission as a function of the angle  $\theta$  between the direction of observation and the perpendicular to the wind velocity vector in the coordinate system in which the Apollo spacecraft is at rest. The lamp output (integrated over wavelength of all spectral components) is assumed to be  $10^{13}$  photons/sec for the oxygen 130.4-nm triplet and  $3 \times 10^{12}$  photons/sec for the nitrogen 120.0-nm triplet.

A practical complication is introduced in performing this experiment because the resonance radiation in the emitted beam can be scattered resonantly by the gas to be studied. Some of this radiation will be emitted in a direction to enter the spectrometer slit, although it is a relatively small amount of the total scattered light because the scattering is virtually isotropic. If one considers the light traveling in a certain direction from the light source (treated as a point source) and calls the number of photons crossing unit area per second at a distance  $x$  from the source  $I_L(\lambda)$ , the number of these scattered per second will be

$$\int_{x_0}^{\infty} \int_L I_L(\lambda) n \sigma(\lambda) \exp \left[ -2n \int_0^x \sigma(\lambda) dx' \right] d\lambda \frac{dx}{4\pi x^2} \quad (8-7)$$

where  $x_0$  is the distance from the light source at which the outgoing beam crosses the spectrometer field of view. To evaluate the actual counting rate due to these scattered photons, it is necessary to evaluate the overlap of the outgoing beam with the effective spectrometer field of view. For example, the field of view is filled gradually and not abruptly at a distance  $x_0$  along the beam. This evaluation is being conducted for the instrument

actually flown. A reasonable approximation for the counting rate from resonance fluorescence  $R_F$  is

$$R_F = \frac{FA_M A_{SM} A_S r^3 QT}{4\pi p^2 \Omega} \int_{x_0}^{\infty} \frac{dx'}{x'^2} \int_0^{\infty} I_L(\lambda) n(x) \sigma(\lambda) \exp \left[ - \int_0^x 2n\sigma(\lambda) dx \right] d\lambda \quad (8-8)$$

where

$A_M$  = the lamp collimating mirror area (3.3 by 5.7 cm)

$A_{SM}$  = the area of the collecting mirror (5.5 by 3.7 cm)

$A_S$  = the area of the spectrometer slit (0.2 by 5.7 cm)

$p$  = the focal length of the collecting mirror (16.5 cm)

$x_0$  = 75 cm

The contribution of resonance fluorescence under the same conditions assumed in the absorption calculation is shown in figure 8-2. The fluorescence contribution varies with the angle between

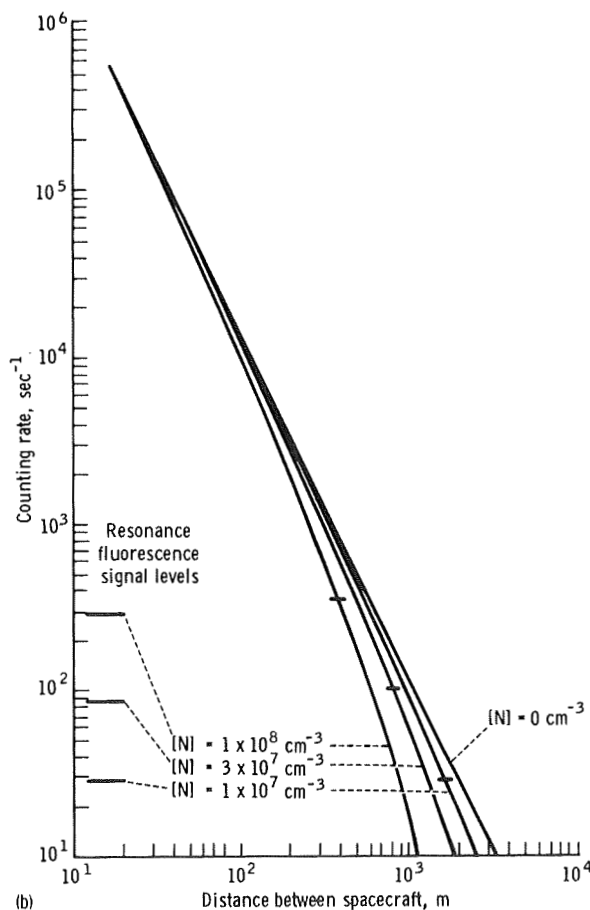
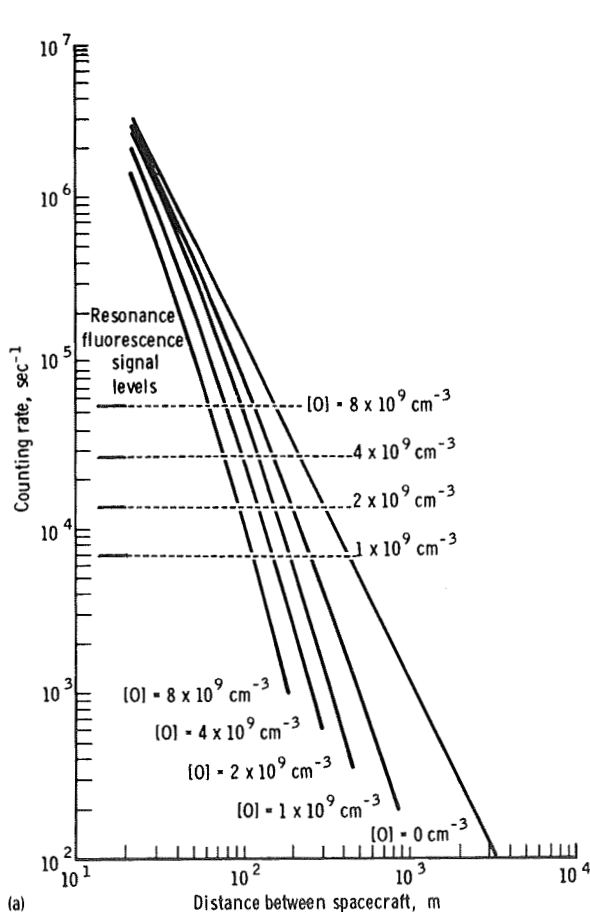


FIGURE 8-2.—Spectrometer signal as a function of spacecraft separation distance (where [O] and [N] are the density of oxygen and nitrogen, respectively). (a) Oxygen atoms. (b) Nitrogen atoms.

direction of observation and velocity vector and reaches a maximum where the transmitted light reaches a minimum; i.e., when the wind velocity component in the direction of observation is zero. The resonance fluorescence contribution to the observed counting rate as a function of time (or angle) must be evaluated independently so that it can be subtracted from the total counting rate to obtain the contribution due to transmitted (or absorbed) radiation alone; also to be subtracted are background signals from airglow.

The heart of the experimental apparatus is the Apollo 17 Ebert-Fastie spectrometer. It was equipped with a new grating drive cam that rotated the grating to scan from 129.65 to 131.15 nm in 2.5 seconds, from 119.25 to 120.75 nm in 4.5 seconds, from 129.65 to 131.15 nm again in 2 seconds, from 134.85 to 136.35 nm in 1.25 seconds, and from 148.55 to 150.05 nm in 1.25 seconds. The light output of each lamp was pulsed with a pulse duration of 0.1 second; the sequence was the O lamp alone, the N lamp alone, and both lamps off.

The resonance lamp light sources, the retroreflector array, and the optical transmitting and receiving systems had to be designed around

the spectrometer in such a way as to maximize the signals received. The spectrometer choice was governed by availability and by the schedule for experiment preparation. The instrument has an entrance slit of 0.2 by 5.7 cm, with an f/5 collecting aperture corresponding to a solid angle of  $12^\circ$  by  $12^\circ$ . The ultraviolet lamps have a 1-cm source diameter and emit into a solid angle of approximately  $56^\circ$  full width, or 0.74 sr. The flux from each lamp is collimated by a mirror placed 12 cm from the lamp. Because the source diameter in the lamps is 1 cm, the beam leaves the collimating mirror with a spread of approximately  $5^\circ$ .

In designing the corner reflector array, it was necessary to consider that the optimum diameter of the mirror that focuses the returned light on the spectrometer slit equals the width of an individual corner reflector. The corner reflectors must be packed efficiently into an array of convenient diameter. The arrangement adopted was a 10-cm array diameter, and each reflector was 3.3 cm wide (fig. 8-4). In this case, the focusing mirror diameter was 3.3 cm, and the mirror was placed 16.5 cm from the slit to fill the slit aperture laterally.

TABLE 8-I.—Spectral Parameters for Atmospheric Absorption Experiment

Species	Spectral line, nm	Absorption cross section at 300 K ( $\sigma_0$ ), $\text{cm}^2$ (a)	Relative lamp intensity $F_i$	Relative atmospheric populations at 1050 K
O	130.217	$1.6 \times 10^{-13}$	0.542	<sup>b</sup> 0.613
	130.487	1.6	.337	<sup>b</sup> .297
	130.601	1.6	.120	<sup>b</sup> .090
N	119.955	3.8	.500	1.000
	120.022	2.5	.333	1.000
	120.071	1.3	.167	1.000

<sup>a</sup> $\sigma_0(T_G) = \sigma_0(300 \text{ K})\sqrt{300/T_G}$ . The values of  $\sigma_0(300 \text{ K})$  are calculated from the oscillator strengths given in reference 8-5.

<sup>b</sup>The relative atmospheric populations for atomic oxygen are calculated from the following formulas.

$$n_{130.2}/n_{\text{total}} = 5/(\text{sum})$$

$$n_{130.5}/n_{\text{total}} = [3 \exp(-228.24/T_G)]/(\text{sum})$$

$$n_{130.6}/n_{\text{total}} = [\exp(-326.16/T_G)]/(\text{sum}),$$

$$\text{where } (\text{sum}) = 5 + [3 \exp(-228.24/T_G)] + [\exp(-326.16/T_G)]$$



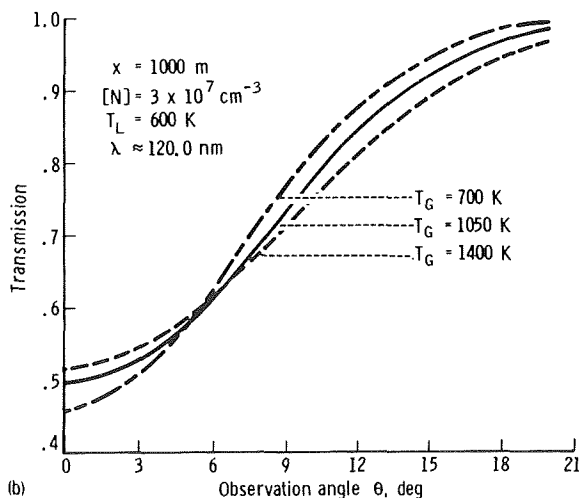
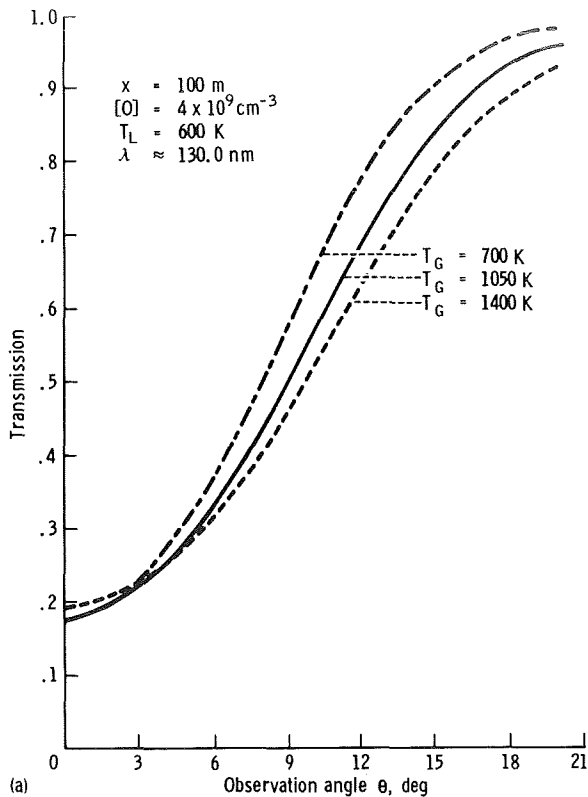


FIGURE 8-3.—Variation of atmospheric transmission as a function of the observation angle. (a) Oxygen atoms. (b) Nitrogen atoms.

The geometry of the optical transmitting and collecting system is defined in figure 8-5. Light originating from a point on a collimating mirror will return from the corner reflector and pass through a region centered at that point on the mirror but twice as large in linear dimensions as the corner reflector (neglecting diffraction effects). For example, light originating from point  $x$  on the O mirror in figure 8-6 will return through the 6.6-cm dashed-line region (hexagonal). It is reasonable to put the collecting mirror in the space bounded by the collimating mirrors and allow the dimensions to be 3.3 by 5.7 cm. The contribution to the collected light originating from point  $x$  is then the shaded overlap of the collecting mirror and the hexagonal area 6.6 cm in diameter and centered at point  $x$ . The size of the return beam from all points on the collimating O mirror is shown by the broken line. The collecting mirror must be protected from stray light coming from the lamps by means of baffling because the most intensely illuminated region is that adjacent to the collimating mirror.

Figure 8-7 shows how the fluorescence and transmitted signals should vary with wavelength around 130.4 nm. This calibration was done by convoluting the previously computed signal intensities in each of the three components of the oxygen triplet with the spectrometer slit function. The latter was assumed to be triangular with a full width of 1.15 nm at half maximum. The case shown is for an Apollo-Soyuz separation of 100 m, an oxygen density  $[O]$  of  $4 \times 10^9 \text{ cm}^{-3}$ , a lamp temperature  $T_L$  of 600 K, and a gas temperature  $T_G$  of 1050 K. The curves are normalized. The difference in wavelength at the peak occurs because most of the transmitted signal is in the weaker 130.5- and 130.6-nm components, whereas most of the fluorescence signal is from the 130.2-nm line.

A third light source was incorporated in the apparatus to provide bright visual light illuminating the same field of view as the ultraviolet sources. The collimating lamp, marked "Visible" in figure 8-6, provided input to a star tracker with output in the spacecraft to indicate to the astronaut whether the retroreflector array was being illuminated by the lamp beams, and, more importantly, whether the retroarray was in the spectrometer field of

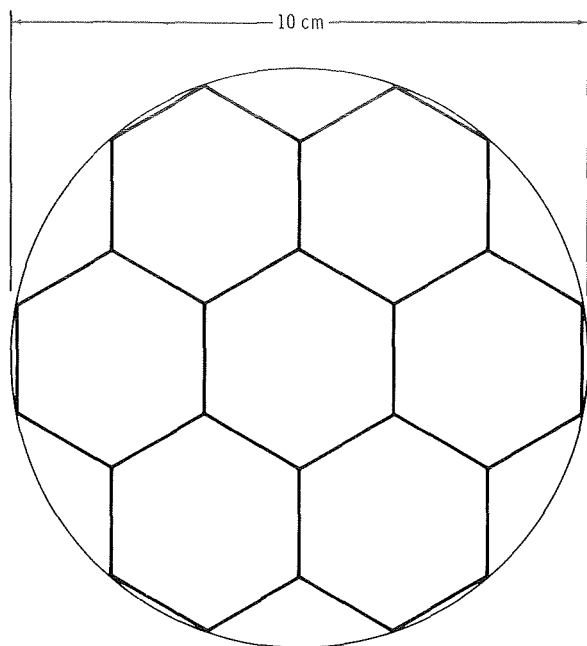


FIGURE 8-4.—Arrangement of mirrors in the retroreflector array.

view ( $\pm 0.35^\circ$  in pitch). A backup to the star tracker was provided by the crew optical alignment sight (COAS), through which the retroreflector could be seen. The COAS was provided with a reticle marked in degrees in the pitch and yaw directions.

A door was provided that was closed when data were not being taken. The inside surface of the door was blackened. However, small reflecting cylinders, one for each of the ultraviolet sources, were fitted in the door. These cylinders provided a means of in-flight calibration. The counting rate as a function of grating position was obtained with the flight unit during thermal-vacuum (TV) checks of the instrument for comparison with calibration runs made during flight.

The reflectivity of the retroreflectors was measured as a function of wavelength. The transmission  $T$  of the full receiving system, the external optics, and the telescope were also measured at the John Hopkins University with the cooperation of W. G. Fastie. The quantum

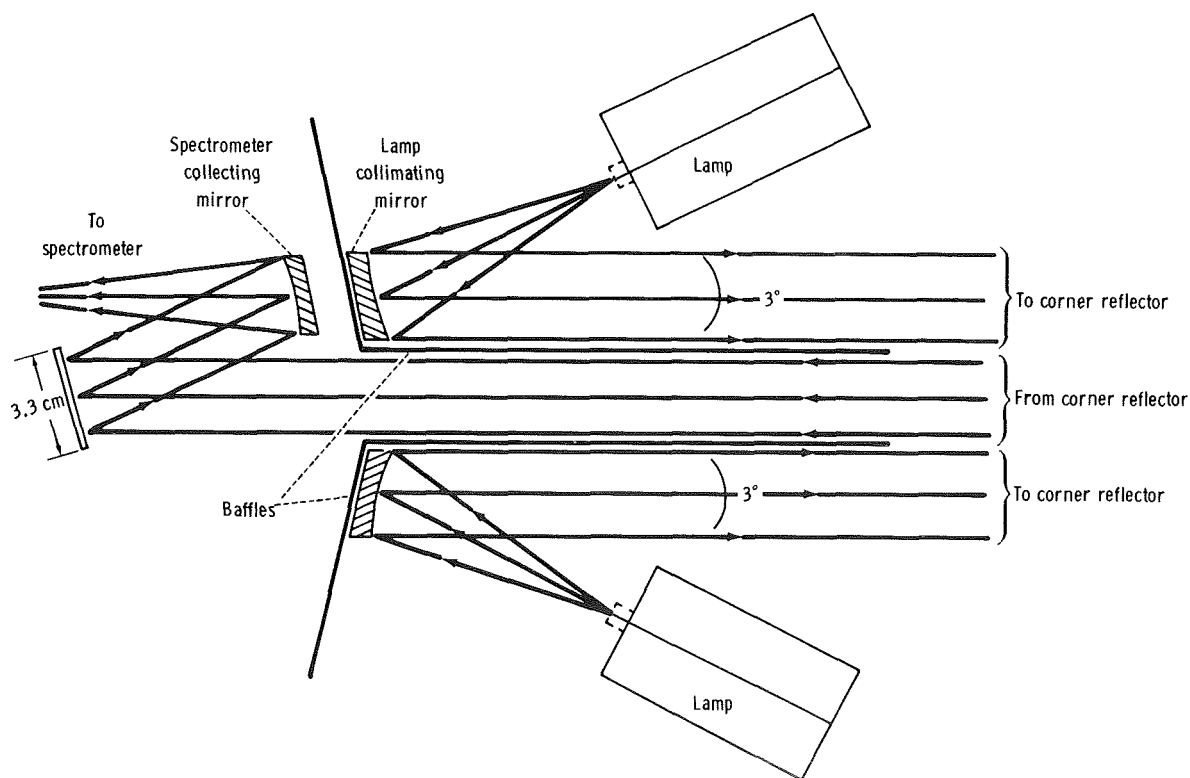
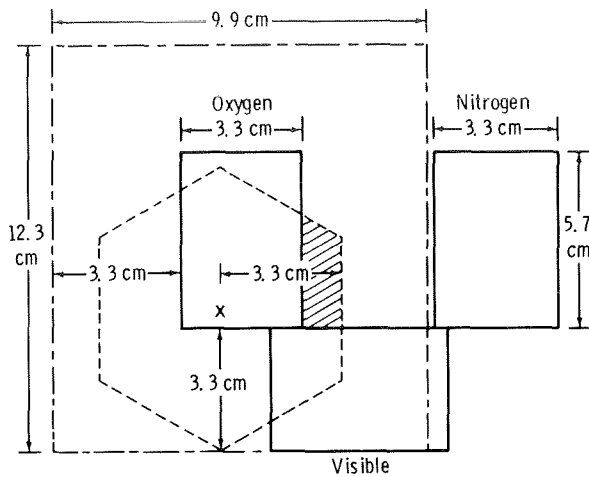


FIGURE 8-5.—Schematic diagram of optical transmitting and collecting system.



--- Return beam dimensions from single point on lamp mirror  
 --- Return beam dimensions from entire lamp mirror

FIGURE 8-6.—Geometry of return beam from the retroreflector array.

efficiencies of the detectors  $Q$  for both flight and backup units were also measured. Pertinent data are shown in tables 8-II to 8-V.

The flight lamps and backup lamps were calibrated to determine the flux of photons emitted. For this calibration, a monochromator and a double ionization chamber (for the 120.0- and 130.4-nm lines) were used, and a measurement of the photocurrent in the monochromator detector (for the 135.6- and 149.3-nm lines) was made. The data obtained for the flight lamps were reduced to absolute intensities by comparison with similar measurements made with the same system on another lamp that had been absolutely calibrated at the University of Pittsburgh. The detector used at Pittsburgh to calibrate the standard lamp had been calibrated by a measurement of its response to radiation at the four wavelengths in question emitted from a beam of O and N atoms of known density excited by electron impact. The flux from the flight lamp is given in table 8-III.

The effective lamp temperatures  $T_L$  were also measured at the University of Pittsburgh by measuring the absorption of their resonance radiation by a column of atoms of known concentration at a temperature of 300 K. The surprising result was that typical effective temperatures for the oxygen lamps were very large, from 2200 to

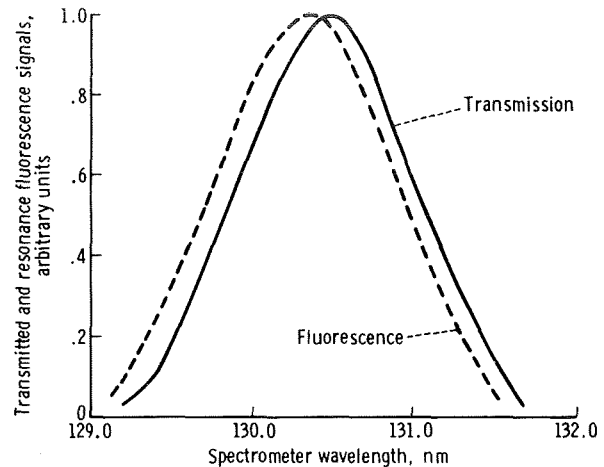


FIGURE 8-7.—Transmitted and resonance fluorescence signals as a function of spectrometer wavelength setting.

3700 K. The high temperature is presumed to be caused by the presence of many atoms that have been dissociatively excited from  $O_2$  into high radiating states of O, and have cascaded into the resonantly radiating state before undergoing many collisions. This was not the case for the nitrogen lamps. The flight lamp temperatures were 2500 K for the oxygen lamp and 400 K for the nitrogen lamp. The UVA experiment was mounted on the Apollo docking module with the field of view forward (plus-X axis).

## RESULTS

The first exercises of the UVA experiment began when the lamps were turned on at 27:00 ground elapsed time (GET) on Wednesday, July 16, 1975. The counting rate as a function of cam position closely reproduced that obtained with the door closed in the last TV tests before the apparatus left the laboratory (table 8-IV). At 28:30 GET, the cover was opened and the spacecraft was pointed toward the star Vega. The purpose of this exercise was to calibrate the COAS and to test the star-tracker system designed to lock the field of view on a target. During this test, the obtaining of resonance fluorescence signals in the oxygen

TABLE 8-II.—Product of Quantum Efficiency and Transmission QT for Flight and Backup Units

Wavelength, nm	Backup unit QT	Flight unit QT
130.4	0.0258	0.0307
120.0	.0129	.0264
130.4	.0272	.0397
135.6	.0258	.0311
149.3	.0151	.0172

TABLE 8-III.—Flight Lamp Fluxes Into 0.74 sr

Flight lamp	Wavelength, nm	Flux, photons/sec
O	130.4	$10.4 \times 10^{13}$
	135.6	1.78
N	120.0	.634
	149.3	1.45

TABLE 8-IV.—Comparison of Counting Rates for Flight and Backup Units

Wavelength, nm	Activity, counts/sec, for -			
	TV test of flight unit	During flight with backup unit	Ratio flight/TV test	Ratio QT backup unit/QT flight unit
130.4	27 310	21 260	0.78	0.84
120.0	21 788	18 359	.84	.78
130.4	27 771	21 709	.78	.69
135.6	6 363	4 268	.67	.83
149.3	13 527	11 881	.88	.88

130.4-nm channels was verified. One problem was discovered, however; the star tracker indicated lock while the COAS indicated star movement from 3° to the right to 2.5° to the left. This difference occurred because a spacer was inserted between the lens and aperture of the star tracker to increase the size of the light spot on the photocathode and thereby to change the slope of the star-tracker response curve. This change moved the focal point approximately 0.25 cm in front of the aperture and enlarged the star-tracker field of view to the limits of the star-tracker tube, 5.5°, due to vignetting. To avoid operating with the retroreflector out of the field in yaw (even though the star tracker indicated it was in the field), the chart on the COAS reticle was marked at  $\pm 1.5^\circ$  and the crew was instructed to prevent straying of the retroreflector image beyond these limits. In fact, the crew was asked to keep the retroreflector as near as possible to the center of the COAS.

Five additional data-taking exercises were performed. After the final undocking on July 19, 1975, the Apollo vehicle assumed a stationkeeping position 18 m ahead of the Soyuz vehicle as the

two spacecraft approached the morning terminator. The UVA power was turned on at approximately 98:55 GET, 30 minutes before the first observational exercise, to permit stabilization of the lamps and the photomultiplier tube. During this period, calibration data were obtained using the door reflectors. Table 8-IV presents results for comparison with those obtained during the final TV tests conducted at the Applied Physics Laboratory of Johns Hopkins University. The counting rates during flight were approximately 0.8 of those obtained on the ground. This effect can be attributed to use of the detector head from the backup unit to replace that of the flight unit on the launch pad shortly before flight because of an electronics problem. A comparison of the ground-test product of QT values for the two units (table 8-IV) shows that the ratios are about the same as the flight to ground-based counting rate ratios. At 99:25 GET, the Soyuz crew activated circuits to unlatch covers over the Soyuz retroreflector arrays. Two arrays were mounted on top of the vehicle, one facing upward, and the other facing starboard. A third array was mounted on the rear of

TABLE 8-V.—Retroreflector Reflectivities

Wavelength, nm	Reflectivity from -	
	Aft	Top
130.4	0.60	0.57
120.0	.56	.54
135.6	.55	.52
149.3	.52	.49

the spacecraft facing aft. The Apollo crew verified with binoculars that the covers on the top-mounted retroreflectors had opened. (If the starboard array had not opened, a contingency plan would have permitted a Soyuz yaw so that its aft-mounted retroreflectors could be used in the experiment). Power to the UVA was briefly turned off while the door of the instrument was opened after the terminator had been passed. (The power-down precaution was necessary so that large flashes of light would not damage the detectors as the door was being opened or closed.) Beginning 18 minutes before the data-gathering run, the Apollo vehicle moved out of the orbital plane (fig. 8-8) until it was 150 m from the Soyuz vehicle and oriented so that the retroreflector could be illuminated. At this time, the angle between the perpendicular to the Soyuz velocity vector and the Apollo vehicle was  $15^\circ$ . The Apollo vehicle then was maneuvered through a  $33^\circ$  circular arc sweep passing through the normal to the velocity vector while the crew attempted to keep the retroreflector illuminated following procedures described previously. Both the star-tracker output and the COAS observations indicated that a lock was obtained. A problem occurred during the first several minutes of the run because the Soyuz flashing beacons and orientation lights were not extinguished. After the data-taking maneuver (lasting 10 minutes) was completed, the Apollo vehicle returned to a stationkeeping position 50 m from the Soyuz vehicle but facing in the direction of motion, as the Soyuz yawed  $180^\circ$  to face the Apollo.

For reasons still not understood, no clearly identifiable reflected ultraviolet radiation was detected during this pass. There was a strong 130.4-nm signal that was almost surely resonance

fluorescence, but there were no counts above background in the 135.6-, 149.3-, or 120.0-nm channels. The Apollo crew reported that both the Soyuz window and the retroreflector were illuminated, and two possible explanations for failure were considered. One was that the reflectivity of the retroreflector had been seriously degraded during the flight. The other was that a window reflection was registered by the star tracker as a reflection from the retroreflector. The second explanation is not consistent with the fact that, through the COAS, an illuminated retroreflector was seen centered in the field of view. It was decided, therefore, not to risk using the side-looking retroreflector during the scheduled run at 500 m separation but to request performance of a Soyuz  $90^\circ$  yaw maneuver to enable use of the aft-looking reflector.

The procedure followed during the 500-m data take was very similar to that described at 150 m (fig. 8-9). It occurred during the next eclipse period. Calibration data with the door closed were obtained starting at 100:30 GET (about 35 minutes before the run). The Apollo vehicle

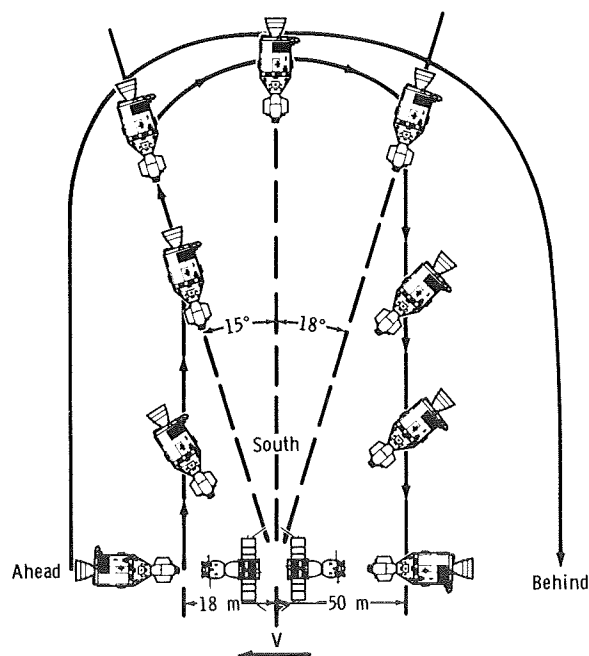


FIGURE 8-8.—Illustration of the 150-m out-of-plane data take (V = velocity vector).

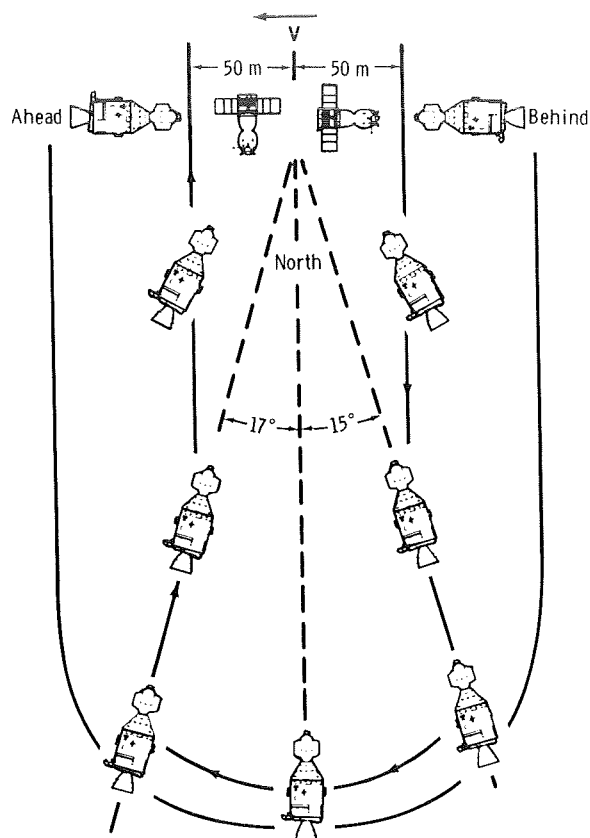


FIGURE 8-9.—Illustration of the 500-m out-of-plane data take.

maneuvered, as shown in the figure, to a position 500 m from the Soyuz vehicle out of the orbital plane and  $15^\circ$  behind. The Apollo vehicle then executed a circular sweep through  $32^\circ$  ( $-15^\circ$  to  $+17^\circ$ ) in a horizontal plane that contained the Soyuz vehicle; the maneuver required 10 minutes. Very early in this maneuver, clear indication was obtained in all UV channels that reflected radiation was being received by the UVA spectrometer. Reflected data were received (as indicated in the 135.6-nm channel) throughout the sweep. Figure 8-10 is an example of the strip-chart records showing a complete spectral scan taken during the sweep for comparison with a spectrum obtained from the UVA door just before the sweep (fig. 8-11). The observed ratio of the counting rates at 130.4 and 135.6 nm was  $5.7 \pm 0.5$  from 101:17:38.13 to 101:17:40.25 GET. (The sweep began at 101:17:37 GET.) The ratio obtained from the door (after correction for the reflectivity of

the door) was 5.72. The ratio of 130.4 to 135.6 nm obtained during the run is shown in figure 8-12. There was an anomaly during the run; the 135.6-nm counting rate dropped by a factor of 5.5 from a plateau of about 250 counts to about 45 counts between 101:17:39.37 and 101:17:41.49 GET. It remained at 45 counts thereafter. A similar effect occurred in the 149.3-nm channel. These anomalies are being analyzed.

During the warmup period for the next eclipse pass, the signals reflected from the door were normal during the first several minutes; this observation indicates that no change in the lamp output, collimating mirror reflectivity, or receiver *QT* was responsible for the drop in signal during the second part of the 500-m pass. However, the calibration signal dropped by a factor of approximately 4 in all channels during the last several minutes of the warmup period and remained low after the door was opened for the 1000-m data take. As shown in figure 8-13, these data were obtained in the orbital plane during separation of the Apollo and Soyuz vehicles. The upward-looking retroreflector was used, and the range varied from 800 to 1300 m during the sweep from  $+15^\circ$  to  $-15^\circ$  with the vertical.

Some reflected signals were detected, although the retroreflector was only in the field of view sporadically. Use of the COAS and the star tracker was very difficult because bright moonlight was illuminating the top of the Soyuz spacecraft. An attempt was made to use the COAS to keep the Apollo vehicle pointed toward the Soyuz beacon and navigation lamps instead of trying to lock on the retroreflector as in the out-of-plane observations.

After the Apollo departed the neighborhood of the Soyuz, two resonance exercises were performed. During an eclipse phase, the Apollo X-axis was oriented normal to the orbital plane and one full orbit (from 105:10 to 106:46 GET) of resonance fluorescence and airglow background data was obtained. This exercise was followed during the next eclipse phase (from 106:55 to 107:10 GET) with an observation of the resonance fluorescence signal obtained with the Apollo X-axis still oriented normal to the orbital plane and with the Apollo vehicle executing a slow roll through  $360^\circ$ . The purpose of this exercise was to

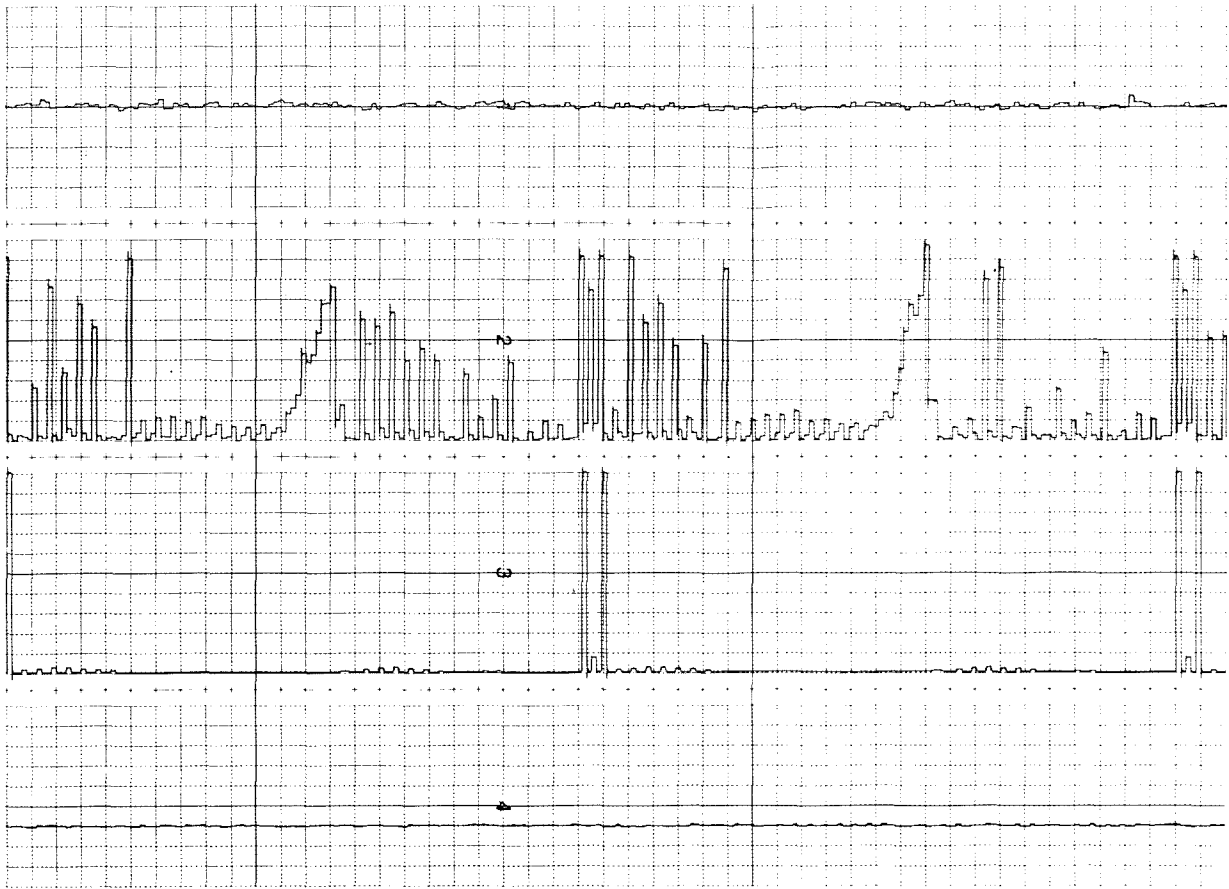


FIGURE 8-10.—Strip-chart record taken during the 500-m data take.

determine the variation in population of thermal O atoms between the ram side of the docking module and the lee side (fig. 8-14). The atoms near the aperture consist of ambient undisturbed atmosphere and atoms that have been scattered from the vehicle. Obviously, the higher density will be on the ram side of the vehicle. Some of the atoms striking the vehicle will have become thermalized, and then reflect. Some will recombine and become  $O_2$  molecules. The recombining fraction should be determinable from the data obtained, because the 130.4-nm fluorescence signal was found to depend strongly on the roll orientation.

The resonance fluorescence counting rate was expected to be approximately  $3.5 \times 10^4$  counts/sec at  $\theta = 0^\circ$  and approximately  $10^4$  counts/sec at  $\theta = 10^\circ$  if the oxygen density was  $10^9 \text{ cm}^{-3}$ . The transmitted signal was expected to

be approximately  $3 \times 10^4$  counts/sec at  $\theta = 0^\circ$  and approximately  $7.5 \times 10^4$  counts/sec at  $\theta = 10^\circ$  for the same density. These were the values predicted when the spacecraft velocity was 7.8 km/sec and the O temperature was 777 K, as they were during the flight. The temperature was determined from the 10.7-cm solar flux and the  $A_p$  index (measurement of magnetic activity at the poles).

If it is assumed that during the 150-m data take all the signal was due to resonance fluorescence, the observed counting rates of only approximately  $5.8 \times 10^3$  counts/sec at  $\theta = 0^\circ$  are approximately a factor of 6 lower than expected. Similarly, if a presumed contribution of  $5.8 \times 10^3$  counts/sec from resonance fluorescence is subtracted from a counting rate of approximately  $7 \times 10^3$  counts/sec at  $\theta = 0^\circ$  during the 500-m data take, the result ( $1.1 \times 10^3$  counts/sec) is too low by a

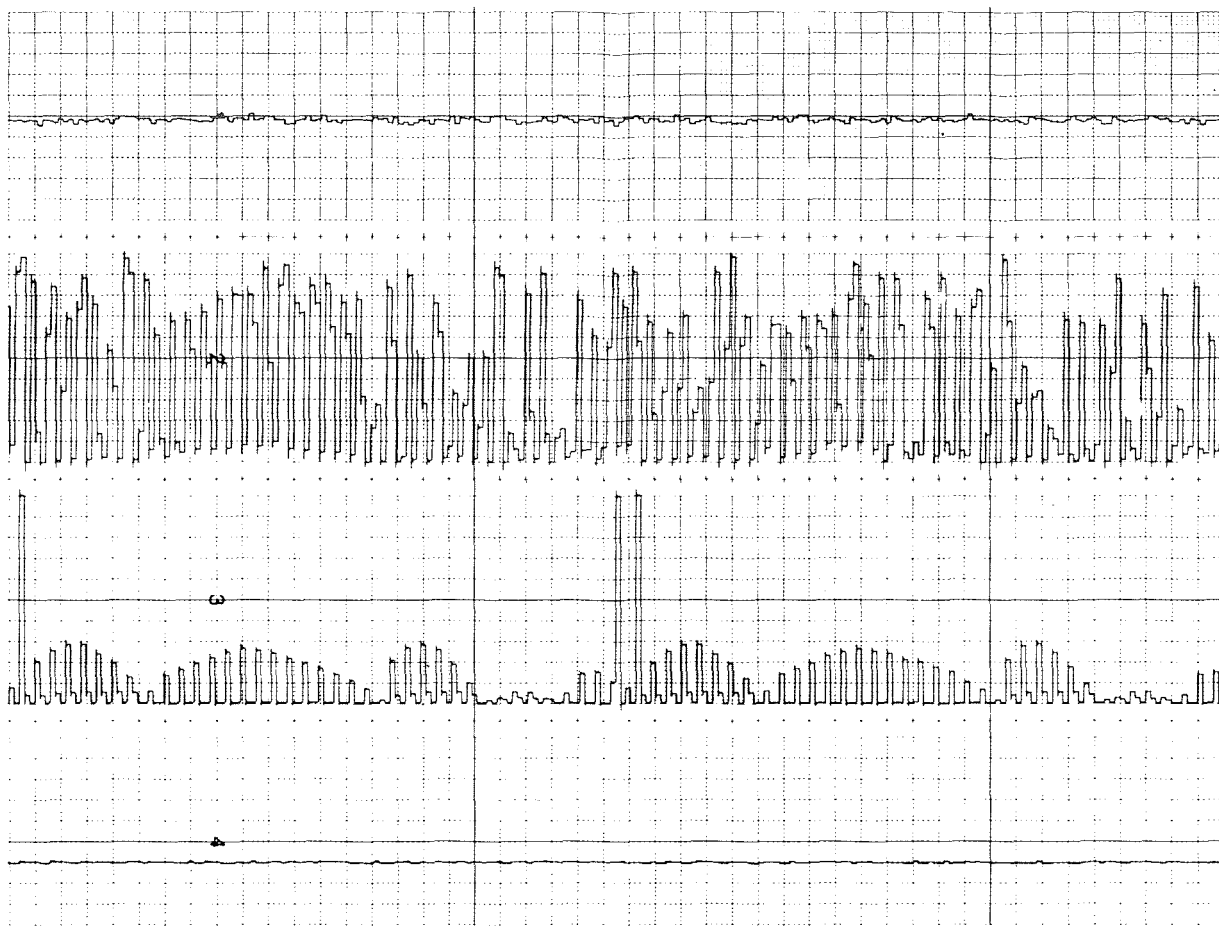


FIGURE 8-11.—Strip-chart record taken just before the 500-m data take.

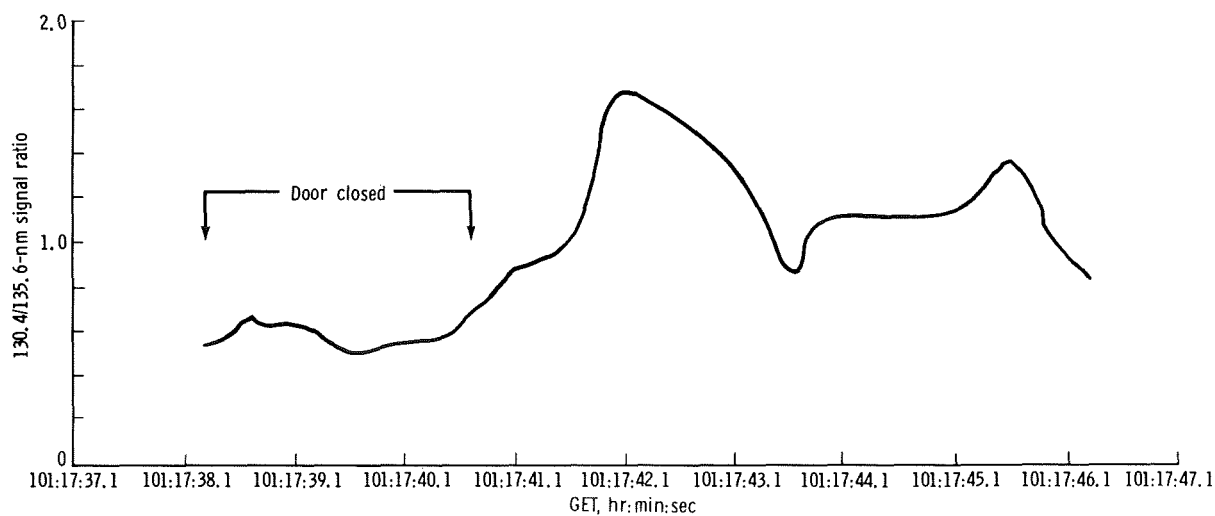


FIGURE 8-12.—Ratio of the 130.4- to 135.6-nm signal during the 500-m data take.



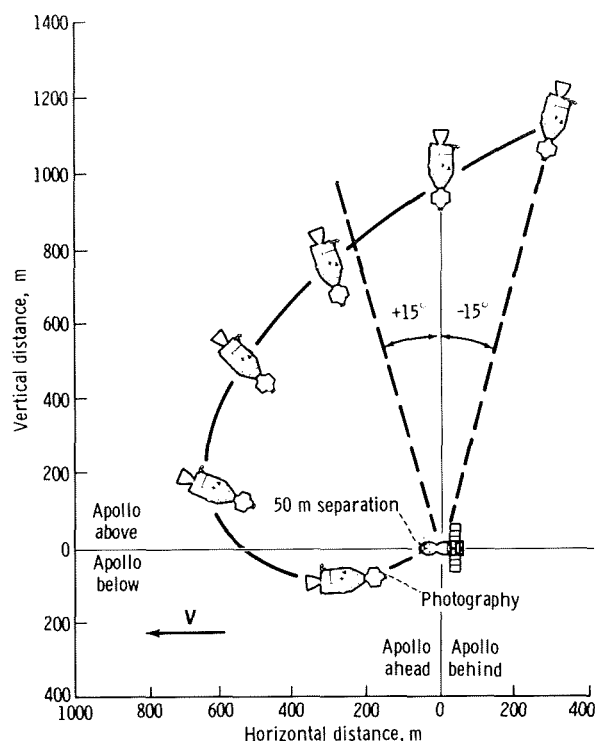


FIGURE 8-13.—Illustration of the 1000-m in-plane data take.

factor of 25. Even if the degradation in the 135.6- and 149.3-nm signals is presumed to indicate a drop in reflectivity of the retroreflector by a factor of 2500/500 (or 5) between the beginning of the data take and the time  $\theta$  reached  $0^\circ$ , the corrected counting rate becomes  $6 \times 10^3$  counts/sec. This value is still approximately a factor of 5 lower than expected. The conclusion is that, for reasons unknown, the radiance in the beam leaving the collimating mirror was lower than expected by a factor of approximately 5. Thus, the data have been analyzed inferring relative values only.

Counting rates as a function of  $\theta$  obtained during the 150- and the 500-m data takes are displayed in figure 8-15. An unexpected lack of symmetry exists about  $\theta = 0^\circ$  in the case of the 130.4-nm signal during the 150-mm data take. Although the variation with  $\theta$  for  $\theta < 0$  resembles that expected for pure resonance fluorescence, the counting rate remains almost independent of  $\theta$  as the latter increases toward high positive values. The data obtained during the  $360^\circ$  roll maneuver executed later in the flight show a very significant

increase in fluorescence caused by atom pileup on the ram side of the spacecraft. As shown in figure 8-8, during the period when  $\theta$  was negative, the field of view of the spectrometer was entirely in the wake, whereas during the period when  $\theta$  was positive, a portion of atmosphere on the ram side of the spacecraft was in the field of view. This is believed to be responsible for the asymmetry.

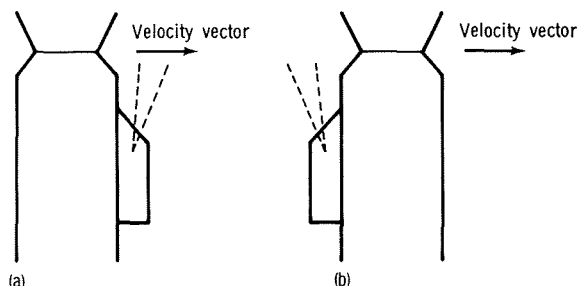


FIGURE 8-14.—Collecting aperture orientation on Apollo docking module. (a) Ram side. (b) Lee side.

The investigators have assumed that, during the 150-m data take, the signal was caused entirely by resonance fluorescence, whereas the 500-m data contain contributions from reflection and fluorescence. To obtain the variation of transmitted signal with  $\theta$ , the fluorescence contribution has been assumed to be the same during the 500-m data take as it was during the 150-m data take for the same values of  $\theta$ . As suggested by the calibration data taken after the 500-m data take, it was also assumed that the decrease in signal during the 500-m pass was caused by deterioration of the corner reflectors. Hence, it can be corrected by use of the 135.6-nm signal. Figure 8-16 is a plot of the resonance absorption signal  $S$  as a function of  $\theta$  where  $S(\theta)$  is calculated as follows:

$$S(\theta) = \left[ R_{130.4}(\theta, 500 \text{ m}) - R_{130.4}(\theta, 150 \text{ m}) \right] \left[ \frac{2500}{R_{135.6}(\theta, 500 \text{ m})} \right] \quad (8-9)$$

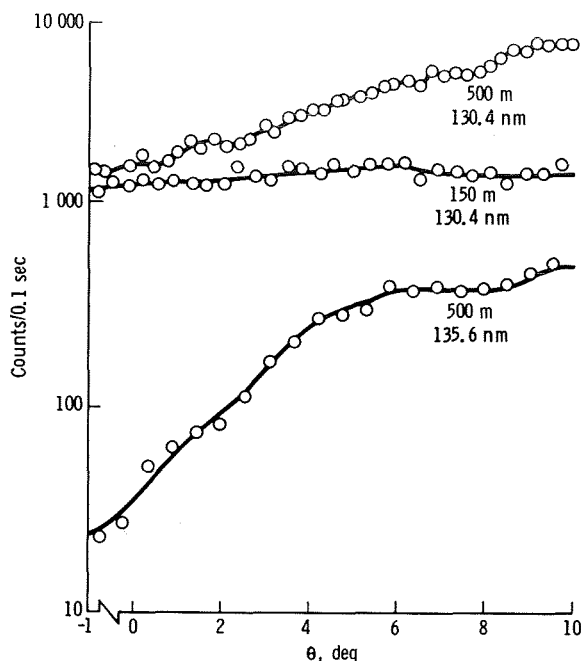


FIGURE 8-15.—Counts/0.1 sec obtained at 130.4 nm during the 150-m data take and at 130.4 nm and 135.6 nm during the 500-m data take.

where  $R$  represents the measured counting rates. Because  $R$  at 135.6 nm remained constant at 2500 counts/sec until  $\theta$  reached  $6^\circ$ , it was assumed that this rate represented the unperturbed 135.6-nm counting rate.

The results have been analyzed in several ways. In figure 8-16, curves showing the theoretical variation in counting rate with  $\theta$  in arbitrary units can be compared with the observed values of  $S(\theta)$ . A least-squares fit of theoretical  $S(\theta)$  curves with the data indicates a value for the oxygen density of

$$[O] = (1.2 \pm 0.5) \times 10^9 \text{ cm}^{-3} \quad (8-10)$$

On the other hand, because the data between  $\theta$  values of  $4^\circ$  and  $8^\circ$  show much less scatter than those obtained at large  $\theta$  (when the lamps were still coming into a steady state) and at small  $\theta$  (when the reflected signal was low), a fit of  $S(\theta)$  to the observed data for  $4^\circ < \theta < 8^\circ$  gives

$$[O] = (1.15 \pm 0.36) \times 10^9 \text{ cm}^{-3} \quad (8-11)$$

Finally, it is appropriate to compare the resonance fluorescence signal  $S_R$  to the transmitted signal  $S_T$  for consistency. The ratio of  $S_R$  at  $\theta = 0^\circ$  and  $S_T$  for any value of  $\theta$  (for instance,  $8^\circ$ ) is a unique function of  $[O]$ . The observed value for  $S_R(0^\circ)/S_T(8^\circ)$  indicates a value for the oxygen density

$$[O] = (1.15 \pm 0.06) \times 10^9 \text{ cm}^{-3} \quad (8-12)$$

In summary, the experiment results predict

$$[O] = (1.15 \pm 0.2) \times 10^9 \text{ cm}^{-3} \quad (8-13)$$

In the case of N, the 149.3-nm reflected line experienced the same degradation with  $\theta$  as the 135.6 [O] line. During the 150-m data take, the resonance fluorescence counting rate at 120 nm was only  $6.1 \pm 1.3$  counts/sec. During the 500-m data take, no significant variation in the transmitted 120.0-nm signal could be seen after a correction was made for the variation in the 149.3-nm counting rate. The value of  $S_T$  was  $400 \pm 68$  counts/sec. For the nitrogen density  $[N]$ , the ratio of  $S_T$  to  $S_R$  of  $66 \pm 18$  gives

$$[N] = \left( 8.6^{+2.7}_{-1.7} \right) \times 10^6 \text{ cm}^{-3} \quad (8-14)$$

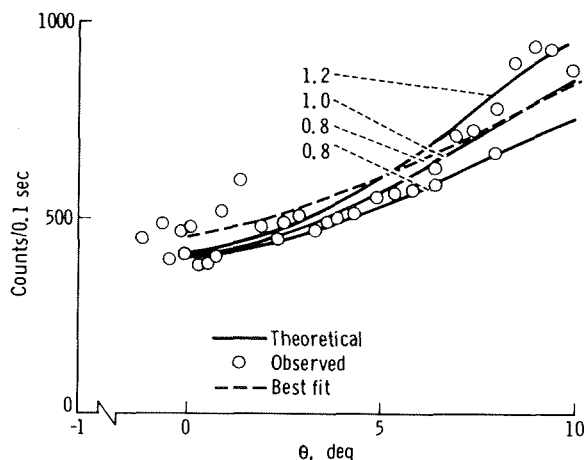


FIGURE 8-16.—Counts/0.1 sec obtained by equation (8-9) compared to theory in units of  $10^9$  oxygen atoms/cm<sup>3</sup>. (Numbers indicate the assumed oxygen densities.)

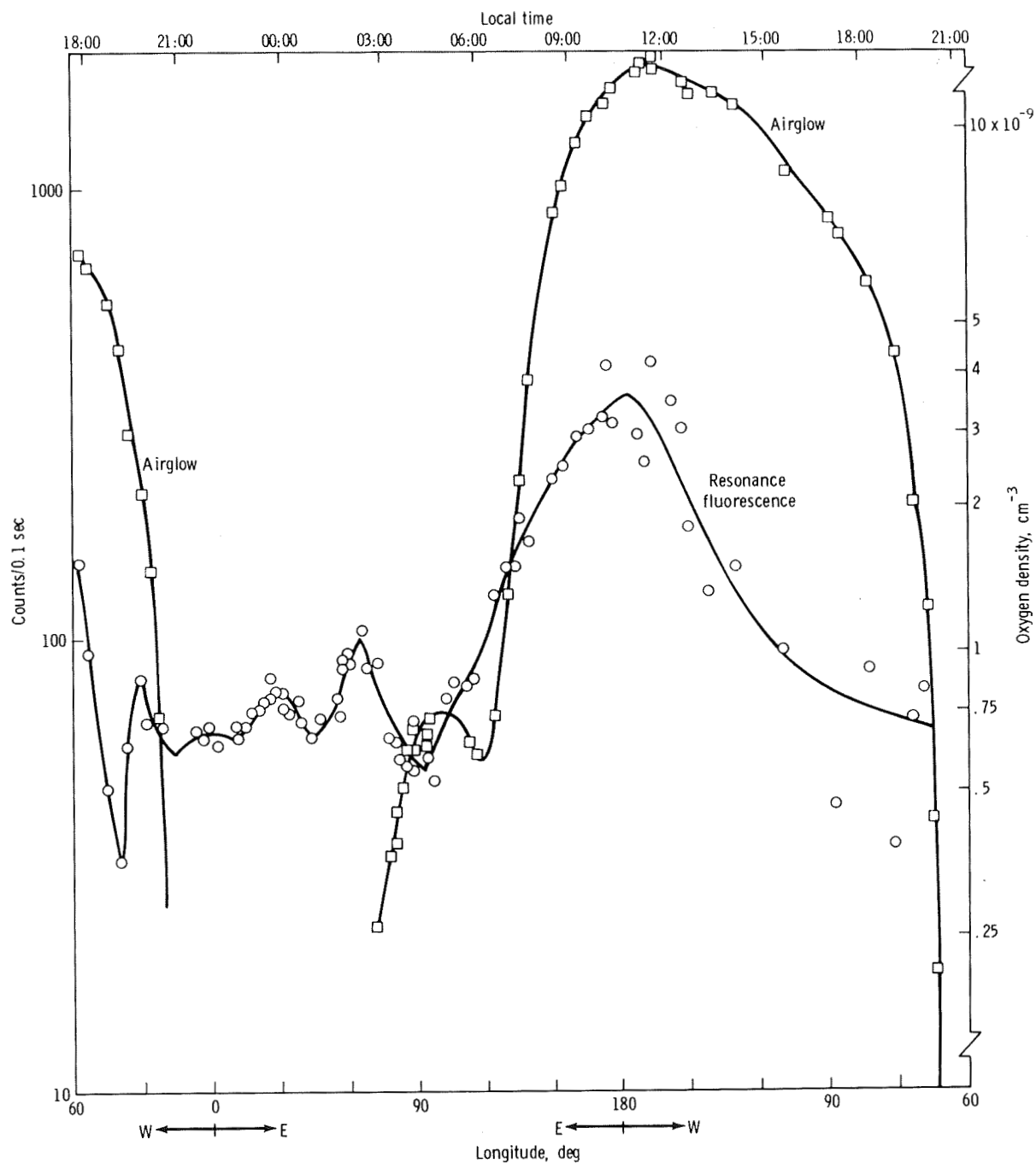


FIGURE 8-17.—The 130.4-nm resonance fluorescence and atomic oxygen density inferred from it during an entire orbit. The 130.4-nm airglow counting rate is also plotted.

The data obtained during the resonance fluorescence/airglow orbit (105:10 to 106:46 GET) are shown in figure 8-17. Correcting for the 6.7-fold decrease in sensitivity that occurred just before the 1000-m data take, the oxygen densities inferred are indicated as well. The oxygen airglow component was obtained from the signal at 130.4 nm when no lamp was illuminated. The apparent increase in ambient oxygen density during the day is inconsistent with what is known about the atmosphere at 225 km. This inconsistency is attributed to atoms that somehow had outgassed from the Apollo vehicle when it was in sunlight. It is significant that the maximum apparent density occurred when the Sun was at local noon.

Twice during this orbit (22:30 local time and latitude 10° N, 10:30 local time and latitude 10° S), the Apollo passed under Atmosphere Explorer (AE), which was at a 340-km altitude. Extrapolating the AE oxygen density to 234 km (which was the altitude of Apollo at 22:30 local time) by means of the Orbiting Geophysical Observatory 6 model would give  $1.0 \times 10^9 \text{ cm}^{-3}$  for the density. The Apollo resonance fluorescence value was  $0.92 \times 10^9 \text{ cm}^{-3}$ . At latitude 10° S, 10:30 local time, the AE extrapolation called for  $1.32 \times 10^9 \text{ cm}^{-3}$  and the fluorescence value was  $4.8 \times 10^9 \text{ cm}^{-3}$ . During the 500-m data take, AE was at latitude 35° S and the local time was 08:00. The oxygen density extrapolated to Apollo altitude was  $1.5 \times 10^9 \text{ cm}^{-3}$ . The agreement between the AE measurements and those of this experiment is considered to be quite satisfactory.

The results of the 360° roll maneuver were that the apparent oxygen density varied from approximately  $0.46 \times 10^9 \text{ cm}^{-3}$  in the wake to  $4.3 \times 10^9 \text{ cm}^{-3}$  in the ram direction, which showed the extreme enhancement of density caused by the reflection of atmospheric gas from the spacecraft.

## REFERENCES

- 8-1. Philbrick, C. R.; and McIsaac, J. P.: Measurements of Atmospheric Composition Near 400 KM. Space Research XII, vol. 1, Academie-Verlag (Berlin), 1972, pp. 743-749.
- 8-2. Ghosh, S. N.; Hinton, B. B.; et al.: Atomic Nitrogen in the Upper Atmosphere Measured by Mass Spectrometers. J. Geophys. Res., vol. 73, no. 13, July 1968, pp. 4425-4426.
- 8-3. Hickman, David R.; and Nier, Alfred O.: Measurement of the Neutral Composition of the Lower Thermosphere Above Fort Churchill by Rocket-Borne Mass Spectrometer. J. Geophys. Res., vol. 77, no. 16, June 1972, pp. 2880-2887.
- 8-4. Fastie, William G.; Feldman, Paul D.; et al.: A Search for Far-Ultraviolet Emissions From the Lunar Atmosphere. Science, vol. 182, no. 4113, Nov. 1973, pp. 710-711.
- 8-5. Lin, Chornng-Lieh; Parkes, David A.; and Kaufman, Frederick: Oscillator Strength of the Resonance Transitions of Ground-State N and O. J. Chem. Phys., vol. 53, no. 10, Nov. 1970, pp. 3896-3900.

# 9. Stratospheric Aerosol Measurements

## Experiment MA-007

*T. J. Pepin,<sup>a†</sup> M. P. McCormick,<sup>b</sup> W. P. Chu,<sup>c</sup> F. Simon,<sup>a</sup> T. J. Swissler,<sup>d</sup> R. R. Adams,<sup>b</sup>  
K. H. Crumbly,<sup>b</sup> and W. H. Fuller, Jr.<sup>b</sup>*

### ABSTRACT

The Apollo-Soyuz Test Project Stratospheric Aerosol Measurements Experiment was flown to demonstrate that direct solar occultation measurements by photometers and from photographs can be used for defining stratospheric aerosol concentrations. Supporting ground-truth data provided by laser radar and balloonborne dustsonde are used with the remote-sensing data to investigate the uniqueness of aerosol optical models. The results show a 1.5 times higher peak aerosol concentration in the Northern Hemisphere than in the Southern Hemisphere.

### INTRODUCTION

This experiment was designed to demonstrate the feasibility of remotely sensing aerosols in the stratosphere from a low-orbiting manned spacecraft. Increasing interest in the stratosphere has led to the investigation of methods for remote sensing from Earth-orbiting satellites. Information gained from the Stratospheric Aerosol

Measurements (SAM) Experiment performed during the Apollo-Soyuz Test Project (ASTP) mission will be used in the design of remote-sensing equipment for future satellite missions.

The instrument used for making these stratospheric aerosol measurements consisted of a photometer and associated electronics that provided a signal to the command module (CM) telemetry system. A Hasselblad data camera (HDC) equipped with special infrared (IR) film and filter was used to photograph the sunset and sunrise events. The experiment technique involved directly measuring solar intensity (photometer) and Sun shape (photographs) in the spectral region centered at approximately 0.84  $\mu\text{m}$ . Immediately before satellite night, as the spacecraft approached the shadow of the Earth, the line of sight to the Sun passed first through the upper layers of the atmosphere and then steadily down into the lower layers of the troposphere. During the 1.5 minutes (approximately) required for the instrument line of sight to pass through the lower 150 km of the atmosphere, the solar intensity was recorded by the photometer, and solar disk shape changes were recorded in photographs. The same set of measurements was made at satellite dawn as the spacecraft emerged from the shadow of the Earth.

The total extinction coefficient was obtained from the variation of the solar intensity as a function of total air mass distributed along the line of sight. At the effective wavelength of the photometer and the photographic system, the extinction

---

<sup>a</sup>University of Wyoming.

<sup>b</sup>NASA Langley Research Center.

<sup>c</sup>Old Dominion University.

<sup>d</sup>Systems and Applied Sciences Corporation.

<sup>†</sup>Principal Investigator.

was principally produced by the atmospheric aerosols; the measurements are being used to determine the aerosol concentration.

To verify the performance of the SAM Experiment, ground-truth data were acquired by dustsonde (a balloonborne aerosol optical counter) and a lidar system (ground-based laser radar). The dustsonde was flown from the Richards-Gebaur Air Force Base (lat. 38.8° N, long. 94.7° W) near Kansas City, Missouri, at the same time and place of the ASTP second sunset SAM. The lidar measurements were also made from Richards-Gebaur Air Force Base on Earth nights bracketing and during the second sunset SAM.

### THE SAM INSTRUMENT

The photometer (fig. 9-1) used for the SAM Experiment utilizes a pin diode detector having a 10° field of view (FOV), which was used to look at the Sun through the CM window at a wavelength centered at approximately 0.84  $\mu\text{m}$ . The detector was used in the photovoltaic mode to detect the solar signal, and samples were taken at a rate of 10 samples/sec using a 12-bit analog-to-digital converter. The signal output of the converter was recorded and transmitted by the CM data system.

The photometer was equipped with a projection sight system consisting of a post whose shadow was projected onto a grid that could be observed by the astronaut to ensure that the photometer system was properly aligned with respect to the Sun. The instrument also included a green light to verify that the power was properly connected and included a switch that the astronaut could activate to send a known signal over the telemetry system to verify proper installation of the photometer in the CM.

### CAMERA SYSTEM

The photographic portion of the experiment consisted of a series of timed IR photographs of spacecraft sunrises and sunsets taken through the CM window with an HDC. The 250-mm-focal-length (12.5° by 12.5° FOV), f/5.6 lens was fitted with a quality glass IR filter capable of obtaining

at least three orders of magnitude blocking in the visible and the ultraviolet. Kodak multispectral IR aerial film (ESTAR-AH base) SO-289 was used in two 70-mm Hasselblad magazines. Each magazine contained film for 50 frames with an additional 1 m reserved for sensitometric calibration exposures. The HDC had a self-contained battery power supply for shutter activation and film advance. An onboard intervalometer provided a contact closure to the HDC every 2.5 seconds during the experiment to trigger the camera automatically. Timing with SAM data was to be provided by an audio channel of the spacecraft tape recorder.

### BALLOONBORNE "DUSTSONDE"

Figure 9-2 is a schematic drawing of the University of Wyoming balloonborne dustsonde used in this program for the ground-truth *in situ* aerosol measurement that was made from the Richards-Gebaur Air Force Base. The mode of operation of the dustsonde is described in the following discussion.

Air sampled on balloon ascent and parachute descent is pumped at approximately 0.75 liter/min in a well-defined stream through the focal point of the condenser lens in the 2.5-liter scattering chamber where individual particles scatter light into the microscopes. The light pulses that can be observed with the microscopes are detected and amplified by the photomultipliers. By pulse-height discrimination and careful laboratory calibration with aerosols of known size and index of refraction, the integral concentration of aerosol particles larger than 0.3 and 0.5  $\mu\text{m}$  in diameter can be determined.

Two photomultipliers were used to enhance the signal-to-noise ratio by requiring coincident events from the two detectors. The background noise for the system was mainly due to Rayleigh scattering from the air molecules in the chamber at low altitude and from cosmic-ray scintillation in the photomultiplier glass at high altitudes. The background was measured approximately every 15 minutes during the flight by passing filtered air through the chamber. For the system used in the Kansas City flight, the background was negligible

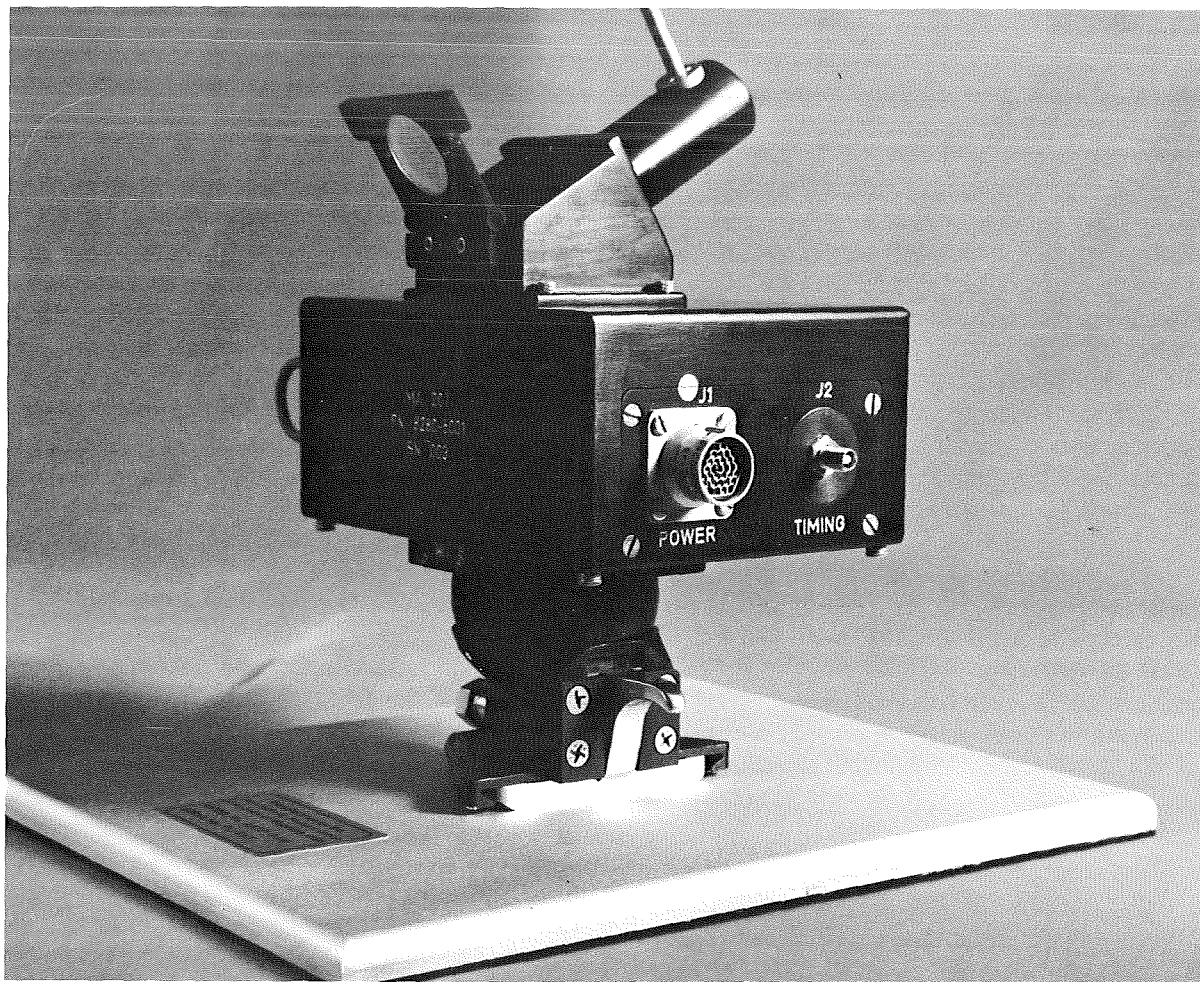


FIGURE 9-1.—The photometer used for making stratospheric aerosol measurements.

above a 10-km altitude. Corrections for the background have been used below this altitude. The dustsonde was also equipped with a rawinsonde temperature element for recording the atmospheric temperature profile (ref. 9-1).

### LIDAR

Ground-based lidar measurements were used as part of the ground truth for the experiment. Generally, laser radars operate in the following manner. A Q-switched laser emits a pulse of nearly monochromatic light approximately 30

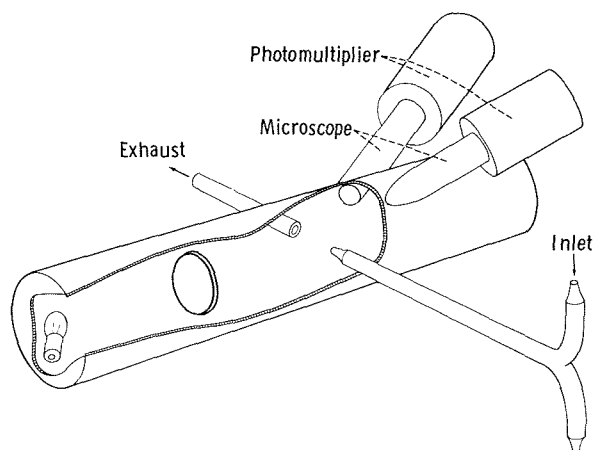


FIGURE 9-2.—Schematic drawing of the University of Wyoming dustsonde used for ground-truth measurements.

nanoseconds in duration. Molecules and suspended particulate matter (aerosols) scatter and/or absorb this radiation as the pulse propagates through the atmosphere. A small portion of this light is scattered directly back toward the laser. A receiver composed of mirrors and/or lenses collects this backscattered radiation and diverts it onto a photodetector, the output of which is measured as a function of elapsed time after laser emission, or range. The backscattered energy incident on the photodetector is examined spectrally at or near the laser output wavelength with color filters, interference filters, or spectrometers. This enhances the signal-to-noise ratio by reducing unwanted background radiation and determines whether elastic or inelastic techniques will be used.

The lidar measurements for the SAM experiment were provided by the NASA Langley Research Center (LaRC) 122-cm (48 in.) laser radar system (fig. 9-3), which consists of two temperature-controlled lasers (ruby and neodymium-doped glass) mounted on either side of an f/10 Cassegrainian-configured telescope

composed of a 122-cm (48 in.) diameter, f/2, all-metal primary and a 25.4-cm (10 in.) diameter secondary. The output from the detector package is recorded by a high-speed data acquisition system. Analog signals are amplified and bandwidth limited, digitized at a 5- or 10-MHz rate with 8-bit accuracy, and recorded on magnetic tape. A 16-bit-word storage computer is used to control the data acquisition system and to process the data. An X-band microwave radar, coincident with the laser system axis, is used to ensure safe operation in the atmosphere. A rotating shutter reduces laser fluorescence after Q switching. The entire system is mobile and can scan in elevation and azimuth at a slow rate of 1°/sec (ref. 9-2).

## METHOD OF INVERSION

The SAM inversion scheme employed for the inversion of the SAM results presented in this paper is based on an onion-skin model of the atmosphere. For this model, the atmosphere is divided into a number of homogeneous, spherical layers that are considered to have uniform aerosol concentrations. Figure 9-4(a) shows a cross section of the measurement geometry and illustrates the path lengths of solar rays at different atmospheric layers. Fig. 9-4(b) shows the inversion geometry and illustrates the solar intensity contribution transmitted through the different layers as seen from the ASTP instrument during a sunset event.

As the bottom limb of the Sun becomes tangent to each of the layers of the onion-skin atmospheric model, the intensity can be computed from limb darkening and refraction by summing the intensities over the layers above. For example, following the notation for the layers identified in figures 9-4(a) and 9-4(b), one finds that when the lower limb is tangent to the first and second layers, the observed intensities are given by

$$\left. \begin{aligned} I_1 &= I_{10}^{\odot} + I_{11} \\ I_2 &= I_{20}^{\odot} + I_{21} + I_{22} \end{aligned} \right\} \quad (9-1)$$

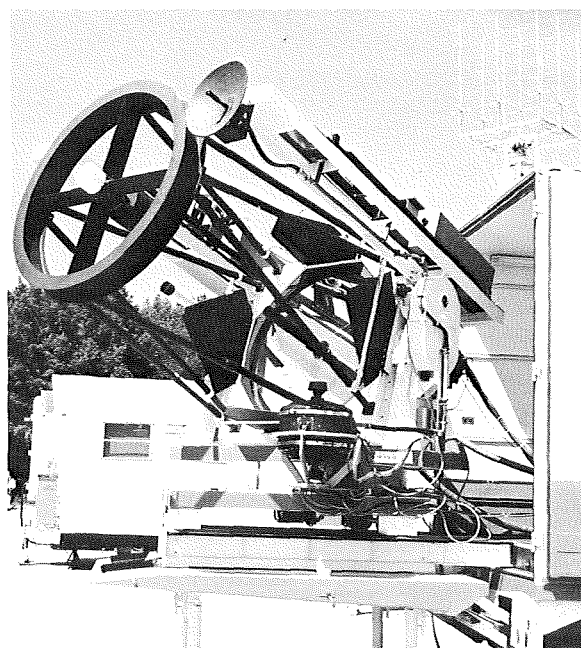


FIGURE 9-3.—The NASA Langley Research Center 122-cm (48 in.) lidar system.



where, in general,  $I_1$  and  $I_2$  are the observed intensities and  $I_{10}^\odot$  and  $I_{20}^\odot$  are the intensities above the upper layer of the inversion model (above the point at which extinction is observed). The intensities  $I_{11}$ ,  $I_{21}$ , and  $I_{22}$  are the transmitted intensities to be determined by inversion. Using the Lambert-Beer law, equation (9-1) can be written in the form

$$\left. \begin{aligned} I_1 &= I_{10}^\odot + I_{11}^\odot \exp(-\beta_1 P_{11}) \\ I_2 &= I_{20}^\odot + I_{21}^\odot \exp(-\beta_1 P_{21}) + I_{22}^\odot \exp(-\beta_1 P_{21} - \beta_2 P_{22}) \end{aligned} \right\} \quad (9-2)$$

where  $I_{ni}^\odot$  is the portion of the unattenuated solar intensity through the  $i$ -th layer that contributes to the observed intensity  $I_n$ ;  $P_{ij}$  is the path length in the  $j$ -th layer for the solar ray tangent to the  $i$ -th layer; and  $\beta_i$  is the total extinction at the wavelength of the SAM system in the  $i$ -th layer. Equation (9-2) yields

$$\left. \begin{aligned} \beta_1 &= \frac{-1}{P_{11}} \ln \left( \frac{I_1 - I_{10}^\odot}{I_{11}^\odot} \right) \\ \beta_2 &= \frac{-1}{P_{22}} \ln \left( \frac{I_2 - I_{20}^\odot - I_{21}^\odot \exp(-\beta_1 P_{21})}{I_{22}^\odot} \right) - \beta_1 \frac{P_{21}}{P_{22}} \end{aligned} \right\} \quad (9-3)$$

This process can be continued as the sunset event occurs, thus allowing the determination of the vertical profile of the total extinction. The aerosol extinction profile can then be obtained by subtracting the molecular extinction contribution.

## RESULTS

### Photometry

The SAM Experiment was designed to observe four events on July 22, 1975. During Apollo revolution 95, measurements were made of a sunset observation (00:07:04 UT) off the coast of New Jersey (lat. 39°10' N, long. 72°45' W)<sup>1</sup> and of

<sup>1</sup>These are the geometric coordinates of the tangent point of the 0-km-altitude grazing ray of the Sun.

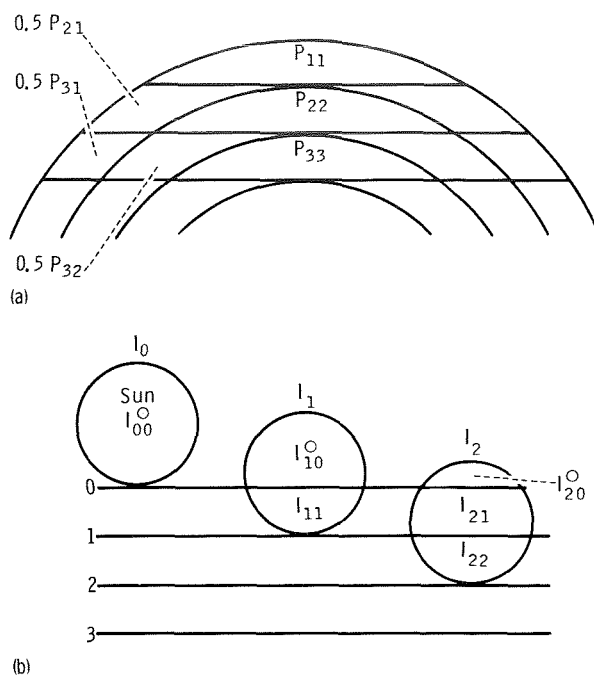


FIGURE 9-4.—Diagram of atmospheric model and inversion geometry. (a) Cross section of the onionskin atmospheric model showing the ray path lengths, where  $P_{ij}$  is the path length in the  $j$ -th layer for the solar ray tangent to the  $i$ -th layer. (b) Inversion geometry showing the contributions to the total transmitted Sun intensity, where  $I_n$  is the observed intensity for the  $n$ -th layer,  $I_{11}$ ,  $I_{21}$ , and  $I_{22}$  are the transmitted intensities to be determined by inversion, and  $I_{ni}^\odot$  is the portion of the unattenuated solar intensity that contributes to  $I_n$ .

a sunrise observation (00:45:52 UT) over the Indian Ocean off the coast of Australia (lat. 43° S, long. 99°55' E). During Apollo revolution 96, a sunset observation (01:37:52 UT) was taken near Kansas City, Missouri (lat. 38°57' N, long. 95°06' W), followed by a sunrise observation (02:14:39 UT) over the Indian Ocean (lat. 42°55' S, long. 77°39' E). The SAM photometer was used to obtain radiometric measurements during each of these four events, and the measured photometric intensities have been inverted using the inversion procedure outlined previously to obtain total extinction as a function of altitude. Figures 9-5(a) and 9-5(b) illustrate the inverted results for the sunset events and sunrise events, respectively. The sunrise events took place in the Southern Hemisphere; the sunset events, in the Northern Hemisphere. The total extinction is greater at the

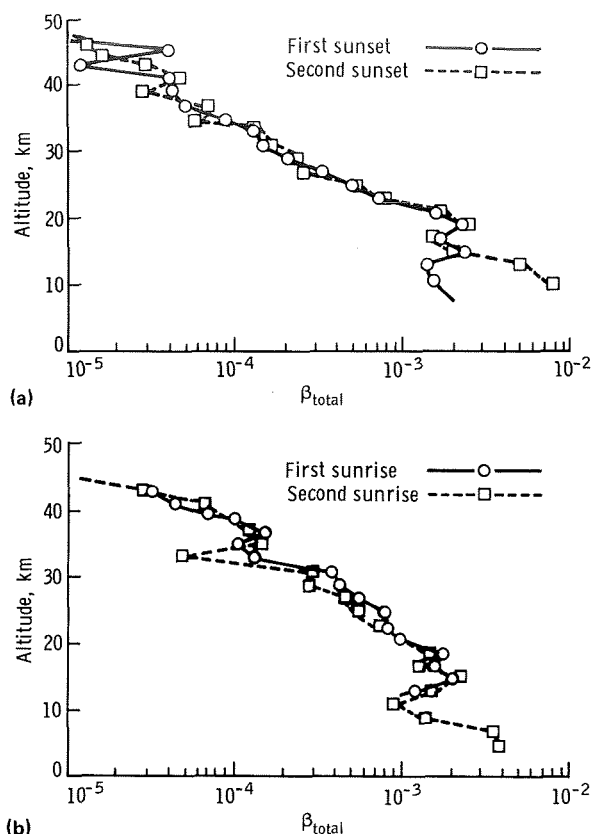


FIGURE 9-5.—Inverted total extinction ( $\beta_{total}$ ) profiles for the four events observed. (a) First and second sunset events, Northern Hemisphere. (b) First and second sunrise events, Southern Hemisphere.

peak of the stratospheric aerosol layer in the Northern Hemisphere than was observed for the Southern Hemisphere by a factor of 1.5. This difference is interpreted as being due to the difference in aerosol content at the time of the ASTP flight. The difference in aerosol content is believed to be due to the injection of material from the Volcan de Fuego in Guatemala (lat.  $14.5^\circ$  N, long.  $90.9^\circ$  W), which erupted in October 1974 (ref. 9-3). The general meridional circulation of injected mass into the atmosphere would normally be northward during the fall and winter seasons in the Northern Hemisphere. This movement reverses in the summer, accounting for the buildup of aerosols in the Southern Hemisphere. This cross-hemispheric transport was beginning at the time of the ASTP mission. Dustsonde obser-

vations by Laby<sup>2</sup> near Melbourne, Australia, were made in April and August of 1975. The April flight showed low aerosol concentration, whereas the August flight showed a factor of 3.5 enhancement in the peak of the stratospheric aerosol concentration. These results are consistent with the three-dimensional circulation model of Cunnold et al. (ref. 9-4).

### Photography

Photographs were made of the first sunrise and the second sunset with the HDC. Figure 9-6 is a composite of frames AST-28-2400 to AST-28-2406 taken during the first sunrise. These photographs have been printed with high contrast to show the observed refracted images of the solar disk and have been superimposed on a grid showing the horizon and tangent altitudes. Figure 9-7 shows frame AST-28-2402, an "isodensity tracing" of this frame, and an outline of the theoretical computed shape of the Sun as expected for the orbital and atmospheric conditions present. The distribution of the observed isophotes is due to limb darkening, extinction by atmospheric constituents, and the effects of refraction. These photographs confirm, at spacecraft altitude, that effects due to refraction must be considered in the design of solar occultation experiments. The photographs taken during the SAM events are currently being analyzed to substantiate theoretical models that are under development for use in future occultation experiments.

### Ground-Truth Data

Data from the dustsonde balloon flight launched on July 21, 1975, at 23:58 UT are shown in figures 9-8 to 9-10. Figure 9-8 contains the measured temperature profile, figure 9-9 illustrates the measured aerosol concentration as a function of altitude for particles larger than  $0.3 \mu\text{m}$  in diameter, and figure 9-10 shows the aerosol

<sup>2</sup>Private communication, 1975.

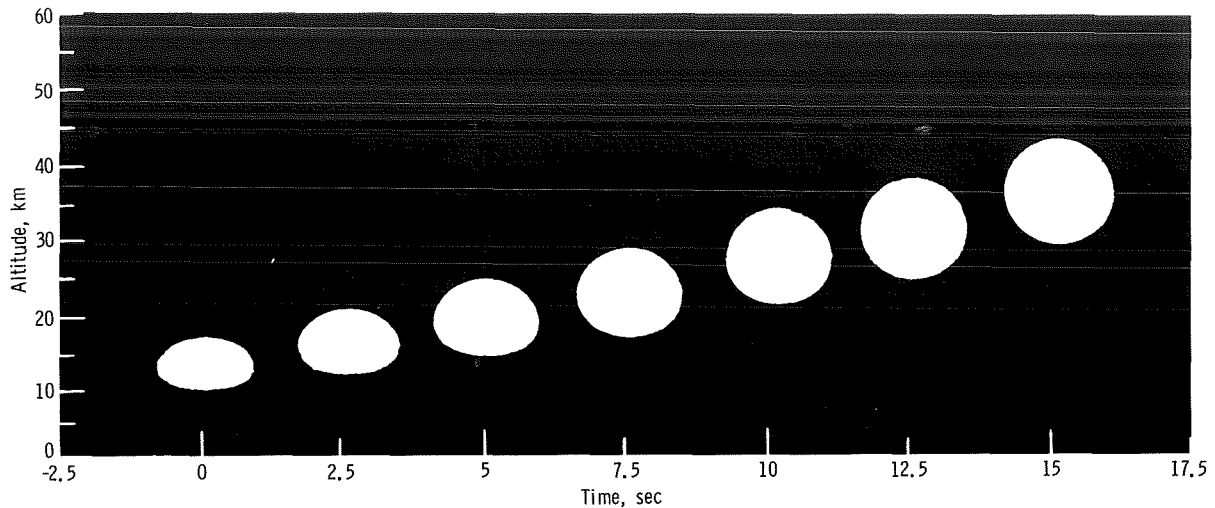


FIGURE 9-6.—Composite of photographs taken during first sunrise event (AST-28-2400 to 2406).

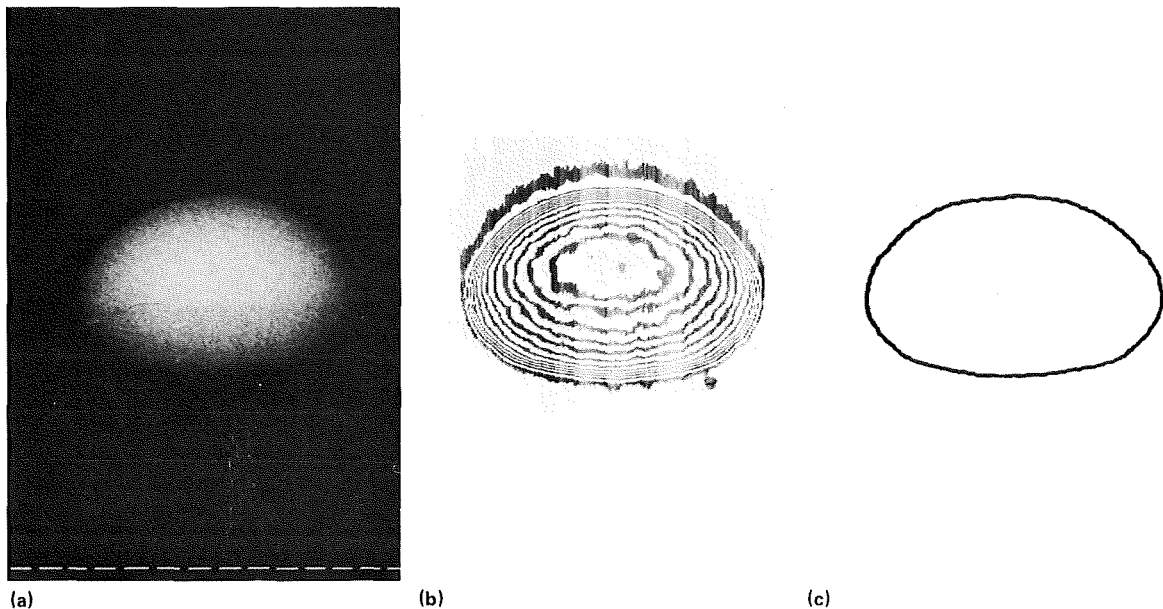


FIGURE 9-7.—Sun-shape comparisons. (a) High-contrast Sun photograph (AST-28-2402). (b) Isodensity tracing. (c) Expected refracted Sun shape.

count ratio (ratio of particles greater than  $0.3 \mu\text{m}$  in diameter to particles greater than  $0.5 \mu\text{m}$  in diameter) as a function of altitude.

The LaRC lidar system was used during the nights of July 22 and July 23 to obtain laser backscatter measurements of the stratospheric aero-

sols. Figure 9-11 shows the backscatter ratios obtained during the measurements made on July 23 at 07:30 UT, and figure 9-12 shows the measured backscatter ratios obtained on July 22 at 04:51 UT. (Backscatter ratio is the ratio of total observed backscatter to molecular backscatter.)

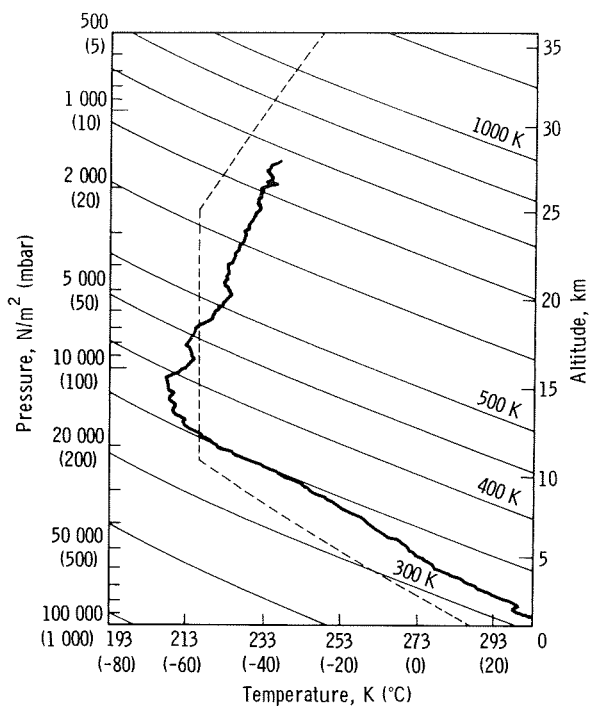


FIGURE 9-8.—Measured temperature profile above Kansas City, Missouri.

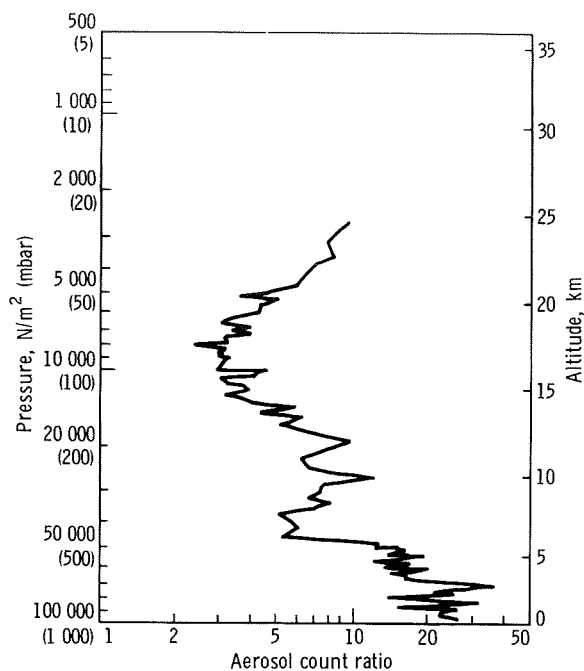


FIGURE 9-10.—Ratio of measured aerosol count for particles  $>0.3 \mu\text{m}$  diameter to particles  $>0.5 \mu\text{m}$  diameter above Kansas City, Missouri.

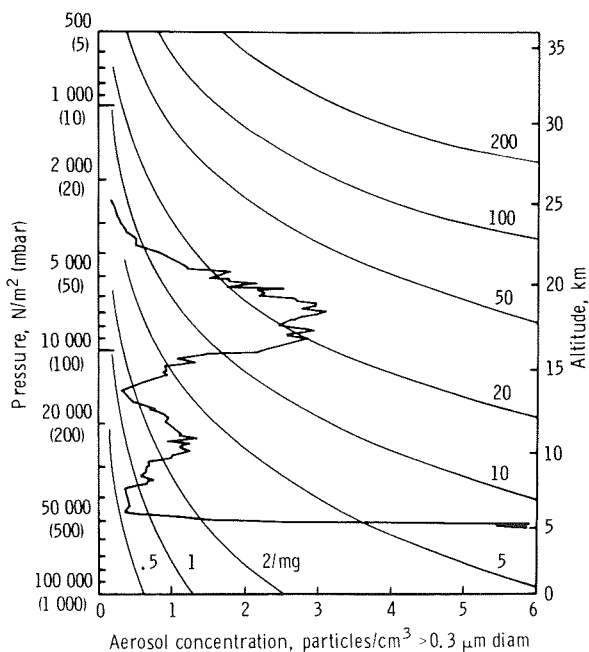


FIGURE 9-9.—Measured dustsonde aerosol concentration ( $>0.3 \mu\text{m}$  diameter) above Kansas City, Missouri. Curved lines indicate mixing ratio.

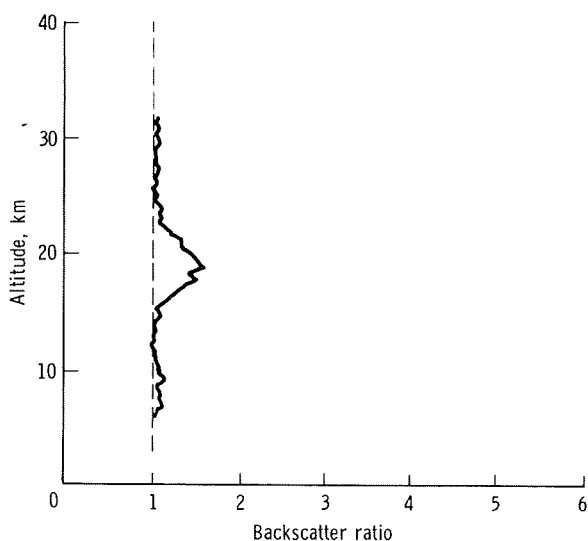


FIGURE 9-11.—Profile of lidar aerosol backscatter ratio taken at Kansas City, Missouri, on July 23, 1975, at 07:30 UT (normalized at 28.53 km).

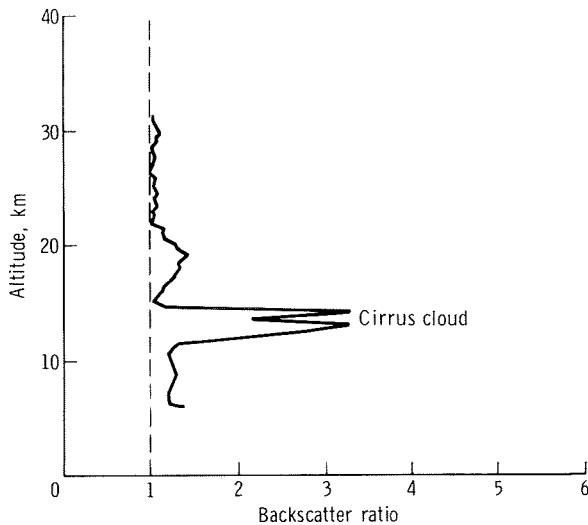


FIGURE 9-12.—Profile of lidar aerosol backscatter ratio taken at Kansas City, Missouri, on July 22, 1975, at 04:51 UT.

### COMPARISON OF RESULTS

The balloon dustsonde measurements of number density of particles greater than  $0.3 \mu\text{m}$  diameter and the aerosol count ratio have been used as a function of altitude to fit various size distributions. These size distributions have been used to predict the SAM photometer measurements of the aerosol extinction observed during the second sunset event and the lidar observations of the backscatter ratio. Figure 9-13 is a comparison plot of the SAM results and the Mie-scattering computations performed using the log-normal aerosol size distribution developed by Pinnick et al. (ref. 9-5). This distribution was adjusted as a function of altitude so that the total number and mode radius fit the dustsonde observations. For these calculations, the index of refraction for the stratospheric aerosol was taken to be  $1.43 - 0i$ ,  $1.50 - 0i$ , and  $1.60 - 0i$  (where  $i = \sqrt{-1}$ ). The complex part of the index of refraction was found to have little effect on the extinction calculations.

Figures 9-14 and 9-15 show the comparisons between the lidar backscatter ratios observed on the nights of July 22 and July 23, respectively, and the computed backscatter ratios for index of refraction  $1.43 - 0i$ ,  $1.50 - 0i$ , and  $1.60 - 0i$ . These backscatter ratios were computed using the same

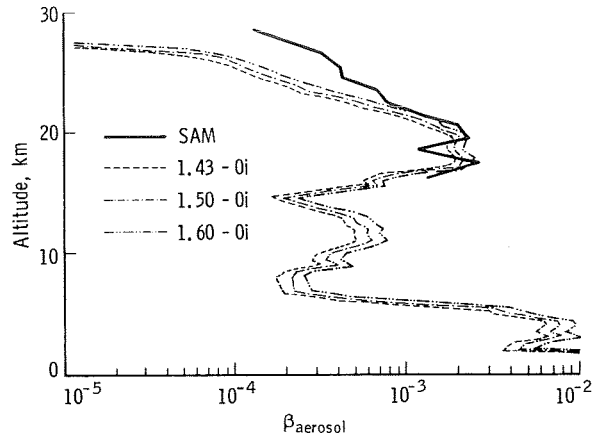


FIGURE 9-13.—Comparison of SAM results on July 22, 1975 (second sunset event), and Mie computations of dustsonde results on July 22, 1975, for different optical properties of the aerosols ( $\beta_{\text{aerosol}} = \text{aerosol extinction}$ ).

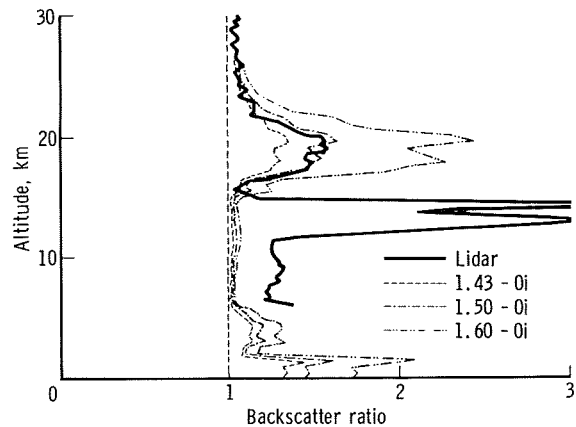


FIGURE 9-14.—Comparison of lidar results of July 22, 1975, and Mie computations of dustsonde results on July 22, 1975, for different optical properties of the aerosols.

size distribution fits to the dustsonde observations that were used for the previously mentioned SAM extinction dustsonde comparisons. The large enhancement at approximately 13 km in the July 22 lidar data is due to cirrus clouds.

Results of the three different techniques agree in the placement of the peak altitude of aerosol concentration, and they are consistent with a single size distribution and particle index. The

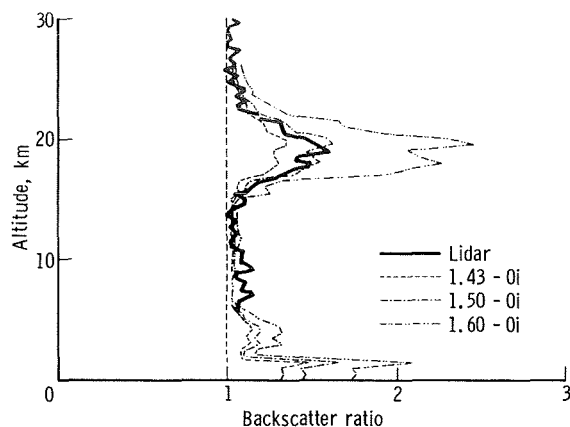


FIGURE 9-15.—Comparison of lidar results of July 23, 1975, and the Mie computations of dustsonde results on July 22, 1975, for different optical properties of the aerosols.

authors would like to point out that the log-normal distribution used to fit these observations is not necessarily unique. Other distributions might fit as well. For example, if the total number density of stratospheric aerosols is assumed to be  $10 \text{ particles/cm}^3$ , then results of the three different techniques are found to agree with a log-normal distribution for an aerosol index of refraction of 1.43, which is consistent with a sulfuric acid aerosol composed of 75 percent sulfuric acid and 25 percent water.

### CONCLUSIONS

The SAM Experiment was performed by the ASTP crewmen as planned. The experiment demonstrated that solar occultation is a viable remote-sensing technique for measuring the vertical extinction of stratospheric aerosols. The solar photo-

graphs corroborated the refraction model needed for future solar occultation experiments. The inversion process that was used to reduce the SAM data was confirmed by the agreement with the ground-truth lidar and dustsonde measurements, and these data show that the solar occultation, lidar, and dustsonde data agree in altitude distribution and in yielding a consistent stratospheric aerosol size distribution model. In addition, the inversions from the SAM Experiment show a significant difference between the Northern and Southern Hemispheres with peak aerosol concentration at least 1.5 times greater in the Northern Hemisphere than in the Southern Hemisphere during the time of the ASTP flight.

### REFERENCES

- 9-1. Rosen, James: Simultaneous Dust and Ozone Soundings Over North and Central America. *J. Geophys. Res.*, vol. 73, no. 2, Jan. 15, 1968, pp. 479-486.
- 9-2. McCormick, M. P.; and Fuller, W. H., Jr.: Lidar Applications to Pollution Studies. Paper presented at Joint Conference on Sensing of Environmental Pollutants (Palo Alto, Calif.), Nov. 8-10, 1971. (AIAA Paper 71-1056.)
- 9-3. McCormick, M. P.; and Fuller, W. H., Jr.: Lidar Measurements of Two Intense Stratospheric Dust Layers. *Appl. Opt.*, vol. 14, no. 1, Jan. 1975, pp. 4-5.
- 9-4. Cunnold, D.; Alyea, F.; Phillips, N.; and Prinn, R.: A Three-Dimensional Dynamical-Chemical Model of Atmospheric Ozone, *J. Atmos. Sci.*, vol. 32, no. 1, Jan. 1975, pp. 170-194.
- 9-5. Pinnick, R. G.; Rosen, J. M.; and Hofmann, D. J.: Stratospheric Aerosol Measurements III: Optical Model Calculations. *J. Atmos. Sci.*, vol. 33, no. 2, Feb. 1976, pp. 304-314.

# 10. Doppler Tracking

## Experiment MA-089

*G. C. Weiffenbach,<sup>a†</sup> M. D. Grossi,<sup>a</sup> and P. W. Shores<sup>b</sup>*

### ABSTRACT

The Doppler Tracking Experiment was designed to test the feasibility of improved mapping of the Earth's gravity field by means of the low-low satellite-to-satellite tracking method and to observe variations in the electron density of the ionosphere between two spacecraft. Data were taken between 01:01 and 14:37 UT on July 24, 1975. Baseline data taken earlier, while the docking module was still attached to the command and service module, indicated that the equipment operated satisfactorily.

The ionospheric data contained in the difference between the Doppler signals acquired at the two experimental frequencies are of excellent quality. The data represent valuable satellite-to-satellite observations, never made before, of wave phenomena in the ionosphere. The gravity data were corrupted by an unexpectedly high noise level of as-yet-undetermined origin, with periods greater than 150 seconds, which prevented unambiguous identification of gravity-anomaly signatures.

### INTRODUCTION

Interest has recently focused on mass density anomalies with scale sizes of 100 to 700 km in the

upper mantle of the Earth. It is likely that these anomalies are important factors in the physics of the mantle and plate tectonics and in the reconstruction of important aspects of the Earth's evolution, such as continental drift. Small-scale anomalies near the surface of the Earth have been studied for many years by means of surface gravimetry; and large-scale anomalies, greater than 2000 km, have been investigated for almost 20 years by observing artificial-satellite orbit perturbations. The spacecraft-to-spacecraft Doppler Tracking Experiment (MA-089) conducted by the Smithsonian Astrophysical Observatory (SAO) during the Apollo-Soyuz Test Project (ASTP) mission was designed to determine gravity features having an intermediate horizontal scale of 250 to 1000 km. The ASTP mission was particularly suitable for this experiment because it provided two platforms with a controlled separation within the same orbit at an altitude low enough for enhanced sensitivity to these short-wavelength gravity anomalies.

The experiment consisted of measuring (by means of a phase-coherent, dual-frequency, very-high-frequency link) the relative velocity, or Doppler shift, between the docking module (DM) and the command and service module (CSM). Both orbiting at a height of 220 km, these two modules had an initial separation of 310 km, which increased to 430 km by the end of the data take. From their relative-velocity data, localized anomalies in the Earth's gravitational field should be measured with a threshold sensitivity of better than 0.15 mm/sec<sup>2</sup> (15 mgal). The geometric range rate induced by the ionosphere was removed by the dual-frequency (162 and 324 MHz) correction.

---

<sup>a</sup>Smithsonian Astrophysical Observatory.

<sup>b</sup>NASA Lyndon B. Johnson Space Center.

<sup>†</sup>Principal Investigator.

A secondary goal of the experiment was to measure changes in the integrated electron concentration and other ionospheric properties along a radio path between the CSM and the DM and between the DM and the ground.

Since the time available for the Doppler Tracking Experiment was limited to 12 hours, complete global coverage was not expected to be possible; therefore, the experiment was meant to serve solely as a feasibility demonstration.

## THEORY

### Measuring the Earth's Gravity Field

The structure of the Earth's gravity field has been of considerable scientific interest for some time because it provides one of the few available clues to the internal distribution of mass in the Earth. The recent development of the plate-tectonics hypothesis has placed added emphasis on the need for information on those particular features in the gravity field that have horizontal wavelengths of 100 to 700 km.

Evidence from studies of seismic-wave propagation shows that the outer portion of the Earth consists of (1) a high-velocity zone, the lithosphere, which generally includes the crust and uppermost mantle, has significant strength, and is approximately 50 to 80 km thick under the oceans and somewhat thicker under the continents; (2) a low-velocity zone, the asthenosphere, which is a layer of low effective strength on a geologic time scale and extends from the base of the lithosphere to a depth of several hundred kilometers; and (3) the lower remaining portion of the mantle, the mesosphere, which may have strength and is relatively passive in tectonic processes.

The plate-tectonics concept is based on the observation that large blocks or plates of the rigid lithosphere, some thousands of kilometers in horizontal extent, appear to be moving ("floating" on the yielding asthenosphere) with respect to one another at average long-term rates of approximately 1 to 15 cm/yr (ref. 10-1). One manifestation of this plate motion is continental drift. Most

large earthquakes, volcanic activity, mountain building, and tsunami generation, plus some terrestrial mineral resources, are located at the boundaries of the lithospheric plates. In fact, nearly all large-scale geological and geophysical phenomena occurring on the Earth's surface appear to be intimately related to this global pattern of plate motions. Thus, the subject of plate tectonics is of considerable scientific and practical interest. However, no satisfactory theory of the mechanism or mechanisms producing plate motion is available. It is very probable that both thermal convection and chemical convection in the asthenosphere are involved in some way, and most current theories include one or both processes. In any event, there is little question that knowledge of the density field in the upper portion of the Earth, to a depth of 700 km or so, would be of considerable importance in determining the basic mechanisms underlying plate motion.

The distribution of mass within the Earth uniquely determines the external gravity field. Hence, measurements of the latter contain information on the density field (although it should be noted that the external field does not define the unique internal mass distribution). As a rough approximation, a density anomaly within the Earth will produce a lateral variation in the external gravity field with a scale comparable to the depth of the anomaly. Thus, the density field within the upper mantle at depths of approximately 100 to 700 km will generally be reflected in horizontal variations of the gravity field having wavelengths of 100 to 700 km. This fact suggests that measurements of intermediate-wavelength (100 to 1000 km) features in the gravity field will be fundamental to advancing the understanding of plate tectonics.

The intermediate-wavelength structure of the Earth's gravity field is of interest for another reason. The surface of the ocean contains topographic signatures of current systems, eddies, storm surges, tsunamis, barometric loading, etc., all of which are of considerable practical importance. There is great interest in developing methods for maintaining frequent surveillance of these phenomena over the world's ocean. One very promising approach is to map the topography



of the ocean with satellite-borne radar altimeters. The third Geodetic Earth Orbiting Satellite (GEOS-3), launched by NASA in April 1975, has such an altimeter.

However, the mean-sea-level surface also contains the topographic imprint of the Earth's gravity field, i.e., the geoid. Geoid undulations must be mapped and removed from the measured ocean topography before it will be possible to identify the signatures of oceanographic parameters uniquely. All the previously mentioned oceanic features have topographic structures with significant lateral components in the range 100 to 1000 km. The estimated geoid accuracy needed for this purpose is 10 cm in geoid height.

Measuring the Earth's gravity field has been a continuing occupation of geodesists for many years. The traditional method has been to use gravimeters at fixed locations in land areas and on-board ships, submarines, and, more recently, aircraft. This method provides accurate measurements of the detailed structure of the gravity field, particularly on land. However, surface gravimetry has several deficiencies: the cost and time involved in covering large geographic areas (particularly in rough terrain), the reduced accuracy of gravimeters on mobile platforms, and the loss in accuracy of large-scale gravity variations synthesized from gravimeter data.

More recently, the structure of the gravity field has been calculated by way of orbital dynamics from accurate tracking of artificial satellites. Because satellite orbits are uniquely determined by the forces acting on the satellite and because gravity is by far the dominant force, the gravitational force can be inferred from the observed orbits and an appropriate orbit theory. This orbital-dynamics approach has been used successfully to measure the large-scale structure of the gravity field with considerable accuracy. However, the orbital-dynamics approach is not suitable for measuring intermediate- or short-wavelength gravity-field features. Specifically, spherical-harmonics terms of degree higher than 20 are impractical, both because of the rapidly increasing complexity of the theory and its computer mechanization and because of the need for many more satellites in different orbits. Thus, this

method is restricted, for practical reasons, to gravity features having horizontal wavelengths greater than 2000 km.

### The Gravity Field From Satellite-to-Satellite Velocity Measurements

Artificial satellites can be used in another way to measure intermediate-sized gravity features. Employed in the SAO Doppler Tracking Experiment, the method is based on calculating the gravitational force acting on a spacecraft directly from changes in its measured velocity. Figure 10-1 is a simplistic diagram of this method; it pictures a satellite in Earth orbit. The density of the model Earth is assumed to be homogeneous except for an excess mass  $M$  at some point under the orbit. As the satellite approaches  $M$ , the added gravitational force exerted by  $M$  will accelerate the satellite. As the satellite moves away from  $M$ , the corresponding retarding force will reduce the satellite velocity. By measuring the time history of the velocity variation during the period when the satellite is under the influence of  $M$ , the size, position, and magnitude of the excess mass  $M$  can be deduced. This approach was used to discover and measure lunar mascons (ref. 10-2).

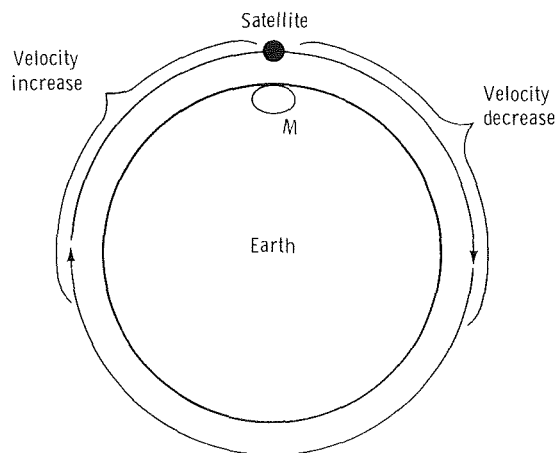


FIGURE 10-1.—Velocity changes associated with a gravity anomaly.

Of course, the actual situation for the experiment is more complex, not only because of the internal mass distribution of the Earth and its effects on the satellite trajectory, but also because the velocity of the satellite must be measured from another satellite. A detailed analysis of more realistic cases has been reported by Schwarz (ref. 10-3). Wolff (ref. 10-4), Comfort (ref. 10-5), and Vonbun (ref. 10-6) have also contributed to the investigation of this method.

From surface-gravimeter data for the United States, Schwarz constructed arrays of  $1^\circ$  by  $1^\circ$ ,  $2^\circ$  by  $2^\circ$ , and  $5^\circ$  by  $5^\circ$  gravity anomalies and computed the theoretical range-rate variations that would be observed between two spacecraft in orbit over these simulated gravity fields. Orbital altitudes of 200, 300, and 700 km and satellite-to-satellite separations of 200 to 600 km were used in various combinations. Noise was added to the computed range-rate data. Schwarz then inverted the process to determine the accuracy with which the simulated gravity anomalies could be recovered from the computed, noisy, range-rate (Doppler) data.

The results of Schwarz's computer experiments are briefly summarized as follows.

1. The structure of the gravity field can be determined from measurements of the variations in range rate between two spacecraft in the same nominal orbit.

2. The lateral scale of the shortest wavelength gravity feature that can be recovered using this method is approximately equal to the orbital altitude.

3. The accuracy of the recovered gravity anomalies is approximately  $0.1 \text{ mm/sec}^2$  (10 mgal), for an accuracy of  $0.5 \text{ mm/sec}$  (1 standard deviation) in range rate between spacecraft, where each measurement is averaged over 16 to 32 seconds.

4. The ephemerides of the two spacecraft need not be determined to high accuracy; orbital errors as large as 1000 m have little effect on the solutions.

Schwarz's computer experiments suggest rather convincingly that the ASTP Doppler Tracking Experiment should produce accurate determinations of gravity anomalies having horizontal

wavelengths in the range of 300 to 1000 km over those geographic regions for which measurements are obtained. The lunar-mascon experiment confirms this conclusion even though the geometry was somewhat different because one of the "spacecraft" terminals was located on the Earth.

Useful data can be obtained when the spacecraft are within line of sight of each other, when the line between them lies above the troposphere, and when their separation is greater than 200 km. It is important to note that gravity-field information is obtained only for those particular geographic regions where the Doppler measurements are made. The scientific usefulness of the experiment thus depends on the geographic coverage.

The accelerations produced by atmospheric drag and radiation pressure on the spacecraft contribute to the measured range rates and thus constitute systematic errors in the determination of the gravity field. The acceleration caused by radiation pressure was computed for solar flux incident on the side of the spacecraft. In this case, the area-to-mass ratio is approximately  $0.02 \text{ cm}^2/\text{g}$ . The pressure exerted by direct solar radiation was taken as  $4.5 \times 10^{-10} \text{ N/cm}^2$  ( $4.5 \times 10^{-5} \text{ dyn/cm}^2$ ); therefore, the resulting acceleration is approximately  $1 \times 10^{-6} \text{ cm/sec}^2$ , which is negligible.

The acceleration produced by atmospheric drag  $a$  was computed for the case in which the spacecraft velocity vector is parallel to its long axis, with an effective area-to-mass ratio  $A/m$  of  $0.005 \text{ cm}^2/\text{g}$ . The following equation was used:

$$a = \frac{C_D}{2} \frac{A}{m} \rho v^2 \quad (10-1)$$

where the drag coefficient  $C_D$  is 2,  $\rho$  is the atmospheric density, and  $v$  is the spacecraft velocity. When  $\rho = 2.8 \times 10^{-13} \text{ g/cm}^3$  at an altitude of 200 km, an acceleration of  $0.0084 \text{ mm/sec}^2$  is obtained. For the 10-second averaging time of the Doppler observations, the velocity change is thus  $0.084 \text{ mm/sec}$  for each data-sample period.

If drag accelerations are reasonably smooth, as is expected, it should be possible to separate the

gravity variations satisfactorily even at a spacecraft altitude of 200 km. Alternatively, the drag forces appear small enough that they can be modeled to sufficient accuracy. In any event, the drag effects are large enough that they must be computed accurately by using the measured orbital and altitude motions of both spacecraft.

### **Ionospheric Studies Using Satellite-to-Satellite Doppler Data**

If a radiofrequency (RF) Doppler link is used between two spacecraft to obtain range-rate data, information about the electron concentration between the spacecraft can also be obtained. In fact, the effects of the ionosphere must be identified before accurate range rates can be determined. Consequently, a secondary goal of the Doppler Tracking Experiment was to analyze the resulting ionospheric information. In addition, it should be possible to probe traveling ionospheric disturbances with the satellite-to-satellite link and to detect the boundaries of turbulent regions of the ionosphere.

The analysis of ionospheric information is an extension of well-known methods (differential Doppler) of measuring the time change of the integrated electron concentration and other properties of the ionosphere along a radio path between a terminal moving within or above the ionosphere and a station on the ground. Before artificial-satellite flights, these techniques were used in suborbital rocket flights to measure ionospheric parameters (refs. 10-7 and 10-8). Since 1957, much information based on the use of multifrequency Doppler links between satellites and ground stations has been published (refs. 10-9 to 10-17).

A fundamental problem in space-to-ground Doppler links is that the differential Doppler shift between two coherent, harmonically related frequencies is connected to the time derivative of the columnar electron content and not to the columnar content itself. This difficulty can be removed if simultaneous measurements are made of Faraday rotation. When Faraday rotation is not observed, the problem is not adequately determined, and inversion of differential Doppler data into

columnar content strongly depends on the presence of horizontal gradients in that region of the ionosphere swept through by the space-to-ground radio path while the spaceborne terminal is in motion.

The ASTP Doppler Tracking Experiment introduced a new feature, namely, measurements of horizontal gradients at a height near 220 km by use of a dual-frequency radio link between spacecraft in the same orbit.

In the case of a probe transmitting at frequency  $\omega_1$  through the ionosphere with a receiver on the ground

$$\Phi_1(t) = \frac{\omega_1}{c} \int_0^{r(t)} n_1(r) dr \quad (10-2)$$

when the spacecraft is at a height  $r(t)$  and where  $c$  is the velocity of light in free space and  $n_1(r)$  is the index of refraction for frequency  $f_1$  at height  $r$ . The symbol  $\Phi_1(t)$  denotes the phase shift imparted at the frequency  $f_1 = \omega_1/2\pi$  to the transmitted signal due to passage through the ionosphere, and its time derivative (time derivatives throughout are indicated by dots) is

$$\dot{\Phi}_1(t) = \frac{\omega_1}{c} \frac{d}{dt} \int_0^{r(t)} n_1(r) dr \quad (10-3)$$

The change of phase path with time is due in part to the spacecraft motion and in part to temporal changes of the index of refraction along the vertical between the spacecraft and the ground. If there are no temporal changes in the index of refraction along the path, and if the spacecraft is assumed to be at height  $r_0$  at time  $t_0$ , the resulting equation is

$$\dot{\Phi}_1(t_0) = \frac{\omega_1}{c} \dot{r}(t_0) n_1(r_0) \quad (10-4)$$

where  $\dot{r}(t_0)$  is the range rate at time  $t_0$ . If there are temporal changes, equation (10-4) becomes

$$\dot{\Phi}_1(t_0) = \frac{\omega_1}{c} \left[ \dot{r}(t_0) n_1(r_0) + \int_0^{r(t)} \frac{\partial n_1(r)}{\partial t} dr \right] \quad (10-5)$$

where the term

$$\int_0^{r(t)} \frac{\partial n_1(r)}{\partial t} dr$$

represents the temporal variation of the columnar refractivity in the entire vertical path between the spacecraft and the ground. The problem is not adequately determined, and unless this variation is otherwise measured or becomes negligibly small, the inferring of  $n_1(r_0)$  from  $\dot{\Phi}_1(t_0)$  is affected by error.

When the effects of the Earth's magnetic field and the collision frequency on the index of refraction are disregarded, equation (10-4) can be rewritten as

$$\dot{\Phi}_1(t_0) = \frac{\omega_1}{c} \dot{r}(t_0) \left( 1 - \frac{2\pi e^2 N}{m\omega_1^2} \right) \quad (10-6)$$

where  $N$  is the electron density and  $e$  and  $m$  are the charge and the mass of the electron, respectively;  $2\pi e^2/m = 1587.6$  if  $N$  is expressed in electrons per cubic meter and if  $\omega_1$  is expressed in radians per second. From equation (10-4), the local index of refraction (and, hence, the electron density) at the spacecraft height can be determined by monitoring the received Doppler shift and by knowing, independently, the velocity of the spacecraft and the frequency radiated. With a single frequency, it is necessary to know these two parameters very accurately. However, by adding a

second frequency,  $\omega_2$ , the equation of the differential Doppler shift in the spacecraft-to-ground link, when temporal changes are neglected, becomes

$$\begin{aligned} \delta\dot{\Phi} &= \dot{\Phi}_1(t) - \frac{\omega_1}{\omega_2} \dot{\Phi}_2(t) \\ &= \frac{\omega_1}{c} \frac{d}{dt} \int_0^{r(t)} [n_1(r) - n_2(r)] dr \\ &= \frac{\omega_1}{c} \dot{r}(t_0) [n_1(r_0) - n_2(r_0)] \quad (10-7) \end{aligned}$$

where  $\dot{\Phi}_2$  is the Doppler shift at frequency  $f_2 = \omega_2/2\pi$  and  $n_2(r)$  is the index of refraction at frequency  $f_2$  and height  $r$ . If the refractive effects of the Earth's magnetic field and the collision frequency are disregarded, the results are

$$\delta\dot{\Phi} = \frac{\omega_1}{c} \dot{r}(t_0) \frac{2\pi e^2 N}{m} \left( \frac{\omega_1^2}{\omega_1^2 \omega_2^2} \right) \quad (10-8)$$

Equation (10-8) shows that the contribution to the measurement error arising from an error in estimating the link's frequencies is virtually eliminated.

Equation (10-6) indicates that an error in frequency contributes directly to the error in  $\dot{\Phi}_1(t_0)$ . However, equation (10-8) shows that the error in frequency must now be multiplied by the quantity  $(n^2 - 1)/\omega_1^2$ , which is usually very small. For instance, if  $\omega_1/\omega_2 = n = 2$  and if  $\omega_1 = 2\pi \times 300 \times 10^6$  rad/sec, then  $(n^2 - 1)/\omega_1^2 = 8.6 \times 10^{-19}$ ; therefore, the influence of the frequency error in the overall error of  $\dot{\Phi}_1(t_0)$  is eliminated.

When the spacecraft trajectory is not vertical, other analytical expressions, which have already been developed by several authors, must be used. However, these expressions show that the problem is inadequately determined even in the planar

approximation. The difficulty was partly alleviated in this experiment by the fact that the DM-to-CSM dual-frequency link measured the horizontal gradients in the orbital plane at the ASTP orbital height

$$\begin{aligned} \delta\dot{\Phi} &= \dot{\Phi}_1(t) - \frac{\omega_1}{\omega_2} \dot{\Phi}_2(t) \\ &= \frac{\omega_1}{c} \frac{\partial}{\partial t} \left[ \int_{DM}^{CSM} n_1(x) dx - \int_{DM}^{CSM} n_2(x) dx \right] \end{aligned} \quad (10-9)$$

where  $x$  is the coordinate of the line joining the CSM and the DM. By assuming that the two spacecraft remained at a constant separation (had a relative velocity of zero), the results obtained will be

$$\delta\dot{\Phi} = \frac{\omega_1}{c} \int_{DM}^{CSM} \frac{\partial}{\partial x} [n_1(x) - n_2(x)] \frac{\partial x}{\partial t} dx \quad (10-10)$$

where  $\partial x / \partial t$  is known from orbital-mechanics considerations. By neglecting the refractive effects of the Earth magnetic field and the collision frequency, equation (10-10) can be rewritten as follows.

$$\delta\dot{\Phi} = \frac{\omega_1}{c} \frac{2\pi e^2}{m} \left( \frac{\omega_1^2 - \omega_2^2}{\omega_1^2 \omega_2^2} \right) \int_{DM}^{CSM} \frac{\partial N}{\partial x} \frac{\partial x}{\partial t} dx \quad (10-11)$$

The horizontal gradient of the electron content  $\partial N / \partial x$  can therefore be obtained from the measured values of  $\delta\dot{\Phi}$  in the DM-to-CSM path. Before it can be used in the processing of the data,

however,  $\partial N / \partial x$  must be known all along the vertical  $z$ . In fact, what is needed is the function

$$\int_0^z \frac{\partial N}{\partial x} z dz$$

and not just  $\partial N / \partial x$  at the ASTP orbital height of 220 km. Therefore, a model must be constructed of  $(\partial N / \partial x) z$  in the lower ionosphere, with the constraint of satisfying both the value measured at 220 km by the DM-to-CSM link and a value equal to zero measured at the bottom of the ionosphere. A linear variation of the gradient between these two values thus seems to be an acceptable assumption.

The investigators were unable to observe Faraday rotation (rotating Doppler) in either link. In the DM-to-CSM link, the transmitting antenna was linearly polarized and the receiving antenna was circularly polarized; and in the DM-to-ground link, there was no provision for recording signal strength.

### Analysis of DM Motion About the Center of Mass

Knowledge of the orientation of the two spacecraft is required for an exact evaluation of the forces acting on their centers of mass. Atmospheric drag and radiation pressure depend on the orientation, and, in principle, the gravitational force depends to second order; but these forces are small enough that only crude orientation information is necessary. However, the observed Doppler signal measures the relative velocity of the antenna phase centers of the DM transmitter and the CSM receiver, which includes the antenna motion around the respective center of mass of these two bodies. To reconstruct the relative motion of the centers of mass, the rotational motion of the DM must be reconstructed from Doppler measurements of the relative velocity of the antenna phase center.

Whereas telemetry data were available on CSM motion (such as gyro rate and gimbal position), the only existing direct information on the orientation of the DM was obtained from the Doppler

signals and from the photographs taken from the CSM during the first 5 minutes after separation. To simulate the motion of the DM, the fundamental assumption was made that the DM is a rigid body (taken with its origin at the DM center of mass and with its axes coincident with the principal axes of the central inertia ellipsoid) subjected only to thermal expansion and contraction. With respect to a reference system, uncertainties exist in (1) the initial conditions, (2) the position of the antenna center, and (3) the geometry and orientation of the radiation pattern. In constructing the equations of motion, the investigators considered all the torques acting on the DM and selected those that had a measurable effect, namely, gravitational torque, atmospheric effects, radiation-pressure effects, and magnetic-torque effects.

As a straightforward method, the investigators chose to integrate the three Eulerian equations considered to be first-order differential equations in  $\omega_1$ ,  $\omega_2$ , and  $\omega_3$  (components of the angular velocity with respect to the body-fixed axes), plus nine first-order auxiliary equations in the direction cosines of the body-fixed axes with respect to an inertial frame. The Eulerian equations are

$$\begin{aligned} A\dot{\omega}_1 - (B - C)\omega_2\omega_3 &= T_1^* \\ B\dot{\omega}_2 - (C - A)\omega_3\omega_1 &= T_2^* \\ C\dot{\omega}_3 - (A - B)\omega_1\omega_2 &= T_3^* \end{aligned} \quad (10-12)$$

where  $A$ ,  $B$ , and  $C$  are the principal moments of inertia of the DM with the ordering  $A < B < C$ ;  $\dot{\omega}_1$ ,  $\dot{\omega}_2$ , and  $\dot{\omega}_3$  are the components of the angular acceleration; and  $T_1^*$ ,  $T_2^*$ , and  $T_3^*$  are the components of the applied torque about the body-fixed axes  $x$ ,  $y$ , and  $z$ , respectively. If  $\mathbf{i}$ ,  $\mathbf{j}$ , and  $\mathbf{k}$  are the unit vectors along the body-fixed principal axes and  $\mathbf{I}$ ,  $\mathbf{J}$ , and  $\mathbf{K}$  are the unit vectors of the inertial

coordinate system, then the direction cosines  $\alpha_i$ ,  $\beta_i$ , and  $\gamma_i$  are defined as follows:

$$\begin{aligned} \mathbf{I} &= \alpha_1 \mathbf{i} + \alpha_2 \mathbf{j} + \alpha_3 \mathbf{k} \\ \mathbf{J} &= \beta_1 \mathbf{i} + \beta_2 \mathbf{j} + \beta_3 \mathbf{k} \\ \mathbf{K} &= \gamma_1 \mathbf{i} + \gamma_2 \mathbf{j} + \gamma_3 \mathbf{k} \end{aligned} \quad (10-13)$$

Then, since  $d\mathbf{I}/dt = 0$ ,

$$\begin{aligned} \dot{\alpha}_1 \mathbf{i} + \dot{\alpha}_1 \boldsymbol{\omega} \times \mathbf{i} + \dot{\alpha}_2 \mathbf{j} + \dot{\alpha}_2 \boldsymbol{\omega} \times \mathbf{j} \\ + \dot{\alpha}_3 \mathbf{k} + \dot{\alpha}_3 \boldsymbol{\omega} \times \mathbf{k} = 0 \end{aligned} \quad (10-14)$$

where  $\boldsymbol{\omega}$  is the angular velocity vector. Expanding the cross products, the following three scalar first-order differential equations are obtained:

$$\begin{aligned} \dot{\alpha}_1 &= \alpha_2 \omega_3 - \alpha_3 \omega_2 \\ \dot{\alpha}_2 &= \alpha_3 \omega_1 - \alpha_1 \omega_3 \\ \dot{\alpha}_3 &= \alpha_1 \omega_2 - \alpha_2 \omega_1 \end{aligned} \quad (10-15)$$

The second and third parts of equations (10-13) can be differentiated to obtain similar equations for  $\dot{\beta}_i$  and  $\dot{\gamma}_i$ :

$$\begin{aligned} \dot{\beta}_1 &= \beta_2 \omega_3 - \beta_3 \omega_2 \\ \dot{\beta}_2 &= \beta_3 \omega_1 - \beta_1 \omega_3 \\ \dot{\beta}_3 &= \beta_1 \omega_2 - \beta_2 \omega_1 \end{aligned} \quad (10-16)$$

and

$$\begin{aligned}\dot{\gamma}_1 &= \gamma_2 \omega_3 - \gamma_3 \omega_2 \\ \dot{\gamma}_2 &= \gamma_3 \omega_1 - \gamma_1 \omega_3 \\ \dot{\gamma}_3 &= \gamma_1 \omega_2 - \gamma_2 \omega_1\end{aligned}\quad (10-17)$$

The set of first-order differential equations (eqs. (10-12) and (10-15) to (10-17)) can then be integrated numerically, provided that  $T_1^*$ ,  $T_2^*$ , and  $T_3^*$  are suitably specified as functions of time or of  $\omega_i$ ,  $\alpha_i$ ,  $\beta_i$ , and  $\gamma_i$ .

To integrate the preceding equations numerically, only the gravitational torque was used. In one case, the DM was considered initially to be tumbling about its axis at a rate of 3°/sec normal to a fixed orbital plane. In another case, with the same initial conditions, the orbital plane was allowed to precess at a rate of 5.5°/day. After 4 hours, the amplitude of the modulation of  $\omega_3$  was unchanged, remaining at approximately  $1.8 \times 10^{-5}$  rad/sec, and the modulations of  $\omega_1$  and  $\omega_2$ , although increasing secularly, were less than  $5 \times 10^{-7}$  rad/sec. The effects of gravitational torque are therefore negligible. The same conclusion must be applicable to the effects of the other torques considered previously.

While analyzing the data, it was found that the tumble period changed from 70.5 to 71.9 seconds; this phenomenon remains unexplained. Several possibilities were examined, but none have any observational support. Among them is the possible variation of the inertia tensor of the DM. This variation might result in part from secular effects due to an increase in mean temperature; the periodic component of the temperature change explains reasonably well the variation of the tumbling rate when the DM moved from sunlight to shadow. Other possibilities include the motion of unsecured items inside the DM that might have been subjected to the field of forces, such as centrifugal, established in the DM. These centrifugal forces, combined with the periodic thermal variation, may increase the moment of inertia about the tumbling axis and thus cause a

decrease in the tumbling rate. Although some perplexity remains in this aspect of the problem, it appears from the data that the fundamental characteristics of the motion can be described accurately enough, at least in a first approximation, by assuming, as the investigators did, that the motion of the DM is that of a rigid body free of torque during properly limited intervals of time.

The results of the analysis confirm the importance of accurately reconstructing the motion of the DM about its center of mass and the shape and orientation of the antenna radiation phase pattern to remove from the raw Doppler data those components that are unrelated to the gravity field. The Doppler accuracy required implies such a detailed reconstruction that even the thermal behavior of the DM and the relative lack of rigidity of the vehicle, perhaps due to somewhat loosely clamped parts in its interior, have a substantial effect that is capable of jeopardizing the gravity experiment.

Unfortunately, the harmonic components removed from the raw Doppler spectrum were within the spectral band of the gravity-anomaly-induced signals. Therefore, their removal, although fully justified because they were attributable to the DM rotational motion, partly affected the detectability of gravity anomalies. Another peculiar occurrence, which is due to the geometry of the DM, is the fact that the precessional period of the DM is almost exactly equal to three times the tumbling period.

## EQUIPMENT

Several pieces of equipment were built for the Doppler Tracking Experiment. A dual-frequency transmitter (fig. 10-2) and monopole antenna were mounted on the DM; the service module carried a receiver and signal processor (fig. 10-3) together with a circularly polarized dual-frequency antenna; in the CSM with the astronauts was a pair of small tape recorders used to store the data for postflight analysis.

Special tape-reading equipment was used during prelaunch system tests and for reading the data from the flight tapes. In the latter application,

the tape reader was controlled by, and fed data to, a standard commercial minicomputer.

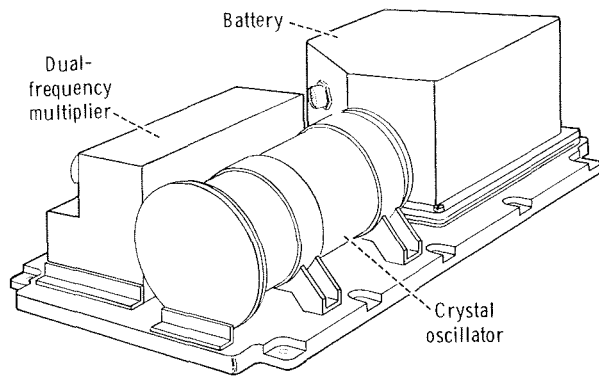


FIGURE 10-2.—The Doppler tracking transmitter.

### Transmitter

The transmitter, which weighed approximately 7 kg, consisted of a highly stable crystal oscillator, frequency multipliers, amplifiers, and a diplexer. The diplexer combined the two frequencies for transmission from a single antenna. A block diagram of the transmitter is shown in figure 10-4. To save battery power for the operational phase of

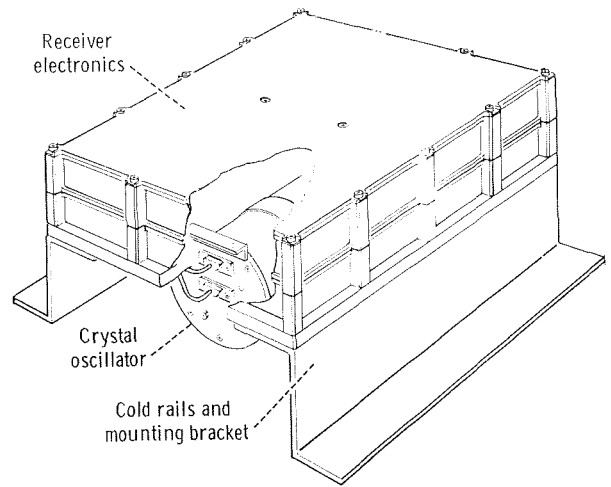


FIGURE 10-3.—The Doppler tracking receiver and signal processor.

the experiment, the transmitter was powered directly from the spacecraft during the 50-hour warmup period required by the oscillator. The frequency of the oscillator was set for 5.06 MHz. Its excellent stability (1.5 parts in  $10^{12}$  over both 10- and 100-second averaging intervals) was preserved by carefully insulating it from environmental changes over a temperature range of 255 to 311 K ( $0^{\circ}$  to  $100^{\circ}$  F). A single multiplier chain

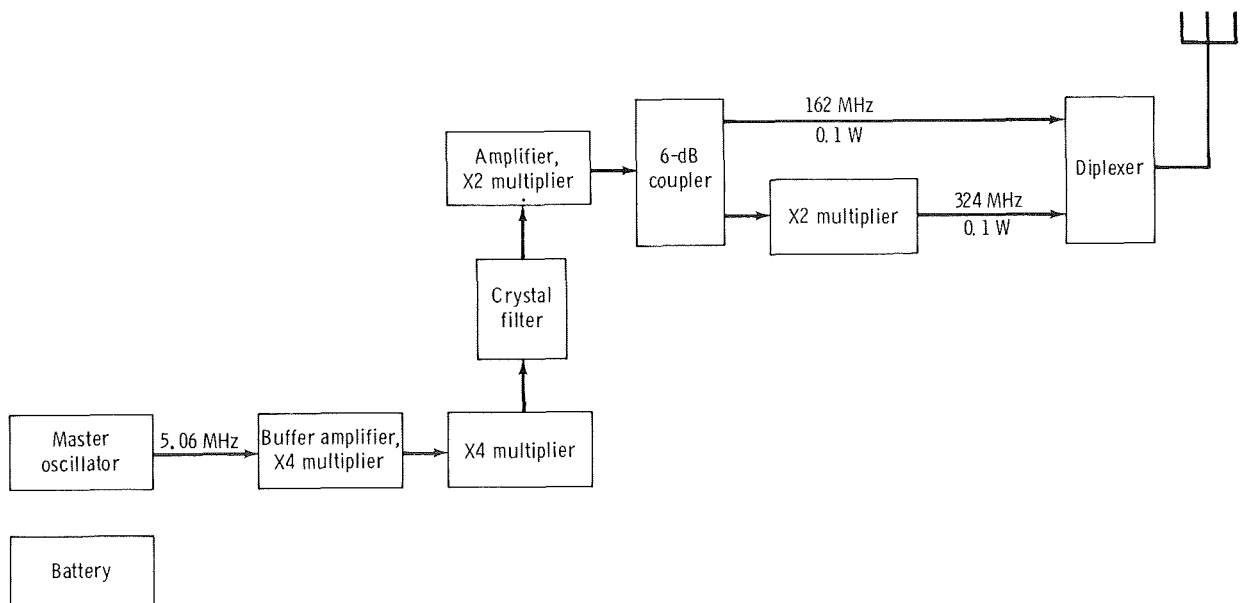


FIGURE 10-4.—Block diagram of the transmitter.



multiplied, amplified, and filtered the oscillator output and drove a power divider. One of the power-divider outputs drove the 162-MHz input of a diplexer; the second was frequency-doubled and was used to feed the 324-MHz diplexer input. The diplexer provided input isolation and filtering. At least 100 mW of output power was delivered to the dual-frequency antenna at each of the two frequencies.

### Receiver and Signal Processor

The receiver, which also weighed approximately 7 kg, is shown in block diagram form in figure 10-5. It provided the processor with a Doppler output compatible with transistor-to-transistor logic for each input frequency. The frequency and phase variations of the 162- and 324-MHz inputs were retained through the use of second-order phase-lock loops. Thus, the receiver outputs were actually band-pass-filtered and constant-amplitude replicas of the input signals, translated from 162 and 324 MHz to 1 kHz. The choice of 1 kHz as the center frequency for the processor represented a compromise between a

desire for high accuracy (requiring a low frequency) and the need to avoid the ambiguity that could result if the Doppler signal shifted this frequency negatively by more than 1 kHz. Because the maximum anticipated Doppler shift was approximately 350 Hz, a 1-kHz center frequency left an adequate margin without significantly degrading the attainable measurement accuracies.

The receiver was powered internally by means of dc-to-dc converters, regulators, and filter circuitry. Less than 50 W of spacecraft power was needed to operate both the receiver and the tape recorder.

Both the transmitting and the receiving antennas were dual-frequency units. The former was a vertical monopole that acted as a quarter-wave antenna at frequencies of 162 and 324 MHz. At 324 MHz, an inductor near the midpoint of the antenna isolated the top section from the bottom; at 162 MHz, the inductor acted as a small loading coil. The receiving antenna was approximately 1 m square and contoured to fit against the side of the service module. This antenna was a strip-line conformal array in which tuned stubs were used to couple its sections at 162 MHz and to isolate the sections at 324 MHz.

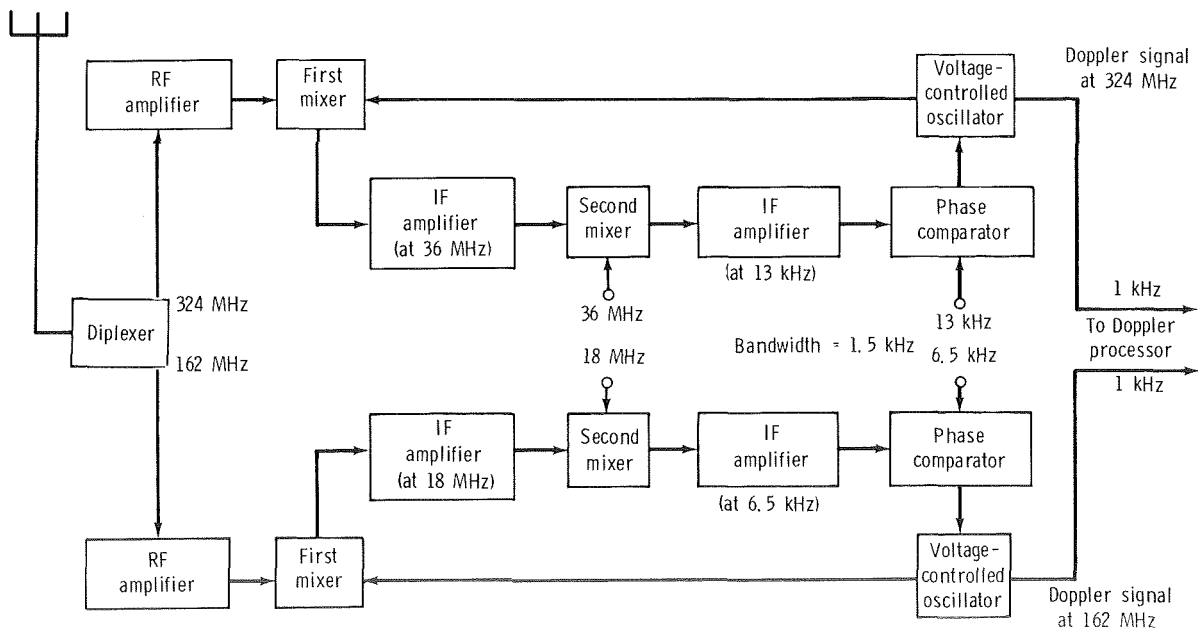


FIGURE 10-5.—Block diagram of the receiver.

A 5.0-MHz reference-frequency input to the synthesizer and the timing reference for the Doppler processor were supplied by an oscillator that was identical, except for its frequency, to that in the transmitter. The synthesizer (having output frequencies, derived by frequency multiplication and division, that were phase coherent with the reference) provided all local-oscillator injections and phase-detector references. When required, band-pass filters were used to obtain outputs of sufficient spectral purity.

A diplexer at the receiver input divided the single input from the dual-frequency antenna into two channels. A preamplifier and a mixer followed the diplexer. These stages had a noise figure of less than 8 dB and a first intermediate-frequency (IF) image-rejection capability of greater than 60 dB. For each channel, a second IF

image-rejection capability of at least 60 dB was achieved by means of a crystal filter. The first IF amplifier included two automatic-gain-controlled stages, and the second included four active filters with amplitude limiting at each stage. The second IF amplifier was followed by sine and cosine phase detectors and filters; the first developed the loop filter voltage fed to the voltage-controlled oscillator (VCO), and the second provided both the automatic-gain-control voltage for the first IF amplifier and a lock/out-of-lock signal to the Doppler processor. The VCO module output fed to the first mixer was derived by multiplying and filtering the output of a crystal VCO having a frequency of 22.5 MHz.

When an out-of-lock signal was received, the processor responded by supplying the phase-detector module with one signal to change the

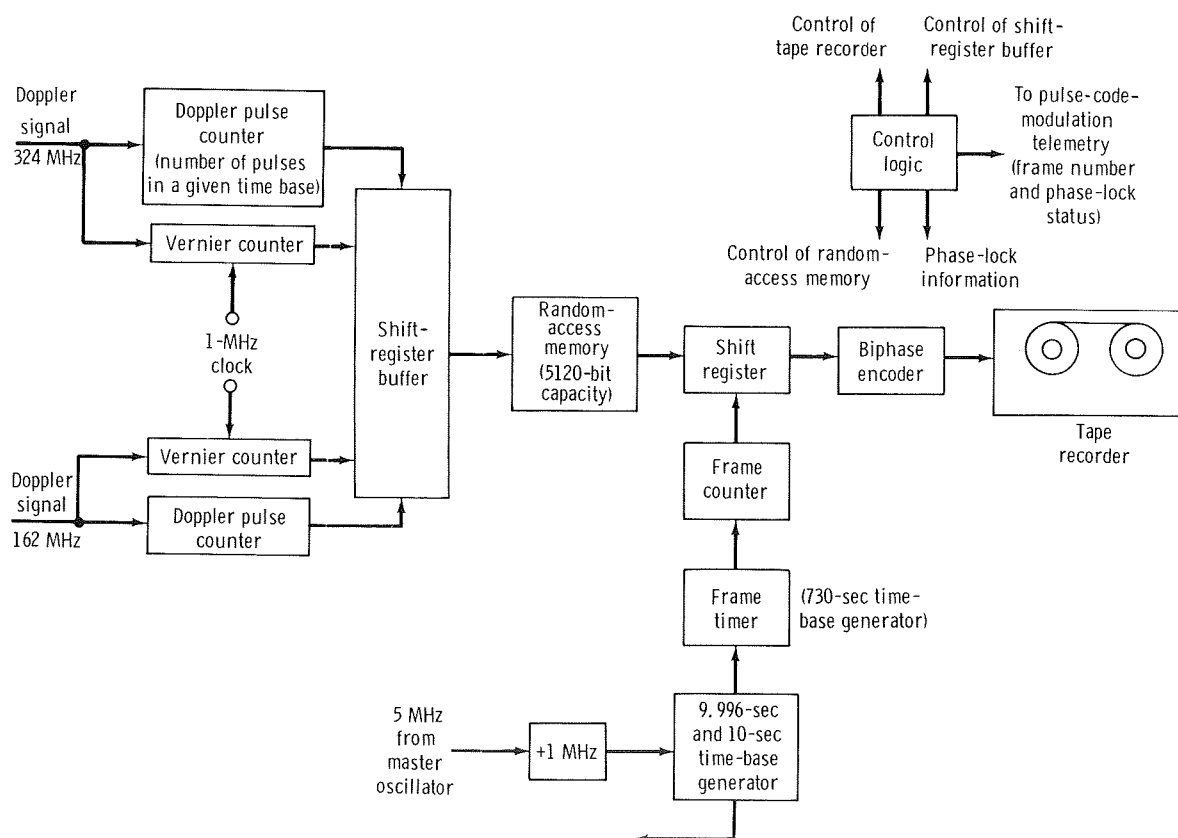


FIGURE 10-6.—Block diagram of the Doppler processor.

phase-lock-loop bandwidth from 5 to 100 Hz and another signal to inject a sweep voltage into the loop. The difference between the sweep ( $\pm 5$  and  $\pm 2.5$  kHz at 324 and 162 MHz, respectively) and the expected Doppler shift allowed for changes in the central-voltage-to-frequency transfer characteristics of the oscillator. When lock was acquired, the signal voltages changed state, the sweeping voltage was removed, and the loop bandwidth was restored to 5 Hz.

The processor received Doppler frequency information from the receiver, extracted the desired information, and recorded and stored this information simultaneously on two tape recorders in the CSM (fig. 10-6). The Doppler frequency averaging interval counted by the processor is shown in figure 10-7. A 10-second counter identified the time instants  $t_0$ ,  $t_2 = t_0 + 9.996$  seconds,  $t'_0 = t_0 + 10$  seconds,  $t'_2 = t_2 + 10$  seconds, etc. The points  $t_1$  and  $t_3$  were determined by the first positive-going zero crossing that occurred after times  $t_0$  and  $t_2$ , respectively. For each channel, an associated vernier up/down counter was enabled at time  $t_0$  and counted the number of 1-microsecond clock pulses observed before it was disabled at time  $t_1$ . It was enabled again at time  $t_2$ , when it down-counted the number of clock pulses in the interval  $t_2 - t_3$ . Simultaneously, zero-crossing counters counted the number of positive-going zero crossings in the interval  $t_0 - t_2$  for each channel. These time counts and zero-crossing counts constituted the raw data associated with each observation interval. The counters were reset and the entire process was restarted at time  $t'_0$ .

The average frequency  $\hat{f}$  observed during a processor cycle was determined from these tape-recorded data by dividing the number of zero crossings  $Z$  by the observation time:

$$\hat{f} = \frac{Z}{9.996 + \Delta t} \quad (10-18)$$

where  $\Delta t$  represents the contents of the vernier counter. Because the zero-crossing counters and the vernier counters were 15 and 13 bits wide, respectively, an unambiguous measurement of any Doppler frequency shift less than or equal to  $\pm 750$  Hz was ensured.

The Doppler processor also performed other functions. For example, it monitored lock/out-of-lock signals from the receiver; when an out-of-lock condition occurred, the processor reestablished lock status and loaded out-of-lock data into a format that could be detected during subsequent data reductions. In addition, the Doppler processor supplied high-channel phase-lock status information to the astronauts by means of a panel meter, as well as that information together with frame numbers to the telemetry channel. From this phase-lock status information, spacecraft maneuvers could have been performed to regain high-channel lock if required. (It was assumed that a high-frequency-channel lock implied a low-frequency-channel lock because of the higher signal-to-noise ratio on the low-frequency channel.) From the telemetered frame number, the

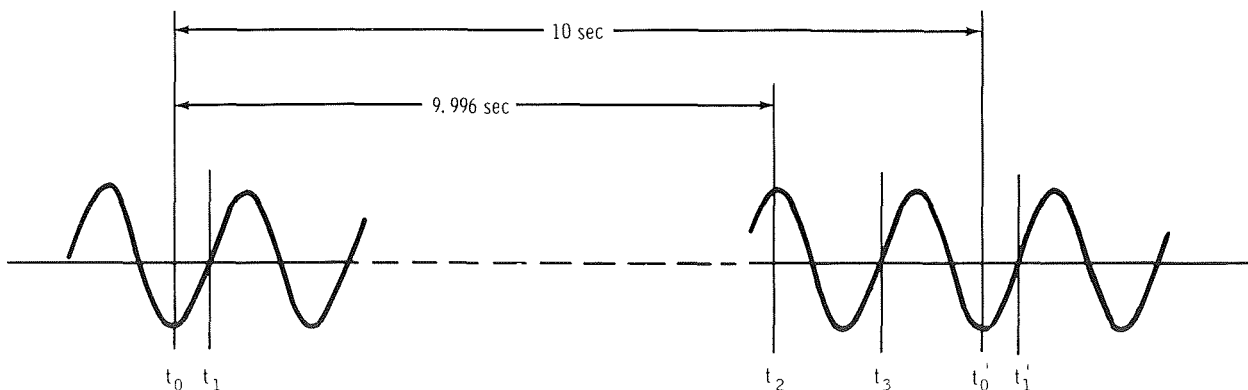


FIGURE 10-7.—Counting interval of the Doppler processor.

tape-recorded data were correlated with the position of the CSM/DM pair relative to the Earth. In another function, data on pitch, roll, and yaw rates of the CSM were received and recorded by the processor to enable the effect of the CSM motion on the Doppler shift to be compensated for during data reduction. Finally, 7-bit parity words were generated by the processor as a protection against substitution and synchronization errors.

Every 10 seconds, a data word was formatted by means of a random-access memory, shift registers, a frame counter, and a microprogramed controller. This data word consisted of the number of zero crossings and the  $\Delta f$  values for both low- and high-frequency channels, plus information on roll, pitch, and yaw rates and parity. After 73 words were stored as a frame, the frame number was appended and the data were serially transferred to the tape recorders at a 972-Hz bit rate through a biphase encoder. Recording time required was approximately 5.2 sec/frame.

### Testing

The system was tested for oscillator stability and low noise before flight by observing the 10-second integrated-frequency measurements produced by the signal processor. The interval during flight between experiment activation and DM jettison also provided a measurement of system performance. On the ground or when the two spacecraft were docked during flight, neither Doppler shift nor ionospheric effects are possible. Thus, the time variation in the sequence of frequency measurements at each frequency indicated the stability of the transmitter oscillator relative to that of the receiver oscillator. The difference between simultaneous 324- and 162-MHz observations tested the balance of the circuitry.

Table 10-I gives the root-mean-square (rms) scatter among a small sample of data points observed at factory acceptance testing, at the NASA John F. Kennedy Space Center before the equipment was installed, on the launch pad, and in orbit. In the first two tests, the backup transmitter was used; the flight system noise in the pad test was attributed to the fact that insufficient time

TABLE 10-I.—Root-Mean-Square Scatter During Testing

Test	Scatter, mm/sec, at —	
	162 MHz	324 MHz
Acceptance	4.2	0.9
Preinstallation	1.0	1.2
Pad	3.7	3.5
Orbit	1.8	1.8

had been allowed for stabilization of the oscillator temperature-controlled crystals.

The rms calculated for the entire "orbit" data set differs somewhat from the tabulated value since it includes longer term fluctuations and the frequency shift induced by g-loading the crystals when the CSM and the DM were rotated at 5°/sec just before separation. The rms difference between channels during this time (based on a small sample) was 1.4 mHz.

### DATA

The Doppler Tracking Experiment had three prime sources of data: spacecraft-to-spacecraft Doppler data and related information recorded in the command module; ground tracking data from the NASA unified S-band (USB) network, from the Defense Mapping Agency Tranet Doppler tracking network, and from a number of geocivers coordinated by the Applied Physics Laboratory; and telemetry from the CSM showing the start of each data frame and a receiver-lock indicator. These sources are described in more detail in the following subsections.

In addition, the astronauts photographed the DM shortly after it was jettisoned from the CSM. The film, which contained approximately 390 images of the DM taken at approximately 0.5-second intervals, was used to make a first estimate of the DM rotational motion.

### **Tape-Recorded Data**

The data recorded onboard the CSM were arranged in groups called words (73 words constituted a frame). The first 8 bits in each frame gave its number, a sequential count that started when the receiver was turned on. The 73 data words followed the frame number; the first word was 87 bits long, and the rest were 69. All data groups appeared with the least significant bit first, except for the frame number, which, for reader synchronization, had its most significant bit first, thereby ensuring 127 frames (nearly 26 hours of observing time) wherein the first bit was zero.

In a Manchester biphase code generated by the signal processor, the data were to have been recorded in the CSM on a parallel pair of tape recorders. One recorder failed to run; postmission investigation revealed that the tape had become stuck to one of the heads. Fortunately, the other tape contained signals of high quality. There were no parity errors and no dropouts.

In all, 109 frames were recorded. Frame 0 contained no useful information and was generated by the signal processor only to ensure that the various registers were correctly set for the start of frame 1. Frames 1 to 15 contained data taken while the CSM and the DM were docked and constituted the final test of the equipment. Frames 16 to 41 included the period during which the CSM was maneuvered to attain a position approximately 300 km from the DM. The observational data began with frame 42, which started at 01:01:56 UT on July 24, 1975 (204:41:56 ground elapsed time), shortly after the start of orbital revolution 126. Since the receiver was turned off during frame 109, which was therefore not recorded, the data ended with frame 108, completed at 14:37:06 UT on July 24.

The Doppler measurements were continuous except for two gaps due to loss of receiver lock. One gap occurred in frames 59 to 61, and the other in frames 101 to 103.

### **Ground-Based Observations**

The CSM was tracked by the NASA USB network, consisting of 18 stations. Eleven USB sta-

tions reported a total of 1754 observations made during 15 passes between 00:43:00 and 15:50:00 UT; 832 observations that were made at low elevation angles were rejected. The limit for range measurements was 5°; for range differences, 8°.

The DM was observed by 19 Tranet stations and 13 geociever stations. Between 00:00:00 and 24:00:00 UT, 216 geociever observations were recorded on 46 passes and 928 Tranet observations from 64 passes. From these 1144 observations, 492 were rejected because of elevation angles less than 8°.

### **Telemetry Data**

For all times when the CSM was within range of a receiving station, the telemetry stream included a signal from the receiver indicating whether or not it was locked onto an incoming signal. Every 12 minutes 10 seconds, the start of a new frame and its number were indicated. These data, recorded on strip charts together with time signals generated at the NASA Lyndon B. Johnson Space Center, formed the basis for correlating Doppler data and spacecraft position.

### **DATA REDUCTION**

The data-processing phase consisted of a series of computerized steps to remove from the raw data a number of corrupting effects, leaving only random system noise and the "signatures" of gravity anomalies. Both theoretical models and filtering techniques were applied. The procedure involved four basic operations: (1) point-by-point calculation and removal of the ionospheric propagation effects, (2) separate determinations of the CSM and DM orbits so that a predicted range difference could be computed for each data point, thereby taking into account all orbital effects including gravitational perturbations (except small-scale anomalies), (3) point-by-point subtraction of the calculated range differences from the observations, and (4) reduction of the rms scatter of the residuals by calculating and subtracting the com-

ponents arising from rotational motions of the spacecraft.

The ionospheric-correction technique, which is described fully in references 10-18 and 10-19, is simply the classical two-frequency correction that includes the frequency-dependent phase shift imposed by the ionosphere. Figure 10-8 is a sample of the raw data as recorded onboard the CSM; figure 10-9 shows the differential Doppler signal due to the ionosphere. Removal of the ionospheric contributions left the data, as shown in figure 10-10, with periodic excursions as large as 3 m/sec.

### Orbit Determination

To suppress the large-scale variations shown in figure 10-10, a range difference was calculated for each data point from high-precision orbits of the DM and the CSM and subtracted from the observed values. The orbits were determined independently by directly integrating the equations of motion for each spacecraft and differentially correcting the initial conditions to optimize the fit to ground-based observations (Tranet Doppler observations of the DM and USB radar range and range-rate observations of the CSM).

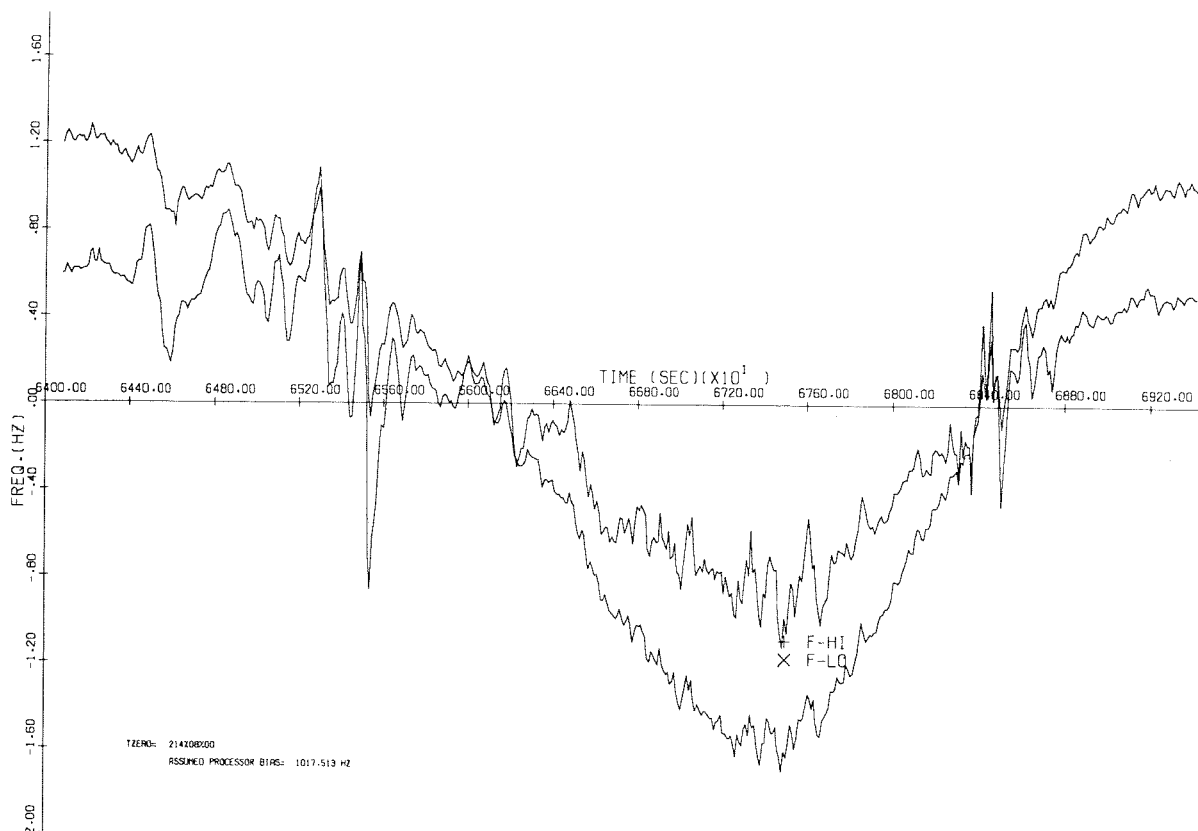


FIGURE 10-8.—Raw Doppler data as recorded onboard the CSM.

The SAO primary orbit-determination program was used to compute approximate orbits, which formed the basis for the starting set of initial conditions. To determine an appropriate set of initial conditions, it was first necessary to eliminate pass-bias errors due to oscillator uncertainties from the observed Tranet range-difference data. This procedure was accomplished by means of a series of orbit determinations within consecutive overlapping time intervals of 0.4 day spanning a total period of 2 days from modified Julian day (MJD) 42616.0 to 42618.2. To calculate the apparent fre-

quency drift of the oscillator, a regression line was subsequently fitted to this set of biases. The slope of the regression line was found to indicate a frequency drift in 1 day of 0.417 Hz per 300 MHz, whereas the mean offset was found to be 18.4 Hz per 300 MHz. After the biases were determined, each Tranet observation was corrected and the resulting set of data was used as input to the precision orbital integration package.

An additional parameter estimated from the set of 0.4-day arcs was the DM area-to-mass ratio  $A/m$ . For a circular orbit (ref. 10-20),  $A/m$  is given

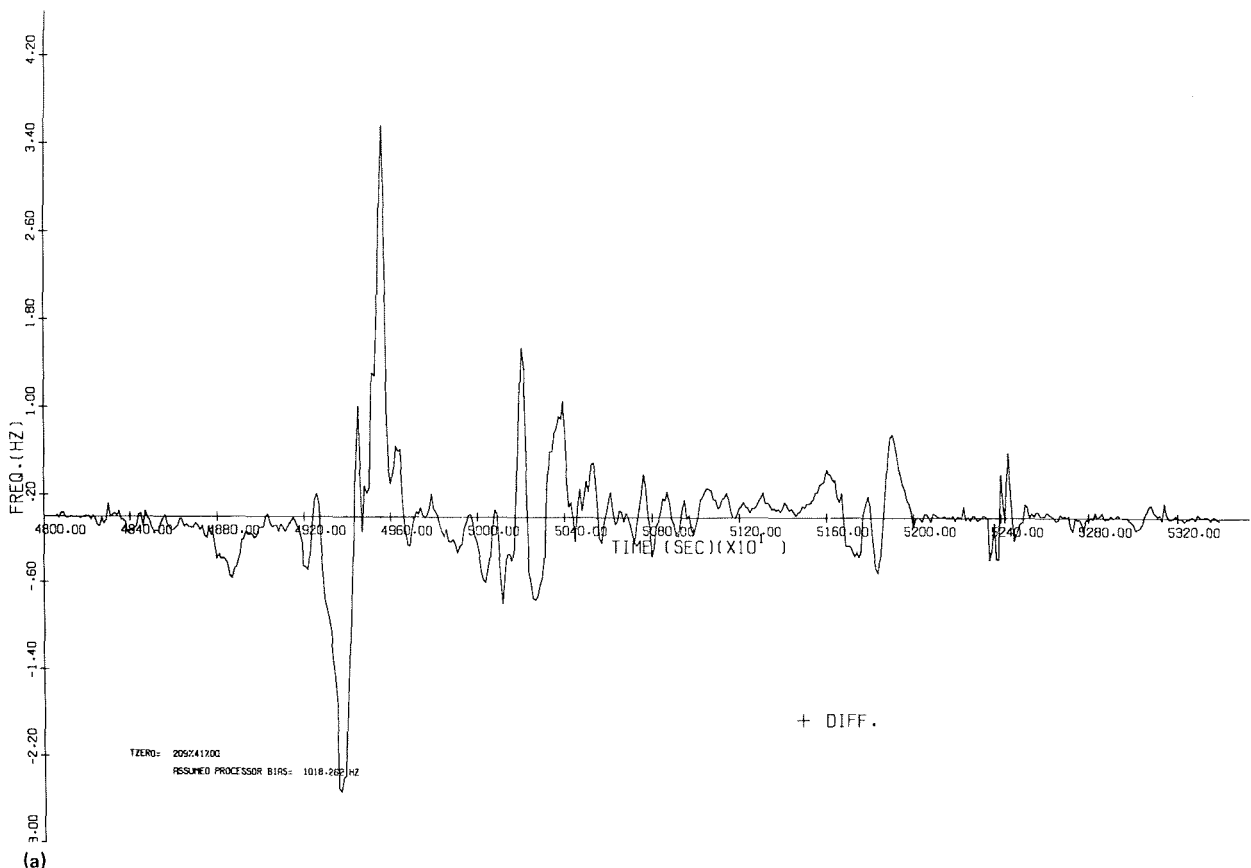


FIGURE 10-9.—Differential Doppler shift due to the ionosphere for four consecutive orbital revolutions. (a) Revolution 129. (b) Revolution 130. (c) Revolution 131. (d) Revolution 132.

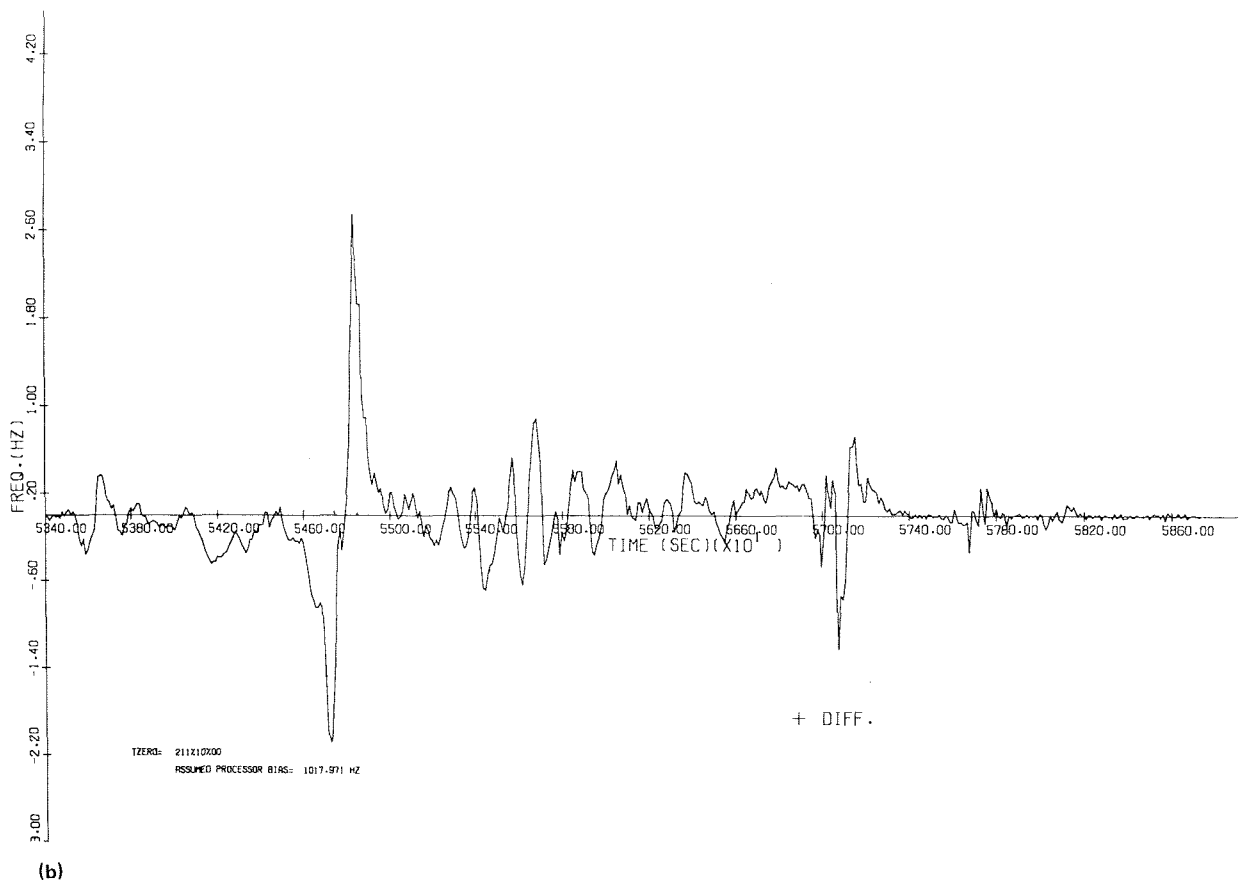


FIGURE 10-9.—Continued.

by

$$\frac{A}{m} = \frac{\dot{P}}{3\pi a \rho C_D} \quad (10-19)$$

where  $\dot{P}$  is the rate of change of the orbital period,  $a$  is the semimajor axis,  $\rho$  is the atmospheric density, and  $C_D$  is the drag coefficient. Since the computer program provides the first and second time derivatives of the mean anomaly  $M$ , the value of  $\dot{P}$  was obtained from

$$\dot{P} = - \frac{\ddot{M}}{2\dot{M}} \quad (10-20)$$

By assuming  $C_D = 2.0$ ,  $\rho = 10^{-13} \text{ g/cm}^3$ ,  $a = 6.587 \times 10^8 \text{ cm}$ ,  $\dot{M} = 16.237 \text{ rev/day}$ , and  $\ddot{M} = 9.932 \times 10^{-3} \text{ rev/day/day}$ , an area-to-mass ratio for the DM of  $0.030 \text{ cm}^2/\text{g}$  was derived.

Once the pass biases, the area-to-mass ratio, and the orbital elements had all been estimated from the orbital processor, the final orbit determinations were performed by means of a precision numerical-integration package. This package consisted of a core integrator program of the Adams-Moulton type developed at the NASA Jet Propulsion Laboratory; step size and integration order were automatically chosen according to the desired accuracy. The gravity field, which was obtained from reference 10-21, included spherical-harmonic coefficients through degree and order 12. To compute lunisolar forces, positions of the



Sun and Moon were derived from reference 10-22. Atmospheric drag  $D$  was given by (ref. 10-20)

$$D = \frac{dv^2}{2} \frac{A}{m} C_D \quad (10-21)$$

where  $v$  is the velocity of the satellite and  $C_D = 2$ . The atmospheric density variation over the orbit was represented by a polynomial in time fitted with 1 percent accuracy to 500 points/rev along the nominal trajectory. The densities of these 500 points were calculated from Jacchia's static-diffusion model 39H.

Because an accurate area-to-mass ratio was not known for either satellite, the value of  $A/m$  selected was the one that minimized the standard error of the calculated orbit. Starting with an estimate of 0.030 from the orbit-computation program, the investigators varied the value of  $A/m$  for the DM from 0.01 to 0.06. The standard error of the DM orbit had a minimum value of approximately 10 m for  $A/m = 0.035 \text{ cm}^2/\text{g}$ . The CSM area-to-mass ratio was taken as  $0.002 \text{ cm}^2/\text{g}$ , and varying it had little effect. The mean elements for the DM and the CSM are given in table 10-II. Orbits for the DM were calculated every 0.2 day, and the orbital elements are plotted in figure 10-11. Table 10-III contains the initial conditions used in the numerical-integration program.

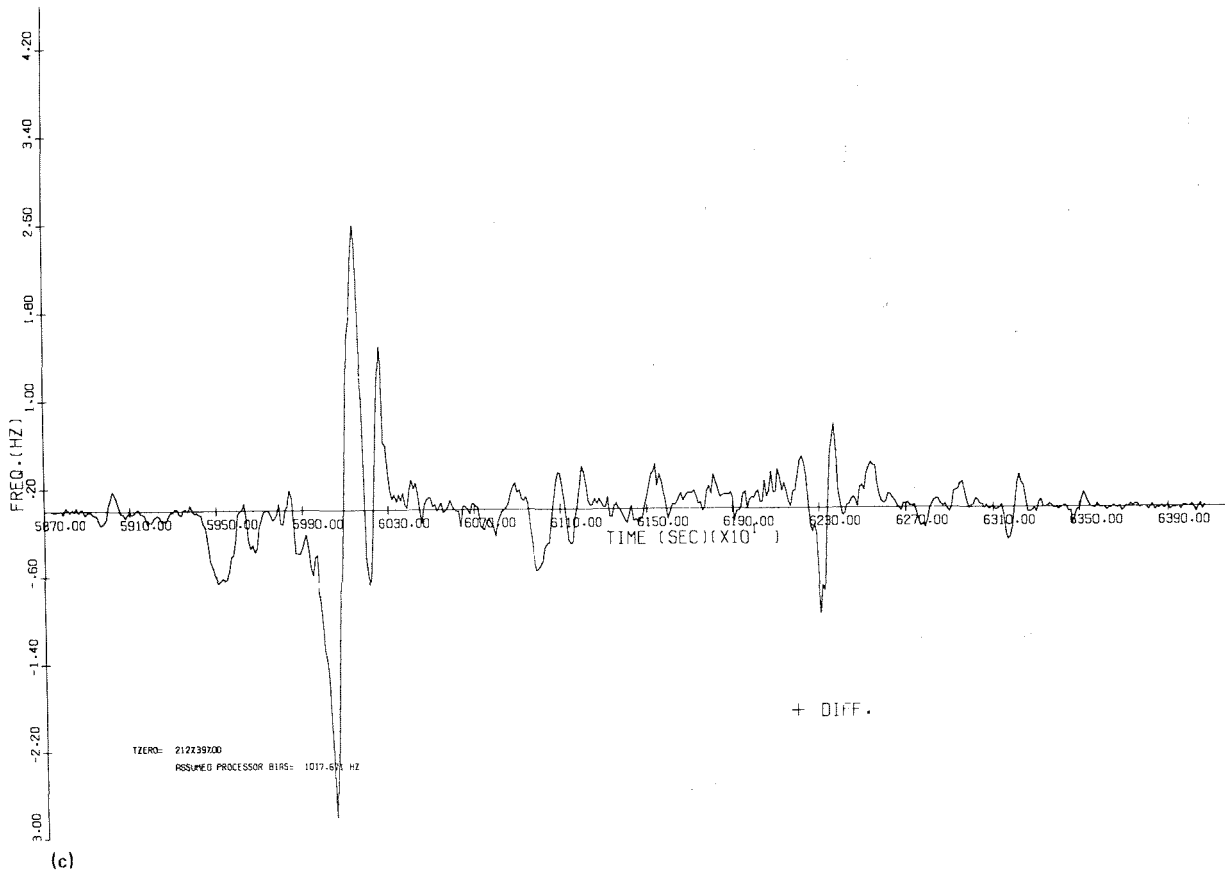


FIGURE 10-9.—Continued.

TABLE 10-II.—Instantaneous Elements for the  
DM and the CSM

[Epoch = 42617.008305567 MJD]

Element	DM	CSM
X, cm .....	$3.369937 \times 10^8$	$3.478627 \times 10^8$
Y, cm .....	$4.567079 \times 10^8$	$4.345419 \times 10^8$
Z, cm .....	$-3.352690 \times 10^8$	$-3.531287 \times 10^8$
$\dot{X}$ , cm/sec .....	$-2.859357 \times 10^5$	$-2.672850 \times 10^5$
$\dot{Y}$ , cm/sec .....	$5.536761 \times 10^5$	$5.779922 \times 10^5$
$\dot{Z}$ , cm/sec .....	$4.650151 \times 10^5$	$4.461675 \times 10^5$

TABLE 10-III.—Orbital Data for the DM  
and the CSM

[Epoch = 42617.008305567 MJD]

Orbital element	DM	CSM
Semimajor axis, km ...	6590.818	6590.843
Eccentricity .....	0.001194	0.001237
Inclination, deg .....	51.7704	51.7657
True anomaly, deg ....	98.984865652	97.558757298
Longitude of ascending node, deg .....	81.3086	81.3114
Argument of perigee, deg .....	220.5304	219.3008

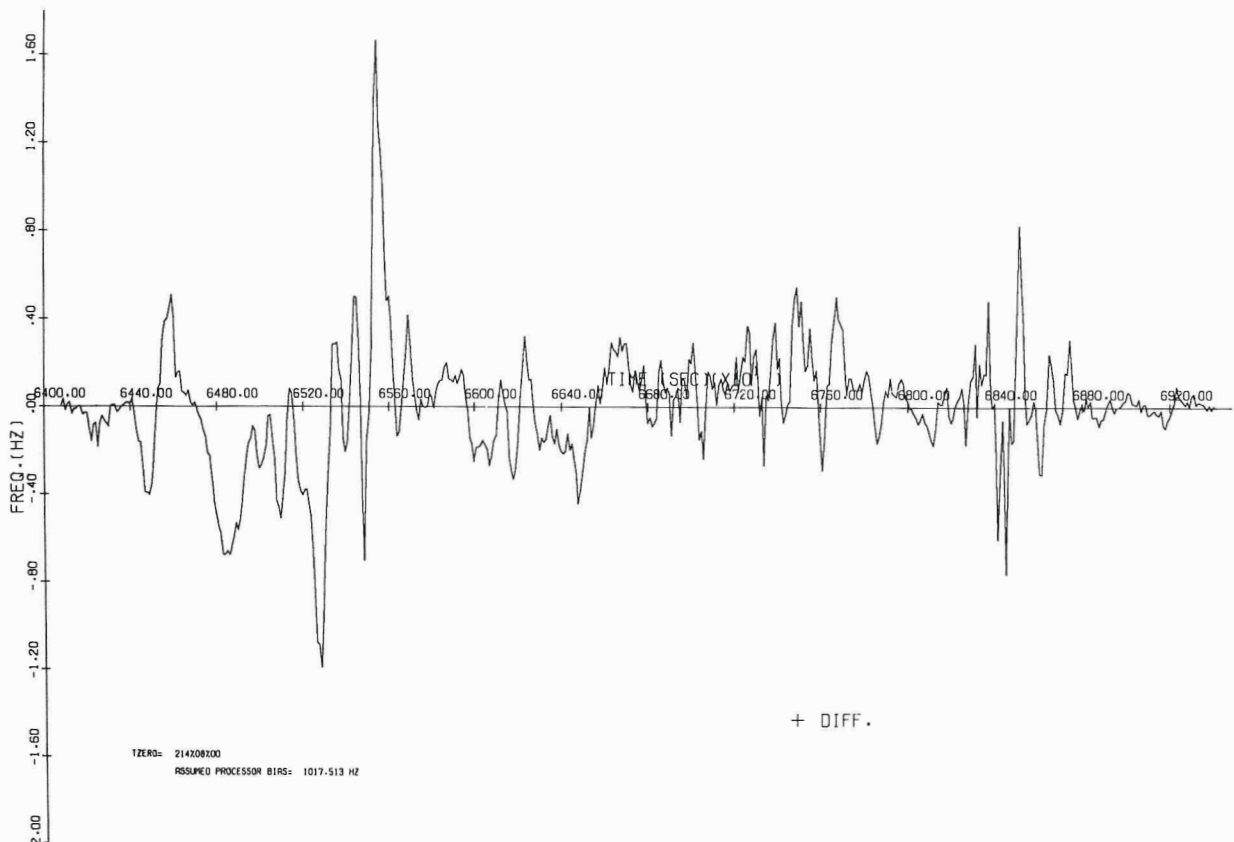


FIGURE 10-9.—Concluded.

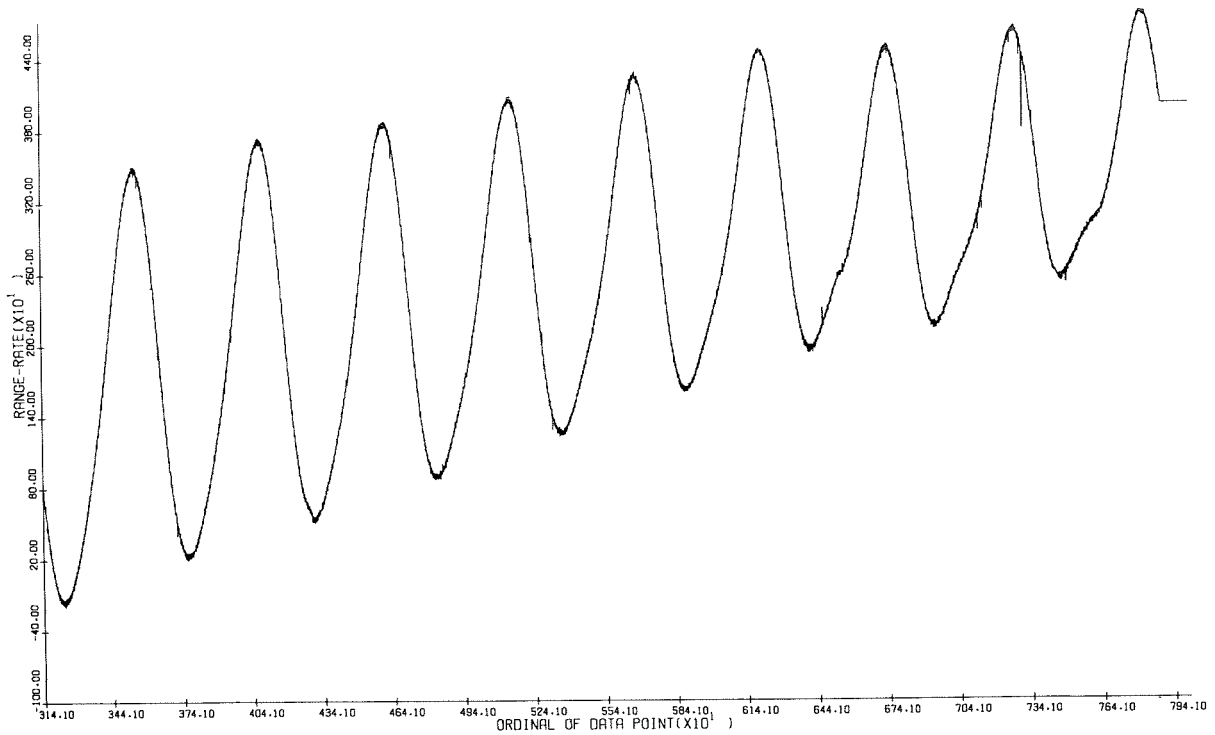
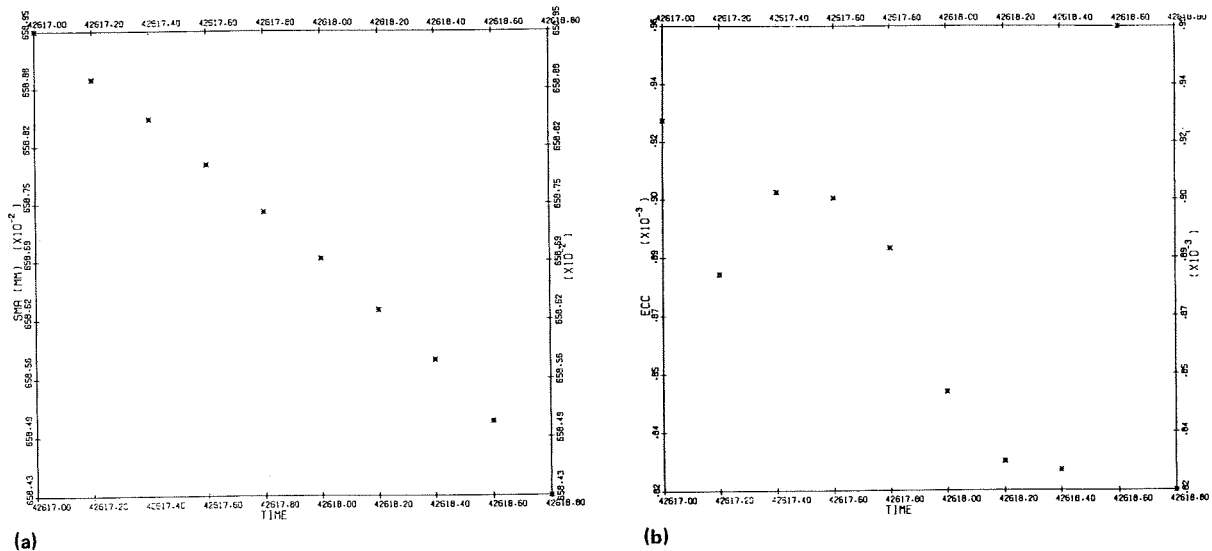


FIGURE 10-10.—Doppler data after removal of ionospheric contribution showing large-scale variations.



(a)

(b)

FIGURE 10-11.—Mean orbital elements for the DM plotted every 0.2 day. Times are modified Julian days. (a) Semimajor axis. (b) Eccentricity. (c) Inclination. (d) Longitude of ascending node. (e) Argument of perigee.

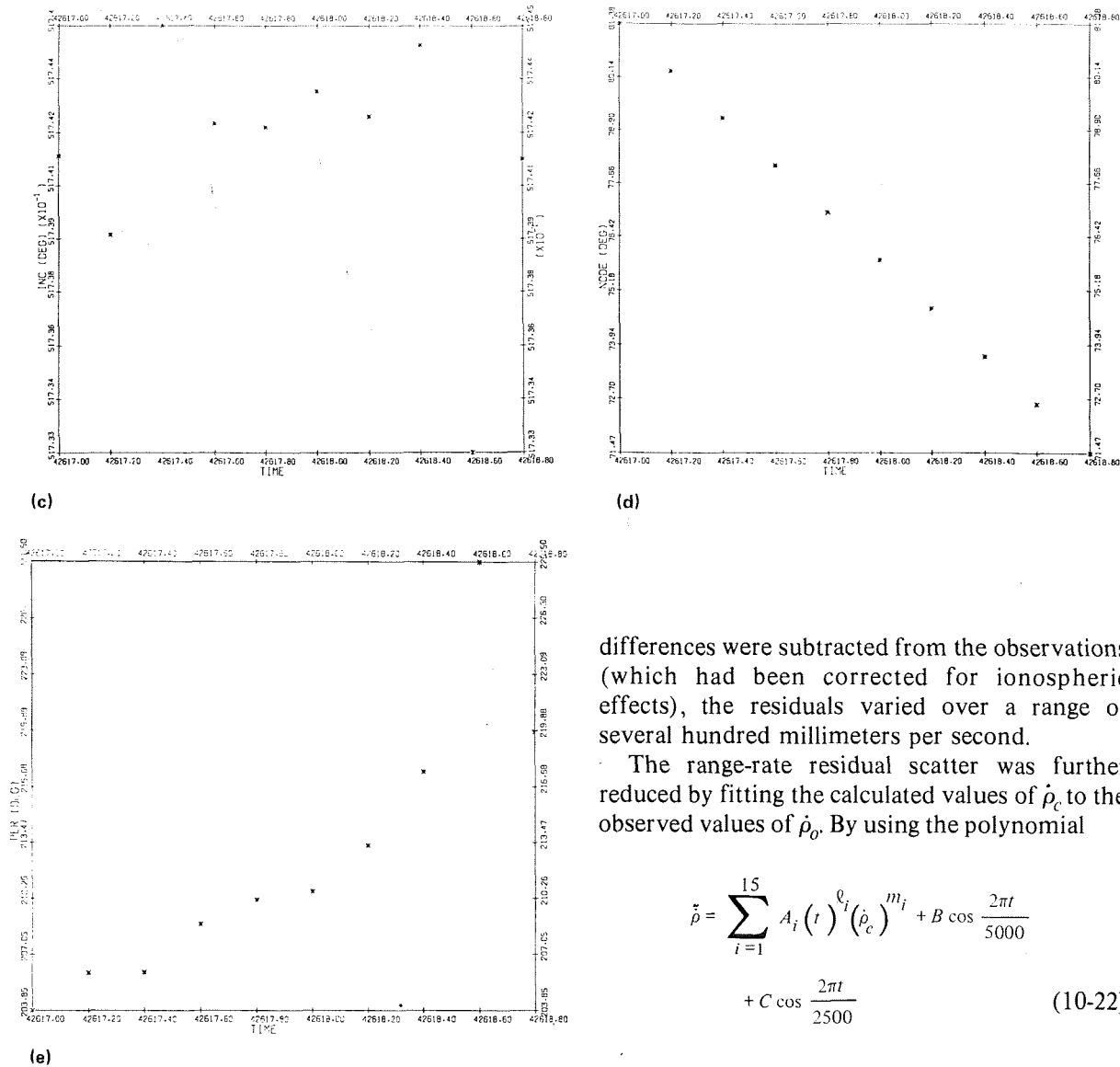


FIGURE 10-11—Concluded.

### Comparison of Calculated and Observed Range Differences

Once the initial conditions were established, an ephemeris for each spacecraft was calculated. This ephemeris was the basis from which a predicted DM/CSM "Doppler signal" was computed for every 10-second interval throughout the lifetime of the experiment. When these calculated range

differences were subtracted from the observations (which had been corrected for ionospheric effects), the residuals varied over a range of several hundred millimeters per second.

The range-rate residual scatter was further reduced by fitting the calculated values of  $\dot{\rho}_c$  to the observed values of  $\dot{\rho}_o$ . By using the polynomial

$$\begin{aligned} \dot{\rho} = & \sum_{i=1}^{15} A_i (t)^{\ell_i} (\dot{\rho}_c)^{m_i} + B \cos \frac{2\pi t}{5000} \\ & + C \cos \frac{2\pi t}{2500} \end{aligned} \quad (10-22)$$

where  $2\pi t$  is the orbital period and the values of exponents  $\ell_i$  and  $m_i$  ranged from 1 to 4, and where  $A_i$ ,  $B$ , and  $C$  were determined in an iterative manner by means of a least-squares estimator. This process was repeated eight times, by using  $\widehat{\dot{\rho}_c}$  as a new value for  $\dot{\rho}_c$  each time, to reduce the scatter in the observed residuals minus the computed residuals to 20 mm/sec. The "corrections"  $\Delta v$  added to the range rate  $\dot{\rho}_c$  calculated from the two orbits were then subjected to a Fourier analysis to ensure that the estimator had suppressed only the orbital component of the intervehicular range rate and had not introduced any "high-frequency"

components (wavelengths shorter than approximately 1000 seconds) that might be mistaken for gravity anomalies.

amplitudes, periods, and phases of the rotational range-rate components. The form of the polynomial was

### Determination of CSM and DM Rotation

A significant contribution to the residual scatter arises from the fact that the observed range differences were from antenna to antenna, whereas the calculated differences were between the centers of mass of the CSM and the DM. Therefore, the next step was to model the motions of the antennas relative to the centers of mass so that their effects could be removed from the residuals.

Because the receiving antenna was so nearly on the line between the centers of mass of the two spacecraft, CSM rotational motions greater than  $0.1^\circ/\text{sec}$  over 10-second intervals would be required to generate Doppler signals of 1 mm/sec. Fourier spectra of the rate-gyro data were examined together with the data. Since no evidence of motions approaching  $0.1^\circ/\text{sec}$  was found (except when the CSM was maneuvered to reacquire Applications Technology Satellite 6 after the astronauts' sleep period), no further effort was devoted to modeling CSM motions.

The DM signature was determined by finding the periods of the dynamical motion for individual segments of the data-take interval. Segmentation boundaries were closed on the times of entry into and exit from the Sun-Earth shadow. A nonlinear least-squares polynomial processor was developed and employed to determine the

$$\begin{aligned} \dot{\rho} = & A_1 \cos \frac{2\pi t}{P+p} + A_2 \cos \frac{2\pi t}{P-p} + \dot{A}_3 \cos \frac{2\pi t}{P} \\ & + A_4 \cos \frac{2\pi t}{\frac{P}{2}} + A_5 \cos \frac{2\pi t}{\frac{P}{3}} + A_1 \sin \frac{2\pi t}{P+p} \\ & + A_2 \sin \frac{2\pi t}{P-p} + A_3 \sin \frac{2\pi t}{P} + A_4 \sin \frac{2\pi t}{\frac{P}{2}} \\ & + A_5 \sin \frac{2\pi t}{\frac{P}{3}} \end{aligned} \quad (10-23)$$

where  $P$  is the period of rotation and  $p$  is the period of nutation, or coning. The DM rotational period was close to 72 seconds, but both periods increased with time. By assuming a linear increase,  $\dot{\rho}_{DM}$  was calculated for each data point and removed from the residuals. These steps reduced the scatter by a factor of 2.

Finally, the baseline was flattened by a 40-point averaging technique, and a filter to remove periods shorter than 50 seconds was applied. By this means, residuals were reduced to an rms amplitude of 6.5 mm/sec.

A sample of the reduced data is shown in figure 10-12. A Fourier spectrum of the entire data run is shown in figure 10-13. Times of the data take and other information are given in table 10-IV.

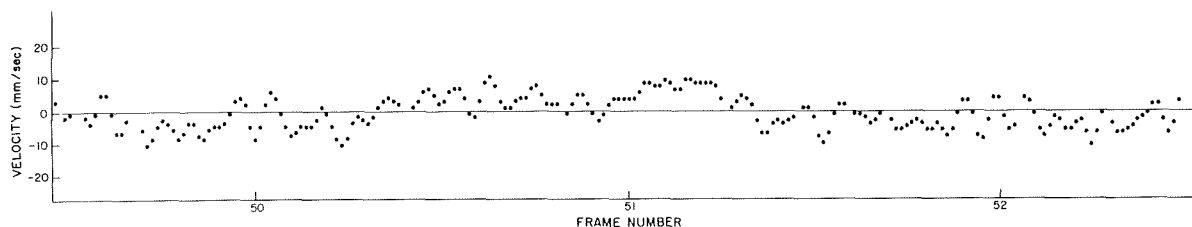


FIGURE 10-12.—Sample of reduced Doppler data. The ordinate is the relative velocity between spacecraft during revolution 126.

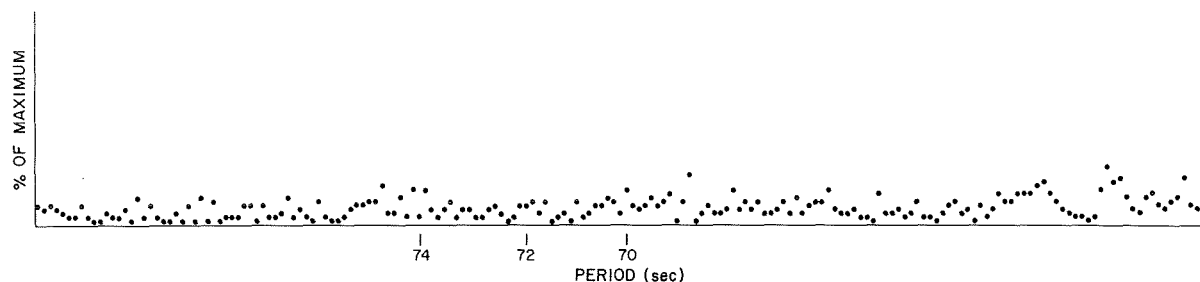


FIGURE 10-13.—Fourier spectrum of reduced Doppler data.

TABLE 10-IV.—Times of Data Take  
[July 24, 1975]

Revolution number	Revolution start time, UT, hr:min	Frame/word at meridian crossing
126	00:56	47/31
127	02:34	54/50
128	04:12	61/69
129	05:47	69/15
130	07:20	76/34
131	08:52	83/56
132	10:24	91/03
133	11:58	98/22
134	13:34	105/41

## RESULTS

The results of this rather involved analysis are discussed in two main parts. The first refers to the ionospheric observations, highly successful though not completely analyzed. The second part describes the inconclusive search for gravity signatures in the satellite-to-satellite velocity data.

The experiment design anticipated a signal-to-noise ratio near 1. With data from other sources — the Goddard Geodynamics Experiment (MA-128), surface-gravity measurements, or GEOS-3 altimetry, for example — or with a longer data take, unambiguous identification of gravitationally induced velocity variations would be possible and, thereby, the feasibility of this technique could be demonstrated. Unfortunately,

noise levels more than twice the value expected precluded such positive identifications.

## Early Results From the Ionospheric Experiment

Differential Doppler data were collected in both DM-to-CSM and DM-to-Earth paths by using the links shown schematically in figure 10-14. The goals of the ionospheric experiment were as follows (refs. 10-18, 10-19, 10-23, and 20-24):

1. To measure the time changes of the columnar electron content between the two spacecraft, from which horizontal gradients of electron density at the height of 220 km (along the orbital path of the CM/CSM pair) could be derived.

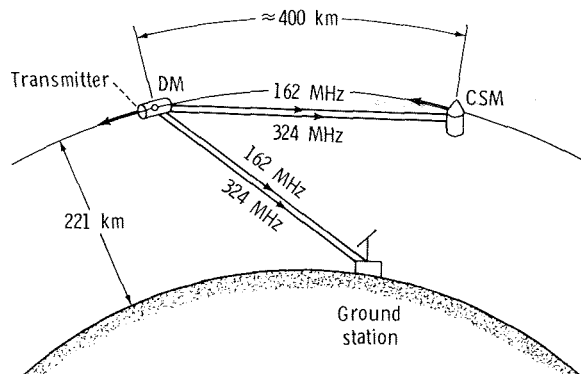


FIGURE 10-14.—Schematic diagram of Doppler links.

2. To measure the time changes of the spacecraft-to-ground columnar electron content, from which an averaged columnar content and the electron density at the DM could be derived under some simplifying assumptions. (Because horizontal gradients at orbital heights were measured simultaneously, a secondary goal was to investigate the increase in accuracy obtained by performing these inversions.)

3. To observe traveling ionospheric disturbances with both the DM-to-CSM and the DM-to-Earth links.

4. To detect boundaries of turbulent regions of the ionosphere, such as the aurora oval and the equatorial region.

The data-collection phase of the experiment was highly successful. The DM-to-CSM link collected samples of differential Doppler data over a period of nearly 14 hours from nine orbital revolutions on July 24. Through the courtesy of the Defense Mapping Agency, DM dual-frequency emissions were recorded on Earth by eight Tranet and geociever tracking stations on 235 passes. Table 10-III contains orbital data for both the DM and the CSM.

Consistent with preflight expectations, the resolution of the Doppler measurements was  $1\sigma \approx 3$  mHz in 10-second integration time. The oscillators of the Doppler links performed as specified, with a stability of a few parts in  $10^{12}$  over a 10- to 100-second integration interval.

Block diagrams of the instrumentation can be found in reference 10-23. Figure 10-15 is a schematic representation of the raw data used in the experiment, and the data-reduction and data-processing flow adopted is shown in figure 10-16.

The differential Doppler shift is defined as  $\delta\dot{\Phi} = \dot{\Phi}_1 - (f_1/f_2)\dot{\Phi}_2$  where  $\dot{\Phi}_1$  and  $\dot{\Phi}_2$  are the Doppler shifts at the higher ( $f_1$ ) and lower ( $f_2$ ) frequencies of the link. In this case,  $f_1 = 324$  MHz and  $f_2 = 162$  MHz; therefore,

$$\delta\dot{\Phi} = \dot{\Phi}_1 - 2\dot{\Phi}_2 \quad (10-24)$$

In the path from the DM to the CSM, the following relationship applies:

$$\delta\dot{\Phi} = \left( 40.3/2\lambda_1 \right) \left[ \left( 1/f_2^2 \right) - \left( 1/f_1^2 \right) \right] d/dt \int_{DM}^{CSM} N ds \quad (10-25)$$

where wavelength  $\lambda_1 = c/f_1$ ,  $c$  being the velocity of light in free space.

Under the assumptions that the two terminals of the link were in nearly coincident circular orbits and that the temporal variations of the ionosphere could be disregarded while the Doppler samples were being taken, the differential Doppler shift  $\delta\dot{\Phi}$  is a measure of the electron-density gradients at the ASTP orbital altitude averaged over a length  $\Delta x$  corresponding to the integration time of the Doppler sample:

$$\frac{\partial N}{\partial x} = \frac{\lambda_1 f_1^2 f_2^2}{40.3(f_2^2 - f_1^2)} \frac{\delta\dot{\Phi}}{v_0 \Delta x} \quad (10-26)$$

where  $v_0$  is the common orbital velocity of the two terminals. The applicable equations for DM-to-Earth paths are provided in reference 10-25.

Figures 10-17 and 10-18 represent the DM-to-CSM differential Doppler records obtained during revolutions 127 and 131. Table 10-IV contains the starting time of each orbit and the serial number of the frame and word recorded when the DM crossed the meridian containing the subsolar point (SSP). Each frame has 73 words, each 10 seconds long, so that, for example, the start of revolution 126 corresponds to  $(47 \times 73 + 31) \times 10 = 34\,620$  seconds from reference time zero, which was set at the beginning of the link operation.

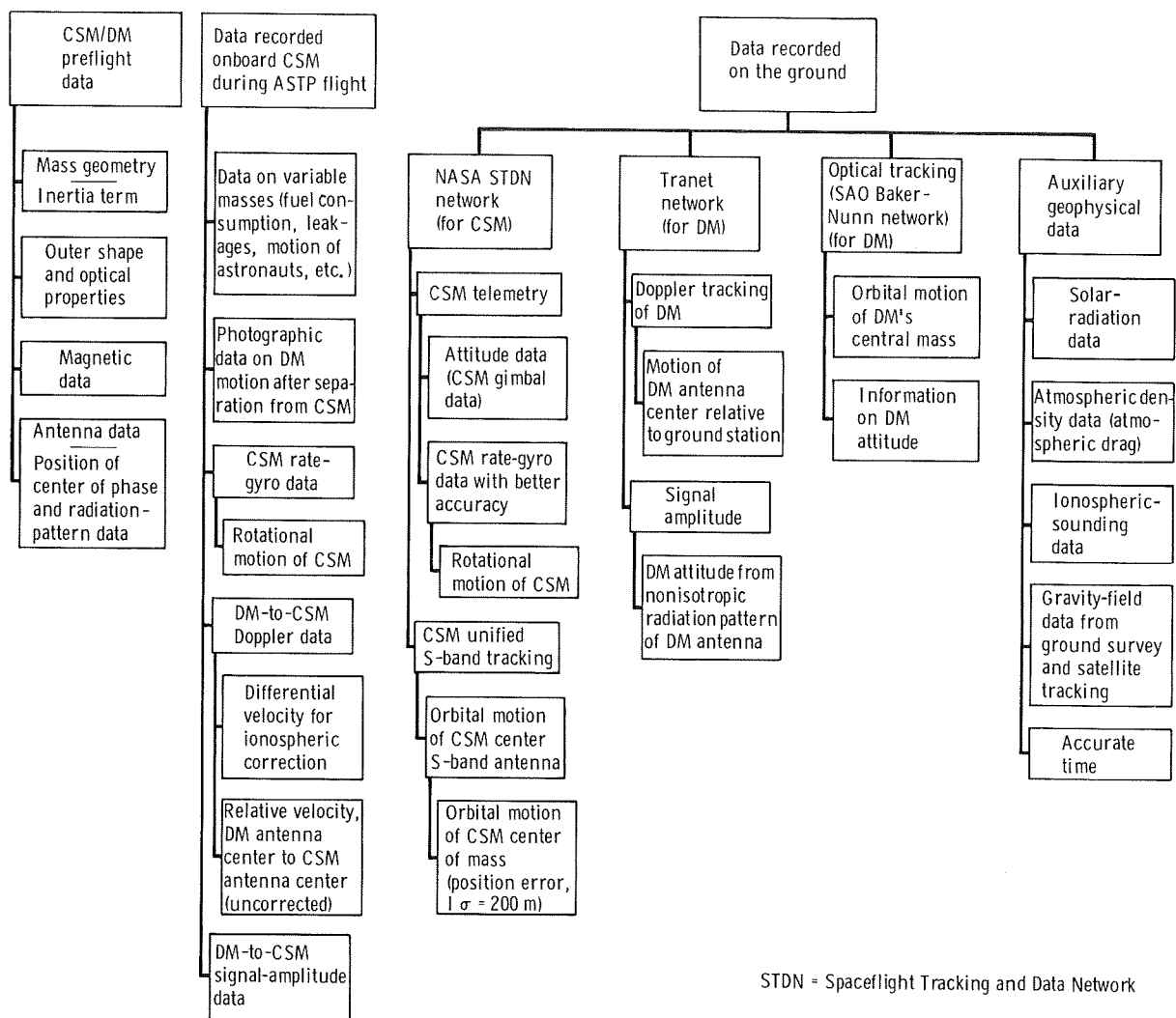


FIGURE 10-15.—Block diagram of the raw data.



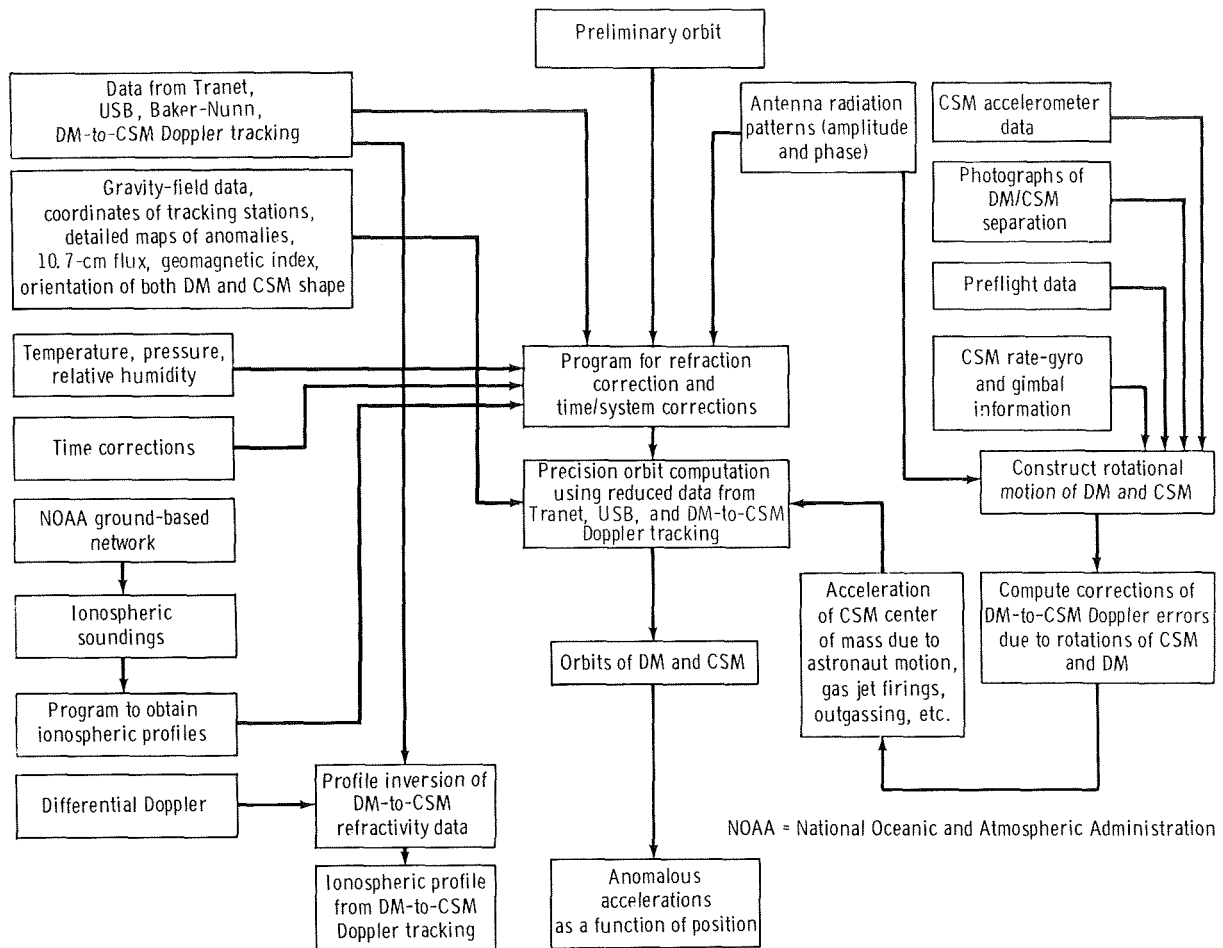


FIGURE 10-16.—Simplified diagram of data reduction and processing.

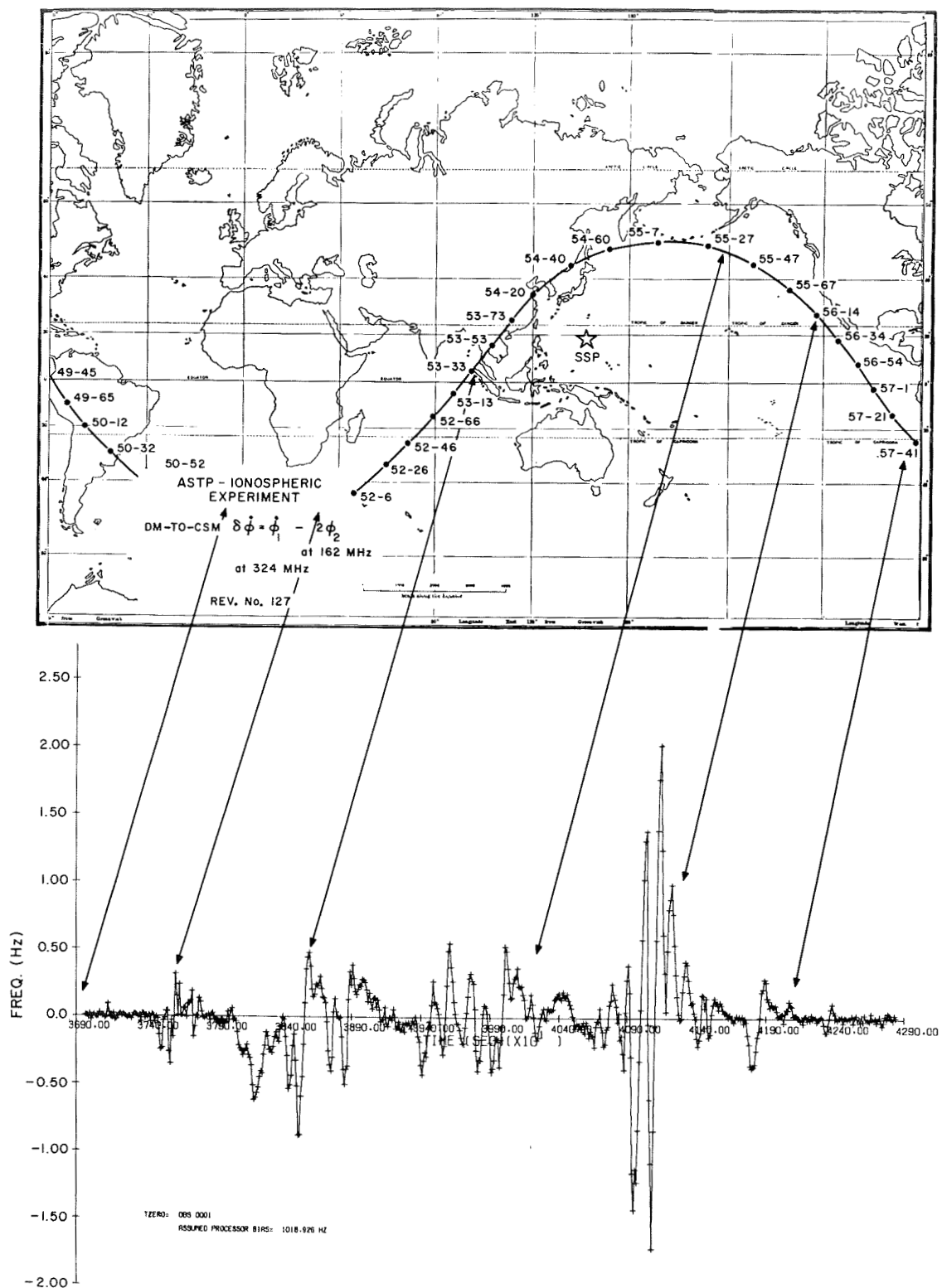


FIGURE 10-17.—Map of revolution 127 with differential Doppler plot.

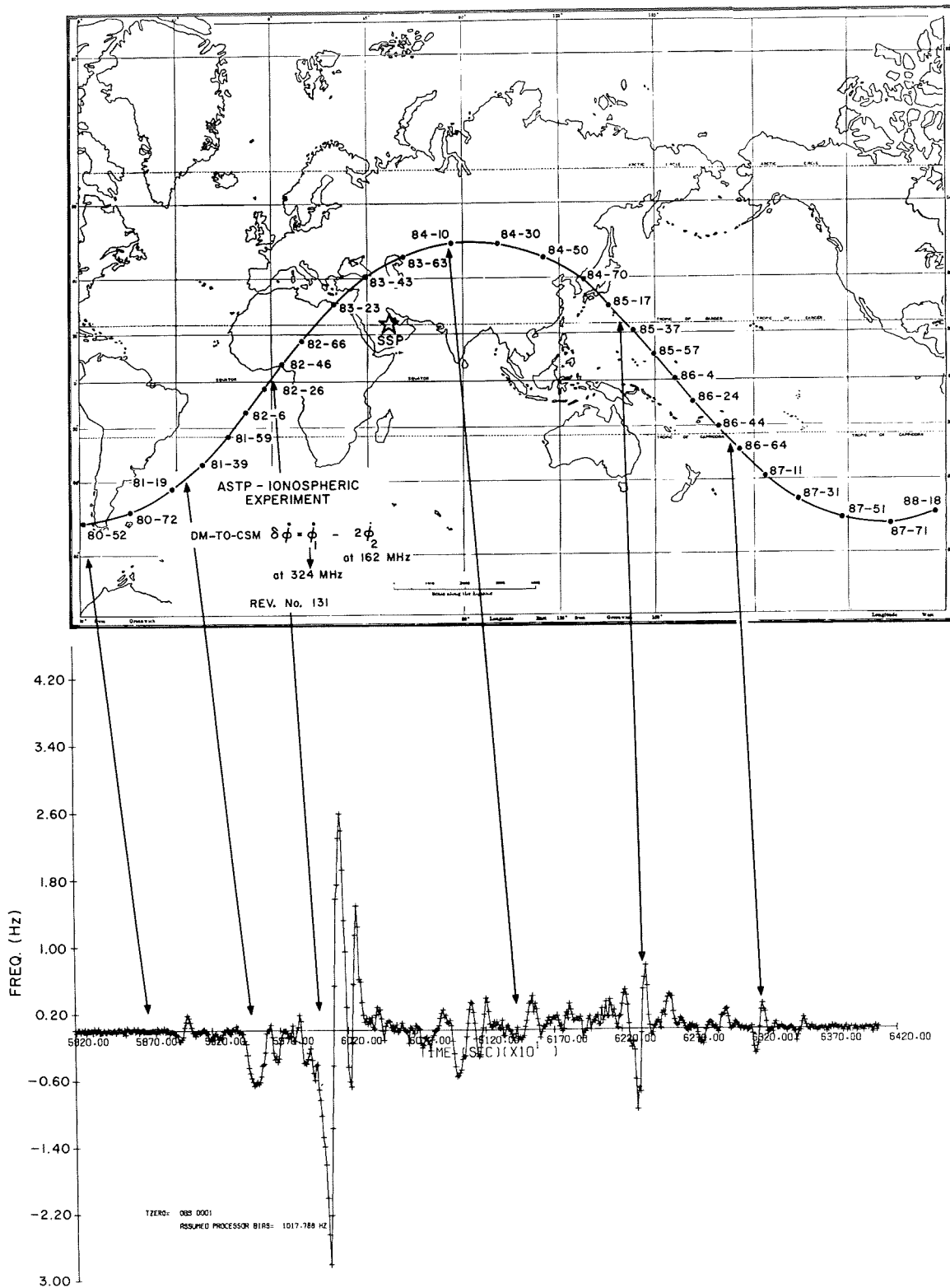


FIGURE 10-18.—Map of revolution 131 with differential Doppler plot.

It can be seen that sharp horizontal gradients of electron density have been detected. From equation (10-26),  $\partial N / \partial x = 2.62 \times 10^5 \times \delta \Phi$  electrons/m<sup>3</sup>/m. The figures show that gradients as large as  $\approx 10^6$  electrons/m<sup>3</sup>/m are not uncommon for a day such as July 24, which was magnetically quiet and was characterized by an electron density at a 220-km height that varied from  $\approx 3 \times 10^9$  electrons/m<sup>3</sup> (nightside) to  $\approx 5 \times 10^{11}$  electrons/m<sup>3</sup> (dayside). Most of the gradients are encountered at the equatorial crossings and are most likely related to the equatorial F-layer irregularities.

The nine-cycle waveform shown in figure 10-17 is suggestive of a dayside traveling ionospheric disturbance characterized by the following parameters (preliminary model).

<i>Parameter</i>	<i>Value</i>
Apparent spatial wavelength along the orbital track at 220-km height, km.....	$\approx 800$
Estimate of the spatial wavelength as it would be observed from the ground, km.....	690
Spatial extent along the orbital track at 220-km height, km.....	$\approx 7200$
Estimate of peak-to-peak electron-density perturbation, percent....	35
Estimate of velocity, m/sec.....	$\approx 700$
Estimate of the period as it would be observed from the ground, min.....	16

During the ASTP ionospheric experiment, the first spacecraft-to-spacecraft horizontal sounding of the ionosphere at a height of 220 km was performed. In addition, data were acquired that are expected to add new and useful information to the literature on ionospheric electron-density structures at a height that is important and that had never been probed before. Furthermore, it is expected that the experiment will contribute to a better understanding of the manner in which

horizontal gradients of electron density influence the accuracy of ionospheric columnar measurements performed by transmitting radio emissions from satellites to the Earth.

At the time this report was written, analysis was continuing both for the data collected with the DM-to-CSM link and for the space-to-ground data collected by the ground-based network of stations that participated in the experiment.

### Results From the Gravimetric Experiment

Among the effects controlling the satellite-to-satellite relative velocity are local variations in gravity. Experiment MA-089 was designed to detect anomalous gravity, i.e., gravity-field variations having wavelengths between 250 and 1000 km. The observed Doppler shift, or velocity difference, also contains other large variations due to the gross relative orbital motion and to the relative motion of the transmitting and receiving antennas with respect to the centers of mass of the CSM and the DM. Additional contributors to the observed relative velocity are the radiation patterns of the antennas and other accelerations on the vehicles (such as air drag, radiation pressure, and astronaut motion). As the analysis proceeded, each of these effects was eliminated, leaving a clean Doppler signal that was free of all extraneous effects and contained the Doppler shift due to anomalous gravity.

*Estimated gravity signal.*—In the section entitled “The Gravity Field From Satellite-to-Satellite Velocity Measurements,” general considerations were used to estimate the gravity signal expected to be detected by means of Experiment MA-089. More detailed simulations were performed during the data-analysis phase of the experiment. These simulations included the actual satellite configuration and physical characteristics, such as the area-to-mass ratio, and environmental factors, such as the atmospheric density. From these simulations, for example, for a satellite spacing of 310 km, a satellite height of 210 km, and a gravity anomaly of 1 mm/sec<sup>2</sup> (100 mgal) in a 100-by 100-km block, a peak-to-peak variation of 1.00 mm/sec should be observable when the satellite pair is directly over an anomaly. Such anomalies

are common; 69 anomalies greater than 1.5 mm/sec<sup>2</sup> (150 mgal) have been observed in terrestrial data, and fourteen 100- by 100-km anomalies greater than 2 mm/sec<sup>2</sup> (200 mgal) have been found. For a 300- by 300-km, 1-mm/sec<sup>2</sup> (100 mgal) anomaly, the peak-to-peak variation would be 7.05 mm/sec; no anomalies of this size and magnitude have been observed. Although detailed calculation of the peak-to-peak variation in velocity requires use of numerical-integration programs, it can be approximated by

$$\Delta v \propto \frac{L^2}{2} \frac{\Delta g_0}{r^3} x \frac{\Delta x}{r^3} \quad (10-27)$$

Here,  $L$  is the half-width of the mean gravity anomaly  $\Delta g_0$ ,  $x$  is the downtrack distance,  $r$  is the distance of the midpoint of the two satellites from the anomaly, and  $\Delta x$  is the distance between the spacecraft. Therefore, the signal is roughly proportional to the gravity anomaly and the spacecraft spacing and is proportional to the square of the anomaly size.

The preceding estimate is a measure of the effect of a single gravity anomaly. Because Experiment MA-089 was sensitive to many anomalies, a granularity was produced in the observed Doppler signal. The root mean square of this granularity was calculated for a number of orbital tracks from a fine-grained gravity model based on the observed 1° by 1° anomalies. The additional short-wavelength signal has an rms of 2.1 mm/sec.

*Error budget.*—When the 11 000-second duration of data take (while the CSM and the DM were still connected) was adopted as the integration time, an rms noise level of 2.26 mm/sec was found. When an integration time of 10 to 100 seconds was used, a noise level of 1.8 mm/sec was obtained. These results are consistent with the expected behavior of the oscillator at the two integration times considered. These data are shown in figure 10-19. The Fourier transform of the 11 000-second-long sample has little structure, with a mild maximum near 300 seconds. Since the signal strength during this data-take interval was very large, the previously indicated noise levels can be attributed to oscillator stability.

A worst-case signal-to-noise ratio for the data with the CSM antenna misaligned by 35° with respect to the DM and with no multipath is as follows:

Separation	162 MHz	324 MHz
350 km	37 dB	31 dB
500 km	33 dB	27 dB

System design required, as a minimum, a 22-dB signal-to-noise ratio. For a worst-case 500-km separation, the contribution is 2.32 mm/sec.

The multipath effects are variegated; first of all, they influence the signal-to-noise ratio as follows:

Separation	162 MHz	324 MHz
350 km	29 dB	23 dB
500 km	23 dB	17 dB

In addition, there is a multipath-induced error due to the erratic behavior of a phase-lock loop if several carriers are present within its bandwidth. Multipath, if present, would boost the total error to 3.50 mm/sec. However, multipath can occur only over the ocean, which is a good reflecting surface for very high frequencies. No discernible difference appeared between the noise level over land and that over oceans, so multipath was ruled out.

Therefore, an expected signal of 2.1 mm/sec, for a 1-mm/sec<sup>2</sup> (100 mgal) anomaly, and an expected noise of 2.32 mm/sec produce a signal-plus-noise to noise ratio of only 1.26 in a 100-second integration time. Consequently, Experiment MA-089 can be expected to reveal reliably only gravity signatures larger than 1 mm/sec<sup>2</sup> (100 mgal), and those are, unfortunately, not expected to be numerous.

*Data analysis.*—The Doppler signal observed after ionospheric effects had been removed is given in figure 10-10. The data spanned 48 910 seconds with 4891 data points, and 83 individual points were eliminated. The equipment lost lock twice. The relative velocity of the two spacecraft is quite evident in the figure, thus demonstrating to zeroth order that the experiment obtained good data.

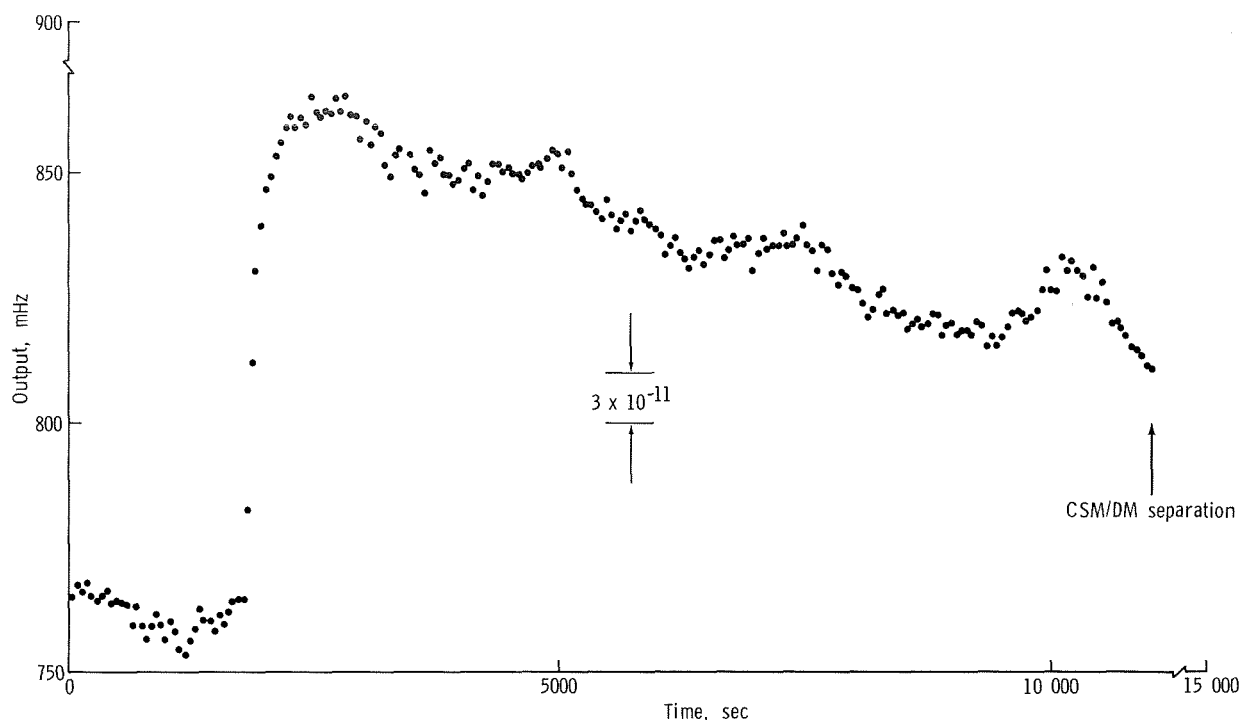


FIGURE 10-19.—Initial 11 000 seconds of 324-MHz Doppler data. Vertical scale shows the output of the receiver Doppler processor with a 1020-Hz instrument bias subtracted.

As described in the section entitled "Data Reduction," the data were processed in a series of steps. In the first level, the gross orbital data were subtracted and an rms Doppler signal of 1.5 m/sec was left, consistent with the accuracy of the orbits derived from ground tracking data. These residuals are given in figure 10-20(a). The long-period orbital effects were further reduced by means of polynomial smoothing, in which the orbital velocity determined from ground tracking data was used as the argument. This smoothing effectively eliminated all observable orbital effects, leaving an rms signal of 49 mm/sec, as shown in figure 10-20(b).

The second level of processing removed the Doppler shift due to the rotation of the DM antenna about the center of mass and to the antenna pattern. A high-pass filter, designed to pass all frequencies in the Fourier transform with periods shorter than 400 seconds, was applied to all the data. This filtering corresponds, roughly, to eliminating gravity signatures 3000 km and longer. When the DM dynamics analysis was repeated by

using unfiltered data, the same results were found. The Fourier transform of these filtered data is given in figure 10-21, in which the spectral lines associated with the DM rotation are easily identified. The width of the lines is, in part, attributable to the facts that the rotational period of the DM continually increased during data acquisition and that the period changed discontinuously as the satellite passed from sunlight to Earth shadow.

Because of these two rotational-period effects, the velocity data were analyzed in sections. The orbit was divided into 17 intervals, 9 of complete Sun illumination and 8 of complete shadow. By using the periods and their rate of change determined by a Fourier transform of the data, the periodic velocity variations were computed and subtracted from the data. The periods of rotation for each Sun/shadow interval are shown in table 10-V. Amplitudes of the components are given in table 10-VI. The phase of each component is not given, since it refers to an arbitrary origin. The internal consistency of the amplitudes and the

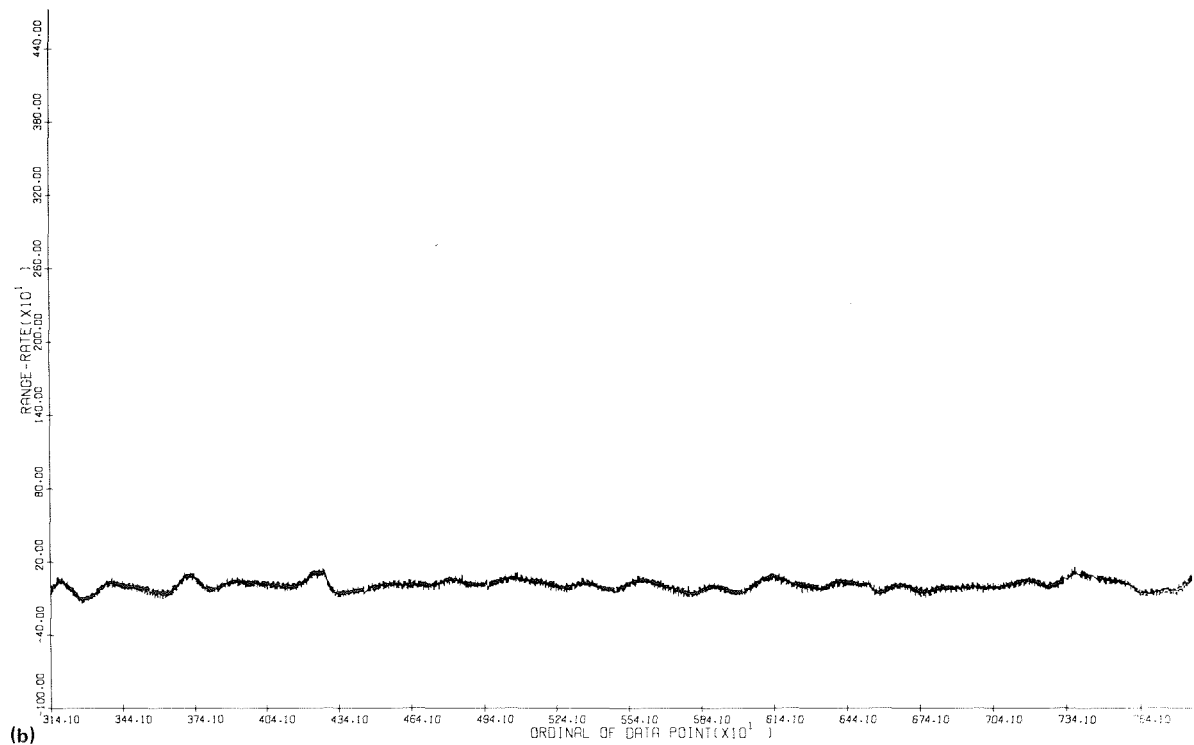
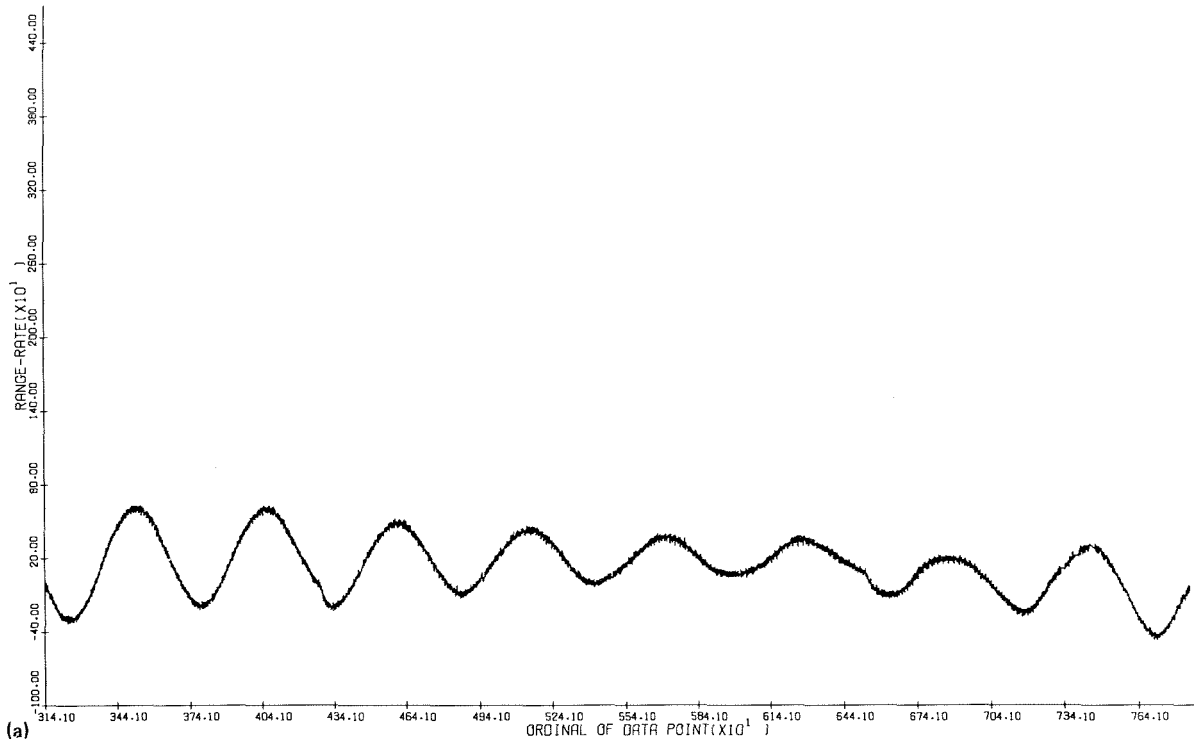


FIGURE 10-20.—Relative velocity after removal of ionospheric and orbital effects. (a) Before polynomial smoothing. (b) After polynomial smoothing.

periods strongly suggests that the investigators' understanding of the dynamics of the DM rotation and the antenna radiation pattern was correct. Figure 10-13 is a typical Fourier transform of one section of the reduced data. Table 10-VII also includes the rms signals for each subset of data; the values range from 9.41 to 11.80 mm/sec.

During data acquisition, the CSM was three-axis stabilized, rolling  $360^\circ$  per orbital revolution to keep the receiver antenna pointed toward the DM. A sample of rate-gyro data is shown in figure 10-22. Pitch and yaw were typically similar, seldom exceeding  $0.05^\circ/\text{sec}$ . Roll remained close to  $0.06^\circ/\text{sec}$ , the orbital rate.

Because the center of the receiving antenna was 475 mm from the center of gravity, measured along the longitudinal axis, a pitch rotation of  $0.05^\circ/\text{sec}$  would result in an antenna line-of-sight motion of only 0.4 mm/sec. Simultaneous pitch and yaw could raise this value to approximately 0.6 mm/sec because the antenna was approximately halfway between the  $y$ -axis and the  $z$ -axis. Because of the small amplitude of these motions, they were not modeled.

The primary contribution from atmospheric density to the Doppler signal was at the orbital period. This information was completely removed during orbit computation, polynomial smoothing, and high-pass filtering. To contribute to the observed noise spectrum, any remaining local variations in atmospheric density would have to be of the order of the density with 100-km wavelength. Gravity waves or microstructures of this magnitude and wavelength are extremely unlikely at these altitudes.

From the Fourier spectra shown in figures

10-13 and 10-21, it can be seen that significant energy remains in the frequency band around  $1/24 \text{ sec}^{-1}$ . This energy could be residual noise from the 24-second signal generated by the third harmonic of the DM antenna radiation pattern or aliasing of periods shorter than  $1/f_m$ , the reciprocal Nyquist frequency. A high-frequency signal at this level is not anticipated to be due to the Earth's gravity field. In any event, this spectral energy was eliminated.

To remove the high-frequency noise, a filter, centered on 24 seconds, was constructed to subtract periods less than 30 seconds. This filter was applied  $n$  times to give an rms approaching  $(2.1^2 + 2.82^2)^{1/2} = 3.6 \text{ mm/sec}$ , corresponding to expectations. The resulting changes in the rms scatter are shown in table 10-VII.

A typical time history of the filtered data is given in figure 10-12, in which no obvious structure that could be interpreted as a gravity signal can be seen. As a further test of the validity of the observations, a predicted Doppler shift was generated from surface-gravity observations, and a

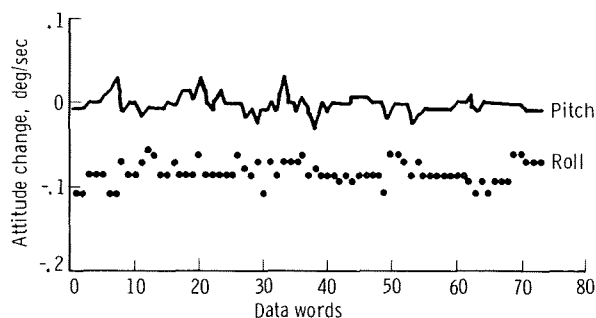


FIGURE 10-22.—Pitch and roll data for CSM from frame 60.

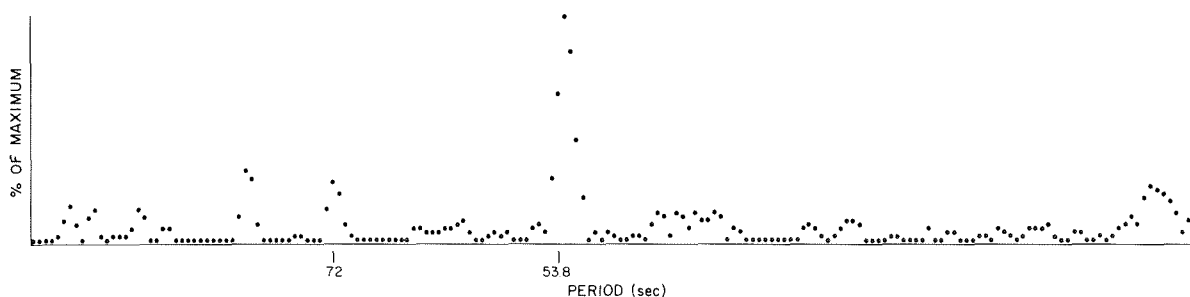


FIGURE 10-21.—Fourier spectrum of smoothed data showing effects of DM rotation.



TABLE 10-V.—DM Rotational Periods

Time, MJD	Interval	Periods, sec					State
		53	24	72	36	108	
42617.0699	1	53.094	23.656	71.457	35.908	108.609	Sunlight
42617.1060	2	53.222	23.755	71.345	34.930	109.155	Shadow
42617.1315	3	53.331	23.811	71.779	36.080	109.189	Sunlight
42617.1677	4	53.483	23.868	71.426	35.894	109.494	Shadow
42617.1931	5	53.547	23.940	72.016	36.246	109.661	Sunlight
42617.2293	6	53.695	23.993	71.763	36.019	109.952	Shadow
42617.2548	7	53.790	24.046	72.351	36.400	109.525	Sunlight
42617.2909	8	53.865	24.087	71.880	35.745	110.411	Shadow
42617.3164	9	53.953	24.168	72.562	36.542	109.828	Sunlight
42617.3525	10	54.049	24.188	72.202	36.065	110.709	Shadow
42617.3780	11	54.132	24.233	72.954	36.691	110.595	Sunlight
42617.4142	12	54.234	24.261	72.625	36.212	111.719	Shadow
42617.4396	13	54.343	24.388	73.303	36.795	111.107	Sunlight
42617.4758	14	54.359	24.398	72.812	36.816	111.770	Shadow
42617.5012	15	54.657	24.470	73.619	36.984	111.180	Sunlight
42617.5374	16	54.596	24.405	73.058	36.635	110.381	Shadow
42617.5629	17	54.844	24.560	73.820	37.133	111.766	Sunlight

TABLE 10-VI.—Amplitudes of DM Rotational Components for Five Periods

Time, MJD	Interval	Amplitude, mm/sec, for period of —				
		108 sec	72 sec	53 sec	36 sec	24 sec
42617.0699	1	6.33	4.82	19.62	5.74	6.73
42617.1060	2	5.76	5.13	19.98	6.68	6.05
42617.1315	3	5.58	5.00	19.91	5.58	7.33
42617.1677	4	5.50	4.19	20.59	5.39	6.58
42617.1931	5	5.90	5.54	18.80	5.60	7.55
42617.2293	6	5.62	5.14	20.16	6.14	6.58
42617.2548	7	6.14	5.08	18.88	5.36	7.70
42617.2909	8	5.38	4.72	19.73	6.47	6.81
42617.3164	9	5.29	5.45	19.73	5.90	8.00
42617.3525	10	5.24	5.38	20.63	7.24	7.85
42617.3780	11	5.24	5.15	19.59	5.78	8.30
42617.4142	12	5.00	5.20	20.96	7.39	8.75
42617.4396	13	5.82	5.50	20.00	6.32	6.66
42617.4758	14	5.20	6.26	17.93	7.41	8.23
42617.5012	15	4.55	6.09	18.73	5.69	6.73
42617.5374	16	3.98	3.15	15.84	5.13	7.10
42617.5629	17	5.20	6.07	17.50	8.80	8.45

TABLE 10-VII.—Root Mean Square of  $\dot{p}$   
Residuals After Multiple Filtering  
(Values in millimeters per second)

Interval	Number of filter applications				
	0	1	4	6	8
1	9.41	6.03	5.26	5.11	5.01
2	10.27	6.61	6.11	6.03	5.98
3	9.56	6.05	5.15	4.98	4.86
4	11.80	9.41	9.03	8.96	8.91
5	10.09	7.17	6.38	6.16	6.01
6	10.20	6.30	5.40	5.22	5.12
7	11.27	8.38	7.65	7.46	7.34
8	10.20	5.96	5.04	4.83	4.69
9	10.03	6.29	5.41	5.21	5.08
10	9.80	5.38	4.52	4.35	4.24
11	10.15	6.49	5.57	5.37	5.24
12	9.97	5.67	4.77	4.56	4.42
13	9.99	6.99	6.07	5.86	5.72
14	9.84	5.42	4.53	4.40	4.33
15	10.13	7.54	6.43	6.08	5.85
16	9.94	8.76	7.45	7.09	6.84
17	9.73	5.90	4.92	4.74	4.64

cross-correlation function, based on a single anomaly, was calculated. The result is a cross correlation not significantly different from zero; in other words, the predicted velocity would correlate equally well with many subsets of the data.

A summary of the data analysis appears in table 10-VIII, which gives the rms left after each step of the reduction. The noise remaining in the data is too large for any firm conclusion to be drawn about the Earth's gravity field.

## CONCLUSIONS

The Doppler Tracking Experiment had two goals: (1) to perform a feasibility test of the low-low satellite-to-satellite method as a scheme capable of measuring gravity-field anomalies and (2) to perform satellite-to-satellite horizontal sounding of the ionosphere.

The ionospheric data collected during the experiment are of excellent quality. The differential Doppler noise was as low as expected, and the experiment provided valuable satellite-to-satellite observations, never made before, of wave

phenomena occurring in the ionosphere at the ASTP orbital height.

The gravity data were, on the contrary, corrupted by a level of single-frequency Doppler noise higher than expected. No good explanation for this occurrence has yet been found, but whatever its origin, this high level of noise has thus far prevented any reliable identification of gravity-anomaly signatures in the data.

TABLE 10-VIII.—Root Mean Square of the  
Data After Each Analysis Step

Step	Effect removed	rms, mm/sec
1	Gross orbital motion	48
2	Low-frequency noise	18
3	DM rotation	<sup>a</sup> 7 to 12
4	High-frequency noise	3.6
Anticipated value		3.6

<sup>a</sup>After step 3, the noise level was too high for any signal to be observed. Presumably, step 4, consisting of four applications of a low-pass filter, in addition to eliminating the high-frequency noise, also removed an excessive amount of the desired signal.

## Ionospheric Experiment

The results of the ionospheric experiment are as follows:

1. Changes in the columnar electron content between the two spacecraft were accurately measured. From these, horizontal gradients of electron density at the height of 220 km were derived. Gradients as high as  $10^6$  electrons/m<sup>3</sup>/m were repeatedly observed both in the dayside ionosphere (typical density of approximately  $5 \times 10^{11}$  electrons/m<sup>3</sup>) and in the nightside ionosphere (typical density of approximately  $3 \times 10^9$  electrons/m<sup>3</sup>). Most of these gradients were encountered at the equatorial crossings and are most likely related to equatorial F-layer irregularities.

2. Traveling ionospheric disturbances were

detected. Most noticeable was a nine-cycle ionospheric wave found off the coast of California during revolution 127 (frame 56, word 14, July 24, 1975, 01:54:36 UT), characterized by a peak-to-peak electron-density perturbation of 35 percent, by a wavelength of 690 km (as the traveling ionospheric disturbance would be observed from the ground), and by a spatial extent of approximately 7200 km along the ASTP orbital track.

3. Spacecraft-to-ground differential Doppler data were collected for SAO by the Defense Mapping Agency from 235 passes of the docking module, covering the entire surface of the Earth. Although the processing of the data has not yet been completed, the investigators are confident that this part of the ASTP ionospheric experiment will contribute to the understanding of the manner in which horizontal gradients of electron density influence the accuracy of the ionospheric columnar measurements performed by using radio emissions from satellites to the Earth. The results of this part of the experiment will be published in the technical literature.

### Gravity Experiment

The gravity-experiment results are summarized as follows:

1. Detailed computations verified that a  $1\text{-mm/sec}^2$  (100 mgal),  $1^\circ$  by  $1^\circ$  gravity anomaly would give rise to a  $1.00\text{-mm/sec}$  peak-to-peak differential velocity for the two spacecraft.

2. The satellite-to-satellite range-rate measurement was made. The equipment revealed gross orbital motion, which was verified at a  $1\text{-m/sec}$  level with orbits determined independently from unified S-band and Doppler data. After the gross long-period effects had been eliminated with these independent orbits, the satellite-to-satellite data had an rms (signal plus noise) of  $48\text{ mm/sec}$ .

3. The differential Doppler signal due to the motion of the CSM about its center of mass was always within  $1\text{ mm/sec}$ , as specified.

4. The tumbling motion of the DM about its center of mass was very clearly discernible in the Doppler observations. The Fourier transform of the data is given in figure 10-21. The principal

periods were as follows:

<i>Approximate period</i>	<i>Phenomenon</i>
72 seconds	Spin rate around the CSM
208 seconds	Period of precession
53 seconds	Harmonics combination of 72- and 208-second periods
36 seconds	Second harmonic of the 72-second period due to tesseral harmonics of the antenna radiation pattern
24 seconds	Third harmonic of the 72-second period due to tesseral harmonics of the antenna radiation pattern

Detailed analysis of the Fourier spectra revealed a significant lengthening of the period over the lifetime of the mission and a significant change in the rotational period of the DM as it passed from shadow to sunlight and vice versa. Figure 10-23 contains the mean period for each complete sunlight and shadow portion. The consequence of this large variation is that the phase of the motion and, to a lesser extent, the amplitude are not preserved throughout the mission; therefore, analysis of each orbital segment must be performed separately.

5. Once the periodic motions were removed, the total system noise was found to be between  $9.41$  and  $11.80\text{ mm/sec}$  for each subset taken separately.

6. The Doppler residuals for a sample of the data set are given in figure 10-12. The remaining noise level, both from a scan of the figure and from the Fourier statistics, precludes an unambiguous detection of specific gravity anomalies. This fact applies to both filtered and smoothed data.

7. One explanation for the high noise level is the degradation of one or both of the satellite

oscillators. As discussed in the section entitled "Orbit Determination," frequency offsets were recovered from the ground tracking data. Although a relatively high rejection rate of passes did occur, the stability of the transmit oscillator was measured to be within specification.

8. The main conclusion is that the total system noise level was sufficiently large to prevent detection of gravity anomalies. Attempts to determine the source of the noise level were not successful. The Fourier spectra of the residuals revealed no significant energy density, showing only clustered broadband noise. The DM motion about its center of gravity has been completely understood, to the point of determining its physical parameters (moments of inertia, antenna position, spin rate, and antenna radiation patterns). Therefore, a plausible explanation for this high noise level remains unidentified as yet. It can be concluded that, with the spatial wavelength implied by the CSM/DM separation, gravity anomalies at the ASTP orbital height produce intervehicular range rates of less than 2.32 mm/sec. This undesirably high threshold sensitivity is, in part, determined by the fact that the stability of the oscillator worsens as the integration time increases beyond 100 seconds.

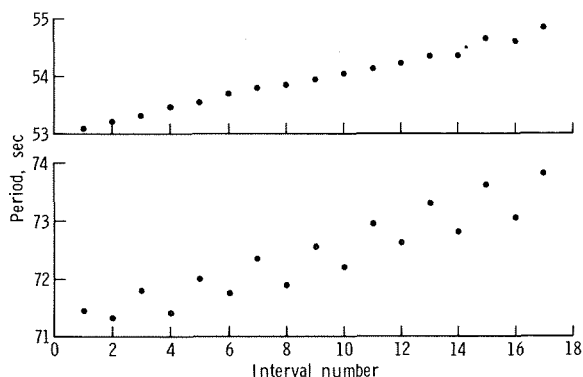


FIGURE 10-23.—Mean period for each sunlight and shadow portion of the DM rotation for 53- and 72-second periods. (See table 10-V.)

## REFERENCES

- 10-1. Isacks, Bryan; Oliver, Jack; and Sykes, Lynn R.: Seismology and the New Global Tectonics. *J. Geophys. Res.*, vol. 73, no. 18, Sept. 15, 1968, pp. 5855-5899.
- 10-2. Muller, P. M.; and Sjogren, W. L.: Mascons: Lunar Mass Concentrations. *Science*, vol. 161, no. 3843, Aug. 16, 1968, pp. 680-684.
- 10-3. Schwarz, C. R.: Gravity Field Refinement by Satellite to Satellite Doppler Tracking. NASA CR-117404, 1970.
- 10-4. Wolff, Milo: Direct Measurements of the Earth's Gravitational Potential Using a Satellite Pair. *J. Geophys. Res.*, vol. 74, no. 22, Oct. 15, 1969, pp. 5295-5300.
- 10-5. Comfort, G. C.: Direct Mapping of Gravity Anomalies by Using Doppler Tracking Between a Satellite Pair. *J. Geophys. Res.*, vol. 78, Oct. 10, 1973, pp. 6845-6851.
- 10-6. Vonbun, F. O.: The ATS-F/Nimbus-E Tracking Experiment. Rotation of the Earth, Paul Melchior and Shigeru Yumi, eds., D. Reidel Publ. Co. (Dordrecht, Holland), 1972, pp. 112-120.
- 10-7. Jackson, John E.; and Seddon, J. Carl: Ionosphere Electron Density Measurements With the Navy Aerobee Hi Rocket. *J. Geophys. Res.*, vol. 63, no. 1, Mar. 1958, pp. 197-208.
- 10-8. Seddon, J. C.: Propagation Measurements in the Ionosphere With the Aid of Rockets. *J. Geophys. Res.*, vol. 58, 1953, pp. 323-335.
- 10-9. Alpert, Ya. L.: A Method for Investigating the Ionosphere With Artificial Satellites. *Usp. Fiz. Nauk*, vol. 64, 1958, p. 3.
- 10-10. Alpert, Ya. L.: On the Results of Ionosphere Investigations With the Help of Coherent Radio Waves Emitted by Satellites. *Space Research V*, Proceedings of the Fifth International Space Science Symposium, D. S. King-Hele, P. Muller, and G. Righini, eds., North-Holland Publishing Co. (Amsterdam), 1965, pp. 652-686.
- 10-11. Alpert, Ya. L.: Radio Wave Propagation in the Ionosphere. *The Ionosphere*, vol. 1, second ed. Consultants Bureau (New York), 1973, pp. 61-77.

- 10-12. Alpert, Ya. L.: On Radio Methods of Ionospheric Investigations by Means of Coherent Radio Waves Emitted by Satellites. Paper presented at COSPAR/URSI Symposium on Beacon Satellite Investigations of the Ionosphere Structure and ATS-6 Data (Moscow), Nov. 1974.
- 10-13. Garriott, Owen K.: The Determination of Ionospheric Electron Content and Distribution From Satellite Observations, Part 1, Theory of the Analysis. *J. Geophys. Res.*, vol. 65, no. 4, Apr. 1960, pp. 1139-1150.
- 10-14. Garriott, Owen K.: The Determination of Ionospheric Electron Content and Distribution From Satellite Observations, Part 2, Results of the Analysis. *J. Geophys. Res.*, vol. 65, no. 4, Apr. 1960, pp. 1151-1157.
- 10-15. De Mendoza, F.: Ionospheric Studies With the Differential Doppler Technique. *Radio Astronomical and Satellite Studies of the Atmosphere*, J. Aarons, ed., American Elsevier (Amsterdam), 1963, pp. 289-312.
- 10-16. Misyura, V. A.; Solodovnikov, G. K.; and Migunov, V. M.: Gradients of the Integral Electron Content in the Ionosphere. *Geomagn. & Aeron.*, vol. 4, 1964, pp. 872-874. (Primary source—*Geomagn. i Aeronomiya*, vol. 4, 1964, pp. 1124-1126.)
- 10-17. Tyagi, T. R.: Determination of Total Electron Content From Differential Doppler Records. *J. Atmos. Terrestrial Phys.*, vol. 36, July 1974, pp. 1157-1164.
- 10-18. Grossi, Mario D.; and Gay, Ray H.: Doppler Measurements of the Ionosphere on the Occasion of the Apollo-Soyuz Test Project. Part I: Computer Simulation of Ionospheric-Induced Doppler Shifts. Special Rep. No. 366, Smithsonian Astrophysical Observatory (Cambridge, Mass.), July 10, 1975.
- 10-19. Gay, Ray H.; and Grossi, Mario D.: Doppler Measurements of the Ionosphere on the Occasion of the Apollo-Soyuz Test Project. Part II: Inversion of Differential and Rotating Doppler Shifts. Special Rep. No. 367, Smithsonian Astrophysical Observatory (Cambridge, Mass.), July 11, 1975.
- 10-20. King-Hele, Desmond: *Theory of Satellite Orbits in an Atmosphere*. Butterworths (London), 1964.
- 10-21. Gaposchkin, E. M., ed.: 1973 Smithsonian Standard Earth (III). Special Rep. No. 353, Smithsonian Astrophysical Observatory (Cambridge, Mass.), Nov. 28, 1973.
- 10-22. *The American Ephemeris and Nautical Almanac for the Year 1975*. U.S. Government Printing Office, 1973.
- 10-23. Grossi, M. D.: Spacecraft-to-Spacecraft Ionospheric Measurements on Occasion of the Apollo-Soyuz Test Project. *Proceedings of the Beacon Satellite Investigations of the Ionosphere Structure and ATS-6 Data*, Acad. Sci. USSR (Moscow), vol. 1, 1975, pp. 84-91.
- 10-24. Gay, R. H.; and Grossi, M. D.: The Ionospheric Experiment of the Apollo-Soyuz Test Project. Paper presented at the American Geophysical Union Meeting (Madison, Wis.), Sept. 1975.
- 10-25. Al'pert, Ja. L.: On Ionospheric Investigations by Coherent Radiowaves Emitted From Artificial Earth Satellites. *Space Sci. Rev.*, vol. 18, 1976, pp. 551-602.



# 11. Geodynamics

## Experiment MA-128

*F. O. Vonbun,<sup>a†</sup> W. D. Kahn,<sup>a</sup> W. T. Wells,<sup>b</sup> and T. D. Conrad<sup>b</sup>*

### ABSTRACT

The Apollo-Soyuz Test Project Geodynamics Experiment was performed to assess the feasibility of tracking and recovering high-frequency components of the Earth gravity field by utilizing a synchronous orbiting tracking station such as Applications Technology Satellite 6. Gravity anomalies of  $0.05 \text{ mm/sec}^2$  (5 mgal) or larger having wavelengths of 300 to 1000 km on the surface of the Earth are important for geologic studies of the upper layers of the Earth crust. Two prime areas of data collection were selected for this experiment: the center of the African Continent and the Indian Ocean Depression centered at latitude  $5^\circ \text{ N}$  and longitude  $75^\circ \text{ E}$ .

Results show that the detectability objective of the experiment was achieved in both areas as well as in several additional anomalous areas around the globe. Gravity anomalies of the Karakoram and Himalayan mountain ranges, of ocean trenches, and of the Diamantina Depth are specific examples.

The more complicated aspect of the experiment was that of recovering the magnitude of the gravity field perturbations that produced the signatures in the experiment data residuals. Recovery of discretely distributed gravity anomalies has been successfully accomplished for the prime

area; i.e., the Indian Ocean Depression. Residual patterns over other geographic areas also indicate possible gravity anomalies, which are the subject for further investigation.

Comparisons of values of the recovered gravity anomalies with surface gravity measurements (ground truth) are generally in good agreement. It is estimated that the accuracy of the recovered anomalies is approximately  $\pm 0.10 \text{ mm/sec}^2$  ( $\pm 10 \text{ mgal}$ ) or better.

### INTRODUCTION

The objectives of the Apollo-Soyuz Test Project (ASTP) Geodynamics Experiment were threefold.

1. To demonstrate the detectability of short-wavelength (i.e., 300 km and larger) features of the Earth gravity field

2. To evaluate the "high/low" satellite-to-satellite tracking (SST) concept for geodynamics applications

3. To test the recoverability of short-wavelength features of the Earth gravity field

This experiment was the culmination of an effort to utilize synchronous orbiting tracking stations for NASA missions (ref. 11-1). The use of a

---

<sup>a</sup>NASA Goddard Space Flight Center.

<sup>b</sup>Washington Analytical Services Center, Inc., Riverdale, Maryland.

<sup>†</sup>Principal Investigator.

low-orbiting (approximately 230 km) spacecraft, such as Apollo-Soyuz, continuously tracked by a synchronous satellite has, for the first time, led to the detection of short-wavelength Earth gravity anomalies (ref. 11-2).

The Apollo-Soyuz spacecraft, flying in a low orbit, is particularly sensitive to gravity anomalies. For example, the ratio of sensitivity to the 25th-degree terms of the Earth gravity potential having a wavelength of approximately 1600 km is approximately 13 to 1 when going from a Geodetic Earth Orbiting Satellite 3 (GEOS-3) type orbit (840 km) to the lower Apollo orbit (223 km). Thus, the ASTP mission presented an excellent opportunity to test the SST concept. Normal satellite perturbation methods used previously for computing the Earth gravity field cannot be used for such short wavelengths because this would require a spherical harmonic expansion to an order and degree of 120 or larger.

During the course of the ASTP mission, MA-128 experiment data were collected for 108 revolutions; 28 revolutions were originally scheduled for the experiment and the remaining 80 revolutions were targets of opportunity. In all the experiment revolutions analyzed, it has consistently been shown that gravity field signatures in the 500- to 1000-km-range wavelengths manifested themselves on the experiment data residuals. The more complicated problem of recovering the magnitude of the gravity anomalies producing the aforementioned perturbations will now be considered.

## MATHEMATICAL METHODS

The gravitational field of the Earth is generally represented in terms of a finite spherical harmonic series expansion having coefficients determined from a combination of satellite ground tracking data and surface gravimetric data. Such a limited representation of the global geopotential does not adequately "model" local variations in the gravity field because the short wavelengths of these local variations would require a field expansion

to a degree and order of approximately 100 to 200. This is considered impractical if not impossible. However, rather small local gravity anomalies are important for geologic investigations of the upper crust as well as for studies of the ocean topography. This experiment provided an opportunity to improve knowledge of the terrestrial gravitational field in localized areas by directly measuring local gravity variations through detection of small velocity changes (1 to 10 mm/sec) of the low-orbiting spacecraft. Before the gravity anomaly analyses are discussed, some basic information about the tracking system will be presented. Figure 11-1 is a schematic of the Applications Technology Satellite 6 (ATS-6)/Apollo communication links. The Apollo spacecraft was connected with Madrid by two links: the ATS-6 link and a direct ground link. This provides a total loop for the measurements that will be used to reduce the errors in the system. The emphasis in this report is on the link from Madrid to ATS-6 to Apollo and back. Figure 11-2 depicts the range rates that were actually measured during the experiment. The system was constructed to measure the total range rate between the ground station (in this case Madrid) and the Apollo spacecraft in Earth orbit. The total range rate is the sum of the range rates between Madrid and ATS-6  $\dot{r}_1$ , ATS-6 and Apollo  $\dot{r}_2$ , Apollo and ATS-6  $\dot{r}_3$ , and ATS-6 and Madrid  $\dot{r}_4$  (ref. 11-3). This analysis concentrates only on variations of the range rate between Apollo and ATS-6  $\dot{\rho}_A$ , which is a dot product of the spacecraft velocity vector  $\mathbf{v}$  and the unit vector between Apollo and ATS-6  $\hat{\rho}^0$  as seen in figure 11-2.

$$\dot{\rho}_A = \hat{\rho}^0 \cdot \mathbf{v} \quad (11-1)$$

One of the first experiment tasks was to evaluate the noise characteristics of the total system. An analysis performed before the experiment was the basis for a predicted range-rate noise level of approximately 0.05 cm/sec using a 10-second integration time (fig. 11-3). The actual experimental



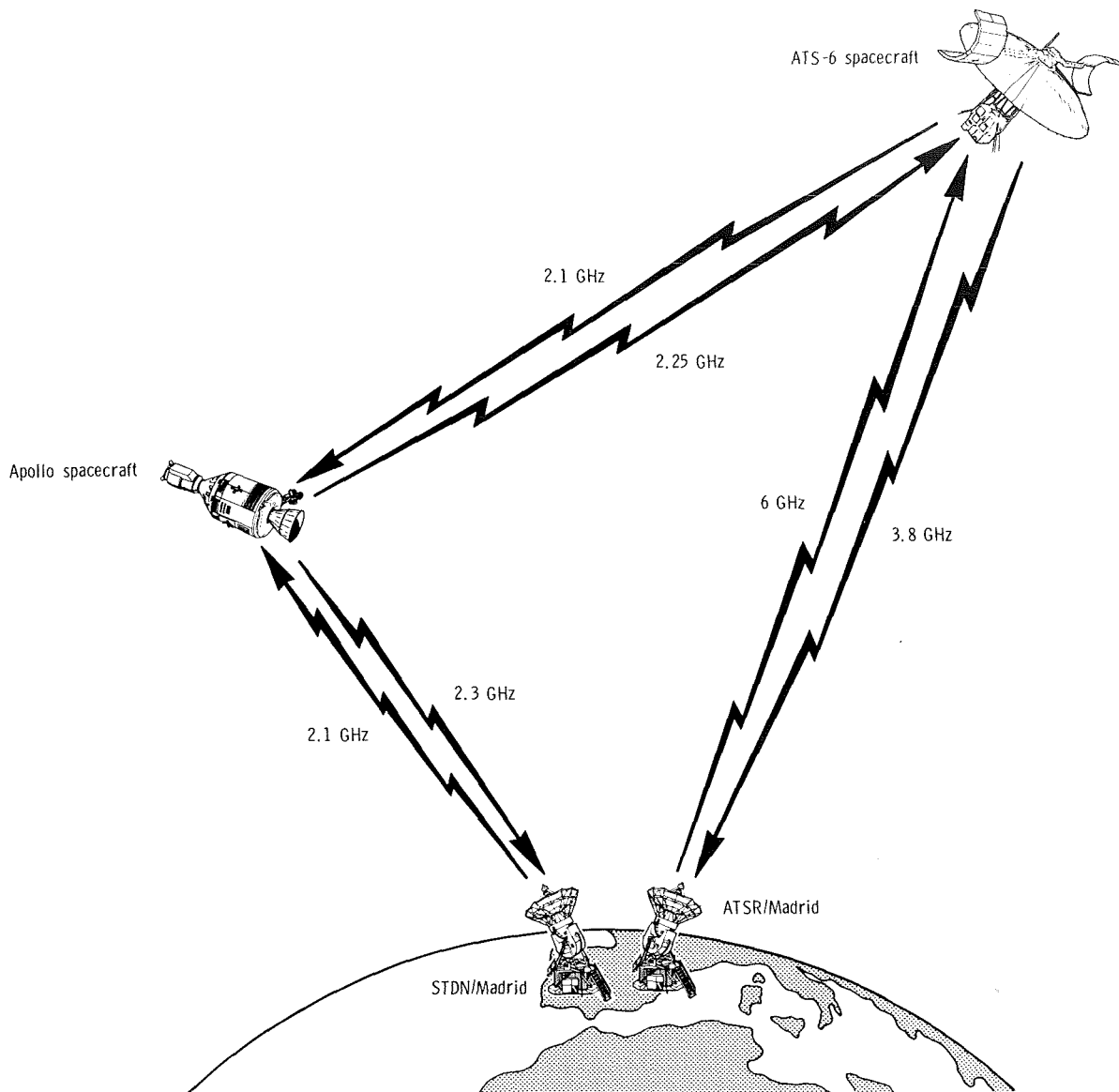


FIGURE 11-1.—Schematic of the ATS-6/Apollo communication links for operations with ATS-6 in the Eastern Hemisphere. The ATS ranging station is designated ATSR; the Spaceflight Tracking and Data Network station is designated STDN.

range-rate noise level, approximately 0.03 cm/sec, was lower than predicted. These values were obtained using a small portion of an orbit to minimize possible orbit modeling errors. These noise values have been rather consistent throughout all the experimental arcs analyzed.

Two approaches were taken to test the detectability of gravity anomalies. The first approach consisted of assuming a single mass anomaly  $\Delta m$  and of computing, in a simple analytical manner, the expected variation of the spacecraft velocity  $\Delta v$  due to this anomaly (ref. 11-2). The velocity

variations in the radial and horizontal components, respectively, are then

$$\Delta v_{\rho} = -\frac{\Delta m}{m} v_{horiz} \left\{ \frac{1+x}{2(1-x)^2} \frac{\Delta \theta}{\sqrt{1 + \frac{x}{(1-x)^2} \Delta \theta^2}} + \frac{1}{2\sqrt{x}} \ln \left[ \frac{\sqrt{x}}{1-x} \Delta \theta + \sqrt{1 + \frac{x}{(1-x)^2} \Delta \theta^2} \right] \right\} \quad (11-2a)$$

$$\Delta v_{\theta} = v_{horiz} \frac{\Delta m}{m} \left( \frac{1}{\sqrt{1+x^2-2x \cos \Delta \theta}} - 1 \right) \quad (11-2b)$$

where  $x = \frac{R-d}{R+H}$

$$\Delta \theta = vt$$

$$t \approx 0 \text{ to } 150 \text{ seconds}$$

$$R = \text{radius of the Earth}$$

$$d = \text{anomaly depth}$$

$$H = \text{satellite altitude}$$

Equations (11-2a) and (11-2b) assume that the spacecraft travels directly over the anomaly and are only valid for variations in true anomaly of as much as  $\pm 5^\circ$ , which corresponds to approximately 1.5 minutes of flight time. The dashed curve in figure 11-4 represents the radial velocity variation due to a  $0.05 \text{ mm/sec}^2$  (5-mgal) anomaly ( $4^\circ$  by  $4^\circ$ ). The size of the anomaly block is roughly twice the orbital height and represents the area of sensitivity of a spacecraft in orbit to an

anomaly on the ground (ref. 11-4). Because of the extremely low noise in the data and the actual geometry (i.e., the spacecraft was not directly over the mass and it was an extended mass rather than a point mass), a second approach, using computer simulation techniques, was necessary to improve the analytical results.

The dotted line in figure 11-4 depicts the result of the computerized analysis. As shown in figure 11-2, the value  $\dot{\rho}$  is defined as (ref. 11-5)

$$\dot{\rho} = \dot{r}_1 + \dot{r}_2 + \dot{r}_3 + \dot{r}_4 \quad (11-3)$$

This is the range rate as actually measured at the Madrid Applications Technology Satellite Ranging (ATSR) station. However, only the range rate between the Apollo spacecraft and the ATS-6 spacecraft  $\dot{\rho}_A$ , which is the dot product of the spacecraft orbital velocity vector  $\mathbf{v}$  and the unit vector  $\rho^0$  between Apollo and ATS-6, is of interest (eq. (11-1)). The ATS-6 orbit is almost independent of any gravity variations because of its extreme height (36 000 km); therefore, the range rate between ATS-6 and Madrid can simply be subtracted from the measured range rate. That is,

$$\dot{\rho}_A \approx \dot{\rho} - \dot{\rho}(\text{ATS-6/Madrid}) \quad (11-4)$$

which reduces to 1, the quantity needed for further analyses. This range rate is, however, a function of the state vectors and the gravity field.

$$\dot{\rho}_A = f(X_A, X_{ATS}, G) \quad (11-5)$$

where  $X_A$  and  $X_{ATS}$  are the Apollo and ATS-6 state vectors, respectively, and  $G$  represents the gravity field. The major aim in this experiment was to determine the relationship between surface gravity anomalies  $\Delta g$  and the Apollo/ATS-6 range-rate variations  $\Delta \dot{\rho}_A$ . Again, because only

the variation in  $\dot{\rho}_A$  is of interest, equation (11-5) is varied as follows.

$$\begin{aligned} \Delta \dot{\rho}_A \approx & \frac{\partial f}{\partial X_A} \left( \frac{\partial X_A}{\partial X_A^0} \right) \Delta X_A^0 + \frac{\partial f}{\partial X_{ATS}} \left( \frac{\partial X_{ATS}}{\partial X_{ATS}^0} \right) \Delta X_{ATS}^0 \\ & + \frac{\partial f}{\partial X_A} \left( \frac{\partial X_A}{\partial G} \right) \Delta G \end{aligned} \quad (11-6)$$

$$\Delta \dot{\rho}_A \approx (\Delta \mathbf{v}_\theta + \Delta \mathbf{v}_\rho) \cdot \mathbf{\rho}^0$$

is equal to the observed-computed range rate.

The sensitivity coefficient  $(\partial X_A / \partial G)$  is now contained in equation (11-6) together with  $\Delta G$ , and thus relates the actual measurements with the gravity potential variation  $\Delta G$ . Because local

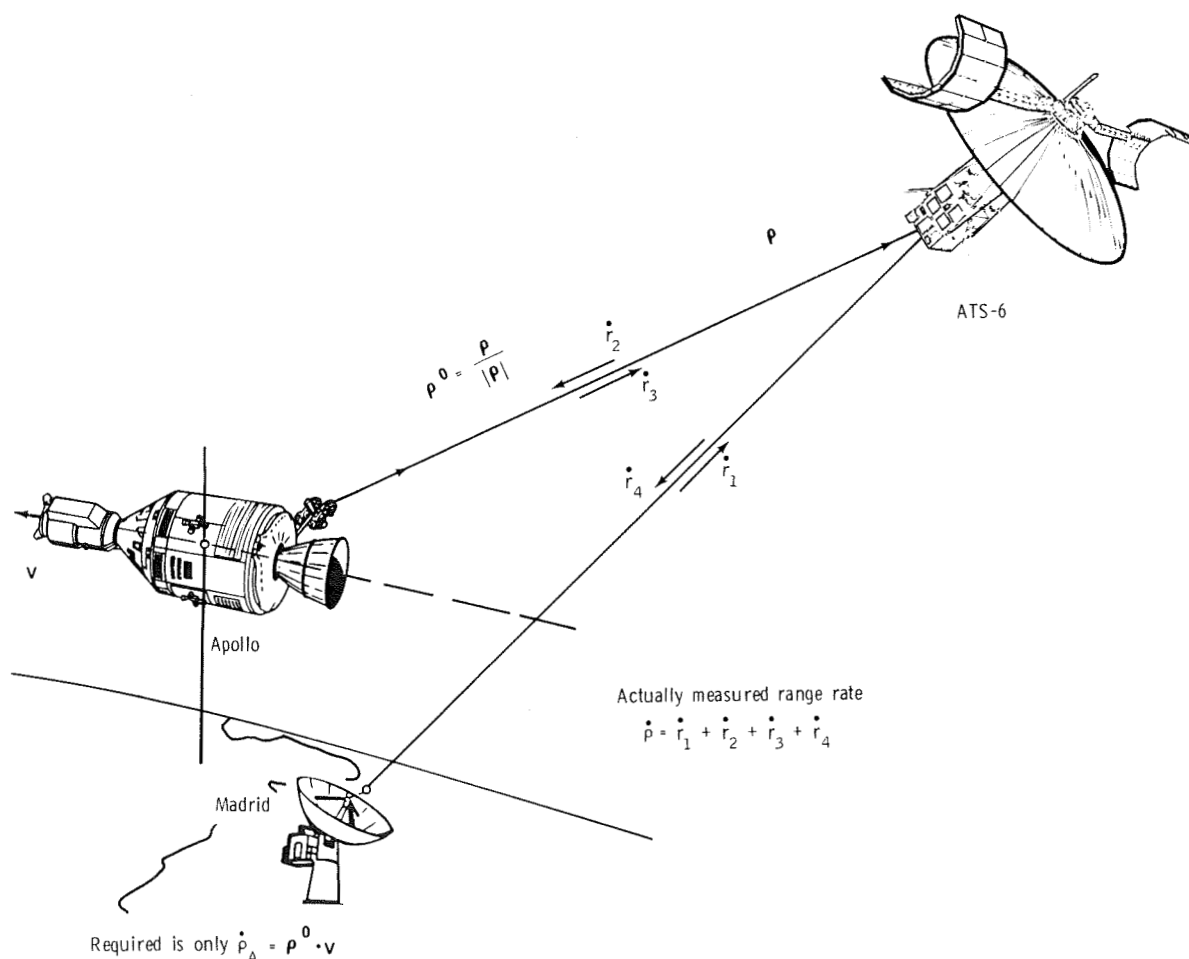


FIGURE 11-2.—Schematic showing range-rate measurement for the ATS-6 and Apollo vehicles.

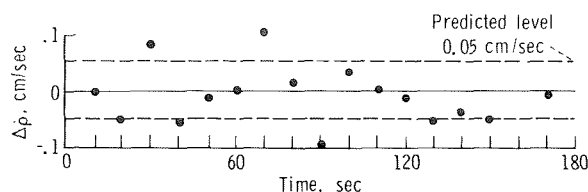


FIGURE 11-3.—Tracking systems range-rate noise characteristics measured from Madrid to ATS-6 to Apollo-Soyuz to ATS-6 to Madrid.

anomalies are being observed over a very brief time (as seen in fig. 11-2, approximately a few minutes), the first two terms on the right side of the series expansion can be neglected. Thus, equation (11-6) reduces to

$$\Delta \dot{\rho}_A \approx \frac{\partial f}{\partial X_A} \left( \frac{\partial X_A}{\partial G} \right) \Delta G \quad (11-7)$$

This sensitivity coefficient can now be computed using Newton's equation of planetary motion.

$$\ddot{X}_A = \frac{\partial V}{\partial X_A} = F(X_A, G) \quad (11-8)$$

Differentiating equation (11-8) with respect to  $G$  yields

$$\frac{\partial \ddot{X}_A}{\partial G} = \frac{\partial F}{\partial X_A} \left( \frac{\partial X_A}{\partial G} \right) + \frac{\partial F}{\partial G} \quad (11-9)$$

Because  $(\partial X_A / \partial G)$  is the variable to be determined, equation (11-9) can be rewritten in the following manner, assuming interchangeability of differential operators; that is

$$\begin{aligned} \frac{\partial \ddot{X}_A}{\partial G} &= \frac{d^2}{dt^2} \left( \frac{\partial X_A}{\partial G} \right) \\ &= \frac{\partial}{\partial X_A} \left( \frac{\partial V}{\partial X_A} \right) \left( \frac{\partial X_A}{\partial G} \right) + \frac{\partial}{\partial G} \left( \frac{\partial V}{\partial X_A} \right) \end{aligned} \quad (11-10)$$

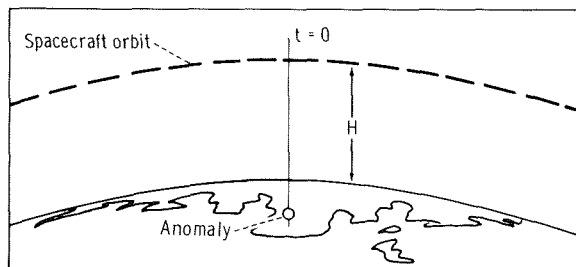
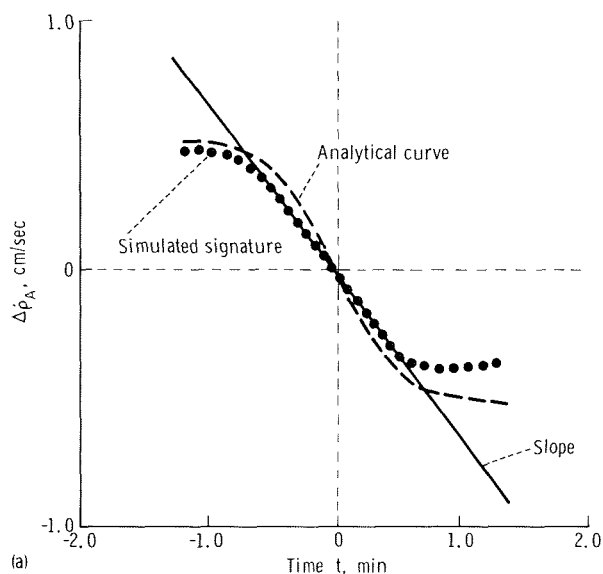


FIGURE 11-4.—Analytical and computer-simulated range-rate signature for a  $4^\circ$  by  $4^\circ$ ,  $0.05 \text{ mm/sec}^2$  (5-mgal) anomaly. (a) Plot. (b) Schematic.

where  $V = U + T$

$U$  = the normal potential of the Earth gravity field in spherical harmonics

$$T = \frac{R}{4\pi} \iint_{\sigma} \Delta g S(\psi) d\sigma$$

$\Delta g = \Delta G + \Delta g_{LOC}$  using  $\Delta g_{LOC}$  as the local average anomaly of a block ( $4^\circ$  by  $4^\circ$ , as an example)

$T$  = the disturbing potential due to the anomalies  $\Delta g$

$R$  = the radius of a sphere having a volume equal to that of the spheroid

$S(\psi)$  = the Stokes function

$\sigma$  = an element of surface area

Introducing  $U$  and  $T$  into equation (11-10) yields

$$\frac{d^2}{dt^2} \left( \frac{\partial X_A}{\partial G} \right) = 2 \frac{\partial^2}{\partial X_A} (U + T) \left( \frac{\partial X_A}{\partial G} \right) + \frac{\partial^2}{\partial X_A \partial G} (U + T) \quad (11-11)$$

Equation (11-11) is now solved for the sensitivity coefficient  $(\partial X_A / \partial G)$  by numerical integration. Using equation (11-7), the computed sensitivity coefficient is correlated and the relationship between  $\Delta \dot{\rho}_A$  and  $\Delta G$  is established. The following procedures were used in detecting the gravity anomalies.

An orbit of one to one and one-half revolutions was computed for the Apollo spacecraft using the Goddard Earth Model 1 (GEM-1) (ref. 11-6) gravity field and all available tracking data (ground station as well as SST). From these Apollo orbits, together with the ATS-6 orbit, the range rates  $\dot{\rho}_A$  between ATS-6 and Apollo were computed. These computed range rates were subtracted from the actual measured ones to yield

the  $\Delta \dot{\rho}_A$  shown in figures 11-5 and 11-6. These values of  $\Delta \dot{\rho}_A$  are finite rather than zero because the gravity field, which would necessarily include all the gravity anomalies, is not known to a very high accuracy. To obtain more precise knowledge of the gravity field, of course, is the essence of this experiment.

## DETECTABILITY

Experimental data were collected in the Eastern Hemisphere region where the Apollo-Soyuz spacecraft was in range of the ATS-6 satellite (which was positioned over the Equator at approximately longitude  $35^\circ$  E). The duration of each Apollo orbit visible to ATS-6 was approximately 50 minutes, or slightly greater than one-half an orbital revolution. To eliminate occultation effect (appendix A), the actual SST data passes used were limited to approximately 40 minutes. All data were successfully collected using the ATS-6 spacecraft and the Madrid ATSR station as the prime ground station. Preliminary results confirm that the range-rate noise of 0.05 cm/sec, computed before the experiment, was improved by the experimental data, which show an average noise of approximately 0.03 cm/sec (fig. 11-3). Figure 11-7 shows the groundtrack of Apollo revolution 115, which coincidentally passed over anomalies in the African area. The effect of the anomalies is apparent in the residual plot.

Figure 11-8 shows three orbital passes (revolutions 8, 23, and 53) that passed over both the Indian Ocean Depression and the Himalayan mountain range. Figures 11-5 and 11-6 depict the actual measurement residuals obtained; that is, the observed minus the computed values. The Indian Ocean Depression can be "seen" in the actual data. The shape of the range-rate variations from the Indian Ocean Depression actually fits the expected shape computed in a manner similar to those shown in figure 11-4. Detectability of the gravity field perturbations has thus been demonstrated to be manifested in the expected form of

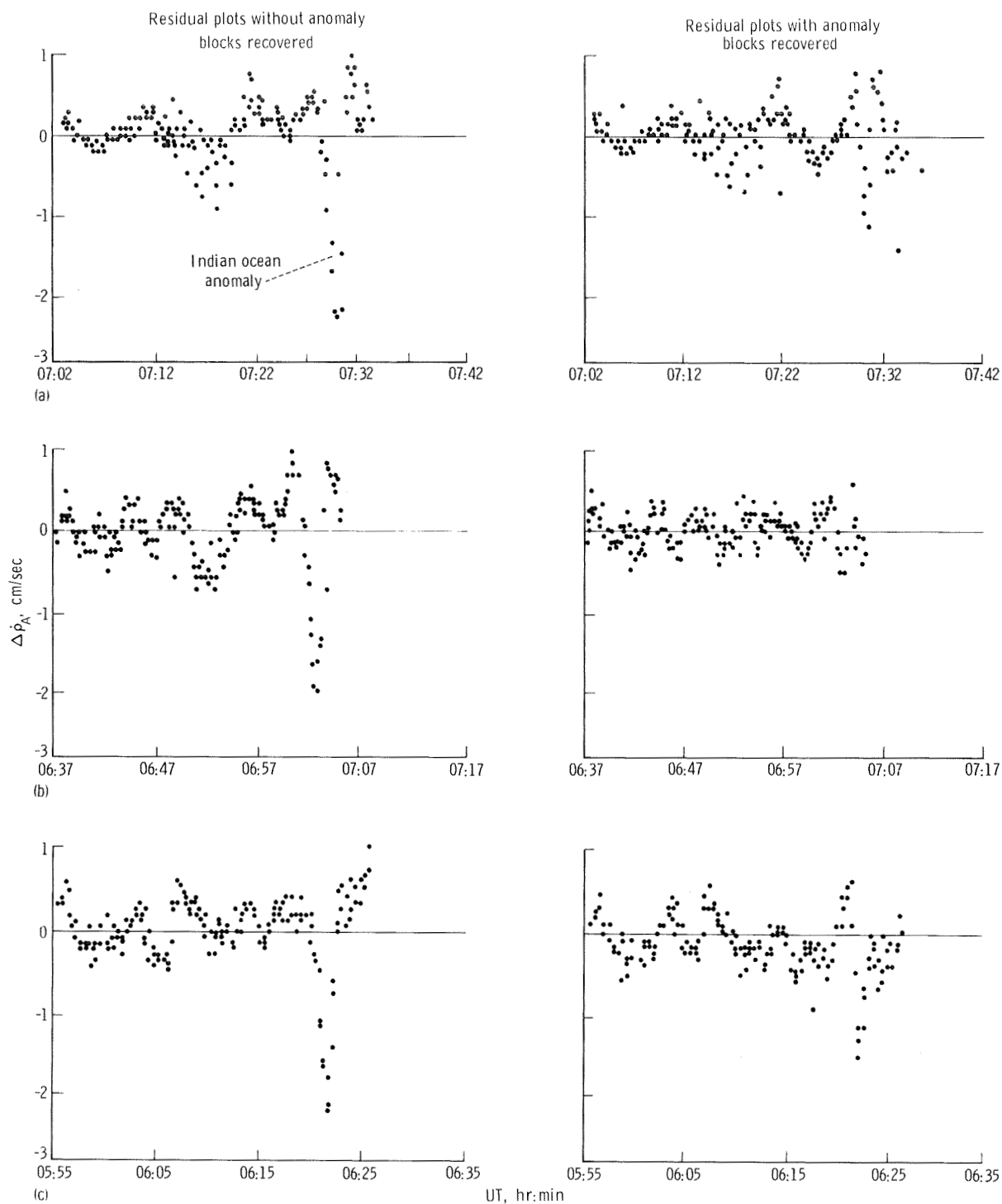


FIGURE 11-5.—Residual plots for ascending revolutions 8, 23, and 53 both with and without anomaly blocks recovered. The GEM-1 reference gravity field model was used. (a) Revolution 8, July 16, 1975. (b) Revolution 23, July 17, 1975. (c) Revolution 53, July 19, 1975.

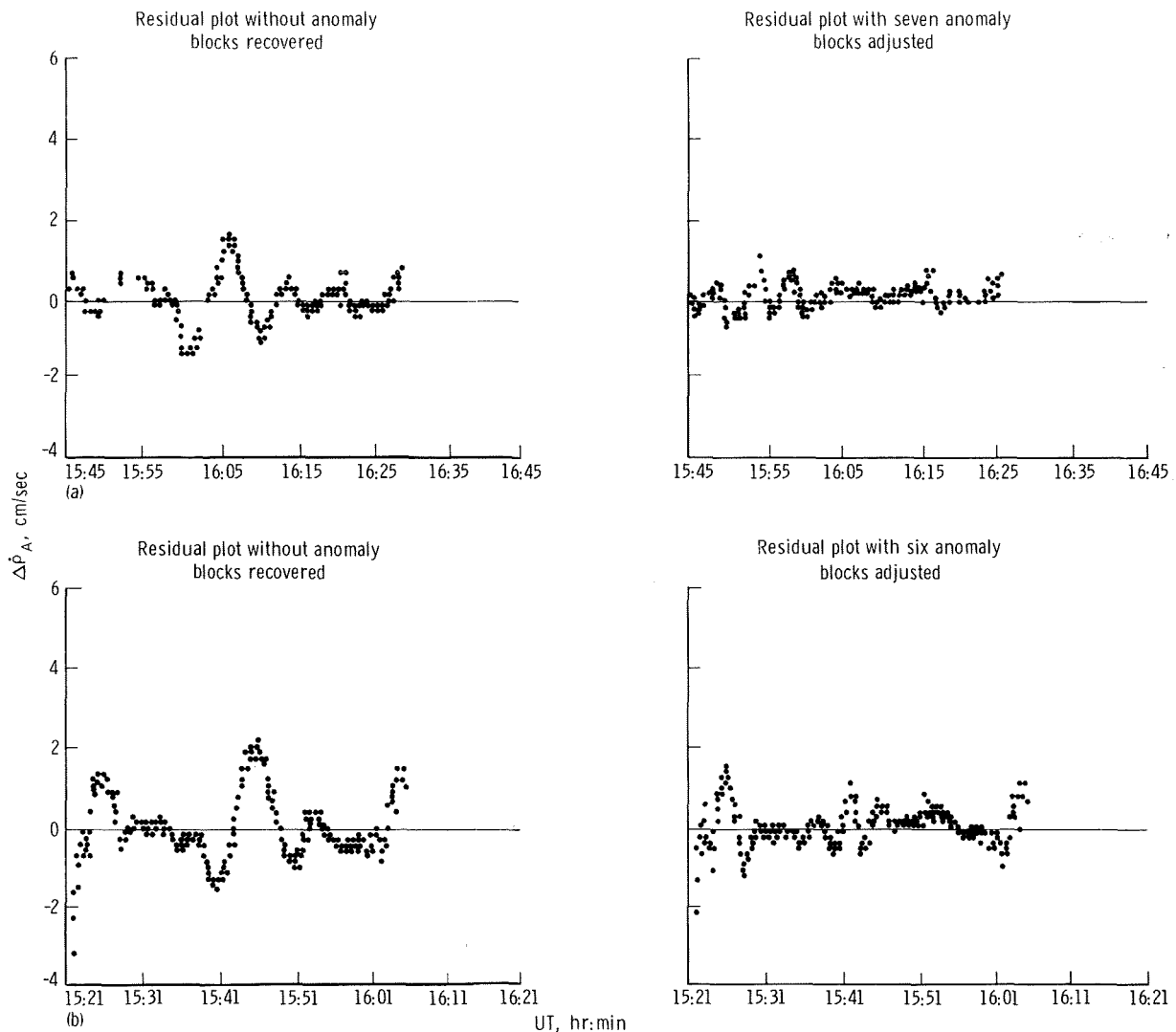


FIGURE 11-6.—Residual plots for descending revolutions 120 and 135 both with and without anomaly blocks recovered. The GEM-1 reference gravity field model was used. (a) Revolution 120, July 23, 1975. (b) Revolution 135, July 24, 1975.

small velocity variations of the spacecraft. The peak values of these variations could, in most cases, be closely correlated with anomalies shown on the detailed map of the global geoid. Other features may have been detected but cannot be verified at this time because of a lack of surface gravimetric data in these areas, particularly in the southern portion of the globe. It may be assumed, however, that the detected gravity signatures in

the southern part of the Earth represent existing anomalies that are not well known.

Orbit determination required for the proper analysis of the experimental data involves the use of SST range-rate data together with direct ATS-6 tracking data and unified S-band tracking data. The error analysis performed indicates that one- and two-revolution arcs are superior for minimizing the effects of unmodeled error in the detection and recovery of gravity anomalies.

Longer arcs seem to introduce larger errors because the influence of the Earth gravity field errors on the orbit errors becomes more pronounced as the arc length increases. Shorter arcs, however, also have rather large errors because not enough tracking data are available. Thus, the use of one- to two-orbit revolutions for the analyses seems to be a good optimum. Air-drag corrections have been used for Apollo-Soyuz orbit determination. The SST data were used only during those periods judged free of onboard propulsion activities. Because the antenna is separated from the spacecraft axis by approximately 3 m, any attitude motion (correction) of the spacecraft (rotation of the spacecraft) is transformed into a range rate between the Apollo-Soyuz spacecraft and the ATS-6 spacecraft. One could therefore quite wrongly interpret a spacecraft rotation as a gravity anomaly. Detailed analysis of attitude control has

not yet been performed; however, attitude data are available and will be used to further refine the range-rate residuals measured between the Apollo-Soyuz and ATS-6 vehicles. The SST data were corrected for ionospheric effects before processing.<sup>1</sup>

## RECOVERY OF GRAVITY ANOMALIES

Groundtracks of some of the ASTP MA-128 experiment revolutions analyzed for gravity anomaly recovery are shown in figure 11-8. Note the center of the prime experiment region, i.e., the Indian Ocean Depression, is represented by block C. Another geographic feature that can be correlated with large variations in the residual signature is in the boundary region between the Eurasian

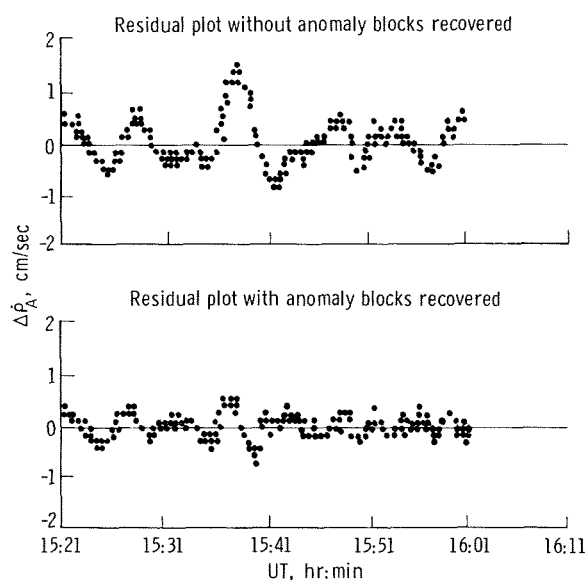
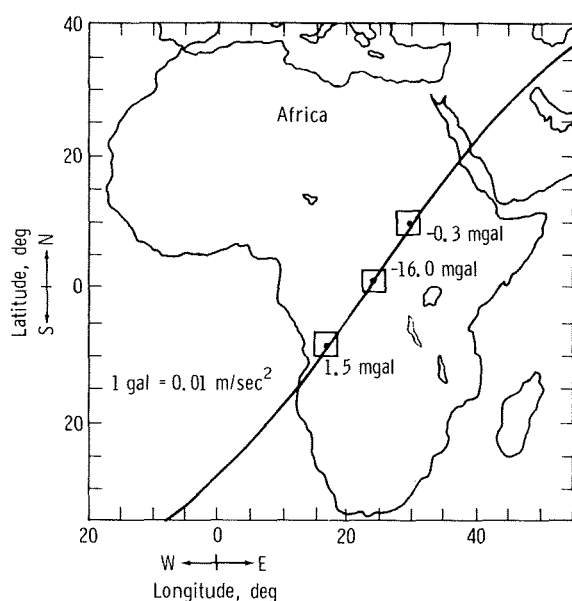


FIGURE 11-7.—Groundtrack and residual plot for revolution 115, July 24, 1975. Recovered value for  $4^\circ$  by  $4^\circ$  anomaly blocks is indicated along the trajectory.

<sup>1</sup>Ionospheric corrections applied to these data were supplied by R. B. Bent, Atlantic Science Corp., Melbourne, Florida (private communication).



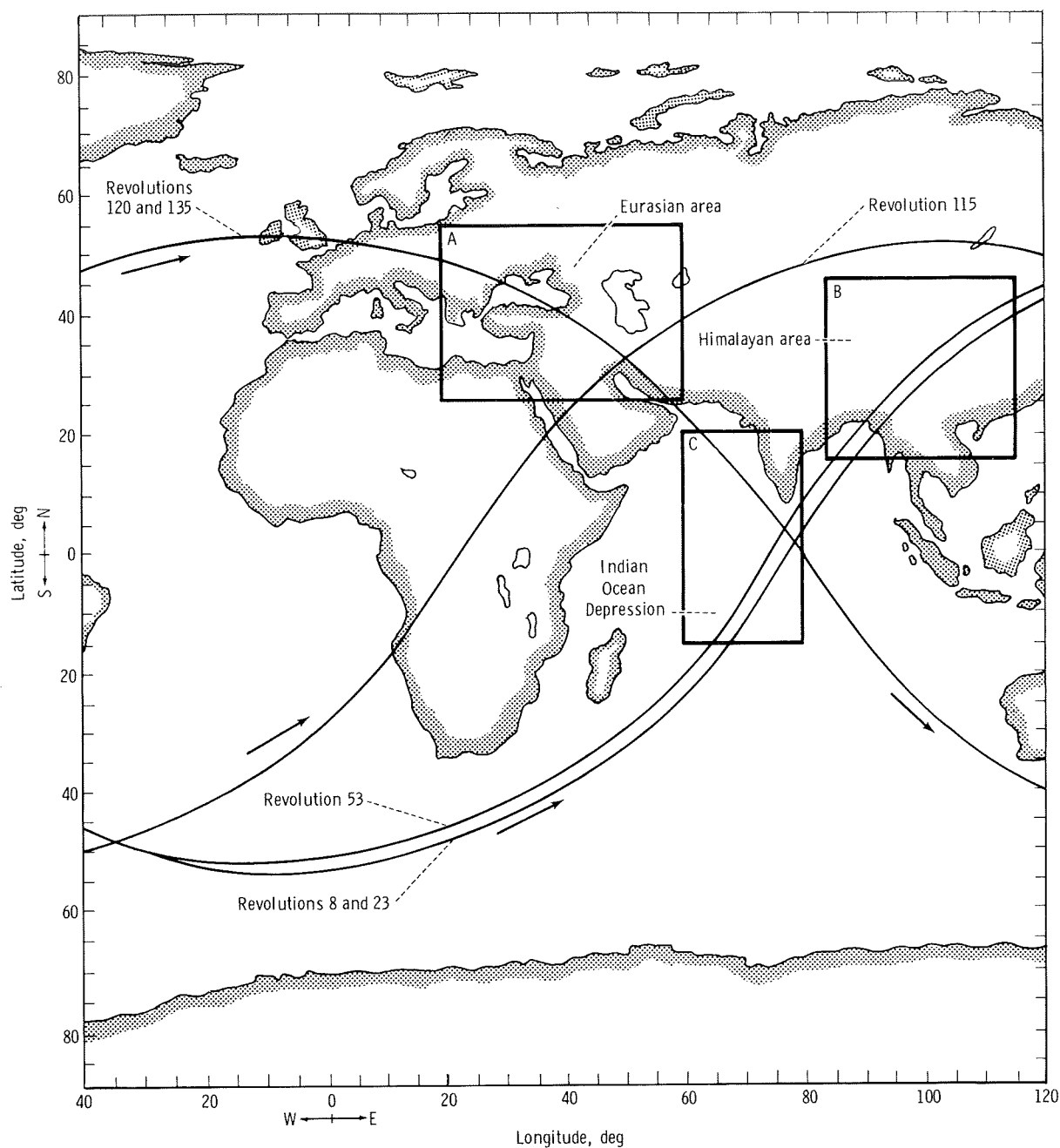


FIGURE 11-8.—Apollo spacecraft groundtracks. "A" represents the Eurasian area; "B," the Himalayan area; and "C," the Indian Ocean Depression.

and African tectonic plates. One revolution (115), which was one of the targets-of-opportunity revolutions, passed over West Central Africa in a region where geoid undulations vary between  $\pm 20$  m. In addition, this revolution is in the vicinity of a large magnetic anomaly, namely the Bangui Anomaly centered at approximately latitude  $3^\circ$  N and longitude  $18^\circ$  E.

Based on an analysis of the residual patterns (ref. 11-7), the location of blocks for recovery of gravity anomalies was made for each experiment revolution separately by placing the block where the residuals change sign. The parameters estimated were the orbital parameters for the Apollo spacecraft, the ATS-6 satellite orbital parameters, and the gravity anomalies. The size of each anomaly block chosen was  $4^\circ$  by  $4^\circ$ . The latter dimension for the blocks is consistent with the region of sensitivity of the Apollo spacecraft.

In the prime experiment area, i.e., the Indian Ocean Depression, three ascending and two descending revolutions were used for recovery of  $4^\circ$  by  $4^\circ$  gravity anomaly blocks in the vicinity of the geometric center of this feature. The ascending revolutions were 8, 23, and 53 and the descending revolutions were 120 and 135. Figure 11-8 shows the groundtrack of each of these revolutions, and figure 11-9 shows in detail the groundtrack and associated  $4^\circ$  by  $4^\circ$  anomalies recovered. This area was denoted in figure 11-8 as "C." In figures 11-9 and 11-10, attention is focused on the fact that blocks in similar geographic regions obtained independently from parallel passes are in excellent agreement. (See figure 11-9 for value and ground truth<sup>2</sup> comparison.) Closer inspection of figure 11-9 yields an even more striking result, which is that values obtained for the anomaly blocks using the aforementioned ascending and descending revolutions are of comparable values for similar geographic location. (See blocks in figure 11-9 contained in  $10^\circ$  by  $10^\circ$  block centered at latitude  $0^\circ$ , longitude  $75^\circ$  E.)

Another recovery of a consistent set of gravity anomaly magnitudes for  $4^\circ$  by  $4^\circ$  anomaly blocks was obtained during revolutions 120 and 135 (fig. 11-10). The geographic area for which the gravity anomalies were recovered corresponds to the area known as the Zagros Thrust Zone (ref. 11-8), which is at the juncture of the African and Eurasian tectonic plates.

Figures 11-5 and 11-6 contain SST range sum rate residuals both before and after the estimation of the gravity anomalies. Initially, the anomaly adjustment reduced the overall magnitude of the residuals but it does not entirely remove systematic signatures. Further analyses have shown that placement of the anomaly blocks to be estimated is "critical." Results have been obtained that lead to the conclusion that the estimate for the magnitude of anomaly blocks is within close agreement for small deviations in the placement of blocks.

The technique of fitting a cubic spline to calculate residual derivatives (i.e., accelerations), used successfully by Muller and Sjogren (ref. 11-7) for the recovery of lunar gravity anomalies, was used for this application. Eleven blocks were placed at the points along the orbit at which peak accelerations occurred. After again solving for the state vectors for the Apollo spacecraft, the ATS-6 satellite, and the magnitude of the 11 anomaly blocks, the residuals were reduced by a factor of 2. The remaining systematic pattern in the residuals appears to correlate with the spacecraft attitude control motion. This latter effect is being studied in greater detail. The residual patterns resulting from the use of this technique are shown in figure 11-5.

Revolution 115, one of the unscheduled revolutions, proved to be of great importance, both from the aspect of detectability and recoverability. During this revolution, the Apollo spacecraft passed over two anomalies in Africa. In fact, during the interval that Apollo passed over Africa, the

---

<sup>2</sup>Ground truth is obtained from a set of surface gravity data collected from multiple sources. The anomalies derived from this data set do not necessarily coincide with the recovered anomaly blocks under the Apollo orbit.

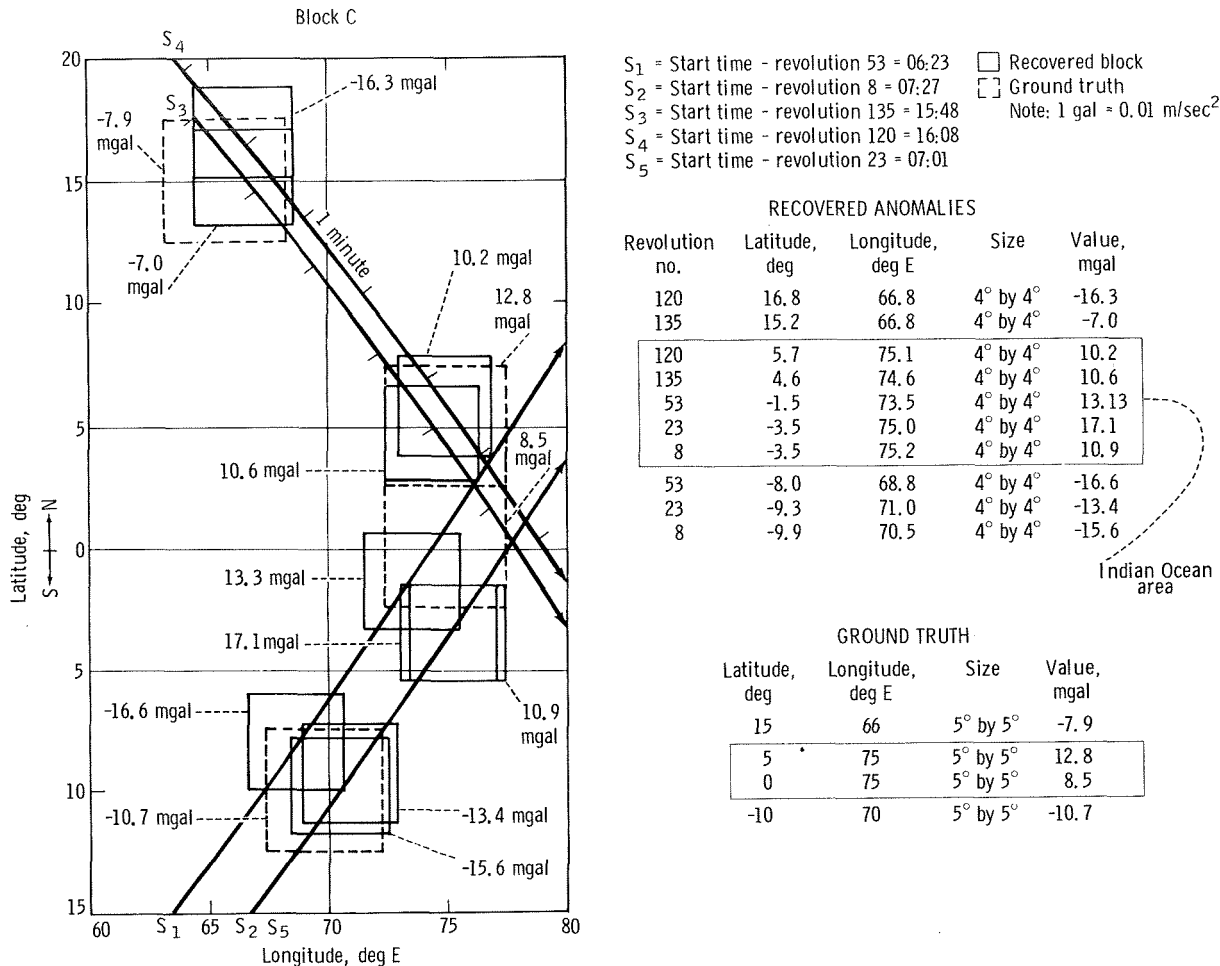


FIGURE 11-9.—Detailed groundtrack of gravity anomaly recovery for the Indian Ocean area together with recovered anomalies and ground truth. Boxed data represent the Indian Ocean area.

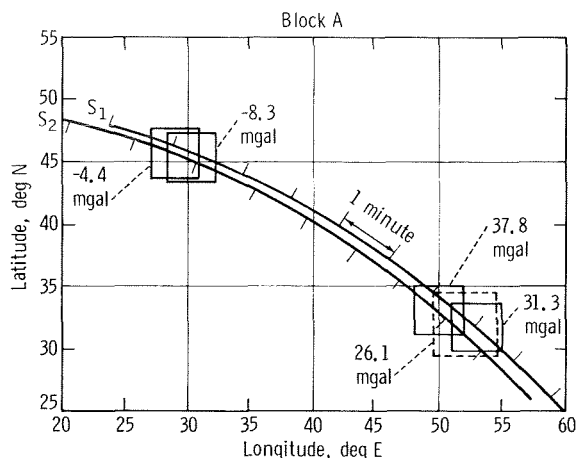
spacecraft was directly underneath the ATS-6 satellite. Therefore, the rate of change of the range sum rate residuals was a direct measure of the anomalous gravitational acceleration.

The residual pattern before adjusting anomaly blocks (fig. 11-7) exhibited a large residual signature allegedly due to gravity field perturbations. At this point in the analysis it was felt that a better

technique for placement of anomaly blocks was needed.

## SUMMARY AND CONCLUSIONS

The high/low SST technique can be utilized for Earth gravity anomaly detection. Anomalies having dimensions equal to or longer than the height



$S_1$  = Start time - revolution 120 = 15:57

$S_2$  = Start time - revolution 135 = 15:36

□ Recovered block

□ Ground truth

Note: 1 gal = 0.01 m/sec<sup>2</sup>

#### RECOVERED ANOMALIES

Revolution no.	Latitude, deg N	Longitude, deg E	Size	Value, mgal
135	45.5	29.2	4" by 4"	-4.4
120	45.4	30.5	4" by 4"	-8.3
135	33.1	50.0	4" by 4"	37.8
120	31.7	52.9	4" by 4"	31.3

#### GROUND TRUTH

Latitude, deg N	Longitude, deg E	Size	Value, mgal
32	52	5" by 5"	26.1

FIGURE 11-10.—Detailed groundtrack of gravity anomaly recovery for the Eurasian area together with recovered anomalies and ground truth.

of the low spacecraft and having values of approximately 0.05 mm/sec<sup>2</sup> (5 mgal) have been detected with a good 10:1 signal-to-noise ratio. The 0.05-cm/sec range rate, conservatively computed before the experiment, was actually improved by the measured noise of 0.03 cm/sec. For all the passes examined, it was possible to correlate the measured range-rate residuals with known geoidal features of short wavelength (approximately 300 km). It was further demonstrated that the range-rate signatures could be repeated orbit by orbit; thus, confidence in the experiment data has been increased.

The results which have been described in this report clearly show that the ASTP Geodynamics Experiment goals have been met; that is, the high/low configuration SST technique for detectability and recoverability of gravity anomalies is successful. This technique represents another source with which the geopotential can be mapped and modeled. Thus, the entire 108 experiment revolutions collectively form a data set that is "rich" in scientific information for geodynamic investigations.

Further analyses using the Geodynamics Experiment data will range from the developing of an improved model for the geopotential to the correlating of experiment data with bathymetric features and plate tectonic boundaries within the ATS-6 visibility region of the Apollo spacecraft. Correlations will also be made with satellite-to-satellite range sum rate data and altimeter data obtained from the GEOS-3 program.

#### REFERENCES

- 11-1. Vonbun, F. O.; and Mengel, J. T.: Tracking and Communications for Planetary Manned Missions. J. Spacecraft & Rockets, vol. 5, no. 5, July 1968, pp. 863-865.
- 11-2. Vonbun, F. O.: The ATS-F/Nimbus-E Tracking Experiment. Rotation of the Earth, Paul Melchoir and Shigeru Yumi, eds., D. Reidel Publ. Co. (Dordrecht, Holland), 1972, pp. 112-120.
- 11-3. Schmid, P. E.; and Vonbun, F. O.: The ATS-F/Nimbus-F Tracking and Orbit Determination Experiment. 1974 IEEE Intercon Technical Program Papers, 1974, pp. 34/6-1 and 34/6-2.
- 11-4. Schwarz, Charles R.: Gravity Field Refinement by Satellite to Satellite Doppler Tracking. NASA CR-117404, 1970.
- 11-5. Bryan, J.: ATS-F/GEOS-C Satellite to Satellite Tracking Data Processing Consideration. NASA TM X-70736, 1974.
- 11-6. Lerch, Francis J.; Wagner, Carl A.; et al.: Gravitational Field Models for the Earth (GEM 1 & GEM 2). NASA TM X-65970, 1972.

- 11-7. Muller, P. M.; and Sjogren, W. L.: Mascons, Lunar Mass Concentrations. *Science*, vol. 161, no. 3482, 1968, pp. 680-684.
- 11-8. Lomnitz, Cinna: *Global Tectonics and Earthquake Risk*. Elsevier Scientific Publishing Co. (New York), 1974.



## 12. Light Flash Observations

### Experiment MA-106

*T. F. Budinger,<sup>a†</sup> C. A. Tobias,<sup>a</sup> R. H. Huesman,<sup>a</sup> F. T. Upham,<sup>a</sup> T. F. Wieskamp,<sup>b</sup>  
J.-U. Schott,<sup>c</sup> and E. Schopper<sup>c</sup>*

#### ABSTRACT

There were 82 visual events reported by two dark-adapted crewmembers during a 90-minute orbit at an altitude of 225 km. Silver chloride crystal events for that orbit totaled 69 stopping protons and alpha particles per square centimeter and 304 heavy ions with linear energy transfer of 150 MeV cm<sup>2</sup>/g or greater. Frequency of visual observations near the geomagnetic poles corresponds to calculated abundances of ions with linear energy transfer greater than 5 keV/μm in tissue. Alpha particles from nonelastic nuclear collisions of fast protons on carbon, nitrogen, and oxygen in the retina or the abundance of stopping protons can explain the low frequency of events in the South Atlantic Anomaly for this mission compared to the high frequency during Skylab 4 at a 443-km altitude.

#### INTRODUCTION

During the last six Apollo missions and on a few occasions during Skylab, the crews made both scheduled and unscheduled observations of the frequency and character of tiny starlike, brief flashes of white light or pencil-thin streaks of light

(refs. 12-1 to 12-6). These observations can be summarized as follows. After approximately 17 minutes of dark adaptation, tiny dots and thin streaks of white light were seen at frequencies of approximately 3 events/min by crewmembers when on translunar or transearth coast or over the polar part of Skylab orbits. When near the South Atlantic Anomaly (SAA), where the proton flux is more than 1000 times greater than in other parts of the orbit, the frequency increased to approximately 9 events/min for Skylab altitudes of 443 km (ref. 12-6). Examples of the type of phenomena seen are shown in figure 12-1, which is based on descriptions by Apollo and Skylab crews as well as laboratory experiments with accelerated charged particles.

Astronaut Edwin E. Aldrin, Jr., first reported these visual phenomena. They were predicted in 1952 by C. A. Tobias (ref. 12-7), who hypothesized that astronauts were likely to see flashes of light from cosmic particles when they were outside the shielding provided by the Earth's magnetic field. The site of action of these particles, and whether cosmic particles actually caused the light flash phenomenon, were subjects of conjecture in 1970 when this phenomenon was first reported. Many known causes for luminous phosphenes exist, including ionizing radiation, mechanical pressure, electrical currents, magnetic fields, stimulation of the cerebral cortex, and pathological conditions of the central nervous system. For example, flashes can be seen during stages of retinal detachment, and the retina is sensitive to externally applied currents as small as 0.3 mA. In 1970, these phenomena were believed to be caused by ionizing heavy nuclei such as carbon,

<sup>a</sup>Lawrence Berkeley Laboratory, University of California at Berkeley.

<sup>b</sup>Lawrence Livermore Laboratory.

<sup>c</sup>University of Frankfurt.

<sup>†</sup>Principal Investigator.

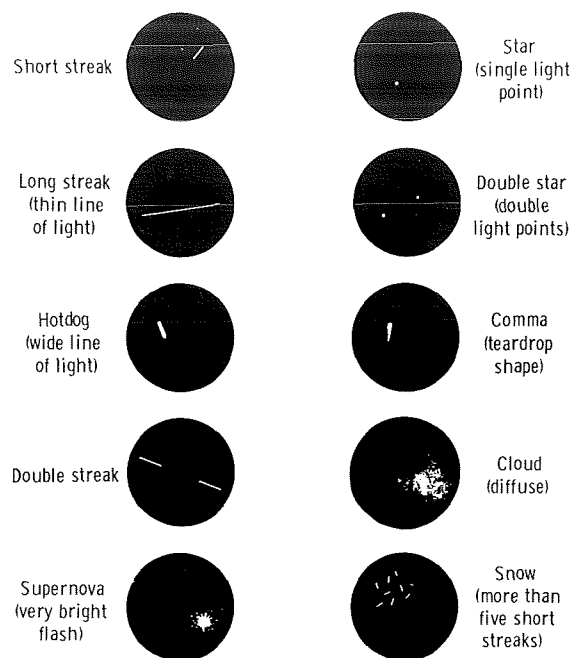


FIGURE 12-1.—Reproduction of visual events noted in space and in cyclotron experiments.

nitrogen, and oxygen, which traverse the spacecraft and the body at frequencies of 1 to 2 nuclei/min  $\cdot$  cm<sup>2</sup> when outside the Earth's magnetic shielding. Of continuing controversy is the conjecture that the major mechanism for these visual phenomena is Cerenkov radiation (refs. 12-8 to 12-11).

In 1970, a series of experiments was conducted to determine whether carbon, nitrogen, and oxygen of approximately 300 MeV/amu and other ions with equivalent ionizing characteristics could cause qualitatively the same phenomena seen by astronauts. Ionizing particles with linear energy transfer (LET) of approximately 10 keV/ $\mu$ m or greater caused similar phenomena in a series of experiments using neutrons of 630 MeV energy, neutrons of approximately 8 MeV energy, helium ions from the 467-cm (184 in.) cyclotron at 230 MeV/nucleon, and nitrogen ions accelerated to approximately 260 MeV/nucleon at the Bevatron (refs. 12-12 to 12-15). These experiments demonstrated that ionization or electronic excitation from cosmic particles could adequately account for the light flash phenomenon. Cerenkov light is

produced by particles at velocities greater than those used in the experiments just described; therefore, it was concluded that, whereas Cerenkov radiation might cause similar phenomena, it was not the predominant mechanism. It is still unclear as to the exact mechanism whereby the retina is stimulated by ionizing particles at velocities below those necessary for emission of Cerenkov light. Experiments in which nitrogen ions were stopped in nine positions in the cerebral cortex have shown that the brain and the optic nerve are not stimulated by ions (ref. 12-15). The mechanisms by which cosmic particles can produce visual sensations are electronic excitation resulting in near-ultraviolet (UV) radiation in the vicinity of the retina, ionization by the primary cosmic particle along the track through the retina, local ionization by the products of a nonelastic collision between a high-velocity proton and carbon, nitrogen, or oxygen, or a shock wave phenomenon from energetic charged particles passing through the tissue matrix.

The purpose of this experiment was to ascertain quantitatively the frequency, character, latitudinal dependence, and identity of cosmic particles that cause the light flash phenomenon. The ultimate objective was the assessment of radiation hazards of long-term Earth-orbiting and interplanetary missions. The special features of this experiment included measurement of the characteristics of the cosmic-particle environment in the vicinity of the eye, measurement of dark adaptation, and continuous onboard accumulation of the light flash observations from astronauts and particle detectors throughout one complete orbit.

## EQUIPMENT

The equipment for the experiment consisted of two dark adaptation masks, two pushbuttons, two cosmic-particle detector boxes, and a control and power unit that housed a data tape. The masks and pushbuttons were manned by two crewmembers, and the control and power unit was controlled by the third crewmember, who monitored the experiment (figs. 12-2 and 12-3).



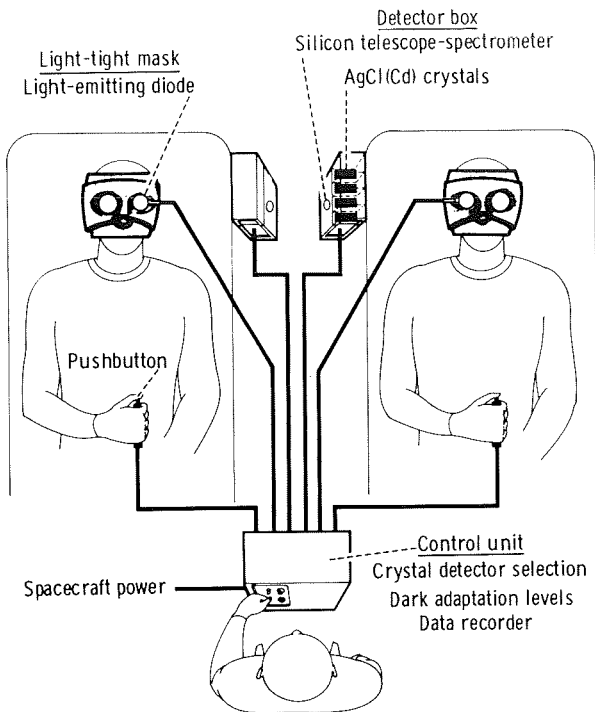


FIGURE 12-2.—Experiment layout.

### Dark Adaptation Masks

Each dark adaptation mask was made of Lexan plastic approximately 2 mm thick and was fitted with a light-emitting diode (LED) behind a pinhole aperture approximately 2 cm from one eye. The masks, held to the head by straps, were fabricated from molds of each crewmember's head. Plaster of paris head casts were made from these molds. The Lexan masks were then made by pressing near-molten Lexan over these head casts. The resulting mask was nearly light tight. To ensure a perfect light-tight fit, a foam rubber insert was used and each mask was then custom fitted to each crewmember.

The effective brightness of the LED was controlled by the duration of a constant voltage. The duration ranged from 5 microseconds to 1.7 milliseconds in six different levels and produced the expected response on normal subjects in terms of the rapidity with which each level of dark adaptation was reached. Level 5 was reached approximately 15 minutes after commencement of dark adaptation.

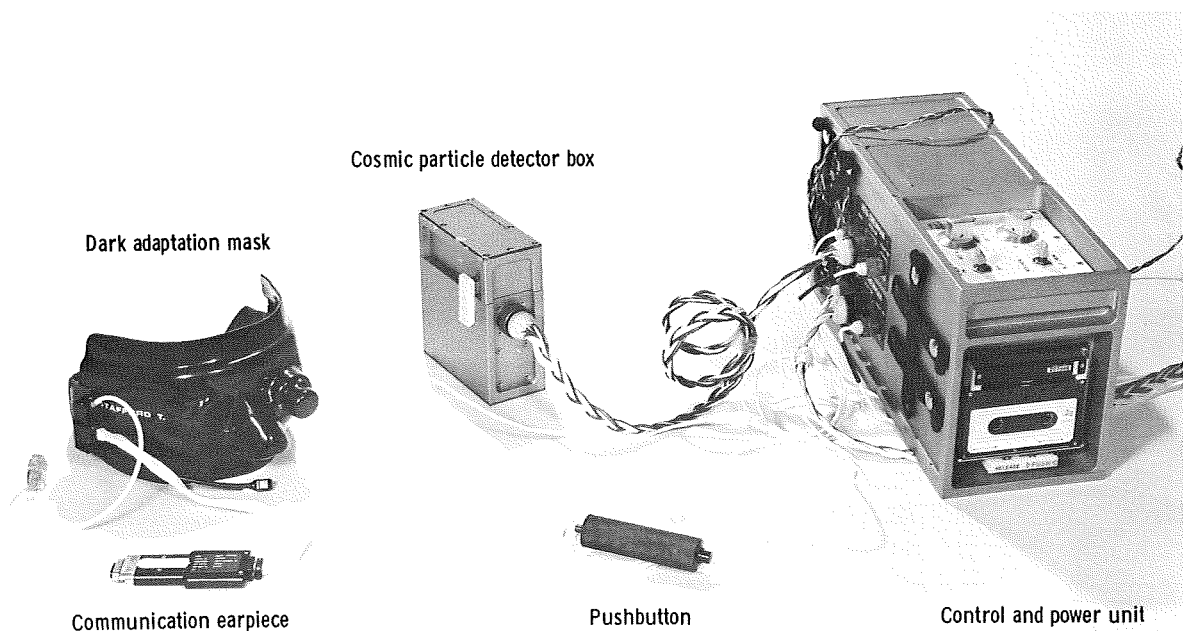


FIGURE 12-3.—Experiment hardware.

### Detector Boxes

Each of the two detector units contained silver chloride (cadmium doped) ( $\text{AgCl}(\text{Cd})$ ) crystals and a silicon solid-state telescope-spectrometer. The location of the detector boxes in the command module is shown in figure 12-4. Each detector box was composed of two units. The first unit (4.1 by 5.5 by 12.7 cm) was an aluminum housing in which there were four compartments (each 1.84 by 3.5 by 2.75 cm) for  $\text{AgCl}(\text{Cd})$  crystals and small lights. The  $\text{AgCl}(\text{Cd})$  crystals were 1- by 2-cm wafers 0.03 cm thick. Two crystals were placed in each compartment on either side of two white 6-V lights, which were filtered to give predominantly yellow light by using yellow plastic sheets (Kapton, 0.06 cm thick) between the lights and crystals.

The  $\text{AgCl}(\text{Cd})$  crystals are nuclear particle detectors developed in Germany (ref. 12-16). They are similar to nuclear emulsions but have a unique property that allows evaluation of the time during which a particle traverses the detector. A nuclear particle passing through the crystal leaves a latent track of dislocated electrons and displaced silver or cadmium atoms. Within a few minutes, the migration of electrons and atoms returns the crystal to its original condition. However, if the crystal is exposed to visual spectrum photons, the latent track is fixed or stabilized. Hours or weeks later, if the crystal is exposed to UV light, the stabilized but still invisible tracks are developed, leaving a permanent record of the nuclear particle track. The distribution of residual silver around the track is related to the charge and velocity of the ion as well as to the intensity and spectrum of

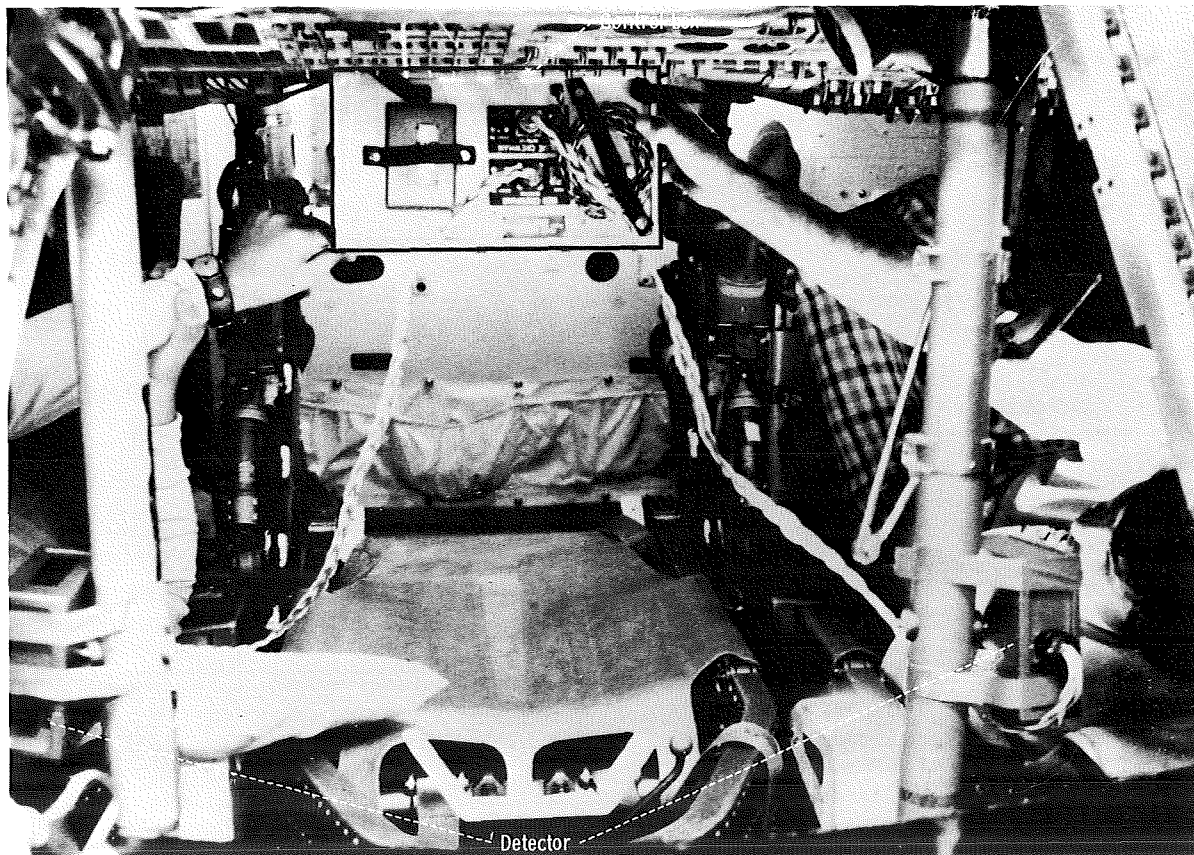


FIGURE 12-4.—Location of equipment in spacecraft.

near-UV light used to develop the stabilized tracks. The time period between implantation of a latent track and fading is a few minutes, but the period between the time a stabilized track is made and fading is more than 1 week. Crystals were loaded into each of four compartments so that the particle environment could be measured in the four sectors of the orbit corresponding to the northern latitudes, the equatorial latitudes, the SAA, and the remaining minutes of the orbit over the Pacific Ocean.

The second unit (4.3 by 9.6 by 12.7 cm) of each detector box housed the electronic detector, which consisted of two sets of silicon solid-state wafers. Each set consisted of two individual wafers 1.7 cm in diameter and 0.03 cm thick. On each wafer were four active strips, each 3 mm wide, separated by 0.5 mm. The telescope was made by rotating one wafer 90° from the other. This set of two wafers gave 16 possible combinations (4 by 4) for particle position. The second set of two wafers was placed 1.5 cm from the first set, and a 0.5-cm-thick copper energy degrader was placed between the sets. This arrangement allowed measurement of the trajectory and energy loss of particles passing through the telescope. The threshold for the device is 100 MeV cm<sup>2</sup>/g.

### Pushbuttons

Events noted by astronauts were recorded on digital tape by means of a handheld pushbutton switch.

### Control and Power Unit

The control and power unit consisted of power distribution, logic circuits, and a digital cassette tape recorder that received 16-bit word groups from the observer pushbuttons and the silicon detectors. Word groups from the silicon detectors contained information on the trajectory and energy loss of particles that passed through the silicon detector. Elapsed time and detector selector switch position information were also recorded.

## EXPERIMENT PROTOCOL

Two revolutions were devoted to this experiment. During revolution 110, the silicon telescope-spectrometer was deployed for measurement of the trajectory, atomic charge  $Z$ , and velocity of cosmic particles with a stopping power of 10 keV/ $\mu$ m or greater. During revolution 111, the Apollo commander and the command module pilot made continuous observations of visual sensations while dark adapted. The docking module pilot operated the experiment control unit, which received data from the silicon detectors as well as from AgCl(Cd) crystals that were used to register particle tracks in four sectors of the orbit corresponding to northern latitudes, equatorial latitudes, the SAA, and southern latitudes.

The experiment commenced with the detector-alone orbit according to the Flight Plan at approximately 13:40 UT on July 22, 1975. The detector-manned orbit, revolution 111, began according to the Flight Plan at approximately 14:45 UT, at which time the spacecraft was maneuvering to proper attitude because the attitude for revolution 110 was not optimum. Approximately 10 minutes later, the observing crewmembers had reached dark adaptation. The first light flash was reported at 15:00 UT at latitude 49° N when the spacecraft was approaching the northernmost point of the orbit. At each event, a pushbutton signal from the observing astronaut was recorded on the digital tape and the verbal description was recorded on the onboard tape recorder. The docking module pilot switched the lighting for the AgCl(Cd) crystal compartments according to the Flight Plan at 17, 29, and 54 minutes after commencement of revolution 111. The experiment was terminated at 16:50 UT. In accordance with the Flight Plan, the digital tapes, voice tapes, detector boxes, and masks were returned to the experimenters. The digital tapes were transported to the Lawrence Berkeley Laboratory for analysis, and the AgCl(Cd) crystals were transported to the University of Frankfurt.

## PROCEDURES FOR DATA REDUCTION

### Observed Events

Descriptions of the events observed by the crewmembers were recorded on the onboard voice recorder. The tapes were transcribed, and each event was related to the orbital position of the spacecraft. Events from the silicon detectors and pushbuttons and the status of the control unit were read from the digital tape by a specially constructed microprocessor. The pushbutton events and time marks were related to the verbal reports. The energy and trajectory information was inadequate because of a paucity of recorded events.

The AgCl(Cd) crystals were transported to the University of Frankfurt, where they had been produced and calibrated. These crystals were analyzed for the abundance of tracks that are related to protons, alpha particles, or heavier ions.

### Calculations of Expected Particle Dose

The characteristics of the cosmic-particle environment inside the spacecraft were determined by converting the spectrum and abundance of particles outside the spacecraft to the number of particles with various LET values and residual ranges, using shielding data for 512 sectors of solid angle around the spacecraft. The shielding data of equivalent thickness of aluminum were supplied by the NASA Lyndon B. Johnson Space Center. Spacecraft position and orientation were obtained from mission ephemeris data supplied after the flight. Cosmic-ray abundances for free space for  $Z > 3$  were obtained from Webber et al. (ref. 12-17), and the abundances for hydrogen and helium were obtained from Smith et al. (ref. 12-18). The spectra were assumed to be the same as those for carbon and oxygen, which were obtained from Juliusson (ref. 12-19). For trapped protons, the model environment AP7 of Lavine and Vette (ref. 12-20) was used.

These free-space abundances were converted to the abundance outside the spacecraft at a 225-km altitude using the spacecraft orbit parameters of

$B^1$  and  $L^2$  data obtained from the 99-term field of Hendricks and Cain (ref. 12-21) extrapolated to 1975. Vertical rigidity cutoffs for cosmic particles at an altitude of 20 km were obtained from Shea and Smart (ref. 12-22). Translation to orbit altitudes (ref. 12-23) and nonvertical directions was performed (ref. 12-24).

The energy-range relationship was derived from an empirical formula that gives range  $R$  as a function of kinetic energy:

$$R = \frac{\alpha A}{Z^2} \left( \frac{E}{A} \right)^\beta \quad (12-1)$$

where  $A$  is the atomic number,  $Z$  is the charge, and  $E$  is the energy in MeV/amu.

For passage of ions through the spacecraft, aluminum shielding is assumed. Thus, the constants are  $\alpha = 2.811 \times 10^{-3}$  and  $\beta = 1.775$ . The stopping power  $S$  is given as

$$S = \frac{Z^2}{\alpha \beta} \left( \frac{E}{A} \right)^{1-\beta} \quad (12-2)$$

Energy transfer in the eye is calculated using equation (12-2) and  $\alpha = 1.88 \times 10^{-3}$  and  $\beta = 1.802$ , corresponding to the passage of ions through water.

## RESULTS

### Visual Observations

The distribution of visual events reported by astronauts is shown along the track line in figure 12-5. Histograms depicting the frequency of events in time and with respect to latitude are shown in figure 12-6. Because the spacecraft

<sup>1</sup>Geomagnetic field strength.

<sup>2</sup>Distance from the center of the Earth in Earth radii.

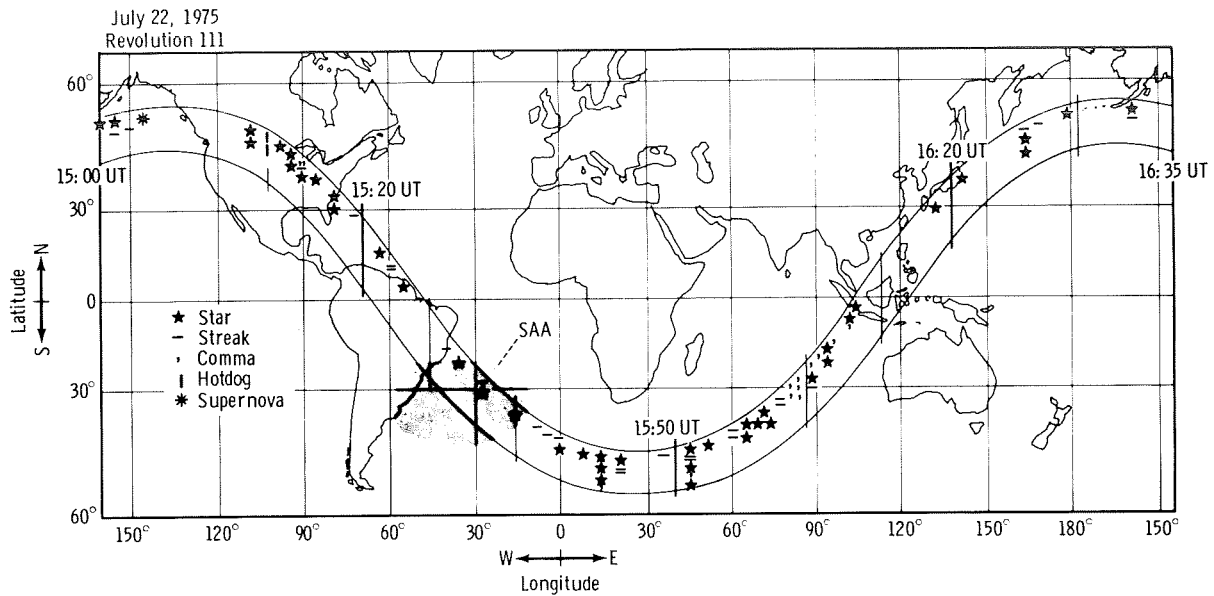


FIGURE 12-5.—Orbit track and distribution of reported events.

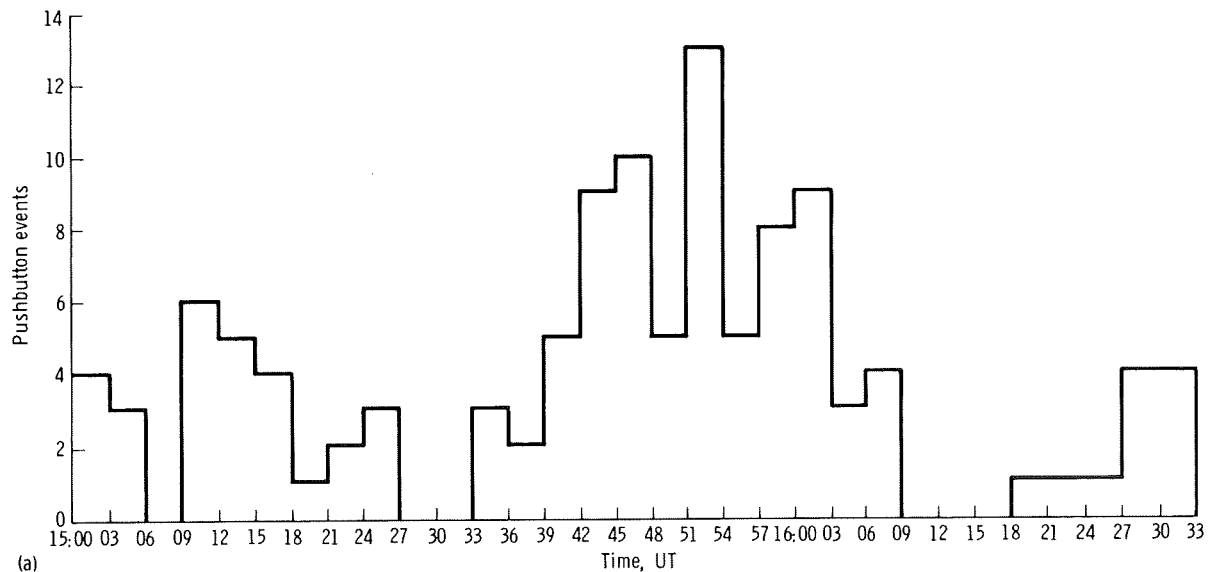


FIGURE 12-6.—Histograms of pushbutton events by time and latitude. Except for a few cases, pushbutton events agree with verbal reports. (a) Intervals of 3 minutes. (b) Intervals of 5° latitude. (c) Intervals of 5° latitude normalized by time intervals.

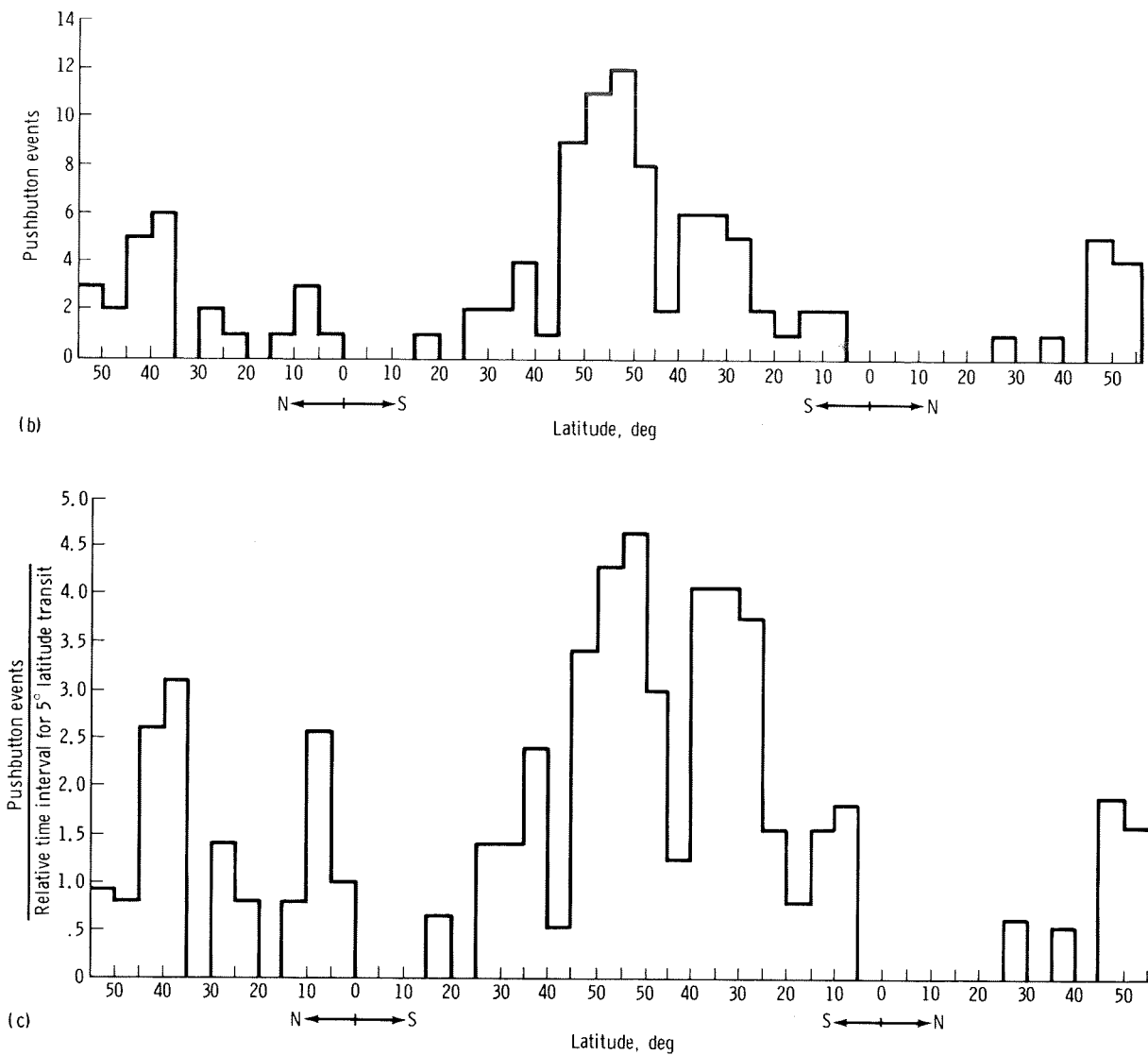


FIGURE 12-6.—Concluded.

TABLE 12-I.—Summary of Events

Track sector	Stars (a)	Streaks (b)	Commas	Total
Northernmost point of orbit to Florida	12	6	2	20
Florida to Brazil	2	3	0	5
SAA	2	1	0	3
SAA to completion of orbit	27	16	11	54

<sup>a</sup>Includes events expressed as supernovas in figure 12-1.<sup>b</sup>Includes events expressed as hotdogs in figure 12-1.

TABLE 12-II.—Visual Flux and Particle Flux From AgCl (Cd) Detectors

UT (July 22, 1975), hr:min	Lat.	Long.	Visual events		Stopping protons and alpha particles		Heavy ions, $LET \geq 15 \text{ keV}/\mu\text{m}^a$	
			No. reported	No./hr	Events, $\text{cm}^{-2} \text{ sector}^{-1}$	Flux, $\text{cm}^{-2} \text{ hr}^{-1}$	Events, $\text{cm}^{-2} \text{ sector}^{-1}$	Flux, $\text{cm}^{-2} \text{ hr}^{-1}$
14:56	43° N	179° E	20	71	$14.0 \pm 1.4$	49	$70.0 \pm 4.8$	250
15:13	38° N	90° W						
15:25	3° N	47° W	5	25	$11.3 \pm 1.3$	55	$81.0 \pm 5.2$	405
15:43	48° S	1° W	3	10	$16.7 \pm 2.0$	56	$64.5 \pm 5.7$	215
16:32	52° N	160° W	54	66	$26.7 \pm 3.8$	33	$89.0 \pm 9.4$	108

<sup>a</sup>Number does not include star events, which are approximately 35 per compartment.

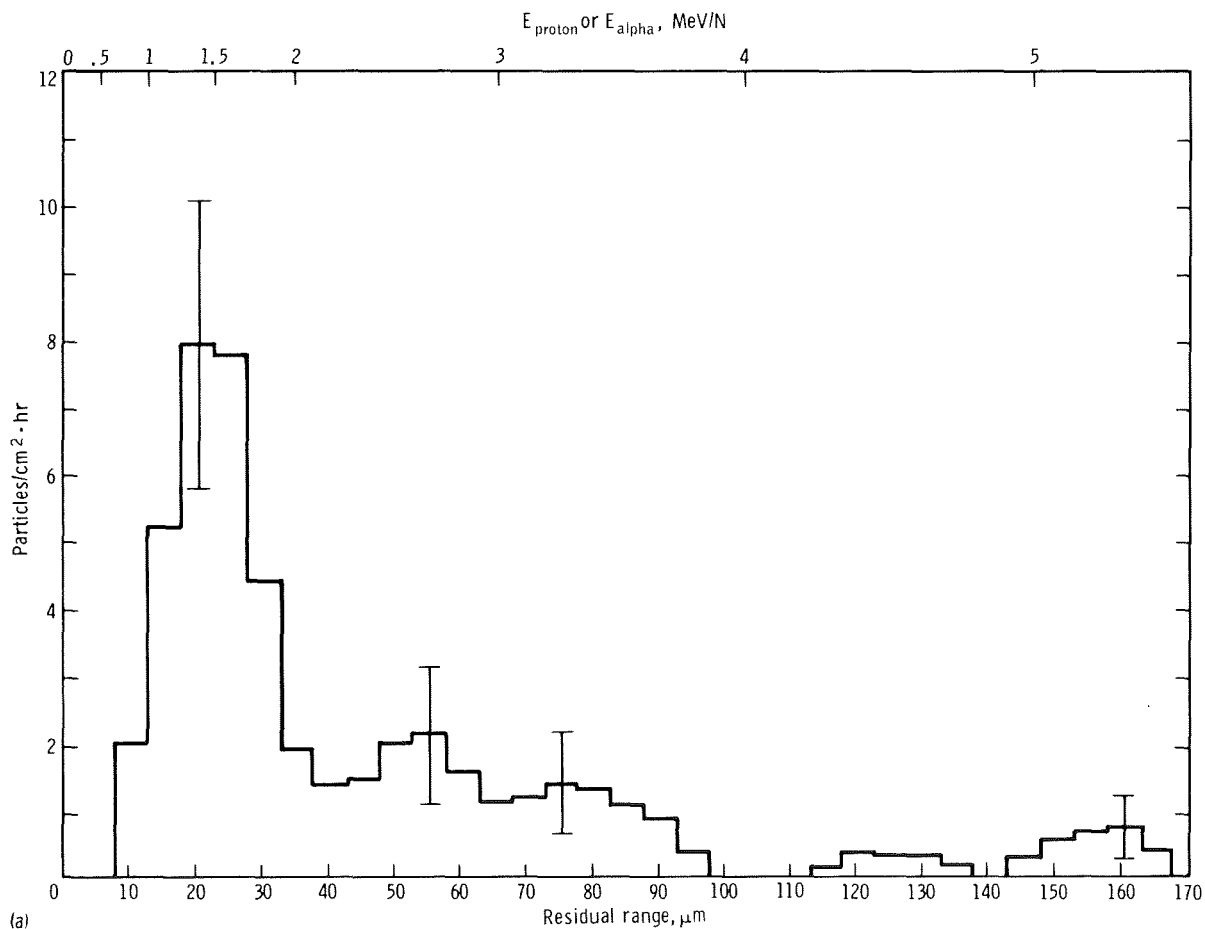


FIGURE 12-7.—Residual range distribution of protons and alpha particles (July 22, 1975). (a) Compartment 1, 14:56 to 15:13 UT. (b) Compartment 2, 15:13 to 15:25 UT. (c) Compartment 3, 15:25 to 15:43 UT. (d) Compartment 4, 15:43 to 16:32 UT.

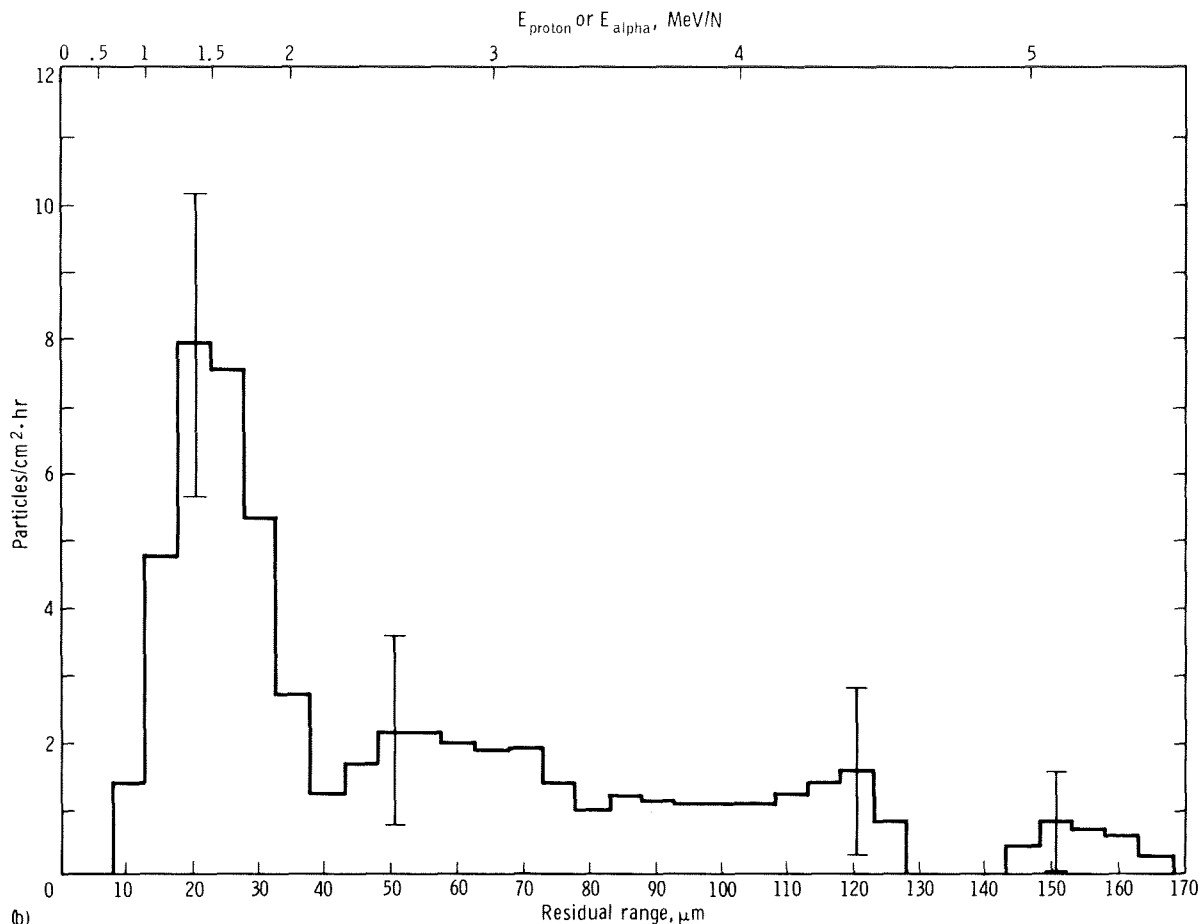


FIGURE 12-7.—Continued.

transited latitudes for varying time intervals, normalization to equal time intervals is shown in figure 12-6(c). A total of 82 events was reported by the two astronauts (table 12-I). No increased activity in the SAA and no graying of the darkened visual fields occurred.

### Crystal Detectors

The AgCl(Cd) detectors from the four compartments corresponding to the four sectors of the orbit were analyzed for two categories of events (table 12-II). The first category includes protons

and alpha particles that could be seen to enter and stop within the AgCl(Cd) layer equivalent to a tissue thickness of 600 μm. The number of particles was tabulated as a function of residual range for each of the four compartments (fig. 12-7). The second category includes those tracks with an LET greater than 15 keV/μm of tissue, which refers to alpha particles of 5 MeV/amu or less kinetic energy and heavier particles. The flux of stopping alpha particles and protons was corrected for known latency of the crystals and normalized to a unit area of 1 cm². The flux of the heavier particles was normalized to 1 cm², but no latency correction was used because this correction varies



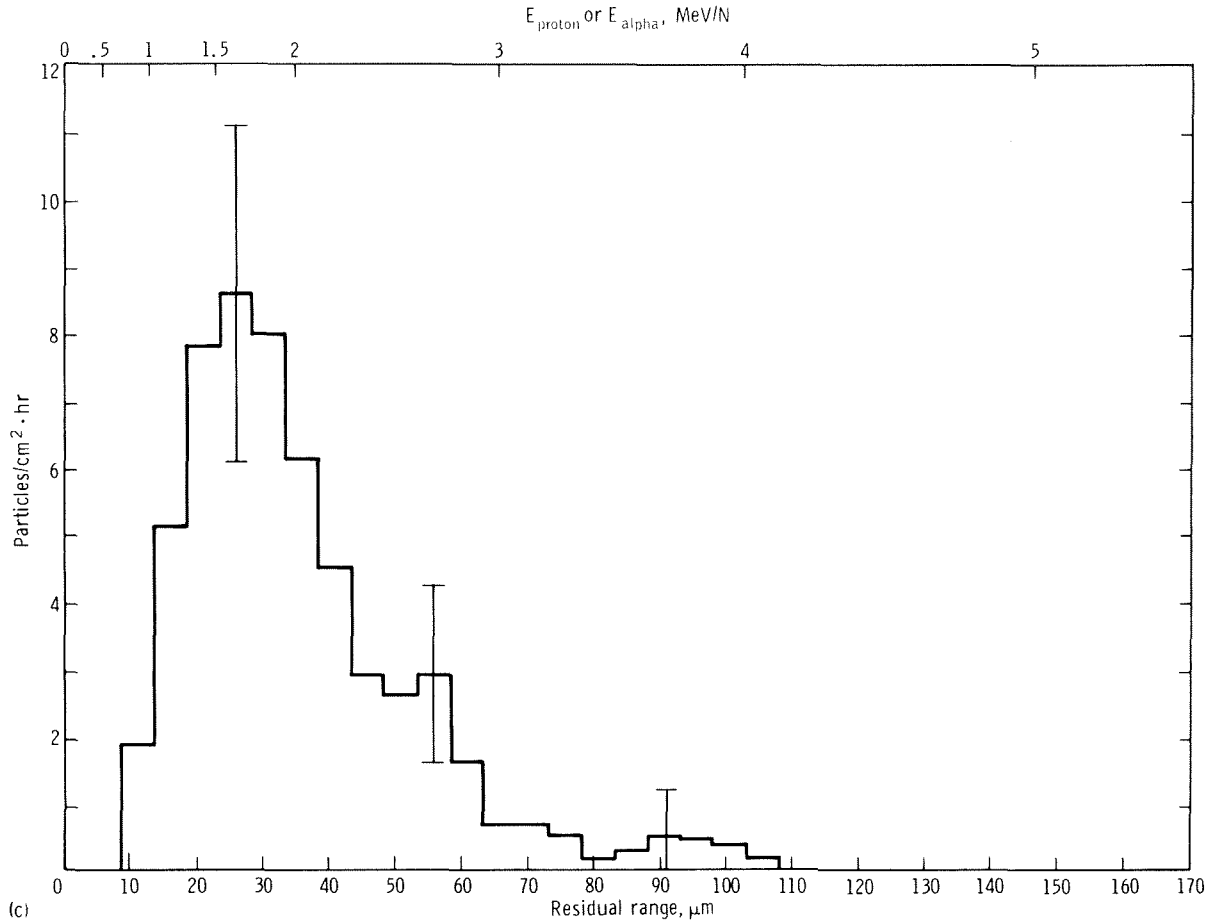


FIGURE 12-7.—Continued.

with the particular ion. Star events were reported in arbitrary units and were of constant abundance in the crystals examined.

The maximum calculated abundances of primary cosmic particles at the north magnetic pole and of trapped protons at the SAA are shown as a function of energy loss in table 12-III. The fluxes are those that are expected at the right-eye position of the right-hand couch in the Apollo spacecraft. The fluxes for 443 km were greater because of less shielding in the observing position during the Skylab 4 mission (ref. 12-6). Distribution of abundances for revolution 111 is shown for various LET ranges in figure 12-8(a). The abun-

dance of trapped protons is shown for LET ranges in figure 12-8(b).

## DISCUSSION

### Primary Cosmic Particles

The frequency of reported light flash events is strongly dependent on latitude. At the points of closest approach to the geomagnetic poles, the observed events occur at one to two per minute;

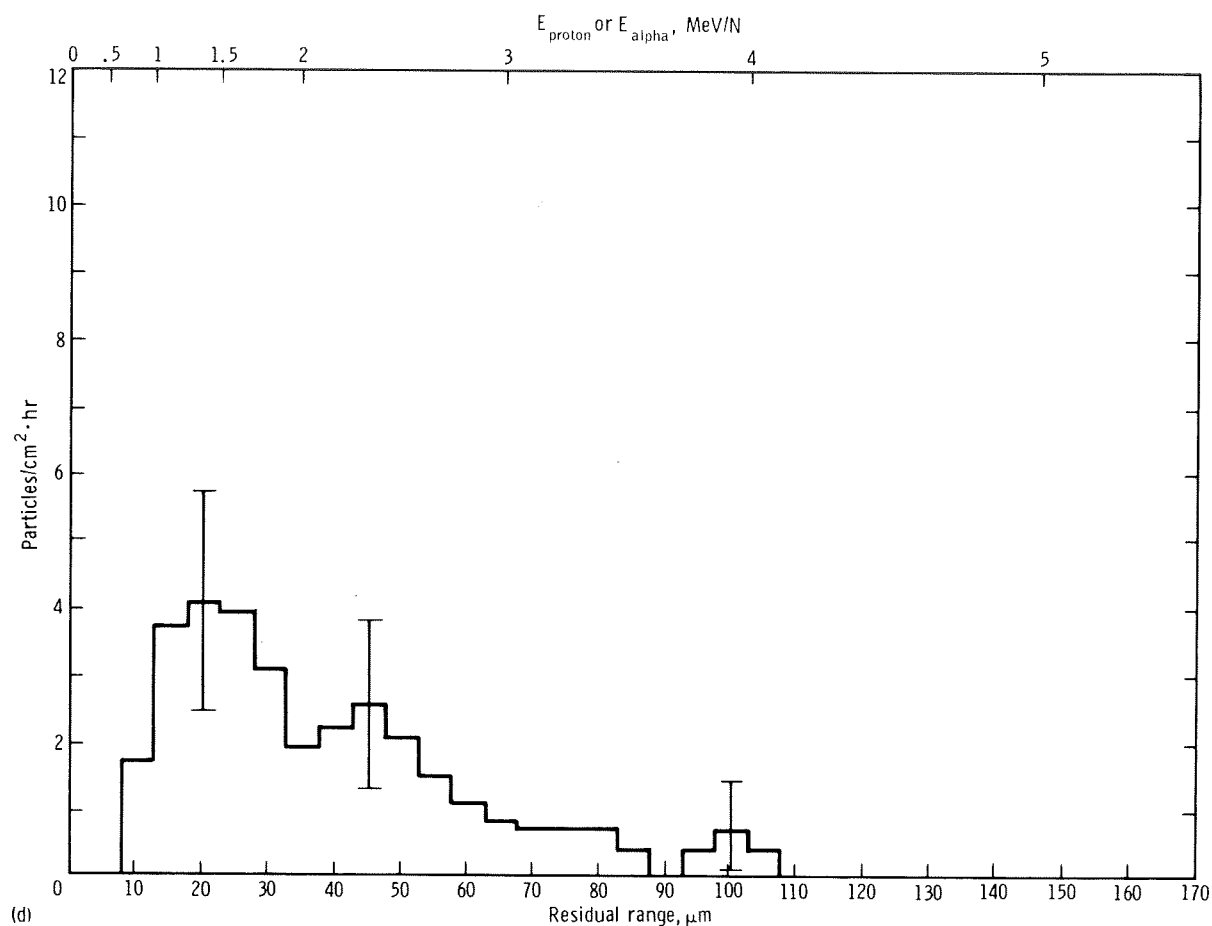


FIGURE 12-7.—Concluded.

TABLE 12-III.—Maximum Abundance of Particles at Right Astronaut Eye

Energy loss, keV/ $\mu$ m	Protons at SAA, no.	Primary cosmic particles at the north magnetic pole <sup>a</sup> no./( $3 \text{ min} \cdot 4 \text{ cm}^2$ )		
		Alpha	$6 \leq Z \leq 9$	Cosmic total
$\geq 0.5$	114 200	117	10	135
$\geq 1$	5 813	51	10	67
$\geq 5$	241	.4	6	10
$\geq 10$	53	.07	3	6
$\geq 15$	22	.03	2	4
<sup>b</sup> $\geq 15$	<sup>b</sup> 318	<sup>b</sup> .08	<sup>b</sup> 2	<sup>b</sup> 4
$\geq 20$	11	.02	1	3
$\geq 25$	7	.01	.5	2

<sup>a</sup>South magnetic pole maximum abundances are 8 percent less.<sup>b</sup>For 443-km altitude of Skylab 4 but shielding of Apollo.

however, no events were observed near the Equator (fig. 12-6(c)). These observations are consistent with the change in abundance of cosmic particles with latitude (figs. 12-6 and 12-8(a)), which was also noted during the Skylab 4 mission (ref. 12-6). The increased rate of visual events near the south geomagnetic pole can be explained by the increased dark adaptation of the crewmembers. The observed event rate correlates with a cosmic particle abundance for heavy particles with energy losses  $\geq 5 \text{ keV}/\mu\text{m}$  (fig. 12-8(a)). The previous experiments indicate that the threshold for high-efficiency visualization of primary events is  $10 \text{ keV}/\mu\text{m}$  (refs. 12-13 and 12-15), but the calculated flux for ions of  $10 \text{ keV}/\mu\text{m}$  and greater is too low to correspond to the observed rate (table 12-III

and fig. 12-8(a)). This discrepancy could be resolved by increasing the abundances by a factor of 2, which might be appropriate because the calculations did not include the change in the modulation of the cosmic spectrum associated with the solar cycle.

The  $\text{AgCl}(\text{Cd})$  detector results (table 12-II) suggest that 60 events of  $15 \text{ keV}/\mu\text{m}$  or greater would be observed during 3-minute intervals in the northernmost portions of the orbit. The highest observed event rate at high latitudes was only 14 events/3 min near the south magnetic pole. This rate would imply a 23-percent efficiency; however, near the Equator, where only a few events were observed, the detectors recorded the equivalent average of  $73 \text{ events}/4 \text{ cm}^2 \cdot \text{min}$ .

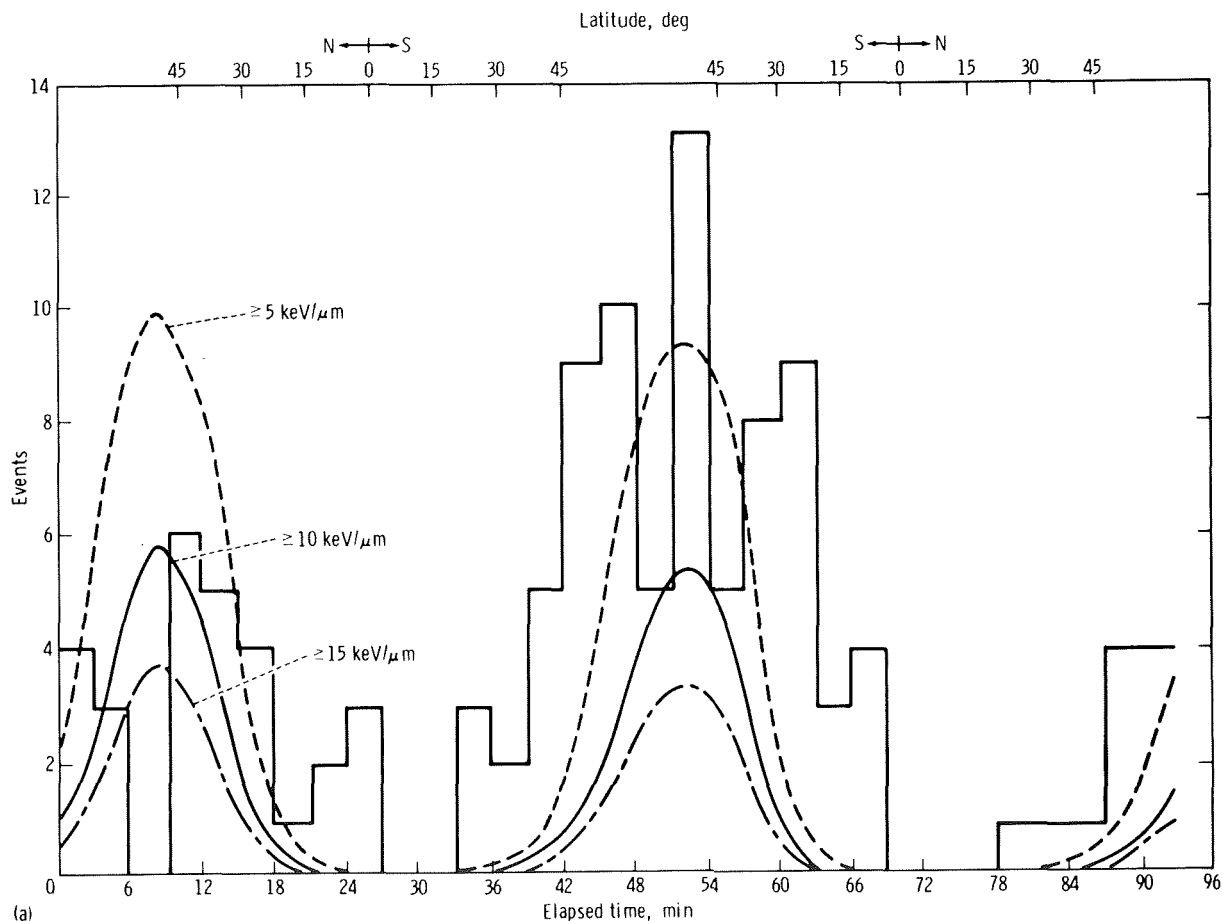


FIGURE 12-8.—Comparison of calculated abundances (curves) to observed events (histograms). (a) Cosmic particles.  
(b) Trapped protons.

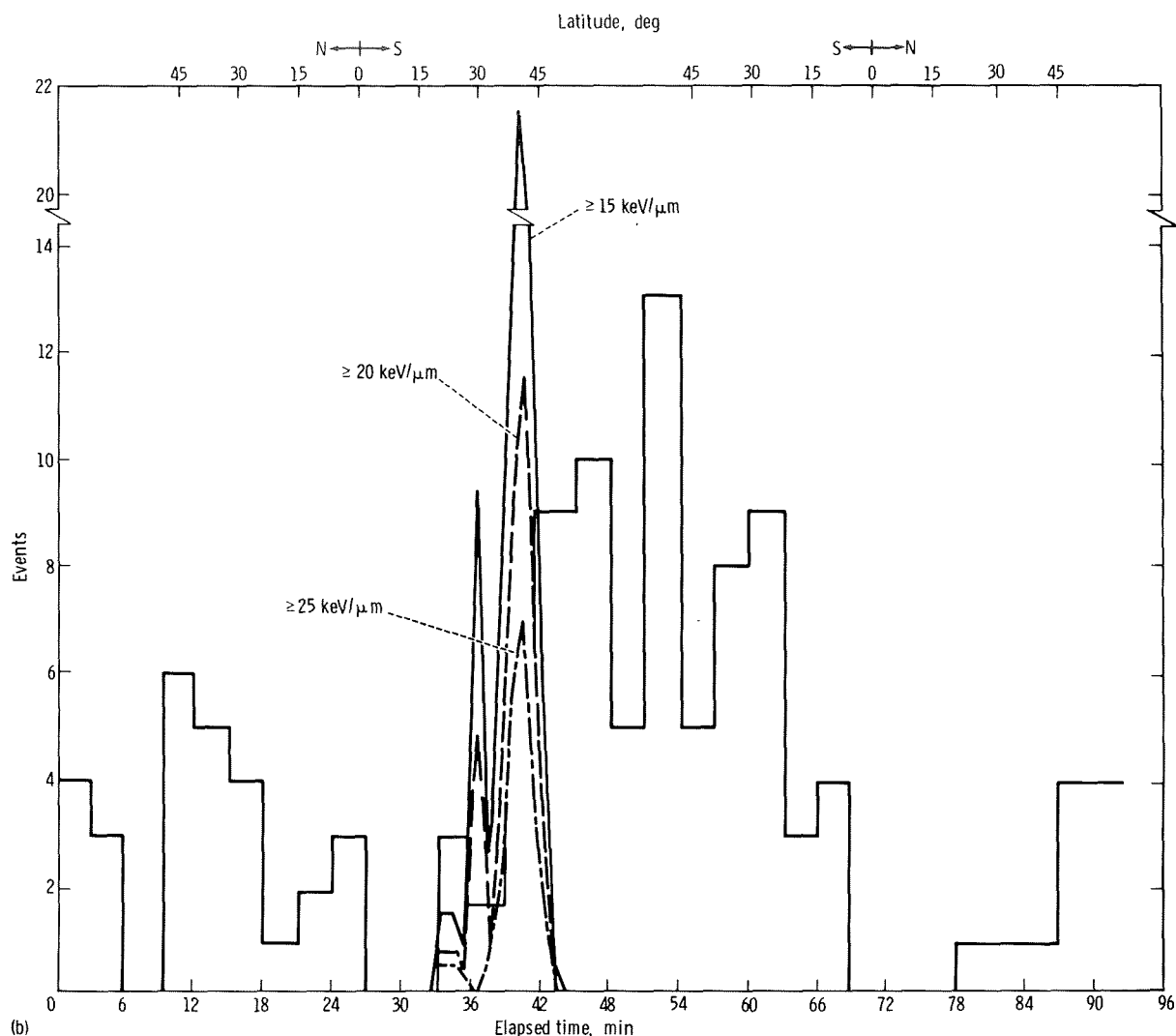


FIGURE 12-8.—Concluded.

These results are not consistent. An explanation is that the fading time from the heavy ions is long relative to the orbit sectors; thus, good identification of the very heavy particle environment in each sector cannot be expected. Particles interacting in the crystals hours before the experiment might have been included in the count.

Better time discrimination is expected from the stopping protons and alpha particles (table 12-II). Assuming the complete retina target area is  $4 \text{ cm}^2$ , the efficiency of visualizing these events is 36 percent for the northernmost sector; but here also,

the efficiency diminishes to only 8 percent for the SAA. Thus, the AgCl(Cd) detector data do not correlate well with either the observed event rate or the calculated abundances.

### South Atlantic Anomaly Observations

There were no reports of a high frequency of flash phenomena through the SAA, as might be expected from a previous Skylab 4 report of markedly increased flash activity (ref. 12-6). Only

four events were reported in this region for Apollo-Soyuz (fig. 12-5), whereas 112 events were reported in a 12-minute period through the SAA during Skylab 4. At the 225-km altitude of Apollo-Soyuz, the proton flux of particles ( $\text{LET} \geq 15 \text{ keV}/\mu\text{m}$ ) is 14 times less than at the 443-km altitude of Skylab 4. Also, the shielding of the Apollo command module is much greater than that of Skylab. The Apollo command module shielding was  $3.0$  to  $3.5 \text{ g/cm}^2$  of aluminum over a

solid angle of  $0.27\pi \text{ sr}$  and  $3.5$  to  $5.5 \text{ g/cm}^2$  over  $0.77\pi \text{ sr}$  solid angle, whereas the observations from Skylab were made in a minimum shielding area of  $1.5$  to  $2.0 \text{ g/cm}^2$  over  $1.5\pi \text{ sr}$ .

The distribution of protons near the astronauts' eyes along the orbit is shown in figure 12-8(b). Although the abundance of protons with energy loss  $\geq 15 \text{ keV}/\mu\text{m}$  is great enough to explain the few events seen in the SAA region at latitude  $35^\circ \text{ S}$  (fig. 12-6(b)), a group of events that correspond to

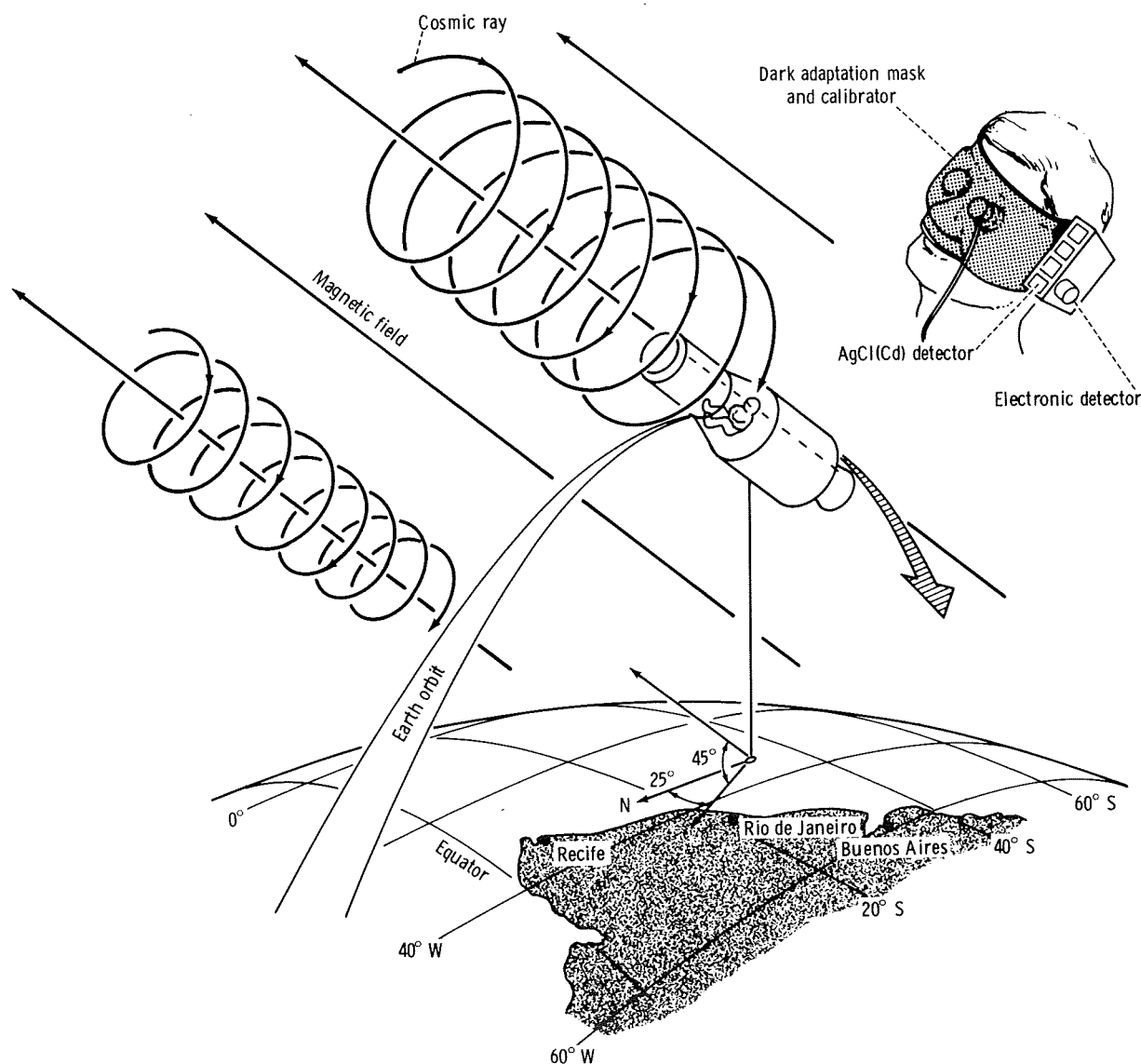


FIGURE 12-9.—Orientation of the spacecraft and astronauts during passage over the SAA.

the SAA cannot be statistically separated. Care was taken to orient the spacecraft and crewmembers so that the particle trajectories would cross the posterior eye orbit tangentially (fig. 12-9). From accelerator experiments, as well as a consideration of maximum path length in the retina, this orientation optimizes the efficiency of the human eye and the AgCl(Cd) crystal detectors. The hypothesis that protons with an LET of  $\geq 15$  keV/ $\mu$ m cause these observed streaks is questionable because these protons have a range of only 100  $\mu$ m and could not cause a streak because they would intersect 10 retinal rods or less.

An alternate explanation for events seen in the SAA, particularly at higher altitudes, is the mechanism of proton nonelastic nuclear collision with carbon, hydrogen, and oxygen in tissues of the retina. This mechanism is similar to that proposed for neutron interactions, which also cause discrete flashes (refs. 12-12 and 12-13). If the average cross section for interactions such as ( $p$ ,  $p'$ ,  $3\alpha$ ) on carbon, nitrogen, or oxygen is assumed to be approximately 45 fm<sup>2</sup> (450 mb) in the proton energy range of 175 MeV or less, only 1 event/3 min would occur during Apollo-Soyuz; however, at the Skylab 4 altitude, the flux of protons was 23 times greater than at the Apollo-Soyuz altitude of 225 km (table 12-III). Under the reduced shielding conditions of Skylab 4, 51 times more protons would interact with the eye tissues of one observer, or 26 events might be observed during a 3-minute interval. The average rate was 28 events/3 min. Thus, the nuclear collision hypothesis for the origin of light flashes in the SAA has some validity.

### ACKNOWLEDGMENTS

The following persons made important contributions to this project: W. Greenberg, University of California at Berkeley; J. Kucala, Lawrence Livermore Laboratory; and R. Dowling, F. Goulding, B. Moyer, J. Walton, and R. Walton, Lawrence Berkeley Laboratory.

### REFERENCES

- 12-1. Chapman, P. K.; Pinsky, L. S.; Benson, R.E.; and Budinger, T. F.: Observations of Cosmic Ray Induced Phosphenes. Proceedings of the National Symposium on Natural and Manmade Radiation in Space, E. A. Warren, ed. NASA TM X-2440, 1972, pp. 1002-1006.
- 12-2. Budinger, T. F.; Tobias, C. A.; et al.: Light Flash Phenomenon Seen by Astronauts. Proceedings of the Colloquium on Space Biology Related to Post-Apollo Program. ESRO, Paris, France, 1971, p. 209.
- 12-3. Benson, R. E.; and Pinsky, L. S.: Visual Light Flash Phenomenon. Sec. 27, Pt. C, of the Apollo 16 Preliminary Science Report. NASA SP-315, 1972.
- 12-4. Pinsky, L. S.; Osborne, W. Z.; and Bailey, J. V.: Visual Light Flash Phenomenon. Sec. 27 of the Apollo 17 Preliminary Science Report. NASA SP-330, 1973.
- 12-5. Pinsky, L. S.; Osborne, W. Z.; et al.: Light Flashes Observed by Astronauts on Apollo 11 Through Apollo 17. Science, vol. 183, no. 4120, Mar. 8, 1974, pp. 957-959.
- 12-6. Pinsky, L. S.; Osborne, W. Z.; Bailey, J. V.; and Hoffman, R. A.: Light Flashes Observed by Astronauts on Skylab 4. Science, vol. 188, no. 4191, May 30, 1975, pp. 928-930.
- 12-7. Tobias, C. A.: Radiation Hazards in High Altitude Aviation. J. Aviation Med., vol. 23, 1952, p. 345.
- 12-8. Fazio, G. G.; Jelley, J. V.; and Charman, W. N.: Generation of Cerenkov Light Flashes by Cosmic Radiation Within the Eyes of the Apollo Astronauts. Nature, vol. 228, no. 5268, Oct. 17, 1970, pp. 260-264.
- 12-9. McNulty, P. J.: Light Flashes Produced in the Human Eye by Extremely Relativistic Means, Nature, vol. 234, no. 5323, Nov. 12, 1971, p. 110.
- 12-10. McNulty, P. J.; Pease, V. P.; et al.: Visual Sensations Induced by Relativistic Nitrogen Nuclei. Science, vol. 178, no. 4056, Oct. 13, 1972, p. 160.
- 12-11. McNulty, P. J.; Pease, V. P.; and Bond, V. P.: Visual Sensations Induced by Cerenkov Radiation. Science, vol. 189, no. 4201, Aug. 8, 1975, pp. 453-454.
- 12-12. Tobias, C. A.; Budinger, T. F.; and Lyman, J. T.: Radiation-Induced Light Flashes Observed by Human Subjects in Fast Neutron, X-ray, and Positive Pion Beams. Nature, vol. 230, Apr. 30, 1971, pp. 596-597.

- 12-13. Budinger, T. F.; Bichsel, H.; and Tobias, C. A.: Visual Phenomena Noted by Human Subjects on Exposure to Neutrons of Energies Less Than 25 Million Electron Volts. *Science*, vol. 172, no. 3978, May 21, 1971, pp. 868-870.
- 12-14. Tobias, C. A.; Budinger, T. F.; and Lyman, J. T.: Biological Effects Due to Single Accelerated Heavy Particles - Problems of Nervous System Exposure in Space. In *Life Sciences and Space Research XI*, P. H. A. Sneath, ed., Akademie-Verlag (Berlin), 1973, p. 233.
- 12-15. Budinger, T. F.; Lyman, J. T.; and Tobias, C. A.: Visual Perception of Accelerated Nitrogen Nuclei Interacting With the Human Retina. *Nature*, vol. 239, no. 5369, Sept. 22, 1972, pp. 209-211.
- 12-16. Schott, J.-U.: *Eigenschaften von AgCl(Cd)-Kristallen als Teilchenspur-Detektoren*. Ph. D. Thesis, Institut für Kernphysik der Johann Wolfgang Goethe-Universität Frankfurt Am Main, 1974.
- 12-17. Webber, W. R.; Damle, S. V.; and Kish, J.: Studies of the Chemical Composition of Cosmic Rays with  $Z = 3-30$  at High and Low Energies. *Astrophys. Space Sci.*, vol. 15, Feb. 1972, pp. 245-271.
- 12-18. Smith, L. H.; Buffington, A.; et al.: A Measurement of Cosmic-Ray Rigidity Spectra Above 5 GV/c of Elements From Hydrogen to Iron. *Astrophys. J.*, vol. 180, no. 3, Mar. 1973, pp. 987-1010.
- 12-19. Juliusson, E.: Cosmic Rays at Very High Energies. Vol. I, Proceedings of the 13th International Cosmic Ray Conference, 1974, pp. 373-377.
- 12-20. Lavine, J. P.; and Vette, J. I.: Models of the Trapped Radiation Environment. Vol. VI - High Energy Protons. NASA SP-3024, 1970.
- 12-21. Hendricks, S. J.; and Cain, J. C.: Magnetic Field Data for Trapped-Particle Evaluations. *J. Geophys. Res.*, vol. 71, no. 1, Jan. 1, 1966, pp. 346-349.
- 12-22. Shea, M. A.; and Smart, D. F.: A Five by Fifteen Degree World Grid of Calculated Cosmic-Ray Vertical Cutoff Rigidities for 1965 and 1975. Vol. 4, Proceedings of the 14th International Cosmic Ray Conference, 1975, pp. 1298-1304.
- 12-23. Smart, D. F.; and Shea, M. A.: A Study of the Effectiveness of the McIlwain Coordinates in Estimating Cosmic-Ray Vertical Cutoff Rigidities. *J. Geophys. Res.*, vol. 72, no. 13, July 1, 1967, pp. 3447-3454.
- 12-24. Smart, D. F.; and Shea, M. A.: An Analysis of Trajectory-Derived Penumbra Widths. Vol. 4, Proceedings of the 14th International Cosmic Ray Conference, 1975, pp. 1309-1314.





# 13. Biostack III

## Experiment MA-107

*Horst Bücker,<sup>a†</sup> M. Delpoux,<sup>b</sup> S. Fogel,<sup>c</sup> M. Freeling,<sup>c</sup> E. H. Graul,<sup>d</sup> G. Horneck,<sup>a</sup> A. R. Kranz,<sup>a</sup> H. Planel,<sup>b</sup> W. Rüther,<sup>d</sup> U. Scheidemann,<sup>a</sup> C. Thomas,<sup>a</sup> C. A. Tobias,<sup>c</sup> B. Toth,<sup>a</sup> T. Yang,<sup>c</sup> O. C. Allkofer,<sup>e</sup> R. Beaujean,<sup>e</sup> E. V. Benton,<sup>f</sup> W. Enge,<sup>e</sup> R. Facius,<sup>a</sup> H. Francois,<sup>g</sup> W. Heinrich,<sup>h</sup> D. Hildebrand,<sup>a</sup> C. Jacquot,<sup>i</sup> R. Kaiser,<sup>i</sup> J. P. Massué,<sup>i</sup> E. Obst,<sup>a</sup> D. D. Peterson,<sup>f</sup> R. Pfohl,<sup>i</sup> G. Portal,<sup>g</sup> G. Reitz,<sup>a</sup> E. Schopper,<sup>a</sup> M. Schäfer,<sup>a</sup> J.-U. Schott,<sup>a</sup> and G. Siegmone<sup>e</sup>*

### ABSTRACT

The Biostack III Experiment onboard the Apollo spacecraft during the Apollo-Soyuz Test Project complemented the Biostack I and II experiments of the Apollo 16 and 17 missions. The objectives of these experiments were to study the biological effects of individual heavy cosmic particles of high-energy loss (HZE) not available on Earth, to study the influence of additional space-flight factors, to obtain knowledge on the mechanism by which HZE particles damage biological materials, to get information on the spectrum of charge and energy of the cosmic ions in the spacecraft, and to estimate the radiation hazards to man in space.

For these purposes, the Biostack experiment includes a wide spectrum of biological objects, and various radiobiological end points are under investigation. Bacterial spores, protozoa cysts, plant

seeds, shrimp eggs, and insect eggs were included in the Biostack experiment packages together with different physical radiation detectors (nuclear emulsions, plastics, silver chloride crystals, and lithium fluoride thermoluminescence dosimeters). The biological objects in the Biostack are stacked alternately between physical detectors of HZE particle tracks. By using special arrangements of biological objects and physical track detectors, individual evaluation of tracks was obtained that permitted the identification of each penetrating particle in relation to the possible biological effect along its path. A precision micromanipulator was developed that allowed the transfer of a single bacterial spore from the flight plates to the nutrient medium, thus permitting observation of the growth of known hit spores for changes in development, growth kinetics, and cell morphology. The response of the different biological objects to space flight and HZE particle bombardment varied in degree, presumably depending on the ability of the organism to replace the cells damaged by a hit. The results help to estimate the radiation hazard during long-duration space missions.

### INTRODUCTION

Although the contribution of high-energy-loss (HZE) particles to space-radiation exposure is only approximately 1 percent, the biological importance cannot be neglected. During space flight,

<sup>a</sup>University of Frankfurt.

<sup>b</sup>University of Toulouse.

<sup>c</sup>University of California.

<sup>d</sup>University of Marburg.

<sup>e</sup>University of Kiel.

<sup>f</sup>University of San Francisco.

<sup>g</sup>Atomic Energy Commission, Republic of France.

<sup>h</sup>University of Siegen.

<sup>i</sup>University of Strasbourg.

<sup>†</sup>Principal Investigator.

HZE particles that are difficult to attenuate by shielding may penetrate or stop in biological tissue; each particle leaving behind a track of extremely high energy deposition. The passage of a single HZE particle may result in serious biological impairment or injury, as has been demonstrated in the space-flight experiments of Biostack I onboard Apollo 16 (ref. 13-1) and Biostack II (ref. 13-1) and Biocore (ref. 13-2) onboard Apollo 17. An urgent need exists for determining the hazard of HZE-particle exposure to man in space (especially during long-duration or repeated flights (ref. 13-3)) and to other living systems that may be involved in space flight.

The objective of the Apollo-Soyuz Test Project (ASTP) Biostack III experiment was to confirm, complement, and expand the information gained from the Biostack I and II experiments on the biological effects of individual HZE particles of cosmic radiation and on the influence of additional random space-flight factors. The ASTP dosimetric and radiobiological data of Biostack III were compared with Biostack I and II data from lunar flights to examine the differences inside and outside of the geomagnetic field. The results may contribute to an estimation of the radiation hazards to man in space and to a lowering of the radiation risk by ensuring maximum possible shielding against HZE particles in the design and construction of future space vehicles.

## EQUIPMENT AND PROCEDURES

During the 218 hours of the ASTP mission, the Biostack III experiment was stored in the R-1 compartment of the Apollo command module (fig. 13-1), where shielding to ambient cosmic radiation was minimal. The same storage area was used for Biostack I and II onboard Apollo 16 and 17.

The Biostack III experiment was contained in two cylindrical aluminum containers designated III/A and III/B (fig. 13-2). Container III/A had the same design as the Biostack I and II experiments (ref. 13-1) and enclosed a stack of 277 sheets, which were layers of different biological objects inserted between different track detectors. This method permitted the localization of each HZE

particle trajectory in the biological layer and the correlation of potential biological effects with the characteristics of the responsible HZE particle (ref. 13-4). Eight biological experiments were accommodated in container III/A, and two biological experiments in container III/B in stack B1 (table 13-I). In addition, seven dosimetric experiments were performed (table 13-II). The silver chloride (AgCl) crystals required illumination by yellow light to stabilize the particle tracks; therefore, container III/B was equipped with small lamps, a filter system, and batteries. Container III/B also contained two further detector stacks (III/B2 and III/B3) for dosimetric studies.

In addition to the postflight procedures used for Biostack I and II (refs. 13-1 and 13-4), new techniques were developed and used (ref. 13-5). Pinpoint etching of plastic detectors improved the accuracy of localizing particle tracks in relation to biological objects to within  $\pm 0.2 \mu\text{m}$ . A computer-supported track measurement system aided in the determination of which internal seed structures

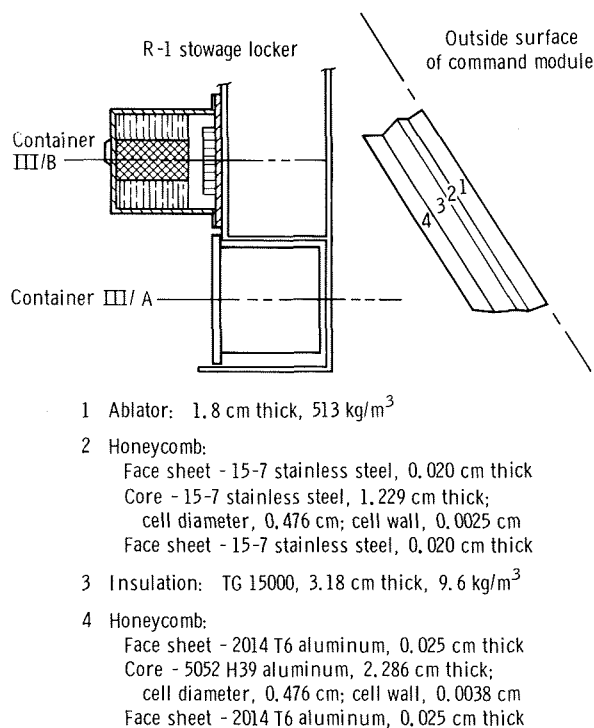


FIGURE 13-1.—Stowage location of the Biostack experiment and structural shielding of the Apollo command module.

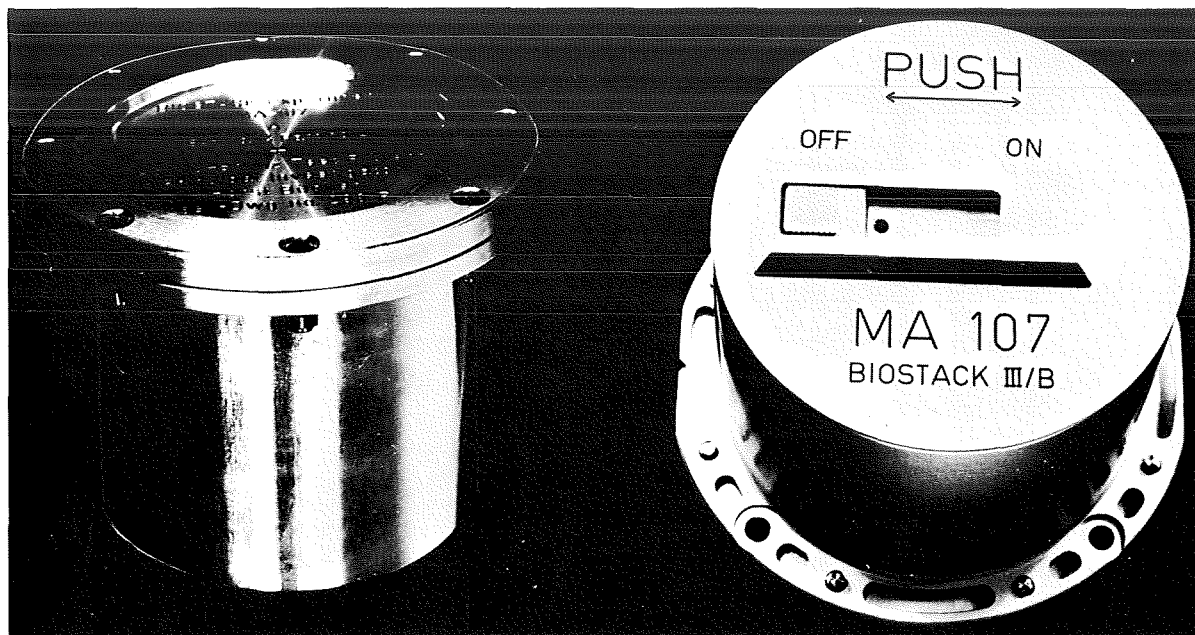


FIGURE 13-2.—Biostack III/A and III/B containers.

had been crossed by an HZE particle. High-precision micromanipulation of single bacterial spores permitted the observation of each spore around a particle track for changes in development, for changes in growth and colony formation, and for induction of mutations. Track decoration by copolymerization was attempted in plastic detectors. After obtaining the complete set of Biostack III data, a multifactorial analysis will be performed to detect relationships between the different parameters and condense them into factors; correlations among the factors will then be calculated.

### DOSIMETRIC DATA

The total dose of space radiation was measured by thermoluminescence dosimeters (TLD) in stack III/A at the top, middle, and bottom and in stack III/B2 at both ends of the stack. The results are shown in table 13-III. (The bottom of the stack in III/A was closest to the outside wall of the spacecraft, i.e., closest to the "space" environment; the top of the stack had the greatest prox-

imity to the spacecraft cabin environment. Stack III/B was oriented conversely (fig. 13-1).)

The 600- $\mu\text{m}$ -thick K2 nuclear emulsion plates were analyzed to obtain dosimetric data on particles of charge  $Z=1$  and  $Z=2$  and on nuclear disintegration stars; the dose from particles of charge  $Z>2$  was estimated (table 13-IV). The dose was approximately 0.015 mJ/kg and was nearly the same for these three components of cosmic radiation.

The sensitivity of the 200- $\mu\text{m}$ -thick AgCl detectors in stack III/B1 was comparable to that of K2 nuclear emulsions. The threshold of sensitivity (defined by the threshold of recognizability of a grainy track at the opacity  $O = 0.2$ ) corresponds to

$$\left. \begin{aligned} \text{LET} &\approx 10 \text{ MeV cm}^2/\text{g} \\ &\approx 6 \text{ keV}/\mu\text{m AgCl} \\ &\approx 1.1 \text{ keV}/\mu\text{m tissue} \end{aligned} \right\} \quad (13-1)$$

where LET is the linear energy transfer. This means that protons of energies  $<28$  MeV, alpha

TABLE 13-I.—*Biostack III Biological Experiments*

<i>Biological object</i>	<i>Effects investigated</i>	<i>Track detector (a)</i>	<i>Biostack III location</i>	<i>Investigators</i>	<i>Affiliation</i>
Monocellular: <i>Bacillus subtilis</i> spores	Spore outgrowth, growth, and mutation	CN AgCl Lexan	A B	R. Facius, D. Hildebrand, G. Hölztz, G. Horneck, M. Schäfer, and B. Toth	University of Frankfurt
Plant: <i>Arabidopsis thaliana</i> seeds	Growth, morphogenesis, and mutation	CN Lexan	A	A. R. Kranz, U. Scheidemann, and C. Thomas	University of Frankfurt
<i>Nicotiana tabaccum</i> seeds	Growth, development, and mutation	K2	A	M. Delpoux	University of Toulouse
<i>Zea mays</i> seeds	Growth, differentiation, morphogenesis, and mutation	CN Lexan	A	C. A. Tobias, T. Yang, M. Freeling, and S. Fogel	University of California
Animal: <i>Artemia salina</i> eggs	Early steps of development	K2	A	H. Planel	University of Toulouse
	Development, morphogenesis, and histology	K2 CN	A	W. Rüther and E. H. Graul W. Heinrich	University of Marburg University of Siegen
		AgCl	B	W. Rüther and E. H. Graul	University of Marburg
<i>Tribolium confusum</i> eggs	Development and morphogenesis	K2	A	W. Rüther and E. H. Graul	University of Marburg
<i>Carausius morosus</i> eggs	Development and morphogenesis	K2	A	W. Rüther and E. H. Graul	University of Marburg

<sup>a</sup>AgCl - silver chloride, CN - cellulose nitrate, K2 - nuclear emulsion.

TABLE 13-II.—*Biostack III Dosimetric Experiments*

Detector	Description	Physical data investigated	Detectors included -				Investigators	Affiliation
			A	B1	B2	B3		
CN	Track detector Area sensitive Tissue comparable	Particles with $LET_{1000} > 1 \text{ GeV cm}^2/\text{g}$ (Parameters measured: energy, charge, pathlength, and $LET_{1000}$ )	X	X	X	X	W. Enge, O. C. Allkofer, K. P. Bartholomä, R. Beaujean, and K. Fukui W. Heinrich E. V. Benton and D. D. Peterson R. Facius, D. Hildebrand, G. Reitz, and M. Schäfer	University of Kiel  University of Siegen University of San Francisco University of Frankfurt
Lexan	Track detector Area sensitive Tissue comparable	Particles with $LET_{1000} > 3 \text{ GeV cm}^2/\text{g}$ (Parameters measured: energy, charge, pathlength, and $LET_{1000}$ )	X		X		W. Enge, O. C. Allkofer, K. P. Bartholomä, R. Beaujean, and K. Fukui W. Heinrich E. V. Benton and D. D. Peterson	University of Kiel  University of Siegen University of San Francisco
Cellulose triacetate (CTA)	Track detector Area sensitive Volume sensitive Tissue comparable	Particles with $LET_{1000} > 1.5 \text{ GeV cm}^2/\text{g}$ (Parameters measured: energy, charge, pathlength, and LET) Primary particles with $LET > 2.0 \text{ GeV cm}^2/\text{g}$ Attenuated particles with $LET > 0.5 \text{ GeV cm}^2/\text{g}$ Stars and other HED-event indications	X		X	X	D. Hildebrand, C. Thomas, and G. Reitz	University of Frankfurt
K2	Track detector Volume sensitive	Particles with $LET > 10 \text{ MeV cm}^2/\text{g}$ (Parameters measured: LET, charge group, pathlength, dose contribution, and all HED events)	X	X	X		R. Kaiser, J. P. Massué, and R. Pfohl	Center of Nuclear Research, Strasbourg

TABLE 13-II.—*Concluded*

Detector	Description	Physical data investigated	Detectors included -				Investigators	Affiliation
			A	B1	B2	B3		
K5	Track detector Volume sensitive	Particles with LET > 10 MeV cm <sup>2</sup> /g (Parameters measured: LET, charge group, pathlength, dose contribution, and all HED events) Quasi-homogeneous component	X	X			R. Kaiser, J. P. Massué, and R. Pfohl	Center of Nuclear Research, Strasbourg
AgCl	Track detectors Volume sensitive	Particles with LET > 10 MeV cm <sup>2</sup> /g (Parameters measured: LET, charge group, pathlength, and all HED events)		X			E. Schopper, J.-U. Schott, and E. Obst	University of Frankfurt
Thermo- luminescence dosimeter (TLD)	Total dose measurement	Total dose	X		X		H. François and G. Portal	Atomic Energy Commission, Republic of France

TABLE 13-III.—*Total Dose of Cosmic Radiation  
Measured by TLD in Biostack III*

Container	Position in the container	Total absorbed dose, mJ/kg	Mission absolute dose, mJ/kg	Mission dose rate, $\mu$ J/kg hr
<i>Flight unit</i>				
III/A	Bottom	1.10	0.99	4.54
	Middle	1.21	1.10	5.04
	Top	1.35	1.24	5.69
III/B2	Middle	1.15	1.03	4.72
	Bottom	1.13	1.01	4.63
<i>Ground control</i>				
III/A	Bottom	0.113	--	--
	Middle	.109	--	--
	Top	.106	--	--
III/B2	Middle	.117	--	--

TABLE 13-IV.—*Dosimetric Data From K2 Nuclear  
Emulsions of Biostack III*

Phenomena	Fluence	Dose, mJ/kg
Particles, Z = 1 and Z = 2	8800/cm <sup>2</sup>	0.014
Particles, Z > 2	<sup>a</sup> 88/cm <sup>2</sup>	.015
Stars	13 000/cm <sup>3</sup>	.013

<sup>a</sup>Estimated

particles of energies  $< 200$  MeV/nucleon, and particles of  $Z \geq 4$  at all energies are detected. The fluence of particles of  $LET > 10$  MeV  $cm^2/g$  is shown in table 13-V.

The HZE particles with  $LET > 0.8$  GeV  $cm^2/g$  were recorded in the cellulose nitrate (CN) plastic detectors. The dosimetric data obtained to date are

shown in table 13-VI. Nuclear disintegration stars have been detected on the surface of the CN Kodak (CN<sub>K</sub>) sheets of the *Bacillus subtilis* unit. Micrographs of etch cones from stars having prongs cut by the foil surface are shown in figure 13-3. A mean of 0.35 stars per square centimeter of surface was found.

TABLE 13-V.—Dosimetric Data From AgCl Detectors of Biostack III

[ $LET > 10$ MeV $cm^2/g$ .]	
All particles, particles/ $cm^2$ .....	$1500 \pm 100$
Stopping protons, particles/ $cm^2$ .....	50
Stopping alpha particles, particles/ $cm^2$ .....	70
Disintegration stars, stars/ $cm^3$ of AgCl .....	3500
Disintegration stars, stars/g of AgCl .....	$\approx 6300$

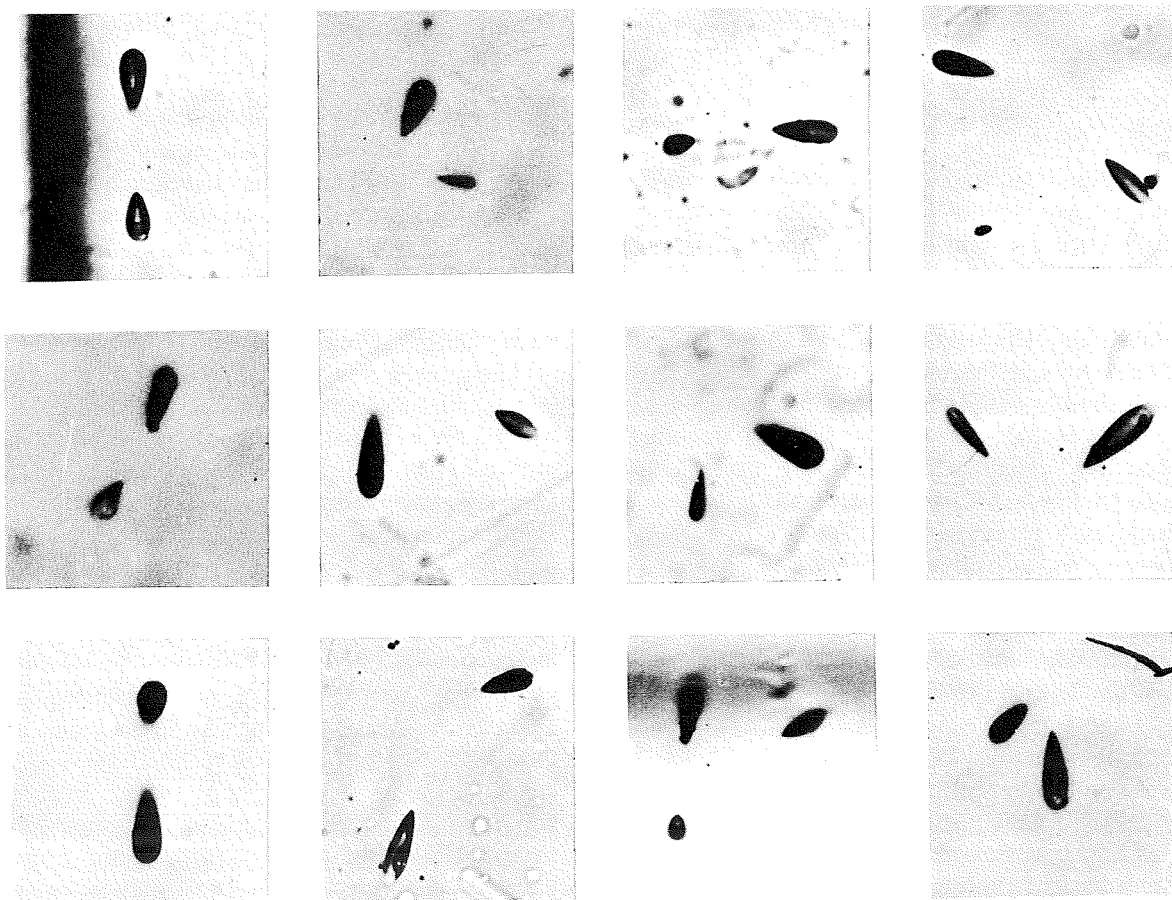


FIGURE 13-3.—Stars cut by a CN<sub>K</sub> surface, found in foils K3-29 and K3-32.

TABLE 13-VI.—Dosimetric Data From Scanning of Selected CN Plastic Detectors of Biostack III

Stack	Direction (a)	Detector designation		Thickness, $\mu\text{m}$	Threshold $x$ (where $LET > x$ ), $\text{MeV cm}^2/\text{g}$	Fluence, tracks/cm <sup>2</sup>				
		Layer no. (b)	Foil no.			Total	Etched through	Two cones	One cone	Stopping track
III/A	Space	K2	2	250	$1.0 \times 10^3$	--	2.5	--	--	--
		K2	54	100	.8	6.4	--	--	--	--
		K3	29	100	.8	3.5	--	--	--	--
		K3	32	100	.8	3.3	--	--	--	--
		K3	47	250	1.0	1.69	.52	0.34	0.49	0.34
		K3	50	250	1.0	1.86	.54	.31	.54	.47
		K3	53	250	1.0	1.38	.65	.21	.36	.16
		K3	56	250	1.0	1.79	.52	.34	.36	.57
		K3	59	250	1.0	1.56	.34	.39	.39	.44
		K3	62	250	1.0	1.03	.39	.31	.31	.03
		K13	2	250	1.0	--	1.8	--	--	--
		K13	22	250	1.0	2.0	--	--	--	--

<sup>a</sup>The lower layer numbers were closest to the outside wall of the spacecraft; i.e. closest to the "space" environment. The higher layer numbers had the greatest proximity to the spacecraft cabin environment.

<sup>b</sup>The prefix "K" in this column was used for designating the stack assembly used for the flight.

## BIOLOGICAL DATA

The biological objects that were hit by an HZE particle were identified from analyses of the adjacent track detector sheets (either nuclear emulsions or CN). The results of these analyses are summarized in table 13-VII. The developed K2 emulsions, which were attached to the biological layer, showed the HZE particle tracks together with shadows of the biological objects of the adjacent layer (ref. 13-6). In the partly translucent seeds of *Arabidopsis thaliana*, the internal structure that was hit was determined from the attached CN Daicel (CN<sub>D</sub>) detector (fig. 13-4) by a computer-supported method (ref. 13-5, table 13-VIII). The etch cones of HZE particles that hit a corn seed (fig. 13-5) were measured in the adjacent plastic sheets to obtain the energy loss and the charge (fig. 13-6). In the *Bacillus subtilis* spore layer, molded onto CN, the pinpoint etching technique of single particle tracks (ref. 13-5) enabled a highly precise experimental determination of the particle penetration point. After determining the experimental penetration point, the so-called impact parameter  $b$ , which is the closest distance between the center of the hit spore and the particle trajectory, was calculated.

Table 13-IX shows the frequency distribution of *Bacillus subtilis* spores for  $b$  values given in discrete intervals of  $1 \mu\text{m}$ . The micrographs shown in figure 13-7 illustrate the procedure. Measurements on AgCl crystals that carried a *Bacillus subtilis* spore layer resulted in 23 spores with  $b \leq 0.6 \mu\text{m}$ . The energy loss of the responsible particles has been determined and is presented in table 13-X.

The growth and development studies and the genetic studies on the biological objects that were hit are still in progress and only preliminary data are available. Outgrowth, growth, and colony-forming ability were investigated in 242 *Bacillus subtilis* spores of an impact parameter  $b < 6 \mu\text{m}$  and were compared with the growth characteristics of the flight controls ( $b > 50 \mu\text{m}$ ) and the ground controls (fig. 13-8). Growth was significantly reduced in spores of  $b < 4 \mu\text{m}$ . This result is surprising, but it is also important because dosimetric calculations for the  $\delta$ -electrons predicted  $b \approx 0.5 \mu\text{m}$  for this reduced survival instead of the  $b < 4 \mu\text{m}$ . Shock waves from the penetrating particles are probably responsible for this effect. Further deviations from normal development were also observed, such as swelling of the first vegetative cell, which did not divide (fig. 13-9).



TABLE 13-VII.—*Biological Objects Hit or in the Vicinity of an HZE Particle*

Biological object	Detector designation		Track detector (b)	Objects/layer	Objects hit/layer	Total objects hit
	Layer no. (a)	Foil no.				
<i>Bacillus subtilis</i> spores	K3	30	CN <sub>K</sub>	≈ 10 <sup>9</sup>	<sup>c</sup> 38	<sup>d</sup> 461
	K3	54	CN <sub>D</sub>	≈ 10 <sup>9</sup>	<sup>c</sup> 115	
	K3	55	CN <sub>D</sub>	≈ 10 <sup>9</sup>	<sup>c</sup> 119	
	K3	60	CN <sub>D</sub>	≈ 10 <sup>9</sup>	<sup>c</sup> 84	
	K3	61	CN <sub>D</sub>	≈ 10 <sup>9</sup>	<sup>c</sup> 105	
<i>Arabidopsis thaliana</i> seeds	K4	11	CN <sub>D</sub>	≈ 10 000	7	<sup>d</sup> 18
	K4	12	CN <sub>D</sub>	≈ 10 000	11	
<i>Nicotiana tabaccum</i> seeds	K11	2	K2	1164	47	78
	K11	4	K2	1164	31	
<i>Zea mays</i> seeds	K12	1	CN	80	41	90
	K12	2	CN	80	49	
<i>Artemia salina</i> eggs	K5	5	K2	≈ 9000	69	<sup>d</sup> 139
	K5	7	K2	≈ 9000	70	
<i>Tribolium confusum</i>	K9	5	K2	≈ 6000	57	123
	K9	7	K2	≈ 6000	66	
<i>Carausius morosus</i> eggs	K10	2	K2	370	82	147
	K10	4	K2	370	65	

<sup>a</sup>The prefix "K" in this column was used for designating the stack assembly used for the flight.

<sup>b</sup>The prefix "K" in this column is part of the manufacturer's emulsion designation; e.g., K2.

<sup>c</sup>Spores in the neighborhood of a track.

<sup>d</sup>In progress.

 TABLE 13-VIII.—*Area of Arabidopsis Thaliana Seeds Hit by an HZE Particle*

Seed no.	Area hit	Seed no.	Area hit
Foil no. K4 - 12		Foil no. K4 - 11u	
1	Cotyledones	1	Cotyledones
2	Cotyledones	3	Cotyledones
3	Cotyledones	4	Cotyledones
7	Cotyledones	5	Cotyledones
9	Cotyledones	6	Cotyledones
10	Cotyledones	2	Root, cotyledones
6	Root	7	Root, cotyledones
4	Root, cotyledones, meristem <sup>a</sup>		
8	Root, one cotyledone		

<sup>a</sup>Questionable.

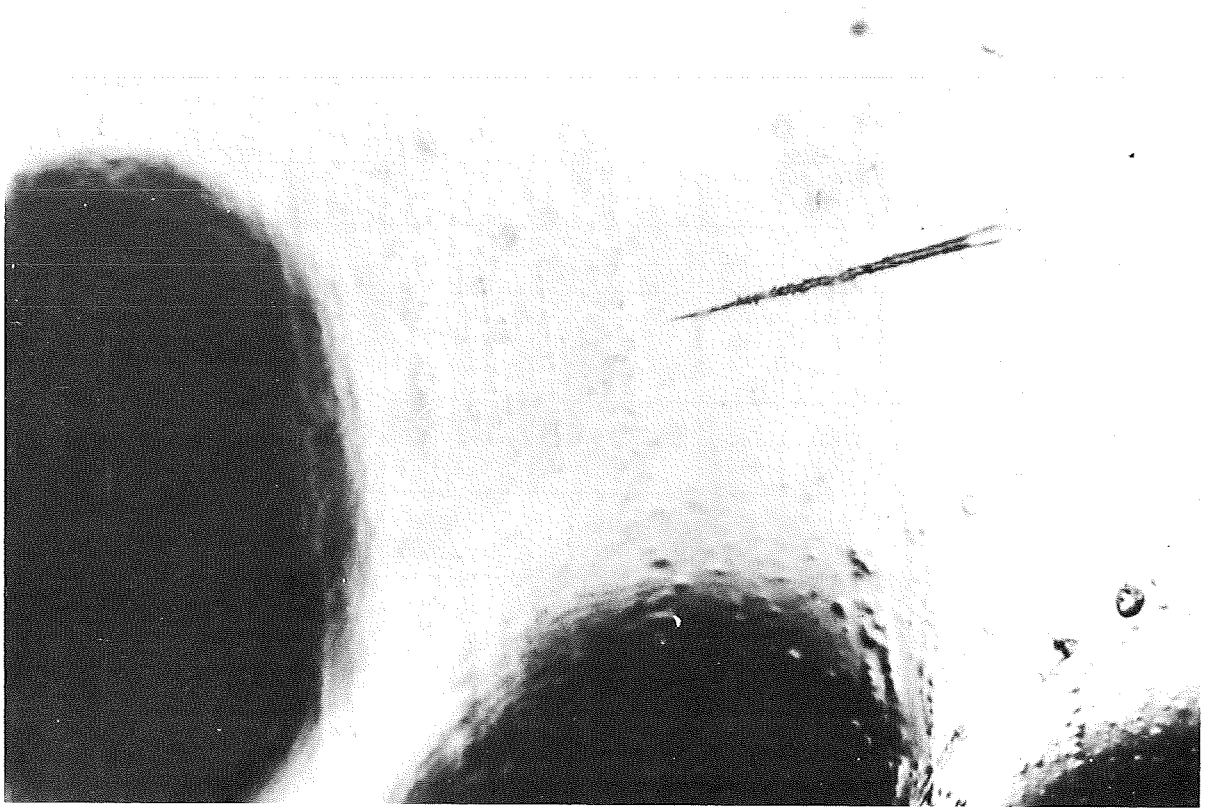


FIGURE 13-4.—Etch cone of an HZE particle track in  $\text{CN}_D$  covered with *Arabidopsis thaliana* seeds in polyvinylalcohol.

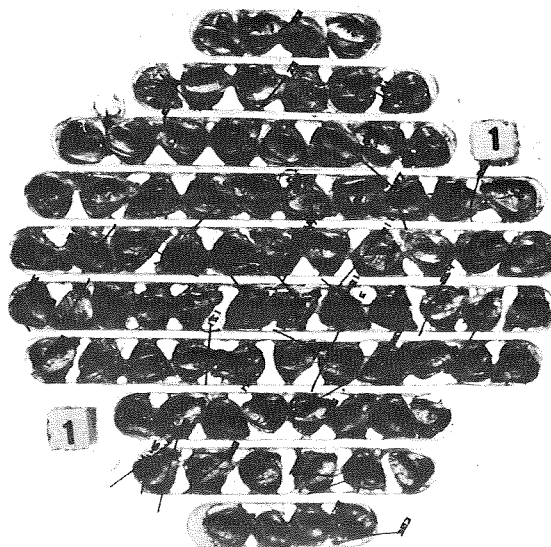


FIGURE 13-5.—Projection of HZE particle tracks in the layer of corn seeds.

TABLE 13-IX.—Impact Parameter  $b$  of *Bacillus Subtilis* Spores of Biostack III

Impact parameter $b, \mu\text{m}$	Number of spores in 1- $\mu\text{m}$ interval
0	22
1	59
2	71
3	67
4	50
5	27
6	14
7	12
8	5
9	3
10	4
11	2
>12	3

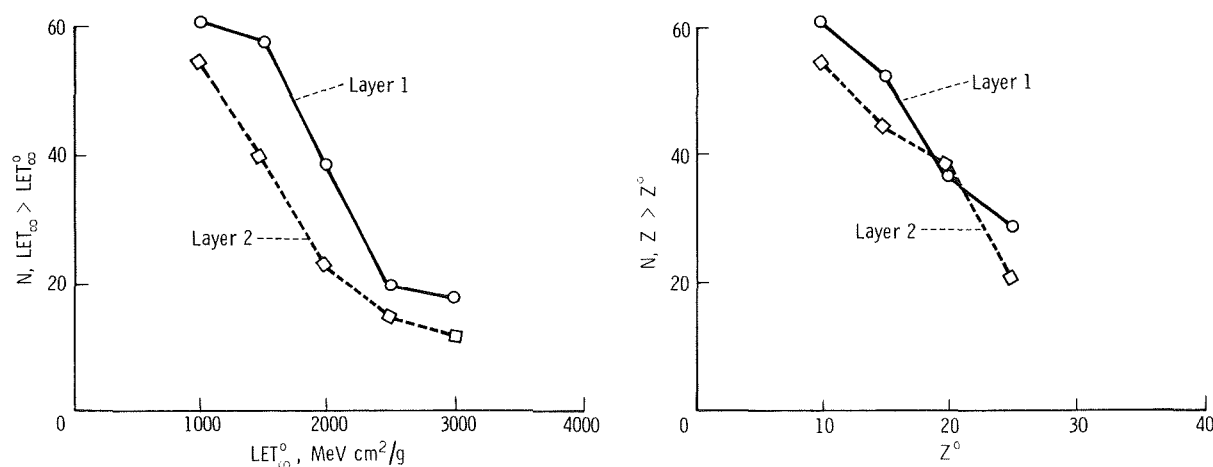
 TABLE 13-X.—Impact Parameter  $b$  and Energy Loss of Particles Penetrating the *Bacillus Subtilis* Spore Layer [Data from AgCl crystal measurement]

Spores with $b \leq 0.6 \mu\text{m}$	LET of the particle, $\text{MeV cm}^2/\text{g}$
15	$\leq 100$
20	$< 500$
3	$> 500$

The *Zea mays* studies are still underway. Sixteen days after the seeds were planted, the embryonic and first leaf were checked. For first-leaf growth comparison, table 13-XI gives averages of flight and ground controls together with first-leaf growth of flight seeds having received direct hits of HZE particles. Note that some seeds which were hit showed significant retardation in growth and development. The length of the first leaf of seed 9 of layer 1 was 101.5 mm, which was much shorter than the average for controls. Also, the width of the first leaf in seed 12 of layer 1 was 7 mm, which was approximately 40 percent smaller than the controls. Two flight seeds that were hit (seed 10 of layer 1 and seed 15 of layer 2) did not germinate. In addition, seed 6 of layer 2, which germinated slowly and appeared to be a dwarf plant, received two hits of HZE particles. Only one seed from the control group did not germinate.

During the growth of *Arabidopsis thaliana*, 44 endpoints were followed, which comprised the growth of the embryo and the development of the rosette leaves, the shoot, the flowers, and the pods. At this time, no significant difference has been found between the flight seeds hit and the controls.

Most of the animal eggs hit by an HZE particle showed serious damage during development. In


 FIGURE 13-6.—Integral LET and atomic number  $Z$  spectra for HZE particle hits in *Zea mays* embryos. (Where  $N$  is the number of particles of energy loss greater than the energy loss specified in terms of  $\text{LET}_\infty > \text{LET}_\infty^0$ , and where  $N$  is the number of particles of  $Z > Z^0$ .)

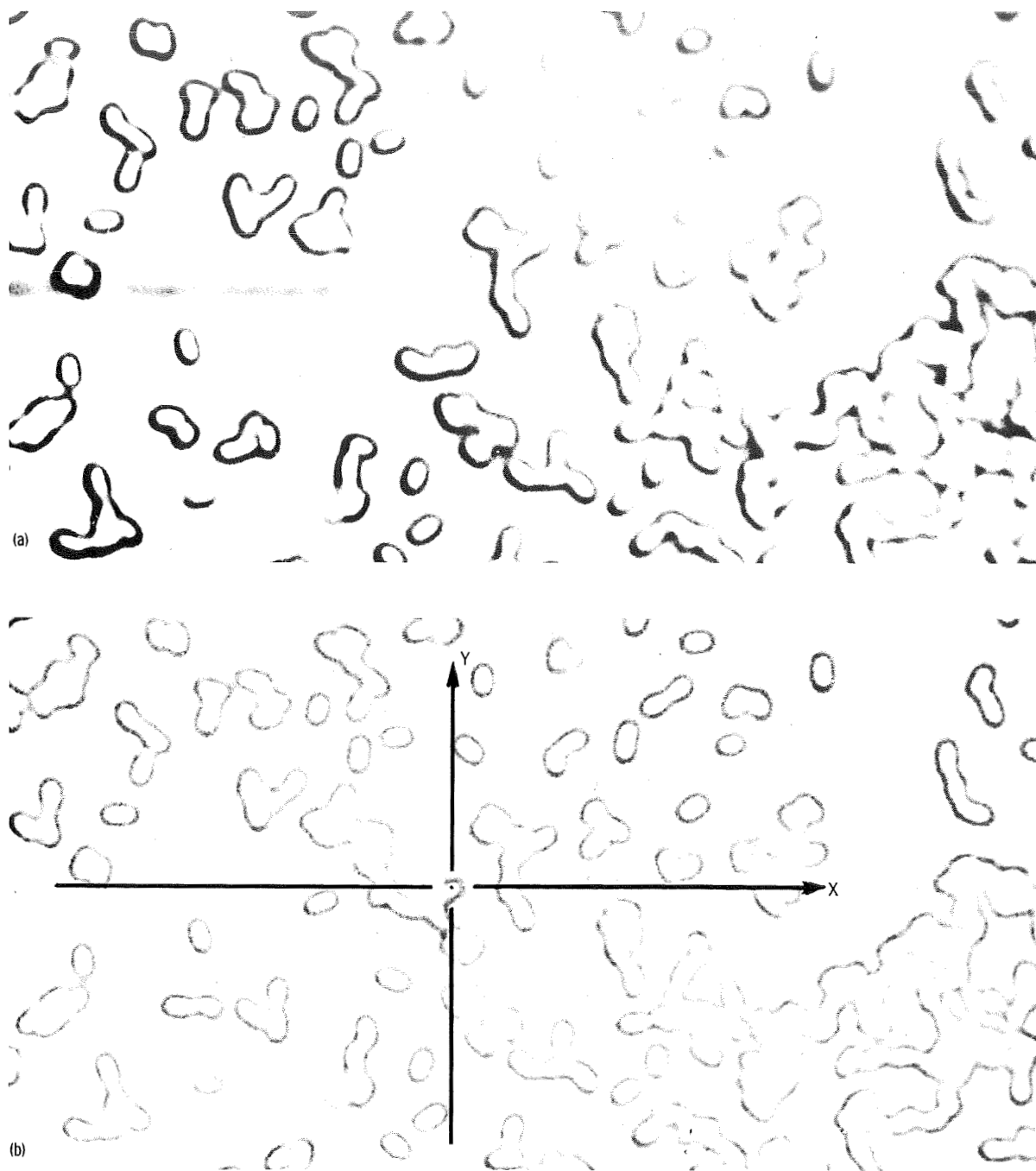


FIGURE 13-7.—Determination of the impact parameter  $b$ . (a) After spore removal by manipulation and breakthrough etching. (b) Spore configuration before manipulation.

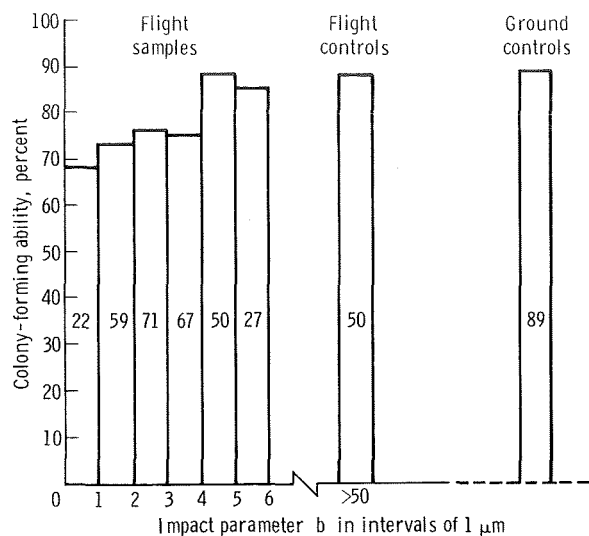


FIGURE 13-8.—Colony-forming ability of *Bacillus subtilis* spores relative to impact parameter *b*. Numbers within the bars indicate the number of evaluated spores.

*Artemia salina* eggs, the hatching rate was significantly reduced and developmental anomalies were frequently observed. Histological studies on anomalous larvae showed cellular and tissue damage primarily at the extremities and the abdomen. These changes may be due to the differentiated dynamics of the developmental processes of the egg. The observations generally confirmed the results of the previous Biostack experiments.

### COMPARISON OF DATA WITH OTHER SPACE-FLIGHT EXPERIMENTS

The flux of HZE particles measured in CN of the ASTP Biostack III is in agreement with the Skylab results. The flux values for these two missions, both of which were near-Earth-orbital satellites with an orbit inclination of 50°, are given

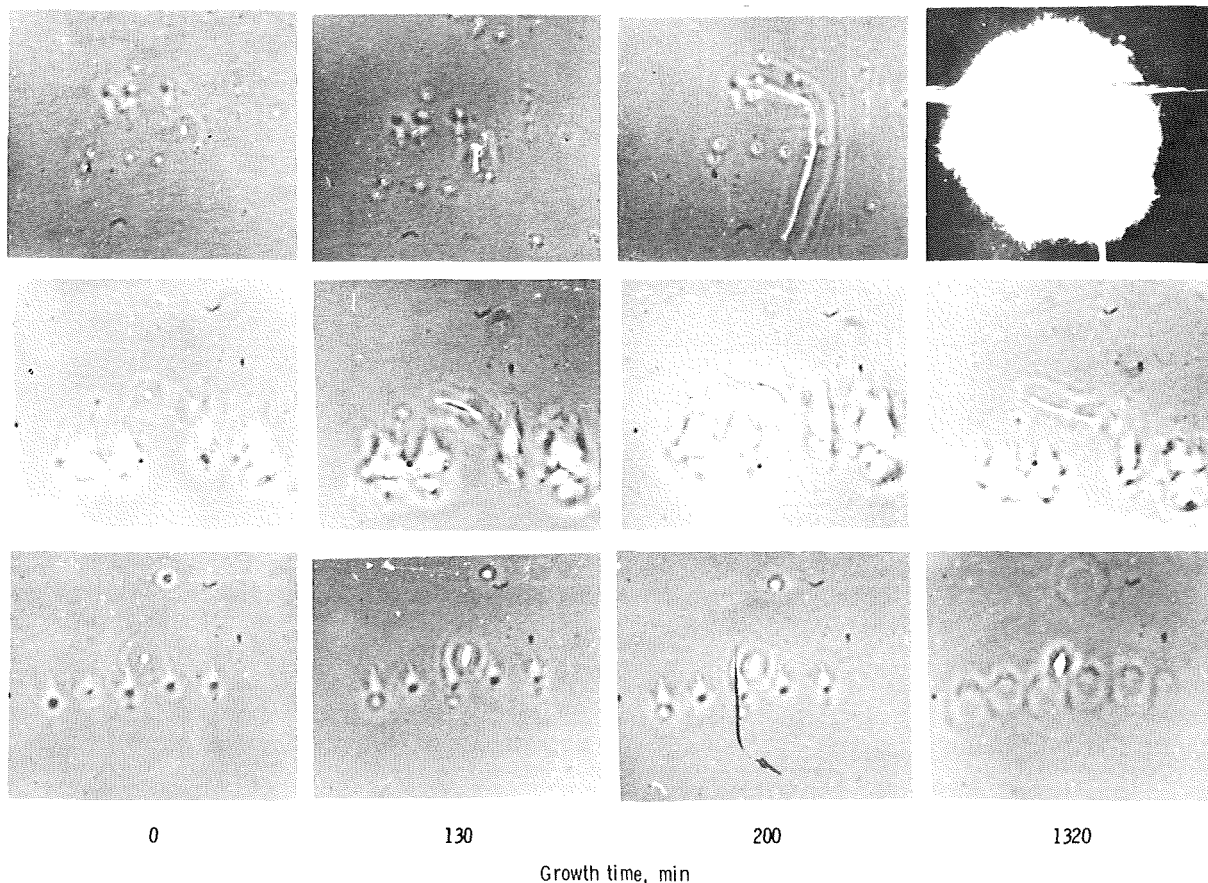


FIGURE 13-9.—Growth anomalies in the first vegetative cell from *Bacillus subtilis* spores of  $b < 4 \mu\text{m}$ .

TABLE 13-XI.—*First-Leaf Growth of Flight Sample Zea Mays Seeds Hit by Heavy Particles and Comparison With Averages of Ground and Flight Controls*

(a) *Flight samples*

Seed no.	Track no.	LET, MeV cm <sup>2</sup> /g	Z	First leaf	
				Length, mm	Width, mm
Layer no. 1					
3	82	≧2660	13 to 15	130.5	11
6	161	3140	25 to 26	121.5	12
8	122	2250	20 to 23	125.5	12
9	46	1770	≧14	101.5	12
10	{ 46	1770	≧14	(a)	(a)
	{ 77	2860	21 to 23	(a)	(a)
12	163	1690	15 to 19	127.5	7
13	207	3310	22 to 26	121.5	11
16	50	1910	9 to 10	115.5	12
Layer no. 2					
5	184	2880	21 to 26	123.5	12
6	{ 184	2880	21 to 26	(b)	(b)
	{ 212	1600	17 to 21	(b)	(b)
7	216	1920	21 to 26	127.5	12
8	218	1830	≧14	115.5	13
11	154	1350	12	121.5	12
12	180	≧2590	≧17	127.5	13
13	178	1590	18 to 26	131.5	12
14	178	1590	18 to 26	134.5	13
15	210	1610	19 to 26	(a)	(a)
16	210	1610	19 to 26	126.5	12
17	223	1380	16 to 26	130.5	12
				<sup>c</sup> 123.87	<sup>c</sup> 11.75

(b) *Comparison with controls*

Sample	Average length, mm	Average width, mm
Flight seeds hit by heavy particles	123.87	11.75
Ground control (32 seeds)	122.59 ± 2.16	12.33 ± 0.15
Flight control (32 seeds)	122.53 ± 1.89	10.91 ± 0.47

<sup>a</sup>Not germinated.

<sup>b</sup>Plant too small to be measured.

<sup>c</sup>Average.

in table 13-XII. The slightly higher flux value for the ASTP mission occurred because the ASTP samples were etched for a longer duration than the Skylab samples.

Table 13-XIII presents a comparison of the dosimetric data of Biostack III with those of Biostack I and II. Although during the Earth-orbital ASTP flight the total dose of space radiation and the HZE particle fluence were approximately one order of magnitude lower than during the lunar flights, the frequency of nuclear disintegration stars was nearly twice the value of that of Biostack II. Therefore, during the postflight evaluation of Biostack III, increased attention is being given to potential biological injury that might be caused by stars. Little is known about their biological effect. The expected data may contribute to the appraisal of potential hazards of nuclear disintegration stars to man not only during space flight (ref. 13-7) but also during very-high-altitude aircraft flights, because this radiation component reaches its maximum at an altitude of approximately 20 km (ref. 13-8). Dosimetric data on nuclear disintegration stars measured in nuclear emulsions at different altitudes are presented in table 13-XIV.

TABLE 13-XII.—HZE Particle Flux of ASTP and Skylab

Mission	HZE particle flux <sup>a</sup> , cm <sup>-2</sup> day <sup>-1</sup>
ASTP	0.38 ± 0.05
Skylab:	
Command module	0.28 ± 0.12
Astronauts	0.27 ± 0.08

<sup>a</sup>Corresponds to etch-through tracks in CN plastic etched at 313 K (40° C) in 6.25N sodium hydroxide. The ASTP samples were etched for 18 hours, the Skylab samples for 10 hours.

TABLE 13-XIII.—Dosimetric Data of Biostack I, II, and III

Space flight	Flight duration, hr	Biostack experiment	Space radiation dose, mJ/kg		HZE particles				Stars		
			Space side	Cabin side	Detector	Number cm <sup>-2</sup> hr <sup>-1</sup>	Detector (a)	Dose, mJ/kg	Detector (a)	Number cm <sup>-2</sup> hr <sup>-1</sup>	Dose, mJ/kg
Apollo 16	266	I	6.45	5.75	CN	0.07	K2	0.033	K5	56	0.026
Apollo 17	304	II	7.50	7.15	CN	.07	K2	.035	K2	37	.011
ASTP	218	III	.99	1.24	CN	.009	K2	b.015	K2	60	.013

<sup>a</sup>Prefix "K" refers to the manufacturer's emulsion designation.

<sup>b</sup>Estimated.

*TABLE 13-XIV.—Dosimetric Data Comparison of Nuclear Disintegration Stars for Different Flights*

<i>Data source</i>	<i>Altitude</i>	<i>Detector (a)</i>	<i>Stars, cm<sup>-3</sup> day<sup>-1</sup></i>
ASTP Biostack III	Earth orbital	K2 AgCl	1450 640
Apollo 17 Biostack II	Lunar	K2	950
Apollo 16 Biostack I		K5	1360
Balloon GRBS, <sup>b</sup> 1969	21 000 m	G5	930
Balloon GRBS, 1970	35 000 m	G5	530
Balloon GRBS, 1974	35 000 m	G5	670
NASA jet aircraft	15 000 m	G5	1000

<sup>a</sup>Prefixes "K" and "G" are part of the manufacturer's emulsion designations.

<sup>b</sup>Groupe de Recherches Biologique Spatiale of the University of Toulouse.

## REFERENCES

- 13-1. Bückner, Horst: Biostack - A Study of the Biological Effects of HZE Galactic Cosmic Radiation. Biomedical Results of Apollo. NASA SP-368, 1975, pp. 343-354.
- 13-2. Haymaker, Webb; Benton, Eugene V.; and Simmonds, Richard C.: The Apollo 17 Pocket Mouse Experiment (Biocore). Biomedical Results of Apollo. NASA SP-368, 1975, pp. 381-403.
- 13-3. Grahn, Douglas, ed.: HZE-Particle Effects in Manned Space-Flight. National Research Council, Radiobiological Advisory Council, National Academy of Sciences, Washington, D.C., 1973.
- 13-4. Bückner, H.; and Horneck, G.: Studies on the Effects of Cosmic HZE-Particles on Different Biological Systems in the Biostack Experiments I and II Flown Onboard of Apollo 16 and 17. Radiation Research, Proceedings of the Fifth International Congress of Radiation Research, 1975, pp. 1138-1151.
- 13-5. Bückner, H.; Facius, R.; et al.: Biostack III Experiment MA-107. Sec. 14 of Apollo-Soyuz Test Project Preliminary Science Report. NASA TM X-58173, 1976.
- 13-6. Pfohl, R.; Kaiser, R.; Massué, J. P.; and Cüer, P.: Experimental Methods of Correlation Between the Trajectories of Cosmic Heavy Ions and Biological Objects: Dosimetric Results From the Biostack Experiment on Apollo 16 and 17. COSPAR Life Sciences and Space Research XII, 1974, pp. 57-64.
- 13-7. Schaefer, H. J.: Das Höhenprofil der kosmischen Strahlendosis Die natürliche Strahlenexposition des Menschen. Georg Thieme Verlag (Stuttgart), 1974, pp. 2-9.
- 13-8. Allkofer, O. C.: Dosimetry at SST Altitude. Paper presented at the 8th International Conference on Nuclear Photography and Solid State Track Detectors, Bucharest, Rumania, 1972.



# 14. Zone-Forming Fungi

## Experiment MA-147\*

T. D. Rogers,<sup>a</sup> M. E. Brower,<sup>a</sup> and G. R. Taylor<sup>b†</sup>

### ABSTRACT

*Streptomyces levoris* Kras was used as an experimental test microorganism during the Apollo-Soyuz Test Project to study alternating vegetative mycelial and spore ring periodicity during space flight. Four cultures were launched in each of the spacecraft (Apollo and Soyuz). During the joint space-flight activities, two cultures from each spacecraft were exchanged. Selected duplicate cultures were maintained as controls in both the United States and the U.S.S.R. Spore ring morphology was periodically documented by photographing the specimens at approximately 12-hour intervals during the preflight, flight, and postflight periods of the experiment. A decreased growth-rate periodicity in the space-flight cultures was in part attributed to the reduced temperature in the spacecraft; however, one or more physical factors of space flight (weightlessness, etc.) may also have been involved. One of the four cultures grown in the reduced temperature environment of the Apollo spacecraft had a growth rate more rapid than that of the ground controls. Three of the space-flight cultures developed double spore rings during the period immediately after flight. This anomaly was attributed to the return to the Earth's gravity. The absence of spores in portions

of one ring formed during space flight may have been caused by nutritional defects or media abnormality. Extensive studies will be required to determine the cause of this defect. There was no visible evidence of wedges in the cultures that would suggest naturally occurring or radiation-induced mutagenic alteration during space flight.

### INTRODUCTION

The manifestation of various cyclic biological phenomena (biorhythms) of living organisms is in part or totally controlled by genetic, biochemical, and biophysical aspects. The occurrence of rhythmic events (biorhythms, circadian clocks, periodicities, oscillations, etc.) of man and other organisms has been a subject of interest and investigation for many years (refs. 14-1 to 14-4). Even though some space-flight studies have involved higher organisms having demonstrable biorhythms (refs. 14-5 to 14-8), there has been no previous investigation of the space-flight effects on the biorhythm or periodicity features of a microorganism. The opportunity to investigate this phenomenon in a microorganism was provided during the Apollo-Soyuz Test Project (ASTP) mission in July 1975.

*Streptomyces levoris* Kras exhibits a distinct periodicity of vegetative mycelial growth, which alternates with spore production. This growth characteristic results in a culture morphology in which uniform rings of mycelium and spores develop in an alternating pattern. When this microorganism is grown under known conditions using a defined biochemical medium and controlled temperature and light, increments of time

---

\*This experiment was performed jointly and in collaboration with I. G. Akoev and associates of the Institute of Biophysics, U.S.S.R. Academy of Sciences, Pushchino, U.S.S.R. The joint experiment designation was AS-1.

<sup>a</sup>Northrop Services, Inc., Houston, Texas.

<sup>b</sup>NASA Lyndon B. Johnson Space Center.

<sup>†</sup>Principal Investigator.

can be directly correlated with biological activity. Consequently, any deviation from the normal morphological pattern can be directly related to a specific time period. *Streptomyces levoris*, therefore, provided a suitable biological test system to investigate influences of space flight on the rhythms of vegetative and spore phase characteristics of both growth-rate periodicity and culture morphology during the ASTP preflight, flight, and postflight periods.

The Zone-Forming Fungi Experiment is one of the five experiments conducted as joint investigations by representatives of the United States and the U.S.S.R. The objectives of the U.S. participation in this experiment were (1) to study the effects of space flight on the biorhythms of *Streptomyces levoris* by comparing the growth-rate periodicity of the vegetative and spore phases within each culture, (2) to investigate the possible alteration of spore morphology and development by examination using the scanning electron microscope, and (3) to compare the effects of a 12-hour phase shift in growth periodicity features of the microorganism in cultures that were exchanged during the joint activities of the space flight. Additional studies were performed by and will be independently reported by U.S.S.R. investigators.

## MATERIALS AND METHODS

Optimum growth of *Streptomyces levoris* (known as *Actinomyces levoris* Kras in the U.S.S.R.) was achieved by incubation at a temperature of 300 K (27° C) on an agar-based medium of inorganic salts, glucose, and yeast extract. Cultures were initiated by singlepoint inoculation of spores on the agar-based medium in 60- by 5-mm petri dishes 6 days preceding the ASTP flight. Phasing of the vegetative and spore production cycles was accomplished in both the United States and the U.S.S.R. by using a 12-hour light-dark period (100 to 200 lux) from 9:00 a.m. to 9:00 p.m. local time. The light-dark cycle was maintained until the cultures were selected for the experiment and placed in the experimental devices 4 days after inoculation.

When grown at a temperature of 300 K (27° C) on a defined medium, the first spore ring typically appears on the third day. Thereafter, one complete cycle of vegetative mycelium and subsequent spore phase generally occurs with a periodicity of 24 to 26 hours for 10 to 14 days. Because of nutritional depletion and metabolic waste diffusion within the media, the growth becomes slower after approximately 2 weeks.

A series of cultures from which the ASTP experimental specimens were selected was initiated 6 days before flight in both the United States and the U.S.S.R. at 9:00 a.m. local time at the respective laboratories. Because of logistics and certain preflight time-line constraints, it was necessary to select the cultures initiated in the United States and to place them in the devices 2 days before flight. The cultures initiated in the U.S.S.R. were selected and placed in the space-flight devices on the day of launch.

Two cultures of *Streptomyces levoris*, each contained in a 60- by 5-mm petri dish, were placed in each flight device (fig. 14-1). Two flight devices (four cultures) were prepared for launch in the

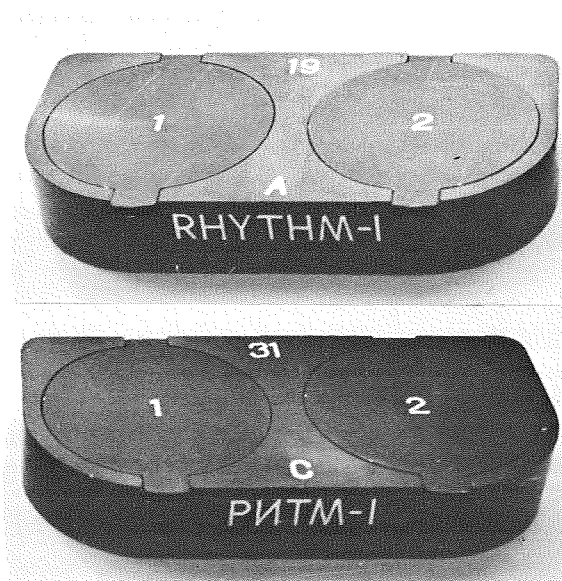


FIGURE 14-1.—Examples of the experiment devices. The "A" series was used by the United States and the "C" series by the U.S.S.R. Each device holds two petri dishes (60 by 5 mm), which are designated as "1" and "2."

Apollo spacecraft and two identical devices with matching cultures were prepared as U.S. ground controls. A similar procedure was followed by the U.S.S.R. representatives.

The main body of each device consisted of separable halves that were composed of anodized aluminum. A protective glass, fitted with a biologically nonreactive siliconized rubber ring, was inserted beneath the movable lid in the top half of each device. This glass served as a protective cover and enabled observation and photography of the cultures. The bottom half of the device, which included the petri dishes with cultures, spacing rings around the dishes, and siliconized rubber rings below the dishes, was fitted with the top half of the device to complete the assembly. The components of the experimental device are shown in figure 14-2. Radiation detectors of Lex-

an and cellulose acetate were placed beneath each petri dish as well as in the movable lid. The detectors would serve to evaluate visible points of alterations within the cultures in conjunction with particle tracks in the detectors. The bacteriophage T4Br+ was incorporated into an agar medium and dried to form a thin film. These films were placed in the flight devices beneath the lower layer of plastic dosimeters so that specific genetic alterations of the bacteriophage deoxyribonucleic acid, induced by the action of high-energy particles, could be studied (ref. 14-9). Data related to dosimetry and to the T4Br+ bacteriophage will be reported by the U.S.S.R. investigators.

Following assembly of the devices to be launched in the Apollo spacecraft, both the flight and control cultures were placed in a "Thermocont," or portable incubator, and were maintained

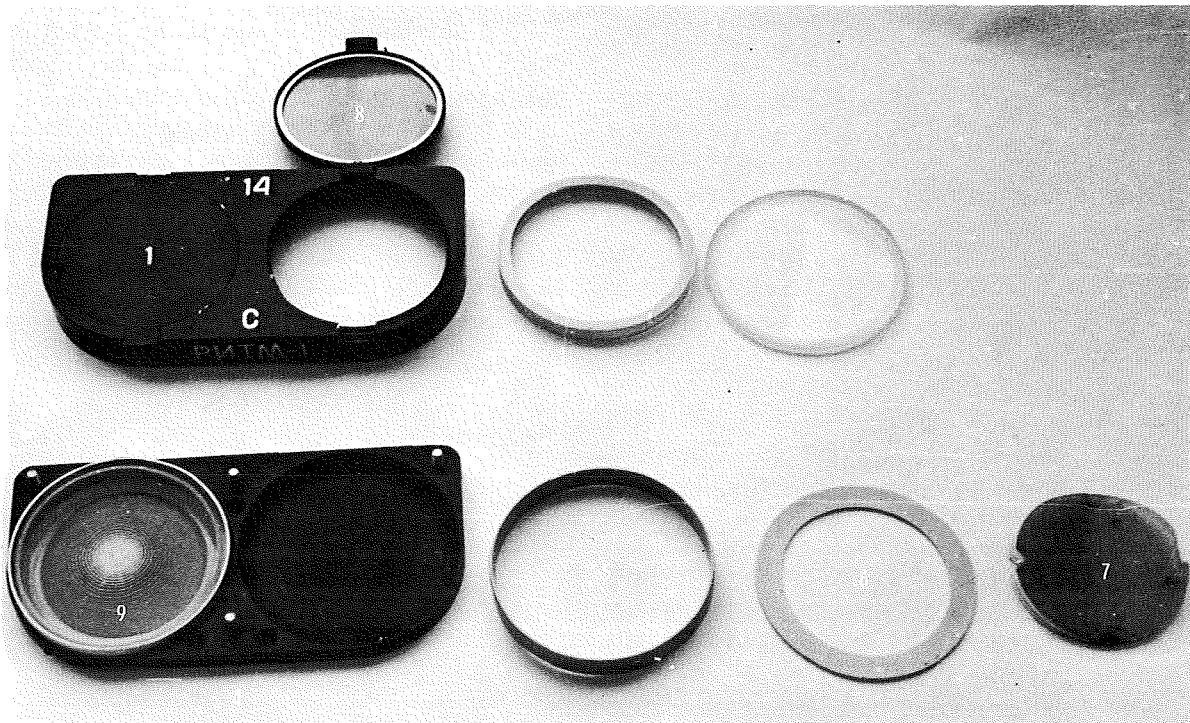


FIGURE 14-2.—Photograph of the components of a flight device. (1) Upper half of device with movable covers. (2) Siliconized rubber ring that fits around the protective glass. (3) Protective glass and rubber ring, which are inserted into the upper half of the device and serve to protect the specimen in the petri dish. (4) Bottom half of the device. (5) Metal spacing ring. (6) Siliconized rubber washer that fits in the well of the lower half of the device. (7) Radiation detector, which is positioned in the bottom of the device under the petri dish. (8) Radiation detector in the movable cover. (9) Petri dish and specimen.

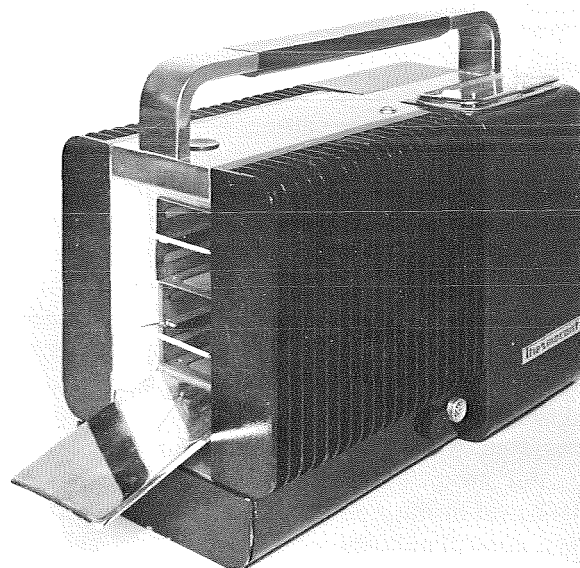


FIGURE 14-3.—The ac/dc portable incubator (transport container) "Thermocont" that was used to maintain cultures at a temperature of 300 K (27° C) during various phases of the experiment in the United States and the U.S.S.R.

at a temperature of 300 K (27° C) during transport to the launchsite (fig. 14-3). The control cultures were maintained in the incubator during the entire course of the experiment. Following recovery, the flight specimens were again placed in the portable incubator and maintained at a temperature of 300 K (27° C) until termination of the experiment. A similar procedure was followed by both laboratories.

Photography of the specimens was begun at the time the cultures were assembled in the flight devices. Both control and flight specimens were photographed at 12-hour ( $\pm 3$  hours) intervals until termination of the experiment. A Nikon 35-mm camera (fig. 14-4), equipped with a 55-mm lens (f/2.8) and adapted with a special framing device to facilitate focusing, was used for photography. The photographs were used to provide a comparative basis for growth analyses.

The U.S. experiment consisted of three time periods.

1. Preflight—Cultures were initiated on July 9, 1975. Specimens for the experiment were selected and placed in the devices on July 13. The control and flight specimens were transported from the NASA Lyndon B. Johnson Space Center (JSC) to

the NASA John F. Kennedy Space Center (KSC), where the flight specimens were placed onboard the Apollo spacecraft on July 15, 1975.

2. In-flight—The flight specimens were launched from KSC on July 15 and were recovered at the splashdown site in the Pacific Ocean on July 24. On July 17, during the joint activity phase of the mission, space-flight crewmen of Apollo and Soyuz each exchanged one device containing two cultures (fig. 14-5). Following the Apollo launch, the controls were returned to JSC and then transported to the Apollo recovery site on July 21.

3. Postflight—Following recovery of the space-flight cultures on July 24, the flight devices were transported with the controls to JSC. From the time of recovery until the experiment was terminated on August 11, 1975, all specimens were maintained at a temperature of 300 K (27° C) in the portable incubator.

Similar time lines were followed by the U.S.S.R. investigators. However, the U.S.S.R. in-flight period was July 15 to 21 and the U.S.S.R. postflight period was July 21 to August 16.

To facilitate preliminary comparison of data in the respective periods, August 1 was selected as the cutoff date for the postflight period, although the experiment was continued until August 11 in the United States and August 16 in the U.S.S.R. On August 29, following termination of the experiment, the Thermocont and specimens from

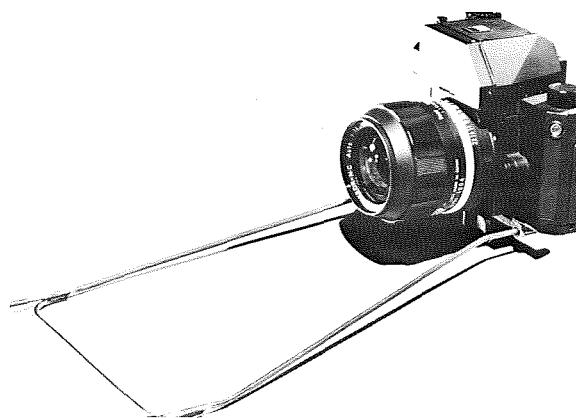


FIGURE 14-4.—Photographic apparatus used in the United States during both ground-support and Apollo in-flight photography of the experiment.



FIGURE 14-5.—Photograph of ASTP crewmen exchanging the culture devices. The exchange occurred on July 17, 1975.

the United States were shipped to the laboratory in the U.S.S.R. On October 7, the radiation detectors were marked for position and were removed from the flight and control devices in the presence of science representatives of both the United States and the U.S.S.R.

## RESULTS AND DISCUSSION

The general scheme of the experiment was performed according to the project outline. All the flight and control cultures of *Streptomyces* exhibited growth during the preflight, flight, and postflight periods of the experiment without apparent contamination.

Cultures were initiated July 9 for the experiment in both the United States and the U.S.S.R. At the respective launch times on July 15, the rate of vegetative growth and the subsequent spore

ring development (biorhythm) were different. The difference in growth rate and frequency between the two sets of cultures continued throughout the experiment.

The total number of spore rings formed by the control and flight cultures at the end of each of the three periods is shown in table 14-I. Since there was a 3-day difference between the U.S. and U.S.S.R. in-flight time lines, the average growth rate per day for each culture during each experiment period is also shown. The latter value provides a more uniform basis of comparison between cultures.

The controls cultured in the United States grew at the same rate when compared with each other within a given time period, with the exception of culture number 2 of device A-25, which exhibited a slight decrease in growth rate during the postflight period. (See table 14-I.) During the preflight period, the flight cultures (A-19 and

A-22) had growth rates identical to those of the controls. At the end of the flight period, the flight specimens were noticeably different from the controls in growth rate and frequency.

The temperature profile in the Apollo spacecraft is shown in figure 14-6. Even though the reduced and variable temperature would cause a decreased growth rate, this factor alone does not explain the difference observed in the flight cultures during the flight period. The growth rate of the in-flight cultures would have decreased uniformly had temperature been the only factor

involved. One or more physical factors of space flight (weightlessness, magnetic field forces, and possible solar effects) appear to have invoked various effects on the growth-rate periodicity, because the space-flight cultures exhibited different types of growth patterns and biorhythms. Some of the more apparent differences are (1) increased growth rate of number 2 of A-22, which grew more rapidly during flight at a reduced temperature compared to the other space-flight cultures or the controls, (2) differences in reduced growth rate of space-flight

TABLE 14-I.—Growth-Rate Comparison of *Streptomyces Levoris* During ASTP

Status	Device	Culture	Preflight period <sup>a</sup>		Flight period <sup>b</sup>		Postflight period <sup>c</sup>	
			Number of rings <sup>d</sup>	Growth rate <sup>e</sup>	Number of rings <sup>d</sup>	Growth rate <sup>e</sup>	Number of rings <sup>d</sup>	Growth rate <sup>e</sup>
United States								
Control	A-24	1	4.0	1.0	9.5	0.61	13.0	0.44
		2	4.0	1.0	9.5	.61	13.0	.44
	A-25	1	4.0	1.0	9.5	0.61	13.0	0.44
		2	4.0	1.0	9.5	.61	12.5	.38
Flight	A-22	1	4.0	1.0	8.0	0.4	12.0	0.5
		2	4.0	1.0	10.0	.66	15.0	.63
	A-19 <sup>f</sup>	1	4.0	1.0	7.0	0.5	13.0	0.55
		2	4.0	1.0	7.0	.5	13.0	.55
U.S.S.R.								
Control	C-35	1	3.0	0.75	6.1	0.52	9.5	0.31
		2	3.0	.75	6.1	.53	9.3	.29
	C-36	1	2.0	0.5	6.0	0.67	9.2	0.29
		2	2.0	.5	6.2	.7	11.5	.48
Flight	C-31	1	3.0	0.75	5.0	0.33	9.3	0.39
		2	2.8	.7	4.8	.33	8.5	.33
	C-12 <sup>g</sup>	1	2.5	0.63	7.3	0.53	10.3	0.38
		2	2.3	.58	6.3	.44	9.2	.36

<sup>a</sup>U.S. and U.S.S.R. preflight period—July 9 to 15.

<sup>b</sup>U.S. flight period—July 15 to July 24; U.S.S.R. flight period—July 15 to July 21

<sup>c</sup>U.S. postflight period—July 24 to August 1; U.S.S.R. postflight period—July 21 to August 1.

<sup>d</sup>Total number of rings at the end of each period.

<sup>e</sup>Number of spore rings formed per day during each period.

<sup>f</sup>Exchanged from Apollo to Soyuz on July 17.

<sup>g</sup>Exchanged from Soyuz to Apollo on July 17.



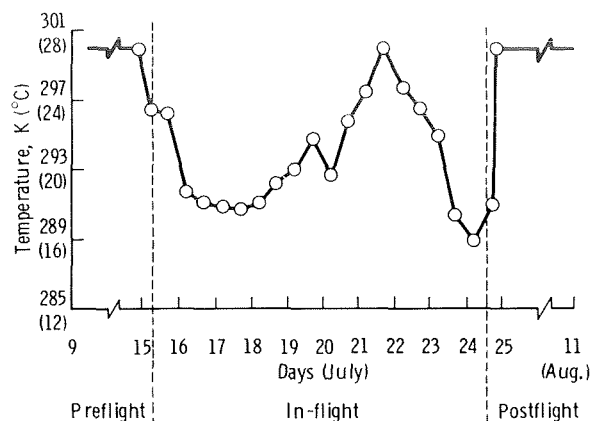


FIGURE 14-6.—Temperature profile in the Apollo spacecraft during the ASTP mission. Each point represents the average temperature for a 12-hour period.

cultures maintained at the same temperature (e.g., no. 1 of A-22 as compared with no. 2 of A-22, no. 1 of C-12 as compared with no. 2 of C-12), and (3) differences between the flight cultures of each group (A-22 and A-19, C-31 and C-12). Direct comparison of flight cultures was made difficult by the exchange of devices during flight.

Spore morphology during the flight period was distinct and, in general, exhibited no alteration of growth pattern. Spores failed to form in two distinct areas of the last in-flight spore ring of A-19 culture number 1 (fig. 14-7). At first, it was suspected that this void area in the spore ring was the result of radiation effects; however, in a postflight radiation experiment in which *Streptomyces* cultures were subjected to neon ions at radiation dose levels of 1 to 100 J/kg (100 to 10 000 rads), not a single aberration of this nature was observed. No other explanation for this type of aber-

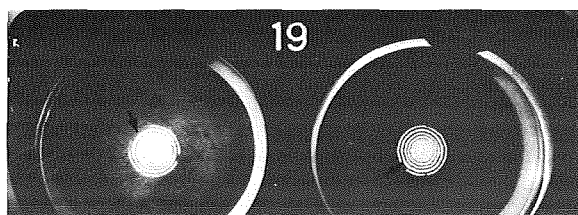


FIGURE 14-7.—Photograph of culture A-19. The last in-flight spore ring in which spores failed to form is indicated by arrows.

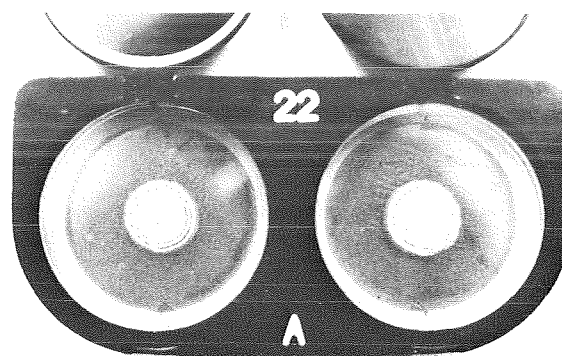


FIGURE 14-8.—Photograph of culture A-22 showing spore ring offset and subsequent spiral ring formation.

ration is suggested at this time, especially in view of the fact that a number of variables are known to have been involved in comparisons of the space-flight cultures with each other or with ground controls.

Spore ring offsets and subsequent spiral ring formation (fig. 14-8) also occurred during the flight period in number 2 of A-22. Similar offsets and spirals were observed in the ground controls.

Unusual double spore rings were formed during the period immediately after flight in cultures of device A-19 and in culture number 2 of device C-31 (fig. 14-9). Although such formations may be coincidental, it is also possible that the dynamics of physical forces related to reentry and landing of

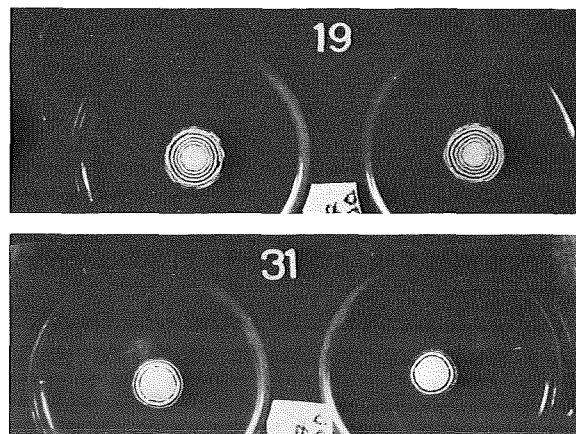


FIGURE 14-9.—Photographs of cultures A-19 and C-31 showing double spore rings formed during the period immediately after flight.

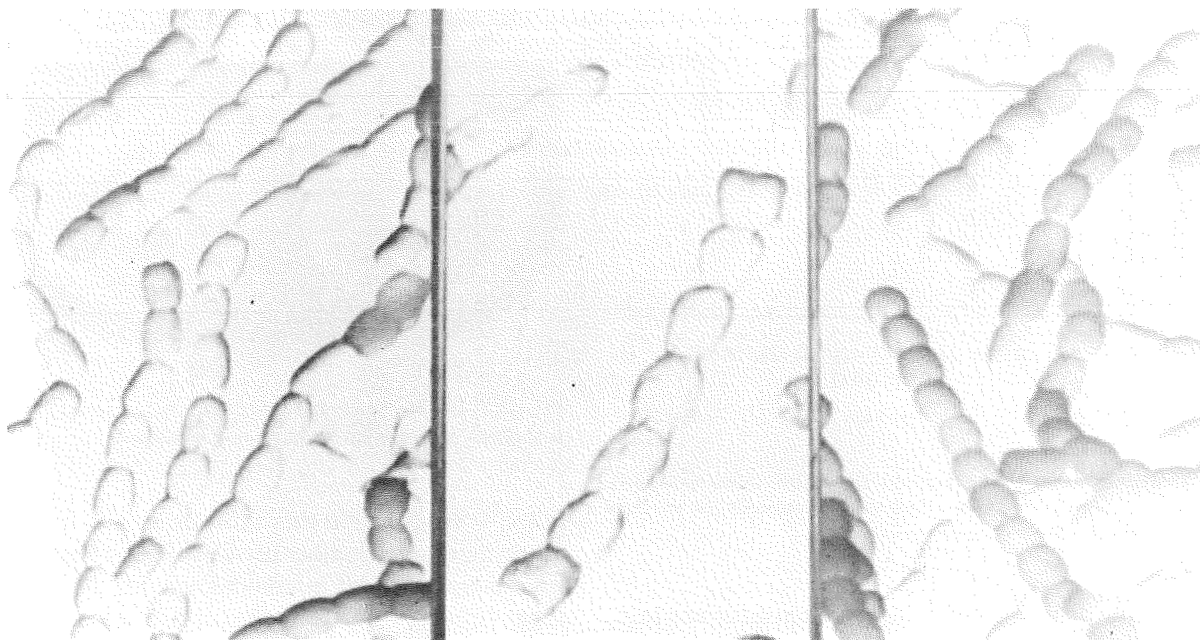


FIGURE 14-10.—Scanning electron micrographs of representative spores from control cultures.

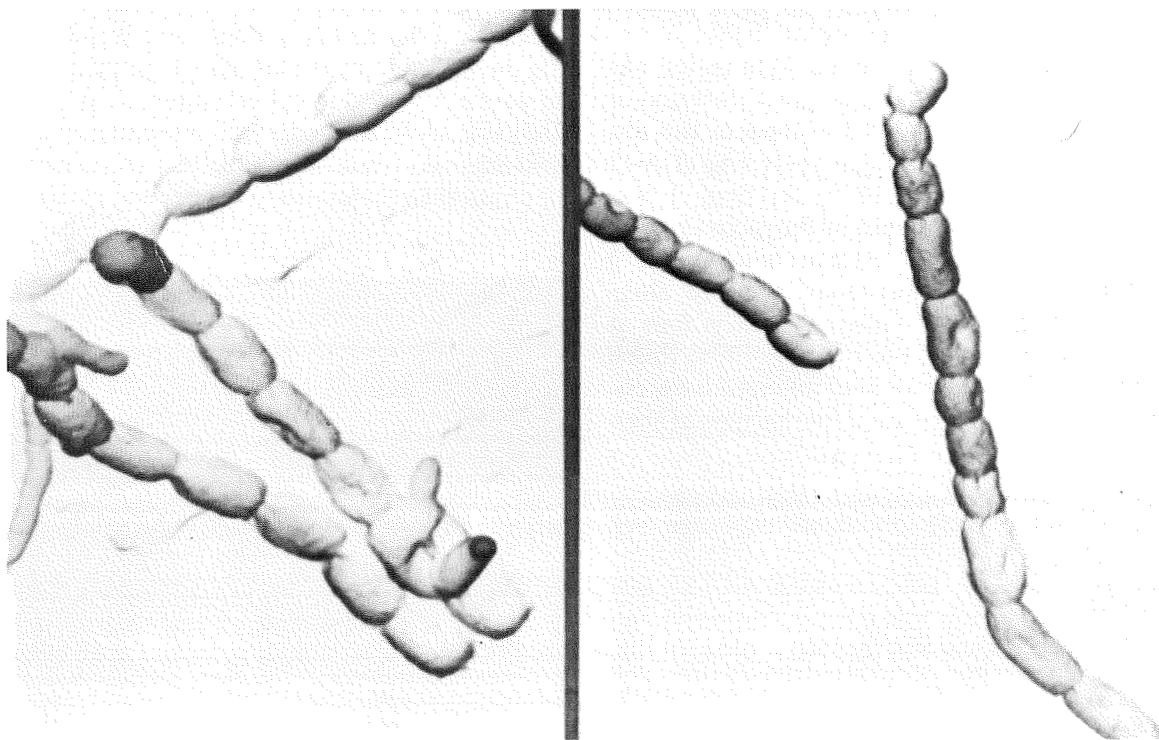


FIGURE 14-11.—Scanning electron micrographs of irregular and elongated spores from spore rings formed during flight in culture 2 of A-22.



the Soyuz spacecraft may have contributed to the growth pattern aberrations. The subsequent spore rings in the cultures developed in a normal pattern, and this type of aberration was not observed in the Apollo flight specimens.

Postflight subculturing of the U.S. and the U.S.S.R. control and space-flight cultures revealed little or no difference in the growth rates of spore ring formation when grown on the standard culture medium.

Before inoculation of cultures for the space-flight experiment, an attempt was made to standardize procedures and components of the nutritional medium; however, specific chemicals were not obtained from the same sources in all cases. The differences in growth rate observed between the two sets of cultures (U.S. and U.S.S.R. initiated cultures) were probably due to a slight difference in the medium rather than an inherent biorhythm difference between the source cultures for the experiment.

Preliminary examination with a scanning electron microscope revealed an irregular and elongated spore morphology in a portion of both the flight cultures when compared with the controls (fig. 14-10). Spores of number 2 of A-22 exhibited a greater deviation from the normal spore morphology than did any of the other space-flight cultures (fig. 14-11); however, spores that formed during the postflight period appeared similar to those of the controls. Investigations are in progress to determine if this abnormal spore morphology will appear in subcultures.

## SUMMARY

Cultures (U.S. device A-19 and U.S.S.R. device C-12) were exchanged on July 17 during the ASTP joint activities phase. Because the respective cultures had been initiated on July 9 at 9:00 a.m. local time in both the United States and the U.S.S.R., there was a 12-hour time differential (time phase shift). The purpose of exchanging one set of cultures during the space flight was to observe the effect, if any, of the time differential relative to growth-rate biorhythm. Because of the diversity of growth-rate patterns exhibited by the flight specimens, it was not possible to determine

whether the time phase shift affected the biorhythm in the exchanged flight specimens. (See table 14-I.)

There is an ordered oscillation of cellular events that is visibly manifest in *Streptomyces levoris* and that results in the intrinsic rhythm of the vegetative and spore phases. It is also important to keep in mind that within the context of this experiment, the temperature, nutritional medium factors, and light conditions could have contributed to the overall results.

Although differences were observed in the biorhythm of *Streptomyces levoris* during space flight, the differences were not uniform. Furthermore, because all cultures did not react in the same manner during flight and because there were distinct preflight frequency differences between the two groups of cultures, statistical analysis of the data was not possible.

It appears that the single most variable factor related to the experiment was lack of temperature control for the space-flight specimens. Although the general temperature profile can be repeated on subcultures under laboratory conditions, the influence of weightlessness and other space-flight factors cannot be reconstructed to provide a meaningful analysis for correlative purposes.

The results obtained from this experiment indicated that space flight did affect the biorhythm of *Streptomyces levoris* vegetative and spore phases. However, the extent to which these cultures were affected cannot be accurately determined because of the action of such variables as temperature, nutritional medium, and the physical force factors associated with the launch and recovery process.

## REFERENCES

- 14-1. Cold Spring Harbor Symposia on Quantitative Biology: Biological Clocks, Vol. XXV. The Biological Laboratory (Cold Spring Harbor, Long Island, N.Y.), 1960.
- 14-2. Bünning, Erwin: The Physiological Clock: Endogenous Diurnal Rhythms and Biological Chronometry. Springer-Verlag (Berlin), 1964.
- 14-3. Aschoff, Jürgen, ed.: Circadian Clocks. North-Holland Publ. Co. (Amsterdam), 1965.

- 14-4. Oatley, K.; and Goodwin, B. C.: The Explanation and Investigation of Biological Rhythms. Biological Rhythms and Human Performance. Academic Press (New York), 1971, pp. 1-38.
- 14-5. Winget, Charles M.: Significance of Biorhythms in Space Flight. Proceedings of the 1973 Lyndon B. Johnson Space Center Endocrine Program Conference. NASA TM X-58155, 1975, pp. 3-1 to 3-11.
- 14-6. Montgomery, P. O'B., Jr.; Cook, J. E.; et al.: The Response of Single Human Cells to Zero Gravity. The Proceedings of the Skylab Life Sciences Symposium, Vol. II. NASA TM X-58154, 1974, pp. 467-491.
- 14-7. Young, Richard S.; Tremor, John W.; et al.: The Effect of Weightlessness on the Dividing Eggs of *Rana pipiens*. The Experiments of Biosatellite II. NASA SP-204, 1971, pp. 251-271.
- 14-8. Von Borstel, R. C.; Smith, R. H.; Whiting, Anna R.; and Grosch, D. S.: Mutation and Physiologic Responses of *Habrobracon* in Biosatellite II. The Experiments of Biosatellite II. NASA SP-204, 1971, pp. 17-39.
- 14-9. Akoev, I. G.; Yurov, S. S.; et al.: Mutagenic Action of Secondary Radiation of 70 GeV Protons. *Studia Biophysica*, vol. 41, 1973, pp. 167-180.

# 15. Microbial Exchange

## Experiment AR-002\*

G. R. Taylor,<sup>a†</sup> K. D. Kropp,<sup>b</sup> M. R. Henney,<sup>b</sup> S. S. Ekblad,<sup>b</sup> A. A. Baky,<sup>b</sup> T. O. Groves,<sup>b</sup> T. C. Molina,<sup>b</sup> J. G. Decelle,<sup>b</sup> C. F. Carmichael,<sup>b</sup> N. J. Gehring,<sup>b</sup> E. L. Young,<sup>b</sup> I. L. Shannon,<sup>c</sup> W. J. Frome,<sup>a</sup> and N. R. Funderburk<sup>d</sup>

### ABSTRACT

The purpose of the Microbial Exchange Experiment was to evaluate components of the infectious disease process in space flight by measuring alterations in three factors: (1) the composition of the microbial populations inhabiting the crewmembers and the spacecraft, (2) the ability of each crewmember's defense mechanism to resist infection, and (3) the ability of certain microorganisms to originate infections. The impetus for performing the experiment arose from the variety of in-flight and ground-based microbial studies in the United States and the U.S.S.R., the results of which have suggested that the conditions of space flight may alter man and microorganisms in such a way that the normal fine balance between them may be adversely affected. The monitoring of two separate crews, which differed microbiologically and immunologically, provided an opportunity to study

in-flight cross-contamination patterns. Because the Apollo-Soyuz Test Project crewmembers came from widely different geographical and ecological areas, it was possible to identify specific, naturally occurring, marker microorganisms for detailed analysis.

This report evaluates the operational aspects associated with the experiment, the activities of medically important microorganisms recovered from the six Apollo crewmembers (three prime and three backup) and four Soyuz crewmembers (two prime and two backup), and the activities of the major groups of microorganisms recovered from the 10 sample sites of each crewmember. Most activities were performed as planned, and a large percentage of the anticipated data was obtained. A variety of potential pathogens was recovered from each of the prime and backup crewmembers before and after flight. However, no disease events were reported. *Candida albicans* and *Staphylococcus aureus* (type 52, 52A, 80, 81) were shown to be transferred from one crewmember to another during the flight. No other medically significant changes in the microbial population were observed.

Within the microbial population of the 10 sampled crewmembers, there was no significant difference between the total load of aerobic bacteria inhabiting the integumentary surface of each, or between the total microbial load in the upper respiratory tract of each. The total load recovered from each crewmember on the day of return from space flight was not significantly different from the preflight mean, contraindicating discernible

---

\*The Microbial Exchange Experiment is one of five experiments that incorporated joint activities of the U.S. and U.S.S.R. crews. The joint experiment designation was "Experiment AS-2."

<sup>a</sup>NASA Lyndon B. Johnson Space Center.

<sup>b</sup>Northrop Services Incorporated, Houston, Texas.

<sup>c</sup>The University of Texas at Houston, Dental Branch.

<sup>d</sup>University of Texas Health Science Center at San Antonio, Texas.

<sup>†</sup>Principal Investigator.

flight-affected changes in the size of the population of aerobic bacteria. The theories that proposed "simplification" of the microbial population, "dysbacteriotic" changes in the oral autoflora, and alteration in the immune potential were evaluated. No data were obtained to corroborate these hypotheses.

## INTRODUCTION

The problems concerning the occurrence of microbial contamination and infectious diseases during space flight have been evaluated repeatedly following U.S. and U.S.S.R. manned missions. Scientists in the U.S.S.R. have been concerned with crew microbiological profiles and natural bactericidal activity since their first manned mission. Twelve years ago, Alekseyeva (ref. 15-1) reported that the composition and properties of the autoflora of cosmonauts remained within normal limits during preflight evaluations but that there were occasional postflight changes. An increase in oral autoflora was accompanied by dysbacteriosis in which the normal throat flora were almost entirely crowded out by Gram-negative, non-hemolytic diplococci. It was also reported that an increase in the number of microbes in the deep layers of the skin was caused by the appearance of masses of hemolytic micrococci (ref. 15-1). More recently, Nefedov et al. (ref. 15-2) have reported that alterations in microbial flora have been observed on several flights and appear to be dependent on "environmental parameters," the duration of the exposure to different environmental factors, and the work-rest schedules. The same authors point out that one of the most consistent phenomena appears to be the interchange of microorganisms between subjects (ref. 15-2). The advent of the U.S.S.R. space station, Salyut, enabled in-flight samples to be taken from the three crewmembers. Postflight analyses of these samples revealed changes in autoflora and microbial interchange.<sup>1</sup> However, the death of the crewmembers prevented postflight sampling and analysis.

The interest of U.S.S.R. investigations in autoflora has not been restricted to cosmonauts. Alekseyeva and Volkova (ref. 15-3) have reported

studies with "space dogs" (dogs that have experienced space flight) since 1960. They reported that whereas acceleration and vibration on the ground had no effect on the microflora, the space dogs had intestinal bacilli in their mouths after 2 days of space flight. The authors interpreted the presence of intestinal bacilli to be a result of a space-flight-mediated decrease in the immunological activity of the subjects.

The interest of the U.S.S.R. space agency concerning this research, and the philosophy that led to participation in the Microbial Exchange Experiment, was offered during the first meeting of the U.S.-U.S.S.R. Joint Working Group in Space Biology and Medicine in Moscow.<sup>2</sup> During the meeting, U.S.S.R. investigators made the following observation.

The results of the study of the automicroflora of the integumentary tissues of the cosmonauts, indicating the development of dysbacteriotic changes in its composition during the space flight, have necessitated more detailed scientific studies in this area. Studies to clarify the role of the environment of objects in space in terms of the appearance of unfavorable changes in the composition of the automicroflora of the cosmonauts are most important in this respect.

Corresponding NASA studies began with comparisons between preflight and postflight specimens collected during one of the Gemini flights (ref. 15-4). In this first U.S. microbial analysis, the investigators reported a decrease in the number of types and an increase in the total number of microorganisms recovered after the flight. Also, there was evidence of microbial transfer between

---

<sup>1</sup>L. I. Kakurin, data presented at the second meeting of the U.S.-U.S.S.R. Joint Working Group in Space Biology and Medicine, NASA Lyndon B. Johnson Space Center, May 1972.

<sup>2</sup>Data presented at the first meeting of the U.S.-U.S.S.R. Joint Working Group in Space Biology and Medicine, Moscow, 1971.

the crewmembers. When evaluating these findings in reference to the total clinical picture, Berry (ref. 15-5) indicated that the observed microbial changes may not be compatible with the health and welfare of the crewmembers. In a survey of 26 chamber tests conducted by the National Academy of Sciences between 1962 and 1970, evidence was presented which indicates that microbial exchange is not infrequent and that it may contribute to medically significant events (ref. 15-6).

Detailed analyses of preflight and postflight samples from Apollo 14 crewmembers revealed (1) an intercrew transfer of *Staphylococcus aureus*, (2) an 830-percent increase in the quantitation of aerobic bacteria, and (3) a transfer of microorganisms from crewmembers to the command module hardware (ref. 15-7). A dramatic postflight reduction in the number of mycological species recovered from the Apollo 14 crewmembers was also observed with the Apollo 15 crew (ref. 15-8).

With the advent of the Skylab missions, it became possible to evaluate the microbial alterations resulting from space flights with durations as long as 85 days. Complete autoflora studies were conducted on each of the prime crews (refs. 15-9 and 15-10). Preliminary evaluations show that, although gross contamination of the Skylab environment did occur and although there were several in-flight disease events (presumably of microbial origin), such events did not prove to be limiting hazards for long-term space flight. Evaluation of the major groups of microorganisms, comprising the microbial population tested, tended to support the theory of microbial simplification for anaerobic bacteria (refs. 15-2, 15-11, and 15-12) but not for other microbes. Intercrew transfer of pathogens was indicated. The data did not support the theory of postflight microbial shock (refs. 15-12 to 15-14).

The review by Fox (ref. 15-15) indicates clearly that the results of the early NASA autoflora studies were analogous to those studies performed in the U.S.S.R. Both studies have indicated significant alterations in the microbial population as well as definite transfer of species between crewmembers.

The Microbial Exchange Experiment was designed to monitor quantitatively the microbial

load of all crewmembers and of selected inner surfaces of both the Apollo and Soyuz spacecraft and to evaluate the status of certain components of the immune mechanism of each crewmember. To accomplish this objective, an evaluation of the normal autoflora and immunocompetence level of each crewmember was established before flight and through repeated sampling and analyses. Therefore, quantitative and qualitative changes occurring during or after flight could be measured and evaluated, and instances of intercrew transfer of marker organisms could be identified. At the same time, certain immunological parameters of the blood and saliva of each crewmember were studied to detect changes in the ability of the individual to resist infection.

## METHODS AND MATERIALS

### Baseline Microbial Specimen Collection

Specimens were to be collected from the 5 prime and 5 backup crewmembers and from 15 areas on the inner surfaces of each spacecraft at specific times before, during, and after the flight as given in table 15-I. During each preflight and postflight sampling period, 10 microbial specimens were collected from each crewmember (table 15-II). Calcium alginate swabs, wetted in 0.3-millimolar phosphate buffer, were used to sample each of the seven body surface areas. This swab technique was the only collection method compatible with the flight program. Although it is recognized that subsurface microbes may be overlooked by this method, procedures for sampling subsurface areas were not acceptable. Dry calcium alginate swabs were used to sample the surfaces of the tonsils and the posterior pharyngeal vault before collection of the gargle specimen. For the latter sample, the subject gargled with 0.3-millimolar phosphate buffer followed by a repeated rinse of the teeth with the same solution. Swabs were placed in 5 cm<sup>3</sup> of 0.3-millimolar phosphate buffer for transport to the laboratory. Analysis of all samples was initiated within 1 hour of specimen collection.

TABLE 15-I.—Sample Collection Schedule

Sample	Day of collection											
	Days before flight (a)						During flight	Days after flight (a)				
	F-45	F-30	F-15	F-7	F-1	F-0		R+0	R+3	R+7	R+15	R+30
Blood		X	X		X		X	X <sup>b</sup> X	X <sup>b</sup>			
Spacecraft microflora											X <sup>b</sup> X <sup>b</sup> X <sup>b</sup>	
Saliva	X	X	X	X		X	X	X	X <sup>b</sup> X <sup>b</sup> X <sup>b</sup>			
Crew microflora	X	X	X	X			X	X				

<sup>a</sup>F-0 = day of launch and R+0 = day of recovery.

<sup>b</sup>Prime crewmembers only.

TABLE 15-II.—Sample Collection Sites

Sample designation	Sample area
Hair	20-cm <sup>2</sup> area of hair (and scalp) on top of head
Ears	Right and left external auditory canals with two revolutions of each swab in each ear canal
Neck	20-cm <sup>2</sup> area below hairline at base of neck
Nares	Internal area of both nostrils
Throat	Surfaces of tonsils and posterior pharyngeal vault
Hands	20-cm <sup>2</sup> area on right and left palms
Axillae	20-cm <sup>2</sup> area below hair on each side
Groin	5-cm strip from rear to front on right and left inguinal area between legs
Toes	Area between the two smallest toes of each foot
Gargle	10 cm <sup>3</sup> of phosphate buffer used as gargle and washed through oral cavity three times

### In-Flight Microbial Specimen Collection

In addition to the baseline samples previously described, in-flight samples were obtained from all five prime crewmembers and both spacecraft between 77:40 and 78:30 ground elapsed time (GET). A specially developed sample collection device was used for this set of samples (fig. 15-1). This device consisted of a cotton-tipped Teflon swab on a capillary tube that contained conservation fluid to keep the microorganisms alive. Each swab was housed within an airtight case to prevent desiccation. Groups of swabs were organized in Beta-cloth retaining bags (fig. 15-2). One bag of this type was provided for each of the following: (1) swabs used for Soyuz spacecraft samples, (2) swabs used for Apollo spacecraft samples, (3) swabs used for Apollo commander (ACDR) and Soyuz commander (SCDR) samples that were taken in the Soyuz, (4) swabs used for Soyuz flight engineer (SFE), docking module pilot (DMP), and command module pilot (CMP) samples that were taken in the Apollo spacecraft.

All four sets of swabs were launched in the Soyuz spacecraft. The two kits to be used in the Apollo were transferred from the Soyuz at the end of the first joint activity (58:20 GET) and

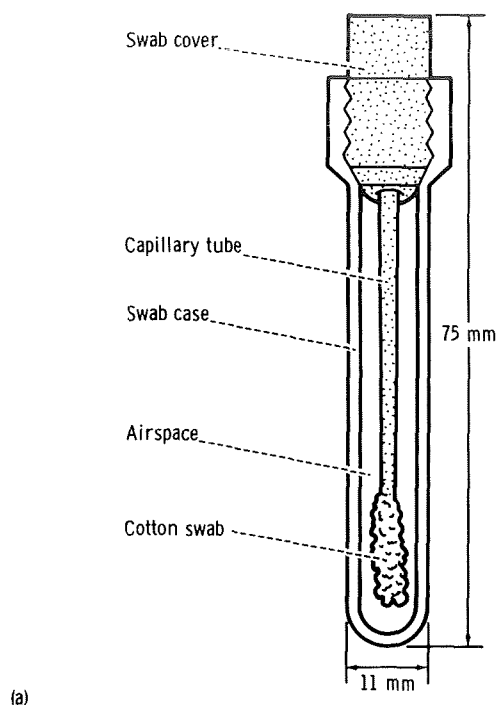


FIGURE 15-1.—In-flight collection of microbial samples. (a) Microbial collection device. (b) Use of device in the Soyuz spacecraft by the SCDR. (c) Use of device in the Soyuz spacecraft by the ACDR.



returned to the Soyuz near the end of the last joint activity (79:50 GET). All samples collected during flight were returned to Moscow for preliminary analysis and division between the U.S. and U.S.S.R. laboratories as outlined in the following discussion. In-flight samples consisted of the first six areas outlined in table 15-II as well as the spacecraft sites presented in table 15-III. It should be noted that Soyuz spacecraft samples C-7 through C-15 were taken from the part of the spacecraft not returned to Earth. Accordingly, these samples were not collected after the flight. To assist in spacecraft sample collection, black lines demarking a 100-cm<sup>2</sup> area had previously been painted at each of the specified sites as shown in the examples illustrated in figure 15-3.

Because the specimens collected during flight had to be returned to the laboratory for analysis, considerable delay was unavoidable. To equate results from these specimens with results from specimens collected before and after flight, a

group of samples was collected the morning of launch and immediately upon return from the flight. These samples were held at room temperature for 4 days to simulate the delay imposed on the in-flight specimens. These comparative specimens were collected from all 10 crewmembers and both spacecraft using the same type swabs used during flight.

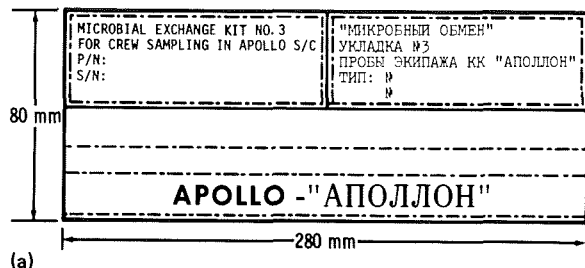
### Collection of Salivary Parotid Fluid

Saliva from the parotid gland was collected from each of the 10 crewmembers before flight and from the 5 prime crewmembers after flight according to the schedule shown in table 15-1. The special saliva collection device, shown in figure 15-4, was attached by pressure to the inner surface of the oral cavity over the opening of the parotid duct. The parotid fluid was collected for 10 minutes with the flow being stimulated by a sour

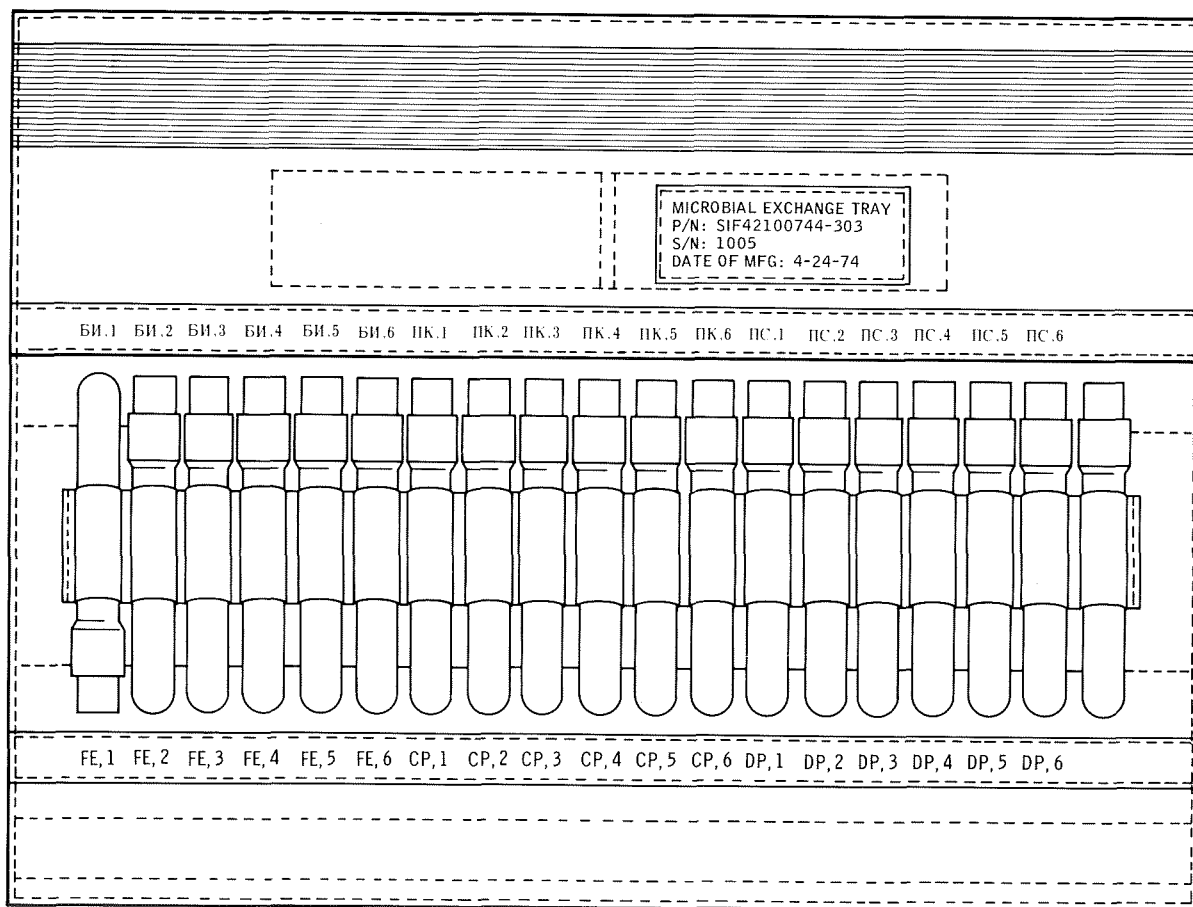
candy drop placed in the subject's mouth. The resulting saliva was frozen at 233 K ( $-40^{\circ}$  C) and stored for future analysis. No saliva was collected during the flight.

### Blood Collection and Serum Preparation

Venous blood was collected from the antecubital fossae of each of the 10 participating crewmembers before flight and from the 5 prime crewmembers after flight as outlined in table 15-I. From each sample, whole blood was allowed to clot for serum separation. The resulting serum was used to determine humoral antibody levels and bactericidal activity.



(a)



(b)

FIGURE 15-2.—Beta-cloth sample collection kit used for crewmember samples in the Apollo spacecraft. (a) Closed kit. (b) Open kit showing sample collection devices in place.



TABLE 15-III.—Location of Sampling Sites on Inner Surfaces of Spacecraft

Sample no.	Location in Soyuz	Sample no.	Location in Apollo
C-1	SCDR couch seat	A-1	Left X-X headstrut
C-2	SFE couch seat	A-2	Right X-X footstrut
C-3	Control panel in the descent vehicle	A-3	Crew couch, right stabilizer beam
C-4	Surface of gas mixture regulator	A-4	Tunnel area
C-5	Surface near bulkhead hatch in descent vehicle	A-5	Right floodlight
C-6	Descent vehicle hatch cover under the handwheel	A-6	Left rotational hand controller pistol grip (both sides)
C-7	Flush side of sanitary device in the orbital module (OM)	A-7	Right girth shelf above panel 278
C-8	Top of food locker table in OM	A-8	Panel 325 below window
C-9	Couch seat in OM	A-9	Above left girth shelf (above U-3)
C-10	Surface of food locker in OM near panel	A-10	Cover plate, ORDEAL stowage locker (U-3)
C-11	Front surface of the couch backrest in the OM	A-11	B-6 door behind waste stowage bag
C-12	Grid near fan in OM	A-12	Inside door of food locker (L-3)
C-13	Floor surface near OM food locker	A-13	Top of video tape recorder module
C-14	Transfer hatch under the handwheel	A-14	Panel 251, waste management dump
C-15	Surface of transfer hatch	A-15	Forward of panel 225

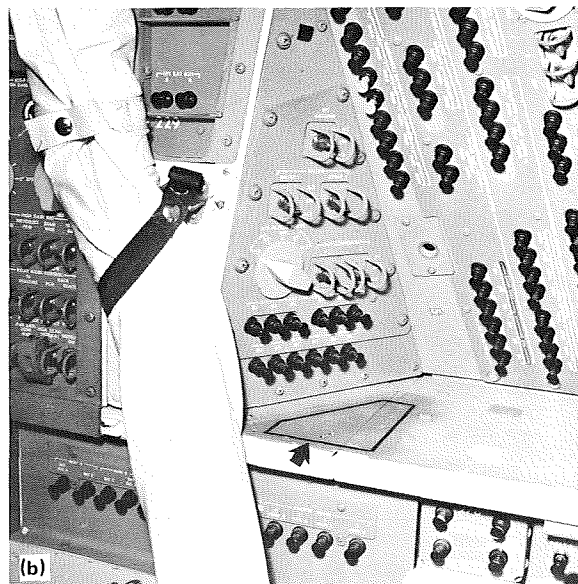
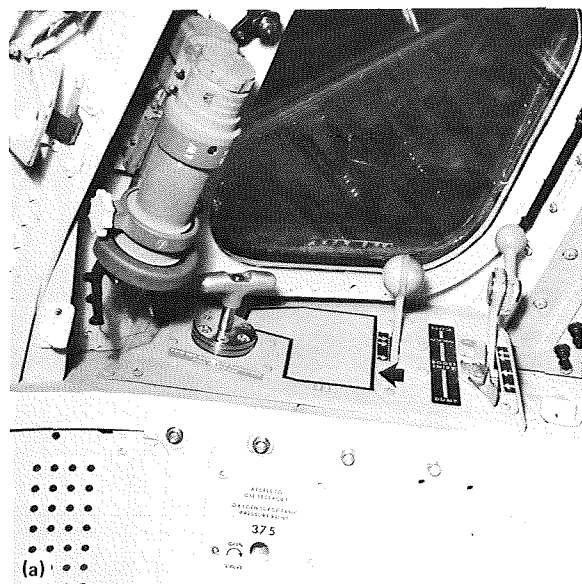


FIGURE 15-3.—Demarcation lines on internal surfaces of Apollo and Soyuz spacecraft. (a) Panel 325 below window in Apollo (S74-33254). (b) Right girth shelf above panel 278 in Apollo (S74-33259). (c) Demarcation lines in Soyuz (AST5-311).

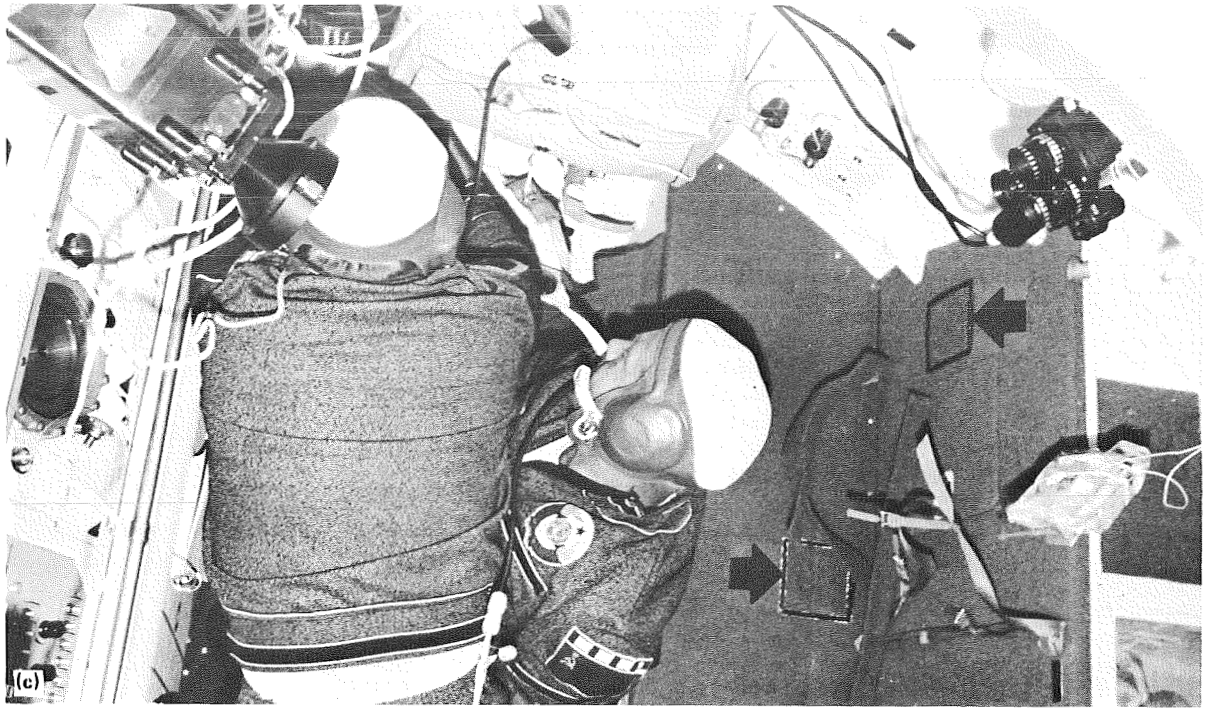


FIGURE 15-3.—Concluded.

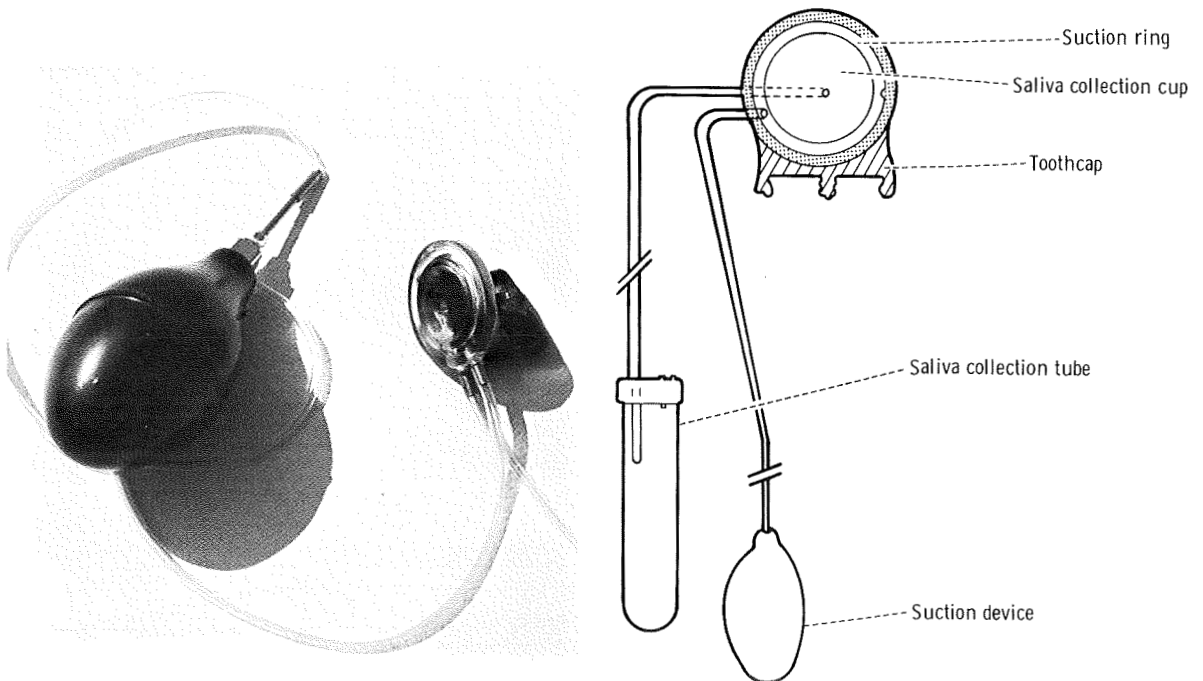


FIGURE 15-4.—Saliva collection device used to obtain salivary parotid fluid.

### Preliminary Analysis of Microbial Specimens and Distribution of Test Materials

The contents of each swab and gargle sample were serially diluted under aseptic conditions and subsequently inoculated onto the surface of the nutrient media as previously outlined (ref. 15-16). The variety of media, number of plates inoculated, dilution ranges, and incubation conditions were selected on the basis of what was required to isolate and quantitate the autoflora components present in each sampled area. A common methodology, composed of analytical procedures acceptable to both the U.S. and U.S.S.R. investigators, was used to ensure comparability of data (ref. 15-17). A general schematic summary of the preliminary steps required for specimen distribution is presented in figure 15-5. Following incubation under the appropriate conditions, all resulting colonies on every culture plate were categorized and counted. Subsequently, one sample of each morphologically different colony type was transferred from each dilution series to the appropriate nutrient media and appropriately stained. Following verification that a pure culture

was obtained, one aliquot of each culture was stored by the laboratory in which it was identified (the host laboratory), and another complementary aliquot was made available to the guest laboratory. The guest laboratory was to have had access to an isolate from each different type of colony grown on the incubated plates.

### Division of Responsibility for Specimen Analysis

The analytical procedures required for performance of the Microbial Exchange Experiment were divided between the laboratories in the United States and the U.S.S.R. (table 15-IV). The U.S. Principal Investigator was responsible for identification of all filamentous fungi, nonlactose-fermenting Gram-negative rods, and members of the genus *Haemophilus*. The U.S.S.R. Principal Investigator was responsible for the identification of yeasts and yeastlike fungi, Gram-positive catalase-negative cocci, Gram-negative cocci, and lactose-fermenting Gram-negative rods. The responsibility for identification of Gram-positive

TABLE 15-IV.—Division of Responsibility for Specimen Analysis

Activity	Responsible laboratory	
	U.S.	U.S.S.R.
Collection of specimens from astronauts and Apollo spacecraft	X	
Collection of specimens from cosmonauts and Soyuz spacecraft		X
Identification of filamentous fungi	X	
Identification of yeasts and yeastlike fungi		X
Identification of Gram-positive catalase-positive cocci	X	X
Identification of Gram-positive catalase-negative cocci		X
Identification of Gram-negative cocci		X
Identification of nonlactose-fermenting Gram-negative rods	X	
Identification of lactose-fermenting Gram-negative rods		X
Identification of <i>Haemophilus</i> sp.	X	
Bacteriophage typing of <i>Staphylococcus aureus</i>	X	
Antibiotic sensitivity testing of <i>Staphylococcus aureus</i>		X
Determination of immunoglobulin levels in parotid fluid	X	
Determination of steroid, urea nitrogen, uric acid, calcium, and potassium levels in parotid fluid	X	
Determination of lysozyme levels in parotid fluid		X
Determination of bactericidal activity of serum		X
Measurement of viral antibody titers in serum		X
Measurement of specific microbial antibody levels in serum	X	
Determination of leukocyte differential count	X	

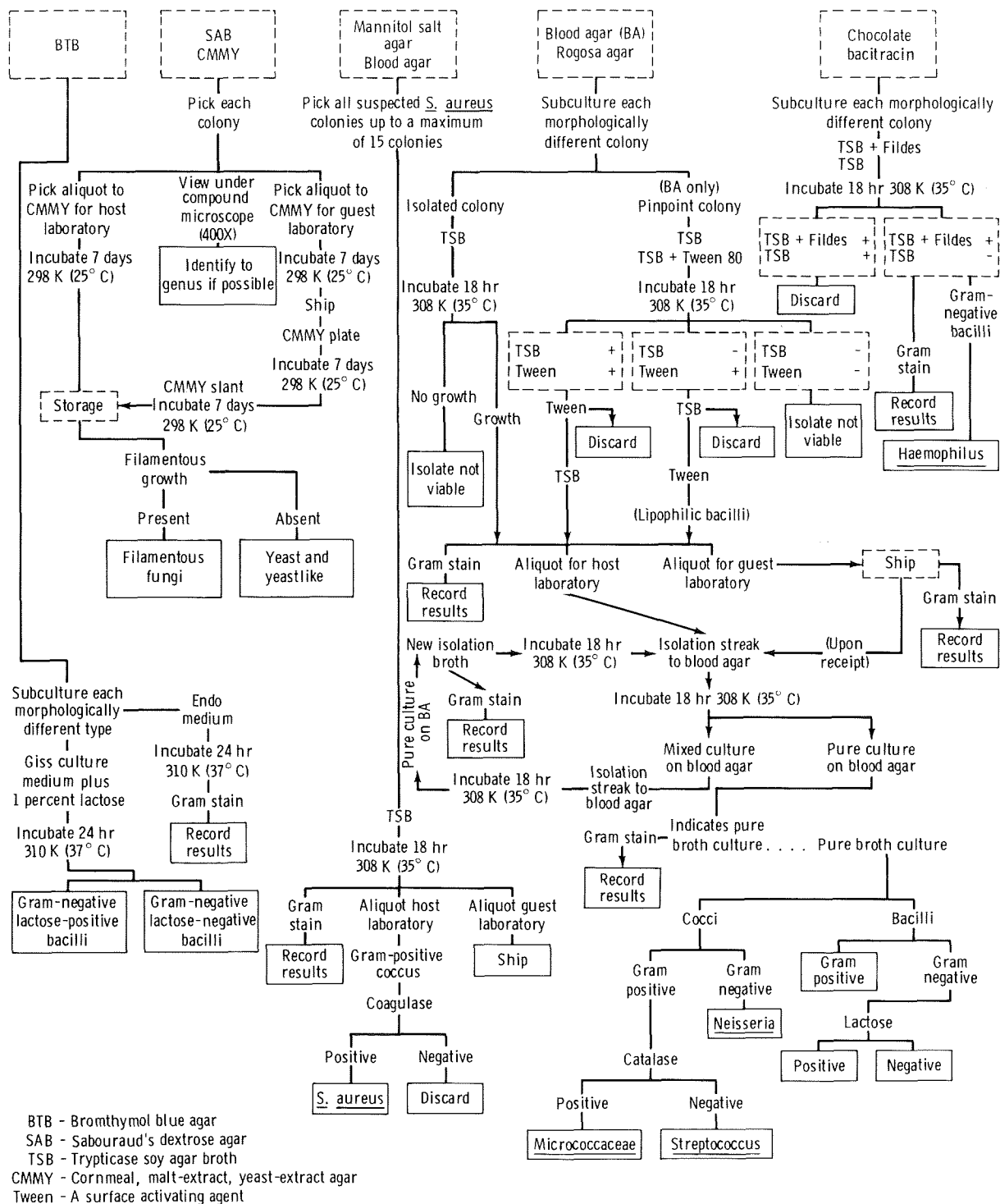


FIGURE 15-5.—Schematic diagram for identifying microorganisms.

catalase-positive cocci was shared by both laboratories. In addition to these microbial identifications, the responsibility for specific tests was divided as shown in table 15-IV.

The proper collection of preflight and postflight samples from the cosmonauts and the Soyuz spacecraft was the responsibility of the U.S.S.R. Principal Investigator. The proper collection of preflight and postflight samples from the astronauts and the Apollo spacecraft was the responsibility of the U.S. Principal Investigator. The safe and expeditious return of samples collected during flight was the responsibility of the U.S.S.R. Principal Investigator. The preliminary analysis of all samples, culminating in and including distribution of specimens to both U.S. and U.S.S.R. investigators, was the responsibility of the Principal Investigator of the country in which the sample was collected. All preliminary specimen analyses conducted in the U.S.S.R. laboratories were to be conducted in the presence of a science representative of both the United States and the U.S.S.R. Although this arrangement was also available in the U.S. laboratories, the U.S.S.R. investigators had the option of exercising this procedure. These joint activities were to include dilution and plating of specimen materials, isolation of microbial colonies, and evaluation of growth properties on the initial isolation media. Crewmembers and spacecraft were sampled independently.

## RESULTS AND DISCUSSION

### Analysis and Evaluation of Operational Activities

The extent to which each objective of the experiment was accomplished is evaluated together with a discussion of any reported anomalies.

1. The normal microbial autoflora level and the immunocompetence level of each crewmember were identified. The collection of five sets of preflight saliva and microbial samples and of two sets of serum samples for each of the prime and

backup crewmembers provided adequate establishment of baselines for U.S. crewmembers. However, data pertaining to the total microbial load could not be retrieved from microbiology specimens collected in the U.S.S.R. All serum samples, with the exception of those taken from the backup SCDR 15 days before launch, were received in a condition that permitted the required analysis. All the astronaut saliva samples, with the exception of the CMP samples, were collected as planned. (An alternate collection method was used for the CMP that provided an adequate but not optimum saliva sample.) All cosmonaut saliva samples were collected in a manner different from that agreed upon and therefore were not usable in this study.

2. The identification of qualitative and quantitative changes in crew and spacecraft microbial populations and the evaluation of demonstrable intercrew microbial exchange occurring during flight were necessary for proper analysis. The most important marker microorganisms were properly monitored in the U.S. and U.S.S.R. laboratories, allowing for a reasonably thorough evaluation of intercrew microbial exchange. Likewise, shifts in many of the major components of the autoflora could be evaluated. Variations in the total autoflora could be calculated only for the Apollo crew.

3. Selected microorganisms were to be critically evaluated to detect postflight changes in their ability to be pathogenic, infective, or toxic in man. Several of the microorganisms that are most useful for these evaluations were repeatedly isolated from Apollo-Soyuz crewmembers. Although these are protracted studies and have not yet been completed, the prognosis for satisfying this objective is very good. Thirty-day postflight samples of cosmonauts were not collected.

4. Immunological parameters of blood and saliva were to be evaluated to detect postflight changes in the ability of crewmembers to resist infection. The required astronaut specimens were obtained and analyzed as planned. Data from cosmonaut specimens were less complete because of incomplete blood collection and different saliva collection techniques.

### Microbiological Analysis of Apollo-Soyuz Test Project (ASTP) Crewmembers

On early Apollo missions, before strict protective measures were instituted, in-flight infections were not unusual (ref. 15-18). In-flight illness of microbial origin was, however, completely absent from the Apollo 14 through 17 missions (ref. 15-19). There is no doubt that the implementation of extensive preventive measures (ref. 15-20), following the clinically significant Apollo 13 mission, was a contributing factor. Preflight monitoring of pathogenic and potentially pathogenic species identified certain potential problems so that appropriate prophylaxis or treatment could be administered before the flight or could be provided during the flight. This procedure was highly effective and was recommended for all future U.S. manned space flights (ref. 15-19). Similar analyses conducted during the three Skylab missions indicated that, whereas there were several in-flight disease events and gross contamination of the orbital workshop did occur, such events did not prove to be limiting hazards for long-term space flight (ref. 15-10). The ASTP mission, a unique space flight in which two teams of crewmembers from different geographical areas joined in space with two different spacecraft, presented an unusual opportunity for cross-contamination. Accordingly, it was necessary to identify and trace all aerobic bacterial species as well as all microorganisms of potential medical importance present in the population.

**Total microbial load.**—One method of detecting important autoflora changes is to monitor alterations in the size of the bacterial population inhabiting the body of the test subject. Accordingly, the number of viable bacterial cells recovered from the skin sites of all five prime crewmembers was determined and is illustrated in figure 15-6(a). These data show no significant differences between subjects, indicating that Apollo and Soyuz crewmembers retained approximately the same microbial load on their skin despite the geographical and cultural differences involved. The data in figure 15-6(a) also show that the values obtained immediately after space flight were within the preflight range, demonstrating that the population

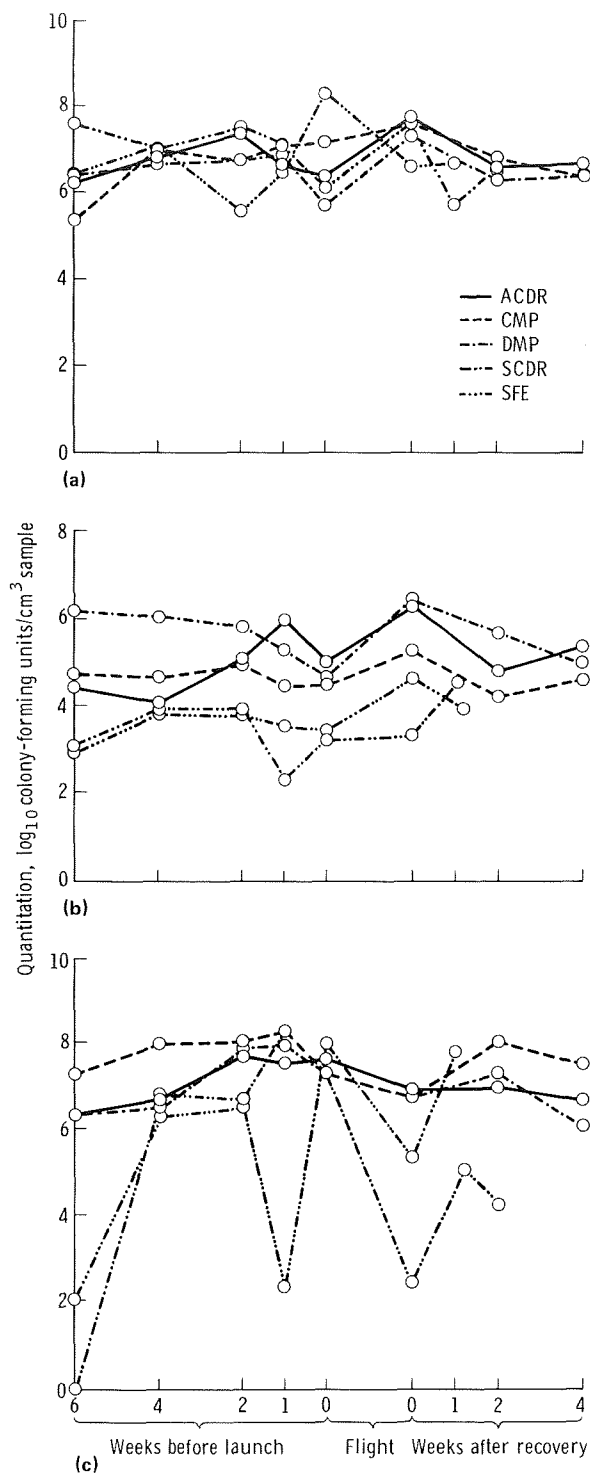


FIGURE 15-6.—Number of aerobic bacterial cells recovered from crewmembers. (a) Cells in skin samples. (b) Cells in nasal cavity. (c) Cells in oral cavity.

of aerobic bacteria (measured in terms of total viable cells) inhabiting the integumentary surfaces was stable following space flight, and that no medically important alterations occurred.

Analyses of the bacterial load recovered from the nasal and oral cavities of ASTP crewmembers were likewise determined and are presented in figures 15-6(b) and 15-6(c), respectively. The upper respiratory tract samples obtained from the cosmonauts yielded counts that were generally lower and more variable than those obtained from astronaut specimens. Even with this variability, the resulting data show that the space flight had no demonstrable effect on the total bacterial load recovered from the oral and nasal cavities.

*Contamination of spacecraft internal surfaces.*—Multiple sites within the Apollo and the Soyuz spacecraft were sampled before, during, and after the flight. Subsequent analyses resulted in the data illustrated in figure 15-7. Most sampled areas were not sterile before flight and thus afforded a potential source of contamination to the crews. Contamination within the Soyuz spacecraft was increased (by one order of magnitude) the day of return from space flight, a response similar to those previously reported for other space flights (refs. 15-7, 15-17, and 15-21). Contamination with-

in the Apollo spacecraft was measurably decreased after the flight. This situation was probably the result of prolonged contact of the sampled surfaces to a dinitrogen tetroxide and nitrous oxide gas mixture that had inadvertently entered the spacecraft during the landing procedure. It is important to note that this toxic gas affected the contamination level of spacecraft surfaces but did not measurably influence the autoflora of the crewmembers. This occurred because the autoflora components were better protected from outside affectors and had a significantly shorter contact time with the toxic gas.

*Gram-negative rods.*—A number of different microbes that occur normally in the intestinal tract, or are associated with intestinal infection, are placed in the enteric group of microorganisms. The normally occurring members of this group are generally considered to be of potential medical importance when recovered repeatedly, or in large numbers, from sites other than the lower digestive tract. A complete analysis of the specific Gram-negative rods recovered from Apollo and Soyuz crewmembers has previously been presented (ref. 15-16). Accordingly, these data are only summarized in this report.

It has previously been reported (refs. 15-2 and 15-22) that the Gram-negative rod component of the autoflora could change during or following confinement in a closed environment and that this change could result in "dysbacteriosis," such as a flooding of the oral cavity with a particular species. The data presented in figure 15-8 show that, when considered as a unit, the quantitation of Gram-negative rods is too variable to establish any flight-affected alteration. This is to be expected because these species are mostly transient to the human body rather than being true members of the autoflora (except in the lower gastrointestinal tract, which was not evaluated in this study). There was, however, an increase in the number (incidence) of cosmonaut body sites from which Gram-negative rods were recovered upon return from the space flight. This spreading of bacteria to previously uncontaminated sites probably resulted from the altered hygiene regimen used onboard the Soyuz spacecraft.

Of the Gram-negative rods recovered, only members of the genus *Haemophilus* are indigenous

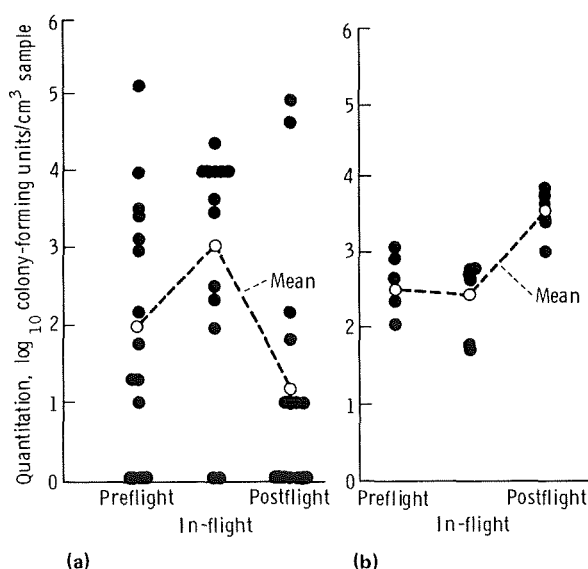


FIGURE 15-7.—Number of aerobic bacterial cells on spacecraft internal surfaces. (a) Apollo. (b) Soyuz.

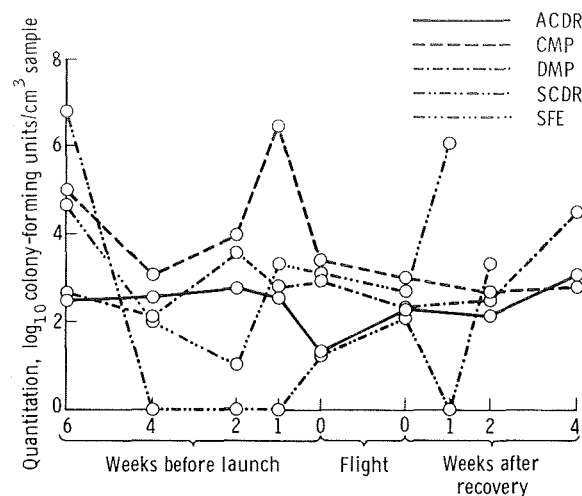


FIGURE 15-8.—Number of Gram-negative rods recovered from crewmembers. (The genus *Haemophilus* is excluded.)

to the human autoflora, being continually present in the oral cavity. Therefore, it is possible to evaluate changes within a single genus of Gram-negative rods only with these microorganisms. The data illustrated in figure 15-9 show that there was a quantitative decrease in the recovery of *Haemophilus* in both prime and backup crewmembers immediately preceding the flight. This

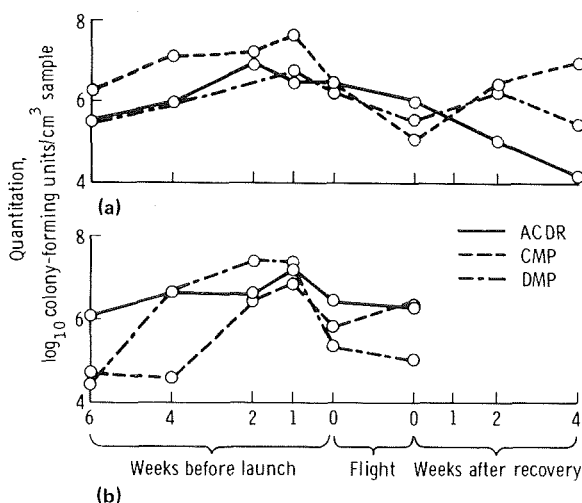


FIGURE 15-9.—Number of *Haemophilus* cells in oral cavity samples from Apollo crewmembers. (a) Prime crew. (b) Backup crew.

decrease coincides with the preflight maintenance of these subjects in protective isolation, a procedure that has been shown to minimize the probability of preflight and in-flight infections in previous space flights (refs. 15-19 and 15-23). The load of *Haemophilus* cells in the oral cavity of all three of the ASTP prime crewmembers was significantly reduced during the flight but remained constant in the nonflight control group. This demonstrates a decrease in the relative importance of these potential pathogens to the autoflora during space flight.

None of the observations previously discussed support the view that Gram-negative rods undergo unfavorable dysbacteriologic changes following space flight. Therefore, those few instances in which such changes have been reported should be considered to be coincidental with, and not a function of, space flight.

*Candida albicans*.—This species, which has long been recognized as a normal component of the indigenous autoflora of man, has frequently been recovered from the crewmembers of previous space flights and space simulation missions (refs. 15-8, 15-19, 15-24, and 15-25). Because *C. albicans* has been identified as the causative agent for serious oral cavity disease, its presence in the mouth of ASTP crewmembers was carefully monitored. Analysis of the data presented in reference 15-16 indicates an intracrew transfer of this species to the Apollo commander during flight. No such transfer occurred with the Apollo backup controls, although *C. albicans* was routinely carried in the mouth of the backup Apollo CMP. Among the Soyuz cosmonaut microbial population, *C. albicans* was recovered only from the prime FE 33 and 15 days before launch, and therefore was not considered of medical importance during the flight.

*Staphylococcus aureus*.—Although *S. aureus* microorganisms are not uncommon skin and nasal contaminants, all strains are potential pathogens. The results of several space-flight-simulation studies have suggested increases in the toxigenic activity, virulence, or pathogenicity of this species with stressful confinement of the human host (refs. 15-2, 15-22, and 15-26). The strains of *S. aureus* recovered from the 10 ASTP crewmembers are presented in table 15-V. A more



TABLE 15-V.—*Staphylococcus Aureus* Strains Carried by Crewmembers

Flight status	Position	Quantitation (a)		Predominant bacteriophage type carried
		Preflight mean	Postflight	
Apollo				
Prime	ACDR	3.04	1.95	Not typeable
	CMP	2.06	0	53, 83A, 85
	DMP	1.10	1.30	52, 52A, 80, 81
Backup	ACDR	1.65	0	3A, 3C
	CMP	3.80	3.86	55, 71
	DMP	3.23	4.83	29, 53, 54, 75, 79, 80
Soyuz				
Prime	SCDR	2.82	3.36	53, 54, 80, 81
	SFE	3.15	4.65	6, 42D, 42E, 47, 53, 81
Backup	SCDR	2.27	(b)	6, 53, 75, 85
	SFE	2.48	(b)	52, 53

<sup>a</sup>Quantitations given as  $\log_{10}$  colony-forming units/cm<sup>3</sup> sample.

<sup>b</sup>No sample collected.

complete analysis is presented in reference 15-16. These data show that each crewmember carried a different strain, each of which is expressed as a numbered bacteriophage type. Type 52, 52A, 80, 81 was carried by the Apollo prime DMP and was transferred to the ACDR during flight. There was no transfer demonstrated between crews.

A postflight increase in the incidence of *S. aureus* has previously been reported (ref. 15-19). This could not occur during the ASTP mission because of the universal presence of this species before flight. However, there was a measurable increase in the number of *S. aureus* cells recovered from prime Soyuz crewmembers immediately after the flight. Although recovery incidence and quantitation of this medically important species was unusually high, no disease events were reported.

**Total load of potential pathogens.**—Several authors have warned that returning space travelers may experience a "microbial shock" and may respond negatively to renewed contact with potentially pathogenic microorganisms that were absent in the space-flight environment (refs.

15-12, 15-14, and 15-18). These warnings were based on the assumption that contact with potential pathogens during space flight would be very limited, resulting in a reduction of immunocompetence. However, there was no demonstrable decrease in the incidence of medically important microorganisms recovered from the ASTP crewmembers on recovery day, a finding that supports earlier reported results (refs. 15-7, 15-19, and 15-24). Accordingly, no postflight disease events were reported. Therefore, neither the proposed simplification of the population of medically important microorganisms, nor the theorized postflight microbial shock, could be supported by the results of this study.

#### Evaluation of Immunological Parameters

The effect of space flight on man's immune system has been the subject of much speculation. Ginsberg (ref. 15-27) has reviewed the mechanisms of natural and acquired immunity and has concluded that the factors which contribute to our

natural, nonspecific immunity could be the most impaired during space travel. Nefedov et al. (ref. 15-2) have reported experiences with human subjects at the Soviet Arctic and Antarctic Institutes. Upon contact with healthy replacements, mass disease erupted among subjects who had resided for months in isolation during which only sterile food was consumed. Additionally, studies of animal resistance to infection performed in space-flight simulators have shown that these conditions may reduce the ability of test subjects to resist infectious challenge by viruses (ref. 15-28) and by staphylococci (ref. 15-29) and may cause a reduction of antibody titer and spleen weight when given an antigenic challenge (ref. 15-30). Hypokinesia and acceleration studies have been reported to produce impairment of properdin, neutrophil phagocytosis, salivary lysozyme, skin bactericidal activity, and increased incidence of inflammatory diseases (ref. 15-31).

A variety of humoral immunological responses were noted for three subjects after being confined in a Skylab simulator for 56 days (ref. 15-32). The most significant of these was a rise in the serum immunoglobulins IgG and IgM. Likewise, salivary muramidase increased before entry into the chamber, again at a point midway in the confinement, and once more at the conclusion of the chamber study. During Apollo missions 7 through 11, increases related to illness were observed in IgG, IgM, IgA, haptoglobin, ceruloplasmin, and  $\alpha_2$  macroglobulin (ref. 15-18). Alterations not related to illness were also sometimes observed.

Although many components of the immune mechanism have been studied in connection with U.S. and U.S.S.R. space flights, the response of specific antibodies, produced in response to microorganisms carried by one or more crewmembers, has not yet been evaluated. Accordingly, such a study was incorporated into the Microbial Exchange Experiment and the data were correlated with the appropriate microbial population as well as with salivary IgA and lysozyme levels.

*Analysis of parotid saliva.*—Automatic, individualized parotid fluid collectors (fig. 15-4) were fabricated to fit the biting surfaces of the molar teeth so that each individual could collect his own parotid secretion with no difficulty. These

devices were prepared by the United States for each of the 10 ASTP crewmembers. For reasons that are not readily apparent, the collection devices were not properly used by the U.S.S.R. cosmonauts and parotid fluid of sufficient quantity and quality for detailed analyses was not received for study. Among the U.S. crewmembers, the collecting device could not be used on the prime CMP because of an anomaly in the opening of the parotid duct. Accordingly, data are included only for the remaining two prime and three backup crewmembers.

Laboratory analyses were directed primarily toward establishing rates of flow and studying concentrations of secretory IgA and lysozyme as they might be affected by the mission experience. A summary of the resulting data is shown in table 15-VI. The readings from samples collected from prime crewmembers the day of return from space flight are generally lower than the preflight mean. However, because similar variations occurred in the control (backup crew) population, none of these changes can be shown to be space-flight related. Therefore, there is no reason to suspect that changes in the oral autoflora during space flight are initiated (or influenced) by changes in the IgA or lysozyme content of parotid fluid.

Analyses were continued with samples collected 7, 15, and 30 days after landing of the Apollo spacecraft. Analyses of these data also failed to show any significant ( $p \leq 0.05$ ) alteration in the measured parameters, with the exception of an increase in IgA in the prime DMP sample collected on day R+15. Following exposure to a toxic mixture of dinitrogen tetroxide and nitrous oxide during landing, the crewmembers were treated with medications potentially capable of effecting a reduction in some measured parameters. It is important to note that, notwithstanding this treatment, no significant decreases were observed.

*Analysis of blood.*—The serum from the blood of U.S. and U.S.S.R. crewmembers was reacted against antigenic preparations of the bacteria *Staphylococcus aureus*, *Streptococcus* sp., *Haemophilus influenzae*, *Escherichia coli*, and the yeast *Candida albicans*. All of these species were isolated from the crew autoflora. In addition, preparations of *Salmonella typhi* "O" antigen and

TABLE 15-VI.—Analysis of Parotid Saliva From Apollo Crewmembers

Parameter	Subject	Preflight mean	Postflight reading and t-test values for comparison to preflight mean							
			R+0		R+7		R+15		R+30	
			Reading	t	Reading	t	Reading	t	Reading	t
Flow rate, cm <sup>3</sup> /min	Prime ACDR	0.414	0.16	-1.30	0.49	0.39	0.18	-1.20	0.56	-0.75
	Prime DMP	.530	.43	-.51	.39	-.72	.35	-.91	.38	-.77
	Backup ACDR	.702	.85	.76	--	--	--	--	--	--
	Backup CMP	.386	.37	-.08	--	--	--	--	--	--
	Backup DMP	.390	.54	.77	--	--	--	--	--	--
IgA content, mg %	Prime ACDR	5.36	3.3	-1.85	3.5	-1.67	5.4	0.04	5.4	0.04
	Prime DMP	2.96	.8	-1.94	1.4	-1.40	6.7	3.36	5.2	2.01
	Backup ACDR	3.90	2.5	-1.26	--	--	--	--	--	--
	Backup CMP	5.34	5.1	-.22	--	--	--	--	--	--
	Backup DMP	6.88	2.9	-3.57	--	--	--	--	--	--
Lysozyme content, mg %	Prime ACDR	0.514	0.06	-2.01	0.08	-1.92	0.40	-0.50	0.98	2.06
	Prime DMP	.378	.38	.01	.22	-.70	.68	1.34	.59	.94
	Backup ACDR	1.112	1.10	-.05	--	--	--	--	--	--
	Backup CMP	1.058	.97	-.39	--	--	--	--	--	--
	Backup DMP	1.264	1.43	.74	--	--	--	--	--	--

TABLE 15-VII.—Titers of Species-Specific Antibodies in Serum From Prime Crewmembers<sup>a</sup>

Species	Sampling time	Prime crewmember				
		ACDR	DMP	CMP	SCDR	SFE
<i>Staphylococcus aureus</i>	F-30	64	8	8	8	0
	F-15	64	8	0	8	0
	R+0	8	8	0	8	0
<i>Streptococcus sp.</i> (beta haemolytic)	F-30	16	16	16	32	16
	F-15	16	16	16	32	16
	R+0	16	16	16	32	16
<i>Haemophilus influenzae</i>	F-30	1024	1024	256	64	256
	F-15	1024	1024	256	64	256
	R+0	1024	1024	128	64	128
<i>Escherichia coli</i>	F-30	8	8	0	2048	>8192
	F-15	8	8	0	1024	>8192
	R+0	8	8	0	1024	1024
<i>Salmonella typhi</i> ("O" antigen)	F-30	64	32	64	64	16
	F-15	32	32	64	64	16
	R+0	32	32	64	128	16
<i>Bacillus abortus</i>	F-30	0	0	>8192	>8192	0
	F-15	0	0	>8192	4096	0
	R+0	0	0	>8192	4096	0
<i>Candida albicans</i>	F-30	32	8	16	8	16
	F-15	32	8	8	8	32
	R+0	32	8	0	8	16

<sup>a</sup> Values given are reciprocal of titer. Zero denotes titer of less than 1/8.

*Bacillus abortus* antigen were likewise reacted against crew serum. The resulting data, expressed as the reciprocal of the highest serum dilution (titer) sustaining a reaction, are presented in table 15-VII. These data illustrate only two significant postflight changes. With *S. aureus*, the titer in the serum of the ACDR was reduced from 1/64 to 1/8 on the day of return from flight (R+0). Likewise, the titer of anti-*E. coli* antibody in the serum of the SFE was reduced from greater than 1/8192 to 1/1024 postflight. Because these were unusual isolated incidences and because all other titers remained essentially unchanged, it must be concluded that this space flight did not effect a demonstrable change in the presence of species-specific antibody.

The results of lysozyme measurements are shown in table 15-VIII. In addition to the considerable variation among individuals, there was a

TABLE 15-VIII.—Levels of Lysozyme in Blood of Prime Crewmembers

Crewmember	Lysozyme level, $\mu\text{g}/\text{cm}^3$		
	F-30	F-15	R+0
ACDR	13.0	13.0	14.5
DMP	10.0	10.0	10.0
CMP	15.0	15.0	15.2
SCDR	12.5	12.5	12.5
SFE	7.4	7.4	10.0

general trend for lysozyme levels to be elevated the day of return from space flight. However, the magnitude of the change was erratic and could not be correlated with the actual space flight. Therefore, these data alone cannot be used as evidence that blood lysozyme levels are affected by space flight.

## REFERENCES

- 15-1. Alekseyeva, O. G.: Some Natural Immunity Factors and Cosmonaut Auto flora During the Training Period and Following the Flights of "Vostok," "Vostok 2," "Vostok 3," and "Vostok 4." *Problemy Kosmicheskoi Biologii* (Problems in Space Biology), Vol. IV. U.S.S.R. Academy of Sciences Publishing House (Moscow), 1964, pp. 278-289.
- 15-2. Nefedov, Yu. G.; Shilov, V. M.; Konstantinova, I. V.; and Zaloguyev, S. N.: Microbiological and Immunological Aspects of Extended Manned Space Flights. *Life Sciences and Space Research*, IX, COSPAR, Akademie-Verlag (Berlin), May 1971, pp. 11-16.
- 15-3. Alekseyeva, O. G.; and Volkova, A. P.: Influence of Space Flight Factors on the Bactericidal Activity of the Body. *Problemy Kosmicheskoi Biologii* (Problems in Space Biology), Vol. I. U.S.S.R. Academy of Sciences Publishing House (Moscow), 1962, pp. 201-209.
- 15-4. Wheeler, H. O.; Kemmerer, W. W.; Dietlein, L. F.; and Berry, C. A.: Effects of Space Flight Upon Indigenous Microflora of Gemini Crew Members. *Bacteriological Proceedings*, 1967, p. 16.
- 15-5. Berry, Charles A.: Preliminary Clinical Report of the Medical Aspects of Apollo 7 and 8. NASA TM X-58027, 1969.
- 15-6. Vargosko, Andrew J.; Gordon, Francis B.; and Wilkins, Judd R.: Microbiological Studies on Man in Closed Environmental Systems. App. B of Infectious Disease in Manned Spaceflight. National Academy of Sciences (Washington, D.C.), 1970, pp. 137-211.
- 15-7. Taylor, Gerald R.: Apollo 14 Microbial Analysis. NASA TM X-58094, 1972.
- 15-8. Taylor, Gerald R.; Henney, Mary R.; and Ellis, Walter L.: Changes in the Fungal Auto flora of Apollo Astronauts. *Appl. Microbiol.*, vol. 26, no. 5, Nov. 1973, pp. 804-813.
- 15-9. Brown, Lee R.; Frome, William J.; et al.: Skylab Oral Health Studies. The Proceedings of the Skylab Life Sciences Symposium. NASA TM X-58154, 1974, pp. 75-97.
- 15-10. Brockett, R. M.; Ferguson, J. K.; et al.: Skylab Environmental and Crew Microbiology Studies. The Proceedings of the Skylab Life Sciences Symposium. NASA TM X-58154, 1974, pp. 121-143.
- 15-11. Lebedev, K. A.; and Petrov, R. V.: Immunological Problems of Closed Environments and Gnotobiology. *Uspekhi Sovremennoy Biologii*, vol. 71, no. 2, 1971, pp. 235-252. (Translation available from Joint Publications Research Service, Washington, D.C.)
- 15-12. Luckey, T. D.: Potential Microbic Shock in Manned Aerospace Systems. *Aerospace Med.*, vol. 37, no. 12, Dec. 1966, pp. 1223-1228.

- 15-13. Dobronravova, N. M.; Kortayev, M. M.; et al.: Variation in Overall Body Tolerance During a 62-Day Exposure to Hypokinesia and Acceleration. *Space Biol. & Med.*, vol. 1, no. 6, Mar. 1968, pp. 101-108. (Primary source - *Kosmicheskaya Biologiya i Meditsina*, vol. 1, 1967, pp. 66-70. (In Russian.))
- 15-14. Spizizen, J.: Microbiological Problems of Manned Space Flight. *Life Sciences and Space Research*, IX, COSPAR, Akademie-Verlag (Berlin), May 1971, pp. 65-68.
- 15-15. Fox, Leo: The Ecology of Microorganisms in a Closed Environment. *Life Sciences and Space Research*, IX, COSPAR, Akademie-Verlag (Berlin), May 1971, pp. 69-74.
- 15-16. Taylor, G. R.; and Zaloguyev, S. N.: Medical Microbial Analysis of Apollo-Soyuz Test Project Crewmembers. NASA TM X-58180, 1976.
- 15-17. Taylor, G. R.; and Zaloguyev, S. N.: Methods for Microbiological and Immunological Studies of Space Flight Crews. NASA TM X-58185. (To be published.)
- 15-18. Berry, Charles A.: Summary of Medical Experiences in the Apollo 7 Through 11 Manned Spaceflights. *Aerospace Med.*, vol. 41, no. 5, May 1970, pp. 500-519.
- 15-19. Taylor, Gerald R.: Recovery of Medically Important Microorganisms From Apollo Astronauts. *Aerospace Med.*, vol. 45, no. 8, Aug. 1974, pp. 824-828.
- 15-20. Wooley, Bennie C.: Apollo Experience Report - Protection of Life and Health. NASA TN D-6856, 1972.
- 15-21. Taylor, G. R.: Space Microbiology. *Ann. Rev. Microbiol.*, vol. 40, 1974, pp. 23-40.
- 15-22. Shilov, V. M.; Lizko, N. N.; Borisova, O. K.; and Prokhorov, V. Ya.: Changes in the Microflora of Man During Long-Term Confinement. *Life Sciences and Space Research*, IX, COSPAR, Akademie-Verlag (Berlin), May 1971, pp. 43-49.
- 15-23. Ferguson, James K.; Taylor, Gerald R.; and Mieszkuc, Bernard J.: Microbial Investigations. Biomedical Results of Apollo. NASA SP-368, 1975, pp. 83-103.
- 15-24. Zaloguyev, S. N.; Shinkareva, N. M.; and Utkina, T. G.: State of the Automicroflora of Skin Tissues and Certain Natural Immunity Indices in the Astronauts A. G. Nikolaev and V. I. Sevastianov Before and After Flight. *Kosmicheskaya Biologiya i Meditsina*, vol. 4, no. 6, 1970, pp. 54-59. (Translation available from Joint Publications Research Service, Washington, D.C.)
- 15-25. Zaloguyev, S. N.; Utkina, T. G.; and Shinkareva, N. M.: The Microflora of the Human Integument During Prolonged Confinement. *Life Sciences and Space Research*, IX, COSPAR, Akademie-Verlag (Berlin), May 1971, pp. 55-59.
- 15-26. Chukhlov, B. A.; Ostrovnikov, P. B.; and Ivanova, S. P.: Development of Staphylococcal Infections in Human Subjects Under the Influence of Some Spaceflight Factors. *Space Biol. & Med.*, vol. 5, no. 6, 1971, pp. 91-98. (Primary source - *Kosmicheskaya Biologiya i Meditsina*, vol. 5, 1971, pp. 61-65. (In Russian.))
- 15-27. Ginsberg, H. S.: Immune States in Long-Term Space Flights. *Life Sciences and Space Research*, IX, COSPAR, Akademie-Verlag (Berlin), May 1971, pp. 1-9.
- 15-28. Giron, David J.; Pindak, Frank F.; and Schmidt, Jerome P.: Effect of a Space-Cabin Environment on Viral Infection. *Aerospace Med.*, vol. 38, no. 8, Aug. 1967, pp. 832-834.
- 15-29. Schmidt, Jerome P.; Cordaro, Joseph T.; and Ball, Robert J.: Effect of Environment on Staphylococcal Lesions in Mice. *Appl. Microbiol.*, vol. 15, no. 6, Nov. 1967, pp. 1465-1467.
- 15-30. Coyne, Robert V.; and Ackerman, G. Adolph: Effects of a Space-Cabin Atmosphere on the Immune Response: I. Depression in Spleen Weights and Antibody Titers. *Aerospace Med.*, vol. 40, no. 11, Nov. 1969, pp. 1219-1223.
- 15-31. Mikhaylovskiy, G. P.; Dobronravova, N. N., et al.: Variations in Overall Body Tolerance During a 62-Day Exposure to Hypokinesia and Acceleration. *Space Biol. & Med.*, vol. 1, no. 6, 1968, pp. 101-108. (Primary source - *Kosmicheskaya Biologiya i Meditsina*, vol. 1, no. 6, 1967, pp. 66-70. (In Russian.))
- 15-32. Ritzmann, S. E.; and Levin, W. C.: Investigation of Man's Immune System. Skylab Medical Experiments Altitude Test, NASA TM X-58115, 1973, pp. 6-9 to 6-14.



# 16. Cellular Immune Response

## Experiment MA-031

*B. Sue Criswell<sup>a†</sup> and Kathy Cobb<sup>a</sup>*

### ABSTRACT

Significant changes in the responsiveness of peripheral blood lymphocytes to phytohemagglutinin (PHA) occurred in the cellular immune response of three crewmembers during the 9-day flight of the Apollo-Soyuz Test Project. Parameters studied were white blood cell concentrations, lymphocyte numbers, B- and T-lymphocyte distributions in peripheral blood, and lymphocyte responsiveness to PHA, pokeweed mitogen, Concanavalin A, and influenza virus antigen.

### INTRODUCTION

The health status of crewmembers before space flight has been a prime concern of NASA throughout the Apollo series of lunar landings and the Apollo-Soyuz Test Project (ASTP). The crews were selected long before the mission and were carefully monitored to determine their immunological responsiveness before flight. The humoral immune response was studied, and serum immunoglobulins (G, A, and M), C-3 complement component, and other serum proteins were quantitated (ref. 16-1). Significant elevations in IgA following space flight were reported. The cellular immune response was studied in 21 Apollo crewmembers for Apollo missions 7 to 13.

Lymphocyte reactivity to phytohemagglutinin (PHA) (nonspecific mitogen) challenge only was reported by Fischer et al. (ref. 16-2). No significant change in lymphocytic responsiveness was reported. In comparison, in Skylab 3 and 4 studies, the functional capacity of the lymphocytes (again PHA responsiveness only) was depressed (ref. 16-3), and a suppression in the T-lymphocyte numbers was noted in this laboratory.

The cellular immune response of the three ASTP crewmembers was studied before and after the 9 days of flight. The findings are compared with lymphocytic changes that were noted during the Skylab mission. Briefly, as previously stated, the functional capacity of lymphocytes at splashdown of Skylab 3 and 4 was depressed along with a suppression in the T-lymphocyte numbers. In the ASTP study, which involved a shorter flight, functional suppression was again noted but no quantitative changes in lymphocytes occurred.

### METHODS AND MATERIALS

Samples of heparinized peripheral venous blood (10 cm<sup>3</sup>) were obtained from the three ASTP crewmembers and compared with similar samples from the three Skylab 4 crewmembers. In Skylab, no cultural studies were performed by this laboratory. All samples were processed within 1 to 24 hours after collection. Before separation, total leukocyte (white blood cell (WBC)) counts were performed using a hemacytometer and/or a Coulter counter, and differential counts were determined using slide preparations stained with Wright's stain.

---

<sup>a</sup>Baylor College of Medicine.

<sup>†</sup>Principal Investigator.

### **Lymphocyte Preparation**

Lymphocytes were also separated by Ficoll-Hypaque gradient centrifugation according to Böyum's method (ref. 16-4) or by using a Technicon lymphocyte separator. Cells in the resulting suspension of mononuclear cells were washed three times in minimum essential medium (MEM); they were then adjusted to a final concentration of  $1 \times 10^6$  cells/ml.

### **Lymphocyte Classification**

The B-lymphocyte distributions were determined by enumerating the percent of 200 mononuclear cells with surface immunoglobulins detected by the immunofluorescent antibody technique described in reference 16-5.

The E-rosette-forming lymphocytes (T-cells) were determined by the method of Jondahl et al. (ref. 16-6). A concentration of  $1 \times 10^6$  lymphocytes was mixed in 0.25 ml of MEM and added to 0.25 ml of a 0.5-percent sheep red blood cell (SRBC) suspension. After mixing, the tubes were incubated at 310 K (37° C) for 5 minutes, centrifuged at 500g for 3 minutes, and incubated in ice water for 2 hours. Approximately half the supernatant was removed, and the top layer of cells was gently resuspended; 200 lymphocytes were counted with 3 or more adhering SRBC's used as criteria for E-rosetted lymphocyte.

### **Lymphocyte Responsiveness in Microculture to PHA, PWM, and Con A**

Purified lymphocytes ( $1 \times 10^5$  cells) in MEM containing 40-percent fetal calf serum (FCS) were placed in culture plates, and the antigens were diluted in MEM (containing Pen-Strep and L-glutamine) in the following concentrations: 0.01 ml PHA/ml MEM; 0.01 and 0.05 ml pokeweed mitogen (PWM)/ml MEM; and 25 and 50  $\mu$ g Concanavalin A (Con A)/ml MEM. The diluted antigens in 0.1-ml aliquots (in duplicate) were placed in the appropriate well. The cultures were incu-

bated in a humidified carbon dioxide atmosphere at 310 K (37° C) for 3 days for PHA and 5 days for Con A and PWM. On the day of harvest, samples were treated as described in the following section on the influenza virus antigen cultures.

### **Lymphocyte Responsiveness to Influenza Virus Antigen by Thymidine Incorporation**

An inactivated monovalent type A influenza virus vaccine containing 1600 chick cell agglutinating units/ml of a Hong Kong strain ( $H_3N_2$ ) was dialyzed against phosphate-buffered saline (PBS) and stored at 203 K (-70° C) until used for tests. Separated lymphocytes were added in 0.1-ml aliquots (in duplicate) for each dilution of influenza antigen, and the cultures were incubated in a humidified carbon dioxide incubator at 310 K (37° C) for periods of either 2 or 3 days. On the day of harvest, the cells were pulsed for 2 hours with 37 billion disintegrations/sec (1  $\mu$ Ci) methyl  $^3$ H-thymidine and then harvested with an automated harvester onto glass-fiber filter strips; they were then counted in a liquid scintillation counter. Data were expressed as counts per minute (CPM)/ $1 \times 10^6$  lymphocytes, and the stimulation index (SI) was calculated by dividing the mean result for stimulated cultures by that for the unstimulated cultures. Allantoic fluid was used separately as a control on the reactivity of each individual crewmember to chick embryo proteins.

## **RESULTS**

### **White Blood Cell Quantitation**

For the ASTP and the Skylab 4 crewmembers, table 16-I shows the mean and 1 standard deviation of the WBC count and the lymphocyte count for respective days preflight and postflight. Normal laboratory values are given for comparison. In the ASTP crew, significant increases in WBC numbers were noted on R+0 (day of splashdown) and R+1, which represented polymorphonuclear leukocyte increases. Individual variation in WBC



TABLE 16-I.—Preflight and Postflight Leukocytic Response of ASTP and Skylab 4 Crewmembers

Sample day (a)	WBC/mm <sup>3</sup> , mean $\pm$ 1 SD <sup>b</sup>	Lymphocyte count/mm <sup>3</sup> , mean $\pm$ 1 SD
ASTP		
F-30	6 640 $\pm$ 1830	2820 $\pm$ 480
F-15	5 830 $\pm$ 2020	2420 $\pm$ 440
F-5	6 530 $\pm$ 560	3040 $\pm$ 550
R+0	11 110 $\pm$ 4210	1950 $\pm$ 490
R+1	13 530 $\pm$ 610	3020 $\pm$ 810
R+8	9 560 $\pm$ 2580	3500 $\pm$ 900
R+13	6 600 $\pm$ 1510	2270 $\pm$ 400
Normal laboratory value	7 110 $\pm$ 2400	3000 $\pm$ 1200
Skylab 4		
F-30	6013 $\pm$ 254	1940 $\pm$ 670
F-15	5243 $\pm$ 699	1820 $\pm$ 213
F-7	5903 $\pm$ 1517	2023 $\pm$ 699
F-1	5206 $\pm$ 645	1987 $\pm$ 206
R+0	8980 $\pm$ 5560	1177 $\pm$ 381
R+1	6230 $\pm$ 1265	2757 $\pm$ 349
R+3	7370 $\pm$ 1528	2280 $\pm$ 479
R+7	5977 $\pm$ 1498	2320 $\pm$ 585
R+14	4840 $\pm$ 881	1827 $\pm$ 118

<sup>a</sup>F-30 is 30 days before lift-off, R+0 is recovery (splashdown) day, R+1 is recovery plus 1 day, etc.

<sup>b</sup>SD = standard deviation.

values (a range of 3300 to 14 410) was noted among the three Skylab 4 crewmembers at R+0, which is reflected in the large standard deviation in table 16-I. However, all values were within clinically normal ranges. Less variation was noted for total lymphocyte values, as reflected by the mean and standard deviation shown in table 16-I. All values at R+0 were decreased below their previous baseline values.

The results of the T-lymphocytes, B-lymphocytes, and nonreactive lymphocytes of ASTP crewmembers are given in table 16-II. Fluctuations are indicated, but values remain within the 1 standard deviation for normal laboratory values. In contrast, highly significant changes were noted in B and T cell distributions of the Skylab 4 crewmen (fig. 16-1).

#### Lymphocyte Responsiveness in Culture to PHA, PWM, and Con A

Cultural studies were performed on samples from the ASTP mission only. The culture findings for the nonspecific mitogens are shown in table 16-III. The stimulation indexes for PHA dropped at R+0 and at R+1 for all three crewmembers. By R+8, the three crewmembers were back within normal ranges. Interestingly, a reverse situation is indicated for the Apollo commander (ACDR) at R+0 with Con A stimulation enhanced. Other crewmembers began and remained at low-level ranges for Con A throughout the preflight and postflight periods. Considerable individual variation was noted in the PWM data and no consistent trend was obtained.

TABLE 16-II.—Results of the T-Lymphocytes, B-Lymphocytes, and Nonreactive Lymphocytes

Sample day	T-lymphocytes, $1 \times 10^5/\text{ml}$ (mean $\pm$ 1 SD)	B-lymphocytes, $1 \times 10^5/\text{ml}$ (mean $\pm$ 1 SD)	Nonreactive lymphocytes, $1 \times 10^5/\text{ml}$ (mean $\pm$ 1 SD)
F-30	16.5 $\pm$ 6.1	7.1 $\pm$ 0.4	4.7 $\pm$ 2.1
F-15	12.9 $\pm$ 4.9	4.7 $\pm$ 0.2	6.7 $\pm$ 0.5
F-5	17.9 $\pm$ 2.8	5.4 $\pm$ 0.9	7.1 $\pm$ 3.7
R+0	13.0 $\pm$ 5.6	5.3 $\pm$ 1.2	1.2 $\pm$ 1.2
R+1	19.1 $\pm$ 3.8	7.0 $\pm$ 3.5	4.2 $\pm$ 1.8
R+8	25.3 $\pm$ 4.4	5.8 $\pm$ 1.9	3.9 $\pm$ 3.6
R+13	14.4 $\pm$ 3.2	5.6 $\pm$ 1.2	2.6 $\pm$ 1.0
Normal laboratory value	15.9 $\pm$ 6.3	5.1 $\pm$ 3.0	8.5 $\pm$ 5.6

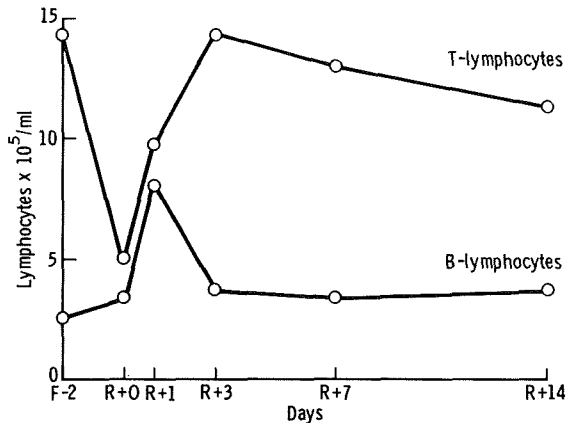


FIGURE 16-1.—Mean Skylab 4 B- and T-lymphocyte responses preflight and postflight.

### Influenza Virus Antigen Stimulation

One of the three ASTP crewmembers responded to influenza virus Hong Kong strain antigen in cultures. All three astronauts responded to influenza virus England strain preflight. Because these antigens are quite variable in response patterns even in known and diagnosed influenza illnesses, changes or losses in reactivity are not completely understood. Total lack of reactivity may reflect influenza susceptibility.

### DISCUSSION

Significant changes were found for all three ASTP crewmembers in the responsiveness of the lymphocytes to PHA. No significant quantitative changes were noted among the lymphocytic population. Variations were noted in the stimulation indexes of the subjects for Con A and PWM; however, because of the rapid exchange of cells between different compartments in the body, variation in the indexes may be expected. Again, an overall suppression at R+0 was found.

The ASTP crewmembers experienced contact with toxic gases upon splashdown. The exposure was severe enough to create concern for lung inflammation; this concern resulted in corticosteroid treatment on R+1. Samples were collected on R+0 before the administration of the steroid. Consequently, it is likely that the increased immunosuppressions noted by cultural responses on R+1 for all mitogens and on R+8 for Con A were attributable to the steroid therapy. Most cortisone preparations are known to affect the lymphocytic reaction. The depressions observed at R+0 were due to either space flight or possibly the toxic gas exposure a few hours before the analysis. No data are available on the effects of toxic gases on lymphocytic responses. Similar depressions in lymphocytic responsiveness were observed in Skylab 3 and 4 data; both of these missions were of much longer duration than ASTP

TABLE 16-III.—*Lymphocytic Response to PHA, PWM, and Con A*

Sample day	Subject (a)	Stimulation indexes		
		PHA	Con A	PWM
F-30	ACDR	34	3	5
	CMP	34	26	50
	DMP	41	16	114
	Mean of three	36 $\pm$ 4	15 $\pm$ 12	56 $\pm$ 55
F-15	ACDR	65	25	43
	CMP	47	11	14
	DMP	95	12	41
	Mean of three	69 $\pm$ 24	16 $\pm$ 8	33 $\pm$ 16
F-5	ACDR	66	12	27
	CMP	46	32	29
	DMP	74	6	34
	Mean of three	63 $\pm$ 15	17 $\pm$ 14	30 $\pm$ 4
R+0	ACDR	38	151	100
	CMP	11	11	24
	DMP	12	12	11
	Mean of three	20 $\pm$ 15	58 $\pm$ 80	45 $\pm$ 48
R+1	ACDR	9	20	40
	CMP	21	49	11
	DMP	5	6	4
	Mean of three	12 $\pm$ 8	25 $\pm$ 22	25 $\pm$ 15
R+8	ACDR	72	12	11
	CMP	45	18	11
	DMP	18	8	9
	Mean of three	45 $\pm$ 27	13 $\pm$ 5	10 $\pm$ 1
Normal laboratory value	Mean	69	67	50
	Range	10 to 282	10 to 277	10 to 170

<sup>a</sup>ACDR, CMP, and DMP indicate Apollo commander, command module pilot, and docking module pilot, respectively.

(ref. 16-3). However, in more comparable missions of similar lengths (the Apollo series) no changes in lymphocytic responsiveness were reported (ref. 16-2).

The ASTP crewmembers showed no change in the quantity of B- or T-lymphocytes present in the peripheral blood. In contrast, the Skylab 4 crewmembers showed significant change. The principal difference between the two missions appeared to be due to the length of time in space. Various disease states have been shown to exhibit proportional as well as quantitative changes in these cells. Although the crewmembers appeared to have no overt disease processes upon return, they did appear to experience a similar stress

phenomenon on the body to create the depression observed in lymphocytes. Because no in-flight blood samples were analyzed for lymphocytic responsiveness, it is not known if the suppression begins immediately after a 9-day stay in space or is a result of splashdown stresses. For Skylab 3, Leach et al. (ref. 16-7) reported increased in-flight urinary cortisol levels compared with baseline values. The greatest increase was immediately upon launch; however, values remained increased throughout the flight. Because cortisol, in high doses, is known to control the immune response, the depressions in lymphocytic responsiveness in this instance may be related to *in vivo* cortisol control.

## REFERENCES

- 16-1. Fischer, C. L.; Gill, C.; et al.: Effects of the Space Flight Environment on Man's Immune System: I. Serum Proteins and Immunoglobulins. *Aerospace Med.*, vol. 43, no. 8, Aug. 1972, pp. 856-859.
- 16-2. Fischer, C. L.; Daniels, J. C.; et al.: Effects of the Space Flight Environment on Man's Immune System: II. Lymphocyte Counts and Reactivity. *Aerospace Med.*, vol. 43, no. 10, Oct. 1972, pp. 1122-1125.
- 16-3. Kimzey, S. L.; Johnson, P. C.; Ritzmann, S. E.; and Mengel, C. E.: Hematology and Immunology Studies: The Second Manned Skylab Mission. *Aviat. Space and Environ. Med.*, vol. 47, no. 4, Apr. 1976, pp. 383-390.
- 16-4. Böyum, A.: Separation of Leukocytes From Blood and Bone Marrow. *Scand. J. Clin. Lab. Invest.*, vol. 21, suppl. 97, 1968, p. 7.
- 16-5. DeFazio, Sally R.; Criswell, B. Sue; et al.: A Paraprotein in Severe Combined Immunodeficiency Disease Detected by Immuno-electrophoretic Analyses of Plasma. *J. Clin. Exp. Immunol.*, vol. 19, no. 3, 1975, pp. 563-570.
- 16-6. Jondahl, M.; Holm, G.; and Wigzell, H.: Surface Markers on Human T and B Lymphocytes. 1. A Large Population of Lymphocytes Forming Nonimmune Rosettes With Sheep Red Blood Cells. *J. Exp. Med.*, vol. 136, no. 2, Aug. 1, 1972, pp. 207-215.
- 16-7. Leach, C. S.; Johnson, P. C.; and Rambaut, P. C.: Metabolic and Endocrine Studies: The Second Manned Skylab Mission. *Aviat. Space and Environ. Med.*, vol. 47, no. 4, Apr. 1976, pp. 402-410.

# 17. Polymorphonuclear Leukocyte Response

## Experiment MA-032

R. Russell Martin,<sup>a†</sup> Glenn A. Warr,<sup>a</sup> Margaret J. Putman,<sup>a</sup> Diane H. Kentor,<sup>a</sup> and Carolinda L. Holleman<sup>a</sup>

### ABSTRACT

Serial blood samples were obtained from the three crewmembers of the Apollo-Soyuz Test Project and from eight normal control subjects over an interval beginning 30 days before flight and ending 30 days after termination of the space flight. A laboratory was established onboard the recovery ship U.S.S. *New Orleans* (LPH-11) to perform tests on leukocytes from blood samples obtained immediately after recovery and on the following day. Inhalation of propellant gases by the crewmembers and the inception of corticosteroid therapy on the day following recovery provided an opportunity to investigate the possible effects of these factors on leukocyte function. The tests performed included total leukocyte count, differential count, measurement of leukocyte adhesion, evaluation of leukocyte migration and chemotaxis, assessment of phagocytic ability, and testing for cytoplasmic granules that stained for leukocyte acid and alkaline phosphatase. Together, these observations present a variety of *in vitro* studies that correlate with the function of polymorphonuclear leukocytes within the body.

### INTRODUCTION

Various physiological, hematological, and serological measurements have been obtained

from crewmembers throughout the manned space flight program. Erythrocytes and lymphocytes have been intensively studied, but considerably less information has been obtained concerning the possible effects of space flight and weightlessness on polymorphonuclear leukocyte (PMN) function. Because these phagocytic cells are important in the defense of the body against infection and because an increasing number of clinical conditions have been recognized in which decreased PMN function is associated with increased susceptibility to infection, a variety of experiments were designed to test PMN function *in vitro* in relation to the events of the Apollo-Soyuz Test Project (ASTP). The goal of this experiment was to attempt to identify any measurable PMN alterations that might have a significant effect on planning future space missions of longer duration.

The experiment proceeded basically as planned, and all desired blood samples were obtained during the baseline, postflight, and later convalescent periods. The unplanned inhalation of propellant gases by the crewmembers during reentry and their subsequent hospitalization with the administration of adrenal corticosteroid therapy provided an opportunity to evaluate these factors in relation to leukocyte function (refs. 17-1 to 17-3).

The results of this experiment successfully documented that no consistent abnormality in PMN function (detectable by the *in vitro* methods used) occurred in the ASTP crewmembers as a result of the 9-day space flight. The experimental design was limited by the inability to test blood samples during the space flight. A broader experience, including studies performed on specimens obtained during weightlessness, will be required before final conclusions can be drawn.

<sup>a</sup>Baylor College of Medicine.

<sup>†</sup>Principal Investigator.

## MATERIALS AND METHODS

The *in vitro* techniques used in the present experiment have been adapted from methods developed in this laboratory and in use among investigators of leukocyte function in other laboratories. The tests were first standardized using leukocytes obtained from a variety of normal control subjects. Control subjects for the experiment itself included the three members of the backup flightcrew and four volunteers from among the investigators conducting experiments onboard the U.S.S. *New Orleans*. Because it was not possible to obtain blood samples from the control subjects and from the crewmembers at exactly the same time, one control subject donated two separate blood samples (one with the other controls in the morning, and the other with the crewmembers in the afternoon). The similar results obtained with both specimens from the same individual indicated that all test systems were working properly for both groups of specimens. One additional control subject was not onboard the recovery ship but was available to serve as a control during the hospitalization of the crewmembers in Honolulu, Hawaii, 8 days after recovery.

After the blood was drawn, a portion was promptly added to sedimentation fluid containing dextran to sediment the erythrocytes. Leukocytes for phagocytosis and chemotaxis experiments were harvested from the leukocyte-rich plasma layer following sedimentation at room temperature for 45 to 60 minutes. A portion of the blood was anticoagulated with heparin at a concentration of 10 units/ml. This specimen was used to prepare slides for histochemical staining for acid phosphatase and alkaline phosphatase as well as for differential leukocyte counts (ref. 17-4). This blood specimen was also used in tests of leukocyte adhesion, using columns containing 50 mg of nylon fiber packed into a tuberculin syringe, with equilibration at 310 K (37° C) (ref. 17-5). Chemotaxis experiments were performed using a variation of the Boyden chamber technique developed in this laboratory (ref. 17-6). Similarly, phagocytosis studies were conducted using Lab-

tek tissue culture slides and previously described techniques (ref. 17-7). Total white blood cell counts were performed on duplicate specimens using a Coulter counter.

## RESULTS

All blood samples were obtained from the Apollo commander (ACDR), command module pilot (CMP), and the docking module pilot (DMP) during the interval from 30 days before flight (F-30) to 30 days after recovery (R+30). The backup crewmembers were studied during the preflight period and served as a normal control group for this interval. Four other subjects (A, B, C, and D) were studied both in preflight testing and during the testing onboard the recovery ship. One additional subject (E) had served as an earlier control in the preflight period and was available in Honolulu to serve as a control during the hospitalization of the crewmembers beginning on day R+8.

The total white blood cell counts were reasonably stable and reproducible for each subject (table 17-I). Preflight values for the DMP were low, particularly on day F-5. Elevated leukocyte counts were noted for all three crewmembers for 2 days after recovery as well as on day R+8 (when corticosteroid administration was also a factor).

The differential leukocyte counts for the study group are presented in table 17-II. The values in tables 17-I and 17-II were used to calculate the total PMN counts presented in table 17-III. The total PMN counts were very reproducible within the same individual subjects studied serially. The low total PMN counts from the DMP on day F-5 indicates that the decrease in total leukocytes on that day was accompanied by a proportional decrease in the PMN's.

The leukocyte alkaline phosphatase is a histochemical test that generally correlates with the amount of PMN activation. The number of positive cells for this enzyme generally paralleled the total number of PMN's (table 17-IV(a)). A weighted value can be assigned to positive leukocytes by grading the reaction of individual

TABLE 17-I.—Total Leukocyte Counts

[Cells/mm<sup>3</sup> of blood]

Subject	Day of observation						
	Before flight			After recovery			
	F-30	F-15	F-5	R+0	R+1	R+8	R+30
ACDR	8512	5567	9605	7 192	11 427	7 200	7076
CMP	6005	6375	4913	13 448	14 395	10 000	5304
DMP	5157	4324	3631	7 036	11 582	9 800	4127
A	7495	5139	5453	6 880	7 673	--	--
B	6757	8210	7429	5 329	6 344	--	--
C	7967	6306	5209	4 502	5 390	--	--
D	--	5364	<sup>a</sup> 6991 <sup>b</sup> 7397	<sup>a</sup> 7 259 <sup>b</sup> 7 479	7 074	--	<sup>a</sup> 6012 <sup>b</sup> 6384
E	6549	--	--	--	--	5 500	--
ACDR <sup>c</sup>	7736	5209	6009	--	--	--	--
CMP <sup>c</sup>	8679	8613	7516	--	--	--	--
DMP <sup>c</sup>	6043	7298	4592	--	--	--	--

<sup>a</sup>Morning sample.<sup>b</sup>Afternoon sample.<sup>c</sup>Backup crewmember.

TABLE 17-II.—Differential Leukocyte Counts

[Expressed as percent]

Subject	Cell type	Day of observation						
		Before flight			After recovery			
		F-30	F-15	F-5	R+0	R+1	R+8	R+30
ACDR	Lymphocyte	51	40	55	23	25	27	46
	Neutrophil	46	57	42	74	73	64	46
	Eosinophil	2	1	1	1	1	6	3
	Basophil	0	1	1	0	1	0	1
	Monocyte	1	1	1	2	0	3	4
CMP	Lymphocyte	40	56	51	12	19	39	43
	Neutrophil	55	38	46	86	77	53	52
	Eosinophil	3	2	0	0	2	3	3
	Basophil	0	0	0	0	0	0	1
	Monocyte	2	4	3	2	2	5	1
DMP	Lymphocyte	56	60	68	14	17	42	42
	Neutrophil	38	36	29	79	80	52	52
	Eosinophil	3	2	1	0	0	2	3
	Basophil	1	1	0	0	0	0	0
	Monocyte	2	1	2	7	3	4	3
A	Lymphocyte	65	32	53	66	54	--	--
	Neutrophil	24	51	34	23	38	--	--
	Eosinophil	8	13	10	3	3	--	--
	Basophil	1	1	0	1	3	--	--
	Monocyte	2	3	3	7	2	--	--

TABLE 17-II.—Concluded

Subject	Cell type	Day of observation						
		Before flight			After recovery			
		F-30	F-15	F-5	R+0	R+1	R+8	R+30
B	Lymphocyte	45	38	42	45	41	--	--
	Neutrophil	49	58	51	51	52	--	--
	Eosinophil	3	2	2	0	2	--	--
	Basophil	2	0	0	0	1	--	--
	Monocyte	1	2	5	4	4	--	--
C	Lymphocyte	39	30	31	52	47	--	--
	Neutrophil	58	65	61	41	48	--	--
	Eosinophil	2	3	5	5	3	--	--
	Basophil	0	1	2	0	0	--	--
	Monocyte	1	1	1	2	2	--	--
D	Lymphocyte	--	38	50/48	41/42	38	--	47
	Neutrophil	--	59	46/49	50/54	56	--	48
	Eosinophil	--	0	0/1	4/2	2	--	2
	Basophil	--	0	0/0	0/0	1	--	0
	Monocyte	--	3	4/2	5/2	3	--	3
E	Lymphocyte	33	--	--	--	--	38	--
	Neutrophil	63	--	--	--	--	56	--
	Eosinophil	2	--	--	--	--	2	--
	Basophil	0	--	--	--	--	0	--
	Monocyte	2	--	--	--	--	4	--
ACDR <sup>a</sup>	Lymphocyte	46	41	54	--	--	--	--
	Neutrophil	45	53	42	--	--	--	--
	Eosinophil	2	4	1	--	--	--	--
	Basophil	2	0	1	--	--	--	--
	Monocyte	5	2	2	--	--	--	--
CMP <sup>a</sup>	Lymphocyte	44	36	42	--	--	--	--
	Neutrophil	51	61	55	--	--	--	--
	Eosinophil	1	0	1	--	--	--	--
	Basophil	1	1	0	--	--	--	--
	Monocyte	3	2	2	--	--	--	--
DMP <sup>a</sup>	Lymphocyte	49	52	50	--	--	--	--
	Neutrophil	46	43	45	--	--	--	--
	Eosinophil	1	1	0	--	--	--	--
	Basophil	2	0	0	--	--	--	--
	Monocyte	2	4	5	--	--	--	--

<sup>a</sup>Backup crewmember.

cells from 0 to 4+. A number of cells of each degree of reactivity are multiplied by the activity score and the total value for 100 representative cells is calculated. When this was done, the crewmembers were noted to have somewhat ele-

vated values during both the preflight and postflight periods (table 17-IV(b)). This higher value was also noted in the values obtained from the CMP of the backup crew. A further weighted value can be calculated by determining the mean



TABLE 17-III.—Total PMN Counts

[Cells/mm<sup>3</sup> of blood]

Subject	Day of observation						
	Before flight			After recovery			
	F-30	F-15	F-5	R+0	R+1	R+8	R+30
ACDR	3916	3173	4034	5 322	8 342	4608	3255
CMP	3303	2423	2260	11 565	11 084	5300	2758
DMP	1960	1557	1053	5 558	9 266	5096	2146
A	1799	2621	1854	1 582	2 916	--	--
B	3311	4762	3789	2 718	3 299	--	--
C	4621	4099	3177	1 846	2 587	--	--
D	--	3165	<sup>a</sup> 3215 <sup>b</sup> 3625	<sup>a</sup> 3 360 <sup>b</sup> 4 039	3 961	--	<sup>a</sup> 3487 <sup>b</sup> 3064
E	4126	--	--	--	--	3080	--
ACDR <sup>c</sup>	3481	2761	2524	--	--	--	--
CMP <sup>c</sup>	4426	5254	4134	--	--	--	--
DMP <sup>c</sup>	2780	3138	2066	--	--	--	--

<sup>a</sup> Morning sample.<sup>b</sup> Afternoon sample.<sup>c</sup> Backup crewmember.

staining intensity of those leukocytes that are positive (table 17-IV(c)). Again, the crewmembers tended to have somewhat higher values than the normal controls, although these values are not statistically significant.

The total number of PMN's staining for the lysosomal enzyme acid phosphatase was similarly determined (table 17-V(a)). The DMP again had low values during the preflight period, with a decrease to 990 positive cells on day F-5. All crewmembers had an elevation in the number of cells staining for acid phosphatase during the immediate postflight interval. The total acid phosphatase scores (table 17-V(b)) and the mean acid phosphatase scores (table 17-V(c)) were not significantly different from the values determined in concurrent controls.

In tests of leukocyte adhesion, samples of heparinized blood were passed through nylon columns and the percentage of leukocytes adhering to the columns was calculated (table 17-VI). This test is usually reproducible if repeated for the same individual, but it is known to be influenced by high levels of steroids or by aspirin ingestion (which lower adhesion), and by inflammation

(which increases adhesion). Two of the three crewmembers (the CMP and the DMP) had decreased leukocyte adherence on day F-5. However, the concurrent controls also had generally decreased adherence values in tests performed on that day, although the extent of the decrease varied among the control individuals. The control tests were much more stable on the day of recovery (R+0) and on day R+1, possibly making the decreases in PMN adherence in members of the prime crew significant. However, because of the fluctuations observed, serial values of the prime crew are not definitely different from those obtained from the controls.

The ability of leukocytes to migrate in a modified Boyden chamber was measured both without a chemotactic stimulant (table 17-VII(a)) and in response to the chemotactic agent casein (table 17-VII(b)). A chemotactic index, expressed as the ratio of migration with casein compared to the migration with no chemotactic agent, is presented in table 17-VIII. In general, the migration of leukocytes, as quantitated by this method, remains within the normal range for this laboratory throughout the period of observation. A slightly

TABLE 17-IV.—Leukocyte Alkaline Phosphatase

(a) Total number of positive PMN's (cells/mm<sup>3</sup> blood)

Subject	Day of observation						
	Before flight			After recovery			
	F-30	F-15	F-5	R+0	R+1	R+8	R+30
ACDR	3564	2665	3066	4630	7841	4986	3255
CMP	2246	1696	1379	6708	8867	4876	2758
DMP	1274	1246	853	3390	8710	4790	2146
A	1673	1835	1224	886	1866	--	--
B	1788	3000	1819	1250	1188	--	--
C	3050	2090	1334	591	905	--	--
D	--	<sup>a</sup> 3023	<sup>a</sup> 2348	<sup>a</sup> 1742	3129	--	<sup>a</sup> 2301
		<sup>b</sup> 2216	<sup>b</sup> 2683	<sup>b</sup> 2585			<sup>b</sup> 1900
E	<sup>a</sup> 2630	--	--	--	--	2587	--
	<sup>b</sup> 3260						
ACDR <sup>c</sup>	1949	2098	1565	--	--	--	--
CMP <sup>c</sup>	4116	4729	3307	--	--	--	--
DMP <sup>c</sup>	2029	2479	1364	--	--	--	--

(b) Total score of positive PMN's

Subject	Day of observation						
	Before flight			After recovery			
	F-30	F-15	F-5	R+0	R+1	R+8	R+30
ACDR	144	128	96	138	133	158	117
CMP	106	89	69	68	95	130	101
DMP	91	119	94	90	129	160	88
A	93	103	72	80	87	--	--
B	58	82	48	50	45	--	--
C	89	60	43	33	37	--	--
D	--	<sup>a</sup> 93	<sup>a</sup> 89	<sup>a</sup> 63	104	--	<sup>a</sup> 71
		<sup>b</sup> 94	<sup>b</sup> 88	<sup>b</sup> 83			<sup>b</sup> 73
E	<sup>a</sup> 101	--	--	--	--	113	--
	<sup>b</sup> 111						
ACDR <sup>c</sup>	67	104	74	--	--	--	--
CMP <sup>c</sup>	151	145	96	--	--	--	--
DMP <sup>c</sup>	95	117	82	--	--	--	--

<sup>a</sup> Morning sample.<sup>b</sup> Afternoon sample.<sup>c</sup> Backup crewmember.

TABLE 17-IV.—*Concluded*

(c) Mean score of positive PMN's

Subject	Day of observation						
	Before flight			After recovery			
	F-30	F-15	F-5	R+0	R+1	R+8	R+30
ACDR	158	152	126	159	141	166	144
CMP	156	127	113	117	119	141	120
DMP	140	149	116	148	137	170	117
A	141	147	109	143	136	--	--
B	107	130	100	109	125	--	--
C	135	118	102	103	106	--	--
D	--	<sup>a</sup> 126 <sup>b</sup> 134	<sup>a</sup> 122 <sup>b</sup> 119	<sup>a</sup> 131 <sup>b</sup> 130	132	--	<sup>a</sup> 108 <sup>b</sup> 118
E	<sup>a</sup> 131 <sup>b</sup> 141	--	--	--	--	135	--
ACDR <sup>c</sup>	120	137	119	--	--	--	--
CMP <sup>c</sup>	162	161	120	--	--	--	--
DMP <sup>c</sup>	130	148	124	--	--	--	--

<sup>a</sup>Morning sample.<sup>b</sup>Afternoon sample.<sup>c</sup>Backup crewmember.

decreased migration was noted on day R+8; but, conversely, migration of leukocytes from a normal control was increased on this day. Because this test was performed at a temporary facility in Honolulu, comparative values obtained under the same field conditions are not available to determine whether migration was actually depressed or whether this decrease was a result of the testing conditions. The chemotactic index was preserved normally in the tests performed on day R+8.

The phagocytic capacity of PMN's was measured by allowing leukocytes to form monolayers in slide culture and then adding heat-killed staphylococci for varying periods of time. The percentage of PMN's that were phagocytic was determined microscopically over intervals

from 3 to 15 minutes (table 17-IX). Although some fluctuations occurred, the PMN's from the prime crewmembers following space flight retained the ability to ingest staphylococci. When the normal number of phagocytic PMN's was calculated, increased numbers of phagocytes were found in the prime crewmembers following recovery (table 17-X). This increase in phagocytic PMN's parallels the total increase in the leukocyte count. When the number of leukocytes containing large numbers of staphylococci (five or more) was calculated, the values for the prime crewmembers were not as markedly elevated compared to those obtained from the controls (table 17-XI). The uptake of heat-killed staphylococci was not altered in any measurable degree by the space flight.

TABLE 17-V.—*Leukocyte Acid Phosphatase*(a) *Total positive PMN's (cells/mm<sup>3</sup> of blood)*

Subject	Day of observation						
	Before flight			After recovery			
	F-30	F-15	F-5	R+0	R+1	R+8	R+30
ACDR	3877	2697	3711	2759	6090	5196	3255
CMP	3303	2399	1966	9715	9754	5194	2758
DMP	1960	1557	990	4724	7413	5096	2146
A	1799	2569	1557	1187	2295	--	--
B	3311	4619	3334	2419	2705	--	--
C	4621	4099	2828	1329	2173	--	--
D	--	<sup>a</sup> 4085 <sup>b</sup> 3165	<sup>a</sup> 3216 <sup>b</sup> 3625	<sup>a</sup> 3630 <sup>b</sup> 4039	3961	--	<sup>a</sup> 3487 <sup>b</sup> 3063
E	<sup>a</sup> 3415 <sup>b</sup> 3507	--	--	--	--	3080	--
ACDR <sup>c</sup>	3481	2733	2297	--	--	--	--
CMP <sup>c</sup>	4426	5201	3473	--	--	--	--
DMP <sup>c</sup>	2780	3138	1756	--	--	--	--

(b) *Total PMN score*

Subject	Day of observation						
	Before flight			After recovery			
	F-30	F-15	F-5	R+0	R+1	R+8	R+30
ACDR	117	91	100	79	74	124	156
CMP	124	116	95	92	98	107	151
DMP	130	121	99	91	87	134	159
A	125	123	88	78	92	--	--
B	124	112	93	97	84	--	--
C	116	145	99	80	86	--	--
D	--	<sup>a</sup> 99 <sup>b</sup> 96	<sup>a</sup> 108 <sup>b</sup> 93	<sup>a</sup> 89 <sup>b</sup> 84	87	--	<sup>a</sup> 155 <sup>b</sup> 156
E	<sup>a</sup> 126 <sup>b</sup> 89	--	--	--	--	125	--
ACDR <sup>c</sup>	124	122	100	--	--	--	--
CMP <sup>c</sup>	150	120	106	--	--	--	--
DMP <sup>c</sup>	120	129	91	--	--	--	--

<sup>a</sup> Morning sample.<sup>b</sup> Afternoon sample.<sup>c</sup> Backup crewmember.

TABLE 17-V.—*Concluded*

(c) Mean PMN score

Subject	Day of observation						
	Before flight			After recovery			
	F-30	F-15	F-5	R+0	R+1	R+8	R+30
ACDR	118	107	109	110	101	125	156
CMP	124	117	109	110	111	141	151
DMP	130	121	105	107	109	134	159
A	125	126	105	104	103	--	--
B	124	115	106	109	102	--	--
C	116	145	111	111	102	--	--
D	--	<sup>a</sup> 116 <sup>b</sup> 114	<sup>a</sup> 117 <sup>b</sup> 109	<sup>a</sup> 110 <sup>b</sup> 105	102	--	<sup>a</sup> 155 <sup>b</sup> 156
E	<sup>a</sup> 126 <sup>b</sup> 105	--	--	--	--	125	--
ACDR <sup>c</sup>	124	123	110	--	--	--	--
CMP <sup>c</sup>	150	121	126	--	--	--	--
DMP <sup>c</sup>	120	129	107	--	--	--	--

<sup>a</sup> Morning sample.<sup>b</sup> Afternoon sample.<sup>c</sup> Backup crewmember.

TABLE 17-VI.—Percentage of PMN Adherence

Subject	Day of observation						
	Before flight			After recovery			
	F-30	F-15	F-5	R+0	R+1	R+8	R+30
ACDR	94.1	--	89.6	88.1	77.3	91.4	74.2
CMP	81.3	78.8	53.2	61.6	80.3	65.4	56.2
DMP	87.0	89.5	62.3	76.9	77.0	81.9	74.4
A	96.8	89.0	81.0	88.5	90.9	--	--
B	89.2	89.6	81.6	83.1	89.4	--	--
C	94.0	93.8	78.7	81.6	85.3	--	--
D	--	<sup>a</sup> 84.4 <sup>b</sup> 84.2	<sup>a</sup> 56.4 <sup>b</sup> 85.5	<sup>a</sup> 81.4 <sup>b</sup> 94.3	75.6	--	<sup>a</sup> 77.9 <sup>b</sup> 72.6
E	76.8	--	--	--	--	70.9	--
ACDR <sup>c</sup>	80.5	75.2	67.2	--	--	--	--
CMP <sup>c</sup>	80.5	93.1	67.4	--	--	--	--
DMP <sup>c</sup>	80.4	84.1	52.0	--	--	--	--

<sup>a</sup> Morning sample.<sup>b</sup> Afternoon sample.<sup>c</sup> Backup crewmember.

TABLE 17-VII.—Leukotaxis

(a) Random PMN migration (mean number of cells per high-power microscopic field)

Subject	Day of observation						
	Before flight			After recovery			
	F-30	F-15	F-5	R+0	R+1	R+8	R+30
ACDR	9.6	2.3	10.7	10.0	6.9	3.9	6.3
CMP	22.3	13.4	16.0	7.4	12.9	5.6	10.3
DMP	19.5	3.6	10.9	7.7	12.8	1.7	5.6
A	5.6	7.8	9.9	4.2	3.9	--	--
B	4.7	13.9	5.3	6.1	5.6	--	--
C	6.4	5.0	29.2	5.2	3.2	--	--
D	--	<sup>a</sup> 31.5 <sup>b</sup> 16.3	<sup>a</sup> 11.1 <sup>b</sup> 6.5	<sup>a</sup> 4.8 <sup>b</sup> 5.2	9.3	--	10.6
E	7.7	--	--	--	--	2.7	--
ACDR <sup>c</sup>	2.4	9.0	25.9	--	--	--	--
CMP <sup>c</sup>	8.0	20.9	9.2	--	--	--	--
DMP <sup>c</sup>	2.5	1.7	7.6	--	--	--	--

(b) PMN chemotaxis to casein (mean number of cells per high-power microscopic field)

Subject	Day of observation						
	Before flight			After recovery			
	F-30	F-15	F-5	R+0	R+1	R+8	R+30
ACDR	70.9	76.4	70.8	45.2	82.9	27.2	50.3
CMP	48.4	41.2	73.5	88.7	65.2	40.9	44.7
DMP	76.0	8.3	50.2	78.7	64.5	17.6	39.2
A	22.6	41.6	63.5	73.5	81.6	--	--
B	29.9	33.2	35.9	56.4	38.8	--	--
C	37.9	21.8	45.7	12.2	60.8	--	--
D	--	<sup>a</sup> 68.5 <sup>b</sup> 52.6	<sup>a</sup> 100.4 <sup>b</sup> 93.2	<sup>a</sup> 68.0 <sup>b</sup> 74.7	72.8	--	76.1
E	79.7	--	--	--	--	20.4	--
ACDR <sup>c</sup>	20.1	28.2	83.1	--	--	--	--
CMP <sup>c</sup>	24.0	48.0	82.8	--	--	--	--
DMP <sup>c</sup>	12.1	29.0	114.4	--	--	--	--

<sup>a</sup> Morning sample.<sup>b</sup> Afternoon sample.<sup>c</sup> Backup crewmember.

TABLE 17-VIII.—Chemotactic Index of Leukotaxis

[Stimulated migration/random migration]

Subject	Day of observation						
	Before flight			After recovery			
	F-30	F-15	F-5	R+0	R+1	R+8	R+30
ACDR	7.38	33.20	6.64	4.52	11.97	7.03	7.94
CMP	2.17	3.07	4.58	12.03	5.07	7.31	4.36
DMP	3.90	2.29	4.63	10.22	5.04	10.54	7.06
A	4.04	5.33	6.40	17.37	20.76	--	--
B	6.36	2.39	6.77	9.29	6.93	--	--
C	5.92	4.36	1.57	2.34	19.00	--	--
D	--	<sup>a</sup> 2.18 <sup>b</sup> 3.21	<sup>a</sup> 9.04 <sup>b</sup> 14.40	<sup>a</sup> 14.26 <sup>b</sup> 14.36	7.80	--	7.20
E	10.35	--	--	--	--	7.47	--
ACDR <sup>c</sup>	8.28	3.13	3.21	--	--	--	--
CMP <sup>c</sup>	3.02	2.29	9.03	--	--	--	--
DMP <sup>c</sup>	4.89	17.58	15.20	--	--	--	--

<sup>a</sup>Morning sample.<sup>b</sup>Afternoon sample.<sup>c</sup>Backup crewmember.

## DISCUSSION

The PMN is a critical cell in the defense of the host against bacterial infections. The ultimate function of this cell is the phagocytosis and killing of microorganisms that invade the tissues of the body. A sequence of earlier functions is critical, however, if the PMN is to be present in adequate numbers to influence the course of bacterial infection. Leukocytes are delivered to the tissues through the circulating blood, in which they are brought to tissues where potential infections occur. To be effective in controlling infection in tissue spaces, the leukocyte must first adhere to the surface of a blood vessel, work its way through

the walls of the small blood vessels, migrate through the tissue spaces, and collect in adequate numbers in the area of inflammation accompanying early infection. Abnormalities in PMN function that impair performance at any one of these steps can potentially cause increased susceptibility to infection.

The series of *in vitro* tests of PMN function used in this experiment was designed to systematically examine the different steps in which the PMN participates in the inflammatory response. Defective adhesion of PMN's has not been definitely documented to increase susceptibility to infection, although several clinical conditions in which infections are a problem are also

TABLE 17-IX.—Percentage of Phagocytic PMN's

Subject	Time interval, min	Day of observation						
		Before flight			After recovery			
		F-30	F-15	F-5	R+0	R+1	R+8	R+30
ACDR	3	9	5	5	30	1	22	10
	6	15	14	21	70	5	38	15
	10	7	24	19	72	19	38	21
	15	26	41	18	89	30	51	12
CMP	3	5	4	6	3	4	4	13
	6	11	9	7	5	4	23	17
	10	13	15	9	31	11	29	21
	15	23	28	18	37	22	15	9
DMP	3	7	6	8	6	6	3	7
	6	8	13	11	10	9	8	5
	10	6	12	8	23	17	15	25
	15	13	28	16	20	23	27	18
A	3	6	6	9	3	18	--	--
	6	13	4	15	3	31	--	--
	10	11	17	31	8	41	--	--
	15	14	29	45	28	31	--	--
B	3	14	9	20	25	13	--	--
	6	25	10	20	54	17	--	--
	10	18	16	10	89	25	--	--
	15	30	26	16	96	29	--	--
C	3	14	4	9	6	6	--	--
	6	15	8	23	12	20	--	--
	10	41	16	10	15	29	--	--
	15	20	20	14	14	57	--	--
D	3	--	a <sub>6</sub> b <sub>12</sub>	a <sub>14</sub> b <sub>9</sub>	a <sub>4</sub> b <sub>7</sub>	5	--	a <sub>3</sub> b <sub>10</sub>
	6	--	a <sub>7</sub> b <sub>12</sub>	a <sub>14</sub> b <sub>17</sub>	a <sub>9</sub> b <sub>15</sub>	8	--	a <sub>8</sub> b <sub>11</sub>
	10	--	a <sub>10</sub> b <sub>25</sub>	a <sub>22</sub> b <sub>12</sub>	a <sub>18</sub> b <sub>16</sub>	7	--	a <sub>24</sub> b <sub>13</sub>
	15	--	a <sub>22</sub> b <sub>24</sub>	a <sub>12</sub> b <sub>17</sub>	a <sub>35</sub> b <sub>38</sub>	32	--	a <sub>15</sub> b <sub>19</sub>
E	3	10	--	--	--	--	18	--
	6	16	--	--	--	--	27	--
	10	22	--	--	--	--	48	--
	15	18	--	--	--	--	42	--
ACDR <sup>c</sup>	3	4	3	3	--	--	--	--
	6	15	8	14	--	--	--	--
	10	20	13	18	--	--	--	--
	15	18	25	19	--	--	--	--

<sup>a</sup> Morning sample.<sup>b</sup> Afternoon sample.<sup>c</sup> Backup crewmember.



TABLE 17-IX.—Concluded

Subject	Time interval, min	Day of observation						
		Before flight			After recovery			
		F-30	F-15	F-5	R+0	R+1	R+8	R+30
CMP <sup>c</sup>	3	6	2	5	--	--	--	--
	6	12	14	10	--	--	--	--
	10	22	15	11	--	--	--	--
	15	13	20	18	--	--	--	--
DMP <sup>c</sup>	3	5	--	8	--	--	--	--
	6	7	--	11	--	--	--	--
	10	22	--	12	--	--	--	--
	15	17	--	9	--	--	--	--

<sup>c</sup>Backup crewmember.

accompanied by reduced *in vitro* leukocyte adhesion (corticosteroid therapy, acute alcoholism). Defective leukocyte migration and decreased phagocytosis and intracellular killing of microorganisms have been demonstrated in patients who are more susceptible to bacterial infections. This experiment did not test the capacity of PMN's from the crewmembers to kill intracellular bacteria, because of the difficulties in conducting these studies under field conditions onboard the recovery ship. The absence of any substantial change in the function studies performed suggests that a 9-day space mission does not impair PMN function to any significant extent. This finding is further substantiated by the fact that crewmembers returning from space flight have not exhibited increased clinical susceptibility to infection.

The PMN is present in the circulating blood for only a matter of hours as the cells travel from the bone marrow, where they are produced, to the tissues. As a result of this rapid turnover in leukocytes, changes in the metabolism or in the

well-being of the host may be reflected by alterations in the circulating leukocytes. Histochemical staining for granules containing acid phosphatase or alkaline phosphatase has been used to detect alterations in PMN's. In this experiment, changes in these measurements in the blood samples from the crewmembers generally paralleled the total PMN counts, as reflected in total leukocyte and differential counts.

Although blood samples were obtained from the crewmembers within 1.5 hours of reentry, the PMN population sampled at that time was probably substantially different from the PMN population that was circulating during weightlessness. Before definitive statements on the possible effects of weightlessness and space flight on PMN function can be asserted, it will be necessary to perform tests on cells actually obtained during a mission. In addition, it is conceivable that a flight of longer duration might result in substantially different effects. This area of investigation should be pursued during future space flights.

TABLE 17-X.—Number of Phagocytic PMN's

[Cells/mm<sup>3</sup> of blood]

Subject	Time, min	Day of observation						
		Before flight			After recovery			
		F-30	F-15	F-5	R+0	R+1	R+8	R+30
ACDR	3	352	159	202	1597	83	1155	326
	6	587	444	847	3725	417	1994	488
	10	274	762	767	3832	1585	1994	684
	15	1018	1303	726	4737	2502	2676	391
CMP	3	165	97	154	359	443	212	359
	6	363	218	179	599	443	1219	469
	10	429	264	230	3710	1219	1537	579
	15	760	678	461	4429	2438	795	248
DMP	3	137	100	84	342	556	153	150
	6	157	217	116	569	834	408	107
	10	118	201	84	1310	1575	764	537
	15	255	468	169	1140	2131	1376	386
A	3	108	157	167	47	525	--	--
	6	234	105	278	47	904	--	--
	10	199	446	575	127	1196	--	--
	15	252	760	834	443	904	--	--
B	3	464	429	758	679	429	--	--
	6	794	476	758	1468	561	--	--
	10	596	762	379	2419	825	--	--
	15	993	1238	606	2609	957	--	--
C	3	647	164	286	111	155	--	--
	6	693	328	731	222	518	--	--
	10	1895	656	317	277	751	--	--
	15	924	820	445	258	1476	--	--
D	3	--	a <sub>245</sub>	a <sub>489</sub>	164	198	--	a <sub>105</sub>
		--	b <sub>379</sub>	b <sub>326</sub>			--	b <sub>306</sub>
	6	--	a <sub>286</sub>	a <sub>489</sub>	370	317	--	a <sub>279</sub>
		--	b <sub>379</sub>	b <sub>616</sub>			--	b <sub>337</sub>
	10	--	a <sub>409</sub>	a <sub>769</sub>	740	277	--	a <sub>837</sub>
		--	b <sub>791</sub>	b <sub>435</sub>			--	b <sub>398</sub>
	15	--	a <sub>899</sub>	a <sub>386</sub>	1439	1286	--	a <sub>523</sub>
		--	b <sub>760</sub>	b <sub>616</sub>			--	b <sub>582</sub>
E	3	206	--	--	--	--	554	--
	6	330	--	--	--	--	832	--
	10	412	--	--	--	--	1478	--
	15	742	--	--	--	--	1294	--

<sup>a</sup> Morning sample.<sup>b</sup> Afternoon sample.

TABLE 17-X.—Concluded

Subject	Time, min	Day of observation						
		Before flight			After recovery			
		F-30	F-15	F-5	R+0	R+1	R+8	R+30
ACDR <sup>c</sup>	3	139	83	76	--	--	--	--
	6	522	221	353	--	--	--	--
	10	696	359	454	--	--	--	--
	15	626	690	479	--	--	--	--
CMP <sup>c</sup>	3	266	105	207	--	--	--	--
	6	531	736	413	--	--	--	--
	10	974	788	455	--	--	--	--
	15	575	1051	744	--	--	--	--
DMP <sup>c</sup>	3	139	--	165	--	--	--	--
	6	195	--	227	--	--	--	--
	10	612	--	248	--	--	--	--
	15	473	--	186	--	--	--	--

<sup>c</sup>Backup crewmember.

TABLE 17-XI.—Number of Phagocytic PMN's With Five or More Staphylococci

Subject	Time, min	Day of observation						
		Before flight			After recovery			
		F-30	F-15	F-5	R+0	R+1	R+8	R+30
ACDR	3	0	0	0	426	0	367	33
	6	0	64	0	852	334	840	0
	10	0	159	81	1277	834	525	98
	15	157	571	121	2076	1501	1102	163
CMP	3	0	0	0	120	0	0	28
	6	33	24	0	120	111	106	0
	10	33	97	51	2513	443	265	110
	15	33	145	26	3351	1108	424	28
DMP	3	0	0	0	57	278	0	0
	6	0	17	0	0	278	0	0
	10	20	0	11	456	648	204	64
	15	0	117	0	513	1019	204	129

TABLE 17-XI.—Concluded

Subject	Time, min	Day of observation						
		Before flight			After recovery			
		F-30	F-15	F-5	R+0	R+1	R+8	R+30
A	3	0	0	0	0	58	--	--
	6	18	0	37	0	117	--	--
	10	18	26	297	63	233	--	--
	15	0	184	222	233	204	--	--
B	3	33	48	0	163	132	--	--
	6	0	0	0	462	330	--	--
	10	0	286	0	1142	495	--	--
	15	331	667	75	1359	627	--	--
C	3	92	0	0	0	0	--	--
	6	0	0	0	55	129	--	--
	10	508	82	0	148	285	--	--
	15	231	328	32	148	751	--	--
D	3	--	a <sub>0</sub> b <sub>0</sub>	a <sub>70</sub> b <sub>0</sub>	41	0	--	a <sub>0</sub> b <sub>0</sub>
	6	--	a <sub>0</sub> b <sub>0</sub>	a <sub>70</sub> b <sub>0</sub>	0	40	--	a <sub>35</sub> b <sub>61</sub>
	10	--	a <sub>82</sub> b <sub>32</sub>	a <sub>0</sub> b <sub>0</sub>	205	119	--	a <sub>105</sub> b <sub>92</sub>
	15	--	a <sub>286</sub> b <sub>379</sub>	a <sub>0</sub> b <sub>0</sub>	1234	634	--	a <sub>105</sub> b <sub>30</sub>
E	3	0	--	--	--	--	92	--
	6	0	--	--	--	--	185	--
	10	0	--	--	--	--	400	--
	15	7	--	--	--	--	462	--
ACDR <sup>c</sup>	3	0	0	0	--	--	--	--
	6	104	0	25	--	--	--	--
	10	104	0	25	--	--	--	--
	15	104	110	101	--	--	--	--
CMP <sup>c</sup>	3	44	0	0	--	--	--	--
	6	133	53	0	--	--	--	--
	10	133	158	83	--	--	--	--
	15	89	158	83	--	--	--	--
DMP <sup>c</sup>	3	28	--	0	--	--	--	--
	6	28	--	0	--	--	--	--
	10	167	--	0	--	--	--	--
	15	83	--	0	--	--	--	--

<sup>a</sup> Morning sample.<sup>b</sup> Afternoon sample.<sup>c</sup> Backup crewmember.

## REFERENCES

- 17-1. Wintrobe, M. H.: *The Leukocytes in Clinical Hematology*. Lea and Febiger (Philadelphia), 1962, p. 214.
- 17-2. White, A.: *Hormonal Steroids, Biochemistry, Pharmacology, and Therapeutics*. Proceedings of the First International Congress of Hormonal Steroids, vol. I, Academic Press (New York), 1964, p. 571.
- 17-3. McCall, C. E.; Katayama, I.; Cotran, R. S.; and Finland, M.: Lysosomal and Ultrastructural Changes in Human "Toxic" Neutrophils During Bacterial Infection. *J. Exp. Med.*, vol. 129, Feb. 1969, pp. 267-293.
- 17-4. McCall, C. E.; Caves, J.; Cooper, R.; and DeChatelet, L.: Functional Characteristics of Human Toxic Neutrophils. *J. Infect. Dis.*, vol. 124, July 1971, pp. 68-75.
- 17-5. McGregor, R. R.; Spagnuolo, P. J.; and Lentnek, A. L.: Inhibition of Granulocyte Adherence by Ethanol, Prednisone, and Aspirin, Measured With an Assay System. *N. Engl. J. Med.*, vol. 291, Sept. 1974, pp. 642-646.
- 17-6. Martin, R. R.; Warr, G. A.; Couch, R.; and Knight, V.: Chemotaxis of Human Leukocytes: Responsiveness to *Mycoplasma Pneumoniae*. *J. Lab. Clin. Med.*, vol. 81, Apr. 1973, pp. 520-529.
- 17-7. Cline, M. J.: A New White Cell Test Which Measures Individual Phagocyte Function in a Mixed Leukocyte Population. I. A Neutrophil Defect in Acute Myelocytic Leukemia. *J. Lab. Clin. Med.*, vol. 81, Feb. 1973, pp. 311-316.



# 18. Killifish Hatching and Orientation

## Experiment MA-161

*H. W. Scheld,<sup>a†</sup> A. Baky,<sup>b</sup> J. F. Boyd,<sup>b</sup> V. B. Eichler,<sup>c</sup> P. M. Fuller,<sup>d</sup> R. B. Hoffman,<sup>e</sup> J. R. Keefe,<sup>d</sup>  
K. P. Kuchnow,<sup>f</sup> J. M. Oppenheimer,<sup>g</sup> G. A. Salinas,<sup>b</sup> and R. J. von Baumgarten<sup>h</sup>*

### ABSTRACT

In the Apollo-Soyuz Test Project Killifish Hatching and Orientation Experiment, the killifish *Fundulus heteroclitus* was used as a model system for the study of embryonic development and vestibular adaptation in orbital flight. The experiment package consisted of two parts: a series of staged embryos in five individual compartments of a polyethylene bag and a series of pre-conditioned juvenile fish in a similar bag. Embryos at 32, 66, 128, 216, and 336 hours after fertilization at the time of launch were chosen to represent key stages of development; development preflight occurred at a constant temperature of 295 K (22° C). Juvenile fish were reared from hatching for 21 days in specific visual environments.

Experiment packages were mounted on the docking module wall and photographed periodically during the mission to record the swimming activity of the fish and the condition of

the eggs. At splashdown, vestibular sensitivity of the juvenile fish and of hatchlings from the eggs was tested in a rotating, striped drum. Subsequently, additional vestibular orientation tests during parabolic-trajectory flight, light-orientation tests, and geotaxis tests were performed. Samples of juveniles and hatchlings/embryos were fixed for microscopic examination at splashdown and at selected times thereafter. Testing for assessment of normalcy of vestibular function is continuing as the fish mature.

Juvenile fish in a null-gravity environment exhibited looping swimming activity similar to that observed during the Skylab 3 mission. Hatchlings from the 336-hour egg stage also were reported to have looped. At splashdown, both juveniles and hatchlings exhibited a typical diving response suggesting relatively normal vestibular function. The juveniles exhibited swimming patterns indicative of abnormal swim bladders. Rotating-drum tests confirmed that no radical changes in vestibular function had occurred; subsequent tests in maturing fish (6 to 8 months) suggest subtle changes in the geotactic response of the 32-hour flight fish and increased sensitization to environmental influences in 32-, 66-, and 128-hour flight fish as compared to controls. Extensive examination by light and electron microscopy of 66-hour through 336-hour groups has revealed no significant differences between flight and control animals in the embryological development of the central nervous system, the peripheral vestibular apparatus, the eye, or the cardiovascular system. The 32-hour group is still being investigated.

---

<sup>a</sup>Baylor College of Medicine.

<sup>b</sup>Northrop Services, Inc.

<sup>c</sup>Wichita State University.

<sup>d</sup>University of Louisville.

<sup>e</sup>NRC-NASA Resident Research Associate.

<sup>f</sup>Texas A. & M. University.

<sup>g</sup>Bryn Mawr College.

<sup>h</sup>University of Mainz, Germany.

<sup>†</sup>Principal Investigator.

## INTRODUCTION

The Apollo-Soyuz Test Project (ASTP) killifish experiment was the second in a series of experiments to evaluate the hazards inherent in the exposure of living organisms to the space environment during critical portions of the life cycle or for extended periods. The points of primary emphasis were the function and development of the vestibular system and calcium deposition, particularly as it relates to otolith development.

The experimental organism was *Fundulus heteroclitus* (Walbaum), a small shallow-water minnow common along the Atlantic coast. This organism has been used in experimental embryology for many years, and its biology and developmental relationships are well known (refs. 18-1 to 18-3). *Fundulus* was used as a test organism at the NASA Lyndon B. Johnson Space Center (JSC) during the lunar quarantine. Subsequently, the methodology for continuous laboratory production of fertile eggs was developed in this laboratory (ref. 18-4).

The Beaufort, North Carolina, strain of *Fundulus* used in these experiments produces an egg having a transparent, tough chorion. Development may thus be observed from the first cleavage to hatching; and, during this time, the egg may be manipulated extensively without undue stress on the developing embryo. The approximately 2-week period of development is convenient for most laboratory experiments, and the resulting hatchling is relatively large (approximately 1 cm long) with much of the length taken up by the head. The vestibular region, the eyes, and the brain are correspondingly large at this stage. Thus, given the limitations of the available flight conditions, the *Fundulus* embryo presents a useful system for preliminary investigations.

## EXPERIMENT BACKGROUND AND DESCRIPTION

A *Fundulus* experiment was included on the Skylab 3 mission in an abbreviated and informal demonstration form. The Skylab package consisted of a plastic bag containing 2 juvenile fish in a compartment with 250 ml of synthetic seawater (21 parts per thousand of dissolved solids) and 50

fertilized eggs (4 days past fertilization) in a separate compartment with 50 ml of seawater. Initially, the juveniles exhibited obvious disorientation reactions (swimming rapidly in loops and circles), but over a period of several days in orbit, they gradually adapted to the weightless environment and to dependence on visual cues for orientation (ref. 18-5). In this state of adaptation, the locker door surface to which the plastic aquarium was attached apparently served as "down." Adaptation was not complete, however, and occasional disoriented swimming activity occurred. Nearly all the 50 eggs hatched in space, and because of a delay in hatching of the flight fish, several returned alive to Earth. However, a series of unfortunate events resulted in the death of these animals shortly after return. The space-hatched *Fundulus* fry exhibited no observable tendency toward disoriented swimming activity, and their apparent dependence on visual orientation cues both onboard the Skylab spacecraft and on the recovery ship suggested the possible absence of vestibular input. Preservation of the returned hatchlings was insufficient to prevent deterioration and did not permit definite conclusions regarding the condition of the vestibular system. Typical otoliths, however, were not visible in microscopic sections of the flight fish.

The ASTP killifish experiment was designed to confirm and extend the Skylab 3 observations of vestibular disturbance and embryonic development. Calcium loss has been observed in humans after exposure in space, and otolith development is, in fact, largely concerned with calcium metabolism. Therefore, observations of otolith development are important not only because of the importance of the vestibular system in balance but also because of the possible use of the otolith as a model for space research on calcium metabolism in general.

The Skylab observations also raised several questions regarding mechanisms of vestibular disturbance and adaptation in the *Fundulus* and its usefulness as a model for vestibular research. The primary questions asked in the ASTP experiment were related to the rate of adaptation, which is only sketchily known from the Skylab experiment, and the role of the visual system in orientation and adaptation to null-gravity conditions.



### Experimental Design

The experiment consisted of a two-part experimental package (fig. 18-1) that was exposed in orbital flight and of four control treatment packages. Except for the treatment designated "launch control," all packages contained the experimental materials enumerated in table 18-I. The following control packages were used.

1. Transport control (package C-I): This package was transported with the flight package. During the mission, it was exposed to a constant temperature (296 K (23° C)) and to the predicted atmospheric pressure and oxygen (O<sub>2</sub>) partial pressure profile of the ASTP spacecraft. Recovery processing and return to JSC paralleled those of the flight treatment package.

2. Laboratory air control (package C-II): Immediately after packing, the fish and egg packages were placed in a 295-K (22° C) incubator under standard atmospheric conditions until recovery. Subsequent handling was similar to that for the

flight treatment package.

3. The 48-hour-lag control in ASTP-simulated air (package C-III): Eggs were fertilized and packages prepared on a schedule precisely 48 hours behind the flight schedule. All timing and conditions of preparation of flight packages were duplicated. At launch time, the package was exposed to a simulated launch vibration profile and then placed in an environmental chamber for exposure to simulated spacecraft atmosphere. Atmosphere (O<sub>2</sub> partial pressure) and temperature were programed to duplicate the averaged readings of the spacecraft sensors. Recovery activities paralleled those of the flight treatment package.

4. Launch control: Smaller samples of eggs (10) and fish (2) were prepared in parallel with the flight controls and the 48-hour-lag controls and were transported with these treatment packages. At lift-off, these samples were fixed in cold trialdehyde fixative to provide a record of developmental condition at lift-off.



FIGURE 18-1.—Experimental package consisting of fish packet and egg packet.

TABLE 18-I.—*Experimental Packages**(a) Egg package with five compartments*

Compartment	Number of eggs		Age of embryos at launch, hr (a)	Nominal stage of embryogenesis
	Launch	Return		
1	100	100	32	Mid-to-late gastrulation
2	100	100	66	Statolith precursors appear
3	100	100	128	Vestibular development completed
4	100	100	216	Vestibular system functional
5	50	50	336	Full development; able to hatch

*(b) Fish package with five compartments*

Compartment	Number of fish		Preconditioning	Flight background
	Launch (b)	Return		
1	6	5	Neutral background	White
2	6	5	Vertical bars	Barred
3	6	5	Horizontal bars	Barred
4	6	<sup>c</sup> 0	Black overhead	Black
5	6	6	Blinded	White

<sup>a</sup>Development occurred at a constant temperature of 295 K (22° C).<sup>b</sup>Age of fish at launch was approximately 21 days.<sup>c</sup>All fish in this compartment were dead.**Experiment Theory**

The embryo development portion of the experiment was designed to isolate the effects of exposure to a null-gravity environment in progressively more advanced stages of embryo development. The ages were selected as probable average times for the onset of key stages of development with particular reference to the vestibular system and otolith development. Development time varies somewhat within the population but is essentially complete by 9 to 11 days, and most of the eggs may be stimulated to hatch at the end of 14 days under standard laboratory conditions. Thus, in a majority of the flight treatment eggs, all subsequent embryogenesis was completed in the near-null-gravity conditions of orbital flight. The three later

stages, 128, 216, and 336 hours, were theoretically capable of hatching during the mission. One experiment objective was to observe and record swimming activities of the hatchlings from these eggs to confirm the observations of apparent adaptation in the Skylab hatchlings.

Embryos of different ages (table 18-I(a)) were obtained by stripping ova and milt from adult *Fundulus* (ref. 18-4) and combining these to effect fertilization at the given prelaunch times. Fertilized eggs were then incubated in plastic petri dishes containing synthetic seawater (21 parts per thousand of dissolved solids) at a constant temperature of 295 K (22° C). Each petri dish contained a maximum of 50 eggs that were washed daily with filter-sterilized synthetic seawater to ensure removal of metabolic products and to reduce the population of contaminant

microorganisms. Between 30 and 26 hours before launch, all eggs were sorted, given a final wash, and sealed into the compartments of the plastic flight package.

The vestibular adaptation portion of the experiment was designed to extend previous observations of *Fundulus* swimming behavior in a null-gravity environment. The cause of the observed disorientation in the fish is largely unknown, although the vestibular system is presumed to be primarily responsible. The observed adaptation during the Skylab 3 mission was apparently based partly on a switch to dependence on the visual system for orientational cues. The entire process is of more than passing interest because it parallels in many ways the patterns reported for human adjustment to weightlessness, and findings regarding vestibular adaptation in fish could usefully be applied to humans (ref. 18-5). Because of time and space limitations, the experimental scheme was not intended to produce profound conclusions; it was simply an attempt to refine previous measurements of rate of adaptation and to define the nature of the visual stimulus (light direction or background surface) in the apparent habituation of fish to null-gravity conditions. Of equal importance was the observation of readaptation of the partly space-adapted fish to one-g conditions.

The experiment package consisted of several small plastic-film bags (fig. 18-1), each containing a number (table 18-I(b)) of *Fundulus* fry (immature fish 21 days old at time of launch) that had been reared from hatching in tanks presenting different visual environments. The swimming activity of the fish was recorded with a motion picture camera at various times during the flight with the objective of measuring general rate of adaptation as well as orientation patterns and relative rates of adaptation of the visually conditioned fish.

### Data Collection

The data yield of the experiment consisted of visual observations from the flight, motion picture recordings of the condition and activity of experimental animals during and after the flight, animals for microscopic examination that were fixed at recovery and at subsequent selected sam-

pling times, and results of behavioral tests taken at recovery and at various times during the maturation of the fish.

The primary objective of the histological sampling was to detect anatomical differences in the flight animals that could be correlated with behavioral differences and to record any observable readjustments that might occur in the developing animals after their return. Samples of juvenile fish were fixed in trialdehyde fixative at splashdown and several weeks later following completion of behavioral testing. To provide a picture of progressive changes, hatchlings and unhatched eggs were sampled at recovery, at approximately daily intervals for the first week after splashdown, and again at 2 weeks, 1 month, and 6 months. Analysis involved, as a first stage, serial sectioning of the fixed animals for light and electron microscopy of the head and body cavity and examination for anomalous development of the vestibular apparatus, the central nervous system, the eye, and the cardiovascular system. Of particular interest was the degree of calcification of cartilage and of the otoliths.

Postflight testing was performed on both fry and hatchlings from the flight and control treatment packages with the objective of detecting and measuring differences in orientation behavior attributable to null-gravity exposure during development. The tests employed were the rotating striped-drum test, the light-orientation test, the geotaxis test, and brief exposure to null-gravity conditions during parabolic-trajectory flight. A final test, to be conducted when the fish are fully mature, will measure and analyze locomotor activity.

The classical fish otolith tests (ref. 18-6) were based on measurements of the fish longitudinal-axis tilt from the horizontal when the direction of water currents or of illumination is varied. At the University of Mainz, an additional otolith test that works especially well with very young and small fish has been developed. The fish tank containing the unrestrained fish is placed inside first a vertical and later a horizontal rotating striped drum. In the vertical drum, the fish visually lock with the stripes and swim around inside the drum, keeping pace with the moving stripe (fig. 18-2(a)). In the horizontal drum, the fish are prevented from

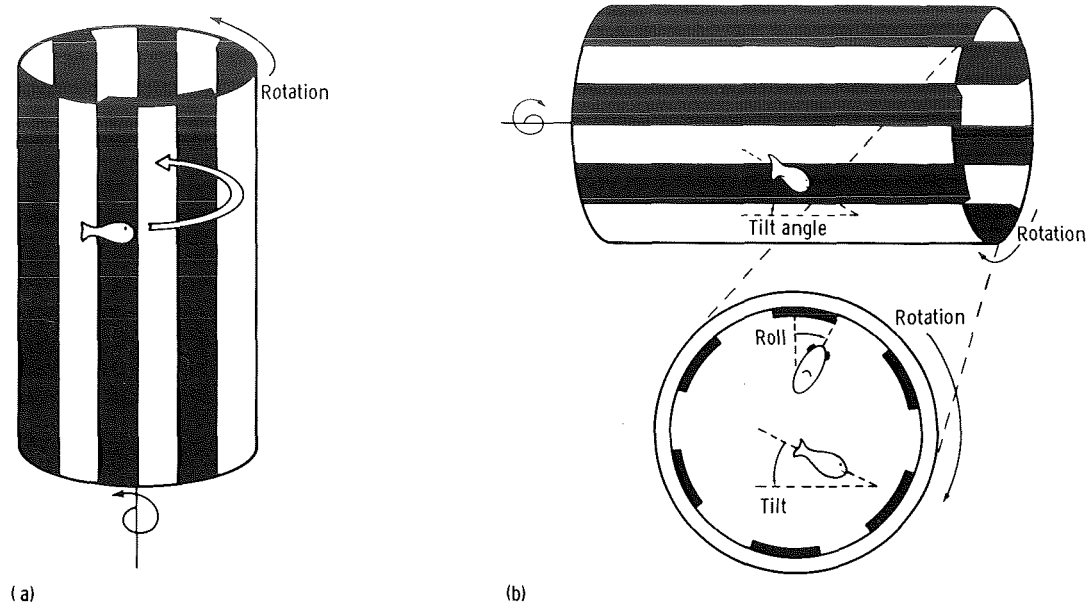


FIGURE 18-2.—Orientation in rotating drum. (a) Vertical position. (b) Horizontal position.

looping solely by action of the otolith system (fig. 18-2(b)). However, if the fish face the stripes, their bodies are tilted in the direction of stripe movement. The fish that are turned  $90^\circ$  away from the stripes roll to a measurable degree in the direction of the drum rotation, but again are prevented from tilting further by the action of their otolith system. Abnormal tilt indicates a lowered sensitivity of the otolith system. The rotating-drum test was employed as the initial vestibular test given to the returned flight fish on the recovery ship. Testing began within 8 hours of splashdown and continued for 5 days. In this test, the fish were inside a sealed tank that was placed inside the drum for varying times of at least 1 minute in both horizontal and vertical drum positions. Tilt angle and movements were recorded by a motion picture camera for later single-frame analysis.

In addition to the rotating striped-drum test, a light-orientation test was given to the juvenile fish to further evaluate their ability to orient in the geogravitational environment after a 9-day exposure to weightlessness. Although it is well known that fish maintain their relative vertical orientation by integrating sensory information from the influences of both gravity and light (ref.

18-6), it was not known whether the exposure only to light cues during a 9-day period would affect this integration when the fish were reintroduced into the normal one-g environment.

In the normal geogravity environment, fish maintain their equilibrium orientation by static and optic stimuli. If these stimuli do not operate in the vertical direction, the fish takes a position between the vertical plane and the incidence of the light (ref. 18-7). For example, if a light is placed in a darkened chamber at a  $90^\circ$  angle relative to the vertical plane, the fish will roll about its body axis toward the light and the dorsal fin will form a  $30^\circ$  to  $60^\circ$  angle relative to the vertical plane. (The exact magnitude of the angle varies with species of fish and other environmental factors such as light intensity and dark adaptation.) Normally, fish live in an environment in which light is overhead and therefore represents a reference for the vertical in addition to the sensing of gravity. The fish rolls toward the light source to accommodate its sensory inputs in the new  $90^\circ$  test environment. If the light intensity is increased, the fish will roll even farther toward the light, up to a point. If gravity is increased (as in a centrifuge), the fish will roll back toward the gravitational vertical. The static vestibular sense is

the more dominant of the two systems, but if it is damaged (as in ablation studies), the fish will orient strictly with respect to the dominant light direction. Therefore, the light-orientation test was an attempt to measure a possible modification of the gravitational receptors due to a 9-day exposure to null-gravity conditions. In this test, each juvenile fish was placed in a clear plastic cylinder and its dorsal fin orientation was measured after a 40-W bulb was placed 14 cm to the right of the fish (90° relative to the vertical plane) for 30 minutes and then to the left for the same period. Dark adaptation was permitted for 1 minute before each test interval, and right and left tests were randomized. Each fish was given one trial (left and right orientations) in any given test day. All fish were tested sequentially until four trials per fish were made over a period of several days.

A geotaxis test developed at JSC was employed for further testing of maturing fish after 6 months. In this test, a fish is gently placed just below the meniscus of the synthetic seawater in a graduated cylinder filled to the 500-ml mark. The amount of time spent in the upper half of the cylinder is recorded over a 2-minute interval as a measure of the geotaxis response. This diving response is very strong in most *Fundulus heteroclitus*; therefore, the test was a measure of whether or not this innate vestibular program was modified by an exposure to null-gravity conditions during embryonic development.

### Experiment Execution

Execution of the flight portion of the experiment was, relatively, the simplest part. The prepared flight package was transported to the launch site in a T-38 aircraft between 26 and 23 hours before launch and placed in a storage locker of the command module approximately 9 hours before launch. At approximately 30 hours after launch, the metal and glass cloth flight container was opened and the experimental packages were mounted on the docking module wall for the duration of the mission. Motion pictures were taken of the fish package at this time. No photography or observations were scheduled during the joint

phase of the mission because of the heavy demands placed on the crew during that time. Daily observations were recorded in the flight notes, and motion pictures were made on mission day 6 and all subsequent days of the mission. Following photography on mission day 9, the packages were returned to the flight container and stored for reentry.

The flight package was removed from the command module 6 hours after recovery and was photographed to record initial swimming activity. Hatching was induced by agitation on a rotary shaker, and samples of eggs, hatchlings, and juvenile fish were killed and fixed for microscopic examination. Additional samples were fixed at approximately 24-hour intervals for 7 days after recovery, at 2 weeks, and again at 1 month. Upon return of experimental materials to the laboratory 2 days after recovery, selected specimens were injected with tritiated thymidine and killed after a 1-hour exposure.

Testing for vestibular sensitivity by the rotating-drum method was begun as soon as the juvenile fish and hatchlings were removed from the flight packages and was continued for several days after splashdown. At 5 days, selected groups were tested for orientation in parabolic-trajectory flights. Continued testing of the animals remaining after sampling for histology included light-orientation tests during the first several weeks following splashdown and tests of geotactic response at 6 to 8 months. A final series of tests to be conducted when the fish reach a length of approximately 7.5 cm will include analysis of oriented locomotor behavior patterns as a final sensitive assay of alterations in the vestibular system.

Following return of the experimental materials to JSC, hatchlings and juveniles were maintained in small plastic dishes containing aerated synthetic seawater. After several weeks of observation and light-orientation testing, all juveniles were fixed. Initially, the hatchlings produced after each daily shaking were maintained separately, but after the early intensive sampling for histology, the various daily hatches were pooled. After approximately 2 months, hatchlings were transferred to polycarbonate mouse cages and critical groups including the 32-, 66-, and 128-hour

hatchlings of flight and control animals were separated out and maintained under a 16:8 light-dark cycle. During geotaxis testing, all animals were also adapted to a 12:12 light-dark cycle so that measurements could be made on the same subject under the influence of two different photo periods. At 9 months, the members of the critical groups were separated into individual containers and thereafter maintained on a 12:12 light-dark cycle.

There are currently no plans for further sacrifice of animals for microscopy until other aspects of the experiment have been completed. Surviving animals are being raised to maturity; when they are of adequate size, they will be tested for possible alterations in oriented locomotor behavior by employing the techniques and apparatus of Kleerekoper (refs. 18-8 to 18-10). Upon completion of behavioral testing, egg and milt production will be induced (ref. 18-4) and a second generation initiated.

## RESULTS

Because of the long-term nature of some observations and the complexity of analyses, this report does not present the final results of the experiment. Status of the experiment is updated, preliminary results and expected trends are reported, and the directions to be taken in completion of the experiment and in planning future sequels to this experiment are suggested.

## Vestibular Behavior of Juvenile Fish

*In-flight activity.*—Three points were examined with respect to orientation in the juvenile fish: the influence of previous environment on initial orientation behavior during the flight, the ability to adapt to weightlessness and the nature and relative importance of the cues employed in adaptation, and the effect of exposure in flight on the ability to orient after return to a one-g environment. Initial observations of orientation were lost because of an improperly seated camera magazine. Subsequent observations on mission days 6 to 9 showed looping activity similar to that observed on the Skylab 3 mission. Single-frame analysis of the flight films indicate that, by day 6, the fish were partially habituated and were largely orienting belly to the wall or back to the camera. Looping appeared to occur only after disturbance of the flight package. The data suggest that sighted controls (compartment 1) and blinded controls (compartment 5) showed a greater tendency to loop than those reared in the presence of specific visual environments. Fish in compartment 4 died of unknown causes before the end of the mission; hence, observations on these should be suspect. Although numerical trends seem to suggest some effect of visual conditioning on adaptation, analysis of the data (table 18-II) indicates no statistically significant difference among treatments.

*Recovery.*—Upon opening of the flight package 6.5 hours after splashdown, juvenile fish exhibited

TABLE 18-II.—Effects of Visual Preconditioning on Adaptation as Measured by Numbers of Fish Looping Over 4 Days of Observation

Compartment	Treatment	No. of fish looping	Total fish	Proportion of looping fish	Time filmed, sec.	Value of F	
						Calculated (a)	Tabulated (b)
1	Normal control	10	20	0.50	41	--	--
2	Vertical bar acclimated	8	20	.40	78	1.39	2.28
3	Horizontal bar acclimated	5	20	.25	91	2.56	2.77
4	Black overhead acclimated	2	14	.14	82	4.12	5.80
5	Blinded	11	17	.65	102	1.11	2.07

<sup>a</sup>Compared to controls.

<sup>b</sup>The significance level is 5 percent.

typical fright-diving responses. After recovery from their initial fright, most fish swam belly down in a nearly normal position. No marked impairment of the vestibular function could be deduced from the spontaneous swimming pattern. Slight differences of behavior compared to the behavior of control fish were observed. During the first hours after space flight, the experimental fish spent more time at the bottom of the bags or at the bottom of the tank in the test drum than did the controls. The specific density of the experimental juvenile fish seemed slightly increased compared to the controls, as was deduced from the faster sinking rate between movements and the steeper angle of attack during periods of horizontal swimming. However, these differences were small compared to the control fish, and further single-frame analysis is required to determine whether this observation is statistically significant. Investigation of the development of the swimming bladders in the juvenile fish that were fixed for histological examination would be interesting and might confirm the hypothesis for this behavior.

*Striped-drum test.*—The first striped-drum tests of the experimental fish were conducted approximately 6.5 hours after recovery. Tests were performed with fish from compartments 1, 2, and 3; the fish in compartment 4 were dead on recovery. The fish of compartment 5 were blind and therefore could not be optokinetically stimulated. The juvenile fish at this time showed no significant change of vestibular behavior when compared to the behavior of the control fish. Tests of the recovered fish in the vertical drum with horizontal movement of the stripes showed that all tested fish followed the horizontal stripe movement well and swam in continuous circles around the axis of the drum. From this observation, it can be concluded that the optomotoric function in the juvenile fish was undamaged. However, the juvenile fish exhibited a slight tendency, only during the first test, to follow less well the movement of the vertical stripes than did the controls. Because these changes were below the significance level of the method, it can only be concluded that the otolithic system was essentially intact and operational in the recovered fish.

*Parabolic flight tests.*—Several parabolic flight

tests were made with juvenile normal *Fundulus* fish, control fish of different ages, and flight juvenile fish. The tests showed that during the 25-second weightless periods, most *Fundulus* fish display the looping behavior at one time or another, as described earlier by von Baumgarten et al. (ref. 18-5).

Looping in weightlessness usually occurs when the fish start to swim forward spontaneously. Fish that are at rest or are trapped in corners or folds of the aquarium or bag often do not loop. The rate of looping typically increases during one looping episode. The direction of looping is mostly forward but it can be sideways in some fish. When the aircraft increases velocity during the parabola and the air bubbles in the fish tank indicate the presence of a longitudinal (X-axis) gravito-inertial vector, the fish turn their bellies into the direction of the gravitational pull and loop sideways.

Some fish occasionally roll around the longitudinal axis instead of looping. The roll direction of these "twisters" can change from clockwise to counterclockwise; however, one direction was always prevalent for any one fish. The opposite direction of roll usually started when the original roll was suddenly stopped by an obstacle (folds or corners of fish container). A possible explanation for the alternating direction of roll would be that in weightlessness the first roll movement starts because of a weight difference (imbalance) between the two utricular otoliths. The compensating impulses, which allow the proper equilibrium on the ground, would cause an imbalance in weightlessness. A sudden stop of such a roll movement would cause postrotational effects in the semicircular system and consequently would be followed by temporary counter-rotation of the fish.

The experimental juvenile fish tested in parabolic aircraft flight 4 days after recovery looped as much as the control fish. It can be concluded from this that after 4 days on the ground, there were no "savings" preserved in these fish that would allow them to swim more normally in weightless conditions.

*Light-orientation tests.*—The results of light-orientation tests on the juvenile fish are presented in table 18-III as the group means of the roll angles for the light orientations. The C-I group was omit-

TABLE 18-III.—Group Responses to Light-Orientation Tests of Juvenile *Fundulus heteroclitus*

Group	N <sup>a</sup>	Roll angle about body axis, deg				
		Trial 1	Trial 2	Trial 3	Trial 4	Mean
Left						
A	7	34.3	27.9	36.4	−10.7	22.0 ± 19.2
C-II	12	12.1	34.6	22.5	30.4	24.9 ± 8.6
C-III	6	23.3	2.5	35.8	35.8	24.4 ± 13.6
Right						
A	7	−8.6	7.1	−21.4	−20.7	−10.9 ± 12.6
C-II	12	−26.2	−23.8	−7.9	−18.3	−19.1 ± 7.1
C-III	6	−3.3	−39.2	−16.7	−29.2	−22.1 ± 13.5

<sup>a</sup>Number of samples.

ted because only four juveniles survived and two died midway through the test period. The roll angles were highly variable for all groups, and the mean values for each group for four trials were similar. There were no significant differences. The ASTP flight juveniles were slightly more variable, particularly for 90° light orientations on the right side of the fish, but this deviation is mentioned only for the sake of data completeness.

The light orienting of the *Fundulus heteroclitus* appears to be much more stable in adults than in juveniles.<sup>1</sup> Several competing responses in the juvenile *Fundulus* apparently increase the difficulty of obtaining a reliable measure of the roll orientation. It is possible to place an adult in a clear plastic cylinder and position its body perpendicular to the light rays for 30 minutes, thereby enabling observation of a slow roll to a final angle toward the light. However, the juvenile will frequently bend itself into a U-shape or become wedged upside down in the same type of tube.

On mission day 9, an attempt was made to measure the light-orienting responses of the groups of juveniles in each of the five compartments. The lights were turned off in the spacecraft, and the camera photolight was held at a 45° angle from the camera line of sight to the fish packages. The crewmembers reported that the

fish did not orient themselves with respect to light direction but seemed to be aligning their bodies with respect to the "bottom" of the fish packages adjacent to the spacecraft wall. It is difficult to believe that light direction was not the major influence for orientation while the fish were in a weightless environment, but it may be possible that a contrast gradient due to the cards in the "bottom" of the package or some type of tactile reference was the major influence. The crew reported that this light-orientation experiment was photographed but this cannot be confirmed from present techniques for viewing the flight films.

*Otolith structure.*—Because of the negligible effects of flight on orientation capability of either juveniles or hatchlings, it was considered unlikely that otolith degeneration would have occurred to a measurable extent. However, because of the availability of the material and the belief that some information on the otolith form could be useful in future studies, limited examinations were conducted.

Because the standard staging tables identify fish only during the embryonic period (while contained within the egg membranes), fish for baseline experiments were selected by size rather than developmental stage. The otoliths of *Fundulus* hatchlings that were less than 10 mm in body length; swimming fry of 20, 30, and 40 mm; juvenile fish of 50, 60, and 70 mm; and mature adults of 80, 90, and 100 mm were dissected from

<sup>1</sup>Hoffman, unpublished observations.



living animals and fixed immediately in cold 2.5 percent glutaraldehyde fixative in standard incubation medium for 24 hours. Following a wash in distilled water, they were postfixed for 1 hour in 1 percent osmic acid. The washed and dried specimens were coated with evaporated gold-palladium and examined at low to moderate magnification in a scanning electron microscope.

Following the return of the flight fish, the otoliths were compared by the established procedure with otoliths from control animals maintained on Earth. Light micrographs of vestibular systems dissected from the right sides of flight and control juveniles are shown in figure 18-3.

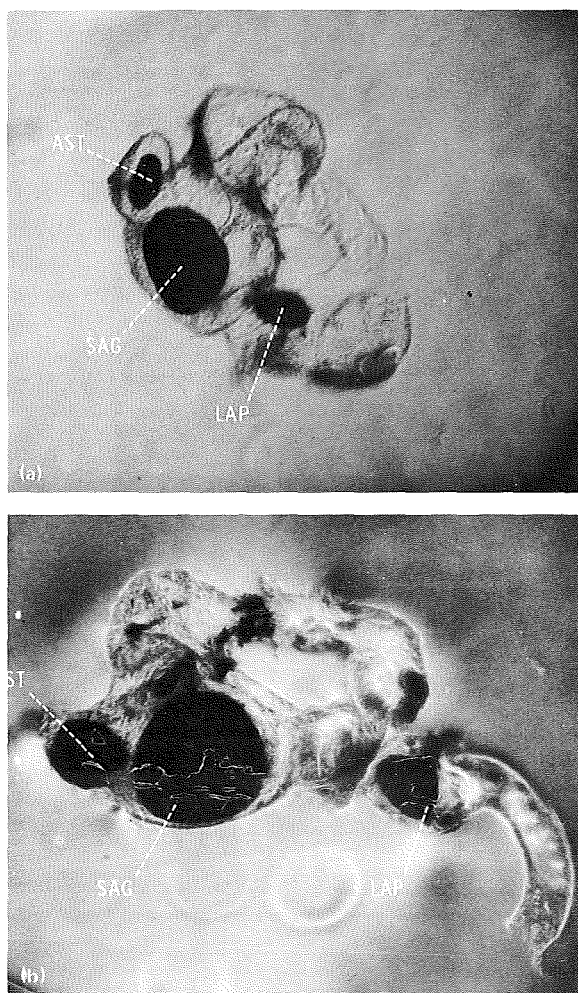


FIGURE 18-3.—Light micrographs of dissected vestibular tissues from the right sides of fish. LAP, lapillus; SAG, sagitta; AST, asteriscus (52 $\times$ ). (a) Control fish. (b) Flight fish.

Both fish were 12 mm long. The large (sagittae) stones are shown as they appear at 200 $\times$  magnification under a scanning electron microscope (figs. 18-4(a) and 18-4(b)). The medial surfaces shown are characteristically grooved and sculptured; the lateral surfaces (not shown) are smooth with concentric "growth rings." In larger

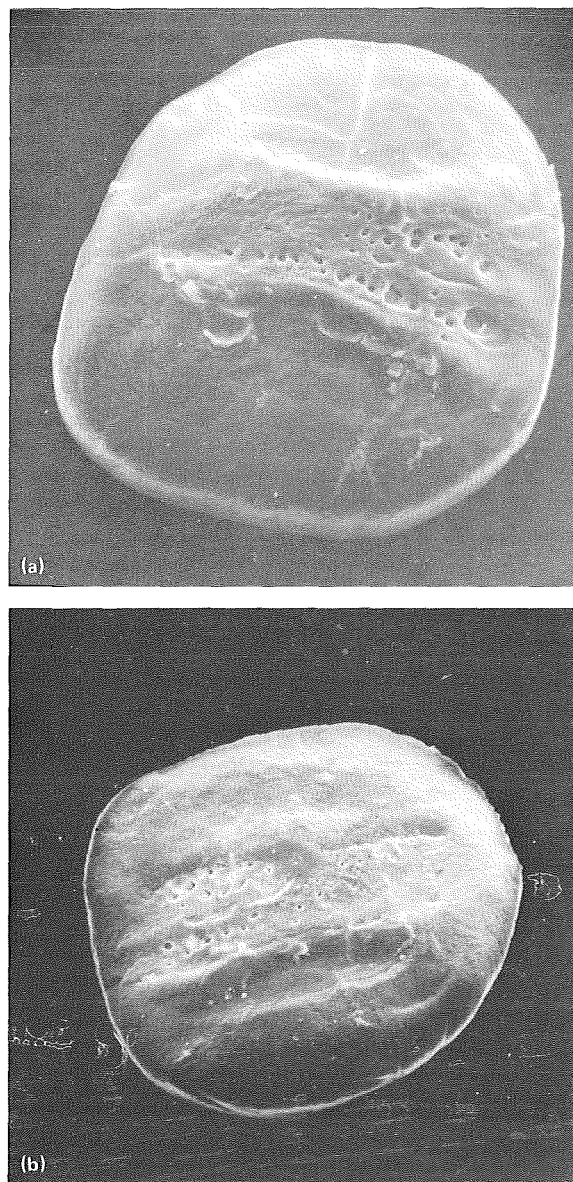


FIGURE 18-4.—Scanning electron micrographs of sagittae. (a) Medial view of left sagitta of flight juvenile (200 $\times$ ). (b) Medial view of right sagitta of controlled juvenile (200 $\times$ ). (c) Medial groove of a 30-mm-long juvenile (1240 $\times$ ).



FIGURE 18-4.—Concluded.

fish, "crystalline" projections appear in the groove as shown in the scanning micrograph of a stone from a 30-mm-long fish examined during baseline studies (fig. 18-4(c)). None of the scanning electron microscopic examinations revealed recognizable differences in size, shape, or surface structure between flight and control juveniles.

### Embryo Development

*Development rate.*—It was recognized at the outset that lack of synchrony in development could present problems in the interpretation of results. Although fertilization of all embryos in a given age group occurred within the space of a few minutes, variability in development rate was such that two to three distinguishable developmental stages were represented in this group at any given time.<sup>2</sup> Thus, it was possible to know only as an average the developmental stage at which each age group was exposed. Theoretically, this point could have been quite important; however, operational constraints prevented the selection and flight exposure of specific developmental stages; and, for

the purposes of this particular experiment, the practical significance seems to have been relatively small.

Hatching, similar to development, is a variable affair. A population of embryos that theoretically has developed more or less uniformly to the point of hatching at between 9 and 15 days will, if left undisturbed, emerge a few at a time over a period of several weeks. Under such circumstances, the uniform sampling and testing of experimental animals would have been a tedious and complicated operation at best. It was found, however, during the course of preflight baseline testing, that if fully developed but sporadically emerging embryos were subjected to a short period (5 to 20 minutes) of vigorous agitation, all individuals apparently physiologically ready to emerge would do so within a period of approximately 20 minutes following cessation of the agitation. Conversely, embryos grown under conditions of continuous agitation would commence wholesale emergence within a short time after cessation of agitation.<sup>3</sup> The circumstantial evidence suggests that one strong stimulus to emergence is a change in the pattern of vestibular stimulation.

By employing the periodic shaking technique, the majority of an age group could be induced to emerge over a period of a few days by a regimen consisting of 20 minutes of vigorous agitation of the culture vessel every 24 hours. (Typically, this was accomplished in 100-mm petri plates on a rotary shaker at 100 excursions per minute.) Thus, the process of hatching could be compressed into a minimum time and, in addition, a means was available for positively assessing the end point of embryonic development in terms of ability to emerge.

A real count of hatching was rendered impossible by the sampling of unhatched eggs for microscopic study, but a relatively close approximation was obtained by applying the formula

$$T_n = T_{n-1} + O_n + \frac{O_n}{R_n + O_n} (F_n - S_n) \quad (18-1)$$

<sup>2</sup>Boyd, unpublished observations.

<sup>3</sup>Scheld and Boyd, unpublished observations.

where  $T_{1,2,3,...n}$  is the theoretical cumulative hatch for days 1,2,3,... $n$ ;  $O_{1,2,3,...n}$  is the observed hatch on days 1,2,3,... $n$ ;  $R_{1,2,3,...n}$  is the total unhatched individuals remaining after shaking on day 1,2,3,... $n$ ;  $F_{1,2,3,...n}$  is the sum of unhatched eggs fixed up to the day selected; and  $S$  is the sum of the fixed individuals (eggs) that had been calculated as theoretically hatched up to the day in question.

These data were analyzed by methods described by Baky (ref. 18-11) for analysis of binomial data. Comparisons were made of ultimate hatch and of 75 percent hatch time as an index of hatching rate. The results of these comparisons are summarized in tables 18-IV and 18-V.

There is some small possibility that the atmospheric environment of the spacecraft may

have been more favorable for development, as indicated by slightly higher hatch in the C-I and C-III treatments that attempted to duplicate spacecraft environments. In general, however, the final hatch of the flight group was significantly different from the pooled controls at the 5-percent level for at least the youngest age groups (table 18-IV). Pooled 66-hour controls missed significance by only a very small margin. If ultimate development can be considered an index of health, and anomaly rates are not different, then it seems reasonable to conclude that flight has had some beneficial effect on health of the organisms. And if the assumption is made that onset of ability to hatch is an index of overall development rate, then it must be concluded that there was a definite

TABLE 18-IV.—Percent Final Hatch for Flight, C-I, C-II, and C-III Groups Over the Five Development Stages Exposed to Zero-g Conditions and Allowed to Continue Development for the Duration of the 9-Day Mission

Development stage, hr	Hatchability, percent			
	Flight	C-I	C-II	C-III
32	<sup>a</sup> 100	94	96	<sup>b</sup> 94
66	<sup>a</sup> 97	93	93	<sup>a</sup> 96
128	<sup>a</sup> 99	<sup>a</sup> 100	88	<sup>a,b</sup> 98
216	<sup>a</sup> 100	<sup>a</sup> 98	92	<sup>a,b</sup> 98
336	100	98	98	98

<sup>a</sup>Significant at the 5-percent level.

<sup>b</sup>Pooled controls that were significantly different.

TABLE 18-V.—Time to Achievement of 75 Percent Hatch for Flight, C-I, C-II, and C-III Groups Over the Five Development Stages Exposed To Zero-g Conditions and Allowed to Continue Development for the Duration of the 9-Day Mission.

Development stage, hr	Time to 75 percent hatch, days			
	Flight	C-I	C-II	C-III
32	<sup>a</sup> 15	23	26	21
66	<sup>a</sup> 15	23	26	21
128	<sup>a</sup> 15	25	27	24
216	18	19	19	22
336	23	23	24	25

<sup>a</sup>Significant at the 1-percent level.

trend toward a higher rate of development in flight-exposed eggs. The trend is quite apparent in plotted cumulative hatching curves (fig. 18-5) and is statistically significant at the 1-percent level when 75 percent hatching times are compared.

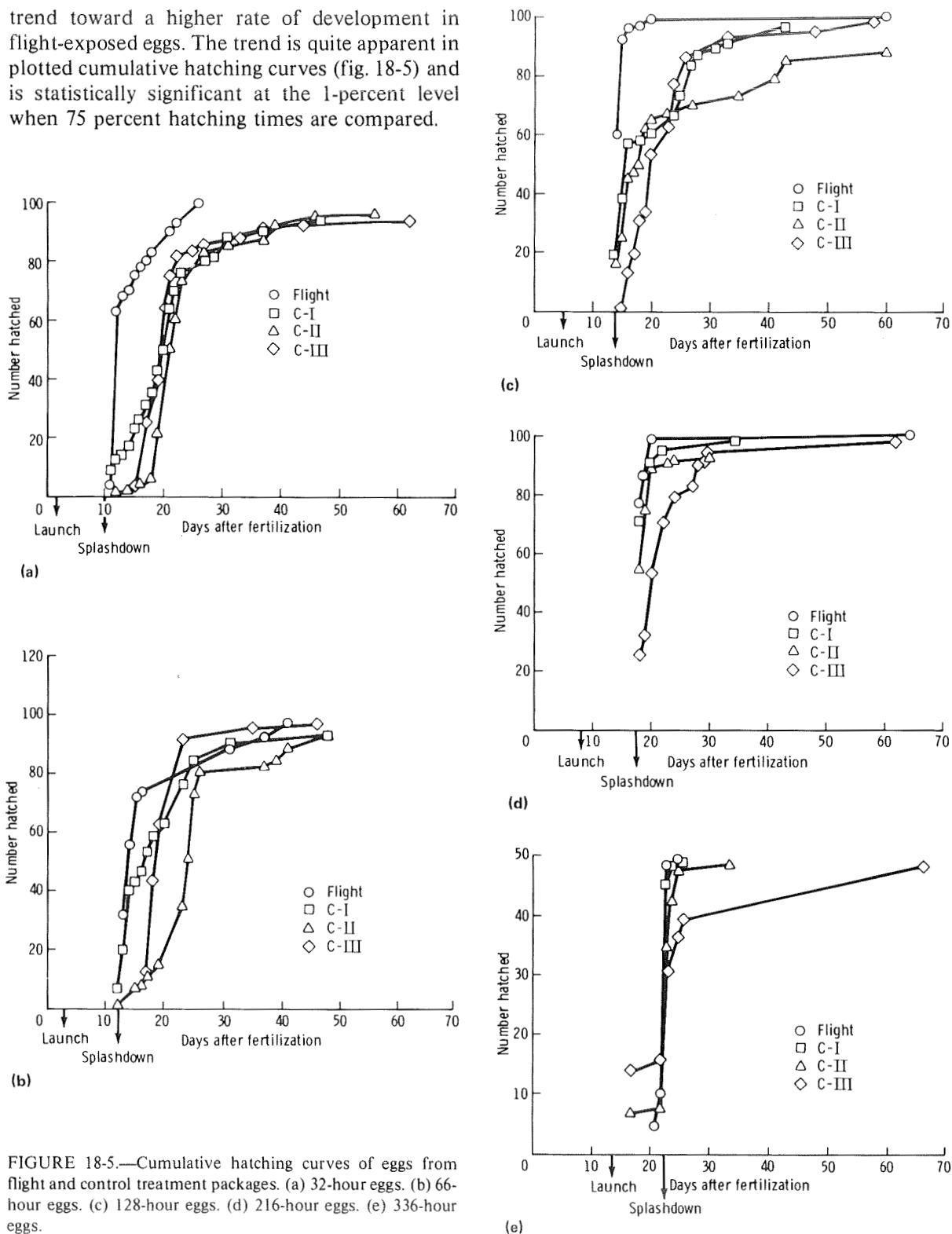


FIGURE 18-5.—Cumulative hatching curves of eggs from flight and control treatment packages. (a) 32-hour eggs. (b) 66-hour eggs. (c) 128-hour eggs. (d) 216-hour eggs. (e) 336-hour eggs.

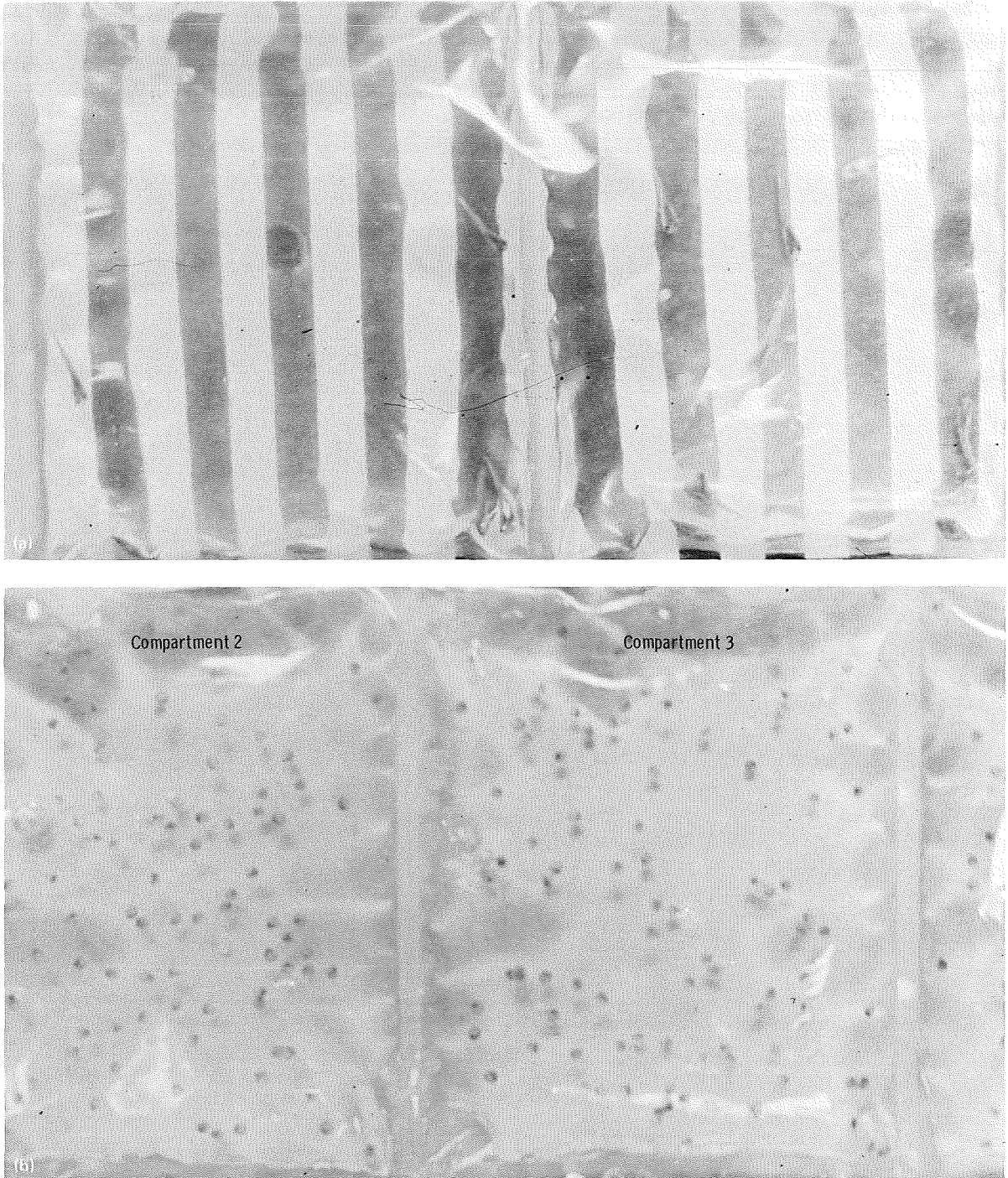


FIGURE 18-6.—Photographs of flight and control animals taken mission day 8. (a) Flight juveniles that were preconditioned in a vertically striped environment are in compartment 2, those preconditioned in a horizontally striped environment are in compartment 3. (b) Flight 66-hour eggs in compartment 2 and 128-hour eggs in compartment 3. (c) Flight 216-hour eggs in compartment 4 and 336-hour eggs in compartment 5. (d) Control III 216-hour eggs in compartment 4. (e) Control III 336-hour eggs in compartment 5.



Similar observations of increased rate or efficiency of metabolic activity may have been made in Biosatellite II experiments; for example, the increased density of *Salmonella* growth (Experiment P-1135) (ref. 18-12) or increased *Tradescantia* flower production (Experiment P-1123) (ref.

18-13). Factors related to the promotion of more favorable conditions for dissipation of toxic metabolites or more efficient utilization of oxygen by the very even distribution of eggs within the available fluid volume (fig. 18-6) may have been solely responsible. It seems possible, however,

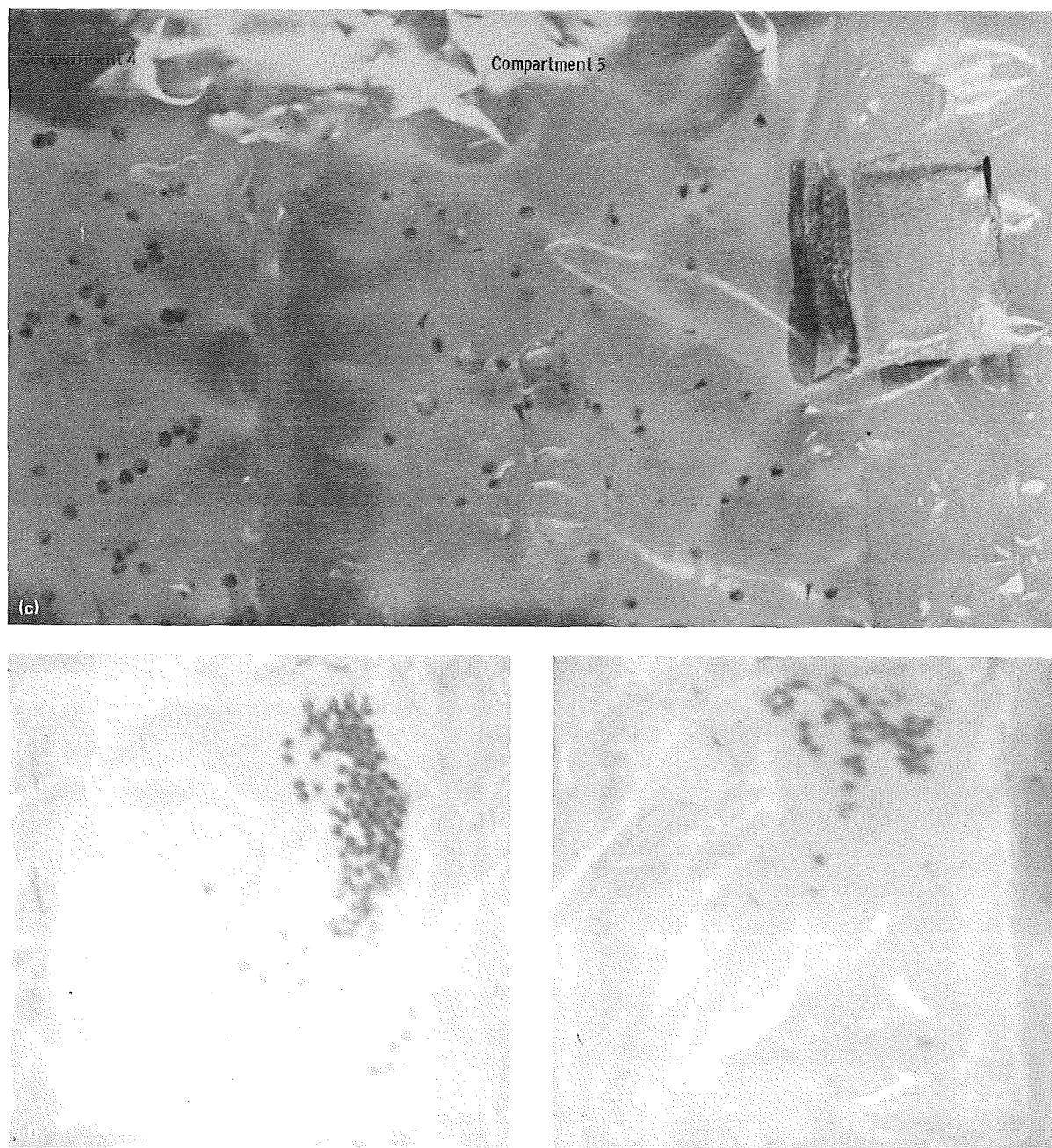


FIGURE 18-6.—Concluded.

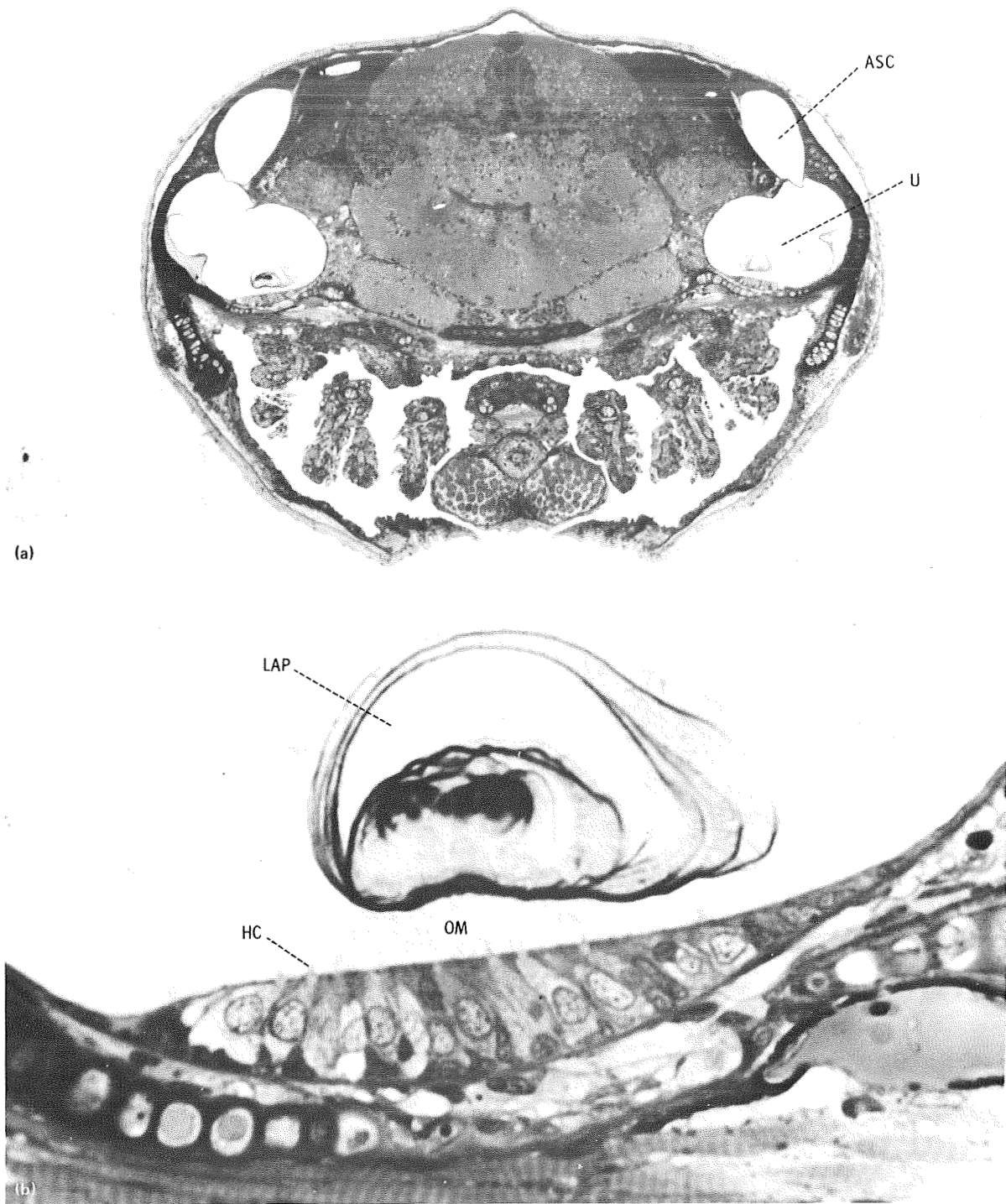


FIGURE 18-7.—Cross section of the head region of flight and control hatchlings at the level of the utricle (ASC, anterior semicircular canal; U, utricle; LAP, lapillus (utricular otolith); HC, hair cell, OM, otolithic membrane; arrow, metachromatic dense bodies). (a) Flight 128-hour sample at 20 $\times$  magnification. (b) Flight 128-hour sample at 200 $\times$  magnification. (c) Flight 128-hour sample at 200 $\times$  magnification. (d) Control I 128-hour sample at 200 $\times$  magnification.

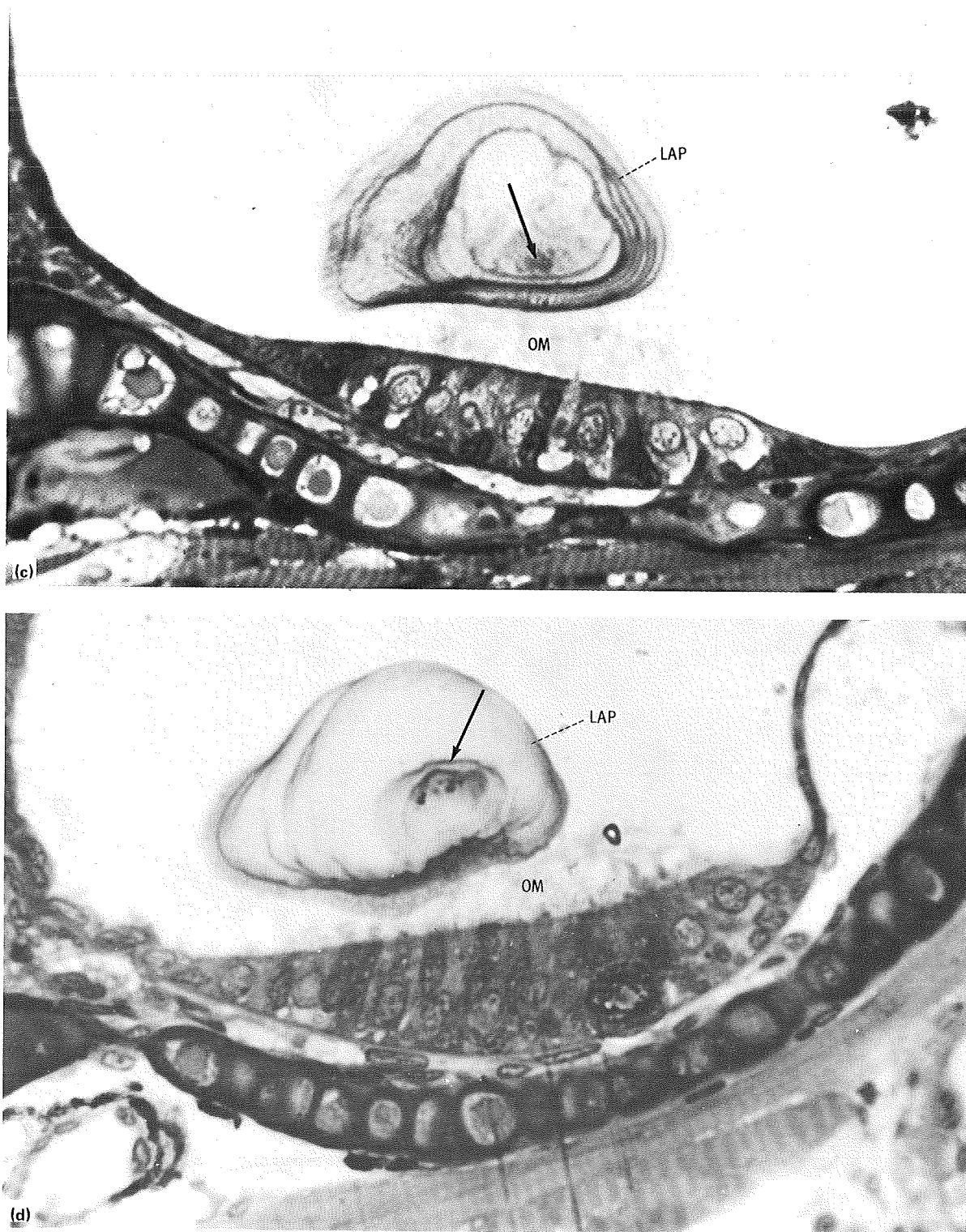


FIGURE 18-7.—Concluded.



that absence of the necessity to expend energy to maintain structural integrity against gravitational force could also impart a small but additively significant advantage in growth rate. Although a profound biological significance cannot be attached to this observation, it is worth noting as at least a possible indirect effect of zero-g conditions, which could have significance in the future for applied aspects of space flight.

*Microscopic examinations.*—Initial histological and ultrastructural analyses of the four oldest age categories (66 hour through 336 hour) have been completed, and no significant differences between flight and ground control treatments were detected in the embryological development of the central nervous system, the peripheral vestibular

apparatus, the eye, or the cardiovascular system. In all of these groups, the peripheral vestibular system developed fully with complete expression of the maculae of the sacculus and utricle (figs. 18-7 and 18-8). The statoliths of the sacculus (*lapillus*) and utricle (*sagitta*) followed normal sequence development, and the lagenal statolith (*asteriscus*) initiated development between posthatching days 4 and 6 in all groups (figs. 18-9(a) and 18-9(b)). Except for a decrease in the extent and content of the vitreous cavity, ocular development was judged to be normal (figs. 18-9(c) and 18-9(d)). Difficulties in maintaining the proper components within the fixative solution during the long preflight storage interval apparently contributed to osmotic collapse of the

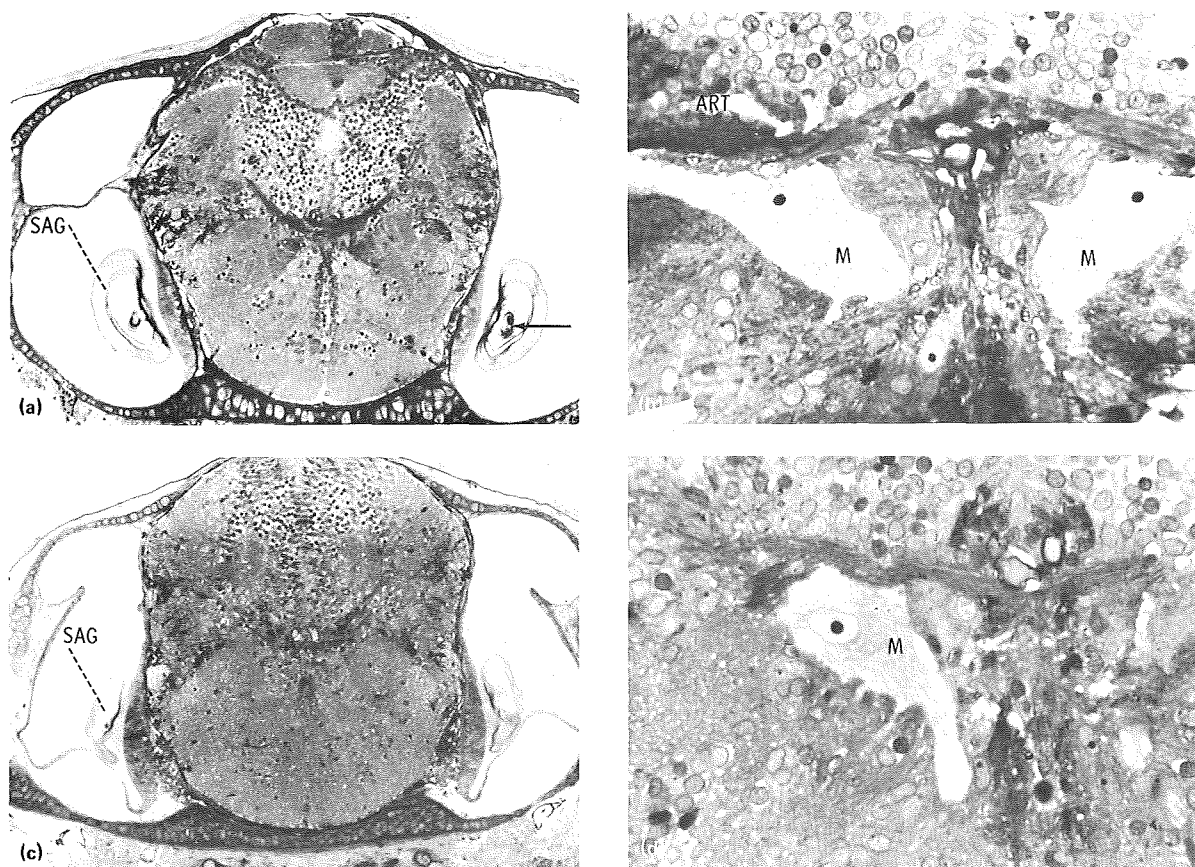


FIGURE 18-8.—Cross section of the head region of flight and control hatchlings at the level of the sacculus (SAG, sagitta (saccular otolith); M, Mauthner cell; ART, process artifact; arrow, metachromatic dense body). (a) Flight 128-hour sample at 23.8 $\times$  magnification. (b) Flight 128-hour sample at 90 $\times$  magnification. (c) Control 128-hour sample at 23.8 $\times$  magnification. (d) Control 128-hour sample at 90 $\times$  magnification.

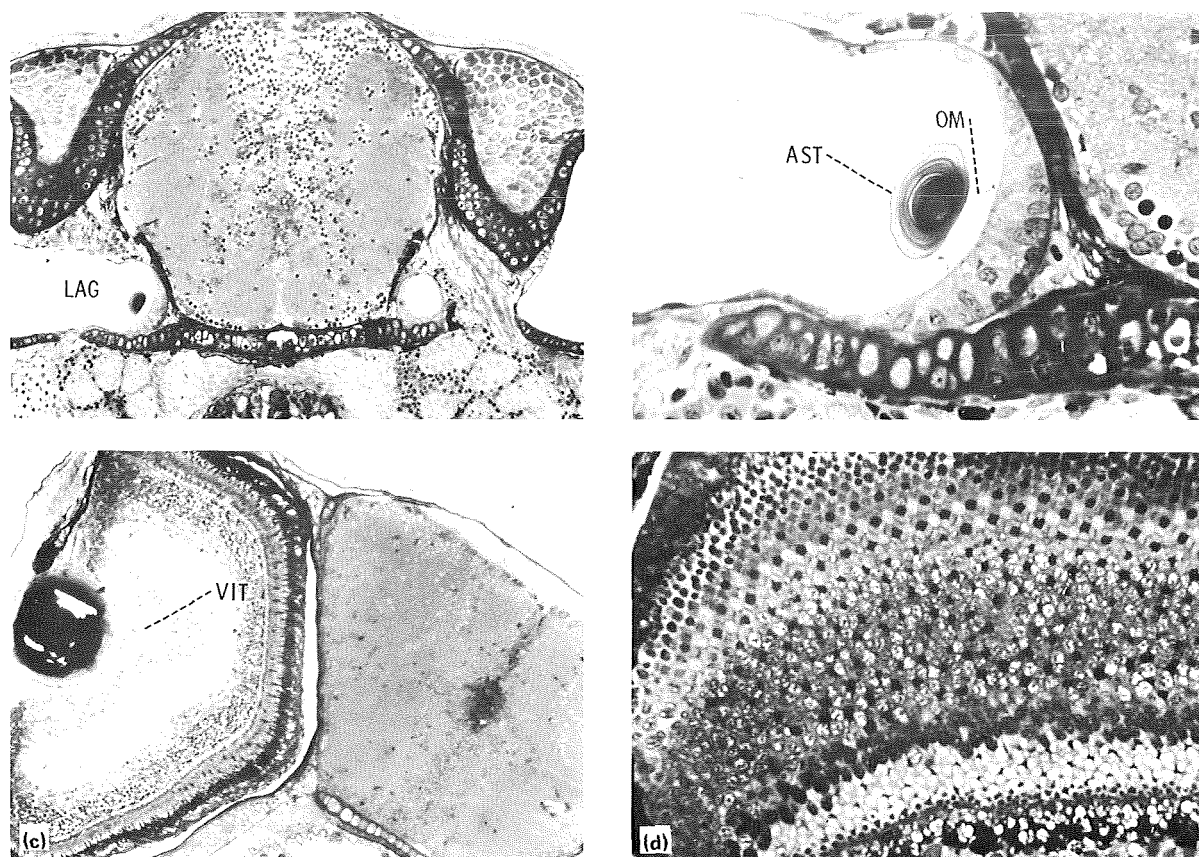


FIGURE 18-9.—Cross sections of the head regions of flight hatchlings at the level of lagena and the eye (LAG, lagena; AST, asteriscus (lagenar otolith); VIT, vitreous body; OM, otolithic membrane; ART, process artifact). (a) Flight 128-hour sample showing the lagena at  $24.4\times$  magnification. (b) Flight 128-hour sample showing the lagena at  $92\times$  magnification. (c) Flight 128-hour sample showing the eye at  $24.4\times$  magnification. (d) Flight 128-hour sample showing the retina at  $92\times$  magnification.

eyes during fixation and to pooling of plasma proteins in both experimental and control groups of animals. Ultrastructural analyses of the developing statoliths and sensory maculae have revealed no differences between matched groups of animals (figs. 18-10(a) and 18-10(b)). Both sustentacular and hair cells followed normal developmental parameters. Central projections and vestibular ganglia contained normal cellular complement and projection configuration. Cartilage development and calcification was identical in flight and control categories (fig. 18-10(c)).

Preliminary analysis of the specimens treated with tritiated thymidine at selected post-splashdown periods has also failed to reveal any significant alterations in the patterns of cellular

proliferation within the vestibular, ocular, or central nervous systems of the oldest stages flown. Cells of the ependyma and cortical neuroepithelium, the *planum semilunatum* of the maculae, and the *ora serrata* of the retina were heavily and consistently labeled in all groups. Further analysis of these animals is now underway to ensure statistical confidence in the morphological observations.

The youngest age category flown, 32 hours after fertilization, was at the mid-to-late gastrula stage at the time of lift-off and orbital insertion, and would be expected to reveal the most significant effects of such an experience. Analysis of these animals is still in progress.

Several factors must be pointed out with



FIGURE 18-10.—Electron micrographs of calcified areas in the vestibular region of flight and control hatchlings (CH, chondrocyte; FIB, fibrocyte; CAL CART, calcified cartilage; DB, metachromatic dense body; SAG, sagitta (saccular otolith)). (a) Saccular otolith of flight 128-hour sample at 6000 $\times$  magnification. (b) Saccular otolith of control 128-hour sample at 6000 $\times$  magnification. (c) Calcified cartilage of flight 128-hour sample at 32 000 $\times$  magnification.

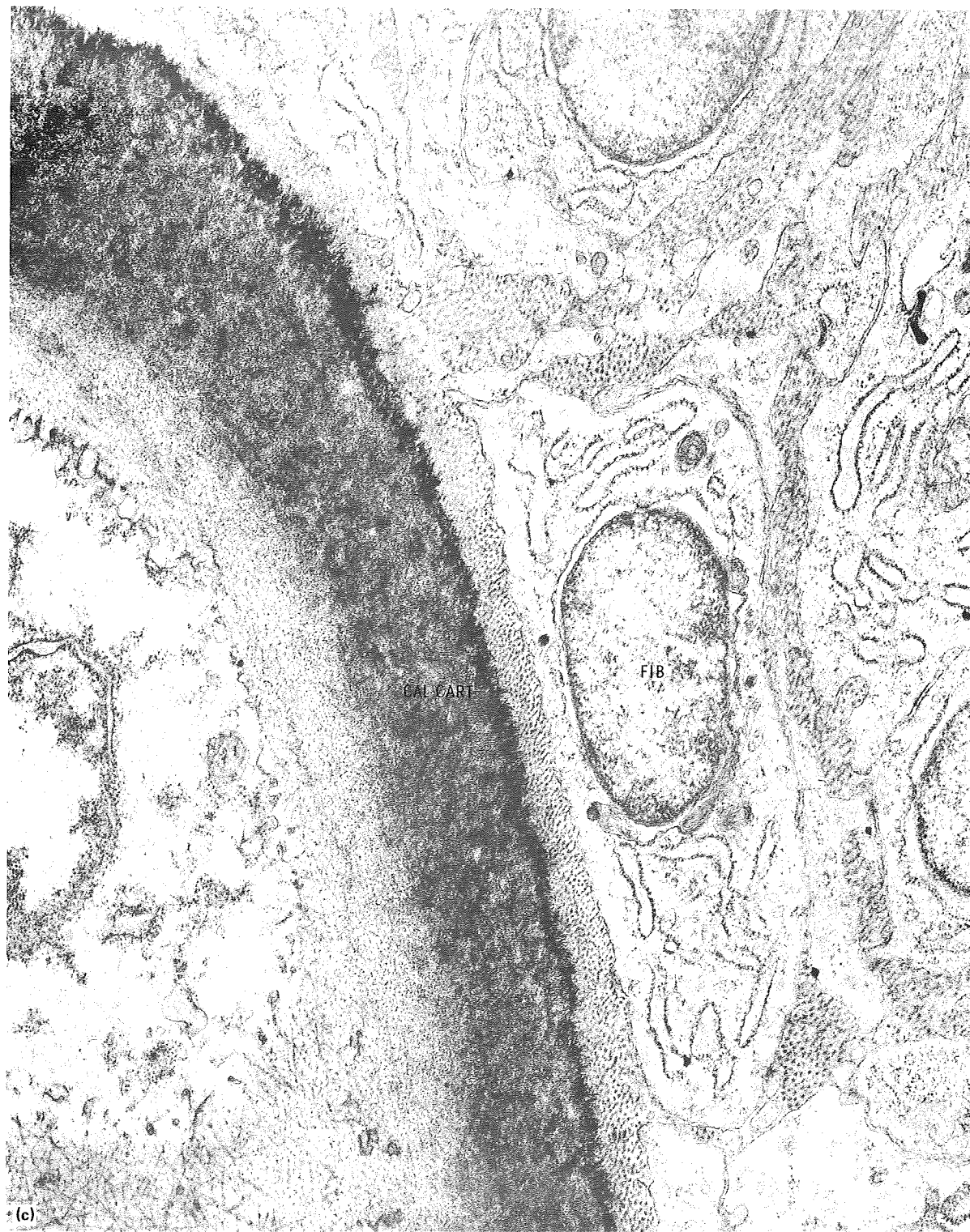


FIGURE 18-10.—Concluded.



respect to the normal development of the *Fundulus heteroclitus* embryos in this experiment. *Fundulus* eggs develop freely within a natural aquatic environment and as such are not dependent on a maternal-fetal interaction. Such a system would actually be facilitated by the conditions found during space flight in which the eggs are randomly dispersed throughout the aquarium and the diffusion and distribution of metabolites is assured. The necessity of packaging and transporting to launch site precluded the analysis of earlier, potentially more susceptible, stages of development. The earliest stages achievable were already mid-to-late gastrulae at the time of insertion, well past the prime sequence of most critical embryonic interactions with respect to vestibular initiation, retinal and lens inception, and central nervous system inductions. Finally, the duration of the mission (9.5 days) is a minimal-duration period of sensory deafferentation.

The foregoing factors should not detract, however, from the primary critical significance of the normal development of these embryos during conditions of space flight. They should, however, suggest the continuing need for a critical analysis of longer term earlier stage embryos as well as the need to extend these studies to a model system entailing maternal-fetal interactions.

*Vestibular behavior in flight.*—Theoretically, three out of the five age groups should have been capable of hatching in flight at some time during the 9-day mission. In fact, only approximately 20 percent of the oldest group (the 336-hour eggs) hatched during flight. The eggs of this group were fully developed but unhatched at the time of launch. The delayed hatching observed on Skylab 3 was thus confirmed. The probable reasons for delay have already been discussed in the preceding subsection. The observed reaction supports the theory that vestibular stimulation is a cue for emergence.

No looping behavior was observed in hatchlings on Skylab 3. This was originally interpreted as an indication of either the absence of a functional vestibular system or of complete habituation of the hatchlings. The 336-hour hatchlings that did emerge during flight exhibited occasional looping behavior, as reported by the crew. The fact that no looping of these animals was observed

in flight films would suggest that habituation of the hatchling fish might have been somewhat better than that of juveniles. Because no hatching occurred in any of the younger groups, it is still not possible to confirm or reject the Skylab observations. The 128-hour group would have been most similar to the Skylab animals.

*Recovery.*—Although little hatching occurred during flight, the stimulation of handling subsequent to splashdown, the agitation caused by movement of the packages during initial photography, and the standard stimulating shake were enough to cause wholesale emergence of all but the youngest group (fig. 18-5).

The control treatment groups, which had been maintained under static conditions, exhibited similar but less striking emergence patterns. As noted in the discussion of hatching rates, hatchlings exhibited a strong diving response. Testing on the rotating striped drum indicated normal reaction, with the possible exception of the 128-hour postshake hatchlings, which exhibited a slightly increased tendency to follow the stripes in the initial test only, suggesting a possible temporary hyposensitivity of the vestibular system.

Flight hatchlings exposed to short periods of weightlessness during parabolic flights at 5 days past recovery also exhibited looping behavior that was indistinguishable from that of the controls. Thus, whatever habituation might have been observed during exposure in flight was lost soon after return to a one-g environment.

*Postflight vestibular testing.*—At approximately 6 months of age, the hatchlings from the flight treatment group were subjected to a geotaxis test. The test consisted of placing each fish in a filled 500-ml graduated cylinder and measuring the amount of time spent in the upper half during a 2-minute interval. The test was administered three times to each fish in the 32-hour, 66-hour, and 128-hour groups after preconditioning under two separate light-dark cycles (12:12 and 16:8). The 32-hour flight fish were found to spend, on the average, 70 percent more time in the upper half of the graduated cylinder than did the control fish ( $p < 0.05$ ). There were no significant differences for the other two groups (table 18-VI(a)). For all three flight treatment groups there was a highly correlated relation ( $r = 0.85$ ) between the number

TABLE 18-VI.—Analysis of Geotactic Response in 6- to 8-Month Hatchlings From Flight and Control Treatment Groups for Four Variables<sup>a</sup>

(a) Comparison of treatment effects

Development stage, hr	L(1)		L		W		G	
	Apollo	Control	Apollo	Control	Apollo	Control	Apollo	Control
32	34.33	31.91	28.28	26.91	419	345	<sup>b,c</sup> 20.07	11.49
66	<sup>c</sup> 36.54	<sup>c</sup> 36.54	<sup>c</sup> 30.00	<sup>c</sup> 30.38	<sup>c</sup> 515	<sup>c</sup> 531	8.82	10.11
128	30.75	32.63	25.58	27.03	312	385	9.18	9.18

(b) Correlation analysis including a fifth variable  $n^d$

Variable	Apollo					Control				
	G	n	L(1)	L	W	G	n	L(1)	L	W
G	1.00	<sup>e,f</sup> 0.85	−0.53	−0.53	−0.56	1.00	<sup>f</sup> 0.12	−0.34	−0.32	−0.38
n	<sup>e,f</sup> .85	1.00	<sup>e</sup> −.79	<sup>e</sup> −.79	<sup>e</sup> −.83	.12	1.00	<sup>e</sup> −.88	<sup>e</sup> −.86	−.85
L(1)	−.53	<sup>e</sup> −.79	1.00	<sup>e</sup> 1.00	<sup>e</sup> .99	−.34	<sup>e</sup> −.88	1.00	<sup>e</sup> .99	<sup>e</sup> .97
L	−.53	<sup>e</sup> −.79	<sup>e</sup> 1.00	1.00	<sup>e</sup> .99	−.32	<sup>e</sup> −.86	<sup>e</sup> .99	1.00	<sup>e</sup> .94
W	−.56	<sup>e</sup> −.83	<sup>e</sup> .99	<sup>e</sup> .99	1.00	−.38	<sup>e</sup> −.85	<sup>e</sup> .97	<sup>e</sup> .94	1.00

<sup>a</sup>G, geotaxis; L(1), length; L, length without tail; W, weight.

<sup>b</sup>Significant; different from control.

<sup>c</sup>Significant; different from other stages.

<sup>d</sup>Number of fish per tank.

<sup>e</sup>Significant at the 5-percent level.

<sup>f</sup>Significant difference between flight and control fish.

of fish in a home tank and the geotaxis parameter under study (table 18-VI(b)). This correlation did not occur for control fish and cannot be explained in terms of any size differences.

The diving response is very strong in most *Fundulus heteroclitus* and, therefore, was considered to be a measure of whether or not the innate vestibular programming was modified by an exposure to null-gravity conditions during embryonic development. The finding of a behavioral difference in the 32-hour group was not unexpected, because behavioral testing is a sensitive measure of subtle effects of environmental influences. The 32-hour and 66-hour groups were considered more likely to be affected in a minor way than other developmental stages, because the vestibular apparatus was not completely formed at the time normal gravity influence was removed. The correlation between population size and orientation behavior was, however, unexpected. Considering this finding and the observations that the geotaxis parameters for experimental fish, but not control fish, tended to vary with the photoperiod (although not significantly), there is an indication

that the experimental fish are more sensitive to environmental factors (at least for the case of crowding and photoperiod). These findings are minor, but further investigation is needed to ensure that exposure to weightlessness during critical periods of development does not produce any profound effects.

## ACKNOWLEDGMENTS

The investigators wish to acknowledge the significant contributions made to this research by Thomas J. Price and his associates of the National Marine Fisheries Service, Atlantic Estuarine Research Center, Beaufort, North Carolina, and by Thomas B. McKee and his associates of the Nutrition-Physiology Section, Fish Commission, Clackamas, Oregon. Without their interest and assistance, respectively, in trapping wild *Fundulus* breeding stock and in providing the diet for the breeding colony, the *Fundulus* research program and the resultant flight experiments would not have been possible.

## REFERENCES

- 18-1. Armstrong, Philip B.; and Child, Julia Swope: Stages in the Normal Development of *Fundulus heteroclitus*. Biol. Bull., vol. 128, no. 2, Apr. 1965, pp. 143-168.
- 18-2. Oppenheimer, Jane Marion: The Normal Stages of *Fundulus heteroclitus*. Anatomical Record, vol. 68, no. 1, Apr. 1937, pp. 1-15.
- 18-3. Trinkaus, J. P.: *Fundulus*. Methods for Study of Development, N. K. Wessells and F. Wilt, eds., Thomas Y. Crowell (New York), 1967, pp. 113-122.
- 18-4. Boyd, John F.; and Simmonds, Richard C.: Continuous Laboratory Production of Fertile *Fundulus heteroclitus* (Walbaum) Eggs Lacking Chorionic Fibrils. J. Fish. Biol., vol. 6, no. 4, 1974, pp. 389-394.
- 18-5. Von Baumgarten, R. J.; Simmonds, R. C.; Boyd, J. F.; and Garriott, O. K.: Effects of Prolonged Weightlessness on the Swimming Pattern of Fish Aboard Skylab 3. Aviation, Space and Environmental Medicine, vol. 46, no. 7, July 1975, pp. 902-906.
- 18-6. Von Holst, E.: Über den Lichtrackenreflex bei fischen. Publ. Staz. Zool. Napoli., vol. 15, 1935, pp. 143-158.
- 18-7. Pfeiffer, Wolfgang: Equilibrium Orientation in Fish. Int. Rev. Gen. Exp. Zool., vol. 1, 1964, pp. 77-111.
- 18-8. Matis, J. H.; Kleerekoper, H.; and Gensler, P.: Non-Random Oscillatory Changes in Orientation of the Goldfish (*Carassius auratus*), in an Open Field. Anim. Behav., vol. 22, no. 1, 1974, pp. 110-117.
- 18-9. Matis, J. H.; Childers, D. R.; and Kleerekoper, H.: A Stochastic Locomotor Control Model for the Goldfish (*Carassius auratus*). Acta Biotheor., vol. 23, no. 2, 1974, pp. 45-54.
- 18-10. Kleerekoper, H.; Matis, J. H.; Timms, A. M.; and Gensler, P.: Locomotor Response of the Goldfish to Polarized Light and Its e-Vector. J. Comp. Physiol., vol. 86, no. 1, 1973, pp. 27-36.
- 18-11. Baky, A.: Applied Statistical Tests for Binomial Laboratory Data With Concentration on Hatchability of Fish Eggs in Space Experimentation. Northrop Services Inc., Report No. 1976-1.
- 18-12. Mattoni, R. H. T.; Ebersold, W. T.; et al.: Induction of Lysogenic Bacteria in the Space Environment. The Experiments of Biosatellite II, Joseph F. Saunders, ed., NASA SP-204, 1971, pp. 309-324.
- 18-13. Sparrow, A. H.; Schairer, L. A.; and Marimuthu, K. M.: Radiobiologic Studies of Tradescantia Plants Orbited in Biosatellite II. The Experiments of Biosatellite II, Joseph F. Saunders, ed., NASA SP-204, 1971, pp. 99-122.





# 19. Electrophoresis Technology

## Experiment MA-011

*R. E. Allen,<sup>a†</sup> G. H. Barlow,<sup>b</sup> M. Bier,<sup>c</sup> P. E. Bigazzi,<sup>d</sup> R. J. Knox,<sup>e</sup> F. J. Micale,<sup>f</sup>  
G. V. F. Seaman,<sup>e</sup> J. W. Vanderhoff,<sup>f</sup> C. J. Van Oss,<sup>d</sup> W. J. Patterson,<sup>a</sup>  
F. E. Scott,<sup>a</sup> P. H. Rhodes,<sup>a</sup> B. H. Nerren,<sup>a</sup> and R. J. Harwell<sup>a</sup>*

### ABSTRACT

Experiment MA-011, Electrophoresis Technology, was designed to test electrophoresis hardware that would continue the development of technology for electrophoretic separation of materials in the near-zero-g environment of space. Experimental difficulties identified during the Apollo 14 and Apollo 16 electrophoresis demonstrations, if not successfully eliminated, would have severely limited any future separations by electrophoresis of biological materials in space.

The experimental hardware generally functioned as planned. Frozen live cells were successfully transported into space, electrophoretic processing was performed, and viable cells were returned to Earth. A separation of the three types of fixed red blood cells (rabbit, human, and horse) was demonstrated. The human lymphocytes, however, showed no apparent migration. Problems relating to this experiment will be discussed in detail in this report.

The separation of human kidney cells produced the most exciting data. Analysis shows

electrophoretic separation throughout the entire column with at least four bands of viable cells. The isotachopheresis experiment definitely demonstrated the isotachopheretic separation of biological cells in a near-zero-g environment.

### INTRODUCTION

The Electrophoresis Technology Experiment demonstrated the concept of static free-fluid electrophoresis in the unique environment of space and verified electrophoresis experiment concepts by operation in this environment. The objectives were as follows:

1. To conduct engineering and operational tests of a space-rated static electrophoresis separation apparatus
2. To further current research efforts through separation of similar cellular species
3. To reduce or eliminate electro-osmosis through the application of a low zeta potential coating to the inner surfaces of the columns
4. To apply biological samples precisely without perturbing the subsequent electrophoresis
5. To maintain viable biological samples during all phases of the experimental procedure
6. To demonstrate isotachopheresis of red blood cells in space

The experiment equipment consisted of four major elements: (1) an electrophoresis unit (EU), (2) a cryogenic freezer (CF), (3) eight experiment columns (six electrophoresis, two isotachopheresis), and (4) eight sample insertion slides.

---

<sup>a</sup>NASA George C. Marshall Space Flight Center.

<sup>b</sup>Abbott Laboratories, Chicago, Illinois.

<sup>c</sup>Veterans Administration Hospital, Tucson, Arizona.

<sup>d</sup>State University of New York, Buffalo, New York.

<sup>e</sup>University of Oregon Health Sciences Center, Portland, Oregon.

<sup>f</sup>Lehigh University, Bethlehem, Pennsylvania.

<sup>†</sup>Principal Investigator.

The following biological materials were contained in the sample slides for the eight experiment stages.

1. Columns 1 and 5, three species of fixed red blood cells: rabbit, human, and horse

2. Columns 2 and 6, human peripheral blood lymphocytes

3. Columns 3 and 7, human fetal kidney cells

4. Column 4 (isotachophoresis), fixed rabbit and human red blood cells; column 8, (isotachophoresis), fresh rabbit and human red blood cells

To perform the experiment, a crewmember removed an electrophoresis or isotachophoresis column from its storage location and installed it in the EU. Fluid couplings were secured to each electrode chamber of the electrophoresis columns only. The slide containing a specific frozen sample was next removed from the cryogenic freezer and inserted into the column. A camera mounted on the EU cover photographed critical control positions and digital readouts during each column operation. Following each electrophoresis separation, the electrophoresis columns were frozen by the thermoelectric (TE) module and then removed from the cradle. The crewman then quickly removed each electrode chamber from the frozen columns and placed the column in the CF for return to Earth. The isotachophoresis columns were neither frozen nor returned but only photographed in orbit during their operation.

## BACKGROUND

### Electrophoresis

Most biological materials, when dissolved or suspended in a selected aqueous medium, have a characteristic electric charge, and the migration velocity per unit electric field strength (defined as the electrophoretic mobility of the material) is thus fixed (ref. 19-1). If the mobility difference between biological species is small, separation can be enhanced by increasing the length of the column. Electrophoresis can be conducted in liquid media, or free solutions, but problems arise because of disturbances in the bulk of the fluid. Two major causes of these disturbances are sedi-

mentation of the particles or solute being separated and thermal convection generated by Joule heating of the column during electrophoresis. Although various techniques have been developed to overcome these problems on Earth, the elimination of gravity-induced sedimentation and thermal convection can be accomplished best in the near-zero-g environment of space.

Electrophoresis in a free fluid was first demonstrated in space during the Apollo 14 mission. Three materials of different molecular weight, deoxyribonucleic acid (DNA), hemoglobin, and soluble dyes, were to be photographed periodically during electrophoresis in 10-cm (4 in.) long by 0.64-cm (0.25 in.) diameter cylindrical columns. Before operation of the apparatus, the sample materials were isolated in small cavities in a plastic slide that was arranged for insertion in a slot intersecting the separation columns. The experiment was initiated by pushing the slide so that the sample cavities coincided with the separation columns. The diameter of the sample cavity was made slightly smaller than the column diameter so that electrophoresis of the sample would occur away from the walls, where electro-osmotic streaming would be less intense.

Particular problems encountered during the demonstration included a misaligned sample insertion assembly that injected the samples near the column walls, poor photography from a handheld camera, and bacterial degradation of the DNA and hemoglobin because of the long storage time. However, a separation was measured between two dyes, and operation of the fluid and electrical systems was normal. The overall results indicated the validity of fluid electrophoresis investigation; therefore, plans were made and apparatus was developed for a second demonstration during the Apollo 16 mission.

The Apollo 16 electrophoresis demonstration was performed using the basic operating elements of the Apollo 14 demonstration, but a nonbiological sample material, polystyrene latex, was used (ref. 19-2). These stable, nondegradable particles were used as models for living cells. Two sizes of latex particles were run separately and collectively to provide comparative data (ref. 19-3). An automatically operated camera, mounted rigidly on the apparatus, photographed a clock, a thermometer,

a column current meter, and the position of the migrating materials. These photographs provided better technical data on electrophoresis in space than had been obtained previously. The sample insertion mechanism was redesigned to provide more reliable release of the samples in the columns. Although each sample was inserted correctly, the insertion mechanism allowed buffer to leak out of the columns before the electrophoresis began, and a bubble formed in each column. The sample bands were severely distorted by electroosmosis, which caused buffer flow along the walls of the columns counter to the direction of electrophoretic migration of the latex particles. Although the parabolic bands observed in space were explained by subsequent analysis, a clear separation of the two sizes of polystyrene latex particles was not obtained because of the electroosmosis. Electrophoresis according to size did occur in the columns containing single species of the latex, and the photographs clearly show distinct boundaries and sharply defined fronts. The deleterious effects of gravity-induced sedimentation and thermal convection on particle electrophoresis can be seen by comparing the results of the Apollo 16 electrophoresis demonstration with those of ground experiments.

For the Apollo-Soyuz Test Project (ASTP), experiment plans included reuse of the parts of the Apollo 14 and Apollo 16 systems that operated correctly, improvement of the techniques used to accomplish sample insertion, elimination of the charge condition along the column walls, and avoidance of bacterial degradation by using proven sterile techniques. A sample insertion technique was devised to ensure precise injection of the sample into the electrophoresis column without affecting the properties of the sample or disturbing the fluid column. The Apollo 14 method of inserting a thin rectangular vane containing cylindrical sample disks into the column was slightly modified and used. Buffer leakage and bubble formation were avoided by specific design techniques. Each sample disk was kept frozen, and the entire insertion slide was stored in a CF that was kept at liquid-nitrogen (77 K ( $-196^{\circ}\text{C}$ )) temperatures.

The advantages of a separate insertion vane containing frozen samples are as follows:

1. The frozen disks can be inserted into the column and allowed to thaw in contact with the buffer while any fluid disturbances induced by the sample insertion are damped.

2. Agglutination and sedimentation of the sample material in storage can be avoided by rate freezing a well-mixed sample on the ground.

3. The freezing preserves the viability of the live biological materials.

### Isotachophoresis

Isotachophoresis is a relatively new technique of electrophoretic separation in which a discontinuous electrolyte system is used at the site of sample injection (ref. 19-4). The boundaries between species of different mobility are sharply defined and stabilized by electrical forces. Adjacent compartments of sample components that may not be distinguishable by zone electrophoresis may be resolved by isotachophoresis. The boundaries are highly self-recuperative and will reform if stirred or disrupted by other factors, including convection. The concentration of each substance within a compartment is uniform and remains constant throughout the run once the separation has been achieved. Because of this uniformity, higher concentrations of components can be handled with no deterioration of the sharp boundaries.

### EXPERIMENT SAMPLE SELECTION

The samples selected for the Electrophoresis Technology Experiment were fixed red blood cells, human lymphocytes, human kidney cells, and fresh human and rabbit red blood cells. Eight columns were processed during the experiment; the columns and samples are shown in table 19-I.

#### Red Blood Cells

To assess the resolution and sharpness of the bands formed by electrophoresis in space, a well-characterized particle species is required.

TABLE 19-I.—Columns and Samples Processed in Space

Type of electrophoresis	Column no.	Sample
Zonal	1 and 5	Fixed <sup>a</sup> rabbit, human, and horse red blood cells
	2 and 6	Human lymphocytes
	3 and 7	Human kidney cells
Isotachophoresis	4	Fresh rabbit and human red blood cells
	8	Fixed <sup>a</sup> rabbit and human red blood cells

<sup>a</sup>Formaldehyde fixed.

Although polystyrene latexes were the model particles for the Apollo 16 demonstration, the red blood cells used on the ASTP flight (erythrocytes fixed in a formaldehyde fixative) provide an almost indestructible sample material resistant to mechanical stress, hemolytic agents, and surface modification. These fixed red blood cells are stable for months under varying temperature conditions, and extensive electrophoresis mobility measurements of the cells using a variety of buffers have been published (ref. 19-5). Each type of cell was selected to be morphologically distinguishable under microscopic examination. The red color of the cells makes them clearly distinguishable on the photographs made in orbit. The isotachophoresis experiment used fresh red blood cells.

### Lymphocytes

The interest in specific lymphocytes stems from the increased emphasis in the field of immunology. Initial interest in immunology grew out of the knowledge that persons who survive an infectious disease seldom contract that disease again. The two major types of immune mechanisms are humoral and cellular. Humoral immunity is characterized by the circulating antibodies that originate from B lymphocytes. Cellular immunity is mediated by means of T lymphocytes and is responsible for delayed allergic and transplant-rejection reactions. With

the increasing emphasis on cell interactions and the cellular basis of immunology, a simple method of obtaining pure fractions of cells from heterogeneous populations is desirable. From examination of microelectrophoretic data, differences in cell surface charge are known to exist (ref. 19-6), and differences in electrophoretic mobility have been measured. The significance of the cell separation is of great practical and theoretical importance. Many unresolved questions in immunology depend on the availability of pure lymphocyte subpopulations; such subpopulations are needed to study the nature of the interaction between T and B cells in antibody formation and the nature of the recently described interaction between the classes of T cells in reactions of cell-mediated immunity. More specifically, interest has developed in the clinical use of various soluble lymphocyte products (lymphokines) in a manner analogous to the use of antisera. Several other lymphocyte products, such as the factors modifying inflammatory cell behavior, are also important. The fractionation of these different lymphokines depends on the earlier separation of the specific lymphocyte populations responsible for their production. To date, none have been fractionated to any significant extent.

### Kidney Cells

The isolation and production of the enzyme urokinase (UK) has interested biomedical

laboratories for more than 20 years (ref. 19-7). This enzyme is capable of effecting the conversion of plasminogen to plasmin. This conversion is necessary to accomplish blood clot lysis. Originally, UK was extracted from urine; however, at least 1500 liters of urine were required to produce a single UK unit dose consisting of 4 million CTA (Committee on Thrombolytic Agents) units. The production cost was \$1200/CTA unit dose. Another source was subsequently discovered; UK has been isolated from cultures of cells located in the cortex of the kidney as follows. Human fetal kidneys are trypsinized to disperse the cells and then tested for viability. The cells are grown out in cultures on mass tissue propagators from which the UK is harvested. Currently, the demand for UK greatly exceeds the capability to produce it. Bernik and Kwaan (ref. 19-8) in 1969 observed that only approximately 5 percent of the cells in the cortex of the kidney produce UK. Obviously, if these "producing cells" could be isolated and subjected to subculturing techniques, a twentyfold increase in the yield and a corresponding reduction in the cost of this lifesaving drug might result. Electrophoresis has been used to try to isolate these "producing cells." The disadvantages of separation on Earth are the loss of resolving power due to sedimentation of the cells and convective mixing due to the heating effects of electrophoresis. Under zero-g conditions, these disadvantages should be eliminated or minimized.

As outlined, the kidney cell portion of Experiment MA-011 consisted of taking to orbit a mixture of frozen human kidney cells, separating them by electrophoresis, refreezing the resulting bands, and returning them to Earth. They were then grown out in tissue culture and assessed for UK production. In addition, extensive analyses were conducted to characterize the separated cells. The information from these analyses, as well as the data from the tissue culturing, has contributed extensively to the understanding of this very important source of UK.

## EQUIPMENT

The experiment equipment consisted of four major elements: (1) an EU, (2) a CF, (3) eight ex-

periment columns (six for electrophoresis and two for isotachophoresis), and (4) eight sample slides containing the experiment specimens. In addition to this experiment hardware, performance of the experiment required the following items of support equipment: (1) a 70-mm electric camera, (2) an 80-mm lens and extender tube, (3) an intervalometer, and (4) an EU power cable. As stated, the materials used as samples in the experiment consisted of fixed red blood cells of three different types (rabbit, human, and horse), lymphocytes, and human kidney cells. In addition to the slides processed, several control slides containing samples of the biological materials were stored in the CF at launch and remained there throughout the ASTP mission to allow assessment of the effects of space flight on the biological materials.

A general description of experiment operation follows. An electrophoresis or isotachophoresis column was removed from its storage location and installed on the EU column cradle. Fluid couplings were secured to each electrode chamber of the electrophoresis columns only. Then, the proper sample slide with a frozen sample was removed from the CF and inserted into the column. The 70-mm camera, mounted on the EU cover, photographed the experiment column during a run. After each electrophoretic separation was completed, the column was frozen in place on

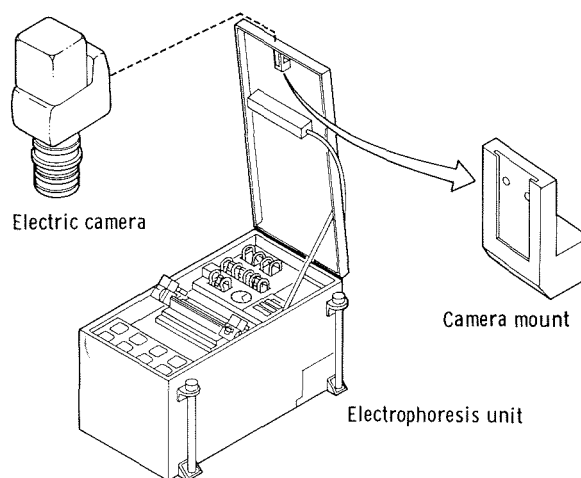


FIGURE 19-1.—Electrophoresis unit with camera.

the EU by the TE module. The frozen column was removed from the column cradle, the electrode chambers were removed and discarded, and the column was placed in the CF for return to Earth. Isotachopheresis specimens were neither frozen nor returned but only photographed. Duplicate electrophoretic separations were performed using each of the three sample materials. The two isotachopheretic separations (runs 4 and 8) were performed using rabbit and human red blood cells. Run number 4 contained formalin-fixed red blood cells and run number 8, fresh red blood cells.

A detailed description of each major hardware element and its subelements is provided in the following paragraphs.

### Electrophoresis Unit

The EU (fig. 19-1) was the apparatus in which the experiment was performed. External envelope dimensions of the unit (cover closed), excluding mounting lugs and fasteners, were 20.32 by 20.32 by 40.64 cm (8 by 8 by 16 in.). Launch weight was 13.61 kg (30 lb). The EU was designed to be mounted on the Electrophoresis Experiment (MA-014) adapter rack near command module locker A-6 with four thermally stable fasteners. Subassemblies provided by the EU were as follows.

1. Controls and displays
2. Fluorescent light assembly for illumination of the experiment columns during processing
3. Thermoelectric module for cooling and freezing the electrophoresis columns
4. Self-contained power supplies that required only an external 208-V ac (115-V line-to-neutral), three-phase, 400-Hz connection
5. Buffer solution reservoir
6. Buffer solution circulation pump
7. Phase separator assemblies for removing gases liberated in the buffer solution
8. Electrical circuitry and plumbing required by the experiment
9. Cover with one knurled screw fastener latch to protect the EU when not in use
10. Camera attachment assembly for mounting the camera to the EU cover
11. Individual storage compartments for eight

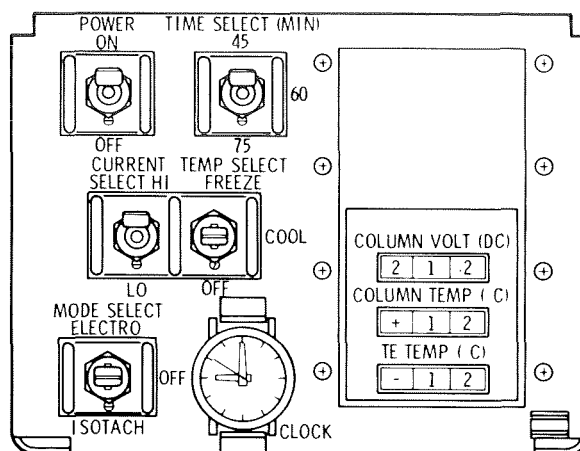


FIGURE 19-2.—Electrophoresis unit control and display panel.

experiment column assemblies

The EU control and display panel (fig. 19-2) is described as follows. In the ON position, the POWER switch energizes the fluorescent light assembly and the EU digital displays and also activates the TE module cooling blower.

The TEMP SELECT switch has positions FREEZE, COOL, and OFF. The FREEZE position is selected to freeze the electrophoresis column after each electrophoresis separation has been accomplished. A thermoelectric temperature controller allows a minimum temperature of approximately 233 K ( $-40^{\circ}\text{C}$ ). When the COOL position of the switch is selected, the temperature controller will control the TE units to temperatures as high as 278 K ( $5^{\circ}\text{C}$ ). The switch is placed in this position at the beginning of viable cell electrophoresis separations and remains in COOL until the separation is accomplished. Because performance of the isotachopheresis portion of the experiment required neither cooling nor freezing of the column, the OFF position was used for isotachopheresis.

The MODE SELECT switch has positions ELECTRO, OFF, and ISOTACH. The ELECTRO position is selected to perform the electrophoresis. When the ISOTACH position of the switch is used to perform the isotachopheresis, the buffer pump, which is not needed for this part of the experiment, does not operate.



The TIME SELECT (MIN) switch is used to select a time period of 45, 60, or 75 minutes for experiment operation.

The CURRENT SELECT switch is used to select the level of current flow through the experiment column to either 4.00 mA (HI) or 1.31 mA (LO). The electrophoresis samples were processed with the switch in the HI position, whereas the LO position was used for isotachopheresis.

The COLUMN VOLT (DC) digitally displays the voltage sensed across the experiment column electrodes. The range of the display is from 0 to 999 V in increments of 1 V, with an accuracy of  $\pm 2$  percent.

The COLUMN TEMP ( $^{\circ}\text{C}$ ) displays the buffer solution temperature in the electrophoresis column. The range of the display is from  $-99^{\circ}$  to  $99^{\circ}$  C in increments of  $1^{\circ}$  C, with an accuracy of  $\pm 2$  percent.

The TE TEMP ( $^{\circ}\text{C}$ ) displays the temperature of the thermoelectric module assembly cold plate. The range of this display is from  $-99^{\circ}$  to  $99^{\circ}$  C in increments of  $1^{\circ}$  C, with an accuracy of  $\pm 2$  percent.

The purpose of the EU clock (a commercial panel-mounted wristwatch) is to enable time correlation of the photographs taken during the experiment process. A metric scale is mounted next to the experiment column cradle. The scale is marked from 0 to 130 mm in 1-mm increments to provide distance information in photographing the biological specimens as the specimens move through the column during the experiment. A portable fluorescent light assembly mounted on the EU cover supplies the illumination required both for viewing the electrophoresis and isotachopheresis processes in the experiment columns and for photography. The fluorescent light tube, contained inside a polycarbonate tube for protection, is permanently bonded to its electrical receptacles.

The EU contains a TE assembly consisting of four three-stage thermoelectric coolers to remove heat from the electrophoresis columns during the experiment and to freeze the columns after each separation has been performed. The four coolers are mounted on a heat sink that is cooled by a flow of  $0.09 \text{ m}^3/\text{sec}$  ( $190 \text{ ft}^3/\text{min}$ ) free air by a 208-V ac, three-phase blower. The cradle holding the

electrophoresis columns during the experiment is attached to the TE assembly cold plate. The cold plate contains a thermistor device to sense the cold plate temperature. A thermal cover joins the column cradle to provide thermal continuity around the periphery of the column. The thermal cover is designed to remain in place for all freezing operations and during electrophoresis of lymphocytes and human kidney cells. The column assemblies can be isolated from the TE cradle by using special thermal spacers or slide devices.

A buffer solution reservoir is mounted on a removable tray that forms a part of the EU structure. The tray is attached to the EU by screw fasteners. The reservoir contains a cylindrical rubber diaphragm with a hemispherical end and has a buffer solution capacity of 57.7 ml. The buffer solution enters the reservoir from a phase separator assembly and is then delivered from the reservoir to the buffer solution pump. The reservoir was covered with a hydrophobic felt cover to ensure containment of the buffer solution if the diaphragm ruptured.

A double peristaltic pump, mounted on one side of the EU removable tray assembly next to the buffer solution reservoir, circulates the buffer solution through the fluid system to allow removal by the phase separators of gas bubbles

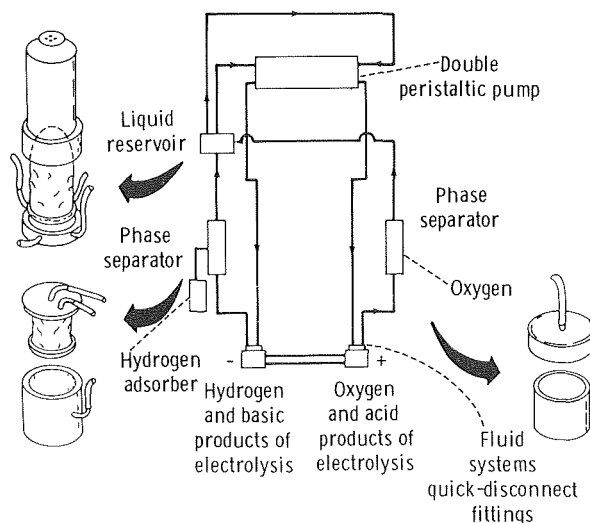


FIGURE 19-3.—Electrophoresis fluid system schematic.

generated at the electrophoresis column electrodes. The pump receives buffer solution from one side of the fluid system (e.g., the column anode side) and circulates it to the other end of the column (fig. 19-3). The capacity of the pump is 35 ml/min.

Two phase separator assemblies are located on the EU removable tray assembly. The phase separators are identical and consist of two cylindrical membranes. One membrane is hydrophilic (porous polyethylene) and the other is hydrophobic (porous polytetrafluoroethylene). The buffer and gas mixture enters between the membranes. The hydrophobic membrane allows passage of gas to either the cabin atmosphere or the hydrogen adsorber, and the hydrophilic membrane allows passage of liquid to the storage reservoir. One separator is connected to the column anode side of the fluid system and removes the oxygen gas liberated in the buffer solution at the anode. The oxygen is vented to cabin air. The other separator is connected to the cathode side of the fluid system and removes hydrogen gas liberated at the cathode. The hydrogen is then routed to the hydrogen adsorber assembly. The separator assemblies return the liquid buffer solution to the reservoir.

The hydrogen adsorber assembly is connected to the phase separator assembly to remove hydrogen bubbles from the buffer solution. The hydrogen gas is adsorbed on a mixture of precipitated palladium (palladium black) and silica gel contained in a fine-filament fiberglass bag in the adsorber canister.

### Cryogenic Freezer

The CF (fig. 19-4) was used to freeze the experiment samples before insertion into the experiment columns for processing and to maintain the frozen electrophoresis columns after the separations had been accomplished. The sample slides were launched in the CF, and the frozen electrophoresis columns were returned to Earth in the CF.

The CF consists of two flasks (one contained within the other). The space between the flasks is evacuated for thermal insulation. The inner flask

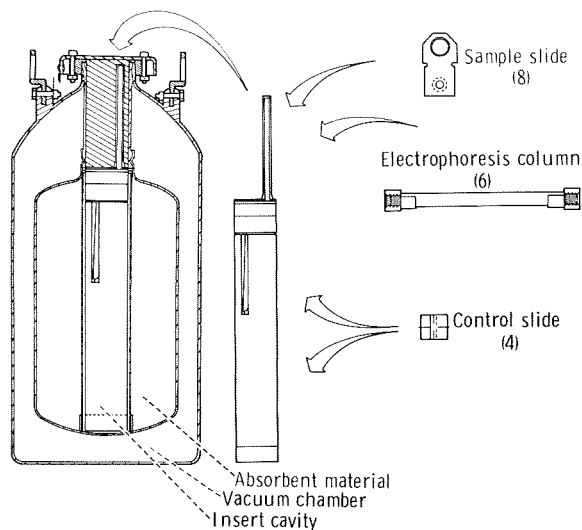


FIGURE 19-4.—Cryogenic freezer.

has an outside diameter of 31.12 cm (12.25 in.) and has a cavity to accommodate a cylindrical sample storage canister with dimensions of 4.98 cm (1.96 in.) diameter and 48.26 cm (19 in.) length. The maximum launch weight of the CF, when charged with liquid nitrogen, is 10.4 kg (22.9 lb).

The cooling medium used in the CF was liquid nitrogen, which was contained in the inner flask and surrounded the sample canister cavity. The CF maintained the samples at a temperature no higher than 188 K ( $-85^{\circ}\text{C}$ ) for 20 days. The sample canister had space for eight experiment sample slides with samples, one experiment sample column for the German Electrophoresis Experiment (MA-014), and three cylindrical cavities for return of the electrophoresis columns (two columns per cavity).

### Electrophoresis Columns

Six electrophoresis columns (fig. 19-5) were stowed in individual compartments at one end of the EU. Each column consisted of a transparent Pyrex glass tube 0.953 cm (0.375 in.) outside diameter by 0.635 cm (0.25 in.) inside diameter. The tube was 15.24 cm (6 in.) long and was split lengthwise and rejoined with a flexible adhesive



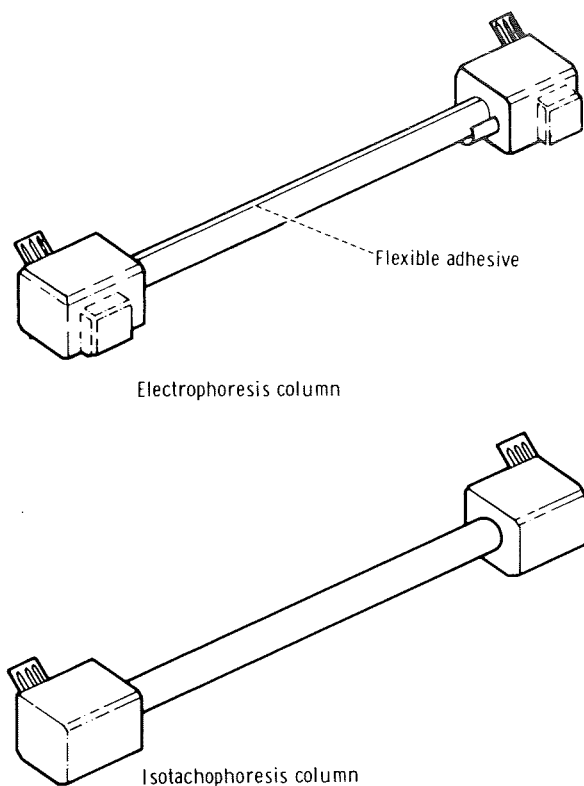


FIGURE 19-5.—Electrophoresis and isotachophoresis column assemblies.

(RTV 140) to allow for expansion of the buffer solution when the electrophoresis columns were frozen. A thermistor bonded to the tube wall at the center of the length of each tube was used to monitor the column temperature for display on the EU COLUMN TEMP (°C) display.

The inside surfaces of the glass columns were stringently cleaned, coated with Z-6040 ( $\gamma$ -glycidoxypolytrimethoxysilane, Dow Corning) and then coated with methylcellulose in order to obtain a stable, biocompatible surface with close to zero zeta potential. Confirmation of the adequacy of the coating was obtained by experimentally determining the electrophoretic velocity of fixed red blood cells in the coated columns. The ends of the tubes were plugged with a fritted glass disk containing a 3-percent agarose gel. The columns were filled before flight with a sterile buffer solution. Each column was sealed in a polyvinylidene chloride bag that was then placed

in a fine-filament fiberglass bag. Attached to the polyvinylidene chloride bag was a wiper used to wipe the female electrical connectors before column installation. Each end of the electrophoresis column has an electrode chamber assembly containing a platinum electrode, a printed circuit electrical connector, and a mating EU buffer solution connector.

The electrode chamber assemblies were removable for disposal after the column had been frozen in the EU. The electrode chamber assembly containing the column cathode had a cavity into which the sample slide was inserted for experiment operation. A blank slide was contained in the cavity before experiment operation. The blank slide had a 0.13-cm (0.05 in.) inside-diameter threaded hole used for preflight filling of the column with buffer solution. The opening was sealed after filling. (The assembly electrical schematic is shown in figure 19-6.)

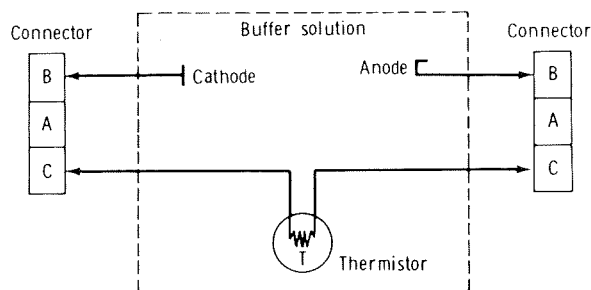


FIGURE 19-6.—Electrophoresis column electrical schematic.

The buffer used in the electrophoresis columns consisted of a mixture of 1.76 mmol  $\text{Na}_2\text{HPO}_4$ , 0.367 mmol  $\text{KH}_2\text{PO}_4$ , 6.42 mmol  $\text{NaCl}$ , 0.336 mmol  $\text{Na}_2\text{EDTA}$ , 222 mmol glucose, and 514 mmol glycerol in water.<sup>1</sup> It has a hydrogen-ion concentration (pH) of  $7.30 \pm 0.10$  at 293 K (20° C) and a calculated ionic strength of 0.0097 mol/liter. At 298 K (25° C), the conductivity was 0.96 mmho/cm; the density, 1.022; and the dynamic viscosity, 0.00111 N-sec/m<sup>2</sup> (0.0111 P).

<sup>1</sup>Na, sodium; H, hydrogen; P, phosphorus; O, oxygen; K, potassium; Cl, chlorine; and EDTA, ethylenediaminetetraacetic acid.

The buffer was demonstrated to be compatible with the column coating, all the components of the EU system, and the candidate materials to be flown on the mission. The mobilities of fixed rabbit, human, and horse red blood cells in this buffer were 1.60, 1.96, and 2.60  $\mu\text{m sec}^{-1} \text{ V}^{-1} \text{ cm}^{-1}$ , respectively.

### Isotachophoresis Columns

Two isotachophoresis columns (fig. 19-5) were stowed in individual compartments in the EU. Each column consisted of a glass tube having dimensions of 0.97 cm (0.38 in.) outside diameter, 0.64 cm (0.25 in.) inside diameter, and 15.24 cm (6 in.) length. Each end of the tube had an assembly containing a flat, disk-shaped, three-lobed electrode (one electrode assembly with a silver anode and the other with a palladium cathode), a rubber diaphragm, and a printed circuit electrical connector.

The assembly containing the palladium cathode had a cavity into which the sample slide was inserted for experiment operation. A blank slide was contained in the cavity before processing the column. The blank slide had two 0.13-cm (0.05 in.) inside-diameter threaded holes used to fill the column with buffer solution before flight.

The isotachophoresis occurred in a column containing a leader buffer of 0.62 ml of 85 percent phosphoric acid in 500 ml water, with 42 g of dextrose and 276 g of glycerol, adjusted to a pH of 7.4 in 1 liter of distilled water. The terminator buffer contained 2 g of serine, 42 g of dextrose, and 276 g of glycerol, adjusted to pH 8.2 in 1 liter of glass distilled water.

### Sample Slides

Each sample to be processed during the experiment was mounted in a slide assembly (fig. 19-7). Before processing, the slides were stowed in the CF sample canister. Each slide assembly was contained in a tetrafluoroethylene cover 0.13 mm (0.005 in.) thick that had a removal tab 5.08 cm (2 in.) long of the same material. The slides were removed from the CF sample canister by grasping

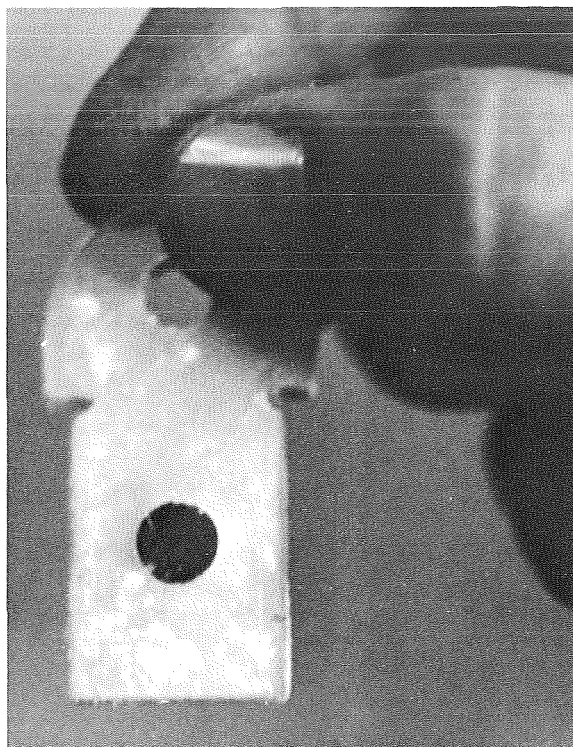


FIGURE 19-7.—Sample slide containing frozen sample.

the removal tab and pulling the slide out of the canister. Every two slides removed from the canister exposed a return storage space in the canister for two electrophoresis columns. In addition to the slides to be processed, four “control” slides with sample material were stowed in spaces on the circumference of the sample canister. Two control slides contained lymphocytes and two contained kidney cells. These “control” slides were designed to assess the effects of the flight environment on the viable sample materials; they were returned to Earth without processing.

Each sample slide was numbered to correspond to the appropriate column. The slides were removed from the canister and inserted into the experiment column electrode (cathode) chamber assembly for processing in numerical order. Each slide was discarded together with the electrode chamber assemblies after each electrophoresis column was frozen for return. The entire isotachophoresis column was discarded after processing.

## RESULTS

In the laboratory, the frozen buffer containing the processed samples was separated from the glass electrophoresis columns. These frozen ice columns were sliced into sections for processing by each Co-Investigator. In slicing the columns, several critical requirements had to be satisfied: (1) the frozen column had to be sliced at 233 K ( $-40^{\circ}\text{C}$ ) or colder; (2) contamination from the slicing mechanism was to be minimized (e.g., heating and particulates from the cutting device were to be avoided); (3) the slices had to be between 0.5 and 5.0 mm long; (4) each slice had to be contained aseptically; and (5) the slicing procedure had to be recorded photographically. After a thorough search of the literature, no existing device was found that could satisfactorily meet all these requirements. Therefore, a device was designed, constructed, and tested for this specific purpose (ref. 19-4). As shown in figure 19-8, the slicing assembly consisted of an extraction assembly in which the frozen flight column was placed. The extraction rod was used to push the ice column into a Teflon tube contained in the slicing assembly. After proper alignment, the razor blade was used to slice "coins" from the frozen column. The 5-mm coins were captured, bagged, and stored at 77 K ( $-196^{\circ}\text{C}$ ). The entire slicing assembly was operated in a laminar flow hood and in a sterile manner. Subsequent analyses of the

cultured kidney cells proved that no detectable contamination resulted from the operation of this device.

The EU, the CF, and the data-collection assembly met the required objectives with satisfactory experimental results. However, the fluid connect lines (located in the electrode housings) of some of the columns were clogged during assembly, and, without a fluid purge of the electrode housing, chemical and gas products of electrolysis accumulated in the electrode region. This accumulation triggered changes in the buffer that were manifested as column voltage fluctuations and pH changes in the column fluid. These anomalies were observed in columns 2, 5, and 6; operations of the other columns appeared normal.

The experimental results are reported according to the order in which the samples were processed. The electrophoresis experiments are presented first, and the isotachophoretic runs are reported in the last subsection.

### Fixed Red Blood Cells

The analyses of the electrophoretic columns containing fixed rabbit, human, and horse red blood cells (columns 1 and 5) consisted of mobility tests and morphological examinations. Both flight photographs and the sliced samples were used.

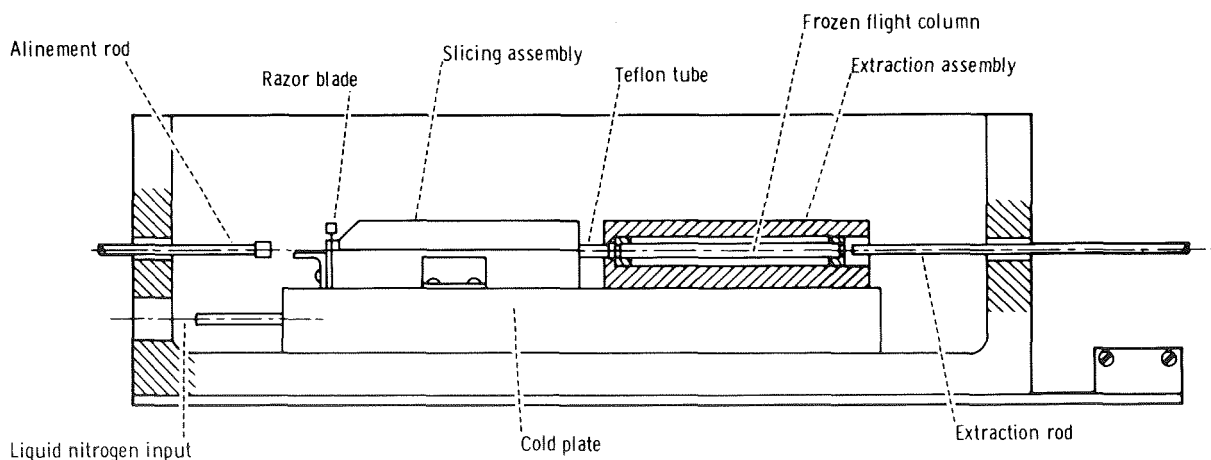


FIGURE 19-8.—Cross section of slicing assembly.

The number of red blood cells loaded in the sample slide was  $5.22 \times 10^6$  rabbit cells/0.06 ml,  $3.44 \times 10^6$  human cells/0.06 ml, and  $7.26 \times 10^6$  horse cells/0.06 ml. The volume of the sample slide for electrophoresis was 0.06 ml.

A major problem in the preparations for the flight experiment was the elimination of electro-osmosis. If present, the fluid flow due to electro-osmosis would cause the cells in the center of the flight column to travel faster than those near the column wall. This effect produces "bullet shaped" bands and reduces the resolution capability of the apparatus. A methyl cellulose coating technique was used to coat the inside walls of the electrophoresis column to eliminate the electro-osmotic flow (ref. 19-9). After use of the coating, electro-osmotic flow was reduced from approximately  $4.5 \mu\text{m sec}^{-1} \text{V}^{-1} \text{cm}^{-1}$  to less than  $0.3 \mu\text{m sec}^{-1} \text{V}^{-1} \text{cm}^{-1}$ . With this lower level of electro-osmotic flow ( $0.3 \mu\text{m sec}^{-1} \text{V}^{-1} \text{cm}^{-1}$ ), the bands were predicted to be spread to approximately 2.5 times the length computed for zero electro-osmotic flow after 60 minutes of run time. Not all of this spread would be observable to the naked eye because the concentrations of cells at the boundaries would be lower than the threshold for direct visualization.

In subsequent examinations of the flight photographs, two indications of electro-osmosis were investigated: (1) band-front boundary curvature, which became more pronounced as the run time increased; and (2) longitudinal spread of the bands in excess of that predicted in the absence of electro-osmotic flow.

The band fronts were planar in appearance with no signs of pronounced curvature for

column 1. Problems that might interfere with this visual assessment are (1) the optical aberration as a result of viewing bands through a cylindrical tube wall, (2) the haziness of the flight photographs, and (3) the definition of the band boundaries as seen by the naked eye. However, the band fronts appeared planar on visual inspection of the flight photographs.

The spreading behavior of the bands was analyzed by plotting the displacement of the band boundaries from the sample slide as a function of run time. The data were collected by visual examination of 20 flight photographs taken at 3-minute intervals during the 60-minute run of column 1. The bandwidths at 60 minutes were taken from the straight curve fits to the boundary migration data. The results are shown in table 19-II. The bands were slightly more compressed than expected. Thus, it was concluded that no band spreading occurred that was due to electro-osmosis.

The electrophoretic mobility of the particles in the band boundaries was computed from the plot of band boundary migration against run time. The data in table 19-II show that the calculated mobility at 298 K (25° C) for the fast band was 2.36 for the band front and  $2.21 \mu\text{m sec}^{-1} \text{V}^{-1} \text{cm}^{-1}$  for the rear boundary. These values are slightly lower than the predicted average of  $2.38 \mu\text{m sec}^{-1} \text{V}^{-1} \text{cm}^{-1}$  for horse cells as observed in ground-based analytical particle electrophoresis. The front of the slower band complex corresponded to the mean value for human cells of  $1.94 \mu\text{m sec}^{-1} \text{V}^{-1} \text{cm}^{-1}$ , but the rear boundary had a mobility of 1.70, which is higher than the 1.56 average value observed for rabbit red blood cells

TABLE 19-II.—Observed and Predicted Bandwidth Values of the Formalin-Fixed Red Blood Cells

Band	Bandwidth, mm		Electrophoretic mobility at 298 K (25° C), $\mu\text{m sec}^{-1} \text{V}^{-1} \text{cm}^{-1}$	
	Observed	Predicted	Observed	Predicted
Fast (horse)	8 to 10	15 to 18	2.21 to 2.36	2.38
Slower band complex (human and rabbit)	20	30	1.70 to 1.96	1.56 to 1.94

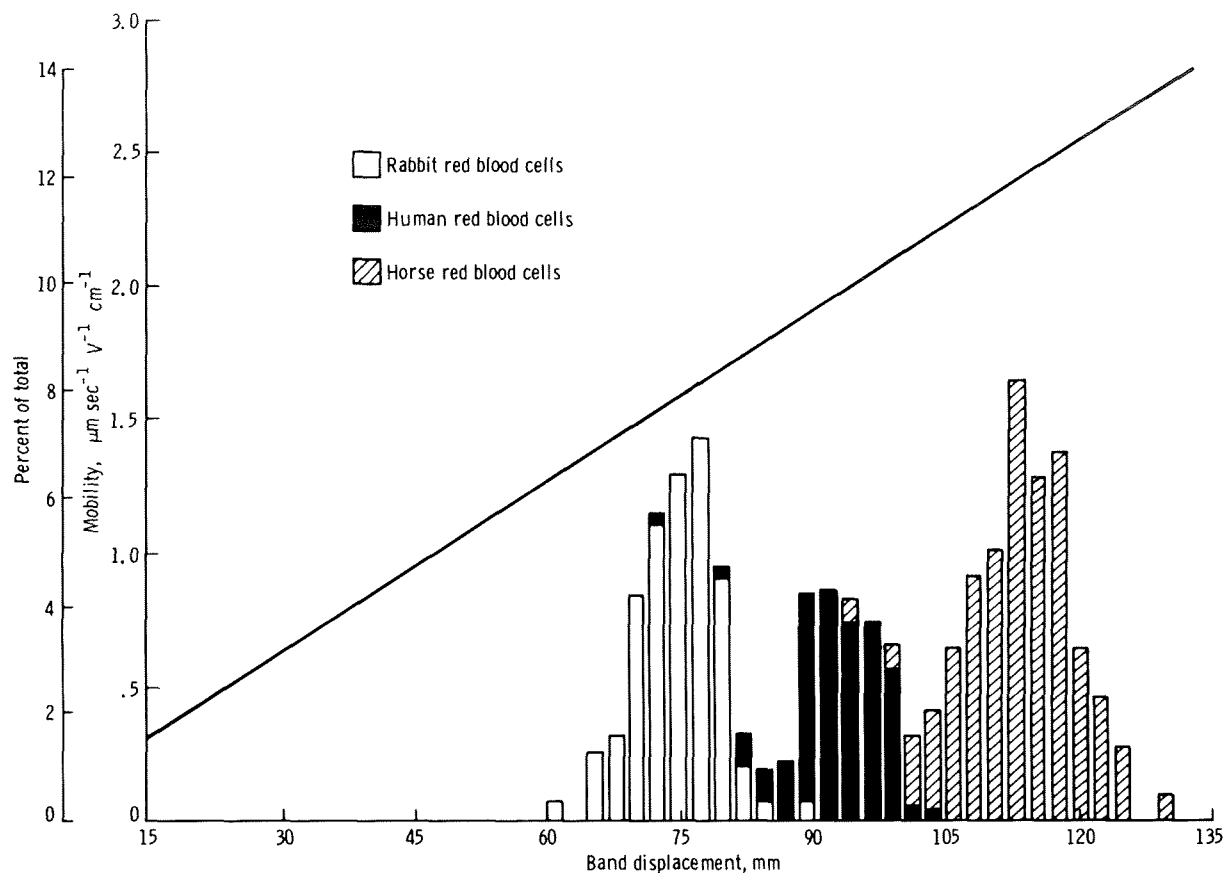


FIGURE 19-9.—Predicted band intensities at various migration distances. Straight line establishes mobilities measured at 298 K (25° C) during ground-based experiments.

in the ground-based experiments. The predicted red blood cell band intensities as a function of migration distance are shown in figure 19-9. This figure was constructed from the observed electrophoretic mobility distributions for each of the red blood cell populations and the number of each cell type loaded in the sample slide. The straight curve establishes the mobilities measured at 298 K (25° C) in A-1 buffer during ground-based experiments. The outside ordinate gives the percentage of the total number of cells in the sample slide found in each bar of the histogram. From figure 19-9, it can be seen that the location of visibly dense bands should be as follows: rabbit,  $\approx 70$  to 81 mm; human,  $\approx 88$  to 100 mm; and horse,  $\approx 105$  to 123 mm.

In figure 19-10, the observed band locations for column 1 at 60 minutes are compared with the

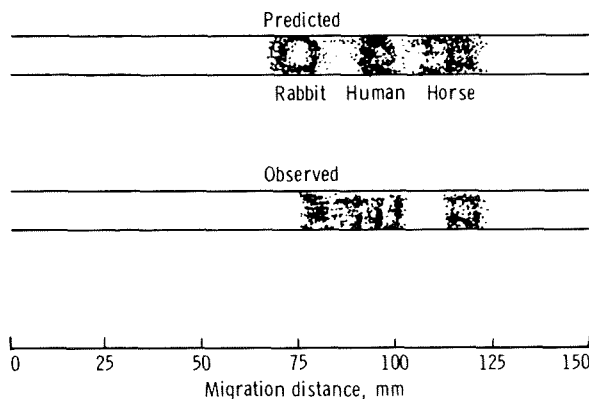


FIGURE 19-10.—Predicted and observed visual migration of formalin-fixed red blood cells. The observed migration of cells is from column 1 of the flight experiment.

predicted locations. The observed band locations were taken from the plot of band migration against run time, because the visualization of the bands was difficult at the end of the run. The fast band corresponded well with the predicted location for horse red blood cells, and the front of the slower band complex corresponded with the predicted human red blood cell location. The rear boundary of the slower band complex was 1 to 1.5 cm farther into the tube than predicted for rabbit cells. Overall, the bands were slightly more compressed than expected, and the separation between horse and human cells was greater than predicted.

The analysis of the flight photographs showed good general agreement between the observed migration behavior of the red blood cell bands and the predicted behavior. Small discrepancies were found and have not yet been explained. Some of these discrepancies may relate to factors not included in the predictive model of the experiment (such as radial and longitudinal thermal gradients in the flight column, compression of the voltage field in the sample disk aperture, and red blood cell concentration effects).

In column 5, two specific instances of sudden disruption of boundaries are indicated in the flight photographs (figs. 19-11 to 19-14). These disper-



FIGURE 19-11.—Flight photograph of electrophoresis column 5 (AST-26-2182).

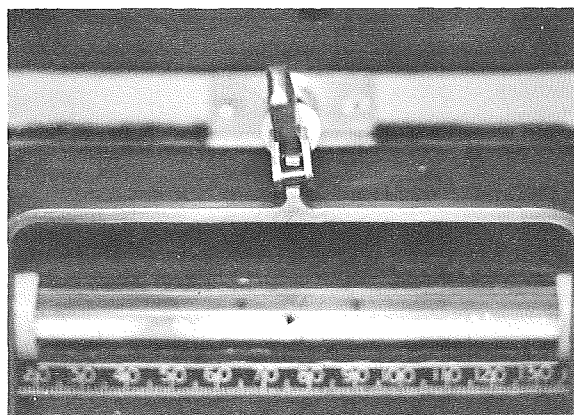


FIGURE 19-13.—Flight photograph of electrophoresis column 5 (AST-26-2186).

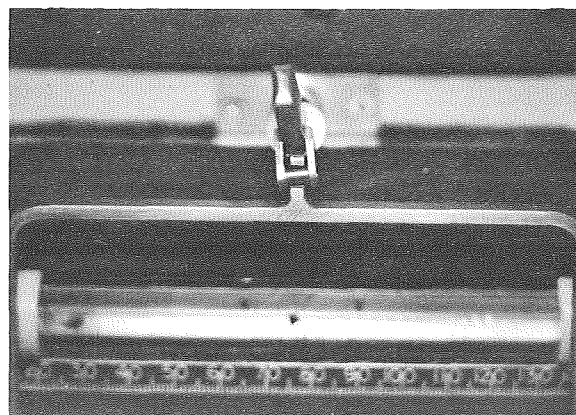


FIGURE 19-12.—Flight photograph of electrophoresis column 5 showing disruption of boundaries seen in figure 19-11 (AST-26-2183).

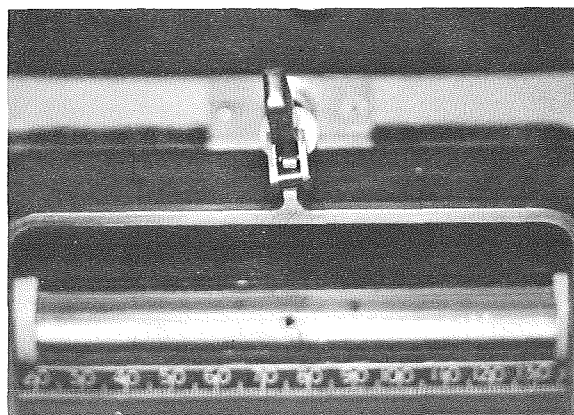


FIGURE 19-14.—Flight photograph of electrophoresis column 5 showing disruption of boundaries seen in figure 19-13 (AST-26-2187).

sions occurred between the time of the photographs shown in figures 19-13 and 19-14. The disruptions probably were caused by random motion of the apparatus or, perhaps, of the spacecraft.

During the sample slicing operation for column 1, the column walls fractured and the column was distorted. The samples were collected in the hope that minimal mixing and contamination had occurred. In the case of column 5, the flight experiment had not functioned properly due to blockage of the electrode buffer circulation ports. This was believed to produce a fluid flow through the electrophoresis column that opposed the direction of particle migration and carried electrolysis products into the column. The sample slicing was performed as planned for column 5.

The calculated recovery of fluid volume was 75 percent for column 1 and 93 percent for column 5. The histograms of cell count compared with the computed distance from the column sample slide are shown for columns 1 and 5 in figure 19-15.

In figure 19-15(a), only six fractions were obtained from the region of the column containing the red blood cell bands. These were placed in the sample histogram starting from the distal end of the column from the sample slide because 25 percent of the column fluid had not been recovered and the earlier sample slices were shown to contain consistently less volume than calculated. The histogram agreed well with the locations of cells in the flight photographs, but this agreement may be fortuitous because cell typing and electrophoretic data indicated considerable mixing of cell types. The recovery of cells was 70 percent of the theoretical value.

In figure 19-15(b), no discrete bands were shown in the histogram for column 5, which is in agreement with the flight photographs. The recovery of cells was 90 percent of the theoretical yield. The front of the continuous band was located at  $\approx 80$  mm in the flight photographs in contrast to the location of the cells in the sample slices, where the front was at  $\approx 60$  mm. In sample slices 7 to 10, the pH decreased from 7.9 to 6.5 and reached values of 3 to 4 in slices at larger migration distances.

The cells in three sample slices from each column were examined by analytical particle electrophoresis to determine whether they dis-

played the electrophoretic mobility distributions expected from their locations in the flight column. Data were collected for 100 cells from each sample.

The samples from column 1 slices 1, 3, and 4 all had similar electrophoretic mobilities and the particle analysis is not consistent with flight photographs. Their mean mobilities were all in the range from 2.05 to 2.17, which suggests that the cells had either been mixed, contaminated during the column breakage, or mixed before freezing. The cells in sample slices 5, 8, and 11 from column

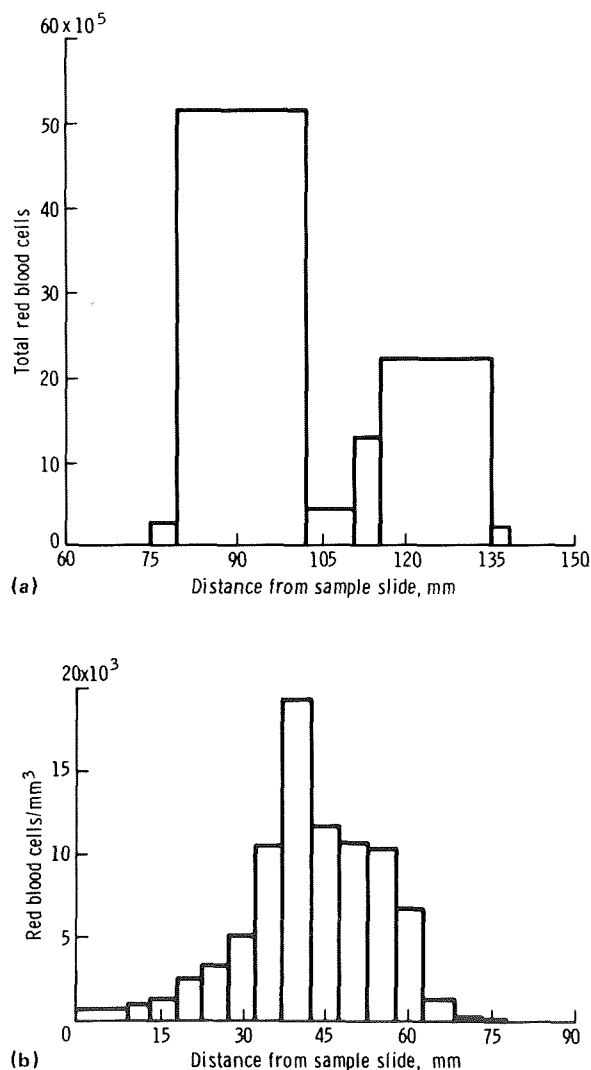


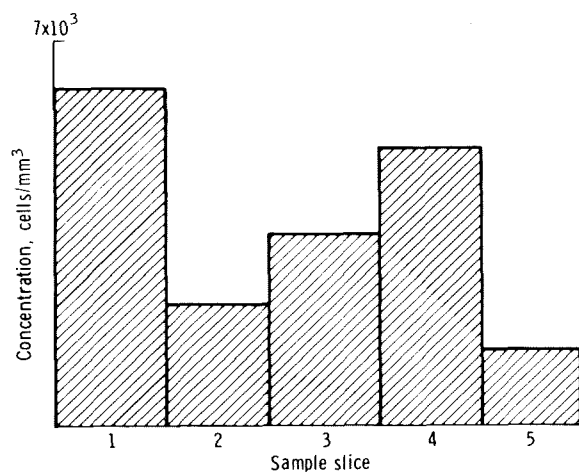
FIGURE 19-15.—Histogram showing cell counts. (a) Column 1. (b) Column 5.

5 showed a trend from lower to higher electrophoretic mobilities, respectively, but the separation was not large.

Estimations made of the numbers of each cell type from the electrophoretic mobility data were in general agreement with the morphological typing estimations (figs. 19-16 and 19-17). For column 1, the typing data showed similar distributions of the three cell types in each of the sample slices in contrast to the expected behavior. This finding supported the suggestion that the samples had been mixed either when the column broke or before freezing. As expected, the data for column 5 show that there were enrichments of rabbit cells in the slow region of the band (left end of column) and horse cells in the fast region (right end of column).

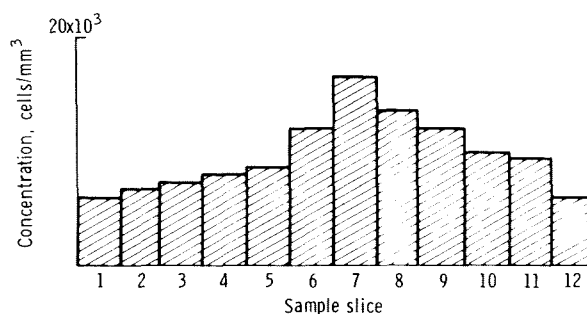
The results of the postflight sample slice

analyses indicate that the samples from column 1 are of little use in interpreting the behavior of the flight experiment. The column 5 data show partial separation of cells according to their electrophoretic mobilities. Electro-osmosis, which is a major obstacle to successful electrophoretic separations in a closed cylindrical tube apparatus, was eliminated in the ASTP electrophoresis experiment. The coating techniques developed for this purpose significantly increased the resolution capability of the electrophoresis unit and will be useful for ground-based and future space electrophoretic applications. The red blood cell bands were planar and showed no signs of longitudinal spreading. The MA-011 electrophoresis unit has demonstrated the capability of separating small volumes of sample cells on the basis of their electrophoretic mobilities.



Sample slice	Cell type		
	Rabbit	Human	Horse
Mobility, percent			
1	19	22	59
3	11	17	72
4	12	38	50
Morphology per 100 cells			
1	17	26	57
3	19	48	33
4	15	31	54

FIGURE 19-16.—Mobility and morphological data from column 1.



Sample slice	Cell type		
	Rabbit	Human	Horse
Mobility, percent			
5	18	60	22
8	24	48	28
11	23	42	35
Morphology per 100 cells			
1	56	38	6
2	66	31	3
3	60	40	0
4	64	36	0
5	36	57	7
6	47	41	12
7	31	32	37
8	17	41	41
9	12	27	61
10	11	23	66
11	10	34	56

FIGURE 19-17.—Mobility and morphological data from column 5.



### Human Lymphocytes

Approximately  $1.5 \times 10^7$  human lymphocyte cells were loaded into the 0.06-ml volume of each sample slide. Migration of the cells was not detected in either column. In column 2, current was established for less than 3 minutes because of fluid line blockage, which resulted in the formation of gaseous products around the electrodes. These gas bubbles blocked the current and prevented operation of the experiment. In addition, the cell viability was only 6 percent (table 19-III). No explanation can be found for this observation; the pH of the column fluid varied from 6.69 to 6.85, which should not kill the cells.

In column 6, current existed for approximately 30 minutes. In this case, the electrode housings were returned and an investigation confirmed that the right electrode chamber fluid lines were blocked. This condition resulted in an acid pH throughout the column. The pH of the fluid in column 6 was 2.54 on the left end, 2.28 in the center, and 2.21 on the right end. As would be expected, the viability of the lymphocytes was only 1 percent (table 19-III).

In addition, the control cells that were taken into orbit but not thawed showed an unusually low viability (table 19-III). The authors have deduced that, because of the small size of the control slides, these lymphocytes froze and thawed

TABLE 19-III.—Cell Count and Viability Results of Human Lymphocytes

Fraction no.	Count per sample	Viability, percent	Fraction no.	Count per sample	Viability, percent
Column 2			Column 6		
Left end	364 000	6	Left end	392 000	0 (clumps)
1	44 800	6	1	427 000	1
2	50 800	0	2	856 800	0 (clumps)
3	1 120	0	3	851 200	0
4	0	--	4	6 160	0
5	560	0	5	0	--
6	0	--	6	0	--
7	0	--	7	0	--
8	0	--	8	0	--
9	0	--	9	0	--
10	0	--	10	0	--
11	0	--	11	0	--
12	0	--	12	0	--
13	0	--	13	0	--
14	0	--	14	0	--
15	0	--	15	0	--
16	0	--	16	0	--
17	0	--	17	0	--
18	0	--	18	0	--
19	0	--	19	0	--
20	0	--	20	0	--
21	0	--	21	0	--
22	0	--	22	0	--
23	0	--	23	0	--
24	0	--	24	0	--
25	0	--	Right end	0	--
26	0	--	Ground control C	1 290 000	19
Right end	0	--	Flight control C	2 360 000	14
Ground control A	1 420 000	46			
Flight control A	3 620 000	13			

faster than the prescribed rate. In preflight tests, the cells routinely showed a recovery of 55- to 63-percent viability when frozen and thawed using the sample keys. These sample keys are much larger than the control slides, although their cell compartments are the same size.

These data are not adequate for conclusions related to the feasibility of space electrophoresis of human lymphocytes. As an application of this work, however, the freezing of human granulocytes, by the same method developed for the freezing of human lymphocytes for ASTP, appears most promising and is being pursued further. The viability of human granulocytes, using the ASTP method, after freezing and thawing is approximately 82 to 86 percent. Also, their phagocytic activity appears undiminished. During simulation of, and in preparation for, the flight experiments, a one-g method for preparative cell electrophoresis was developed that enabled separation of the fastest migrating cells (the T lymphocytes) in a pure state (ref. 19-10).

### Human Kidney Cells

For the human kidney cell experiments, approximately  $2.0 \times 10^6$  cells were loaded into the sample slide. Only column 3 was subjected to electrophoresis in orbit; during orbital operations, the crewmembers discontinued the processing of column 7.

The frozen slices obtained from column 3 were thawed rapidly at 310 K (37° C), centrifuged, and resuspended in growth media. These fractions were weighed and the pH determined (table 19-IV). An aliquot was taken so that a viable cell count could be made; and, based on this information, the cells were cultured. The distribution of viable cells is shown in figure 19-18, in which approximately four subpopulations of cells can be identified.

After 28 days, only fractions 11 to 19 had reached confluency. The other fractions were removed from the culture plates and tested for UK activity by the fibrin plate method (ref. 19-11). These fractions showed no fibrinolytic activity. The disposition of the confluent plates and of the subcultures is shown in table 19-V. The

cells that were put on production media were tested at various times for UK activity; the cells that were subcultured were removed from the dishes with EDTA and then recultured.

Table 19-VI shows the results of the UK production obtained with the primary and subculture 1 cells after 35 days on production media. There is an obvious enrichment of UK activity in fraction 15. An increased production is also apparent in several other fractions. A control experiment with the same cells cultured using ground-based conditions resulted in the value of 0.28 UK units per 100 cells. The subculture 2 cells did not produce UK when placed on production media. Some of the cells from subculture 2 were analyzed for electrophoretic mobility distribution, and the results of three such fractions are shown in figure

TABLE 19-IV.—Weight and pH of Sample Slices From Column 3

Fraction no.	Weight, g	pH
Right	0.3231	7.25
Left	.27805	7.05
1	.15400	7.8
2	.15110	7.9
3	.14195	7.8
4	.16695	7.8
5	.16320	7.85
6	.15825	7.6
7	.14845	7.85
8	.16250	7.75
9	.17195	7.75
10	.15805	7.85
11	.15435	--
12	.17765	7.65
13	.15620	7.55
14	.10100	7.45
15	.13340	7.5
16	.13925	7.65
17	.20405	7.25
18	.14975	--
19	.12015	7.45
20	.14915	--
21	.16115	--
22	.16695	7.45
23	.16230	--
24	.15635	--
25	.18545	--
26	.11970	7.4

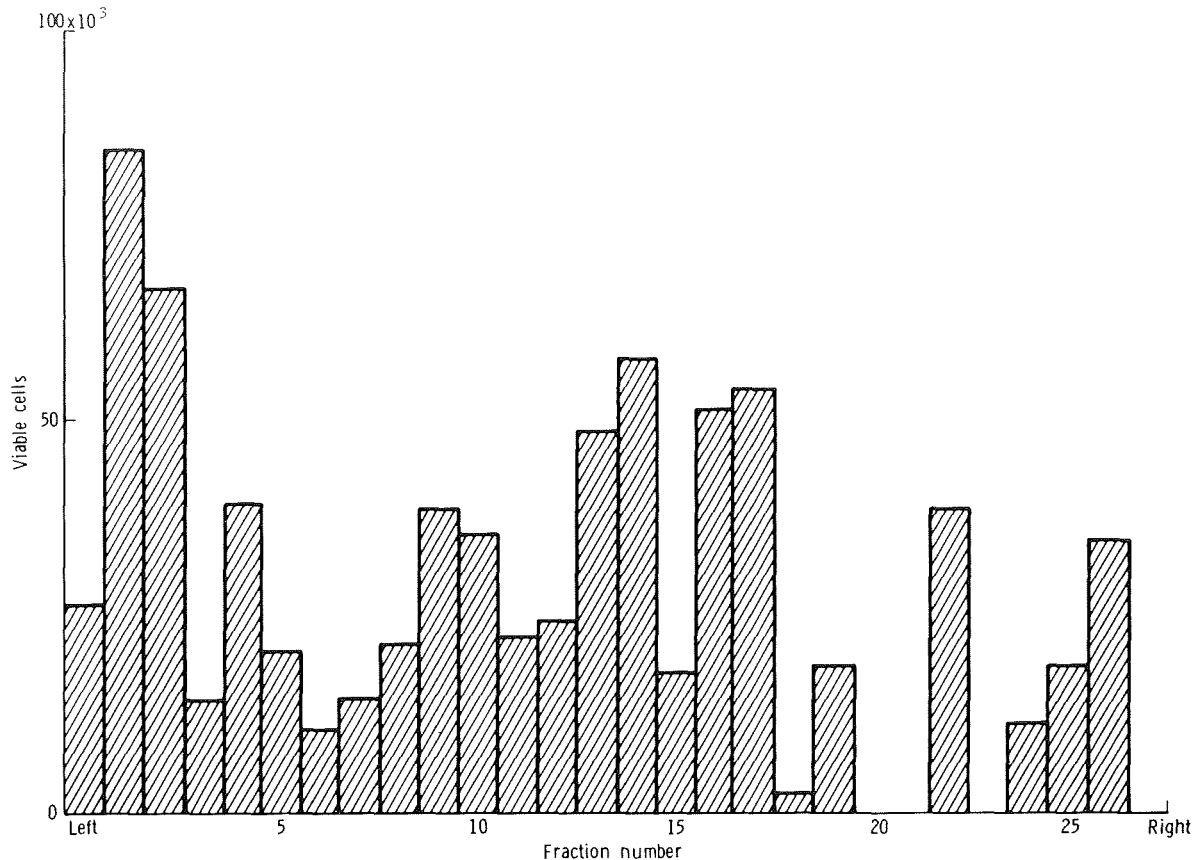


FIGURE 19-18.—Histogram of viable kidney cells for each sample slice in column 3.

19-19. The cells of subculture 1 were also tested for the presence of human granulocyte conditioning factor (HGCF), and the results are shown in table 19-VII. It is evident that the highest concentration of these HGCF-producing cells was in a separate band (fraction 17).

These results show that cells can be separated under sterile conditions and returned from orbit in such a manner that they retain their ability to grow in culture. Electrophoresis in space resulted in good separation of the kidney cells into subpopulations, with an indication of at least three and maybe four subpopulations. This result is in agreement with the best data obtained using the endless belt electrophoresis. Although subpopulations have been observed using the endless belt apparatus, sterile collection of these bands has not been possible. Whereas each fraction from the

ASTP flight showed viable cells by the stain technique (ref. 19-12) and they all attached to the glass surface, only the few fractions between 11 and 20 multiplied. The reason for this is not known. The only possible explanation is that the "non-growers" were more sensitive to unfavorable conditions and therefore could not recover to grow in culture.

During the final quarter of this study, analyses were made for erythropoietin activity. All assays were performed using a standard with a potency of 2.2 units/mg. The harvests from the primary culture, subculture 1, and subculture 2 were assayed for erythropoietin activity. The results, reported in table 19-VIII, are the average of two sets of assays. The results are most encouraging because the peak activity for erythropoietin is found in fraction number 14. This is a different

TABLE 19-V.—Disposition of Cultures From Column 3

<i>Fraction no.</i>	<i>Condition</i>	<i>Disposition</i>
<i>Confluent primary kidney cell cultures</i>		
11	Confluent	Production
13	Confluent	Production
14	Confluent	Subculture <sup>a</sup>
15	Confluent	Production
16	Confluent	Subculture
17	Confluent	Production <sup>b</sup> ; subculture <sup>b</sup>
19	Confluent	Subculture
Flight control B	Confluent	Production
Flight control D	Confluent	Production
<i>Kidney cell subculture 1</i>		
14-1	Confluent	Subculture
14-1	Confluent	Production
16-1	50 percent confluent	Production
16-1	50 percent confluent	Reculture <sup>c</sup>
17-1	Confluent	Subculture
17-1	Confluent	Production
19-1	Confluent	Subculture
19-1	Confluent	Production
<i>Confluent kidney cell subculture 2</i>		
14-2	Confluent	Production
14-2	Confluent	Mobility <sup>d</sup>
17-2	Confluent	Production
17-2	Confluent	Mobility
19-2	Confluent	Production
19-2	Confluent	Mobility

<sup>a</sup>Two 35-mm petri dishes.<sup>b</sup>One 35-mm petri dish.<sup>c</sup>No growth resulted from this subculture.<sup>d</sup>Electrophoretic mobility determination.

fraction than for either UK (fraction 15) or HGCF peak (fraction 17). These data indicate that a different subpopulation of cells is responsible for each activity assayed.

In summary, these data indicate an enrichment of UK-producing cells in the area centering around fraction 15. These results can be interpreted to show an incomplete resolution between a producing cell population and a non-producing population. Considering that the experimental conditions (buffer run time, etc.) were not optimized for kidney cells but generalized for three different separations, these results are not

surprising. This lack of optimization is probably the reason for the failure of the cells to produce farther than subculture 2, when normally under optimized growth conditions the cells produce to subculture 7. It also appears that the bands that produced HGCF and erythropoietin do not coincide with that band of cells that produce UK. This is a very interesting finding and indicates that these products are most likely not produced by the same cell.

The analytical mobility data of the subculture 2 show each fraction at this stage to have a rather broad distribution. This was disappointing

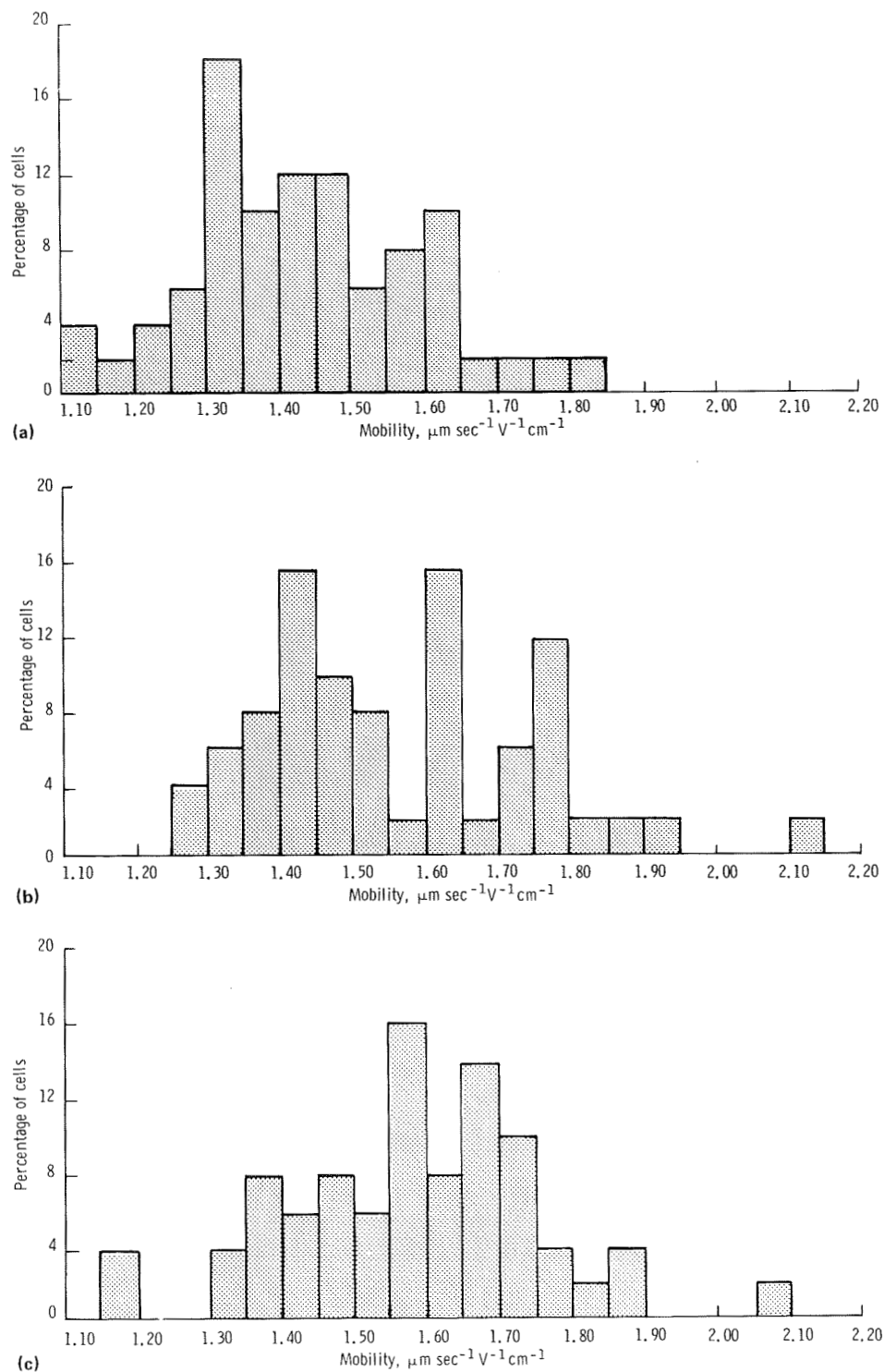


FIGURE 19-19.—Analytical electrophoretic mobility distribution. (a) Cell subculture 2 of fraction number 14. (b) Cell subculture 2 of fraction number 17. (c) Cell subculture 2 of fraction number 19.

TABLE 19-VI.—Units of UK Produced From Primary and Subculture 1 Kidney Cells Separated in Flight Column 3

Fraction no.	UK assay, units/disk	Viable cells	UK, units/100 cells
<i>Primary</i>			
11	45	$0.07 \times 10^5$	0.64
13	535	.696	.77
15	240	.12	2.0
17	225	.744	.3
B control <sup>a</sup>	61	.068	.9
D control <sup>a</sup>	81	.288	.3
<i>Subculture 1</i>			
14-1	85	$0.60 \times 10^5$	0.14
16-1	124	.132	.94
17-1	205	.9	.23
19-1	359	.222	1.62

<sup>a</sup>Samples taken as controls on the ASTP mission.

TABLE 19-VII.—Levels of HGCF Found in Various Fractions of Subculture 1

Fraction no.	HGCF, no. of colonies formed <sup>a</sup>
14-1	40
16-1	65
17-1	123
19-1	0

<sup>a</sup>Number of colonies formed was corrected for control plate.

because a rather sharp mobility distribution was anticipated. The explanation for this finding may be that the starting fraction is heterogeneous and the cell attachment and growth pattern is a random event that can broaden at each reculture level. It also must be remembered that the mobility data were taken from subculture 2 cells and not from the original cells separated during the ASTP flight. Further analyses should help prove this point and are in progress.

TABLE 19-VIII.—Units of Erythropoietin Produced From Primary Culture, Subculture 1, and Subculture 2 Kidney Cells Separated in Flight Column 3

Fraction number	Erythropoietin activity, units/ml
<i>Controls<sup>a</sup></i>	
B	0.8
D	0
<i>Primary</i>	
13	(b)
15	(b)
17	(b)
<i>Subculture 1</i>	
14-1	1.1
17-1	.9
19-1	1.65
<i>Subculture 2</i>	
14-2	5.0
17-2	2.0
19-2	1.0

<sup>a</sup>Samples taken as controls on the ASTP mission.

<sup>b</sup>Inhibitory.

### Isotachophoresis

A disadvantage of isotachophoresis is that the sample compartments are contiguous to each other and never separate to form an intermediate zone of clean buffer. (The buffer in front of the sample is called the "leading buffer" and the buffer that is behind the inserted sample is called the "terminator buffer.") If separation is desired, a so-called "spacer ion" of suitable intermediate mobility must be added. As will be discussed subsequently, this is of crucial importance for isotachophoresis. A further complication is that the heating of the column is not uniform; i.e., the progressively lower mobility compartments are exposed to proportionately higher potential gradients to ensure identical mobility. The temperature is a complicated function of both radial cooling and frontal migration of each compartment. The highest temperature is reached in the terminator buffer. This characteristic caused considerable concern in the design of the ASTP experiment, and it caused both the applied field and the duration of each experiment to be limited to an absolute minimum that was deemed compatible with sample resolution.

The sharpness of isotachophoretic boundaries gives rise to equally steep concentration (i.e., density gradients); thus, gravity effects are even more difficult to overcome than in zone electrophoresis. Because of gravity, protein isotachophoresis has always been conducted only in gels; and, at the beginning of the planning for the ASTP experiment, there was no ground-based apparatus in which cell isotachophoresis could be conducted. Therefore, the ASTP experiment provided a unique opportunity to study cell isotachophoresis.

Approximately 6 months before the ASTP flight, a new apparatus for cell isotachophoresis was developed as a result of extensive ground-based research. The apparatus utilized boundary stabilization through rotation of a horizontal tube, and the apparatus, named Rotofor, permitted the first ground-based work on cell isotachophoresis. Unfortunately, the leadtime for the ASTP experiment preparation was too short to permit as thorough an evaluation as desired.

From the beginning of the planning for the ASTP experiment, the possibility of processing

either fixed or fresh red blood cells was considered. Freezing fixed cells presented no problems, but freezing fresh cells was more difficult. Although low-temperature storage of erythrocytes is well documented, the particular requirements of isotachophoresis called for a freezing mixture with low overall electrolytes and substitution with a buffer suitable for isotachophoresis. This latter requirement presented the greatest problem. Many of the usual leader/terminator buffers, although compatible with the freezing of the red cells, caused cell aggregation during an actual isotachophoresis run. Using the Rotofor instrument, nonaggregating buffers were eventually found. In addition, the proposal to use liquid nitrogen as the freezing agent, together with the prescribed method of thawing (direct contact of the frozen cells with buffer at ambient temperature), imposed further limitations on the method of freezing red blood cells. The toxicity of dimethyl sulfoxide, which is widely used in red blood cell preservation, precluded its use in the manned flight experiment. Glycerol, therefore, seemed the most suitable cryoprotectant, especially in view of its electrophoretic inertness.

The primary buffer variables investigated were concentrations of glycerol and dextrose, which were necessary to preserve isotonicity in the freezing mixture. In addition, the influence of variable cooling rates on red blood cell recovery was studied. Good recovery (60 percent) of fresh red blood cells was obtained using a freezing mixture containing 4.2 percent dextrose and 2.8 to 3.5 M glycerol. Since these results were based on a freezing temperature of 194 K ( $-79^{\circ}\text{C}$ ), the study was extended by using liquid nitrogen for freezing. It was found that, over a wide range of red blood cell concentrations in the freezing mixture (5 to 50 percent hematocrit), no modification in the composition of the cryoprotectant was necessary.

A ground-based problem encountered in isotachophoresis of red blood cells was aggregation. This aggregation was initially absent but became apparent several minutes after application of the current, and it increased progressively during a run. Several leader/terminator buffer combinations were tried, including 2-amino 2-(hydroxymethyl-1, 3-propanediol) hydrochloride, acetate, or cacodylate as leader and

threonine, alanine, or asparagine as terminator; all of these caused aggregation. The combination that prevented aggregation was the use of phosphate as leader and serine as terminator.

Using nonfrozen red blood cells in phosphate serine buffer systems, isotachopheresis separation of cells from hemoglobin (or various added dyes) was easily achieved. Characteristically sharp boundaries were always obtained, a proof that in isotachopheresis, these cells do behave analogously to proteins or other ionic constituents. However, fractionation of mixtures of sheep and rabbit cells or human and rabbit cells (i.e., separation into two clearly defined zones) was not achieved. Again, the customary assortment of spacers was used, including ampholines and amino acids. The addition of ampholines caused spreading of boundaries, proving that at least some ampholin fractions possessed mobilities comparable to the two cell populations. Lack of visible separation can be interpreted in terms of an interaction between the red blood cells and ampholine, resulting in randomization of cell mobilities. The situation was radically different with frozen mixtures of fresh cells. These cells readily separated in isotachopheresis even without the addition of spacers. Because freezing always results in partial hemolysis of the cell population, this was interpreted as showing that hemolysis liberated a spacer of suitable mobility to act as a spacer. No attempts were made to characterize this spacer. Attempts to use the supernatant from frozen fresh cells to separate fixed cells were not productive. For the ASTP experiment, it was therefore proposed to fly one sample of fixed cells and one sample of frozen fresh cells.

Isotachopheresis column 4 was processed using rabbit and human formalin-fixed red blood cells. The concentration of these cells, when loaded, was the same as that for columns 1 and 5. The volume of live red blood cells loaded into the sample slide (number 8) was provided in the following manner. Human and rabbit cells were prepared at a 40-percent hematocrit each. Equal volumes of each concentration were loaded into the sample slide. The final concentration was  $450 \times 10^6$  cells/0.098 ml. The isotachopheresis sample slides had a slightly larger volume (0.098 ml) than that

of the electrophoresis slides (0.06 ml).

On the day of the ASTP flight experiment, two sample slides containing duplicate samples of the fresh frozen flight cells were removed from liquid nitrogen, thawed, examined for free hemoglobin, and submitted to isotachopheresis in the Rotofor, using aliquot portions of the flight buffer. Free hemoglobin was found to correspond to a hemolysis of 52 percent of the cells, considerably higher than the usual hemolysis of less than 20 percent that was routinely observed in previous experiments. The decreased recovery of cells did not affect the ASTP experiment because sufficient cells survived to form good bands, and, indeed, the cell mass was clearly visible in both ground-based and ASTP runs. One might have expected the formation of a third isotachopheresis band containing free hemoglobin. Unfortunately, an isotachopheresis run in the Rotofor, under conditions of amperage and duration that duplicated the conditions of the ASTP flight, did not result in the expected separation of the two cell populations and/or hemoglobin. The migration distance was also lower than expected; the sample migrated only 30 mm in 45 minutes. The boundaries were quite diffuse and did not present the usual sharp fronts of other isotachopheresis cell runs. At the time of this experiment, there was no explanation for the lack of sample resolution. The lack of characteristically sharp boundaries is frequently observed during early stages of isotachopheresis before the sample is fully resolved and a steady state is reached. Lack of boundary sharpness is particularly pronounced in the presence of large amounts of ampholines, which provide a continuous mobility spectrum spacer. Migration velocity is also usually reduced during the resolving period of a mixture containing large amounts of ampholines, and visible samples frequently appear to remain stationary, whereas, in fact, higher mobility ampholine fractions are advancing into their proper position along the column.

Thus, this ground-based control experiment had all the appearances of isotachopheresis of a sample in the presence of a great excess of ampholines. At this time, only limited importance was assigned to this ground-based control experiment. The limited amount of available control-frozen cells prevented the exploration of this cell



behavior. In view of the similarly reduced migration velocity of the cells in the ASTP experiment, this control experiment proved to be highly significant. Its implication will be discussed, correlating it with the increased hemolysis of the sample.

### Evaluation of the Photographic Record of the Flight Experiment

Isotachopheresis of the formalin-fixed red blood cells was run in column 4. Photographs taken at various times are shown in figure 19-20. The photographic record is not as good as desired because the film was underexposed and the visibility is particularly poor at the ends of the column. The photographs were taken at 3-minute in-

tervals. The first frame showed the current off; the following frames, covering a timespan of 40 minutes, showed the current on; and the last three frames showed the current off again. Thus, because no record was made at precisely the time the switches were turned on and off, it is not certain whether the current was on for 40 minutes, for 46 minutes, or for some interim time period. The migration velocity appears to be 10 mm in 9 minutes, or very close to the predicted velocity of 1 mm/min. A different velocity is obtained, however, if the entire timespan of migration is considered. The last photograph (fig. 19-20(d)) was taken at a minimum of 40 minutes and a maximum of 43 minutes of migration; thus, the overall migration rate was 0.725 or 0.675 mm/min, depending on the exact time of current application.

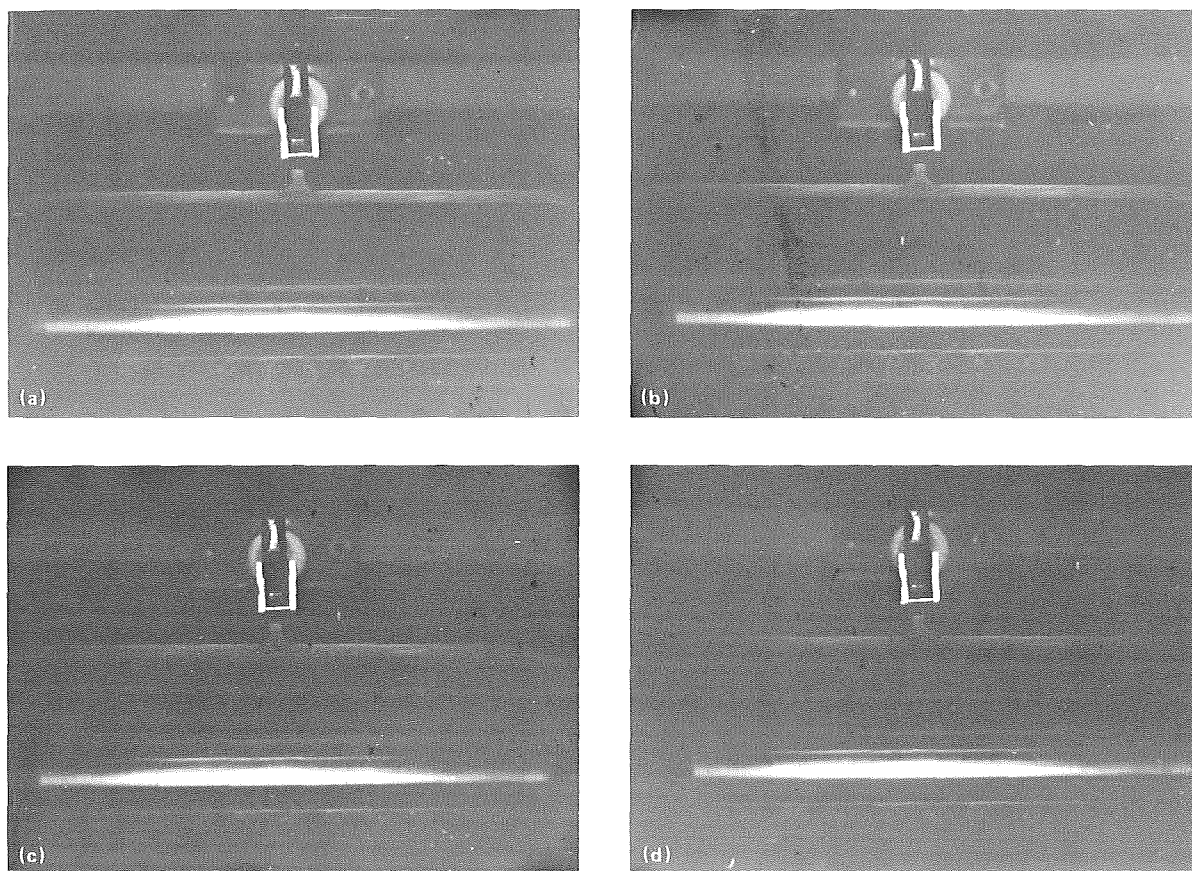


FIGURE 19-20.—Flight photographs of column 4. The sample is formalin-fixed rabbit and human red blood cells. (a) After 31 minutes of isotachopheresis. (b) After 34 minutes of isotachopheresis. (c) After 37 minutes of isotachopheresis. (d) After 40 minutes of isotachopheresis.

This value represents a substantially lower migration rate than expected.

The first visible boundary (fig. 19-20(a)) appears slightly fuzzy; but the last boundary, four frames later, is sharp and flat, as expected in isotachophoresis. The initial voltage was 113 V, and the final voltage was 133 V. This increase is characteristic of isotachophoresis. On the basis of the ground-based experiment, the predicted initial voltage would have been 106 V; thus, in this regard, there is excellent agreement.

The isotachophoresis of fresh-frozen cells occurred in column 8 (fig. 19-21). The quality of the photographs is somewhat better than for the first isotachophoresis run, and the column is visible past the 15-mm mark. In the case of column 8, the experiment was performed twice by the

crewmembers; the first portion of the run showed that no current was applied and, consequently, no migration occurred. For unknown reasons, the run was repeated and the remaining 39-minute timespan showed the current to be on. This second run was initiated, however, at least 70 minutes after insertion of the sample specimen into the column. Thus, there is considerable uncertainty as to the position of the sample at the beginning of the run.

An overall migration rate of 1 mm/min was predicted for both samples. The last four frames of the fixed cells confirm this migration rate, but the overall migration rate appears to be substantially lower than expected (presumably only 0.675 mm/min). For the fresh cells, the migration rate was still lower, being in the range of 0.55 to 0.64

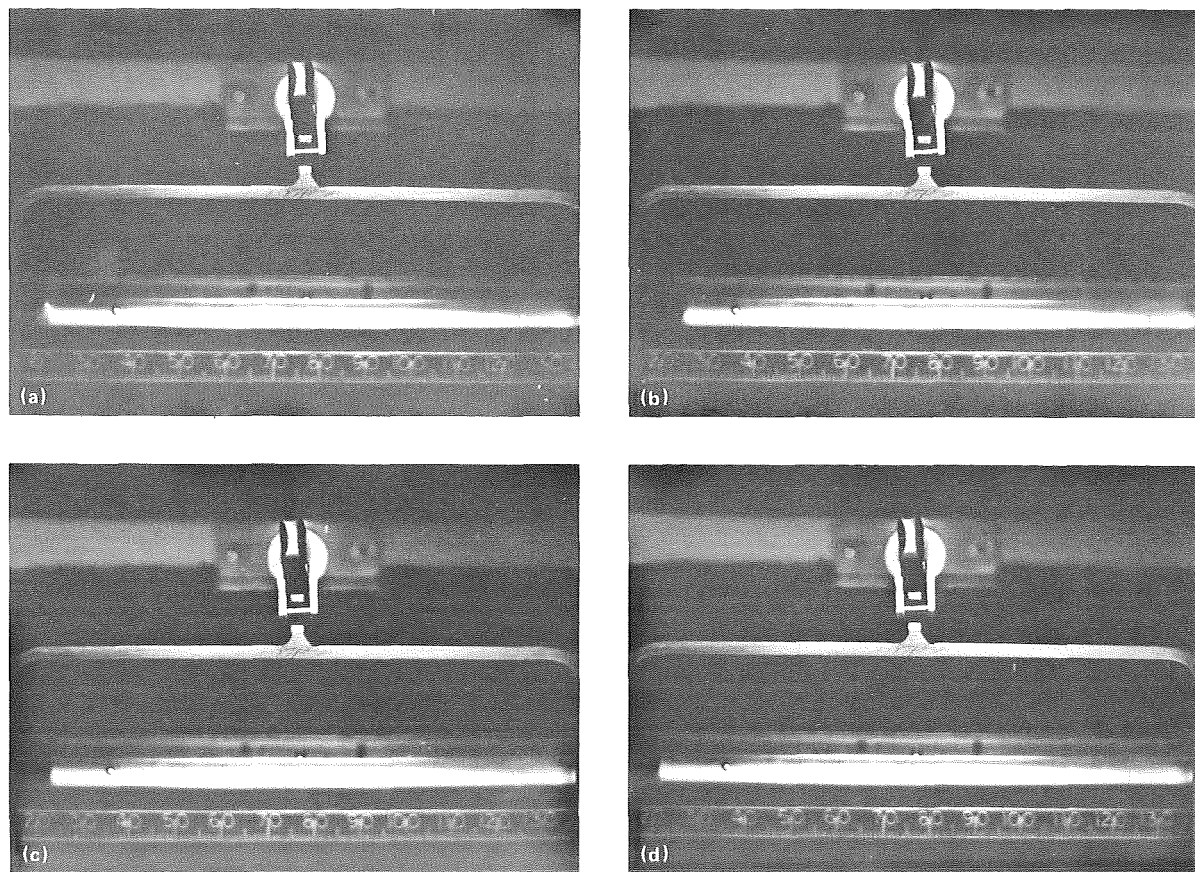


FIGURE 19-21.—Flight photographs of column 8. The sample is fresh frozen rabbit and human red blood cells. (a) After 30 minutes of isotachophoresis. (b) After 33 minutes of isotachophoresis. (c) After 36 minutes of isotachophoresis. (d) After 39 minutes of isotachophoresis.

mm/min, depending on the mode of calculation.

Interpretation of the mobility differences is difficult because there are several possible contributing factors: (1) there is an inherent uncertainty concerning overall duration of each run because the exact time of power application was not recorded; (2) for column 8, there appear to be unexplained periods of power failure; and (3) the position of the sample at the beginning of the fresh cell run is uncertain, as previously mentioned, due to the insertion of the sample at least 70 minutes before the onset of migration. Thus, it is not certain whether, during either of the isotachophoresis experiments, the photographs taken at 3-minute intervals represent a true record of run times. It is conceivable that power may have been flickering, but this was not observed during ground-based runs. Although measurements of advancing fronts in the fixed cell show constant increments, this is not the case with the fresh cell run.

One must assume, therefore, that none of the mentioned factors contributed to the observed reduction in migration velocity. That is, the same reduction in migration of the fresh cells in the ground-based control experiment was obtained when performed in the Rotofor using a duplicate of the flight sample. It will be remembered that this sample had an unusually high hemolysis. The reason for this high hemolysis is inexplicable. During the month before submission of flight samples, the cell preparation and freezing procedures were conducted numerous times, with innumerable individual samples, and uniform results were obtained. The separation of the two cell populations in frozen fresh cell isotachophoresis is predicated, however, on the liberation of an unidentified spacer. It is possible that the freezing procedure liberates not only a colorless spacer with intermediate mobility between the two populations, but also a spacer with a mobility higher than that of the human cells. Thus, a leading band of colorless spacer may be present. Increased hemolysis may account for greater quantity of either spacer, and thus result in slower initial migration rate, while the components of the mixture are resolved. As previously mentioned, this occurs whenever an excess of ampholines is used. Thus, the reduced rate of fresh cell migra-

tion may have been caused by excessive hemolysis, the sample not having reached a steady state in the time allotted.

A similar explanation may account for the discrepancy in the migration rate of fixed cells. That is, colorless fast ions may have been in the sample, thus retarding initially the migration rate of these cells. The sample, however, achieved a steady state of migration by the time the photographic record was obtained, as judged by the cell migration velocity.

In summary, the two isotachophoresis experiments did not run for a sufficient time to permit visualization of rear or intercompartmental boundaries. Nevertheless, the experiment shows the great advantage of isotachophoresis in the sharpness of the frontal boundary and in the concentration of the migrating zones. Thus, the main potential advantage of isotachophoresis is the quality of sample it may fractionate. With respect to cells, however, one must specify that the future of isotachophoresis depends on finding proper spacers.

## SUMMARY

The basic objectives of the Electrophoresis Technology Experiment were to conduct engineering and operational tests of a space-rated static electrophoresis separation apparatus and to further current research efforts through separation of similar cellular species. In addition, special effort was made to improve existing concepts in several areas. A method was needed that would allow for the precise application of the sample without affecting the subsequent electrophoresis. This improvement was accomplished by inserting the sample as a frozen disk. Attempts were made to separate and return viable lymphocytes and kidney cells. This goal was accomplished with the kidney cells but not with the lymphocytes. A technique was needed to demonstrate viable candidate preservation after separation. This preservation was accomplished for the first time in space by using a thermoelectric module to freeze the sample at a prescribed rate after separation was completed. The experiment allowed, therefore, the testing and evaluation of many important aspects

related to space-flight electrophoresis. In almost all cases, the concepts developed were proven operationally or shown to offer significant improvements over past efforts. Of particular interest was the low zeta potential coating. The minimization of electro-osmosis in this experiment provided a breakthrough sought since before the Apollo 14 separation attempts.

In summary, this experiment provided a significant step forward in the development of a biological processing facility in space. All areas of concern — i.e., sample preservation, sample collection and return, biocompatible systems, and sterile operating environment — were considered in this experiment. The accomplishments were significant and encouraging. The performance of electrophoretic separations in space without sedimentation and heat convective-mixing problems was demonstrated. The isotachopheresis of large living biological particles can be achieved. Scientists limited by Earth gravity problems can now use space-flight operations in the processing of particles that are difficult to separate or purify on Earth.

## REFERENCES

- 19-1. Shaw, Duncan J.: *Electrophoresis*. Academic Press (New York), 1969.
- 19-2. McKannan, E. C.; Krupnick, A. C.; Griffin, R. N.; and McCreight, L. R.: *Electrophoresis Separation in Space — Apollo 14*. NASA TM X-64611, 1971.
- 19-3. Wiersema, P. H.; Loeb, A. L.; and Overbeek, J. Th. G.: Calculation of the Electrophoretic Mobility of a Spherical Colloid Particle. *J. Colloid & Interface Sci.*, vol. 22, no. 1, July 1966, pp. 78-99.
- 19-4. Bier, M.; Hinckley, J. O. N.; and Smolka, A. J. K.: Potential Use of Isotachopheresis in Space. *Protides of the Biological Fluids: 22nd Colloquium*, H. Peeters, ed., Pergamon Press (New York), 1975, pp. 673-678.
- 19-5. Seaman, G. V. F.: *Electrokinetic Behavior of Red Cells*. *Red Blood Cell*, Vol. 2, Douglas N. Surgenor, ed., Academic Press (New York), 1975.
- 19-6. Donald, D.; Hutchinson, F.; Macleod, T. M.; and Raffle, E. J.: *Electrophoretic Mobility of Human Lymphocytes — An Investigation of the Technique of Cytopherometry*. *J. Immunological Methods*, vol. 6, nos. 1 and 2, 1974, pp. 151-156.
- 19-7. White, Wilfrid F.; Barlow, Grant H.; and Mozen, Milton M.: The Isolation and Characterization of Plasminogen Activators (Urokinase) From Human Urine. *Biochemistry*, vol. 5, no. 7, July 1966, pp. 2160-2169.
- 19-8. Bernik, Maria B.; and Kwaan, Hau C.: Plasminogen Activator Activity in Cultures From Human Tissues. An Immunological and Histochemical Study. *J. Clin. Invest.*, vol. 48, no. 7, Apr. 24, 1969, pp. 1740-1753.
- 19-9. Patterson, William J.: Development of Polymeric Coatings for Control of Electro-Osmotic Flow in ASTP MA-011 Electrophoresis Technology Experiment. NASA TM X-73311, 1976.
- 19-10. Gillman, Cetewayo F.; Bigazzi, Pierluigi E.; Bronson, Paul M.; and Van Oss, Carel J.: Preparative Electrophoresis of Human Lymphocytes. I. Purification of Nonimmunoglobulin-Bearing Lymphocytes by Electrophoretic Levitation. *Prep. Biochem.*, vol. 4, no. 5, 1974, pp. 457-472.
- 19-11. Brakman, P.: *Fibrinolysis. A Standardized Fibrin Plate Method and a Fibrinolytic Assay of Plasminogen*. Scheltema and Holkema (Amsterdam), 1967.
- 19-12. Phillips, H. J.: *Tissue Culture, Methods and Applications*. Kruse and Patterson, eds., Academic Press (New York), 1973, p. 406.
- 19-13. Haglund, Herman: *Isotachopheresis — A Principle for Analytical and Preparative Separation of Substances Such as Proteins, Peptides, Nucleotides, Weak Acids, Metals*. *Sci. Tools*, vol. 17, no. 1, 1970, pp. 2-13.

## 20. Electrophoresis

### Experiment MA-014

*K. Hannig,<sup>a†</sup> H. Wirth,<sup>a</sup> and E. Schoen<sup>b</sup>*

#### ABSTRACT

A continuous, free-flow electrophoresis study was conducted during the Apollo-Soyuz Test Project mission to investigate and evaluate the increase in sample flow rate and sample resolution achievable in space. This electrophoresis technique is one of the most valuable methods to separate and analyze biological particles, such as living cells, without decreasing their biological activity. Gravity-induced thermal convection and sedimentation limit the effectiveness of separation by this method. The electrophoresis equipment was designed for the separation of four mixtures of biological cells with variable sample flow rates, buffer flow rates, and electric field gradients. Separation quality was assessed by measuring the light from a quartz lamp through the electrophoresis channel and on to a photodiode system.

The data evaluation indicates that all monitored systems operated correctly during the experiment. The optical system produced a light that was too bright to discern true cell distributions, but final analysis of scientific data by computer processing shows the expected distribution of separated cells.

#### INTRODUCTION

The scientific requirements of the Electrophoresis Experiment (EPE) on the

Apollo-Soyuz Test Project (ASTP) flight resulted from a study concerning the application of electrophoresis in future biological experiments on Spacelab. That study examined the possibility of separating vital cells or other biological materials in the space environment.

To understand the specific function of cells and their membrane systems, research is needed concerning the problem of separation and characterization of particles performing individual functions. Of particular importance in studying cooperative interactions in biological processes is the isolation of the interacting systems in the most homogeneous and still functioning form. These problems are not only of a fundamental theoretical interest but are also of practical importance to elucidate normal and pathological processes in biology.

The reason for using electrophoresis to investigate these problems concerns the properties of the cell membrane surface, which is the site of many important biological phenomena. Transformation and differentiation processes are often accompanied by changes of the cell surface charge density. Charge density, however, determines the electrophoretic behavior; i.e., the electrophoretic mobility. Therefore, electrophoresis is a highly efficient method of separating cells or other biological particles according to functional criteria. Furthermore, cell electrophoresis is one of the few physicochemical processes that can be applied to living cells without producing damage or loss of viability.

Because electrophoresis is established as one of the most effective separation methods used in biological study, it is considered an essential tool for investigation in space. The expectation was that the separation capability would be increased

---

<sup>a</sup>Max Planck Institut für Biochemie, Munich.

<sup>b</sup>Messerschmitt Bölkow Blohm GmbH, Munich.

<sup>†</sup>Principal Investigator.

at zero-g, resulting in new applications that depend on improved resolution.

The EPE concept was based on a new electrophoretic principle known as "carrier-free continuous-deflection electrophoresis" (free-flow electrophoresis). The technique was developed by K. Hannig at the Max Planck Institut and is patented in Germany and the United States. By this method (fig. 20-1), the sample to be separated is introduced continuously into a separation chamber, in which a buffer solution flows laminarly. An electric field is generated perpendicular to the direction of flow. Particles having different surface charge densities are deflected from the flow direction of the buffer by an angle determined by the flow rate and the electrophoretic mobility of the particles. After leaving the lower end of the separation chamber, the separated zones can be collected continuously or analyzed by evaluating the deflection and the density distribution of the fractions.

Because this electrophoresis system is a continuous procedure, it should be applicable for routine use in solving a variety of separation problems in a future Spacelab. The EPE was designed to verify the theoretically expected better and higher capacity separations in the free-flow electrophoresis system under zero-g conditions.

### EFFICIENCY OF FREE-FLOW ELECTROPHORESIS

The decisive advantages of free-flow electrophoresis result from the principle of continuous operation in a flowing medium. In contrast to most of the usually applied foil- or gel-electrophoresis methods, this method does not accomplish stability by an open-pore carrier medium, but rather permits the medium to flow freely in a narrow gap. To obtain the necessary stability, the capillary forces at the gap walls are used. Under one-g conditions, this method succeeds when the gap width is less than 1.0 mm. This width is also sufficient for an undisturbed electrophoretic migration of larger particles in the electrical field. Unlike the discontinuous electrophoresis method that is stabilized by porous media, the range of application of

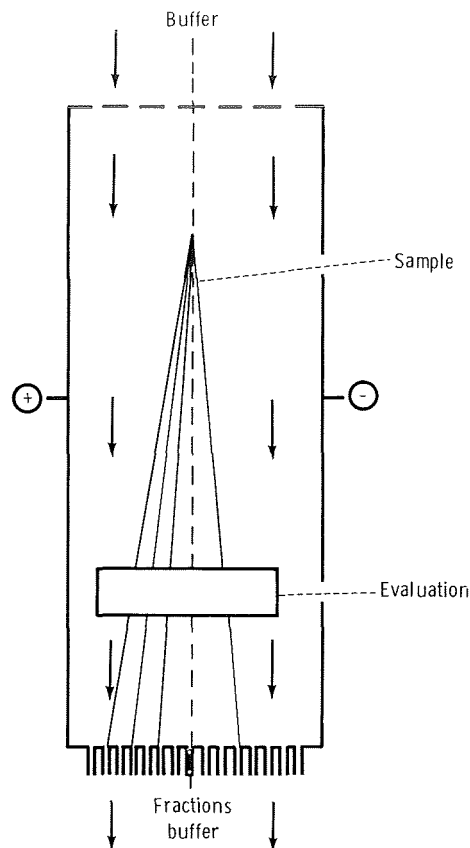


FIGURE 20-1.—Illustration of the principle of free-flow electrophoresis.

electrophoresis for preparative purposes can be expanded to include bulk-colloidal mixtures such as suspensions of viruses, bacteria, and cells and their membrane systems. A further advantage of electrophoresis in flowing medium with continuous operation is that the samples to be examined can be quickly exchanged without interrupting the experimental process.

The capability of quickly switching to the optimal experimental conditions combined with a completely automated operation makes this electrophoretic principle applicable to routine analytical separation problems. Thus, it would be possible to separate as many as 100 samples/hr to obtain analytical data concerning the composition of the samples to be examined.

As in every physical process, the effectiveness of free-flow electrophoresis is limited by some methodologically determined disturbances. In the

use of electrophoresis under zero-g conditions, it is necessary to distinguish between effects caused by gravitation (i.e., sedimentation and thermal convection) and effects independent of gravitation. Under zero-g conditions, sedimentation and convection can be eliminated and thus a higher throughput with larger separation chamber gap dimensions can be obtained.

The resolution of electrophoretic separation is, however, hindered by a methodologically caused band broadening, which also exists under zero-g conditions. The band-broadening effects result mainly from (1) the Poiseuille velocity profile of the liquid curtain, (2) the electro-osmotic velocity profile, and (3) the temperature gradient through the liquid curtain thickness; the temperature gradient increases with liquid curtain thickness and electric power (fig. 20-2). The thermal diffusion caused by the extremely short separation times in free-flow electrophoresis can be ruled out.

The extent of the previously mentioned effects on the resulting band broadening has been theoretically and experimentally examined. The

results are reported in reference 20-1, from which the following remarks were taken.

An analytical Free-Flow Electrophoresis apparatus permitted easy observation of all these parameters. It could be shown that the opposing tailing effects of electro-osmosis, and the temperature gradient to the effect of the velocity profiles can be compensated for by appropriate adjustment of the chamber wall zeta potential. (The velocity profile of the liquid curtain flow causes a tailing of the separated bands in the direction of electrophoretic migration, whereas the electro-osmotic velocity profile counteracts this effect.) The experiments showed that there are additional broadening effects due to other not clearly defined parameters. It was observed that the sample inlet geometry plays a considerable role in band broadening. The practical relevance of this observation is that band broadening is reduced if samples are centered in the middle of the liquid curtain. Furthermore, sample bandwidths should be adjusted to values with a starting bandwidth of less than half the liquid curtain thickness. Under such conditions, the bandwidth was reduced so as to approach theoretical values.

These considerations and the experimental results reveal decisive advantages of free-flow electrophoresis, as opposed to static systems, regarding obtainable separation sharpness and sample throughput. However, one limitation occurs if the method of "isoelectric focusing" or "isotachopheresis" is applied for special separation problems. Because of the discontinuous buffer systems required (pH or ion strength gradients), the free-flow system appears to be less suitable.

### ELECTROPHORESIS UNDER ZERO-G CONDITIONS

The efficiency of electrophoresis under one-g conditions is limited. Gravity effects such as heat convection, sedimentation, and buoyancy limit

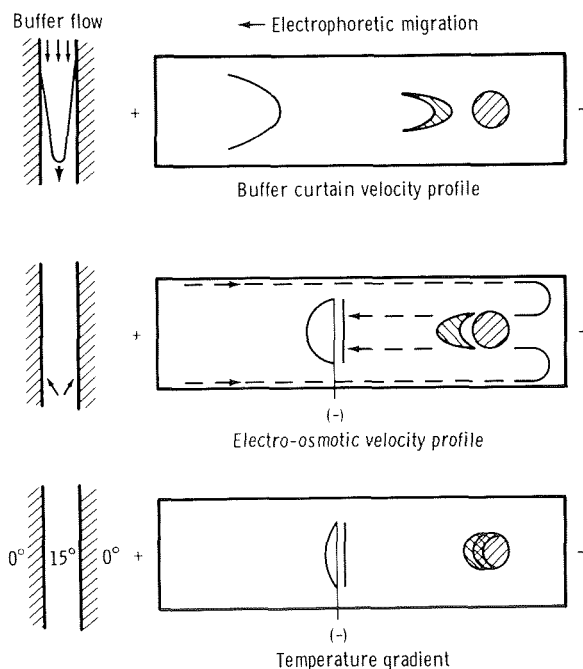


FIGURE 20-2.—Band-broadening effects in free-flow electrophoresis.



the application with respect to flow rates and resolution. To avoid convection under one-g conditions, the cross section and dimensions of the electrophoresis separation chamber must be kept small. (The thickness of the buffer film is normally 0.5 to 1 mm.) Under zero-g conditions, there are theoretically no limits in this respect. However, one limit is set by the need for effective removal of the Joule heat, especially when working with biological materials. (Depending on environmental conditions, this limit occurs at a layer thickness of 5 to 10 mm.) Considering this limitation, with a possible tenfold larger buffer film thickness, an increase of up to tenfold in sample throughput can be achieved because of the lack of convection disturbances.

A simultaneous improvement of separation sharpness is, however, not to be expected. As previously discussed, the factors influencing separation sharpness in the EPE are essentially methodological and are not dependent on gravitation. An optimization of separation sharpness can be achieved under one-g conditions if the experimental requirements are fulfilled (suitable separation chamber wall potential and less sample throughput).

The significance of applying electrophoresis in the Spacelab as the preferred separation method for sensitive biological material becomes particularly evident in connection with important biological experiments conducted under zero-g conditions. The use of electrophoresis may assist in clarifying many phenomena, such as growth, metabolism, genetics, and immune responses, which occur differently in zero-g conditions than in one-g conditions. The two main purposes for conducting electrophoresis experiments in space are (1) to analyze purity and to isolate samples for medical and biological research, and (2) to develop separation methods for commercial and other applications on a preparative scale.

Many proposals also merit further investigation. These proposals concern the effect of gravity on cell functions and the ability of cells or whole organisms to adapt to changes in gravity. One example is the cultivation of cells, the investigation of their synthesis efficiency, and their contact inhibition without gravity. Assuming that it is possible to isolate highly purified cell populations

grown under zero-g conditions, the state of weightlessness will offer an excellent opportunity to examine the phenomena of cell differentiation and the exchange of information between different cells.

Some of the necessary operational conditions can be tested only with complete absence of sedimentation. The clarification of these phenomena is not only of great scientific interest but also of practical significance for the regulation of detailed biological processes.

The importance of new findings of this kind for medicine can be anticipated. These investigations require a separation method that allows separation of the carriers of specific syntheses or of the synthesis products themselves. This purpose may be fulfilled in Spacelab by using electrophoretic separation methods. However, the applicability of space electrophoresis for the production of biological material for commercial purposes cannot yet be predicted. At this point, researchers are just learning how electrophoresis in space is to be used. The EPE can therefore be essentially regarded as a pilot experiment.

The main purposes of EPE and the problems to be clarified were as follows.

1. Applicability of electrophoresis in space
2. Performance of separation experiments with greater throughput
3. Investigation of temperature and velocity effects with a chamber of larger gap width
4. Investigation of separation capability in zero-g conditions
5. Proof of the possibility of separating preparative quantities of living cells
6. Determination of necessary modifications in the construction of the apparatus for use in space

## METHODS AND PROCEDURES

### Equipment Design

The design goal for the EPE apparatus (fig. 20-3) was to develop experimental equipment meeting the ASTP spacecraft requirements. The apparatus functions automatically, requiring



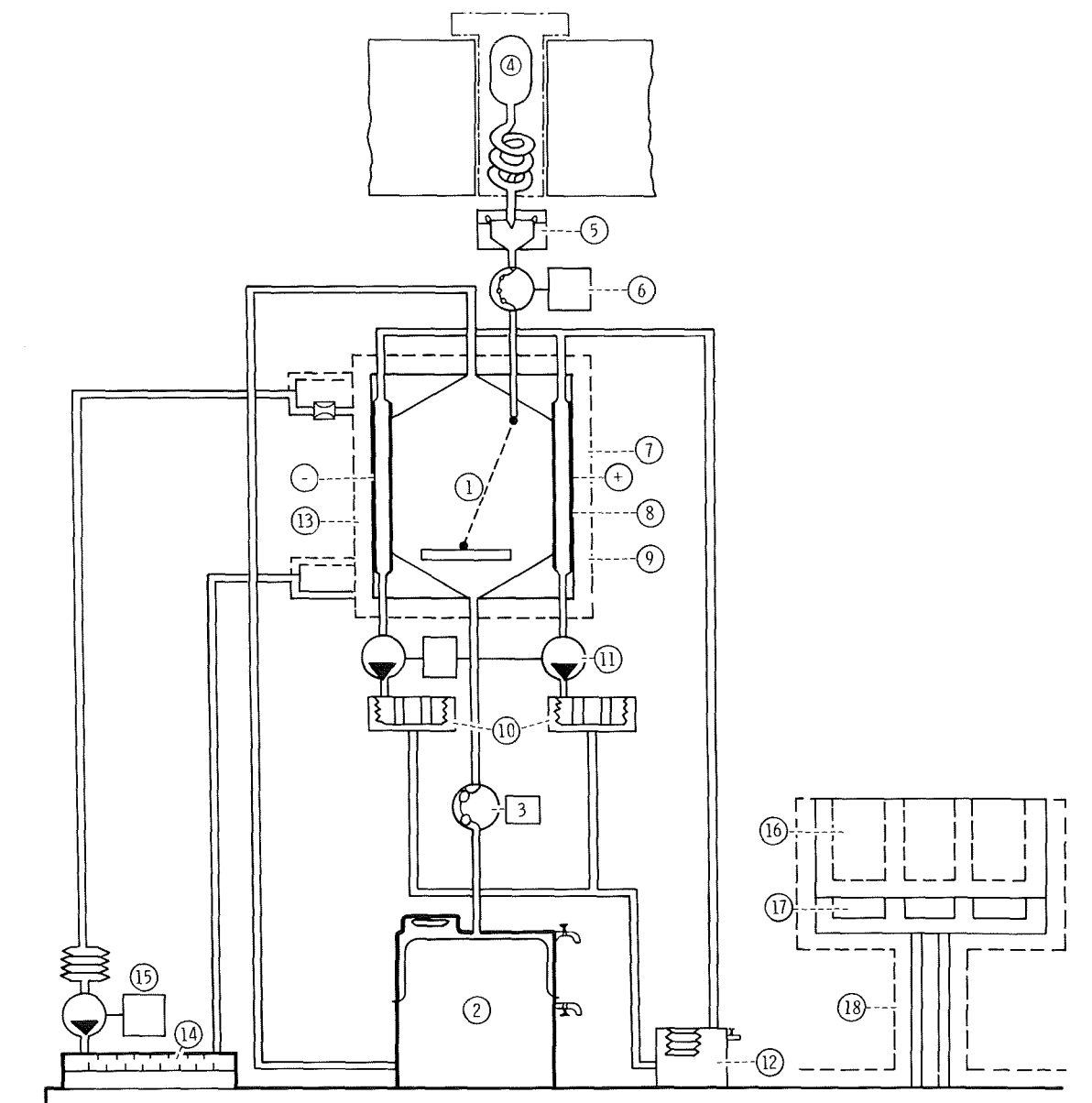


FIGURE 20-3.—Functional diagram of experiment. Buffer system: (1) separation chamber, (2) chamber buffer/waste container separated by diaphragm (3) peristaltic pump and motor for buffer flow. Sample system: (4) sample container (exchangeable), (5) sample inlet, (6) peristaltic pump and motor for sample flow. Electrode system: (7) electrode chamber, (8) electrodes, (9) ion exchange membranes, (10) phase separators ( $O_2 + H_2$ ) and gas absorbers (palladium black), (11) gear pump and motor for electrode purging, (12) electrode buffer container. Chamber cooling system: (13) separation-chamber cooling plates, (14) Peltier heat exchanger, (15) gear pump and motor for coolant flow. Freezer system: (16) sample storage, (17) Peltier cooling unit, (18) heat transfer plate.

minimal crew intervention. Known biological samples were used and it was not necessary to collect the separated biomaterial fractions. An

optoelectronic analysis of the separation was performed. A preparative separation was not used. A quantitative evaluation (by use of an optical

system) is sufficient to determine the applicability of the method and to study the sharpness of separation.

The separation chamber is the main part of the apparatus. It consists of two cooling plates that are adjusted to be exactly parallel to supply laminar flow and form a gap of approximately a 28- by 3.8-mm cross section. Along the sides, electrodes (180 mm long) provide the electric field perpendicular to the chamber buffer flow. The electrodes are separated from the chamber buffer by ion-exchange membranes. The electrodes are located in channels purged by the electrode buffer to remove the hydrogen and oxygen ( $H_2$  and  $O_2$ ) gases generated by the electrolytic processes. The gases are separated from the fluid and absorbed by means of catalysis. The fluid flow is kept constant by controlled pumping at a rate sufficient to transport the total volume of gas generated. The electrode buffer is separated from the cell buffer, which has a lower concentration, by the two ion-exchange diaphragms.

During the experiment sequence, the walls of the separation chamber were cooled down and the temperature was controlled at the operational condition of  $278 \pm 3$  K ( $5^\circ \pm 3^\circ$  C). The buffer leaves the storage container and enters the separation chamber somewhat upstream of the sample inlet to achieve a constant laminar flow in the separation chamber parallel to the electrodes. After having passed the separation chamber, the mixture of sample and chamber buffer entered the waste container, which is combined with the storage container but separated by a membrane. The angle of deflection for a particular particle was determined by the separation buffer flow rate and the field gradient. The program included two flow rates for each sample so that the influence of buffer velocity could be studied.

The sample containers were designed so that no air entered the circuit and none of the samples were split when the containers were inserted into the equipment. The containers have a volume of 2 ml, consist of a metal tube with handling knob, and are totally gold plated. On the upper end, they are closed by a pressure exchange membrane and sealing. The lower end has a bore connected to a needle with a valve that is opened by inserting the

container into the sample inlet closed by a rubber sealing.

The sample containers were stored in a freezer at 273 to 278 K ( $0^\circ$  to  $5^\circ$  C). For experimental operation, they were removed from the freezer and inserted into the equipment so that the sample flow entered the buffer flow. This flow was directed by a peristaltic pump similar to that of the buffer flow circuit.

The separation was evaluated by optoelectronic methods. By this method, a narrow slit across the downstream end of the separation chamber, parallel to the electric field, is illuminated. The light passes through the quartz plates of the separation chamber and is attenuated as a function of the density of the biomaterial distribution. On the other side of the chamber, the light intensity, related to the cell density, is measured with a photodiode array.

### Experiment Electronics

The experiment equipment was programed and controlled by electronic units that performed the following functions.

1. Control of the flow rates; i.e., motor speeds for driving the pumps
2. Power supply
3. Program sequencing, which provided the program of the experiment operations
4. Thermoelectric temperature control
5. Self-check and NO-GO indications
6. Data acquisition, evaluation, and processing
7. Data recording
8. Switching and displaying of experiment operations and experiment states

The main purpose of the program sequencer was to operate the experiment automatically as much as possible, thereby reducing crewmember participation. The program sequencer was designed to perform the following functions (fig. 20-4):

1. Timing of functions such as precooling or purging
2. Generating nominal values for voltage and flow rates according to the sequence step

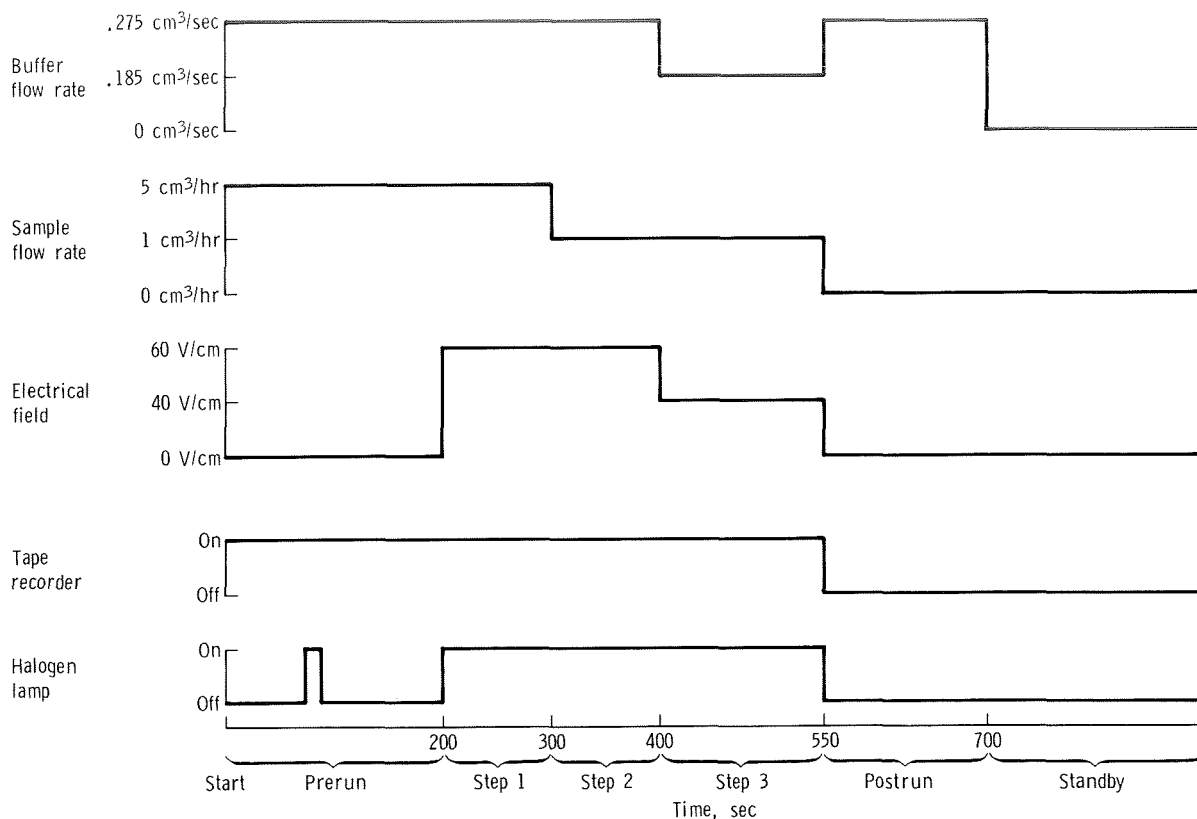


FIGURE 20-4.—Electrophoresis experiment sequence.

3. Collecting and processing GO/NO-GO information from experiment subsystems

4. Switching subunits "on" or "off" according to the program

5. Providing time, frequency, and voltage references

All experimental data were recorded in digital form by two redundant tape recorders that were integrated into the experiment. Both recorded digital data at a bit rate of 2.5 kilobits/sec.

### Experiment Hardware

*Fluid circuits.*—The experiment hardware incorporated four independent fluid circuits.

1. The chamber buffer circuit provides laminar flow for the chamber buffer, which passes from the sample inlet to the quartz window through the separation chamber. The buffer is stored in the

chamber buffer container, which at the same time serves to collect the waste chamber buffer leaving the separation chamber. The container halves are separated from one another by a diaphragm that prevents waste buffer from mixing with unused buffer. Thus, the buffer circuit has a constant volume so that there is no need for complicated volume and pressure compensating systems.

2. The sample circuit is used to ensure defined insertion of the biological samples into the separation chamber.

3. The electrode buffer circuit aids in transporting the gases produced at the electrodes to the phase separator where they are separated from the fluid and absorbed by means of catalysis.

4. The coolant circuit is used to keep the temperature of the separation chamber constant (278 K (5° C) wall temperature).

Chamber buffer and sample flow is achieved by

means of peristaltic pumps (figs. 20-5 and 20-6). Coolant and electrode buffer are fed using gear pumps.

*Electronics.*—The following major problems were solved through the use of electronic equipment (fig. 20-7).

1. Drive and revolutions-per-minute control of motors
2. Control of experiment sequence
3. Temperature control of sample freezer and separation chamber
4. Data acquisition, processing, and storage
5. Automatic functional check of systems and indicators (GO/NO-GO)

*Acquisition of scientific data.*—The scientific data were obtained through measurement of the absorption of shortwave light passing through the separation chamber to reach the line of measurement (fig. 20-8). After having passed the quartz window of the separation chamber, light from a filtered source is focused onto the optical center of a lens with the aid of a condenser. An image of this line of measurement is projected onto a photodiode array measuring the local brightness of the individual image points.

The photodiode array (fig. 20-9) is composed of 128 photodiodes 12.5 mm in length. Their photovoltages are successively scanned and recorded in digital form on a magnetic tape as a measure of the

local brightness. The data rate is approximately 2.5 kilobits/sec with a brightness resolution of approximately 1 percent per step.

*Samples.*—The equipment was designed for the successive runs of a total of four samples. Each sample had a volume of 1.6 cm<sup>3</sup> usable for analysis. The first three samples were stored at 277 K (4° C) in a sample freezer in the experiment package. The fourth sample was stored in a freezer in the space vehicle and was kept at the temperature of the liquid nitrogen until use. The crew had to insert and exchange the samples; therefore, the containers were designed so that simple handling was ensured, fulfilling at the same time the functional requirements of (1) no entrance of air when inserting the samples into the sample inlet and (2) no escape of fluid when exchanging the samples.

*Experiment sequence.*—To determine the effects of the individual parameters, the essential parameters influencing the separation were changed in several steps. Each sample was subjected to the same sequence as follows.

1. During the prerin, the sample circuit was refilled with sample fluid and any possible remainders of the previous sample were removed from the separation chamber.
2. During experiment step 1, the following settings were made.

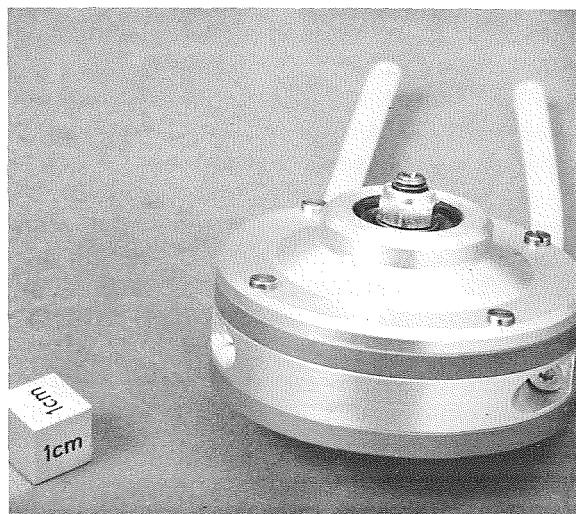


FIGURE 20-5.—Peristaltic pump (weight approximately 150 g) used in chamber buffer circuit and in sample circuit.

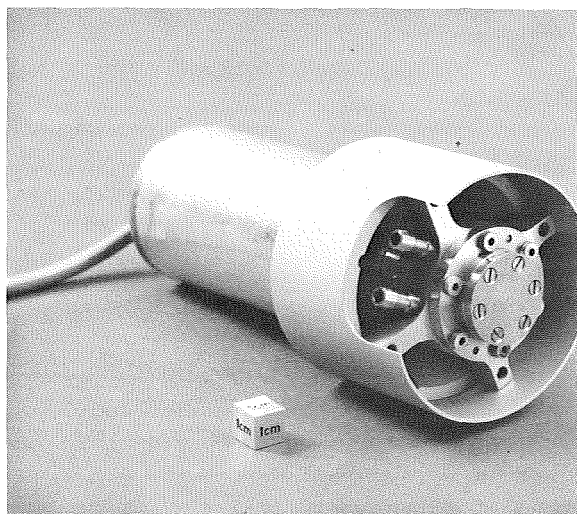


FIGURE 20-6.—Gear pump with motor as used in electrode buffer circuit and in coolant circuit.

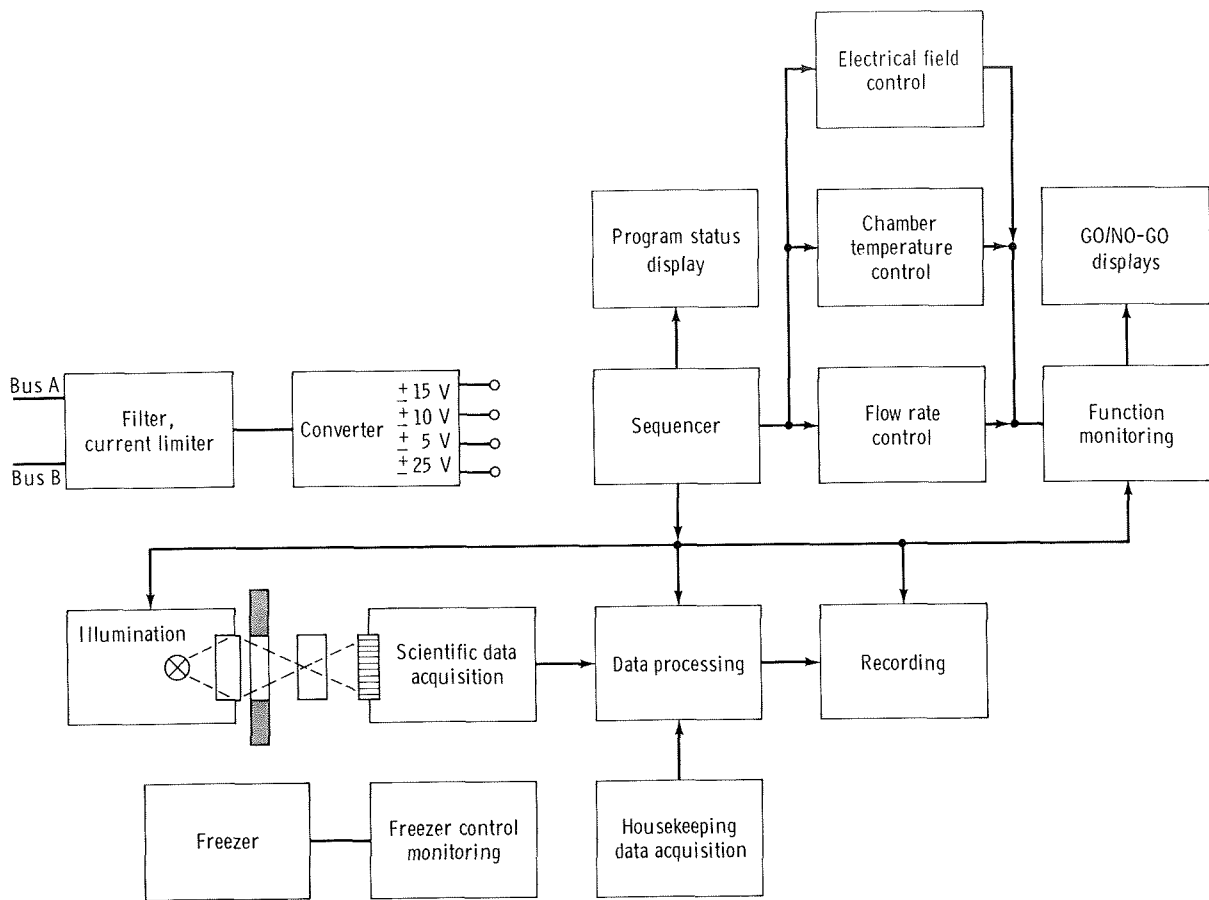


FIGURE 20-7.—Electronics block diagram.

Electric field: 60 V/cm  
 Buffer flow rate: 0.275 cm<sup>3</sup>/sec  
 Sample flow rate: 5 cm<sup>3</sup>/hr

3. During step 2, the sample flow rate was decreased from 5 to 1 cm<sup>3</sup>/hr, maintaining the two other conditions.

4. During step 3, the electric field intensity and the buffer flow rate were reduced to two-thirds of their original values, keeping the flow rate constant (1 ml/hr).

The experiment sequence is shown in figure 20-4.

*Overall experiment.*—The components of the experiment (figs. 20-10 to 20-12) were mounted on a baseplate that also accommodated the heat exchanger and the Peltier elements for control of the chamber temperature.

Special consideration was given to the design to

ensure that the equipment was capable of functioning satisfactorily with the cover removed; that all components could be exchanged as easily as possible, and that the major maintenance work, such as sterilizing the fluid circuits and fueling the systems, could be performed with the cover closed.

### Cell Sample Preparation

The following samples were prepared for the electrophoresis experiment.

1. Rat bone marrow cells
2. Mixture of human and rabbit erythrocytes
3. Rat spleen cells
4. Rat lymph node cells with the addition of human erythrocytes as markers (Sample 4 was the only frozen sample.)

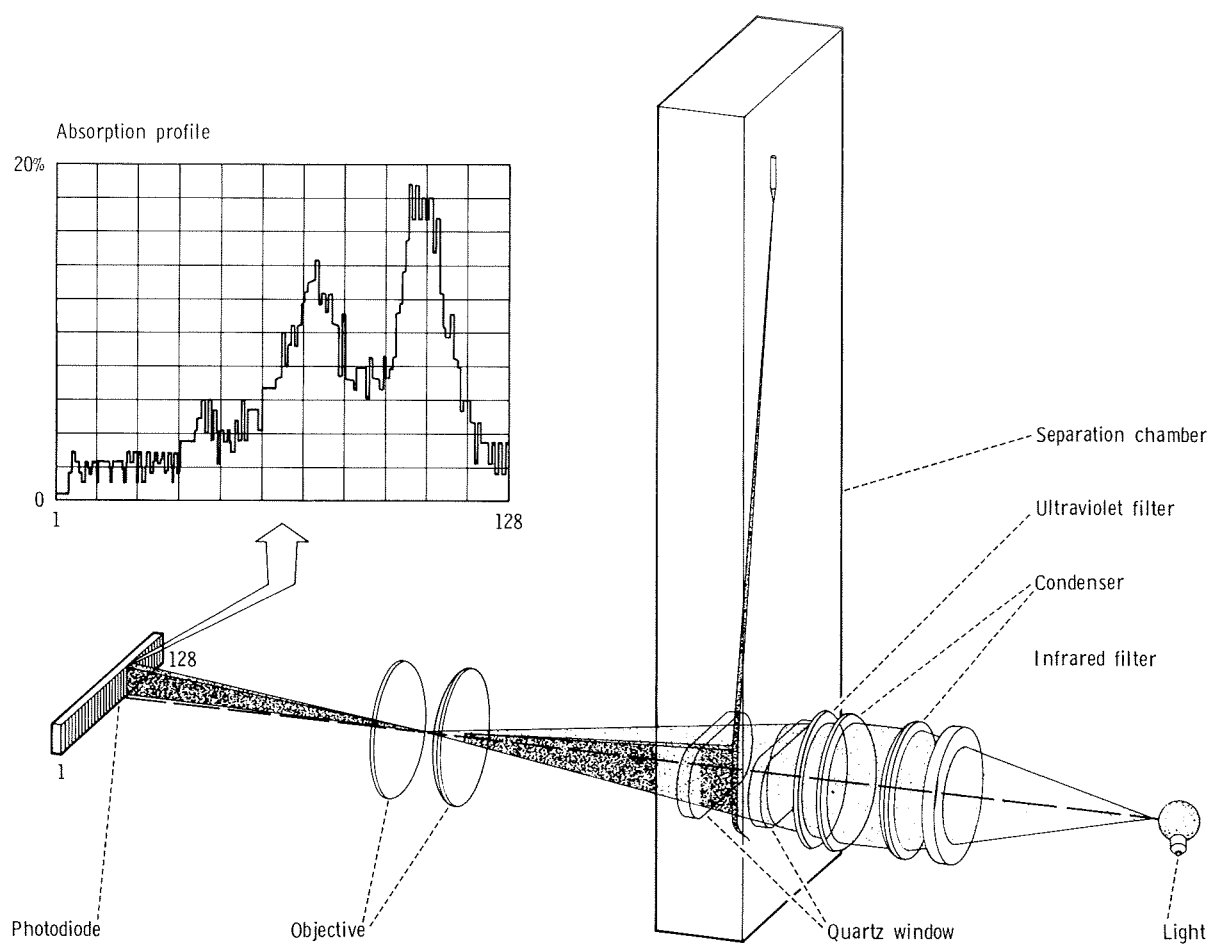


FIGURE 20-8.—Illustration of the principle of sample absorption measurement.

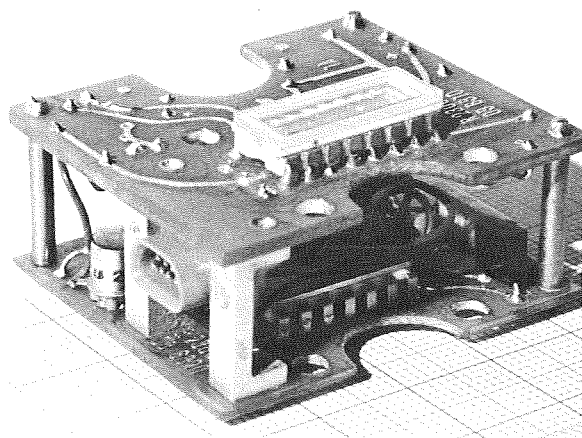


FIGURE 20-9.—Photodiode array integrated into shift register and amplifier unit.

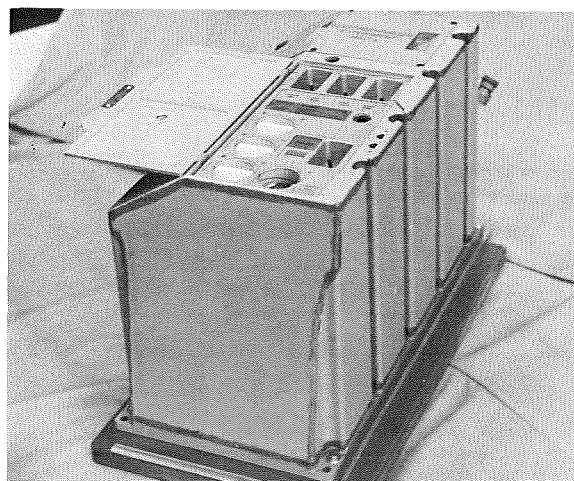


FIGURE 20-10.—Electrophoresis experiment flight unit with protective cover open.

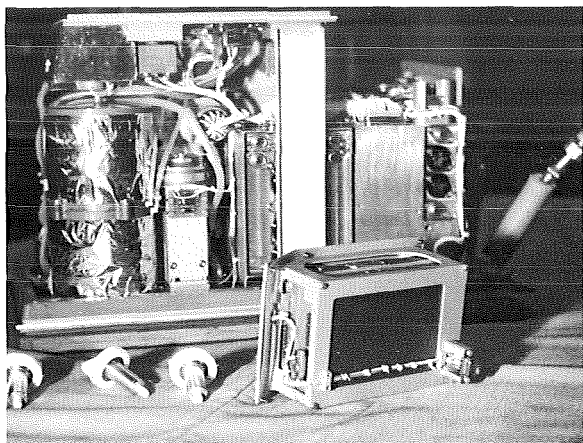


FIGURE 20-11.—Electrophoresis experiment flight unit opened, showing sample container and tape recorder module in the foreground. Components of the experiment shown are the 1.3-liter buffer container (left), the buffer pump with motor and the electrode buffer pump (center), and the electronic components (right).

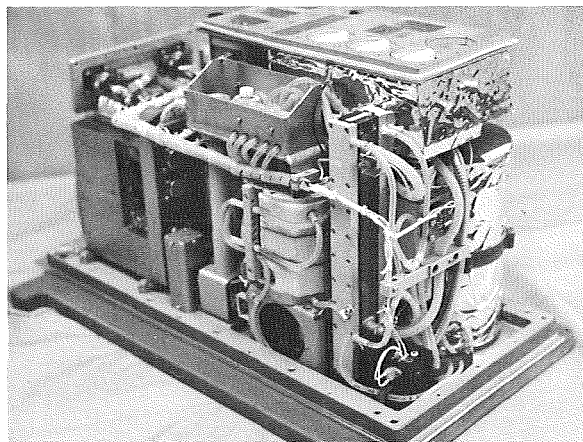


FIGURE 20-12.—Front view of experiment unit. On the right side is the buffer container, and above it the sample freezer and the control panel with sample containers installed. In the foreground is the separation chamber with the hose connections for buffer, coolant, and samples; and below are parts of the optical system. Adjacent to the separation chamber is the electrode buffer container, and above it is the service board for fueling and ventilation. The phase separator is shown below the service board.

With the exception of sample 2 (erythrocytes), all samples were freshly prepared on July 14, 1975, 15 to 20 hours before lift-off. They were stored at

277 K (4° C) for approximately 45 hours before the start of the experiment. Sample 2 (erythrocytes) had been prepared 2 weeks in advance at the Max Planck Institut für Biochemie in Munich, and the cells were preserved by fixation in 2 percent glutaraldehyde. The preparation of cells from different lymphatic organs was accomplished under sterile conditions (autoclaved material, clean bench) at 277 K (4° C) in the NASA John F. Kennedy Space Center (KSC) laboratory.

Bone marrow cells of rats (Wistar) were prepared, and cells were flushed out of the bones with Puck TC solution combined with 2.5 percent bovine serum albumin (33 percent) by using a syringe. A single-cell suspension was prepared by passing the cells several times through a plastic syringe without a needle. The cells were then washed twice (150 g, 10 minutes) with the same buffer and finally resuspended in ampholine buffer.

Cells from spleen and lymph nodes of the rats were prepared by teasing the organs in Puck TC solution at 277 K (4° C) with injection needles. Cells were washed twice with the same solution (150 g, 10 minutes), filtered through cotton wool, and resuspended in ampholine buffer.

For sterile tests, cell suspensions and buffer solution were spread on blood-agar dishes and incubated for 5 hours at 301 K (28° C). This test, as well as light microscopical control, showed no bacterial contamination of cell suspensions and buffer solutions. The viability of the prepared cells (tested with trypan-blue exclusion test) was more than 90 percent in each sample.

All containers of the flight unit were sterilized with formaldehyde (2.5 percent) and washed five times with 20 ml of sterile ampholine buffer. A special apparatus for filling the sample containers was sterilized in the same way. At 4 days before Apollo lift-off, the special "deep freezing container" was filled with a 0.8-ml mixture of rat lymph node cells ( $25 \times 10^6$  cells/ml) and human erythrocytes ( $30 \times 10^6$  cells/ml) and kept in liquid nitrogen. At 14 hours before Apollo lift-off, the other three sample containers were filled with 1.4 ml of the following preparations.

1. A mixture of fixed human erythrocytes

( $30 \times 10^6$  cells/ml) and fixed rabbit erythrocytes ( $50 \times 10^6$  cells/ml)

2. Native bone marrow cells of the rat ( $80 \times 10^6$  cells/ml)

3. Native spleen cells of the rat ( $80 \times 10^6$  cells/ml)

The exact composition of all buffer systems used for cell preparation and for electrophoretic separation is shown in table 20-I.

## RESULTS

The experiment began on schedule on July 16, 1975, and lasted for one complete Earth orbit. Radio communication from the Apollo spacecraft confirmed that, according to the signal lamps, all functions were operating properly.

### Evaluation of Housekeeping Data

The housekeeping data indicated that the experiment functioned correctly during the mission. The data were examined individually and compared with the values recorded during qualification testing of the equipment (December 1974). In this way, apart from the functional proof, a good

evaluation can be made as to the functional reliability of the equipment for a relatively long period. The results of this evaluation are summarized in table 20-II and figure 20-13.

## Discussion of Results

*Program.*—The program sequencer was functioning satisfactorily during all of the four runs. Program sequence and schedule were as planned (fig. 20-13).

*Chamber cooling.*—The controller used for chamber cooling was functioning properly. During precooling in the prerun, the chamber was cooled to 277.2 K (4.1° C) for each sample, this minimum value being reached toward the end of the prerun. From part I to the end of part II, the temperature control circuit was overloaded during all of the four sample runs. The chamber temperature rose beyond the nominal values of 278 K (5° C) to 280.9 K (7.8° C) (sample 1), 280.6 K (7.5° C) (samples 2 and 3), and 280.3 K (7.2° C) (sample 4), respectively. The maximum value was reached in each case at the end of part II.

In part III, the chamber temperature was again reduced continuously to a final value of 279 K (5.9° C). The circuit was no longer overloaded and

TABLE 20-I.—Buffer Solutions<sup>a</sup>

Description	Electrode buffer	Chamber buffer	Ampholine buffer
Substance, g/liter			
Triethanolamine .....	5.16	1.71	--
Potassium acetate .....	0.90	0.30	0.61
Glucose .....	0.90	14.61	--
Sucrose .....	--	7.88	--
Calcium acetate .....	--	0.033	0.05
Magnesium acetate .....	--	0.46	--
Glycine .....	--	--	21.55
Ampholine (pH 3.5 to 10) .	--	--	20 000
Characteristic			
Conductivity, $\mu$ mho .....	2500	900	900
Osmolarity, mOsmol .....	--	$\approx$ 300	$\approx$ 300
pH .....	7.2	7.2	7.2

<sup>a</sup>Buffer solutions mixed with distilled water.



TABLE 20-II.—Results of Housekeeping Data Evaluation

<i>Item</i>	<i>Nominal</i>	<i>Mission</i>	<i>Qualification</i>
EPE sequence prerun/parts I and II . . . . .	(a)	(a)	(a)
EPE sequence part III . . . . .	(a)	(a)	(a)
Reference voltage, V . . . . .	9.9 to 10.1	9.96 to 9.98	10.00
Chamber temperature, K (°C) . . . . .	276 to 280 (3 to 7)	277.1 to 280.6 (4 to 7.5)	277 to 279 (4 to 6)
Coldplate temperature, K (°C) . . . . .	278 to 280 (5 to 7)	278.9 to 279.4 (5.8 to 6.3)	--
Amplifier supply, V . . . . .	14.2 to 15.8	15.05	15.0
Amplifier supply, V . . . . .	-14.2 to -15.8	-14.8	-14.82
Logic supply, V . . . . .	9 to 11	9.8	9.95
Recorder supply, V . . . . .	4.5 to 5.5	4.75 to 5.0	4.8
Diode array supply, V . . . . .	24.0 to 25.0	24.7 to 24.8	-25.0
Motor supply, V . . . . .	20 to 27	20.8 to 23.6	<sup>b</sup> 22.5
Electrical field (60 V/cm), V/cm . . . . .	58 to 62	61 to 61.7	61
Electrical field (40 V/cm), V/cm . . . . .	39 to 41	40	41
Peltier current, percent . . . . .	0 to 100	10 to 85	10 to 85
Lamp supply . . . . .	--	--	--
Reference voltage, V . . . . .	9.9 to 10.1	10.00 to 10.01	-10.01
Reference voltage, V . . . . .	9.9 to 10.1	10.0	-10.00
Reference voltage, V . . . . .	9.9 to 10.1	10.02 to 10.026	9.99
Reference voltage, V . . . . .	9.9 to 10.1	10.00	10.00
Display supply, V . . . . .	4.5 to 5.5	4.70	5.05
Auxiliary motor supply, V . . . . .	20 to 28	22 to 26	<sup>b</sup> 24.2
Speed motor 2 . . . . .	(a)	(a)	(a)
Speed motor 1 . . . . .	(a)	(a)	(a)
GO/NO-GO events . . . . .	(a)	(a)	(a)

<sup>a</sup>Satisfactory.<sup>b</sup>KSC test, Oct. 1, 1975.

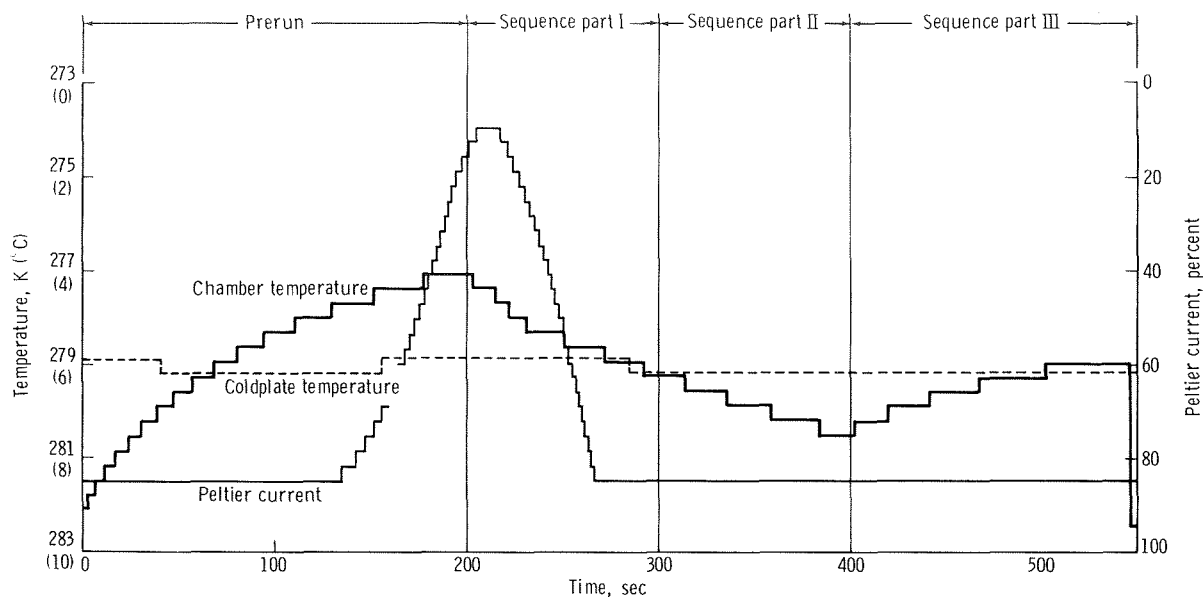


FIGURE 20-13.—Temperature profiles of the experiment during the mission (applicable for all four samples).

reached its nominal temperature, as shown by the extrapolation. The latter behavior, which differs from that in part I and part II, was due to the more than 50 percent reduction in heat transformation during part III of the sequence.

During the testing, an improvement in the temperature behavior was recognizable, which, as experience has shown, results from desalting of the electrode buffer and, thus, a decrease in the conductivity of this buffer as a function of operating time.

Overloading of the temperature control circuit during parts I and II of the sequences resulted from the following.

1. The conductivity of the chamber buffer was set to 800  $\mu\text{mho/cm}$  at a temperature of 283 K ( $10^\circ\text{C}$ ) for the mission. Desalting of the electrode buffer, in principle, results in approximately a 10-percent increase in the conductivity of the chamber buffer in the separation chamber so that a mission conductivity of approximately 880  $\mu\text{mho/cm}$  was obtained. Compared with the nominal value (750  $\mu\text{mho/cm}$ ), a current increase of 18 percent, or a power increase of approximately 35 percent, was achieved.

2. Upon completion of the hardware design, the conductivity of the electrode buffer was increased to 2500  $\mu\text{mho}$  so that the electrode buffer

cross section no longer affected the overall resistance of the separation chamber. This led to another current increase of approximately 10 percent, compared to the nominal value (20 percent power increase).

3. The modification of the cooling pump brought about a 30-percent reduction in coolant flow rate so that the stability reserve preventing the coolant circuit from overloading was depleted.

The assessments, based on the performance parameters thus modified, have shown that the cooling system behavior must have been as shown during the mission. As indicated in table 20-III, the temperatures as a whole did not exceed the prescribed performance limits.

*Electric fields.*—The prescribed field voltages in both ranges (i.e., 60 and 40 V/cm were maintained with a high degree of accuracy during all four sample runs (table 20-II).

*Supply voltages.*—The supply voltages were within the prescribed tolerance range; minor deviations of the mission data from the comparison values obtained during qualification testing are irrelevant.

*Illumination.*—As a result of the weightlessness, the circuit process in the halogen lamp was disturbed so that the helix temperature during the mission was higher than that under one-g condi-

TABLE 20-III.—Temperature Behavior of Experiment

Sample no.	Temperature, K (°C)			
	Chamber (initial)	Minimum (end of prerun)	Maximum (end of part II)	Minimum (end of part III)
1	282.5 (9.4)	277.2 (4.1)	280.9 (7.8)	279 (5.9)
2	282.2 (9.1)	277.2 (4.1)	280.6 (7.5)	279 (5.9)
3	282.2 (9.1)	277.2 (4.1)	280.6 (7.5)	279 (5.9)
4	282.5 (9.4)	277.2 (4.1)	280.3 (7.2)	279 (5.9)

tions. To obtain information about the excessive lighting, the transient phenomena of the illumination unit were determined at the beginning of each lamp check performed before each mission sequence, and the final lighting value was defined through extrapolation.

The transient phenomena of the illumination unit are shown in figure 20-14. Assuming that the transient follows the exponential law, the following equation applies approximately.

$$y = y_{\infty}(1 - T\dot{y}) \quad (20-1)$$

where  $y$  is brightness,  $\dot{y}$  is its derivative, and  $T$  is time. Time constant  $T_1$  is then given by

$$T_1 = \frac{1}{\dot{y}_1} \left( 1 - \frac{y_1}{y_{1\infty}} \right) \quad (20-2)$$

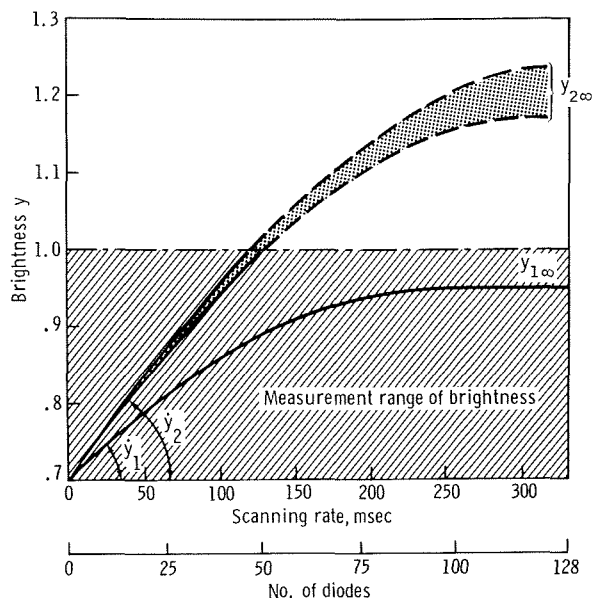
Assuming that  $T_1$  of the curve for normal lighting and  $T_2$  of the curve for excessive lighting are approximately equal, a conditional equation is obtained for the final value  $y_{2\infty}$  from the curve for excessive lighting

$$y_{2\infty} = \frac{y_2}{1 - \left( 1 - \frac{y_1}{y_{1\infty}} \right) \frac{\dot{y}_2}{\dot{y}_1}} \quad (20-3)$$

Using the values shown in figure 20-14, then  $y_1 = y_2 = 0.7$  (lower end of measuring range),  $\dot{y}_1 = 1.677 \times 10^{-3} \text{ sec}^{-1}$  (with  $y_1 = 0.7$ ),  $\dot{y}_2 = 2.5 \times 10^{-3}$  to  $2.85 \times 10^{-3} \text{ sec}^{-1}$  (with  $y_2 = 0.7$ ), and  $y_{1\infty} = 0.95$  (final value of normal curve). The probable final value of the photodiode array subjected to excessive lighting is given by  $1.18 \leq y_{2\infty} \leq 1.27$ .

**Reference voltages.**—The reference voltages registered on channels 136 and 147 to 150 are decisive for the reproducibility of the data. The deviations of the reference voltages from the values obtained during qualification testing show the level of confidence of the calibration curves. None of the voltages revealed a deviation larger than 3.6 percent.

**Lamp voltage.**—After a modification of the illumination system performed on a short-term



$y_{1\infty}$ = Final value at nominal exposure	} During preinstallation test
$\dot{y}_1$ = Derivative at nominal exposure	
$y_{2\infty}$ = Final value at overexposure	} During mission
$\dot{y}_2$ = Measured derivative at overexposure	

FIGURE 20-14.—Transient behavior of the illumination system.

basis, adaptation of the brightness sensor from 40 to 10 W was abandoned because of cost and schedule reasons; therefore, no data were supplied by this channel.

*Motor speeds of peristaltic pumps.*—The motor speeds were within the prescribed tolerance range. Stepper motors were used; therefore, only two stable states are possible, which means that the motors either run at nominal speed or they do not run at all. In addition, the NO-GO indicators and the event combination (in channel 161) confirmed that the motors were operating correctly.

*NO-GO and status checks.*—No NO-GO was recorded throughout the mission. The experiment status was displayed as requested by the program.

*Interfaces.*—The coldplate temperature ranged between 279 and 279.3 K (5.9° and 6.2° C) throughout the mission. The terminal voltages of bus A and bus B were within the prescribed tolerance range, as derived from the evaluation of channels 142 and 152 (uncontrolled voltages).

*Tape recordings.*—The tape recordings could be read correctly by the unit tester. The synchronization and bit errors were smaller than 1 percent. Of the total of 7500 frames, approximately 50 could not be read. The errors essentially were due to data failures during starting and stopping of the tape recorder at the beginning and end of the sequences (four samples and preinstallation test).

### Evaluation of Scientific Data

The scientific data revealed that the light for the optical detection of the separation must have been too bright. The lamp check showed excessive lighting that resulted in a saturation of the photodiodes in the optical detection system. The quantitative estimate of error revealed that the light must have been 35 percent too bright, although the lamp check indicated normal functioning during the preinstallation check. For this reason, only absorptions above 25 percent were registered. This amount corresponds to the maximum expected absorption of the separated fraction zone.

In the entire separation process, no "true" cell distribution curve was obtained. The baseline of registration in all cases was above the maximum absorption obtained in the peaks. Because of this

finding, an analysis of the experiment seemed impossible at first. However, during the stationary phase of the separation (after adjustment to constant experimental conditions), i.e., during 90-second separation time, irregularly occurring pulses (called "events") were recorded. This pattern reflected the expected course of the separation curves (fig. 20-15). These pulses seemed to be caused by cell aggregation in the region of the separated bands. This assumption was confirmed in the following two ways.

1. An aliquot of the sample used in the ASTP flight was separated under the same conditions on lift-off day at KSC, in an identical apparatus but under one-g conditions (electrophoresis engineering model (EM) with a 0.7-mm buffer film thickness). In addition to the expected cell distribution curves (fig. 20-15), analysis of this undisturbed tape showed stray pulses caused by cell aggregation that had a greater absorption. The accumulation at the same location (frequency distribution of the events) during a separation time of approximately 2 minutes yielded the distribution curves (fig. 20-15).

2. To check this finding and to obtain a reliable interpretation, such separations were repeated many times with the EM apparatus, and each experiment was performed and evaluated with normal and increased lighting. It was clearly established that only the analysis of the periodically occurring cell aggregations at the measuring location was representative of the actual cell distribution. The difficult evaluation and coordination of indirect information was performed with the aid of a computer.

Based on these studies, assertions can be made regarding the following samples.

1. Bone marrow cells: Although only a few events (73) could be analyzed because of the tendency of these cells to form no aggregations, the distribution curve is that of an excellent separation.

2. Mixture of human and rabbit erythrocytes: Because of the weak tendency of these fixed cells to form aggregations, insufficient information was available for computation.

3. Spleen cells: The best result was obtained with this sample. The amount of information (358 events) was sufficient to identify fine details of

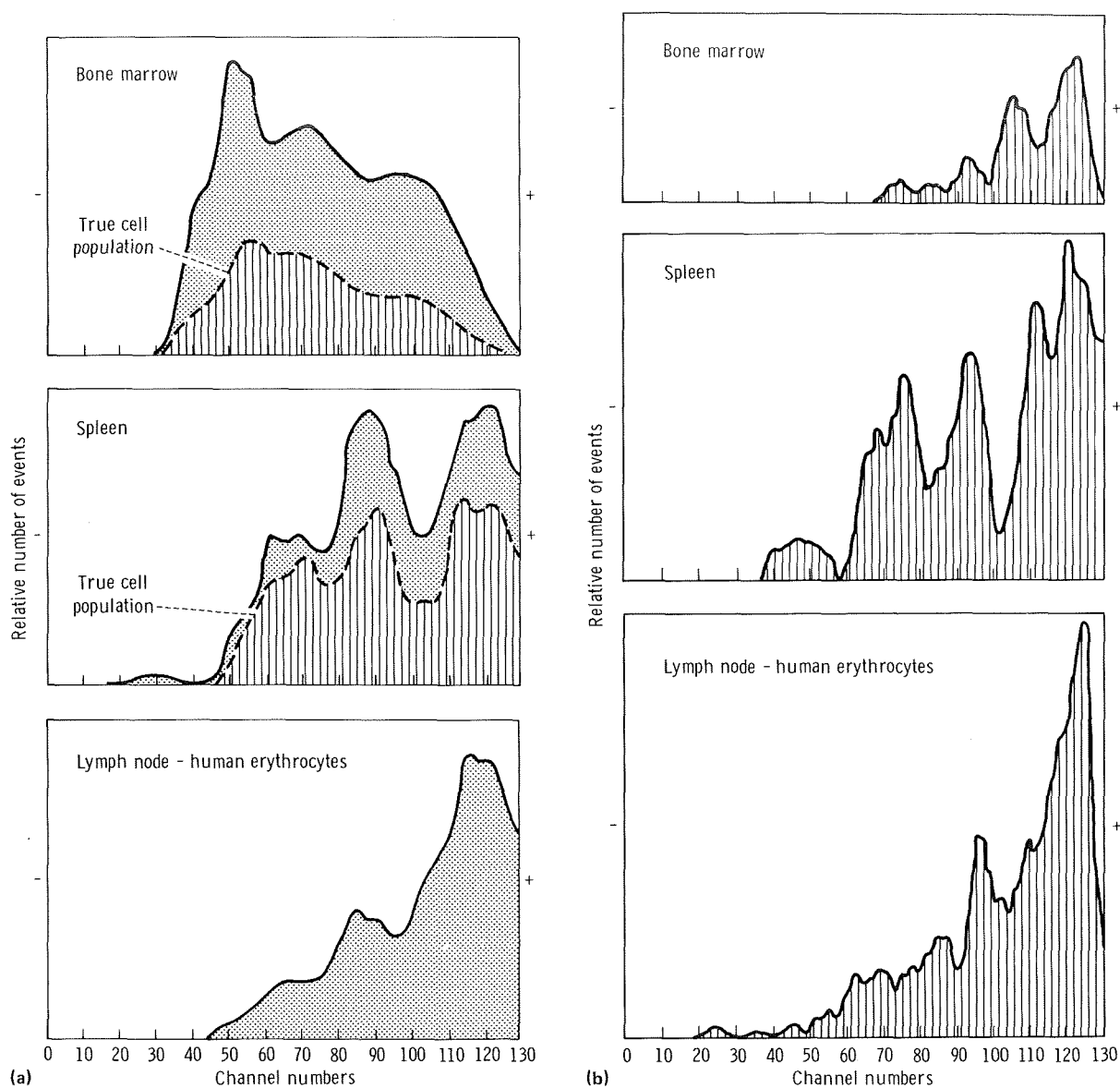


FIGURE 20-15.—Sample separation under zero-g and one-g conditions. (a) zero-g conditions. (b) One-g conditions.

the separation. The separation in erythrocyte peak can sometimes be indicated in good separations under normal one-g conditions as well. This finding indicates an essentially good separation sharpness under zero-g conditions.

4. Lymph node cells with the addition of human erythrocytes (frozen sample): A large number of events (549) were detected. A good separation effect, similar to sample 3, was inferred here as well as under zero-g conditions.

### Postflight Examination

Postflight examination of the flight unit, which took place in Munich, yielded the following information.

1. All housekeeping data were within the tolerance range.
2. The buffer and sample amounts corresponded to the required specification according to the volume measurement carried out.

3. Buffer samples collected in the container revealed no extraordinary bacterial contamination despite the long storage period. Microscopic investigation for the presence of cell particles in the separation buffer (collection container) was positive.

4. The expected remainder of the cell suspension, more than 3 months old, was found in the examined sample containers. However, the gold-plated containers revealed unexpected corrosion.

5. All buffer tube systems were intact and penetrable. The pump systems were still fully operational.

This information clearly reveals that the course of buffer and sample and the electronic system must have operated accurately. Surprisingly, the error in the optical detection system shown by the tape (saturation of the photodiodes) was at first not identifiable. Both the current and the voltage of the lamp were normal. By contrast, the light intensity measured by the diode array was, as expected, too low, because of turbidity. The cause of this phenomenon can be considered as either a fault in the electrical contact that occurred during the flight or an increase in lamp helix temperature that occurred under zero-g conditions. The latter could be explained by the absence of thermal convection in the gas-filled tube.

## SUMMARY

The applicability of free-flow electrophoresis under zero-g conditions of the space flight was confirmed. The technical problems arising from the special environmental conditions in a Spacelab can be controlled. This observation applies to the technical concept of the electrophoresis experiment apparatus as well as the manual operation by crewmembers. In particular, it was demonstrated that the buffer flow systems operated despite the

more difficult conditions imposed by a closed system. The effective removal of gases from the electrode buffer (electrolytic products) by the measures used was a necessary part of this experiment.

In a separation chamber of large cross section, the temperature conditions required for biological material could be fulfilled. This also applies for the correct laminar buffer flow.

A sample throughput greater than tenfold was achieved by the expansion of the separation chamber cross section, possible in space flight, and with otherwise similar chamber dimensions. (In the fast sequence (fig. 20-4, step 1),  $7 \times 10^6$  cells/min were separated.) Despite the error that occurred in the optical detection system, it was demonstrated that the separation sharpness corresponded at least to that of analytical separations under one-g conditions. Whether an improved separation sharpness is possible with a fivefold decreased sample insertion rate (fig. 20-4, steps 2 and 3), in contrast to one-g conditions, could not be determined because of the reduced source of information (sensitivity) caused by the lamp error. This is of little importance because such measurements can also be conducted under one-g conditions, as already shown. Also, the separation sharpness depends on other influences as well (e.g., zeta potential on the wall).

The possibility of separating living cells under zero-g conditions was demonstrated. The cell aggregations that formed in the cell suspensions need not correspond to a decrease in cell viability.

## REFERENCE

- 20-1. Hannig, K.; Wirth, H.; Neyer, B.; and Zeiliter, K.: Theoretical and Experimental Investigations of the Influence of Mechanical and Electrokinetic Variables on the Efficiency of the Method. *Z. Physiol. Chem.*, vol. 356, Aug. 1975, pp. 1209-1223.

# 21. Multipurpose Electric Furnace

## Experiment MA-010

*A. Boese,<sup>a†</sup> J. McHugh,<sup>b</sup> and R. Seidensticker<sup>b</sup>*

### ABSTRACT

Experiments on solidification, crystal growth, and other processes involving phase changes in various type materials were performed in the multipurpose electric furnace developed for the Apollo-Soyuz Test Project. Phase changes were conducted at elevated temperatures (as high as 1423 K (1150° C)) in systems comprising selected combinations of solid, liquid, and vapor phases. Because of the near-zero-g environment aboard the spacecraft, the liquid and vapor phases were essentially quiescent, and phases of different density had little or no tendency to separate.

### INTRODUCTION

The Multipurpose Electric Furnace Experiment facility for the Apollo-Soyuz Test Project (ASTP) was based on a similar furnace (denoted M-518) that was operated onboard the Skylab. The furnace was used to heat and cool material samples in space and thereby take advantage of the lack of thermal convection and sedimentation during the liquid or gaseous phase of the material. Seven experiments in solidification and crystal growth from vapor or melts were performed: Surface-Tension-Induced Convection (MA-041),

Monotectic and Syntectic Alloys (MA-044), Interface Markings in Crystals (MA-060), Zero-g Processing of Magnets (MA-070), Crystal Growth From the Vapor Phase (MA-085), Halide Eutectic Growth (MA-131), and Multiple Materials Melting (MA-150). These experiments are described in sections 22 to 29, respectively.

The motivating concept for the MA-010 experiment was that, at the present stage of the space-processing program, there are many useful preliminary space experiments that can be performed simply by applying prescribed heating and cooling programs and/or known temperature distributions to selected experimental samples of materials. For example, the simple process of growing a Bridgman crystal of a pure metal by directional solidification becomes an interesting new experiment in space because convective heat and mass transport will be largely suppressed in the melt. Many other similar examples exist.

The guiding design requirement for the multipurpose electric furnace system was to produce an apparatus that provided the widest possible flexibility in applying predetermined temperature distributions and temperature/time sequences within the constraints imposed by existing interfaces. Although the Skylab multipurpose furnace met all expectations of performance and reliability, it was apparent that improvement in function could be obtained with some specific modifications for ASTP. The system consisted of three essential parts: the furnace, a programmable electronic temperature controller that provided the desired temperatures, and a helium rapid cooldown system (fig. 21-1).

---

<sup>a</sup>NASA George C. Marshall Space Flight Center.

<sup>b</sup>Westinghouse Research Laboratories, Pittsburgh, Pa.

<sup>†</sup>Principal Investigator.

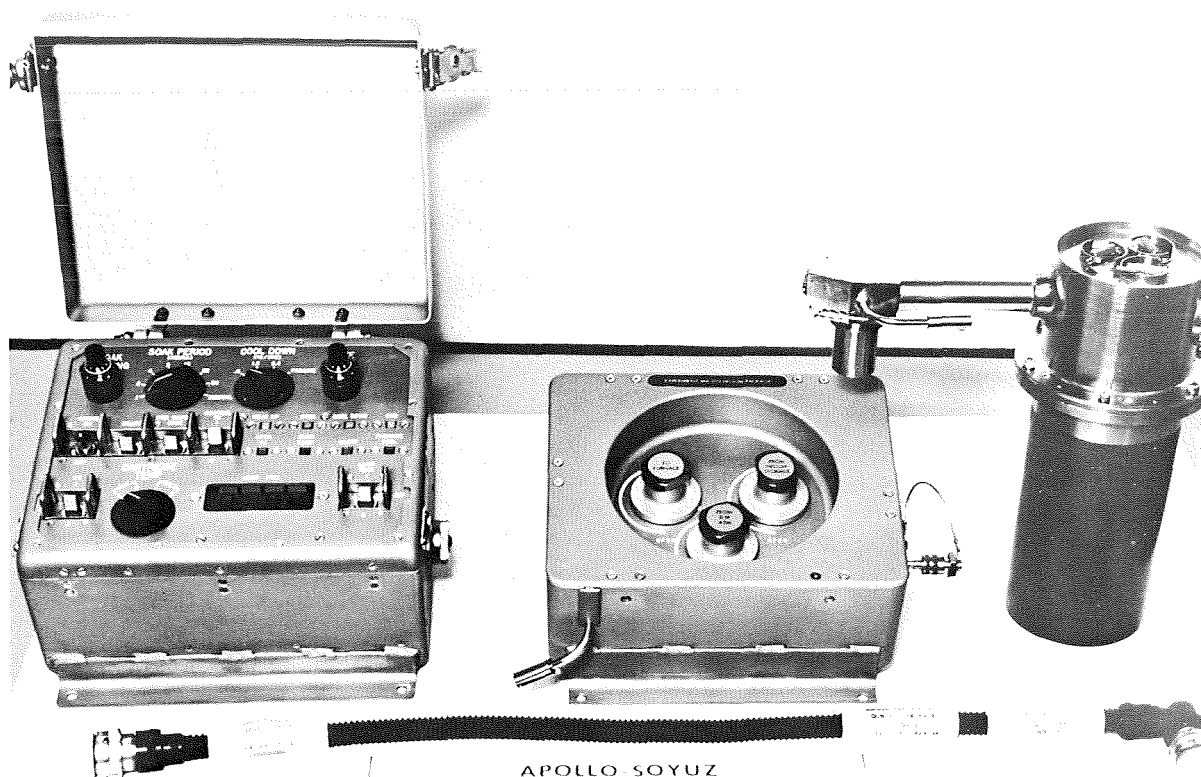


FIGURE 21-1.—Multipurpose electric furnace system.

## SYSTEM DEVELOPMENT

### Furnace

The design of the ASTP multipurpose furnace was prompted by two major considerations: the need for higher operating temperatures and the desire for reduced power requirements. The variety of materials experiments proposed for the ASTP mission required temperatures in excess of the approximately 1273-K (1000° C) limit of the Skylab system. Furthermore, the reduced heat dissipation capability of the ASTP vehicles dictated that these higher temperatures be obtained with no increase in power requirements (205 W).

Experience with the Skylab furnace facility indicated that somewhat higher temperature operation would be possible without any modification; however, the power requirements would be excessive. Therefore, the initial effort of the

redesign was to reduce the intrinsic heat loss. The predicted performance of the redesigned system was sufficiently encouraging that even higher temperature operation appeared feasible if it were compatible with the furnace materials, especially the heating elements. Accordingly, the high-temperature components of the furnace were carefully evaluated and, where necessary, materials were changed or assembly techniques modified to provide reliable operation.

Analysis of the Skylab furnace indicated that one significant source of heat loss was the "piping" of radiation between the heat shields. This loss could be reduced by providing a "mitered" closure of the radiation shields at both the cold and hot ends of the furnace. This type of construction would, in essence, provide a "nested can" shield configuration in which radiation leaks would occur only through the necessary clearance gaps in the shields. The efficiency of the shield



system was also increased by using two interstitial shields of 0.0127-mm (0.0005 in.) thick molybdenum foil between adjacent main shields.

Conductive heat loss through the heat leveler support tubes was also reduced. In the Skylab system, the heat leveler assembly was mechanically supported by three stainless steel (Type 310) gradient tubes that had outside diameters of 2.223 cm (0.875 in.) and walls that were 0.040 cm (0.016 in.) thick. These tubes had a combined thermal conductance of approximately 0.15 W-cm/K, which would result in a conductive loss of approximately 21 W with a furnace temperature of 1423 K (1150° C). In the modified furnace, the wall thickness of the support tubes was cut to 0.020 cm (0.008 in.), which would reduce the loss by half.

The design target maximum temperature of 1423 K (1150° C) for the heat leveler necessitated a reexamination of the heater elements. The first characteristic considered was the specific loading of the heater wires. This parameter controls the temperature difference between the wire and the workpiece; e.g., the graphite heat leveler. If the loading is too large, then the heater wire may be forced to run too hot in order to transfer the requisite power to the work. Several variations of heater design, including single and multiple ribbon heaters, were investigated. It was found, however, that the double, noninductive winding used for the Skylab furnace was nearly optimum when the additional constraint of heater resistance was imposed. The specific loading of approximately 1 W/cm<sup>2</sup> would impose a wire temperature only approximately 50 K (50° C) greater than the heat leveler temperature.

The next factor investigated was the suitability of Kanthal A-1 as heater material. Although this material is suitable for use to 1598 K (1325° C) in air, it is not recommended for use in vacuum at temperatures over 1273 K (1000° C). This warning is based on the rapid evaporation of a component from the alloy and was verified by tests performed on bare wires in ultrahigh vacuum. Sample filaments burned out after 2 hours or less at a surface temperature of 1473 K (1200° C). The heater winding, however, is not a bare wire operating in ultrahigh vacuum.

A second test was performed with a Kanthal A-1 heater wound on a salvaged Skylab heater form. In this configuration, the wire is completely surrounded by high-purity alumina. In the test facility, this heater form was filled with a graphite block to simulate the heat leveler and heavily insulated with Fiberfrax to reduce heat losses. After 144 hours of operation, the windings were still operating; however, the heater resistances had changed considerably. Examination of the disassembled unit revealed that evaporation of a volatile component had occurred and the wire was seriously degraded.

A further modification of the configuration was considered, namely embedding the heater wires in high-purity alumina cement. The life test was then repeated. The Kanthal was wound on the heater form and fired in air at 1273 K (1000° C) to form a surface oxide. A slurry of alumina powder was applied and air dried, and the heater form was then fired at 1273 K (1000° C). Finally, the test setup was reassembled. After 100 hours of operation at approximately 1473 K (1200° C), the heater resistances had changed by only 1.3 percent. Because the test time was roughly 10 times longer than the anticipated operating requirements, this design was adopted for incorporation in the prototype furnace.

Coincident with the requirement for higher temperature operation of the modified furnace, it became necessary to evaluate the higher temperature suitability of the structural materials used in the Skylab furnace design. It was immediately obvious that the only portion of the design that might be doubtful was that part of the structure in close thermal proximity to the heating element. Furthermore, it was clear that the limiting condition was that of the combined effects of graphite, alumina, and stainless steel as they exist at higher temperature in the multipurpose furnace atmosphere and pressure environment. In the Skylab furnace design, these materials are in direct physical contact.

To evaluate the limiting of this materials combination, a series of compatibility tests was carried out under conditions that approximated the multipurpose furnace environment. Alumina was promptly shown to be inert in these conditions at

the intended temperature. The margin of safe temperature for the graphite/stainless steel combination, however, was found to be very small. The intended maximum design temperature for graphite and stainless steel is 1423 K (1150° C) in the modified design. The tests indicated that this materials combination exhibited no harmful degradation at 1498 K (1225° C) but degraded seriously at 1523 K (1250° C). Thus, a furnace overtemperature of approximately 75 K (75° C) would be allowable insofar as graphite and stainless steel reaction is a concern. Although a margin of that value is probably adequate, it was desirable to provide a better choice of materials.

As a consequence, nickel was proposed as a replacement for the stainless steel, and the graphite and nickel combination was evaluated. This combination exhibited no harmful degradation even at 1560 K (1287° C), and it was deemed unnecessary to extend the evaluation to higher temperatures. The conclusion was that the graphite-nickel-alumina combination was safe to at least 1560 K (1287° C) and that the resulting overtemperature margin of 137 K (137° C) was more than adequate. The stainless steel was thus replaced with nickel in the temperature-critical areas in the modified multipurpose furnace.

A predictable consequence of increased multipurpose furnace temperature is increasingly reduced thermocouple electrical isolation resistance. This occurrence is a natural property of the magnesia insulation in the prefabricated swaged thermocouples and has the effect of reducing the resistance between the Chromel-Alumel wires and the Inconel sheaths, which, in the Skylab furnace, were electrically grounded to the furnace structure. This effect was acceptable at the 1273 K (1000° C) maximum temperature for which the Skylab furnace was designed. Because this effect is strongly temperature dependent, however, it was unacceptable at the higher (1423 K (1150° C)) maximum furnace temperature and thus required compensating design changes.

Greatly increased thermocouple resistance to a ground was obtained by electrically insulating the Inconel sheaths from the grounded furnace structure. This was accomplished in the high-temperature region by the installation of high-

purity alumina sleeves and in the low-temperature region by Teflon sleeves. Additionally, the control thermocouple Inconel sheaths were electrically connected to the regulated 10-V supply that biases the control thermocouples. This arrangement in effect applies a guard potential to the sheaths and thus eliminates the effect of the small remaining electrical leakage which exists with the insulating sleeves. The Inconel sheaths of the four measuring thermocouples were allowed to float electrically.

Experience disclosed that the seals of the access ports for the Skylab multipurpose electric furnace were not suitable for repeated use because of the excessive force required for removal. No seal leakage was ever detected. Because rotating and reciprocating seals are used routinely in high-vacuum systems, it appeared very likely that the problem with the Skylab furnace was not a fault of design principle but was rather a fault of design detail dimensions. A new design was developed.

The Skylab furnace was evacuated by evacuating the chamber in which it was situated. The ASTP furnace was evacuated through a pump line leading from the furnace through the docking module wall to space. The furnace vacuum connection was redesigned to allow for this change. The Skylab fitting was replaced by a 2.54-cm (1 in.) diameter elbow that terminated in a welded connection to the docking module pump line.

### Helium Package

The Skylab multipurpose furnace was evacuated during the entire time period required for each experiment. The modified furnace, if evacuated, required as much as 20 hours of passive cooling to reach the allowed touch temperature. For the ASTP mission, cooldown periods of such duration would seriously limit the number of experiments that could be fitted into the permitted time frame. To minimize this problem, a helium rapid cooldown system was developed. With this system, the time required for cooldown was reduced to as little as 3 hours.

Rapid cooling may be provided through selective control of the heat loss of the furnace. For

minimum thermal transfer, the heat shields require a high-vacuum environment, but the thermal transfer will be greatly increased if the vacuum environment is replaced by helium. Fortunately, only a very small amount of helium is required for this purpose; approximately  $1.01 \text{ kN/m}^2$  (0.01 atm) approaches the maximum effectiveness. For the multipurpose furnace, the volume required to produce  $1004.13 \text{ kN/m}^2$  (9.91 atm) is approximately  $0.16 \text{ cm}^3$  of helium at standard conditions. Within the  $1.01\text{-kN/m}^2$  (0.01 atm) range, the thermal transfer is weakly dependent on pressure, and it is consequently not necessary to provide a precise volumetric measure for each dosage. The helium package was designed so that successive doses of helium would be provided at slightly reduced volume.

A schematic representation of the helium package is shown in figure 21-2. During each experiment before rapid cooldown, all helium package valves must be closed. Immediately before operation of the package, the docking module valve in the overboard vacuum line to the furnace must be closed. To initiate rapid cooldown, two valve operations are required: (1) valve B must be opened momentarily to pressurize the helium dosage cavity from the helium storage tube, and (2) valve A must be opened momentarily to release the helium dosage into the

furnace. No further valve manipulation is required during the rapid cooldown period.

When cooldown is completed and the allowed touch temperature has been reached, the experiment cycle is completed. Before the furnace is opened, it should be pressurized to the same value as the docking module. This is accomplished with the helium package by momentarily opening valves A and C simultaneously and thus allowing the docking module atmosphere to flow into the furnace until the pressure is equilibrated.

### Control Package

The control package for the multipurpose electric furnace system (fig. 21-3) was modified to meet a new set of requirements for the ASTP mission. These modifications included several changes of the system operating functions; mechanical modifications were also made to meet new interface requirements. A listing of these modifications and a brief description of each is presented in the following paragraphs. In addition to these items, a number of minor electronic component changes were made to provide additional safety margins in circuitry operation.

*Increase in maximum control temperature.*—To facilitate higher temperature experiments, the gain of the control thermocouple amplifier was altered to permit a maximum controlled heat leveler temperature in excess of  $1423 \text{ K}$  ( $1150^\circ \text{ C}$ ).

*Variable controlled cooldown rate.*—To provide more constant solidification velocities in the experiments, circuitry was incorporated to decrease the cooldown rate continuously during the controlled cooldown portion of the experiment. A control was provided to enable selection of the amount of cooldown rate variation.

*Shorted control thermocouple protection.*—To protect the furnace from overheating should the control thermocouple become shorted, an additional shutdown circuit was incorporated in the control package. This circuit continuously monitors both HOT-1 and HOT-2 measuring thermocouples and automatically shuts off the furnace heaters if either of these thermocouples exceeds a preset limit temperature (nominally set at  $1463 \text{ K}$  ( $1190^\circ \text{ C}$ )).

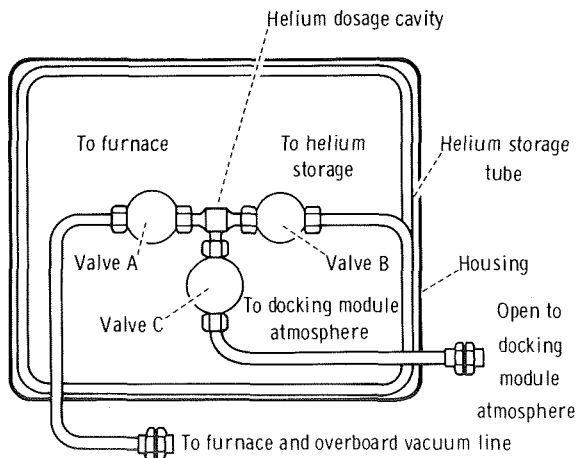


FIGURE 21-2.—Schematic representation of the helium rapid cooldown system.

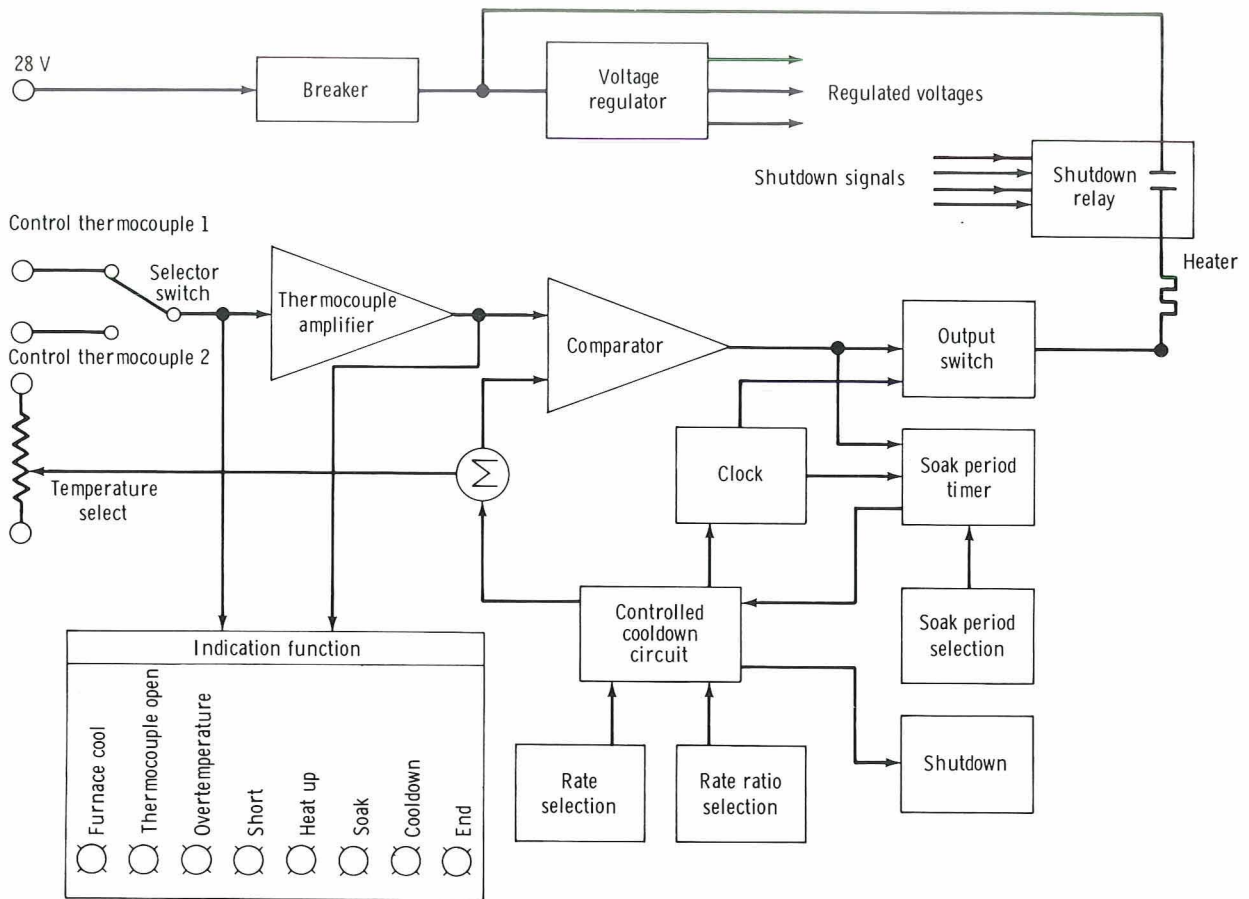


FIGURE 21-3.—Schematic representation of the furnace control system.

*Mechanical interface modifications.*—A new mounting mechanism and a new control cable between the control package and the furnace were designed to facilitate the ASTP system configuration. The input power and telemetry cable was provided by the vehicle integration contractor.

The operation of the ASTP control package is very similar to the operation of the Skylab control package described previously.

## SUMMARY

The entire multipurpose electric furnace system performed perfectly, as had been predicted

from the ground-based testing, with one minor exception. The rapid cooldown helium system did not respond during the first experiment. It could not be ascertained whether this was a facility or an operational problem, but the system performed nominally on all subsequent experiments. Table 21-I describes the thermal cycles for the flight experiments and shows how they compare with the ground-based tests. The soak temperatures were well within the tolerances requested by the Principal Investigators.

Temperature profiles of the multipurpose electric furnace are shown in figures 21-4 to 21-10 for the seven ASTP experiments discussed in the following sections.

TABLE 21-I.—Experiment Thermal Cycles

Experiment	Heat-up time, hr: min		Soak temperature, K (°C)		Cooldown
	Ground test	Flight	Ground test	Flight	
MA-041	1:10	1:37	962 (689)	965 (692)	Extended
MA-044	2:45	3:15	1428 (1155)	1422 (1149)	Normal
MA-060	3:15	3:45	1393 (1120)	1396 (1123)	Normal
MA-070	2:30	3:07	1348 (1075)	1354 (1081)	Normal
MA-085	1:12	1:15	898 (625)	898 (625)	Normal
MA-131	2:10	2:23	1293 (1020)	1293 (1020)	Normal
MA-150	3:12	2:52	1338 (1065)	1339 (1066)	Normal

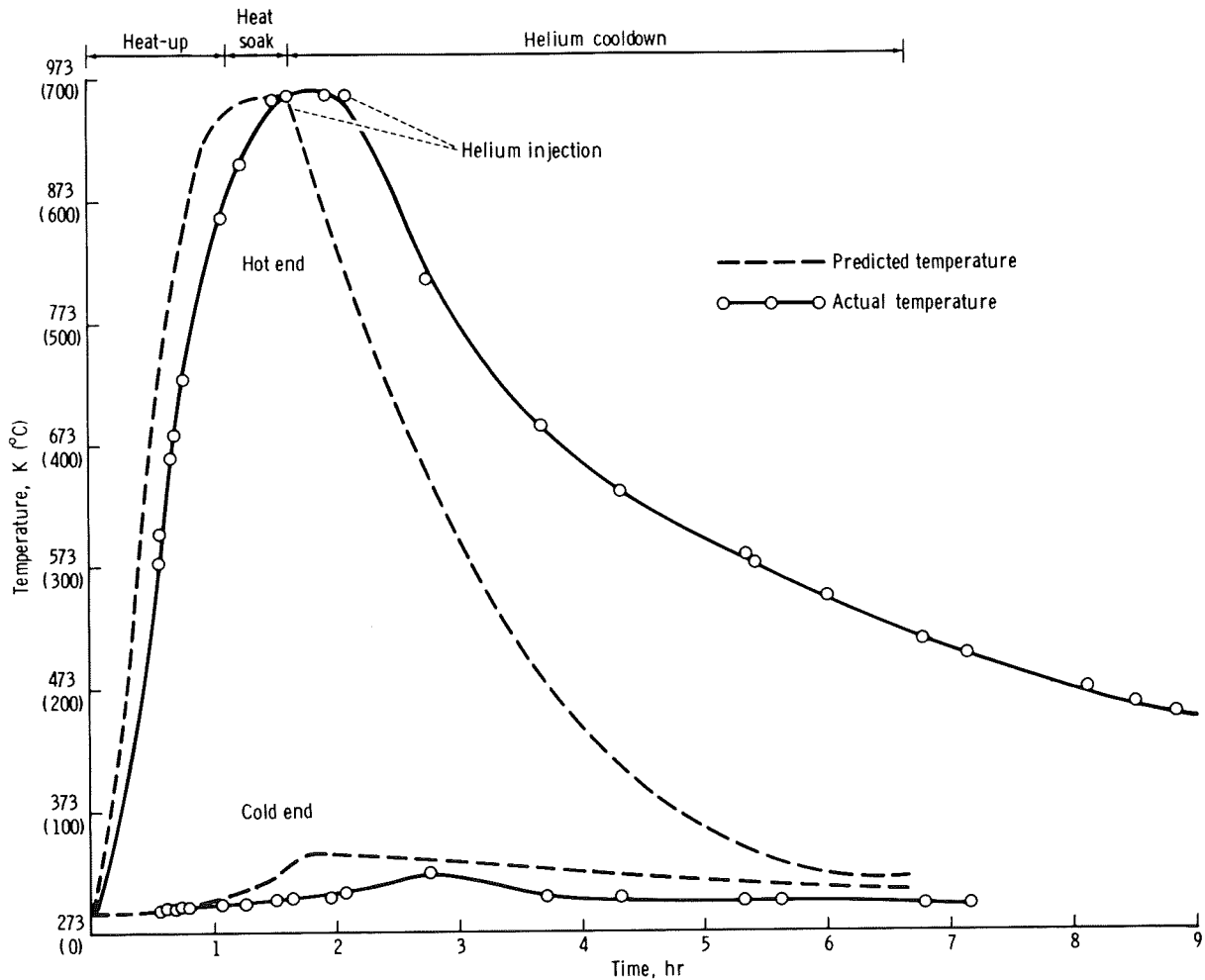


FIGURE 21-4.—Temperature profile for Surface-Tension-Induced Convection (MA-041).

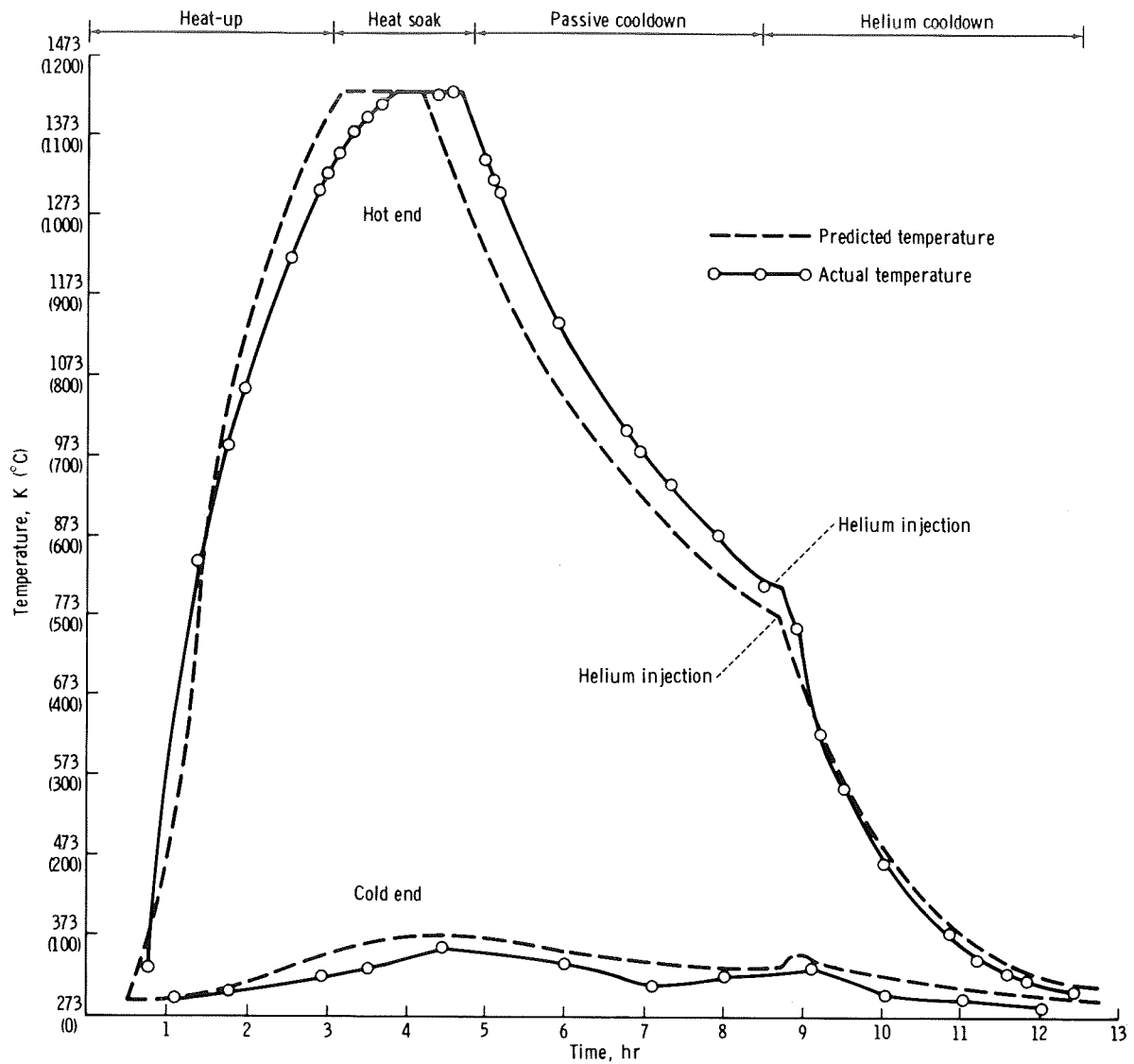


FIGURE 21-5.—Temperature profile for Monotectic and Syntectic Alloys (MA-044).

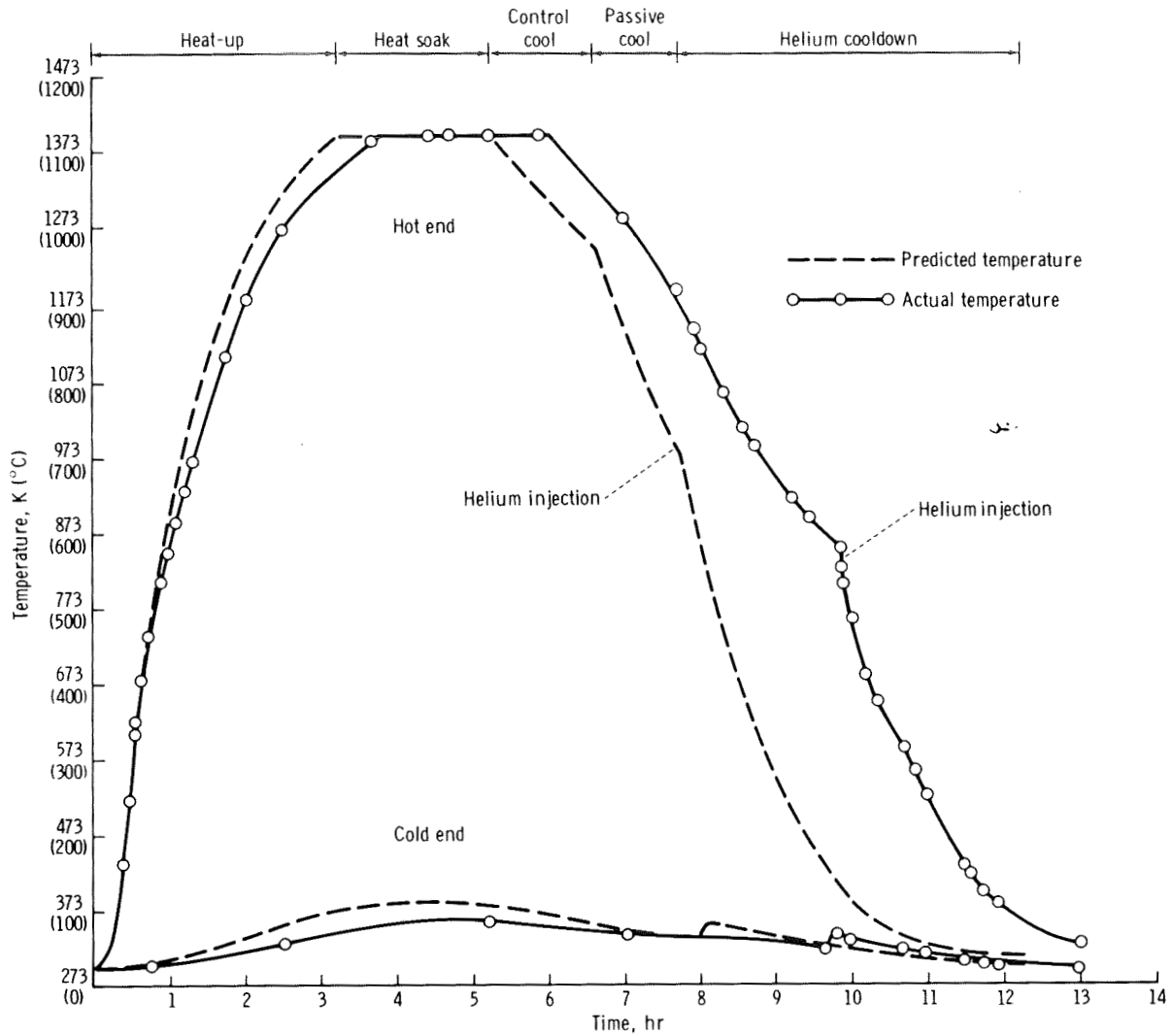


FIGURE 21-6.—Temperature profile for Interface Markings in Crystals (MA-060).

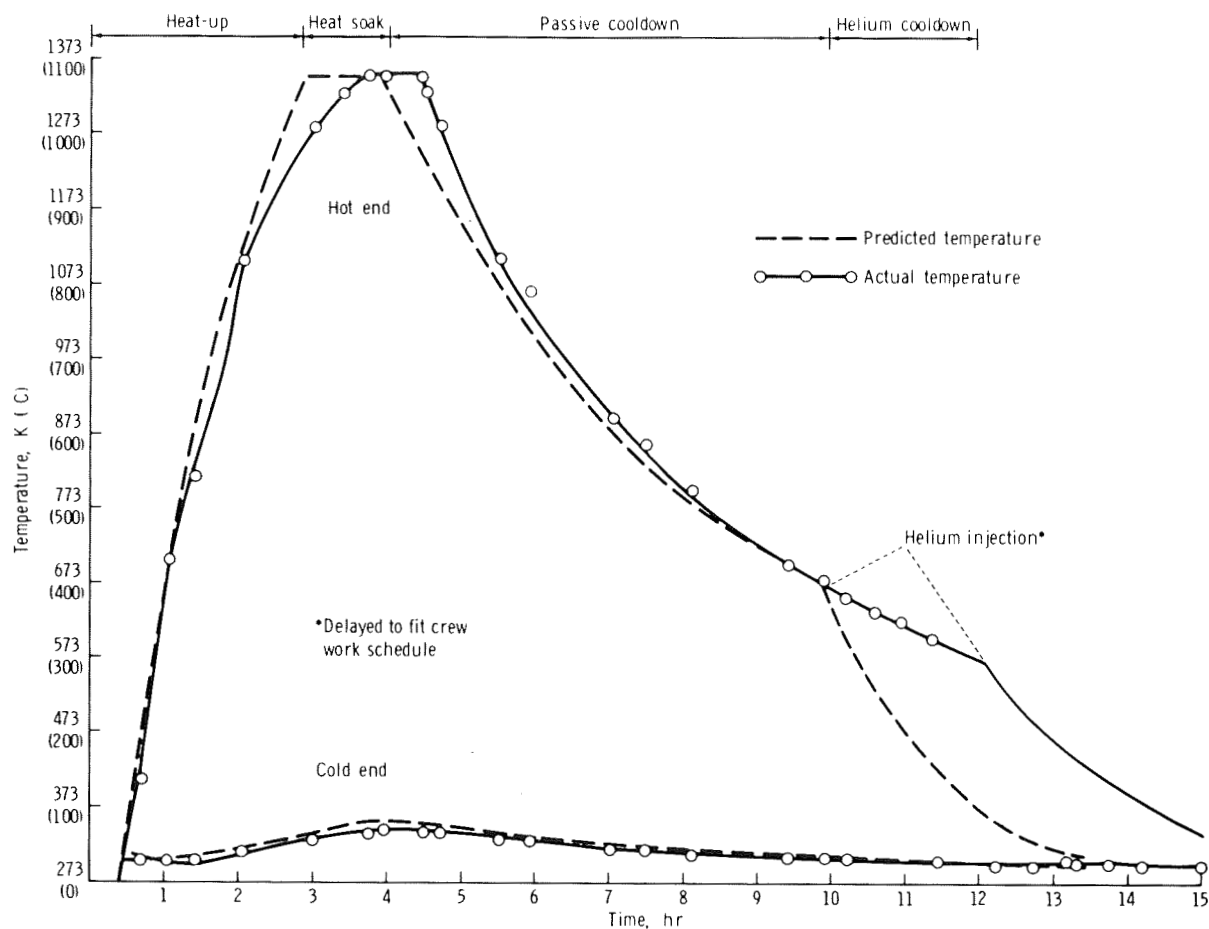


FIGURE 21-7.—Temperature profile for Zero-g Processing of Magnets (MA-070).



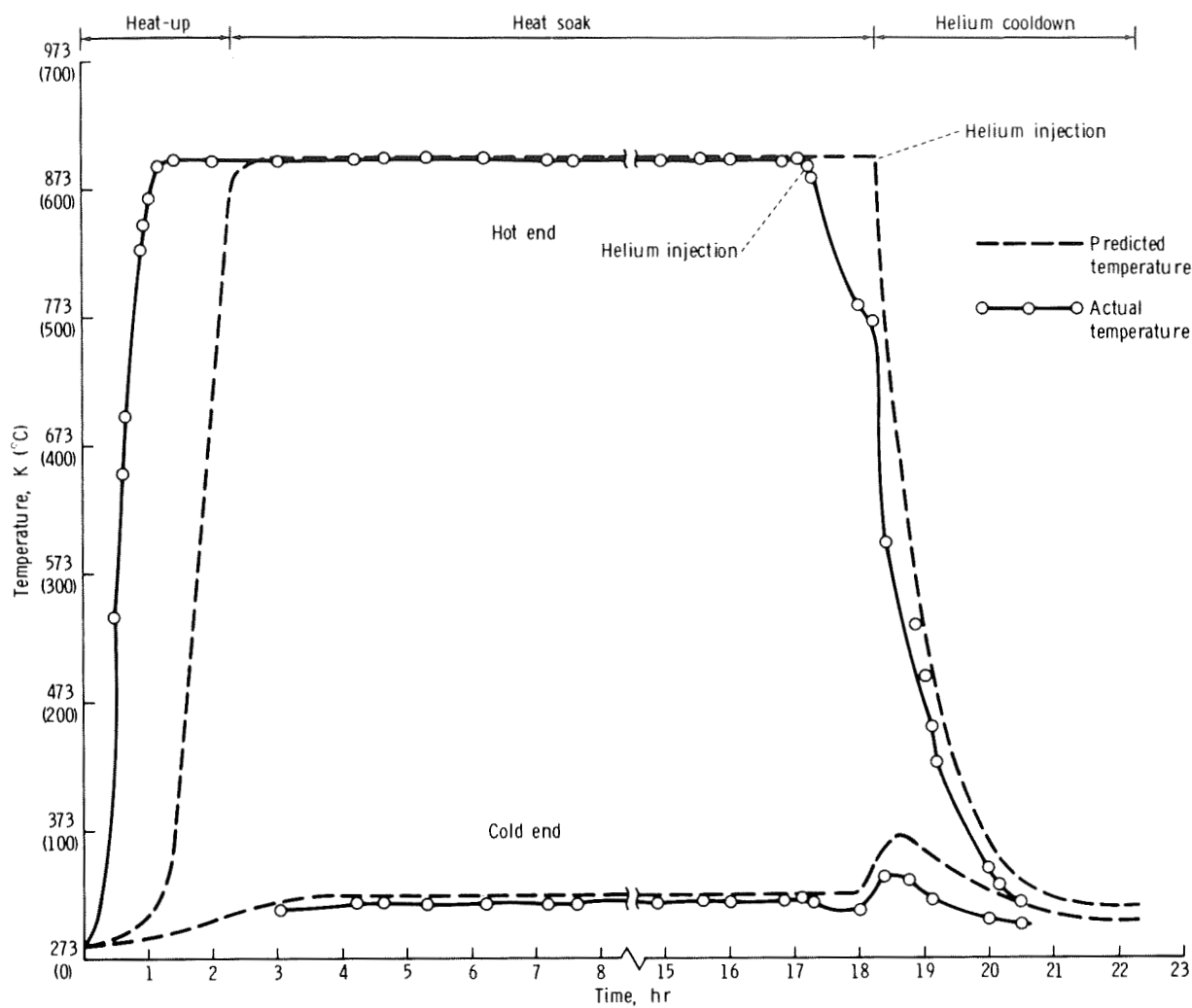


FIGURE 21-8.—Temperature profile for Crystal Growth From the Vapor Phase (MA-085).

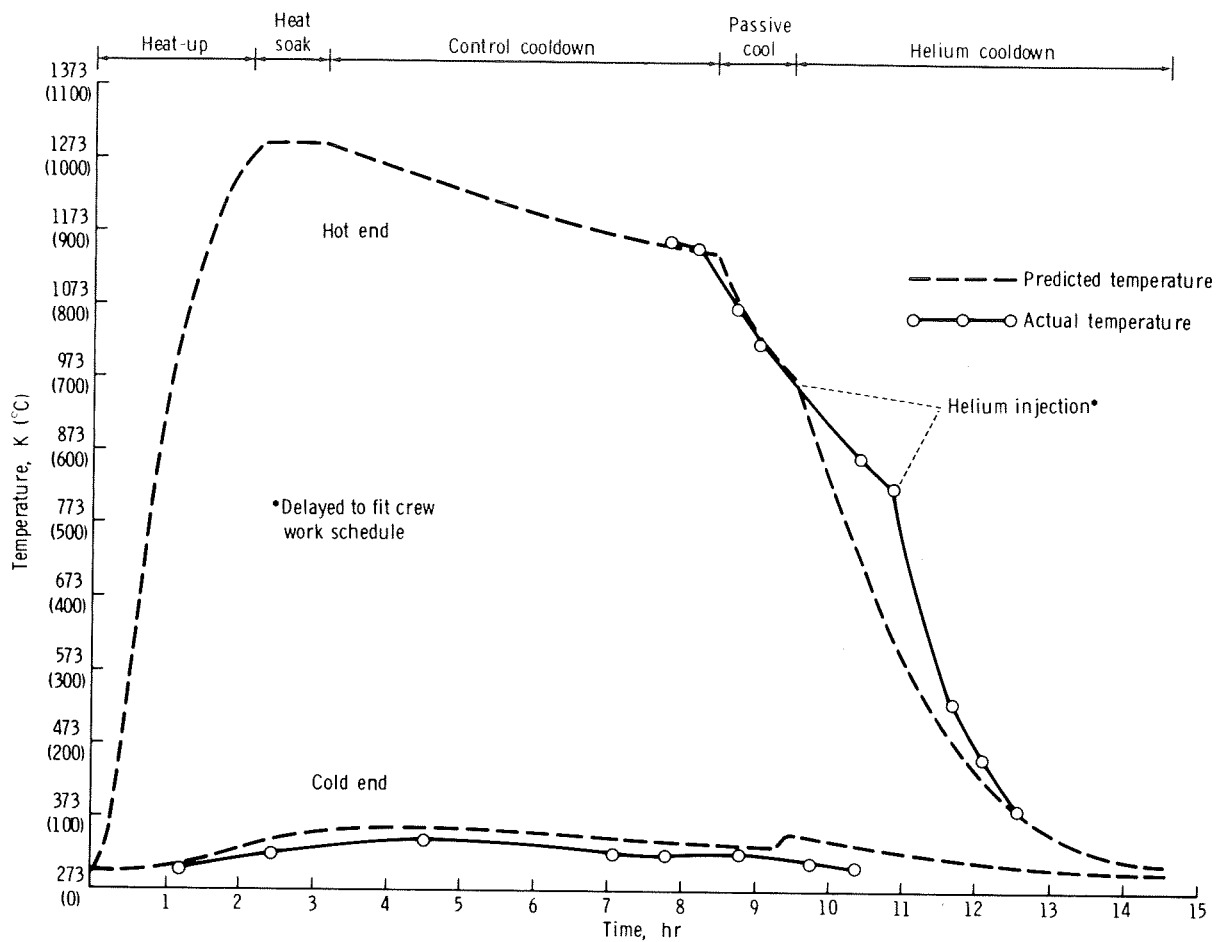


FIGURE 21-9.—Temperature profile for Halide Eutectic Growth (MA-131).

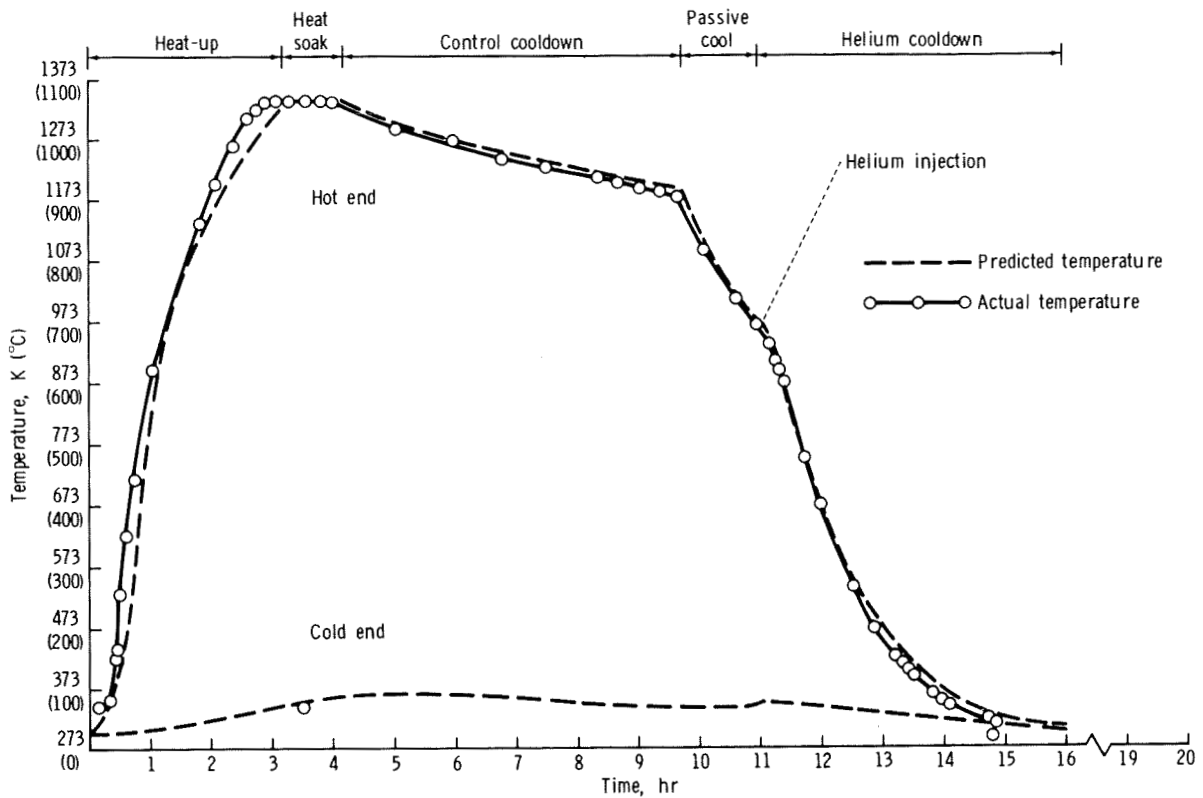


FIGURE 21-10.—Temperature profile for Multiple Materials Melting (MA-150).



## 22. Surface-Tension-Induced Convection

### Experiment MA-041

*R. E. Reed,<sup>†</sup> W. Uelhoff,<sup>a</sup> and H. L. Adair<sup>b</sup>*

#### ABSTRACT

This experiment was designed to detect possible convection caused by a steplike compositional variation in a liquid metal in a microgravity environment. Wetting and nonwetting ampoules were used to determine the extent of the stirring effects if they were present. Because stirring effects can be caused by temperature gradients, the temperature gradients for this experiment were minimized.

Steplike compositional variation was created by pressure bonding a lead-gold alloy (0.05 atomic percent gold) to pure lead. Two diffusion temperatures (923 and 723 K) were used; if no stirring effects were present, it was hoped that the liquid diffusion parameters for gold in lead could be obtained. Convection effects were observed but were not sufficiently large to bring about total mixing in the space-flight specimens. However, they were large enough to prohibit analysis of the pure diffusion process. The most plausible explanation for the flow phenomena observed is convection induced by the Marangoni effect.

Two identical experimental arrangements were used to compare the transport mechanisms of gold in liquid lead in unit gravity and microgravity environments.

#### INTRODUCTION

In the absence of gravity, stirring in a liquid due to density differences caused by thermal or compositional gradients is suppressed. However, other mechanisms resulting in natural convection in a microgravity environment exist and have been described elsewhere (ref. 22-1). One of the most important mechanisms for liquid metals is surface-tension-driven convection (Marangoni effect), which may become predominant in a low-gravity environment. In this case, surface tension differences caused by compositional or temperature gradients have been demonstrated to cause stirring in liquids during experiments performed onboard the Skylab spacecraft. Compositional gradients were created by adding soap solution or grapejuice to a large water globule. The result was a vigorous fluid motion for some moments after the addition. Also, evidence of stirring was detected in the sphere-forming (ref. 22-2) and welding (ref. 22-3) experiments involving electron beam heating; this type of heating causes very steep temperature gradients.

Experiment MA-041 was designed to detect possible convection caused by steplike compositional variation in a liquid metal contained in both wetting and nonwetting ampoules. The general concept of the investigation was to set up a liquid diffusion couple of lead (Pb) and Pb-0.05 atomic percent (at.%) gold (Au) alloy in a microgravity environment. The couples were to be maintained in the molten state for approximately 2 hours, during which the Au would diffuse a distance of approximately 2.5 cm. If there were no convective

---

<sup>†</sup>Principal Investigator (deceased).

<sup>a</sup>Institut für Festkörperforschung, Kernforschungsanlage Jülich, German Federal Republic.

<sup>b</sup>Oak Ridge National Laboratory.

stirring effects between the Pb and the Pb-0.05 at.% Au alloy, a normal concentration-distance profile for Au would be found in the diffusion couples. The use of two diffusion temperatures (923 and 723 K) should enable estimation of the liquid diffusion parameters for Au in Pb. The existence of convective stirring effects should be revealed by means of the autoradiographic technique used for the diffusion analysis. The extent of the convective stirring effects (if present) were to be determined by examination of the wetting and nonwetting containers.

Surface-tension-induced convection could be expected if the specimens were not in contact with the ampoule walls. However, if the specimens touch the walls, the interface tension between the alloy and pure Pb should not be able to create a convection effect according to the fluid dynamic theories by which zero flow is expected at the walls (ref. 22-4). On the other hand, a zinc (Zn) self-diffusion experiment (ref. 22-5) indicated that slight convection occurred in liquid Zn contained in a nonwetting capsule that was heated in a temperature gradient of approximately 45 K/cm. The change in surface tension (not interface tension) with temperature for Zn has been reported to be in the range of  $-0.009$  to  $-0.025 \mu\text{J}/\text{cm}^2 \text{ K}$  ( $-0.09$  to  $-0.25 \text{ erg}/\text{cm}^2 \text{ K}$ ) (ref. 22-6, pp. 403 and 404). Therefore, a surface tension change of approximately 0.5 to 1.5 percent/cm could have occurred in the Zn self-diffusion experiment.

### THE LEAD-GOLD SYSTEM

A Pb/Pb-0.05 at.% Au diffusion couple was selected for this experiment for three major reasons.

1. The melting point of Pb (600 K) was sufficiently low to provide a convenient temperature range for liquid diffusion and to ensure that 0.05 at.% Au would be initially soluble in Pb upon solidification. Any subsequent precipitation of  $\text{Pb}_2\text{Au}$  would be *in situ* and thus would still provide a marker for the original position of the Au. If the precipitation reaction were sufficiently sluggish, the Au could be in solid solution at room temperature. Figure 22-1 is the portion of the Pb-Au phase diagram of interest in this experiment.

The calculated solubility line (curve) shown in figure 22-1 is based on data from reference 22-7.

2. The nuclear properties of Pb and Au make the mixture an ideal diffusion couple to study by neutron activation techniques. The distribution of Au in the Pb matrix can be determined autoradiographically. In this case, samples were neutron irradiated in the center hole of the Bulk Shielding Reactor deuterium oxide tank at Oak Ridge National Laboratory (ORNL) in essentially a pure thermal flux of  $1.2 \times 10^{12} \text{ neutrons sec}^{-1} \text{ cm}^{-2}$ . The nuclear data of interest for Pb and Au are shown in table 22-I. After neutron activation, the Au distribution was determined by placing a polished section of the sample on a nuclear emulsion plate that is sensitive to 0.96-MeV electrons.

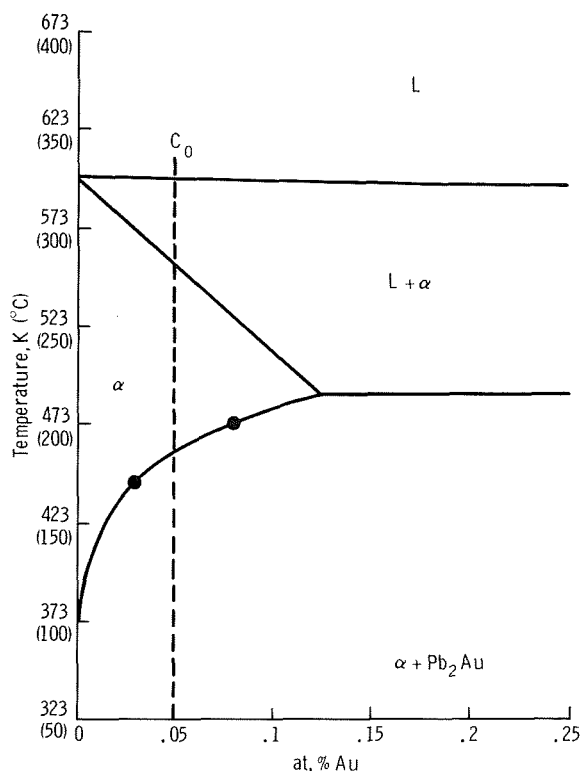


FIGURE 22-1.—The Pb-rich portion of the Pb-Au binary phase diagram, where  $C_0$  is the initial Au concentration,  $\alpha$  is a melting phase, and  $L$  is the liquidus phase. The curve was calculated on the basis of two experimental points in the relationship  $C = A \exp[-(Q/RT)]$ , where  $C$  is the Au concentration,  $A$  is a constant,  $Q$  is activation energy,  $R$  is the gas constant, and  $T$  is temperature (ref. 22-7).

TABLE 22-I.—Nuclear Data for Pb and Au

Property	Element	
	Pb	Au
Nuclear reaction .....	$^{208}\text{Pb}(n,\gamma)^{209}\text{Pb}^a$	$^{197}\text{Au}(n,\gamma)^{198}\text{Au}^a$
Abundance .....	52.3-percent $^{208}\text{Pb}$	100-percent $^{197}\text{Au}$
Thermal-neutron cross section, $\text{m}^2$ (b) .....	$0.0005 \times 10^{-28}$ (0.0005)	$99 \times 10^{-28}$ (99)
Radionuclide .....	$^{209}\text{Pb}$	$^{198}\text{Au}$
Type decay .....	$\beta^-$	$\beta^-$
$\beta^-$ -energy, MeV .....	0.64 (100 percent)	0.96 (96 percent)
Radionuclide half life, hr .....	3.3	64.8

<sup>a</sup> n = neutron;  $\gamma$  = gamma ray.

By calibrating the emulsion sensitivity to  $\beta^-$  radiation using samples of Pb containing known amounts of Au, quantitative analyses of the Au concentration in the experimental samples were made using a microphotometer to read the plates. This technique has been used successfully at ORNL for determination of tungsten and tantalum distributions in niobium (ref. 22-8).

3. It is believed that the Pb-Au system has large variations of surface tension with changes in composition. The variation of surface tension with temperature  $d\sigma/dT$  is well known for Pb from the melting point to a temperature of approximately 1373 K (ref. 22-6, pp. 8 and 400). In fact, the value of  $d\sigma/dT$  ranges from  $-0.0062$  to  $-0.0120 \mu\text{J}/\text{cm}^2 \text{ K}$  ( $-0.062$  to  $-0.120 \text{ erg}/\text{cm}^2 \text{ K}$ ). The variation of surface tension with composition  $d\sigma/dc$  has not been determined for the Pb-Au system. However, a similar system, tin-copper, has been studied (ref. 22-6, p. 258). For tin-copper, a slight negative deviation from a linear relationship was found. Thus, assuming a linear relationship between the surface tension of Pb ( $39.5 \mu\text{J}/\text{cm}^2$  ( $395 \text{ ergs}/\text{cm}^2$ )) and Au ( $112.5 \mu\text{J}/\text{cm}^2$  ( $1125 \text{ ergs}/\text{cm}^2$ )) at a common temperature of 1373 K, the value of  $d\sigma/dc$  can be estimated as approximately  $0.73 \mu\text{J}/\text{cm}^2 \text{ at.}\%$  ( $7.3 \text{ ergs}/\text{cm}^2 \text{ at.}\%$ ). The interfacial energies for the alloy-graphite, lead-graphite, alloy-mild steel, and

lead-mild steel systems that were used in the experiment are not known.

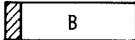
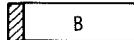
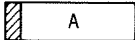
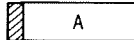
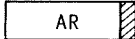
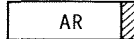
## EXPERIMENTAL DESIGN

A schematic representation of the specimen arrangement in the multipurpose electric furnace is shown in figure 22-2. Because of longitudinal heat flow in the furnace during operation, the specimens melted from left to right with reference to the representation (fig. 22-2) and solidified in the reverse direction; as is shown, six flight specimens were used in the Apollo-Soyuz experiment. The furnace and the cartridges that contained the specimen ampoules were constructed so that each ampoule would experience minimum temperature gradients. Two of the three flight cartridges contained specimens loaded in graphite containers. The two cartridges were identical except for the location of the Pb-0.05 at.% Au alloy. In one cartridge (flight cartridge 2), the alloy was located on the hot end and thus melted first; in the other cartridge (flight cartridge 3), the alloy was located on the reverse end of the specimen and thus melted last and solidified first. This arrangement was designed to determine whether melting or solidification affected the Au concentration

profile. Flight cartridge 1 (fig. 22-2) contained two specimens in mild steel capsules with the Pb-Au alloy aligned so that it melted first. An identical specimen arrangement was used for ground-based tests to provide comparison between the different transport mechanisms in liquid metals processed in space and in a unit gravity environment.

Dimensions of the actual specimens are shown in figure 22-3. The 3-mm-thick Pb-0.05 at.% Au alloy disk was cold-pressure welded to the pure Pb. It should be noted that the total diffusion distance available was approximately 3 cm.

Ampoules (mild steel and stainless steel lined with graphite) used for the specimens described in this report are shown in figures 22-4 and 22-5, respectively. In the graphite-lined container, quartz cloth disks were placed at each end to provide padding for normal handling movements and to adjust the void space in the ampoule. Originally, it was anticipated that specimens attaining the 923-K temperature would be in the liquid state approximately 2 hours and that specimens heated to a temperature of 723 K would be molten approximately 1 hour. Liquid diffusion data for Au in Pb are not available. However, by using the results from the Skylab Zn self-diffusion experiment (ref. 22-5, p. 440), it was possible to estimate some diffusion distances for this experiment. Figure 22-6 contains the calculated Au concentration-distance profiles for a geometry consisting of a 3-mm-thick disk of Pb-0.05 at.% Au alloy

Flight cartridge	Temperature		Type of ampoule wall
	923 $\pm$ 10 K	723 $\pm$ 50 K	
1			Wetting (mild steel)
2			Nonwetting (graphite)
3			Nonwetting (graphite)



 Pb-0.05 at.% Au  
 Pb

FIGURE 22-2.—Schematic arrangement of specimens in multipurpose furnace. (Letters indicate specimen notation used in this report.)

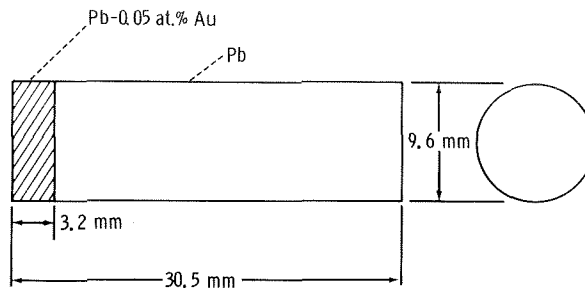


FIGURE 22-3.—Dimensions of MA-041 specimen.

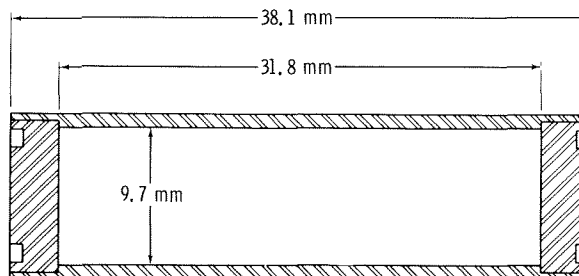


FIGURE 22-4.—Mild steel (type 1015) ampoule assembly for type B specimen capsules.

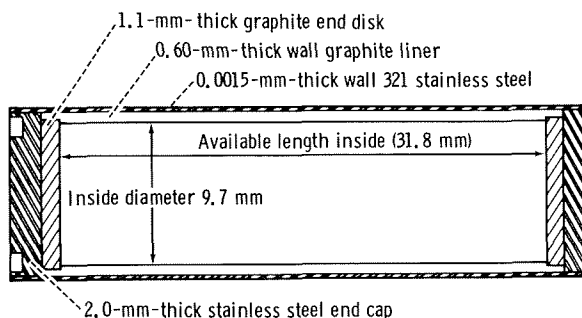
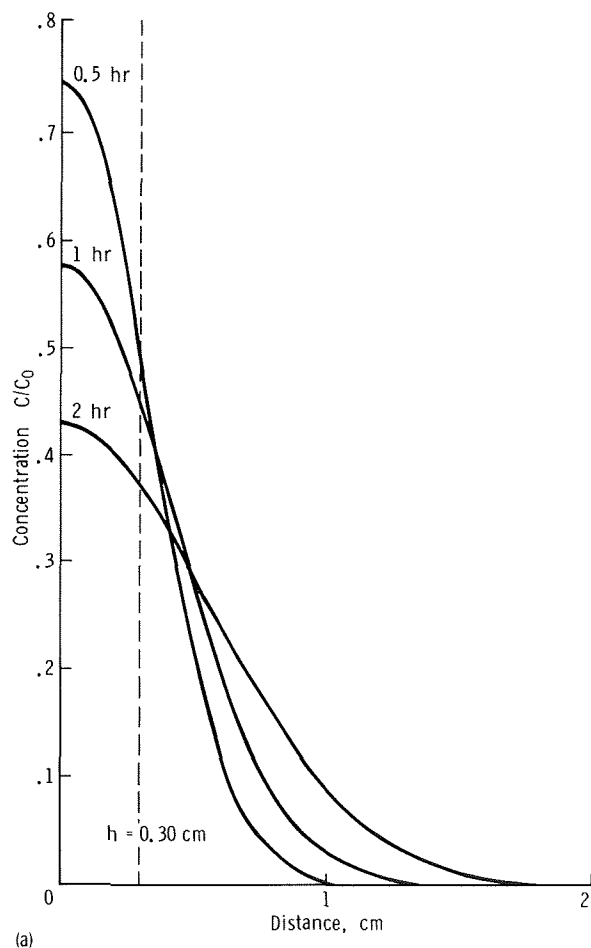


FIGURE 22-5.—Graphite-lined stainless steel assembly for type A and AR specimens.

bonded to pure Pb to form a cylindrical specimen 3 cm long. These concentration-distance profiles were calculated using the solution for an extended source of limited extent from reference 22-9 (pp. 11 to 14). The source width  $h$  was 3 mm; the diffusion temperatures were 673 and 923 K for figures 22-6(a) and 22-6(b), respectively. The diffusivity value  $D$  is calculated from the Zn self-diffusion



results of reference 22-5 (p. 440). Figure 22-6(a), in which an effective diffusion temperature of 673 K is assumed, shows that diffusion distances of approximately 1.5 cm would be achieved in 1 hour. Figure 22-6(b), calculated for 923 K, indicates that a diffusion distance of 2.7 cm would be expected within 2 hours at the diffusion temperature. Assuming an initial concentration of Au in Pb  $C_0$  of 500 atomic parts per million (at. p/m), the Au concentration in the pellet would be reduced to 215 and 130 at. p/m at 673 and 923 K, respectively. These estimated distances and concentrations were within the limits of the experimental design capabilities.



### FURNACE THERMAL CHARACTERISTICS AND OTHER IMPORTANT EXPERIMENTAL PARAMETERS

Temperature-time data monitored on the Apollo-Soyuz mission were obtained by measurements made on the heat-leveler block of the multipurpose furnace (fig. 22-7). Because the furnace operation during flight was longer than planned, a postflight ground-based test (GBT) was performed to duplicate the space-flight furnace operation. The temperature-time curves are shown in figure 22-8. Table 22-II contains the heating and cooling rates for both ground based (GB) and space-flight (SF) specimens at a temperature of 600 K. The approximate solidification rates for both GB and SF specimens were determined by dividing the change in temperature per unit time by the change in temperature per unit length. The results are as follows.

1. 2.5 cm/min for the 923-K-temperature-zone GB specimens
2. 9.0 cm/min for the 723-K-temperature-zone GB specimens
3. 2.5 cm/min for the 923-K-temperature-zone SF specimens
4. 6.0 cm/min for the 723-K-temperature-zone SF specimens

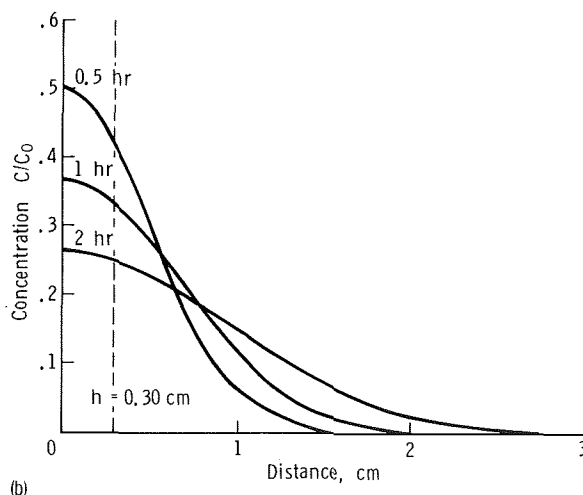


FIGURE 22-6.—Concentration-distance profiles calculated using the solution for an extended source of limited extent (ref. 22-9), where the source width  $h = 3$  mm,  $T$  is the diffusion temperature, and  $D$  is the diffusivity value calculated from Zn self-diffusion data (ref. 22-5, p. 440). (a)  $D = 1.93 \times 10^{-5}$  cm<sup>2</sup>/sec;  $T = 673$  K (400° C). (b)  $D = 5.50 \times 10^{-5}$  cm<sup>2</sup>/sec;  $T = 923$  K (650° C).

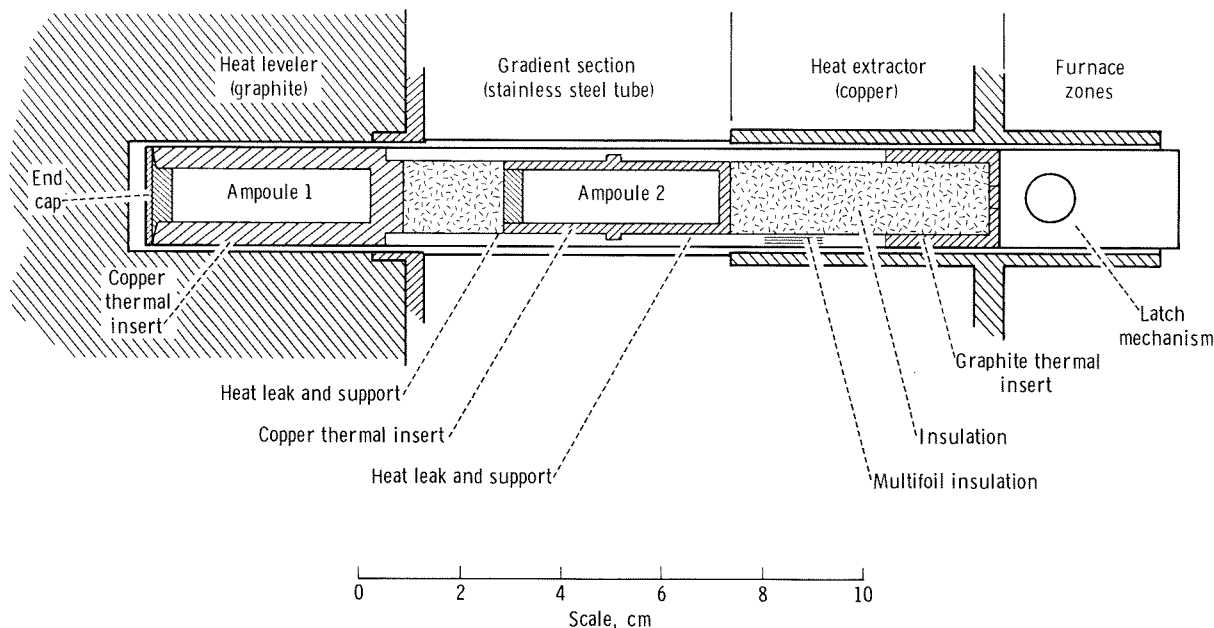


FIGURE 22-7.—Diagram of MA-041 advanced flight cartridge.

It was determined from the flight analyses that ampoules A and B were in the liquid phase for 268 and 82 minutes, respectively. In the GBT-25 experiment, the specimens remained in the liquid phase 226 and 77 minutes for ampoules A and B, respectively.<sup>1</sup> Additional experimental values that must be considered in the experimental analyses are as follows.

1. The relative density difference  $\Delta\rho/\rho$  between the Pb-Au alloy and the pure Pb was  $1.76 \times 10^{-4}$ .
2. The equilibrium distribution coefficient  $K$  of Au in Pb is nearly 0.3.
3. Cooling rates  $dT/dt$ , where  $t$  is time, were in the range of 1 to 10 K/min.
4. The temperature gradient  $G$ , which was purposely kept small to maintain a constant-temperature diffusion rate, was in the range of 0.4 to 2.0 K/cm.
5. The calculated solidification velocity  $V$  was in the range of 2.5 to 9 cm/min.

The average acceleration of the SF specimens during the experiment was less than  $0.0981 \text{ cm/sec}^2$ . Maximum acceleration, which was caused by firing of the reaction control system thrusters, was less than  $5.886 \text{ cm/sec}^2$  for time periods of 15 milliseconds.

### SAMPLE PREPARATION FOR POSTMISSION ANALYSES

Sample numbers for each specimen used in both the ground-based and space-flight experiments are shown in table 22-III. The samples are coded as follows. The "A" suffix indicates specimens in graphite-lined stainless steel containers with the Pb-0.05 at.% Au alloy located at the hot end of the temperature zone. The "AR" suffix indicates specimens in graphite-lined stainless steel containers with the Pb-Au alloy located away from the hot end (i.e., the "reverse" end) of the temperature zone. The "B" suffix indicates specimens in unlined mild steel containers with the Pb-Au alloy located at the temperature-zone hot end,

<sup>1</sup>W. S. Key, Technical Letter ASD-EP 44-22716, Teledyne Brown Engineering, December 16, 1975.

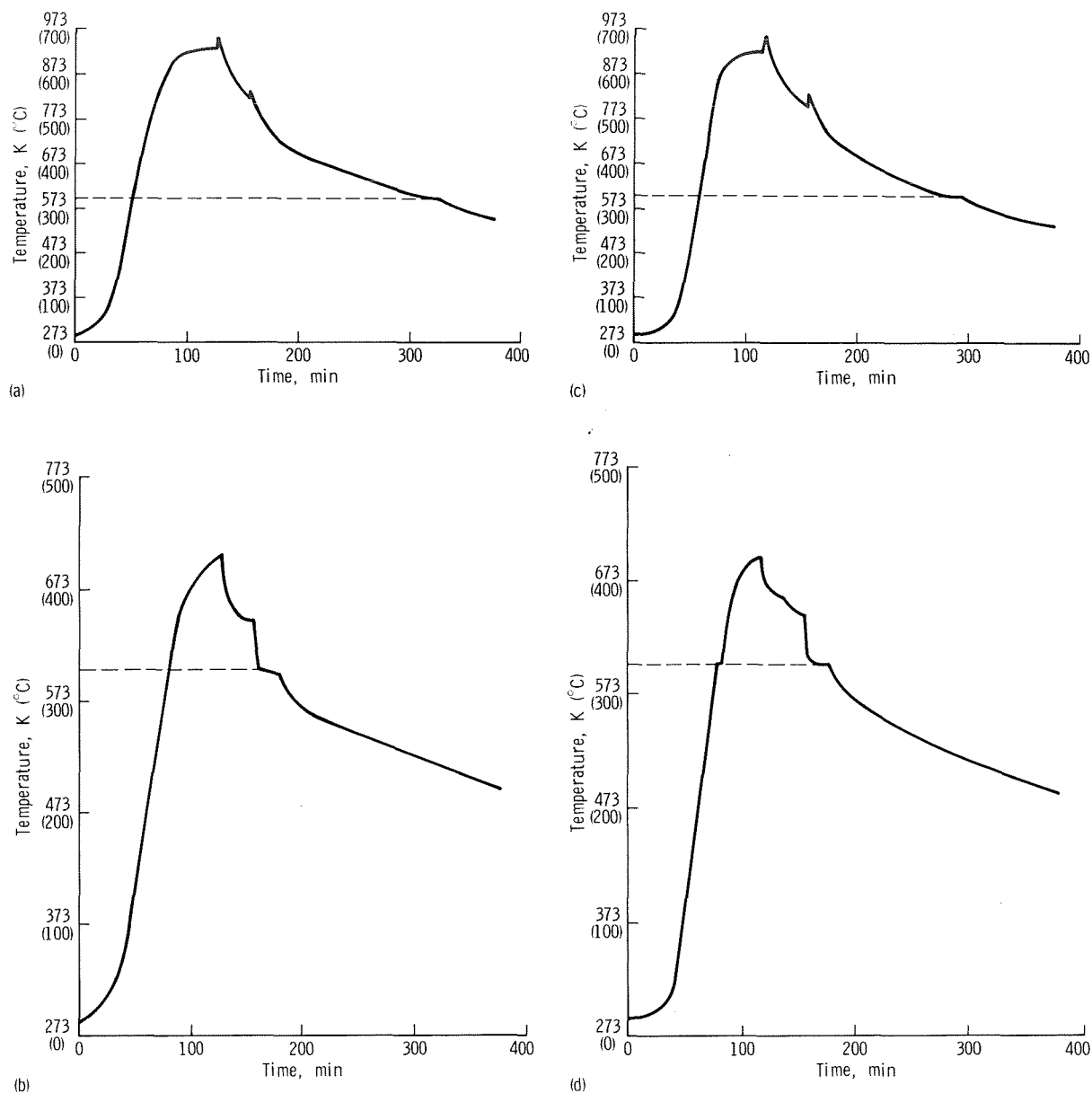


FIGURE 22-8.—Temperature-time history for MA-041 specimens. The dashed line is at 600 K, the melting point of Pb. (a) 923-K SF specimens. (b) 723-K SF specimens. (c) 923-K GB specimens. (d) 723-K GB specimens.

which was the only alloy location in mild steel containers. (See fig. 22-2.)

After completion of the melting experiments (both ground based and space flight), the specimens were returned to the laboratory for sectioning and subsequent analysis. After removal from the nonwetting ampoules, the A and AR speci-

mens were potted in epoxy for longitudinal sectioning. The wetting-type, mild steel ampoules containing the B alloy specimens were mounted in epoxy resin and sectioned longitudinally together with the specimens. The epoxy potting material was then dissolved and each specimen, together

TABLE 22-II.—Heating and Cooling Rates for GB and SF Specimen Ampoules

Characteristic	Temperature history			
	GB specimens <sup>a</sup>		SF specimens <sup>b</sup>	
	923-K zone	723-K zone	923-K zone	723-K zone
Heating rate at 600 K, K/min . . . . .	7	2	11	4
Cooling rate at 600 K, K/min . . . . .	1	10	1	5

<sup>a</sup>Heating and cooling rates based on the slopes of the temperature curves at 600 K at nodes 312 and 322 for GBT-25.<sup>b</sup>Heating and cooling rates based on the slopes of the temperature curves at 600 K at nodes 312 and 322 for the SF ampoules.TABLE 22-III.—Sample Nomenclature and Location for MA-041 Specimens<sup>a</sup>

Container type	Specimen number and location	
	923-K zone	723-K zone
<i>SF specimens</i>		
Graphite	11-A	21-A
Graphite	13-AR	17-AR
Mild steel	12-B	21-B
<i>GB specimens</i>		
Graphite	17-A	14-A
Graphite	11-AR	20-AR
Mild steel	13-B	15-B

<sup>a</sup>Schematic arrangement of specimens is shown in figure 22-2.

with seven Pb-Au alloy calibration disks, was re-mounted in a 5-cm-diameter epoxy mount and metallographically polished.

The specimens were irradiated in the Bulk Shielding Reactor for 4 hours in essentially a pure thermal flux of  $1.2 \times 10^{12}$  neutrons  $\text{sec}^{-1} \text{cm}^{-2}$ . During irradiation, both  $^{209}\text{Pb}$  and  $^{198}\text{Au}$  are formed. The activity of interest is  $^{198}\text{Au}$ , which decays by the emission of 0.960-MeV beta particles and has a half-life of 64.8 hours. The  $^{209}\text{Pb}$  formed during the irradiation is essentially nonexistent after approximately 24 hours, because the thermal-neutron cross section for forming  $^{209}\text{Pb}$  from  $^{208}\text{Pb}$  is small and the  $^{209}\text{Pb}$  half-life is only

3.3 hours. After the radioactive nuclides decayed for 24 to 30 hours, autoradiographs of the specimens were made.

Autoradiographs were made in complete darkness in the same darkroom in which the film was developed after exposure. The polished face of the mount was placed face down on Kodak industrial type R X-ray film, an ultra-fine-grain, single-emulsion film. Exposures were made for durations of 8, 16, 32, 64, 128, and 256 minutes. The film is exposed to  $\beta^-$  emission from the Au in the Pb. Because the range of the 0.960-MeV  $\beta^-$  in Pb is approximately 0.4 mm, only the Au concentration in this layer thickness is detected.

Originally, seven Pb-Au standards of 0, 20, 52, 91, 217, 277, and 393 at. p/m Au were used. The arrangement of the standards and the specimen for the first irradiation is shown in figure 22-9. Beta scattering from the standards distorted the Au concentration profiles in both the GB and the SF specimens in the area of the specimens adjacent to the standards. In addition, beta scattering influenced the radiation values obtained for each standard. Thus, to eliminate the beta-scattering problem, two epoxy mounts were necessary; one contained the Pb-Au standards and one contained the specimen. This arrangement is shown in figure 22-10. The 277 and 393 at. p/m Au standards were not used because the original irradiation verified that all Au concentrations in the specimens were below these values.

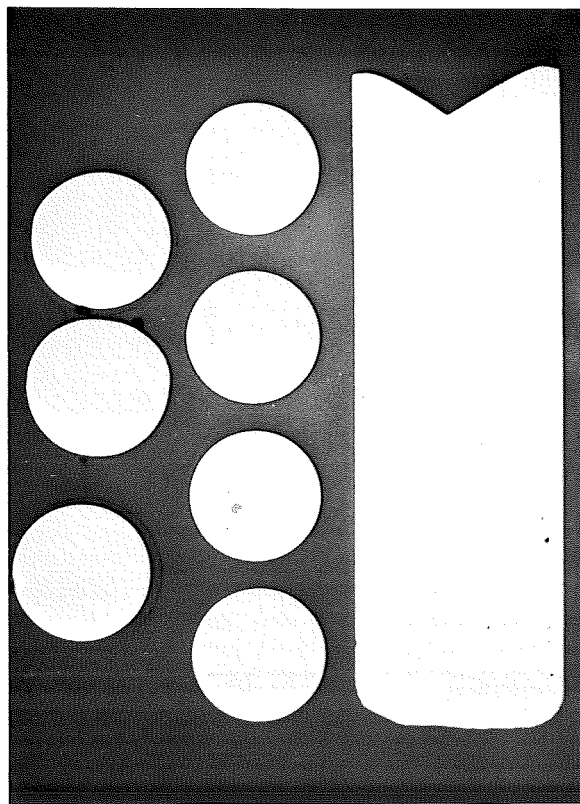


FIGURE 22-9.—Macrograph of the longitudinally cut surface of SF specimen 17-AR and seven Pb-Au standards mounted in epoxy resin.

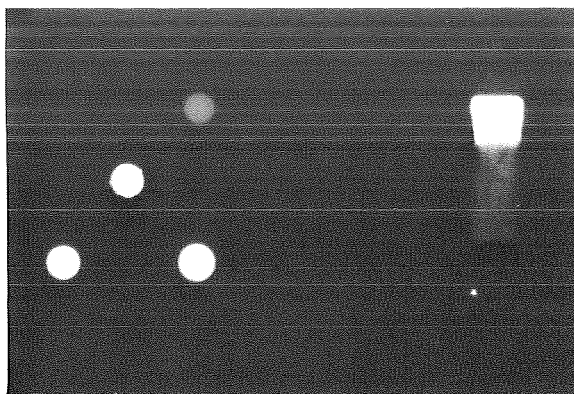


FIGURE 22-10.—This print, taken from a deliberately overexposed autoradiograph, shows the relative locations of the Pb-Au standards (disks) and the specimen during autoradiography. Light areas indicate Au activity.

### EXAMINATION OF SPECIMEN EXTERIORS AND LONGITUDINAL SECTIONS

A visual examination of both the GB and SF specimens after removal from the ampoules revealed no evidence of oxidation.

#### Ground-Based Specimens

The exterior surfaces of the A and AR GB specimens are shown in figures 22-11 to 22-16. A side view of GB specimens 17-A and 14-A, which were mounted vertically in the multipurpose electric furnace and were located in the 923- and 723-K temperature zones, respectively, is shown in figure 22-11. The samples melted from the top to the bottom (fig. 22-11) and, upon cooling, solidified in the reverse direction. The original bond interface of the Pb-Au disks can still be discerned at the top of each specimen. In addition, both specimens show the expected sharp corners at the base.

A bottom view of specimens 17-A and 14-A is shown in figure 22-12. This figure shows the sharp corners as well as ripples due to the quartz spacer cloth. Figure 22-13 is a top view of GB specimen 17-A. Evidence of a solidification pipe, which was not evident for specimen 14-A, can be seen.

A side view of GB specimens 11-AR and 20-AR is shown in figure 22-14. Like the previous

specimens (17-A and 14-A), specimens 11-AR and 20-AR were mounted vertically in the multipurpose electric furnace and were located in the 923- and 723-K temperature zones, respectively. However, the 11-AR and 20-AR Pb-Au alloy disks were located at the bottom and thus melted last and solidified first. Again, the original bond interface and the square corners can be seen at the bottom of the specimens. The top view of specimens 11-AR and 20-AR is shown in figure 22-15. Evidence of a solidification pipe can be seen for specimen 11-AR but not for 20-AR. A bottom view of the two specimens can be seen in figure 22-16. Characteristics to note are the ripples due to the quartz spacer cloth and the Pb-Au bond interface.

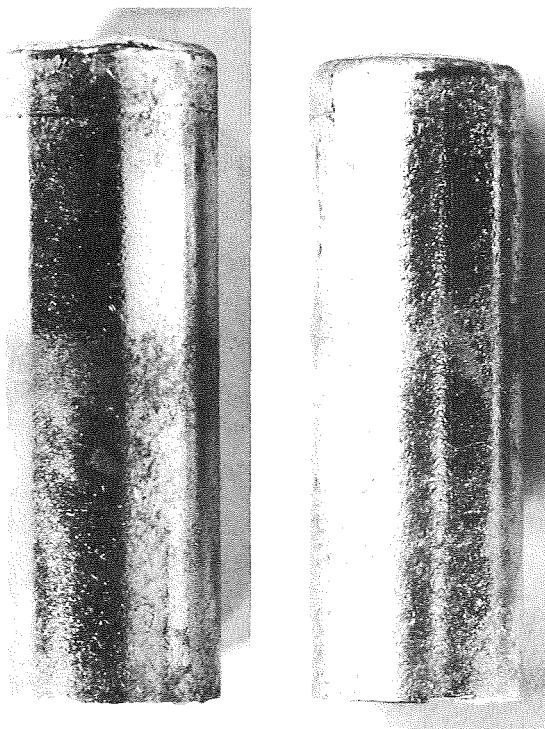


FIGURE 22-11.—Photograph of GB specimens 17-A (left) and 14-A (right), which were located in the 923- and 723-K temperature zones, respectively, of the multipurpose furnace. The specimens are approximately 1 cm in diameter.

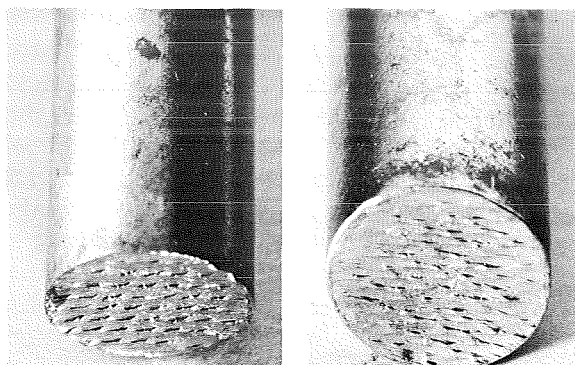


FIGURE 22-12.—Photograph of the lower ends of GB specimens 17-A (left) and 14-A (right).

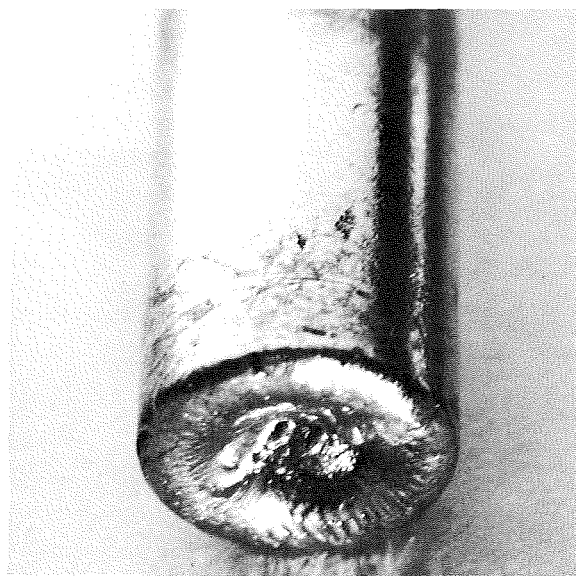


FIGURE 22-13.—Photograph of the upper end of GB specimen 17-A.

Macrographs of the metallographically polished, longitudinally sectioned surfaces of GB specimens 17-A, 11-AR, 14-A, and 20-AR are shown in figures 22-17 and 22-18. The solidification pipe is clearly seen for the two 923-K specimens (figs. 22-17(a) and 22-17(b)). The 723-K

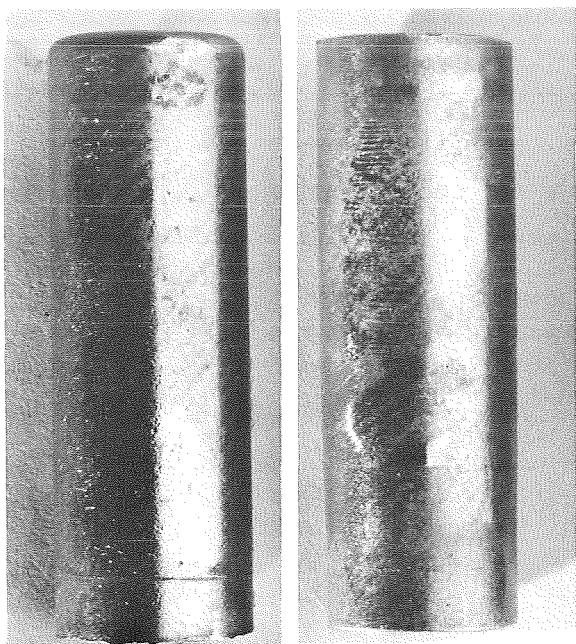


FIGURE 22-14.—Photograph of GB specimens 11-AR (left) and 20-AR (right), which were located in the 923- and 723-K temperature zones, respectively, of the multipurpose furnace.

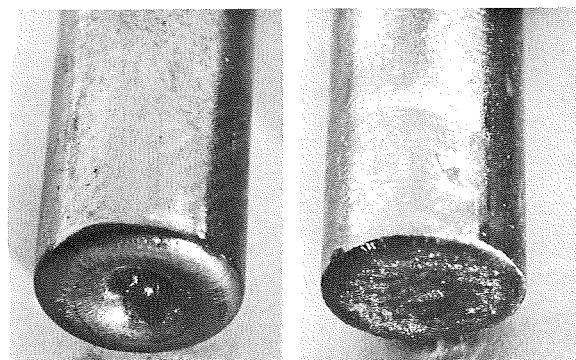


FIGURE 22-15.—Photograph of the upper ends of GB specimens 11-AR (left) and 20-AR (right).

specimens (figs. 22-18(a) and 22-18(b)) have square corners and reveal no evidence of solidification pipes.

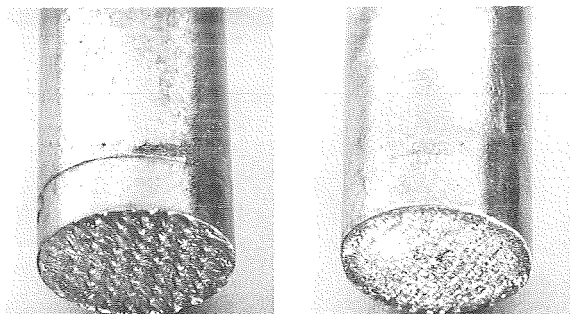


FIGURE 22-16.—Photograph of the lower end of GB specimens 11-AR (left) and 20-AR (right).

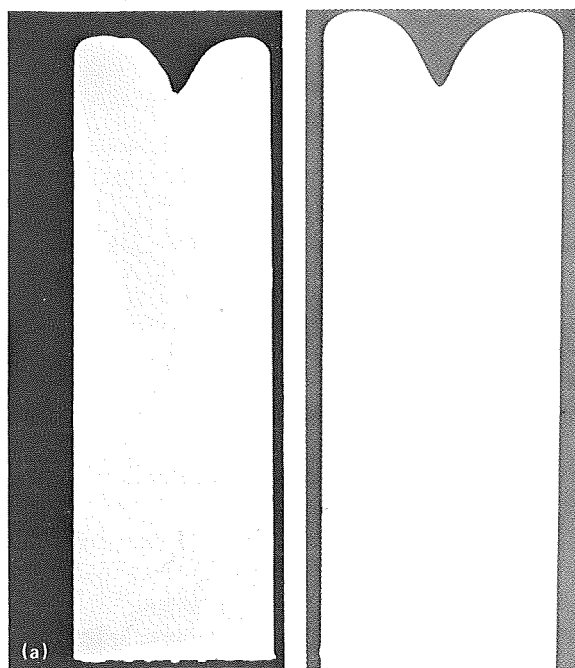


FIGURE 22-17.—Macrographs of metallographically polished, longitudinally sectioned surfaces of 923-K GB specimens. The specimens solidified from bottom to top in a non-wetting ampoule. (a) Specimen 17-A; Pb-Au alloy disk originally located at top. (b) Specimen 11-AR; Pb-Au alloy disk originally located at bottom.

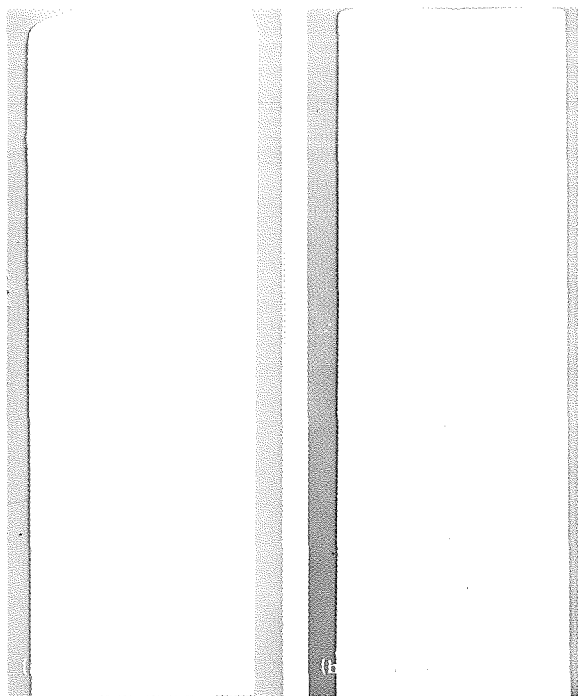


FIGURE 22-18.—Macrographs of metallographically polished, longitudinally sectioned surfaces of 723-K GB specimens. The specimens solidified from bottom to top in a non-wetting ampoule. (a) Specimen 14-A; Pb-Au alloy disk originally located at top. (b) Specimen 20-AR; Pb-Au alloy disk originally located at bottom.

### Space-Flight Specimens

The exterior surfaces of the A and AR SF specimens are shown in figures 22-19 to 22-24. A side view of SF specimens 11-A and 21-A is shown in figure 22-19. Cellular structure at the top is clearly evident for specimen 11-A, which was located in the 923-K temperature zone, but not as evident for the 723-K zone specimen (21-A). The specimens melted from the top to the bottom (fig. 22-19) and solidified in the reverse direction. A bottom view of specimens 11-A and 21-A is shown in figure 22-20. The SF samples have rounded edges and no evidence of ripple marks from the quartz spacer cloth. Figure 22-21 is a top view of specimen 11-A showing the Pb-Au alloy disk region. The cellular structure and the Pb-Au bond interface are clearly distinguishable.

A side view of SF specimens 13-AR and 17-AR is shown in figure 22-22. Again, one can see the

cellular structure for the 923-K-temperature-zone specimen (13-AR) in the Au-rich region at the bottom. This structure is not evident for the 723-K-zone specimen (17-AR). A top view (opposite from the Pb-Au alloy disk) in figure 22-23 reveals evidence of solidification pipes for both specimens. The Pb-Au alloy region for specimens 13-AR and 17-AR is shown in figure 22-24; this end of the specimen melted last and solidified first. The cellular structure and the Pb-Au bond interface can be seen for both specimens.

Macrographs of the metallographically polished, longitudinally sectioned surfaces of the SF specimens are shown in figures 22-25 and 22-26. The macrograph for SF specimen 11-A (fig. 22-25(a)) shows the expected rounded corners. This specimen was located in the 923-K temperature zone. The AR SF specimen from the same temperature zone (fig. 22-25(b)) also has rounded corners. In addition, a large solidification

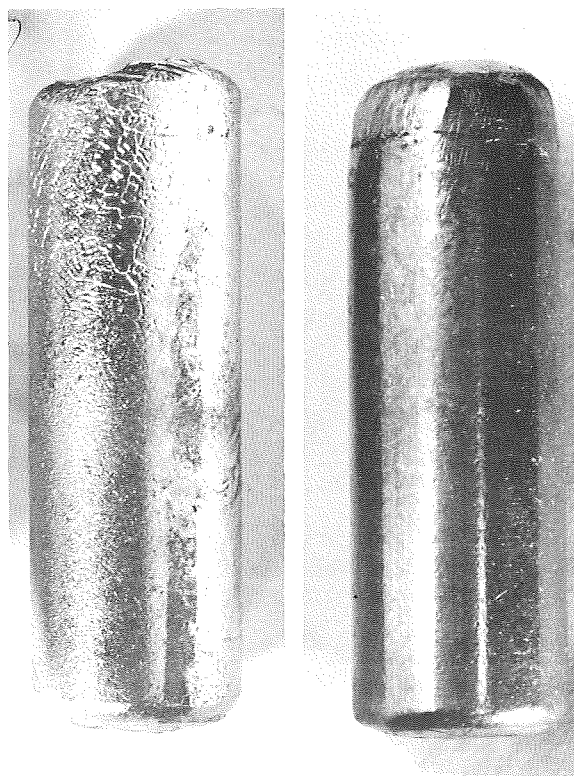


FIGURE 22-19.—Photograph of SF specimens 11-A (left) and 21-A (right), which were located in the 923- and 723-K temperature zones, respectively, of the multipurpose furnace.



pipe was formed at the top of the specimen. Macrographs of the polished longitudinal sections of the 723-K-temperature-zone A and AR SF specimens are shown in figures 22-26(a) and 22-26(b), respectively. These specimens have characteristics similar to those described for the 923-K-zone SF specimens.

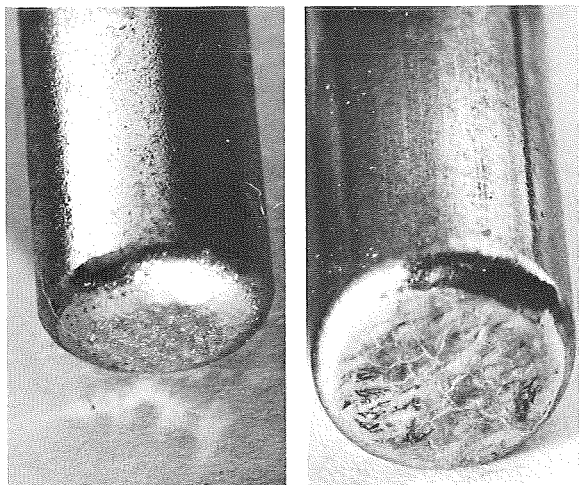


FIGURE 22-20.—Photograph of the lower end of SF specimens 11-A (left) and 21-A (right).

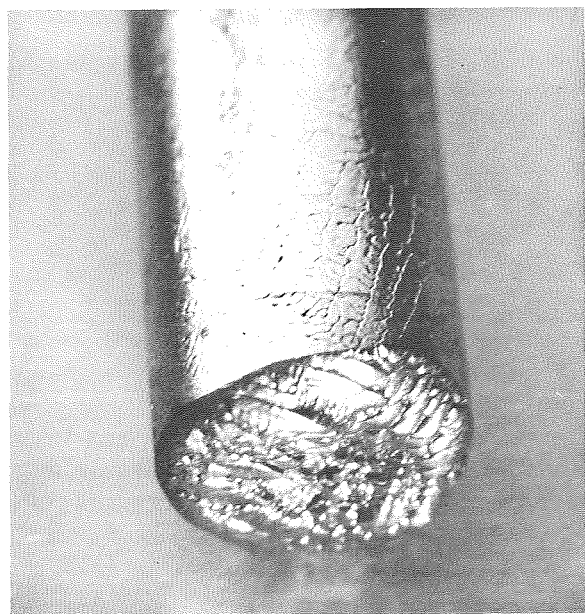


FIGURE 22-21.—Photograph of the upper end of SF specimen 11-A.

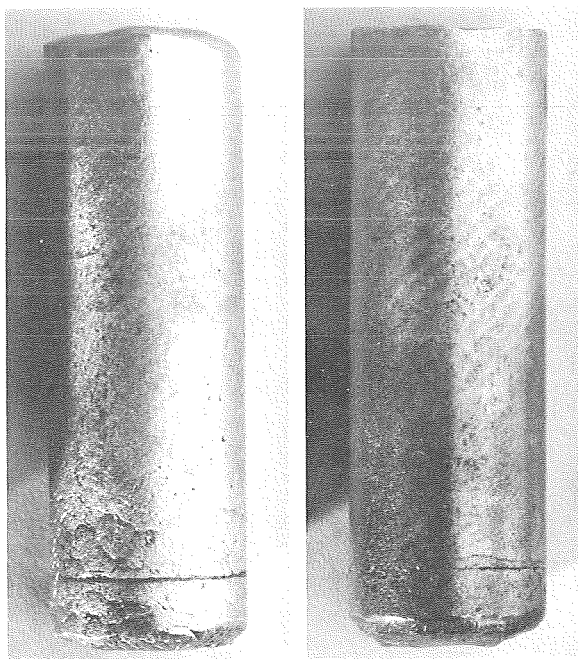


FIGURE 22-22.—Photograph of SF specimens 13-AR (left) and 17-AR (right), which were located in the 923- and 723-K temperature zones, respectively, of the multipurpose furnace.

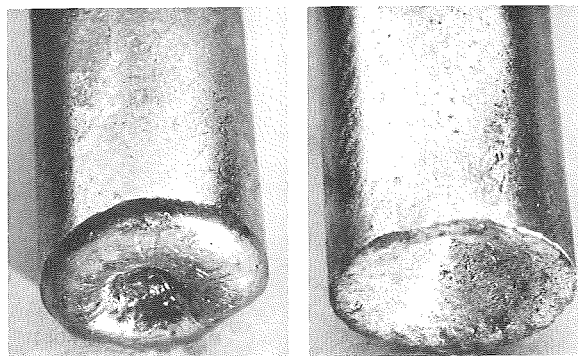


FIGURE 22-23.—Photograph of upper end of SF specimens 13-AR (left) and 17-AR (right).

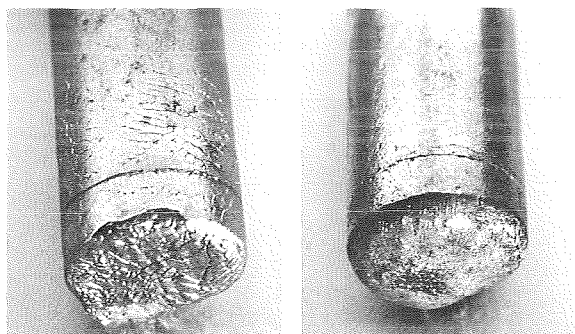


FIGURE 22-24.—Photograph of lower end of SF specimens 13-AR (left) and 17-AR (right).

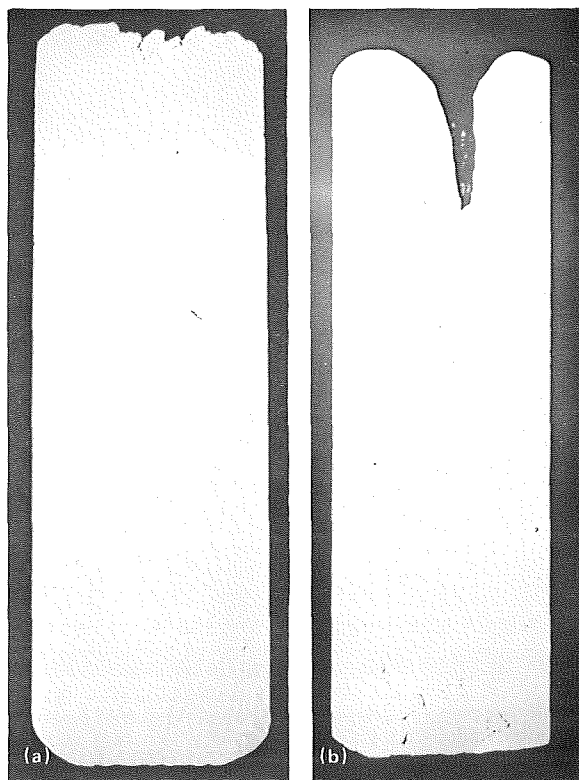


FIGURE 22-25.—Macrographs of metallographically polished, longitudinally sectioned surfaces of 923-K SF specimens. The specimens solidified from bottom to top in a non-wetting ampoule. (a) Specimen 11-A; Pb-Au alloy disk originally located at top. (b) Specimen 13-AR; Pb-Au alloy disk originally located at bottom.

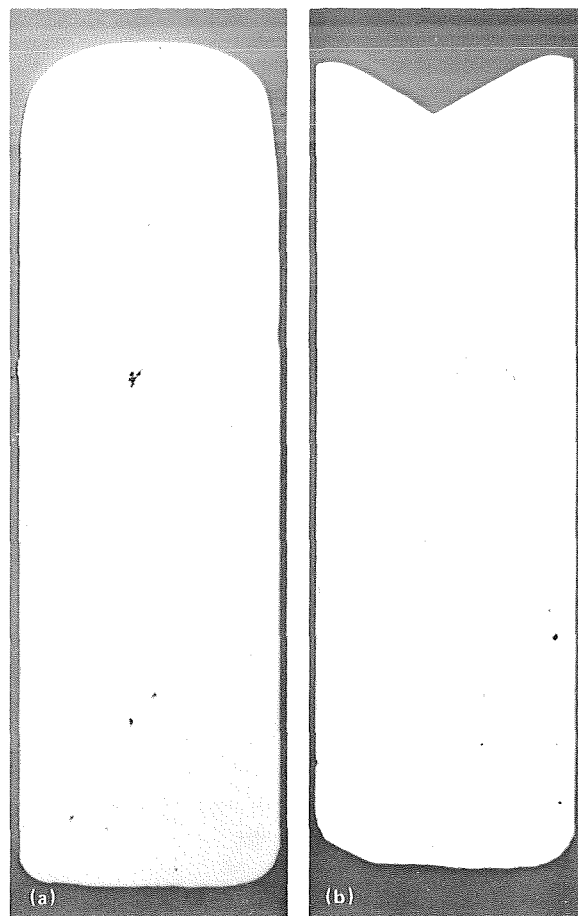
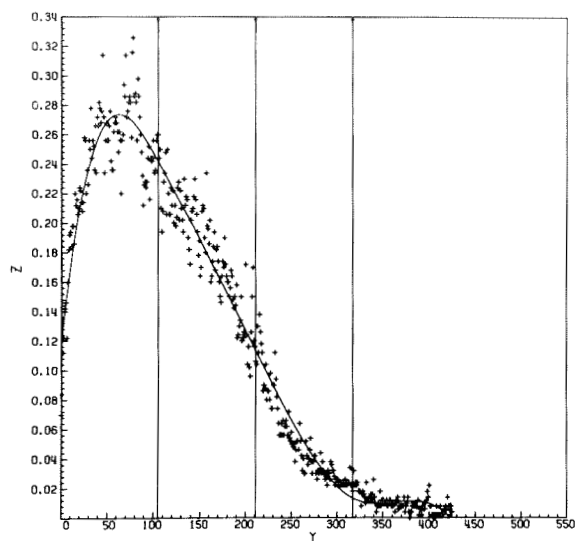


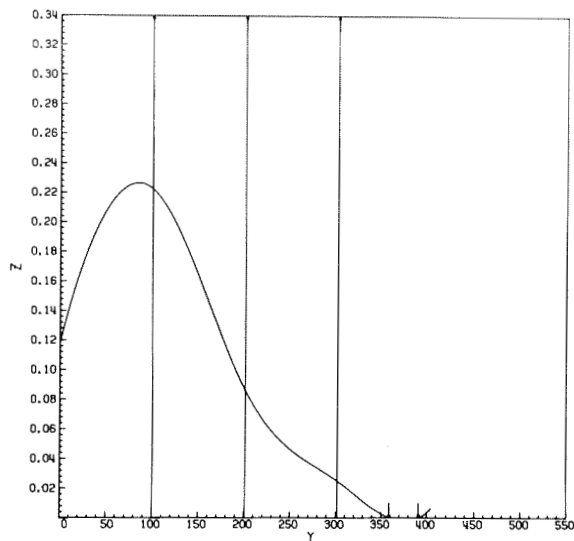
FIGURE 22-26.—Macrographs of metallographically polished, longitudinally sectioned surfaces of 723-K SF specimens. The specimens solidified from bottom to top in a non-wetting ampoule. (a) Specimen 21-A; Pb-Au alloy disk originally located at top. (b) Specimen 17-AR; Pb-Au alloy disk originally located at bottom.

## DIFFUSION ANALYSIS

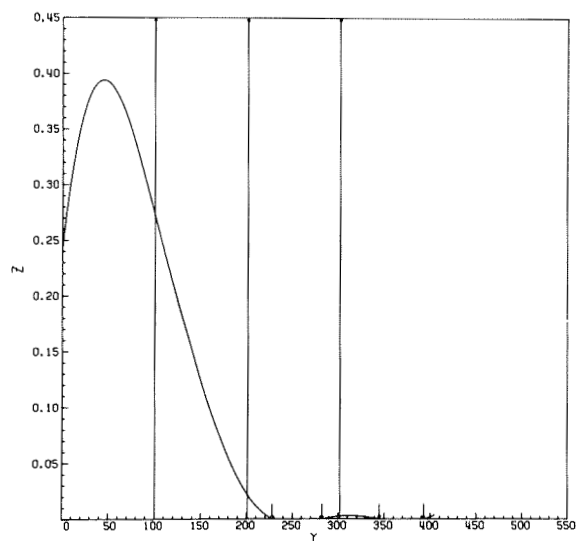
If no convective stirring effects were present during the period in which the samples were molten, a normal diffusion concentration-distance profile would be expected. As shown in figures 22-27(a) to 22-27(d), the right-hand portion of the Au-concentration profiles for the central slices of the SF specimens resemble profiles that would



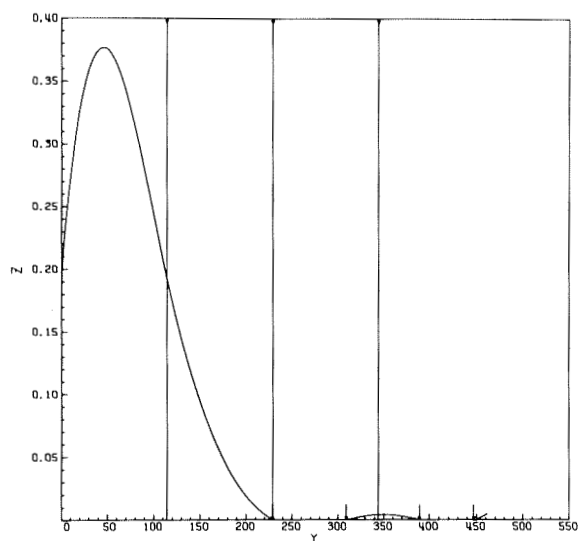
(a)



(b)



(c)



(d)

FIGURE 22-27.—Computer printouts giving central axial Au-concentration profiles for SF specimens. The ordinate  $Z$  represents the percentage of Au with respect to the initial concentration of 500 at. p/m. The abscissa  $Y$  corresponds to a specific column number that can be converted to distance in millimeters by dividing by 14.5 (i.e., 14.5 columns/mm). (a) Specimen 11-A; all data points (approximately 420) are shown. (b) Specimen 13-AR. (c) Specimen 21-A. (d) Specimen 17-AR.

result essentially from diffusion. Thus, an attempt was made to calculate the diffusion constant  $D_0$  and the activation energy  $A$  for the liquid diffusion of Au in Pb by assuming the following definition of diffusion coefficient  $D$ .

$$D = D_0 \exp\left(-\frac{A}{RT}\right) \quad (22-1)$$

where  $R$  is the gas constant (8.314 J/mol K (1.987 cal/mol K)) and  $T$  is temperature. Because of a malfunction in the helium quenching process, the SF specimens stayed molten longer than was initially anticipated. As shown in figures 22-8(a) to 22-8(d), the temperature was not constant but decreased at a slow rate during the cooldown process. Thus, the diffusion coefficients would be expected to have temperature dependency. To solve this problem, according to Crank (ref. 22-9, p.9), one uses the solutions of the diffusion differential equation

$$\frac{\delta C}{\delta T^*} = \frac{\delta^2 C}{\delta x^2} \quad (22-2)$$

where  $C$  is concentration,  $x$  is diffusion distance, and  $T^*$  is defined as

$$T^* = \int_0^t D(t') dt' \quad (22-3)$$

where  $t$  is time. Substituting equation (22-1) into equation (22-3) gives

$$T^* = D_0 \int_0^t \exp\left(-\frac{A}{RT(t')}\right) dt' \quad (22-4)$$

Solving equation (22-1) with the boundary conditions (1) extended source of length  $h$  and constant concentration  $C_0$  and (2) finite specimen length  $\ell$ , one obtains (ref. 22-9, p.15)

$$\frac{C}{C_0} = \frac{1}{2} \sum_{n=-\infty}^{\infty} \left[ \operatorname{erf} \frac{h + 2n\ell - x}{2\sqrt{T^*}} + \operatorname{erf} \frac{h - 2n\ell + x}{2\sqrt{T^*}} \right] \quad (22-5)$$

where integer counter  $n \geq -\infty$ . It is evident that  $T^*$  (eq. (22-4)) is a function of the temperature-time history of the specimens. Because the specimens in this experiment were located in two temperature zones, there are two temperature-time histories and consequently two  $T^*$  values, as follows.

$$T_1^* = D_0 \int_0^{t_1} \exp\left(-\frac{A}{RT_1(t')}\right) dt' \quad (22-6)$$

and

$$T_2^* = D_0 \int_0^{t_2} \exp\left(-\frac{A}{RT_2(t')}\right) dt' \quad (22-7)$$

One method of determining the activation energy is to define a function  $G(A)$  as follows.

$$G(A) = \frac{\int_0^{t_1} \exp\left(-\frac{A}{RT_1(t')}\right) dt'}{\int_0^{t_2} \exp\left(-\frac{A}{RT_2(t')}\right) dt'} = \frac{T_1^*}{T_2^*} \quad (22-8)$$

Using this function, the quotient of the experimentally determined values of  $T_1^*$  divided by  $T_2^*$  defines the actual value of  $G(A)$ . Using the calculated values for the function  $G(A)$  shown in figure 22-28, one should be able to determine the activation energy for the Pb-Au system.

Equation (22-5) was used to obtain the best fit for the concentration profiles for the central slices of the four SF specimens, neglecting the six lowest concentration values shown on the experimental curves. An example of such a fit for SF specimen 13-AR is shown in figure 22-29. The  $T^*$  values obtained for the four SF specimens are shown in table 22-IV. Taking the average value for the two temperature zones and using equation (22-8), a value of 2.12 is obtained for  $G(A)$ . Figure 22-28 indicates that the corresponding activation energy would be extremely small (or negative). This low

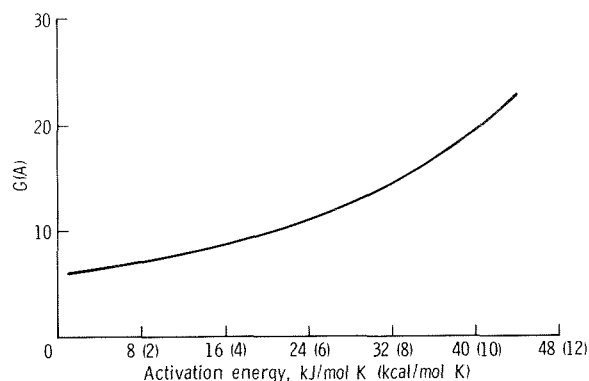


FIGURE 22-28.—Plot of equation (22-8) for the two temperature-time histories of Experiment MA-041 and different activation energies.

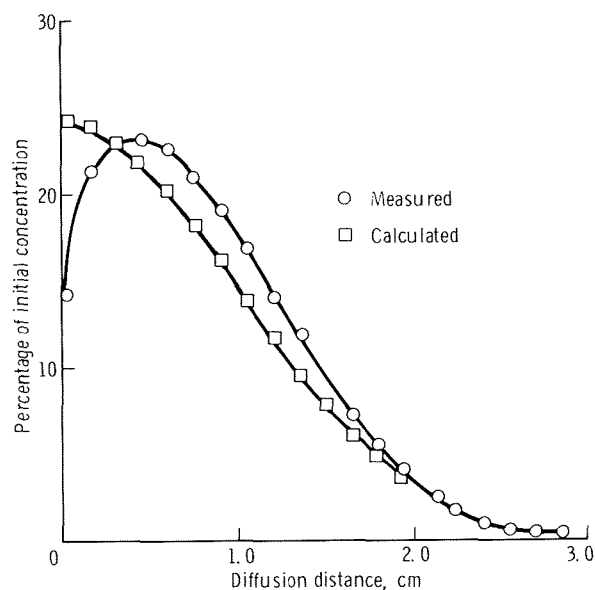


FIGURE 22-29.—Comparison of measured and calculated diffusion profiles for SF specimen 13-AR. The calculated curve was plotted using equation (22-5).

value does not appear reasonable because the reported activation energies for most liquid diffusion systems are greater than 4 kJ/mol K ( $>1$  kcal/mol K) (ref. 22-10, p. 316).

To clarify the discrepancy, the Zn self-diffusion data taken from the Skylab experiment (ref. 22-5, p. 440) were used in conjunction with the two temperature-time histories for this experi-

TABLE 22-IV.— $T^*$  Values for the Four SF Specimens

Specimen	Temperature zone, K	$T^*$ , $\text{cm}^2$
11-A	923	0.39
13-AR	923	.48
21-A	723	.16
17-AR	723	.16

ment to calculate concentration profiles. The calculated concentration profiles, using a  $D_0$  value of  $9.17 \times 10^{-4}$  and an activation energy of 21 589 J/mol K (5160 cal/mol K), are compared with the experimental concentration profiles for SF specimens 11-A and 21-A in figures 22-30(a) and 22-30(b), respectively. Curves 1 and 2 in figures 22-30(a) and 22-30(b) represent the experimental values. Curve 1 represents the actual Au concentration in the central slice. Because of the increased Au concentration in the central region of the SF specimens, it was believed that the true diffusion process would be better represented by a curve adjusted to show no Au increase. Thus, curve 2 was obtained by adjusting the experimental values by the amount of Au-concentration increase in the central region. It is evident that the calculated values for the 923-K SF specimen (fig. 22-30(a)) are in good agreement with the adjusted experimental values, whereas figure 22-30(b) shows that the diffusion process for the 723-K specimen is much more rapid than that calculated from the Zn self-diffusion data. If the temperature-time histories for both temperature zones are assumed correct, there seems to be another mass transport mechanism that occurs predominantly in the beginning. This mechanism is not as evident for the longer soak time, because it is obscured by the diffusion process. Because a process other than diffusion obviously occurred, it is not possible to obtain the true diffusion activation energy and the Au diffusion constant from this experiment. Possible transport mechanisms that could lead to the observed results will be considered in the section entitled "Distributions for SF Specimens."

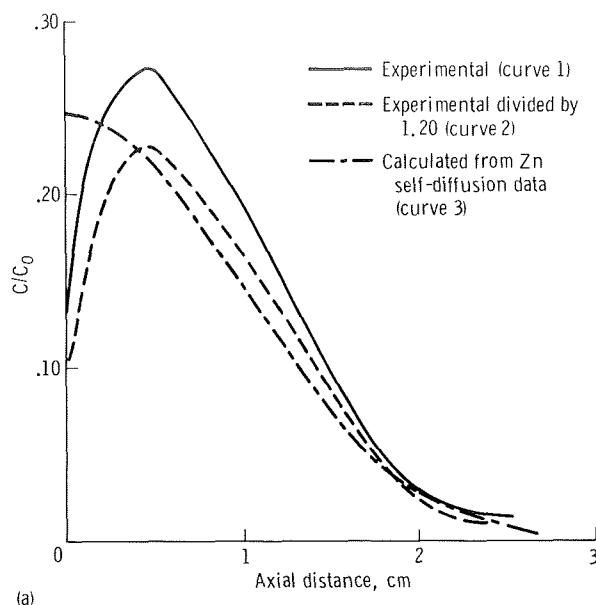
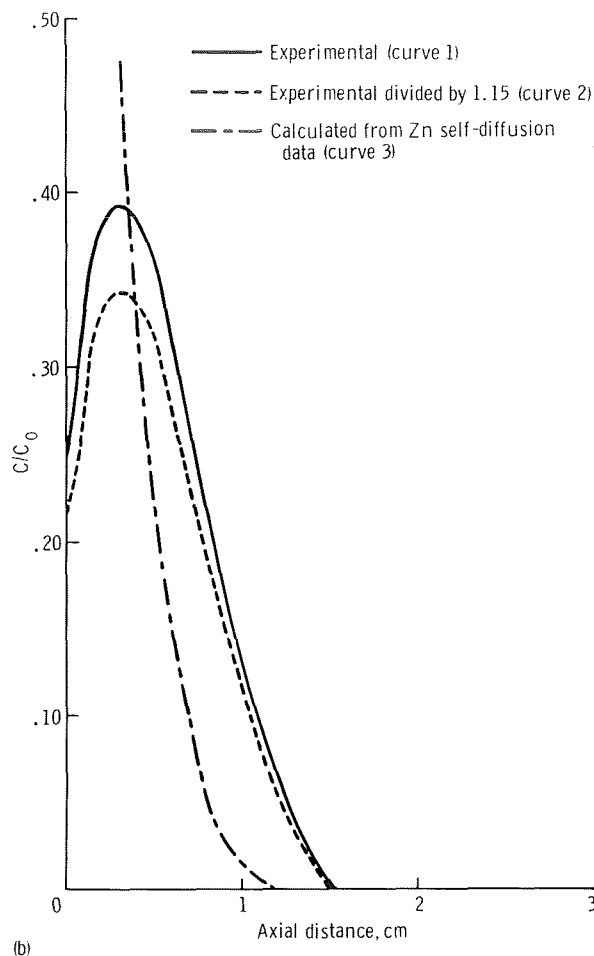


FIGURE 22-30.—Comparison of experimentally determined Au-concentration values with calculated values for SF specimens using Zn self-diffusion data and equation (22-5). (a) Specimen 11-A. (b) Specimen 21-A.

### GOLD-CONCENTRATION DETERMINATION FOR GRAPHITE-LINED CONTAINERS

Gold concentration as a function of location was determined by using the Image Data Processing System (IDAPS) at the NASA George C. Marshall Space Flight Center, Huntsville, Alabama, to scan the specimen autoradiographs. Initially, the autoradiograph of the Pb-Au standards, which had been irradiated and autoradiographed with each specimen, was scanned to establish a calibration curve that related transmittance to Au concentration. This scan was done automatically by the computer-based IDAPS. By using the calibration curve, a table that related all gray values for each specimen to Au concentrations was established. This table permitted the output of the densitometer scan of each specimen to be expressed in Au-concentration units rather than gray values. The scanning interval normally used for each specimen was 70  $\mu\text{m}$ , although a scanning interval of 12.5  $\mu\text{m}$  was used for selected magnified regions to examine speci-



men microstructure. The integration time normally used was 80 microseconds with a signal-to-noise ratio of 34 dB. For the magnifications, an integration time of 1200 microseconds was used with a corresponding signal-to-noise ratio of 46 dB.

The IDAPS provided many possibilities for analyzing the autoradiographs. For this experiment, Au-concentration values for all specimens were obtained and stored on magnetic tape for current and future analyses. For a quick and easier understanding of Au distribution in the specimens, pseudocolors were assigned to particular Au concentration ranges. Using this method, pseudocolor representations showing the Au distribution were obtained. The color scheme used for all specimens is shown in table 22-V.



TABLE 22-V.—Basic Color Scheme  
Relating Pseudocolors to Au Concentrations

Pseudocolor	Au concentration, at. p/m	Percentage of original Au concentration
Black	0 to 5	0 to 1.0
Yellow	6 to 10	1.2 to 2.0
Blue-green	11 to 20	2.2 to 4.0
Red	21 to 40	4.2 to 8.0
Green	41 to 80	8.2 to 16.0
Purple	81 to 120	16.2 to 24.0
Dark blue	121 to 160	24.2 to 32.0
Orange	161 to 254	32.2 to 50.8

### Distributions for GB Specimens

The pseudocolor representations of the Au distributions in the type AR and A GB specimens are shown in figures 22-31 and 22-32. Figure 22-31(a) shows 923-K specimen 11-AR, in which the original Pb-Au alloy disk was located at the bottom. Each large division shown represents approximately 0.24 cm. As can be seen, a large portion of the Au remained at the bottom. In examining the Au-concentration results, one should be aware that a characteristic of the autoradiographic technique is that an "edge" effect occurs when the radioactive disintegrations are recorded on film. This edge effect is caused by the symmetry of the

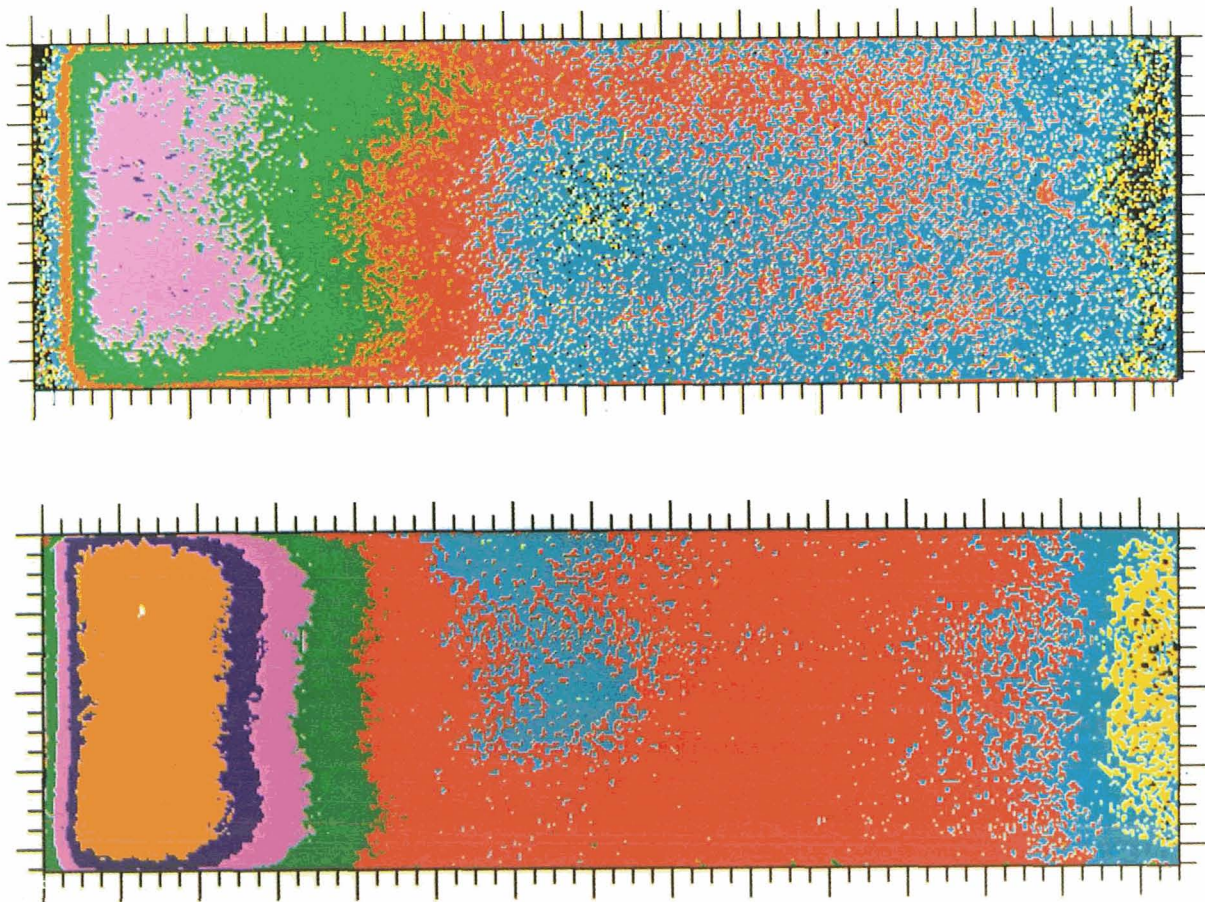


FIGURE 22-31.—Pseudocolor representation of Au concentrations in type AR GB specimens. The pseudocolors are defined in table 22-V. The specimens were mounted vertically in the multipurpose furnace with the original Pb-Au alloy (left side) located at the bottom. The direction of melting was from right to left. (a) Specimen 11-AR; 923-K temperature zone. (b) Specimen 20-AR; 723-K temperature zone.



radioactive disintegrations and is more predominant for  $\beta^-$  particles than for alpha particles because the range of  $\beta^-$  particles in various materials is longer. Thus, at the extreme edge of the samples, the slight decrease in Au concentration recorded is simply a characteristic of the process. The edge effect for all specimens is  $\leq 0.4$  mm, which is the approximate range of the 960-keV  $^{198}\text{Au}$   $\beta^-$  in Pb.

Thermal soak time for specimen 11-AR (fig. 22-31(a)) was approximately 230 minutes, and it is clearly evident that mixing was incomplete. The flow direction is probably indicated by the red color, and mixing probably occurred in the upper portion of the sample. The pseudocolor represen-

tation of the Au distribution for the 723-K GB specimen having the original alloy located at the bottom is shown in figure 22-31(b). Again, it can be seen that most of the Au remained at the bottom of the specimen.

Surprising results were obtained for the GB specimens with the alloy located at the top. Specimens having soak temperatures of 723 and 923 K are shown in figures 22-32(a) and 22-32(b), respectively. Most of the Au "dropped" to the bottom and thus created nearly the same Au distribution for the two temperature zones. Almost identical isograms for the two specimens are shown in figures 22-33(a) and 22-33(b).

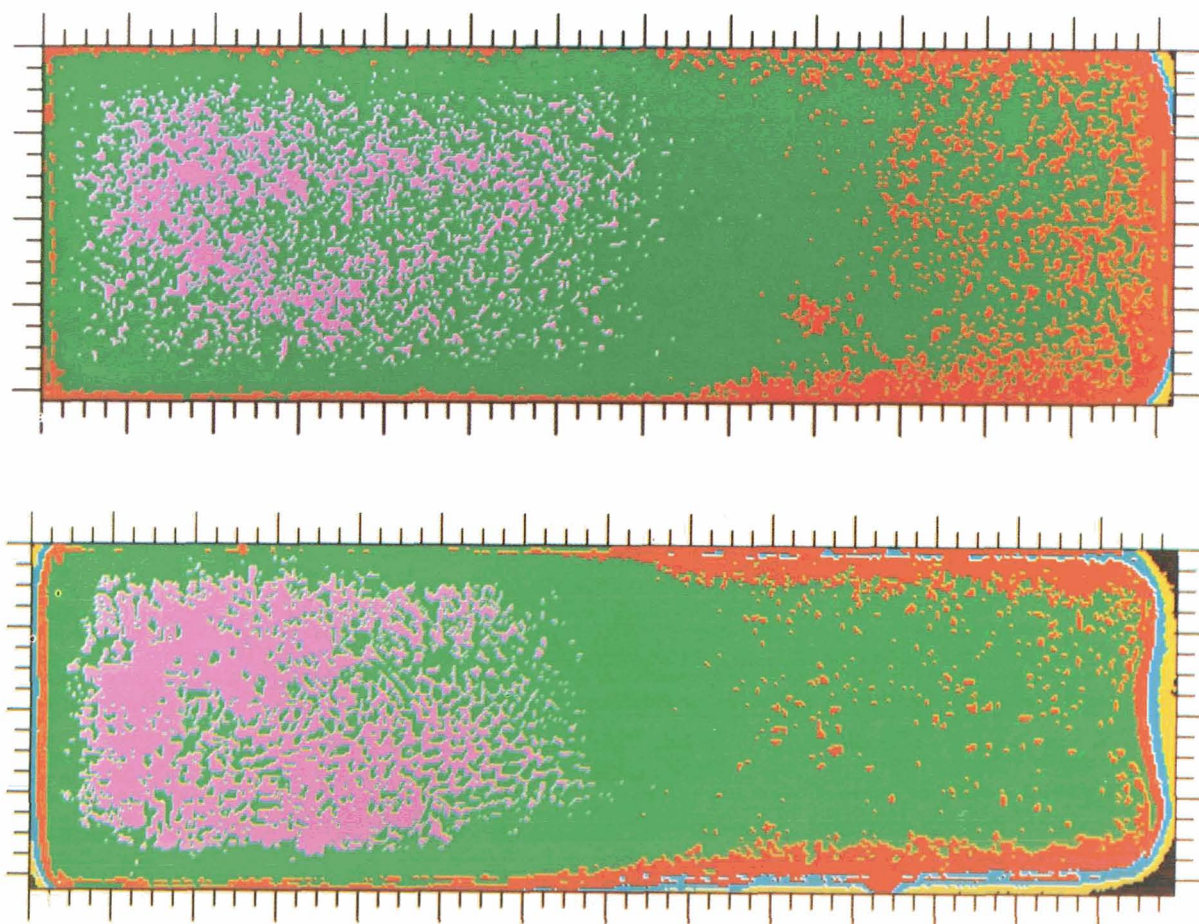


FIGURE 22-32.—Pseudocolor representation of Au concentrations in type A GB specimens. The pseudocolors are defined in table 22-V. The specimens were mounted vertically in the multipurpose furnace with the original Pb-Au alloy (right side) located at the top. The direction of melting was right to left. (a) Specimen 14-A; 723-K temperature zone. (b) Specimen 17-A; 923-K temperature zone.



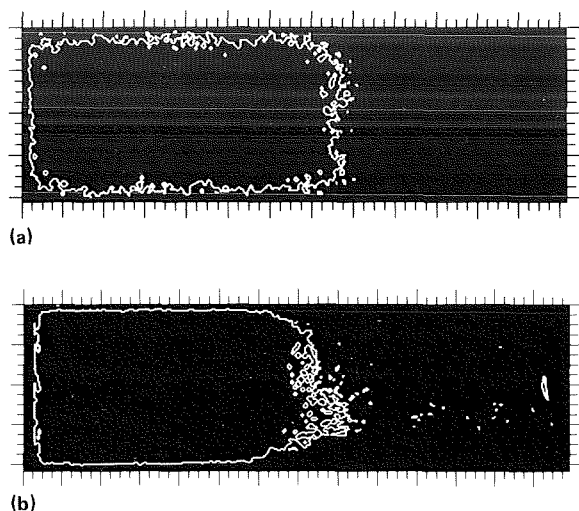


FIGURE 22-33.—Isograms showing the 60 at. p/m Au-concentration region for GB specimens. The direction of melting was from right to left. (a) Specimen 14-A; 723-K temperature zone. (b) Specimen 17-A; 923-K temperature zone.

At least two explanations are possible for the Au movement to the bottom in specimens 14-A and 17-A (figs. 22-32(a) and 22-32(b), respectively).

1. Sedimentation effect: This effect is based on the assumption that an equal distribution of Au in the specimen is obtained and that gravity subsequently causes the Au to settle to the bottom. An estimation of this effect shows that the density difference and Au concentrations are below the levels required for the occurrence of sedimentation.

2. System instability: As was shown by Verhoeven (ref. 22-11), fluid systems with heavier materials at the top can sustain only a certain concentration gradient  $\Delta C/\Delta Z$  before becoming unstable. The concentration gradient can be obtained from the following equation.

$$\frac{\Delta C}{\Delta Z} = \frac{(R_s)_c \cdot \nu \cdot D}{g \cdot \alpha' \cdot r^4} \quad (22-9)$$

where the critical Rayleigh number  $(R_s)_c = 68$ , the kinematic viscosity  $\nu = 1.73 \times 10^{-3} \text{ cm}^2/\text{sec}$ , the diffusion constant  $D \approx 4 \times 10^{-5} \text{ cm}^2/\text{sec}$ , the acceleration due to gravity  $g = 981 \text{ cm/sec}^2$ , the flow distance  $\Delta Z = 2.63 \times 10^3 \text{ cm}$ ,  $r$  is the radius

of the specimen, and  $\alpha' = (1/\rho)(d\rho/dC) = 0.4$  where  $\rho$  is material density and  $C$  is material concentration.

Figure 22-34 is a visual representation of the Pb-Au alloy movement. Because the initial MA-041 concentration gradient was infinite, the Au would be predicted to flow downward to reduce the gradient. Using equation (22-9), one can calculate the Au flow distance required to reach the critical concentration gradient. Calculation of  $\Delta Z$  yields a predicted distance of  $2.6 \times 10^3 \text{ cm}$ . Thus, it is highly probable that the movement of the Au was caused by system instability.

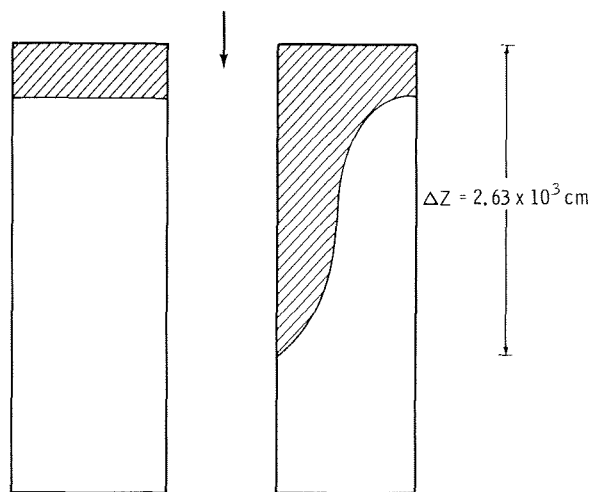


FIGURE 22-34.—Diagram of Pb-Au alloy (shaded) movement to bottom of vertically mounted GB specimens 14-A and 17-A. The diagram is based on the stability analysis of Verhoeven (ref. 22-11) and on equation (22-9).

### Distributions for SF Specimens

Gold-concentration pseudocolor representations used for the type A and AR SF specimens from the 923-K temperature zone are shown in figures 22-35(a) and 22-35(b), respectively. For specimen 11-A, the Pb-Au alloy melted first and solidified last; for specimen 13-AR, the alloy melted last and solidified first. Both specimens have curved radial Au concentration profiles with the larger amount of Au at the cylinder axis gradually decreasing toward the wall. Isograms for

specimens 11-A and 13-AR are shown in figures 22-36(a) and 22-36(b), respectively; the isograms show the 5-, 10-, 20-, 40-, and 80-at. p/m Au concentration lines. To the right of the 5-at. p/m concentration line, the concentration decreases to zero; to the left of the 80-at. p/m concentration line, the Au concentration increases to approximately 140 at. p/m for specimen 11-A and to approximately 115 at. p/m for specimen 13-AR. Although about 120 axial Au-concentration profile lines were obtained for each specimen, only the central lines are shown. As can be seen

from figures 22-27(a) and 22-27(b), which represent the central axial Au-concentration lines from specimens 11-A and 13-AR, respectively, the Au-diffusion distance for specimen 11-A was slightly greater than that for specimen 13-AR. The ordinates in figures 22-27(a) and 22-27(b) represent the percentage of Au with respect to the initial concentration (500 at. p/m); the amount of Au at any point can be obtained by multiplying the ordinate value by 500. The abscissa values can be converted to distance in millimeters by dividing by 14.5.

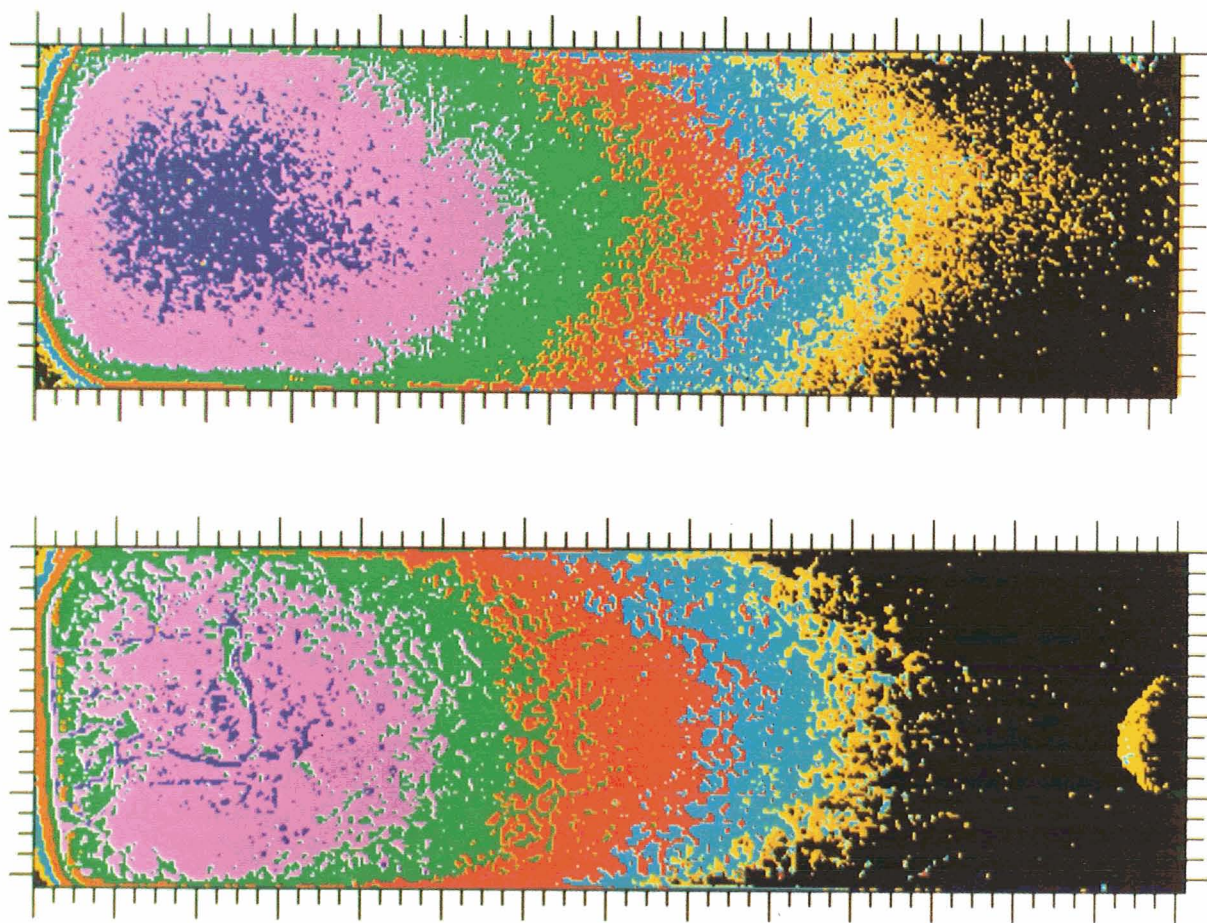


FIGURE 22-35.—Pseudocolor representation of Au concentrations in 923-K SF specimens. The pseudocolors are defined in table 22-V. The original Pb-Au alloy was located on the left-hand side of the specimens. (a) Specimen 11-A; direction of melting was from left to right. (b) Specimen 13-AR; direction of melting was from right to left.

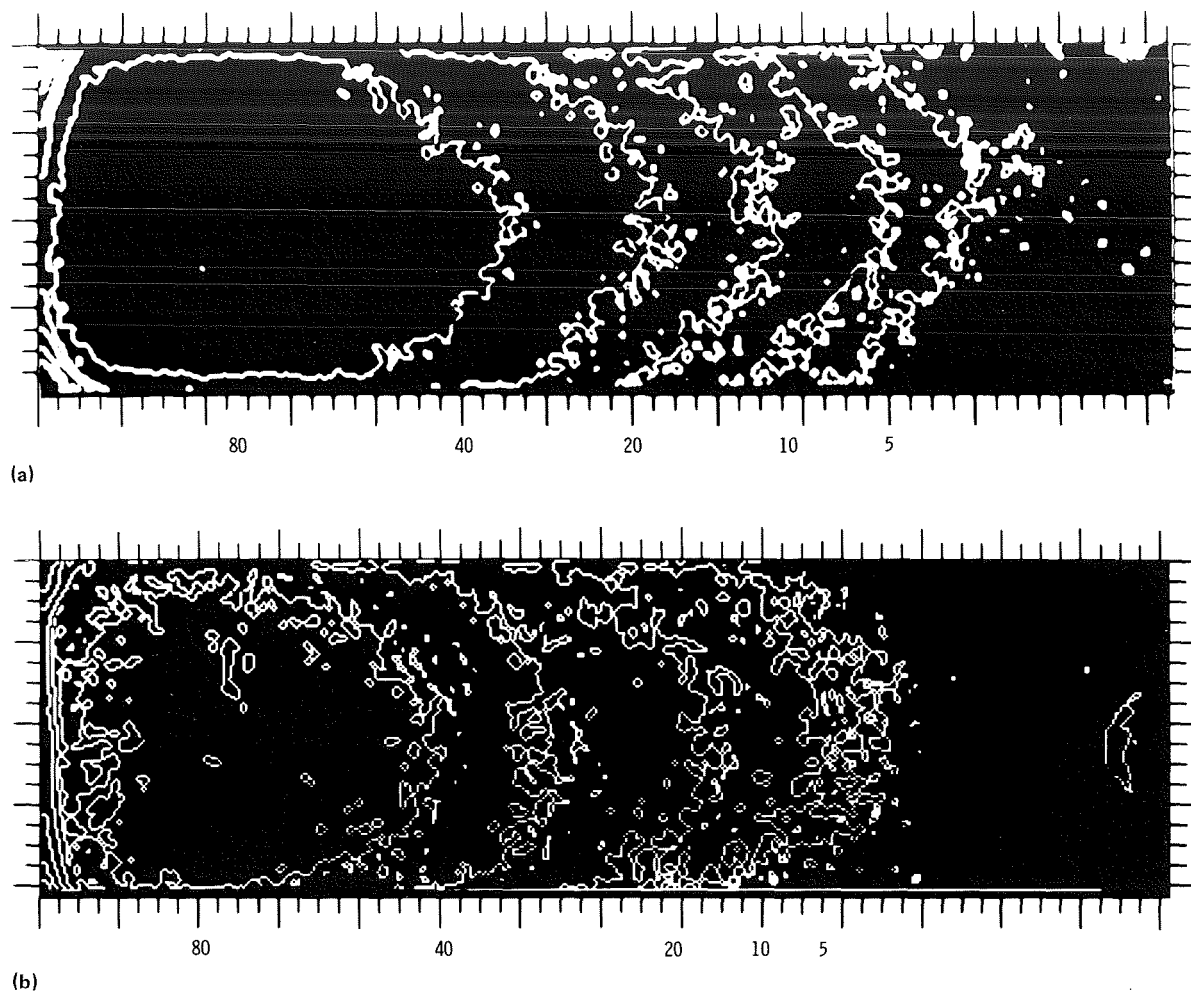


FIGURE 22-36.—Isograms showing the 5-, 10-, 20-, 40-, and 80- at. p/m Au-concentration regions for 923-K SF specimens. (a) Specimen 11-A; direction of melting was from left to right. (b) Specimen 13-AR; direction of melting was from right to left.

Gold-concentration pseudocolor assignments used for SF specimens 21-A and 17-AR, which were located in the 723-K temperature zone of the multipurpose electric furnace, are shown in figures 22-37(a) and 22-37(b), respectively. Gold diffusion into these specimens is approximately equal, as can be seen from the central axial Au-concentration lines shown in figures 22-27(c) and 22-27(d). Curved radial Au-concentration profiles are clearly evident for both specimens, but the curvature appears to be greater for SF specimen

21-A. The only apparent difference between the type A and AR specimens from the 923- and 723-K temperature zones is that the Au-diffusion distance for specimen 13-AR is slightly less than that for specimen 11-A, and the radial concentration curvature is slightly greater for specimen 21-A than for specimen 17-AR. A number of slices were examined for all the SF specimens to determine the location of the maximum Au concentration. The results are shown in table 22-VI. It appears fairly certain that the maximum  $C/C_0$  values



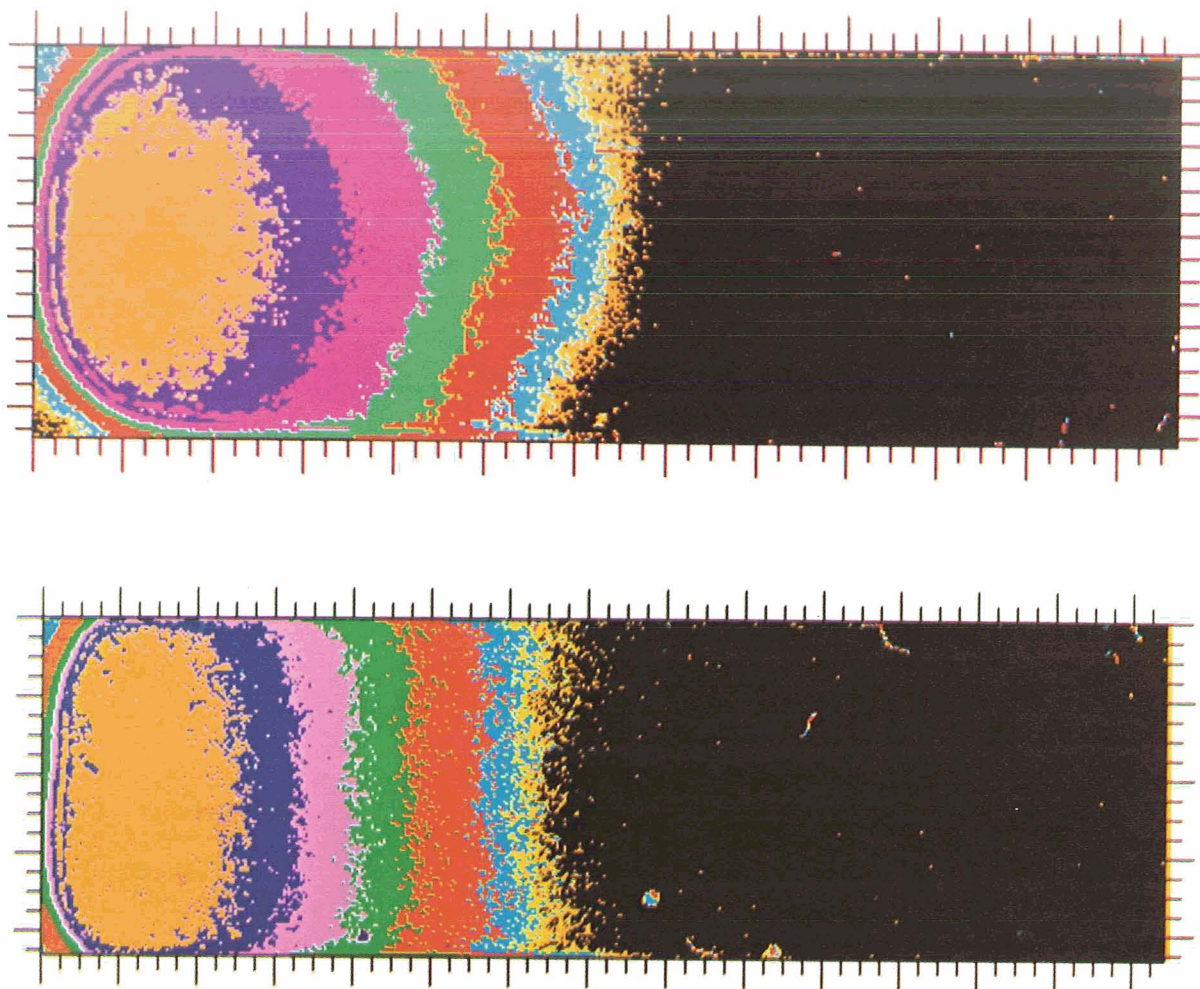


FIGURE 22-37.—Pseudocolor representation of Au concentrations in 723-K SF specimens. The pseudocolors are defined in table 22-V. The original Pb-Au alloy was located on the left-hand side of the specimens. (a) Specimen 21-A; direction of melting was from left to right. (b) Specimen 17-AR; direction of melting was from right to left.

for the 923-K specimens (11-A and 13-AR) were shifted farther into the samples than for the 723-K specimens (21-A and 17-AR).

It appears that the concentration distribution of Au in the SF specimens is not determined simply by diffusion. Independent of the previously discussed diffusion results, there are additional reasons for this conclusion.

1. The occurrence of a maximum Au concentration in the region of the original Pb-Au alloy disk, as shown in table 22-VI

2. The existence of curved Au-concentration profiles in the radial direction for all the SF speci-

mens, as shown in figures 22-35(a), 22-35(b), 22-37(a), and 22-37(b)

3. An increase in the Au concentration in the axial regions

Increase in Au concentration in the axial region was determined by calculating the total Au content in each radial segment and dividing by the initial concentration of the Pb-Au alloy, 500 at. p/m. For example, in figure 22-38(a), the axial Au-concentration increase for SF specimen 11-A is shown. The ordinate represents the total Au content in each segment divided by the initial concentration, and the abscissa shows the location of

TABLE 22-VI.—Data Used to Locate Maximum Au Concentration

Segment no.	Longitudinal location, mm	Maximum $C/C_0$ ratio
<i>Specimen 11-A (923 K)</i>		
6	4.5	0.207
12	4.3	.219
18	4.3	.230
24	4.2	.243
30	4.3	.247
36	4.3	.255
42	4.3	.270
48	4.3	.272
54	4.2	.274
60	4.3	.274
66	4.6	.273
72	4.7	.273
78	4.7	.268
84	4.7	.261
90	4.7	.254
96	4.8	.239
102	4.5	.237
108	4.7	.223
114	4.7	.210
120	4.8	.173
<i>Specimen 21-A (723 K)</i>		
6	3.6	0.270
12	3.4	.304
18	3.4	.324
24	3.4	.342
30	3.3	.352
36	3.2	.360
42	3.2	.388
48	3.1	.388
54	3.1	.389
60	3.1	.395

Segment no.	Longitudinal location, mm	Maximum $C/C_0$ ratio
<i>Specimen 17-AR (723 K)</i>		
6	3.8	0.329
12	3.9	.349
18	3.4	.363
24	3.4	.365
30	3.3	.370
36	3.3	.370
42	3.3	.374
48	3.2	.379
54	3.1	.379
60	3.1	.378
<i>Specimen 13-AR (923 K)</i>		
6	4.1	0.170
12	4.1	.172
18	5.0	.189
24	4.7	.196
30	4.5	.218
36	4.1	.212
42	5.0	.211
48	5.2	.221
54	5.2	.229
60	5.6	.226
66	5.9	.232
72	6.3	.217
78	6.2	.223
84	4.9	.236
90	5.6	.219
96	5.6	.220
102	4.8	.223
108	4.8	.214
114	4.7	.218
120	4.5	.204

each segment of the specimen with respect to the sample axis, which is set equal to zero. A 20-percent Au-concentration increase in the central region was observed for specimen 11-A (fig. 22-38(a)), with a corresponding concentration decrease in the outer radial portions of the specimen. The axial Au-concentration increases in SF specimens 13-AR, 21-A, and 17-AR are shown in figures 22-38(b), 22-39(a), and 22-39(b), respectively.

The following mechanisms were considered as

possible explanations for the Au-concentration distribution in the SF specimens.

1. Melting effects—Radial temperature gradients comparable to longitudinal temperature gradients known to exist might cause variations in Au concentration. Although the magnitudes of the radial temperature gradients are not known, one would expect a difference between the Au-concentration profiles for the type A and AR SF specimens because the melting occurred in opposite directions. However, because the curvature

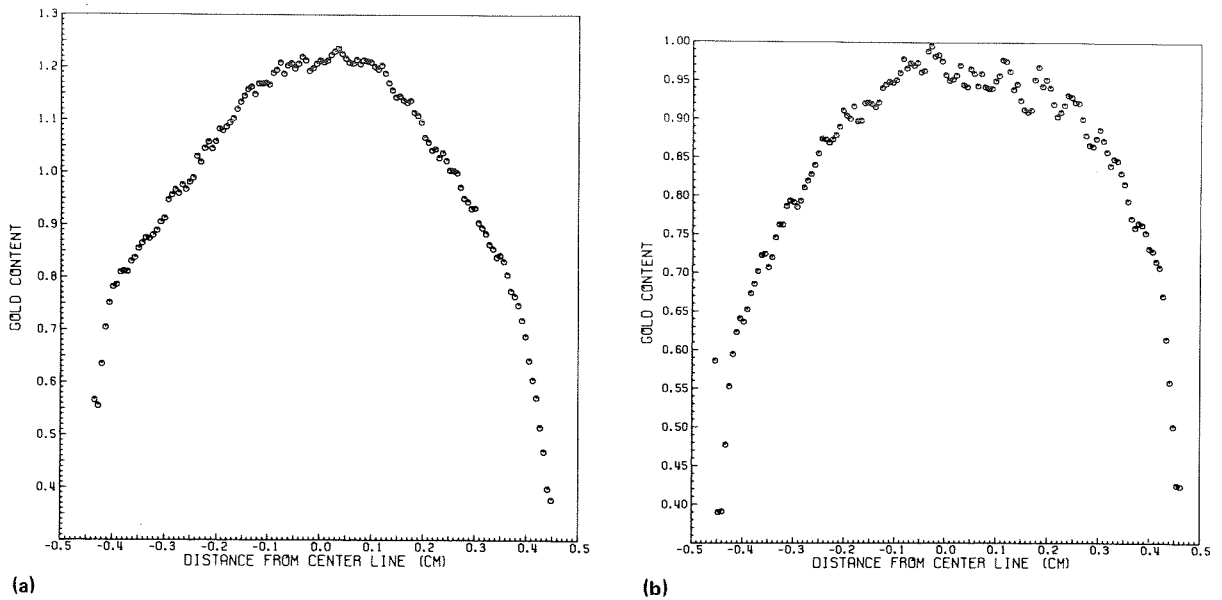


FIGURE 22-38.—Computer printouts showing enhancement of Au in the axial region of 923-K SF specimens. The ordinate represents the percentage of Au for each slice compared to the initial concentration (500 at. p/m). The abscissa represents the radial location of each slice compared to the central slice. (a) Specimen 11-A. (b) Specimen 13-AR.

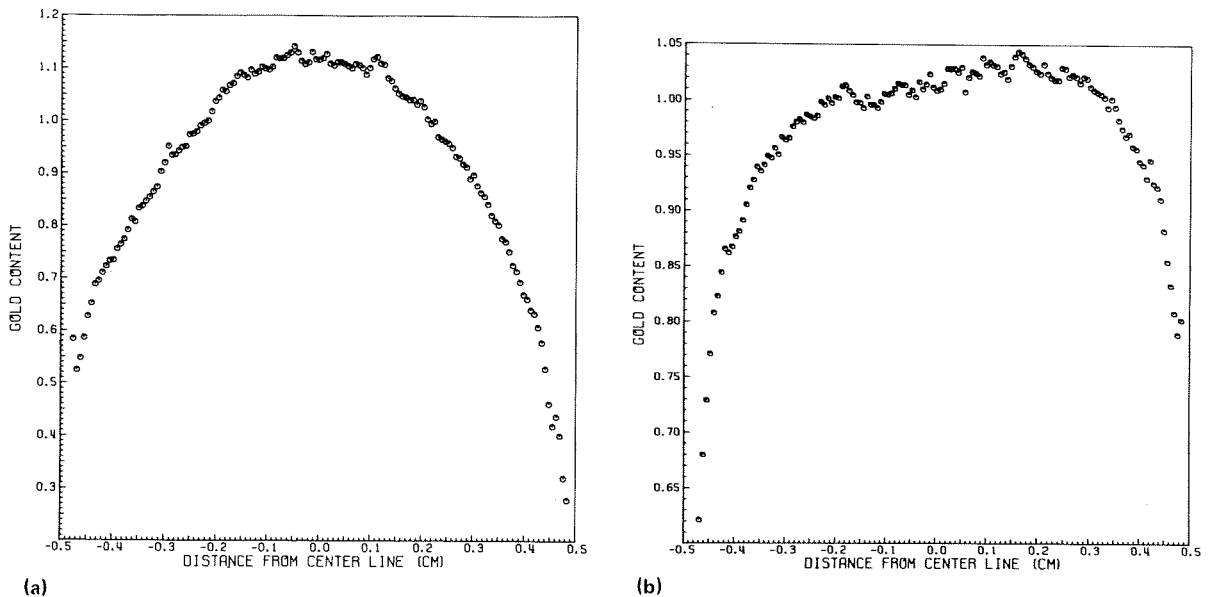


FIGURE 22-39.—Computer printouts showing enhancement of Au in the axial region of 723-K SF specimens. See figure 22-38 for explanation of ordinate and abscissa scales. (a) Specimen 21-A. (b) Specimen 17-AR.

of the Au concentration is the same for both A and AR SF specimens, this explanation is assumed to be invalid.

## 2. Solidification effects

a. Interdendritic flow—According to Mehrabian et al. (ref. 22-12), the curved concentration profiles could be the result of interdendritic flow. However, an examination of the microstructure revealed no dendritic solidification. Curved Au-concentration profiles were observed even in the low Au-concentration regions (0 to 5 p/m), where dendritic solidification would not be expected. Thus, this explanation seems infeasible.

b. Volume shrinkage—Volume shrinkage during solidification in the presence of curved interfaces generally could cause radial concentration distortion. However, in this case, one would expect opposite radial-concentration-profile curvature for the A and AR specimens. Thus, even though the volume shrinkage for lead is 3.1 percent, it apparently had no effect on the final Au-concentration profiles.

Because the experimental arrangement of the A and AR specimens made it possible to exclude melting or solidification effects as an explanation for the curved Au-concentration profiles, the following mechanisms of flow effects while in the liquid state were considered.

1. Radius-dependent diffusion—Radius-dependent diffusion may occur as the result of a radial temperature gradient. However, if a radial gradient existed because of the furnace design, one would assume a higher temperature at the surface of the specimen. In this case, diffusion would occur more rapidly in the surface region and thus would create a resultant concentration curvature opposite to that observed.

2. Flow caused by gas pressure differences—Pressure difference between the meniscus at the left-hand and right-hand sides of the specimen could cause a flow of all the material in one direction. Therefore, the curved concentration profiles are probably not caused by pressure differential since

a. All material would necessarily flow in the same direction.

b. The specimens were sealed in the ampoules at a very low pressure ( $0.133 \text{ mN/m}^2$  ( $1 \times 10^{-6}$  torr)).

3. Meniscus-forming induced flow—Meniscus-induced flow could have contributed to forming the curved Au-concentration profiles. The equilibrium form of the meniscus in a non-wetting container under zero-g conditions is a half sphere. Under this assumption, during the melting process, some material from the outer region would flow to the central region to form the equilibrium shape. Material flow would occur toward the center of the specimen, and part of the material would flow back and form the flow patterns shown in figure 22-40. In Experiment MA-041, such an effect was probably less significant than other effects because the development of the meniscus was impeded by the confining walls of the capsule.

4. Marangoni-effect induced flow—Experimental results can be explained by assuming that induced material flow was caused by either a difference in the interfacial energies between the alloy-graphite or lead-graphite, or a difference in the surface tensions of the alloy and pure Pb according to the contact conditions discussed later. Assuming the interfacial tension of alloy-graphite to be greater than that of Pb-graphite, convection could occur after melting in the region and in the direction shown in figure 22-41 to decrease the difference in the interfacial tensions or the surface tensions. Lead would be transported in the region near the walls to the alloy region and thus would dilute the latter region. A corresponding flow would occur in the specimen center in the opposite direction and would cause the alloy to flow into the pure-Pb region.

An estimate of the Marangoni number  $M_a$  was obtained from the equation

$$M_a = -\Delta\gamma \frac{L}{\eta\psi} \quad (22-10)$$

where  $\Delta\gamma$  is the surface tension difference,  $L$  is the specimen diameter,  $\eta$  is viscosity, and  $\psi$  is

heat diffusivity defined as

$$\psi = \frac{\lambda}{\rho c_v} \quad (22-11)$$

where  $\lambda$  is heat conductivity,  $\rho$  is density, and  $c_v$  is specific heat at constant volume.

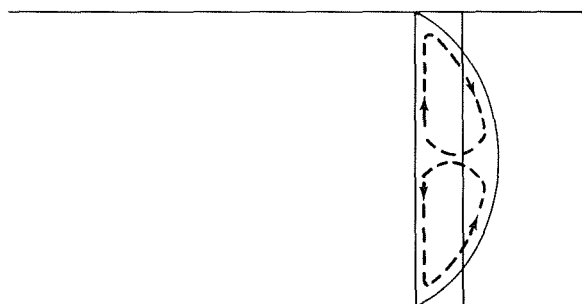


FIGURE 22-40.—Schematic representation of the flow pattern for meniscus-forming induced flow.

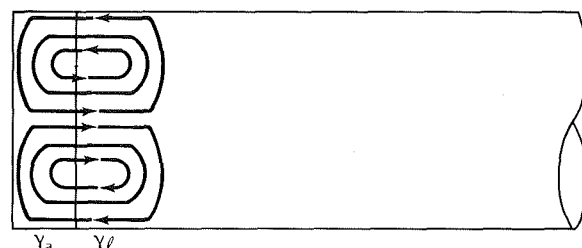


FIGURE 22-41.—Schematic representation of the flow patterns arising from the Marangoni effect, where  $\gamma_a$  and  $\gamma_l$  represent the surface tension of the Pb-Au alloy and of pure Pb, respectively.

Estimation of the Marangoni number was made using available surface tension values of the similar copper-tin system and assuming a surface tension difference of  $0.37 \times 10^{-5}$  N/cm (0.37 dyn/cm) and a specimen diameter of 1 cm. The estimated value of 97 for the 723-K specimens

supports the preceding argument because the critical Marangoni number for zero gravity is zero.

The Marangoni effect can, in fact, be responsible for all the experimental observations, such as the Au-concentration minimums, the occurrence of an Au-concentration maximum not at the beginning of the alloy as in a normal diffusion experiment but at some distance from the end of the specimen, and the low Au concentrations in the outer radial regions of the specimens. In addition, smaller curvatures for the lower temperature specimens can be explained by the same mechanism, because the greater viscosity at the lower temperature would result in a lower flow velocity.

Additional support for induced flow resulting from the Marangoni effect can be found in at least three other experiments.

1. Indium self-diffusion under normal gravity conditions (ref. 23-13)—The capillary method was used to study indium self-diffusion over a wide temperature range. Curved concentration profiles were observed. Nachtrieb (ref. 22-10, p. 314) attributed these results to radial segregation of the indium tracer isotope. On the basis of isotope separation theory, the investigators believe that this explanation is very unlikely.

2. Liquid Zn self-diffusion under near-zero-g conditions (ref. 22-5)—Zinc-65 was pressure bonded to Zn and placed inside a carbon-lined tantalum ampoule. Samples remained in the liquid state for 1 hour. Zinc-65 concentration profiles were determined by sectioning the specimens and gamma-counting each segment to determine the  $^{65}\text{Zn}$  concentration. Results indicated curved concentration profiles in the radial direction attributed by Ukanwa to surface diffusion, capillary attraction, or some sort of surface phenomena.

3. Tea diffusion experiment under near-zero-g conditions (ref. 22-14)—A tea solution was placed in an ampoule containing water, and the diffusion process was monitored. Curved concentration profiles were visually observed by the Skylab astronauts, but no quantitative data were obtained.

The investigators believe that the results of the first two experiments can better be explained by



Marangoni-effect induced flow resulting from surface tension gradients induced by temperature gradients, and that the interfacial or surface tension gradient in the third experiment was caused by concentration differences. The greatest flaw in the preceding explanation is that, according to hydrodynamic theories, Marangoni-effect induced flow should only occur on "free" surfaces. In Experiment MA-041 and the three experiments described previously, it must be assumed that the liquid touched the container walls. Thus, flow caused by interfacial tension gradients can only occur if one assumes a nonzero flow velocity at the walls. According to Scriven<sup>2</sup> and Richardson (ref. 22-4), such an assumption is a violation of the zero-slip boundary condition. On the other hand, the investigators believe that some reasons exist for doubting the applicability of zero-slip boundary conditions in space. The degree of contact of the nonwetting fluid may be different for null gravity than for normal gravity. The fluid may have only partly contacted the ampoule wall; thus, free surfaces could have existed over small regions. The degree of contact is influenced by the different pressures in the fluid. If, in fact, the Marangoni-effect induced flow in Experiment MA-041 was not hindered by total contact, one can assume, in this case, that flow was caused by the difference in the surface tensions rather than in the interfacial tensions.

The best explanation at this time for the experimental results is that a flow induced by the Marangoni effect did occur. The investigators suggest that studies should be made concerning the validity of the nonzero boundary condition in zero gravity with nonwetting materials and different surface structures for the container walls.

#### **GOLD-CONCENTRATION DETERMINATION FOR MILD STEEL CONTAINERS**

The Au-concentration distribution for the specimens in mild steel containers was similar to

that determined for the specimens in graphite-lined containers. Macrographs of the longitudinally sectioned surfaces of mild-steel-contained GB and SF specimens are shown in figures 22-42 to 22-44. As shown by the meniscus shapes, the contact angle in all cases is  $>90^\circ$ . Rough measurements of contact angles indicate a tendency for nonwetting for the GB specimens and nearly total nonwetting for the SF specimens.

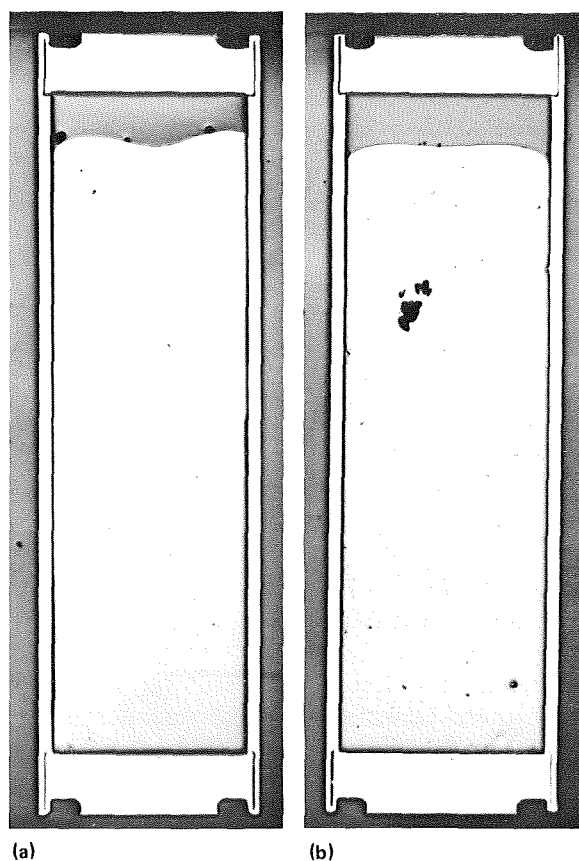


FIGURE 22-42.—Macrographs of metallographically polished, longitudinally sectioned surfaces of GB specimens contained in mild steel ampoules. The specimens were mounted vertically. The original Pb-Au alloy was located at the top. The direction of melting was from top to bottom. (a) Specimen 13-B; 923-K temperature zone. (b) Specimen 15-B; 723-K temperature zone.

<sup>2</sup>L. E. Scriven, personal communication, July 1976.

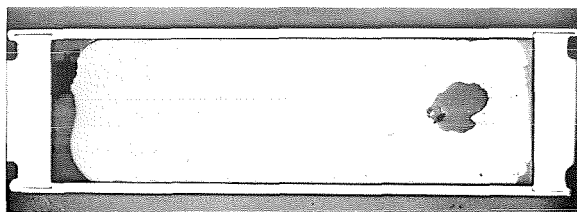


FIGURE 22-43.—Macrograph of metallographically polished, longitudinally sectioned surface of SF specimen 12-B contained in a mild steel ampoule. The specimen was located in the 923-K temperature zone and melted from left to right. The original Pb-Au alloy was located in the vicinity of the large void.

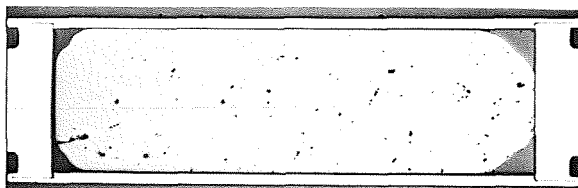


FIGURE 22-44.—Macrograph of metallographically polished, longitudinally sectioned surface of SF specimen 21-B contained in a mild steel ampoule. The specimen was located in the 723-K temperature zone and melted from left to right. The original Pb-Au alloy was located on the left-hand side of the specimen. Dark spots are oxide deposits on the surface.

### EXAMINATION OF SPECIMEN MICROSTRUCTURES

Initial investigations revealed no systematic differences between the microstructures of the GB and SF specimens. Selected areas in the autoradiographs of two SF specimens and one GB specimen were magnified for an examination of the microstructure. The observed microstructures can be classified as follows.

1. Grain and subgrain boundaries
2. Well-developed cell structure
3. Diffuse (little structure)

Examples of these classifications are shown in figures 22-45, 22-46, and 22-47, respectively. Each large division in the figures represents approximately 0.7 mm.

Figure 22-45 is an enlargement of a selected area in the Au-rich region of figure 22-35(b) (SF specimen 13-AR) that contains grain and subgrain

boundaries. The pseudocolor assignment is as shown in table 22-V. Segregation of Au at the grain boundaries is shown by the orange and represents at least a 60-percent increase over the amount of Au in the adjacent grain region. One also can observe that segregation in the grain boundaries is not homogeneous.

Well-developed cell structure is shown in figure 22-46, which is an enlargement of a selected area in the center of figure 22-32(b) (GB specimen 17-A). The pseudocolor assignment for the Au concentrations in figure 22-46 is shown in table 22-VII. Quantitative Au-concentration data for the magnified region of GB specimen 17-A are shown in figure 22-48 for a slice taken parallel to the melting direction. The slice analyzed in figure 22-48 was located approximately 9.5 large divisions from the top of figure 22-32(b). The average cell size calculated from the slice is approximately 0.3 mm. In addition, further examination of the slice reveals a segregation increase of Au at the cell walls of approximately 50 percent compared to the cell interior. Both figures 22-46 and 22-48 reveal that the cell walls are not very sharp; the walls are broadened either during formation or by diffusion in the solid.

An enlargement of a selected area in the Au-rich region of SF specimen 11-A (fig. 22-35(a)) is shown in figure 22-47 to illustrate diffuse microstructure. The pseudocolor representation of the Au concentrations for this magnification is shown in table 22-VII. As one can see, very little structure is present.

Results obtained for the three magnifications represent only a beginning in the examination of the microstructure of both GB and SF specimens.

### SUMMARY

The purpose of the Surface-Tension-Induced Convection Experiment was to observe compositional-induced convection effects. Convection effects were observed but were not sufficiently large to bring about total mixing in the SF specimens. However, they were large enough to prohibit analysis of the pure diffusion process. The most plausible explanation for the flow phenomena observed is convection induced by

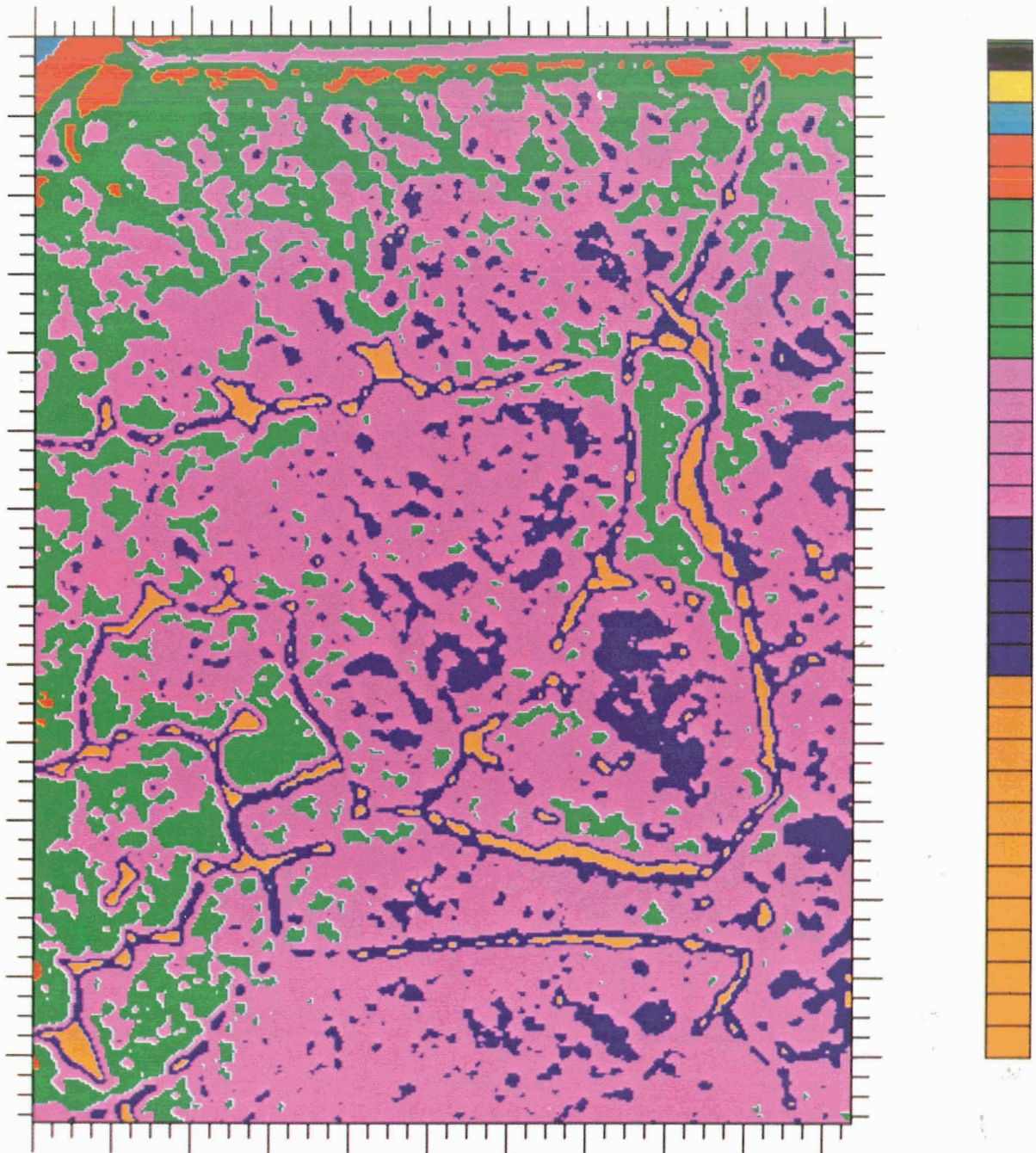


FIGURE 22-45.—Enlarged pseudocolor representation of Au-rich region of 923-K SF specimen 13-AR showing grain and subgrain boundaries. The pseudocolors are defined in table 22-V. The direction of melting was from right to left.



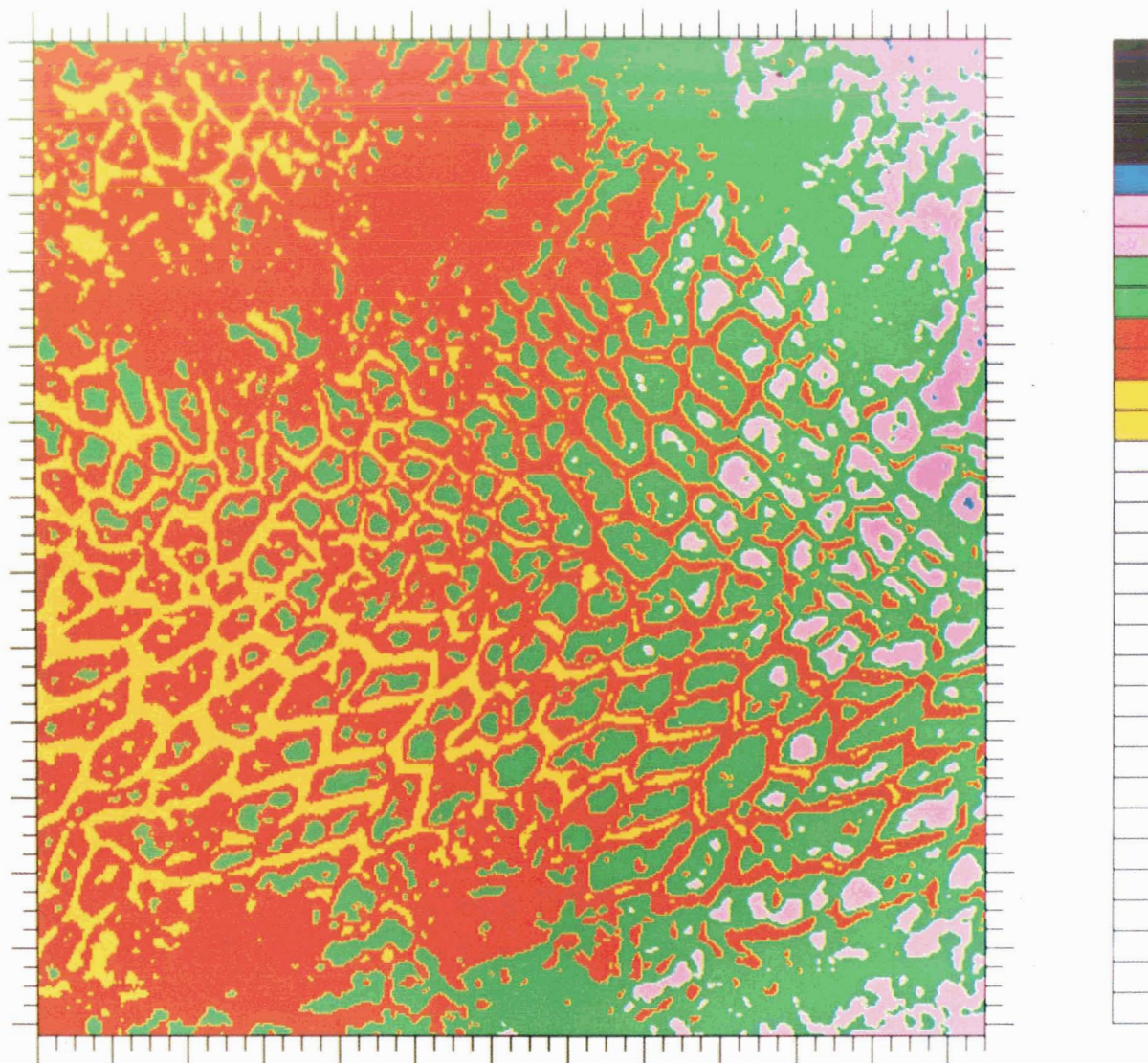


FIGURE 22-46.—Enlarged pseudocolor representation of an area of 923-K GB specimen 17-A showing well-developed cell structure. The pseudocolor Au-concentration assignments are shown in table 22-VII. The direction of melting was from right to left.

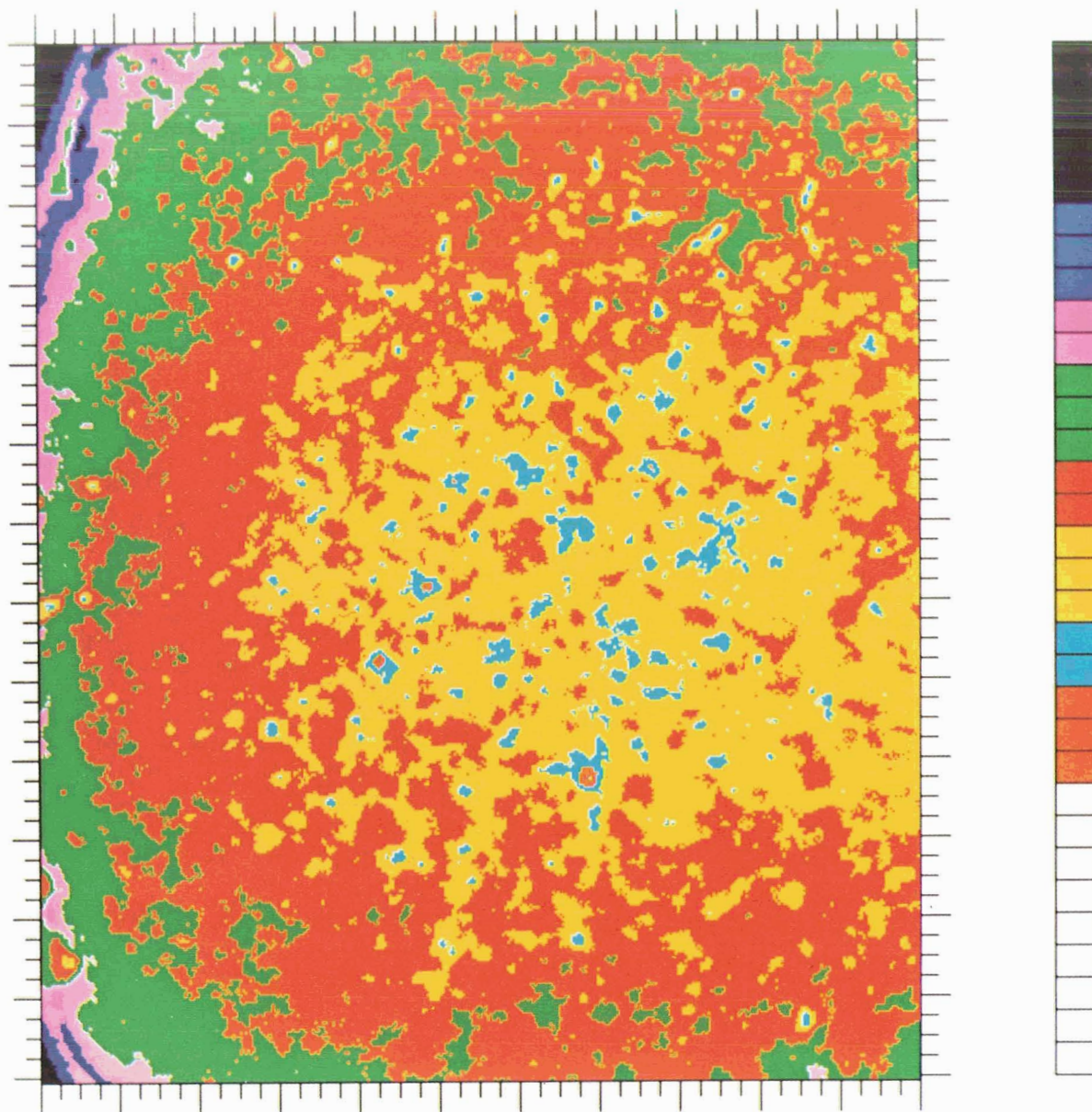


FIGURE 22-47.—Enlarged pseudocolor representation of an area of 923-K SF specimen 11-A showing the lack of cell structure characteristic of diffusion. The pseudocolor Au-concentration assignments are shown in table 22-VII. The direction of melting was from left to right.

TABLE 22-VII.—Pseudocolor Au-Concentration  
Assignments for Magnifications

Pseudocolor	Au concentration, at. p/m	Percentage of original Au concentration
<i>GB specimen 17-A</i>		
Black	0 to 24	0 to 4.0
Blue	25 to 40	5.0 to 8.0
Pink	41 to 55	8.2 to 11.0
Green	56 to 70	11.2 to 14.0
Red	71 to 85	14.2 to 17.0
Yellow	86 to 100	17.2 to 20.0
<i>SF specimen 11-A</i>		
Black	0 to 40	0 to 8.0
Dark blue	41 to 60	8.2 to 12.0
Purple	61 to 80	12.2 to 16.0
Green	81 to 100	16.2 to 20.0
Red	101 to 120	20.2 to 24.0
Yellow	121 to 140	24.2 to 28.0
Light blue	141 to 160	28.2 to 32.0
Red-brown	161 to 180	32.2 to 36.0

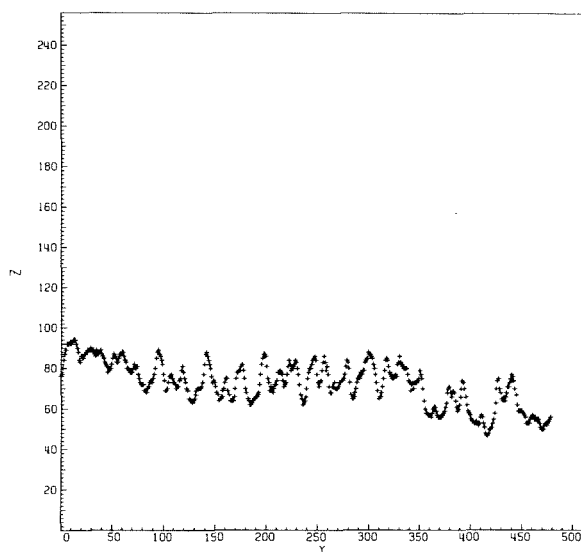


FIGURE 22-48.—Computer printout showing Au-concentration data for a slice parallel to the melting direction of GB specimen 17-A (fig. 22-46). The ordinate represents the Au concentration in atomic parts per million; the abscissa represents the column number, where the corresponding linear distance between two columns on the sample slice is 0.0175 mm.

the Marangoni effect; if this explanation is in fact correct, a violation of the no-slip boundary condition must be assumed. Results for the GB specimens were totally different from those obtained in space; convection was a dominant factor in the GB specimen mixing.

Expected wetting of the mild steel capsules did not occur in space, and only a partial wetting occurred for the GB specimens.

Initial investigation of the microstructures revealed no systematic differences between GB and SF specimens. Segregation resulted in an increase in Au concentration of approximately 50 to 60 percent in the cell walls and grain boundaries.

## REFERENCES

- 22-1. Grodzka, P. G.; and Bannister, T. C.: Natural Convection in Low-g Environments. AIAA Paper 74-156, 1974.
- 22-2. Larson, D. J.: Skylab M553 Sphere Forming Experiment. Proceedings of the 3rd Space Processing Symposium on Skylab Results, Vol. 1. NASA TM X-70252, 1974, pp. 101-113.



- 22-3. McKannan, E. C.; and Poorman, R. M.: Skylab M551 Metals Melting Experiment. Proceedings of the 3rd Space Processing Symposium on Skylab Results, Vol. 1. NASA TM X-70252, 1974, pp. 85-100.
- 22-4. Richardson, S.: On the No-Slip Boundary Condition. *J. Fluid Mech.*, vol. 59, pt. 4, Aug. 7, 1973, pp. 707-719.
- 22-5. Ukanwa, A. O.: M558 Radioactive Tracer Diffusion. Proceedings of the 3rd Space Processing Symposium on Skylab Results, Vol. 1. NASA TM X-70252, 1974, pp. 425-456.
- 22-6. Semenchenko, V. K. (N. G. Anderson, transl.; R. Kennedy, ed.): *Surface Phenomena in Metals and Alloys*. Pergamon Press Ltd. (London), 1962.
- 22-7. Hansen, Max: *Constitution of Binary Alloys*. McGraw-Hill Book Company (New York), 1958.
- 22-8. Reed, R. E.: Redistribution of Tantalum and Tungsten Impurities in Niobium by Electron Beam Float Zone Refining. *J. Crystal Growth*, vol. 19, no. 1, 1973, pp. 61-64.
- 22-9. Crank, J.: *The Mathematics of Diffusion*. Oxford University Press (London), 1956.
- 22-10. Nachtrieb, N. H.: Self-Diffusion in Liquid Metals. *The Properties of Liquid Metals*. Proceedings of the International Conference Held at Brookhaven National Laboratory, Upton, New York, Sept. 1966. Taylor & Francis, Ltd. (London), 1967, pp. 309-323.
- 22-11. Verhoeven, J. D.: Convection Effects in the Capillary Reservoir Technique for Measuring Liquid Metal Diffusion Coefficients. *Trans. Met. Soc. AIME*, vol. 242, no. 9, Sept. 1968, pp. 1937-1942.
- 22-12. Mehrabian, R.; Keane, M.; and Flemings, M. C.: Interdendritic Fluid Flow and Macrosegregation; Influence of Gravity. *Met. Trans.*, vol. 1, no. 5, May 1970, pp. 1209-1220.
- 22-13. Careri, G.; Paoletti, A.; and Vincentini, M.: Further Experiments on Liquid Indium and Tin Self-Diffusion. *Nuovo Cimento*, vol. 10, 1958, pp. 1088-1099.
- 22-14. Bannister, Tommy C.: Science Demonstrations on Skylab in the Material Processing Area. Proceedings of the 3rd Space Processing Symposium on Skylab Results, Vol. 1. NASA TM X-70252, 1974, pp. 491-595.



### IN MEMORIAM

Dr. Richard E. Reed, Principal Investigator for the MA-041 Experiment, exhibited unusual dedication by his continuous participation in this investigation until his untimely death. His colleagues and associates remember him for his unrelenting adherence to the highest standards of scientific research.





## 23. Monotectic and Syntectic Alloys

### Experiment MA-044

*L. L. Lacy<sup>a</sup> and C. Y. Ang<sup>ab</sup>*

#### ABSTRACT

The flight test furnace run of the Monotectic and Syntectic Alloys Experiment was successfully conducted during the Apollo-Soyuz Test Project mission in July 1975. Examination of the returned sample cartridges and the formal comparative characterization of the low-g- and one-g-processed samples of lead-zinc and aluminum antimonide have been completed. The results on aluminum antimonide show that polycrystalline and multiphased material can be homogenized in space under low-g conditions. In terms of reduction of the unwanted second phase, the low-g samples show a homogeneity improvement by factors from 4 to 20 over the one-g counterparts. Furthermore, small amounts of the second phase were formed only along parts of the grain boundaries of the flight samples, whereas the ground-based samples show major grains of the second phase.

Microstructural study on the lead-zinc flight samples shows that complete interdiffusion of lead and zinc had not been achieved, even though the flight data indicated a soak temperature in the miscible region that was 40 K above the published consolute temperature. Dispersion of lead particles in the zinc matrix was observed in both the low-g and one-g samples of lead-zinc. A chemical analysis of cut sections shows that the distribution of lead in zinc in the flight sample follows a diffusional process with a diffusion coefficient of

$\approx 3 \times 10^{-6} \text{ cm}^2/\text{sec}$ , which is about two orders of magnitude smaller than that for miscible liquid metals. Conversely, the one-g samples of lead-zinc have a uniform, dilute concentration of lead in the zinc matrix, an indication that most of the lead phase was removed by sedimentation after it was introduced by convective mixing.

#### INTRODUCTION

Certain potentially useful alloys or material systems are difficult to synthesize on Earth because of sizable differences in specific gravity of the constituents in a molten state; these differences result in undesirable buoyancy and convection influences during homogenization of the melts as well as during the initial stages of solidification and grain growth. Consequently, the near-zero-g condition in space processing was the primary motivation for this experiment. Furthermore, significant discoveries related to microsegregation and kinetics of lattice defects, made as a result of Skylab experiments (refs. 23-1 and 23-2), have shown the value of continuing space-processing experimentation for future manufacturing activities in space.

The purpose of this experiment was to investigate the effects of weightlessness on the melting and solidification of two material systems, lead-zinc (Pb-Zn) and aluminum antimonide (AlSb). The objectives were (1) to investigate phase segregation effects in low g for the immiscible binary Pb-Zn and (2) to determine the influences of low-g solidification on the microstructural homogeneity and stoichiometry of the semiconducting compound AlSb. This report contains a

---

<sup>a</sup>NASA George C. Marshall Space Flight Center; Co-Principal Investigators.

<sup>b</sup>Universities Space Research Association, visiting scientist at George C. Marshall Space Flight Center.

comprehensive summary of evaluation results for two flight samples, two ground-based tested (GBT) samples, and two prototype tested (PT) samples of each material. Additional samples were used for specific tests such as chemical analyses.

### EXPERIMENT CONCEPT AND PROCEDURES

The Pb-Zn monotectic system (ref. 23-3 and fig. 23-1) is characterized by the large miscibility gap  $L_1 + L_2$  in which liquid phases can coexist over a large compositional and temperature range. This system is also characterized by a large den-

sity difference between Pb ( $11.7 \text{ g/cm}^3$ ) and Zn ( $7.14 \text{ g/cm}^3$ ). In the Earth's gravity field, the prevention of gravity separation between Pb and Zn upon solidification is difficult. Negating the effects of gravity in space processing should lead to an optimum mixing of the two phases, resulting in a dispersion of fine particles of superconducting Pb in a Zn-rich composition. Previous results of Apollo 14 (ref. 23-4), Skylab (refs. 23-1, 23-2, and 23-5), and experiments performed on the NASA George C. Marshall Space Flight Center (MSFC) drop tower (refs. 23-6 to 23-8) indicated that stable dispersions of immiscible liquids can be prepared in a low-g environment, whereas similar dispersions prepared on Earth are rapidly separated by such gravity-dependent influences as creaming,

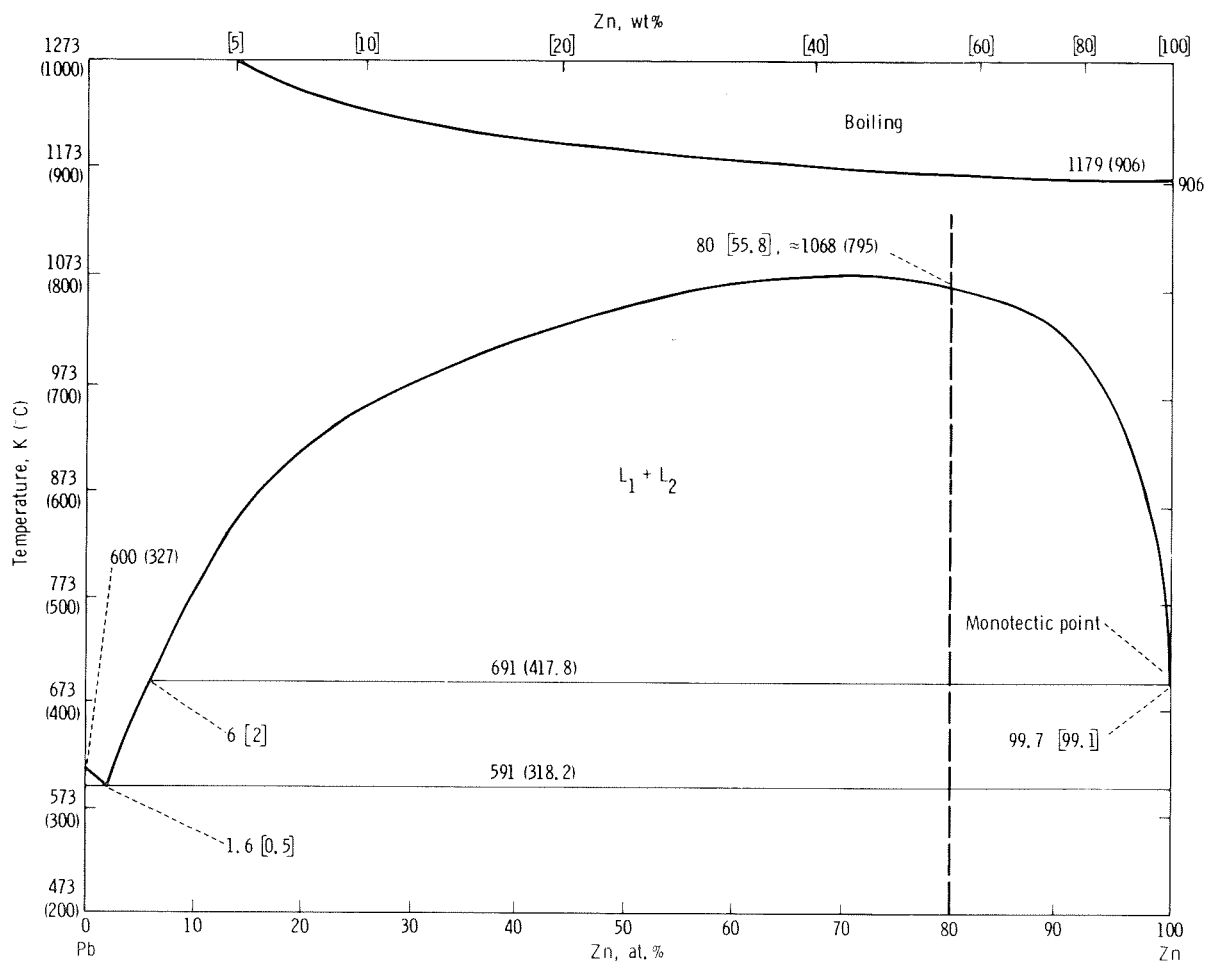


FIGURE 23-1.—Phase diagram for Pb-Zn.

flocculation, and coalescence. The composition selected for the experiment was 20 atomic percent (at.%) Pb and 80 at.% Zn, as shown by the heavy vertical line in figure 23-1. This composition is equivalent to a weight percent (wt%) of 44.2 Pb and 55.8 Zn or a volume percent of 33.2 Pb and 66.8 Zn.

The Pb-Zn samples were prepared from 99.999-percent-pure materials, which were premelted by heating (at a temperature of 1123 K (850° C)) the

samples above the consolute temperature of the binary (1068 K (795° C)) for 10 minutes. Metallographic examination of the PT and GBT samples indicated good interfacial bonds between the gravity-separated layers. To obtain the low-g dispersions of Pb in Zn, the material was again heated 40 K (40° C) above the published value of the consolute temperature and allowed to interdiffuse for 1.5 hours. A thermal history of Pb-Zn for both GBT and flight samples is shown by the

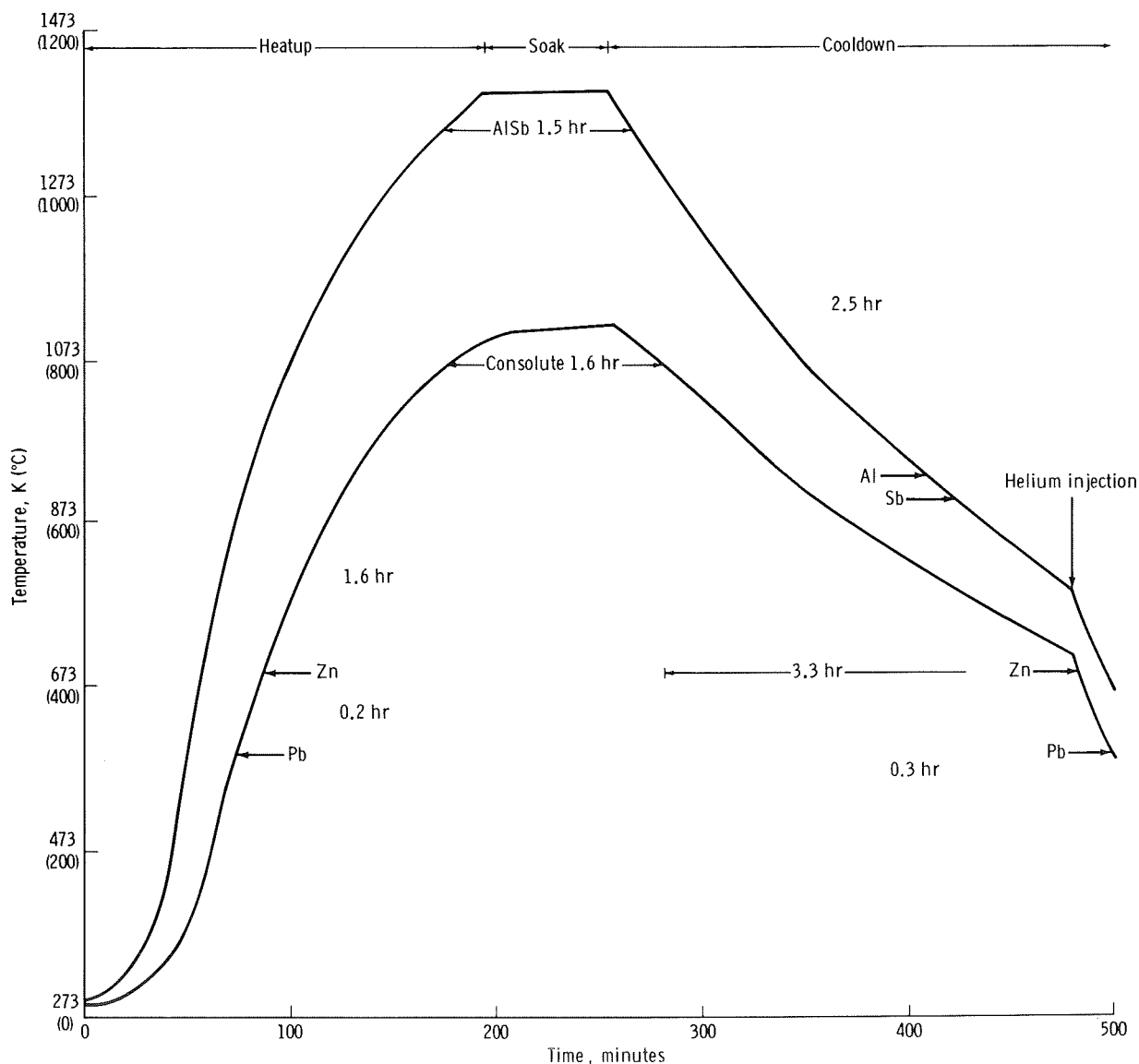


FIGURE 23-2.—Thermal history for AISb and Pb-Zn.

lower curve in figure 23-2. Preflight diffusion analysis indicated that the liquid binary should be easily homogenized into single liquid phase within the 1.5-hour period. During the cooldown portion of the thermal history, it was anticipated that small Pb-rich liquid particles would continuously nucleate and grow in a Zn-rich liquid phase until the monotectic temperature was reached. Therefore, an objective of this investigation was to study the low-g diffusion and kinetics of such dispersions.

The AlSb system (fig. 23-3) has been neglected for many years among the Group III-V semiconducting compounds that are characterized upon solidification by a syntectic transformation of two molten constituents to a constant-composition intermetallic compound (50 at.% Al and 50 at.% Sb). The reasons for this neglect have been difficulties in synthesizing a stoichiometrically homogeneous compound and the problems of high reactivity of the material to moisture (ref. 23-9). With an energy gap of 1.62 eV, AlSb has been theoretically analyzed as a highly efficient solar cell material (refs. 23-10 and 23-11) that may be 30 to 50 percent more efficient than silicon.

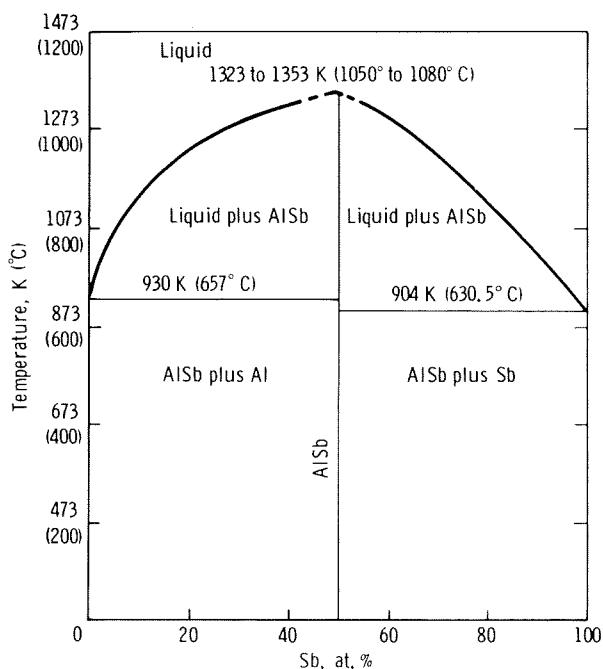


FIGURE 23-3.—Phase diagram for AlSb.

A typical grain of the best commercially available polycrystalline AlSb can be seen in figure 23-4. In addition to the compound phase, the material consists of Al- and Sb-rich phases. A chemical analysis of a 2-gram sample of this starting material indicated that macroscopically, the material has the correct stoichiometric composition of 50.00 at.% of each element and no more than 0.001 wt% oxygen content. In space processing, the compositional homogeneity may be enhanced by minimizing the very large density difference between constituents ( $2.7 \text{ g/cm}^3$  for Al and  $6.62 \text{ g/cm}^3$  for Sb) in the molten state and during crystallite formation upon cooling. Electromotive potential considerations suggest that Al- and Sb-rich phases observed in polycrystalline AlSb synthesized on Earth could cause the high reactivity to moisture. Therefore, an objective of this



FIGURE 23-4.—Typical grain of AlSb starting material.

investigation was to determine whether low-g, liquid-state homogenization and solidification would improve the microstructural and compositional homogeneity of the best commercially available polycrystalline AlSb. A thermal history of the AlSb samples for both flight and GBT is given by the upper curve of figure 23-2. The experiment consisted of heating samples of polycrystalline AlSb 50 K (50° C) above the melting temperature (1353 K (1080° C)) for 1 hour.

A detailed description of sample preparation and experiment design for the ampoules and cartridges can be found in references 23-12 and 23-13. The AlSb and Pb-Zn samples were thermally cycled in the Apollo-Soyuz Test Project (ASTP) multipurpose furnace, which had three furnace cavities; each cavity provided a short hot zone and a longer gradient zone. As shown in figure 23-5, each furnace cartridge contained one AlSb and one Pb-Zn ampoule. Except for the difference in size, the two types of ampoules were

similarly constructed. All sample preparation and ampoule assembly steps, from graphite crucible capping to tungsten-inert-gas welding of the stainless steel containers, were performed in an atmosphere of ultrapure argon gas. Similarly, assembled sample cartridges were thermally processed on the ground under one-g conditions for comparative characterization purposes. The post-ASTP and post-ground-test examination of cartridges and ampoules, including the quick-look evaluation of a limited number of samples, has been previously reported (refs. 23-12 and 23-13).

### EXPERIMENTAL RESULTS AND DISCUSSION

Although the common denominator for both the AlSb and the Pb-Zn experiments is the study of effects of low g on liquid-state heat treatment and solidification, the two types of material

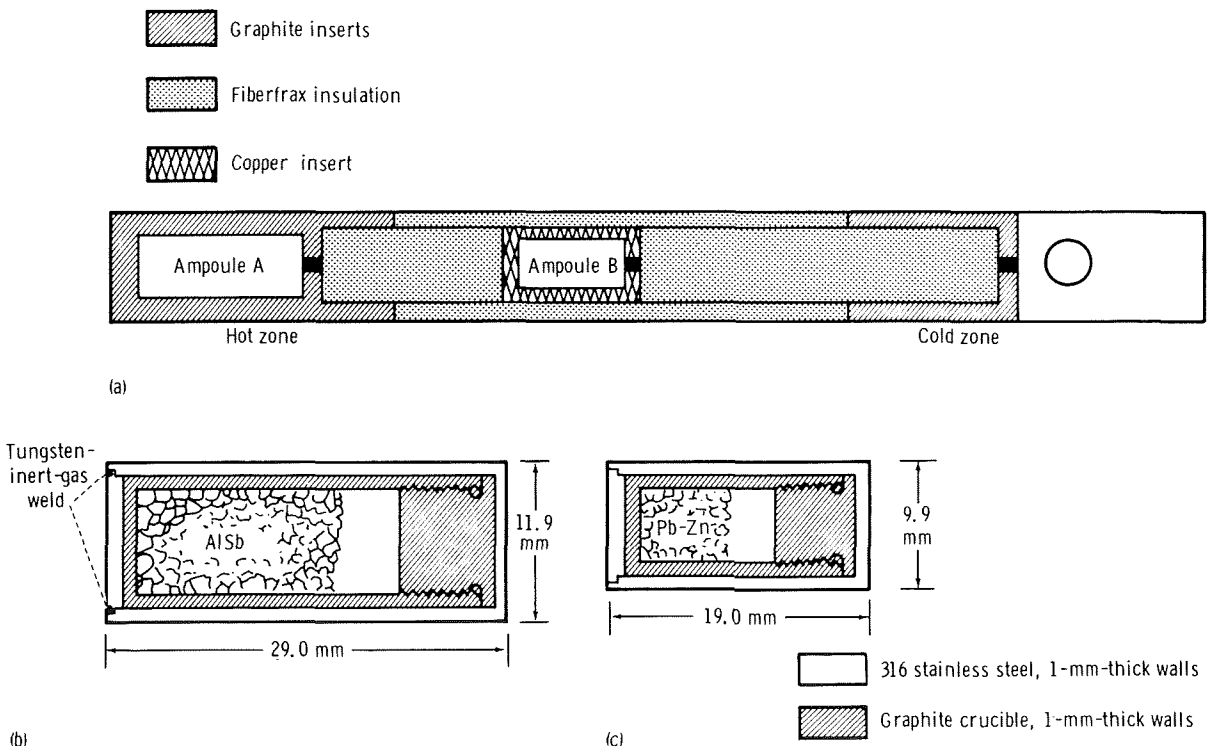


FIGURE 23-5.—Schematic of cartridge assembly and ampoules. (a) Stainless steel cartridge assembly. (b) Ampoule A (AlSb). (c) Ampoule B (Pb-Zn).

systems are quite different in terms of phase equilibria, phase transformations, and anticipated microstructure and properties. Therefore, the experimental results and analyses of the two materials are presented separately in the following discussion.

### Thermal History

The soak temperatures of the flight and GBT samples were determined by using thermocouples

attached directly to the experiment ampoules in instrumented prototype tests. Ampoule temperatures in the PT were determined as a function of two temperatures simultaneously measured inside the multipurpose furnace. The two temperatures measured in the furnace are at the hot end and the cold end of the experiment cartridges. Thus, the thermal history of the flight and GBT samples, shown in figure 23-2, was indirectly calculated from the measured furnace temperature data shown in figure 23-6. In figure 23-6, the hot- and cold-end furnace data for the flight

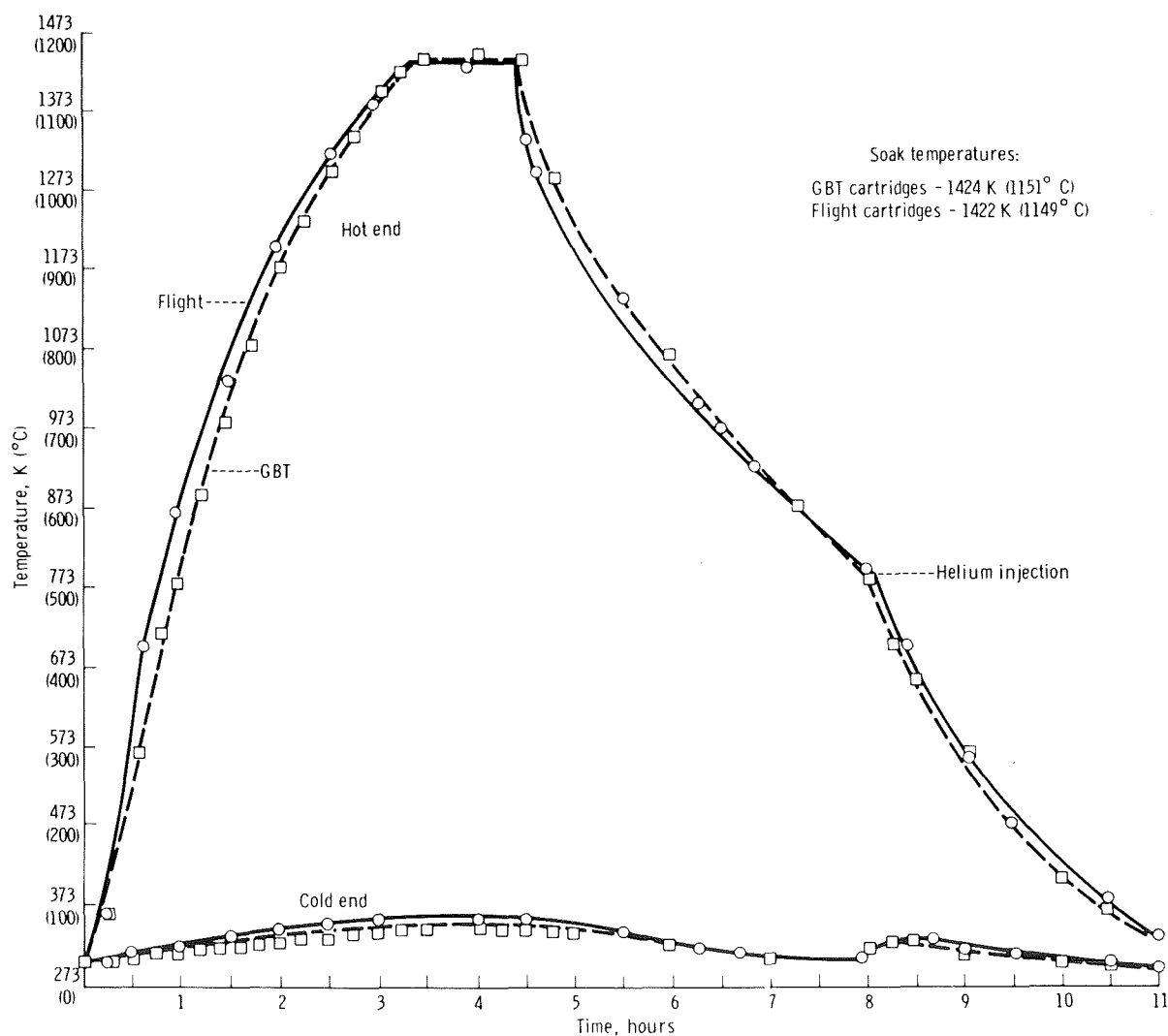


FIGURE 23-6.—Hot-end and cold-end temperatures of experiment cartridges.

and GBT cartridges are compared. The data of figure 23-6 indicate that the flight and GBT samples had essentially equivalent thermal histories.

### Aluminum Antimonide Compound

The results of the AlSb experiment are discussed in the following paragraphs.

*Postflight evaluation and characterization.*—The postflight evaluation and characterization plan for the flight and GBT samples is given in table 23-I. A detailed discussion of task 1 and task 2 and a

quick-look metallographic assessment of one flight sample (A-185) and one prototype sample (A-127) of AlSb are given in reference 23-12. A preliminary analysis of one flight sample (A-185), one GBT sample (A-141), and two PT samples of AlSb can be found in reference 23-13. The completed characterization of the previously mentioned samples and of additional flight, GBT, and PT samples is reviewed here. The characterization tasks to be discussed include metallography, quantitative microstructural analysis, scanning electron microscopy/energy dispersive X-ray analysis (SEM/EDAX), electrical resistivity

TABLE 23-I.—*Postflight Evaluation and Characterization Plan*

<i>Evaluation</i>	<i>AlSb</i>	<i>Pb-Zn</i>
<i>Cartridge examination (task 1)</i>		
Photography	X	X
Radiography (preflight and postflight)	X	X
Disassembly	X	X
<i>Ampoule examination (task 2)</i>		
Photography	X	X
Radiography	X	X
Leak tests (helium)	X	X
Weighing	X	X
<i>Sample characterization (task 3)</i>		
Removal	X	X
Weighing	X	X
Stereoscopic examination (10× to 100×)	X	X
Macrophotography (2× to 10×)	X	X
SEM <sup>a</sup> topography (60× to 1000×)		X
Surface EDAX <sup>b</sup>		X
Microstructure (metallography)	X	X
Quantitative microstructural analysis	X	X
SEM/EDAX (qualitative and quantitative)	X	X
Microhardness testing	X	
Resistivity (4-point probe)	X	X
X-ray diffraction	X	X
Chemical and spectral analysis	X	X
Microchemical analysis (ion microprobe)	X	X
Diffusion analysis	X	X

<sup>a</sup>Scanning electron microscope.

<sup>b</sup>Energy dispersive X-ray analysis.

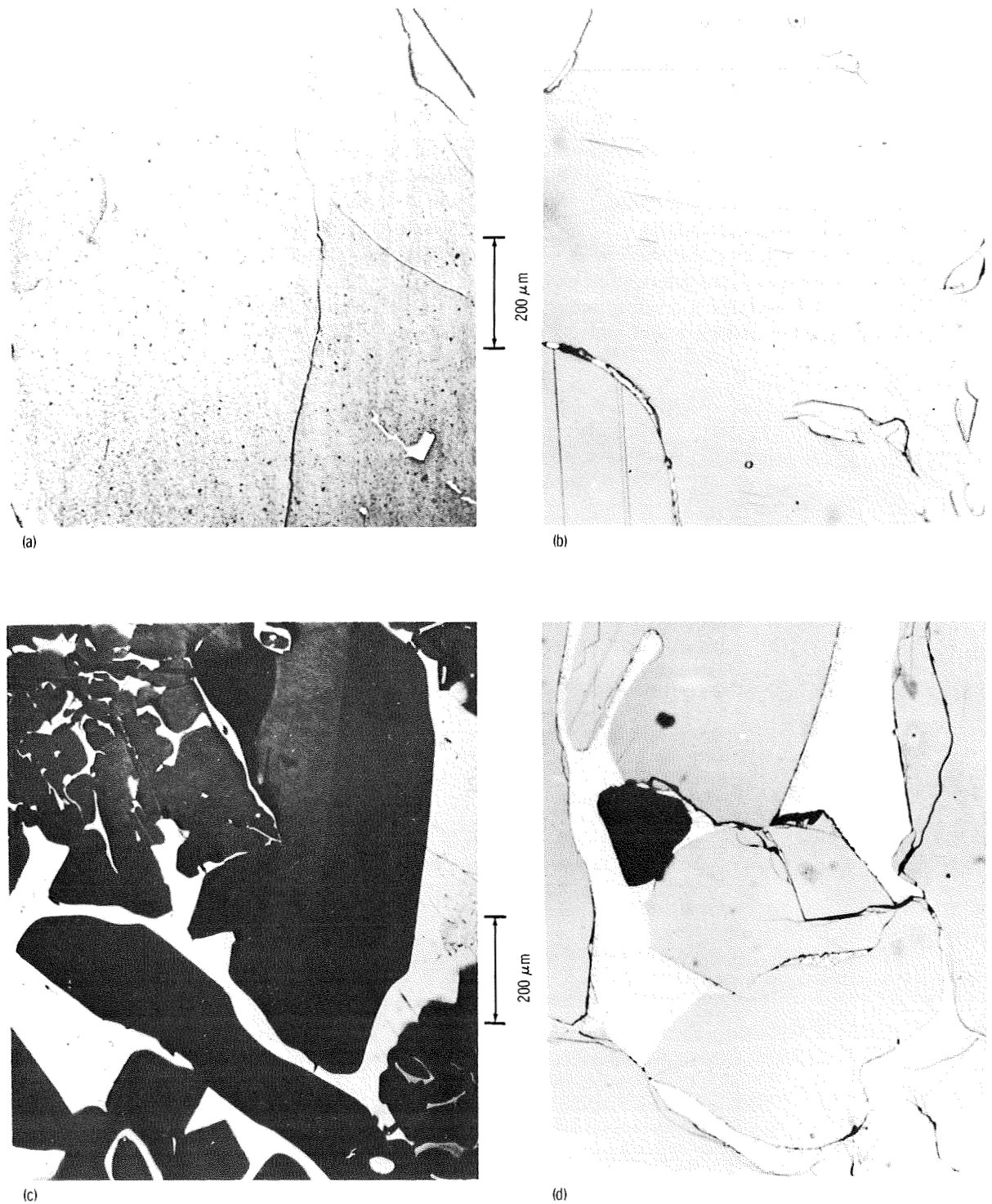
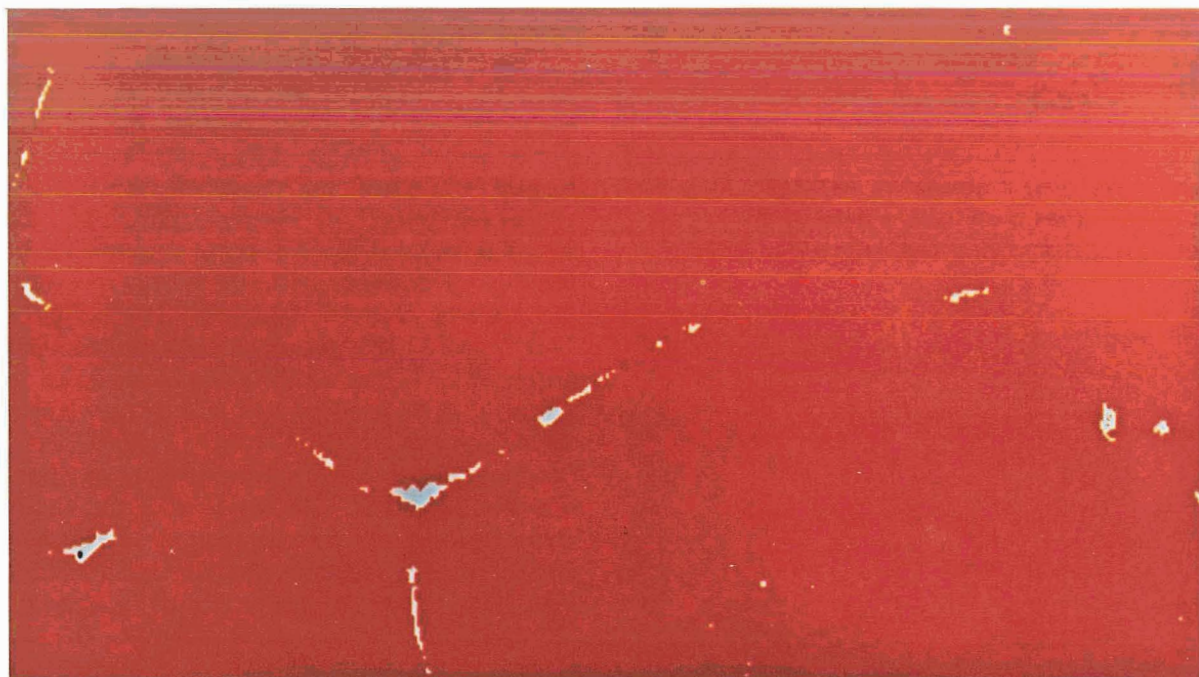
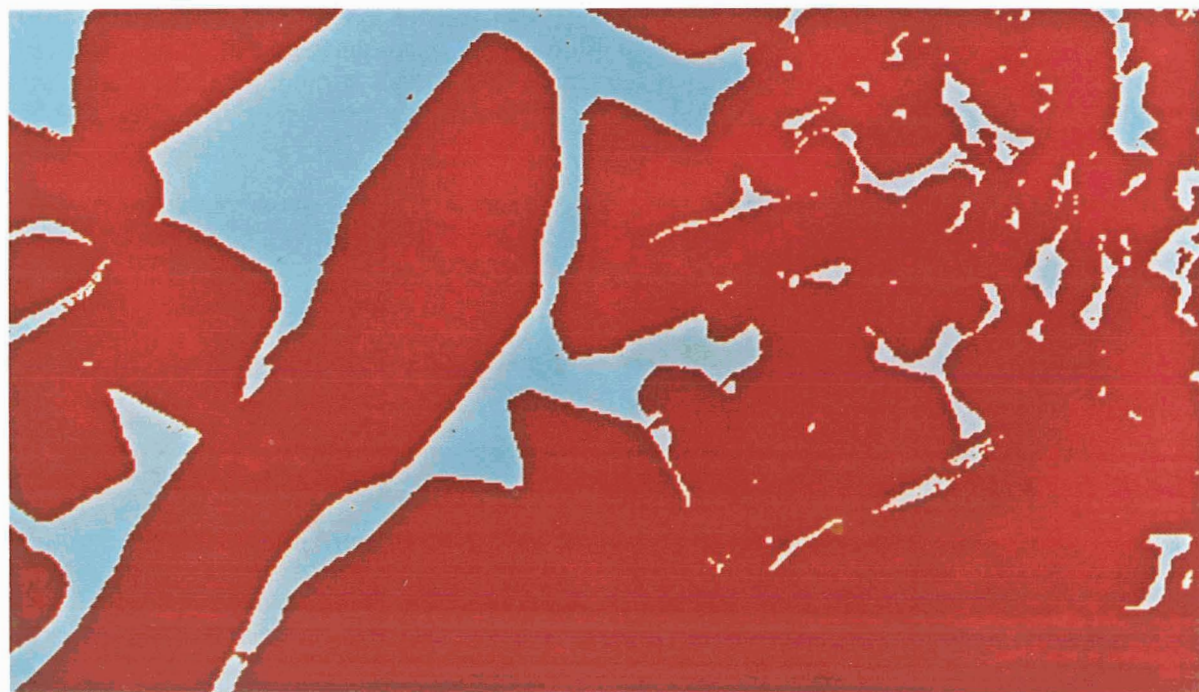


FIGURE 23-7.—Microstructures of low-g and one-g AlSb samples, showing difference in amounts of the primary grains (dark regions) and secondary phases. (a) Low-g sample (A-185). (b) Low-g sample (A-164). (c) One-g sample (PT). (d) One-g sample (GBT).





(a)



(b)

FIGURE 23-8.—Pseudocolor photographs showing microstructures of flight and PT AISb samples. The red areas represent AISb; the blue areas represent a second phase. (a) ASTP sample (A-185). Blue is Al-rich phase. (b) Laboratory sample (PT). Blue is Sb-rich phase.

measurements, X-ray diffraction studies, chemical analysis, and ion-microprobe mass analysis (IMMA).

*Metallography and qualitative microanalysis.*—A comparison of the microstructures of low-g and one-g samples is presented in figure 23-7. The typical unetched microstructure of low-g homogenized AlSb as represented by ASTP sam-

ples A-185 and A-164 in figures 23-7(a) and 23-7(b), respectively, shows that the very small amounts of a second phase (light) are formed along parts of the boundaries of the primary grains (dark) of AlSb compound. In contrast, figures 23-7(c) and 23-7(d), which represent the typical microstructures of the PT and GBT AlSb samples, respectively, show large amounts of the secondary phases not unlike the microstructure of the starting material. (See fig. 23-4.) Figures 23-8(a) and 23-8(b) are pseudocolor photographs of figures 23-7(a) and 23-7(c) in which surface artifacts have been eliminated and the computer-aided technique of digital imaging analysis (DIA) has been used to more clearly present compositional homogeneity. The red areas of the photograph represent the AlSb compound, and the blue areas represent a second phase (Al-rich for the flight sample and Sb-rich for the one-g sample). For these two selected photomicrographs, the area fraction of the secondary phase is 21.6 percent in the one-g sample and 1.7 percent in the flight sample.

Major improvements in microscopic homogeneity are quite evident in the flight samples. The EDAX maps of the one-g and low-g samples, shown respectively in figures 23-9 and

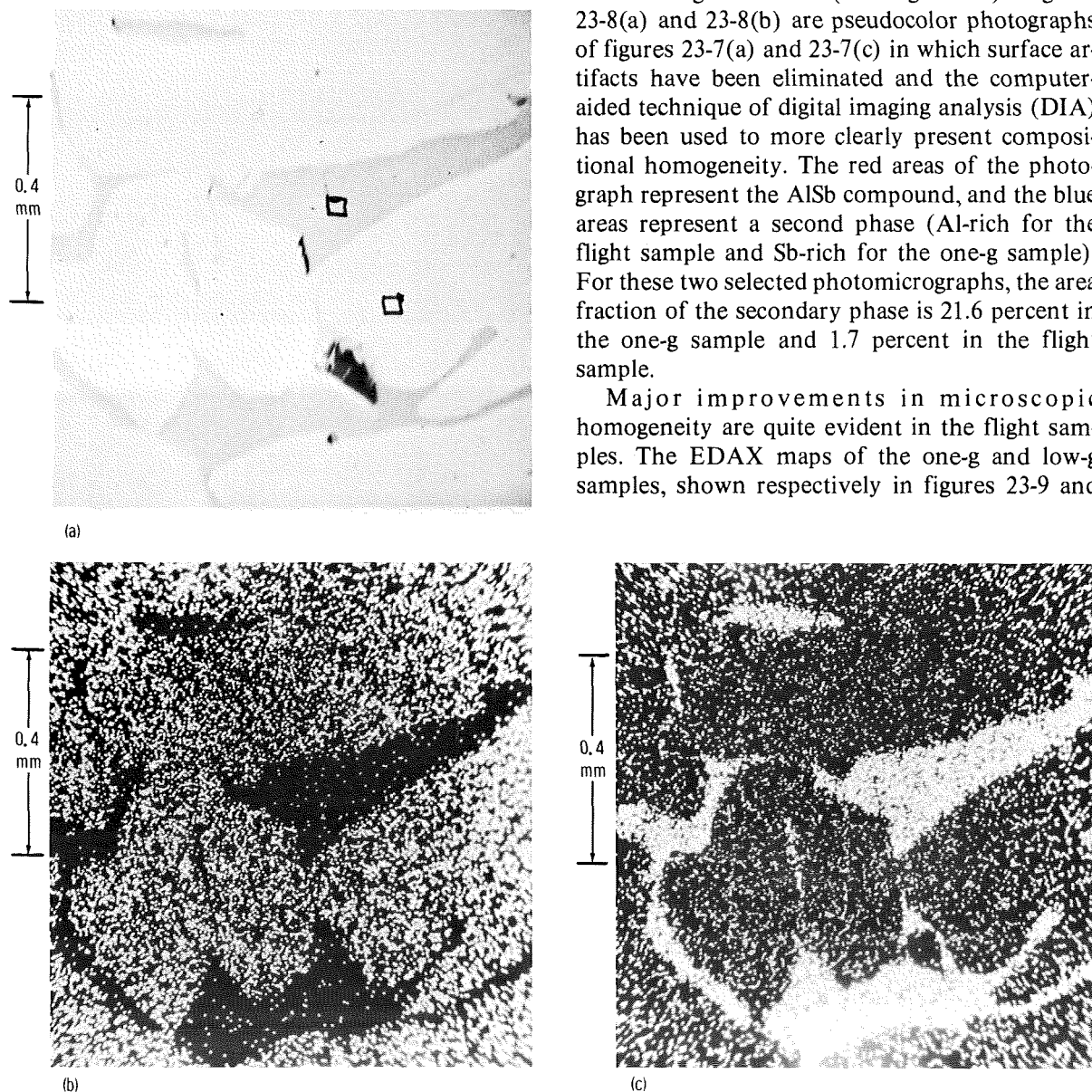


FIGURE 23-9.—SEM/EDAX map of GBT AlSb sample (A-141). (a) SEM photograph. (b) EDAX Sb scan. (c) EDAX Al scan.

23-10, qualitatively identify the gray phase as the compound AlSb and the white phase as an Al-rich phase. (In the SEM photographs (figs. 23-9(a) and 23-10(c)), the secondary phase appears lighter than the compound phase.) Figure 23-11 is a pseudocolor representation of the low-g and equivalent one-g microstructures using DIA. An analysis of the area fraction of the second phase for these two photomicrographs reveals that the flight sample has 1.1 percent of the Al-rich phase as compared to 25.2 percent for the GBT sample.

Thus, for these two selected areas, the Al-rich phase has been reduced by a factor of 23 in the flight sample. Although the photomicrographs represent two selected locations of approximately  $1 \text{ mm}^2$  surface area for the flight and GBT sample, the microstructures typify the salient features observed on a microscopic scale in other parts of the samples. That is, only a small amount of a secondary phase is found along parts of the AlSb grain boundaries for the flight sample, whereas major grains of a secondary or satellite phase are observed in the GBT sample.

To compare the homogeneity of the flight, GBT, and PT samples on a macroscopic scale, figure 23-12 is presented to show the relative location and size of the primary compound phase (red) and secondary phases (blue), determined using a  $20\text{-}\mu\text{m}$  scan across the sample surfaces. The major improvement in macroscopic homogeneity of the flight sample is again evident. The size of the secondary phases for the PT and GBT samples can vary from less than  $20 \mu\text{m}$  to as much as  $1 \text{ mm}$ , whereas the size of the secondary phase can vary from  $3$  to approximately  $30 \mu\text{m}$  in the flight sample. The  $20\text{-}\mu\text{m}$  scan was taken near the bottom of the PT sample, near the top of the GBT sample, and near the hot end of the flight sample.

A large difference in microhardness between the primary compound phase and the secondary

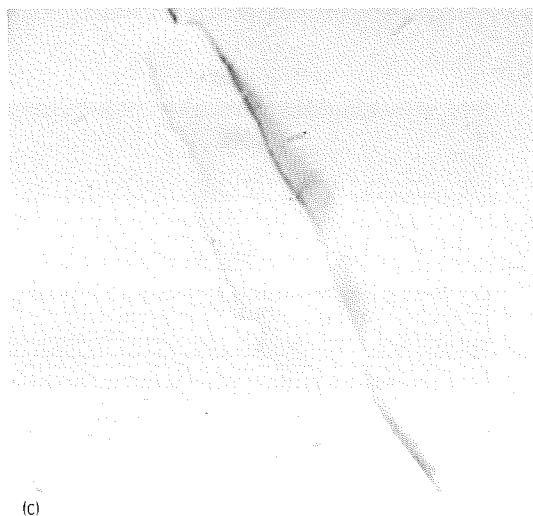
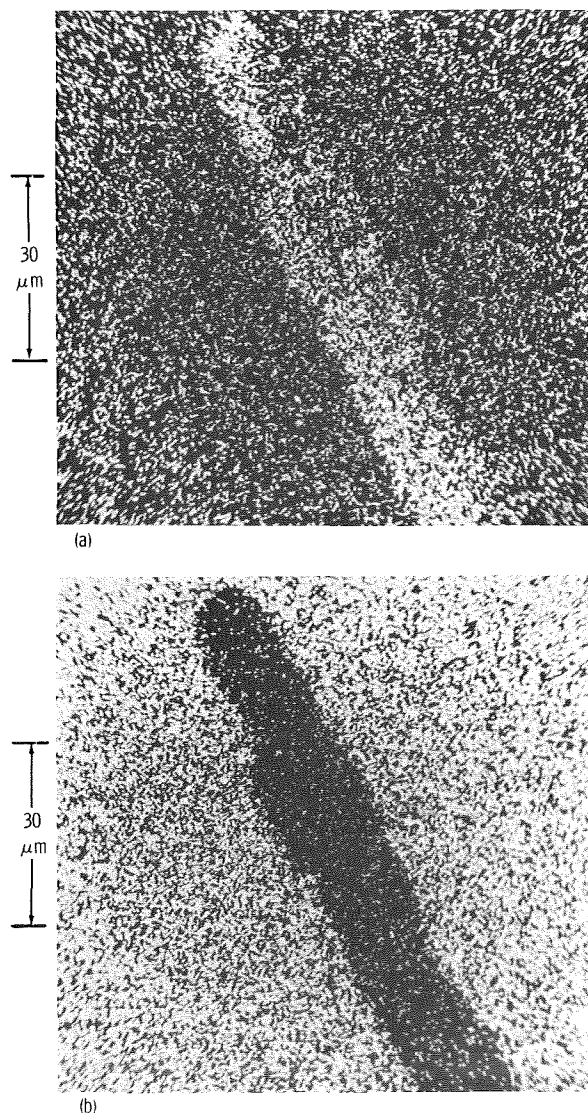


FIGURE 23-10.—SEM/EDAX map of flight AlSb sample (A-185). (a) EDAX Al scan. (b) EDAX Sb scan. (c) SEM photograph.



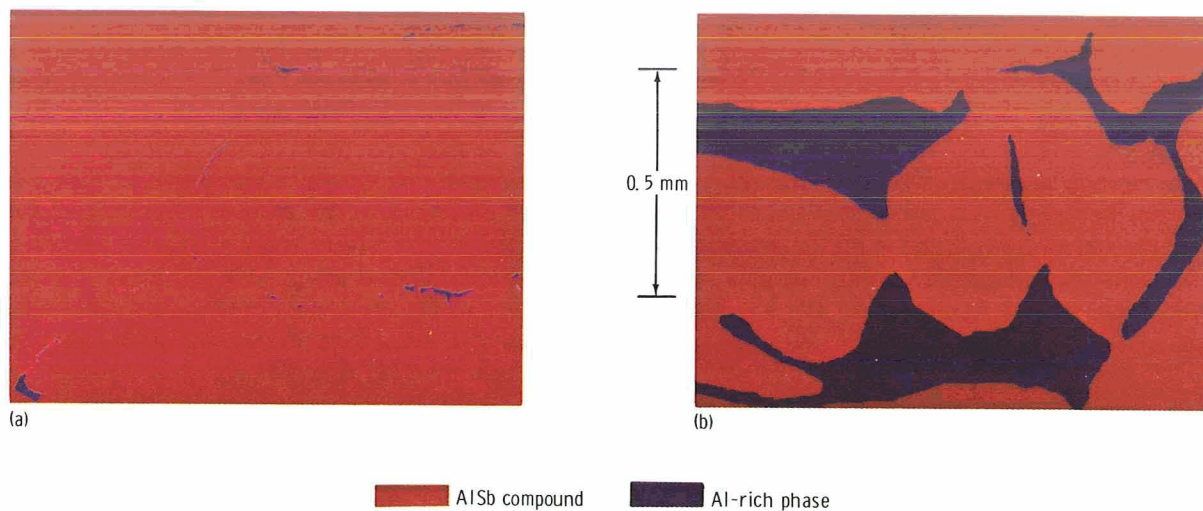


FIGURE 23-11.—Pseudocolor photographs showing microstructures of flight and GBT AlSb samples. (a) Low-g sample (A-185). (b) One-g sample (A-141).

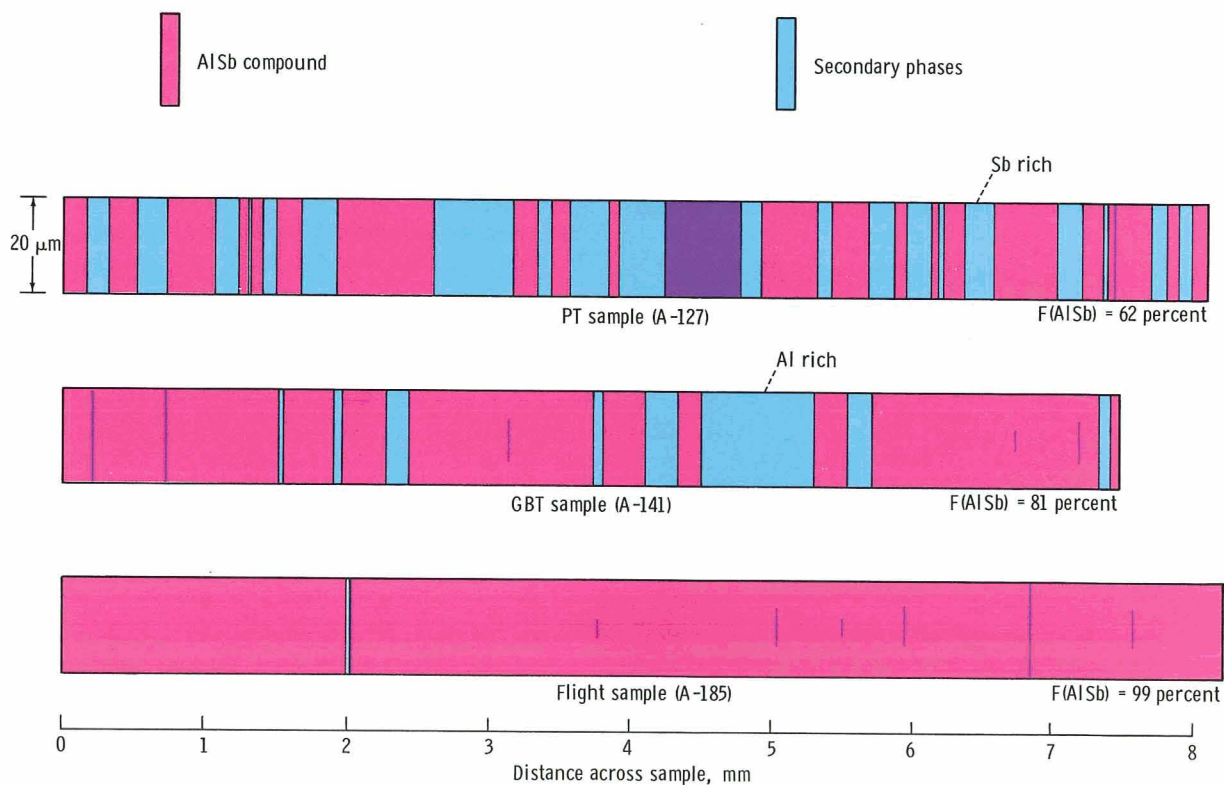


FIGURE 23-12.—Distribution of compound and secondary phases across low-g and one-g AlSb samples determined using 20- $\mu$ m scan. The symbol  $F(\text{AlSb})$  represents the primary compound concentration.

phase also is evident. Microhardness readings taken on a PT sample section indicate that the AlSb phase has a Vickers number of approximately 400, whereas the softer second phase has a hardness number of approximately 60.

**Quantitative microstructural and chemical analysis.**—To obtain a more quantitative comparison of the microstructure, a continuous series of photomicrographs (100 $\times$ ) was taken across the sectional surface of flight sample A-185 and GBT sample A-141. An area analysis for the secondary phase, obtained from the photomicrographs, is shown in figure 23-13. The area fraction of the secondary phase varies from approximately 2 to 22 percent for the GBT sample. As shown in figure 23-13, the secondary phase is nonuniformly distributed on a macroscopic scale for the GBT sam-

ple. For the flight sample, the area fraction varies from approximately 0.7 to 2 percent. Thus, the flight sample is macroscopically much more homogeneous than the GBT sample. Note, also, that the least homogeneous portion of the flight sample contains no more of the secondary phase than the most homogeneous portion of the GBT sample. As also shown in figure 23-13, the ratio of the average area fraction of the GBT sample to the average area fraction of the flight sample is 5.1. One photomicrograph each from the GBT and flight samples was selected to quantitatively compare the microscopic homogeneity of the material. For these selected regions of the samples, the area fraction of the AlSb compound phase was determined as a function of measured area. The results are shown in figure 23-14, which reveals that the flight sample is also more homogeneous in terms of the microscopic areas examined. The average size of the secondary phase was determined for the same photomicrographic data, and the results are shown in figure 23-15. On the average, the secondary phase is 33 times larger in the GBT sample than in the flight sample.

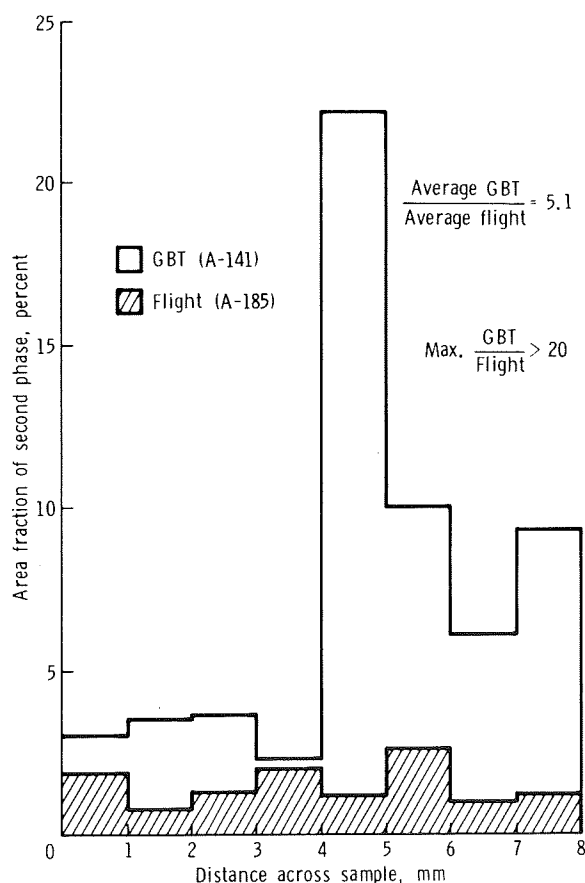


FIGURE 23-13.—Area fraction of secondary phases across flight and GBT AlSb samples.

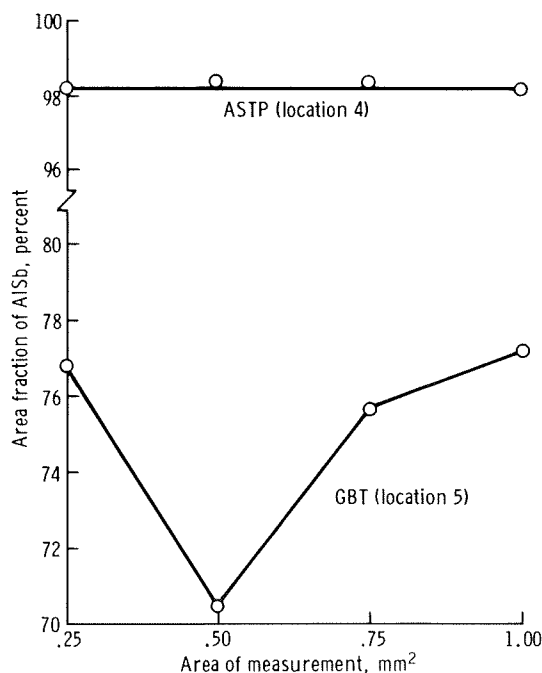


FIGURE 23-14.—Area fraction of compound phase as a function of measured area.

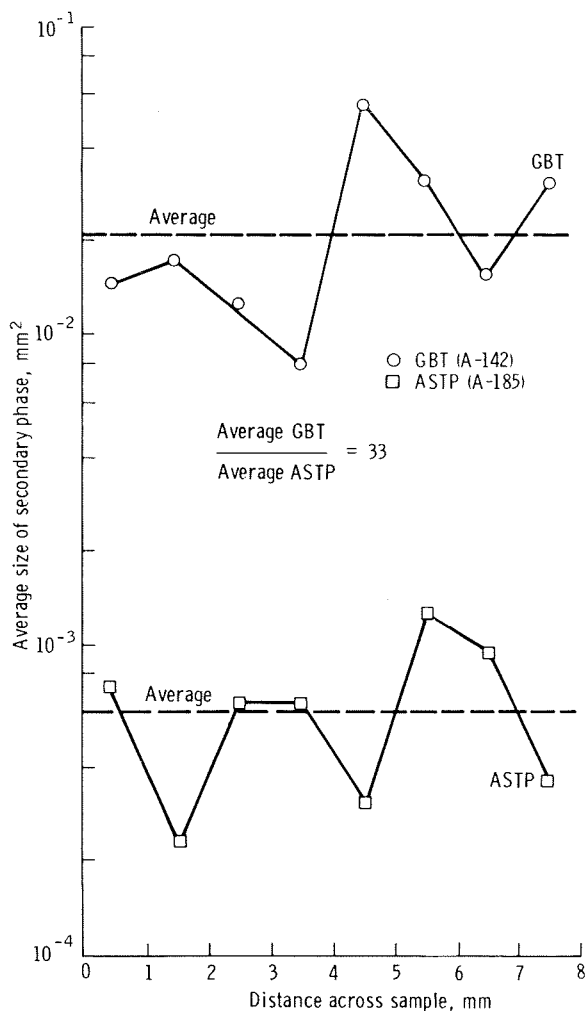


FIGURE 23-15.—Comparison of average size of secondary phases.

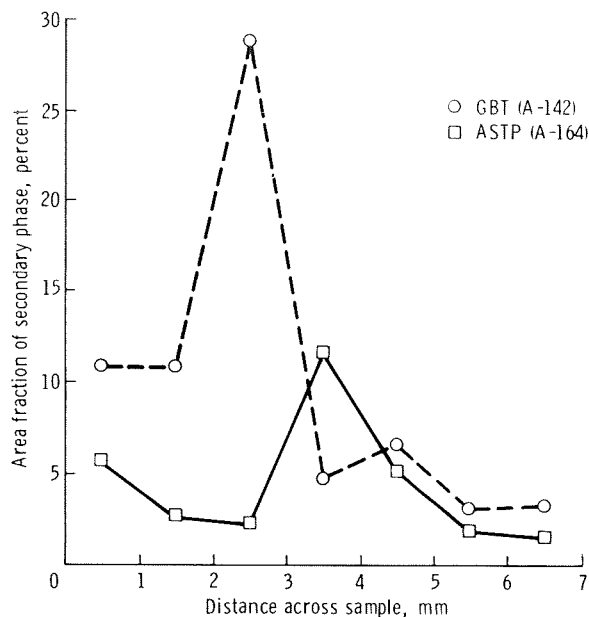


FIGURE 23-16.—Comparison of area fraction of secondary phases for the worst region of flight sample A-164 and a typical region of GBT sample A-142.

A similar quantitative microstructural analysis was performed on flight sample A-164 and GBT sample A-142. The least homogeneous portion of the flight sample was selected for this comparison, and the average reduction in the secondary phase is 2.2 times. The distributions of the second phase across representative segments of the two samples are plotted in figure 23-16.

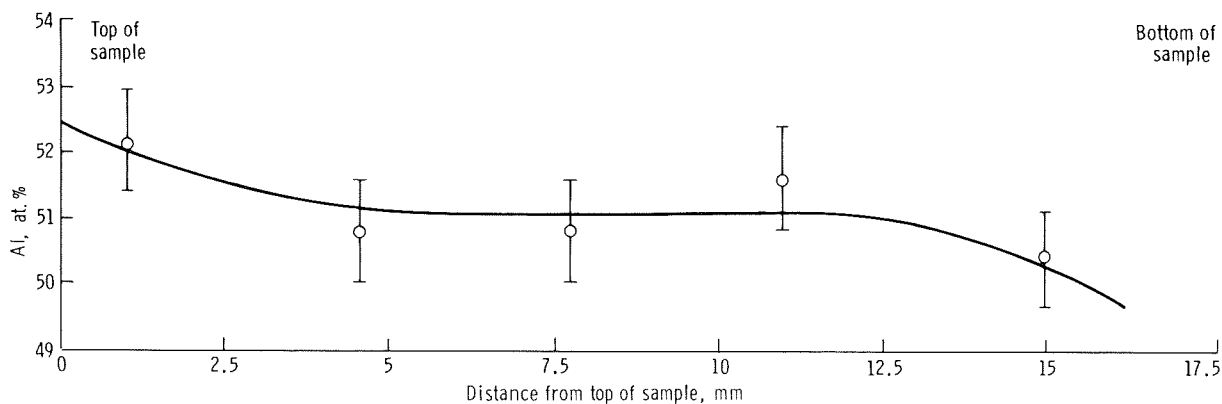


FIGURE 23-17.—Aluminum content in GBT AISb sample (A-165) based on atomic absorption spectroscopy.

A third GBT sample (A-165) was cut into five wafers, which were analyzed for aluminum content using the method of atomic absorption spectroscopy. Results of this quantitative analysis are plotted in figure 23-17 as a function of distance from one end of the sample to the other end. It should be noted that the average Al content in this one-g-processed sample is approximately 1 at.% higher than the theoretical value and that there is a compositional variation from end to end, due perhaps to the influence of gravity during liquid-phase homogenization.

Because the initial SEM/EDAX results gave indications of variation in composition of the two microstructural phases in various samples, an effort has been initiated to use the ion-microprobe mass analyzer (IMMA) for quantitative chemical determination on a microscale. The preliminary IMMA results on PT sample A-132 are plotted in figure 23-18 in terms of ratios of  $\text{Al}^+$  to  $\text{Sb}^+$  ions sputtered off from the two phases at three locations. Because a "standard" has yet to be introduced, these results are considered as semi-quantitative in nature. Nevertheless, the differences in the Al/Sb ratios are significant, indicating that the second phase in this sample has varying compositions from one end of the sample to the other, and that the AlSb compound phase may have a small homogeneity range not unlike many other intermetallic compounds such as  $\text{Cu}_3\text{As}$ ,  $\text{AgZr}$ ,  $\text{BeCo}$ ,  $\text{AlLi}$ , or  $\text{AlPd}_2$ .

Figure 23-19 contains IMMA ion maps for  $\text{Sb}^+$  in the second phases for a low-g and a one-g sample. A comparison of the maps shows that, in the flight sample, the small amount of residual second phase is almost pure Al; whereas, in the GBT sample, the Al-rich phase does contain significant concentrations of Sb.

**Electrical resistivity.**—Aluminum antimonide is a Group III-V semiconducting compound with a typical resistivity (p type) of 10 to 100  $\Omega$  cm. The Al-rich and Sb-rich phases are metallic and should have resistivity values in the range of  $10^{-4}$  to  $10^{-6}$   $\Omega$  cm (i.e., the resistivity of the secondary phases would depend on their precise composition and previous history). Thus, the average resistivity of the AlSb samples would be very sensitive to the relative fraction of the primary compound phase and the secondary phases, because the compound

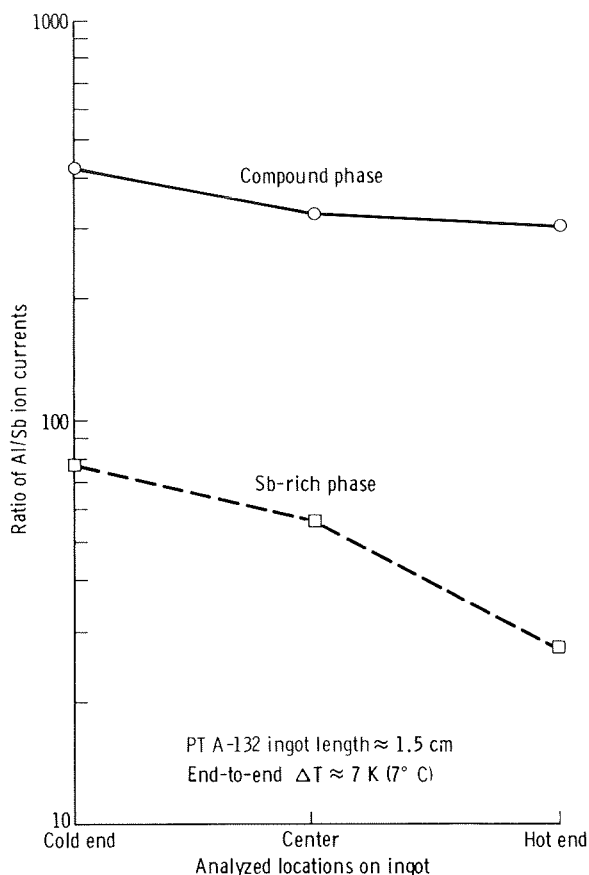


FIGURE 23-18.—IMMA Al/Sb ratios in PT AlSb sample.

phase has a resistivity that is six orders of magnitude larger than the resistivity of the secondary phases. Likewise, those samples that have the largest values of resistivity should contain the highest fraction of the compound phase.

By measuring the resistivity on a cut and polished surface of the sample using a four-point probe, the localized values of resistivity obtained will be a sensitive indication of the quality for the sample at various locations within the material. The electrical resistivity of two prototype samples and one flight sample was determined by using a four-point probe to measure approximately 10 to 20 values at different locations on each sample. The results are shown in table 23-II. The typical or average value of resistivity found for the flight sample was 12  $\Omega$  cm, which indicates that the flight sample consisted almost entirely of the

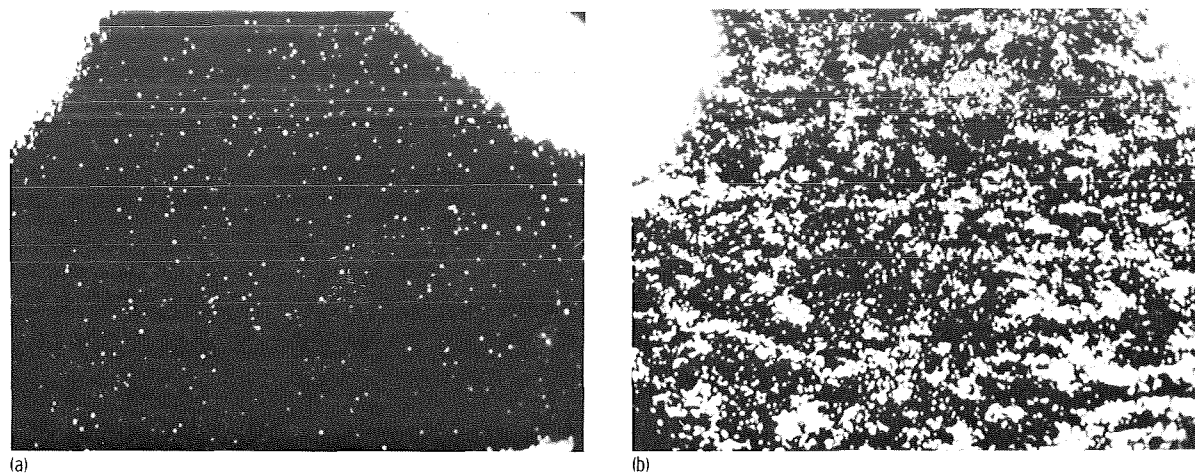


FIGURE 23-19.—IMMA  $\text{Sb}^+$  ion maps for Al-rich phase of flight and GBT AlSb samples. The white areas in the upper corners are the AlSb compound phase. (a) Low-g sample (A-185), 1326 $\times$ . (b) One-g sample (A-141), 975 $\times$ .

TABLE 23-II.—Resistivity of AlSb Samples

Sample	Resistivity, $\Omega \text{ cm}$	
	Typical value	Minimum value
Flight (A-185)	12	0.03
PT (A-132)	.009	.003
PT (A-127)	.003	.002

compound phase. The minimum or “worst” value of resistivity of  $0.03 \Omega \text{ cm}$  found in the flight sample is still a factor of 3 to 10 greater than typical values observed in the two PT samples. The PT samples had typical resistivity values in the range of  $3 \times 10^{-3}$  to  $9 \times 10^{-3} \Omega \text{ cm}$ , which is three orders of magnitude less than expected for the pure compound phase but also several orders of magnitude larger than expected for the secondary phases. Thus, the resistivity measurements tend to support the results and conclusions of the microstructural studies. That is, the flight sample shows major improvements in compositional homogeneity. Additional measurements will be made on the GBT samples.

*X-ray diffraction studies.*—A small amount of material was filed off the outside surface of one flight sample (A-164) at both the top and the bottom, one GBT sample (A-141) at the middle, one PT sample (A-124) at the bottom, and at two loca-

tions from a single crystal of AlSb. The single crystal, which actually consisted of several twins or large single crystalline grains, was obtained from the Battelle Memorial Institute (BMI) for the purpose of comparative characterization. This crystal is assumed to be unique, since the authors have not been able to find any other single crystals of AlSb. Using the Debye-Scherrer technique, X-ray diffraction images were made with  $\text{Cu K}\alpha$  radiation through a nickel (Ni) filter. An optimum exposure time of 2 hours was chosen after verification that a 4-hour exposure time did not reveal additional lines but, instead, increased the background fluorescence. The main results of this analysis are summarized in table 23-III.

All samples, except for PT sample A-124, revealed only the AlSb compound lines. The bottom part of PT sample A-124 had eight additional lines that could be identified as Sb lines. As expected, the lattice constant of AlSb for all samples was the same to within an accuracy of  $\pm 0.0003 \text{ nm}$  and agreed with the best published data (ref. 23-14) and the data of the single crystal. A careful measurement of the highest reflection lines indicated that the primary phase was always forming at the  $50 \pm 1 \text{ at.}\%$  stoichiometric composition. That is, to within an accuracy of 1 at.%, the composition of the compound does not appear to vary between samples or to depend on the extent or the nature of the secondary phases.



TABLE 23-III.—X-Ray Diffraction Study of AlSb Samples

Sample (location)	Lattice constant, nm	Notes
Flight A-164 (top)	0.6133 $\pm$ 0.3	AlSb lines
(middle)	.6134 $\pm$ .3	AlSb lines
GBT A-141 (middle)	.6133 $\pm$ .3	AlSb lines
PT A-124 (bottom)	.6135 $\pm$ .3	AlSb lines + Sb lines
BMI single crystal (no. 1)	.6136 $\pm$ .3	AlSb lines
(no. 2)	.6136 $\pm$ .3	AlSb lines
Published data (ref. 23-14)	.61355 $\pm$ .01	

*Liquid-state homogenization and diffusional analysis.*—The observation that the ASTP samples have a much smaller amount of the secondary or satellite phases compared to ground samples seems to suggest the following: at low- $g$ , intermetallic diffusion dominates in the liquid-state homogenization process; whereas, at one- $g$ , convection-induced segregation hampers the process of compositional homogenization. The results obtained can be explained by assuming that the low- $g$  melts are relatively well homogenized within the 1.5 hours of available diffusion time but that the one- $g$  melts are still relatively inhomogeneous after 1.5 hours. The inhomogeneities that seem to exist in the Earth-based melts are probably caused by the large differences in densities that exist between the Al-rich and Sb-rich phases found in the best commercially available starting material (fig. 23-4).

Based on the preceding premises, a liquid-state homogenization model for the AlSb system may be postulated to analyze the relative importance of gravity and diffusion. Because the starting material consists of Al-rich, Sb-rich, and AlSb phases, some time will be required for liquid-state diffusion to homogenize the material at every location within the melt. If during this time, the Al- and Sb-rich liquid phases are separating or segregating as a result of gravity-driven convection caused by differences in density, the compositional inhomogeneities within the melt may increase. To determine whether gravity or diffusion is the dominant process, a liquid-state homogenization number  $H$  may be defined as a convective or segregation distance divided by diffusion distance. If  $H \gg 1$ , gravity will domi-

nate; if  $H \approx 1$ , gravity will have a smaller effect; and if  $H \ll 1$ , diffusion will dominate. Consider a region of the melt having typical size  $\ell$  and having a density difference  $\Delta\rho$  from the surrounding AlSb melt defined as

$$\Delta\rho = \rho_{\text{AlSb}} - [C\rho_{\text{Al}} + (1 - C)\rho_{\text{Sb}}] \quad (23-1)$$

where  $C$  is the concentration of Al in the inhomogeneous region. If a Stokes' law type of model is used to specify the convective distance and a Fick's law type of model to specify the diffusional distance, then

$$H = \frac{\ell^2 \Delta\rho g}{5\nu} \sqrt{\frac{t_s}{D}} \quad (23-2)$$

where  $\nu$  is the viscosity of the primary fluid phase,  $g$  is acceleration due to gravity, and  $t_s$  is the total soak time for a melt at diffusion rate  $D$ . To determine the influence of gravity relative to diffusion, consider a conservative analysis (which would tend to underestimate the gravitational influences) by selecting  $\ell \leq 0.2$  mm,  $C \approx 0.9$ ,  $D \approx 10^{-4}$  cm<sup>2</sup>/sec,  $\nu \leq 1$  N sec/m<sup>2</sup> (10 P), and  $\Delta\rho \approx 2$  g/cm<sup>3</sup>. Based on these values,  $H \geq 100$  for the ground-based test and  $H \leq 0.1$  for the flight test (assuming  $10^{-3}g$ ).

Thus, these calculations would tend to indicate that convection has an important role in maintaining any inhomogeneities that may exist in Earth-based AlSb melts. Conversely, if the inhomogeneities are localized and if the starting

material is on the average macroscopically 50 at.% of each element, then the calculations would tend to indicate that the melt should rapidly homogenize by liquid-state diffusion in a low-g environment.

These simple calculations are useful in identifying the difficulties of maintaining homogeneous Earth-based melts. It should also be understood that part of the effects observed in this experiment may occur during the nucleation, growth, and solidification of the compound phase.

### Lead-Zinc Immiscible System

Results of the Pb-Zn experiments are discussed in the following paragraphs.

*Miscibility gap in the Pb-Zn system.*—The Pb-Zn system is a classical monotectic binary characterized by a large liquid miscibility gap in the temperature-composition phase diagram. (See fig. 23-1.) Thermodynamically, the two liquids within the immiscible region do not obey the normal solution laws and exhibit large positive deviations from Raoult's linear relationship between activity and concentration. In this miscibility gap, on an atomic scale, the dipole-dipole attractive forces between like atoms (or ions) are much greater than between unlike species. With the large difference in specific gravity ( $Pb/Zn = 11.34/7.14$ ), macroscopic sedimentation of the heavier Pb liquid occurs when the binary melt is held quiescently on Earth in the miscibility gap.

As described previously, the composition selected for the experiment is 20 at.% Pb or 33.2 percent Pb by volume. For this composition, the consolute temperature (immiscible to miscible transition point) is approximately 1068 K (795° C). The starting sample configuration was a layered ingot achieved by heating Pb on top of Zn in the graphite crucible at a temperature of 1123 K (850° C) for 10 minutes, resulting in the sedimentation of Pb through the Zn. Reheating samples of this type under low-g conditions for 60 minutes at a temperature 50 K (50° C) higher than the consolute temperature should promote miscible liquid interdiffusion. It was postulated that, by solidifying the thoroughly interdiffused liquids

under low-g conditions, a microstructure consisting of a dispersion of superconducting Pb in the Zn matrix would be obtained.

The discussions to follow will reveal two important phenomenological observations that must be considered in future investigations (on Earth as well as in space) of immiscible systems similar to Pb-Zn. The first observation is that microscopically complete and total separation of Pb and Zn is difficult to achieve under one-g conditions. The second observation is that, under low-g conditions whereby convection is minimized, the liquid diffusion coefficient within the miscibility gap is smaller than commonly found for miscible metals.

Because of small convection currents, the precise measurement of liquid diffusion parameters in Earth experiments is extremely difficult. However, it is generally agreed that diffusion rates of liquids are orders of magnitude greater than those for the solid phases of the same components. It is also recognized that although the intermolecular geometry of diffusing liquids is not well understood, some geometric order does exist in liquids having similar properties. If one assumes that a range of liquid diffusion lengths exists, an analysis of the root mean square (rms) distance covered by atoms as a function of time will lead to an expression similar to that for the long-range atomic motion in one-dimensional solid diffusion. This liquid diffusion motion in terms of rms distance covered is

$$\overline{x^2} = 2Dt \quad (23-3)$$

where  $D$  is the liquid diffusion coefficient and  $t$  is time. The available experimental data reported in the literature show that liquid metal diffusion coefficients all fall within the range of  $10^{-5}$  to  $10^{-4}$  cm<sup>2</sup>/sec. It was on the basis of this knowledge that optimum mixing of Pb and Zn at a temperature of 1123 K (850° C) was postulated for the soaking period of 1 hour in the ASTP experiment.

The difference between diffusion profiles in miscible liquids (i.e., temperature  $T$  greater than consolute temperature  $T_c$ ) and immiscible liquids

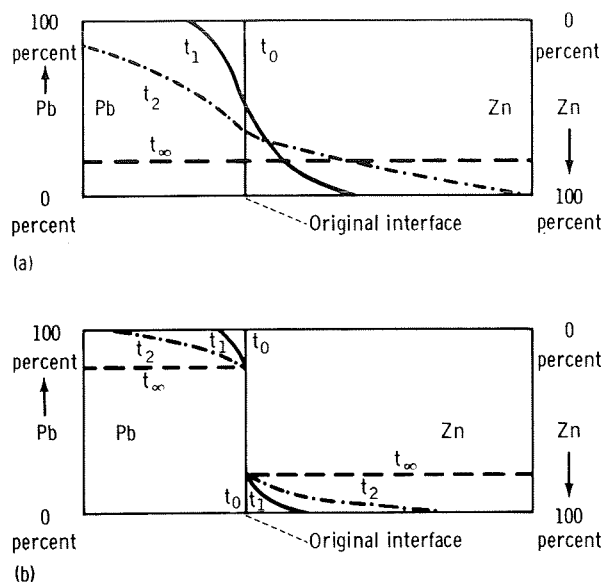


FIGURE 23-20.—Low-g Pb-Zn liquid-state diffusion models. (a) Miscible liquids ( $T > T_c$ ). (b) Immiscible liquids ( $T < T_c$ ).

( $T < T_c$ ) is shown in figure 23-20. The models in figures 23-20(a) and 23-20(b) represent the expected diffusion profiles at times  $t_\infty > t_2 > t_1$  for liquids diffusing from a well-defined interface starting at time  $t_0$ . For miscible liquids, the original interface should quickly disappear or become modified and the concentration gradient should vary continuously and smoothly throughout the sample. After a sufficient time lapse (i.e., identified as  $t_\infty$ ), the two liquids should homogenize into one liquid phase. In contrast to miscible liquids, the model in figure 23-20(b) indicates that the original interface should persist for immiscible liquids even for long diffusion times ( $t_\infty$ ), and that there should be a discontinuity in the concentration gradient at the interface. Within the miscibility gap, the diffusion profiles on both sides of the interface would probably approach those for solid-state diffusion as described by the second Fick's law for change in solute concentration  $C$  as a function of time and distance

$$\frac{\partial C}{\partial t} = D \frac{\partial^2 C}{\partial x^2} \quad (23-4)$$

where  $D$  is again the diffusion coefficient. By analyzing the concentration of Pb in Zn, away from the interface, it should be possible to determine whether the analytical data agree with a solution of equation (23-4) in the form of

$$C = C_0 \left[ 1 - \operatorname{erf} \left( \frac{x}{2\sqrt{Dt}} \right) \right] \quad (23-5)$$

where  $C_0$  is the maximum solubility of Pb in Zn and  $x$  is the distance from the interface. In the discussion of the results that follow, it will be seen that the Pb-Zn system is still immiscible in a near-zero-g environment at a temperature 40 K (40° C) higher than the published value of the consolute temperature and that the diffusion coefficient is one or two orders of magnitude smaller than usually found in Earth-based liquid metals experiments.

**Metallography and microanalysis.**—The GBT samples show almost total and complete separation of the Pb and Zn phases, as can be seen in figure 23-21(a) for a polished and etched (using 5 percent nitric acid ( $\text{HNO}_3$ )) sample. Notice that the ASTP samples also show major separation of the Pb-rich and Zn-rich phases, as shown in figure 23-21(b). Consistent with the immiscible-liquids model of figure 23-20(b), the original Pb/Zn interface is evident. An SEM photograph of the interface on the flight sample is shown in figure 23-22(c); corresponding EDAX microchemical maps of Zn and Pb are also shown in figures 23-22(a) and 23-22(b), respectively. There appears to be a sharp discontinuity in the Pb and Zn concentrations at the interface. The black particles in the upper part of figure 23-22(c) are Pb particles dispersed in a Zn matrix.

The microstructure of the Zn-rich region is shown in figure 23-23 for polished and etched surfaces of the flight sample. Many of the particles seen in the photomicrograph are Pb-rich, as shown by the SEM photographs and EDAX maps of figure 23-24 (flight sample) and figure 23-25 (PT sample). The Pb dispersions in Zn appear to have a higher particle number density in the flight samples. The Pb particles of the flight sample also appear to be more uniform in size and spherical in shape. The particle alinement, evident in figure

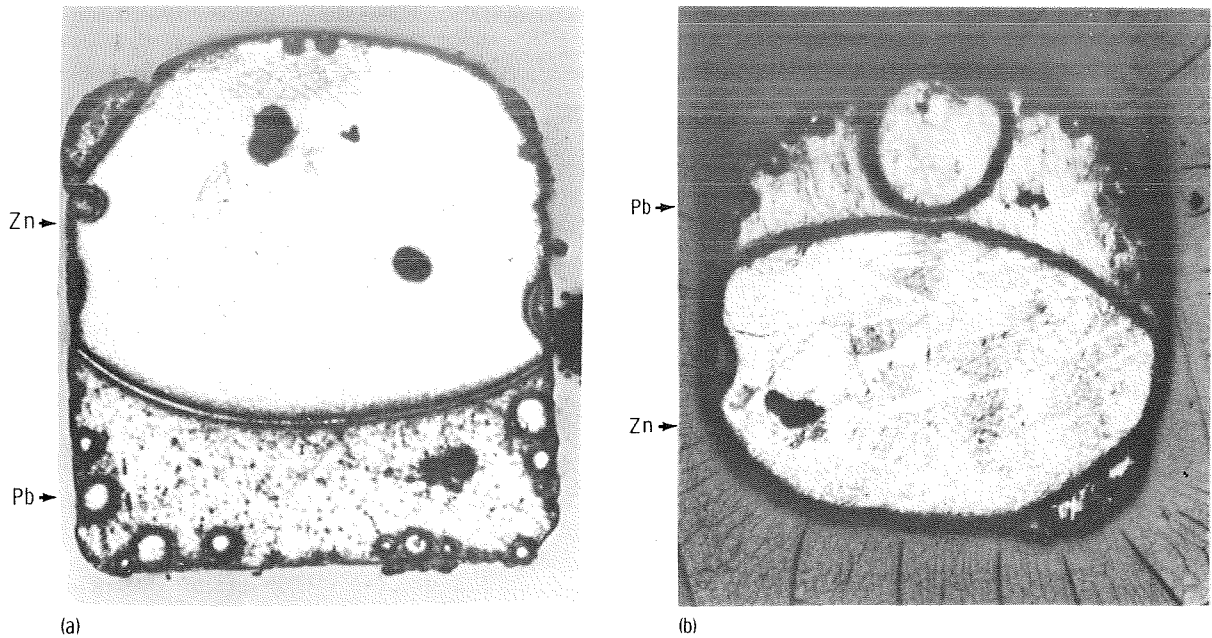


FIGURE 23-21.—Photomacrographs of Pb-Zn flight and GBT ingots. The Pb-rich and Zn-rich portions of the GBT ingots are reversed because of sedimentation. (a) One-g sample (gravity vector downward). (b) Low-g sample.

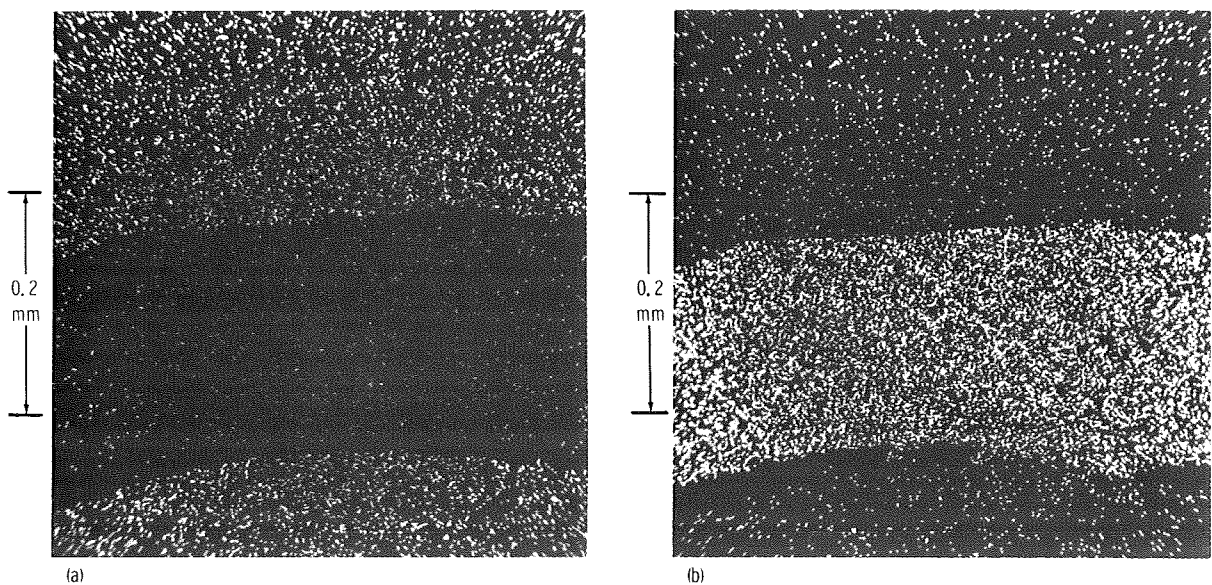


FIGURE 23-22.—SEM/EDAX maps of Pb/Zn interface in flight sample B-186. (a) EDAX Zn scan ( $L_{\alpha}$ ). (b) EDAX Pb scan (M). (c) SEM photograph.

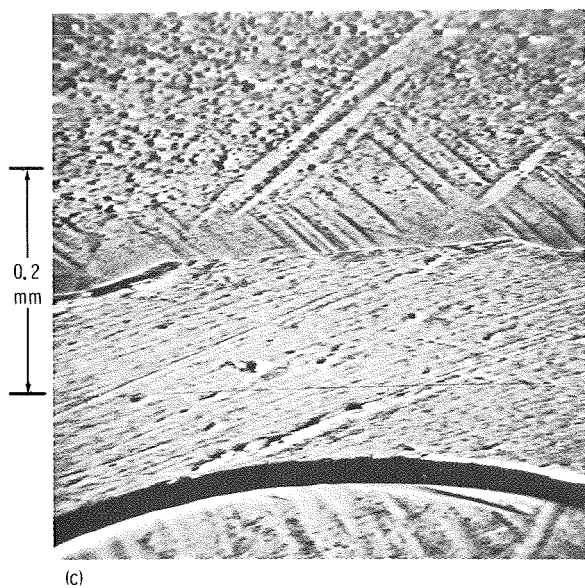
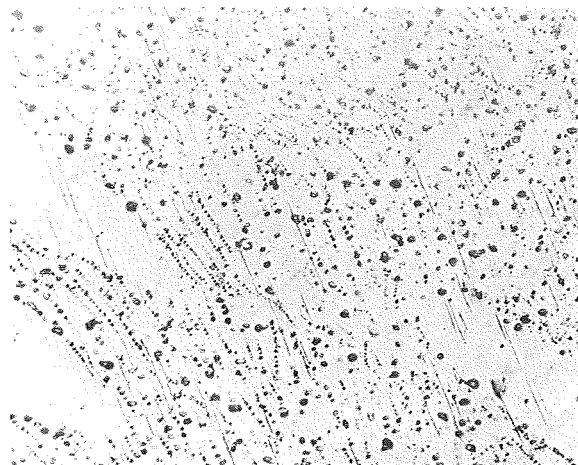
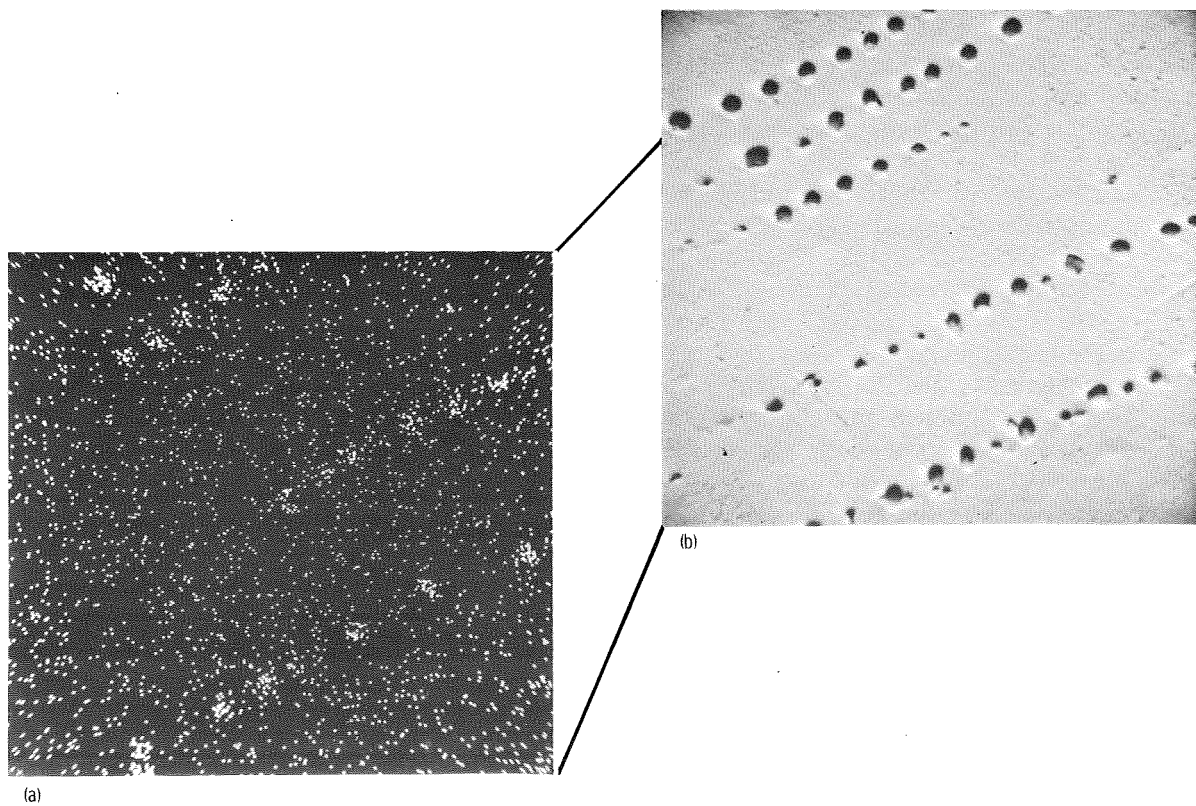


FIGURE 23-22.—Concluded.

FIGURE 23-23.—Microstructure of flight Pb-Zn sample (32 $\times$ ).FIGURE 23-24.—SEM/EDAX map of Zn matrix in flight sample B-186. (a) EDAX Pb scan ( $M_{\alpha}$ ,  $M_{\beta}$ ) (760 $\times$ ). (b) SEM photograph (654 $\times$ ).

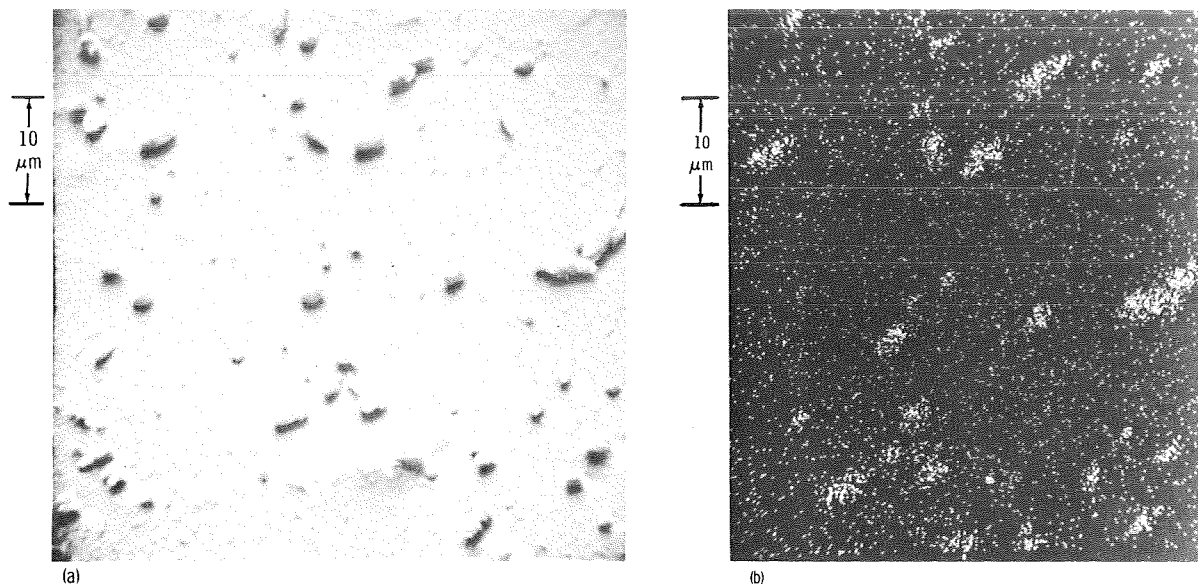


FIGURE 23-25.—SEM/EDAX map of Zn matrix in PT sample B-125. (a) SEM photograph (1332 $\times$ ). (b) EDAX Pb scan ( $M_{\alpha}$ ).

23-24(b), occurs in many of the flight samples and less in the GBT samples. It seems reasonable to attribute the alinement of the microstructure in the flight sample to constitutional supercooling and subsequent nucleation and growth of Pb particles along supersaturated fronts. As previously observed, this phenomenon would be expected to be less evident in the GBT samples because buoyancy forces acting on the individual particle and convective effects acting on the front would tend to destroy the alinement.

It should be noted that the one-g samples were processed in a manner to encourage convective mixing between the Pb and Zn phases. In the one-g samples, the more dense liquid Pb was initially on top of the less dense Zn, resulting in a flow of liquid Pb through the molten Zn. The residual Pb dispersions observed in the GBT samples indicate that total microscopic separation of the phases did not occur in one g. In the next section, it will be shown that the Zn-rich portion of a GBT sample has a dilute and approximately constant concentration of Pb, part of which could be in the monotectic phase.

*Chemical and diffusional analysis.*—One flight sample (B-186) and one GBT sample (B-165) were cut into small sections of approximately 3 mm<sup>3</sup>

each (i.e., approximately 20 mg/section) such that the distance of each section away from the Pb-Zn interface could be determined. These small sample sections were chemically analyzed by means of atomic absorption spectroscopy. The results are shown in figure 23-26. The Zn matrix of the GBT sample (fig. 23-26(a)) contains only a small ( $\approx 0.5$  at.%) and constant concentration of Pb throughout the Zn matrix. This small concentration of Pb represents the combined influence of convective phase mixing during the heatup and soak period and density sedimentation of molten Pb particles during cooldown portions of the experiment. In contrast, the flight sample (fig. 23-26(b)) contains a relatively large (maximum concentration, 3.5 at.%) and monotonically decreasing concentration of Pb away from the Pb/Zn interface.

The data on the flight sample are consistent with the low-g immiscible-liquids diffusion model described in the subsection entitled "Miscibility gap in the Pb-Zn system" and specified by equation (23-5). Equation (23-5) can be best fitted to the data by assuming an equilibrium concentration at the interface  $C_0$  of 8 at.% and a diffusion coefficient of  $2.4 \times 10^{-6}$  cm<sup>2</sup>/sec. The theoretical immiscible-liquids diffusion curve is shown in

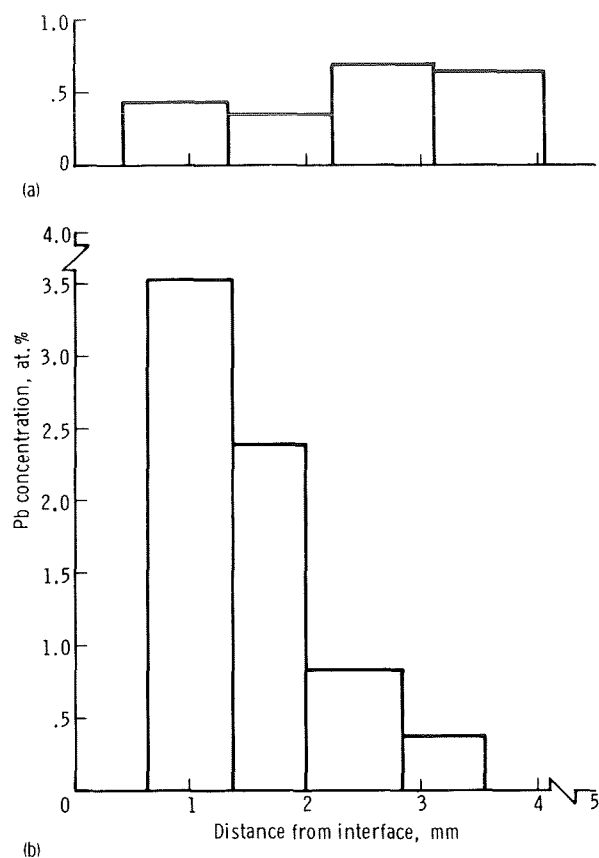


FIGURE 23-26.—Compositional profiling of GBT and flight Pb-Zn samples based on atomic absorption spectroscopy. (a) GBT-2 sample (B-165). (b) ASTP sample (B-186).

figure 23-27. After several attempts, it was concluded that the data could not be fitted with a miscible-liquids diffusion model. The results of the chemical and diffusional analysis is therefore consistent with the microchemical and metallographic analysis in that the combined results show, in the low-g experiment, that Pb and Zn are still immiscible at a temperature of 1108 K (835° C) and that the diffusion coefficient measured in the low-g sample is one or two orders of magnitude smaller than commonly expected. Thus, these experimental results would suggest that there is a significant inaccuracy in the published phase diagram of Pb-Zn.

Pelzel (ref. 23-15) has measured the rate of solution  $K$  in both immiscible and miscible liquid metals. His results appear to follow the diffusion

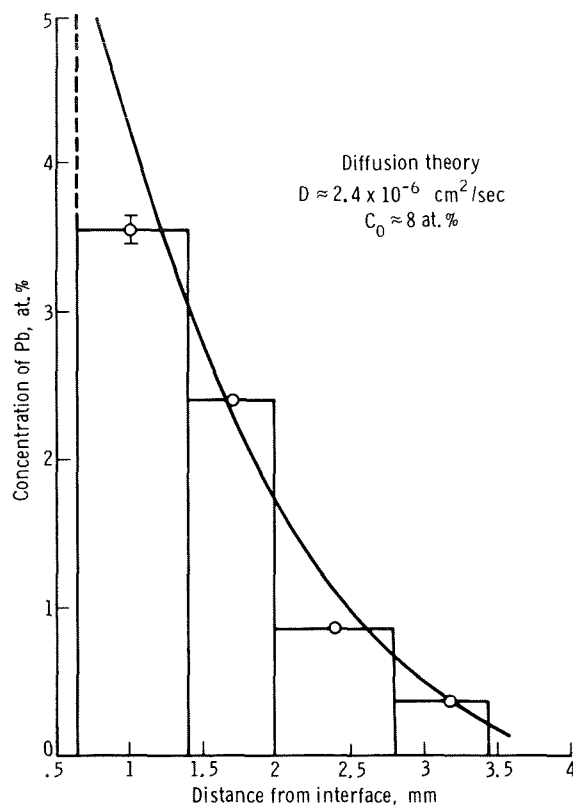


FIGURE 23-27.—Diffusion profile for concentration of Pb in Zn matrix in flight sample. The curve is an optimum fit to the data, based on an immiscible-liquids diffusion model.

models given in the subsection entitled "Miscibility gap in the Pb-Zn system," and he finds that values of  $K$  for the monotectic systems are the same order of magnitude as in experiments in which one of the phases is a solid reaction partner. He also finds that  $K$  is influenced by buoyance or gravitational effects. Using Pelzel's published value of  $K$  for the diffusion of Pb and Zn at a temperature of 773 K (500° C), it is estimated that his Earth-based experiment had an effective diffusion coefficient,  $D \approx 3 \times 10^{-4} \text{ cm}^2/\text{sec}$ , which is two orders of magnitude greater than observed in the ASTP experiment. Thus, the combined results of the low-g experiment and Pelzel's one-g experiment would tend to support the conclusion that liquid metal diffusion is strongly influenced by thermal or density-driven



convection in Earth-based experiments and that, in the low-g experiment, the probability is high that the homogenization temperature of 1108 K (835° C) was not above the miscibility gap.

In summary, the results of the chemical and diffusional analysis would tend to indicate that the Pb-Zn part of the experiment did not perform as initially anticipated for two reasons. First, the Pb-Zn system is apparently still immiscible at a temperature of 1108 K (835° C), which would limit the concentration gradient in the samples and greatly reduce the rate of solution  $K$ . Second, the diffusion coefficient  $D$  is much smaller than was initially expected. The results of the experiment do suggest that the low-g quiescent environment of space is an ideal environment for accurately determining diffusional and kinetic reaction rates that may be difficult, or perhaps in some cases impossible, to determine on the ground.

**Electrical resistivity.**—The previous results and conclusions must be modified if the Pb-Zn samples contained oxides at the interface; such a condition would tend to prevent interdiffusion. The existence of oxides seems improbable because only the highest purity materials were used, the ampoules were sealed under high-purity argon, and previous PT and GBT experiments did not indicate the presence of oxides. Moreover, the sedimentation of Pb through Zn during the initial stage of sample preparation would break up oxide films if present in the starting materials. However, to further test for the presence of oxides at the Pb/Zn interface, a sensitive test that involved measuring the average resistivity of the material in the vicinity of the interface was performed.

The resistivity of the materials was measured on the mounted, polished, and etched sample surfaces using a four-point probe. One flight sample (B-186) and one GBT sample (B-142) were selected for the test. The results of the measurements are presented in figure 23-28, where each measurement point represents the average of 10 separate determinations. The absolute accuracy of the measurement is approximately 5 percent, and the relative accuracy between points is better than 1 percent. Both the ASTP and the GBT resistivity values varied smoothly and continuously across the interface. In neither case was there any evi-

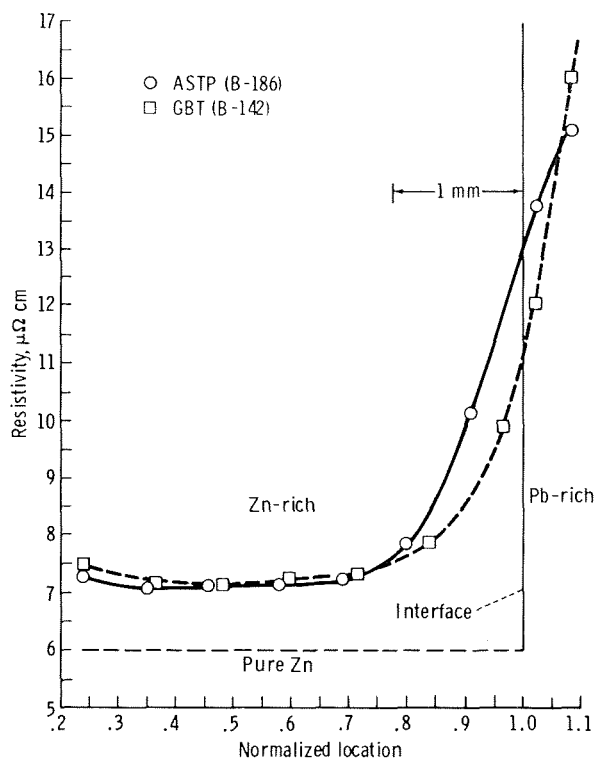


FIGURE 23-28.—Electrical resistivity of Pb-Zn samples.

dence of any oxide layer along the interface. The slightly larger resistivity values associated with the flight sample near the interface were probably caused by the higher concentration of Pb in the Zn matrix found by the chemical analysis.

## CONCLUSIONS

The experiment plan for the ASTP Monotectic and Syntectic Alloys Experiment has been implemented, and the following conclusions have been reached.

### Aluminum Antimonide Compound

1. Liquid-state homogenization of polycrystalline, multiphase AlSb in a low-g environment produces major improvements in macroscopic and microscopic homogeneity. The ASTP-processed material contains an average of 4



and a maximum of 20 times less of the unwanted secondary phase. Very small amounts of an Al-rich phase are found only along parts of the grain boundaries in the flight samples, whereas the ground-processed counterparts show major grains of the Al-rich or Sb-rich phase not unlike the starting material except for the recrystallized grain structure.

2. A diffusional and liquid-state homogenization analysis indicates that gravity-induced convection can severely complicate the homogenization of AlSb melts on Earth and can induce compositional and microstructural inhomogeneity during solidification.

3. Qualitative and semiquantitative energy dispersive X-ray and ion-microprobe mass analyses indicate the possibility of a homogeneity range for the AlSb compound and compositional variations in the secondary phases. A chemical analysis of a one-g sample indicates an overall approximate stoichiometric composition with a small, possibly gravity-induced, longitudinal variation in Al content.

### Lead-Zinc Immiscible System

1. Incomplete liquid-state mixing of Pb and Zn was observed in the ASTP experiment, although the homogenization temperature of 1108 K (835° C) is 40 K (40° C) above the miscibility gap described in the literature. In the flight samples, a dispersion of fine particles of superconducting Pb in the Zn matrix was observed, but the bulk of Pb remained in the same position as before the start of the experiment. The experiment results suggest that there is a significant inaccuracy in the published phase diagram for Pb-Zn.

2. Compositional profiling of a low-g-processed sample indicates a quasi-solid-state diffusion of Pb into Zn with a diffusion coefficient of  $2.4 \times 10^{-6} \text{ cm}^2/\text{sec}$ , which is about two orders of magnitude smaller than expected from ground-based experiments.

3. Difficulty in controlling convective mixing, sedimentation, and density gradients can hinder the analysis of diffusional or other kinetic processes in material systems performed on Earth. The quiescent low-g conditions of orbital flight

provide an ideal environment for studying and accurately measuring such processes by reducing or eliminating the competitive gravity-dependent variables.

### REFERENCES

- 23-1. Proceedings of the Third Space Processing Symposium on Skylab Results, vol. 1. NASA TM X-70252, 1974.
- 23-2. Proceedings of the Third Space Processing Symposium on Skylab Results, vol. 2. NASA TM X-70253, 1974.
- 23-3. Hansen, Max: Constitution of Binary Alloys. McGraw-Hill (New York), 1959, p. 1118.
- 23-4. Yates, I. C., Jr.: Apollo 14 Composite Casting Demonstration. NASA TM X-64641, 1971.
- 23-5. Lacy, L. L.; and Otto, G. H.: The Stability of Liquid Dispersions in Low Gravity. Paper No. 74-1242, AIAA/AGU Conference on Scientific Experiments of Skylab (Huntsville, Ala.), Oct. 30-Nov. 1, 1974.
- 23-6. Lacy, Lewis L.; and Otto, Guenther H.: Electrical Resistivity of Gallium-Bismuth Solidified in Free Fall. AIAA J., vol. 13, no. 2, Feb. 1975, pp. 219-220.
- 23-7. Reger, J. L.: Experimental Development of Processes to Produce Homogenized Alloys of Immiscible Metals, Phase III. NASA CR-149977, 1976.
- 23-8. Otto, Guenther: Studies on Immiscible Alloys. NASA CR-144226, 1976.
- 23-9. Willardson, R. K.; and Beer, Albert C., eds.: Semiconductors and Semimetals. Physics of III-V Compounds. Vol. 4. Academic Press (New York) 1968, p. 59.
- 23-10. Rittner, E. S.: Use of p-n Junctions for Solar Energy Conversion. Phys. Rev., vol. 96, no. 6, Dec. 15, 1954, pp. 1708-1709.
- 23-11. Loferski, J. J.: Theoretical Considerations Governing the Choice of the Optimum Semiconductor for Photovoltaic Solar Energy Conversion. J. Appl. Phys., vol. 27, no. 7, July 1956, pp. 777-784.
- 23-12. Ang, Choh-Y.; and Lacy, Lewis L.: Monotectic and Syntectic Alloys: ASTP Experiment MA-044. NASA TM X-64956, 1975.

- 23-13. Ang, C. Y.; and Lacy, L. L.: Monotectic and Syntectic Alloys: Experiment MA-044. Sec. 24 of the Apollo-Soyuz Test Project Preliminary Science Report. NASA TM X-58173, 1976.
- 23-14. Giesecke, Von G.; and Pfister, H.: Präzisionsbestimmung der Gitterkonstanten von  $A^{III}B^V$ -Verbindungen. Acta Cryst., vol. 11, 1958, pp. 369-371.
- 23-15. Pelzel, E.: Die Lösungsgeschwindigkeit Fester und Flüssiger Metalle in Ruhenden Schmelzen. Z. Metallk., vol. 61, no. 4, Apr. 1970, pp. 289-297.

## 24. Interface Marking in Crystals

### Experiment MA-060

*H. C. Gatos,<sup>a†</sup> A. F. Witt,<sup>a</sup> M. Lichtensteiger,<sup>a</sup> and C. J. Herman<sup>a</sup>*

#### ABSTRACT

Experiment MA-060 was designed to establish the crystal growth and segregation characteristics from the melt in a directional solidification configuration under near-zero-g conditions. The germanium (doped with gallium) system was selected because it has been studied extensively on Earth and because it lends itself to a very detailed macroscopic and microscopic characterization. The interface demarcation technique was incorporated into the experiment because it constitutes a unique tool for recording the morphology of the growth interface into the grown crystal, for determining the microscopic growth rate throughout solidification, and for establishing an absolute time-reference framework for all stages of the solidification process. An extensive study of the germanium crystals grown during the Apollo-Soyuz Test Project was conducted. It was found that single crystal growth was achieved and that the interface demarcation functioned successfully. On the basis of the results obtained to date, there is no indication that convection driven by thermal or surface tension gradients was present in the melt. The gallium segregation, in the absence of gravity, was found to be fundamentally different in its initial and in its subsequent stages from that in the ground-based tests. None of the existing theoretical models for growth and segregation can account for the observed segregation behavior in the absence of gravitational effects. The results strongly sug-

gest the acute need for extensive experimental and theoretical work on Earth before the far-reaching implications of materials processing in space can be understood and exploited.

#### INTRODUCTION

Gravity-induced convection is always present in the melt undergoing solidification because of unavoidable thermal gradients. It has also been established that thermal convection causes uncontrollable variations in the rate of crystal growth (or solidification), which in turn result in compositional inhomogeneities and structural defects. Thus, gravity adversely affects the key parameters of the crystal growth (solidification) process. Furthermore, thermal convection interferes with the study of the processing parameters (i.e., solidification rate, growth interface characteristics, and others) and with the assessment of the relative importance of such parameters in the physical and chemical characteristics of the resulting solids. Since some key materials processing parameters remain essentially unaffected in the absence of gravitational effects, space provides a unique environment and a striking opportunity for materials processing.

The experiment of indium antimonide (InSb) crystal growth during the Skylab missions demonstrated beyond doubt that, in a zero-g environment, virtually ideal conditions for crystal growth can be established, which lead to chemical homogeneity never attained on Earth, and demonstrated that crystal growth and segregation phenomena can be studied directly in the absence of convective interference. On the basis of the

---

<sup>a</sup>Massachusetts Institute of Technology.

<sup>†</sup>Principal Investigator.

Skylab findings, the present experiment was designed to obtain more refined fundamental and quantitative information on the crystal growth and segregation processes. The germanium (Ge) (doped with gallium (Ga)) system was selected because it has been the most extensively studied system during the last 30 years. The following subsections discuss experiment results; related technical information is included in the appendix to this section.

### OBJECTIVES

The specific objectives of the MA-060 experiment for the Apollo-Soyuz Test Project (ASTP) were to determine the following characteristics under near-zero-g conditions.

1. The absence or presence of convective phenomena
2. The surface tension (and/or wetting) characteristics of the melt
3. The microscopic growth-rate behavior during directional solidification
4. The dopant segregation behavior and its dependence on the microscopic growth rate
5. The heat-transfer characteristics of the solidification system

### EXPERIMENTAL APPROACH

To achieve the experimental objectives, single crystals grown on Earth were partially melted and resolidified in space with simultaneous transmission of periodic current pulses across the crystal-melt interface.

The in-flight growth experiments were conducted in the multipurpose furnace (fig. 24-1) originally designed for the Skylab missions (ref. 24-1) and modified for ASTP to meet the higher temperature requirements. The stainless-steel cartridges containing the crystal assemblies were inserted into the three tubular cavities of the furnace. Heat levelers, lateral heat shields, and a heat-extraction system controlled the heat flow from the heating element through the crystal to the heat-extractor plate. With the furnace in this con-

figuration, melting was initiated when appropriate power was applied at the crystal end located within the heating element, and the crystal-melt interface was stabilized after 6 cm of each of the original crystals was melted. Stabilization of the crystal-melt interface (thermal soaking) was achieved by reducing the power duty cycle to 90 percent. After thermal soaking (2 hours), the power system was switched to the cooldown mode, resulting in an average cooling rate of 2.4 K/min (2.4° C/min). This cooling rate was expected to yield a microscopic growth rate ranging from 5  $\mu\text{m/sec}$  at the beginning to 10  $\mu\text{m/sec}$  at the end of the controlled cooldown period. Controlled cooldown was terminated after 1 hour and 23 minutes (estimated regrowth length of approximately 4 cm); the growth system was subsequently switched to the passive cooldown mode for 1 hour and 7 minutes, after which helium was injected into the furnace to accelerate the cooling rate.

To permit growth-interface demarcation (ref. 24-2) by current pulsing, leads were attached to the encapsulated Ge crystals. This was achieved with "graphite cup" electrodes at both ends of the crystals to which platinum leads were attached (fig. 24-2). The platinum leads of the three growth systems were connected in series, with the seed having a positive polarity. A power supply provided 19.1-A/cm<sup>2</sup> current pulses of 55-millisecond duration at 4-second intervals throughout the experiment. The specific cartridge design and the optimized interface-demarcation procedure were established during extensive ground-based tests.

### RESULTS AND DISCUSSION

Upon return to Earth, the crystals grown in space were subjected to an exhaustive growth and segregation analysis based on procedures established during ground-based tests. The primary analytical techniques used were high-resolution etching, Hall-effect measurements, spreading-resistance measurements, and ion-microprobe analysis. Because of the confined geometry that leads to stresses during growth, no defect analysis of the regrown material was performed.

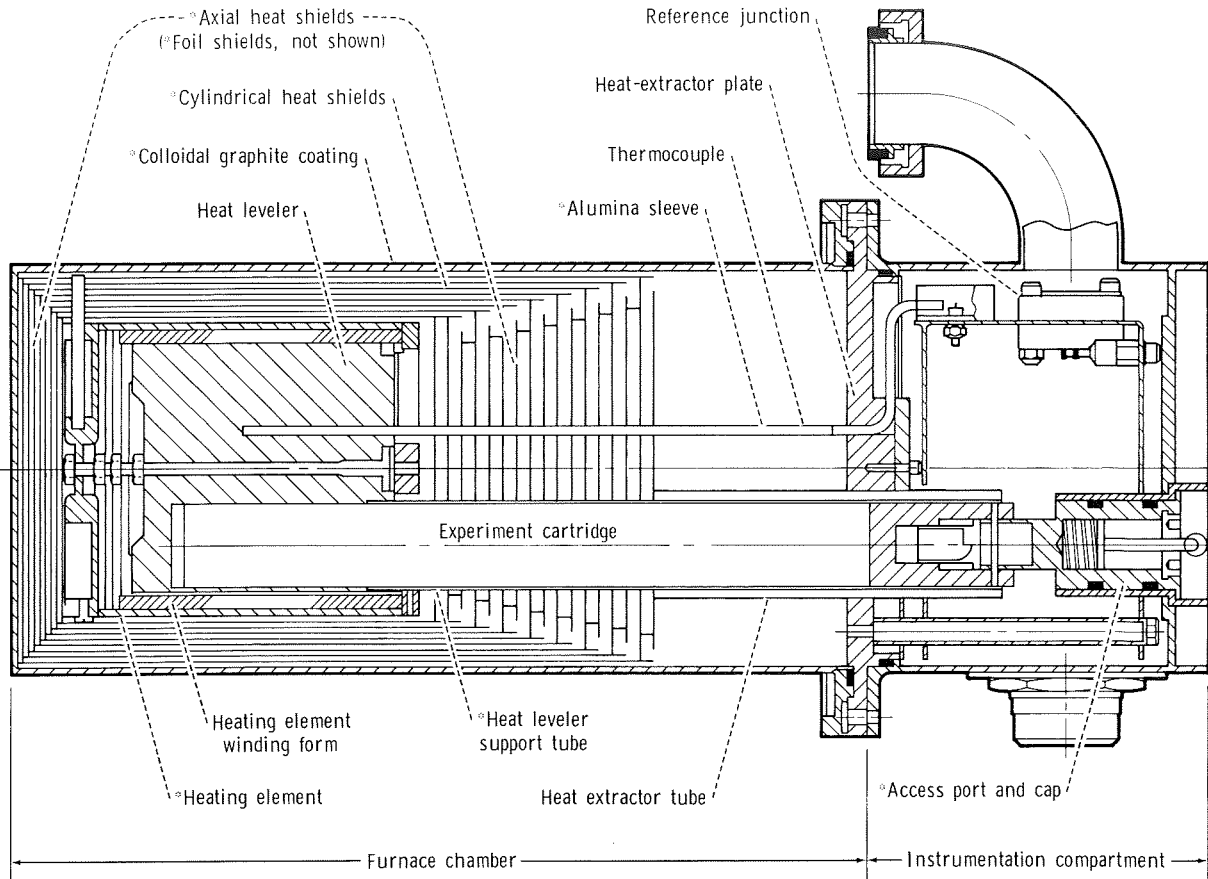


FIGURE 24-1.—Schematic of the multipurpose furnace used for the ASTP crystal growth and solidification experiments. An asterisk indicates design modifications.

### Surface Characterization

All crystals regrown in space could readily be removed from their quartz ampoules (fig. 24-3). In contrast, all crystals grown on Earth could be isolated only by dissolving the quartz ampoules in hydrofluoric acid. This pronounced difference in the behavior of the Earth- and space-grown crystals can be understood on the basis of the morphological characteristics of their surfaces. In interference contrast, it was observed that the surfaces of the space-grown crystals exhibited an irregular network of narrow ridges (fig. 24-4) similar to that observed on InSb crystals grown on Skylab. However, all crystals grown during ground-based tests in the same growth facility ex-

hibited surface features that reflected in detail the unavoidable irregularities of the inner walls of their quartz ampoules. It was therefore concluded that no wetting contact existed between the Ge melts and the confining quartz ampoules during growth in space; whereas, during growth on Earth, the Ge melt was in wetting contact with its confinement. This conclusion is significant because it suggests that effective wetting inversion (first observed during growth of InSb during Skylab) is a phenomenon that may be expected to occur in a multitude of systems subjected to solidification in space. The implications of this effect on materials processing are far reaching with regard to processing technology and possibly to the perfection of materials solidified in partial or total confinement.

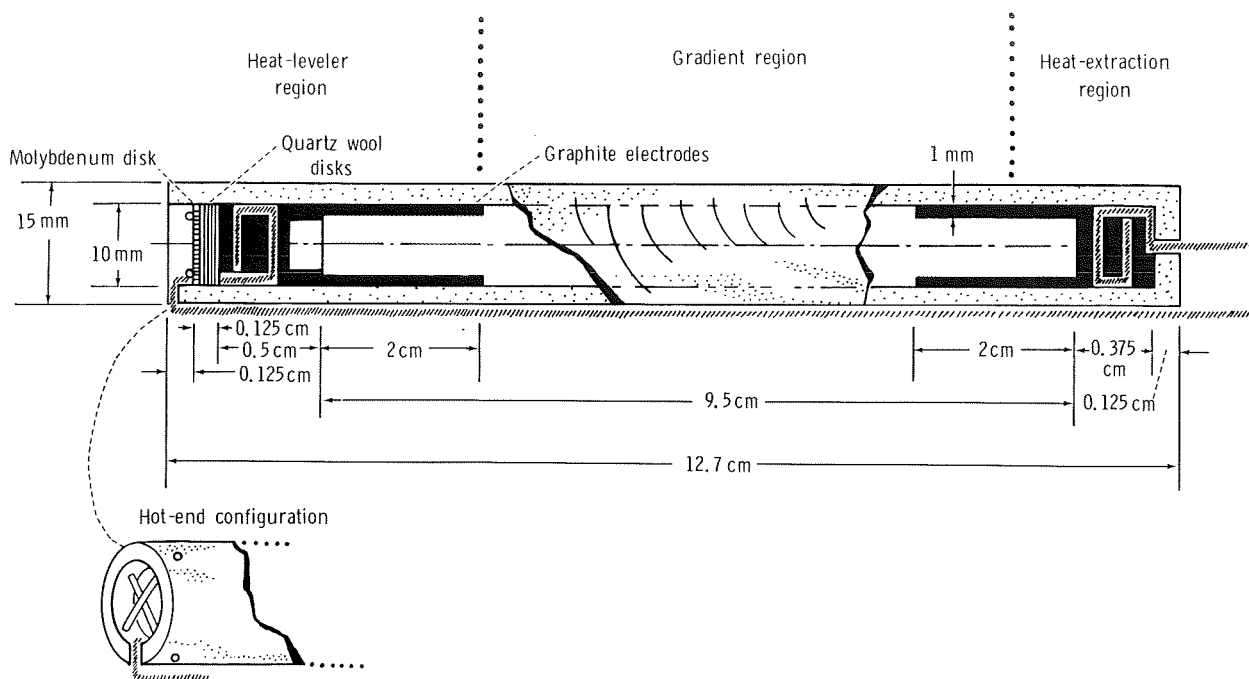


FIGURE 24-2.—Ampoule design permitting interface demarcation through current pulsing during regrowth.

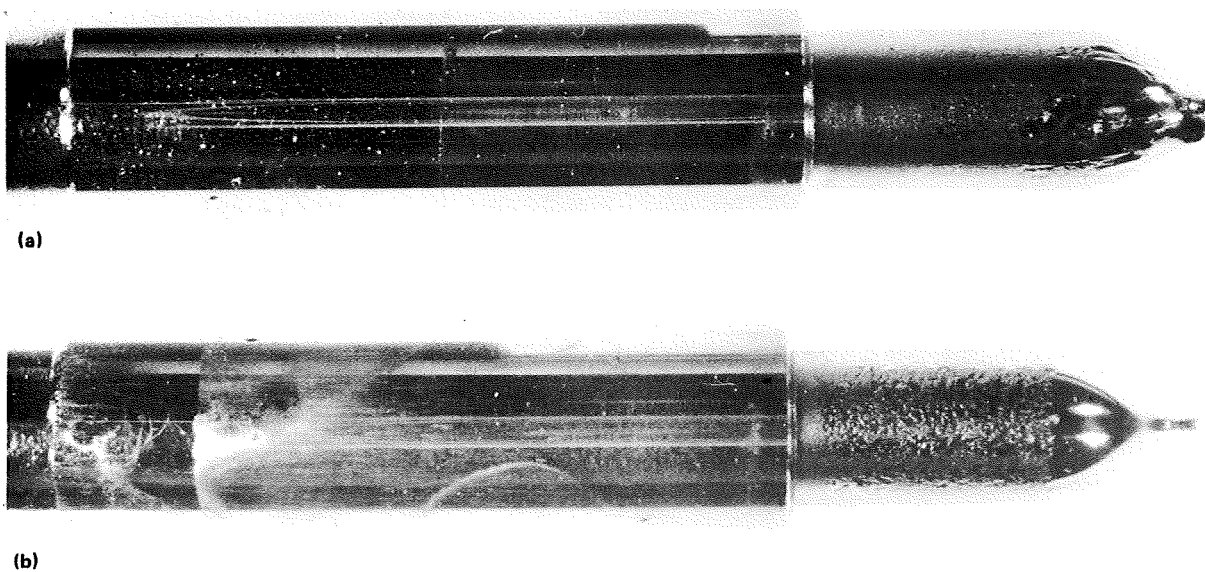


FIGURE 24-3.—Germanium crystals regrown in space (after removal from their quartz ampoules). (a)  $\langle 100 \rangle$  orientation. (b)  $\langle 111 \rangle$  orientation.

In all crystals, the original regrowth interface was identified (fig. 24-3) and appeared as an abrupt increase (0.5 mm) in crystal diameter at the predicted distance of approximately 3.5 cm from the cold end of the crystals. The location indicates the extent of backmelting in space and confirms on a macroscale the proper functioning of the multipurpose furnace.

From the morphological characteristics (absence of twin and grain boundaries), it is evident that single crystallinity in the peripheral region of the space-grown Ge crystal of  $\langle 111 \rangle$  orientation prevailed over the entire length of regrowth. In this respect, growth in space and growth on Earth are conspicuously different because crystals regrown during ground-based tests did not exhibit single crystallinity beyond regrowth of approximately 3 cm. The preservation of single crystallinity in the peripheral region (single crystal shell) is particularly remarkable in view of

the high doping level at which interface instability (due to constitutional supercooling and eventual interface breakdown) is predicted, in fact observed, in the crystal interior. Single crystallinity in the peripheral region was not preserved on the space-grown  $\langle 100 \rangle$  crystal. In this case, grain boundaries were first observed after growth of 3.5 cm, which compares favorably with ground-based tests in which breakdown first occurred after approximately 2 cm of growth.

#### **Bulk Characterization by High-Resolution Etching**

High-resolution etching techniques were refined during ground-based tests to permit the detection of microscopic compositional fluctuations in Ge with a sensitivity of more than  $\pm 0.2$  percent at Ga-dopant levels in excess of  $10^{18}/\text{cm}^3$ .

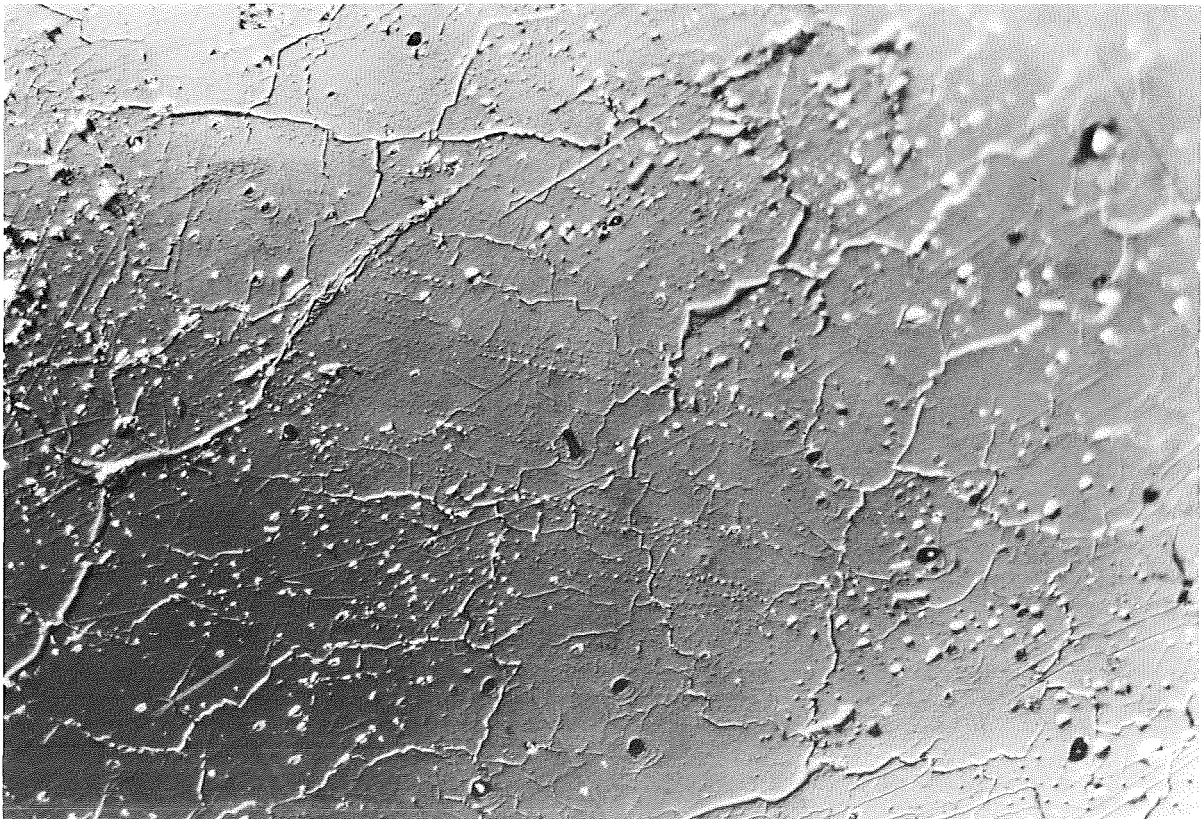


FIGURE 24-4.—Irregular ridge patterns on the surface of the  $\langle 100 \rangle$  Ge crystal regrown in space. (Magnification of  $123\times$ .)



Bulk characterization by etching was performed on longitudinal center cuts of the regrown segments. The exposed surfaces were polished and etched. An etched segment of the  $\langle 111 \rangle$  Ge crystal regrown in space is shown in figure 24-5. Three regions can be identified: the original seed portion (top), a narrow region exhibiting microscopic compositional inhomogeneities (center), and a region exhibiting no compositional fluctuations (bottom). The latter growth region exhibits faint, but distinct, lines that are the current-induced interface demarcations formed at 4-second intervals during regrowth. The spacing of consecutive demarcation lines can be seen to converge to zero (zero growth rate) at the lower end of the bandlike region of perturbed growth

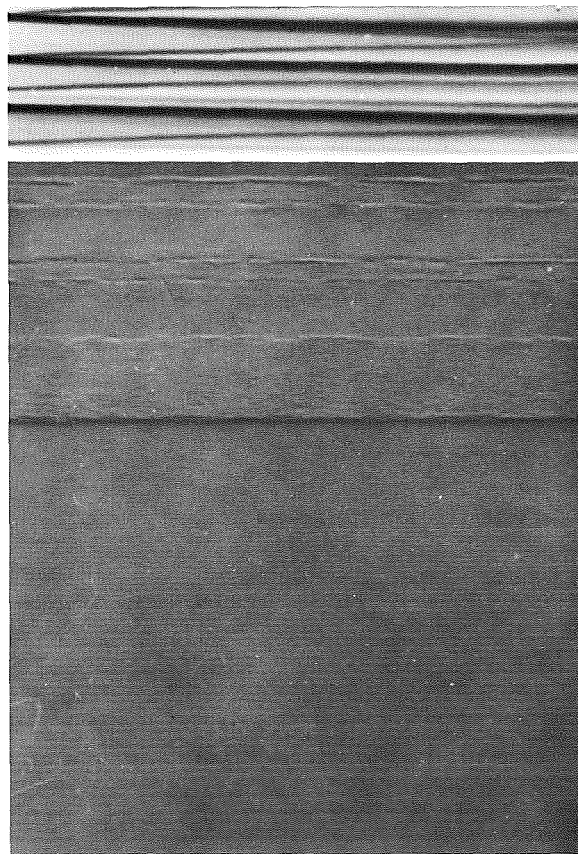


FIGURE 24-5.—Etched segment of the  $\langle 111 \rangle$  Ge crystal regrown in space. Note the seed portion (top) and the controlled regrowth portion (bottom) separated by a band of uncontrolled growth and segregation. (Magnification of 72 $\times$ .)

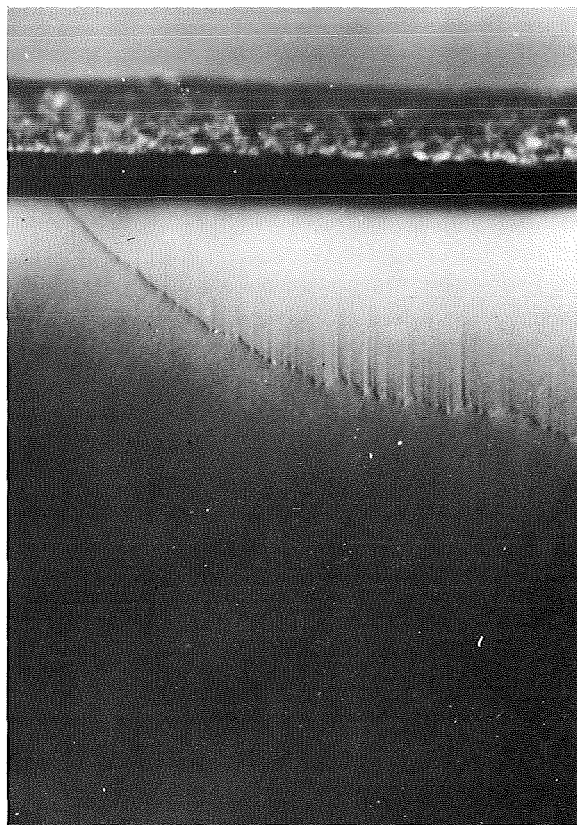


FIGURE 24-6.—Segregation inhomogeneities associated with peripheral facet formation in the  $\langle 111 \rangle$  Ge crystal regrown in space. (Magnification of 182 $\times$ .)

and segregation. Thus, interface demarcation established that the formation of the growth region with compositional fluctuations (band below the original regrowth interface) occurred during the 2-hour thermal soak and preceded the controlled regrowth. Ground-based tests indicated that this growth band reflects thermal instability of the furnace and is attributed to a slight imbalance of heat input and heat loss during the early thermal soak stages.

Etching analysis revealed further that the bulk of the controlled regrowth region of the  $\langle 100 \rangle$  crystal was free of microscopic compositional fluctuations over a growth length of more than 2.5 cm. For regrowth in the  $\langle 111 \rangle$  direction, minor compositional fluctuations of approximately 0.1 percent were observed associated with peripheral



facet formation (fig. 24-6). The nature of these perturbations is not yet understood.

Segregation inhomogeneities associated with interface breakdown due to constitutional supercooling were observed in all crystals after the advancing growth front had moved into the graphite cup. The breakdown in the space-grown material was attributed to deteriorating thermal gradients caused by abrupt changes in the thermal conductivity of the confinement system (in going from quartz to graphite) and the resulting changes in the growth-interface morphology. It is important to note that the onset of instability occurred significantly earlier in the  $\langle 111 \rangle$  crystal and was initiated at the facet to off-facet boundary. Occasionally, the morphological characteristics of the unstable growth interface were much more regular and conforming to theoretical predictions in the space-grown crystals than they were in the Earth-grown crystals (fig. 24-7).

### Growth-Rate Behavior on the Microscale

From interface demarcation lines introduced at 4-second intervals, a quantitative growth-rate analysis on a microscale was performed for all space-grown crystals. The growth-rate data for the crystal grown in the  $\langle 111 \rangle$  direction are shown in figure 24-8. Notice that, during the early stages of the cooling cycle, the microscopic growth rate increased rapidly from  $0 \mu\text{m/sec}$  to approximately  $7 \mu\text{m/sec}$ . After the initial transient region, the rate increase slowed down and, after approximately 2.5 cm of growth, the microscopic growth rate approached  $10.5 \mu\text{m/sec}$ . The growth-rate behavior observed in space (for the cooling rate of  $2.4 \text{ K/min}$  ( $2.4^\circ \text{ C/min}$ )) was virtually identical with that encountered during ground-based tests and indicates that the heat-transfer characteristics of the system are the same in space as they are on Earth. This result indicates that, in the growth configuration used, conductive heat transfer dominates and that the contribution of laminar convection to heat transport, which is present in the ground-based tests, is negligible.

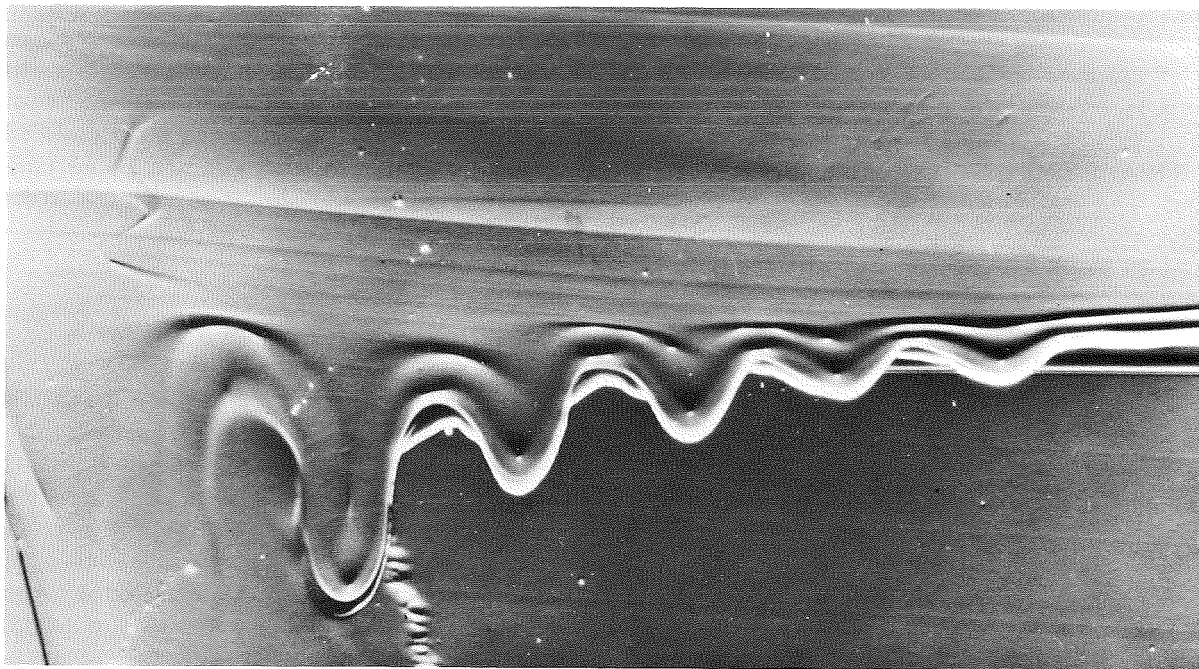
It should be pointed out that all existing theories of segregation assume an initial step function of the growth rate from zero to a finite and con-

stant rate; however, because all real melt-growth systems exhibit an initial transient growth behavior, no quantitative comparison between theory and experiment can be made. In view of these results, the development of a modified segregation theory has been initiated that considers the existence of initial growth-rate transients under convection-free conditions.

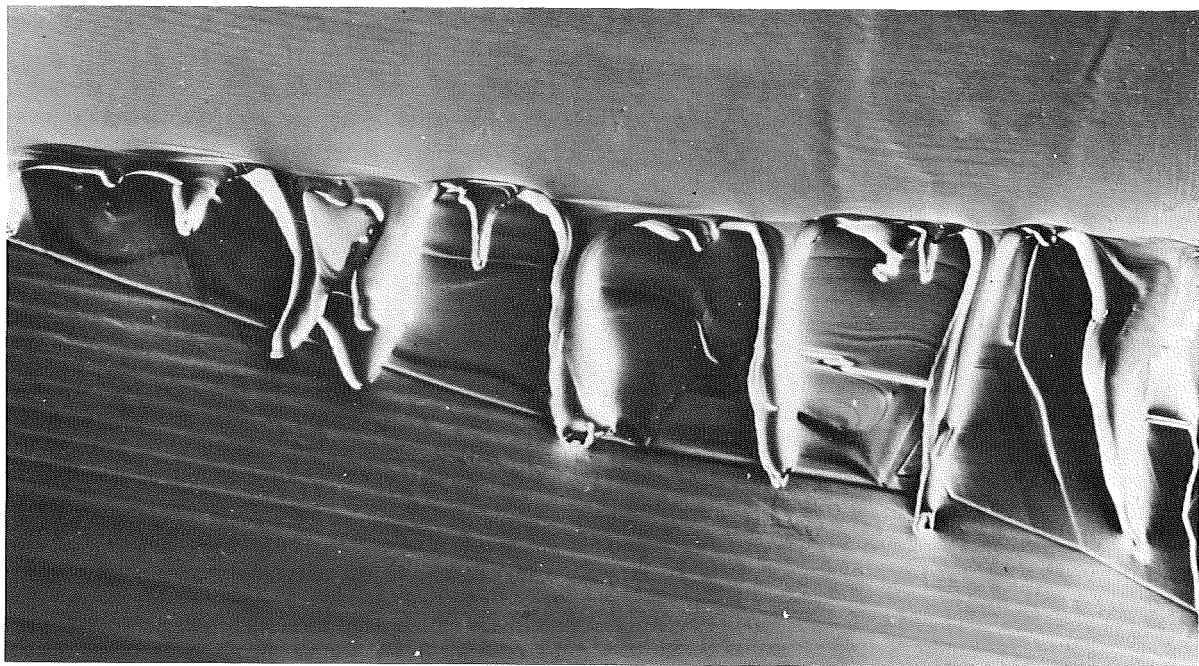
### Dopant Segregation Behavior

Quantitative compositional analyses of crystals regrown in space and on Earth have been obtained by means of spreading-resistance measurements with a linear resolution of  $5 \mu\text{m}$ . The results obtained for the initial regrowth region of crystals grown in the  $\langle 111 \rangle$  direction are shown in figure 24-9. (These regions are the same as those shown in fig. 24-5.) The measurements obtained along the growth direction of an Earth- and space-grown sample identify three regions: the seed regions (marked left), characterized by pronounced compositional fluctuations; the bands of uncontrolled growth (marked center); and the regrown regions with steadily increasing dopant concentration (marked right). Notice that the initial region in the space-grown crystal exhibits a much more rapid dopant concentration increase than the Earth-grown crystal. This behavior reflects the effect of laminar convection on segregation. The results are not, however, as expected with regard to the absolute dopant concentration level. Assuming the equilibrium distribution coefficient  $k_o$  of Ga in Ge to be 0.087 (as generally accepted), the dopant concentration in the initial regrowth region should assume a value of approximately  $9 \times 10^{17}/\text{cm}^3$  instead of the presently measured value of  $2.43 \times 10^{18}/\text{cm}^3$ . Since virtually identical initial dopant concentration levels were observed in both samples, the generally accepted value for  $k_o$  was assumed to be erroneous.

The appearance of growth facets in the space-grown  $\langle 111 \rangle$  crystal enabled the study of facet-segregation behavior in the absence of convective interference. The spreading-resistance measurements (fig. 24-10) show that the dopant concentration on-facet is less than that off-facet by a factor of 0.92. The tracings also show that the



(a)



(b)

FIGURE 24-7.—Frontal interface breakdown during late stages of  $\langle 111 \rangle$  Ge regrowth. (Magnification of  $200\times$ .) (a) Space-grown. (b) Earth-grown.

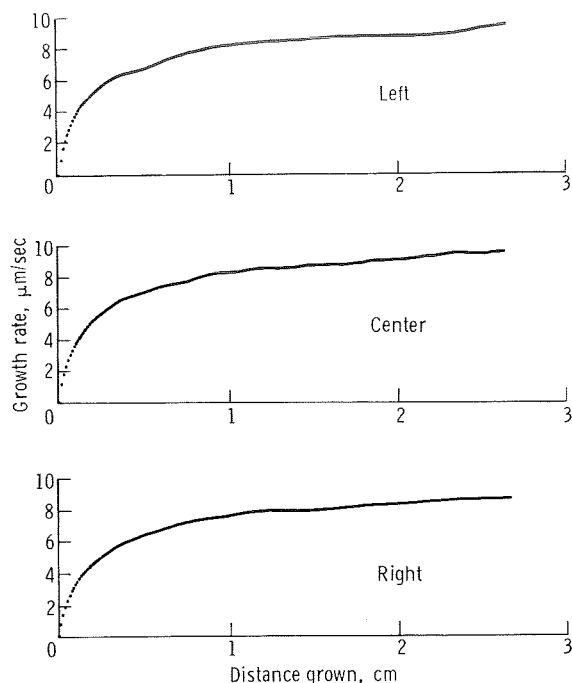


FIGURE 24-8.—Microscopic growth rates of the  $\langle 111 \rangle$  Ge crystal regrown in space.

compositional change on-facet to off-facet occurs over a distance of approximately  $30\ \mu\text{m}$ .

Attempts to analyze quantitatively the initial segregation transient in the regrowth region of the space-grown sample were unsuccessful because of the existing growth-rate transient that is not considered in the theoretical treatments. Because of the unavailability of reliable values for  $k_0$  and for the diffusion coefficient  $D$  (essential for a quantitative segregation analysis), appropriate experiments must be conducted under zero-g conditions to accurately determine these constants.

Compositional analysis on a macroscale, covering the entire length of crystals regrown in space, is still being conducted. The results obtained to date are largely unexpected and as yet unexplained. As shown in figure 24-11, the dopant concentration, as expected, increased steadily over a distance of approximately 1.5 cm from the original regrowth interface. At this distance, the effective distribution coefficient  $k_{\text{eff}}$  approached the value of 1, which is characteristic of diffusion-controlled steady-state segregation. However, with continuing growth and with a steadily in-

creasing microscopic growth rate, the dopant concentration decreased instead of reaching the steady-state value. The dopant concentration continued to decrease over a distance of approximately 1 cm of growth. At this point, interface breakdown due to constitutional supercooling occurred and a further analysis of the segregation behavior was not possible.

There are indications that the observed segregation anomaly is not characteristic of growth under zero-g conditions, but that it was a consequence of the particular geometry of the growth system. In view of the potentially far-reaching implications of these unexpected segregation effects, a complete understanding of their origin is of paramount importance.

## SUMMARY

The results of the MA-060 experiment revealed growth and segregation effects previously not observed on Earth. The majority of these effects cannot be explained by any existing experimental or theoretical models of growth and segregation. This finding has fundamental implications because germanium is the most studied and best understood of all solids. The clear implication is that, although space provides a unique environment for materials processing, exploitation of the unprecedented opportunities of the zero-g environment necessitates the selection of systems and experimental apparatus that have been, or can be, exhaustively investigated on Earth so that zero-g effects on materials processing can be unambiguously identified and quantitatively studied. In addition, extensive research is essential following space experimentation (even on critically selected and well-understood systems) to quantitatively understand the zero-g effects and establish sound guidelines for subsequent space processing. The authors believe that materials processing in the Space Shuttle Program could be a most expensive and unprofitable undertaking unless ground-based investigations on critically selected materials systems are greatly expanded.

*The following material represents an update to the preceding analysis and was added after proofreading.*

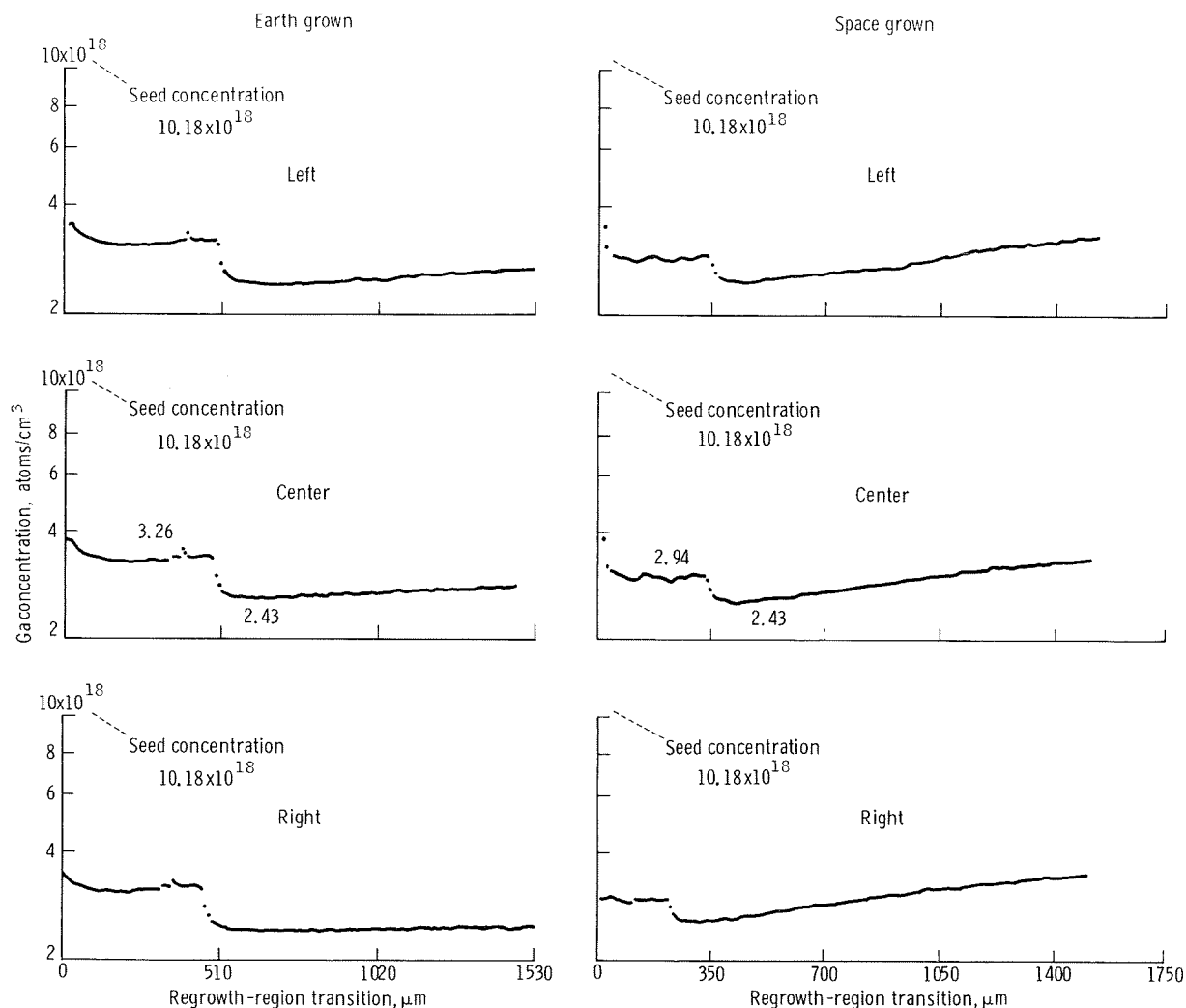


FIGURE 24-9.—Compositional profiles of the initial regrowth region in the  $\langle 111 \rangle$  Ge crystal regrown in space. (Ground-based data are shown for comparison.)

### MACROSEGREGATION ANALYSIS

A comprehensive macrosegregation analysis for both Ga- and Sb-doped Ge crystals grown in space was conducted. It was found that the previously unexplained segregation effects are directly related to the characteristics of the growth interface morphology which in turn are controlled by the thermal configuration provided in the multipurpose furnace. In addition, the analysis showed that the dopant distribution in Ga-doped crystals grown in space is in all respects consistent

with diffusion-controlled segregation. The observed segregation behavior provides no evidence of convection in the melt.

The compositional profiles for the first 2.5 cm of Ga- and Sb-doped Ge crystals grown in space are shown in figure 24-12. These data were obtained from spreading resistance measurements on longitudinal cuts containing the growth axes of the crystal. It can be seen that dopant segregation in both systems has the same basic characteristics: the dopant concentration increases steadily in the direction of regrowth, indicative of transient

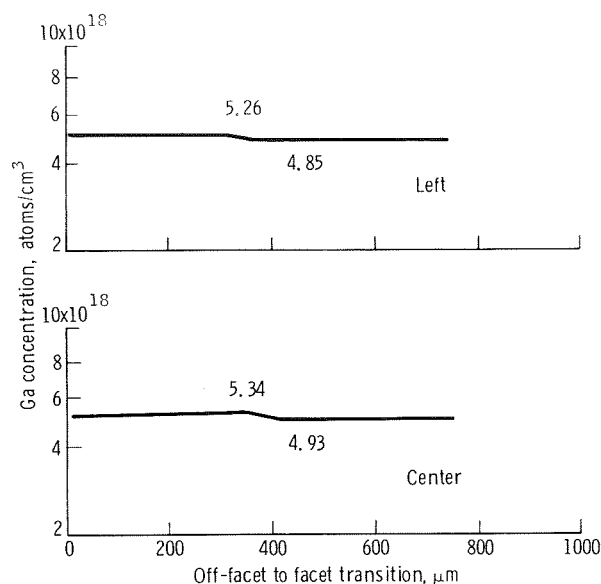


FIGURE 24-10.—Compositional profile of the off-facet to facet transition region in the  $\langle 111 \rangle$  Ge crystal regrown in space.

segregation and consistent with theory. The concentration profiles of both systems show, in addition, longitudinal and radial compositional variations for which the origin could not be explained previously. Of particular concern was the Ga-concentration decrease on the right and center scans of figure 24-12(a), first noticeable at a distance of approximately 1.3 cm from the original regrowth interface. Since this concentration decrease reflects a net decrease of the dopant concentration within the diffusion boundary layer (the microscopic growth rate is still steadily increasing), it could be interpreted as indicative of convective interference. To assess, for the analyzed growth region, the magnitude of effective segregation, average longitudinal dopant concentration profiles were determined by averaging along the growth direction the corresponding concentration values of the left, center, and right scans of figures 24-12(a) and 24-12(b). It is seen in figure 24-13(a) that the averaged dopant concentration profile does not exhibit the pronounced compositional variations observed in the longitudinal scans of figure 24-12(a). The minor compositional variations observed in figures

24-13(a) and 24-13(b) are considered as deficiencies of the averaging process, which by necessity is confined to one plane of the cylindrical crystal. Thus, it is concluded that the concentration variations observed on the longitudinal scans at distances in excess of 1 cm from the original regrowth interface do not constitute changes in segregation brought about by dopant depletion within the diffusion boundary layers; but, rather, that they reflect radial dopant redistribution within the diffusion boundary layer.

As indicated in figure 24-12, the dopant concentration in both systems is radially uniform at the onset of regrowth. With continuing growth, a radial nonuniformity in composition develops with the dopant concentration in the center exceeding significantly that on the periphery. At a distance of approximately 0.3 cm from the original regrowth interface it becomes apparent that radial segregation is asymmetric and, with continuing growth, undergoes pronounced changes. A study of the growth interface morphology (made possible through interface demarcation) reveals that the radial dopant incorporation is in all respects consistent with diffusion-controlled segregation on a nonplanar growth front; thus, the originally established growth interface, which is concave into the crystal, will result in a correspondingly curved boundary layer. Since the diffusive dopant flux away from the growth interface is largest in the normal direction, it will result in a nonuniform dopant distribution within the diffusion boundary layer and correspondingly lead to radially nonuniform dopant incorporation in the growing crystal.

In view of the interdependence of growth interface morphology and radial dopant segregation under diffusion-controlled conditions, a detailed study of the morphology of the crystal melt interface and its changes during growth was conducted. It was found that the growth interface (in both crystals analyzed) is axially asymmetric and changes continuously with growth. In particular, it was observed that pronounced morphological changes take place when the growth interface is located in the region where the radial temperature control changes from axial heat shields to the heat leveler. A comparison of the growth interface morphology and its changes during growth with

radial dopant segregation indicates in all instances a behavior that is consistent with diffusion-controlled dopant redistribution within the diffusion boundary layer.

The preceding analysis, together with the observed compositional homogeneity on a microscale, must be taken as conclusive evidence for the absence of time-dependent convective flows in the Ge melt under the presently used growth configuration.

In the context of the present study, it is important to recognize that time-independent convective melt flows are only consequential if they affect macrosegregation and prevent the establish-

ment of dynamic steady-state conditions for which  $k_{\text{eff}}$  becomes 1 and the composition of the growing crystal becomes constant. Thus, unambiguous evidence for the absence of convective interference with segregation is given by the achievement of constant composition in a grown crystal—as reported for InSb crystal growth during the Skylab missions. In the presently studied systems, because of the small dopant distribution coefficients, constant composition cannot be achieved over the limited growth length; thus, the analysis for residual convection effects must be based on the segregation behavior in the transient region.

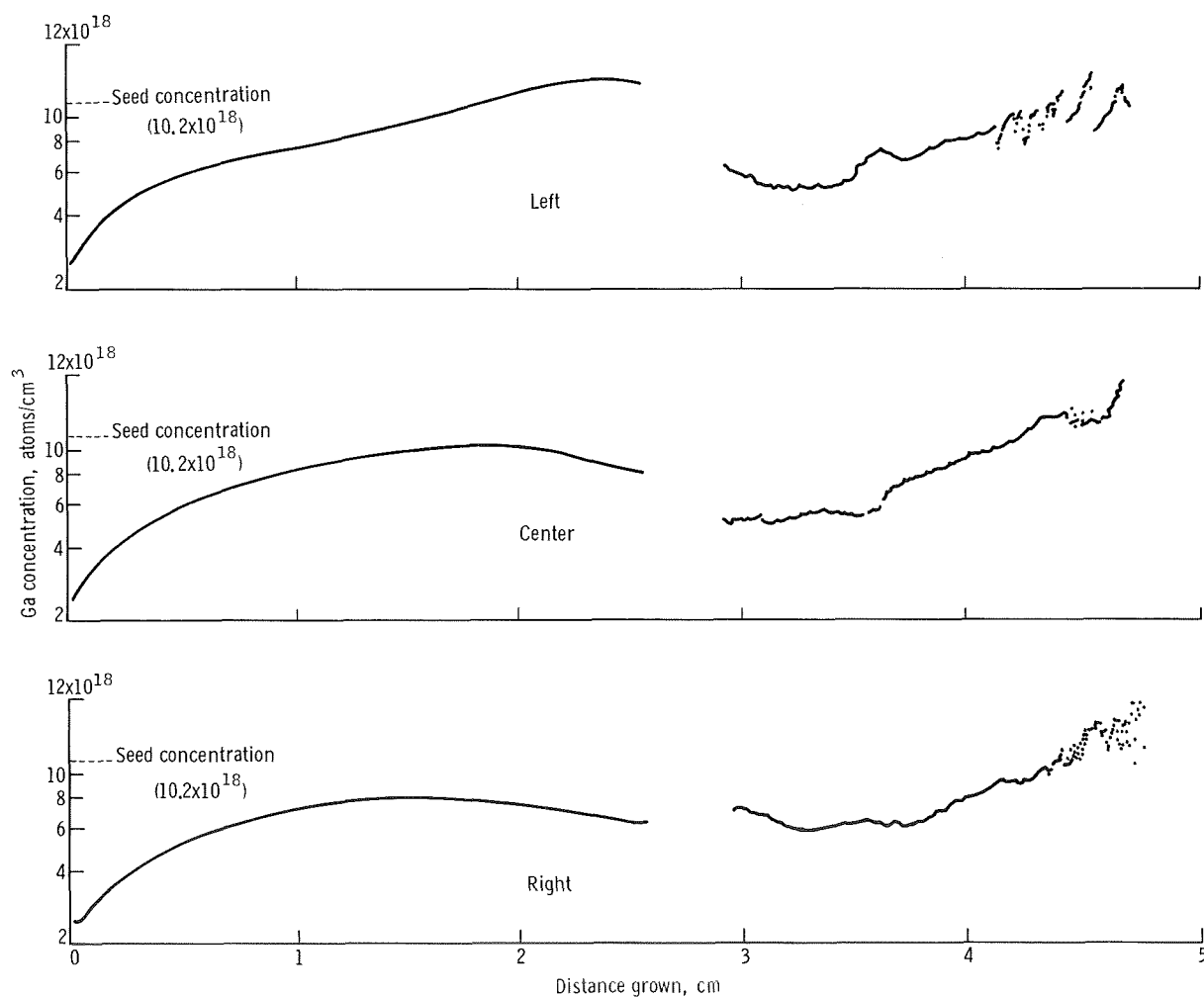


FIGURE 24-11.—Macroscopic compositional profile of the  $\langle 111 \rangle$  Ge crystal regrown in space.

Such an analysis, as indicated earlier, is complicated by three facts: (1) The transient region is associated with a steadily increasing growth rate—conditions for which the theoretical transient segregation in the absence of convection has, as yet, not been determined; (2) the diffusion coefficients for Ga and Sb in Ge melts are not known with adequate precision; the best published data for diffusion of Ga in Ge range from  $D = 7.5 \times 10^{-5}$  to  $1.5 \times 10^{-4}$  cm<sup>2</sup>/sec; and (3) the generally accepted equilibrium distribution coefficients for Ga in Ge range from  $k_o = 0.087$  to 0.12.

Although the existing theoretical treatment of transient segregation in the absence of convective interference (ref. 24-3) assumes a constant rate of growth, it can nevertheless be usefully applied to the present results. According to this theory, the dopant concentration in the growing solid will assume the value  $C_x$  at a distance  $x$  from the origi-

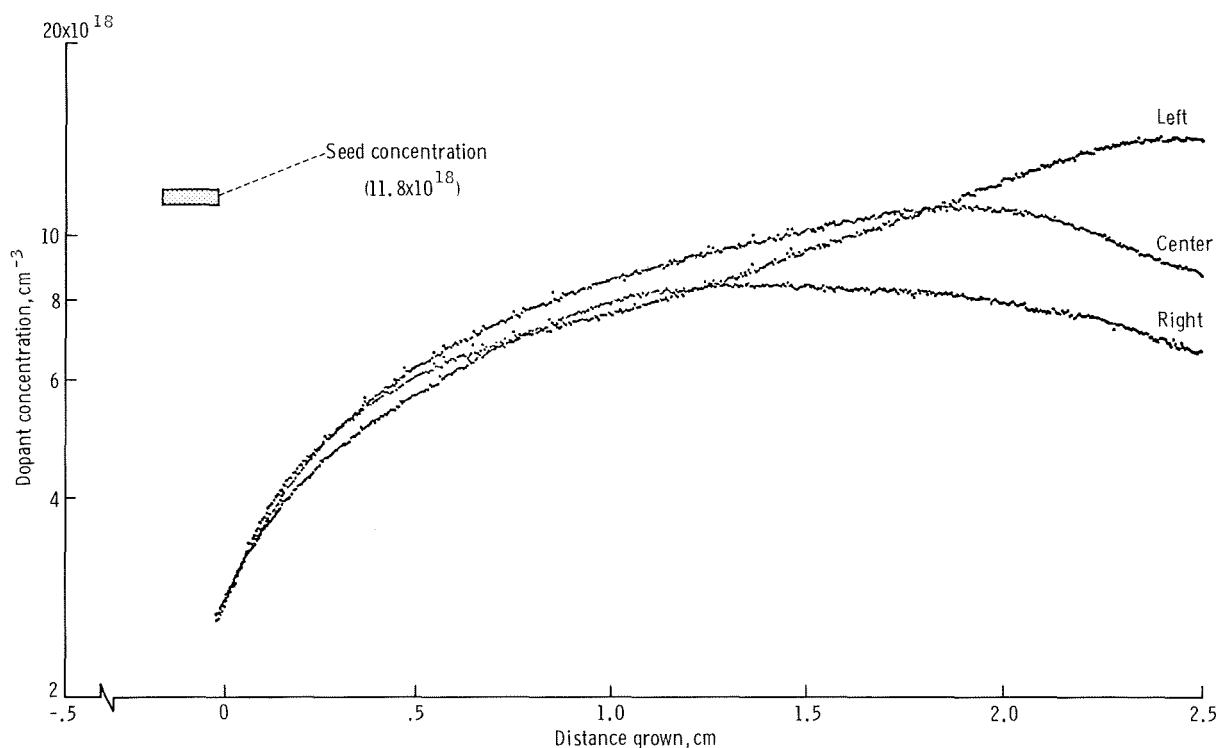
nal regrowth interface

$$C_x = C_L \left\{ (1 - k_o) \left[ 1 - \exp \left( -k_o \frac{R}{D} x \right) \right] + k_o \right\} \quad (24-1)$$

where  $R$  is the microscopic rate of growth and  $C_L$  is the concentration in liquid. For  $x = D/(k_o R)$  (the characteristic distance),  $C_x$  becomes

$$C_x = C_L \left[ \left( 1 - k_o \right) \left( 1 - \frac{1}{e} \right) + k_o \right] \quad (24-2)$$

Therefore, by using a value of  $R$  as the average measured value of  $7 \times 10^{-4}$  cm/sec, it is possible to determine a characteristic distance range ( $x_{\min}$  and  $x_{\max}$  controlled by the spread of accepted values of  $D$  and  $k_o$ ) over which, in the absence of convective interference, the dopant concentration in the solid melt must have risen to the value of  $C_x$ .



(a)

FIGURE 24-12.—Longitudinal composition profiles of Ga- and Sb-doped Ge crystals regrown in space. The three curves give the data obtained by scans performed on the left, center, and right of the investigated axial plane. (a) Ga-doped Ge crystal  $\langle 111 \rangle$ . (b) Sb-doped Ge crystal  $\langle 100 \rangle$ .

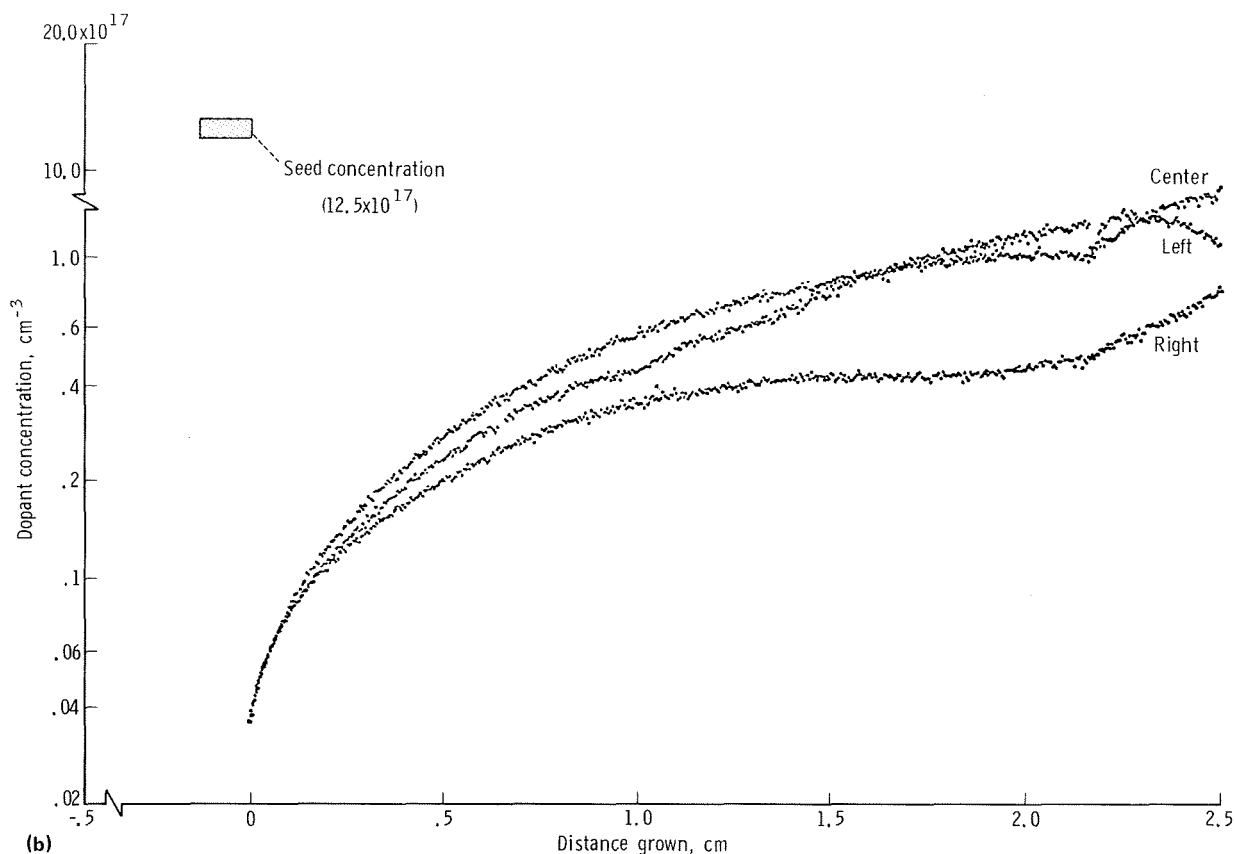


FIGURE 24-12.—Concluded.

It is self-evident that, in the presence of convective interference, the distance  $x$  from the original growth interface at which the value  $C_x$  is reached must exceed  $x_{\max}$ . It is also evident that, if the critical distance  $x$  assumes any value smaller than  $x_{\max}$ , the result may be interpreted as evidence for the absence of convective interference. The results of this analysis for growth of Ga-doped germanium are shown in figure 24-14.

It can be seen that the Ga concentration in the space-grown crystal reached the value  $C_x$  virtually at the calculated distance of  $x_{\min}$  (0.9 cm). In contrast, in the Earth-grown crystal, the critical concentration is reached at a distance well beyond  $x_{\max}$ . Thus, in spite of the uncertainty associated with the required physical constants, the present results are considered as concrete evidence of the

absence of time-independent convective interference with dopant segregation. (The present analysis was not applied to the Sb-doped Ge crystals, because the critical distance is in excess of 6 cm.)

Therefore, the present analysis provides an interpretation of microsegregation and macrosegregation behavior consistent with diffusion control in the microgravity environment established during the ASTP mission. The analysis also shows that the establishment of thermal configurations leading to planar or near-planar solidification fronts is essential for the achievement of radial compositional homogeneity during crystal growth under diffusion-controlled, near-zero-g conditions.



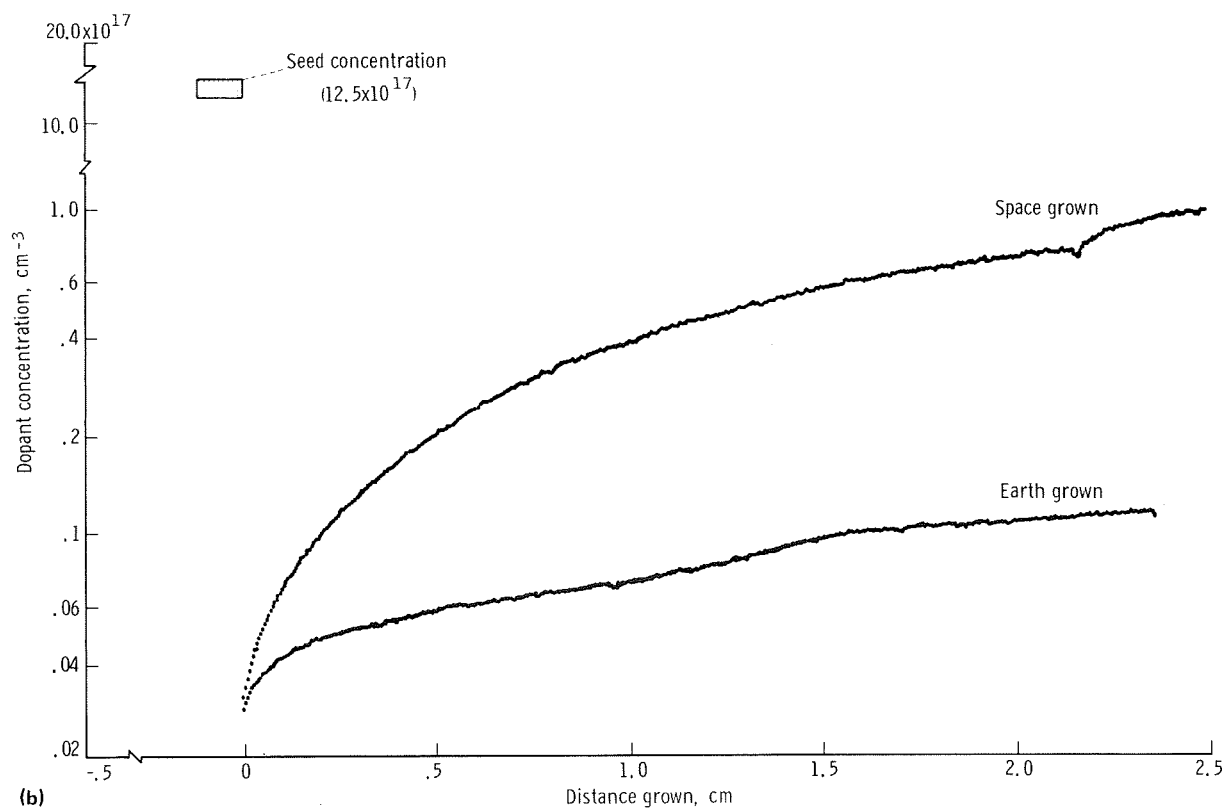
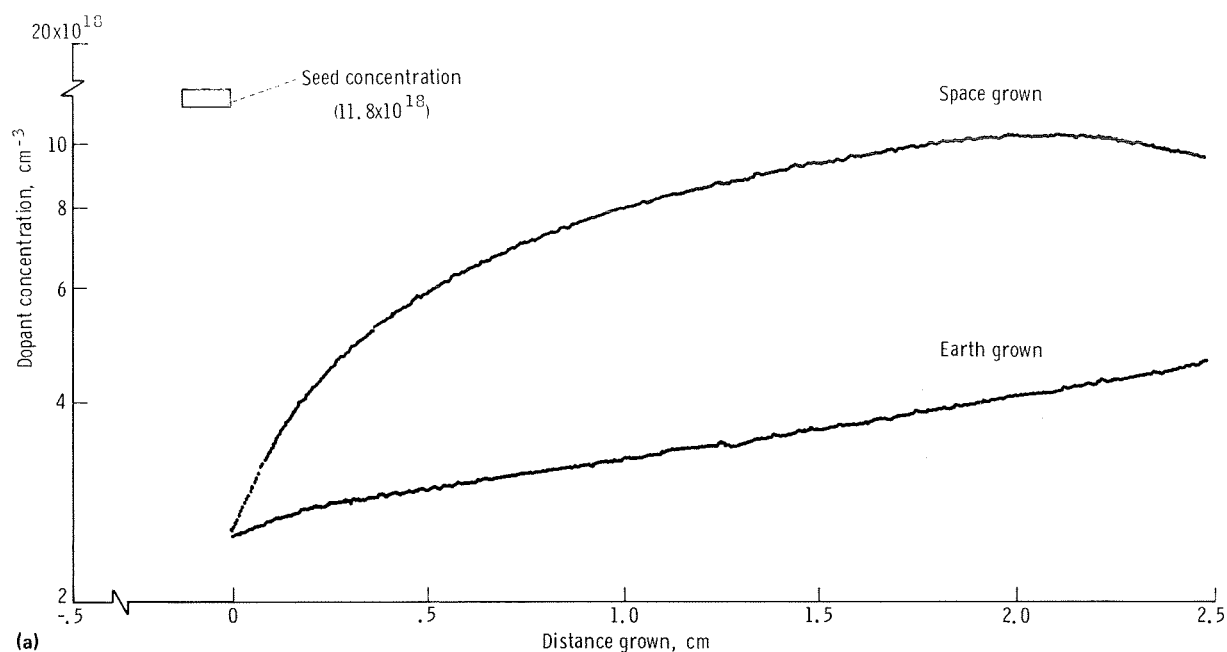


FIGURE 24-13.—Averaged longitudinal composition profiles of Ga- and Sb-doped Ge crystals regrown in space. The data constitute the average of the concentration values of the longitudinal scans shown in figure 24-12. (a) Ga-doped Ge crystal  $\langle 111 \rangle$ . (b) Sb-doped Ge crystal  $\langle 100 \rangle$ .

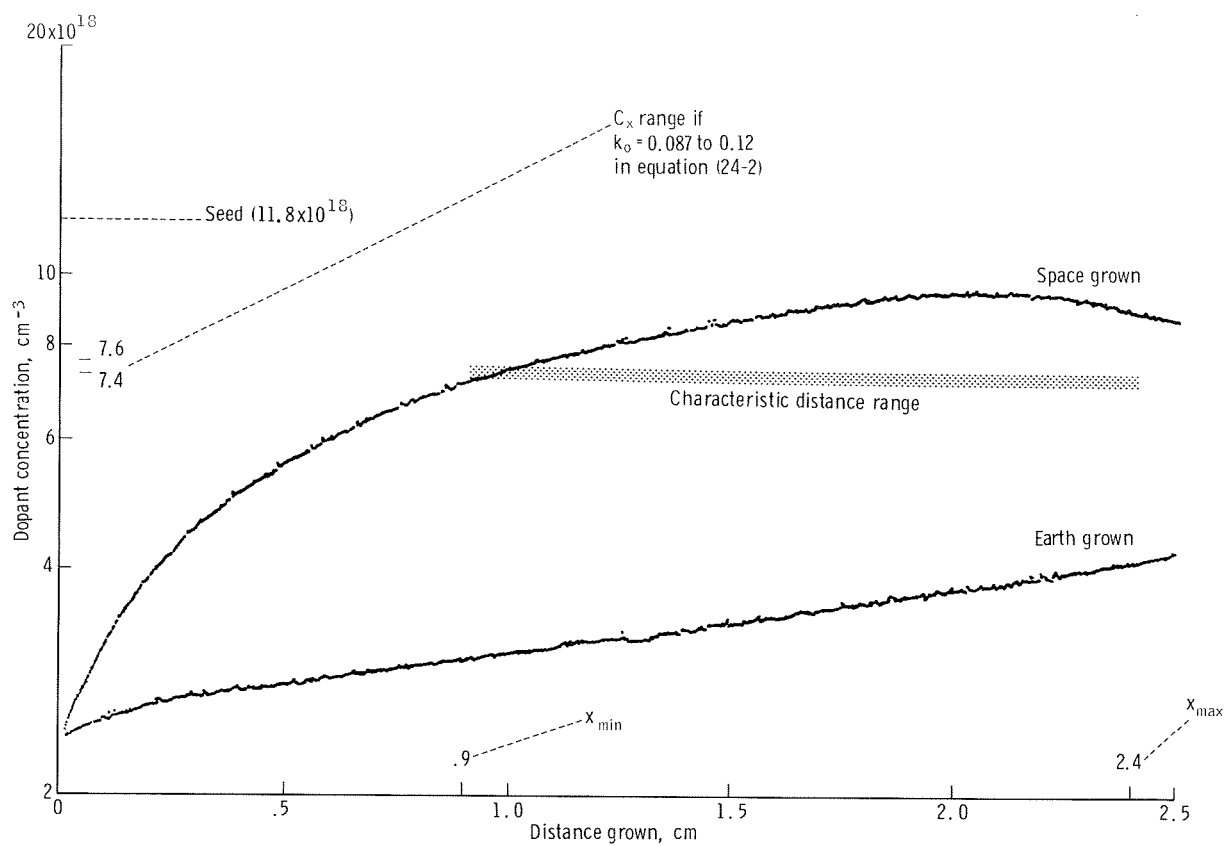


FIGURE 24-14.—Application of transient segregation theory to experimental results of figure 24-13(a). (See text.)

## Appendix — Technical Information

### GROWTH OF GERMANIUM CRYSTALS FOR GROUND-BASED TESTS AND FLIGHT EXPERIMENTS

The 23 germanium (Ge) single crystals that were used for the experiments were pulled from doped melts by the Czochralski technique under the following growth conditions.

1. The Ge charge was 240 g in ATJ graphite crucibles.

2. The dopant elements were gallium (Ga), tin (Sn), and antimony (Sb). (All crystals were singly doped.)

3. The melts were doped to achieve an average dopant concentration in the grown crystals of approximately  $10^{18}$  to  $10^{19}/\text{cm}^3$ .

4. The seed orientation was  $\langle 100 \rangle$  and  $\langle 111 \rangle$ .

5. The protective gas atmosphere was hydrogen ( $\text{H}_2$ ) at a pressure of approximately  $101\,325\text{ N/m}^2$  (760 mmHg).

6. The pulling rate was  $14\text{ }\mu\text{m/sec}$  for Ga-doped crystals and  $7\text{ }\mu\text{m/sec}$  for Sb- and Sn-doped crystals.

7. The seed rotation was 10 rpm; the crucible rotation, 0 rpm.

The crystals (weight,  $\approx 130\text{ g}$ ; length,  $\approx 15\text{ cm}$ ; and diameter,  $\approx 1.5\text{ cm}$ ) were centerless ground to a diameter of 1.046 cm and cut to a length of 9.5 cm. The diameter of both ends of all crystals was reduced to 0.843 cm over a length of 2.06 cm to permit the attachment of graphite cups, which served as the current contacts for interface demarcation. The crystals were subsequently etched in CP-4 (five parts nitric acid ( $\text{HNO}_3$ ), three parts hydrofluoric acid (HF), three parts acetic acid ( $\text{CH}_3\text{COOH}$ ), and bromine ( $\text{Br}_2$ )) to the desired diameter of 0.838 cm. Samples from both ends of all crystals were retained for determining the doping levels.

### AMPOULE DESIGN AND ASSEMBLY

The ampoules confining the growth systems were constructed of heavy-wall quartz tubing (10 mm internal diameter, 16 mm outer diameter), which was centerless ground to a diameter of 1.50 cm and cut to a length of 12.7 cm. Before assembly, the ampoules were etched with HF, rinsed with distilled water ( $\text{H}_2\text{O}$ ), methanol, and acetone, and dried with hot filtered air. The graphite contact cups, machined to yield low-contact resistance with the Ge crystals, were fired at 1873 K ( $1600^\circ\text{C}$ ) in a vacuum of  $13.3\text{ }\mu\text{N/m}^2$  ( $10^{-7}$  torr). The platinum leads were then attached.

The decision was made to use an open ampoule configuration (non-vacuum tight) with 0.10-cm (0.04 in.) platinum current leads and graphite cups at both ends of the crystals as contacting media. The inside length of the graphite cups was 2.0 cm, and they were designed to ensure contact with the melt irrespective of the degree of backmelting. The mechanical contact design required precision machining of the graphite cups and the Ge crystals. The ampoule design was tested in ground-based experiments and was used for the flight experiment without modification.

### PULSE POWER SUPPLY

The results from preliminary experiments showed that growth characterization on a microscale through interface demarcation would require a power supply capable of delivering current pulses of the following characteristics.

1. A pulse-repetition rate of 2 seconds
2. A pulse duration of  $\geq 75$  milliseconds
3. An amplitude of 25 A independent of load-resistance variations up to 1 ohm

The basic design criteria of the pulse power supply and its connection to the three growth ampoules in either parallel, series, or multiplexed (sequential) configurations were evaluated. On the basis of the power available for the MA-060 experiment, a prototype unit to be connected in series with the growth ampoules was designed that delivered 50-millisecond half-width constant current pulses of 15 A amplitude into a resistive load up to 1 ohm with a nominal 4-second repetition rate. The pulse transit time was degraded to 10 milliseconds to minimize electrical isolation requirements for the spacecraft power bus.

### **SAMPLE PREPARATION**

For bulk crystal analysis by interference-contrast microscopy and spreading-resistance measurements, all crystals were cut along the growth direction to obtain 0.2-cm-thick slices containing the crystal axis. These center cuts were mounted on brass disks and the surfaces were ground with a 10- $\mu\text{m}$  abrasive. All samples were subsequently mechanically polished to a Linde A (0.3  $\mu\text{m}$ ) surface finish and chemically polished with a modified Syton HT 30 solution (200 ml of Syton HT 30, 200 ml of  $\text{H}_2\text{O}$ , 5 ml of  $\text{H}_2\text{O}_2$ , and 2 ml of  $\text{CH}_3\text{COOH}$ ). The samples were then etched by immersion for 5 to 8 seconds in a solution of one part HF, one part  $\text{CH}_3\text{COOH}$  and one part  $\text{H}_2\text{O}$ . For quantitative segregation analysis, the specimens were first subjected to spreading-resistance measurements and subsequently investigated by interference-contrast microscopy. This procedure enabled the determination of the microscopic growth rate (from the spacing of consecutive interface demarcation lines) corresponding precisely to the region for which the dopant concentration profile was obtained by the spreading-resistance measurements (the traces of the spreading-resistance probe are visible in interference contrast). Photomicrographs were taken using Contrast Ortho Film (125 ASA).

### **SPREADING-RESISTANCE MEASUREMENTS**

The functional relationship between resistivity and spreading resistance, with its application to

the "spreading resistance probe" technique, has been described by Mazur and Dickey (ref. 24-4). Resistivity and mobility data for Ge at 573 K (300° C) were analyzed by least-squares methods and plotted as a function of impurity concentration (ref. 24-5). This procedure results in the establishment of an exact correlation between spreading resistance and impurity concentration. Thus, spreading-resistance measurements provide a precise method for determining dopant impurity profiles on a microscale (ref. 24-2).

All measurements were obtained with a single probe, which was calibrated against a small segment of the Ge  $\langle 111 \rangle$  flight crystal (0.4 by 0.4 by 0.2 cm) as a standard. The resistivity and carrier concentration of the crystal were determined by Hall-effect measurements at 573 K (300° C) using the Van der Pauw technique (ref. 24-6).

Center slices (0.2 cm thick) were cut with a diamond-wheel from the space-grown crystals and from the corresponding ground-based test crystals. Because of the 2.5-cm traverse limit of the X-axis drive of the probe positioner, each slice had to be cut, which prevented continuous scanning of the sample surfaces.

Large-area ohmic contact to the back side of all samples to be analyzed was made with an evaporated and microalloyed silver layer. The samples were pressure bonded to brass disks using conductive silver paint. The samples were then polished and etched.

Reproducibility of the measurements obtained on stabilized surfaces was better than 2 percent for the  $\langle 111 \rangle$  Ge segments and approximately 5 percent for the  $\langle 100 \rangle$  Ge segments (worst case). Occasional excessive data scatter or systematic drift of the data base could, in all cases, be traced to steps in the sample preparation.

The raw spreading-resistance data were first converted to normalized resistances using a quadratic regression fit, correcting for additional distributed resistances in the external circuitry. Resistivities were calculated from these values without smoothing and were fitted to a computer-generated expression for the concentration-to-resistivity relationship using a spline cubic interpolating polynomial. The resulting concentration values as a function of distance were plotted on a high-speed digital plotter.

## REFERENCES

- 24-1. Morgenthaler, George W.; and Simonson, G. E., eds.: Skylab Science Experiments. Science and Technology, vol. 38, American Astronaut. Soc., 1975.
- 24-2. Witt, A. F.; Lichtensteiger, M.; and Gatos, H. C.: Experimental Approach to the Quantitative Determination of Dopant Segregation During Crystal Growth on a Microscale: Ga Doped Ge. *J. Electrochem. Soc.*, vol. 120, no. 8, Aug. 1973, pp. 1119-1123.
- 24-3. Tiller, W. A.; Jackson, K. A.; Rutter, J. W.; and Chalmers, B.: The Redistribution of Solute Atoms During the Solidification of Metals. *Acta Met.*, vol. 1, 1953, pp. 428-437.
- 24-4. Mazur, R. G.; and Dickey, D. H.: A Spreading Resistance Technique for Resistivity Measurements on Silicon. *J. Electrochem. Soc.*, vol. 113, no. 3, Mar. 1966, pp. 255-259.
- 24-5. Irvin, J. C.; and Sze, S. M.: Resistivity, Mobility and Impurity Levels in GaS, Ge, and Si at 300 Deg. K. *Solid-State Electronics*, vol. 11, 1968, pp. 599-602.
- 24-6. Van der Pauw, L. J.: A Method of Measuring Specific Resistivity and Hall Effect of Discs of Orbiting Shape. *Phillips Res. Rep.*, vol. 13, no. 1, Feb. 1958, pp. 1-9.

## BIBLIOGRAPHY

- Brice, J. C.: *The Growth of Crystals From Liquids*. North-Holland Publishing Co. (Amsterdam), 1973.
- Chalmers, Bruce: *The Principles of Solidification*. John Wiley & Sons, Inc., 1964.
- Gilman, J. J., ed.: *The Art and Science of Growing Crystals*. John Wiley & Sons, Inc., 1963.
- Witt, A. F.; Gatos, H. C.; et al.: Crystal Growth and Steady-State Segregation Under Zero Gravity: In Sb. *J. Electrochem. Soc.*, vol. 122, no. 2, Feb. 1975, pp. 276-283.



# 25. Zero-g Processing of Magnets

## Experiment MA-070

*D. J. Larson, Jr.<sup>a</sup>*

### ABSTRACT

The Zero-g Processing of Magnets Experiment (MA-070) was conducted during the Apollo-Soyuz Test Project mission to study contained solidification of high-coercive-strength magnetic materials in the low-g orbital environment. The magnetic compounds under study, manganese bismuth (MnBi) and copper-cobalt-cerium ((Cu, Co)<sub>5</sub> Ce), are representative of magnetic alloy systems that have the potential for the development of high coercive strength and high energy product.

The samples of 50 atomic percent (at.%) Bi-50 at.% Mn solidified in the low-g environment demonstrated a substantial improvement in the macroscopic chemical homogeneity. The Bi/MnBi directionally solidified eutectic flight samples exhibited markedly superior magnetic properties. Intrinsic coercive strengths in excess of 14 722 kA/m (185 kOe) have been measured in the low-g processed samples at a temperature of 77 K. This strength exceeds the maximum previously published value (8992 kA/m (113 kOe)) by 64 percent. The average value of inductance was improved by 76 percent and the energy product by 57 percent.

Additional results of this experiment indicate that, in the near absence of the gravitational body force, contained fluids will assume a lowest energy configuration that differs significantly from that found terrestrially. These results are of significance to any orbital processing that involves controlled heat transfer to, or from, a contained fluid.

<sup>a</sup>Grumman Aerospace Corporation, Bethpage, New York; Principal Investigator.

### INTRODUCTION

Although permanent magnets are essential to present-day technology, their importance is often overlooked. In fact, since the magnets are usually located inside equipment, most people either are not aware of their presence or take them for granted. However, these permanent magnets are the key components in many devices that are important to everyday life, such as telephone receivers, computers, radar equipment, loudspeakers, electrical meters, microphones, tape recorders, hearing aids, electric clocks, scientific instruments, magnetic door catches, and even children's toys (refs. 25-1 to 25-5).

In recent years, significant improvements in magnetic properties have resulted from the discovery of the exceptionally high anisotropy constants in compounds of cobalt (Co) and platinum (Pt) and of manganese (Mn) and bismuth (Bi) and in the cobalt-rare earth (RE) (and yttrium) systems (refs. 25-6 to 25-8). The magnitude of these improvements can be seen from table 25-I, in which the properties of some commercial magnets are compared with experimentally determined values of high-anisotropy magnets (ref. 25-9).

Because anisotropy energy results from the coupling between the spin of an electron and its orbital motion, the superior magnetic properties of high-anisotropy compounds are related to their crystal structures. The electron orbits are strongly directional and are associated with the lattice symmetry.

Most high-anisotropy compounds have a complex hexagonal lattice symmetry. The C-axis is the unique direction of easy magnetization, and the

TABLE 25-I.—Physical Properties of Magnetic Materials

Material	Energy product (BH) <sub>max</sub> <sup>a</sup> MTA/m (MGOe)	Coercive strength H <sub>c</sub> <sup>a</sup> kA/m (kOe)	Curie Temperature, K (°C)
Alnico	79 577 (10)	159.2 (2)	973 to 1073 (700 to 800)
Barium ferrite	31 931 (4)	238.7 (3)	996 (723)
CoPt	71 620 (9)	397.9 (5)	783 (510)
MnBi (directionally solidified)	<sup>a</sup> 58 092 (7.3)	2387.3 (30)	623 (350)
Co <sub>5</sub> -RE	<sup>b</sup> 190 986 (24)	<sup>bc</sup> 795.8 (10)	<sup>b</sup> 1143 (870)

<sup>a</sup>Powders.<sup>b</sup>Typical values. <sup>c</sup>Values as high as 2228.2 kA/m (28 kOe) were obtained in chill cast specimens of Co<sub>3</sub>Cu<sub>2</sub>Sm (ref. 25-10).

directions within the basal planes are uniformly hard to magnetize (ref. 25-9). The excess energy required to turn the direction of magnetization from an easy direction to a hard direction is the anisotropy energy. The anisotropy constant  $K$  is a measure of this energy and is related to the theoretical upper limit of the coercive strength

$$H_A = \frac{2K}{M_s}$$

where  $M_s$  is the saturation magnetization (ref. 25-11). Values of  $K$  range from 5 to 12 J/cm<sup>3</sup> (5 to 12 × 10<sup>7</sup> ergs/cm<sup>3</sup>) for Co<sub>5</sub>-RE-type compounds (refs. 25-4 and 25-9) and result in values of  $H_A$  from 11 937 to 19 894 kA/m (150 to 250 kOe). Besides the high anisotropy constants and high coercive strength, permanent magnets also must have a high intrinsic magnetization ( $4\pi M_s$ ) and a high Curie temperature ( $T_c$ ).

Because of the brittleness and reactivity of most magnetic compounds, powder metallurgy techniques principally have been used to fabricate high-coercive-strength magnets. Casting and solidification techniques have been possible only in a limited number of systems.

Fabrication of high-coercive-strength magnet materials from the liquid state could lead to a marked reduction in the number of processing steps and hence in cost. The magnets would have theoretical density, the fine particles would be protected from environmental attack, the magnets would have a high degree of particle alignment, and the magnets would only require a minimal amount of final machining. The requirement of

particle refinement and crystallographic and magnetic alignment has led several investigators to consider directional solidification as a means of achieving this morphology.

In space, gravity-driven convection and gravitationally dependent elemental segregation are absent in the liquid state. This fact has important consequences in the directional solidification of eutectic alloys. When grown on Earth, the rod or lamellar structure of the eutectic usually contains many imperfections (faults or terminations) due to local thermal and compositional gradients resulting from convection. It has been suggested that eutectic solidification in the absence of gravity will produce better alignment and fewer imperfections as a result of the reduction of these convection currents. Directional solidification in the orbital environment would then improve the magnetic coercivity and, perhaps, the energy product. The work reported here was undertaken to test the effect of the reduction of gravitationally dependent elemental segregation and convection on high-coercive-strength magnetic composites.

## EXPERIMENTAL PROCEDURE

Three sets of three samples were simultaneously processed in the course of this experiment. Three furnace cartridges, each housing three samples, were used. The sample arrangement within the furnace and each cartridge is shown in figures 25-1 and 25-2. Ampoules 1 and 2 were made from pyrolytic boron nitride; ampoule 3 was composed of fused silica (quartz). The thermal processing



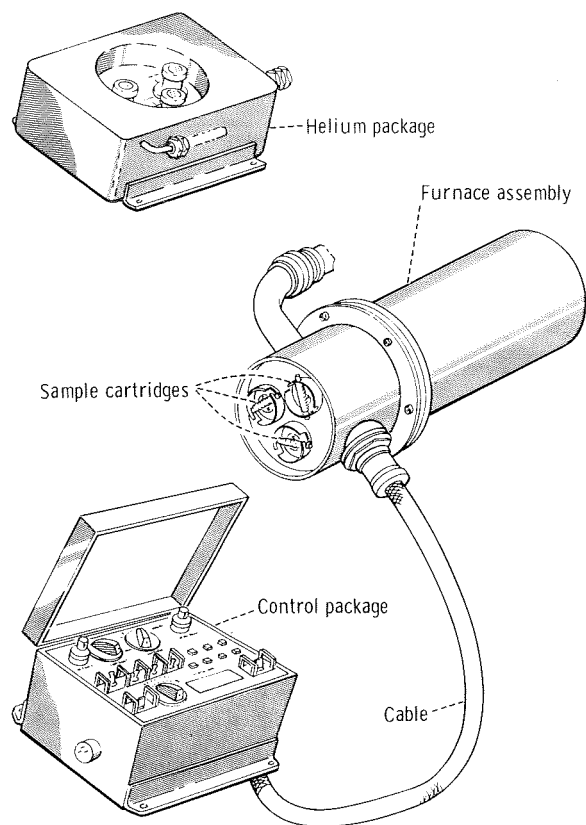


FIGURE 25-1.—The ASTP multipurpose electric furnace system.

was conducted in the multipurpose furnace (ref. 25-12) located in the Apollo-Soyuz Test Project (ASTP) docking module.

Experiment planning was based on thermal results from the prototype test. It was anticipated that the thermal environment for ampoule 1 (fig. 25-2) would be essentially isothermal over the temperature range of solidification. Ampoule 2 was expected to be exposed to a thermal gradient of  $30 \pm 2$  K/cm and ampoule 3 to a thermal gradient of  $60 \pm 3$  K/cm. The flight samples were actually exposed to conditions substantially different from planned conditions, and these differences will be detailed in the following paragraphs.

The prototype test was the only thermal test of the furnace cartridge that was internally instrumented with thermocouples. The prototype furnace differed from the flight furnace in that it was a single-tube furnace. The flight furnace was a three-tube furnace with the tubes equidistant from

the centerline of the furnace and arrayed  $120^\circ$  apart. The geometrical difference between the prototype, ground-based, and flight furnaces resulted in thermal environments that were not radially symmetric. This characteristic will be considered further in the section entitled "Phase Relations and Microstructure."

The longitudinal thermal profiles from the prototype test are shown in figure 25-3;  $T_{HL}$  is the heat-leveler temperature. The furnace temperature histories for the ground-based and flight tests are shown in figure 25-4. The time to reach operating temperature for the flight test was longer than that for the ground-based test, and the hold time was slightly shorter (45 minutes compared to 60 minutes). The cooling rate was greater during the flight test. Because all samples are completely solidified at helium injection, the differences in cooling rate after helium injection are not very significant.

The thermal history deduced for the type 1 flight ampoules is shown in figure 25-5. Because thermal data of this type were not provided for the ground-based test, no direct comparison can be made. It is safe to conclude, however, that the cooling rate of the flight samples was, on the average, 10 percent greater than that of the ground-based samples. The difference in cooling rate was greatest for ampoule 1 and least for ampoule 3.

The thermal gradient was calculated, as a function of time, for ampoule 2 and 3. These calculations were made from analytical data presented in reference 25-13. The variation of the thermal gradient, including the time during which the samples in the type 2 ampoules were directionally solidifying, is shown in figure 25-6. The temperature gradient for ampoule 2 varies from approximately 30 K/cm at the onset of directional solidification to 23.5 K/cm at the conclusion of solidification.

The variation of the thermal gradient in ampoule 3 (ref. 25-13) is shown in figure 25-7 for the lifetime of the experiment, and in figure 25-8 for the duration of the directional solidification. The thermal gradient during the period of maximum superheating was 80 K/cm; however, during the period of solidification, it varied from only 10.9 K/cm at the onset to 8.9 K/cm at the conclusion.

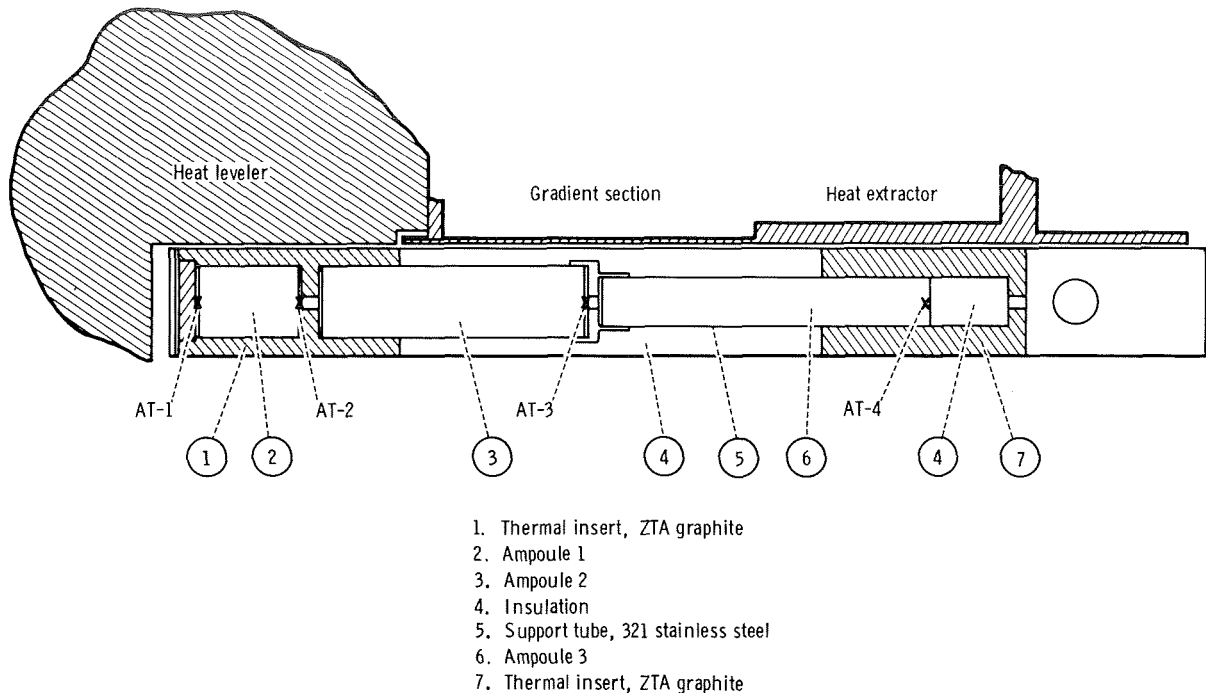


FIGURE 25-2.—Experiment MA-070 cartridge.

The value during solidification is lower than the thermal gradient anticipated from the prototype test by approximately 80 percent.

## EXPERIMENTAL RESULTS

### Fluid Statics

The fluid state before and during thermally controlled solidification is of critical importance to successful plane-front solidification of single-phase and polyphase alloys. This fluid state is complex and involves both static and dynamic components. Many of these fluid effects can be shown to be functionally dependent on gravity vector and level; therefore, it would be anticipated that orbital processing would have a substantial influence on them. The measurements required to conduct *in situ* and postflight dynamic analyses of the flight samples, processed during the ASTP flight, were deemed impossible. Thus, only static fluid analysis was conducted.

Previous orbital plane-front solidification experiments, performed during the Skylab Program,

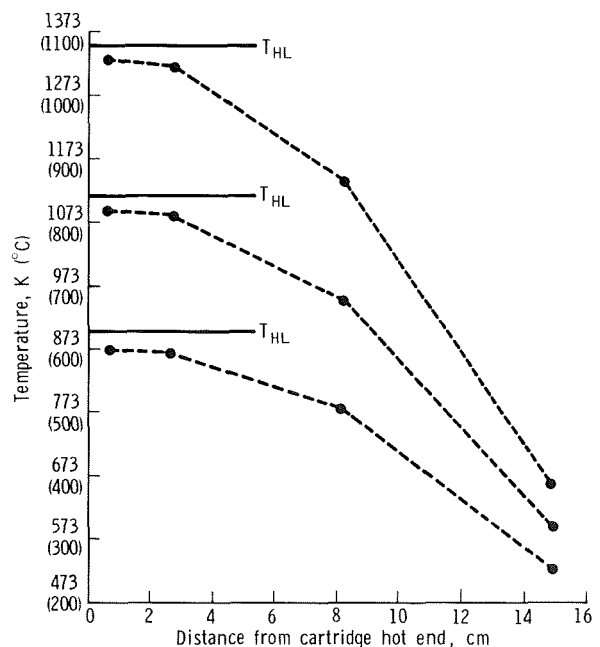


FIGURE 25-3.—Longitudinal temperature distribution within experiment cartridges; prototype test results.

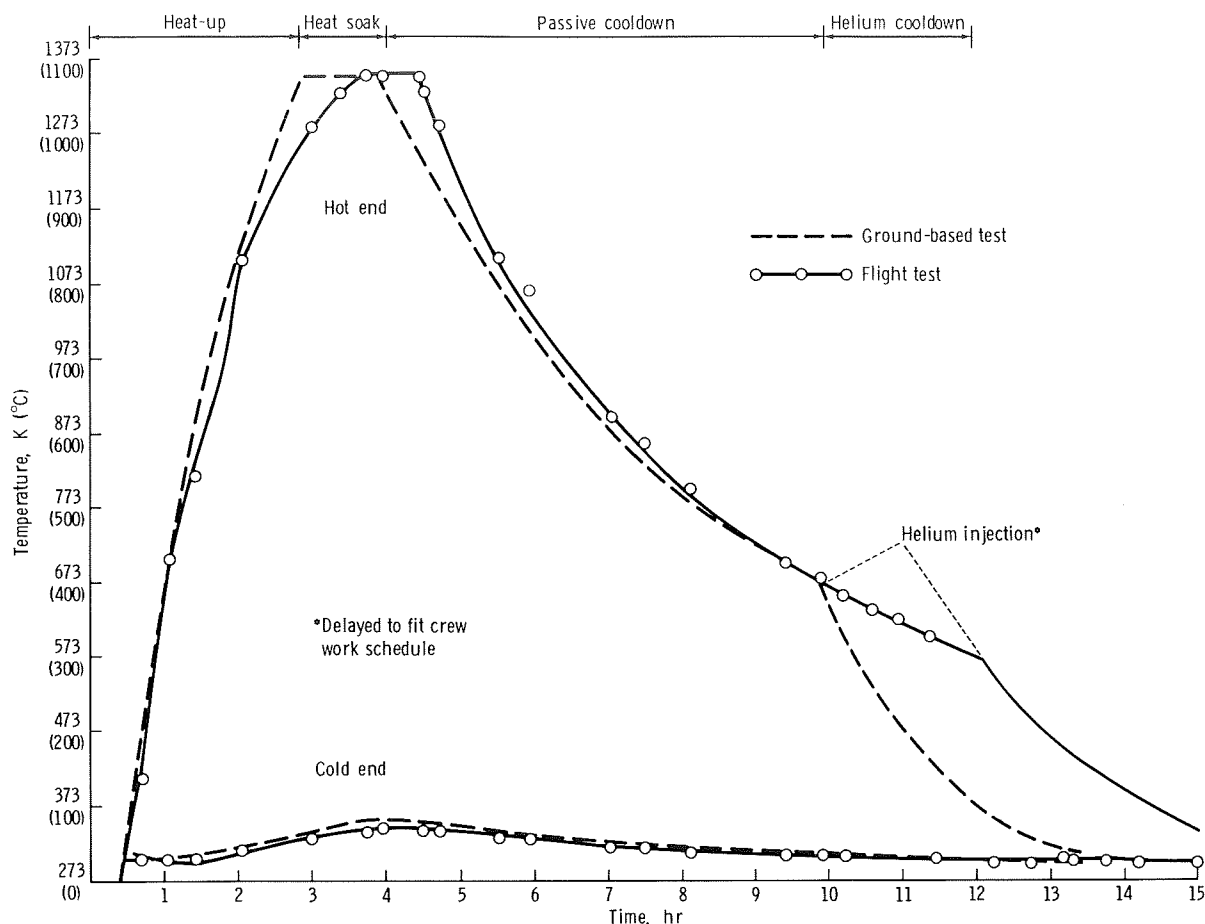


FIGURE 25-4.—Furnace temperature compared to elapsed time for the ASTP ground-based and flight tests.

indicated that the static fluid shape in the orbital environment was appreciably different from the static fluid shape documented terrestrially (refs. 25-14 and 25-15). If the static fluid configuration is changed, the heat flux, the thermal profile, and the solid/liquid-interface geometry may also change. Because these factors are critical to the plane-front solidification process, the success or failure of the experiment may depend on anticipating these changes. Previous work conducted in the drop tower facility at NASA Lewis Research Center (LeRC) has identified the fluid-crucible variables that are of primary consideration in a reduced gravity environment (refs. 25-16 to 25-18). The variables cited in the LeRC work are the fluid/crucible wetting angle  $\theta$ , the thermal gradient  $G$ , the crucible taper, the fluid/crucible fill factor, the crucible diameter to length ratio

$D/L$ , the gravity vector  $g$ , and the magnitude of the gravitational acceleration  $|g|$  (refs. 25-4 to 25-6). The LeRC results on fluid displacement are presented schematically in figure 25-9, and the static fluid configurations and displacements within a cylindrical crucible are illustrated in figure 25-10.

The fluid statics analysis of the samples was initiated while the flight ampoules were still in place in the experiment cartridges. Before the cartridges were disassembled, each was radiographed twice, at 90° angles, and the results were interpreted. A representative radiograph of the three cartridges is shown in figure 25-11. Several points to be noted in figure 25-11 will be detailed in subsequent sections, but may be summarized as follows.

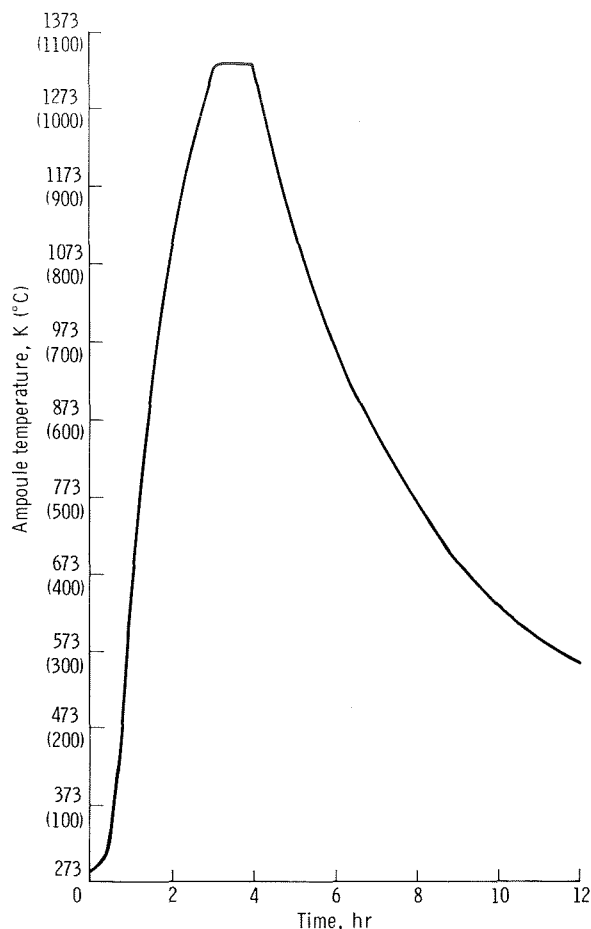


FIGURE 25-5.—Temperature profile for type 1 flight ampoules.

1. The type 1 samples (fig. 25-2) are of differing configurations, and the sample in cartridge 9 has leaked from the inner to the outer crucible.

2. The type 2 samples appear similar, but the sample in cartridge 8 appears higher than the other two.

3. The type 3 samples appear to be at differing heights. The sample in cartridge 9 is the highest, and that in cartridge 8 is the lowest. It is apparent that some material has been lost from ampoule 3 in cartridge 9, and subsequent analysis showed that some material had been lost from ampoule 3 of cartridge 7 as well. These displacement and configurational differences are all explicable on the basis of figures 25-9 and 25-10.

The fluid in the type 1 ampoules (50 atomic

percent (at.%) Bi, 50 at.% Mn) wet the inner crucible (pyrolytic boron nitride), and the crucible had a diameter-to-length ratio of approximately 0.71. The volumetric fill factors were varied within the type 1 ampoules, and the samples were processed isothermally ( $G = 0$ ). The fill factor for the ampoule within cartridge 7 was 0.95, that within cartridge 8 was 0.90, and that within cartridge 9 was 0.85. It was anticipated that variation from type 1 to type 4 fluid configuration would be noted (fig. 25-10). Unfortunately, the sample in cartridge 9 was lost through a vibrational failure; however, samples 7 and 8 were consistent with type 1 and intermediate configurations (type 1/type 4 behavior). This result was indicative of a low wetting angle, as previously mentioned.

The type 2 ampoules housed a wetting liquid (8 at.% cerium (Ce), 92 at.% copper (Cu) and cobalt (Co)) within a crucible. These samples, which were processed in a thermal gradient of approximately  $27 \pm 2$  K/cm, were not totally melted, but were melted back along the seed crystal such that, at peak furnace temperature, the fluid was in contact with a seed crystal. Figure 25-9 shows that a wetting fluid would be expected to be displaced toward the colder end of a thermal

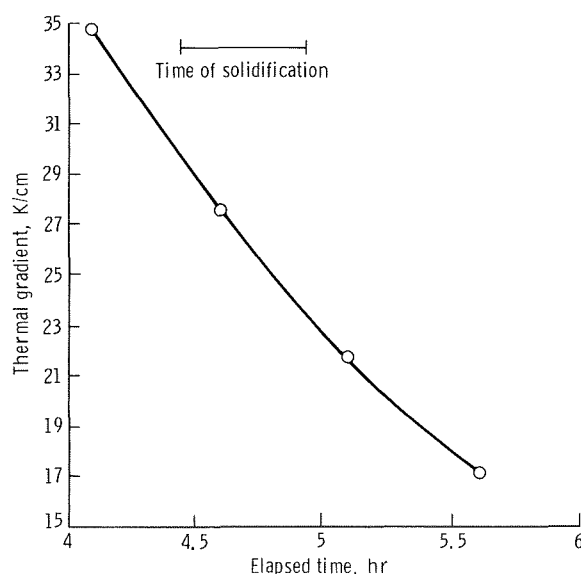


FIGURE 25-6.—Thermal gradient as a function of elapsed time for type 2 flight ampoules.

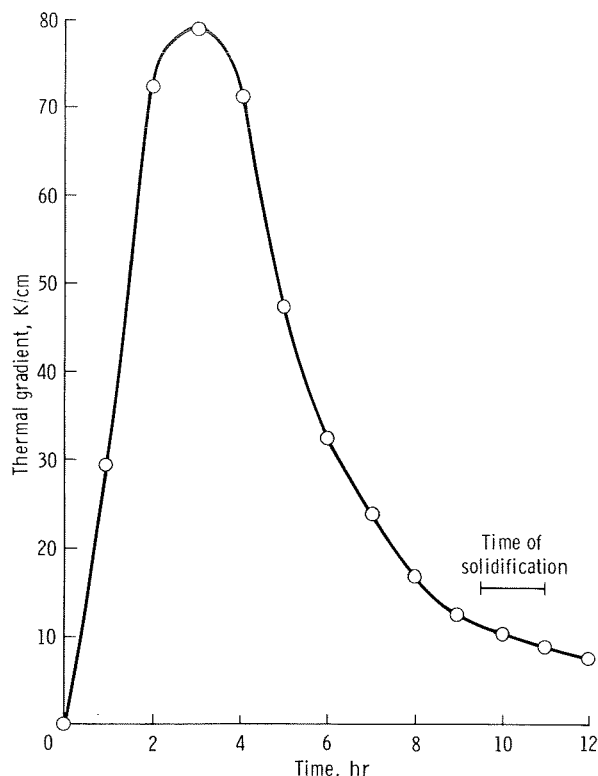


FIGURE 25-7.—Thermal gradient as a function of time for type 3 flight ampoules.

gradient; that is, toward the seed crystal. Because the seed crystal would be mechanically fixed, no fluid displacement would be expected. Therefore, the upward displacement of sample 2 in cartridge 8 must be explained on the basis of mechanical

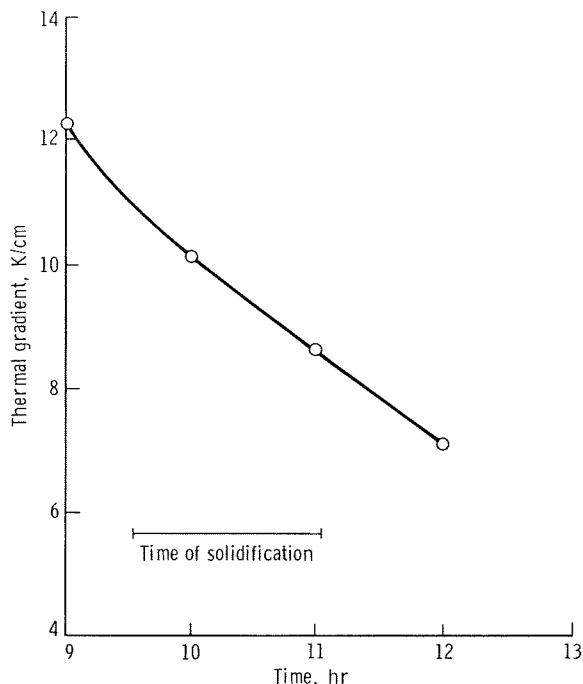


FIGURE 25-8.—Thermal gradient during time of solidification of type 3 flight ampoules.

displacement of the entire seed crystal, prior to the melting and solidification sequence.

The type 3 ampoules were intended to demonstrate the behavior of an unconstrained (no seed crystal), nonwetting fluid (97.8 at.% Bi, 2.2 at.% Mn) in a thermal gradient. The thermal gradient varied from 80 to 10 K/cm during the experiment. These fused silica ampoules had been backfilled

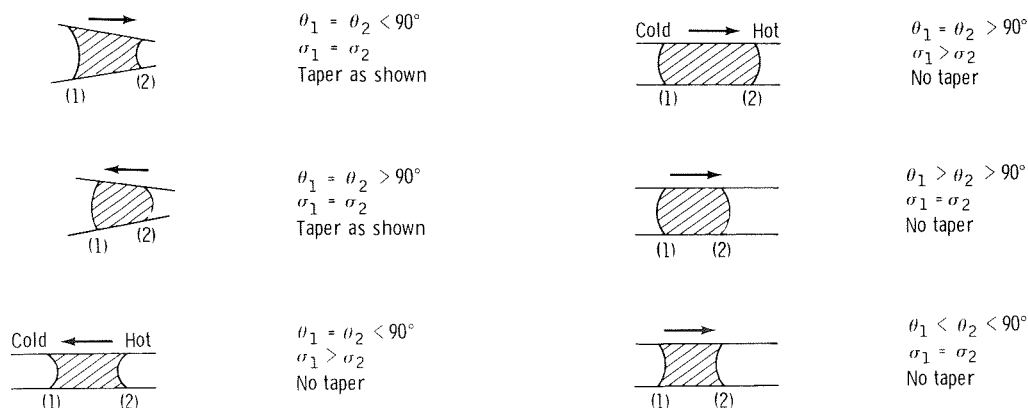


FIGURE 25-9.—Results on fluid displacement in a reduced gravity environment, where  $\sigma$  is surface tension.

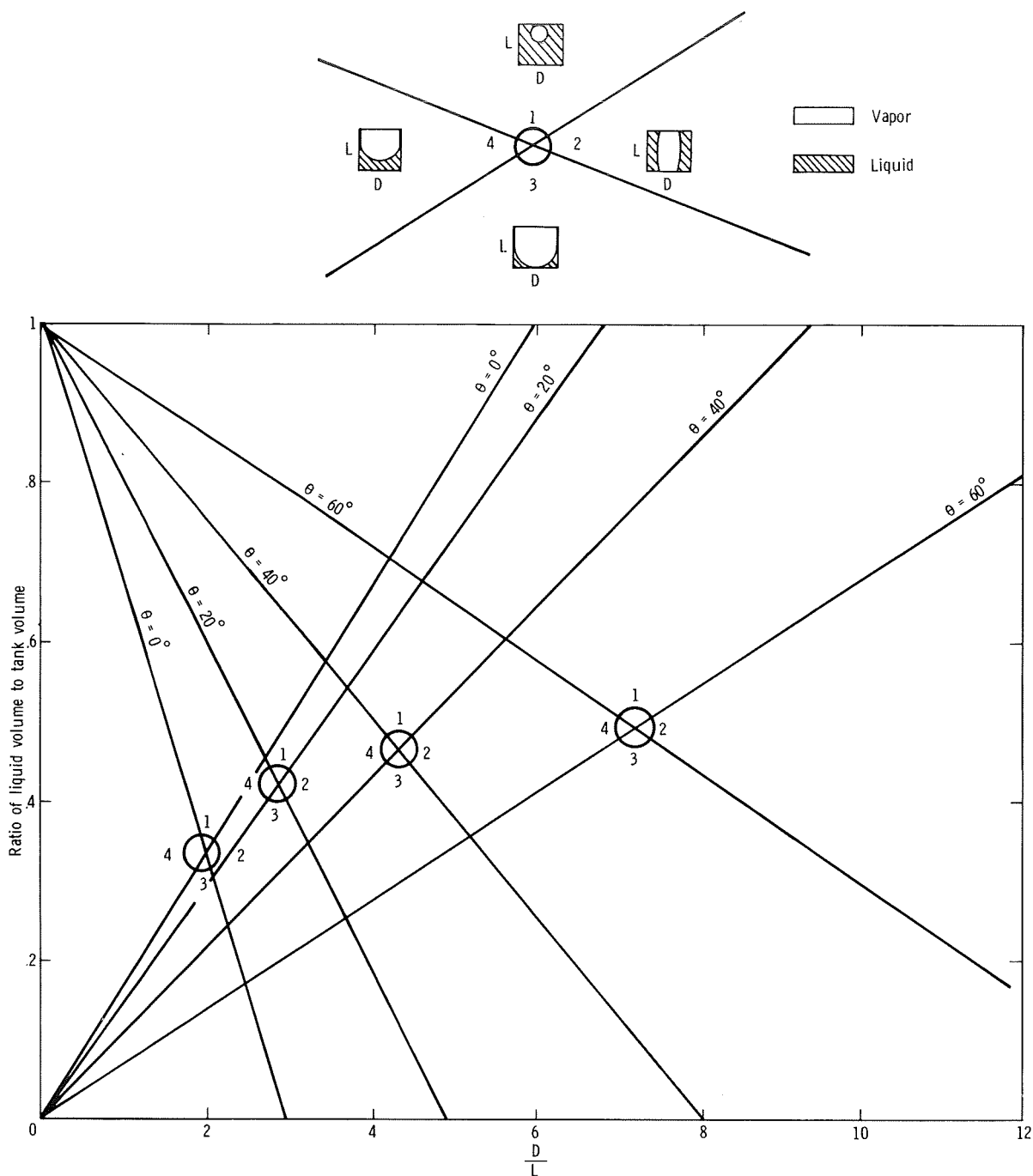


FIGURE 25-10.—Wetting fluid configurations in a cylindrical tank.

with an inert gas (argon) to suppress the possibility of thermal cavitation of the bismuth-rich liquid. Apparently, in the backfilling opera-

tion, a small amount of contaminant oxygen was allowed to enter ampoule 3 of cartridge 8. This small amount of oxygen was sufficient to alter the

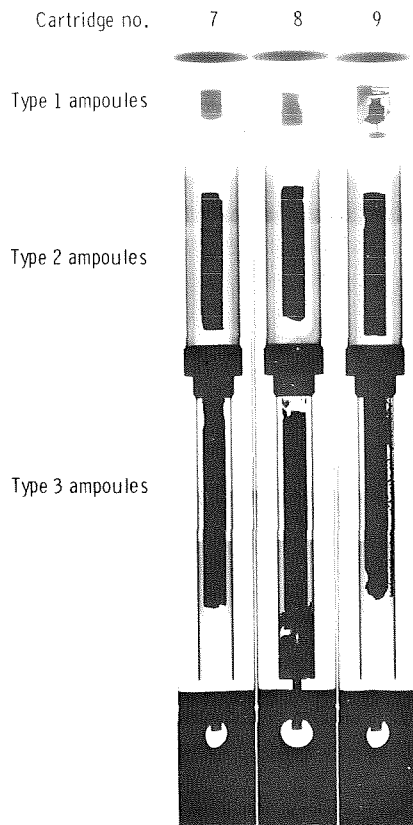


FIGURE 25-11.—X-ray radiograph of the three flight cartridges.

characteristics of the fluid/crucible interface from nonwetting to wetting, with concomitant changes in the fluid displacement behavior.

As would be anticipated from figure 25-9, the nonwetting fluid moved toward the hot end of the ampoule, whereas the wetting fluid moved in the opposite direction. This relative fluid displacement has been mentioned previously. Fluid displacement in the outermost ampoules resulted in the failure of the ampoules. The bismuth-rich fluid expands on solidification. The movement of the fluid toward the hot end of the ampoule resulted in a condition, during the latter stages of solidification, characterized by insufficient free volume in the ampoule to house the resultant solid. The pressure buildup within the ampoules was sufficient to cause cracking. This result should be considered in the planning of subse-

quent solidification experiments in which the fluid expands on solidification.

### Phase Relations and Microstructure

The thermal profile imposed on the type 3 ampoules substantially superheated the bismuth-rich liquid when the furnace was at peak temperature. This superheating necessitated the previously mentioned backfilling operation. To check the compatibility of the quartz ampoule with the superheated bismuth-rich liquid, quartz-bismuth samples were superheated within a differential thermal analysis unit. Results of these studies confirmed the compatibility of the bismuth and quartz at temperatures as high as 1050 K and determined that a liquid phase transition occurred in the liquid bismuth. Similar fluid-state transitions have been reported for other semimetals (ref. 25-19), but not previously for bismuth. The bismuth transition was characterized by large temperature hysteresis and was rate sensitive. At a rate of 10 K/min, the transition occurred at 988 K (715° C) on heating and 858 K (585° C) on cooling.

The samples within the type 1 ampoules (fig. 25-2) were composed of 50 at.% Bi and 50 at.% Mn. Three Bi-Mn phase diagrams have been proposed (refs. 25-20 to 25-22); all three were considered in this experiment. Ground-based investigation before the ASTP flight supported the liquidus results of references 25-21 and 25-22. Investigation performed in the analysis of the flight samples indicates that the phase diagram of reference 25-22, shown in figure 25-12, is preferable. This conclusion is based on qualitative metallographic evidence, and quantitative thermal and chemical analysis is in progress. The quantitative data will determine whether this preliminary conclusion is sound.

The samples in the type 1 ampoules, henceforth denoted as type 1 samples, were processed by isothermal lowering ( $G=0$ ) from a temperature above the liquidus temperature. A characteristic of the ground-based samples was appreciable gravitationally dependent macrosegregation. This chemical macrosegregation resulted in the location of almost all the primary peritectic

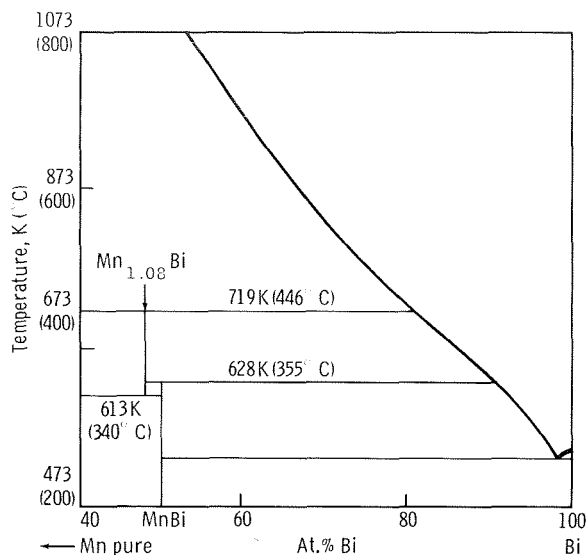


FIGURE 25-12.—Proposed Bi-Mn phase diagram (ref. 25-22).

Mn particles at the top of the sample. The volume fraction of the MnBi phase, determined by quantitative areal analysis, continuously decreased from the top of the ingot to the bottom. This variation, for a ground-based sample exposed to the same thermal cycle as the flight samples, is shown in figure 25-13. The average value for this sample was 29.5 volume percent of primary Mn and MnBi particles. The volume fraction of the primary MnBi phase in the flight samples was more uniformly distributed, and no primary Mn particles were identified. The average volume fraction of primary particles (fig. 25-13) was 35.7 percent, which may be an indication that the pro-

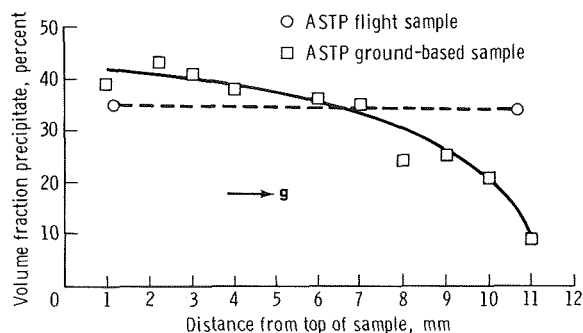


FIGURE 25-13.—Precipitate volume fraction as a function of distance from top of ground-based and flight samples.

peritectic Mn had reacted with the Bi-rich liquid to form MnBi. Because the samples are being conserved for detailed magnetic analysis (discussed in the following subsection), these measurements were made only on the upper and lower ends of the samples.

The flight samples were found to have large primary MnBi particles, lying on or near the surface, transverse to the longitudinal direction of the samples. This characteristic was unexpected and was not typical of the ground-based samples. The structure might indicate that the radial gradient experienced by the flight samples was greater than the longitudinal gradient and thus caused the primary crystallites to grow radially, in the direction of heat extraction. It is possible that gravitationally dependent convective flow caused a more uniform thermal distribution in the ground-based samples, or at least prevented alinement of the primary crystallites.

Some of the ground-based and low-g primary MnBi crystallites appeared to be composed of two distinctly different microstructural regions, as shown in figure 25-14, whereas others did not. This anomaly can be explained on the basis of the phase diagram shown in figure 25-12, in which two compositional modifications of MnBi are proposed. The first, MnBi (I), forms at a temperature of 719 K (446° C) and is manganese rich. The stoichiometric ratio proposed for this compound is  $\text{Mn}_{1.08}\text{Bi}/\text{Bi}_{1.00}$ . This phase decomposes eutectoidally to MnBi (II) plus Mn at a temperature of 613 K (340° C). The MnBi (I) phase forms directly from the melt at a temperature between 719 K (446° C) and 628 K (355° C). The MnBi (II) phase is equiatomic and forms directly from the melt at a temperature between 628 K (355° C) and 542 K (269° C), the eutectic temperature.

When the flight samples are considered, the crystallites forming at temperatures between 719 K (446° C) and 628 K (355° C) would be expected to react with residual liquid between 628 and 613 K to form MnBi (II). This reaction would be subject to the same diffusion barrier limitations common to all peritectic or peritectoid reactions and would not be expected to go to completion. The MnBi (I) core would then thermally decompose at a temperature below 613 K (340° C) to Mn plus MnBi (II). The MnBi (II) formed by way of the



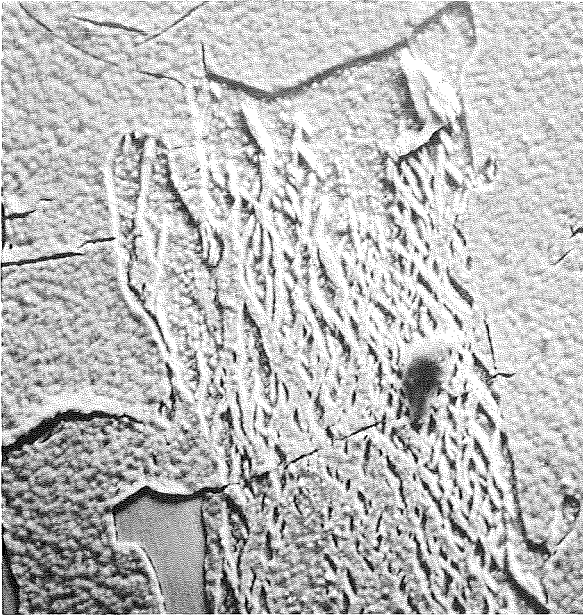


FIGURE 25-14.—Primary MnBi crystallite showing discrete morphological regions (900 $\times$ ).

peritectic reaction would then act as a heterogeneous nucleus for continued MnBi (II) precipitation at a temperature below 628 K (355° C). Sections of crystallites undergoing the preceding sequence would be expected to have a duplex

appearance. The MnBi (II) formed at a temperature below 628 K (355° C), by way of either peritectic reaction (fig. 25-15(a)) or proeutectic precipitation (fig. 25-15(b)), would be expected to appear monolithic, whereas residual MnBi (II) would be expected to show some evidence of the eutectoid decomposition. Crystallites forming at a temperature below 628 K (355° C) would be expected to be monolithic throughout.

The secondary MnBi (II) crystallites were found to be almost normal to the primary MnBi crystallites in the low-g samples (fig. 25-15(a)), whereas they were typically skewed in the one-g samples (fig. 25-15(b)). This may be an indication of decreased fluid motion, although other hypotheses may be proposed to explain the phenomenon.

In addition to having morphological differences, the secondary crystallites were finer in the flight samples than in the ground-based samples. One might have expected the opposite to be true because the rate of cooling through this temperature range was slower for the flight samples than for the ground-based samples. (See figure 25-4).

Processing of the samples in the type 2 ampoules was hampered by experimental limitations. The peak furnace temperature available was 1323

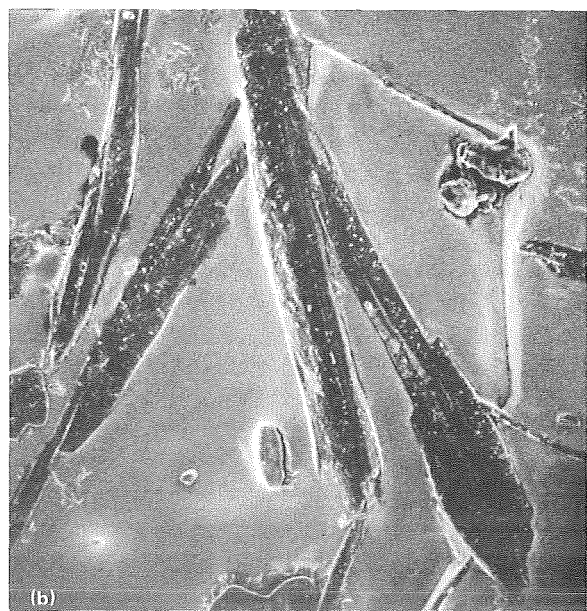
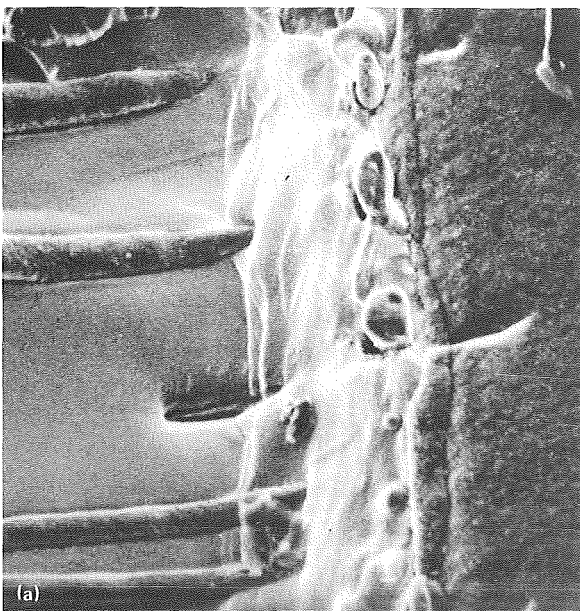


FIGURE 25-15.—Primary and secondary MnBi particles. (a) Flight sample (3750 $\times$ ). (b) Ground-based sample (1500 $\times$ ).

K (1050° C). To process most metallic-rare earth ( $M_5$  - RE) compounds would have required a furnace temperature of 1773 K (1500° C) to 1873 K (1600° C). This experimental constraint required that a serious alloy development program be undertaken. In the development program, varying combinations of copper, cobalt, and iron were considered as the metallic component, and varying combinations of cerium, samarium, and misch metal were considered as the rare earth component. On the basis of the alloy development data,<sup>1</sup> the maximum copper content, with cerium or misch metal alloying additions, provided the lowest liquidus temperatures, but sacrificed magnetic performance to experimental expediency.

In addition to thermal problems, crucible/fluid compatibility problems were encountered. In short, all rare earth liquids are extremely reactive and hence difficult to contain. The results of ground-based studies and literature surveys identified pyrolytic boron nitride as the most promising crucible material. This crucible material did react with the melt but seemed to establish a stable reaction product at the crucible/fluid interface that acted as a barrier to further reaction. Results of ground-based studies showed that the copper-cerium fluid was the least reactive of the fluids investigated.

The thermal and compatibility considerations, in concert, dictated selection of the copper/copper-cerium eutectic as the eutectic composite material for this experiment.

Analysis of the samples processed in the type 2 flight ampoules indicated that directional solidification was not achieved in this experiment. The reaction product at the fluid/crucible interface acted as a heterogeneous nucleation point ahead of the advancing solid/liquid interface, and coordinated eutectic growth was not achieved. Crystallites grew into the melt from the crucible wall.

Directional solidification of high-performance rare earth magnetic composites in orbit is still considered by the author to be an attractive possibility. Ideally, however, it would be conducted in a floating-zone directional-solidification

apparatus that could impose steep thermal gradients on the samples and achieve an absolute temperature of 2000 K ( $\approx 1750^\circ$  C). This would eliminate most of the experimental constraints, and the experiment could be performed properly.

The samples in the type 3 ampoules, henceforth denoted type 3 samples, were 97.8 at.% Bi and 2.2 at.% Mn, the eutectic composition. These samples were totally melted and were solidified in a temperature gradient of approximately 10 K/cm. Although the temperature gradient was substantially lower than anticipated, coordinated eutectic growth was achieved.

The microstructure in the region of initiation of solidification of ground-based and flight samples consisted of large primary bismuth dendrites with Bi/MnBi (II) eutectic in the interdendritic regions. The eutectic in this region was not well aligned with the imposed thermal gradient, as is shown in figure 25-16 for a ground-based sample. As the solidification progressed in the ground-based and flight samples, the primary bismuth dendrites became fewer in number and the interdendritic eutectic became progressively better aligned with the thermal gradient, as shown in figure 25-17 for



FIGURE 25-16.—Primary bismuth dendrites and secondary MnBi/Bi eutectic (650 $\times$ ).

<sup>1</sup>D. J. Larson, Jr., ASTP MA-070 Experiment Final Report, in press.



FIGURE 25-17.—Primary bismuth dendrites and aligned secondary MnBi/Bi eutectic (325 $\times$ ).

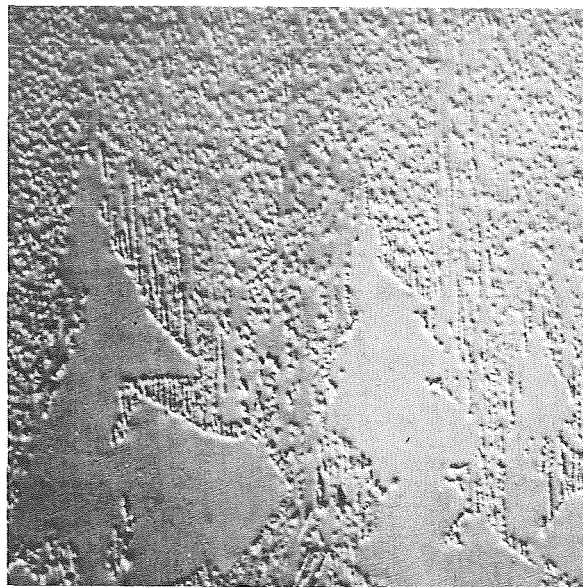


FIGURE 25-18.—Transition from dendritic to coordinated growth (75 $\times$ ).

a ground-based sample. Ultimately, there was a transition from dendritic to coordinated growth in both sample sets, as shown in figure 25-18 for a ground-based sample. The latter region of uniformly distributed and aligned magnetic particles was analyzed magnetically.

The Bi/MnBi eutectic system is a doubly faceted system (ref. 25-23). The rod shape, in cross section, is dependent on the growth rate during solidification. At slow growth rates, the rods have a cross section reminiscent of a chevron; whereas, at rapid rates, the cross section is nearly circular.

The rod cross section of the ASTP ground-based samples was chevronlike, as shown in figure 25-19. This result is consistent with previous findings (ref. 25-24). The rod diameter, however, was smaller in the flight samples than in the ground-based samples, and the cross section was circular. Particle sizes in the flight samples were typically 0.75 to 2.00  $\mu\text{m}$ , whereas the ground-based samples had particles of 2.0 to 4.0  $\mu\text{m}$  diameter. This result is somewhat surprising as it is generally understood that the rod diameter varies in a manner such that the square of the diameter ( $d^2$ ) times the growth rate  $R$  is a constant, over wide ranges of

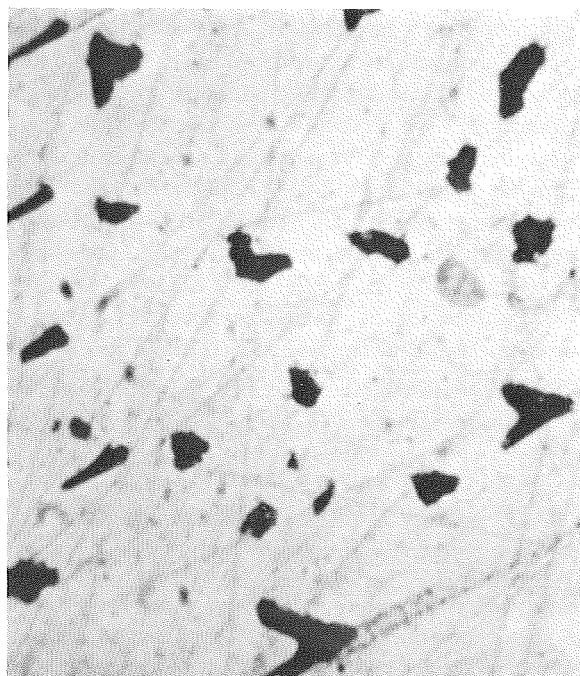


FIGURE 25-19.—Transverse section of ASTP flight sample 8C (2000 $\times$ ).

growth conditions (ref. 25-25). It was not anticipated that the growth rate would vary significantly between the ground-based and flight experiments; therefore, the cause for this variation in  $d$  would seem to reside within the "constant," which was not expected to vary.

Consideration of the various possibilities that would lead to a difference of this magnitude is continuing. One distinct possibility is thermal transport, which should be enhanced in a convectionless environment. This could impact both the solute profile ahead of the advancing interface (i.e., the diffusional coefficient in the previously mentioned constant) and the dendritic to coordinated transition. Although thermal transport would seem to be a likely source of difference, the lower limit of influence has been predicted analytically (ref. 25-26) and the experimental parameters for the ASTP flight experiment would seem to predict only a small influence. Investigation in this area will be pursued.

The refinement of the particle size in the flight experiment was also reflected in the magnetic results. These results will be detailed in the following subsection; however, it is important to note that the flight samples behaved magnetically like samples grown terrestrially about six times faster. This is equivalent to saying that, if  $d^2$  was determined by the ratio of the constant to the growth rate, then, for magnetic equivalence, the flight samples should have a particle diameter approximately 40 percent of the ground-based value. This conclusion is reasonably consistent with the particle size data, when the scatter bands are considered.

Another set of measurements was made to compare the flight samples with the ground-based samples. These measurements were of the MnBi lattice parameter. It was assumed in these measurements that all the MnBi used had 4 atoms/unit cell and was of a  $D_{6h}^4 - P6_3/mmc$  hexagonal structure. The bismuth was assumed to have 2 atoms/unit cell and a  $D_{3d}^5 - R\bar{3}m$  structure. A bismuth rhombohedral angle  $\alpha$  of  $57^\circ 14'$  was assumed throughout this study.

Measurements based on the MnBi  $\{10 \cdot 0\}$  and  $\{21 \cdot 0\}$  reflecting planes were used to calculate the MnBi lattice parameters. Because of the low volume fraction and crystallographic anisotropy

of the samples, it was impossible to consistently use lines other than these. The lattice parameter measured from the ground-based samples, in the coordinated growth region, was  $a_0 = 0.4255 \pm 0.0003$  nm ( $4.255 \pm 0.003$  Å). This value did not vary, within experimental error, over the length of the coordinated growth region. The value measured for the coordinated growth region of one of the flight samples was  $0.4306 \pm 0.0003$  nm ( $4.306 \pm 0.003$  Å). This difference is well beyond experimental error and is worthy of further consideration.

Slowly cooled bulk MnBi samples have been reported to have  $a_0$  lattice parameters varying from 0.425 to 0.427 nm (4.25 to 4.27 Å). Rapidly cooled bulk samples, and samples quenched from high temperatures, have  $a_0$  parameters as large as 0.433 nm (4.33 Å) (quenched from 673 K). The lattice parameter from the flight sample would indicate that it is equivalent to a sample quenched from an intermediate temperature or grown at a higher growth rate. This result is consistent with the investigator's magnetic and particle size conclusions.

### Magnetic Analysis

The optimum morphological array for a magnetic composite consists of fine, elongated, single-domain magnetic particles alined in a matrix, with the easy axis of magnetization parallel to the particle axis (ref. 25-27). The greater the magnetocrystalline anisotropy constant for the magnetic phase, and the finer the discrete magnetic particles (ref. 25-28), the higher the magnetic coercivity.

Directional solidification of magnetic composites is promising because the particle size of the magnetic phase in a rod eutectic is typically on the order of  $1 \mu\text{m}$ , the finely dispersed magnetic phase is protected from contaminating environmental effects, and the easy axis of magnetization of the magnetically anisotropic dispersed phase is frequently the crystallographic growth direction of the magnetic phase. Directional solidification of magnetic composites thus offers the potential for protection, alinement, and refinement of the dispersed magnetic phase.

As mentioned in the section entitled "Phase Relations and Microstructure," directional solidification was not achieved in the type 2 samples, and the magnetic properties of the ground-based and flight samples were essentially the same. The measured intrinsic coercivity  $H_{ci}$  of the magnetic phase was 82.8 kA/m (1.04 kOe) in both cases (within experimental error). As mentioned previously, the evolution of new experimental hardware is required to successfully accomplish the original goal of processing high performance rare earth magnetic composites.

The type 3 samples, however, were successfully processed; and because of their high performance, particularly at cryogenic temperatures, all measurements were made at the Francis Bitter National Magnet Laboratory of the Massachusetts Institute of Technology.

A typical Bitter magnet facility is shown in figure 25-20. The large cooling capability is required because 5 to 10 MW of power is passed through these magnets, depending on which unit is being used.

A standard two-coil pickup was used to make the measurements on the full length of the coordinated growth region. Sample sizes were approximately 2.5 cm long and 5 mm in diameter. A flux integration technique was used to map the B-H curves. The coil circuit used is shown

schematically in figure 25-21 and the integrator circuit is shown schematically in figure 25-22. The H-axis was calibrated from the known calibrated field parameters, and B was calibrated using a VP grade pure nickel standard. Measurements were made with this diagnostic system at 295, 197, and 77 K. Thermal loss problems prevented the investigators from making lower temperature measurements with this apparatus. Measurements were made of field strengths as great as 18.5 T (185 kG).

A typical set of B-H loops for rapidly grown ground-based material, based on test temperature, is shown in figure 25-23. These curves are typical of directionally solidified MnBi dispersed in a Bi matrix. The duplex curve at 77 K was analyzed using the theory of superposition, and the data are

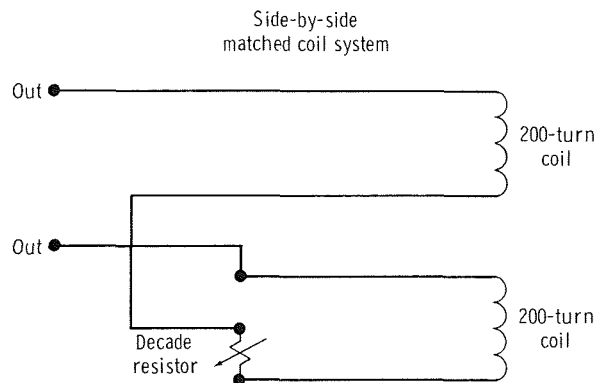


FIGURE 25-21.—Schematic of pickup coil circuit.

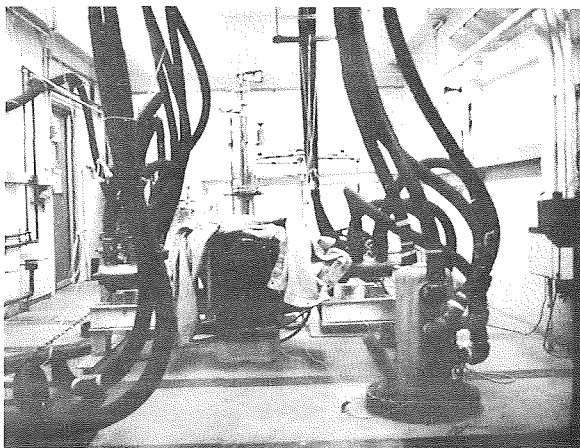


FIGURE 25-20.—Typical magnet facility at the Francis Bitter National Magnet Laboratory.

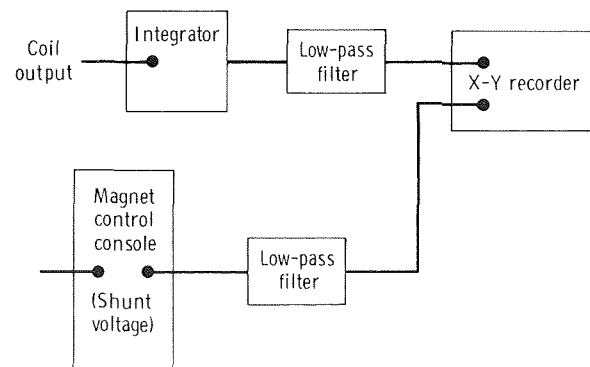


FIGURE 25-22.—Schematic of integrator circuit.

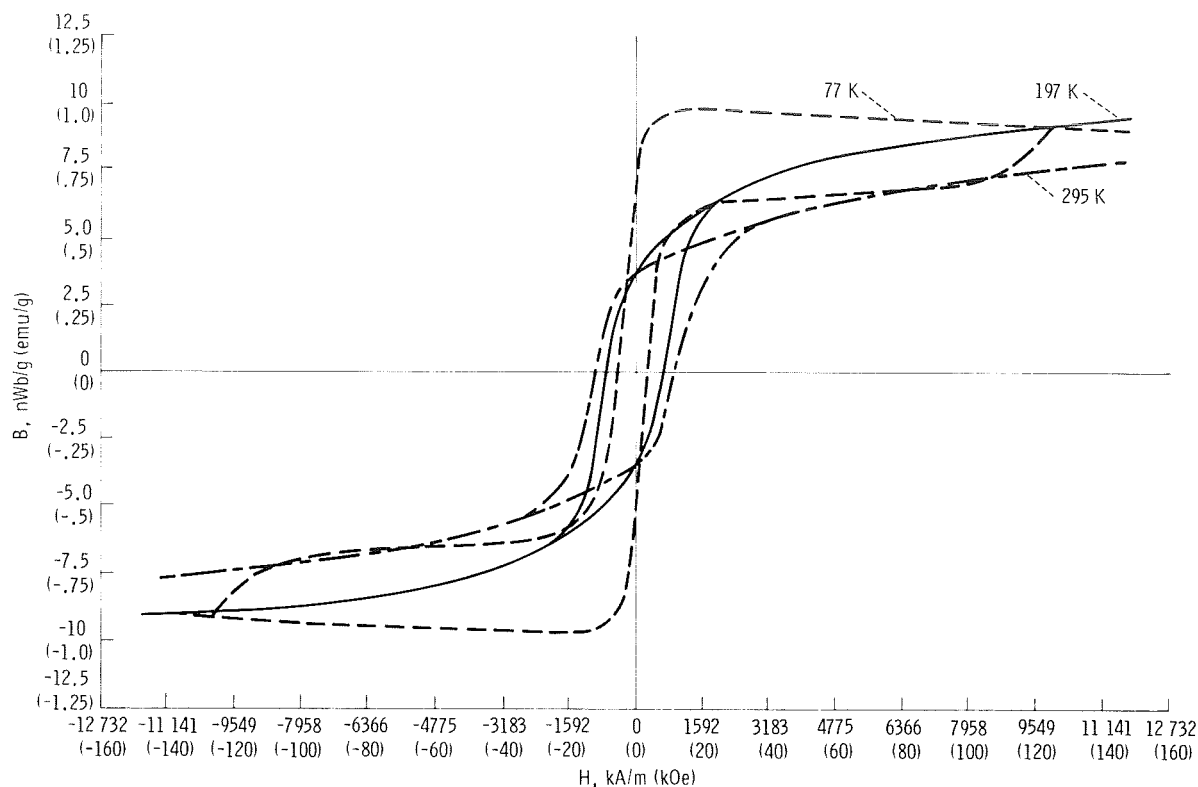


FIGURE 25-23.—Ground-based-sample MnBi/Bi eutectic composite B-H plot for three test temperatures.

reported in the manner of reference 25-24. The duplex loop reduces to two simple B-H loops as shown in figure 25-24.

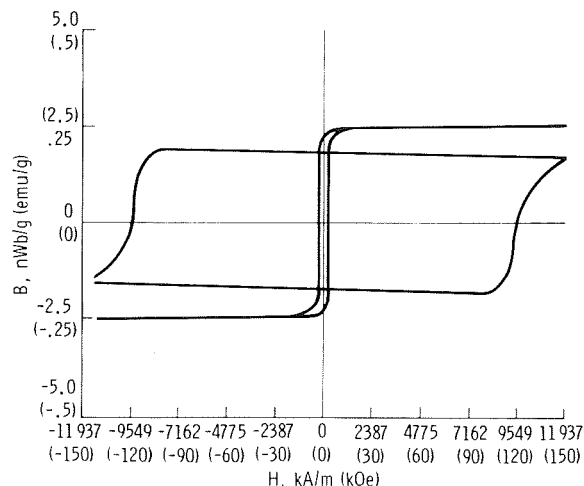


FIGURE 25-24.—Ground-based-sample B-H component loops at 77-K test temperature.

The apparatus previously described was relatively insensitive and prevented further reduction in sample size to enable more selective analyses in the coordinated growth region. A low-frequency vibrating-sample magnetometer was made available, and the general facility and the gearbox that changed the rotary motion to a vertical displacement in the field are shown in figures 25-25(a) and 25-25(b), respectively. The measurement technique and the hardware are fully described in reference 25-29. This apparatus substantially increased the resolution and enabled reduction of sample sizes by a factor of five. Also, measurements transverse to the magnetic flux lines could be made and the region of coordinated growth could be selectively analyzed. An additional advantage was use of the world's largest continuous-field magnet (23.5 T (235 kG)) and inclusion of measurements at a test temperature of 4.2 K.

The average room-temperature data for ground-based, flight, and literature samples are



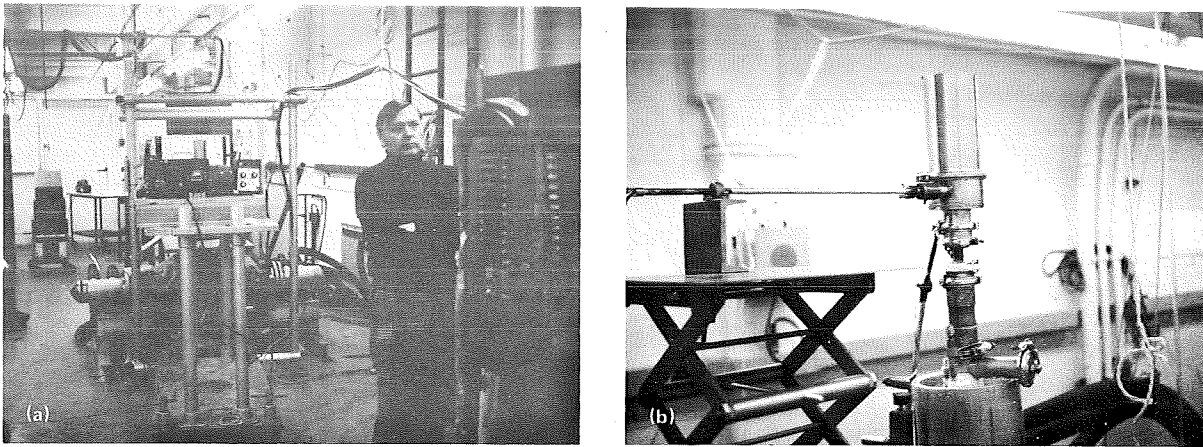


FIGURE 25-25.—Low-frequency vibrating-sample magnetometer. (a) Installation. (b) Gear mechanism.

presented in figure 25-26; the literature data are from reference 25-24. The square root of the growth rate was selected as the abscissa because it is a solidification parameter that should be proportional to the intrinsic coercive strength  $H_{ci}$ . It should be noted, however, that the literature data shown were measured on samples grown in a ther-

mal gradient  $G$  an order of magnitude greater than that of this experiment. Although a steeper thermal gradient might be expected to impact the physical properties, no definitive study to quantify this effect has been made. To that extent, the comparisons are imprecise.

Representative B-H loops for ground-based samples have been shown for the eutectic composite at temperatures of 295, 197, and 77 K in figure 25-23. The configuration at 4.2 K is virtually identical to that at 77 K, except that the intrinsic coercive strength is slightly lower.

The magnetic anisotropy energy (ref. 25-30) and the intrinsic coercive strength, of the room-temperature magnetic phase, have been shown to decrease with temperature. These values are reported to reach zero at temperatures of 85 and 80 K, respectively. Neutron diffraction measurements (ref. 25-31) have suggested that small positive values may be found even at very low temperatures. The  $H_{ci}$  data for the ASTP ground-based and flight samples support the latter contention to a temperature as low as 4.2 K. Representative curves showing the temperature dependence of the room-temperature magnetic phase, from ground-based and flight samples, are shown in figure 25-27.

At temperatures below room temperature, a second magnetic component having extremely high coercivity appears (ref. 25-24). No magnetic property data, as a function of growth rate, have been published for cryogenic temperatures;

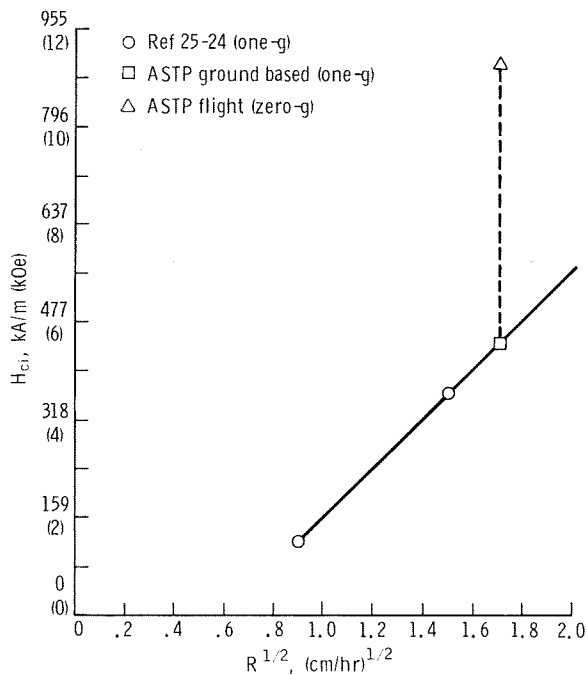


FIGURE 25-26.—Intrinsic coercive strength  $H_{ci}$  compared to the square root of growth rate  $R^{1/2}$  for as-grown Bi/MnBi eutectic composites.

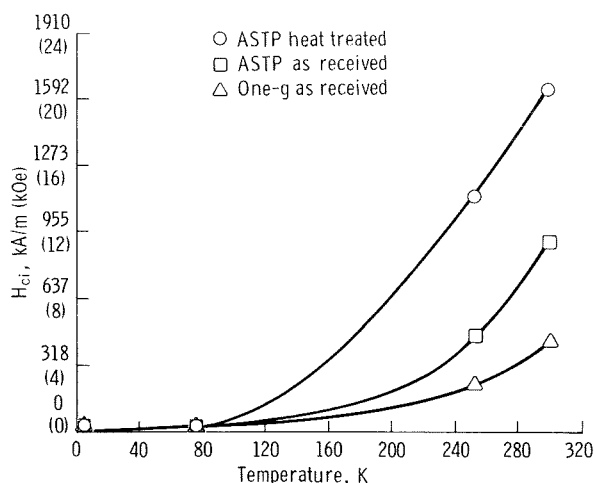


FIGURE 25-27.—Intrinsic coercive strength  $H_{ci}$  as a function of temperature for the room-temperature MnBi phase.

therefore, the ASTP flight-sample low-temperature data have been superimposed on the temperature-dependence results of reference 25-32, as shown in figure 25-28. The literature data shown in figure 25-28 are from samples grown at a rate of 75 cm/hr. It has been reported that the low-temperature component appears only in samples grown at freezing rates in excess of 75 cm/hr (ref. 25-24); however, the ASTP flight data for samples grown at a rate of 3 cm/hr are not consistent with this conclusion.

The average values of intrinsic coercive strength for the ASTP ground-based and flight samples are shown in table 25-II. Work has continued, however, in the analysis of selected sample sections. An unexpected result, but confirmed by other experts on MnBi behavior,<sup>2</sup> is illustrated in figure 25-29. Sections of this type, from the coordinated growth regions of the flight samples, demonstrate the high field coercivity associated with the low-temperature component, but show positive-field "collapse" when field strength is reduced.

Thermal cycling of this sample showed that the positive-field collapse occurred at lower positive fields at 4.2 K than at 77 K. Restated, these results show a wider hysteresis in field strength at 4.2 K than at 77 K.

<sup>2</sup>C. D. Graham, Jr., and M. R. Notis, personal communication.

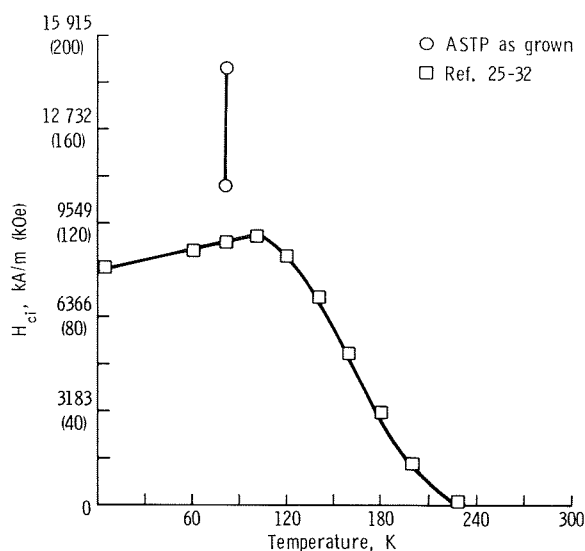


FIGURE 25-28.—Intrinsic coercive strength  $H_{ci}$  as a function of temperature for the low-temperature component.

Some samples were heat treated at 90 percent of the absolute melting point for a period of 24 hours, then furnace cooled. This heat treatment has been reported to substantially improve the

TABLE 25-II.—Intrinsic Coercive Strength as a Function of Test Temperature  
[Average values]

Sample	Temperature, K	Intrinsic coercive strength, kA/m (kOe)
ASTP ground-based	295	437.7 (5.5)
ASTP flight 8C	295	869.0 (10.92)
	253	467.9 (5.88)
	77	10 743.0 (135)
9C	295	1 108.5 (13.93)
	253	870.6 (10.94)
	77	14 721.8 (185)
10C	295	814.9 (10.24)
	77	9 350.4 (117.5)
	4.2	8 116.9 (102)
Heat-treated	295	1 655.2 (20.8)
	243	1 040.9 (13.08)
	77	8 753.5 (110)
	4.2	8 116.9 (102)



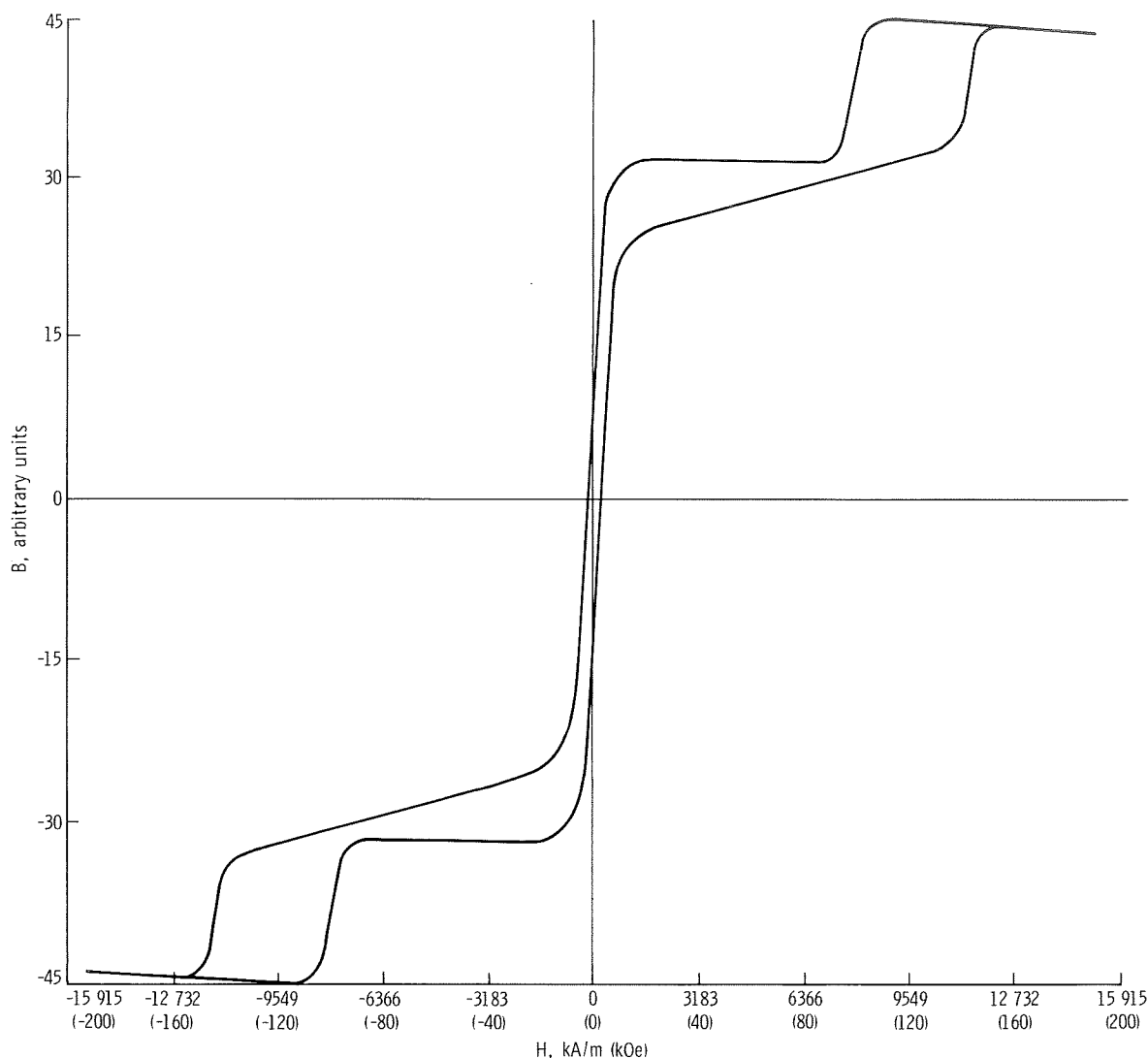


FIGURE 25-29.—As-grown flight sample 9C B-H loop at 77-K test temperature.

room-temperature intrinsic coercive strength. The  $H_{ci}$  of this sample increased from 912.8 to 1655.2 kA/m (11.47 to 20.8 kOe), an 80-percent improvement. The heat treatment squared the B-H loop and increased the value of  $H_{ci}$  at room temperature, as reported in reference 25-24. The temperature behavior of the room-temperature component of the heat-treated flight sample is shown in figure 25-27. Essentially, the magnitudes are different but the behavior as a function of temperature is consistent.

The heat-treated value of intrinsic coercive strength as a function of rod diameter is shown in

figure 25-30. Rod diameter has been selected for the abscissa in this case because the thermal-mechanical state of the composite should be equilibrated. The results indicate that the heat treatment is a determining factor in the final value of  $H_{ci}$ . The ASTP data points are entirely consistent with those presented in the literature for similar heat treatments.

A final room-temperature measurement was made on the heat-treated sample. A B-H curve, with the rods transverse to the magnetic field, was measured and is shown in figure 25-31. As may be seen, the sample was not saturated even at the

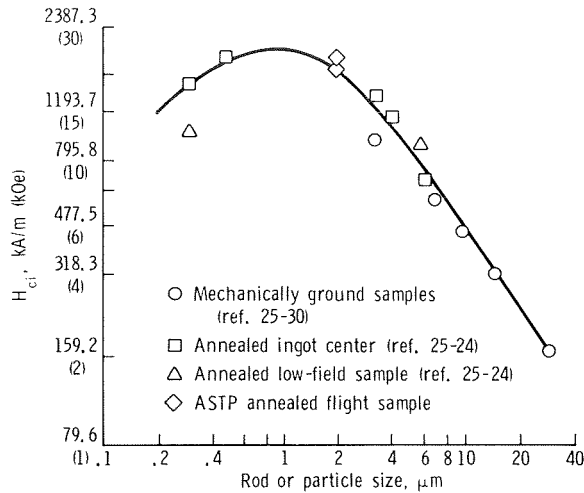


FIGURE 25-30.—Intrinsic coercive strength  $H_{ci}$  at room temperature compared to MnBi particle size, for heat-treated MnBi/Bi eutectic composites and mechanically ground MnBi particles.

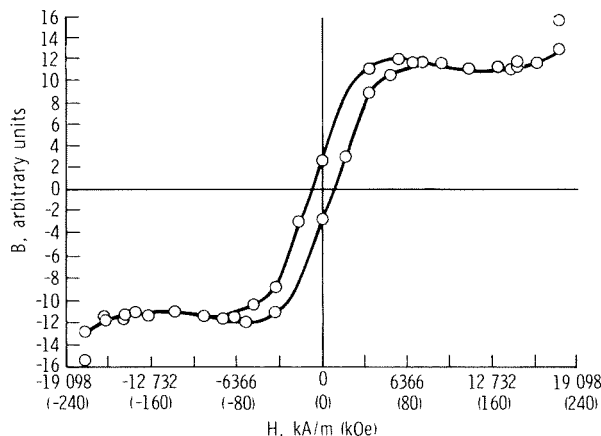


FIGURE 25-31.—Room-temperature B-H loop, with transverse field, for flight sample 11C (heat treated).

highest field strength 22.3 T (223 kG). This result was entirely expected because theoretical estimates (ref. 25-33) of the coercivity in a transverse field predict that saturation will not occur until a field strength of 15 915 to 19 894 kA/m (200 to 250 kOe) has been attained. It would appear that a field of 25 T (250 kG) would be barely adequate for saturation studies.

In addition to intrinsic coercive strength, the

magnetization of the ASTP ground-based and flight samples has also been measured. The average magnetization, for magnetic MnBi/Bi eutectic composites, is reported in the literature to be 6 nWb/g (0.6 emu/g) (ref. 25-24). The average value for the ASTP flight samples of 10.5 nWb/g (1.05 emu/g) is a substantial improvement over the previously mentioned value; however, magnetizations an order of magnitude greater were measured within these samples, on their first exposures to a magnetic field. These results could not be reproduced, and subsequent measurements gave the value of 10.5 nWb/g (1.05 emu/g). This variation in magnetization has been noted in a previous study (ref. 25-32) but remains unexplained. The variation indicates that, although the ASTP average value of magnetization has shown improvement over the literature value, an additional improvement may well be possible with proper processing.

In summary, orbital processing of the eutectic MnBi/Bi composite has led to enhanced values of critical magnetic parameters B and H through particle refinement and alinement. The average improvement within these parameters was 60 percent. Although the precise reason for these improvements has not been ascertained, it seems reasonable to presume that the reduction of detrimental gravitationally dependent phenomena, during solidification, has resulted in these improvements in the as-received composites.

The magnetic results from the as-received type 1 samples showed duplex behavior at room temperature. This behavior could be the result of a shift in the onset temperature of the low-temperature magnetic component from 240 to 295 K, or could result from particle size effects. In addition, substantial differences in magnetic behavior were noted, depending on the orientation of the sample in the field. Because the microstructural analysis of the flight samples has shown that the microstructure is complex but nonrandom and that there are substantial differences in the MnBi particle size, it was decided to defer the magnetic analysis of these samples until all the necessary magnetic analyses of the alined, constant-particle-size eutectic samples have been completed.

## SUMMARY AND CONCLUSIONS

The intent of this project was to study the contained solidification of magnetic materials in a low-g environment. Although the work is not yet complete, the following conclusions may be drawn.

1. Fluid static configurations in a low-g environment were appreciably different than in one-g, but were found to agree well with theory.

2. Bismuth undergoes a liquid phase transition, with large hysteresis, at temperatures of 988 K on heating and 858 K on cooling.

3. The Mn-Bi phase diagram presented in reference 25-22 is to be preferred.

4. Macroscopic chemical segregation due to gravitationally dependent buoyancy forces is minimal in a low-g environment.

5. The number and size distribution of orbitally processed primary crystals is significantly different in the flight samples.

6. The intrinsic coercive strengths of as-grown low-g MnBi/Bi eutectic samples greatly exceed any values previously reported for this magnetic composite (>60 percent).

7. The solidification product from the orbital processing of the Bi/MnBi faceted rod eutectics differs in particle size and shape, lattice parameter, and magnetic properties from equivalently processed terrestrial samples.

## REFERENCES

- 25-1. Polgreen, G. R.: *New Applications of Modern Magnets*. Macdonald & Co. (London), 1966.
- 25-2. Lee, Eric W.: *Magnetism*. Pelican Books (London), 1963.
- 25-3. Iden, D. J.; Ehrenfried, C. E.; and Garrett, H. J.: Present and Future Applications of High-Coercive-Force Magnets. *Magnetism and Magnetic Materials*, AIP Conference Proceedings, no. 5, 1971, p. 1026.
- 25-4. Strnat, K. J.: The Recent Development of Permanent Magnetic Materials Containing Rare Earth Metals. AFML-TR-69-299, Wright-Patterson AFB, June 1970.
- 25-5. Becker, Joseph J.; Luborsky, Fred E.; and Martin, D. Luther: Permanent Magnet Materials. *IEEE Trans. Magn.*, vol. MAG-4, no. 2, June 1968, pp. 84-99.
- 25-6. Hoffer, G.; and Strnat, K.: Magnetocrystalline Anisotropy of  $\text{YCo}_5$  and  $\text{Y}_2\text{Co}_{17}$ . *IEEE Trans. Magn.*, vol. MAG-2, no. 3, Sept. 1966, pp. 487-489.
- 25-7. Strnat, K.; Hoffer, G.; et al.: A Family of New Cobalt-Base Permanent Magnet Materials. *J. Appl. Phys.*, vol. 38, no. 3, Mar. 1, 1967, pp. 1001-1002.
- 25-8. Buschow, K. H. J.; and Velge, W. A. J. J.: Permanent Magnetic Materials of Rare Earth Cobalt Compounds. *Z. Angew. Phys.*, vol. 26, no. 2, 1969, pp. 157-160.
- 25-9. Strnat, K. J.: Cobalt-Rare Earth Alloys as Promising New Permanent Magnet Materials. *Cobalt*, vol. 36, Sept. 1967, pp. 133-143.
- 25-10. Nesbitt, E. A.: New Permanent Magnet Materials Containing Rare-Earth Metals. *J. Appl. Phys.*, vol. 40, no. 3, Mar. 1, 1969, pp. 1259-1265.
- 25-11. Faltermayer, Edmund: The Energy "Joyride" Is Over. *Fortune*, vol. 86, no. 3, Sept. 1972, pp. 99-101.
- 25-12. Prototype Test Report for MA-010 Experiment Cartridges. Tech. Rep. WANL-TME-2867, Westinghouse Electric Corp., Astronuclear Lab., May 1975.
- 25-13. Thermal Analysis of the Apollo Soyuz Test Project MA-070 Experiment in the Flight Environment. Tech. Letter ASD-EP44-22740 (SO-E017-Par III) H72, Teledyne Brown Engineering, Jan. 21, 1976.
- 25-14. Witt, A. F.; Gatos, H. C.; et al.: Steady State Growth and Segregation Under Zero Gravity: InSb. *Proceedings of the Third Space Processing Symposium—Skylab Results*. NASA TM X-70252, 1974, pp. 275-288.
- 25-15. Hasemeyer, Earl A.; Lovoy, Charles V.; and Lacy, L. L.: Skylab Experiment M566 Copper-Aluminum Eutectic. *Proceedings of the Third Space Processing Symposium—Skylab Results*. NASA TM X-70252, 1974, pp. 457-461.
- 25-16. Clodfelter, Robert G.; and Lewis, Roger C.: Fluid Studies in a Zero Gravity Environment. Tech. Note 61-84, Wright-Patterson AFB, June 1961.
- 25-17. Clodfelter, Robert G.: Fluid Mechanics and Tankage Design for Low Gravity Environments. ASD-TDR-63-506, Wright-Patterson AFB, Sept. 1963.
- 25-18. Clodfelter, Robert Glen: Low Gravity Pool Boiling Heat Transfer. APL-TDR-64-19, Wright-Patterson AFB, Mar. 1964.

- 25-19. Vezzoli, Gary C.: Electrical Resistance of Liquid Sulfur to 420° C and of Liquid Selenium to 700° C. *American Ceram. Soc. J.*, vol. 55, no. 2, Feb. 1972, pp. 65-67.
- 25-20. Hansen, Max: *Constitution of Binary Alloys*. McGraw-Hill Book Co., 1958, pp. 318-321.
- 25-21. Willis, B. T. M.; and Rooksby, H. P.: Magnetic Transitions and Structural Changes in Hexagonal Manganese Compounds. *Proc. Phys. Soc. (London)*, vol. 67B, Apr. 1954, pp. 290-296.
- 25-22. Chen, Tu; and Stutius, W. E.: The Phase Transformation and Physical Properties of the MnBi and Mn<sub>1-08</sub>Bi Compounds. *IEEE Trans. Magn.*, vol. MAG-10, no. 3, Sept. 1974, pp. 581-586.
- 25-23. Hunt, J. D.; and Jackson, K. A.: Binary Eutectic Solidification. *Trans. Met. Soc. AIME*, vol. 236, no. 6, June 1966, pp. 843-852.
- 25-24. Boulbes, J. C.; Kraft, R. W.; Notis, M. R.; and Graham, C. D., Jr.: Structural and Magnetic Properties of the Bi-MnBi Controlled Eutectic. *Proceedings of the Conference on In Situ Composites*, Vol. III, National Materials Advisory Board Spec. Publ. 308, Jan. 1973, pp. 61-78.
- 25-25. Cline, H. E.; and Livingston, J. D.: High-Speed Directional Solidification of Sn-Pb Eutectic Alloys. *Trans. Met. Soc. AIME*, vol. 245, no. 9, Sept. 1969, pp. 1987-1992.
- 25-26. Verhoeven, J. D.; Warner, J. C.; and Gibson, E. D.: Effect of Thermotransport Upon Off-Eutectic Composite Growth in Sn-Pb Alloys. *Met. Trans.*, vol. 3, no. 6, June 1972, pp. 1437-1441.
- 25-27. Albright, D. L.; Conard, G. P., II; and Kraft, R. W.: Magnetic Behavior of a Eutectic Alloy Featuring an Aligned Array of Iron Rods. *J. Appl. Phys.*, vol. 38, no. 7, June 1967, pp. 2919-2923.
- 25-28. Stoner, E. C.; and Wohlfarth, E. P.: A Mechanism of Magnetic Hysteresis in Heterogeneous Alloys. *Phil. Trans. Roy. Soc. London*, vol. A240, May 1948, pp. 599-642.
- 25-29. Foner, Simon: Versatile and Sensitive Vibrating-Sample Magnetometer. *Rev. Sci. Instrum.*, vol. 30, no. 7, July 1959, pp. 548-557.
- 25-30. Guillaud, C.: *Ferromagnetism of Binary Alloys*. Ph. D. Thesis, Univ. of Strasbourg, 1943.
- 25-31. Roberts, B. W.: Neutron Diffraction Study of the Structures and Magnetic Properties of Manganese Bismuthide. *Phys. Rev.*, vol. 104, no. 3, Nov. 1, 1956, pp. 607-616.
- 25-32. Boulbes, J. C.: Structural and Magnetic Properties of the Bi-Mn-Bi and Controlled Eutectics. M. S. Thesis, Lehigh Univ., 1971.
- 25-33. Noothoven van Goor, J. M.; and Zijlstra, H.: Structural and Magnetic Properties of a Bi-MnBi Composite. *J. Appl. Phys.*, vol. 39, no. 12, Nov. 1968, pp. 5471-5474.

# 26. Crystal Growth From the Vapor Phase

## Experiment MA-085

*H. Wiedemeier,<sup>a†</sup> H. Sadeek,<sup>a</sup> F. C. Klaessig,<sup>a</sup> M. Norek,<sup>a</sup> and R. Santandrea<sup>a</sup>*

### ABSTRACT

The positive effects of microgravity on crystal quality and fundamental properties of the vapor transport reaction were established by analyzing the results of three transport experiments on multicomponent systems performed during the Apollo-Soyuz mission. The systems employed, consisting of germanium selenide, tellurium, germanium tetraiodide (transport agent), germanium monosulfide, germanium tetrachloride (transport agent), and argon (inert atmosphere), were

1. System A:  $\text{GeSe}_{0.99}\text{Te}_{0.01} - \text{GeI}_4$
2. System B:  $\text{GeS}_{0.98}\text{Se}_{0.02} - \text{GeCl}_4$
3. System C:  $\text{GeS} - \text{GeCl}_4 - \text{Ar}$

The crystallographic analysis is based on a direct comparison of space-grown and ground-based (prototype) crystals, by means of X-ray diffraction, microprobe, microscopic, and chemical etching techniques. The results demonstrate a considerable improvement of the space-grown crystals in terms of chemical and crystalline homogeneity, surface morphology, and bulk perfection relative to ground specimens. The confirmation of greater mass transport rates than predicted for a microgravity environment by existing vapor transport models is of basic scientific and practical importance for the improvement of transport models and techniques on Earth and for the development of a transport model for space

conditions. The internal consistency and agreement between the Apollo-Soyuz Test Project and Skylab results obtained for different compounds, transport agents, and temperature gradients strongly support the validity of these observations. The combined findings of improved crystal quality and high mass transport rates are of technological significance for space-processing applications.

### INTRODUCTION

Crystal growth by chemical vapor transport is of technological importance for the production of bulk- and layer-type single crystalline materials used in various electronic devices. It is well known that the performance characteristics of electronic materials are critically dependent on the degree of chemical homogeneity and crystalline perfection. These material properties are affected by the transport and growth conditions of a given chemical system. Complete control of these growth parameters under ground-based conditions is limited because of the presence of gravity-driven convection. Under otherwise optimal growth conditions on Earth, convective interference with the transport process causes crystalline imperfections.

Crystal growth in a microgravity environment in the absence of convective interference should produce crystals of improved quality and yield fundamental data for the vapor transport process. These expectations were confirmed by the results of Skylab Experiment M556 (Vapor Growth of IV-VI Compounds). In the Skylab experiments

<sup>a</sup>Rensselaer Polytechnic Institute.

<sup>†</sup>Principal Investigator.

(refs. 26-1 and 26-2), representative compounds of Group IV-VI materials, germanium selenide (GeSe) and germanium telluride (GeTe), were transported with germanium tetraiodide (GeI<sub>4</sub>) as a transport agent. The single crystals grown in space are of considerably improved structural perfection compared to corresponding ground-based specimens. The second major result of the Skylab studies is the observation of greater mass transport rates in a microgravity environment than predicted for a diffusion-type transport process. Because of the far-reaching scientific and technological implications of the preceding observations, the Skylab results served as a basis for the definition of the Apollo-Soyuz Test Project (ASTP) experiments. The primary objectives of the ASTP crystal growth by vapor transport experiment were to extend and generalize microgravity crystal growth for a class of compounds and to characterize the unexpected gas motion observed during Skylab missions. For this purpose, new compounds and solid solutions were transported with different transport agents in higher temperature gradients. In addition, an inert atmosphere was used in one of the transport ampoules. Details of the experimental design and chemical systems are discussed subsequently.

This report is based on the current analysis of three transport experiments performed in space. The data reveal improved crystalline perfection for the space-grown material compared to ground-based samples. These results confirm the Skylab observations and extend the conclusions drawn to more complex systems. In addition, the mass transport rates observed in space are considerably greater than predicted by theory. The latter results not only confirm Skylab data, but provide experimental evidence for the cause of the higher than expected mass fluxes.

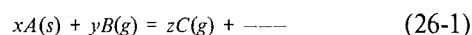
Because of the technological importance of single crystals for solid-state devices and because of their high yield-to-weight ratio, crystal growth by vapor transport is a primary candidate for space-processing applications. A definite purpose of the ground-based and microgravity transport studies is to provide the scientific and technical basis for actual space manufacturing. In addition, knowledge gained from these space experiments

will be of practical use for the improvement of crystal growth techniques on Earth.

## GROUND-BASED STUDIES

### Basic Theory

In a chemical transport reaction (ref. 26-3), a gaseous (g) transport agent  $B(g)$  reacts at a given temperature with the solid (s) source material  $A(s)$  to form exclusively gaseous products  $C(g)$ . This process is represented by the following reaction.



The number of different gaseous products formed depends on the particular chemical system. The vapor species migrate in the reaction vessel from the source to the condensation region, where, at a different temperature, the reverse reaction occurs with formation of the solid. The necessary concentration gradient is established by means of a temperature gradient, which yields different equilibrium constants for the reaction of equation (26-1) and, thus, yields different partial pressures of the gaseous species in the source and condensation zones of the system. According to equation (26-1) the solid  $A$  is transported via the gas phase by means of a chemical reaction; this is distinctly different from transport by sublimation. Under optimal experimental conditions, well-defined single crystals of the source material are obtained by the condensation reaction. Depending on the thermodynamic properties of the transport reaction, a chemical transport can occur from high to low temperature or vice versa. This aspect is of practical importance with respect to the choice of transport agent and condensation temperature. The transport reaction is performed in evacuated, sealed ampoules of fused silica that are conventionally subjected to the desired temperature gradient in a horizontal, two-zone, tubular resistance furnace.

The migration of gas phase species can be described by diffusion and by gravity-driven convection. In a gravitational field and temperature gradient, both transport modes occur simultaneously. It is a unique feature of the vapor transport technique to select experimental conditions so that one or the other mode can be predominant. Under ground-based conditions, the convective contribution to the overall transport process can be minimized but not eliminated. Based on existing models for diffusive and convective gas motion (ref. 26-3), the material flux from the source to the condensation region is affected by the pressure in the transport ampoule. At very low pressures of transport agent, the mass transport rate is controlled by the rate of the heterogeneous solid-gas phase reaction in the source or the condensation region, or both. Under these conditions, the material flux is proportional to the concentration of transport agent. At medium pressures, the transport rate is inversely proportional to the total pressure. The overall transport is diffusion controlled in this range. At higher pressures, the material flux increases with increasing total pressure, indicating the predominance of the convective transport mode. For the conditions of the diffusion- and convection-controlled transport modes, the heterogeneous solid-gas phase reactions in the source and condensation zones are fast.

### Transport Properties of Group IV-VI Compounds

Mass transport rate studies on GeTe (ref. 26-4) and GeSe (ref. 26-5) confirmed the general shape of flux as a function of total pressure curves predicted by the previously described models. Details of the experimental procedures and results have been discussed in references 26-4 and 26-5. The most important observation of these studies is the decrease in crystal perfection with increasing contribution of the convective component to the overall transport process. Transport studies in the Rensselaer Polytechnic Institute (RPI) laboratory on germanium monosulfide (GeS) using germanium tetrachloride ( $\text{GeCl}_4$ ) as a transport agent

and different temperature gradients show the diffusion- and convection-controlled transport regimes in agreement with those of the preceding systems (refs. 26-4 and 26-5). In particular, the changes in crystal morphology and habit of GeS as a function of transport mode reveal the negative effects of convective interference on crystal quality. The previously described ground-based studies and the solid-solution properties of these binary systems led to the definition of mixed systems for two of the three transport experiments performed during the ASTP mission. The chemical composition of the mixed systems is given by the formulas  $\text{GeSe}_{0.99}\text{Te}_{0.01}$  (system A) and  $\text{GeS}_{0.98}\text{Se}_{0.02}$  (system B), respectively, where the decimal subscripts are weight percentages of the compounds and of the elements tellurium (Te) and selenium (Se). The third transport ampoule (system C) contained GeS and a mixture of  $\text{GeCl}_4$  and argon (Ar). In the RPI laboratory, quantitative mass transport rate studies in terms of flux as a function of pressure were performed on these systems in the temperature gradient  $877 \rightarrow 780 \text{ K}$  ( $604 \rightarrow 507^\circ \text{ C}$ ). The transport agent was  $\text{GeI}_4$  for system A and  $\text{GeCl}_4$  for systems B and C. The flux is calculated from the quantity of crystals recovered, the cross section of the ampoule, and the duration of the experiment. The pressure is computed for the mean temperature of the gradient from the amount of transport agent added, assuming ideal conditions and use of  $\text{GeI}_4(\text{g})$  or  $\text{GeCl}_4(\text{g})$ , respectively.

In system C, the partial pressure of argon in the ampoule was approximately twice the pressure of the transport agent  $\text{GeCl}_4$ . In figure 26-1, the system C flux is plotted as a function of transport-agent pressure to be consistent with systems A and B. For comparative purposes, the flux results of the GeS- $\text{GeCl}_4$  system without argon also are included in figure 26-1.

The flux curves of all systems have the same shape as those observed earlier (ref. 26-5). The diffusion-controlled region at lower pressures shows a decrease in flux with increasing pressure. The range of predominantly convective transport is characterized by an increase in flux with increasing pressure.

The leveling of the flux curve for system A at higher pressures is due to the precipitation of the

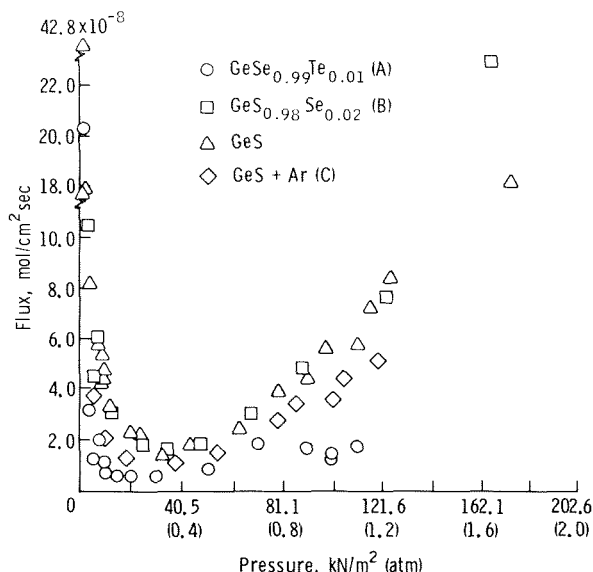


FIGURE 26-1.—Mass transport rates in terms of flux as a function of transport-agent pressure for the temperature gradient 877 → 780 K (604° → 507° C) determined under ground-based conditions.

transport agent, thus establishing a constant saturation pressure in the ampoule. The flux curves in figure 26-1, determined in the RPI laboratory, serve as a basis for the evaluation of the space experiments. For the direct comparison of mass transport rates and crystals obtained on Earth and in space, a set of three ampoules containing the same amounts of starting materials and transport agent as the corresponding ampoules used in the ASTP mission were processed in the prototype furnace. This furnace and the prototype transport conditions were identical to the furnace and conditions used in space, except for gravity.

## EXPERIMENTAL ASTP PROCEDURES

### Apparatus

The transport experiments were performed in the multipurpose electric furnace, which consisted essentially of a cylindrical furnace chamber and an instrumentation compartment. The furnace chamber contained three tubular reaction cavities

for the individual metal cartridges and quartz ampoules discussed subsequently. Because the furnace was heated resistively in one zone at the source region, the desired temperature gradient and stability were achieved by heat shields surrounding the quartz ampoules in the metal cartridges and by appropriate heat shields in the furnace. The temperature gradient employed for those experiments in space was 877 → 780 K (604° → 507° C) with a shallow gradient in the hot zone and a nearly linear gradient between the hot and cold zones of the reaction chamber. During the performance of the transport experiments, the furnace temperatures were constantly monitored at the outside of the metal cartridges in the hot and cold zones. The difference between furnace and actual ampoule temperatures was calibrated under identical ground-based conditions by using thermocouples.

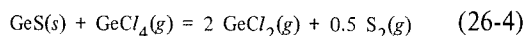
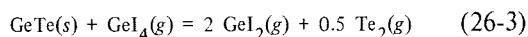
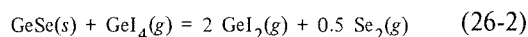
### Ampoule and Sample Preparation

The transport ampoules were made of fused silica tubing of 13.7 mm inner diameter and 150 mm length. Near the rounded end, the ampoules contained two thin silica rods to hold the source material in place. The other ampoule end was sealed after loading at a pressure of 0.1333 mN/m<sup>2</sup> (10<sup>-6</sup> torr) or less. Before loading, the cleaned ampoules (refs. 26-4 and 26-5) were outgassed at a temperature of approximately 1273 K (1000° C) and a pressure of 0.1333 mN/m<sup>2</sup> (10<sup>-6</sup> torr) for 10 hours. The polycrystalline starting materials were synthesized by the repeated annealing at a temperature of approximately 873 K (600° C) of stoichiometric mixtures of the binary compounds GeS, GeSe, and GeTe. The compounds were prepared from high-purity elements (99.999 percent) by annealing and subsequent sublimation of the product (refs. 26-4 and 26-5). The crystallographic identity of all materials was established by means of X-ray diffraction techniques. High-purity GeI<sub>4</sub> (99.999 percent) and GeCl<sub>4</sub> (99.999 percent) were used as transport agents. Ultra-high-purity argon was used as inert gas in one system. The ampoule designated 3A in this experiment contained 1.50 g of GeSe<sub>0.99</sub>Te<sub>0.01</sub> and 123.5 mg of GeI<sub>4</sub>. Ampoule 3B was loaded with 1.50 g of GeS<sub>0.98</sub>Se<sub>0.02</sub> and 59.1



mg of  $\text{GeCl}_4$ . The third ampoule (3C) contained 1.50 g of  $\text{GeS}$ , 61.8 mg of  $\text{GeCl}_4$ , and  $193.53 \text{ kN/m}^2$  (1.91 atm) of argon at the mean temperature of the gradient. The ampoules used for the ground-based prototype tests (2A, 2B, and 2C) were of the same dimensions and contents.

The chemical transport reactions for the binary compounds are shown in the following equations.



The experimental conditions for the ASTP mission are summarized as follows for a temperature gradient of  $877 \rightarrow 780 \text{ K}$  ( $604^\circ \rightarrow 507^\circ \text{ C}$ ).

$$\text{GeSe}_{0.99}\text{Te}_{0.01} \text{ (3A)} \quad P(\text{GeI}_4(\text{g})) = 70.93 \text{ kN/m}^2 \quad (0.70 \text{ atm})$$

$$\text{GeS}_{0.98}\text{Se}_{0.02} \text{ (3B)} \quad P(\text{GeCl}_4(\text{g})) = 95.25 \text{ kN/m}^2 \quad (0.94 \text{ atm})$$

$$\text{GeS (3C)} \quad P(\text{GeCl}_4(\text{g})) = 97.27 \text{ kN/m}^2 \quad (0.96 \text{ atm})$$

$$P(\text{Ar}) = 193.53 \text{ kN/m}^2 \quad (1.91 \text{ atm})$$

where  $P$  indicates component gas pressure. The transport reactions of the mixed systems are analogous. The total pressures in terms of  $\text{GeI}_4(\text{g})$  or  $\text{GeCl}_4(\text{g})$  are calculated for the mean temperature of the gradient and for ideal gas conditions. The partial pressure of argon in ampoule 3C is twice the pressure of the transport agent  $\text{GeCl}_4$ . Thus, the total pressure in ampoule 3C is approximately three times the pressure in ampoule 3B.

### Heating Cycle and Return of Ampoules

The transport ampoules were enclosed in hermetically sealed metal cartridges, which were in-

serted into the multipurpose furnace by the astronauts. Details of the cartridges are described in reference 26-1. After a heatup period of approximately 2 hours, the desired temperature gradient was achieved and maintained for 16 hours. Following termination of the experiment, cooling of the cartridges to ambient temperatures occurred over a period of approximately 4 hours, during which a helium quench was used.

Examination of the opened cartridges at the NASA George C. Marshall Space Flight Center revealed that none of the ampoules had any mechanical damage and that the residual source material in all ampoules was firmly attached to the ampoule wall in the source region. The ampoules were brought to the RPI laboratory for analysis of these experiments.

## RESULTS AND DISCUSSION

The analysis of the transport experiments performed on the ASTP mission is based on X-ray diffraction, microprobe, microscopic, and chemical etching techniques and on mass transport rate measurements. The current results are summarized as follows.

### Crystallographic Identification of Transport Products

The crystallographic identification of space-grown crystals was established by means of Debye-Scherrer and Laue X-ray diffraction techniques. For the Debye-Scherrer method, randomly selected crystals were finely powdered, sealed in thin-walled glass capillaries, and exposed to copper ( $\text{Cu}$ )  $K\alpha$  radiation in a 114.59-mm-diameter X-ray camera. For the Laue method, individual single-crystal platelets were mounted on the crystal holder of a conventional Laue camera and exposed to  $\text{Cu } K\alpha$  radiation. The results in terms of lattice parameters (Debye-Scherrer) and crystallographic orientation of as-grown predominant faces (Laue) are summarized in table 26-I together with corresponding data for ground-based (prototype) crystals.

A comparison of the data in table 26-I shows that the lattice constants of the respective systems

TABLE 26-1.—Crystallographic Parameters of Ground-Based and ASTP Space-Grown Crystals

Location	Lattice parameter, nm (Å)			Orientation
	a <sub>0</sub>	b <sub>0</sub>	c <sub>0</sub>	
GeSe <sub>0.99</sub> Te <sub>0.01</sub> (A)				
Ground Space	0.4385 (4.385) ± 0.0008 (0.008)	0.3838 (3.838) ± 0.0007 (0.007)	1.0791 (10.791) ± 0.0019 (0.019)	(001)
	0.4386 (4.386) ± 0.0008 (0.008)	0.3839 (3.839) ± 0.0007 (0.007)	1.0793 (10.793) ± 0.0020 (0.020)	(001)
GeS <sub>0.98</sub> Se <sub>0.02</sub> (B)				
Ground Space	0.4301 (4.301) ± 0.0009 (0.009)	0.3651 (3.651) ± 0.0008 (0.008)	1.0431 (10.431) ± 0.0020 (0.020)	(001)
	0.4302 (4.302) ± 0.0012 (0.012)	0.3652 (3.652) ± 0.0010 (0.010)	1.0432 (10.432) ± 0.0022 (0.022)	(001)
GeS (C)				
Ground Space	0.4299 (4.299) ± 0.0008 (0.008)	0.3649 (3.649) ± 0.0007 (0.007)	1.0428 (10.428) ± 0.0019 (0.019)	(001)
	0.4301 (4.301) ± 0.0006 (0.006)	0.3651 (3.651) ± 0.0005 (0.005)	1.0430 (10.430) ± 0.0015 (0.015)	(001)

are in excellent agreement. There is no change in the orientation of predominant native faces of single crystals. Within the detection limits of X-ray diffraction techniques, there is no measurable effect of microgravity on the crystallographic parameters of space-grown crystals. The preceding results are expected in view of the relative magnitude of chemical bonding and gravitational forces.

Transmission Laue photographs of  $\text{GeSe}_{0.99}\text{Te}_{0.01}$  ground (2A) and space (3A) crystals indicate considerable differences, as shown in figure 26-2. The diffraction pattern of the ground-based crystal (fig. 26-2(a)) reveals striations and multiplicity of individual diffraction spots. This condition indicates a high degree of strain and structural inhomogeneities of the ground specimen. The Laue pattern of the space crystal (fig. 26-2(b)) reveals the twofold symmetry of the predominant (001)-oriented growth face. The considerably better defined diffraction spots indicate improved crystallographic perfection compared to the ground-based sample.

Corresponding diffraction patterns of  $\text{GeS}_{0.98}\text{Se}_{0.02}$  ground (2B) and space (3B) crystals in figure 26-3 demonstrate a pronounced improvement in crystallinity of the space sample (fig. 26-3(b)) relative to the ground specimen (fig. 26-3(a)). The rather well-defined diffraction spots of the space crystal (fig. 26-3(b)) reveal a considerable degree of crystallographic perfection, which has not been observed for ground crystals obtained under these conditions.

Laue diffraction patterns of GeS ground (2C) and space (3C) crystals grown in the presence of argon indicate in both cases some degree of strain (figs. 26-4(a) and 26-4(b)). Since crystals obtained under these conditions are considerably thinner than those of systems A and B, it is presently difficult to decide whether the observed strain is caused by mechanical handling of the sample or by the inclusion of argon into the crystal lattice.

The combined results of the diffraction studies for systems A and B demonstrate the distinctly improved structural homogeneity and perfection of the crystals obtained in a microgravity environment.

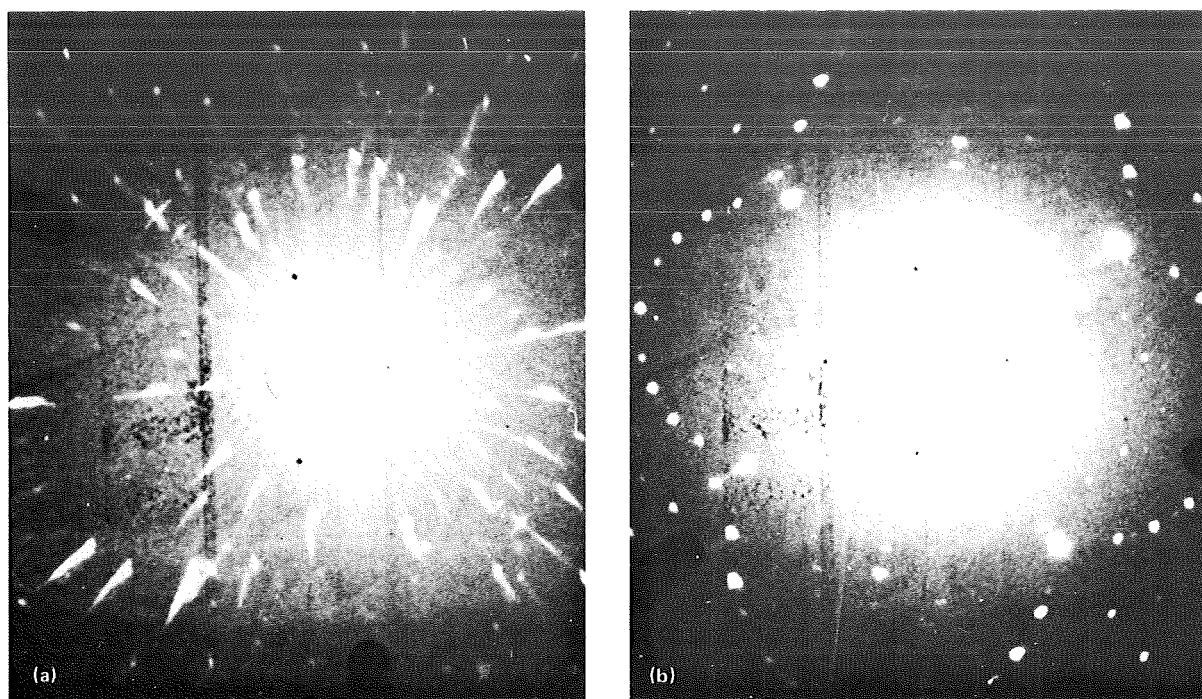


FIGURE 26-2.—Laue X-ray diffraction transmission photographs of (001)-oriented  $\text{GeSe}_{0.99}\text{Te}_{0.01}$  (system A) single-crystal platelets. (a) Ground-based (prototype). (b) Space-grown.

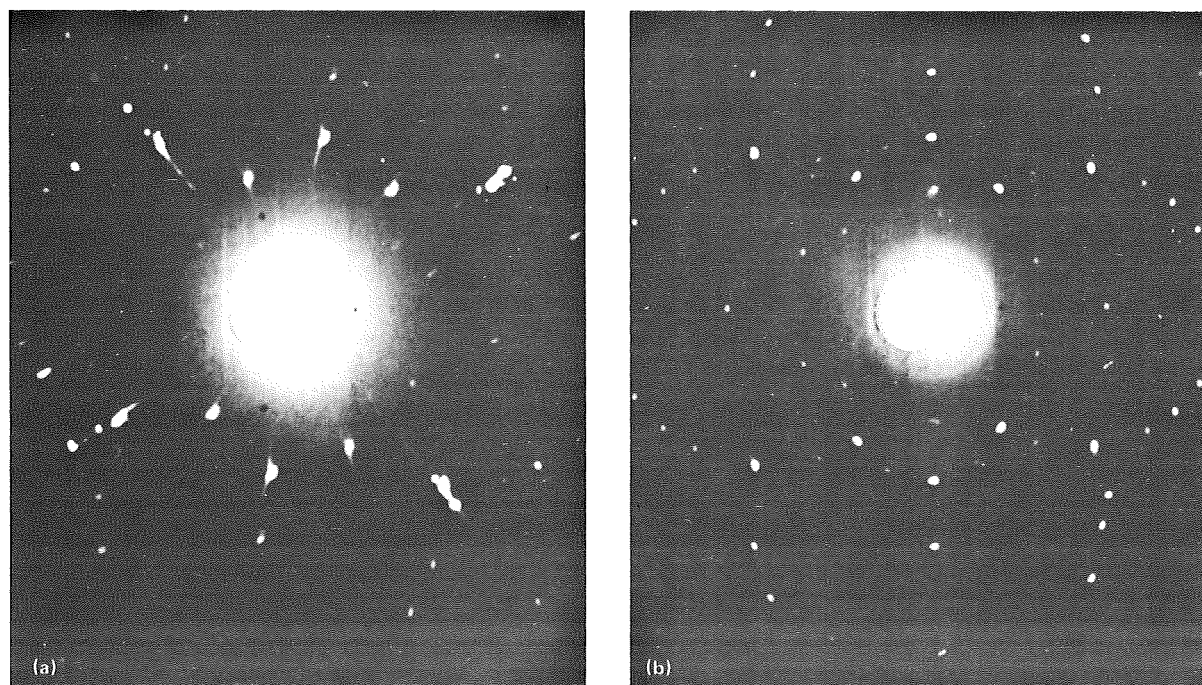


FIGURE 26-3.—Laue X-ray diffraction transmission photographs of (001)-oriented  $\text{GeS}_{0.98}\text{Se}_{0.02}$  (system B) single-crystal platelets. (a) Ground-based (prototype). (b) Space-grown.

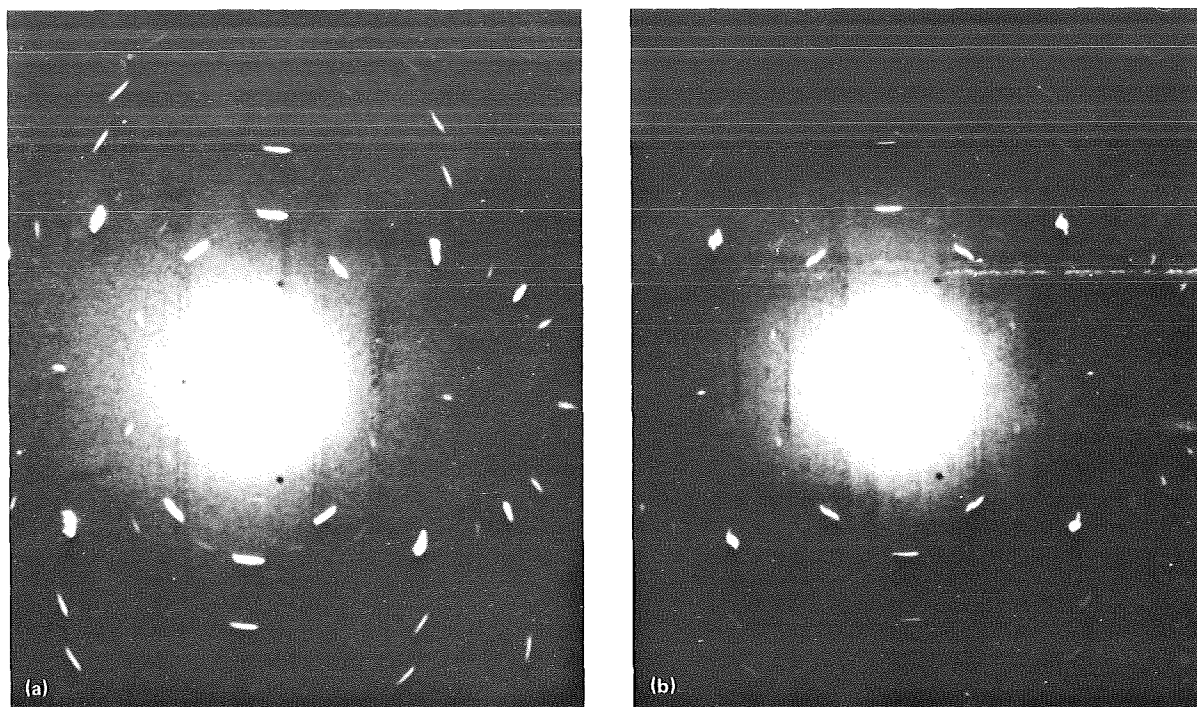


FIGURE 26-4.—Laue X-ray diffraction transmission photographs of (001)-oriented GeS (system C) single-crystal platelets. (a) Ground-based (prototype). (b) Space-grown.

### Chemical Homogeneity of Crystals

To examine the chemical homogeneity of the solid solutions (systems A and B), the distribution of Te in GeSe (A) and of Se in GeS (B) was determined using an electron microprobe analyzer. For this purpose, cleaved faces of ground-based (prototype) and space-grown crystals were used. The relative concentration of Te (in GeSe) and of Se (in GeS) was measured along three directions parallel to the a-axis and the b-axis of the (001)-oriented crystal platelet. Along each direction, intensity measurements were performed at several locations. The results are summarized in table 26-II. The individual data listed are the averages of points along a given direction. The error limits represent the maximum deviation in atomic concentration of individual points from the mean value for all points along that direction. Stoichiometric GeTe and GeSe, respectively, were used as reference samples.

Based on the relative magnitude of the deviations in concentration from the average values, the distribution of Te in the solid solution of starting composition  $\text{GeSe}_{0.99}\text{Te}_{0.01}$  is considerably more homogeneous in the space-grown crystal (3A) than in the ground-based crystal (2A). The differences in homogeneity are about one order of magnitude. The corresponding improvement in the distribution of Se in the space crystal (3B) compared to the ground specimen (2B) for the solid solution of starting composition  $\text{GeS}_{0.98}\text{Se}_{0.02}$  is less pronounced, but measurable. The deviation of the average values from the nominal concentration of Te and Se in the starting materials is due to slightly different transport properties of the binary components of the mixed systems.

Because of the relative differences in atomic radii between sulfur (S), Se, and Te and because of the individual crystal structures of GeS and GeSe (orthorhombic) and GeTe (rhombohedral), one

TABLE 26-II.—Distribution of Te (A) and Se (B) in Ground-Based and ASTP Space-Grown Crystals

System	Concentration, at. %		
	Average all data	Average parallel a-axis	Average parallel b-axis
GeSe <sub>0.99</sub> Te <sub>0.01</sub> (Ground-based, 2A)	1.83 ± 0.6	2.03 ± 0.5	1.59 ± 0.4
		1.71 ± .6	2.07 ± .3
		1.78 ± .4	1.81 ± .4
GeSe <sub>0.99</sub> Te <sub>0.01</sub> (ASTP, 3A)	1.56 ± 0.1	1.59 ± 0.03	1.58 ± 0.04
		1.52 ± .08	1.57 ± .06
		1.56 ± .02	1.58 ± .02
GeS <sub>0.98</sub> Se <sub>0.02</sub> (Ground-based, 2B)	0.395 ± 0.092	0.371 ± 0.068	0.374 ± 0.034
		.399 ± .061	.402 ± .020
		.399 ± .028	.422 ± .015
GeS <sub>0.98</sub> Se <sub>0.02</sub> (ASTP, 3B)	0.462 ± 0.048	0.470 ± 0.014	0.459 ± 0.046
		.448 ± .020	.471 ± .009
		.470 ± .007	.463 ± .007

would expect a more homogeneous mixing to occur in the GeS-GeSe system than in the GeSe-GeTe system. Any improvement in the degree of homogeneity as a result of microgravity conditions should thus be more pronounced for GeSe-GeTe than for GeS-GeSe solid solutions. The experimental observations are in agreement with these expectations.

### Morphological Characterization of Crystals

Before the microscopic investigation of individual single crystals is discussed, it should be noted that a macroscopic view of the deposition pattern of transport agent (GeI<sub>4</sub>) on the system A ampoule walls (fig. 26-5) shows significant differences. The transport agent in the space ampoule (fig. 26-5(a)) is condensed in the form of well-developed, transparent single-crystal platelets and a few needles. The GeI<sub>4</sub> deposition in the ground-based ampoule (fig. 26-5(b)) shows dendritic-type material with a distinct curvature of individual dendrites. The length of these dendrites ranges to approximately 8 mm. The absence of any distinct curvature in the deposition

pattern of the space ampoule (fig. 26-5(a)) reflects the more homogeneous gas motion in a microgravity environment.

Optical photomicrographs of representative GeSe<sub>0.99</sub>Te<sub>0.01</sub> (A) ground (prototype) and space crystals show qualitative differences in surface morphology, as illustrated in figure 26-6. Most of the prototype crystals (fig. 26-6(a)) reveal ragged edges, intergrowth, and stepped surfaces. The space crystals (fig. 26-6(b)) have smoother surfaces and generally better defined edges. The average dimensions of the ground specimens range from approximately 2 to 8 mm in edge length. The slightly smaller sizes of the space material are in agreement with the lower microgravity transport rates observed for this system (table 26-III).

Optical photomicrographs of representative GeS<sub>0.98</sub>Se<sub>0.02</sub> (B) ground (prototype) and space crystals in figure 26-7 reveal distinct morphological differences. The prototype crystals (fig. 26-7(a)) show considerable aggregation, undefined edges, and rough surfaces. The morphological improvement in terms of surfaces and edges of the space crystals is evident from

TABLE 26-III.—Mass Transport Rates Under Ground-Based and Microgravity Conditions

System	Mass flux, mol/cm <sup>2</sup> sec		
	Condition		Extrapolated diffusion mode
	Normal gravity	Microgravity	
GeSe <sub>0.99</sub> Te <sub>0.01</sub> (A)	$7.9 \times 10^{-9}$	$4.2 \times 10^{-9}$	$1.4 \times 10^{-9}$
GeS <sub>0.98</sub> Se <sub>0.02</sub> (B)	22.1	22.1	6.5
GeS + Ar (C)	15.0	13.0	2.8

FIGURE 26-5.—Deposition pattern of transport agent GeI<sub>4</sub> (system A) on ampoule walls. (a) In microgravity environment. (b) Under ground-based conditions.

figure 26-7(b). The average dimensions of the space material range from approximately 1 to 7 mm in edge length. Because the system B transport rates (table 26-III) are the same under both ground and space conditions, the external

morphological differences reflect the absence of convective interference in a microgravity environment. Similar differences in growth habits were observed for GeS crystals (system C).

The external morphological differences of native faces and edges of typical GeSe<sub>0.99</sub>Te<sub>0.01</sub> (A) ground and space crystals are shown in scanning electron photomicrographs in figure 26-8. Rough and partly damaged faces of the ground crystal (fig. 26-8(a)) are contrasted by well-defined surfaces and edges of the space crystal (fig. 26-8(b)). Most of the ground crystals appear to have at least one edge damaged, whereas most of the space crystals have well-developed edges. These results confirm similar observations of the Skylab experiments and indicate homogeneous nucleation, which could occur more frequently under microgravity conditions than on Earth.

Scanning electron photomicrographs of native surfaces of GeS<sub>0.98</sub>Se<sub>0.02</sub> (B) ground (prototype) (fig. 26-9(a)) and space (fig. 26-9(b)) crystals reveal significant morphological differences. The degree of surface perfection of the space material (fig. 26-9(b)) is considerably improved compared to the ground specimen (fig. 26-9(a)). Because the transport rates of system B are the same under ground-based and microgravity conditions (table 26-III), the greater crystalline perfection of the space material is attributed to the absence of convective interference.

To investigate the effects of microgravity forces on the degree of crystalline perfection for the bulk of the material, internal faces of ground



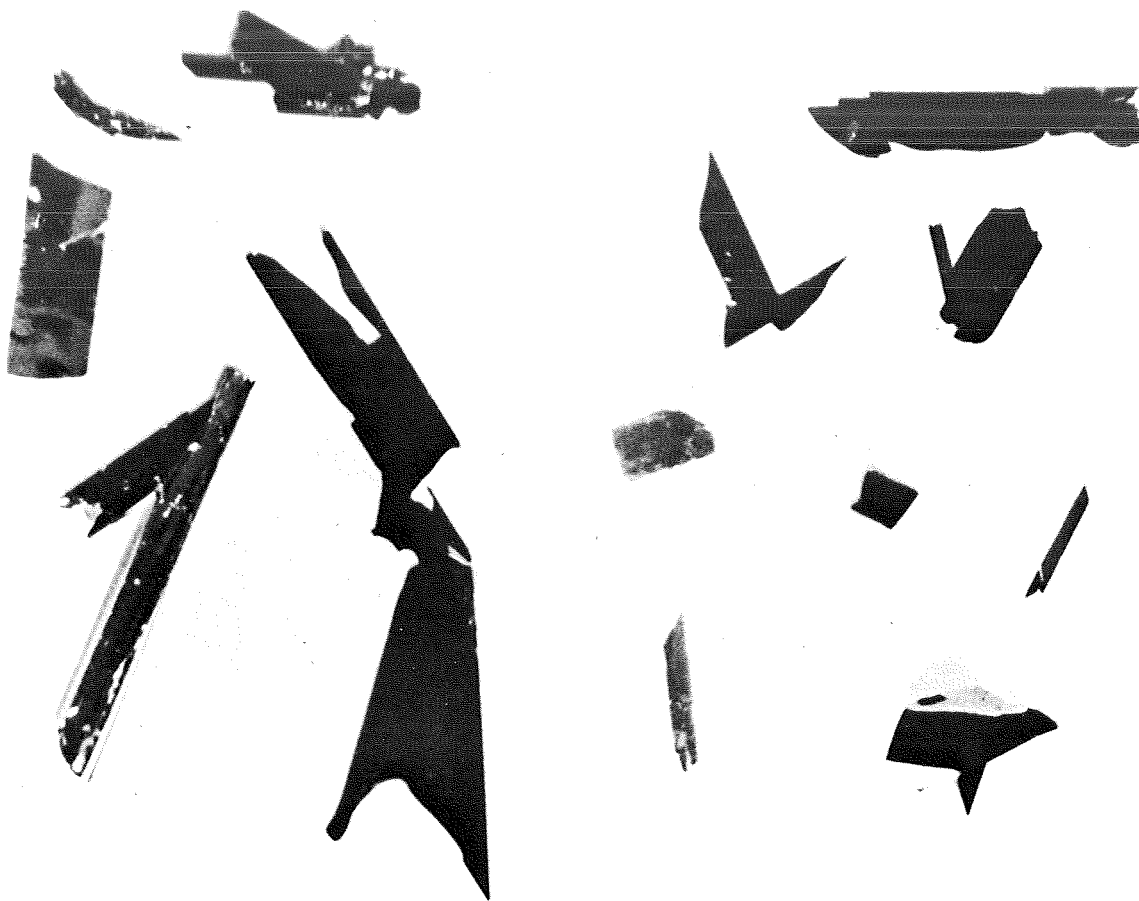


FIGURE 26-6.—Representative crystals of  $\text{GeSe}_{0.99}\text{Te}_{0.01}$  (system A). (a) Ground-based (prototype). (b) Space-grown.

and space crystals were examined by means of chemical etching and optical microscopy. For this purpose, crystal platelets were cleaved parallel to the (001) plane.

An optical photomicrograph of the cleaved face of a ground (prototype) crystal of  $\text{GeSe}_{0.99}\text{Te}_{0.01}$  (system A) shows the presence of large cavities in the bulk of the material (fig. 26-10(a)). After chemical etching, the same area of the crystal is covered with etch pits (fig. 26-10(b)). It is interesting to note that the areas which appear to be mirror smooth at this magnification (fig. 26-10(a)) show a high etch-pit density (fig. 26-10(b)). Etch pits along the walls of the main cavity are also clearly visible. The concentration of etch pits indicates the degree of structural or chemical imperfection in the ground-based material. Similar ob-

servations were made for the majority of investigated crystals.

Application of the same cleaving and etching procedures to space-grown crystals of system A yields distinctly different results, as shown in figure 26-11. The photomicrograph of the cleaved crystal reveals that most of the space material is structurally very uniform (fig. 26-11(a)). The photomicrograph after etching of the cleaved space crystal platelet (fig. 26-11(b)) is practically free of etch pits and thus indicates a high degree of microhomogeneity. The line pattern of the crystal, showing (001) planes of different depth with respect to the native surface, is due to cleavage.

Similar differences in etch patterns were observed for ground-based (prototype) and space-grown  $\text{GeS}_{0.98}\text{Se}_{0.02}$  (B) crystals, as shown in

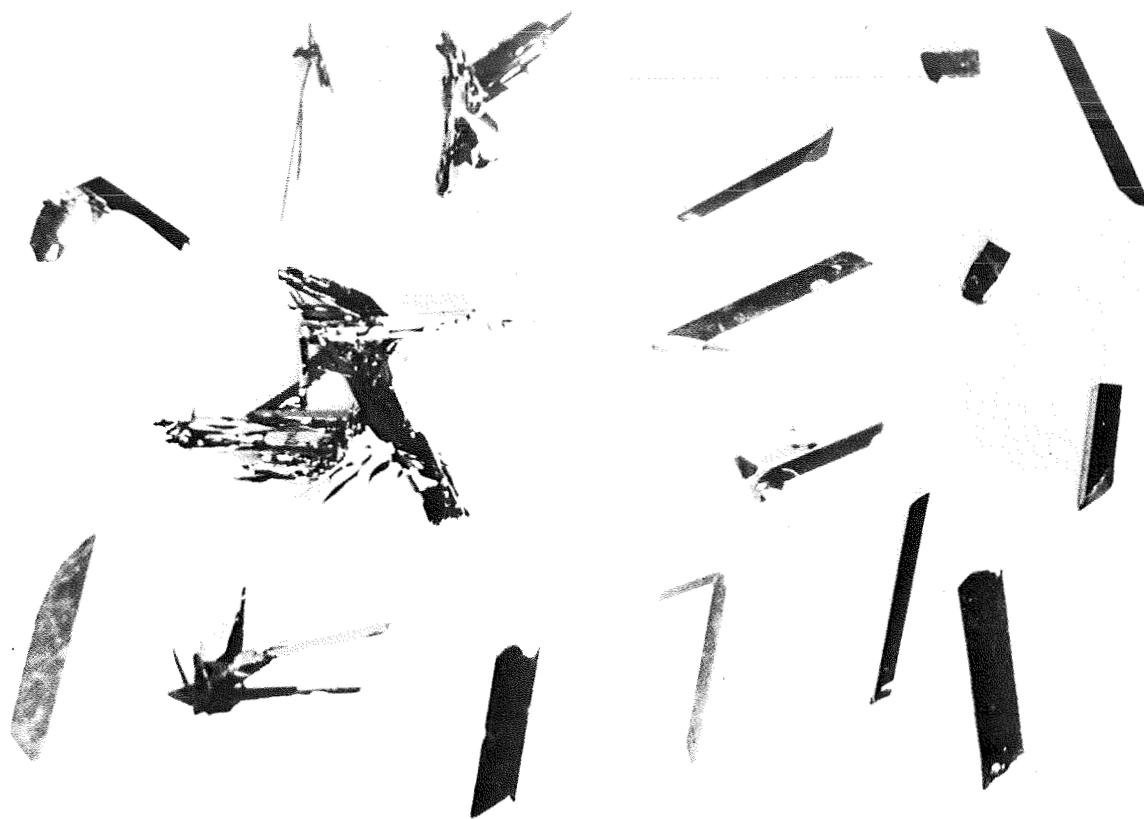


FIGURE 26-7.—Representative crystals of  $\text{GeS}_{0.98}\text{Se}_{0.02}$  (system B). (a) Ground-based (prototype). (b) Space-grown.

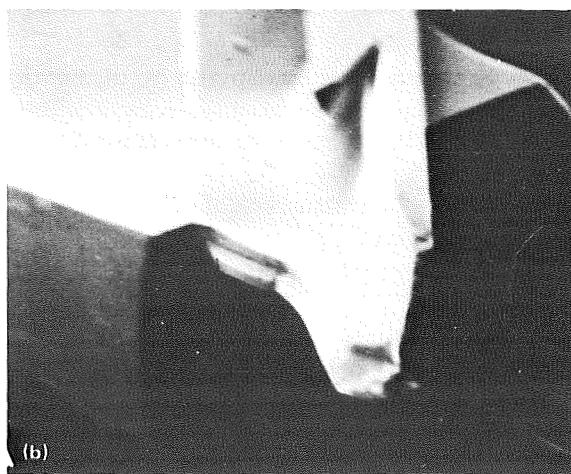
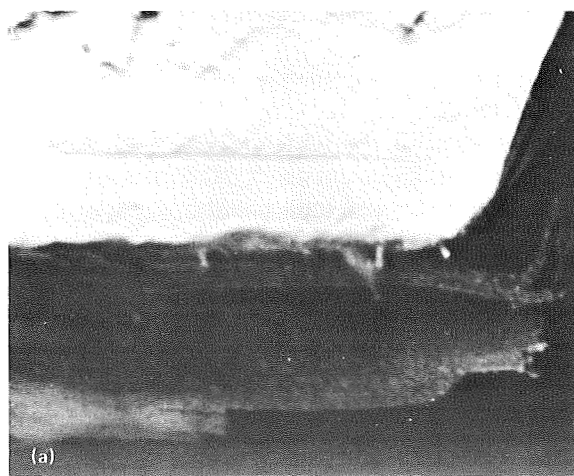


FIGURE 26-8.—Scanning electron photomicrographs (200 $\times$ ) of native faces and edges of  $\text{GeSe}_{0.99}\text{Te}_{0.01}$  (system A) crystals. (a) Ground-based (prototype). (b) Space-grown.



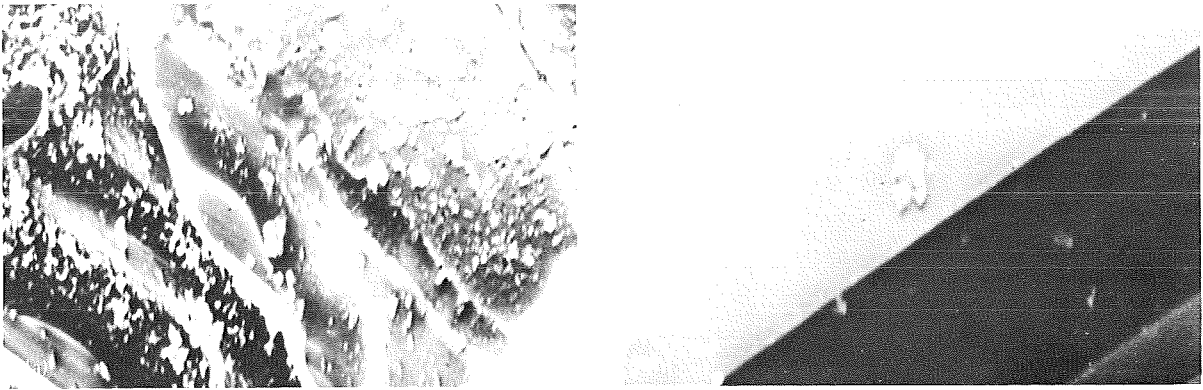


FIGURE 26-9.—Scanning electron photomicrographs (200 $\times$ ) of native faces of  $\text{GeS}_{0.98}\text{Se}_{0.02}$  (system B) crystals. (a) Ground-based (prototype). (b) Space-grown.

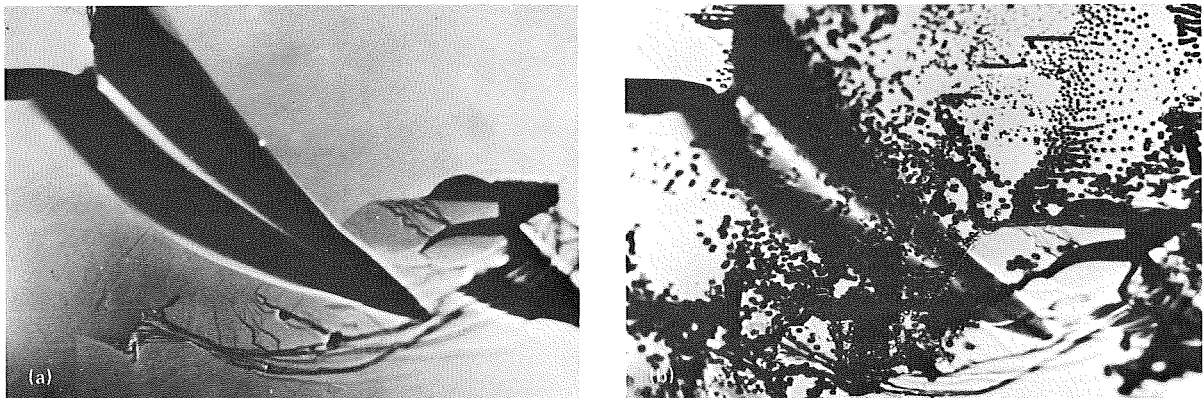


FIGURE 26-10.—Optical photomicrographs (100 $\times$ ) of a cleaved and etched (001) face of a ground-based (prototype)  $\text{GeSe}_{0.99}\text{Te}_{0.01}$  (system A) crystal platelet. (a) Cleaved. (b) Cleaved and etched.

figures 26-12 and 26-13, respectively. For comparative purposes, a ground crystal of above average quality has been selected, as indicated by the cleavage pattern (fig. 26-12(a)). (Most B-type ground crystals contain cavities and elongated channels in the bulk of the material.) Chemical etching of the cleaved (001) face yields large etch pits and lines (fig. 26-12(b)), which are indicative of crystallographic imperfections. This characteristic is in contrast to that revealed by optical photomicrographs of cleaved and etched (001) faces of system B space crystals (figs. 26-13(a) and 26-13(b)). Except for a few isolated etch pits in the crystal plane (fig. 26-13(b)), the bulk of the

material is practically unaffected by chemical etching. This characteristic indicates a high degree of crystalline homogeneity of the space-grown material.

Optical photomicrographs of cleaved and etched (001) faces of GeS (C) ground (prototype) and space crystals are shown in figures 26-14 and 26-15, respectively. Whereas the cleaved faces of the prototype (fig. 26-14(a)) and space (fig. 26-15(a)) crystals appear to be of comparable quality, the corresponding etched faces of the ground (fig. 26-14(b)) and space (fig. 26-15(b)) crystals reveal measurable differences. The prototype material shows a high density of etch pits



FIGURE 26-11.—Optical photomicrographs (125 $\times$ ) of a cleaved and etched (001) face of a space-grown  $\text{GeSe}_{0.99}\text{Te}_{0.01}$  (system A) crystal platelet. (a) Cleaved. (b) Cleaved and etched.

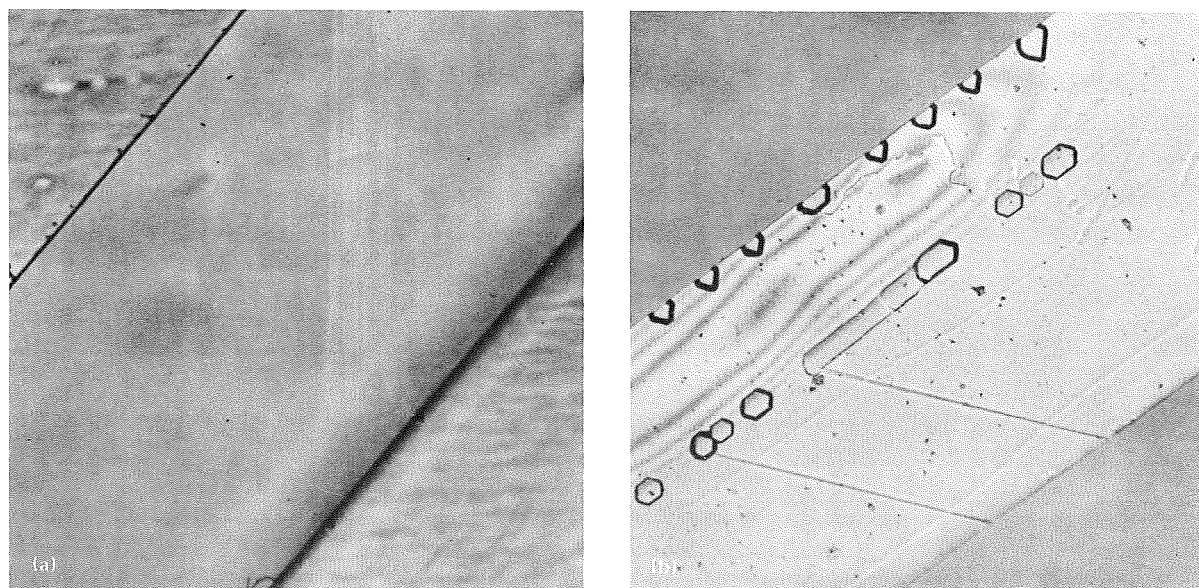


FIGURE 26-12.—Optical photomicrographs (125 $\times$ ) of a cleaved and etched (001) face of a ground-based (prototype)  $\text{GeS}_{0.98}\text{Se}_{0.02}$  (system B) crystal platelet. (a) Cleaved. (b) Cleaved and etched.

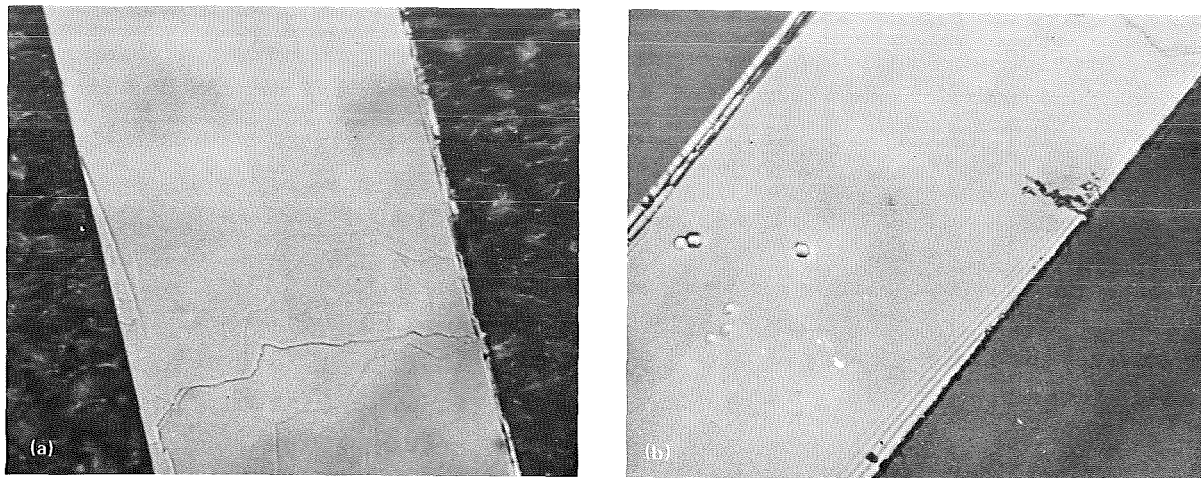


FIGURE 26-13.—Optical photomicrographs (125 $\times$ ) of a cleaved and etched (001) face of a space-grown  $\text{GeS}_{0.98}\text{Se}_{0.02}$  (system B) crystal platelet. (a) Cleaved. (b) Cleaved and etched.

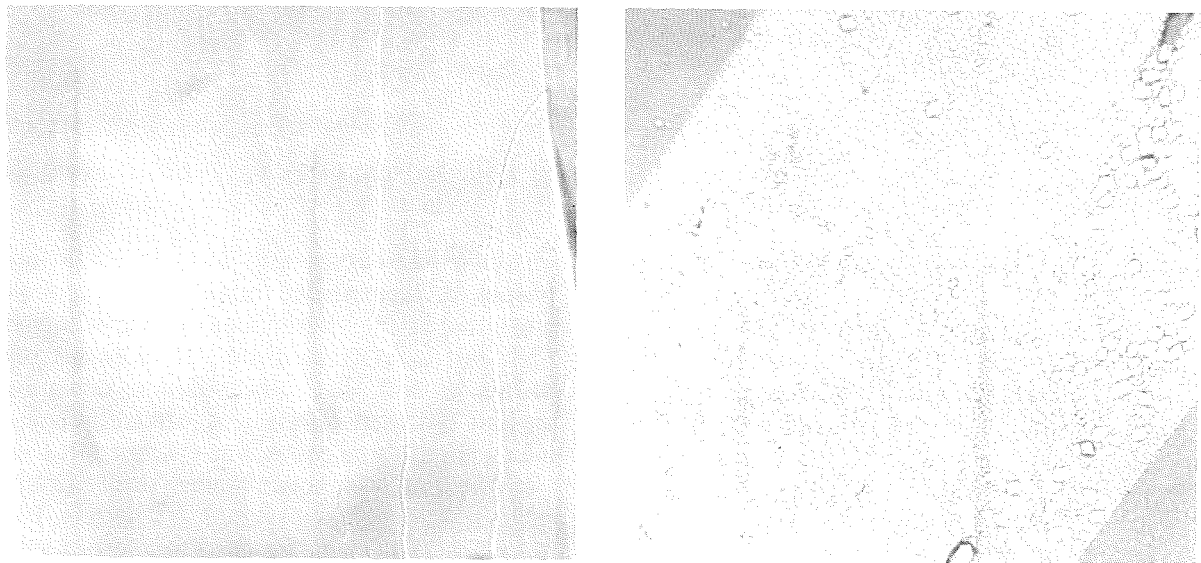


FIGURE 26-14.—Optical photomicrographs (125 $\times$ ) of a cleaved and etched (001) face of a ground-based (prototype) GeS (system C) crystal platelet. (a) Cleaved. (b) Cleaved and etched.

of different sizes (fig. 26-14(b)). The etch pits of the space sample (fig. 26-15(b)) are concentrated in the lower section of the crystal and along the edges, whereas the major part of the plane has a considerably lower pit density than the ground crystal. It was observed that the GeS space crystals (system C) grown in the presence of argon were of slightly lower crystallographic quality than the system A and B space crystals, which were produced in the absence of an inert atmosphere.

Studies are in progress to determine whether these differences are due to the incorporation of argon into the GeS lattice.

These differences in cleavage and etch patterns for the three systems were observed for the majority of investigated space and ground crystals. The combined results of the morphological studies demonstrate the considerably improved crystallographic perfection of the crystals grown in a microgravity environment.

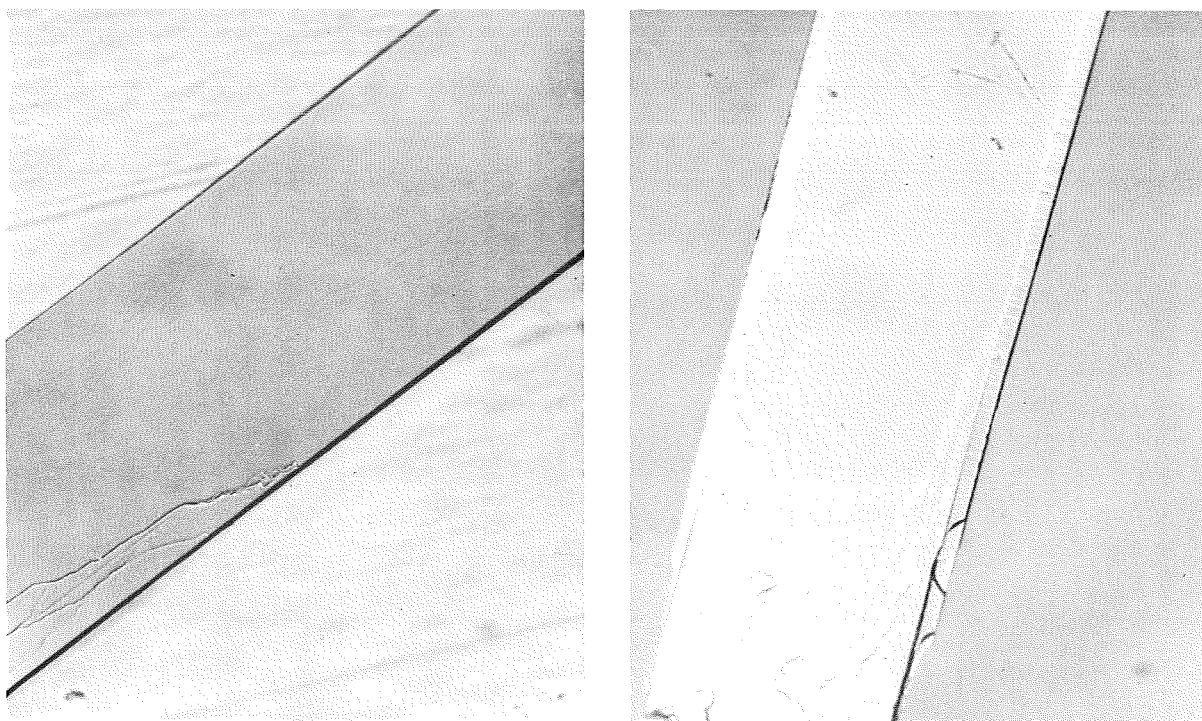


FIGURE 26-15.—Optical photomicrographs (125X) of a cleaved and etched (001) face of a space-grown GeS (system C) crystal platelet. (a) Cleaved. (b) Cleaved and etched.

### Mass Transport Rates

The determination of the mass transport rates observed in a microgravity environment is based on the mass of the transported crystals and on the mass loss of the source materials. The same procedures were applied to determine the fluxes of the ground-based (prototype) systems. The experimental uncertainties associated with the recovery of crystals were combined to yield lower values for the mass flux observed under microgravity conditions. The extrapolated values are based on a graphical extrapolation of the diffusion-controlled region of the respective ground-based experimental flux curves shown in figure 26-1. For this purpose, flux as a function of pressure data were plotted in double logarithmic scales and the resulting straight line was extended to the flux corresponding to the pressure employed in the ASTP experiments. This extrapolation is shown for system A in figure 26-16 and for system B and GeS in figure 26-17. The data of the diffusion-controlled region selected for the extrapolation are near the minimum of the in-

dividual flux curves (fig. 26-1) to obtain upper values for the predicted fluxes. The extrapolations are based on the assumptions that vapor transport in a microgravity environment is by gas phase diffusion and that other known non-gravity-caused transport effects (e.g., streaming) are included in this procedure. The predicted flux value for system C was obtained analytically from the extrapolated identical values for system B and GeS (fig. 26-17) and the argon pressure in system C, considering the different molecular weights of argon and  $\text{GeCl}_4$ . The mass transport properties of system B and GeS (figs. 26-1 and 26-17) and the transport agent ( $\text{GeCl}_4$ ) pressures of systems B and C ( $95.25 \text{ kN/m}^2$  (0.94 atm) and  $97.27 \text{ kN/m}^2$  (0.96 atm), respectively) are the same within limits of error. Therefore, a direct comparison of the effect of argon on the mass flux between systems B and C can be made. In view of the applied evaluation procedures, any differences between observed and predicted (extrapolated) microgravity fluxes are minimized and well outside error limits. The numerical transport results are listed in table 26-III.

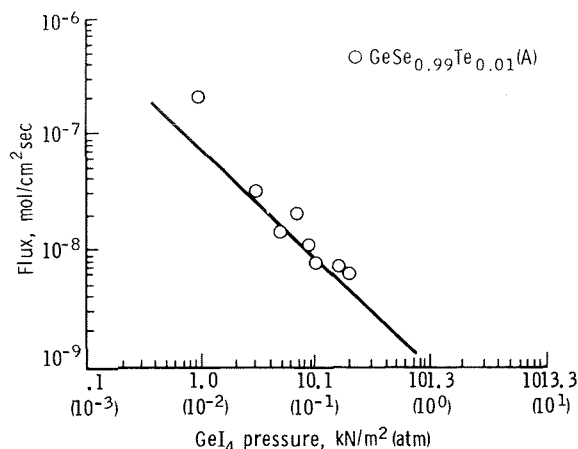


FIGURE 26-16.—Extrapolation of flux as a function of pressure data from the diffusion branch of the ground-based flux curve (fig. 26-1) for system A.

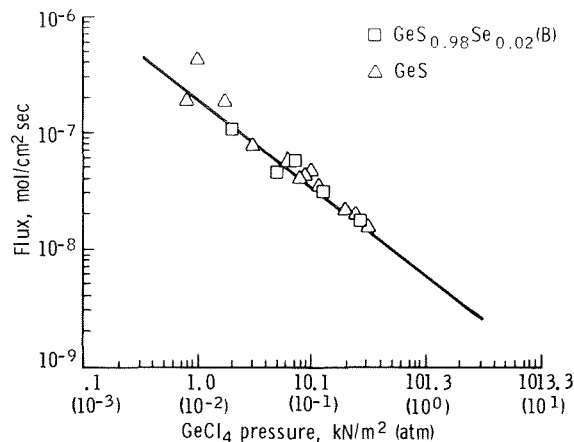


FIGURE 26-17.—Extrapolation of flux as a function of pressure data from the diffusion branch of the ground-based flux curves (fig. 26-1) for system B and GeS.

A comparison of the data in table 26-III reveals a rather significant result. For system A, the microgravity flux is lower than the normal gravity flux but approximately three times greater than predicted for a purely diffusion-type transport. These observations are consistent with the Skylab results. For system B, the normal gravity and microgravity fluxes are the same but the latter is more than three times greater than the transport rate predicted by theory. The pressure of transport agent  $\text{GeCl}_4$  employed for ASTP system B is different from the  $\text{GeI}_4$  pressure of the corresponding Skylab experiment for which the same ground and space fluxes were observed. This fact indicates the importance of the chemical properties of the transport system for flux considerations. For system C, the normal gravity and microgravity fluxes are the same within error limits and the latter is nearly five times greater than predicted. A comparison of the individual flux data of systems B and C demonstrates that the effect of argon on the mass transport rate is the same under normal gravity and microgravity conditions. The observed decrease in flux upon addition of argon is in good agreement with ground-based inert-atmosphere studies, as shown in figure 26-1. These combined results have two important consequences. First, the greater than predicted transport rates observed in a microgravity environment are not caused by gravity fluctuations or any other conditions typical of

spacecraft operations. Second, the effect of argon on the mass flux is independent of gravity and, thus, affects the inherent physicochemical properties of the transport system. These observations are of primary importance for the explanation of the unexpected flux results.

In view of the rather unconventional nature of microgravity transport phenomena, it is necessary to demonstrate independently the validity of the discrepancies between the flux values actually observed in space and those predicted on the basis of a diffusion-type transport. For this purpose, different transport models developed by Schaefer (ref. 26-3), Lever (ref. 26-6), Mandel (ref. 26-7), and Faktor et al. (ref. 26-8) have been used. These models are for vapor transport by diffusion and differ essentially in the treatment of the so-called streaming effect or flow factor and in the thermodynamic calculation of partial pressure gradients. Based on these diffusion models, curves of flux as a function of pressure were computed for the temperature gradients and transport agents of the ASTP, Skylab 3, and Skylab 4 experiments. The "theoretical" flux curves were fitted to the diffusion branch of the experimental ground-based curves (fig. 26-1 for the ASTP mission and accordingly for the Skylab missions) to obtain optimal fit. This procedure yielded the numerical constants required for the calculation of the fluxes for the specific ASTP and Skylab conditions. The results of these computations for the different



models are listed in table 26-IV together with the observed and extrapolated fluxes. A comparison of these data shows that the flux values obtained from the model computations agree within a factor of 2 with the extrapolated values. In no case are the transport rates predicted by the models greater than the observed fluxes. When the uncertainties associated with thermodynamic calculations of partial pressures and transport effects are considered, the agreement between the model calculations and the extrapolation data is close. However, because of these uncertainties, the extrapolated data represent the best flux values for comparison. The combined data demonstrate unambiguously that the microgravity transport rates cannot be explained on the basis of an exclusively diffusion-type process. The internal consistency and close agreement between the flux results of the ASTP and Skylab missions obtained for different chemical systems, eight pressures,

two transport agents, and three temperature gradients strongly support the validity of these observations. The combined results lead to the conclusion that the greater than predicted mass transport rates in a microgravity environment are due to non-gravity-caused transport effects. These unexpected phenomena are related to thermochemical effects of gas phase reactions, which have not been considered in existing vapor transport models.

The latter conclusion is supported by the analysis and application of models for convective vapor transport on Earth developed by Schaefer (ref. 26-3) based on the Hagen-Poiseuille equation and by Klosse and Ullersma (ref. 26-9) using a hydrodynamic approach and the Navier-Stokes equation. An important difference between these two models is their treatment of the convective boundary layer, the fluid layer immediately in contact with the growing crystal and through

TABLE 26-IV.—Mass Transport Rates Observed and Predicted for Microgravity Conditions

System	Mass flux, mol/cm <sup>2</sup> sec					
	Observed	Extrapolated	Modeled			
			Schaefer (ref. 26-3)	Lever (ref. 26-6)	Mandel (ref. 26-7)	Faktor et al. (ref. 26-8)
ASTP (877 → 780 K (604° → 507° C) <sup>a</sup> )						
GeSe <sub>0.99</sub> Te <sub>0.01</sub> (A)	4.2×10 <sup>-9</sup>	1.4×10 <sup>-9</sup>	2.5×10 <sup>-9</sup>	2.7×10 <sup>-9</sup>	2.6×10 <sup>-9</sup>	3.1×10 <sup>-9</sup>
GeS <sub>0.98</sub> Se <sub>0.02</sub> (B)	22.1	6.5	8.9	9.1	9.1	9.5
GeS + Ar (C)	13.0	2.8	3.6	3.7	3.2	5.2
Skylab 3 (797 → 695 K (524° → 422° C) <sup>a</sup> )						
GeSe (A)	5.0×10 <sup>-9</sup>	0.5×10 <sup>-9</sup>	0.80×10 <sup>-9</sup>	0.89×10 <sup>-9</sup>	0.86×10 <sup>-9</sup>	1.1×10 <sup>-9</sup>
GeSe (B)	10.0	2.5	3.4	3.7	3.6	4.2
GeTe (C)	3.0	.5	.84	.87	.87	.92
Skylab 4 (685 → 619 K (412° → 346° C) <sup>a</sup> )						
GeSe (A)	0.8×10 <sup>-9</sup>	0.15×10 <sup>-9</sup>	0.14×10 <sup>-9</sup>	0.14×10 <sup>-9</sup>	0.14×10 <sup>-9</sup>	0.15×10 <sup>-9</sup>
GeSe (B)	1.8	.35	.29	.30	.30	.30
GeTe (C)	1.0	.40	.79	.79	.79	.79

<sup>a</sup>Temperature gradients.

which mass must diffuse. The model based on the Hagen-Poiseuille equation (ref. 26-3) does not include consideration of a boundary layer. In the hydrodynamic model (ref. 26-9), the thickness of the boundary layer depends on the aspect ratio of the enclosure. Preliminary applications of these convection models to the investigators' experimental ground-based flux curves show systematic deviations. The mass fluxes predicted by the first model (ref. 26-3) for convective transport are greater than fluxes observed. The second model (ref. 26-9) agrees with the investigators' experimental results in the initial convection range and predicts fluxes lower than those observed at higher pressures. These deviations from the experimental ground-based data are related to the treatment of the boundary layer in these models (refs. 26-3 and 26-9). In addition, possible thermal effects of gas phase reactions on mass transport and on the boundary layer are not considered in the convection models (refs. 26-3 and 26-9). Theoretical and experimental studies are being conducted to further analyze existing vapor transport models through systematic applications of these models to different transport systems investigated in the RPI laboratory. The immediate purpose of these efforts is the extension of ground-based convection models to agree with experimental results. These modifications combined with the investigators' spaceborne and continued ground experiments will lead to the development of a transport model for microgravity conditions.

On the basis of these results, the transport phenomena observed for the ASTP and Skylab mission experiments are of far-reaching scientific and technological significance. The improvement of ground-based transport models is of basic and practical value for crystal growth theories and techniques on Earth. A transport model for space conditions based on microgravity experiments is of primary importance for actual space-processing applications.

## SUMMARY AND CONCLUSIONS

The original objectives of the crystal growth by vapor transport experiment were to investigate the effects of microgravity forces on the

morphology of single crystals of mixed systems and to determine the mass transport rates of these systems using the chemical transport technique. For this purpose, three vapor transport experiments were performed during the Apollo-Soyuz mission using three chemical compounds, two transport agents, and one inert gas in one common temperature gradient. The analysis of these experiments is based on a direct comparison of X-ray diffraction, microprobe, scanning electron and optical microscopy, and chemical etching studies of crystals obtained under ground-based (prototype) and microgravity conditions. The results demonstrate a considerable improvement in structural and chemical homogeneity, surface morphology, and bulk perfection of the space-grown materials compared to ground-based specimens. In addition to the positive crystallographic results, the confirmation of greater mass transport rates in microgravity than predicted by existing transport models represents the second major achievement of this experiment.

The excellent agreement between the ASTP and Skylab results demonstrates the validity of the observed crystal growth and transport properties in space for a class of technologically useful materials. This confirms the initial predictions concerning the suitability of the vapor transport technique for the growth of higher quality crystals and for the observation of unexpected phenomena in a microgravity environment. These results are of basic scientific and practical importance for the modification of transport models on Earth. The production of high-quality crystals at high mass transport rates is of technological significance for space-processing applications.

## REFERENCES

- 26-1. Wiedemeier, H.; Klaessig, F. C.; Wey, S. J.; and Irene, E. A.: Vapor Growth of GeSe and GeTe Single Crystals in Micro-Gravity. Proceedings of the Third Space Processing Symposium on Skylab Results, vol. 1. June 1974, pp. 235-256.
- 26-2. Wiedemeier, Heribert; Klaessig, Frederick C.; Irene, Eugene A.; and Wey, Song J.: Crystal Growth and Transport Rates of GeSe and GeTe in Micro-Gravity Environment. *J. Crystal Growth*, vol. 31, Dec. 1975, pp. 36-43.

- 26-3. Schaefer, Harald: Chemical Transport Reactions. Academic Press (New York), 1964.
- 26-4. Wiedemeier, H.; Irene, E. A.; and Chaudhuri, A. K.: Crystal Growth by Vapor Transport of GeSe, GeSe<sub>2</sub>, and GeTe and Transport Mechanism and Morphology of GeTe. J. Crystal Growth, vol. 13-14, 1972, pp. 393-396.
- 26-5. Wiedemeier, H.; and Irene, E. A.: The Chemical Transport Rates and Crystal Morphology of GeSe. Z. Anorg. Allgem. Chem., vol. 400, 1973, pp. 59-66.
- 26-6. Lever, R. F.: Multiple Reaction Vapor Transport of Solids. J. Chem. Phys., vol. 37, no. 5, Sept. 1, 1962, pp. 1078-1081.
- 26-7. Mandel, G.: Multiple Reactions and the Vapor Transport of Solids. J. Chem. Phys., vol. 37, no. 6, Sept. 15, 1962, pp. 1177-1180.
- 26-8. Faktor, M. M.; Garrett, I.; and Heckingbottom, R.: Diffusional Limitations in Gas Phase Growth of Crystals. J. Crystal Growth, vol. 9, May 1971, pp. 3-11.
- 26-9. Klosse, K.; and Ullersma, P.: Convection in a Chemical Vapor Transport Process. J. Crystal Growth, vol. 18, Jan.-Mar. 1973, pp. 167-174.



## 27. Halide Eutectic Growth

### Experiment MA-131

*A. S. Yue,<sup>a†</sup> C. W. Yeh,<sup>a</sup> and B. K. Yue<sup>a</sup>*

#### ABSTRACT

Continuous and discontinuous lithium fluoride fibers, embedded in a sodium chloride matrix, have been produced in space and on Earth. The production of continuous fibers in a eutectic mixture was attributed to the absence of convection currents in the liquid during solidification in space. Image transmission and optical transmittance measurements of transverse sections of the space-grown and Earth-grown ingots were made with a light microscope and a spectrometer. Better optical properties were obtained from the space-grown eutectics. This result is attributed to a better alignment of lithium fluoride fibers along the growth direction.

#### INTRODUCTION

When certain binary eutectic mixtures solidify, one of the two phases can form fibers or platelets in a matrix of the second phase. For example, when a eutectic liquid of sodium chloride (NaCl) and sodium fluoride (NaF) solidifies, fibers of NaF (ref. 27-1) form in a matrix of NaCl. Similarly, when a liquid of NaCl and lithium fluoride (LiF) solidifies, LiF will form the fiber phase in the NaCl matrix.

Fiberlike and platelike eutectics produced on Earth are limited in quality by the presence of a banded structure (refs. 27-2 and 27-3), by discontinuity (ref. 27-4), and by faults (refs. 27-5 and

27-6) caused, at least in part, by vibration and convection currents in the melt during solidification. The presence of these defects makes the solid-state eutectic devices inefficient and useless (ref. 27-7).

If the solidification process is performed in a space environment, where there are no vibration and convection currents in the melt, there is reason to believe that continuous fiberlike eutectic microstructures can be produced. The electric, thermomagnetic, optical, and superconducting characteristics of such eutectics will be strongly anisotropic, which suggests the possibility for important applications of the eutectic devices. A Skylab experiment (ref. 27-1) of NaCl-NaF eutectic demonstrated that continuous fibers of NaF embedded in an NaCl matrix could be grown by the directional solidification technique in space.

The objectives of the Apollo-Soyuz Test Project (ASTP) MA-131 experiment were

1. To prepare, in a space environment, fiberlike LiF-NaCl eutectic with continuous LiF fibers embedded in the NaCl matrix. (This eutectic of continuous LiF fibers cannot be produced on Earth because of convection currents and vibration in the melt during solidification.)

2. To extract a few fibers from an ASTP space-grown NaCl-LiF eutectic ingot and also from Earth-grown ingots and to determine whether the extracted fibers were continuous or discontinuous.

3. To calculate the interfiber spacing of the LiF fibers.

4. To measure transmittance as a function of wavelength for the space-grown and Earth-grown ingots (both parallel and perpendicular to the fibers).

<sup>a</sup>University of California at Los Angeles.

<sup>†</sup>Principal Investigator.

## EXPERIMENTAL PROCEDURE

The NaCl-29 weight percent LiF eutectic ingots were prepared from 99.96-percent-pure NaCl and 99.99-percent-pure LiF. The NaCl-LiF ingots were melted and solidified in an induction furnace having an argon atmosphere. After solidification, each ingot was machined to the shape and dimensions shown in figure 27-1 (labeled "sample").

To hold the NaCl-LiF ingot, a graphite crucible was machined from a high-purity graphite rod. Because graphite is a very fragile material, a special method was used to machine the crucibles. The graphite crucibles were calcined in vacuum at a temperature of 1223 K (950° C) for 25 hours.

The eutectic-ingot/graphite-crucible assembly was then loaded into a 304 stainless steel container of the dimensions shown in figure 27-1. The container was constructed from stainless steel tubing with a stainless steel plug heliarc-welded to one end. After the ingot-crucible assembly was loaded, the inner wall of the stainless steel container was coated with a graphite paste where the NaCl-LiF ingot was exposed to the container. A calcined graphite disk (0.025 cm (0.010 in.) thick) was then placed over the end of the ingot. The graphite paste and the disk were used to prevent a reaction between the container and the eutectic when the ingot was later remelted and resolidified. The container was then sealed by heliarc-welding a cap, with a vent hole (no. 60), in place to form the ampoule (fig. 27-1).

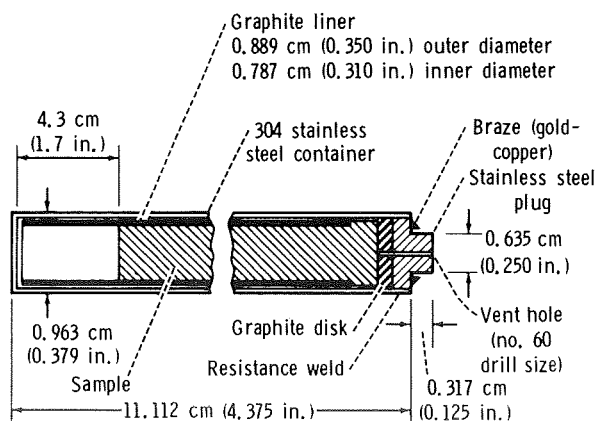


FIGURE 27-1.—Sketch of an ampoule.

Three groups of eutectic-ingot samples were used. The first (group A) was retained at the laboratory for later comparison, the second (group B) was regrown in a prototype furnace for comparison with the space-grown samples, and the third (group C) was the ASTP flight sample.

The resolidification experiment in the Apollo spacecraft was performed in the multipurpose electric furnace (ref. 27-8). A 1.3-cm (0.5 in.) portion of the eutectic ingot adjacent to the graphite disk was left unmelted; the remaining portion of the ingot was melted and resolidified unidirectionally toward the empty space of the ampoule as indicated in figure 27-1.

## RESULTS

The experimental results are presented in five parts: (1) examination of the macrostructures and microstructures of the space-grown and Earth-grown eutectics, (2) extraction of continuous LiF fibers embedded in an NaCl matrix, (3) calculation of the interfiber spacing of the LiF fibers of the space-grown NaCl-LiF eutectic, (4) determination of the image transmission of space-grown and Earth-grown eutectics, and (5) determination of the optical transmittance of space-grown and Earth-grown eutectics.

### Macrostructures and Microstructures

The appearance of the three ampoules after completion of the ASTP experiment is shown in figure 27-2. The surfaces of the stainless steel cylinders and plugs were in perfect condition.

The three space-grown eutectic ingots removed from the ampoules by grinding off the welded ends of each stainless steel cylinder are shown in figure 27-3. Careful inspection of the surface of the ingots revealed no evidence of reaction between the NaCl-LiF eutectic and the graphite container. In sample number 18, one transverse fracture surface occurred at the head portion (fig. 27-3(a)). However, the fracture occurred after resolidification and did not interrupt the growth pattern of the sample.

The solidified eutectic (sample no. 19) that reveals the shape of the meltback interface is shown in figure 27-4. The resolidified portion of

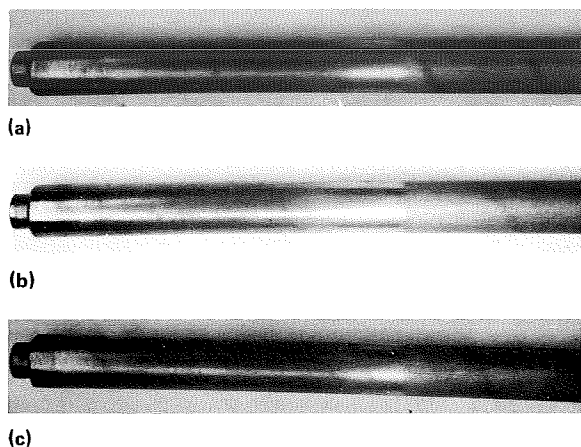


FIGURE 27-2.—Photographs of the three ASTP flight ampoules. (a) Sample number 18. (b) Sample number 19. (c) Sample number 20.

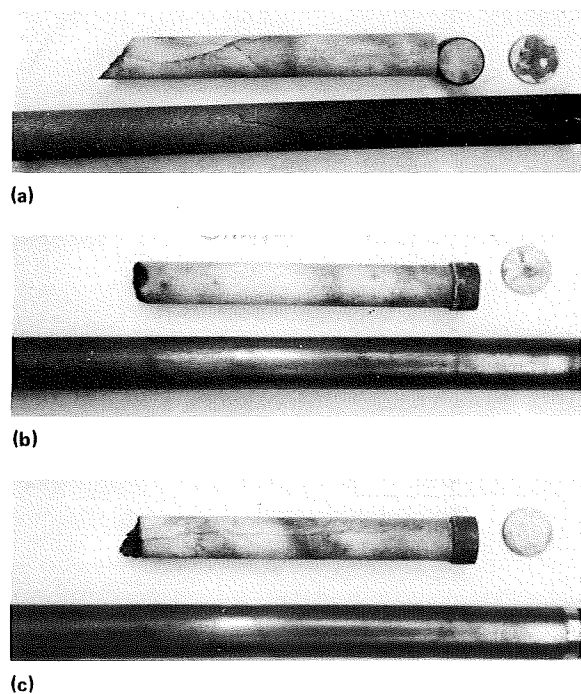


FIGURE 27-3.—Photographs of the ASTP space-grown NaCl-LiF eutectic after removal from ampoules. (a) Sample number 18. (b) Sample number 19. (c) Sample number 20.

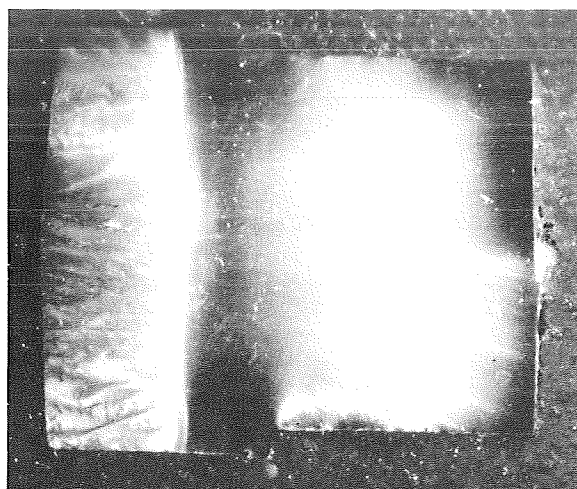


FIGURE 27-4.—Photograph showing the original shape of the solid-liquid interface of the ASTP space-grown NaCl-LiF eutectic (3.8X).

the ingot is on the right of the interface, and the unmelted portion is on the left of the interface. In this eutectic, the remeltback interface is 0.28 cm (0.11 in.) from the left end of the ingot, whereas the same meltback distances of the other two space-grown eutectics are approximately 0.51 cm (0.20 in.). This difference may indicate a slight offset in the positioning of the heat zones in the furnace. A photomicrograph of the solid-liquid interface is shown in figure 27-5, in which the beginning of the solidification process can be seen. The elongated LiF phases (fig. 27-5) grew in a direction perpendicular to the conical solid-liquid interface; therefore, the direction of heat extraction during the onset of solidification probably was not parallel to the growth direction as intended. At a distance not far from the initial solid-liquid interface, as evidenced in figures 27-4 and 27-5, the LiF fibers began to divert toward the periphery of the ingot. Figure 27-6(a), a representative photomicrograph of a longitudinal section of space-grown sample number 19, shows the long, continuous fibers. The eutectic microstructure that resulted when the NaCl-LiF eutectic was grown on Earth in the presence of convection current is shown in figure 27-6(b); this structure reveals that the solidified LiF fibers are short and discontinuous. A representative photomicrograph of a transverse section of a space-grown eutectic is

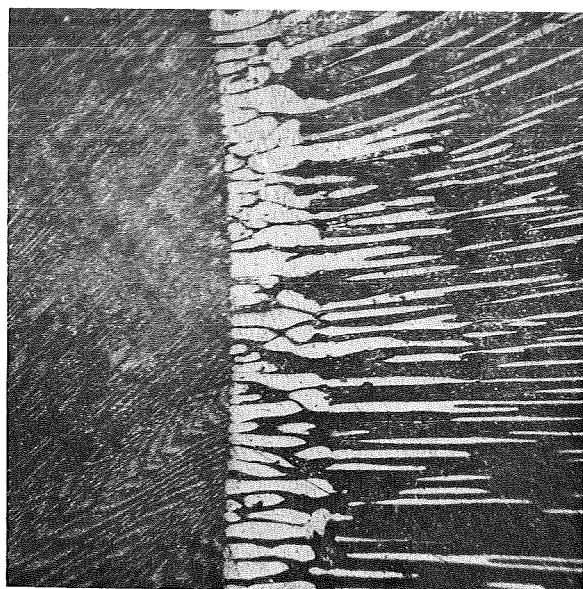


FIGURE 27-5.—Photomicrograph of the original solid-liquid interface (67 $\times$ ).

shown in figure 27-7, which reveals that the fibers tend to be round. Figure 27-8 is a scanning electron micrograph that shows the shapes of the Earth-grown LiF fibers. In this figure, the perspective is a view of the round LiF fibers protruding from the continuous NaCl matrix. Figure 27-9, a corresponding scanning electron micrograph of the space-grown ingot, shows that all the LiF fibers are aligned unidirectionally.

Single-grain eutectic was not produced in the presence of microgravity in space. This finding is evidenced in figure 27-10, which is a transverse section of space-grown sample number 18 and shows the presence of many grains throughout the cross section. Supporting evidence is given in figure 27-11(a), which is a photograph of space-grown sample number 18. Filtered light from a microscope was directed at the lower end of the eutectic. Good alignment of LiF fibers along the longitudinal axis permitted transmission of light from the lower end and propagation through the ingot for a longer distance with a much stronger intensity than with the Earth-grown ingot (fig. 27-11(b)). Light was not transmitted through the upper portion of the space-grown eutectic because, in that portion of the ingot, the fibers were not aligned with the longitudinal axis.

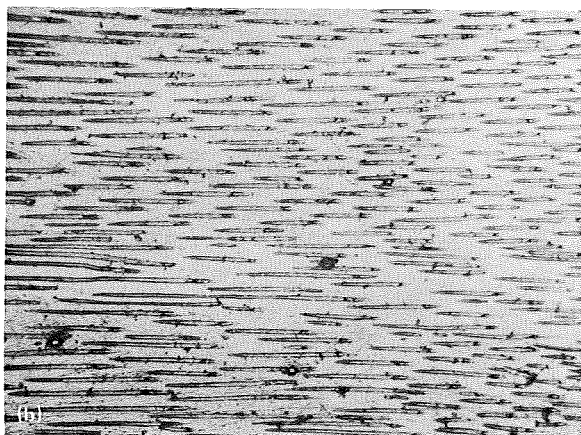
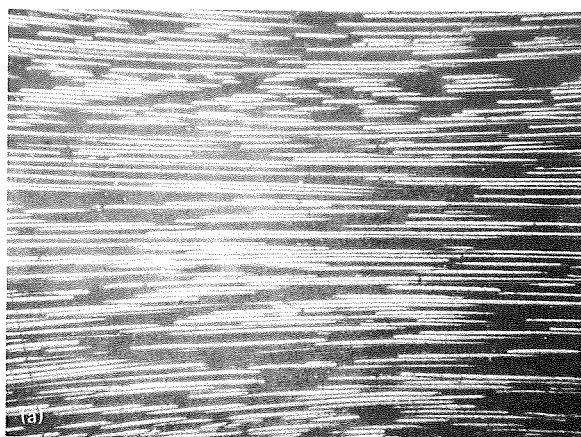


FIGURE 27-6.—Photomicrographs of a longitudinal section of the NaCl-LiF eutectic. (a) Space-grown eutectic (sample no. 19) showing continuous LiF fibers (30.5 $\times$ ). (b) Earth-grown eutectic showing discontinuous LiF fibers (115.5 $\times$ ).

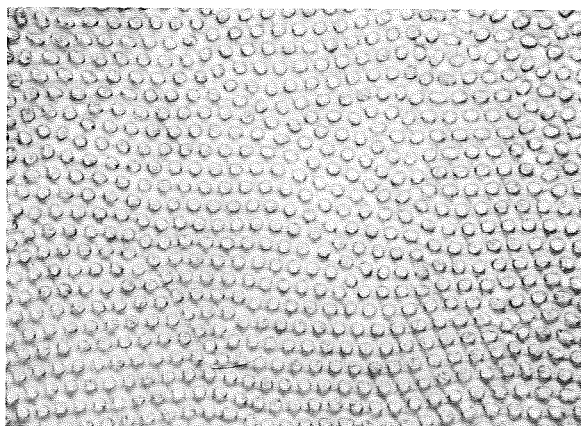


FIGURE 27-7.—Photomicrograph of the transverse section of an ASTP space-grown eutectic showing the round shapes of LiF fibers (205 $\times$ ).



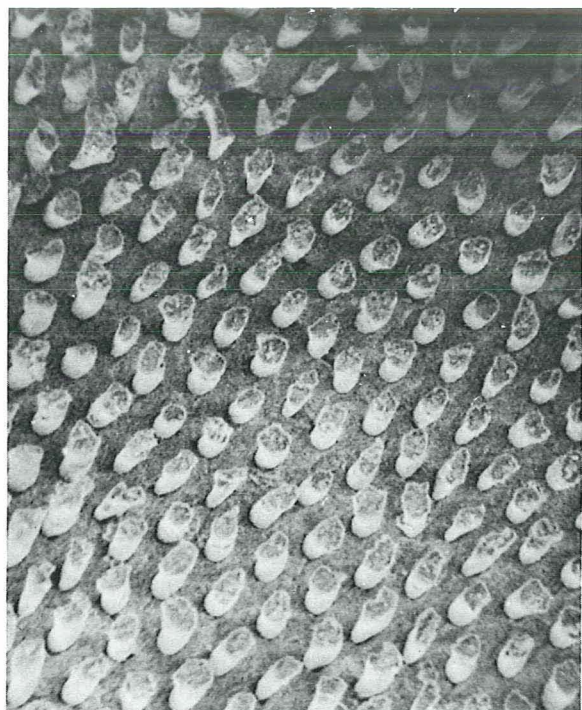


FIGURE 27-8.—Scanning electron micrograph of the Earth-grown LiF fibers (1058 $\times$ ).



FIGURE 27-10.—Photograph of the transverse section of the NaCl-LiF eutectic showing grains and subgrains (sample no. 18, 7.9 $\times$ ).

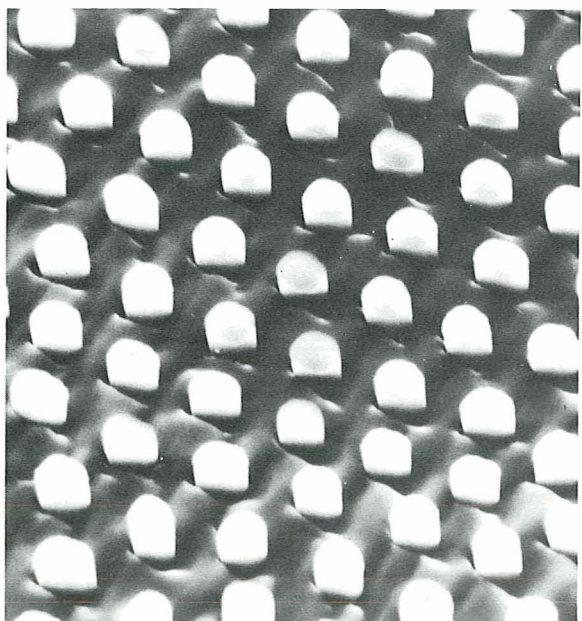


FIGURE 27-9.—Scanning electron micrograph of the ASTP space-grown LiF fibers (1900 $\times$ ).

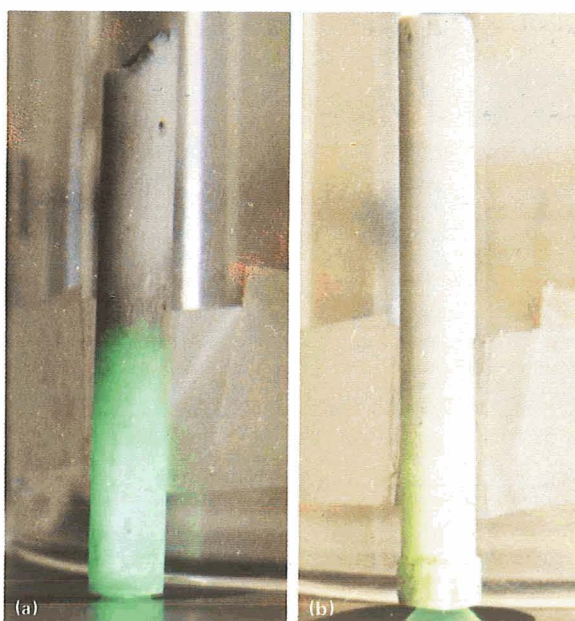


FIGURE 27-11.—Photographs of NaCl-LiF eutectics. (a) ASTP space grown (sample no. 18). (b) Earth grown.

### Lithium Fluoride Fibers

Figure 27-12(a) is a photograph of a space-grown ingot that was taken when the LiF fibers were suspended in methyl alcohol. From this figure, it is evident that the LiF fibers are continuous and straight. When an Earth-grown NaCl-LiF eutectic ingot (from group A) was immersed in the same solution, LiF fibers could also be extracted from the NaCl matrix. However, as indicated in figure 27-12(b), the extracted fibers were short and discontinuous, which is in agreement with prediction. Based on this analysis, it was tentatively concluded that continuous LiF fibers were produced in space.

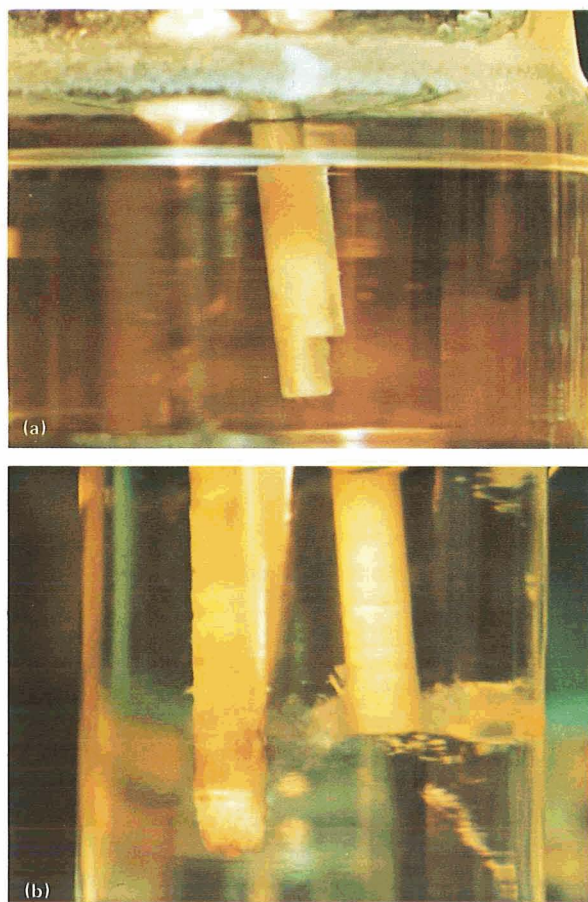


FIGURE 27-12.—Photographs of NaCl-LiF eutectic ingot (2 $\times$ ). (a) ASTP space-grown ingot showing continuous LiF fibers. (b) Earth-grown ingot showing discontinuous and randomly oriented fibers.

### Interfiber Spacing

The measured interfiber distances in space-grown, prototype-furnace-grown, and Earth-grown ingots, at growth rates of approximately 4.5  $\mu\text{m}/\text{sec}$ , are listed in table 27-I. The average fiber diameter of the prototype-furnace-grown and space-grown ingots is 3.6  $\mu\text{m}$ . These measurements indicate no significant difference in interfiber spacing between the space-grown and the prototype-furnace-grown ingots. The interfiber spacing of the Earth-grown eutectic is smaller than that of the space-grown eutectic because the Earth-grown eutectic was subjected to a faster cooling rate during growth.

TABLE 27-I.—Measured Interfiber Distances<sup>a</sup> of Eutectic Ingots

Sample no.	Interfiber distance, $\mu\text{m}$
<i>ASTP space grown</i>	
18	6.68
19	6.41
20	5.41
<i>Prototype furnace grown</i>	
1	6.92
2	7.35
3	6.70
<i>Earth grown</i>	
Laboratory sample	4.5

<sup>a</sup>Growth rates of approximately 4.5  $\mu\text{m}/\text{sec}$ .



### Image Transmission

Image transmission properties similar to those of fiber optic materials were obtained with an Earth-grown NaCl-NaF eutectic (ref. 27-9). Because the eutectic in the referenced case had discontinuous NaF fibers, far better results were expected to be obtained if a similar halide eutectic having continuous fibers was produced in space. Two 2-mm-long cylindrical sections were cut from space-grown (group C) and Earth-grown (group A) NaCl-LiF eutectic ingots. Image transmission experiments were performed on these two sections, and the results are shown in figure 27-13. Figure 27-13(a) shows that an image was transmit-

ted from a source (a sheet of paper containing the word "solar") through the length of the sample (2 mm) to its surface. The transmitted image has the same dimensions as the source, an indication that the LiF fibers are perpendicular to the plane of the paper. However, the transmitted image is not as clear as the original image of the source; therefore, a loss of light through transmission is indicated. Some loss is common to all fiber optic materials (ref. 27-10). An image transmitted through a section of an Earth-grown eutectic was also observed as seen in figure 27-13(b). However, the image is unclear and the dimensions of the letters "S" and "E" are larger than those of the source, an indication that the fibers are diverged away from the source.

### Optical Property

In a previous ground-based study (ref. 27-9), an NaCl-NaF eutectic was found to be a far-field infrared transmitting medium for wavelengths longer than the interfiber distance. Because the NaCl-NaF eutectic used for optical measurement had discontinuous NaF fibers embedded in an NaCl matrix, better results were expected if continuous fibers were obtained. This was indeed the case, as demonstrated in the Skylab experiment (ref. 27-1). Similar experiments comparing transmission properties of space-grown and Earth-grown NaCl-LiF eutectics were conducted for ASTP. A comparison of the far-field infrared transmission of transverse sections of three NaCl-LiF eutectic samples is shown in figure 27-14. The ASTP space-grown eutectic is shown to have the highest transmittance over nearly the entire wavelength range, an indication that it had the highest percentage of fibers parallel to the growth direction. The transmittance result also shows that, over part of the wavelength range, the prototype-furnace-grown eutectic had a lower transmittance than the laboratory-grown eutectic.

The effect of section thickness on transmission for the prototype-furnace-grown eutectics and the ASTP space-grown eutectics is shown in figure 27-15. In both cases, the thinner the section, the higher the transmittance for a fixed wavelength. This observation is in agreement with absorption laws as expected.

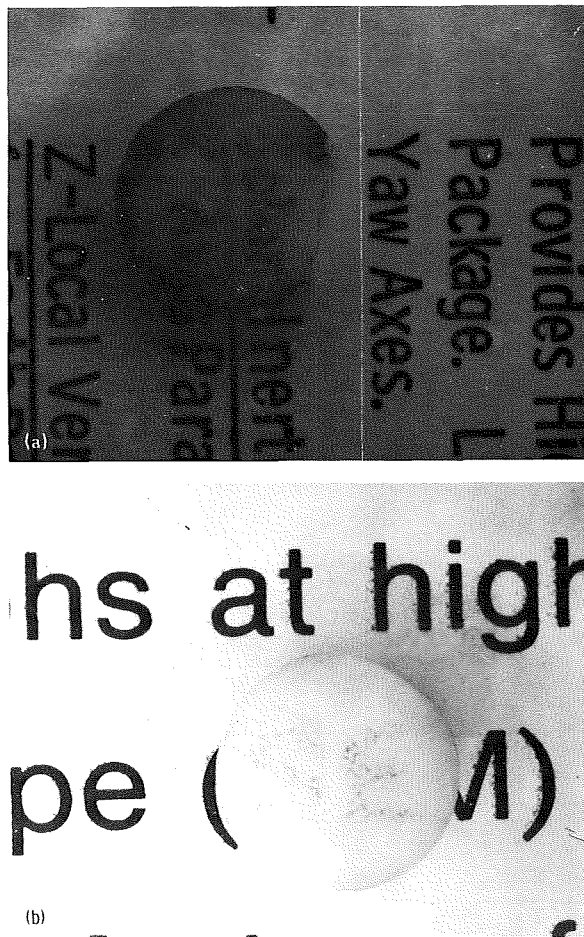


FIGURE 27-13.—Image transmission macrograph of NaCl-LiF eutectics (sample thickness, 2 mm; 3.8 $\times$ ). (a) ASTP space grown. (b) Earth grown.

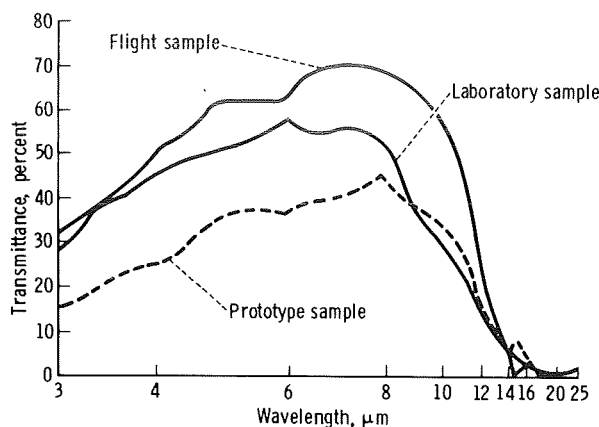


FIGURE 27-14.—Far-field infrared transmission curves of transverse sections of NaCl-LiF eutectics grown on Earth and in space. The sample thickness was 0.0536 cm (0.0211 in.).

Figures 27-16(a) and 27-16(b) show plots of transmittance as a function of wavelength for a longitudinal section of a laboratory-grown eutectic (group A), using polarized light and with the electric field  $E$  parallel and perpendicular to the fiber axes, respectively. Figures 27-17(a) and 27-17(b) show the same curves for the space-grown eutectic (sample no. 18). For both orientations, the transmittance for the space-grown eutectics is lower than it is for the Earth-grown eutectics over the range of wavelengths measured. It is difficult to explain this peculiar phenomenon at the present time.

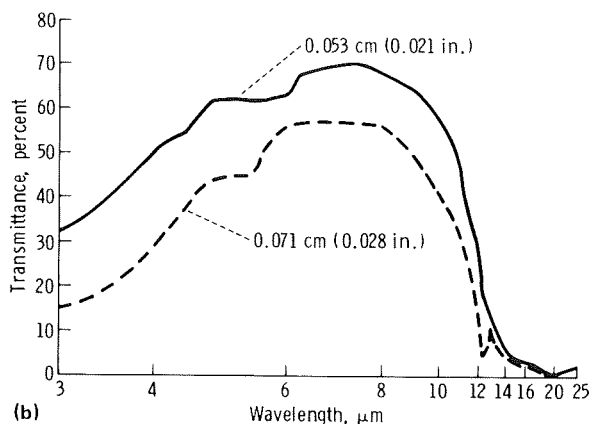
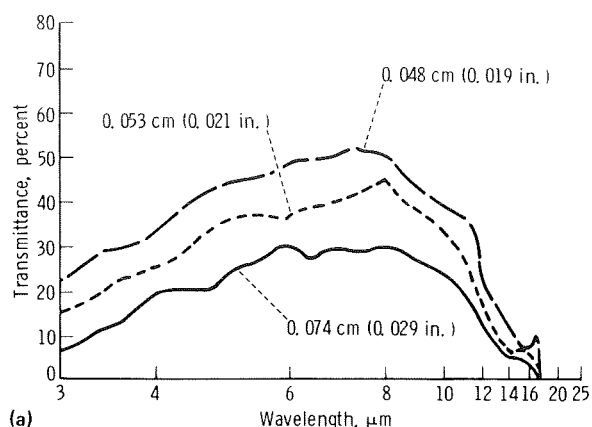


FIGURE 27-15.—Far-field infrared transmission curves of transverse sections of NaCl-LiF eutectics having different thicknesses. (a) Prototype-furnace-grown eutectic. (b) ASTP space-grown eutectic.

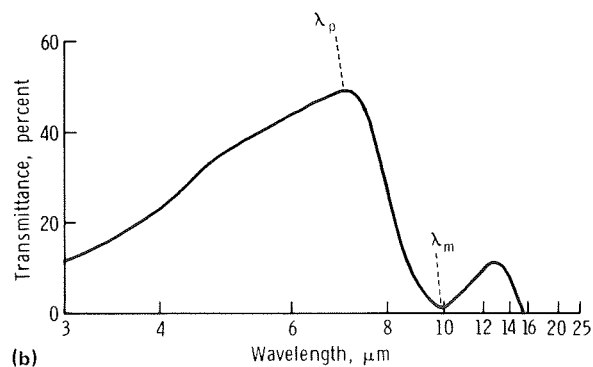
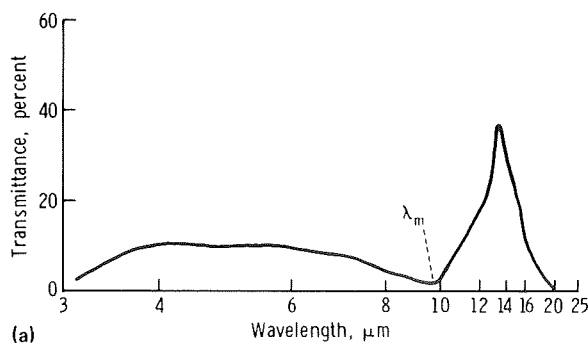


FIGURE 27-16.—Far-infrared transmittance curves of a longitudinal section of a laboratory-grown NaCl-LiF eutectic (group A). (a)  $E_{\parallel}$  fiber axis;  $\lambda_m$  is the maximum wavelength. (b)  $E_{\perp}$  fiber axis;  $\lambda_p$  is the peak wavelength.



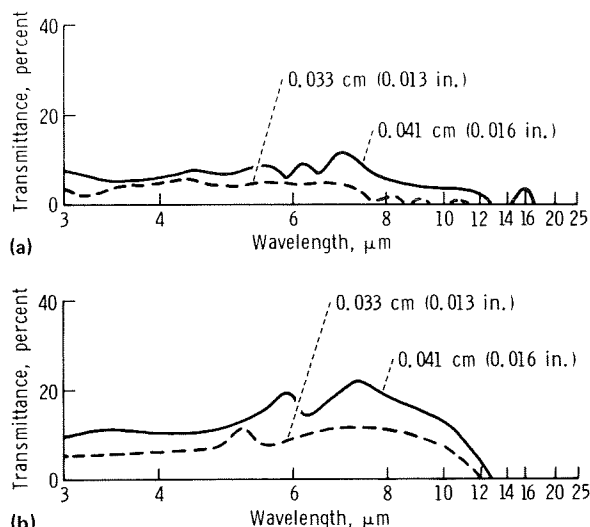


FIGURE 27-17.—Far-infrared transmittance curves of a longitudinal section of the ASTP space-grown NaCl-LiF eutectic of varying thicknesses. (a)  $E \parallel$  fiber axis. (b)  $E \perp$  fiber axis.

## DISCUSSION

### Lithium Fluoride Fibers

In a zero-g environment, there is no gravity-driven convection current in the liquid during solidification, and there is no difficulty in mixing two liquid phases of different densities. Furthermore, vibration levels in the spacecraft are far lower than those on Earth. Consequently, a homogeneous eutectic mixture consisting of continuous fibers can be produced in a space environment, and microstructure (which is sensitive to convection currents and vibration) can develop undisturbed. Accordingly, the success in producing continuous LiF fibers, as evidenced in figure 27-12, is due mainly to the absence of convection current in the melt during resolidification in space.

### Optical Property

Pure NaCl and NaF crystals have approximately 95 percent transmittance per centimeter of thickness up to 15 and 9  $\mu\text{m}$ , respectively, in the far-infrared wavelength region (ref. 27-1). Beyond these wavelength ranges, these crystals

have zero transmittance because of the optical modes of lattice vibration of ionic crystals. If a thin piece of NaCl-LiF eutectic is cut along its fiber axis (longitudinal section), as illustrated in figure 27-18, and is measured in the 2- to 20- $\mu\text{m}$  wavelength region with an infrared spectrometer, typical "transmittance as a function of wavelength" curves with polarized beam parallel and perpendicular to fiber axes are the result (figs. 27-16(a) and 27-16(b), respectively). For the electric field parallel to the fiber axes, the transmittance is near zero over a range of wavelengths for which the maximum wavelength  $\lambda_m$  is less than 10  $\mu\text{m}$ . When the electric field is perpendicular to the fiber axes, the percentage of transmittance increases over a range of wavelengths less than  $\lambda_m$  and reaches a maximum value at a wavelength of 7.2  $\mu\text{m}$ , which is designated a peak wavelength  $\lambda_p$  as indicated in figure 27-16(b). Because a thin NaCl-LiF eutectic sheet has these characteristics, it can be used as a polarizer and a modulator. It can transmit or block light rays at a specified wavelength when the electric field is rotating. The investigators have advanced an explanation that accounts for this phenomenon in terms of two-dimensional Bragg scattering and the polarization effect of Rayleigh scattering.

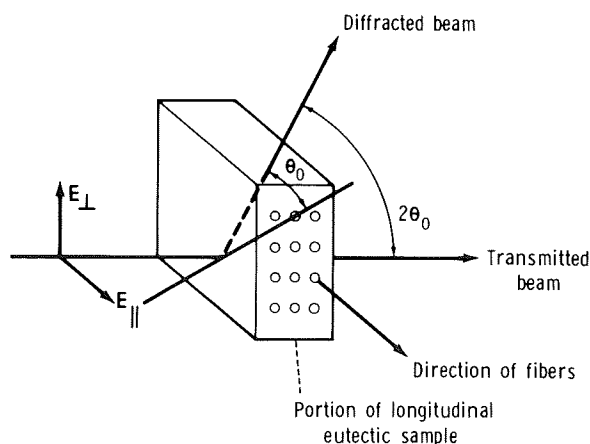


FIGURE 27-18.—Diagram illustrating factors involved in analyzing scattering measurements for transmission through a longitudinal sample section.

### SUMMARY

The following conclusions can be drawn from this investigation.

1. Continuous LiF fibers, regularly arranged in a portion of the NaCl matrix that has been resolidified unidirectionally in a space environment, have been produced.

2. Larger transmittance over a wider wavelength and better image transmission were obtained for transverse sections of the space-grown eutectic ingots.

### REFERENCES

- 27-1. Yue, A. S.; and Yue, J. G.: Solidification of NaCl-NaF Eutectic in Space. AIAA/ASME Conference on Thermophysics and Heat Transfer. AIAA Paper 74-646, July 1974.
- 27-2. Yue, A. S.; and Clark, J. B.: Determination of Eutectic Composition by Zone-Melting Method. Trans. TMS-AIME, vol. 221, no. 2, Apr. 1961, pp. 383-389.
- 27-3. Lemkey, F. D.; and Thompson, E. R.: Nickel and Cobalt Eutectic Alloys Reinforced by Refractory Metal Carbides. Met. Trans., vol. 2, no. 6, June 1971, pp. 1537-1544.
- 27-4. Yue, A. S.: Microstructure of Magnesium-Aluminum Eutectic. Trans. TMS-AIME, vol. 224, no. 5, Oct. 1962, pp. 1010-1015.
- 27-5. Crossman, F. W.; and Yue, A. S.: Unidirectionally Solidified Ti-TiB and Ti-Ti<sub>3</sub>Si<sub>3</sub> Eutectic Composites. Met. Trans., vol. 2, no. 6, June 1971, pp. 1545-1555.
- 27-6. Kraft, R. Wayne, Jr.; and Albright, D. L.: Microstructure of Unidirectional Solidified Al-CuAl<sub>2</sub> Eutectic. Trans. TMS-AIME, vol. 221, no. 1, 1961, pp. 95-102.
- 27-7. Weiss, H.: Electromagnetic Properties of Eutectic Composites (A Critical Review). Met. Trans., vol. 2, no. 6, June 1971, pp. 1513-1521.
- 27-8. Seidensticker, R. G.: System Design Considerations for Free-Fall Materials Processing. Third Space Processing Symposium; Skylab Results, vol. 2, NASA TM X-70253, 1974, pp. 595-601.
- 27-9. Batt, J. A.; Douglas, F. C.; and Galasso, F. S.: Optical Properties of Unidirectionally Solidified NaF-NaCl Eutectic. American Ceram. Soc. Bull., vol. 48, no. 6, June 1969, pp. 622-626.
- 27-10. Payne, D. N.; and Gambling, W. A.: Preparation of Multimode Glass- and Liquid-Core Optical Fibers. Opto-Electronics, vol. 5, no. 4, July 1973, pp. 297-307.

## 28. Multiple Materials Melting (Metals)

### Part of Experiment MA-150\*

*L. I. Ivanov,<sup>a</sup> V. N. Kubasov,<sup>a</sup> V. N. Pimenov,<sup>a</sup> K. P. Gurov,<sup>a</sup> E. V. Demina,<sup>a</sup>  
Yu. S. Malkov,<sup>a</sup> and V. M. Lazarenko<sup>a</sup>*

#### INTRODUCTION

Microgravity in space can be used to develop new technological processes for manufacturing materials. Weightlessness may be particularly beneficial in metallurgical synthesis of the so-called compound materials; i.e., materials composed of a meltable matrix and a heavy, more refractory second phase. The second-phase distribution for the solid-state components can be predetermined on Earth, and this distribution should remain unchanged after the matrix has been melted in conditions of "ideal" weightlessness.

Such materials systems are difficult to synthesize on Earth because of "weight" segregation of the elements, which results in a separation of the constituents in a molten-state matrix. It is believed that compound materials obtained in conditions of weightlessness possess unique physical, electrical, and other properties. Study of microgravity melting and solidification is of particular interest, both scientific and practical, for powdered metals and for alloys containing eutectics.

Equally interesting is the question of conducting basic scientific experiments under the weight-

less conditions of a space flight. For example, the study of laws governing mutual diffusion and growth of intermetallic phases within the diffusion area upon the interaction of solid and liquid metals is of great value for solid-state physics. The physical characteristics of diffusion processes can be investigated more effectively in a microgravity environment because of the much lower convection of space-molten metals compared to Earth-molten metals. The kinetics of these processes and the phase formation in tertiary systems represent yet other interesting points for study.

Therefore, the objectives of the metallic materials part of the Multiple Materials Melting Experiment were to investigate the effects of weightlessness on the following.

1. The feasibility of a metallurgical method of synthesizing compound materials with a predetermined distribution of constituents based on metals with significantly different specific gravities. Aluminum (Al) was chosen as a matrix and tungsten (W) was chosen as a "heavy" component.

2. The mutual diffusion and formation of intermetallic phases as a result of interaction of a meltable matrix (Al) and hard, refractory inclusions (W).

3. The melting and solidification of powdered Al.

Additional studies were made on microgravity melting and solidification of copper aluminum (CuAl) eutectic alloy as it interacts with Al, as well as on the diffusion and formation of intermetallic phases in the tertiary system of solid W, solid rhenium (Re), and liquid Al.

---

\*The Multiple Materials Melting Experiment is one of the five experiments that incorporated joint activities between the U.S. and U.S.S.R. crews. The joint U.S.-U.S.S.R. designation was "Experiment AS-3." The "germanium-silicon solid solutions" part of the experiment is reported in section 29.

<sup>a</sup>Institute for Metallurgy, U.S.S.R.

### EXPERIMENTAL METHOD AND SAMPLE ANALYSIS

The starting composite material prepared for melting in space was an Al cylinder (fused from pellets) 8 mm in diameter and 9 mm high. A rod composed of special WRe alloy (rhenium content  $\approx 30$  wt%), 2 mm in diameter and 4.5 mm high, was fused into the upper part of the Al cylinder along its axis of gravity. Seven W balls (round samples with an average diameter of approximately 1 mm) were fused into the lower part of the cylinder along the plane perpendicular to the cylinder axis. Only high-purity metals were used for sample preparation. Before fusing, the material surfaces were carefully cleaned to remove any possible contaminants.

Samples prepared in this manner were wrapped in aluminum foil and placed in capped graphite crucibles. The crucibles were loaded into quartz ampoules, which were outgassed to approximately  $0.133 \text{ N/m}^2$  (0.001 mmHg) and sealed. Figure 28-1 is an X-ray photograph of one of these ampoules.

The ampoules containing Al powder, obtained by crushing the solid Al sample, were prepared in the same manner. In addition to Al powder, each ampoule contained small pieces of CuAl eutectic alloy (mean diameter,  $\approx 2$  mm) that were insulated from the Al by aluminum foil. Three ampoules for each material were tested in conditions of weightlessness.

Similar samples were prepared for identical ground-based simulation tests. The specimens tested in flight were identified by the following numbers: MA-150-16, MA-150-17, and MA-150-18; the simulation samples were MA-150-9, MA-150-11, and MA-150-12. This report presents the experimental results for flight samples 16 and 17 as well as for ground-based samples 9, 11, and 12.

Both flight and ground-based samples were melted in a multipurpose electric furnace (sec. 21). The ampoules and sample materials were loaded in hermetically sealed cartridges. A disassembled view of the cartridge components is shown in figure 28-2. The fireproof cases used for transporting the cartridges onboard the Soyuz spacecraft are shown in figure 28-3.

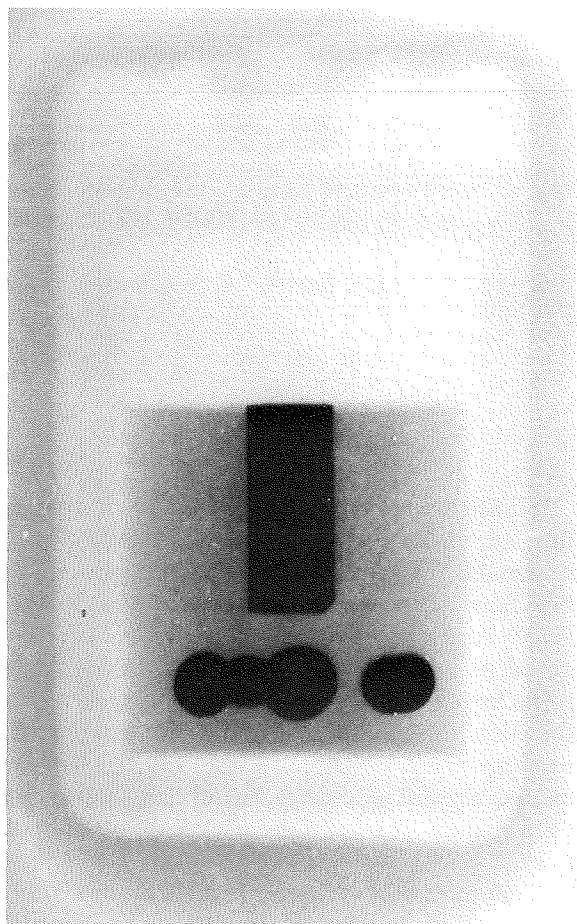


FIGURE 28-1.—X-ray photograph of ampoule containing a mixture of Al and W and WRe alloy. The balls are W; the rod is alloy.

Figure 28-4 is an X-ray photograph of flight cartridges showing the relative positions of compound material, powdered Al, and eutectics (also the germanium silicon crystals discussed in sec. 29). Figure 28-5 shows the thermal profile for the sample processed in flight. The same conditions were applied to ground-based processing.

After completion of the experiment, the ampoules and crucibles were first X-rayed for quick-look examination and then opened. The crucibles with compound material ingots were cut perpendicularly to the crucible axis.

Metallographically polished sections containing WRe rods, or W balls in cross section, were

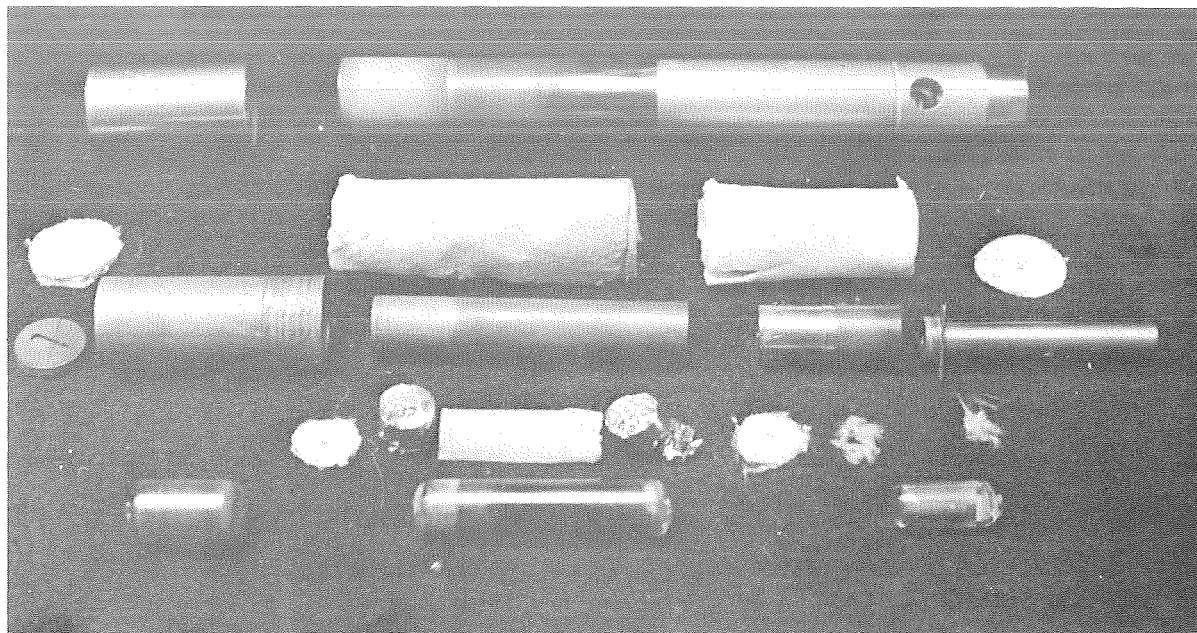


FIGURE 28-2.—Disassembled view of cartridge and ampoule with material specimen.

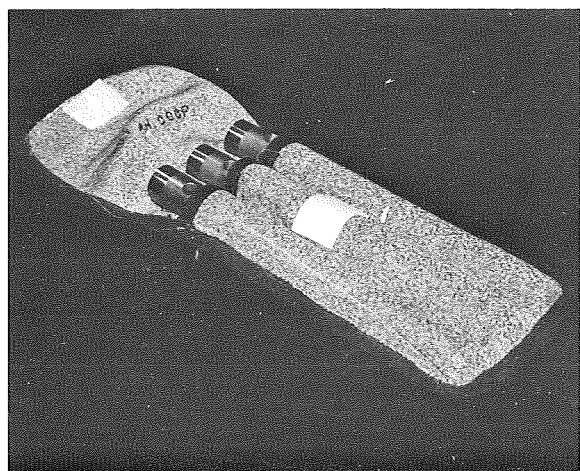


FIGURE 28-3.—Flight cartridges in transport case made of nonflammable cloth.

then prepared. Metallographic sections were also prepared from the pieces of eutectics. In etching the eutectic alloy sections, the following agents were used: 2.5 ml of nitric acid ( $\text{HNO}_3$ ), 2 ml of

hydrogen chloride ( $\text{HCl}$ ), 1.5 ml of hydrogen fluoride ( $\text{HF}$ ), and 94 ml of water ( $\text{H}_2\text{O}$ ).

The polished sections were examined by means of optical microscopy, electron probe microanalysis (ref. 28-1), and electron scanning microscopy.

Phase composition of the microsections was determined by quantitative local X-ray spectral analysis (refs. 28-2 to 28-5). Based on the technique described in reference 28-2, the weight concentration  $c_i$  of the  $i$ -th (heavier) component in a binary system is determined by

$$c_i = f_i^{(1)} f_i^{(2)} \frac{I_i}{I_{io}} \quad (28-1)$$

where  $I_i$  and  $I_{io}$  are the measured intensities of the characteristic radiation for the sample and for the standard, respectively;  $f_i^{(1)}$  is the atomic number correction that considers different stopping power and different incident electron scattering for the sample and for the standard;  $f_i^{(2)}$  is the absorption correction that considers the difference in absorption of the excited characteristic radiation for the

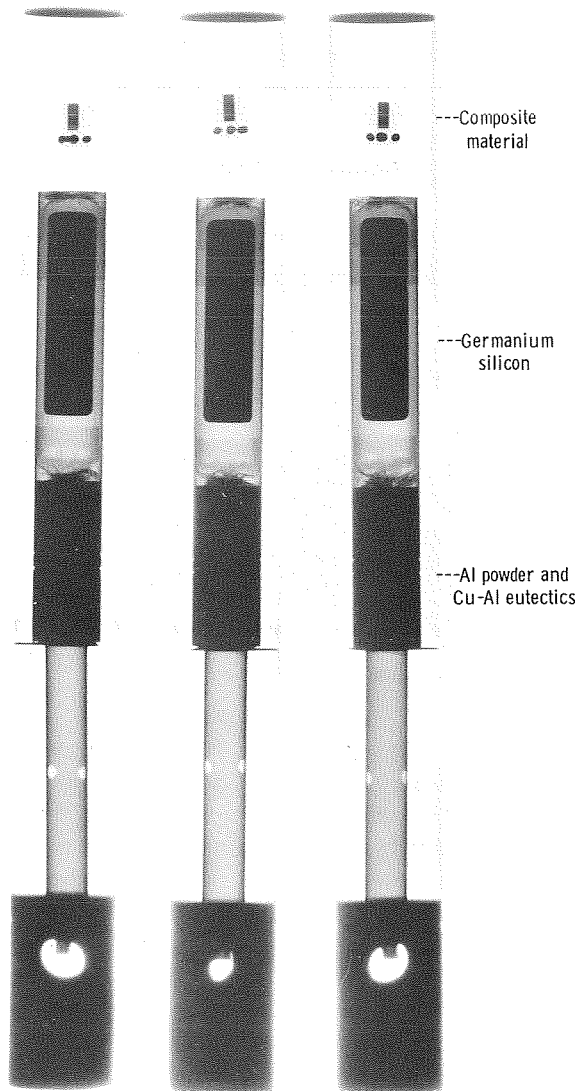


FIGURE 28-4.—X-ray photograph of flight cartridges MA-150-16, MA-150-17, and MA-150-18.

sample and the standard. These corrections are defined by

$$f_i^{(1)} = \frac{1 + 2\delta_i(1 - \beta^{-n})}{1 + 2\delta_i^*(1 - \beta^{-n})} \quad (28-2)$$

$$f_i^{(2)} = \frac{1 + \alpha E_o^n \tau_i^* (1 - \beta^{-n}) \operatorname{cosec} \theta}{1 + \alpha E_o^n \tau_{ii}^* (1 - \beta^{-n}) \operatorname{cosec} \theta} \quad (28-3)$$

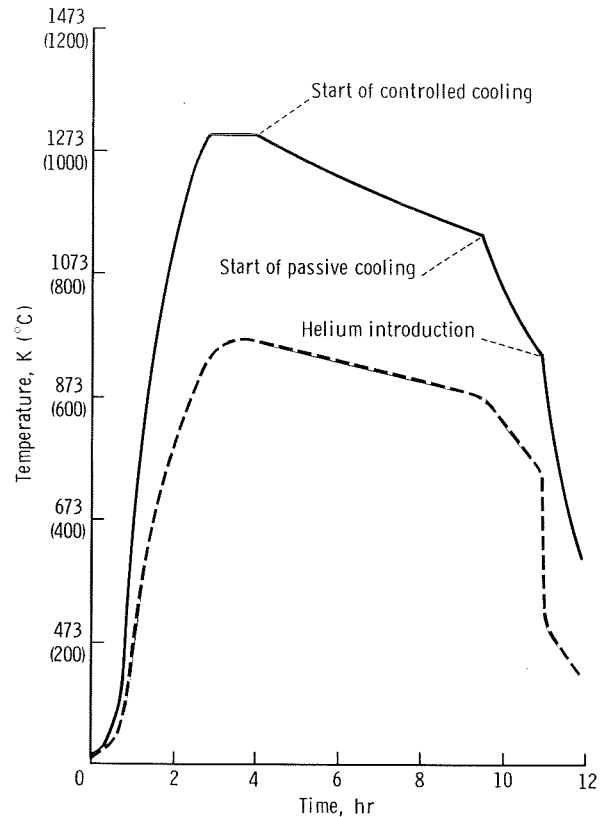


FIGURE 28-5.—Temperature-time profile of microgravity processing. The solid line indicates W-Al and W-Al-Re systems and the dashed line indicates powdered Al and CuAl eutectics.

where

$$\delta_i^* = \sum_k c_k \delta_k$$

$\delta_i$  = electron backscattering factor for the  $i$ -th element

$$\beta = E_o / E_i$$

$E_o$  = initial electron energy corresponding to accelerating voltage

$E_i$  = excitation energy of the studied radiation

$$\tau_i^* = \sum_j c_j \tau_{ij}$$

$\tau_{ij}$  = mass coefficients of the  $i$ -th radiation absorption by the  $j$ -th element in the sample

$\theta$  = angle of departure of radiation from the surface

$\alpha$  = dimensionless parameter equal to  $3.33 \times 10^{-6}$  (ref. 28-2) provided that  $E_o$  and  $E_i$  are given in kiloelectronvolts

and parameter  $n$  is assumed to be 1.62.

However, using methods previously described (refs. 28-3 to 28-5), atomic number and absorption corrections are determined for the ratio

$$c_i = f_i^{(1)} f_i^{(2)} f_i^{(3)} (I_i/I_{io}) \quad (28-4)$$

Here, in contrast to the other methods (ref. 28-2), the atomic number correction consists of two corrections: stopping power  $f_i^{(1)}$  and electron backscattering  $f_i^{(2)}$  and where  $f_i^{(3)}$  is the absorption correction. These corrections are calculated from

$$f_i^{(1)} = \frac{\sum_k c_k \frac{Z_k}{A_k} \ln \left( 0.585 \frac{E_o + E_i}{J_k} \right)}{\frac{Z_i}{A_i} \ln \left( 0.585 \frac{E_o + E_i}{J_i} \right)} \quad (28-5)$$

$$f_i^{(2)} = \frac{1/R_i^*}{1/R_i} \quad (28-6)$$

$$f_i^{(3)} = \frac{\left( 1 + \frac{\chi_i^*}{\sigma_i} \right) \left[ 1 + \frac{h_i \chi_i^*}{(1 + h_i^*) \sigma_i} \right]}{\left( 1 + \frac{\chi_{ii}}{\sigma_i} \right) \left[ 1 + \frac{h_i \chi_{ii}}{(1 + h_i) \sigma_i} \right]} \quad (28-7)$$

where  $E_o$  and  $E_i$  = same values (in electronvolts) as those in reference 28-2

$Z_i$  =  $i$ -th element atomic number

$A_i$  =  $i$ -th element atomic weight

$J_i$  = 11.5 eV

$R_i^* = \sum_k c_k R_k$

$R_k$  = the electron backscattering factor for the  $k$ -th element (ref. 28-5)

$\chi_i^* = \text{cosec } \theta \sum_k c_k \tau_{ik}$

$\chi_{ii} = \tau_{ii} \text{cosec } \theta$

$\tau_{ik}$  = same values as those in reference 28-2

$h_i^* = \sum_k c_k h_k$

$h_k = 1.2 A_k / Z_k^2$

and  $\sigma$  is the Lenard's modification factor associated with  $E_o$  and  $E_i$  by

$$\sigma = \frac{4.5 \times 10^5}{E_o^{1.65} - E_i^{1.65}} \quad (28-8)$$

where  $E_o$  and  $E_i$  are given in electronvolts.

The two methods used to calculate corrections for the systems under study yielded similar results. To determine the unknown concentration in the analyzed specimens, special averaged calibration curves were constructed from the calculation data  $c_i = c_i(I_i/I_{io})$ , where  $i = W$  for the W-Al and W-Al-Re systems; and  $i = Cu$  for the Cu-Al system. A calculation for the tertiary system (W-Al-Re) was made with the same method as that used for the W-Al system (ref. 28-2) because equalities  $\tau_{WW} \approx \tau_{WRe}$ ,  $\tau_{ReRe} \approx \tau_{ReW}$ ,  $\tau_{WAl} \approx \tau_{ReAl}$ , and  $\tau_{AlW} \approx \tau_{AlRe}$  are valid for both W and Re, which are adjacent elements in the periodic table. Figure 28-6 is an example of a W-Al system calibration curve that was used to determine W concentration. In general, the system was analyzed along the lines W  $L\alpha$ , Al  $K\alpha$  (W-Al); W  $L\alpha$ , Al  $K\alpha$ , Re  $L\alpha$  (W-Al-Re); Cu  $K\alpha$ , Al  $K\alpha$  (Cu-Al);  $E_o = 20$  keV.

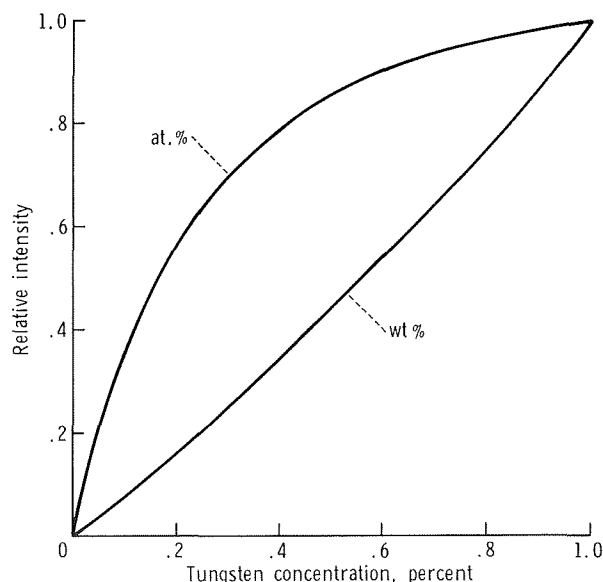


FIGURE 28-6.—Relative intensity of W  $L\alpha$  radiation as a function of concentration for the W-Al system ( $E_o = 20$  keV).

## EXPERIMENTAL RESULTS

### Compound Materials

The X-ray photographs (fig. 28-7) of the ampoules and ingots for both ground-based and flight experiments show evidence that neither of the solidified materials preserved the initial structure (fig. 28-1). Also, the distribution of the refractory inclusions throughout the Al in the flight samples differed from that of the ground-based samples. In the flight samples, the W balls were distributed throughout the bulk of the materials. In the ground-based samples, the cylindrical rod was on the ingot surface and the W balls were at the bot-

tom of the crucible (fig. 28-8). The space-grown ingot (fig. 28-7) is larger and has a different shape than the Earth-grown ingot. The end of the flight specimen at the bottom of the crucible is almost conical.

### Tungsten and Aluminum Matrix Interaction

The W specimens showed a certain distribution throughout the Al. Two patterns were discernible in cross section: an almost circular one and a horseshoelike pattern.

Examination of the specimens by electron scanning microscopy and X-ray spectral analysis

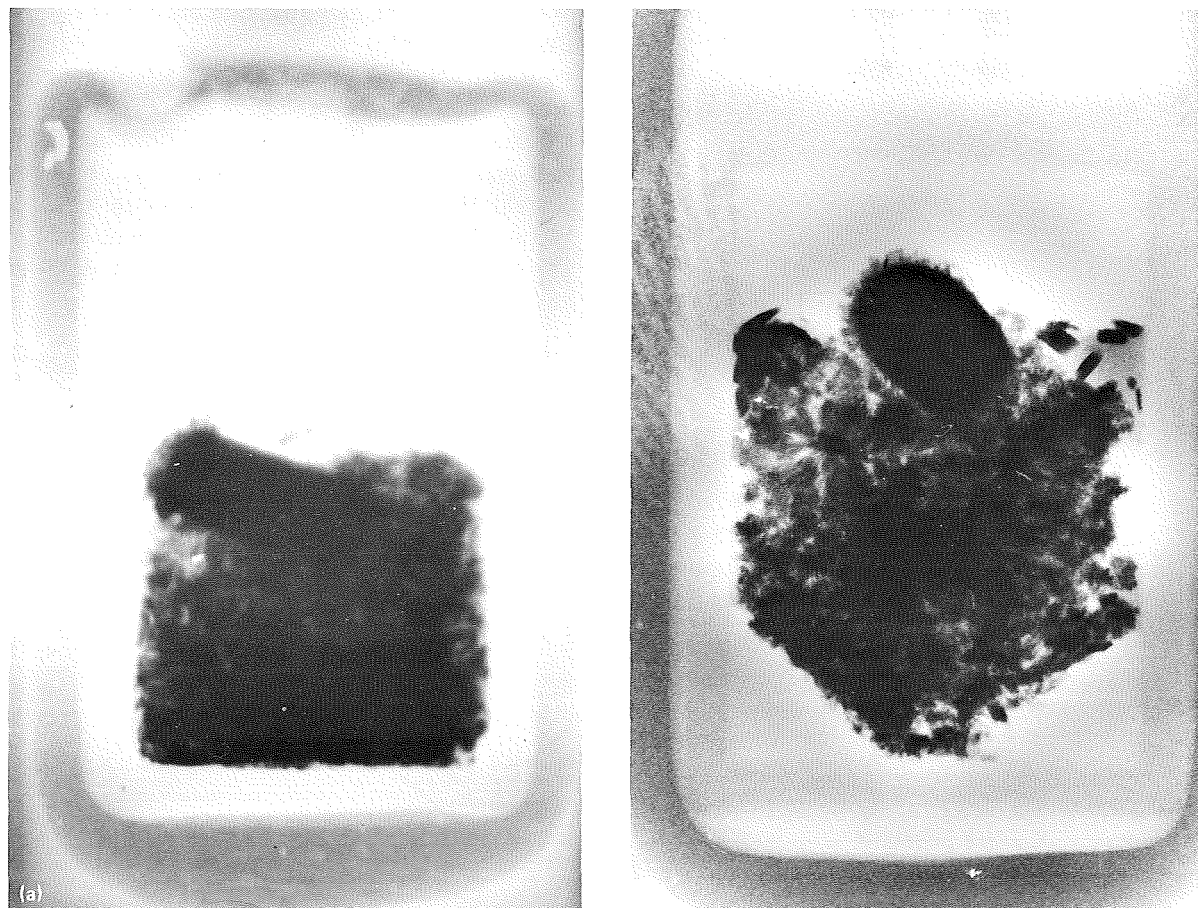


FIGURE 28-7.—X-ray photograph of ampoules with ingots. (a) Earth-grown sample MA-150-11. (b) Space-grown sample MA-150-17.



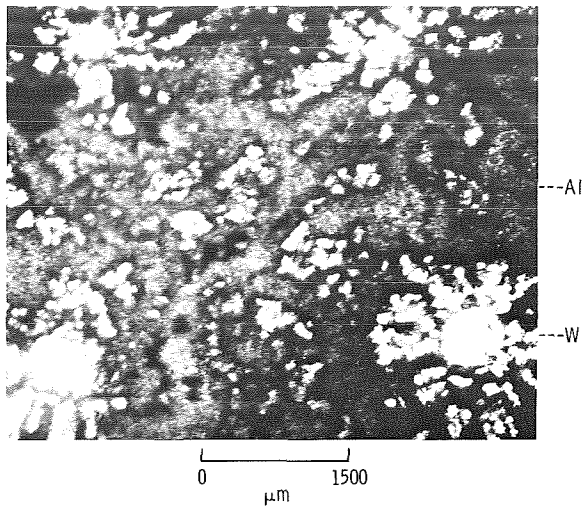
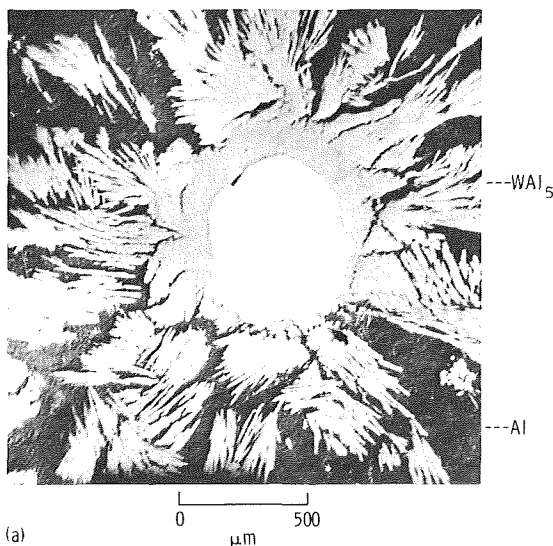


FIGURE 28-8.—Photomicrograph of a sectioned area of ground-based sample MA-150-12 in the plane passing through W samples near the bottom of the crucible.

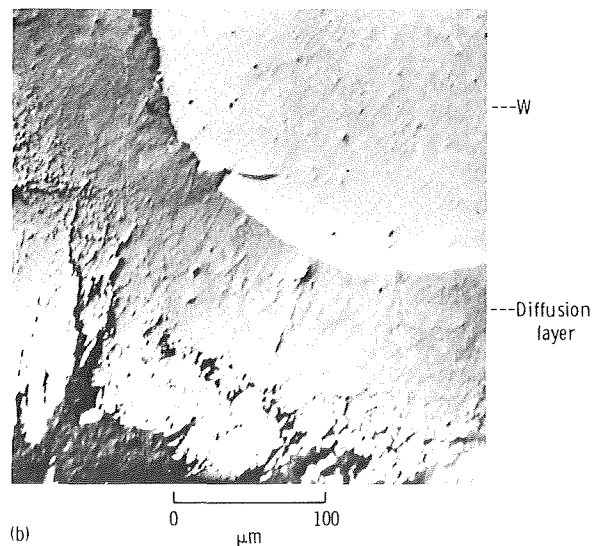
revealed the existence of an area of interaction between W and Al composed entirely of intermetallic phases. The distribution of this interaction area across the ground and flight specimen sections is shown in figures 28-9 to 28-13. These figures show that the area, in all cases, is a diffusion layer that disintegrates farther from the W

into individual, elongated and dendritic sections. The latter are usually separated from the main part (adjacent to W) of the diffusion layer by a layer of Al. The main bulk of the layer, as shown by quantitative X-ray spectral analysis, consists generally of three phases:  $WAl_4$ ,  $WAl_5$ , and  $WAl_{12}$ . Phase boundary concentrations determined for zero-g conditions correspond within measurement accuracy to those determined for one-g conditions, and agree with the W-Al system phase diagram data (fig. 28-14).

The distribution of intensity of the characteristic W  $L\alpha$  radiation for two different sections of the flight specimen diffusion layer is shown in figure 28-15. This figure indicates that, in one section of the diffusion layer (fig. 28-15(a)), phase distribution conforms to the laws of phase growth resulting from mutual diffusion (ref. 28-7) and that, in the second section (fig. 28-15(b)), these laws have not been followed. Ground-based specimens exhibit a similar behavior. It is interesting to note that the diffusion layer in ground-based and flight specimens had an extremely ragged front at the boundary with Al and a better defined front at the boundary with W (figs. 28-9 and 28-11 to 28-13). The  $WAl_5$  phase comprises the main bulk of the layer; it constitutes a base for the "elongated" areas (figs. 28-9 to 28-13). The  $WAl_4$  and



(a)



(b)

FIGURE 28-9.—Electron probe scanning of a sectioned area of ground-based sample MA-150-12. (a)  $WAl_5$  phase region. (b) Tungsten/diffusion layer interface.

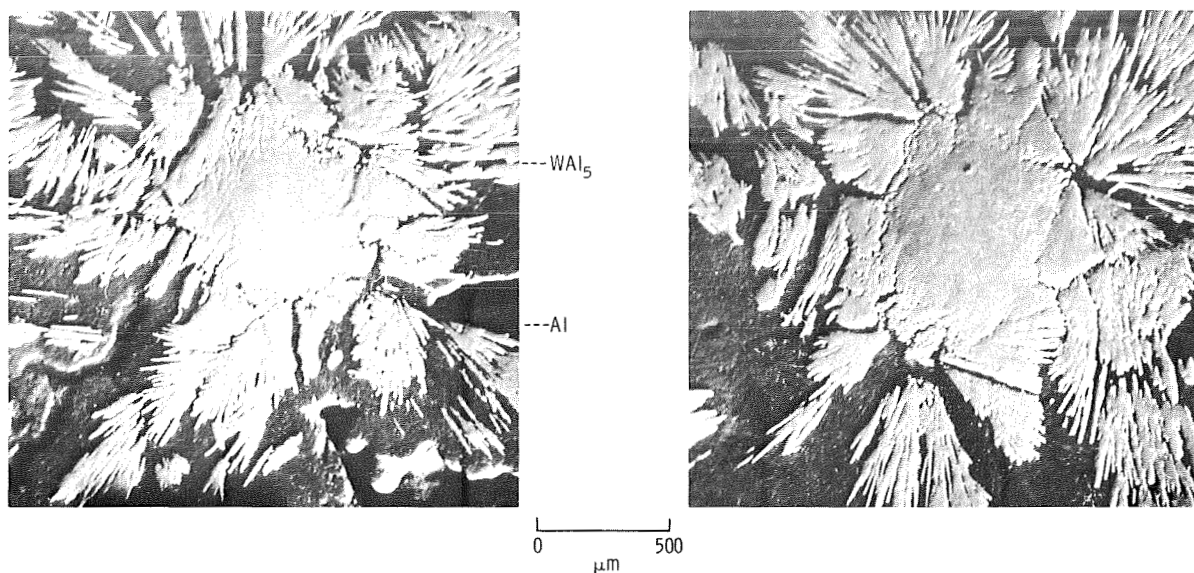


FIGURE 28-10.—Electron probe scanning of two sectioned areas of ground-based sample MA-150-12. Shear plane passes above the W specimens and cuts across the diffusion layer.

$WAl_{12}$  phases are generally not as thick and do not occur in some parts of the layer. Generally, the layer displays a considerable variation in phase thickness and an extreme raggedness of interphase boundaries.

Interestingly, the  $WAl_{12}$  phase in the flight sample (MA-150-16) has a crystalline faceting (fig. 28-12), a fact not observed in ground samples. Furthermore, in ground-based and flight samples, all these phases occur as individual fragments

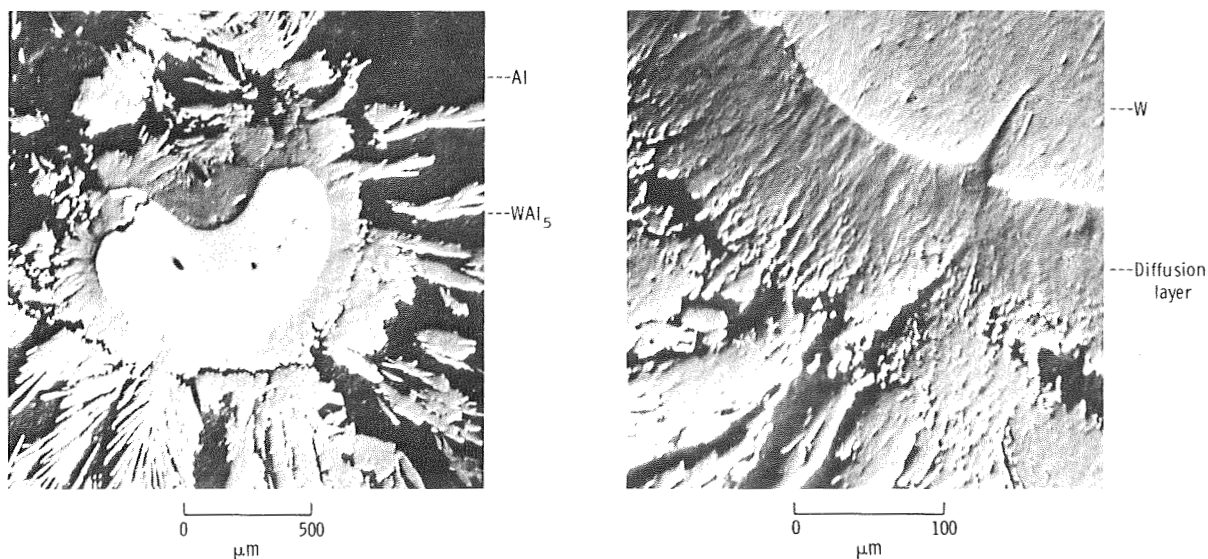


FIGURE 28-11.—Electron probe scanning across a sectioned area of ground-based sample MA-150-12.

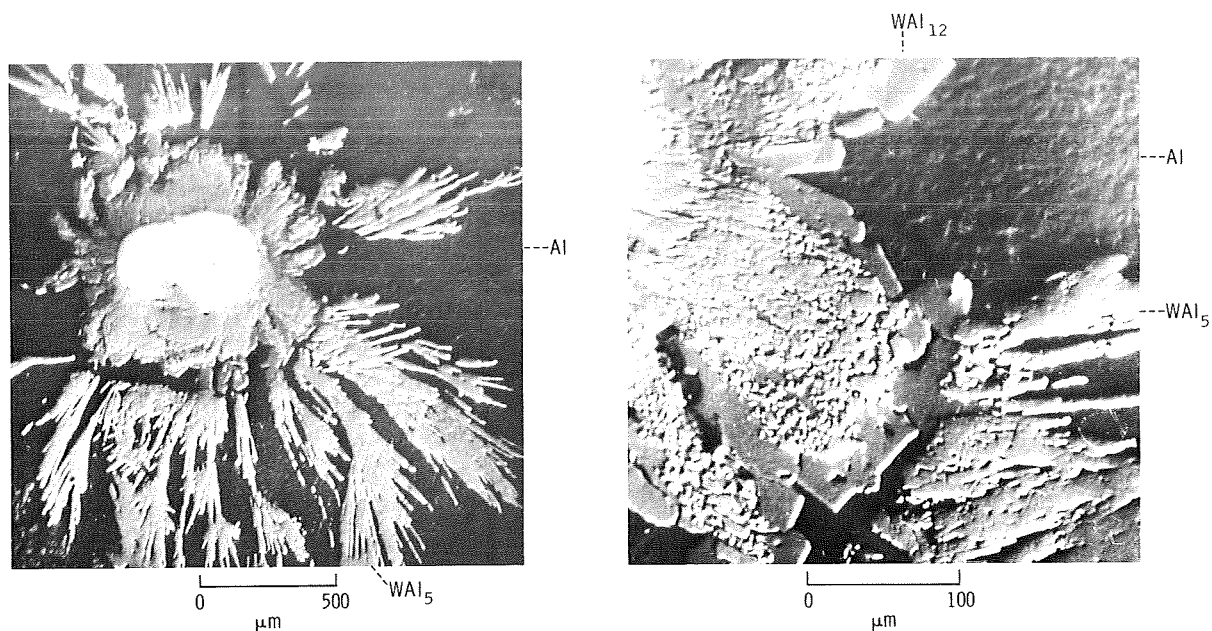


FIGURE 28-12.—Electron probe scanning across a sectioned area of flight sample MA-150-16.

throughout different parts of the ingot within the studied plane of the section. Fragments of  $WAl_4$  and  $WAl_{12}$  phases are irregularly shaped, whereas the  $WAl_5$  phase occurs usually as needlelike fragments (fig. 28-14).

The sectioned areas of ground-based and flight samples, lying far from the diffusion layer and containing the  $WAl_5$  phase, are shown in figures 28-16 to 28-19. An analysis has shown that the “needles” of this phase in flight specimens are

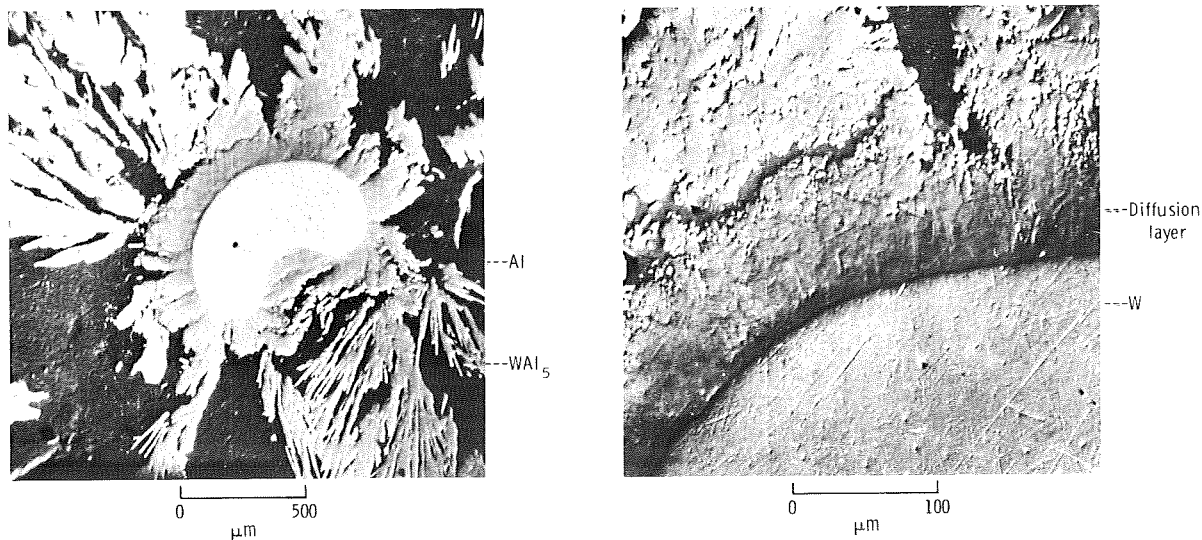


FIGURE 28-13.—Electron probe scanning of a sectioned area of flight sample MA-150-17.

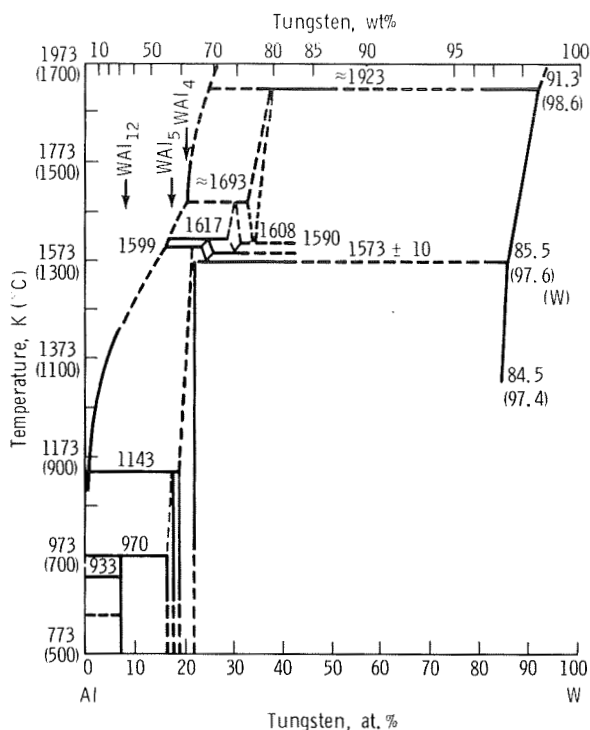


FIGURE 28-14.—Constitutional diagram of the W-Al system based on data from reference 28-6.

thinner and somewhat less disoriented than in ground specimens. However, individual, separated needles of the  $WAl_5$  phase are encountered more frequently in ground-based specimens (fig. 28-18).

For sections of ground-based and flight samples containing W inclusions, microhardness  $H$  was measured for the Al matrix, for W inclusions, and for phases formed as a result of interaction of solid-state W and liquid Al. The results are summarized in table 28-I. The table indicates that the values of microhardness in the samples are compatible within the limits of measurement error. The greatest hardness was determined for the diffusion layer  $WAl_5$  phase. (Hardness of the  $WAl_4$  phase was not measured because of its low thickness in the diffusion layer.)

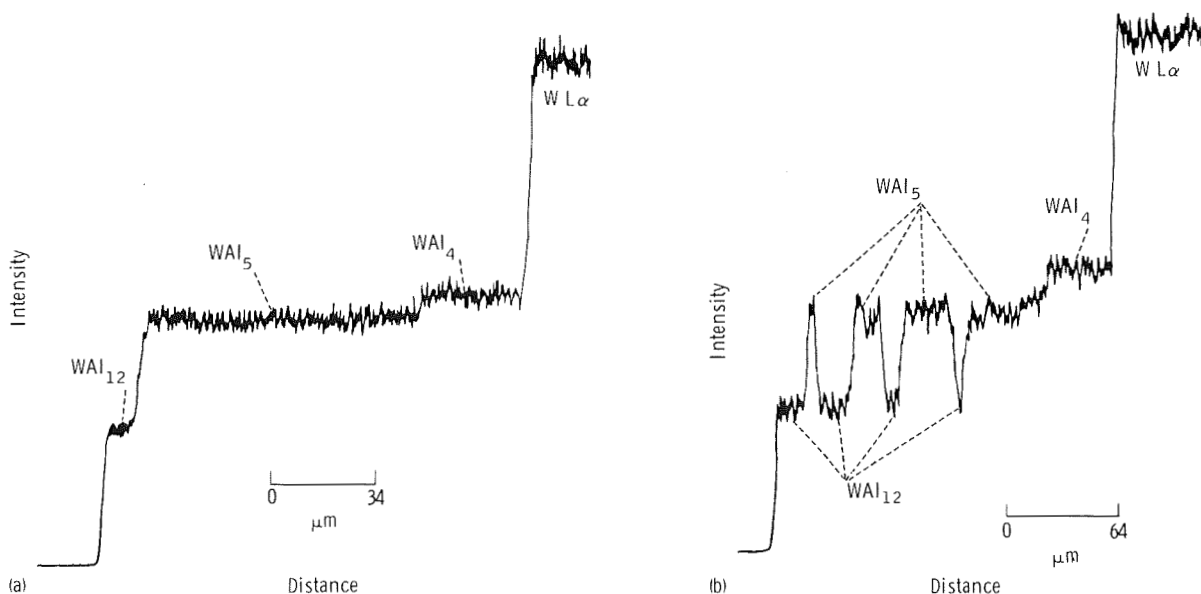


FIGURE 28-15.—Recordings of two types of intensity distributions of characteristic  $W L\alpha$  radiation for two different sections of the W/Al diffusion layer for sample MA-150-17. (a) Section 1. (b) Section 2.

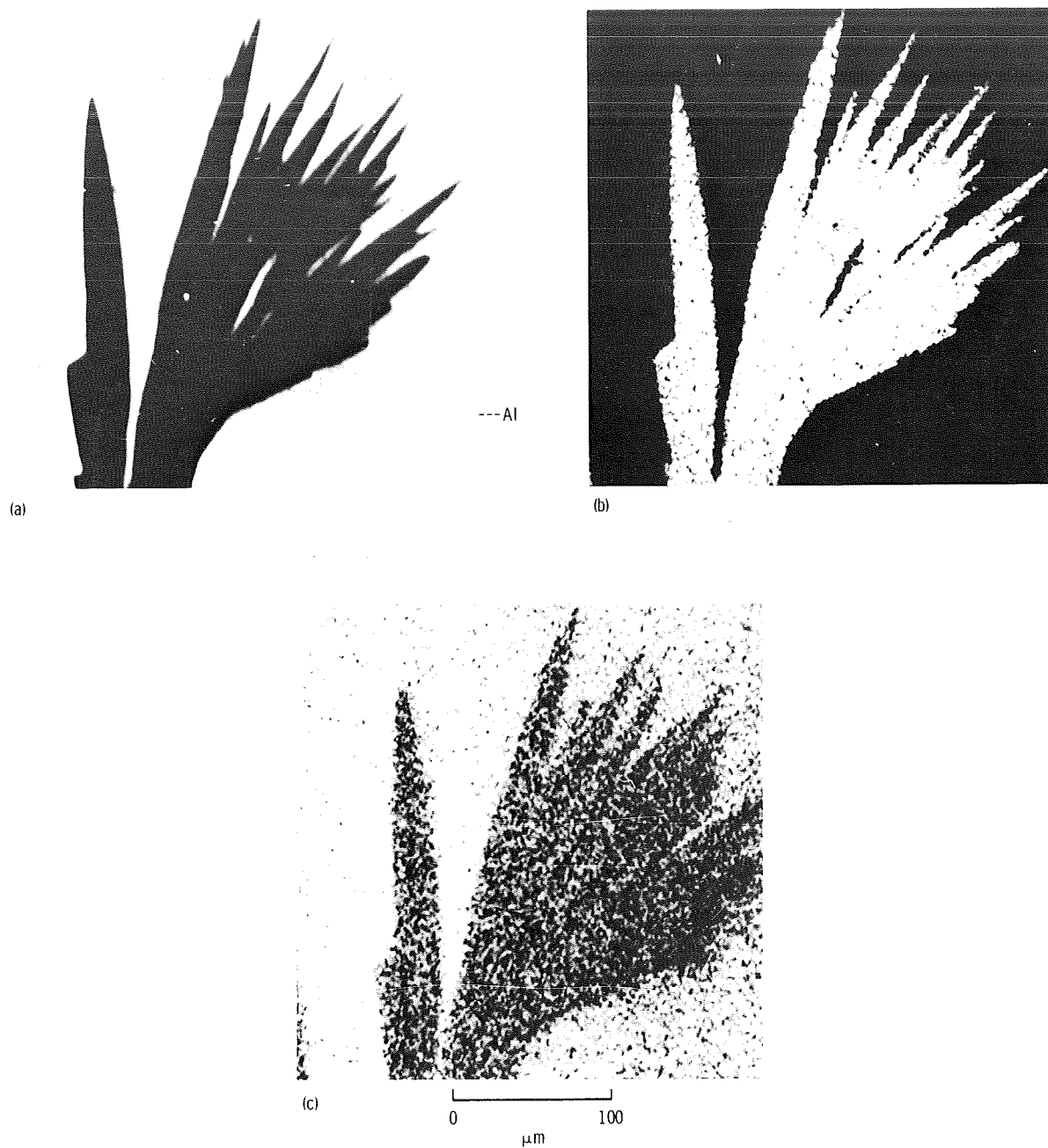


FIGURE 28-16.—Scanning of the  $WAl_5$  phase in a section of ground-based sample MA-150-11. (a) Electron beam scanning. (b) Tungsten  $L\alpha$  radiation. (c) Aluminum  $K\alpha$  radiation.

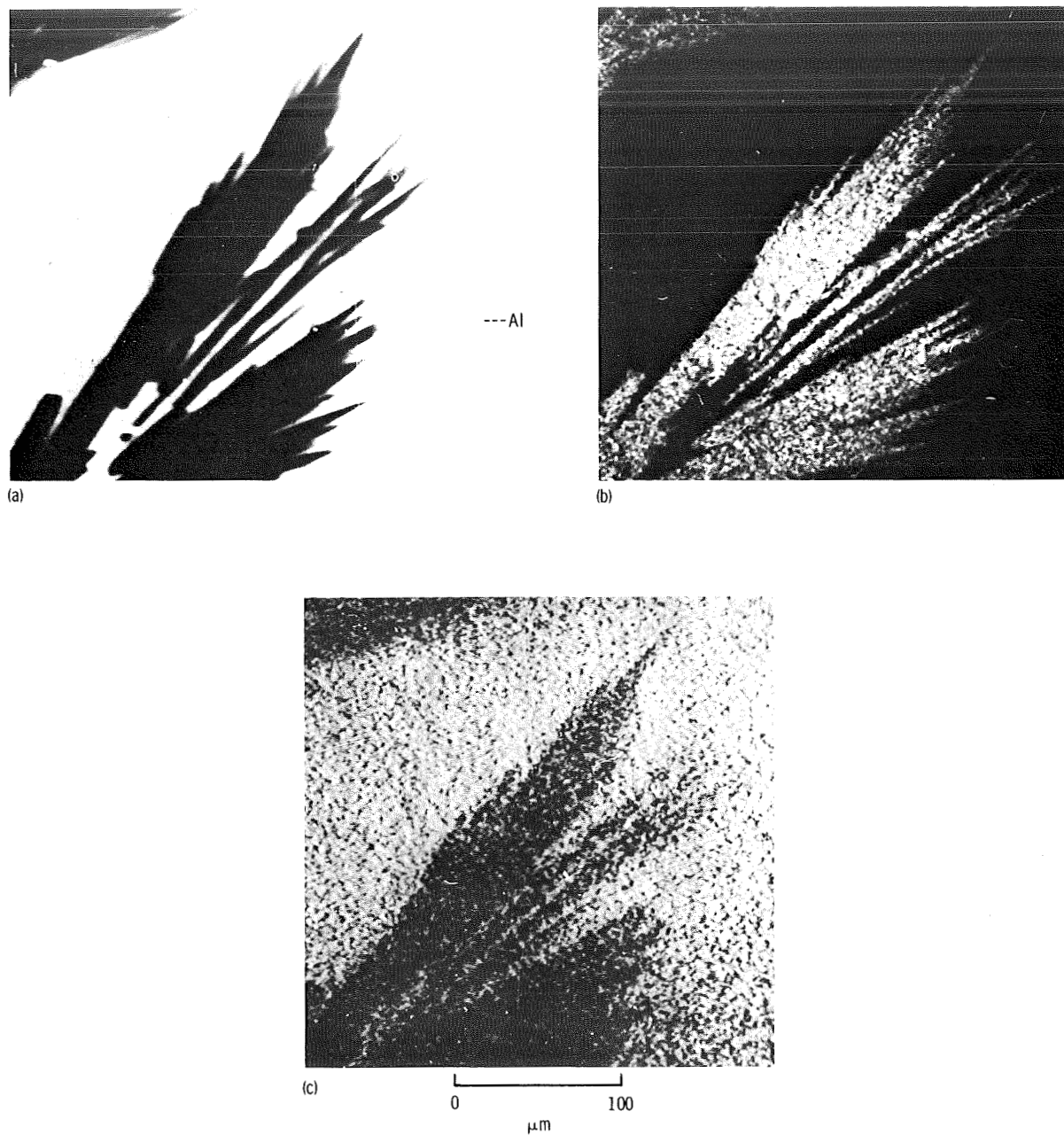


FIGURE 28-17.—Scanning of  $\text{WAl}_5$  phase in metallographically polished flight sample MA-150-16. (a) Electron beam scanning. (b) Tungsten  $L\alpha$  radiation. (c) Aluminum  $K\alpha$  radiation.



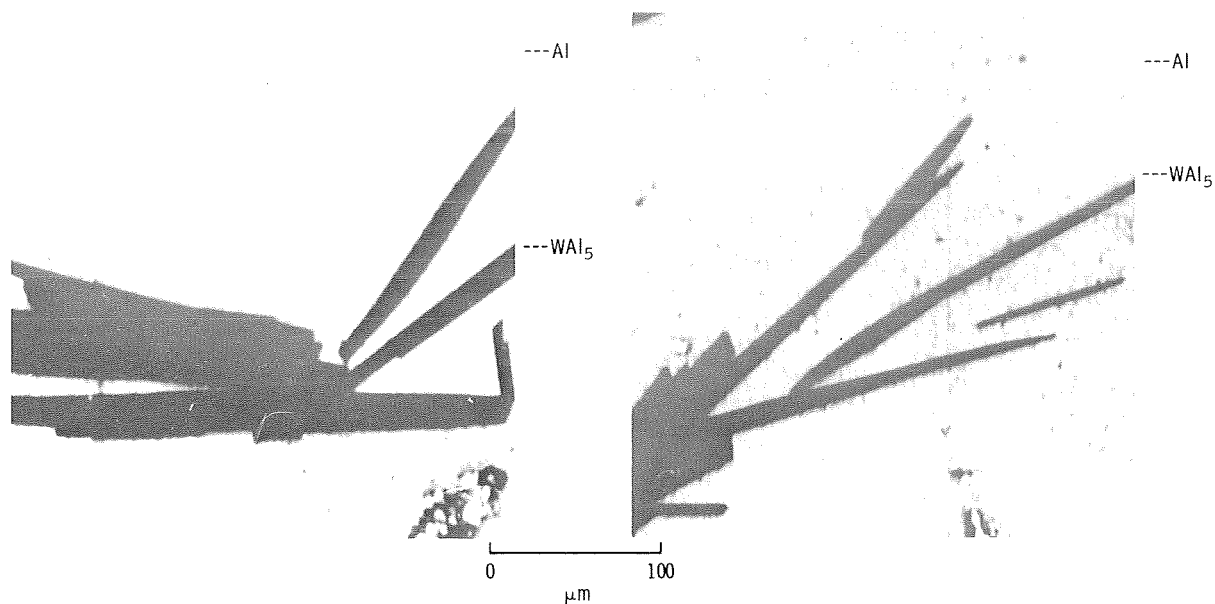


FIGURE 28-18.—Electron beam scanning across two sectioned areas of ground-based sample MA-150-11 containing the WAl<sub>5</sub> phase.

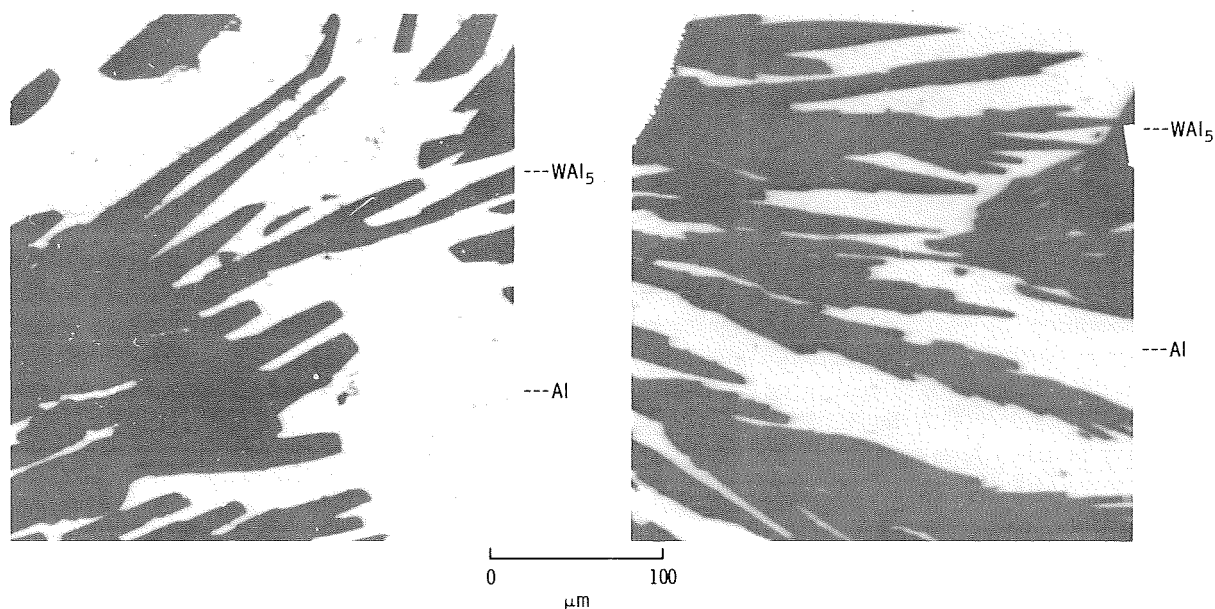


FIGURE 28-19.—Electron beam scanning of flight sample MA-150-16 in two sectioned areas containing the WAl<sub>5</sub> phase.

TABLE 28-I.—Microhardness Measurement Results for Al Matrix,  
W Inclusions, and Interaction Phases

<i>Specimen</i>	<i>Phase</i>	<i>Microhardness H, kg mm<sup>2</sup></i>
MA-150-11 (ground-based)	W - ball-shaped	--
	Al - matrix	21
	WAl <sub>5</sub> - needle-shaped	500
MA-150-12 (ground-based)	W - ball-shaped	470
	W - horseshoe-shaped	500
	Al - matrix	21
	WAl <sub>5</sub> - needle-shaped	500
	WAl <sub>5</sub> - diffusion layer	550
	WAl <sub>12</sub> - --	310
MA-150-16 (flight)	W - horseshoe-shaped	480
	Al - matrix	21
	WAl <sub>5</sub> - needle-shaped	470
	WAl <sub>5</sub> - diffusion layer	550
	WAl <sub>12</sub> - --	390
MA-150-17 (flight)	W - horseshoe-shaped	480
	Al - matrix	21
	WAl <sub>5</sub> - needle-shaped	480
	WAl <sub>5</sub> - diffusion layer	550
	WAl <sub>12</sub> - --	370

### Tungsten-Rhenium Alloy and Aluminum Matrix/Interaction

The section analysis revealed that an interface exists between starting alloy and Al along the entire length of the W-Re rod/matrix contact area (fig. 28-20). The front of this interface is more ragged at the boundary with the Al than at the boundary with the alloy, although the raggedness is approximately of the same type for flight and ground specimens (figs. 28-21 and 28-22).

The X-ray spectral analysis of different parts of the interface in polished sections showed it to be composed of two phases with irregular boundaries. The distribution of the intensity of the characteristic W L $\alpha$ , Al K $\alpha$ , and Re L $\alpha$  radiation in the examined sections is shown in figure 28-23. It is clear from the figure that the distribution of phases conforms to the laws governing their

growth in the process of mutual diffusion in a tertiary system. The conversion of relative intensities into concentrations enabled the construction of concentration curves for the distribution of each constituent in the diffusion layer (fig. 28-24). The boundary concentration values for flight-sample phases correspond, within measurement accuracy, to the respective concentration values obtained for ground-based samples. Both samples show almost identical distribution of corresponding constituents within the same phases. Figure 28-24 also indicates that some difference in phase and diffusion layer thickness exists between flight and ground-based samples. However, the same variation in thickness was observed throughout different areas of the same sample (both flight and ground-based), although the phase adjacent to the alloy was invariably the one with the greatest thickness. In all cases, the X-ray spectral analysis



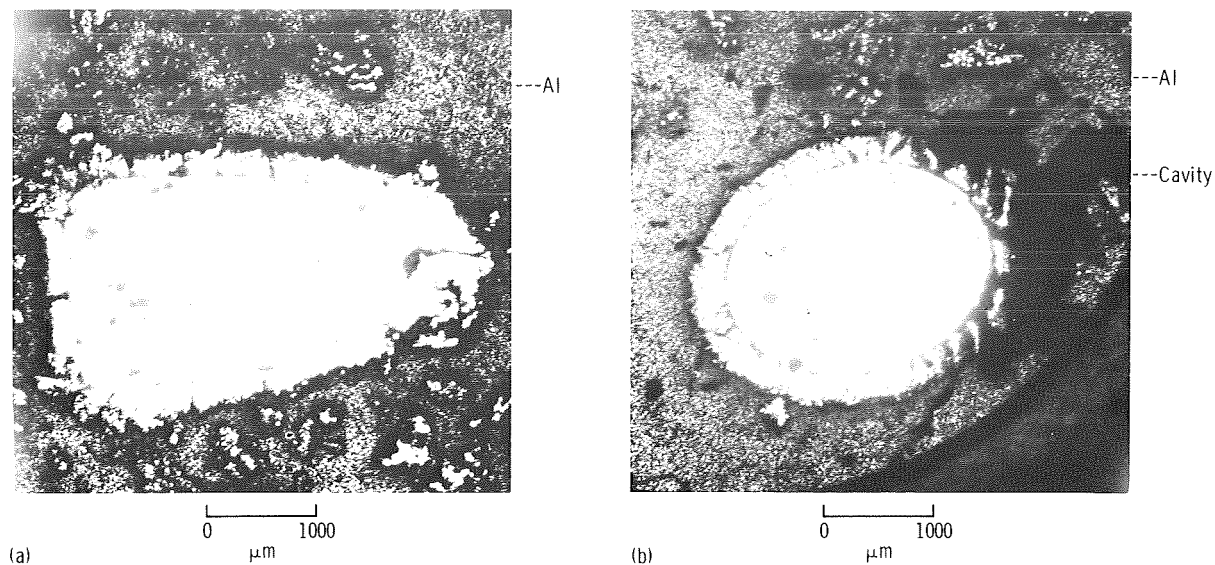


FIGURE 28-20.—Photomicrograph of metallographically polished sections. The WRe alloy and the adjacent diffusion layer are in the center. (a) Ground-based sample MA-150-11. (b) Flight sample MA-150-16.

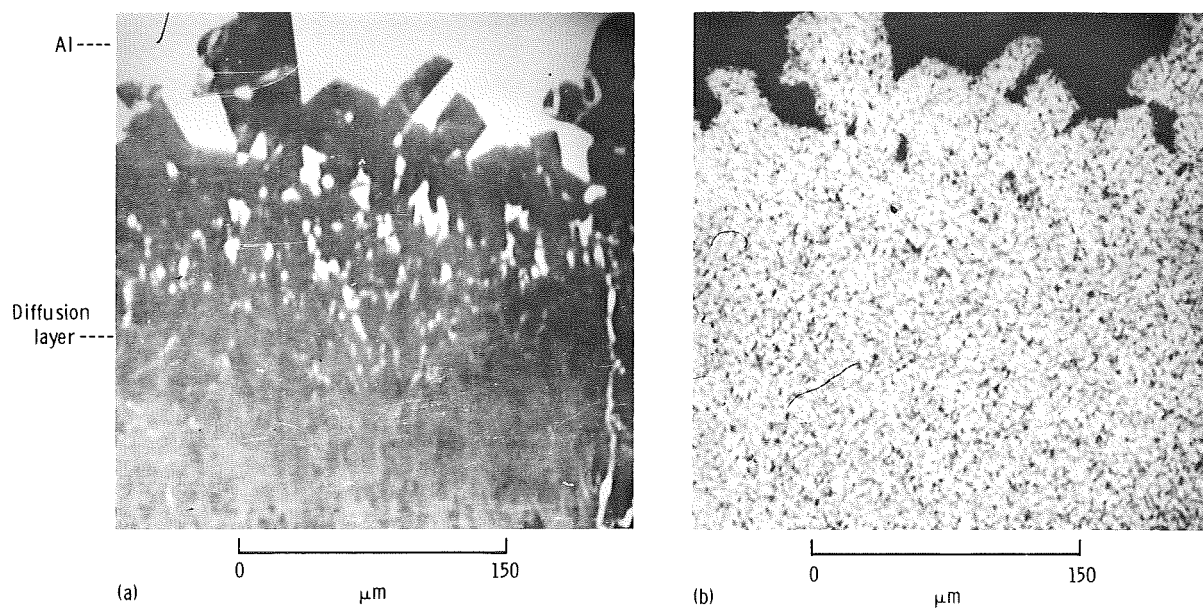


FIGURE 28-21.—Scanning of the diffusion layer in the ground-based sample MA-150-11. (a) Electron beam scanning. (b) Tungsten  $L\alpha$  radiation. (c) Aluminum  $K\alpha$  radiation. (d) Rhenium  $L\alpha$  radiation.

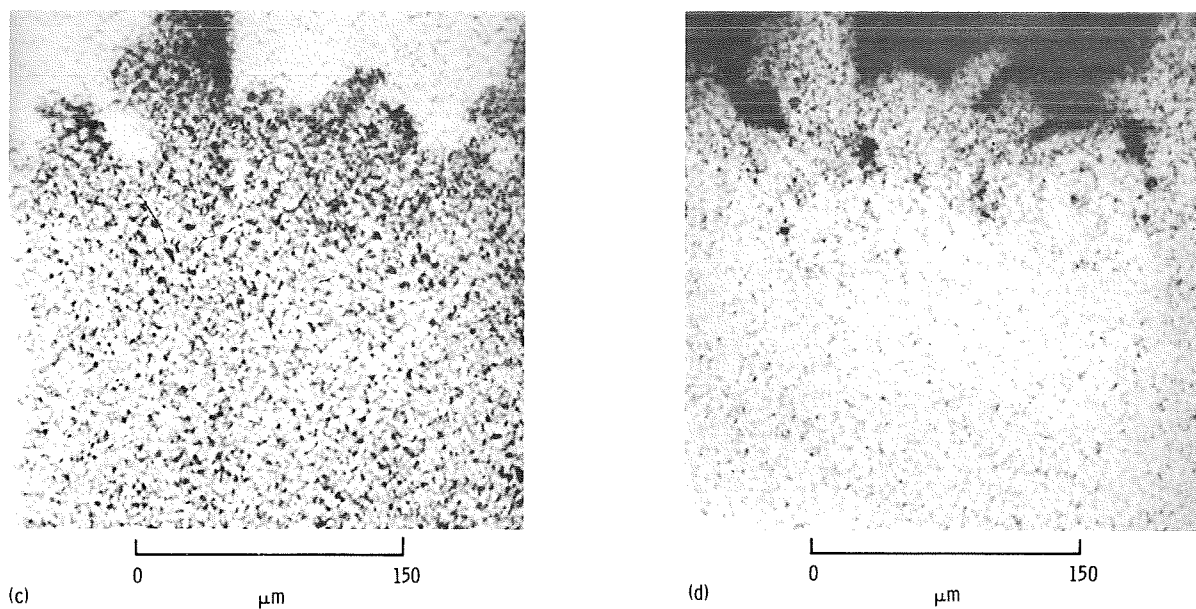
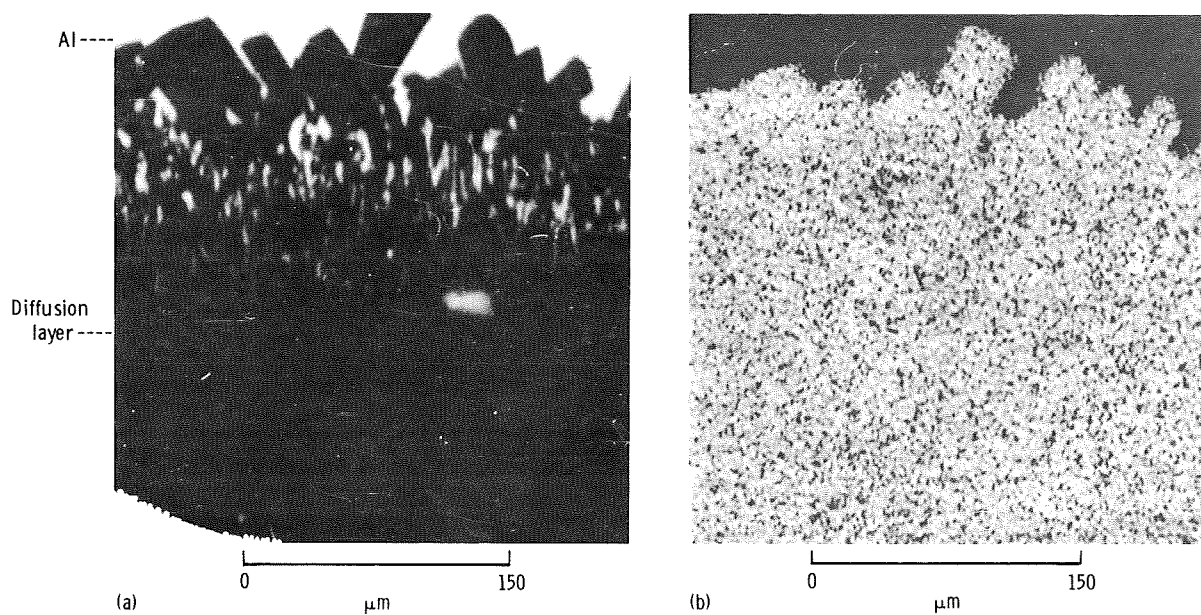


FIGURE 28-21.—Concluded.

FIGURE 28-22.—Scanning of diffusion layer in flight sample MA-150-16. (a) Electron beam scanning. (b) Tungsten  $L\alpha$  radiation. (c) Aluminum  $K\alpha$  radiation. (d) Rhenium  $L\alpha$  radiation.

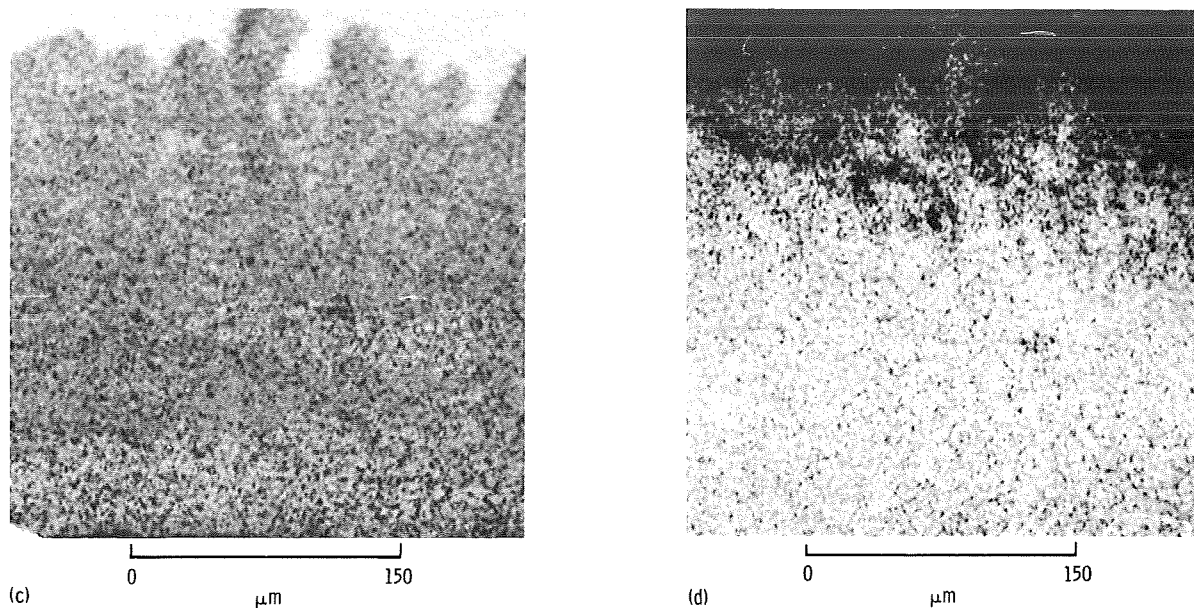


FIGURE 28-22.—Concluded.

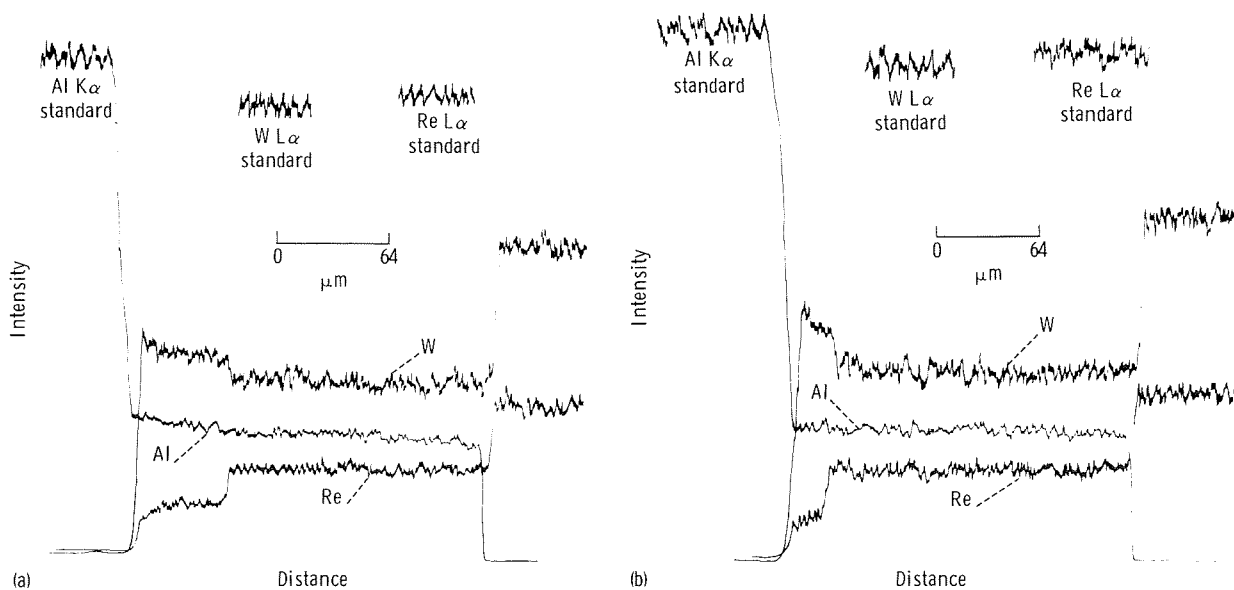


FIGURE 28-23.—Distribution of intensities of W  $L\alpha$ , Al  $K\alpha$ , and Re  $L\alpha$  radiation throughout the diffusion layer. (a) Ground-based sample MA-150-11. (b) Flight sample MA-150-16.

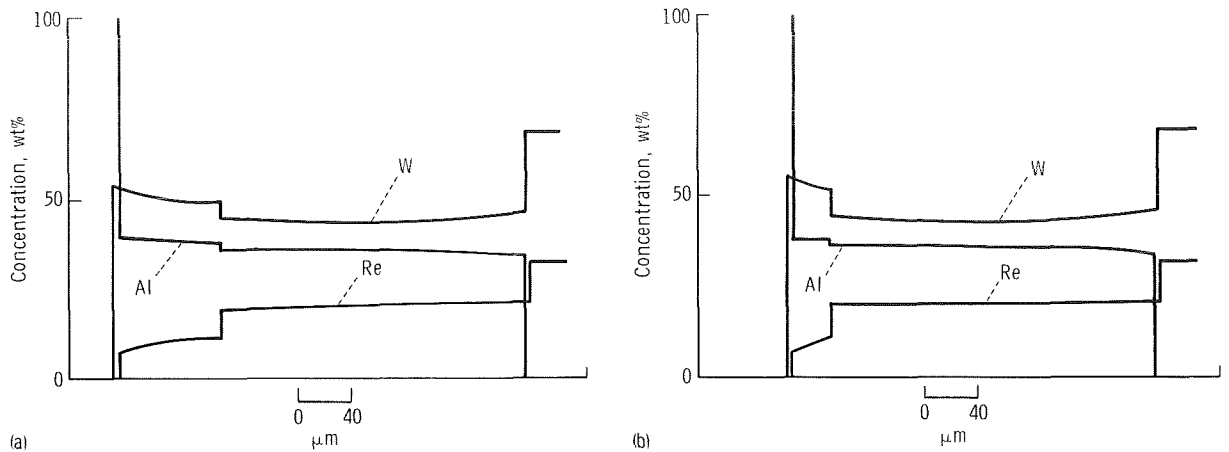


FIGURE 28-24.—Concentration curves showing distribution of W, Al, and Re in the diffusion layer. (a) Ground-based sample MA-150-11. (b) Flight sample MA-150-16.

revealed pure Al inclusions in the diffusion layer, located in the main near the boundary of the two phases (figs. 28-21 and 28-22). On the other hand, single fragments of tertiary phases, varying in size and shape, can be seen in different parts of the section of Al matrix. Examples of such chaotic dispersion of phases across sections are shown in figures 28-25 to 28-30. None of the fragments in the figures appear to be needle-shaped, as was the case with binary system W-Al. A quantitative analysis of a fairly large number of these fragments was made to determine their composition in the studied specimens. The results, averaged

over several close values and normalized to 100 wt%, are shown in table 28-II.

In flight and ground-based specimens, the phase composition in different parts of sections is generally similar to that of the diffusion layers (fig. 28-24). However, one striking feature in flight specimen MA-150-16 is the presence of phase fragments with a higher Al content (more than 60 wt%). Examples of such Al-rich phases are presented in figures 28-29 and 28-30. No Al-rich phases were found in ground specimens. Furthermore, sample MA-150-11 contained fragments of phases composed of W, 45; Al, 38, and Re, 17

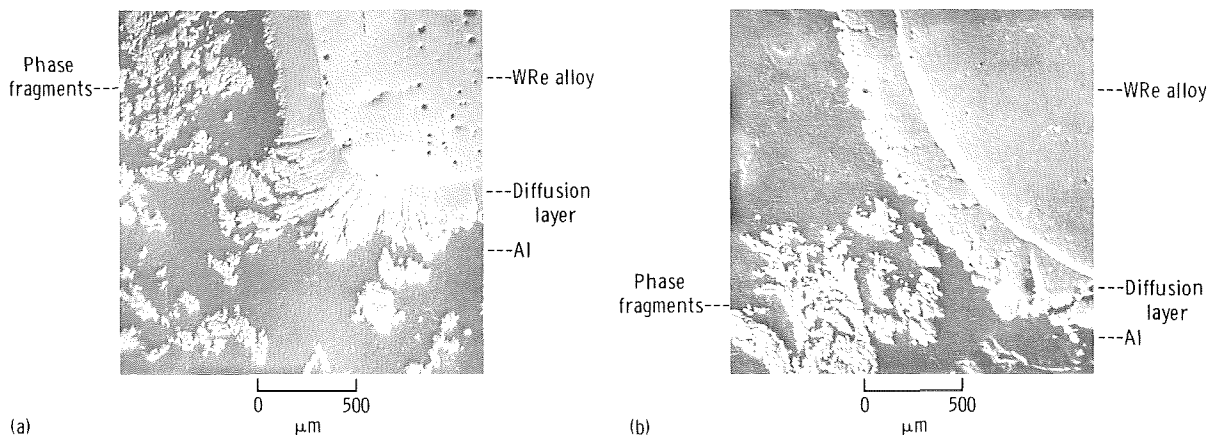


FIGURE 28-25.—Electron probe scanning of metallographically polished sections. (a) Ground-based sample MA-150-11. (b) Flight sample MA-150-16.

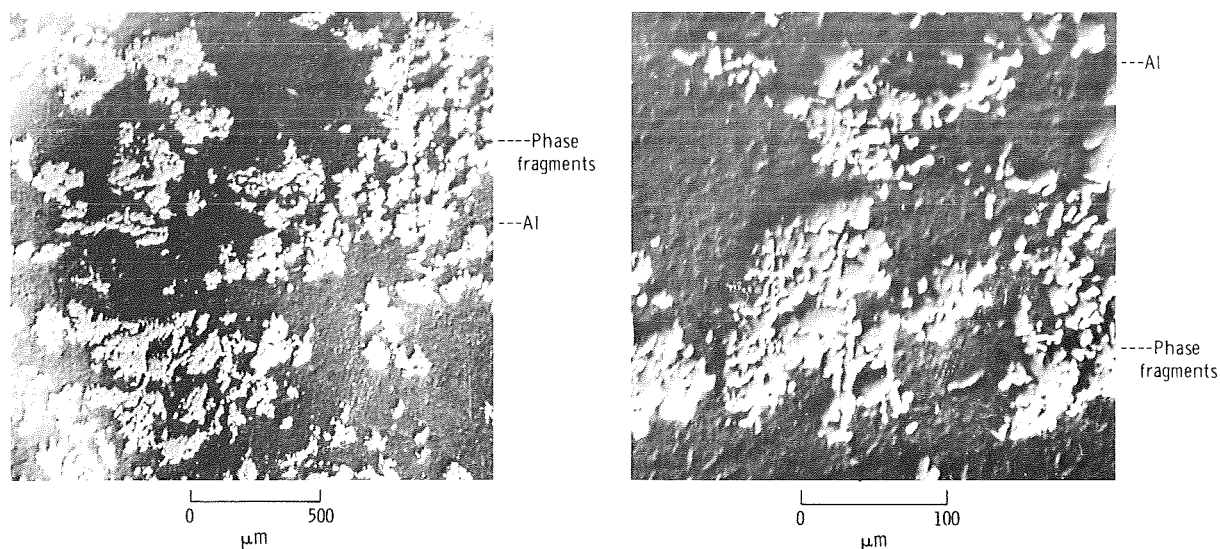


FIGURE 28-26.—Electron probe scanning across a sectioned area of flight sample MA-150-16 containing fragments of W-Al-Re system phases.

TABLE 28-II.—Phase Composition

Sample	Phase composition, wt%		
	W	Al	Re
MA-150-11 (ground-based)	55	39	6
	53	38	9
	59	37	4
	45	38	17
MA-150-12 (ground-based)	55	37	8
	53	38	9
	58	37	5
	60	36	4
MA-150-16 (flight)	56	37	7
	58	39	3
	58	37	5
	60	37	3
	31	66	3
	33	64	3
MA-150-17 (flight)	56	37	7
	55	38	7
	59	39	2
	59	37	4

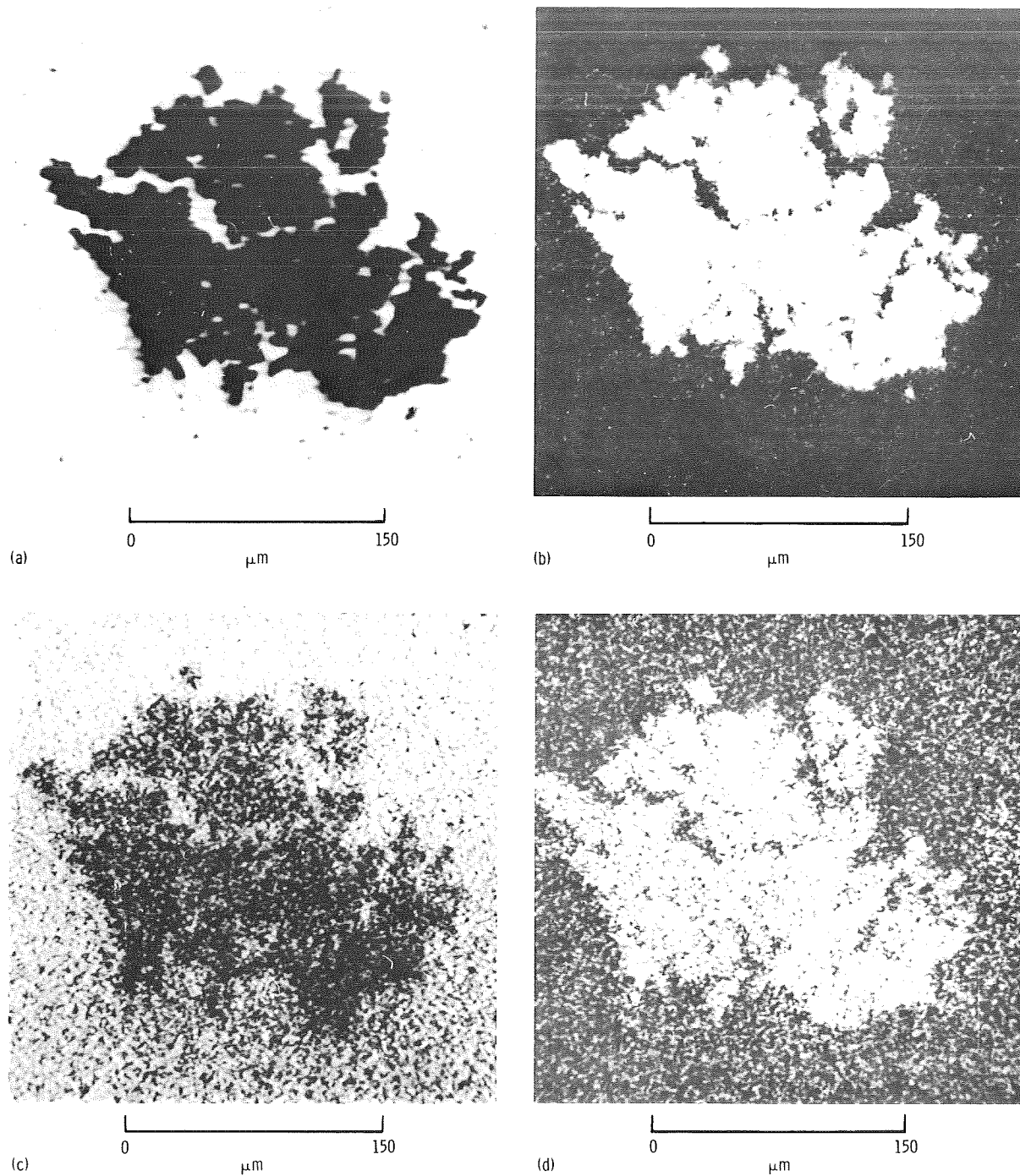


FIGURE 28-27.—Scanning of ground-based sample MA-150-11 in sectioned areas containing the W-Al-Re system phase. The W-Al-Re phase is shown in the center. (a) Electron beam scanning. (b) Tungsten  $L\alpha$  radiation. (c) Aluminum  $K\alpha$  radiation. (d) Rhenium  $L\alpha$  radiation.



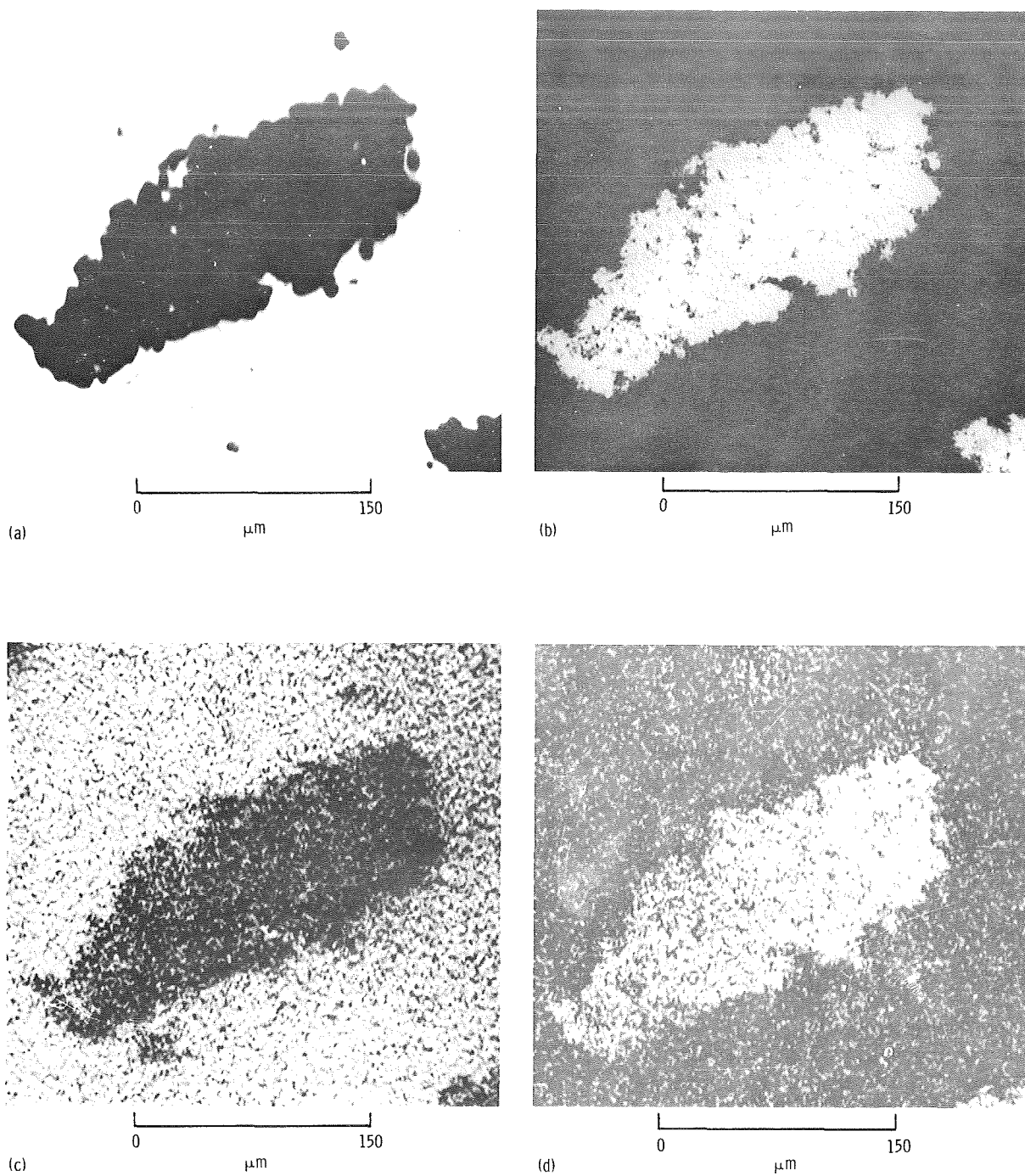


FIGURE 28-28.—Scanning of flight sample MA-150-16 in the sectioned areas containing the W-Al-Re system phase. The W-Al-Re phase is shown in the center. (a) Electron beam scanning. (b) Tungsten  $L\alpha$  radiation. (c) Aluminum  $K\alpha$  radiation. (d) Rhenium  $L\alpha$  radiation.

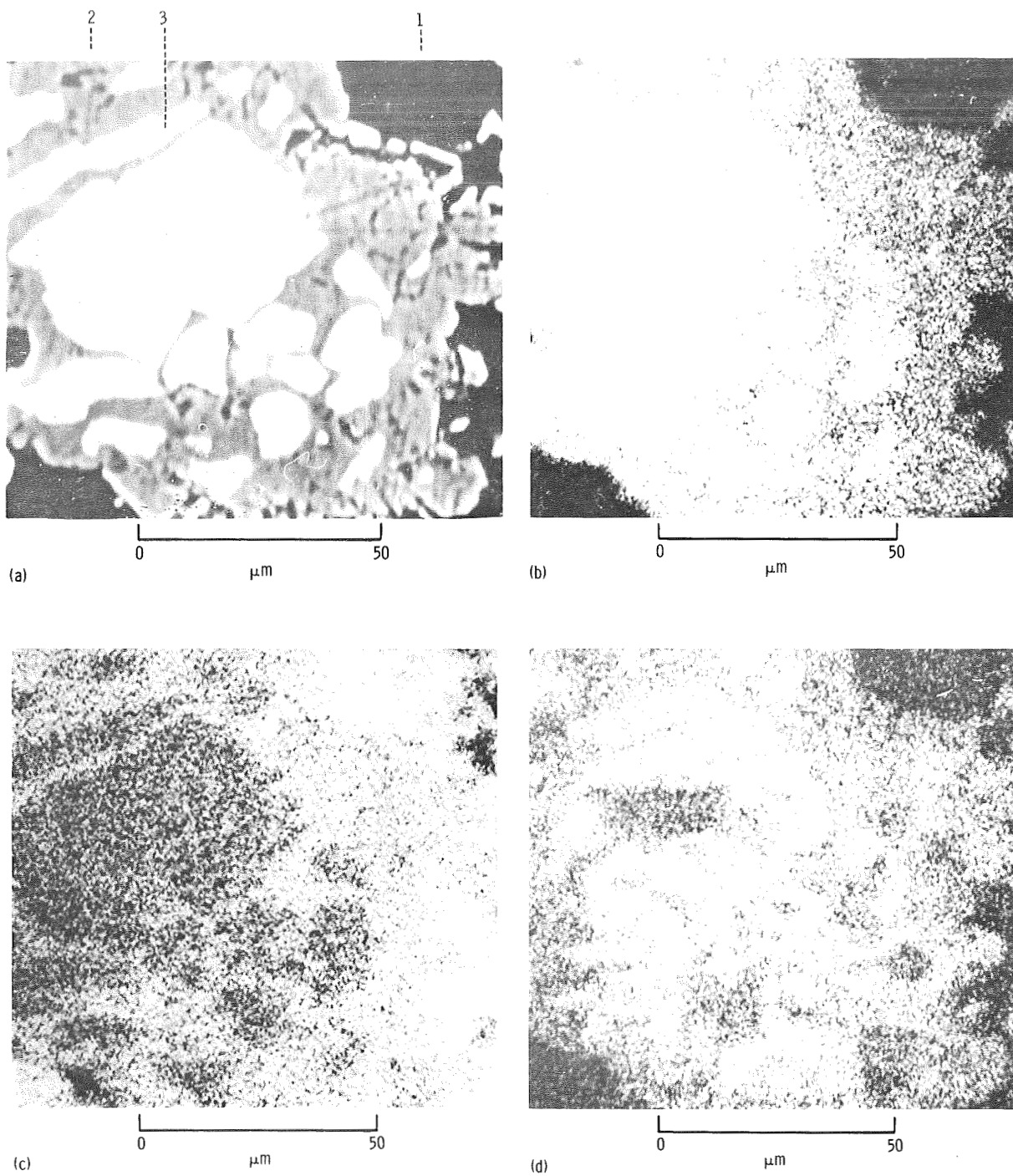


FIGURE 28-29.—Scanning of flight sample MA-150-16 in sectioned areas containing two phases of the W-Al-Re system. (a) Electron beam scanning ("1" indicates the Al, "2" indicates the Al-rich phase (31W 66Al 3Re), and "3" indicates phase 58W 37Al 5Re (table 28-II)). (b) Tungsten  $L\alpha$  radiation. (c) Aluminum  $K\alpha$  radiation. (d) Rhenium  $L\alpha$  radiation.



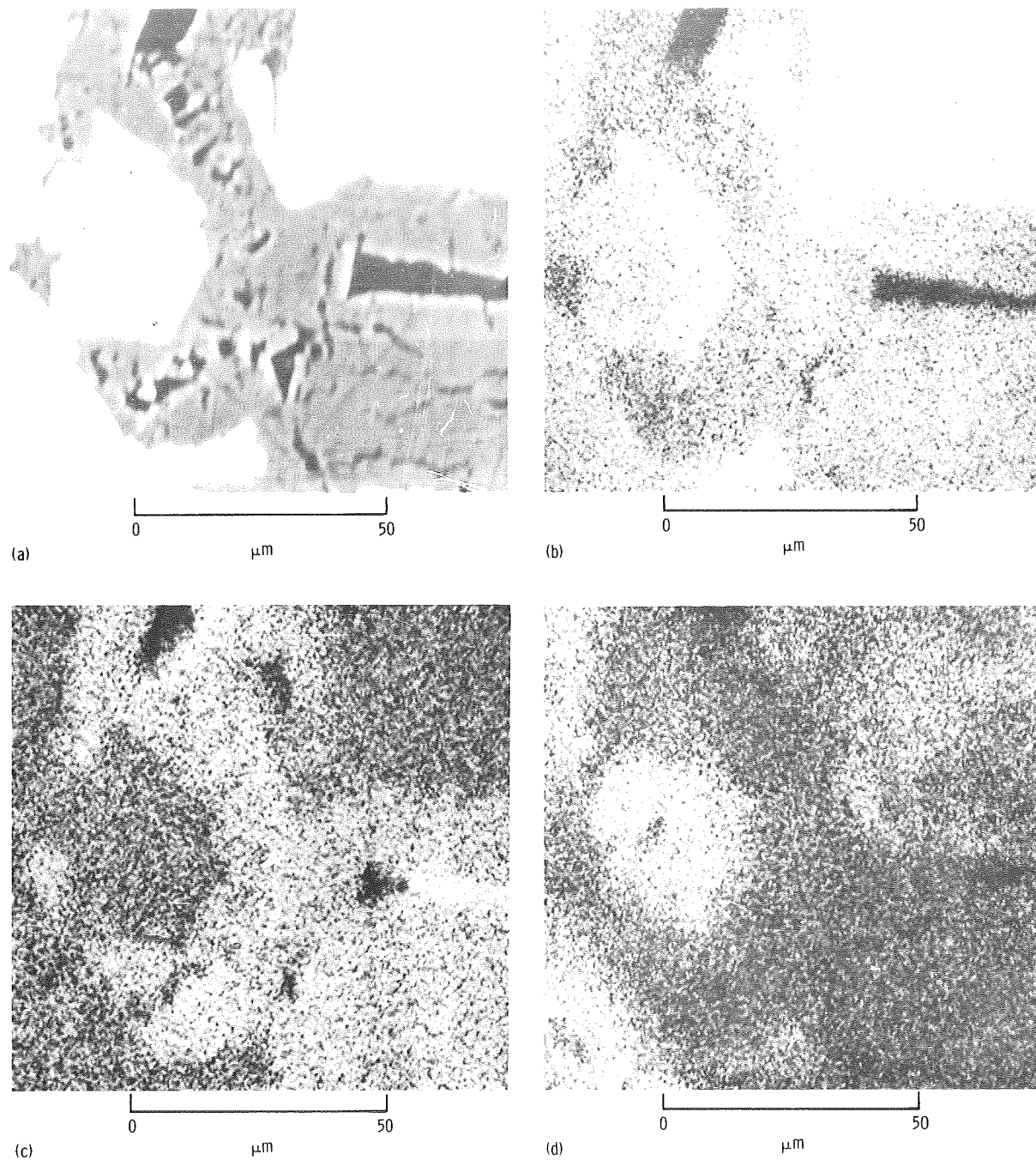


FIGURE 28-30.—Scanning of flight sample MA-150-16 in sectioned areas containing two phases of the W-Al-Re system. (a) Electron beam scanning ("1" indicates the Al, "2" indicates the Al-rich phase (31W 66Al 3Re), and "3" indicates phase 56W 37Al 7Re (table 28-II)). (b) Tungsten  $L\alpha$  radiation. (c) Aluminum  $K\alpha$  radiation. (d) Rhenium  $L\alpha$  radiation.

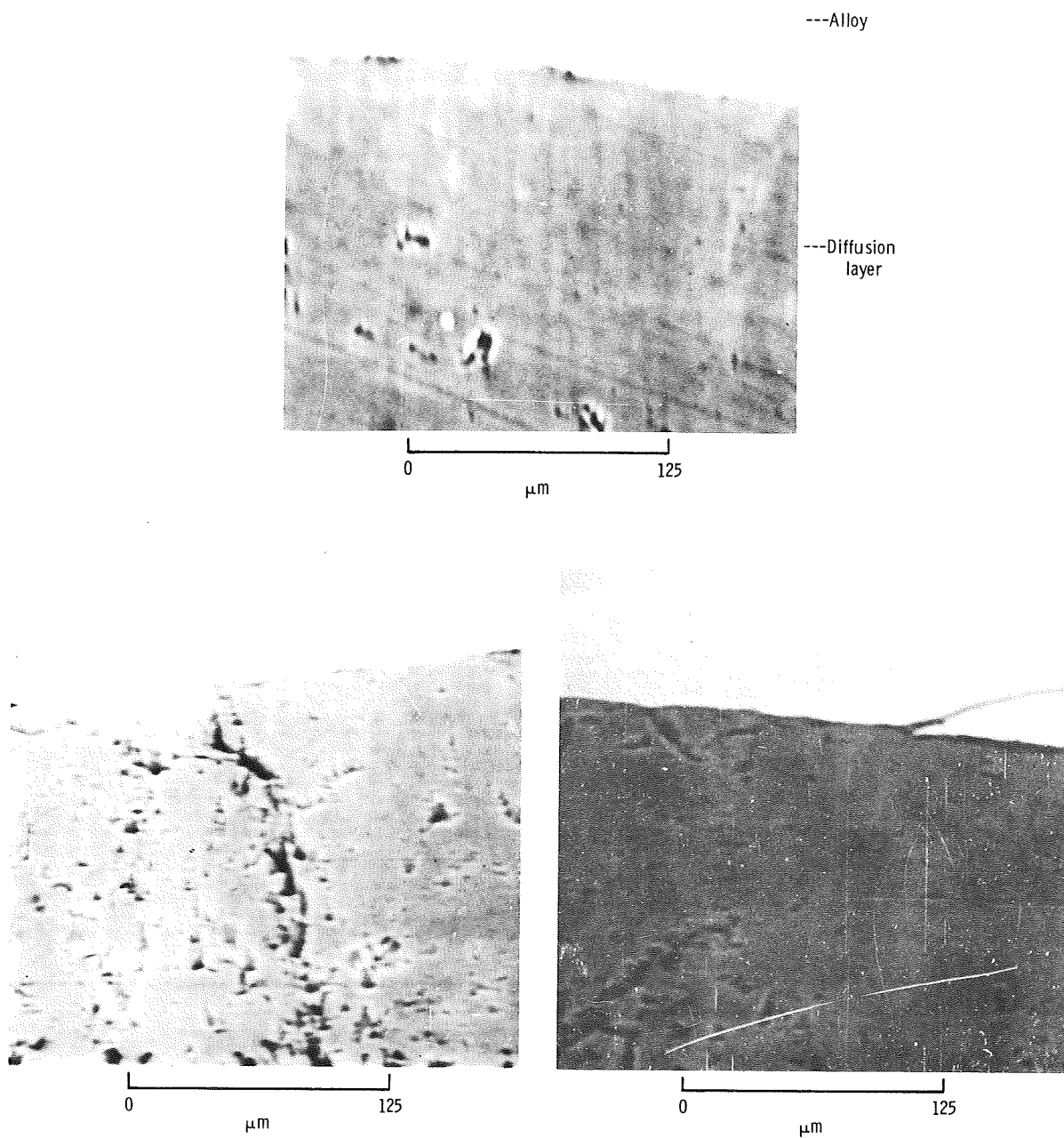


FIGURE 28-31.—Electron beam scanning in different areas of the diffusion layer/WRe alloy interface in ground sample MA-150-11. Pores can be seen in some areas of the diffusion layer.

(wt%). This composition was not observed in the matrix of any other sample (except for the diffusion layer).

Study of the Al/alloy interface revealed that some areas of the diffusion layer are more porous than others (figs. 28-31 and 28-32), the average size of the pores being generally larger in the flight samples. Concentration of pores at the boundary of the diffusion layer and the alloy in flight samples (fig. 28-32) is higher than in ground samples (fig. 28-31).

For further comparison, it should be noted that no appreciable pore formation was observed in the diffusion area between pure W and Al. An increased pore formation was also observed in the Al matrix of the flight ingot.

Microhardness was determined for the WRe alloy, for the Al, and for the diffusion layer phases. The results, summarized in table 28-III, shows the microhardness values of the ground-based sample to be in good agreement with those of the flight sample. The phase in the diffusion layer contiguous to WRe alloy has the highest hardness.

The ingot Al matrix was analyzed for W, Re, carbon, and oxygen content. The first three ele-

ments were not detected in dissolved state in any of the samples. Oxygen content, both in flight and ground-based samples, did not exceed the values corresponding to Al surface oxidation resulting from section preparation.

To evaluate the degree of interaction between liquid Al and the graphite crucible walls, carbon and Al distribution across the Al/crucible contact area was determined. The results provide no evidence of any appreciable interaction between the ingot and the crucible for all examined specimens.

### Aluminum Powder and CuAl Eutectic

In ground-based and flight experiments, Al powder was molded into ingots with almost identical outward appearances (fig. 28-33). Samples had low cohesive strength and damaged easily. This was especially true with flight samples. The disintegration of one such sample into small fragments can be seen in figure 28-33(b). This physical characteristic hindered sample examination. Only scanning microscopy made the quantitative analysis of samples possible. The analysis results for the appropriate ingot sections, presented as

TABLE 28-III.—Microhardness Measurement Results for WRe Alloy, Al, and Diffusion Layer Phases

<i>Specimen</i>	<i>Phase</i>	<i>Microhardness H, kg/mm<sup>2</sup></i>
MA-150-11 (ground-based)	WRe alloy	550
	Al matrix	21
	Phase bordering with alloy <sup>a</sup>	645
	Phase bordering with Al <sup>a</sup>	550
MA-150-16 (flight)	WRe alloy	550
	Al matrix	21
	Phase bordering with alloy	650
	Phase bordering with Al	550

<sup>a</sup>See figure 28-24.

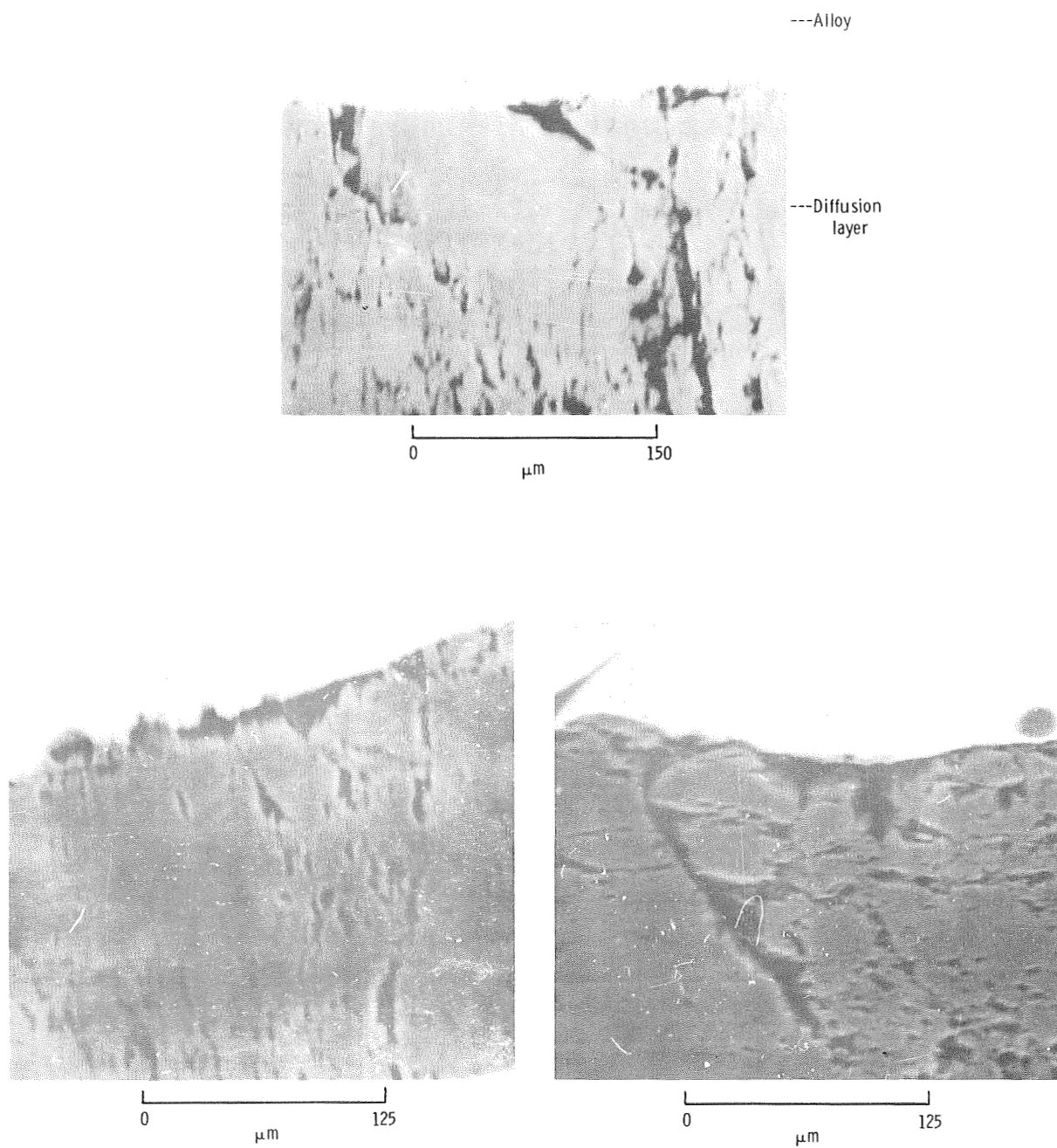


FIGURE 28-32.—Electron beam scanning in different areas of the diffusion layer/WRe alloy interface in flight sample MA-150-16. Pores can be seen at the interface and deep in the diffusion layer.

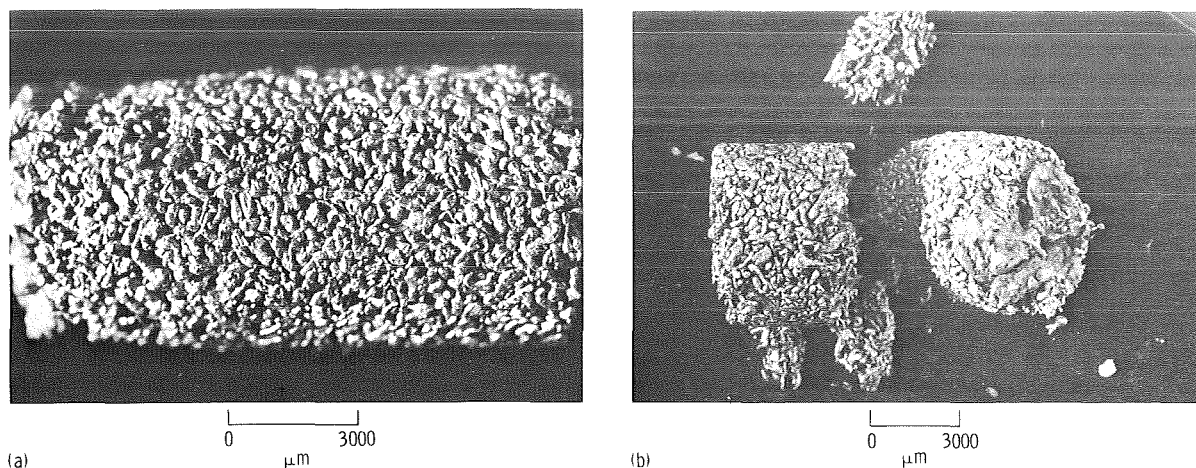


FIGURE 28-33.—Powdered Al sample after the experiment. (a) Ground-based sample. (b) Flight sample.

photographs in figure 28-34, show no evidence of differences between the flight and ground-based samples.

The aluminum foil used to insulate the Al powder from the pieces of eutectics melted completely. Close to the foil, the space- and Earth-grown ingots are somewhat smaller in diameter (fig. 28-33). Fragments of the CuAl eutectic, which in the beginning of the experiment were placed on the bottom of the graphite crucible, failed to melt into one ingot under any experimental conditions. Only a partial fusion of fragments to each other and to the aluminum foil occurred.

The results of metallographic analysis performed on Earth- and space-processed ingots indicate that their original microstructure (laminated eutectic) was not preserved. In both cases, the structure that was formed after melting and subsequent crystallization was composed of  $\alpha$ -solid-solution (Al-based) and second-phase inclusions. This phase, both in flight and ground-based specimens, occurred in small amounts, generally as isolated elongated inclusions.

Figures 28-35 to 28-38 are photographs of sectioned areas containing  $\alpha$ -solid-solution and second-phase inclusions. The photographs were made with electron beam scanning and characteristic Cu  $K\alpha$  and Al  $K\alpha$  radiation. It is apparent

that the results for ground-based and flight samples are very similar.

Quantitative X-ray spectral analysis revealed that the phase Cu content for both ground-based and flight samples constituted  $\approx 33$  at.% (corresponding to the CuAl<sub>2</sub> phase), and that Cu content in  $\alpha$ -solid-solution was within the range of 1.5 to 2 at.%. These results are congruent with the Cu-Al system phase diagram data (ref. 28-6).

## RESULTS AND DISCUSSION

### Compound Material

Different reasons for change in the primary structure of ingots (fig. 28-1) after ground-based and flight-based experiments (fig. 28-7) are discussed in this section. In the first case, two different reasons for displacement of W and alloy are evident: (1) marked difference in specific weight between W (WRe alloy) and Al and, consequently, strong gravitational force and buoyancy exerted on the samples by liquid Al melt, and (2) the effects of liquid Al surface tension.

Different effects of these forces can best be illustrated by comparing the location of the W balls and the rod in the alloy. The rod remained at the



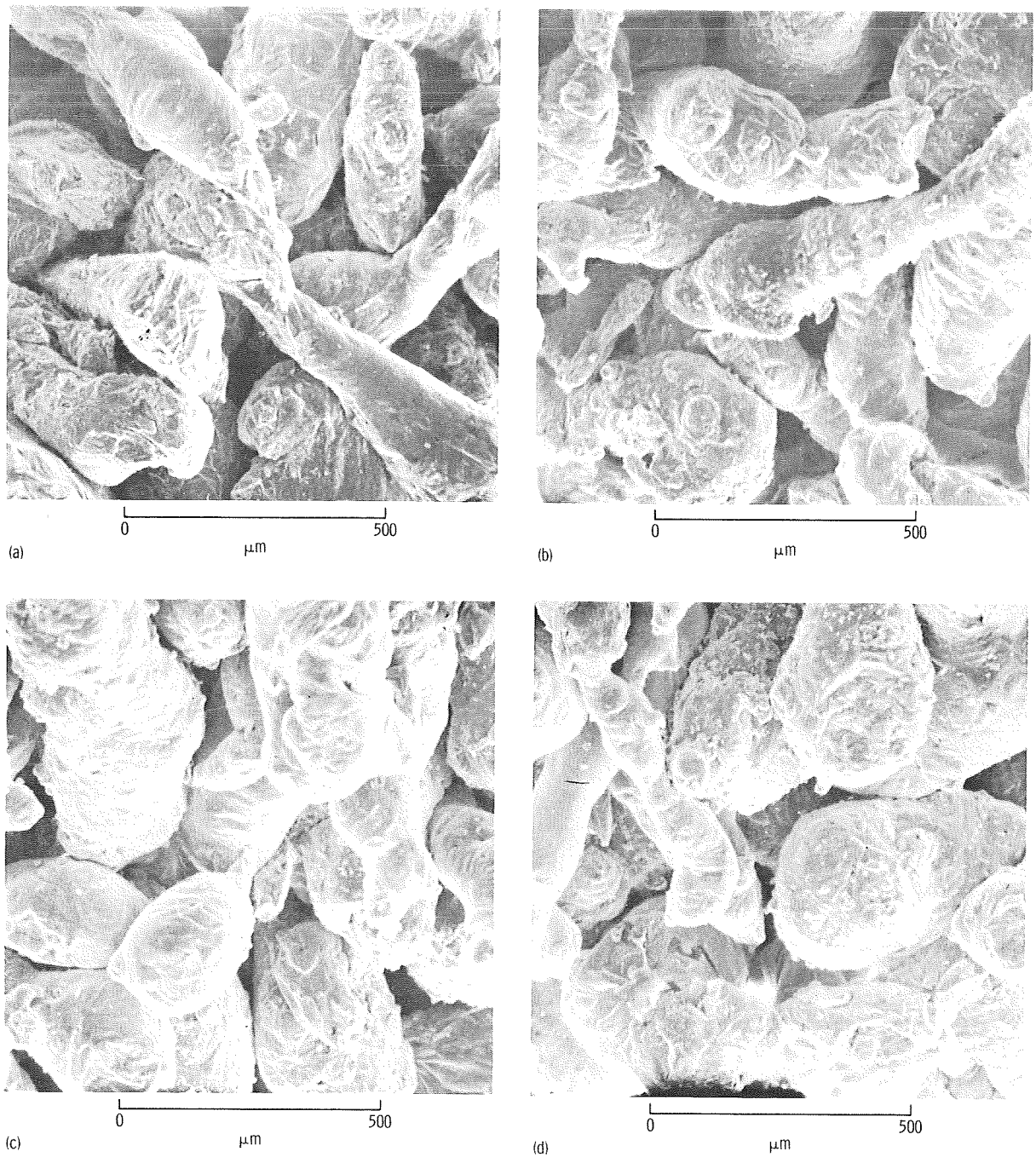


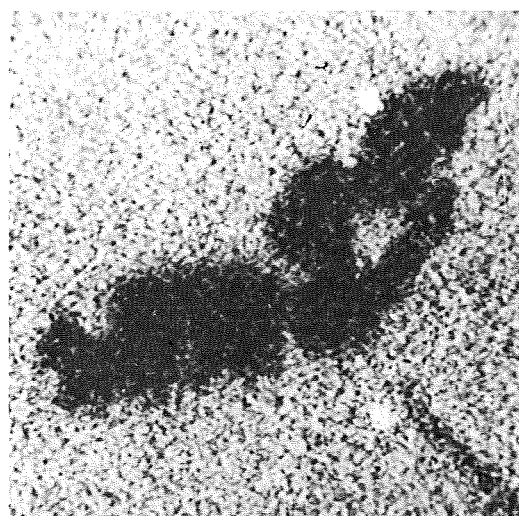
FIGURE 28-34.—Different surface areas of the powdered Al sample. (a) Ground-based experiment (example 1). (b) Ground-based experiment (example 2). (c) Flight experiment (example 1). (d) Flight experiment (example 2).



(a)



(b)



(c)

0 50  
μm

FIGURE 28-35.—Scanning of ground-based sample MA-150-9 in areas containing the  $\alpha_{Al}$  solid solution and  $\theta$  phase of the Cu-Al system. The  $\theta$  phase is in the center. (a) Electron beam scanning. (b) Copper  $K\alpha$  radiation. (c) Aluminum  $K\alpha$  radiation.

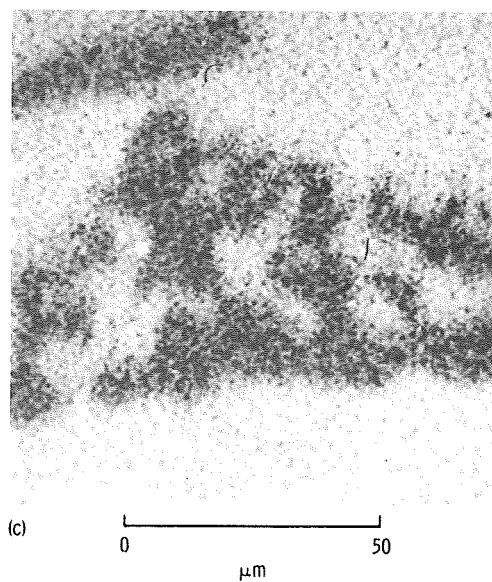
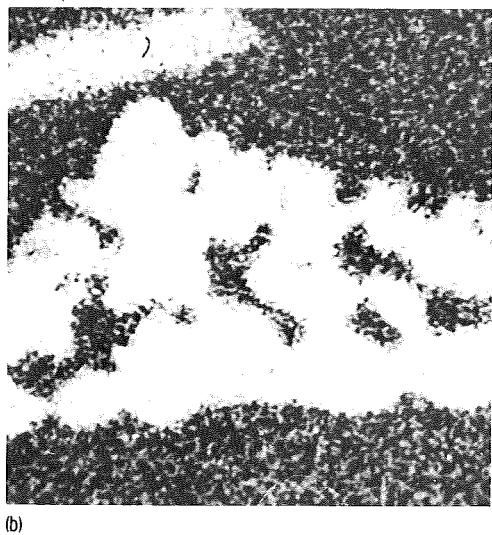
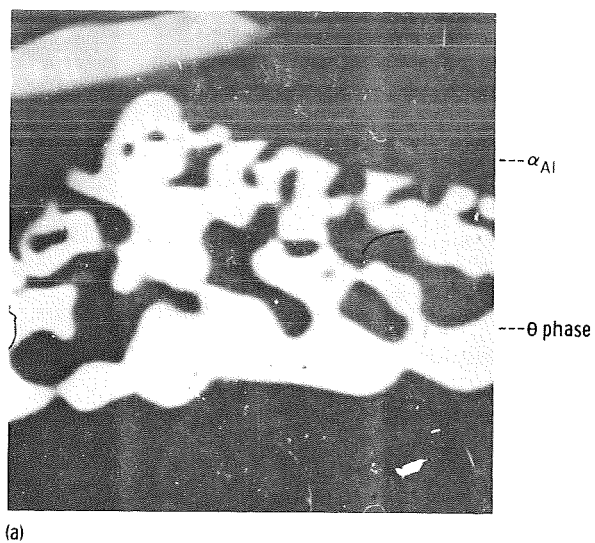


FIGURE 28-36.—Scanning of flight sample MA-150-17 in sectioned areas containing the  $\alpha_{Al}$  solid solution and  $\theta$  phase of the Cu-Al system. (a) Electron beam scanning. (b) Copper K $\alpha$  radiation. (c) Aluminum K $\alpha$  radiation.



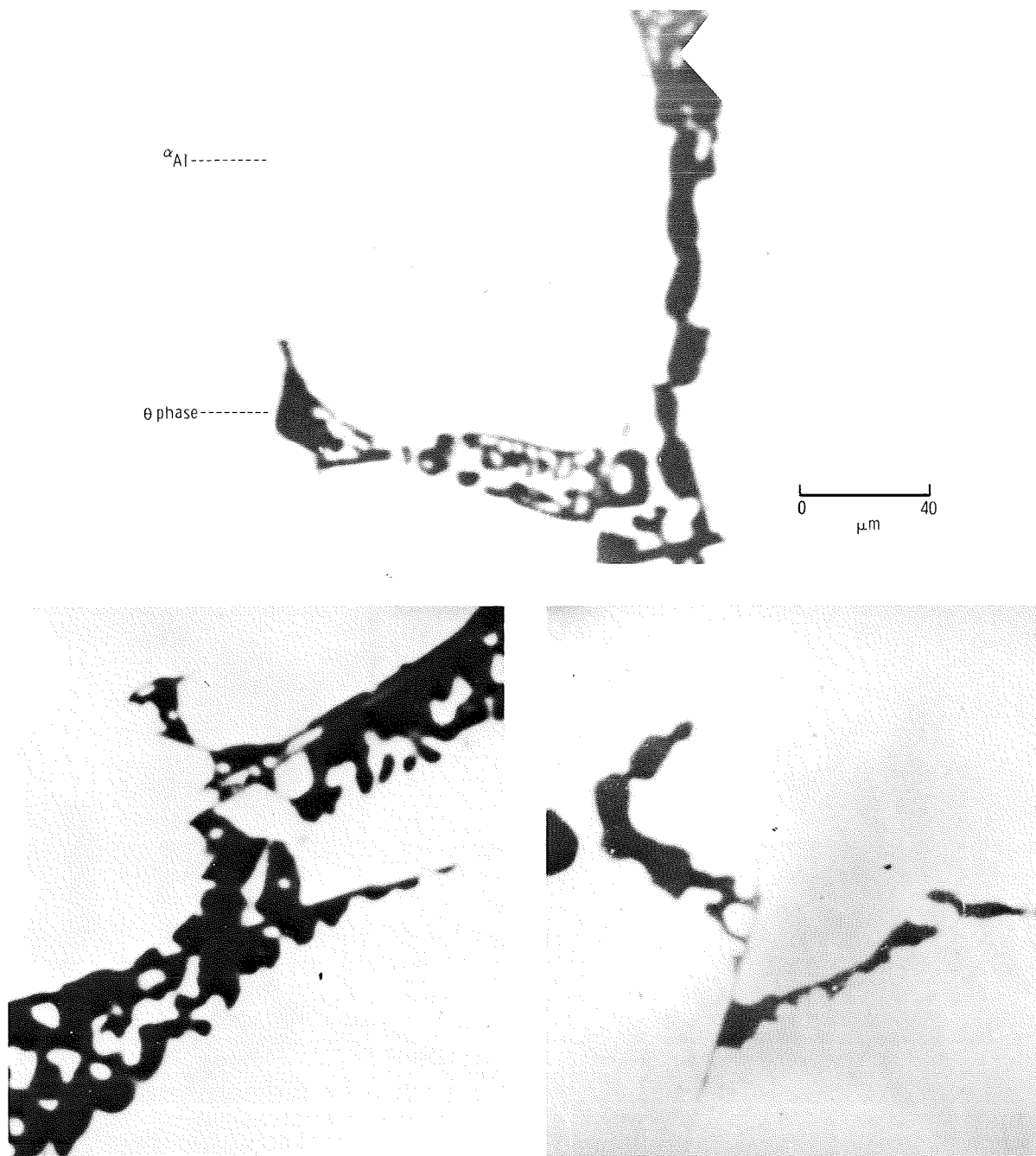


FIGURE 28-37.—Scanning electron photomicrographs of ground-based-sample regions containing the  $\theta$  phase of the Cu-Al system.

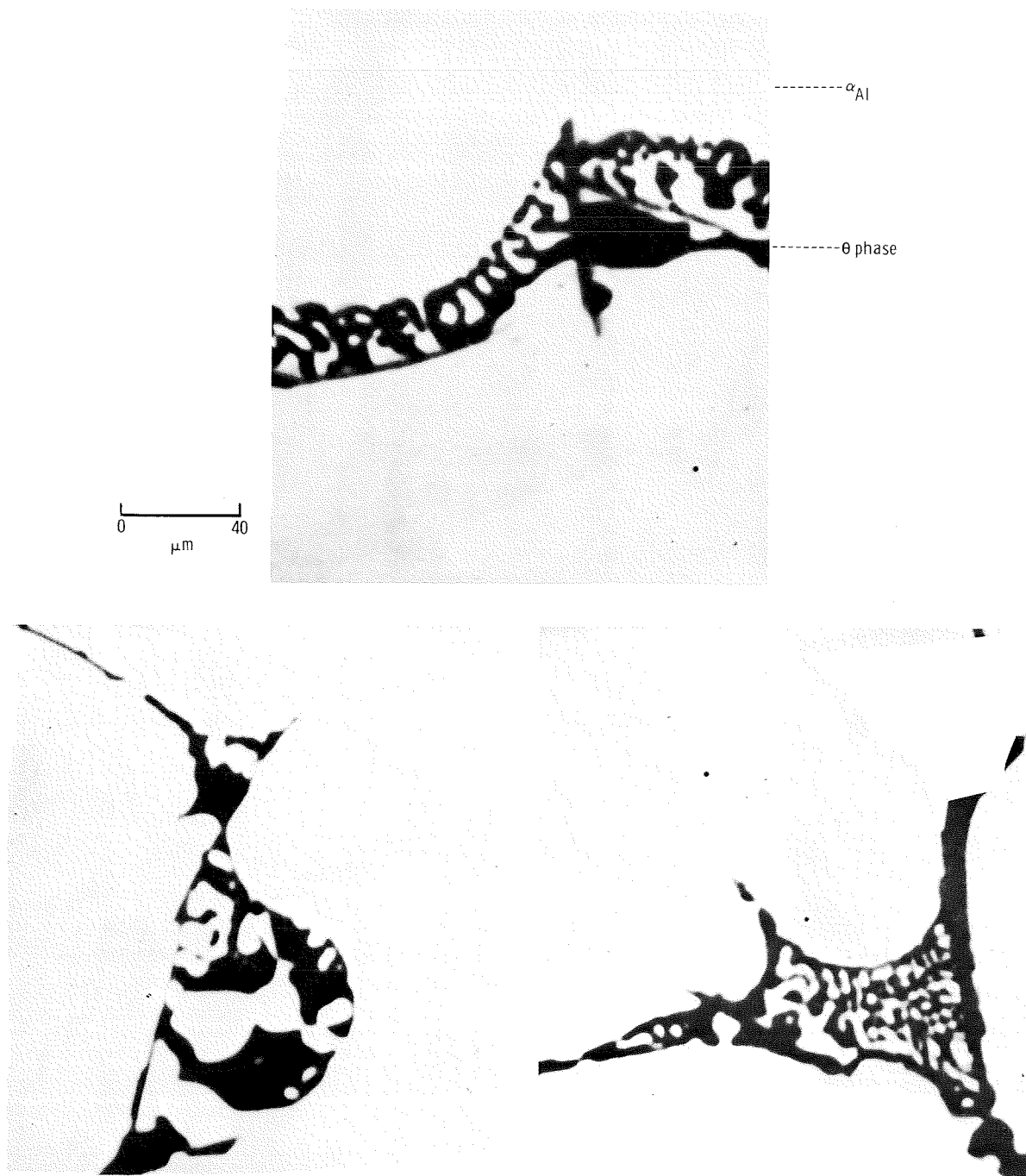


FIGURE 28-38.—Scanning electron photomicrographs of flight-sample regions containing the  $\theta$  phase of the Cu-Al system.

surface (fig. 28-7(a)), whereas the W balls shifted to the bottom. Because the rod was initially located at the ingot surface, it was primarily affected by the Al surface tension; however, deeper in the ingot, the effect of this force on W specimens was quite negligible (symmetry conditions). Also, ingot structural formation could have been strongly affected by the Al melt convection and by the interaction between "composite" system constituents. However, in an "ideal" weightless environment, the effects of gravity and buoyancy should be eliminated and melt convection should be brought to a minimum. Under these conditions, it would be only natural to expect that the predetermined structure of the ingot would remain unchanged.

However, gravitation data for the flight-based multipurpose furnace experiment provide ample evidence that weightlessness during the Apollo-Soyuz Test Project (ASTP) was not "ideal." First, the center of gravity of cartridges and ampoules was not coincident with that of the docked spacecraft. Hence, the specimens were subjected to an acceleration force (ref. 28-8) on the order of  $10^{-5}$ g. Moreover, NASA data indicate that the specimens in ampoules were periodically exposed to accelerations of  $10^{-3}$ g during spacecraft attitude correction and to  $10^{-5}$ g acceleration during spacecraft braking. Burn time was within 0.01 to 0.1 second, and the acceleration vector was approximately in the plane perpendicular to the ampoule axis (its direction was not constant).

The possibility of W balls being displaced from their original position as a result of the aforementioned gravity is discussed here. The W/Al interaction, convection of melt, and possible shape changes of the melt will be disregarded.

Assuming that W specimens are shaped as perfect balls, the motion equation for one ball is

$$ma = F_{\text{gravity}} + F_{\text{viscosity}} + F_{\text{buoyancy}} \quad (28-9)$$

where  $m$  is the ball mass;  $a$  is the ball acceleration; and  $F_{\text{gravity}}$ ,  $F_{\text{viscosity}}$ , and  $F_{\text{buoyancy}}$  are the flight gravity, viscosity, and buoyancy forces, respectively. Considering that all these forces act along one straight line and designating the flight gravita-

tional acceleration as  $g_o$ , equation (28-9) can be written as a scalar equation by substituting appropriate values

$$m \frac{d^2x}{dt^2} = mg_o - 6\pi\eta R \frac{dx}{dt} - \frac{4}{3}\pi R^3 \rho g_o \quad (28-10)$$

where  $F_{\text{gravity}} = mg_o$ ,  $F_{\text{viscosity}} = -6\pi\eta R dx/dt$  (along the slope),  $F_{\text{buoyancy}} = -4/3\pi R^3 \rho g_o$ ,  $R$  is the ball radius,  $\eta$  and  $\rho$  are the viscosity factor and melt density at experiment temperature, respectively,  $x$  is the displacement, and  $t$  is the time. Direction of flight-induced gravity is taken here as a positive direction.

Equation (28-10) can be rewritten as

$$\frac{d^2x}{dt^2} + \alpha \frac{dx}{dt} + \beta = 0 \quad (28-11)$$

assuming that

$$\alpha = \frac{9\eta}{2R^2\rho_W}, \quad \beta = g_o \left( \frac{\rho}{\rho_W} - 1 \right) \quad (28-12)$$

where  $\rho_W$  is the tungsten density.

Of course, no displacement of balls occurs in the absence of gravity. Hence, the initial condition can be written as

$$t = 0, x = 0, \frac{dx}{dt} = 0 \quad (28-13)$$

Solving differential equation (28-11) for these initial conditions, one obtains

$$\frac{dx}{dt} = \frac{\beta}{\alpha} \left( e^{-\alpha t} - 1 \right) \quad (28-14)$$

$$x = -\frac{\beta}{\alpha} \left( \frac{1}{\alpha} e^{-\alpha t} + t - \frac{1}{\alpha} \right) \quad (28-15)$$

These results can also be valid for a one-g environment, substituting gravitational acceleration

$g_o$  by Earth gravity  $g$ . When condition  $\alpha t \ll 1$  in equation (28-15) is met, expanding the exponent into series and restricting calculations to the term of the second order of smallness for  $\alpha t$ , the displacement  $x$  can be written as

$$x = -\frac{\beta t^2}{2} = \left(1 - \frac{\rho}{\rho_W}\right) \frac{g_o t^2}{2} \quad (28-16)$$

This equation defines the law that governs displacement of a spherical body as a function of time. It differs from the standard law of uniformly accelerated motion (when the initial velocity is zero) by the presence of the coefficient  $1 - (\rho/\rho_W)$  that considers the "buoyancy" effect of the melt. Melt viscosity in these conditions has no effect on the body displacement.

It can be proven that condition  $\alpha t \ll 1$  during the flight-based multipurpose furnace experiment was satisfied only when  $t$  was the duration of one "accelerating" impulse. As previously implied,  $t_{\max} \approx 0.1$  second;  $R \approx 5 \times 10^{-2}$  cm;  $\rho_W \approx 19.3$  g/cm<sup>3</sup> (ref. 28-9); and  $\eta \approx 1.4 \times 10^{-6}$  g/cm sec (ref. 28-10) for  $T \approx 1073$  K (800° C). Hence,  $\alpha \approx 1.3 \times 10^{-4}$  sec<sup>-1</sup> and  $\alpha t_{\max} \approx 10^{-5} \ll 1$ .

Thus, equation (28-16) is valid for the impulse gravity conditions and allows an estimation of  $x$  for the duration of one impulse. Displacement of a W ball during one impulse at acceleration  $g_o \approx 4 \times 10^{-3} g \approx 3.9$  cm/sec<sup>2</sup> ( $10^{-3} g$  acceleration can be disregarded), which is the most common force involved in a spacecraft attitude correction maneuver, will now be determined. Considering that  $\rho \approx 2.3$  g/cm<sup>3</sup> (ref. 28-10), equation (28-16) gives  $t_{\min} = 0.01$  second,  $x \approx 1.7$   $\mu$ m,  $t_{\max} = 0.1$  second,  $x \approx 170$   $\mu$ m. Thus, the ball displacement value (in order of magnitude) as a function of impulse duration is within the range of  $1 \mu\text{m} \leq x \leq 200 \mu\text{m}$ .

It must be emphasized that this calculation is an approximation only and that it applies primarily to the stage immediately following Al melting, during which the interaction between W and Al is still negligible. More rigorous analysis is needed for subsequent stages because of the potential formation of liquid solution of W in the Al (hence, changes in  $\rho$  and  $\eta$ ) and because of the

growth of intermetallic phases between W and Al (i.e., continuous changes in mass and shape of a moving body).

The analysis results suggest that gravitation in flight experiments may cause a displacement of W balls (figs. 28-7(b)) during the initial stages of the solid and liquid metal interaction. However, displacement of specimens in subsequent stages may also result from the phase growth interaction of the adjacent specimens and possibly from the microgravity-induced convection and shape changes of the ingots.

As was noted previously, a composite, microgravity-melted ingot is larger than its ground-melted counterpart. Such an increase in size may be attributed to the fact that the air, which is absorbed by the Al and which fills the gaps in the material interface, cannot be completely removed from the melt in a microgravity environment (unlike on Earth); it remains trapped in the melt, causing an increased macroporosity of aluminum and a "swelling" of the ingot. An estimation of possible air-bubble displacement occurring in the melt under the influence of flight gravitation can serve as confirmation of this fact.

The relationship in equation (28-15) can be valid for any spherical inclusion affected by the above forces (eq. (28-9)). Assuming the air density of  $\rho_B \approx 10^{-3}$  g/cm<sup>3</sup> (eq. (28-10)), then equation (28-12) proves that the condition  $\alpha t \gg 1$  (where  $t$  is the duration of an acceleration pulse) was always satisfied for bubbles having a diameter of 1 to 100  $\mu$ m. The inequality obtained indicates  $t \gg 1/\alpha$ , and all the more for  $t \gg \frac{1}{\alpha} e^{-\alpha t}$ . Therefore, for bubble displacement in the melt, equations (28-12) and (28-15) give

$$x = -\frac{\beta t}{\alpha} = -\frac{2R^2}{g} \frac{(\rho - \rho_B)}{\eta} \quad (28-17)$$

Since  $(\rho - \rho_B) > 0$ , the minus on the right side of equation (28-17) indicates that the bubbles are displaced in the direction opposite to that of the flight gravitation force, which always occurs under one-g conditions as well.

Based on equation (28-17), table 28-IV shows estimations of the maximum value of bubble displacement occurring during one impulse  $t_{\max} = 0.1$  second for  $g_0 \approx 4 \text{ cm/sec}^2$ . The table indicates

TABLE 28-IV.—*Estimates of Bubble Displacement*

Bubble diameter, $\mu\text{m}$	Maximum value of displacement, $\mu\text{m}$
1	5
10	$5 \times 10^2$
100	$5 \times 10^4$

that the displacement of bubbles with a diameter of no more than  $100 \mu\text{m}$  did not exceed the mean size of the Al ingot. The presence of such bubbles obviously caused an accumulation of macropores in the bulk of the ingot as well as in the area of the diffusion/alloy interface in the flight sample (fig. 28-32).

### **Tungsten and Tungsten-Rhenium Alloy/Aluminum Interaction**

General physical considerations suggest that, given the temperature of the flight and ground-based experiments, a process of mutual diffusion should occur between solid W and liquid Al. This process should result in the formation of intermediate phases within the diffusion layer, as predicted by the W-Al system constitutional diagram. Furthermore, liquid solution of W may form in the Al as a result of this diffusive interaction (fig. 28-14).

Results of the experiments indicate that three phases were indeed observed, but that each phase was formed under specific circumstances. Thus, the  $\text{WAl}_4$  phase can develop practically at any experimental temperature. On the other hand, the  $\text{WAl}_5$  phase (see constitutional diagram in fig. 28-14) can exist only at temperatures below 1143

K ( $870^\circ \text{C}$ ). Consequently, the  $\text{WAl}_5$  phase developed only during the experiment cooldown specimen, which lasted approximately 1 hour (fig. 28-5).

The markedly greater thickness of the  $\text{WAl}_5$  phase as compared to the  $\text{WAl}_4$  phase, despite the much longer formation time of the latter, can be explained by the fact that the  $\text{WAl}_4$  phase growth occurs at temperatures far below its melting point ( $1599 \text{ K}$  ( $1326^\circ \text{C}$ )), whereas the  $\text{WAl}_5$  phase grows at temperatures close to its melting point. It is not unlikely that the  $\text{WAl}_5$  phase grows at the expense of the  $\text{WAl}_4$  phase by means of "diffusive dilution."

Finally, the third phase ( $\text{WAl}_{12}$ ), which exists at temperatures below  $970 \text{ K}$  ( $697^\circ \text{C}$ ) (fig. 28-14), could grow in the diffusion layer no longer than  $\approx 15$  minutes after the temperature was lowered (fig. 28-5). Hence, its "diffusion" area thickness was very small and in some places impossible to detect.

Another phase formation mechanism to be considered other than diffusion is the precipitation of phases from liquid solution in the process of cooling. This mechanism may, for example, explain the inhomogeneous distribution (fig. 28-15(b)) and the varied thickness of the phases throughout different areas of the Al/W interface. Perhaps the crystalline faceting of the  $\text{WAl}_{12}$  phase in the flight sample can be also attributed to the  $\text{WAl}_{12}$  precipitation from the melt under conditions of lower convection than on Earth.

The presence of convection in the space-flight environment, together with Al penetration along grain boundaries into the phases, may explain the formation of small phase fragments in the Al matrix as well as the dendritic growth of these phases. It should also be noted that a division of the diffusion front into elongated and dendritic sections (figs. 28-9 to 28-13) could be related to finite dimensions of W specimens and to the effect this produced on diffusion. In early stages of the process, when specimen dimensions were "semi-infinite" compared to dimensions of the layer, the diffusion front was dense. However, the already limited amount of W became insufficient to sustain such a front, which soon began to disintegrate. At this stage, the process developed

radially (figs. 28-9 to 28-13). Lower convection of melts in a microgravity environment could be also responsible for the somewhat lower "disorientation" of the needlelike parts of the layer in flight specimens as compared to ground-based specimens (figs. 28-16 to 28-19).

The diffusive reaction between Al and WRe alloy will now be discussed. Analysis has shown that the process of mutual diffusion between solid alloy and liquid Al occurs both in microgravity and one-g environments. As a result, two intermetallic phases (figs. 28-23 and 28-24) of short concentration range are formed in the diffusion layer. Division of the layer into single elongated sections, which is typical of the W-Al system, was not observed. This may be associated with the fact that the starting alloy sample in the experimental temperature/time mode was "semi-infinite" with respect to the diffusion layer thickness.

Similar concentration curves for the distribution of constituents in ground-based and flight samples indicate that microgravity phase formation in the diffusion layer is subject to the same laws as in a one-g environment. However, the lack of reliable structural diagrams for the W-Al-Re system hinders more detailed evaluation. Especially, it does not seem possible to establish the extent to which the boundary concentrations in the diffusion layer phases correspond to the constitutional-diagram-predicted values. Particularly interesting in this respect is the boundary of the W-richest phase and Al. Both in ground-based and flight samples (fig. 28-24), an appreciable increase in W concentration and a decrease in Re concentration (Al content changes are small) were simultaneously noted as one approaches this boundary and becomes farther from the center of the phase. However, how close the boundary concentrations are to the equilibrium values for the specimens studied is unknown.

Equally difficult to explain is the formation of numerous individual fragments of W-Al-Re system phases (figs. 28-25 to 28-30) in the Al matrix. Two mechanisms explaining their formation can be tentatively offered: (1) phase precipitation from the solution in the process of cooling (if the constitutional diagram predicts the existence of such a solution within the experimental temperature range) and (2) separation of phase

crystals from the diffusion layer resulting from grain-boundary diffusion of Al into the phase and from gravity induced convection of the melt.

When the first mechanism is the predominant one, then a structural analysis of phases precipitated from the solution (table 28-II) and of phases grown in the diffusion layer (fig. 28-24) permits an assumption that three phases are present in the W-Al-Re system for the studied temperature range. These phases should have different melting points  $T_{\text{melt}}$ , and their boundary concentrations should be a function of temperature. It follows that the Al-richest phase (more than 60 wt%), detected only in flight specimen MA-150-16 (table 28-II), has the lowest  $T_{\text{melt}}$  value.

However, if the second mechanism predominates, then the absence of liquid solution might suggest the occurrence of a diffusion of Al from the melt into phase fragments that separated from the layer. The formation of phases with increased Al content in flight samples indicates more intensive diffusion of Al in a microgravity environment. However, more experiments are needed before reliable interpretation of these results can be made.

Results obtained from measuring microhardness  $H$  for different phases of the W-Al and W-Al-Re system will now be discussed briefly. An agreement in  $H$  values for the aforementioned systems in ground-based and flight samples (tables 28-I and 28-II) indicates microstructural similarity of the Earth- and space-grown phases. As far as the Al matrix is concerned, the "swelling" of flight-processed melts stems from macroporosity, a fact mentioned previously. The greatest hardness value in the W-Al-Re system is found in the phase having the highest content of Re (fig. 28-24, table 28-III). Of all phases tested for microhardness in the W-Al system, the  $\text{WAl}_5$  phase located in the diffusion layer was found to have the highest values of  $H$ . However, individual "needles" of the  $\text{WAl}_5$  phase have somewhat lower hardness values (table 28-I). This discrepancy may be associated with the fact that the  $\text{WAl}_5$  phase located in the diffusion layer exists within a certain concentration range (allowable by the W-Al system constitutional diagram) and is richer in W than the more homogeneous individual "needles" of this phase.

### Powdered Aluminum and Eutectics

Analysis of results reveals that fusing of powder particles (fig. 28-34) in flight and ground-based samples did not occur. This may be attributed to the fact that each Al particle is protected by an oxide coating, the melting point  $T_{\text{melt}}$  of which is considerably higher than that of pure Al. The presence of this coating prevented inter-particle fusing, although pure Al melting ( $T_{\text{melt}} = 933 \text{ K (660}^\circ \text{C)}$ ) within each particle in the studied temperature range (fig. 28-5) did occur in both flight and ground-based specimens.

The possibility of particles becoming "coupled" in certain areas was higher in the more constant (in value and direction) Earth gravity than in the much lower and more variable orbital gravity. This was a factor that determined the somewhat higher cohesive strength of the ground-processed powdered ingots as compared to the flight-processed ingots.

Preliminary analysis data on the CuAl eutectic failed to demonstrate any substantial effect of weightlessness on the resultant ingot structure. As previously implied, neither flight nor ground-based specimens maintained the original lamellar structure after melting. This may be associated with the following factors: (1) deviation from the originally predetermined composition and (2) alloy cooling conditions (fig. 28-5).

According to the constitutional diagram (ref. 28-6), the ratio of  $\theta$ -phase and  $\alpha$ -solid-solution in a eutectic alloy CuAl should be more or less constant. However, all examined specimens showed higher  $\alpha$ -solid-solution content. This is probably associated with the aluminum foil dissolving in the alloy and the resultant change in the chemical composition of the alloy.

As is well known, cooling conditions can strongly affect the formation of an eutectic microstructure (ref. 28-11). In these experiments, the temperature/time mode led to phase separation and to the disappearance of the original lamellar structure (figs. 28-35 to 28-38).

It should be noted that the Cu content in  $\alpha$ -solid solution (1.5 to 2 at.%) for both types of specimens was higher than normally expected at room temperature and as predicted by the Cu-Al system constitutional diagram. This supersatura-

tion of the solution may be attributed to a rapid cooling of the alloy from 773 K (500° C) (fig. 28-5), a temperature at which the solubility of Al and Cu corresponds to the above values.

### CONCLUSIONS

The results of this preliminary analysis justify a conclusion that, despite a low-g environment on-board the spacecraft, the predetermined distribution of refractory inclusions in composite material was not maintained after the matrix was melted. This may be attributed to the effect of gravity on-board the spacecraft and to the interaction between different constituents of the composite material.

The Al matrix of the space-grown ingots is more porous than it is in Earth-grown ingots. Space-grown ingots are also larger and shaped differently than Earth-grown ingots.

The kinetics of diffusion and phase formation in the solid W (WRe alloy)/liquid Al diffusion area was approximately the same for both ground-based and flight samples. This is evidenced by the similarity in geometrical characteristics of the compared diffusion layers as well as by the analogous phase composition and distribution of the diffusion layer constituents.

At the same time, microgravity diffusion and phase formation processes for the W-Al and W-Al-Re systems exhibit some striking differences. In the binary system, the  $\text{WAl}_5$  phases are thinner than on Earth, are needle-shaped, and have a lower disorientation angle; the  $\text{WAl}_{12}$  phase has a crystalline faceting. In the case of the tertiary system, the distinguishing features include a higher porosity at the diffusion layer/WRe alloy interface, and the formation of phases rich in Al.

Samples of the CuAl eutectics and powdered Al processed under specified temperature/time conditions in space showed no appreciable difference from their Earth-processed counterparts. Experiments with powdered Al demonstrated that a slight excess of temperature above the Al melting point reduces the possibility of individual particles being fused together in a low-gravity orbital environment.

## REFERENCES

- 28-1. Castaing, R.: Application of Electron Probe to Local Chemical and Crystallographic Analysis. Ph.D. Dissertation, Univ. of Paris, 1951. (Translation by P. Duwez and D. B. Wittry, WAL 142/59-7, Calif. Inst. of Technology, 1955.)
- 28-2. Borovskii, I. B.; and Rydnik, V. I.: The Theory of Quantitative Electron Probe Analysis. Quantitative Electron Probe Analysis, K. F. J. Heinrich, ed., National Bureau of Standards, Special Publication 298, U.S. Dept. of Commerce (Washington, D.C.), 1968, pp. 35-52.
- 28-3. Philibert, J.: A Method of Calculating the Absorption Correction in Electron Probe Microanalysis. X-Ray Optics and X-Ray Microanalysis, H. H. Pattee, V. E. Cosslett, and A. Engström, eds., Academic Press (New York), 1963, pp. 379-392.
- 28-4. Reed, S. J. B.: The Present State of Quantitative Electron Probe Microanalysis. Rev. Phys. Technol., vol. 2, no. 2, 1971, pp. 92-115.
- 28-5. Duncumb, P.; and Reed, S. J. B.: Progress Achieved in Calculating the Stopping Power and the Backscattering Coefficient. Physical Bases for X-Ray Spectral Local Analysis, Nauka Press, 1973, pp. 117-138.
- 28-6. Hansen, Max: Constitution of Binary Alloys. Second ed., McGraw-Hill Book Co., 1958.
- 28-7. Gurov, K. P.; Pimenov, V. N.; and Ugaste, Yu. E.: Some Features of Mutual Diffusion in Multiphase System. Physics of Metals and Metallography, vol. 32, no. 1, 1971, pp. 101-107.
- 28-8. Belyakov, I. T.; and Borisov, U. D.: Technology in Space. NASA TT F-16264, 1975.
- 28-9. Shultze, G.: Physics of Metals. MIR Press (Moscow), 1971.
- 28-10. Koshkin, N. I.; and Shirkevich, M. G.: Elementary Physics Manual. FIL Press (Moscow), 1962.
- 28-11. Maltsev, M. V.: Metallurgy of Industrial Nonferrous Metals and Alloys. JPRS-55357, 1972. (Available from the National Technical Information Service.)



## 29. Multiple Materials Melting (Germanium-Silicon Solid Solutions)

### Part of Experiment MA-150\*

*V. S. Zemskov,<sup>a</sup> V. N. Kubasov,<sup>a</sup> I. N. Belokurova,<sup>a</sup> A. N. Titkov,<sup>a</sup> I. L. Shulpina,<sup>a</sup>  
V. I. Safarov,<sup>a</sup> and N. B. Guseva<sup>a</sup>*

#### INTRODUCTION

An experiment on melting and directional crystallization of an antimony (Sb)-doped germanium (Ge) silicon (Si) solid solution was designed for the Apollo-Soyuz Test Project (ASTP) to study the possibility of using microgravity conditions for obtaining solid-solution monocrystals with uniformly distributed components. Solid-solution monocrystals obtained in a microgravity environment in the absence of buoyancy forces and thermal convection were expected to have a more homogeneous and even distribution of components compared to those obtained under normal gravity conditions.

It was anticipated that the absence of convective mixing and the occurrence of mass transfer in the melt, caused by diffusion only, would create conditions for stationary crystal growth and would provide a compositional segregation consistent with these conditions (ref. 29-1). Also, in the absence of uncontrollable convective mixing, laminar distribution of components in a monocrystal is not likely to occur (ref. 29-2).

Antimony-doped Ge-Si solid solutions are favorable materials for studying the previously

mentioned processes, because the distribution coefficient of Si in Ge ( $K_{Si} > 1$ ) and that of Sb ( $K_{Sb} < 1$ ) enable investigation of the behavior of components having different distribution coefficients. Also, because Sb-doped Ge-Si solid solution is a semiconducting material, the precision techniques that are widely used in studying semiconducting materials can be used for a detailed investigation of component distribution in crystal volume and for analyses of defects in crystal structure.

#### PREPARATION AND OPERATION OF THE EXPERIMENT

Cylindrical specimens (ingots) of Sb-doped Ge-Si solid solution were made of monocrystals obtained by means of crystal pulling from the melt, which was continually being fed with Si (ref. 29-3). All monocrystals had the following identical characteristics:  $\langle 111 \rangle$  orientation growth, Si content from 0.7 to 1.0 at.%, Sb content from 1 to  $2 \times 10^{17}$  atoms/cm<sup>3</sup>, dislocation density in the  $\{111\}$  face from  $10^3$  to  $10^4$  cm<sup>-2</sup>, laminar distribution of components with Si-content fluctuations in the layers ranging to 0.1 at.%, and heterogeneity associated with crystal face effect.

The monocrystals were ground so that the ingot diameter would not be smaller than the internal diameter of the quartz ampoule by more than 0.2 mm and so that the crystallographic  $\langle 111 \rangle$  orientation would coincide with the ingot axis. The length of the ingot was  $38 \pm 0.1$  mm.

\*The Multiple Materials Melting Experiment is one of the five experiments that incorporated joint activities between the U.S. and U.S.S.R. crews. The joint U.S.-U.S.S.R. designation was "Experiment AS-3." The "metals" part of the experiment is reported in section 28.

<sup>a</sup>Institute for Metallurgy, U.S.S.R.

The tubes used to fabricate the ampoules were made of quartz that contained total impurities of not more than  $1.2 \times 10^{-3}$  wt%. Before inserting the ingots, the internal surface of each ampoule was coated with graphite by means of acetone pyrolysis.

A schematic diagram of an ampoule containing an ingot is shown in figure 29-1. To increase the mechanical strength of the ampoule, the walls of its rounded end (situated in the hot zone of the furnace) were made thicker than those of the remainder of the ampoule. The corresponding end of the ingot had a spherical shape matching the internal surface of the ampoule. At the other end of the ampoule, where sealing had to be performed, the specimen had a plane surface. Two spacers, which were of the same diameter as that of the specimen and which were made of high-purity graphite that had been additionally annealed in vacuum at a temperature of approximately 1773 K

(1500° C), were located at the plane face; and another spacer consisting of four layers of quartz cloth was located between the two graphite spacers. The ampoules were sealed at  $13.33 \text{ mN/m}^2$  ( $10^{-4}$  torr) to make the quartz tube press the graphite spacers tightly against the specimen.

The ampoules with the ingots were transferred to the United States for insertion into cartridges of a specific design. Both ends of the ampoules were wrapped with copper foil to create the necessary conditions for heat transfer inside the cartridge.

The experiment on melting and crystallization of Ge-Si solid solution was conducted in the three-chamber multipurpose furnace (sec. 21). According to the experiment plan, the ampoule containing the solid solution was to be placed in the furnace gradient zone, in which the following thermal conditions were to be maintained.

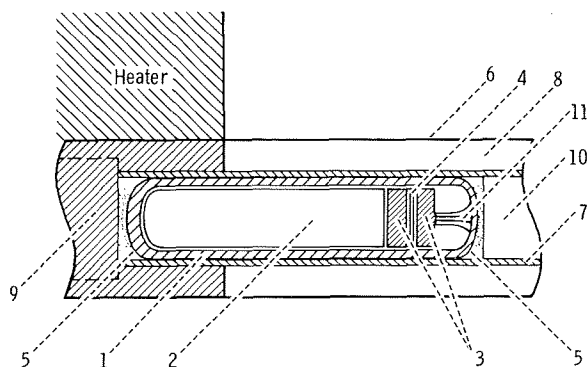
1. A temperature of 1323 K (1050° C) at the hot end and a temperature of 973 K (700° C) at the cold end

2. A thermal gradient along the ampoule from 30 to 40 K/cm (30° to 40° C/cm) when the specimen was in a molten state, and from 10 to 40 K/cm (10° to 40° C/cm) during the cooldown phase

This temperature distribution in the gradient zone would be expected to restrict the melting of the ingot to no more than two-thirds of its length, so that the remainder of it served as a seed for crystallization of the melt.

For the purpose of developing the required thermal mode and perfecting the ampoule and cartridge designs, ground-based thermal simulation experiments using prototypes of the flight ampoules and furnace were conducted in the United States. These experiments helped to obtain the desired temperatures at the hot and cold ends of the furnace. However, during these experiments, the distribution of the temperature along the ampoules containing the solid solution was such that the thermal gradient did not exceed 20 K/cm (20° C/cm) at any point along the ingot. Under these thermal conditions, complete melting of the entire ingot could be expected.

During the experiment in the microgravity environment as well as during the ground-based thermal simulation tests, the temperature cycles were kept in conformity with the plan.



1. Quartz ampoule: outside diameter,  $11.5 \pm 0.1$  mm; length,  $52 \pm 0.05$  mm
2. Ingot: diameter,  $9.5 \pm 0.1$  mm; length,  $38 \pm 0.1$  mm
3. Graphite spacers
4. Spacer consisting of four layers of quartz cloth
5. Copper foil
6. Stainless steel cartridge
7. Stainless steel tube
8. Heat insulation
9. Graphite insert for ampoule 1
10. Copper insert for ampoule 3
11. Quartz tube

FIGURE 29-1.—Schematic diagram of ampoule containing ingot of Ge-Si solid solution.

## CRYSTAL-STUDY TECHNIQUES

Upon experiment completion, the first step (both in thermal simulation tests and during the mission) was an X-ray analysis of the cartridges to detect changes in their internal parts. Then, the cartridges were opened, and the surface, contour, and macrostructure of the crystals were visually inspected. Next, structural perfection of the crystals and the distribution of their components in longitudinal sections and cross sections were investigated.

For this purpose, the specimens were prepared and oriented by means of X-ray techniques so that their longitudinal and cross sections correspond to the planes that are appropriate for investigation; these are  $\{110\}$  and  $\{100\}$  planes. The preparation scheme for monocrystals grown in  $\langle 111 \rangle$  orientation is presented in figure 29-2, where I and III designate the series of samples that was subjected to X-ray-topographical, spectral, electrophysical, and metallographic analyses and where II designates the series of samples for investigation of electrophysical properties.

To determine Si content in crystals, photoluminescence spectra were analyzed (refs. 29-4 to 29-6). Because the size of the investigated area was  $\leq 0.11 \text{ mm}^2$ , a high topographic resolution was obtained. The error in Si-content determination was  $\leq 0.1 \text{ at.}\%$ . Specific resistance was measured by means of conventional four- and two-probe compensation techniques and by the spreading-resistance method (ref. 29-7).

The distribution of Sb along the crystals was determined by measurements of carrier concentration using the Hall-effect method. Samples for these measurements were cut out of the series II sections (fig. 29-2) in regions that were adjacent to the center of the crystal.

The crystal structure was investigated by means of the X-ray diffraction topography methods of Berg-Barrete-Newkirk and of Lang (ref. 29-8). For the Berg-Barrete-Newkirk method, a specific camera was used (ref. 29-9). This camera enables a crystal survey geometry capable of providing a linear resolution of  $3 \mu\text{m}$  and an angular resolution of  $5'$  for copper  $K\alpha$  radiation. The depth of the crystal measurement layer was from 5 to  $25 \mu\text{m}$ . For the Lang method, a standard

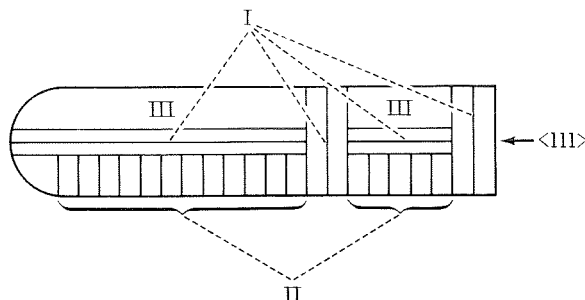


FIGURE 29-2.—Schematic of crystal-sample preparation.

camera with crystal scanning was used, and the linear resolution of molybdenum  $K\alpha$  radiation for this camera was  $5 \mu\text{m}$ .

The detection of dislocations by means of chemical etching permitted an evaluation of microscopic and macroscopic heterogeneities of Ge-Si solid solutions in the investigated crystal face. Chemical etching was performed using ferricyanide etchant (ref. 29-10) on the  $\{111\}$  or the  $\{110\}$  face, which had been previously polished in CP-4A solution. A metallographic microscope with  $90\times$  or  $120\times$  enlargement was used to study the density of dislocations and their distribution in the etched crystal face.

## RESULTS

### Ingot Macrostructure

For the purpose of studying the microgravity ( $\leq 0.006g$ ) effect on melting and crystallization of Ge-Si solid solution and comparing the results with those of other studies on identical crystals obtained under normal gravity conditions, four experiments on Earth and one in space were performed.

The postexperiment X-ray analysis of the flight cartridges revealed no damage to the internal parts of the cartridges; all the ampoules and crystals remained intact. A visual inspection of the crystals, after the cartridges had been opened, showed no macroirregularities, such as cracks, scratches, or cavities.

The results of a preliminary examination of the macrostructure of all crystals obtained under both normal gravity and microgravity conditions are summarized in table 29-I.

The photographs of space-grown crystals are shown in figure 29-3. From the contour of the crystals, a conclusion can be made that the ingot MA-150-16 melted completely and was measurably superheated. Both ends of the crystal had a typical spherical contour, which has never been observed in ground-based crystals. The entire surface of the ingot in cartridge MA-150-18 melted also, but the ingot was less superheated than MA-150-16. The ends of crystal MA-150-18 also had a spherical shape but with a smaller curvature radius compared to that of MA-150-16. An approximately 4-mm-long portion of ingot MA-150-17 appeared unmelted, supposedly an indication that this crystal preserved its seed. Subsequent etching of the crystals showed that MA-150-18 had a monocrystalline structure, whereas MA-150-16 and MA-150-17 were polycrystalline.

It should be noted that all space-grown crystals, both monocrystals and polycrystals, had a specific surface contour (fig. 29-4) never observed in ground-based crystals. Such a contour would indicate that wetting of the graphite-coated ampoule walls by the melt does not occur during crystallization under microgravity conditions.

Two groups of crystals, each containing two ingots, were selected for subsequent measurements. The basic data on these crystals are given in table 29-II.

TABLE 29-I.—Results of External Examination of Ge-Si Solid-Solution Crystals Obtained During Ground-Based Experiments and Under Microgravity Conditions

Cartridge no.	Melted portion of ingot, percent	Structure
<i>Ground-based experiment 1</i>		
MA-150-01	100	Polycrystalline
MA-150-02	100	Polycrystalline
MA-150-03	100	Polycrystalline
<i>Ground-based experiment 2</i>		
MA-150-04	--	--
MA-150-05	100	Polycrystalline
MA-150-06	100	Monocrystalline
<i>Ground-based experiment 3</i>		
MA-150-07	100	Monocrystalline
MA-150-08	100	Monocrystalline
MA-150-09	100	Polycrystalline
<i>Ground-based experiment 4</i>		
MA-150-10	(a)	(a)
MA-150-11	60	Monocrystalline
MA-150-12	80	Monocrystalline
<i>Space-grown</i>		
MA-150-16	100	Polycrystalline
MA-150-17	90	Polycrystalline
MA-150-18	100	Monocrystalline

<sup>a</sup>Was not melted; opened after dynamic tests.

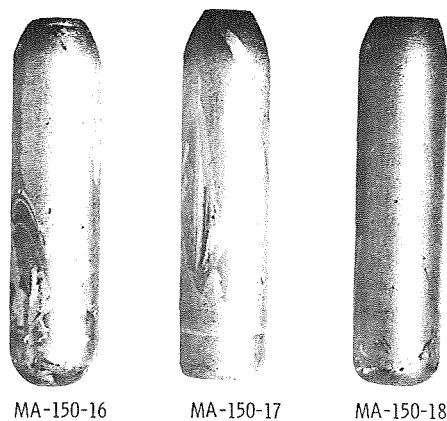


FIGURE 29-3.—Photographs of space-grown crystals.

### Monocrystals Obtained Without Seeding

*Silicon distribution.*—Silicon distribution in space-grown monocrystal MA-150-18 is shown in figure 29-5. Figure 29-5(a) shows Si distribution along one edge of the crystal; figure 29-5(b), along the other. As indicated in figure 29-5, a decreasing Si content with increasing distance from the point of original crystallization is the basic characteristic of impurities with  $K > 1$ . A considerable scattering of Si concentration was noticed in the initial region of the crystal. It is also evident from figure 29-5 that the Si distribution across the crystal diameter was nonuniform. This nonuniformity

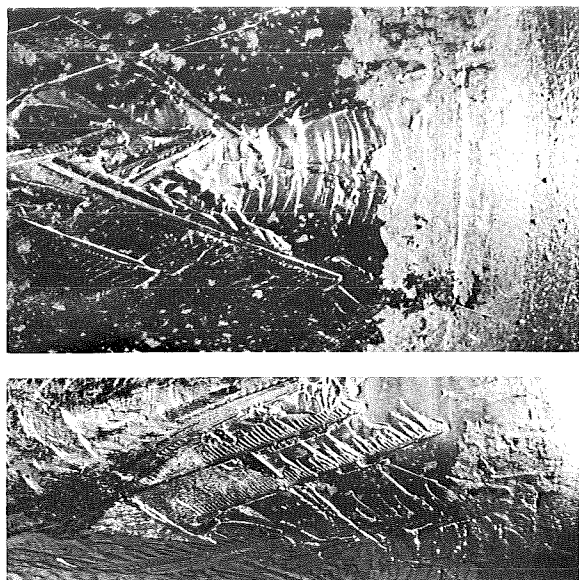


FIGURE 29.4.—Surface of space-grown crystal MA-150-17; areas near the seed.

across the crystal was decreasing toward the end of the crystal. Silicon distribution in the longitudinal section through the center of the crystal is not shown, but it was similar to that shown in figure 29-5(a). The Si distribution throughout the diameter of ground-based crystal MA-150-07, in regions located close to the onset and termination of crystallization, proved to be virtually uniform and, by its form, in agreement with the laws of normal directional crystallization (fig. 29-6).

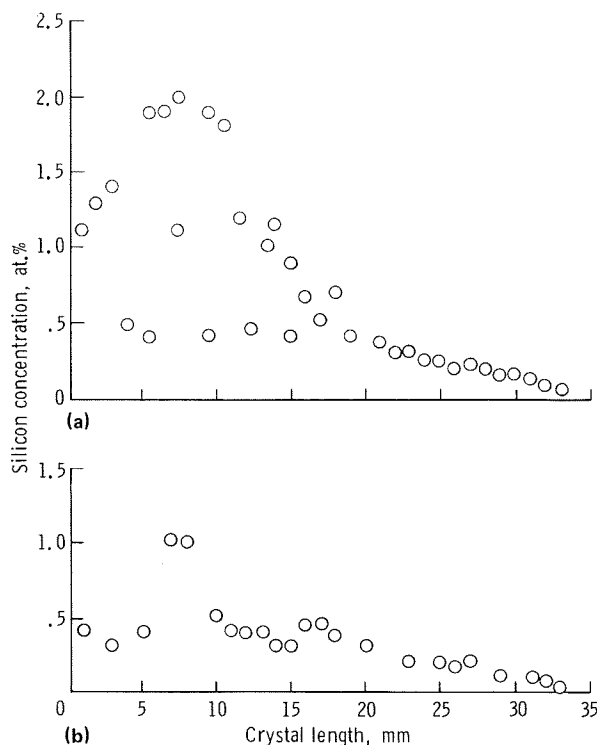


FIGURE 29.5.—Silicon distribution in space-grown monocrystal MA-150-18. (a) Left side of crystal. (b) Right side of crystal.

*Antimony distribution.*—The changes in specific resistance along space-grown crystal MA-150-18 and ground-based crystal MA-150-07, measured on series II samples (fig. 29-2), are shown in figure 29-7. The specific resistance of the space-grown

TABLE 29-II.—Basic Data on Crystals Selected for Measurements

Crystal no.	Growth conditions	Presence of seed	Orientation	Remarks
<i>Group I</i>				
MA-150-18	Space	No	$\langle 110 \rangle$	
MA-150-07	Ground	No	$\langle 100 \rangle$	
<i>Group II</i>				
MA-150-17	Space	Yes	$\langle 111 \rangle$	4-mm-long seed
MA-150-12	Ground	Yes	$\langle 111 \rangle$	7-mm-long seed

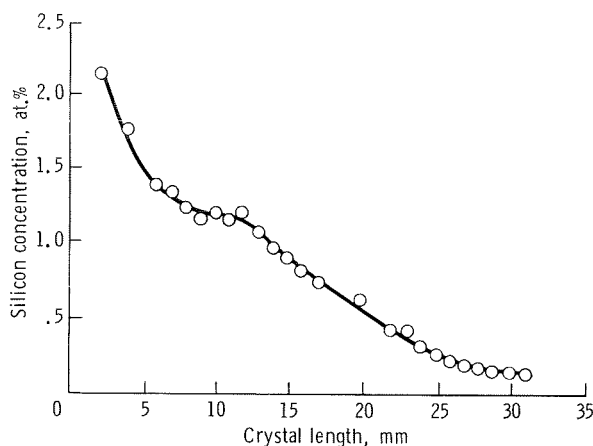


FIGURE 29-6.—Silicon distribution in ground-based monocystal MA-150-07.

crystal remained virtually constant along approximately 20 mm and decreased abruptly only at the end of the crystal, whereas the specific resistance of the ground-based crystal decreased monotonically from the beginning to the end of the crystal. Consequently, the nature of the changes indicates that Sb distribution was uniform throughout a large portion of crystal MA-150-18.

Antimony-content determination by measurements of carrier concentration performed using the Hall-effect method showed that, in crystal

MA-150-18, Sb was distributed uniformly (fig. 29-7), whereas, in the ground-based crystal MA-150-07, the concentration of Sb increased along the entire length of the crystal from the beginning to the end. It is interesting to note that such uniformity of Sb distribution, which occurred during Ge-Si solid-solution crystallization under microgravity conditions, has never been obtained under Earth conditions except when special techniques capable of providing uniform distribution of impurities in a crystal were used.

An analysis of charge-carrier-distribution curves showed that Sb concentration in the area with uniform Sb distribution in the space-grown crystal was approximately  $6 \times 10^{14}$  atoms/cm<sup>3</sup>, whereas it could have been equal to Sb concentration in the melt (i.e.,  $\approx 2 \times 10^{17}$  atoms/cm<sup>3</sup>) if ideal stationary conditions of growth and segregation, depending only on the diffusion in the melt near the crystallization front, were obtained in the microgravity environment. On the other hand, the value  $\approx 6 \times 10^{14}$  atoms/cm<sup>3</sup> is in good agreement with the value of the Sb-distribution coefficient if one accepts that this coefficient is equal to the coefficient of Sb distribution in Ge ( $3 \times 10^{-3}$ ) for a solid solution low in silicon and that the crystal grows from a melt with an Sb concentration of  $\approx 2 \times 10^{17}$  atoms/cm<sup>3</sup>, which is approximately the Sb concentration in the original ingot.

Changes in the Hall mobility of charge carriers along both space-grown crystals and ground-based crystals were similar (fig. 29-7). However, the distribution of Sb throughout the space-grown crystal was nonuniform, Sb concentration changing from one edge of the cross section to the other by two or three times. The nonuniformity was obvious from measurements of specific resistance of crystal MA-150-18 along its three parallel lines (going along the edges and the center of the crystal) and from the nature of spreading-resistance changes in the cross sections.

**Crystal structure.**—Monocrystals MA-150-07 and MA-150-18 had a dendritic structure as the crystal first solidified (figs. 29-8(a) and 29-8(b)); as crystallization continued, the dendritic structure changed to a block structure (figs. 29-9(a) and 29-9(b)). This transition is clearly indicated in photographs of the longitudinal section of the region of initial crystallization (figs. 29-10(a) and

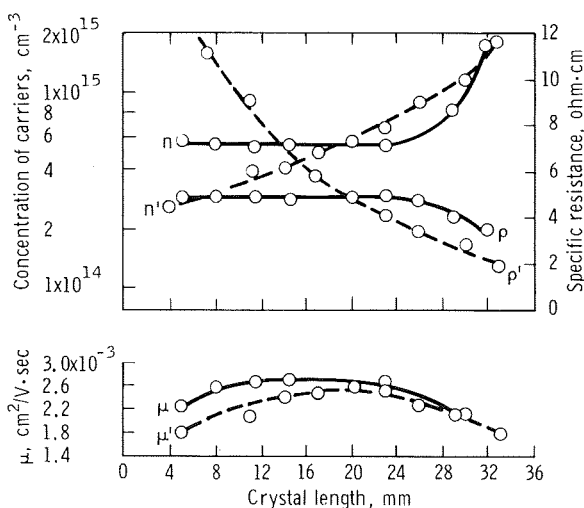
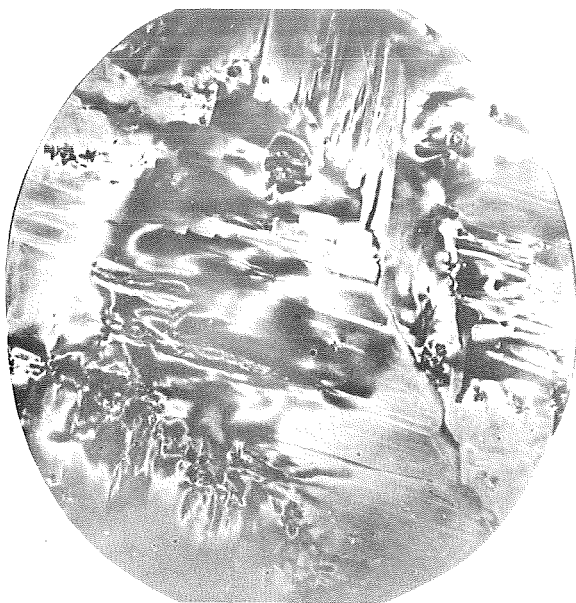


FIGURE 29-7.—Change in specific resistance, in concentration, and in mobility of charge carriers for crystals MA-150-18 ( $\rho$ ,  $n$ , and  $\mu$ , respectively) and MA-150-07 ( $\rho'$ ,  $n'$ , and  $\mu'$ , respectively).



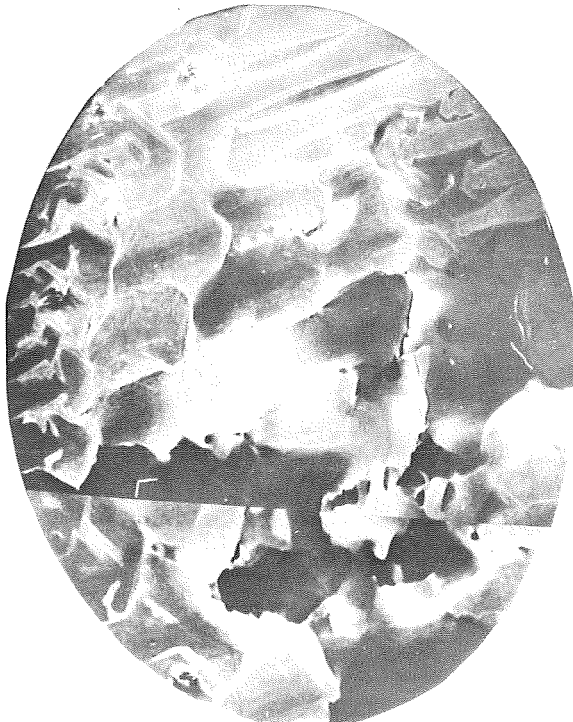
(a)



(a)



(b)



(b)

FIGURE 29-8.—X-ray topographs of cross sections of the initial regions of crystals MA-150-07 and MA-150-18 ( $8\times$ ). (a) MA-150-07 (ground based). (b) MA-150-18 (space grown).

FIGURE 29-9.—X-ray topographs of cross sections of the central regions of crystals MA-150-07 and MA-150-18 ( $8\times$ ). (a) MA-150-07 (ground based). (b) MA-150-18 (space grown).



29-10 (b)). Both space-grown and ground-based crystals had zones of local deformation centers, located mainly in the region of initial crystallization and concentrated near the lateral surface of the crystals (figs. 29-10(a) and 29-10(b)); whereas the central portion of the crystals was almost completely free of such defects. However, an extensive region of microstresses, caused probably by local deformation centers, was observed in the central part. Crystal MA-150-18 had a different number of local deformation centers near

different lateral surfaces. The reason for these defects could be the trapping of separate drops of the melt caused by irregular crystal growth, an indication of the presence of microheterogeneities in the composition of the crystal.

Blocks in different cross sections along the length of crystals differed in size and orientation. This difference can be attributed to microheterogeneities in the composition of the solid solution resulting from radial thermal gradients in the multipurpose furnace.



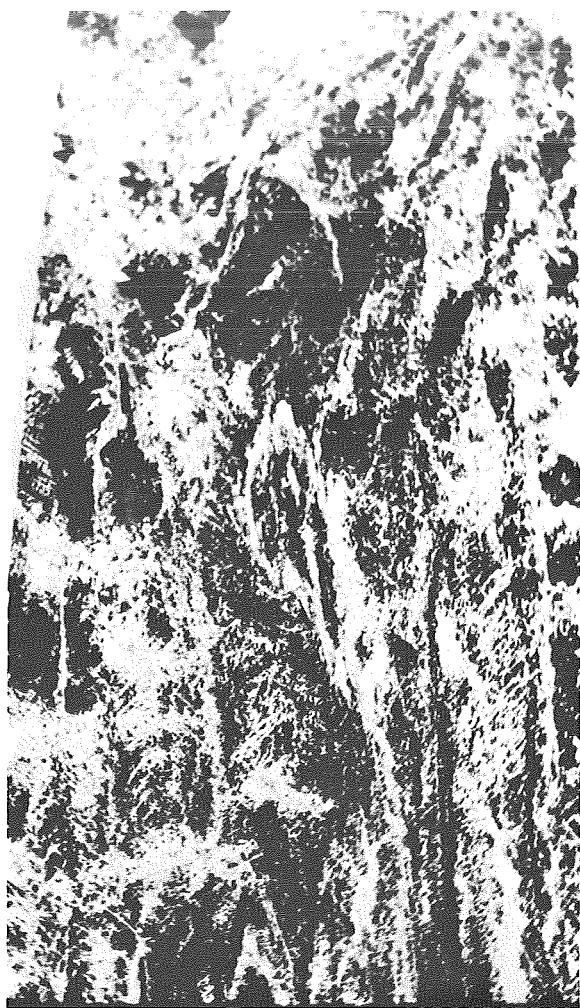
(a)



(b)

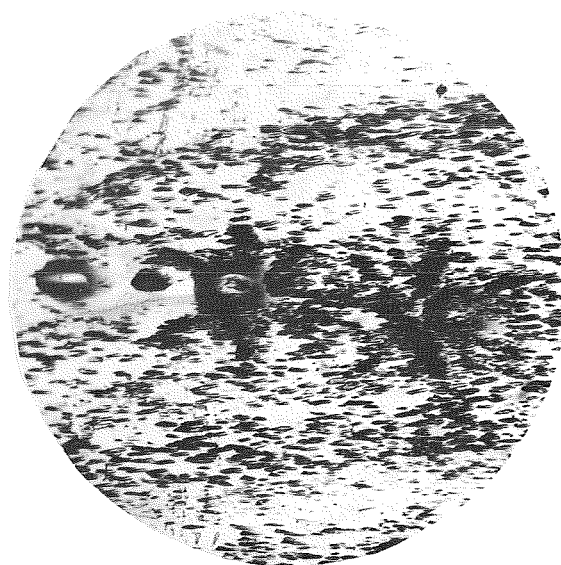
FIGURE 29-10.—X-ray topographs of the longitudinal sections of crystals MA-150-07 and MA-150-18 (10 $\times$ ). (a) MA-150-07 (ground based). (b) MA-150-18 (space grown).





(a)

Photomicrographs in figures 29-11 and 29-12 show the distribution of dislocations in  $\{110\}$  planes of the longitudinal section and cross section of monocrystal MA-150-18. A region with a high density of dislocations (i.e., a region that had the most heterogeneous Si distribution) was observed at the beginning of crystallization, where Si content was the highest. Distribution of dislocations throughout the longitudinal section of this portion of the crystal (fig. 29-11(a)) was in keeping with its structure, as shown by X-ray diffraction topography (fig. 29-10(b)). Local defects are clearly indicated in this region (fig. 29-11(b)). With an Si-content decrease, the density of dislocations diminished, and their distribution



(b)

FIGURE 29-11.—Distribution of dislocations and centers of local deformation in  $\{110\}$  plane of the longitudinal section of crystal MA-150-18. (a) Distribution of dislocations. (b) Centers of local deformation.

throughout the longitudinal section became more uniform.

A cellular structure, which indicates the presence of constitutional supercooling at the front of crystallization, is clearly indicated in the cross section of the central part of the crystal (fig. 29-12). (The X-ray topograph is given in fig. 29-9(b)).

### Crystals Obtained With Seeding

*Silicon distribution.*—The change in Si content throughout ground-based crystal MA-150-12, which had an approximately 7-mm-long seed, is shown in figure 29-13. The curve is composed of several segments that characterize the recrystallization process. The initial segment of the Si-distribution curve corresponds to the approximately 7-mm-long unmelted part of the ingot, which served as a seed for crystallization. Silicon concentration in this region was constant and equaled 0.7 at.%. At the interface of melting and subsequent crystallization, Si concentration

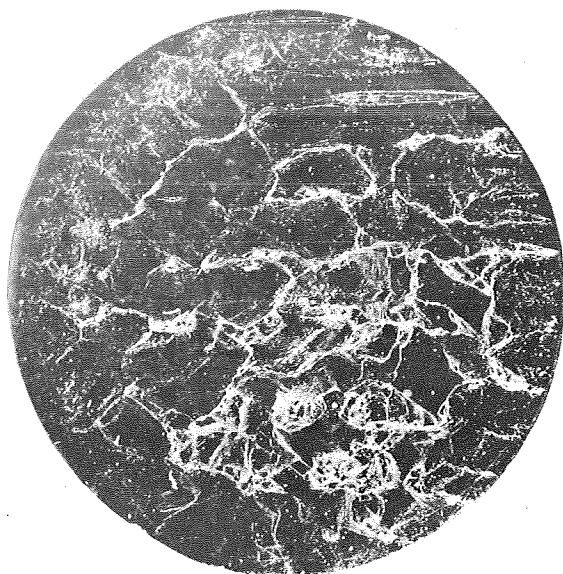


FIGURE 29-12.—Distribution of dislocations in  $\{110\}$  plane of the cross section of crystal MA-150-18.

abruptly increased to a value of 1.6 at.%. In the remaining part of the crystal, the concentration of Si decreased gradually as the crystallization of the melt was in progress. In the ground-based experiment, the effective coefficient of Si distribution in Ge during crystallization was evaluated from the curve in figure 29-13. The value of 2.3 agrees with published data on values of  $K$  for nonequilibrium conditions of crystallization. The Si distribution throughout the cross sections of the crystal was practically uniform, varying by no more than 20 percent.

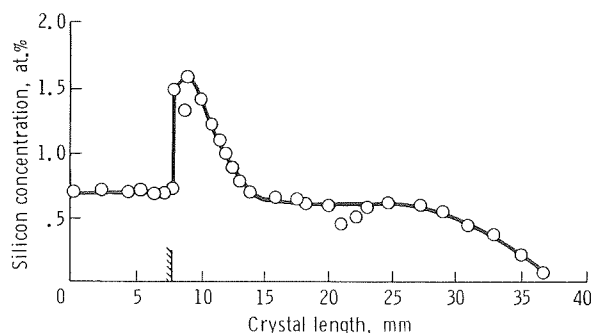


FIGURE 29-13.—Silicon distribution in ground-based crystal MA-150-12.

Silicon distribution in the region of the seed of space-grown crystal MA-150-17 is unusual (fig. 29-14). An increase in Si concentration is observed in two regions, in that of the seed and in that located at some distance from the crystallization boundary. In the section between the two regions, approximately 2 mm long, Si concentration could not be estimated. The anomalous change of composition in the region of the seed can be attributed to regeneration of the seed; namely, to melting of localized areas.

Silicon distribution throughout the cross section of the recrystallized region, which had a polycrystalline structure, was identical to that of the space-grown monocrystal MA-150-18. A change in Si concentration from one edge toward the other was observed in both crystals.

*Antimony distribution.*—Changes in specific resistance and charge-carrier concentration throughout the length of crystals grown with seeding, both under microgravity (MA-150-17) and Earth (MA-150-12) conditions, are shown in figure 29-15. The curves for specific resistance and carrier concentration in the crystals were of the same type as those for monocrystals grown without seeding, except for the region of the seed. The seed region of crystal MA-150-12 had the same specific resistance and carrier concentration as the original ingot. The space-grown crystal MA-150-17 had the same specific resistance value as the original ingot only in the end face that was adjacent to the graphite spacer and was located in

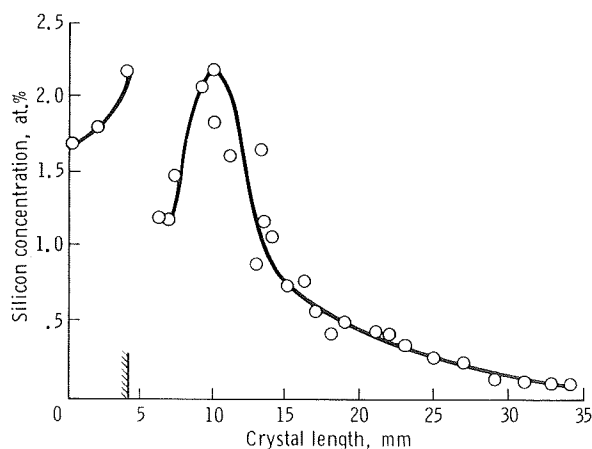


FIGURE 29-14.—Silicon distribution in space-grown crystal MA-150-17.

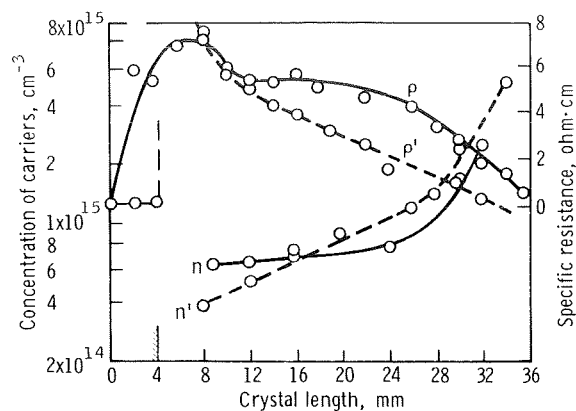


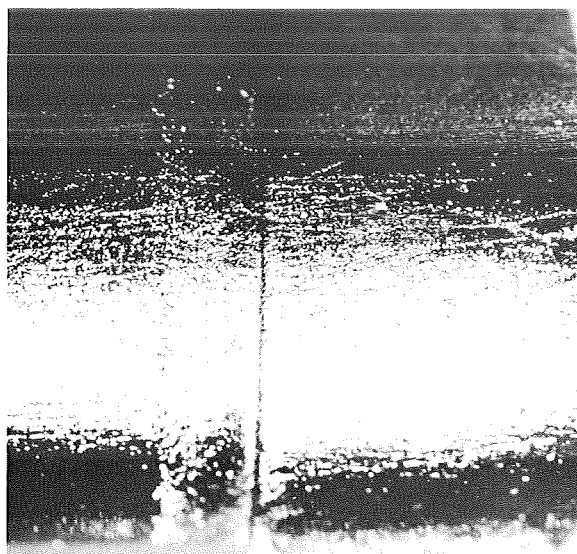
FIGURE 29-15.—Changes in specific resistance and charge-carrier concentration for crystals MA-150-17 ( $\rho$  and  $n$ , respectively) and MA-150-12 ( $\rho'$  and  $n'$ , respectively).

the cold end of the furnace. Strictly speaking, it was only this zone that served as a seed. After that zone, the specific resistance increased abruptly in a 4-mm-long region with an outward contour of a seed. The increase in specific resistance and the nature of Si distribution in this region indicate that, although the seed preserved its original contour, it probably underwent partial melting and recrystallization during the experiment.

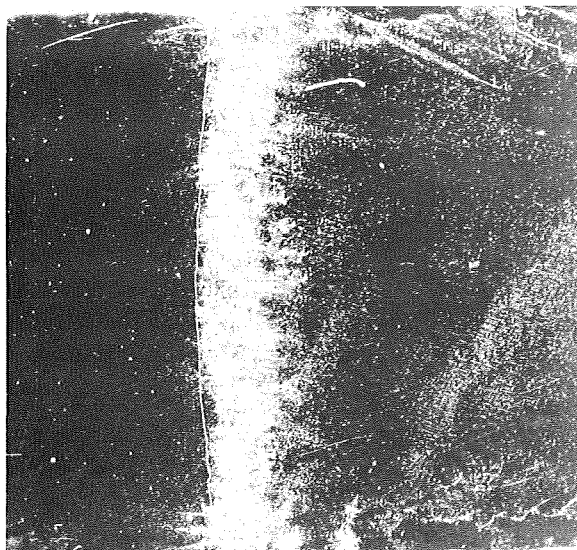
*Crystal structure.*—The most interesting part of the investigation of the structure of space-grown crystal MA-150-17 was the study of the structure of its seed in comparison with the structure of the seed and the region of original recrystallization in ground-based ingot MA-150-12.

Figure 29-16(a) shows the outward appearance of the portion of crystal MA-150-12 that includes the seed, the boundary of melting, and the recrystallized part of the crystal, the diameter of which was somewhat larger than that of the seed. The distribution of dislocations in the  $\{110\}$  plane is shown in figure 29-16(b), and the X-ray topograph of the seeding boundary of this crystal is shown in figure 29-17.

The crystallization interface had a concave (in the direction of the seed) shape and a steplike structure. The region near the crystallization interface had a high density of dislocations and numerous centers of local deformation. The X-ray topography revealed a laminar structure of the seed that was not observed in Ge-Si solid-solution



(a)



(b)

FIGURE 29-16.—Region of the seeding boundary of crystal MA-150-12. (a) Outward appearance. (b) Distribution of dislocations.

monocrystals obtained under microgravity conditions.

The outward appearance of the end of crystal MA-150-17 is shown in figure 29-18(a). The figure shows a sharp boundary line between the seed and the recrystallized portion, which, similar to that of crystal MA-150-12, has a slightly enlarged

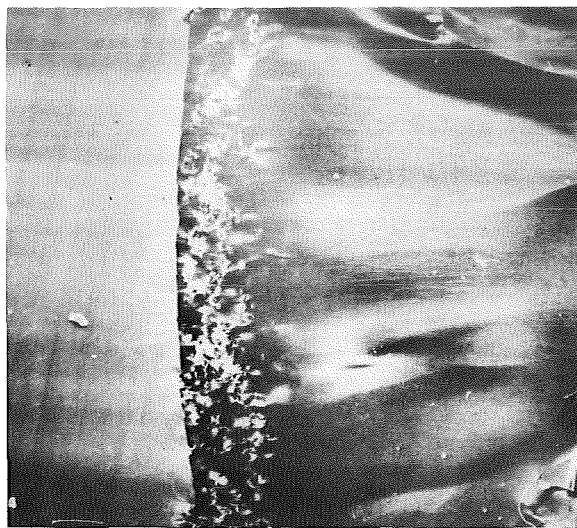
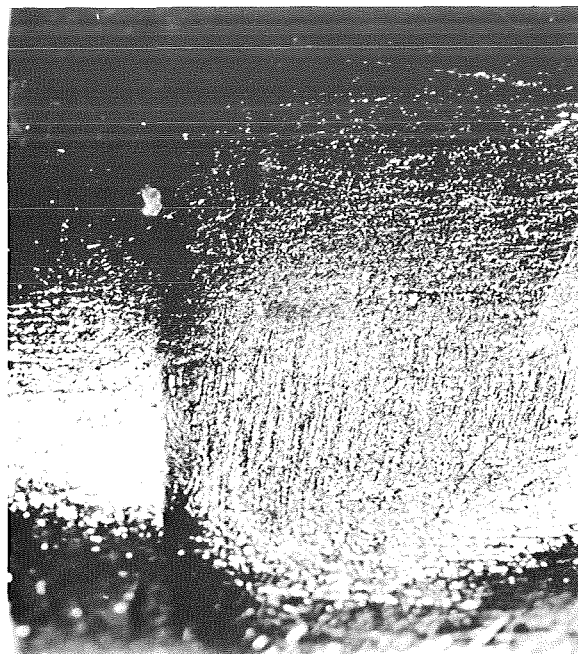


FIGURE 29-17.—X-ray topograph of the seeding boundary region of crystal MA-150-12 ( $9\times$ ).

diameter. However, the macrostructure and the X-ray topograph of this region (figs. 29-18(b) and 29-19) are fundamentally different from those of the ground-based crystal (figs. 29-16(b) and 29-17). The region of the seed in crystal MA-150-17 is of a heterogeneous structure characterized by centers of local deformation located close to each other. Outside this region, local deformation centers are not observed everywhere but in single groups. Furthermore, formation of a block structure with strong microstresses and macrostresses occurred, and the monocrystal changed to a polycrystal.

A detailed investigation of the seed indicated that portions of its surface, which were adjacent to the graphite spacer, began melting in hexagonal patterns (fig. 29-20(a)). The center of the seed surface was distorted. An X-ray topograph of the surface of a sample taken from the opposite end of the seed (fig. 29-20(b)) indicated that, following the hexagon corners, other portions of the crystal along the hexagon sides started melting; but the melting occurred locally, in isolated areas only. The spreading of the melting throughout a section of the crystal is shown in figure 29-20(c), which is a photograph of that portion of the seed adjacent to the region shown in figure 29-19. It should be noted that the radial spreading of the melting regions was unsymmetrical. Considering that



(a)



(b)

FIGURE 29-18.—Region of the seeding boundary of crystal MA-150-17. (a) Outward appearance. (b) Distribution of dislocations.





FIGURE 29-19.—X-ray topograph of the seeding boundary region of crystal MA-150-17 ( $9\times$ ).



(a)



(b)



(c)

FIGURE 29-20.—X-ray topographs of space-grown crystal MA-150-17 ( $8\times$ ). (a) Seed surface adjacent to graphite spacer. (b) Opposite side of specimen shown in figure 29-20(a); thickness of specimen,  $\approx 1$  mm. (c) Seed surface adjacent to the region of crystal MA-150-17 shown in figure 29-19.

microheterogeneities of Si distribution in the layers of the original ingot were  $\approx 0.1$  at.%, it was possible to determine the thermal gradient of the seed region in the longitudinal direction and across the crystal by the size of the regenerated seed. The gradient was approximately 1 K/cm.

Thus, crystal MA-150-17, obtained under microgravity conditions, had no recrystallization boundary. Recrystallization started gradually (2 to 3 mm behind the line visible on the outward surface) and developed consecutively both along the crystal growth and in the radial direction.

### CONCLUSIONS

The investigation of Ge-Si solid-solution crystals obtained under microgravity conditions in the ASTP multipurpose furnace experiment gave the following results.

1. Under microgravity conditions, monocrystals of Sb-doped Ge-Si solid solution were obtained with and without seeding by means of directional crystallization in ampoules.

2. The analysis of Si and Sb distribution in crystals and of their structures has resulted in a series of conclusions concerning melting and crystallization under microgravity conditions.

3. During melting and crystallization under microgravity conditions, convective mixing is either absent or sufficiently negligible to have no effect on the process. The following facts support this conclusion.

- a. Laminar distribution of crystal components was absent.

- b. Cellular structure, which indicates the presence of constitutional supercooling at the crystallization front, was observed.

- c. Regeneration of the seed occurred in the microgravity environment only (in the absence of mixing); complete melting without regeneration of the seed would have occurred under Earth conditions.

4. Crystallization in the microgravity environment did not occur under ideal stationary growth and segregation conditions, which could have been expected considering that directional crystallization occurs in the absence of convective mixing.

5. Crystallization under microgravity conditions revealed the heterogeneous nature of Si and Sb distribution in the cross sections of crystals. The presence of the radial thermal gradient in the multipurpose furnace could be one of the reasons for such Si and Sb distribution.

6. The structure of space-grown crystals correlates with the nature of heterogeneities of Si and Sb distribution in crystals.

7. The type of surface morphology and the contour observed in space-grown crystals have never been observed in ground-based crystals and indicate the absence of wetting of the graphite-coated walls of the ampoule by the melt during melting and crystallization.

8. All original ingots melted completely, an indication that the temperature distribution along the ampoule containing Ge-Si solid solution did not satisfy the optimal conditions planned for the experiment. In the area where the cold end of the ampoule was located and where a part of the ingot had to stay unmelted to serve as a seed, the temperature was 1211 K (938° C) and higher.

9. The regeneration of the seed proves that the thermal gradient in the region of the seed was not higher than 1 K/cm, causing local melting of the seed, a change in its structure, and the formation of a polycrystalline structure during subsequent crystallization. Such thermal conditions were unfavorable for the growth of monocrystals.

### REFERENCES

- 29-1. Tiller, W. A.; Jackson, K. A.; Rutter, J. W.; and Chalmers, B.: The Redistribution of Solid Atoms During the Solidification of Metals. *Acta Met.*, vol. 1, no. 4, 1953, pp. 428-437.
- 29-2. Lodiz, R.; and Parker, R.: Rost monokristallov. (Monocrystal Growth.) MIR Press (Moscow), 1974, pp. 522-524.
- 29-3. Belokurova, I. N.; Kekua, M. G.; Petrov, D. A.; and Suchkova, A. D.: Growth of Single Crystals of Germanium-Silicon Alloys. *Izvest. Akad. Nauk S.S.S.R., Otdel. Tekh. Nauk, Met. i Toplivo*, vol. 1, 1959, pp. 9-12.

- 29-4. Gross, E. F.; Sokolov, N. S.; and Titkov, A. N.: Zero-Phonon Radiative Annihilation of Indirect Excitons in Germanium Crystals with Isoelectronic Substitutional Impurities. *Soviet Phys. - Solid State*, vol. 14, no. 7, 1973, pp. 1732-1734.
- 29-5. Pokrovskii, Ya. E.; Svistunova, K. I.; and Alkeev, N. V.: Effect of Band Structure on the Recombination Mechanism of Condensed Charge Carriers in Germanium, Silicon, and Their Alloys. *Soviet Phys. - Solid State*, vol. 14, no. 11, 1973, pp. 2805-2807.
- 29-6. Safarov, V. I.; and Titkov, A. N.: Indirect Phonon-Free Optical Transitions in Germanium-Silicon Solid Solutions. *Soviet Phys. - Solid State*, vol. 14, no. 2, 1972, pp. 380-383.
- 29-7. Gupta, D. C.; and Chan, J. Y.: A Semiautomatic Spreading Resistance Probe. *Rev. Sci. Instrum.*, vol. 41, no. 2, Feb. 1970, pp. 176-179.
- 29-8. Pryamyie metody issledovaniya defektov v kristallakh. (Direct Methods of Crystal-Defect Studies.) MIR Press (Moscow), 1965, pp. 7-23 and 205-222.
- 29-9. Gross, Ya. G.; Pokornyi, E. G.; et al.: X-Ray Camera for Investigating Defects in Crystals. *Instrum. & Exp. Tech.*, vol. 15, no. 4, 1972, pp. 1246-1248.
- 29-10. Travleniye poluprovodnikov. (Etching of Semiconductors.) MIR Press (Moscow), 1965, pp. 184-187.





# 30. Crystal Growth

## Experiment MA-028

M. D. Lind<sup>a</sup>

### ABSTRACT

The Crystal Growth Experiment assessed a novel process for growing single crystals of insoluble substances by allowing two or more reactant solutions to diffuse toward each other through a region of pure solvent in zero-g. The experiment was entirely successful and yielded crystals of about the expected size, quality, and number.

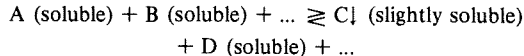
### INTRODUCTION

The objective of this experiment was to investigate the growth of single crystals of insoluble substances by a process in which two or more reactant solutions are allowed to diffuse toward each other through a region of pure solvent. This is a novel method of crystal growth conceived for orbital space flights to take advantage of the absence of gravity-driven convection that, on Earth, predominates over diffusion as a mechanism of material transport. The experiment performed during the Apollo-Soyuz Test Project (ASTP) mission was designed both as a first attempt to determine the feasibility of the method and as a starting point for further development.

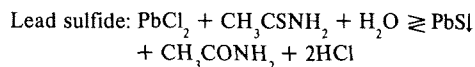
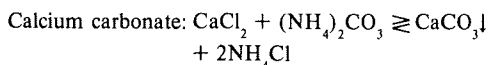
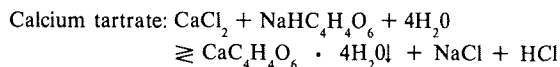
### BASIC THEORY

Because the method of crystal growth used for this experiment is closely related to gel methods

of crystal growth, it is appropriate to present a brief review of gel methods. Gel methods are particularly applicable to the growth of crystals that have very small solubility in the solvent (usually water) that is used. In these methods, two or more reactant solutions, separated by a gel, diffuse slowly together and react according to a chemical equation of the following type as the crystal grows:



The three reactions chosen for experiments on the ASTP flight are examples of this type reaction.



Typical experimental arrangements for gel methods are shown schematically in figure 30-1. In the U-tube arrangement, the crystals normally grow within the gel or at the interfaces with the reactant solutions. In the second arrangement, the crystals can grow in the pure solvent at the center.

The primary functions of the gel are suppression of gravity-driven convection and support of the growing crystal. Diffusion is the predominant mechanism for mixing of the reactant solutions. The crystal grows in a cell of solution, is exposed to the solution on all sides, and has no contact

<sup>a</sup>Rockwell International Science Center; Principal Investigator.

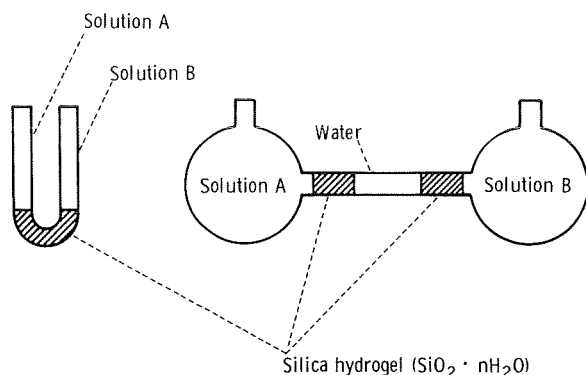


FIGURE 30-1.—Typical experimental arrangements for gel methods of crystal growth.

with container surfaces except those of the flexible gel structure.

The hypothesis for this experiment was based on the assumption that, in an environment of sufficiently low gravity, convection and sedimentation become negligible. Therefore, the gel is not needed for suppressing these processes and can be replaced by a region of pure solvent. Diffusion becomes the predominant mixing mechanism even with no gel present.

The advantage of allowing diffusion to be the predominant mechanism for material transport, whether in gel processes on Earth or in low-gravity processes in space flights, is that the rate of transport can be controlled by varying the concentrations of the diffusing substances and the length of the diffusion path. This is important because the rate of material transport must be compatible with the rate of crystal growth, which may also depend on other kinetic or heat-transfer factors. A diffusion-controlled process can result in better crystal quality through better prediction and control of the parameters involved. It can also result in a better understanding of crystal growth processes through simplification of theoretical treatments and a clearer comparison of the experiment with the theory.

The gel methods of crystal growth, like most aqueous solution growth methods, are advantageous because crystal growth occurs at ambient (room or spacecraft) temperature. This minimizes problems of thermally or mechanically induced strain, phase transformations, volatility of components, contamination by the container, etc., often

inherent in high-temperature growth methods. However, gel methods also have certain disadvantages, including excessive nucleation that results in small crystal sizes, contamination of the crystals by gel constituents or impurities in the gel, and gel instability. The method used for this experiment is expected to overcome all these disadvantages while retaining the advantages.

Much research has been done concerning gel methods of crystal growth. This research has provided much of the background for the design of the ASTP experiment. Information particularly relevant to this experiment can be found in references 30-1 to 30-12. The three crystals (calcium tartrate, calcium carbonate, and lead sulfide) investigated in the ASTP experiments were chosen for the following reasons:

1. They are easy to grow in gel systems.
2. There has been much investigation of their growth in gel systems so that growth conditions are well known, and terrestrial results are readily available for comparison with ASTP results.
3. Calcium tartrate has been an especially important subject for investigations of gel growth mechanisms.
4. Calcium carbonate and lead sulfide have technological importance.
5. Calcium carbonate is a typical example of crystals that are contaminated by gel constituents and therefore can be improved by growth without the gel.

The experimental conditions for the ASTP experiments were based on results of previous gel growth experiments. It was assumed that the diffusion and crystal growth processes would not be very different if the gel was replaced by a region of pure solvent. Because typical gels are 95 to 96 percent solvent and only 4 to 5 percent solid, this assumption was reasonable and appears to have been validated by the ASTP results. To simplify the ASTP experimental apparatus, the usual requirement for precise temperature control was eliminated by choosing crystals that can be grown at ambient temperature without precise temperature control. The other important experimental parameters are selection and concentrations of reactant solutions, reactor dimensions, and hydrogen-ion concentration (pH) of the growth medium (water). The values of these

TABLE 30-I.—Reactant Solutions

Reactor serial number	Compartment B		Compartment A		Compartment C	
	Reactant	Length, cm	Reactant	Length, cm	Reactant	Length, cm
005	0.1M $\text{CH}_3\text{CSNH}_2$	3.30	$\text{H}_2\text{O}$ adjusted to pH = 1.0 with HCl	5.08	Saturated $\text{PbCl}_2$	3.30
006	0.5M $\text{CaCl}_2$	3.30	$\text{H}_2\text{O}$	5.08	0.45M $\text{NaHC}_4\text{H}_4\text{O}_6$	
007	0.5M $\text{CaCl}_2$	3.30	$\text{H}_2\text{O}$	5.08	0.5M $(\text{NH}_4)_2\text{CO}_3$	3.30
008	0.1M $\text{CH}_3\text{CSNH}_2$	3.30	$\text{H}_2\text{O}$ adjusted to pH = 0.5 with HCl	5.08	Saturated $\text{PbCl}_2$	3.30
012	0.5M $\text{CaCl}_2$	4.19	$\text{H}_2\text{O}$	4.19	0.5M $(\text{NH}_4)_2\text{CO}_3$	3.30
013	0.5M $\text{CaCl}_2$	4.19	$\text{H}_2\text{O}$	4.19	0.45M $\text{NaHC}_4\text{H}_4\text{O}_6$	3.30

parameters used in the ASTP experiments are summarized in table 30-I.

As previously implied, much of the behavior of these crystal growth systems could be calculated from known laws of thermodynamics, diffusion, and heat transfer. In general, the required parameters, including equilibrium solubilities as functions of temperature and pH, heats and entropies of fusion, specific heats, diffusion coefficients, thermal conductivity coefficients, etc., were reasonably well known or could be determined in experiments on Earth. However, relationships between supersaturation and nucleation are more difficult to understand, and incomplete knowledge in this area precludes a complete prediction of the behavior of the crystal growth systems chosen for study. Consequently, it was necessary to estimate the best growth conditions on the basis of results of experimental gel growth studies.

## EQUIPMENT

The experimental apparatus consisted of six specially designed and fabricated reactors (fig. 30-2). The entire set of flight hardware is illustrated in figure 30-3. Each reactor had three compartments that were separated by valves operated by the knobs at each end. Each compartment had a separate filling port. The compartments varied in length, as indicated in table 30-I. The reactor covers were flat and transparent to permit photographing the progress of diffusion and

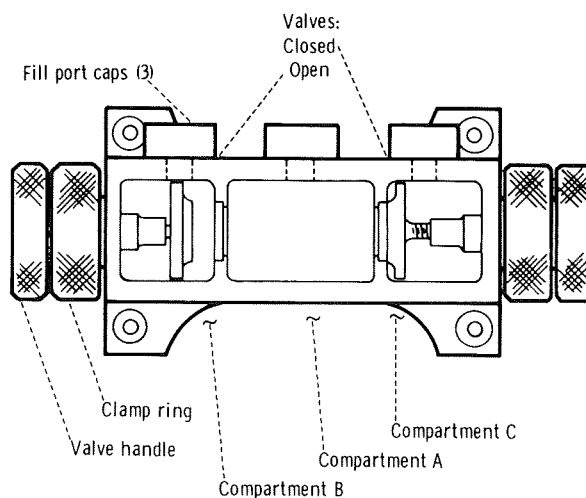


FIGURE 30-2.—Schematic diagram of a reactor.

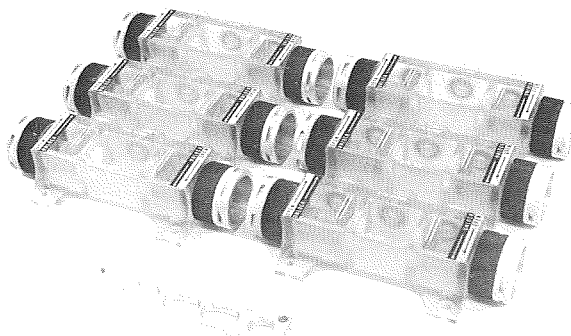


FIGURE 30-3.—Flight hardware.

crystal growth. The reactors were constructed of Lexan polycarbonate resin with silicone rubber gaskets and seals, porous high-density polyethylene diaphragms between the compartments, and aluminum knobs.

Before delivery of the hardware to the launch facility, the reactors (with the intercompartment valves in the closed positions) were filled with the various solutions. The reactant solutions were placed in the outer compartments of each reactor, and the central compartment was filled with water.

The six reactors were mounted in the U-4 locker in the command module. They were accessible in this location, yet out of the way of other operations.

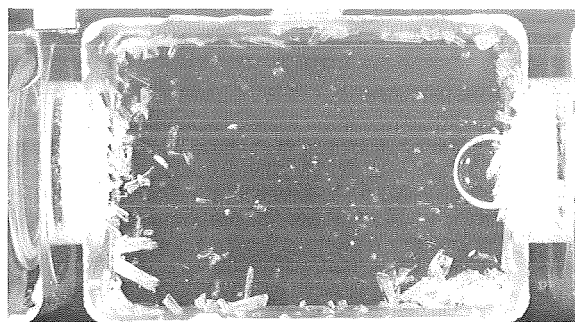
After the joint phase of the flight, at approximately 109 hours ground elapsed time (GET), a crewman activated the experiments by opening the intercompartment valves to allow the reactants to begin diffusing toward the center. A wrench (fig. 30-3) that was included as a contingency measure was not required.

Beginning at the time of activation and at approximately 12-hour intervals for the remainder (116 hours) of the flight, a crewman took color photographs of the six reactors with the Nikon 35-mm camera used for various other photography. A framing device designed and fabricated at the NASA Lyndon B. Johnson Space Center was used to place the camera properly.

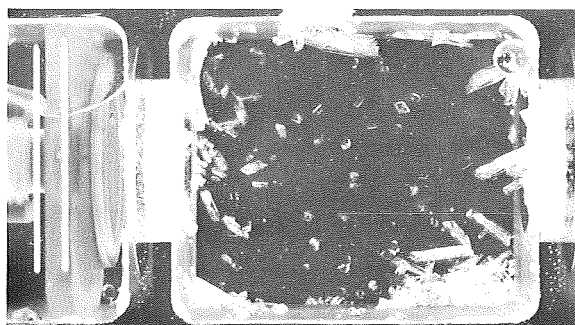
Throughout the flight, the experiment progressed as planned with no problems or anomalies. The performance of the reactors was most satisfactory. There was no evidence of leakage through the intercompartment valves before activation of the experiment, and the valves were opened easily at the proper time to begin the experiment. Photographs of the reactors taken during the flight are of excellent quality and verify that the framing device, camera settings, and lighting were entirely satisfactory.

## DISCUSSION AND RESULTS

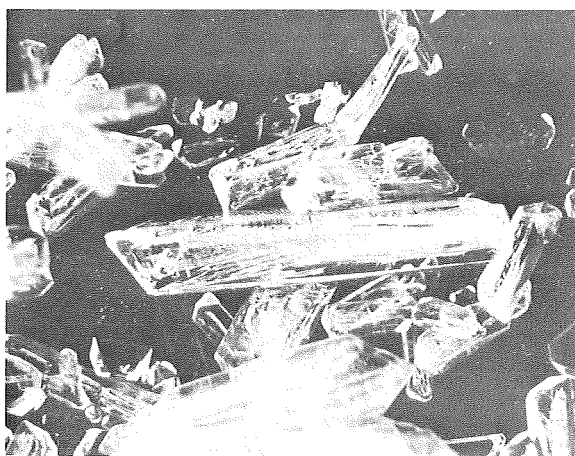
Crystals of about the expected size, quality, and number formed in all six reactors. Experiment results are shown in figures 30-4 to 30-6, which are



(a)



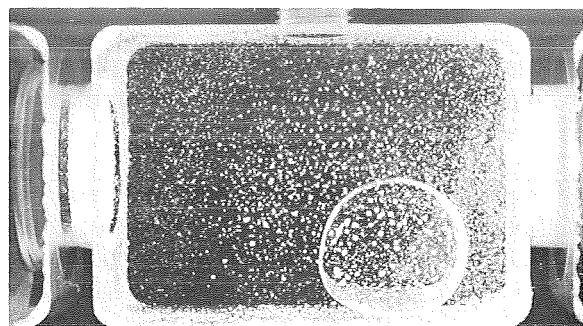
(b)



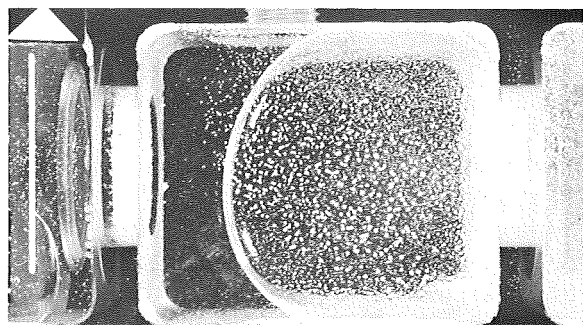
(c)

FIGURE 30-4.—Calcium tartrate. (a) Serial number 006. (b) Serial number 013. (c) Magnified view of calcium tartrate crystals.

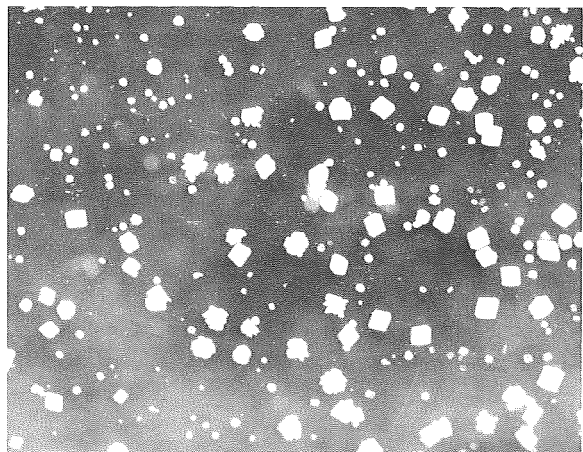
photographs taken after return of the reactors to the laboratory. Upon receipt of the reactors and before opening them, the reactors and their contents were examined visually through the reactor faces with a binocular polarizing microscope of



(a)



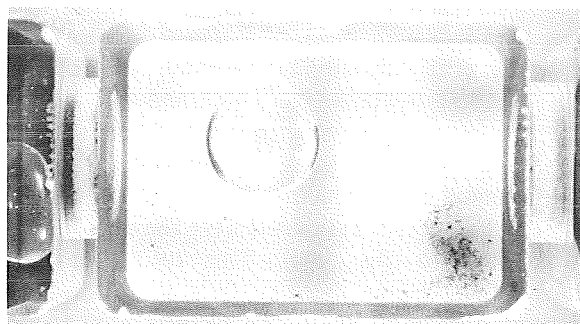
(b)



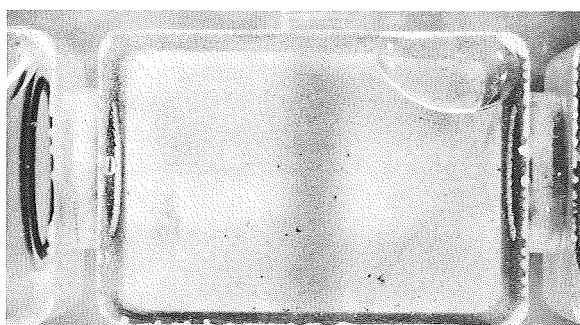
(c)

FIGURE 30-5.—Calcium carbonate. (a) Serial number 007. (b) Serial number 012. (c) Magnified view of calcium carbonate crystals.

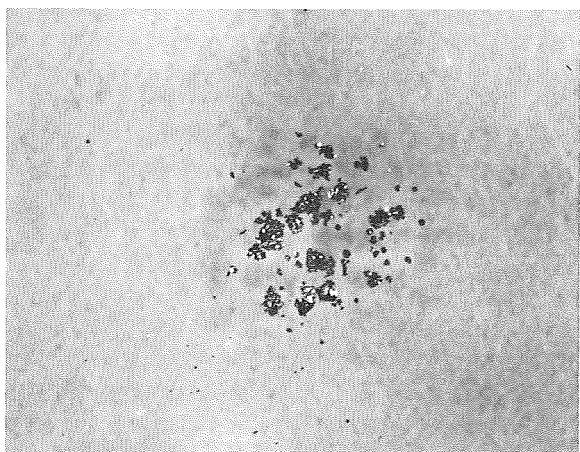
40 $\times$  magnification. The reactors were photographed with 1.5 $\times$  magnification, and representative crystals were photographed through the reactor faces with 10 $\times$  magnification. Following this procedure, representative crystals were removed



(a)



(b)



(c)

FIGURE 30-6.—Lead sulfide. (a) Serial number 005. (b) Serial number 008. (c) Magnified view of lead sulfide crystals.

through the center fill ports for further examination. The identity of each kind of crystal was confirmed by single crystal X-ray diffraction data obtained with Buerger precession and Gandolfi cameras. As expected, the X-ray diffraction data

are identical with those of Earth-grown crystals. For several calcium tartrate crystals, X-ray diffraction topographs were obtained with a Lang camera for comparison with those of Earth-grown crystals. To date, these comparisons indicate about equal crystal quality.

The best crystals obtained were the calcium tartrate crystals (fig. 30-4). This result was not surprising because these crystals are among the easiest to grow by gel methods. Both calcium tartrate reactors produced numerous prismatic crystals with maximum dimensions as large as 2 mm and platelike crystals as long as 5 mm; these crystals have good face development, are very clear, and appear flawless when viewed in the microscope both with unpolarized light and with light transmitted through crossed polarizers. The quality of these crystals is confirmed by X-ray diffraction topographs. There were also a few platelike crystals as long as 10 mm but of somewhat poorer quality. The absence of finely divided precipitate indicated that mixing of the reactant solutions and crystal growth were complete by the time of spacecraft reentry, which was the desired result. Contrary to the experience with gel experiments, the platelike crystals were more numerous and larger than the prismatic crystals. Platelike crystals have been obtained occasionally in gel experiments, but the prismatic habit is more usual. The reasons for this variation in habit and its significance are unknown at this time.

Each of the two calcium carbonate reactors produced numerous well-formed, clear rhombohedral crystals as long as 0.5 mm on an edge (fig. 30-5). These crystals are very similar in appearance to Earth-grown calcium carbonate crystals, both synthetic and natural. Although small, they are large enough to exhibit birefringence. Again, no finely divided precipitate resulted, which indicates that, as desired, mixing of the reactant solutions and crystal growth were complete by the time of spacecraft reentry. Most of the calcium carbonate crystals adhered to the reactor, which implies that, for the calcium carbonate growth, the polycarbonate material is not the best surface for the interior walls of the reactors.

The two lead sulfide experiments were less successful, but both resulted in the production of discrete single crystals with dimensions as large as

0.1 mm (fig. 30-6). In this case, the mixing and reaction were not complete at the time of reentry. A fine precipitate was observed that continued to increase even after return of the reactors to the laboratory. This result indicates that a longer time is needed for successful growth of larger lead sulfide crystals under the conditions used. An alternative way of obtaining better results is to use a somewhat higher temperature to increase the solubility of one of the reactants (lead chloride).

The calcium carbonate crystals are easily visible in the series of photographs taken at 170 hours GET (61 hours after activation of the experiment) and are increasingly visible in subsequent photographs. Selected photographs are shown in figure 30-7. A small number of calcium tartrate crystals also appear in these photographs, but less clearly. The photographs indicate that most of the calcium tartrate crystals must have grown after the last series of photographs was taken. The flight continued for more than 6 hours after the last series of photographs; therefore, it is quite possible that substantial growth occurred after that time. It is very likely that the calcium tartrate crystal growth was complete before reentry, because virtually all the calcium tartrate crystals were free of the reactor walls as if they were grown in low gravity. Repeated experiments in normal gravity have shown that rapid mixing in one-g will result in a much smaller particle size and that the crystals thus formed adhere to the bottom of the reactor. It is reasonable to assume that reactant concentrations were just reaching the values required for calcium tartrate growth at the end of the flight. It was also observed that some additional calcium carbonate crystals grew after the last series of photographs was taken.

The photographs also provide a record of the movement of air bubbles in the reactors during the flight. The air bubbles migrated from the expansion spaces in the fill-port caps during handling of the reactors before flight. It would have been preferable to avoid the presence of the bubbles, but they apparently did not have any significant negative effect on the experiment. In fact, their presence allowed the beneficial effect of a rough evaluation of the accelerations experienced by the reactors. It is interesting to observe that air bubbles in the two calcium tartrate reactors re-



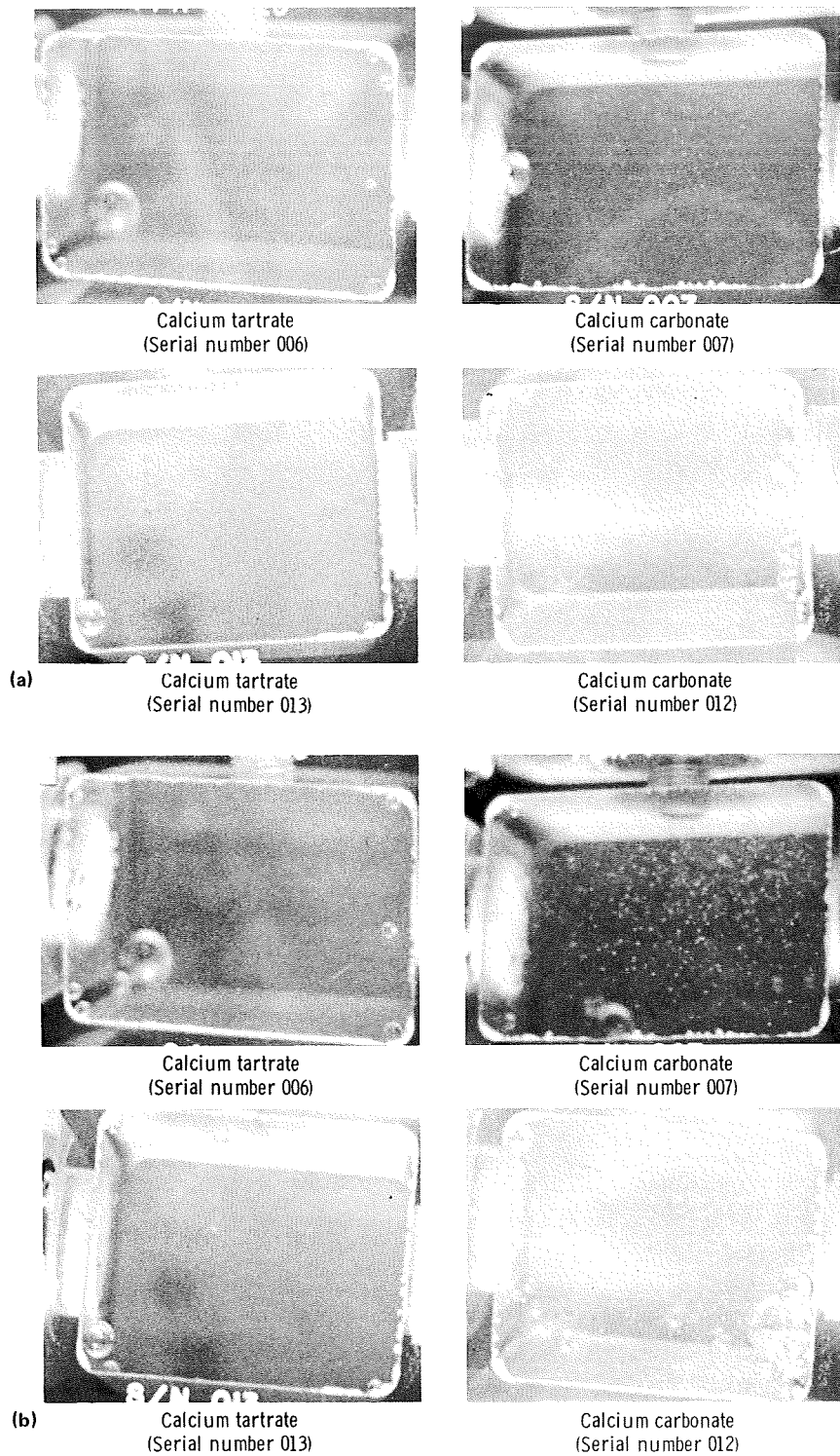


FIGURE 30-7.—Selected photographs of the calcium tartrate and calcium carbonate reactors taken during the flight. (a) 170 hours GET. (b) 218 hours GET.

mained stationary throughout the flight. Bubbles in the calcium carbonate and lead sulfide reactors were more mobile but remained stationary for as long as the 12-hour interval between photographs. The difference in mobility of bubbles in the various reactors is not understood; however, movement of the bubbles shows that accelerations experienced by the reactors during the flight were small.

During the flight, the cabin temperature varied more than had been anticipated and more than was desirable for crystal growth from solutions. The cabin temperature ranged between approximately 297 K (75° F) and approximately 289 K (60° F) during the flight. Solubilities of the reactants and crystalline products are strongly dependent on temperature, and the temperature variations were sufficient to markedly affect the results of this experiment. Such large temperature variations were not expected when the decision was made to neglect temperature control to simplify the experimental hardware.

The crystals grown during the flight are at least as good in size, quality, and number as those obtained by gel methods on Earth in the same length of time. Nucleation was excessive in all six reactors, which indicates the need for considerable refinement of the experimental parameters to suppress nucleation and improve crystal size and quality. Precise temperature control and longer growth times are probably the two main improvements to be made.

## SUMMARY

Results of the Apollo-Soyuz Crystal Growth Experiment successfully proved the feasibility of this novel method of crystal growth and indicate that the method, with further refinement, should yield superior crystals of a variety of materials. It still appears likely that conditions can be optimized to produce larger crystals than can be obtained with gels. High purity remains a major potential advantage of this method. Because of its simplicity, the method should also promote a better understanding of crystal growth theory.

## REFERENCES

- 30-1. Henisch, Heinz K.: *Crystal Growth in Gels*. Pennsylvania State Univ. Press, 1970.
- 30-2. Henisch, H. K.; Dennis, J.; and Hanoka, J. I.: *Crystal Growth in Gels*. *J. Phys. Chem. Solids*, vol. 26, no. 3, Mar. 1965, pp. 493-500.
- 30-3. Nickl, H. J.; and Henisch, H. K.: *Growth of Calcite Crystals in Gels*. *J. Electrochem. Soc.*, vol. 116, no. 9, 1969, pp. 1258-1260.
- 30-4. Barta, Cestmir; Zemlicka, Jan; and Rene, V.: *Growth of Calcium Carbonate and Calcium Sulfate Dihydrate Crystals in Gels*. *J. Cryst. Growth*, vol. 10, no. 2, 1971, pp. 158-162.
- 30-5. Blank, Zvi; and Brenner, Walter: *The Growth of Group II-VI Crystals in Gels*. *J. Cryst. Growth*, vol. 11, no. 3, 1971, pp. 255-259.
- 30-6. Blank, Zvi; and Brenner, Walter: *Research Directed Toward Preparation of Compound Semiconductors by Controlled Diffusion Mechanism in Gels*. AFCRL-70-0252, Air Force Cambridge Res. Labs., L. G. Hanscom Field, Mass., Mar. 1970.
- 30-7. Blank, Zvi; Brenner, Walter; and Okamoto, Yoshiyuki: *The Growth of Lead Sulfide in Silica Gels at Ambient Temperatures — Preliminary Characterization and Effect of Various Organic Compounds as Sulfide Ion Donors*. *Mater. Res. Bull.*, vol. 3, no. 7, 1968, pp. 555-561.
- 30-8. Swift, Ernest H.; and Butler, Eliot A.: *Precipitation of Sulfides From Homogeneous Solutions by Thioacetamide*. *Anal. Chem.*, vol. 28, no. 2, Feb. 1956, pp. 146-153.
- 30-9. Armington, Alton F.; DiPietro, Mary A.; and O'Connor, John J.: *A Study of Some Factors Which Influence the Growth of Cuprous Chloride in Silica Gel*. AFCRL-67-0445, *Phy. Sci. Res. Paper* no. 334, Air Force Cambridge Res. Labs., L. G. Hanscom Field, Mass., July 1967.
- 30-10. Armington, Alton F.; and O'Connor, John J.: *Some Factors Influencing the Growth of Crystals in Gel by the Complex Dilution Method*. *Mater. Res. Bull.*, vol. 3, no. 12, 1968, pp. 923-931.
- 30-11. Kirov, G. K.: *On the Diffusion Method for Growing Crystals*. *J. Cryst. Growth*, vol. 15, no. 2, 1972, pp. 102-106.
- 30-12. Torgesen, John L.; and Peiser, Herbert S.: *Method and Apparatus for Growing Single Crystals of Slightly Soluble Substances*. U.S. Patent 3,371,036, Feb. 27, 1968.



## Appendix A

# Recovery of Atmospheric Parameters From Radio Tracking Data of the Geodynamics Experiment

*P. E. Schmid<sup>a</sup> and S. Rangaswamy<sup>b</sup>*

### INTRODUCTION

The primary goal of the Apollo-Soyuz Test Project (ASTP) Geodynamics Experiment (MA-128) was Earth gravity-field analysis. However, selected segments of MA-128 Doppler tracking data, as measured by the Applications Technology Satellite 6 (ATS-6), are also being studied in terms of lower atmosphere (i.e., tropospheric) effects. Certain results from this atmospheric analysis that have potential widespread application in the field of meteorology are presented in this appendix.

The biasing effects of the troposphere and the ionosphere on radio tracking data have been a subject of continuing study by the NASA Goddard Space Flight Center (refs. A-1 to A-3). This work has led to the development of algorithms that, to the extent possible, remove atmospheric effects from radio and laser tracking data. This research has been part of an NASA effort to improve satellite orbit determination accuracy.

The earlier applied atmospheric research indicated that Doppler tracking of a near-Earth satellite by means of a geostationary satellite near the time of occultation should provide a very pronounced range-rate signature of approximately tens of meters per second. Such a signature is well above the noise level that was observed to be approximately 0.03 cm/sec (ref. A-4) during the experiment. Analysis also indicated that such occultation data would provide a new means of

deducing atmospheric pressure and temperature profiles on a worldwide basis. Such information would be invaluable to meteorologists involved in weather and climate research. The ASTP Geodynamics Experiment data provided the first opportunity to experimentally verify these concepts. The computational techniques and results associated with MA-128 occultation Doppler (range rate) analysis are presented in this appendix.

### COMPUTATIONAL APPROACH

The radio occultation method of measuring planetary atmospheric parameters has been used to study the atmospheres of Mars and Venus (refs. A-5 and A-6). The technique consists of measuring the integral phase change of the tracking signal due to refraction by the atmosphere. During near-Earth occultation, the neutral atmosphere, or troposphere, will introduce the major refractive perturbation. The troposphere can be considered to extend from sea level to a height of approximately 30 km. The corresponding index of refraction varies from approximately 1.000350 at sea level to 1.000004 at the 30-km level. In terms of refractivity  $N$ , this variation corresponds to  $4 < N < 350$ . The ionosphere, which extends from approximately 85 to 1000 km, introduces a refractive effect that is inversely proportional to frequency squared (ref. A-3). Although the ionosphere is not a critical factor for near-Earth occultation, it certainly must be considered during any signature analysis at the centimeter per second level. There are now indications that the

---

<sup>a</sup>NASA Goddard Space Flight Center.

<sup>b</sup>Old Dominion Systems, Inc., Gaithersburg, Maryland.

"Himalayan data anomaly" observed near the end of several MA-128 passes is at least partly due to the steep ionospheric gradients characteristic of this region.

Planetary analysis involved transmission of radio signals from a spacecraft to Earth as the spacecraft passed into the planetary atmosphere just before occultation. In an analogous manner, Earth atmospheric radio occultation can be observed by means of a high satellite, such as the "geostationary" ATS-6, observing a near-Earth satellite in a satellite-to-satellite tracking configuration (refs. A-7 to A-10). During portions of MA-128, this was the desired configuration that provided the first useful data set for evaluating this concept. The "geostationary" ATS-6 satellite is actually in a slightly inclined equatorial orbit. Hence, the Doppler effect between ATS-6 and a ground station is not zero but varies sinusoidally with a period of 24 hours and a peak amplitude of a few meters per second (ref. A-11). The composite Doppler data recorded in this experiment are a result of the two satellite motions (ATS-6 and Apollo) and the coherent two-way Doppler equipment configuration. For the Apollo occultation analysis, the following approximation (ref. A-9) has proved adequate.

$$f_d = (2.256 \times 10^9) \left( -\frac{2}{c} \right) \left[ \left( 1 + \frac{1.7000}{2.256} \right) \dot{r}_1 + \dot{r}_2 \right] \quad (\text{A1})$$

where  $f_d$  is Doppler shift, the ATS-6 to Apollo carrier frequency is 2.256 GHz,  $c$  is the speed of light, 1.7000 is an exact multiplier resulting from the electronics,  $\dot{r}_1$  is the average range rate from the Madrid station to ATS-6, and  $\dot{r}_2$  is the average range rate from Apollo to ATS-6. It should be noted that the "raw data" consist of a measure of accumulated carrier phase change rather than carrier frequency change (ref. A-12). The carrier signal that originated at the Madrid site was transmitted to ATS-6 at 6 GHz, coherently relayed to and from Apollo at a nominal 2 GHz, and returned to Madrid at 4 GHz. The received signal at Madrid was processed in real time by the carrier Doppler extractor, and the data were recorded on standard punched paper tape. In the two-way

2-GHz link between ATS-6 and Apollo, each time the separation changed by one-half wavelength ( $\approx 7.5$  cm), one cycle of Doppler phase was recorded. The path change between Madrid and ATS-6 also contributed to the overall Doppler phase measurement, although to a much lesser extent. That is, the Madrid to ATS-6 range rate was typically on the order of a few meters per second rather than the few kilometers per second associated with the ATS-6 to Apollo link. As shown by equation (A1), the Doppler frequency shift  $f_d$  is directly proportional to the average range rate. The data were recorded and time tagged as "non-destruct T-count" Doppler. In this mode, the accumulated phase change throughout a pass was recorded without clearing the counter while being read out at even time intervals. To obtain the desired resolution, the observed Doppler shift was electronically multiplied by a factor of 100 and offset with a fixed and stable 20-MHz bias signal. The net change in cycle count  $\Delta m$  over any time interval  $\Delta t$  is given by

$$\Delta m = \Delta t (f_b + 100f_d) \quad (\text{A2})$$

where  $f_b$  is a 20-MHz bias added to detect changes in range-rate sign and  $f_d$  is Doppler shift as defined in equation (A1).

As the near-Earth satellite (Apollo in this case) emerges from or enters radio shadow behind the Earth, the signal phase, and hence its time derivative or frequency, is abruptly affected by the presence of the atmosphere. The result is a large perturbation to  $f_d$  (eq. (A1)) of short duration (typically less than a minute). The computational approach was to determine accurately the orbits of ATS-6 and Apollo using all the available ground-tracking data obtained in support of ASTP. Then,  $\dot{r}_1$  and  $\dot{r}_2$  in equation (A1) were computed on the basis of this accurate ephemeris information. The computed data then were used to determine the expected behavior of the data as recorded at Madrid in the form of cycle counts (eq. (A2)). The sudden deviation from predicted behavior in the region of occultation was then attributed to the lower atmosphere. The mathematics for relating this Doppler change to an index of refraction profile of the troposphere (refs. A-13 and A-14)

had been determined before the Apollo launch as part of the Nimbus-6/ATS-6 Tracking and Data Relay Experiment (T&DRE). Although Nimbus-6 was launched on June 12, 1975, before the ASTP mission, the scheduled T&DRE checkout phase precluded occultation experiments until October 1975. Thus, the ATS-6/Apollo-Soyuz configuration provided the first opportunity to check out the foregoing concepts. The term refractivity  $N$ , as suggested previously, is simply a convenient means for representing the index of refraction  $n$ , where

$$n = 1 + N (10^{-6}) \quad (\text{A3})$$

Initially, a model of atmospheric refractivity profile is assumed that, for this particular study, was an exponential of the form

$$N(h) = N_0 \exp(-kh) \quad (\text{A4})$$

where  $N(h)$  is the refractivity at an altitude  $h$  above sea level,  $N_0$  is the refractivity at sea level, and  $k$  is the decay constant. Using some initial estimates of the parameters of this model, one-way range rate between ATS-6 and Apollo is computed for 30 data points at 1-second intervals up to the loss of signal. The computed range-rate values are compared with the observed values, which were derived from the four-way range sum rate by assuming symmetry between the upward and downward paths. The parameters of the model are then adjusted by iterative differential correction until least-squares convergence is reached. The estimated values of the parameters are used to compute the atmospheric refractivity profile.

The refractivity  $N$  of the atmosphere is a function of pressure, temperature, and humidity as given by

$$N = \frac{77.6}{T} \left( P + \frac{4810e}{T} \right) \quad (\text{A5})$$

where  $P$  and  $e$  are the atmospheric total pressure and water-vapor pressure, respectively, in millibars and  $T$  is the temperature in Kelvin (ref. A-15). By assuming a water-vapor profile and by

using the hydrostatic equation, it is possible to deduce values of pressure and temperature (ref. A-13). In this study, ASTP tracking data have been used to derive atmospheric refractivity as well as pressure and temperature profiles, which, for revolution 8, have been independently verified with radiosonde data. As indicated in table A-I, the Apollo-Soyuz tracking data base contains many passes for which the geometry was favorable for this type of occultation analysis. Revolution 8 was one of the first data sets that became available from the Geodynamics Experiment (MA-128) data base; therefore, data from this revolution were used for the initial analysis. However, subsequent data reductions indicate that revolution 8 is typical, and the same consistent results are being obtained from each revolution analyzed. Passes processed to date include revolutions 7, 8, 19, 20, 21, and 22.

Earlier simulations (ref. A-13) showed that the ionospheric effect on the Doppler rate was much smaller than the tropospheric effect and that the Chapman model was quite adequate for the inversion of occultation data. The critical frequency of 4 MHz was taken from vertical incidence data obtained from the meteorological station at Khabarovsk, U.S.S.R. (lat. 48.3° N, long. 135.1° E), which was the only ionosonde station in the general vicinity of the occultation site for which data were available.

## RESULTS

Figure A-1 shows the time variation of the atmospheric bias  $\Delta \dot{r}$  on the one-way range rate just before loss of signal between Apollo and ATS-6 during revolution 8. The range-rate atmospheric bias is defined as

$$\Delta \dot{r} = \overline{\dot{r}_2} - \dot{r}_2 \quad (\text{A6})$$

where  $\overline{\dot{r}_2}$  is the observed one-way range rate between Apollo and ATS-6 and  $\dot{r}_2$  is the true one-way range rate along the line of sight between the two spacecraft computed from the known orbits. The basic observation is the Doppler frequency indicated by equation (A1). The observed range

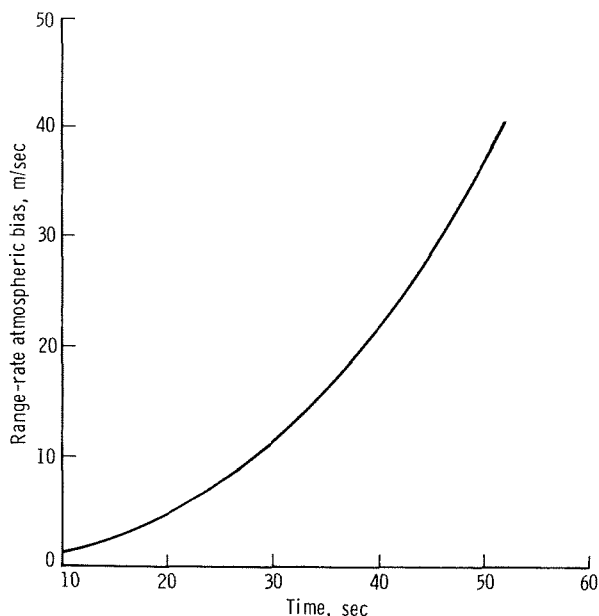


FIGURE A-1.—Time variation of atmospheric bias on the one-way range rate between Apollo and ATS-6. Data are from revolution 8, July 16, 1975, beginning at 07:48 UT. Loss of signal was at 53 seconds.

rate  $\bar{r}_2$  is obtained from equation (A1) by inserting the value of Doppler shift  $f_d$  obtained from the data (eq. (A2)) and by including the value of ATS-6 to Madrid site range rate  $r_1^*$ , as computed using ATS-6 orbit information. The data used in this study to date were obtained during Apollo revolutions 7 and 8 on July 16, 1975. However, a careful survey of the total Doppler tracking data set indicates a large number of "highly probable" occultation passes at both the 1/second and 1/10-seconds data rates. These revolutions are indicated in table A-I. To the extent possible, these data will be used for further verification of the inversion technique presented in this report. The orbits of Apollo, as well as ATS-6, were determined by orbit computation using ground-tracking data. During the ASTP mission, ATS-6 was tracked by stations at Madrid, Spain, and Ahmadabad, India. The ATS-6 satellite was also tracked using the trilateration technique (ref. A-11) with transponders at Madrid, Ascension Island, and Johannesburg, South Africa. The Apollo spacecraft was tracked by the NASA Spaceflight Tracking and Data Network. Occultation during revolution 8 oc-

curred at latitude 48.5° N, longitude 112.7° E. Radiosonde data from the meteorological station at Choybalsan, Mongolian Peoples Republic (lat. 48.0° N, long. 114.5° E) were used for comparison with revolution 8 results. Data for comparison with revolution 7 results have not yet been obtained. Table A-II gives the values of refractivity obtained from occultation data for revolution 8, as well as those derived from radiosonde data from the nearby meteorological station. In the case of

TABLE A-I.—Apollo Revolutions for Which Occultation Data Are Highly Probable

(a) For 1/second data rate

Revolution no.	Date	Stop time, UT, hr:min
6	July 16, 1975	04:38
7		06:15
8		07:49
17		21:54
19	July 17, 1975	00:59
20		02:35
21		04:12
22		05:49
23		07:23
82	July 21, 1975	04:33
83		06:07
84		07:40
85		09:12
87		12:22

(b) For 1/10-seconds data rate

Revolution no.	Date	Stop time, UT, hr:min
5	July 16, 1975	03:01
16		20:24
24	July 17, 1975	08:55
34	July 18, 1975	00:37
35		02:14
37		05:29
45		18:07
46	July 19, 1975	19:41
52		04:15
53		06:45
54		08:26
60		17:50
67	July 20, 1975	04:52
68		06:29
69		07:59
76		19:17
89	July 21, 1975	15:08
98	July 22, 1975	05:48

radiosonde data, the measured temperature, humidity, and pressure are sufficient to compute the reference refractivity profile. The radiosonde data were available only for 00:00 and 12:00 UT. Because the time of occultation was 07:49 UT, the radiosonde data corresponding to the occultation time were obtained by linear interpolation between the 00:00 and 12:00 UT data sets. Although this procedure may not have theoretical justification, the paucity of available data made it a practical necessity. It may be observed from table A-II that the difference between the two sets of refractivity at the 85 000-Pa (850 mbar) level is only 2.2 percent. It is conceivable that even better agreement between profiles would have been achieved had radiosonde data been available at the precise time of occultation. The two profiles provide the same value of refractivity at a height of approximately 6 km.

The occultation-derived refractivity profile was inverted to obtain the pressure profile by using an assumed average water-vapor profile. The technique used is presented in detail in reference A-13. After the pressure profile was obtained, the temperature profile was deduced from it by using equation (A5) and the radiosonde data for water-vapor pressure. The results, shown in table A-III, indicate that the agreement between the radiosonde- and occultation-derived pressure values at the 85 000-Pa (850 mbar) level is a difference of less than 1 percent, thus approaching the accuracy required for meteorological applications. A semilogarithmic plot comparing the two refractivity profiles is given in figure A-2. The Doppler-determined values of refractivity for Apollo revolution 7 occultation are presented in table A-IV.

*TABLE A-II.—Results From Apollo and ATS-6  
Atmospheric Parameters  
[Revolution 8, July 16, 1975]*

Altitude, km	Pressure, Pa (mbar)	Refractivity		Difference, percent
		Occultation derived	Radiosonde derived	
1.407	85 000 (850)	261.44	255.79	2.2
3.016	70 000 (700)	212.36	203.25	4.5
5.650	50 000 (500)	151.09	152.27	.8
7.280	40 000 (400)	122.39	128.75	-4.9
9.260	30 000 (300)	94.75	102.68	-7.7

*TABLE A-III.—Atmospheric Data From Apollo/ATS-6 Occultation Data  
[Revolution 8, July 16, 1975]*

Altitude, km	Pressure, Pa (mbar)		Difference, percent	Temperature, K		Difference, percent
	Radiosonde derived	Occultation derived		Radiosonde derived	Occultation derived	
1.407	85 000 (850)	85 230 (852.3)	0.3	289.6	279.6	3.5
3.016	70 000 (700)	70 600 (706.0)	.9	276.8	268.6	2.9
5.650	50 000 (500)	50 900 (509.0)	1.8	256.5	263.6	2.8
7.280	40 000 (400)	41 350 (413.5)	3.4	242.3	263.0	8.5
9.260	30 000 (300)	32 060 (320.6)	6.9	227.1	262.8	15.7

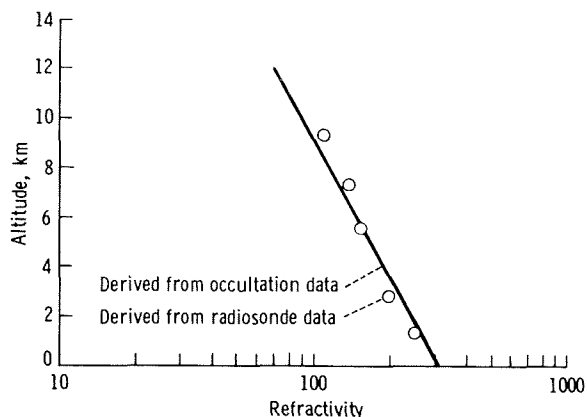


FIGURE A-2.—Refractivity profile from occultation data between Apollo and ATS-6. Data are from revolution 8, July 16, 1975, beginning at 07:48 UT.

TABLE A-IV.—*Doppler-Determined Atmospheric Refractivity Profile*  
[Revolution 7, July 16, 1975]

Altitude, km	Occultation-derived refractivity
1	281.8
2	250.3
3	222.2
4	197.4
5	175.3
6	155.6
7	138.2
8	122.7
9	109.0
10	96.8

## CONCLUSIONS

The analyses performed thus far clearly demonstrate the feasibility of using occultation between a near-Earth and a synchronous satellite to deduce atmospheric pressure and temperature profiles. The agreement of the occultation- and radiosonde-derived pressures and temperatures at

the 85 000- and 70 000-Pa (850 and 700 mbar) levels is quite good considering that the radiosonde-derived reference profile was not exactly coincident in time and location with the occultation-derived profile. Data from Apollo revolutions 19, 20, 21, and 22 have been processed for occultation analysis. The profile extracted from revolution 22 data is very similar to that obtained from revolution 7 data. This similarity is not surprising because the occultation site (i.e., geographical latitude and longitude where the radio path just grazes the Earth) was the same for these two particular revolutions.

The possibility of using radio occultation of signals between two Earth-orbiting satellites to measure meteorological parameters for purposes of weather forecasting was recognized at least as early as 1969 (ref. A-16). These earlier ideas were adapted and refined (refs. A-13 and A-14) for application to the particular case of a geostationary satellite tracking a near-Earth satellite. The MA-128 experiment provided the very first data base to verify these theoretical considerations.

In long-term (i.e., greater than 10 days) weather forecasting, an accurate worldwide initial state of the atmosphere in terms of pressure, temperature, and humidity is essential. At present, such information is obtained from a variety of sources. These sources include balloonborne radiosonde, satellite radiometry, surface observations, and so forth. All such sources require a substantial cost in deploying specialized equipment and in establishing the logistics for worldwide data collection, integration, and distribution. The importance of the occultation scheme, which was demonstrated in this experiment, is that no special instrumentation is required, and worldwide coverage is inherent in the tracking geometry. Therefore, with any near-Earth satellite (such as will be tracked by the forthcoming NASA geostationary Tracking and Data Relay Satellite System (TDRSS)), the tracking data required for operational orbit computation can also be used to extract atmospheric parameters. Such parameters could then be used as a primary input for long-term weather forecasting with no additional expense or complexity beyond that always incurred from routine central facility computer processing together with subsequent distribution to the user community.

## REFERENCES

- A-1. Marini, J. W.: Correction of Satellite Tracking Data for an Arbitrary Tropospheric Profile. *Radioscience*, vol. 7, Feb. 1972, pp. 223-231.
- A-2. Marini, J. W.: Tropospheric Range-Rate Tracking Data Correction. NASA TM X-66071, 1972.
- A-3. Schmid, P. E.; Bent, R. B.; et al.: NASA-GSFC Ionospheric Corrections to Satellite Tracking Data. NASA TM X-70608, 1973.
- A-4. Vonbun, F. O.; Kahn, W. D.; et al.: Geodynamics Experiment MA-128. Sec. 12 of Apollo-Soyuz Test Project Preliminary Science Report, NASA TM X-58173, 1976.
- A-5. Fjeldbo, G.; Kliore, A.; and Eshleman, V. R.: The Neutral Atmosphere of Venus as Studied With the Mariner V Radio Occultation Experiments. *Astron. J.*, vol. 76, 1971, pp. 123-140.
- A-6. Fjeldbo, G.; and Eshleman, V. R.: The Atmosphere of Mars Analyzed by Integral Inversion of the Mariner IV Occultation Data. *Planetary and Space Science*, vol. 16, 1968, pp. 1035-1059.
- A-7. Vonbun, F. O.; and Mengel, J. T.: Tracking and Communications for Planetary Manned Mission. *J. Spacecraft & Rockets*, vol. 5, no. 7, July 1968, pp. 863-865.
- A-8. Vonbun, F. O.: The ATS-F/Nimbus-E Tracking Experiment. Rotation of the Earth, Paul Melchior and Shigeru Yumi, eds., D. Reidel Publ. Co. (Dordrecht, Holland), 1972, pp. 112-120.
- A-9. Schmid, P. E.; and Vonbun, F. O.: The ATS-F/Nimbus-E Tracking and Orbit Determination Experiment. 1974 IEEE Intercon. Technical Program Papers, 1974, pp. 34/6-1 to 34/6-8.
- A-10. Schmid, P. E.; Trudell, B. J.; and Vonbun, F. O.: ATS-6 Satellite-to-Satellite Tracking and Data Relay Experiments. *IEEE Trans. Aerosp. and Electron. Sys.*, vol. AES-11, no. 6, Nov. 1975, pp. 1048-1058.
- A-11. Schmid, P. E.; and Lynn, J. J.: Results of the 3 November 1974 Applications Technology Satellite-6 (ATS-6) Trilateration Test. NASA TM X-70897, 1975.
- A-12. Bryan, J. W.; Lynn, J. J.; and Hinely, A. O.: A User's Guide for Satellite to Satellite System Observations and Data Formats. NASA TM X-70895, 1975.
- A-13. Murray, C. W., Jr.; and Rangaswamy, R.: Recovery of Atmospheric Refractivity Profiles From Simulated Satellite-to-Satellite Tracking Data. NASA TM X-71016, 1975.
- A-14. Rangaswamy, S.: Recovery of Atmospheric Parameters From the Apollo-Soyuz/ATS-F Radio Occultation Data. *AGU Geophysical Research Letters*, vol. 8, Aug. 1976, pp. 483-486.
- A-15. Bean, B. R.; and Dutton, E. J.: Radio Meteorology. National Bureau of Standards, Monograph 92, Mar. 1966, p. 7.
- A-16. Lusignan, Bruce; Modrell, Gary; et al.: Sensing the Earth's Atmosphere With Occultation Satellites. *Proceedings of IEEE*, vol. 57, no. 4, Apr. 1969, pp. 458-467.





## Appendix B

### Abbreviations and Acronyms

ac	alternating current	Con A	Concanavalin A
ACDR	Apollo commander	CPM	counts per minute
A-D	analog to digital	CSM	command and service module
AE	Atmosphere Explorer	CTA	cellulose triacetate
amu	atomic mass unit	D-A	digital to analog
ANS	Astronomical Netherlands Satellite	DAC	data acquisition camera
ANZUS	Australia-New Zealand-United States	dc	direct current
ASTP	Apollo-Soyuz Test Project	DIA	digital imaging analysis
at. %	atomic percent	D/L	diameter to length ratio
ATS	Applications Technology Satellite	DM	docking module
ATSR	Applications Technology Satellite ranging	DMA	Defense Mapping Agency
BMI	Battelle Memorial Institute	DMP	docking module pilot
BTB	bromthymol blue agar	DNA	deoxyribonucleic acid
CEM	channel electron multiplier	DTA	differential thermal analysis
CF	cryogenic freezer	ECE	electrical checkout equipment
CGE	Crystal Growth Experiment	ECS	environmental control system
CM	command module	EDAX	energy dispersive X-ray analysis
CMC	command module computer	EDTA	ethylenediaminetetraacetic acid
CMMY	corn-meal, malt-extract, yeast- extract agar	EM	electrophoresis engineering model
CMP	command module pilot	EMI	electromagnetic interference
CN	cellulose nitrate	EPE	Electrophoresis Experiment
COAS	crew optical alignment sight	EU	electrophoresis unit
Co-I	Co-Investigator	EUV	extreme ultraviolet
		FCS	fetal calf serum
		FOV	field of view

FWHM	full width, half maximum	MEM	minimum essential medium
GB	ground based	MJD	modified Julian day
GBT	ground-based test	MSFC	NASA George C. Marshall Space Flight Center
GEM	Goddard Earth Model	NML	Francis Bitter National Magnet Laboratory (at MIT)
GEOS	Geodetic Earth Orbiting Satellite	NOAA	National Oceanic and Atmospheric Administration
GET	ground elapsed time	NRL	Naval Research Laboratory
GRBS	Groupe de Recherches Biologique Spatiale	OGO	Orbiting Geophysical Observatory
HDC	Hasselblad data camera	OM	orbital module
HED	high-energy deposition	ORNL	Oak Ridge National Laboratories
HeG	helium glow	OSO	Orbiting Solar Observatory
HGCF	human granulocyte conditioning factor	PBS	phosphate-buffered saline
HGD	helium glow detector	PC	polycarbonate
HRC	Hasselblad reflex camera	PGS	preliminary Goddard solution
HVPS	high-voltage power supply	PHA	phytohemagglutinin
HZE	high-charge energy	PI	Principal Investigator
ICRP	International Commission for Radiation Protection	p/m	parts per million
IDAPS	image data processing system	PMN	polymorphonuclear leukocyte
IF	intermediate frequency	PT	prototype tested
IMMA	ion-microprobe mass analysis	PVA	polyvinylalcohol
IR	infrared	PWM	pokeweed mitrogen
ISM	interstellar medium	QT	quantum efficiency and transmission
JSC	NASA Lyndon B. Johnson Space Center	RBE	relative biological effectiveness
KSC	NASA John F. Kennedy Space Center	RCS	reaction control system
LaRC	NASA Langley Research Center	RE	rare earth
LBL	Lawrence Berkeley Laboratory	RF	radiofrequency
LED	light-emitting diode	rms	root mean square
LeRC	NASA Lewis Research Center	RPI	Rensselaer Polytechnic Institute
LET	linear energy transfer	SAA	South Atlantic Anomaly
LFE	Light Flash Experiment	SAB	Sabouraud's dextrose agar
lidar	laser radar		

SAM	stratospheric aerosol measurement	VCO	voltage-controlled oscillator
SAO	Smithsonian Astrophysical Observatory	VHF	very high frequency
SAS	Small Astronomy Satellite	VTR	video tape recorder
SCDR	Soyuz commander	WBC	white blood cell
SD	standard deviation	wt. %	weight percent
SEM	scanning electron microscope	XBT	expendable bathythermograph
SEM/EDAX	electron microscopy/energy dispersive X-ray analysis	Z	atomic number
SF	space flight	ZFF	zone-forming fungi
SFE	Soyuz flight engineer		
SI	stimulation index		
SM	service module		
SMC	Small Magellanic Cloud		
SRBC	sheep red blood cells		
SSP	subsolar point		
SST	supersonic transport or satellite-to-satellite tracking		
STDN	Spaceflight Tracking and Data Network		
T&DRE	Tracking and Data Relay Experiment		
TDRSS	Tracking and Data Relay Satellite System		
TE	thermoelectric module		
TLD	thermoluminescence dosimeter		
TSB	trypticase soy agar broth		
TV	thermal vacuum or television		
Tween	a surface activating agent		
UK	urokinase		
USB	unified S-band		
UT	universal time		
UV	ultraviolet		
UVA	ultraviolet absorption		



## Appendix C

### Units and Unit-Conversion Factors

In this appendix are the names, abbreviations, and definitions of International System (SI) units used in this report and the numerical factors for converting from conventional units to SI units.

#### Names and Symbols of SI Units

<i>Quantity</i>	<i>Name of unit</i>	<i>Symbol</i>	<i>Definition of symbol</i>
<i>SI Base Units</i>			
Length	meter	m	
Mass	kilogram	kg	
Time	second	sec	
Electric current	ampere	A	
Thermodynamic temperature	kelvin	K	
Luminous intensity	candela	cd	
Amount of substance	mole	mol	
<i>SI Derived Units</i>			
Area	square meter	m <sup>2</sup>	
Volume	cubic meter	m <sup>3</sup>	
Frequency	hertz	Hz	s <sup>-1</sup>
Mass density (density)	kilogram per cubic meter	kg/m <sup>3</sup>	
Speed, velocity	meter per second	m/sec	
Angular velocity	radian per second	rad/sec	
Acceleration	meter per second squared	m/sec <sup>2</sup>	
Angular acceleration	radian per second squared	rad/sec <sup>2</sup>	
Force	newton	N	kg • m/sec <sup>2</sup>
Pressure (mechanical stress)	pascal	Pa	N/m <sup>2</sup>
Kinematic viscosity	square meter per second	m <sup>2</sup> /sec	
Dynamic viscosity	newton-second per square meter	N • sec/m <sup>2</sup>	
Work, energy, quantity of heat	joule	J	N • m
Power	watt	W	J/sec
Quantity of electricity	coulomb	C	A • sec
Potential difference, electromotive force	volt	V	W/A
Electric field strength	volt per meter	V/m	
Electric resistance	ohm	Ω	V/A
Capacitance	farad	F	A • sec/V
Magnetic flux	weber	Wb	V • sec
Inductance	henry	H	V • sec/A
Magnetic flux density	tesla	T	Wb/m <sup>2</sup>
Magnetic field strength	ampere per meter	A/m	
Magnetomotive force	ampere	A	
Luminous flux	lumen	lm	cd • sr
Luminance	candela per square meter	cd/m <sup>2</sup>	

**Names of Symbols of SI Units (continued)**

<i>Quantity</i>	<i>Name of unit</i>	<i>Symbol</i>	<i>Definition of symbol</i>
<i>SI Derived Units (continued)</i>			
Illuminance	lux	$\text{lx}$	$\text{lm}/\text{m}^2$
Wave number	1 per meter	$\text{m}^{-1}$	
Entropy	joule per kelvin	J/K	
Specific heat capacity	joule per kilogram kelvin	$\text{J}/(\text{kg} \cdot \text{K})$	
Thermal conductivity	watt per meter kelvin	$\text{W}/(\text{m} \cdot \text{K})$	
Radiant intensity	watt per steradian	$\text{W}/\text{sr}$	
Activity (of a radioactive source)	1 per second	$\text{s}^{-1}$	
<i>SI Supplementary Units</i>			
Plane angle	radian	rad	
Solid angle	steradian	sr	

**Unit Prefixes**

<i>Prefix</i>	<i>Abbreviation</i>	<i>Factor by which unit is multiplied</i>
giga	G	$10^9$
mega	M	$10^6$
kilo	k	$10^3$
centi	c	$10^{-2}$
milli	m	$10^{-3}$
micro	$\mu$	$10^{-6}$
nano	n	$10^{-9}$
pico	p	$10^{-12}$

### Unit Conversion Factors

The following table expresses the definitions of units of measure used in the Apollo-Soyuz Test Project Summary Science Report as exact numerical multiples of coherent SI units and provides multiplying factors for converting to SI units. The first two digits of each numerical entry represent a power of 10. An asterisk follows each number which expresses an exact definition.

<i>To convert from —</i>	<i>To —</i>	<i>Multiply by —</i>
angstrom	meter	−10 1.00*
atmosphere	newton/meter <sup>2</sup>	+05 1.013 25*
Celsius (temperature)	kelvin	$t_K = t_C + 273.15$
foot	meter	−01 3.048*
gram	kilogram	−03 1.00*
inch	meter	−02 2.54*
pound mass (lbm avoir- dupois)	kilogram	−01 4.535 923 7*
torr (0° C)	newton/meter <sup>2</sup>	+02 1.333 22





## Appendix D

### Hardware Vendors

<i>Experiment</i>	<i>Equipment supplied</i>	<i>Vendor</i>
Microbial Exchange (AR-002)	Experiment hardware	General Electric Company Houston, Tex.
Stratospheric Aerosol Measurement (MA-007)	Experiment hardware	University of Wyoming Laramie, Wyo.
Multipurpose Electric Furnace (MA-010)	Experiment hardware	Westinghouse Astronuclear Pittsburgh, Pa.
Electrophoresis Technology (MA-011)	Experiment hardware	Teledyne Brown Engineering Huntsville, Ala.
	Thermoelectric assembly	Ohio Semitronics Columbus, Ohio
	Column assemblies	NASA George C. Marshall Space Flight Center Huntsville, Ala.
Electrophoresis (MA-014)	Experiment hardware	Messerschmitt-Bölkow-Blohm Ottobreuren, West Germany
Crystal Growth (MA-028)	Experiment hardware	Rockwell International Science Center Thousand Oaks, Calif.
	Camera equipment and accessories	NASA Lyndon B. Johnson Space Center Houston, Tex.
Soft X-Ray Observation (MA-048)	Experiment and ground-support equipment (GSE)	Ball Brothers Research Corporation Boulder, Colo.
	Data subsystem	New Mexico State University Las Cruces, N. Mex.

<i>Experiment</i>	<i>Equipment supplied</i>	<i>Vendor</i>
Ultraviolet Absorption (MA-059)	Experiment, optical system, and GSE	Johns Hopkins University Applied Physics Laboratory Laurel, Md.
	Retroreflector optics (built and tested)	Precision Lapping and Optical Company Valley Stream, N.Y.
	Ultraviolet (UV) light source (built)	Intraspace International Inc. Toronto, Ontario, Canada
	UV light assembly (design and assembly)	Lockheed Electronics Houston, Tex.
	Retroreflector mount, UV and incandescent light sources, and GSE	NASA Lyndon B. Johnson Space Center Houston, Tex.
Extreme Ultraviolet Survey (MA-083)	Experiment and GSE	Ball Brothers Research Corporation Boulder, Colo.
	Telescope	Applied Optics Center Burlington, Mass.
	UV filters	Luxel Corporation Santa Barbara, Calif.
Interstellar Helium Glow (MA-088)	Experiment and GSE	Ball Brothers Research Corporation Boulder, Colo.
	Helium pressure vessel	Supplied by NASA
	Helium system valves	Sterer Valves Engineering & Manufacturing Los Angeles, Calif.
	UV filters	Luxel Corporation Santa Barbara, Calif.
Doppler Tracking (MA-089)	Transmitter, receiver, and GSE	Raytheon Company Equipment Division Sudbury, Mass.
	Ultrastable oscillators for transmitters and receivers, crystal filters for transmitters	Frequency Electronics, Inc. New Hyde Park, N.Y.
	Transmitter battery development	Eagle Picher Joplin, Mo.
	Receiving antenna (design and development)	Ball Brothers Research Corporation Boulder, Colo.
	Data recording system	NASA Lyndon B. Johnson Space Center Houston, Tex.

<i>Experiment</i>	<i>Equipment supplied</i>	<i>Vendor</i>
Light Flash (MA-106)	Experiment hardware	Lawrence Livermore Laboratory University of California Berkeley, Calif.
Biostack (MA-107)	Experiment hardware	Messerschmitt-Bölkow-Blohm Ottobreuren, West Germany
Earth Observations and Photography (MA-136)	70-mm cameras, magazines, lenses, and accessories for photography	Victor Hasselblad, Aktiebolag Sweden
	20× binoculars for visual observations	Tasco Sales, Inc. Miami, Fla.
	Standard color chips for visual color comparisons	Munsell Color Company Macbeth Division Baltimore, Md.
	Zoom telescope for visual observations	Bushnell Optical Corporation Pasadena, Calif.
Crystal Activation (MA-151)	Variable intervalometer for sequencing photography; 16-mm camera equipment for complementary strip mapping	Perkin Elmer Corporation Aerospace Division Pomona, Calif.
	Experiment hardware	NASA Goddard Space Flight Center Greenbelt, Md.

National Aeronautics and  
Space Administration

Washington, D.C.  
20546

Official Business

Penalty for Private Use, \$300

SPECIAL FOURTH CLASS MAIL  
BOOK

Postage and Fees Paid  
National Aeronautics and  
Space Administration  
NASA-451



**NASA**

---

POSTMASTER:

If Undeliverable (Section 158  
Postal Manual) Do Not Return